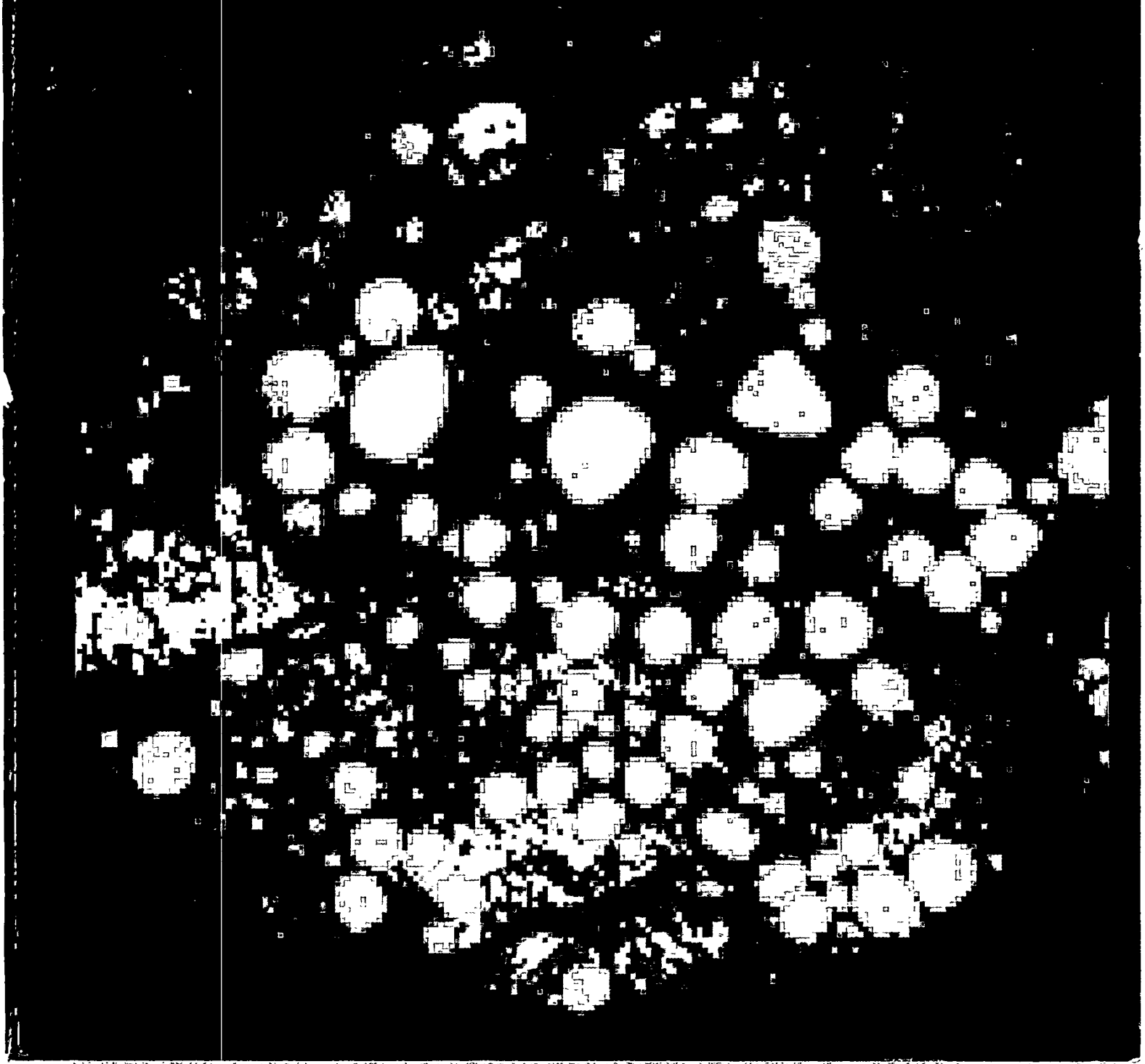
26
8-25-95
NS (2)

BNL

NATIONAL SYNCHROTRON LIGHT SOURCE

ACTIVITY REPORT 1994



BNL 52455
UC400
(General Energy Research)

Front cover, Beamline X1A: Quantitative calcium map of "tendonitis" human shoulder tendon section 0.1 micron thick. The calcium concentration has been mapped to show the distribution and density of the pathogenic mineral deposits in order to study the possible processes responsible for isolating the calcification in rounded islands. The map was made by combining a series of images formed at different energies on the Scanning Transmission X-ray Microscope (STXM) on beamline X1A. The peak brightness represents a calcium concentration of 5.5 micrograms per cm^2. (C.J. Buckley, King's College, London)

DISCLAIMER

This report was prepared as an account of work sponsored by an agency of the United States Government. Neither the United States Government nor any agency thereof, nor any of their employees, nor any of their contractors, subcontractors, or their employees, makes any warranty, express or implied, or assumes any legal liability or responsibility for the accuracy, completeness, or usefulness of any information, apparatus, product, or process disclosed, or represents that its use would not infringe privately owned rights. Reference herein to any specific commercial product, process, or service by trade name, trademark, manufacturer, or otherwise, does not necessarily constitute or imply its endorsement, recommendation, or favoring by the United States Government or any agency, contractor, or subcontractor thereof. The views and opinions of authors expressed herein do not necessarily state or reflect those of the United States Government or any agency, contractor, or subcontractor thereof.

Printed in the United States of America
Available from
National Technical Information Service
U.S. Department of Commerce
5285 Port Royal Road
Springfield, VA 22161

DISCLAIMER

Portions of this document may be illegible in electronic image products. Images are produced from the best available original document.

NATIONAL SYNCHROTRON LIGHT SOURCE

(For the period October 1, 1993 through September 30, 1994)

Editor:
E.Z. Rothman
Layout:
N.A. Wright

May 1995

The National Synchrotron Light Source Department
is supported by the
Office of Basic Energy Sciences
United States Department of Energy
Washington, D.C.

Brookhaven National Laboratory
Associated Universities, Inc.
Upton, New York 11973-5000

DISTRIBUTION OF THIS DOCUMENT IS UNLIMITED

Under Contract No. DE-AC02-76CH00016 with the
United States Department of Energy

MASTER

Introduction

Introduction by the Chairman 2
Denis McWhan
Environment, Safety and Health Update 4
William Thomlinson
User Administration Report 5
Eva Z. Rothman
Users' Executive Committee 6
Jean Jordan-Sweet

Scientific Disciplines

Atomic and Molecular Science 12
Mei-Ling Shek
Energy Dispersive Diffraction 15
Syed B. Qadri
Lithography, Microscopy, and Tomography 18
Gwyn P. Williams
Nuclear Physics 24
Craig E. Thorn
Time Resolved Spectroscopy 31
Jim Long and Jon Levin
UV Photoemission and Surface Science 37
Steve Hulbert and Chi-Chang Kao
X-Ray Absorption Spectroscopy 44
Lars Furenlid
X-Ray Emission Spectroscopy 51
Ken Miyano
X-Ray Scattering and Crystallography 53
Lonny Berman and D. Peter Siddons
X-Ray Topography 60
Michael Dudley

Meetings & Workshops

5th International Synchrotron Radiation Instrumentation Conference: SRI '94 68
Jerry B. Hastings
SRI '94 Workshops 71
Jean Jordan-Sweet
Applications of X-ray Standing Waves in Studies of Surfaces, Films, and Bulk Materials 71
David Heskett and Lonny Berman
X-ray Microbeam Techniques and Applications 72
Slade Cargill and Don Bilderback
Synchrotron Radiation at High Pressure 73
Donald J. Weidner
Technique and Experimental Method for X-ray Absorption Fine-structure Spectroscopy 74
Geraldine Lamble
Computed Microtomography: Techniques and Applications 75
Keith W. Jones and Per Spanne

Operations

VUV Machine 78
Stephen Kramer
VUV Storage Ring Parameters 82
VUV Beamlines 83
Roger Klaffky
X-Ray Machine 85
Norman Fewell
X-Ray Beamlines 87
Roger Klaffky
X-Ray Storage Ring Parameters 90
Injection System Upgrade 91
Eric Blum

Projects

The NSLS Source Development Laboratory (SDL): A Confluence of Opportunities 94
Ilan Ben-Zvi, Eric Blum, Erik D. Johnson, Sam Krinsky, James B. Murphy and Li-Hua Yu
The Accelerator Test Facility (ATF) 97
Ilan Ben-Zvi and Ken Batchelor
NSLS Facility Improvements 98
Bill Foyt

Organization

NSLS Advisory Committees 102
NSLS Staff 104
VUV Beamline Guide 107
X-Ray Beamline Guide 111

Abstracts & Publications

VUV Beamline Abstracts A-1
X-ray Beamline Abstracts B-1
NSLS User Publications C-1
NSLS Staff Publications D-1
BNL Formal and Informal Reports D-4



Beamline X1A: The chemical sensitivity of XANES microscopy used to investigate phase morphology of a sample of liquid crystalline polyester. The micrograph on the left, acquired at 285.0 eV, emphasizes the aromatic content and a discontinuous phase with domains smaller than 100 nm, as well as continuous phases with dimensions of a few microns. The figure at right, taken at 286.8 eV, reverses the contrast between the continuous phases, while there is virtually no contrast between the small features. This demonstrates the different chemical character of these domains. [H. Ade (NCSU), B. Wood and I. Plotzker (DuPont)]

ONE
INTRODUCTION

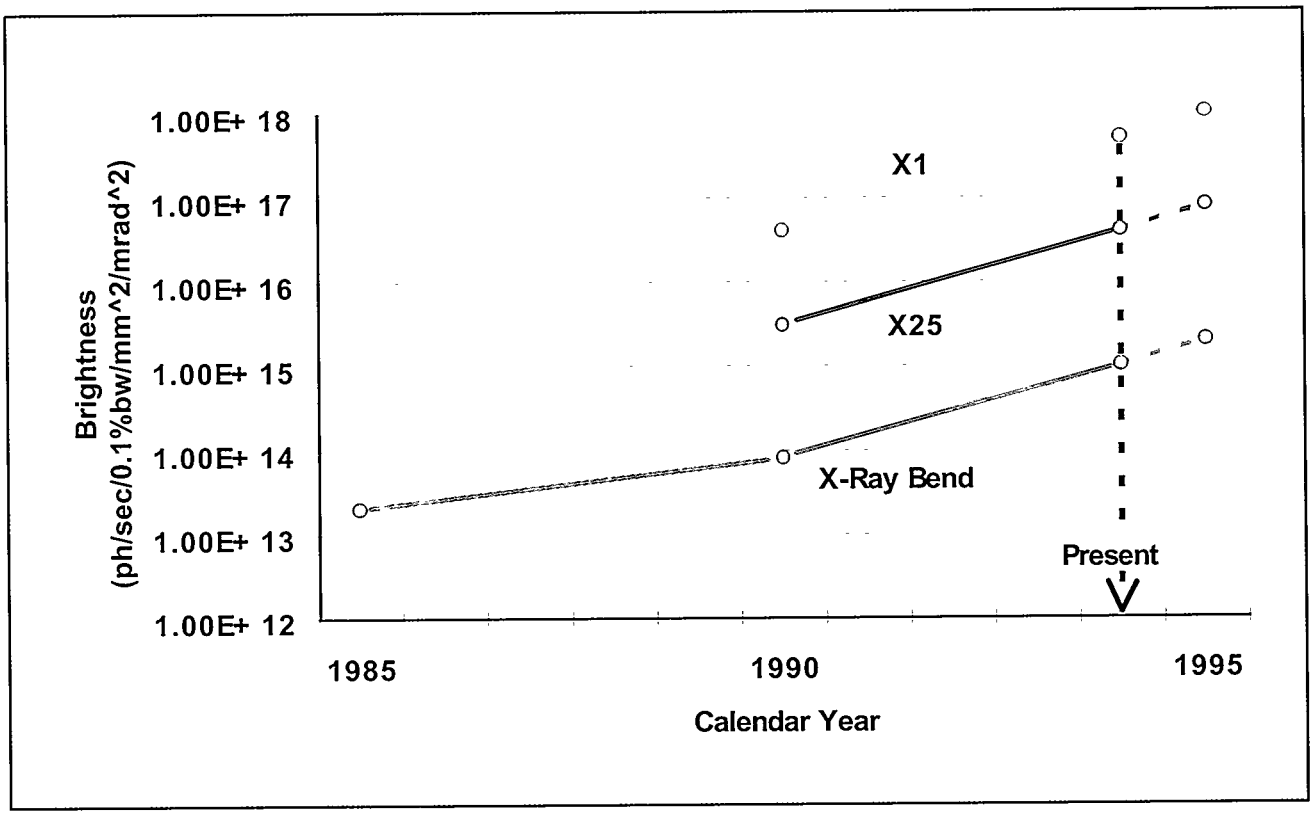


INTRODUCTION

Denis McWhan
NSLS Chairman

It has been another banner year for the NSLS with well over 5000 hours of user beam being supplied with much better than 95% reliability. The facility continues to evolve to meet the changing needs of the users, to provide beams with even higher brightness and to develop new types of insertion devices. The figure below shows how the brightness has evolved over time with increases in current, decreases in emittance and the commissioning of new undulators and wigglers. During the last decade the NSLS has moved toward the performance expected from the third-generation sources. FY 1994 saw the successful commissioning of the first small gap undulator to produce very bright beams in the hard x-ray region. The next new insertion device to be tested will be an elliptically polarized wiggler which can switch from right to left handed circularly polarized light at a frequency of up to 100 Hz. The EPW is a collaboration between the NSLS, the APS, and Novosibirsk. This year has also seen substantial upgrades in the injection system and improvements in the water system thereby decreasing the fill times and reducing long term drifts in beam position, respectively.

The NSLS continues to increase its user support systems. There is an NSLS Home Page on the World Wide Web which allows electronic submission of abstracts for the Activity Report. We hope to extend this capability to General User proposals and experimental Safety Approval Forms in the coming year. A new training film was produced, and GERT training is now transferable to other DOE Laboratories. The building expansion is nearing completion. It will increase the user space by an additional 12,400 square feet leading to each PRT having a set-up laboratory adjacent to their beamlines. The expansion will also provide a new control room and at least one new conference room on the experimental floor.



The PRT system is also evolving. The vast majority of the beamlines are operated by PRTs. The NSLS presently supports General User programs on 18 beamlines and has an additional five beamlines for instrument development and special user experiments. This support is provided by a staff of twelve scientists, three professional staff and five technicians. The user program is supported by an additional 13 people in areas such as User Administration, ES&H, training, building management and user shop and by an Operations Coordinator staff of nine. The beamline staff is clearly too small to fulfill its present commitments. At the same time it is evident that the scarcity of operational funding for the PRTs will require the NSLS and the PRTs to find creative ways in which to make the beamline operations more efficient. The NSLS plans to add an additional two scientists and five professional staff to meet its commitments. At the same time we are working with the PRTs to establish confederations of beamlines which specialize in areas such as x-ray absorption spectroscopy, x-ray powder diffraction and structural biology. This should allow overall cost reductions due to standardization and shared resources.

Finally, we have established an NSLS Source Development Laboratory to do frontier accelerator research leading to fourth-generation sources. The laboratory is housed in Building 729 across the street from the NSLS and a number of key components have been assembled: a 230 MeV electron linac, a 10 meter wiggler loaned to us by Boeing, and a 200 MeV compact storage ring. As funding becomes available we plan to perform key demonstration experiments on our unique free electron laser concept and to study short pulse operation in storage rings.



NSLS Management Group

(front, from left)
Bill Thomlinson, Associate Chairman;
Jerry Hastings, Beamline Support/R&D;
Sam Krinsky, Deputy Chairman;
Marty Woodle, Mechanical Engineering;
Bill Foyt, Assistant to the Chairman.

(back, from left)
Denis McWhan, Chairman;
John Keane, Electrical Systems;
Ilan Ben-Zvi, Accelerator Test Facility
Absent from photo:
Richard Heese, Operations

Environment, Safety and Health Update

William Thomlinson
Associate Chairman
NSLS

This has been the first full year with all ES&H activities reporting to the Associate Chairman and all indications are that it has worked very successfully. The coordination of our excellent resources has provided a solid base for meeting the challenges presented to us in the areas of beamline training, electrical safety, the new Radiation Protection Program and ALARA activities.

After a slow start, the Beam Line Operations and Safety Awareness program has really taken its place as part of our ES&H activities. This formal program in which all users get beamline specific training has proven very effective. To date, we have recorded 1598 individuals as being trained. The program is not yet perfect, but it continues to grow, hopefully reaching everyone who works at the NSLS experimental facilities.

BNL was faced with a serious problem when there was a fire at the experimental facility for the TRISTAN experiment at the High Flux Beam Reactor. Although the fire was contained by shielding, a very small amount of radiation was released to the HFBR experimental hall and environment. BNL established a review team, in parallel with activities of a DOE review team, which determined that one of the main contributing factors was inadequate review procedures for electrical safety of the facility. This lesson was carried back to the NSLS where two students were assigned the task of designing and testing an electrical safety program for the NSLS experimental floors. Many of our beamlines are now growing old and we must insure that they meet the highest levels of electrical safety. The end result of the program was the formulation of a safety review document which will be extended to all beamlines during 1995. Plans for that review are being formulated. The program was tested on four beamlines and the interaction between the NSLS personnel and beamline personnel proved that everyone at the NSLS is concerned about having the very highest standards for safety.

Radiation protection has become codified as a United States Federal Law, G-10 CFR 835/B1 - Rev. 0, Radiation Protection Program. Like all DOE facilities, BNL has responded and will be in full compliance by January 1, 1996. Working with the BNL committee, the NSLS determined that there are not many serious issues raised by the law (at least for the NSLS operations). This law contains mostly the same regulations already being complied with, or about to be complied with, under the present DOE Order 5480.11 and the DOE Radiological Control Manual.

There are two areas of interest to the NSLS user community. The first is the set of regulations concerning recording of total yearly radiation exposure for any individual before being allowed to access the facility. BNL and the NSLS are working to find ways to reduce the impact of that regulation on our issuing of film badges, and hence allowing access to the experimental floor. We do not, at this time, expect any serious problems.

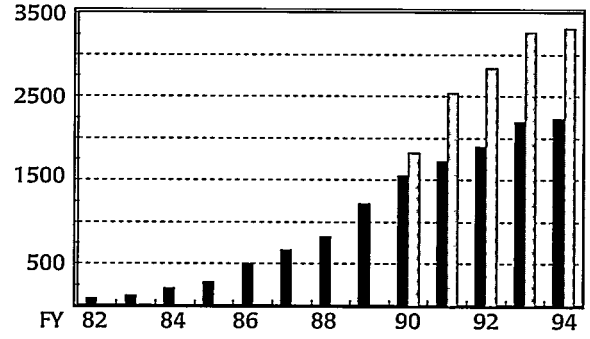
CFR 835 contains a major increase of the emphasis on ALARA (As Low As Reasonably Achievable) with respect to radiation exposure. The NSLS has operated with an ALARA program for many years, but in response we have already increased its formality. More important, our ALARA Committee is formulating a detailed program for the continuing reduction of levels from Booster and VUV Ring operations. Specifically targeted are levels in some of the offices which are presently controlled area. Proposals for new posting and new shielding have been drafted and will be implemented. Levels have already been dramatically reduced and the understanding of neutron vs. gamma doses is on firm footing. The program will now contain measurable goals, improved communication with the staff and users, and increased documentation.

Help is always available to users on ES&H issues. The Operations Coordinators are the front line of safety for the users. They are a skilled group whose mission is to insure safe and efficient use of the facility. Major problems will always be dealt with by our Safety Officer or by the Associate Chairman. It was a very good year, safe and busy. The facility, always safe, is even safer now!

User Administration Report

Eva Z. Rothman
User Administrator
NSLS

During FY 1994 the User Administrators and Directors of the NSLS, SSRL, ALS, and APS met to discuss topics of mutual concern. One item high on the agenda was the way in which statistics are tracked and presented, in particular those involving users. In an ever more competitive arena, it becomes important to identify to which facilities the users go, where the users are from, and the type of research they perform. Synchrotrons are obviously interested in this information to help them attract and keep users, but there are also various agencies in Washington, many of them with great influence over our funding, who request this data. The most visible item was the way in which all the synchrotrons count users - we all agreed that a user is a person who physically comes to the facility for the purpose of carrying out an experiment on beamline. This definition is meant to exclude casual visitors, consultants, contractors, and co-authors or collaborators associated with an experiment but not actually coming to the facility.



Comparison of the old and new methods of counting users. The black bars show actual numbers of users at the NSLS, while the grey show the more recent, and now obsolete, method of counting all registered users.

In accordance with this new definition, both the SSRL and the NSLS have begun counting users in a new way. The NSLS had been counting all laboratory guest appointments that were active during any part of the fiscal year, resulting in counts much higher than the actual number of visitors. The revised statistics, presented in Figure 1, are a more accurate representation of the number of experimenters coming to use the facility within a specified period of time and will be used from now on.

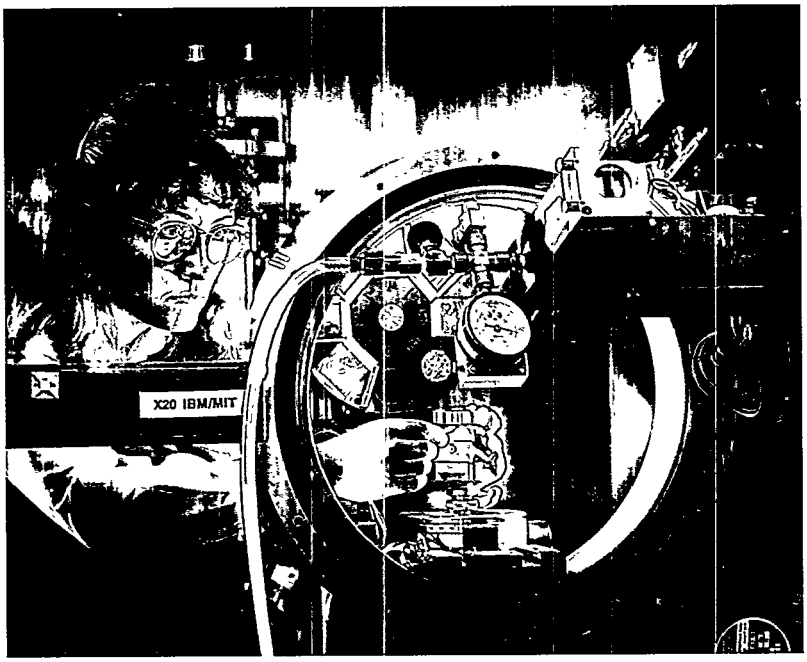
The NSLS has produced a new safety orientation video, which, like its predecessor, must be shown to every user before they can be granted access to the experimental floor. With a tightening of the rules, the radiation portion of the video had to be expanded and the user must now pass a 15-question quiz before they are considered trained. NSLS Training Coordinator Denny Klein worked closely with BNL's S&EP Division to make the GERT (General Employee Radiation Training) portion completely "RadCon compliant", meaning it meets the DOE specifications for the level of training required for receiving a film badge. The SSRL, ALS, and APS are doing the same, and agreed that the GERT training should therefore be transferable among our sites. What does this mean to a user? The user must still take the site-specific training, as required by each facility. If the user can produce a card which shows they have had GERT (RadCon compliant) training at another DOE facility within the past 21 months, they are exempt from the GERT training and the quiz. This is another example of cooperation between facilities that results in benefits to both the facilities and the users.

FY 1994 also brought changes to the NSLS lobby. The receptionist position was dissolved and Nancye Wright was transferred to the User Administration Office. Nancye has taken over the layout of the Activity Report, using the templates and procedures developed for the 1993 Activity Report by graphic designer Keelin Murphy. Besides becoming a key player in the NSLS publication production, Nancye has proven invaluable in keeping training and registration running smoothly in the User Administration Office.

Users' Executive Committee

Jean Jordan-Sweet
IBM
UEC Chair

The Users' Executive Committee serves as a two-way communications channel between the NSLS administration and the user population. It is an advocate of both PRTs and General Users, and works to make our lives at the NSLS as productive, comfortable, and well-informed as possible. The year 1994 has been tough for all of us in several ways, and the UEC has been in the process of re-evaluating its role in this changing environment. The decrease in funding and staffing for PRT home institutions and for the NSLS has damaged research programs and morale. The UEC has a duty to become a "watchdog" for the user community to make sure that services and support for users, as well as reliable and stable ring operations, are not unduly affected by tight budgets and "cost recovery" programs. The Committee also finds itself becoming more polticized. It must use its voice as representative of the most productive synchrotron users group in the nation to convince DOE and Congress of the great value in providing synchrotron facilities with reasonable operating and capital-improvement budgets.



UEC Chair Jean Jordan-Sweet

In October the elected members of the UEC compiled and submitted a detailed response to a questionnaire sent by DOE to "identify potential areas in which expanding facility operations could produce tangible benefits...and examine facility user needs." In parallel, each SPIG representative was invited to submit a response tailored to the needs of the group he or she represents. Anyone wishing to see a copy of the UEC response is welcome to contact me. We now have an essentially new Congress and state government to educate, and aren't even sure where the DOE will be a year from now! On the home front, we will also be getting a new NSLS Chairman in 1995, as Denis McWhan steps up to become the BNL Associate Director for BES Programs. The UEC would like to congratulate Denis, and thank him for his hard work during his tenure as NSLS Chairman.

The UEC met three times in 1994, with each meeting being preceded by a Town Meeting of NSLS staff and users. The NSLS is really stepping into the information age! The User Administration office is very streamlined, with on-line registration, database, and directory; and is now soliciting electronic submission of experimental abstracts via Mosaic and World Wide Web. There are plans to make the 1994 Activity Report available on WWW and CD ROM. In the near future, all NSLS forms will be handled electronically. I predict that within the

next year most beamlines will have a Mosaic "home page", containing information on PRT members, beamline characteristics, schedules of experiments, and even research highlights. Because of this tremendous growth in computer communications, network traffic and computer security have become important issues. The UEC has formed a subcommittee, headed by Peter Siddons, to assess the needs of the NSLS user community for high-speed data transfer lines, to study the range of possible methods and products for computer security, and to make recommendations to the NSLS and users.

Another project that has been in the works for about a year, was first approved for funding in 1991, and will be ready for use in early 1995 is the X1-X11 floor expansion. This not only will provide new space for biology labs, a control room, and some NSLS staff, but will have a positive impact on ALL users. There will now be enough room on the experimental floor for every beamline to have its own lockable lab/setup space. The Space Committee, headed by Steve Ehrlich, has made recommendations to Denis for space assignments, including an expanded lounge area off of the X-Ray Ring.



Users' Executive Committee

(seated around table, clockwise)
Geraldine Lamble (NSLS/NCSU), Peter Siddons (NSLS), Michael Dudley (SUNY - Stony Brook), Paul Lyman (Northwestern U.), David Johnson (Old Dominion U.), Johnny Kirkland (NRL), Craig Thorn (BNL-Physics), and Jean Jordan-Sweet (IBM),

(back, from left to right, standing)
Sue Wirick (SUNY - Stony Brook), Boris Sinkovic (New York U.), David Hanson (SUNY - Stony Brook), Robert Sweet (BNL-Biology), Kevin Smith (Boston U.) and Paul Zschack (ORNL).
Absent from photo are Dan Fischer (NIST), Stephan Ginell (ANL), Syed Qadri (NRL), Eva Rothman (NSLS), and Ke Zhang (U. City Science Center).

VUV and X-Ray Ring operations have been extremely reliable in 1994. In 1995 we should expect to see the start of two new operations modes in the X-Ray Ring. Some beamlines already have had radiation surveys done and are approved to run in "high current" mode, with fills up to 438 mA at 2.584 GeV. More shielding work will be needed to operate in "high energy" mode, where the shift up to 2.8 GeV (at 250 mA) produces more penetrating radiation. The NSLS Beamline Safety Committee is currently developing procedures for making sure beamlines are safe to operate at this energy. Another NSLS committee, under the guidance of Lonny Berman and Steve Hulbert, is completing calculations to identify any heat load problems on various ring, ID, and BM components. A UEC Subcommittee on X-Ray Operations, headed by Lars Furenlid, has polled each beamline and come up with a consensus on how to schedule the two types of operations. It has recommended that two trimesters per year should be used for high current operations, and the third for high energy. Another recommendation,

which wasput into effect immediately, is to have scheduled X-Ray fills.

The Scientific Program Support Committee (SPSC) continued to be led this year by Gwyn Williams and Mike Sagurton. They have been working efficiently and independently to assess and improve the success of General User experiments. In parallel with this, the NSLS R&D staff has implemented a program to provide a scientific contact for each General User group that visits the NSLS. The SPSC has also finally seen some action in the years-long effort to get the experimental floor noise problem sorted out. Sound-absorbing boards (disguised as beamline poster boards...) have been installed around the two rings and soft baffles have been hung up over the VUV floor. If the baffles are successful, they will also be installed over the X-Ray floor. Individual beamlines are still encouraged to solve noise problems in their immediate vicinities due to loud rack-mounted equipment, pumps, etc.

The UEC has had very positive interactions with Staff Services over the last several years. Improvements are continually being made in the area of housing, including the setup of a fully automated reservation system, updating of dorms and apartments, and the formation of a Dormitory Residence Council. The Housing Office made a special effort this year to locate off-site housing for visitors during the overcrowded summer season. Berkner Hall also is being brought into the information age. At our next Users' Meeting on May 8-10, 1995, we can expect to find 10 terminals available for logging into home institutions and sending e-mail. A business center has also been set up with a copy machine, FAX, etc. for conference use.

Because of the impact of SRI'94 on NSLS staff resources and experimenters' travel budgets, we did not host an NSLS Users' Meeting in 1994. The UEC instead organized and ran five workshops on Sunday, July 17, in conjunction with SRI'94. The UEC also paid for invited speakers' travel to each workshop. These workshops were highly successful and had a total attendance of over 220. I wish to thank all of the workshop organizers for their hard work and interesting programs. They were: S. Cargill and D. Bilderback for "X-ray Microbeam Techniques and Applications", D. Heskett and L. Berman for "Applications of X-ray Standing Waves in Studies of Surfaces, Films, and Bulk Materials", G. Lamble for "Technique and Experimental Method for XAFS", K. Jones and P. Spanne for "Computed Microtomography: Techniques and Applications", and D. Weidner for "Synchrotron Radiation at High Pressure." You can read more about these workshops under the "Meetings and Workshops" section of this Activity Report.

Beamline X25: Visualization of the RNA polymerase II transcription machinery, responsible for messenger RNA production in all eukaryotes. The central orange crescent represents the TATA box-binding protein recognizing its DNA target in the promoter or transcription control region of the gene. (Acrylic painting by Irving Geis in collaboration with S.K. Burley, Howard Hughes Medical Institute, Rockefeller University. Acrylic painting copyright by Irving Geis, reproduced by permission.)

TWO SCIENTIFIC DISCIPLINES



ATOMIC AND MOLECULAR SCIENCE

Mei-Ling Shek
NSLS

I. VALENCE ELECTRONIC EXCITATION

The gas phase research on beamline U11 has focussed on the discharge flow-photoionization mass spectrometry of the radicals FO,FCO and NO_3. From the threshold of the photoion efficiency spectrum of NO_3 generated by the reaction $F+HNO_3$, as shown in **Figure 1**, the adiabatic ionization energy for the transition $NO_3(^2A_2')$ -> $NO_3^+(^1A_1')$ is determined for the first time. Moreover, the steep rise at the threshold suggests that the ground state and the cation have the same symmetry, which has been theoretically shown to be D_{3h} for the cation.

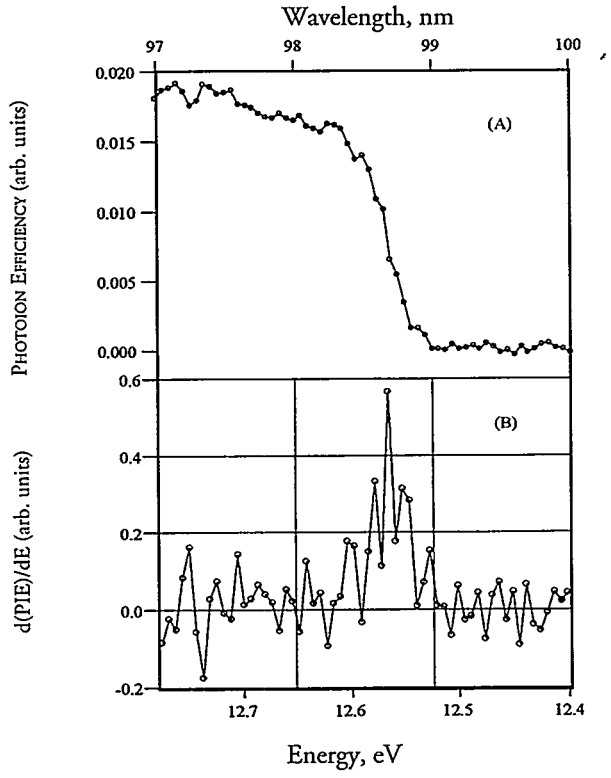


Figure 1 U11: (A) Threshold region of the photoion efficiency spectrum of NO_3. (B) Energy derivative of the spectrum in A, the maximum of which yields the adiabatic ionization energy. A value of 12.57± 0.03 eV is obtained from eight independent threshold measurments. U11 data from P.S. Monks and L.J. Steif (NASA MD), M. Krause (NIST), S.C. Kuo, Z. Zhang and R.B. Klemm (BNL-DAS).

II. INNER-SHELL PHOTOIONIZATION

A new zero kinetic energy (zeke) electron detector based on transverse velocity discrimination has been developed, and used on beamline U13UA for core level excitation studies of Ar, N_2, O_2 and N_2O. By the coincidence detection of Auger and zero-energy photoelectrons, chemical-site-selective molecular Auger electron spectra have been obtained for the first time, as shown in **Figure 2** for N_2O. The terminal N K edge is at 408.5 eV, and the central N K edge is at 412.5 eV. For the terminal nitrogen, comparison between the ordinary and true coincidence Auger spectra suggests that the signal above 373 eV in the ordinary Auger spectrum originates from excitation to Rydberg states instead of N 1s ionization. For the central nitrogen, the true coincidence Auger electron spectrum is free from the contribution from the terminal nitrogen, unlike the ordinary Auger spectrum.

On beamline X1B, energy-dependent high-resolution core level photoelectron spectroscopy has revealed the effects of shape resonances on the coupling between electronic and vibrational excitations. As shown in **Figure 3**, the C 1s photoelectron spectrum of C_2H_4 near the shape resonance has a vibrational fine structure different from that at a higher photon energy. With the use of line shapes accounting for the post-collision interaction between the photoelectrons and Auger electrons, the deduced frequencies of the totally symmetric C-H and C=C

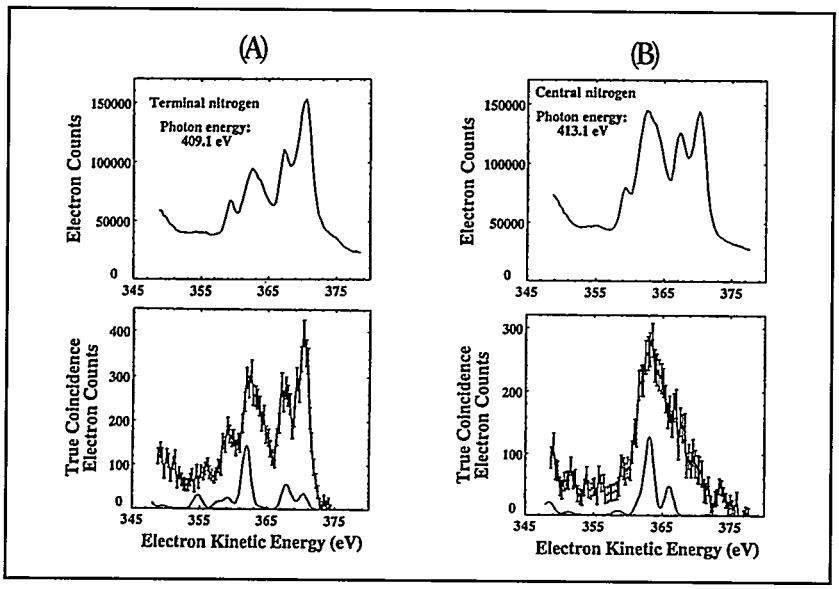


Figure 2 U13UA: (A) Upper panel: Ordinary Auger electron spectrum with photon excitation at the terminal N zeke electron peak in N_2O (409.1 eV). Lower panel: True coincidence Auger spectrum due to terminal N 1s ionization (with error bars) and a simulated theoretical spectrum (lower curve). (B) Upper panel: Ordinary Auger spectrum with photon excitation at the central N zeke electron peak in N_2O (413.1 eV). Lower panel: True coincidence Auger spectrum due to central N 1s ionization (with error bars) and a simulated theoretical spectrum (lower curve). U13UA data from K. Lee (SRRC, SUNY at Stony Brook), S.L. Hulbert (NSLS), P. Kuiper (BNL), D. Ji and D.M. Hanson (SUNY at Stony Brook).

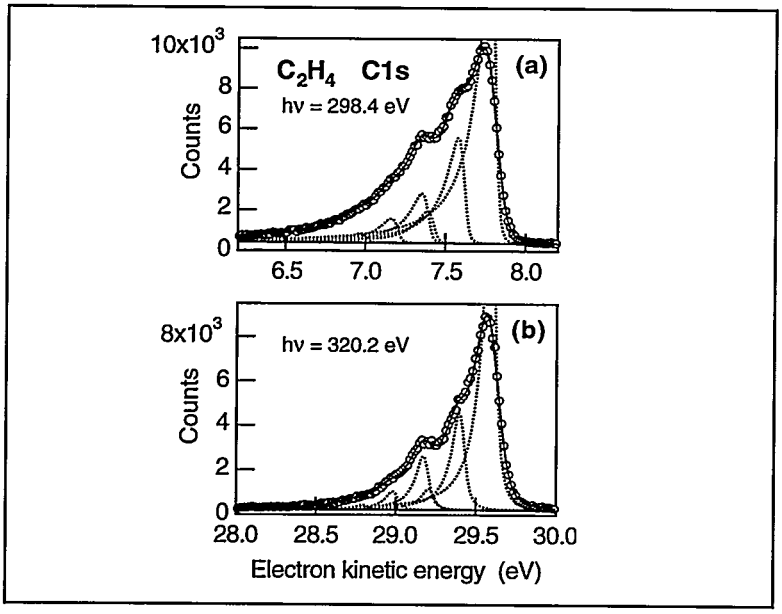


Figure 3 X1B: The C 1s photoelectron specturm of C_2H_4 measured on the shape resonance (a) and at a higher photon energy (b). The open circles are data points. The full line is the result of a least squares fit convoluting post-collision interaction lineshapes (dashed lines) with instrumental resolution. A preliminary analysis gives 415 meV and 190 meV for the totally symmetric C-H and C=C stretching modes, respectively; and a lifetime broadening of 90±10 meV. X1B data from H.M. Koppe, M. Schmidbauer, B.S. Itchkawitz, A.L.D. Kilcoyne, J. Heldhaus and A.M. Bradshaw (Fritz-Haber-Institute, Berlin).

stretching modes suggest a strengthening of the C-H bond and a weakening of the C=C bond in the molecular ion.

On beamline X1B, absolute inner-shell photoabsorption cross-section measurements have also been made on simple molecules containing C, N, O and F, with the use of a high order light suppressor consisting of two plane mirrors at grazing incidence.

On beamline X24A, the development of coincident detection of photoelectrons or Auger electrons with fluorescent x-rays will allow a delineation of complicated core hole de-excitation processes. As a demonstration of the technique, the Ar 1s photoelectron spectrum has been recorded in coincidence with K α and K β x-ray fluorescence. As seen in **Figure 4**, the selected photoelectron spectrum is free from the asymmetric broadening and energy shift characteristic of photoelectrons affectd by post-collision interaction with KLL Auger electrons.

On beamline X24A, the yield of Ar and K ions of different charge states, near their repective K edges, have been studied with time-of-flight measurements in the single-bunch operation mode. Other work includes the photoabsorption spectra of alkali atoms and their spectral identifications by comparison with calculations and with rare gas absorption spectra. The attenuation of photons by He has been accurately measured in the energy range 3 - 5.5 KeV, and is in good agreement with the combined calculated cross-sections for Compton scattering and photoionization. This further verifies the dominance of Compton scattering at high photon energies in recent measure-

ments of the ratio of doubly to singly charged He ions induced by x-rays (see 1993 NSLS Activity Report).

III. APPLIED SCIENCE

On beamline X6B, a total-electron-yield detector has been constructed and used for *in situ* S K edge absorption measurements of both dry and humid atmosphere containing SO_2. An experimental resolution of ~0.5 eV is attained at the S K edge. The x-ray absorption near-edge data in Figure 5 indicate that neither the structural C_{2v} symmetry nor the +4 oxidation state of SO_2 changes with the introduction of gaseous H_2O at room temperature.

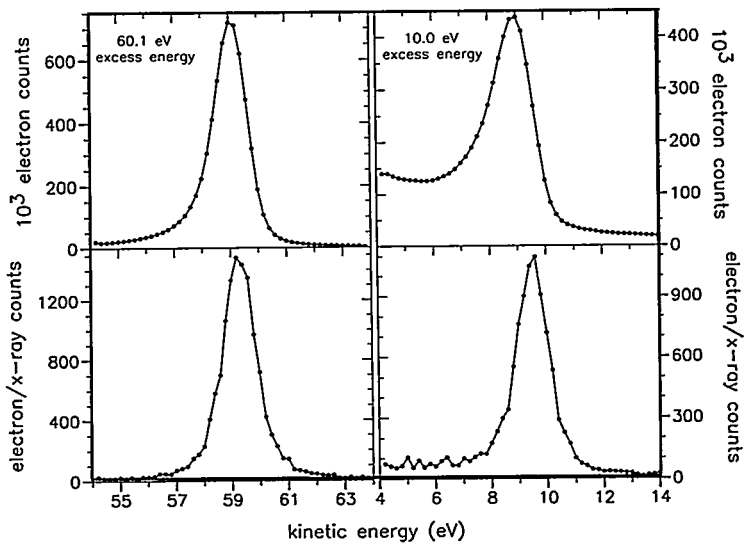


Figure 4 X24A: Ar 1s photoelectron spectra (upper panels) and coincidence spectra between Ar 1s photoelectrons and unresolved Kα and Kβ x-ray fluorescence (lower panels). Results are shown for excitation photon energies 10.0 and 60.1 eV in excess of the threshold (3206.3eV). X24A data: S.H. Southworth and U. Arp (NIST), T. LeBrun (ANL), M.A. MacDonald (Daresbury) and R.D. Deslattes (NIST).

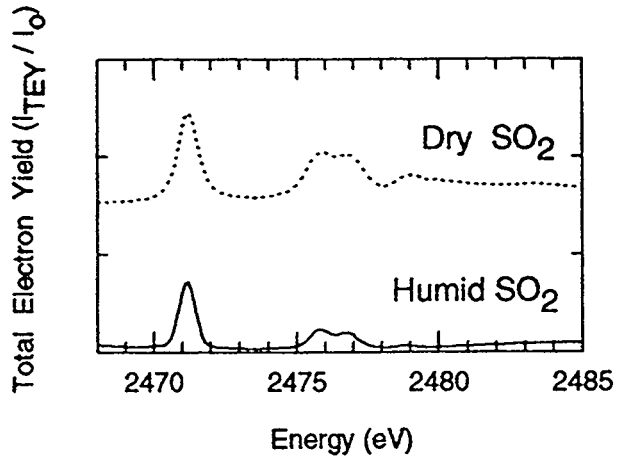


Figure 5 X6B: Similarity of the S K absorption near-edge structure of SO_2 in the absence and in the presence of H_2O (88% relative humidity). X6B data: I. Song, B.I. Rickett, P. Janavicius and J.H. Payer (Case Western Reserve U.) and M.R. Antonio (ANL).

Energy Dispersive Diffraction

Syed B. Qadri
Naval Research Laboratory

In energy dispersive x-ray diffraction (EDXD), the angular variable is replaced by energy variable keeping the angle of the detector fixed. Thus EDXD uses most of the broad energy spectrum of the synchrotron radiation especially the high energy photon (>20 keV). Energy-dispersive techniques have distinct advantage over the angular dispersive x-ray diffraction when there are special constraints such as the sample size and limited exit angle for the diffracted beam as in the case of diamond anvil cells and the presence of other special attachments such as high/low temperature rigs, magnets and electro-chemical cells. The high magnetic field of the superconducting wiggler (4.6-4.7 Tesla) of beamline X17C produces synchrotron radiation with high critical energy (E_c=20 keV), resulting in several orders of higher flux (to 100 keV) over a beamline with a bending magnet. Thus X17C is optimal for ultra high pressure diamond anvil cell experiments and other experiments requiring the greater penetration power of high energy x-rays.

With the advanced evolution of diamond-anvil cell technology, static pressures of several hundred gigapascals (GPa) are generated routinely. Using EDXD techniques, physical properties of materials such as crystal structures, equations of state, and structural phase transitions at extreme pressures have been characterized accurately. Thus the pressure variable has become as significant as the variables temperature and chemical composition in exploring new materials with novel physical and chemical properties. In this brief article, highlights of the most recent work performed using EDXD technique are described.

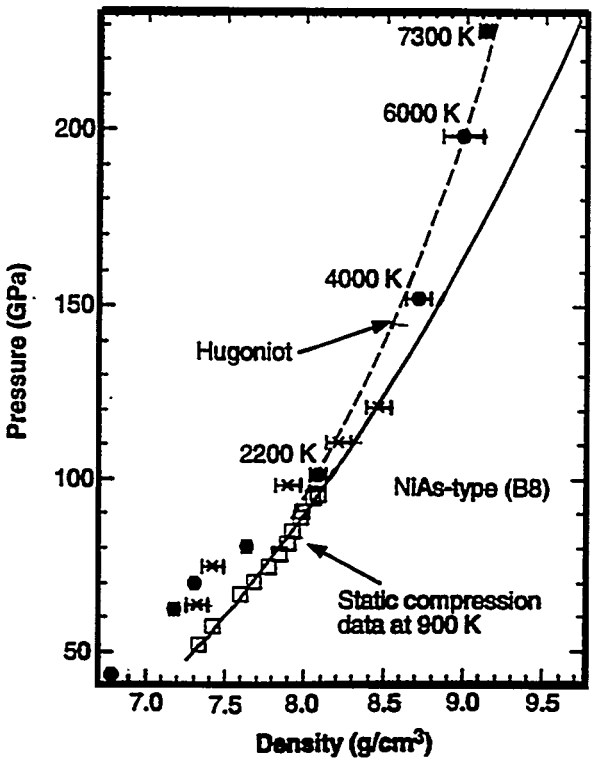


Figure 1 X17C: Densities of the high-pressure NiAs phase of FeO as a function of pressure at 900K compared with the shock compression data. [Y. Fei and H. K. Mao, *Science* **266**, 1678, (1994)].

Fei and Mao from Carnegie Institution of Washington (CIW) performed *in situ* synchrotron x-ray diffraction measurements of FeO at high pressures and temperatures and found the high pressure phase of FeO to be the NiAs structure at a pressure of 96 GPa and 800K. Figure 1 shows the densities of the high pressure NiAs phase of FeO as a function of pressure at 900 K and compares with the shock compression data. FeO is the basic oxide component in the interior of the earth and its behavior at high pressure and high temperature plays an important role in mantle composition and core formation model. FeO is the only monoxide that has been found to have covalent metallic bond formation in the NiAs structure at high pressure and temperature in contrast to other monoxides such as CaO, SrO and BaO which transform from NaCl (B1) to CsCl (B2) at high pressure. This finding opens the possibility of incorporating both oxygen and sulfur in the earth's core [see Y. Fei and H. K. Mao, *Science* 266, 1678, (1994)].

The equation of state and phase stability are the most fundamental properties in understanding the physics of materials at ultra high pressures. However, the reliability of

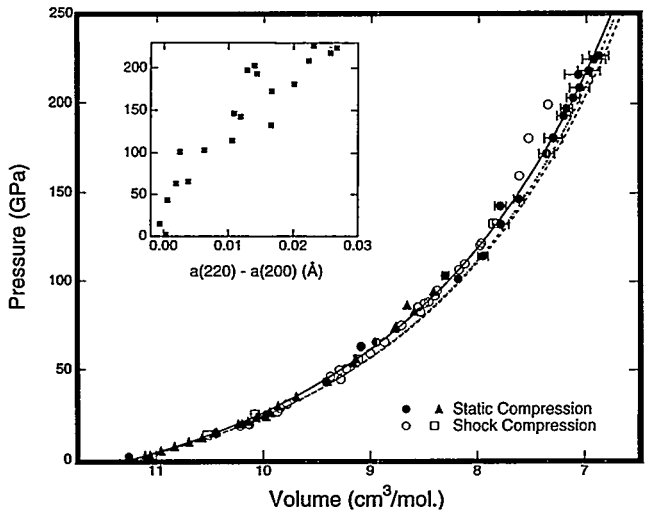


Figure 2 X17C:: Pressure-volume data for MgO. The filled symbols are static compression data and the open symbols are from shock compression. The solid line is a third order Birch-Murnaghan fit to the present data. The inset shows pressure versus the difference in the lattice parameters determined from the (220) and (200) diffraction peaks. [T. S. Duffy, R. H. Hemley, and H. K. Mao, accepted for publication in *Phys. Rev. Lett.*, (1995)].

equation of state at large compression becomes uncertain because of the stress state at multimegabar static pressures. Duffy, Hemley and Mao from CIW examined MgO to 227 GPa using synchrotron x-ray diffraction in a diamond anvil cell and obtained an equation of state taking into account the shear strengths. Figure 2 shows the volume versus pressure data for MgO as obtained from static compression and compares it with shock compression data for MgO. This single equation of state can describe ultrasonic, shock, and static compression for MgO. They showed that it is possible to characterize material strength and elastic anisotropy at ultra high pressure directly from diffraction data. Their results also show that there are significant changes in the degree and character of the elastic anisotropy of MgO at high pressure and that the strength at high pressures differs significantly from predictions based on low-pressure measurements. [This work will be published in *Physical Rev. Letters*, (1995)].

During the past few years, significant progress has been made in the ultra-high pressure studies of solid hydrogen [see H. K. Mao and R. J. Hemley, *Rev. Mod. Phys.* 66, 671, (1994)]. Theoretical calculations carried out have given rise to expect a dense metallic solid, in either an atomic or a molecular metallic state, could possess a number of unusual properties. As a result, the creation of "metallic hydrogen" in the laboratory has become a principal goal of high pressure research. Zha and his co-workers from CIW [C. S. Zha *et al.*, *Phys. Rev. B* 48, 9246, (1993)] developed a technique for studying the elasticity of single crystals of solid hydrogen and related materials at very high pressures. They used this method to determine the second-order elastic modulii of single crystal n-type hydrogen to 24 GPa at 295 K. The method involved the measurements of acoustic velocities as a function of crystallographic direction by Brillouin scattering in a diamond anvil cell with the orientation of the single crystals determined by synchrotron x-ray diffraction.

Some of the other highlights of the work from CIW include the work of Reichlin *et al.* on optical, x-ray, and band structure studies of iodine at several megabars and their findings on the transformation of iodine at 53 GPa and its stability to a pressure of 276 GPa [see R. Reichlin *et al.*, *Phys. Rev. B* 49, 3725, (1994)]. At this pressure, the volume compression is 0.324. Fei and Mao [see *J. GeoPhys. Research* 98, 11875, (1993)] reported the static compression of $Mg(OH)_2$ to 78 GPa at high temperatures. Eggert *et al.* [see *Phys. Rev. B* 49, 15299,

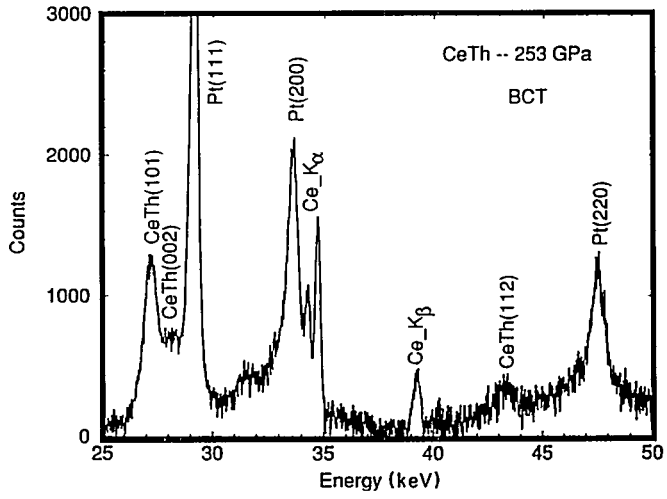


Figure 3 X17C: EDXD spectrum of Ce-Th+Pt mixture at 253 GPa. Pt is used as an internal pressure calibrant. [G. Gu, Y. K. Vohra, U. Benedict, and J-C. Spirlet, *Phys. Rev. B* **50**, 2751, (1994)].

(1994)] measured the compressibility of the $HgBa_2Ca_{n-1}Cu_nO_{2n+2+\delta}$(n=1,2,3) high-temperature superconductors. Fei *et al.* reported [see *J. Chem. Phys.* 99, 5369, (1993)] on the thermal expansivity, bulk modulus, and melting curve of H_2O-ice VII to 20 GPa.

The f-electron metals and their alloys have been the focus of intense experimental and theoretical high-pressure research. Gu *et al.* from U. of Alabama [see *Phys. Rev. B* 50, 2751, (1994)] investigated the ultra high-pressure synthetic diamonds show a great promise for their use as anvils in ultra high pressure research. (This work has been accepted for publication in Advances in *New Diamond Science and Technology*, 1995).

Skelton and associates from the Naval Research Lab (NRL) have studied high temperature superconductors, for evidence of structural inhomogeneities. By illuminating the samples with 10 μm beam, small changes in the c-axis lattice parameters were detected and were interpreted

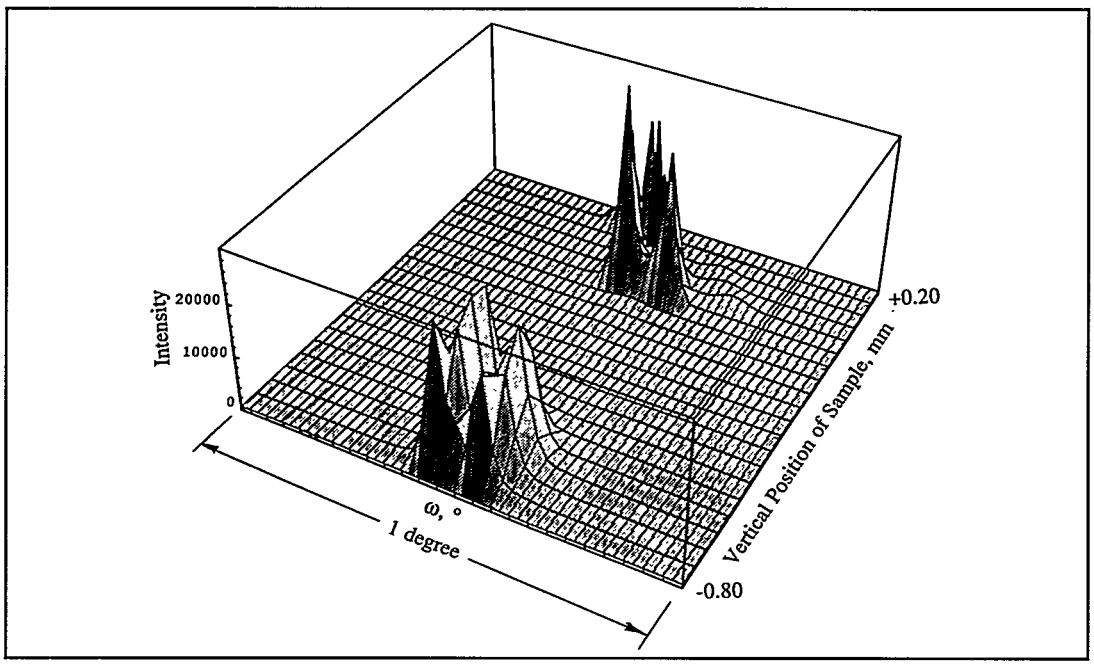


Figure 4 X17C: ω-scans of the (0,0,11) diffraction peak from a single crystal of $YBa_2Cu_3O_{7-\delta}$ as a function of vertical position of the sample.

transformations in the $Ce_{0.43}Th_{0.57}$ alloy up to a pressure of 253 GPa in a DAC utilizing SR x-ray diffraction (Figure 3) and found a phase transition from fcc-to-bct at 17 GPa. This is in contrast to first order isostructural fcc-to-fcc transition under pressure observed in pure Ce. The transition pressure is close to the transition pressure in Ce metal (12 GPa) and is considerably lower than that in Th metal (60 GPa). These results suggested non-linearities in transition pressure as a function of alloying content for f-electron alloys.

Vohra and his co-workers used large gem quality synthetic crystals of both isotopically pure (99.95 % 12C/ 0.05% 13C) and natural abundance (98.9 % 12C/1.1% 13C) diamond in the DAC to produce pressures as high as 253 GPa. Using x-ray diffraction measurements performed at X17C on metal standards of Fe, Cu and Pt, together with their known equations of state, pressures were calculated. The use of isotopically enriched (isopure) as evidence of variations in the oxygen content [see Skelton *et al.*, *Science* 263, 1416, (1994)]. Extended work of ω-scans of the (0,0,11) diffraction peak from a single crystal of $YBa_2Cu_3O_{7-\delta}$ revealed more information on the structural inhomogeneities as shown in Figure 4. A series of ω-scans were taken as the 1mm crystal length is moved through the polychromatic x-ray beam on X17C in 20 μm steps. The apparent loss of a diffraction signal from the central region is evidence of lack of single crystallinity within the core. A diffraction peak is present in this region, but very weak, < 600 counts, versus > 20,000 counts recorded from near the edges of the sample. This work is being expanded to perform automatic step scans throughout the volume of a single crystal and thereby to generate the equivalent of a 3-dimensional topograph, augmented by chemical information via fluorescence scattering excited by the incident photons.

LITHOGRAPHY, MICROSCOPY, AND TOMOGRAPHY

G. P. Williams
NSLS

LITHOGRAPHY

The Extreme Ultraviolet Projection Lithography project work continued at U13, the main emphasis being on optics development and testing. The present goal is to develop the ability to print 0.1 micron features. Diagnostics are an important parallel focus. With the 20X Schwarzschild camera, real time imaging of features down to 0.2 micron were demonstrated using a doped Yttrium Aluminum Garnet single crystal as a phosphor in combination with a CCD camera. One of the images is shown in **Figure** 1. Meanwhile a new 1X camera is under development which uses similar multilayer coated mirrors to image patterns of light of wavelength 13 nm onto resist-coated wafers. Imaging is required to be at the diffraction limit, so the quality of the camera mirrors required is very high. Typical figure errors are dictated to be of the order of 1 nm over several square centimeters of mirror surface. To characterize such mirrors, AT&T has built an interferometer on the undulator beamline U13UB that operates in the EUV spectral range. Initial results are starting to be produced. The first requirement for such an interferometer is to produce a source with a characterized wave front. This is usually achieved by illuminating a pinhole and the light passing through then has the characteristic Airy pattern. **Figure** 2 shows such an Airy pattern generated by a 2.5 micron pinhole. The concentric rings are of the correct radius and intensity to indicate that the wave front

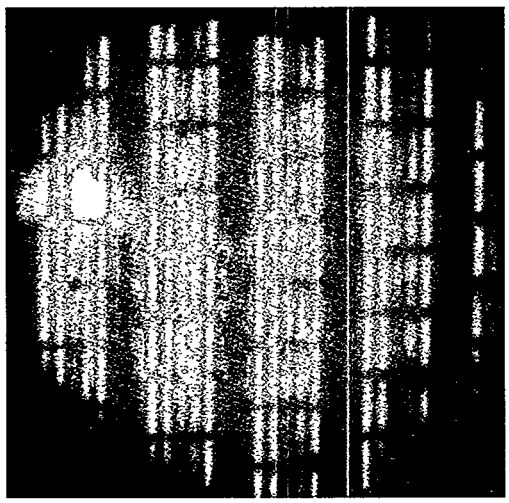


Figure 1 U13UB: Fluorescent visible light from a doped YAG type single crystal placed at the image plane of the camera. Groups of single lines of dimensions 0.5 μm, 0.3 μm, 0.1 μm, 0.2 μm and 0.4 μm are resolved, although the 0.1 μm line is only resolved to a resolution of 0.2 μm as limited by the Raleigh criterion of the visible light optics of the microscope. The bright area to the left of the image is a tear in the Silicon membrane mask.

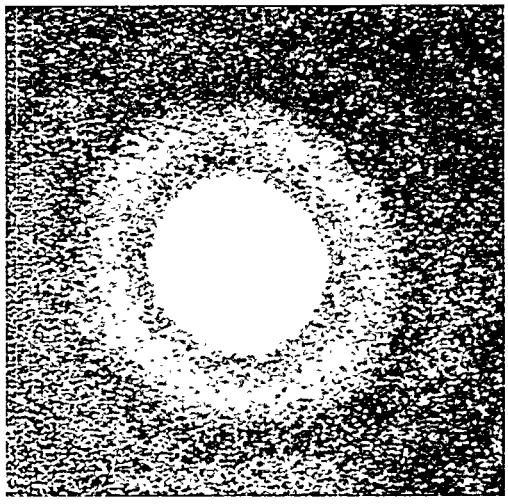


Figure 2 U13UB: Airy pattern from 2.5 μm pinhole with light of wavelength = 13nm.

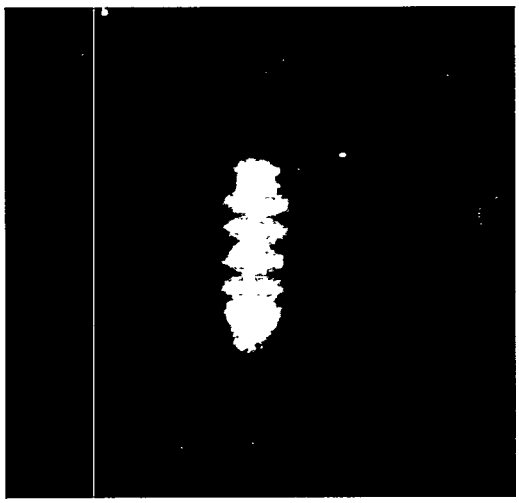


Figure 3 U13UB: Shearing interferogram of a pinhole light source with a spherical wavefront and wavelength of 13nm.

is indeed spherical. This near ideal source can then be used to evaluate the interferometry. Shearing interferometry is used - the wave front being diffracted from a grating and the zero and first orders being allowed to interfere. Thus the wavefront acts as a reference to itself. Shearing interferometry of the point source was accomplished by placing a grating 2mm beyond the pinhole and collecting the light with a CCD camera. The interference pattern is shown in Figure 3. The light is diffracted in the vertical plane and the image shows the overlap of zero, +1 and -1 orders. The horizontal bars are the interference patterns. Analysis of this interferogram indicates that the interferometer can readily establish the wavefront to better than a tenth of a wave. Such an accuracy is typically what will be required to characterize the EUVL camera. In addition, work continued on the evaluation of photoresists when operating at wavelengths of 37.5, 13.9 and 6.8 nm.

MICROSCOPY

Infrared Microspectroscopy;

An infrared microspectroscopy facility using a modified Spectra-Tech IRμs scanning microspectrometer was built in the late spring of 1994, the microscope itself being housed in the U2 clean room. The microscope is owned by the Northrop Grumman Advanced Technology and Development Center and is used for evaluation of semiconductors and devices as well as for studies of some of the new composite structures used in the aerospace industry. The microscope has a built-in Michelson interferometer and takes a full infrared spectrum at each point on the sample with a spatial resolution at the diffraction limit, which for the f/1 optics is approximately equal to the wavelength. Samples are scanned to produce maps. Spectra can be taken in either transmission or reflection. Several other collaborators have also participated in using the instrument, notably Polaroid Corporation and General Electric. The instrument is shown in Figure 4. A white pipe can be seen at the rear of the instrument which brings the collimated synchrotron radiation into the instrument. Below this is a liquid helium cooled Cu/Ge detector which was added to the instrument for linearity reasons. Examples of spectra taken with the instrument by Larry Carr (Northrup Grumman) are shown in Figure 5, in which we see maps of the distribution of oxygen in various forms in a silicon wafer. In Figures 6 and 7 we see a linear map taken of a laminate structure by Carl Zimba of Polaroid Corporation, in which features of dimensions as small as 3 microns are distinguished. (For Figure 7 please see the section divider, Appendices).

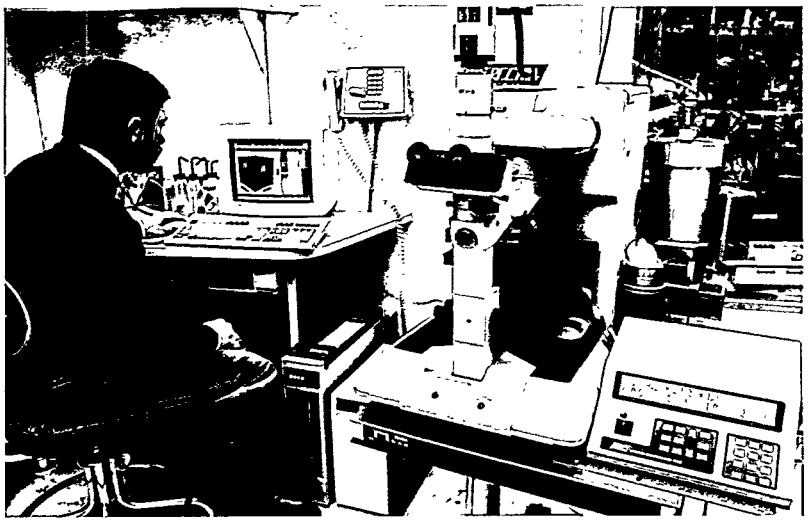


Figure 4 U2B: The infrared microspectroscopy facility at U2B. Larry Carr (Grumman) is operating the modified Spectra-Tech IRμs instrument which uses synchrotron radiation (white pipe entering from back) as the source. The large cylinder on the right is a liquid helium cooled Cu/Ge external detector.

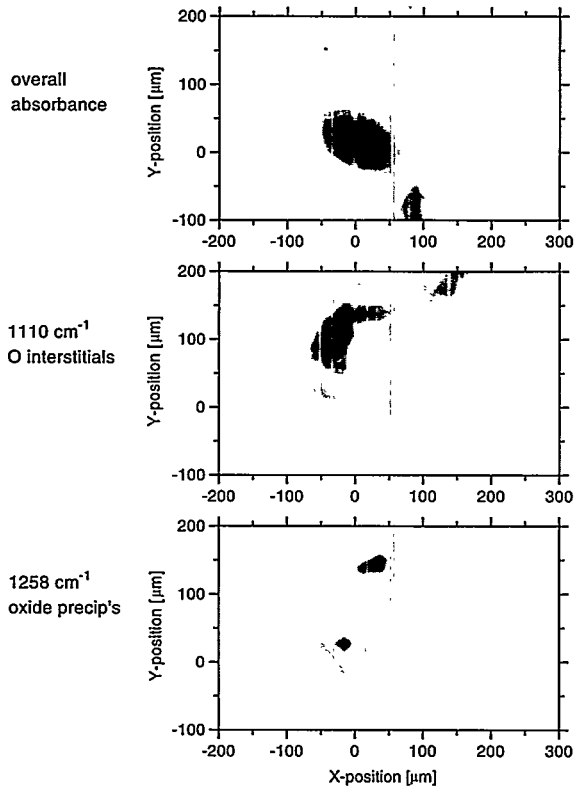


Figure 5 U2B: The absorbance maps demonstrate the ability of scanning infrared microspectroscopy to spatially locate two types of oxygen impurities. Scanning infrared microspectroscopy was performed on a silicon wafer region measuring 500 µm long by 300 µm wide, in 25 µm steps. The spatial variations of the absorbance at three wavelengths are shown, with darker regions corresponding to greater absorption. (a) represents the overall (non-wavelength specific) absorbance, presumably due to a mechanical defect within the wafer situated primarily near the point (0,0). (b) is an absorbance map for the oxygen interstitials (9µm) and (c) shows the distribution of oxides (8µm).

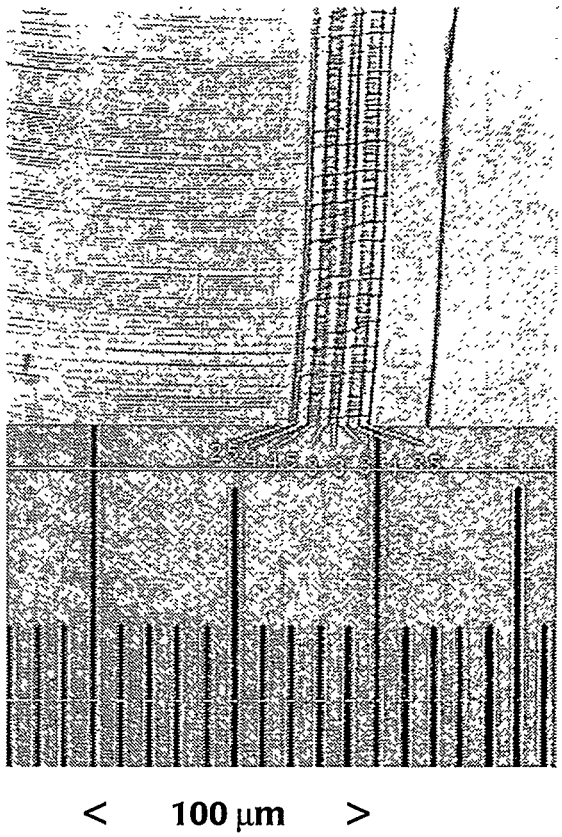


Figure 6 U2B: Micrograph of a polymer laminate sample. Dimensions are in microns. The infrared map generated by a linear scan is shown on the section divider for the Appendices.

X-Ray Microscopy;

At X1 several new demonstration experiments were done in soft x-ray microscopy. Using the scanning microscope, Chris Buckley (King's College, London) did quantitative mapping of calcium in a section of a human shoulder tendon with tendonitis (**Figure 8**, please see cover). Additional biological experiments were carried out on sperm cells from different species by Xiaodong Zhang (SUNY-Stony Brook) and collaborators, who mapped and measured the DNA and protein distributions quantitatively using XANES microscopy to study chromatin structures. An example of this work is shown in **Figure 9**, where a bull sperm head shows a protein-rich equatorial segment which is the part where sperm first interacts with the egg during fertilization. Henry Chapman (SUNY-Stony Brook) and collaborators used dark field imaging techniques in conjunction with gold labelling to

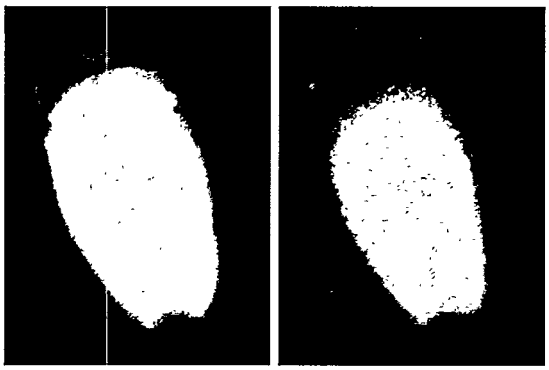


Figure 9 X1A: Distribution of DNA and protein in a bull sperm head. The DNA distribution in the sperm head is quite uniform while the protein distribution has significant variations.

produce images showing individual chromosome distributions also in sperm cells, an example being shown in Figure 10. Steve Lindaas (LBL) and co-workers used a different technique, that of Gabor holography, to produce images of various objects including a critical point dried NIL cell (Figure 11). The x-ray image reveals features that are not seen in visible light. Work also continued on polymers, led by Harald Ade of North Carolina State University and involving many collaborators from DuPont and Polaroid Corporation, among others. In one experiment micrographs were made of a liquid crystalline polyester based on several aromatic monomers. Superb contrast images revealing different phases were obtained. Some of these are shown in Figure 12 (see section divider for Chapter 1).

Photoemission Microscopy;

Other images using yet another technique, that of scanning phototoemission microscopy, were made by Cheng-Hao Ko (SUNY-Stony Brook) and co-workers. Using a new instrument capable of simultaneous multiple energy detection, chemical state mapping can be done in real time at each point, thus eliminating the effects of drift. An example is shown in Figure 13.

Microanalysis;

There were several experiments conducted that do not involve scanning, or the generation of images, but microanalysis. On U2B, Jean-Louis Bantignies (LURE) was able to establish how certain types of oil bond to clays by studying the vibrational bonding modes. At X1, Cody (ANL) and collaborators studied the organic structure of kerogen as well as the photochemical alteration of humic acid, an important reaction intermediate involved in oxidative weathering.

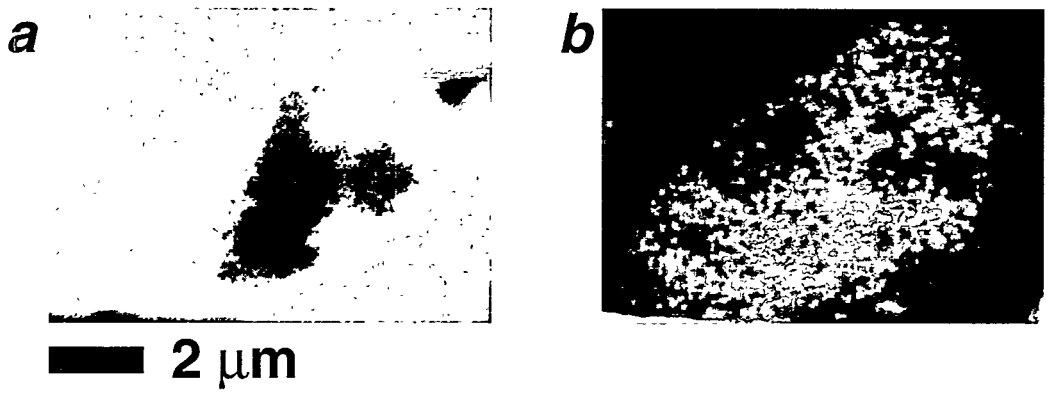


Figure 10 X1A: (a) STXM bright-field image, and (b) STXM dark-field image, of a partially decondensed sperm-cell labelled with 20-nm immunogold, attached by *in situ* hybridization to the telomere sequences of the chromosomes. The bright-field image is a map of the absorption, due mostly to carbon, whereas the dark-field image is a map of the scattering, primarily from the gold.

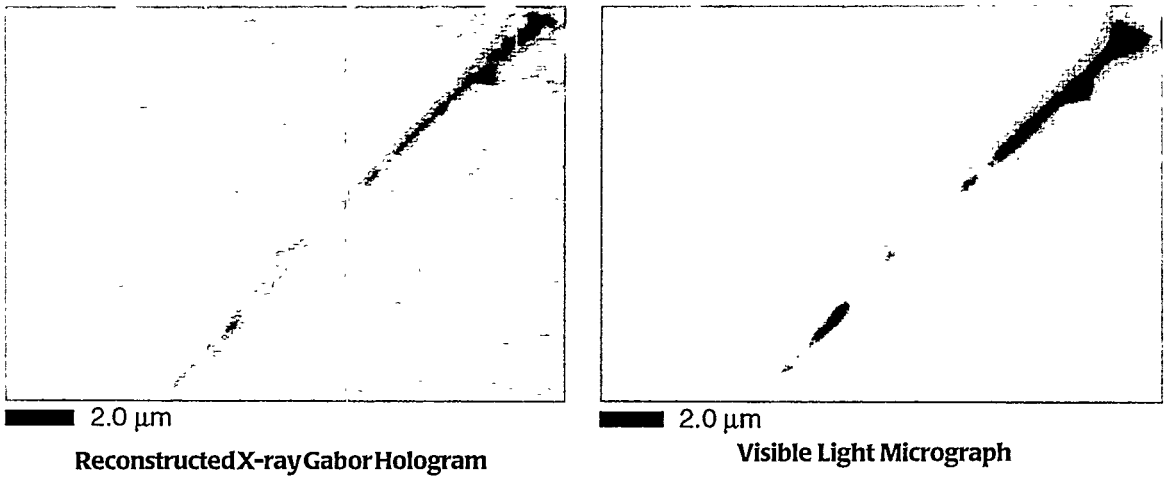


Figure 11 X1A: A subimage from a reconstructed image of a critical point dried NIL cell. An image from a visible light microscope (100x N.A.=0.9) of the same region is shown for comparsion. Small subcellar features as well as a tendril are observed in the x-ray image that are not resolved in the visible light micrograph.

X-RAY FLUORESCENCE MICROPROBE

At X26A, a substantial effort was made (S. Bajt, S. Sutton, and M. Rivers, CARS at the U. of Chicago; K. Jones, BNL-DAS; and P. Bertsch, D. Hunter and P. Nuessle, U. of Georgia) to develop the synchrotron x-ray fluorescence microprobe and, in collaboration with other scientists, apply it to a wide variety of scientific problems. For chemical speciation of transition metals and toxic elements investigative experiments using micro-XANES and pre-edge inelastic scattering (collaboration with A. Hanson, BNL-DAT) were carried out. In addition, research on microfocussing optics was done. A tapered capillary was used with the microprobe for the first time (collaboration with S. Hoffman, CHESS). Tests of Kirkpatrick-Baez mirrors (P. Eng and M. Rivers, CARS) and zone plates (B. Lai *et al.*, ANL) were also carried out on X26C.

Earth, Planetary and Environmental Science;

Trace element analysis and mapping was carried out for a number of materials relevant to earth science. H. Stowell and co-workers (U. of Alabama) studied trace elements in zoned garnets from Alaska. The distribution of these elements gives clues about the formation of these minerals. Richard Reeder (SUNY-Stony Brook) and co-workers studied the sectoral zoning behavior of trace elements in apatite and topaz as well as synthetically grown calcite crystals. Trace element analysis was also carried out on interplanetary dust particles from various sources and heating experiments were run on meteorite microfragments to determine elemental volatility during atmospheric heating (G. Flynn, SUNY-Plattsburgh). Distribution of moderately volatile trace elements in fine-grained chondrule rims very studied by A. Brearley, from U. of New Mexico. Chondrules are often mantled with rim material (low-temperature condensate). Detailed compositional data of this rim material is crucial in understanding the origin, history, and relationship of the chondrules and associated rims. Concentrations and oxidation state microdistributions of Se, Cr and U were measured in contaminated sediments (T. Tokunaga, LBL; P. Bertsch *et al.*, U. of Georgia). Cation partitioning of Fe and Cr between olivine and silicate melt as a function of pressure and temperature (J. Delaney, Rutgers U.), and speciation of Zn in single fluid inclusions in quartz (A. Anderson, St. Francis Xavier U., Canada; and R. Mayanovic, Southwest Missouri State U.) were investigated. Preliminary results of solubility of zerovalent iron in silicate melts (H. Nekvasil *et al.*, SUNY-Stony Brook) and of iodine valence state in contaminated soils (M. Fuhrmann, BNL-DAT) were reported.

Electrochemistry;

Alison Davenport (BNL-DAS) and collaborators used the microprobe to study the passivation of Fe-Cr alloys in an electrochemical cell in real time. Using a cell in which an electrode of graded composition had been produced, they were able to observe a sharp transition in the Fe/Cr ratio evolving with time at potentials where Fe is soluble at a 18-19% Cr.

Plant and Wood Disease;

Manganese is suspected of being involved in a fungal reaction that degrades lignocellulose in wood. B. Illman (U. of Wisconsin) and collaborators used the fluorescence microprobe to detect and map Mn including the oxidation state in southern yellow pine wood. The same group also analyzed Cr distributions in wood treated with chromated-copper-arsenate (CCA) to demonstrate the sensitivity of micro-XANES. Later the method will be used to investigate the bonding of metals to wood which has relevance to leaching. Mn is also suspected of being involved in promoting one of the world's major diseases of wheat, and Darrell Schulze and collaborators (Purdue U.) studied Mn oxidation state distributions in both soils and in wheat rhizospheres using micro-XANES.

Microtomography;

John Dunsmuir (Exxon) and his collaborators at X2B have continued experiments on porous media and in particular, oil reservoir rocks. In addition experiments in collaboration with the Mayo foundation have led to the successful imaging of the rodent cardio-vascular tree, liver vascular and bilary duct systems. Finally, studies have been made in collaboration with researchers from NIST of specimens of concrete before and after sulfur attack.

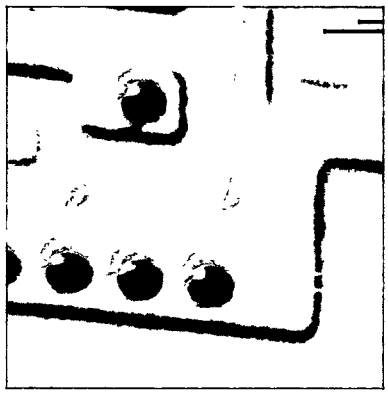
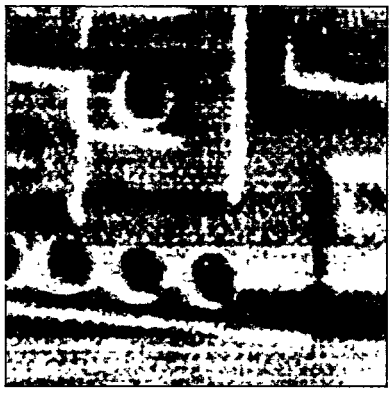


Figure 12 X1A: (a) A fine resolution photoelectron image (tuned to the Nb 3d photopeak) of a Nb circuit. Image size is 120 pixels by 120 pixels with a pixel size of 0.25 μm and a dwell time of 220 ms. The shadowing effect is caused by topological features on the surface.



(b) A sample current image acquired simultaneously with the photoelectron image.

NUCLEAR PHYSICS

Craig E. Thorn
BNL Physics Department

DEUTERON PHOTODISINTEGRATION THROUGH THE Δ (EXPS. L1-3)

Several measurements of the $d(\vec{\gamma},p)n$ reaction have been completed. The experiments include five independent measurements with three different detector systems, different photon endpoints from different laser wavelengths, different polarizations and two different liquid deuterium targets. These measurements overlap in various kinematic regions between 113 and 325 MeV, and the agreement in the regions of overlap is excellent. By taking weighted means of overlapping measurements, a 'net' data base has been constructed, and is available upon request (LEGS Data Release #L1-3.0, March/94). Selections of these results are shown in Figure 1.

As demonstrated in the first phase of these experiments[1], polarization observables in this reaction are particularly sensitive to the short range character of the nuclear tensor force. Calculations by Arenhoevel and collaborators from Mainz were quite successful in describing the results around 200 MeV but showed a systematic departure from the data at the higher energies. This could be due to inadequacies of the phenomenological parameterization used for the short range part of the tensor interaction, but the problem could also lie in an approximation that treated the N-N and N-Δ interactions as indistinguishable. The Δ peaks at about 265 MeV in d(γ,p)n and a better approach at these energies is to treat

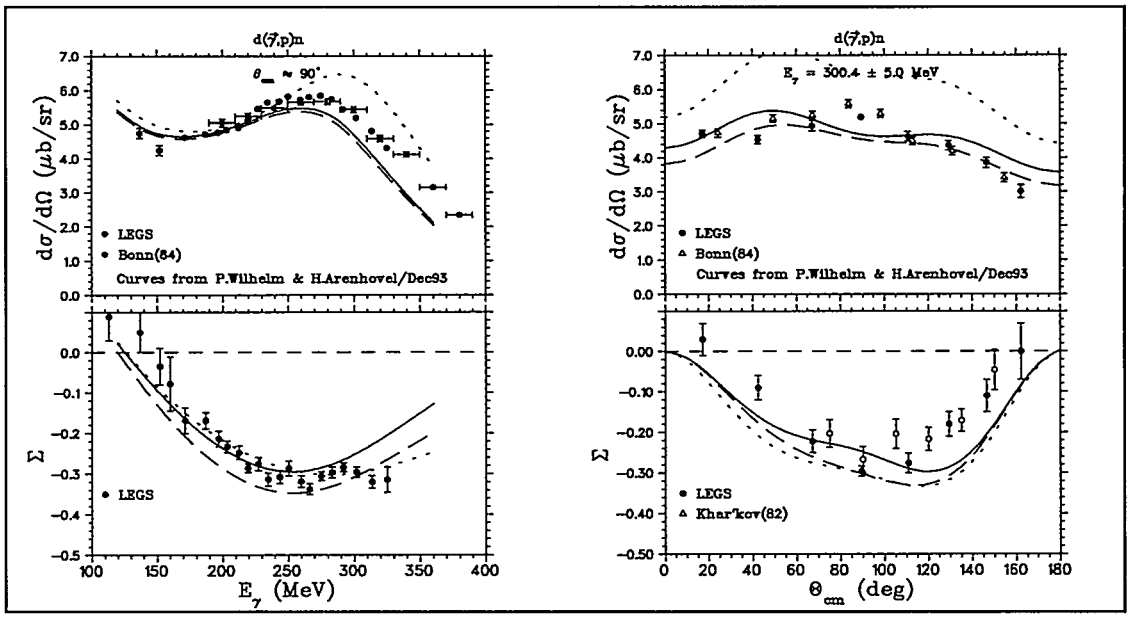


Figure 1 X5: Deuteron PhotoDisintegration results from Release #L1-3.0. The energy dependence of the 90° cross section and linear polarization asymmetry are shown to the left. The angular distribution of these observables at 300 MeV is shown to the right. Bonn[2] and Khar'kov[3] data are also shown. The curves are coupled-channel calculations by Wilhelm and Arenhoevel (see text).

these interactions separately, solving coupled Schroedinger equations. Such calculations have been carried out by Wilhelm and Arenhoevel. The results have been somewhat surprising, and are shown together with a sample of the data in Figure 1. The coupled-channel effects are very large. Including only the first order term involving the γNΔ interaction (dotted curves) significantly overestimates the cross sections in the energy region of the Δ, although the agreement with the polarization asymmetry, Σ, seems quite reasonable. In a more complete treatment, with the γNΔ coupling fixed by the $M_{1+}^{3/2}$ multipole for π-photoproduction, the resulting angular distributions (solid curves of Figure 1) predict a depression of the cross sections near 90° throughout the region of the Δ. This depression is not present in the data. Modifying the γNΔ coupling (dashed curves in Figure 1), a procedure that includes non-resonant Born terms in an effective way, improves the overall agreement in the angular dependence of the cross section but gives a poorer representation of the polarization asymmetry, Σ. This is a difficult problem since very little is known about the NΔ interaction. Work is now in progress to include non-local and relativistic corrections. The combined data from both cross sections and polarization observables imposes stringent constraints upon such calculations.

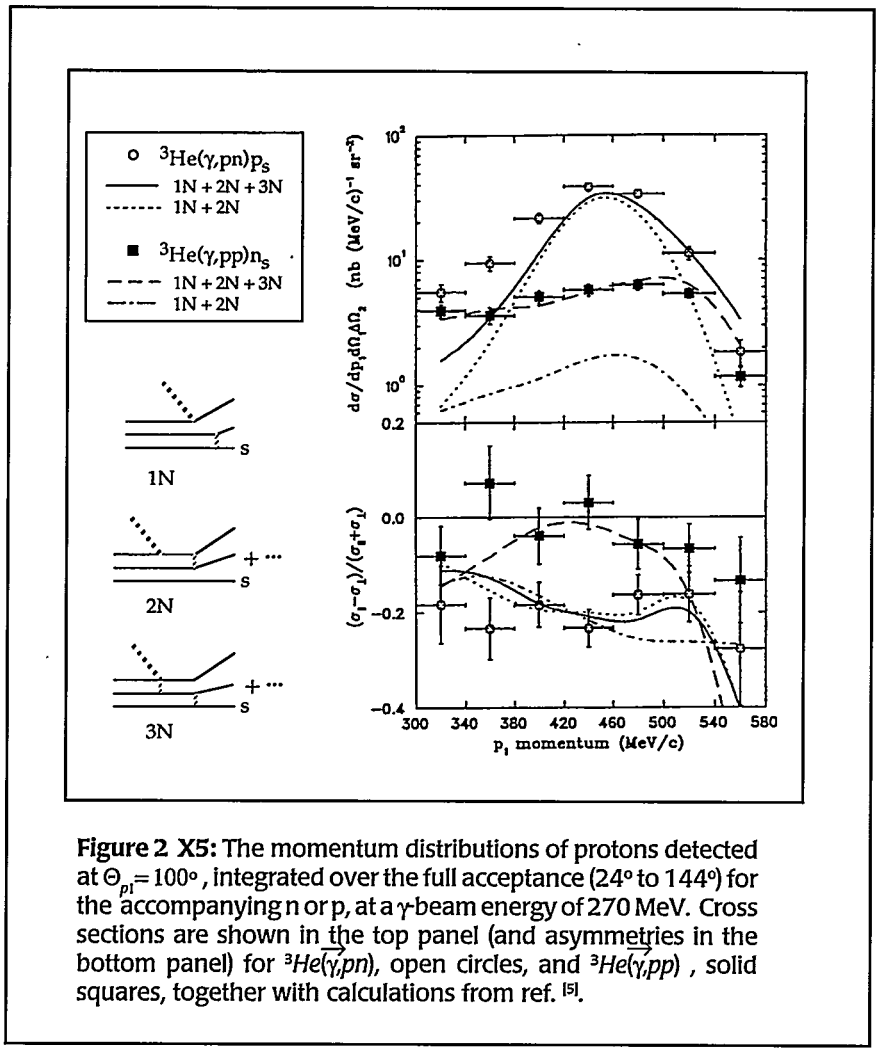


Figure 2 X5: The momentum distributions of protons detected at $\Theta_{p1} = 100°$, integrated over the full acceptance (24° to 144°) for the accompanying n or p, at a γ-beam energy of 270 MeV. Cross sections are shown in the top panel (and asymmetries in the bottom panel) for $^3\vec{He}(\vec{\gamma},pn)$, open circles, and $^3\vec{He}(\vec{\gamma},pp)$, solid squares, together with calculations from ref. [5].

MULTI-NUCLEON CORRELATIONS IN $\vec{\gamma}$ + ^{3}He REACTIONS (EXP. L4)

Both inclusive $^3\vec{He}(\vec{\gamma},p)X$, and the exclusive $(\vec{\gamma},pn)$ and $(\vec{\gamma},pp)$ channels, have been studied in Experiment L4 at LEGS[4,5]. The mass-3 system is the simplest in which 3-body correlation effects might be present, and for which exact calculations can be performed. Measurements from other laboratories (all unpolarized), for both inclusive and exclusive photodisintegration, have suggested that a substantial fraction of the cross section proceeds through the three-Nucleon absorption channel. Calculations of the inclusive (γ,p) channel, which appear to reproduce the unpolarized cross section, do not provide consistent agreement with the beam polarization asymmetry[4].

On the other hand, there is less freedom in modeling the exclusive channels, and the (γ,pp) reaction provides a unique testing ground. The momentum distributions for protons detected at 100°, integrated over the full acceptance (24° to 144°) for an accompanying p or n, are shown in Figure 2 for an average beam energy of 270 MeV[5]. The (γ,pn) cross sections (open circles) are dominated by a large quasi-deuteron component and peak at 460 MeV/c, the expected momentum from deuterium dissociation with the extra proton acting as a spectator. The solid and dotted curves are recent calculations, performed J.-.M. Laget of Saclay, and include contributions from 2N and 2N+3N photon-absorption amplitudes, respectively. The 2N dominates in (γ,pn) and the addition of the 3N component adds very little. However, the analogous 2N mechanism for the pp-channel is suppressed since the diproton has no dipole moment and charged meson-exchange currents cannot contribute. The (γ,pp) cross

sections (solid squares in the upper panel) are much lower than those of the (γ,*pn*) channel, and theoretical predictions that exclude 3N amplitudes (dashed-dot curve) are a factor of 5 lower still, although they exhibit a similar momentum dependence. The addition of 3N absorption to the theory (dashed curve) produces results that are in very good agreement with the data.

Qualitatively similar results have been observed in unpolarized reactions with ^{3}He at other laboratories. However, a recurring objection can be made that, since the shapes of the predictions with (dashed curves) and without (dash-dot curves) the 3N absorption mechanism are so similar, uncertainties in the N-N potential might allow for some adjustment in the overall normalization of the 2N contribution. Experiment L4 has provided the first polarization information on these reaction channels, and the beam polarization asymmetry (lower panel of **Figure 2**) completely rules out this scenario. The predicted (γ,*pp*) asymmetry from 2N amplitudes (dash-dot curve) is large and negative. It is, in fact, quite similar to that observed in deuteron photodisintegration (Exp. L1,3: **Figure 1**) and to that of the (γ,*pn*) channel. Increasing the 2N amplitude would only make the asymmetry more negative. In contrast, the data (solid squares), as well as the predictions including 3N absorption (dashed curve), are nearly zero. There can be no preferred direction when all three nucleons are involved.

NEW MEASUREMENTS OF $p(\vec{\gamma},\pi)$ AND THE E2 EXCITATION OF THE Δ (EXP. L7)

In constituent quark models, a tensor interaction, mixing quark spins with their relative motion, is introduced to reproduce the observed baryon spectrum. This necessarily results in a D-wave component to the nucleon wave function, which breaks spherical symmetry and leads to a static deformation for the proton's first excited state, the Δ resonance. The Δ is photo-excited mainly by M1 radiation. However, the D-state component results in a small E2 transition strength. The magnitude and sign of the E2/M1 mixing ratio are quite sensitive to the internal structure of the proton.

The isospin I=3/2 Δ decays with a 99.4% branch to πN final states, and with an 0.6% γN branch back to the initial state (Compton scattering). There have been many determinations of the I=3/2 photo-pion multipoles. For the most part, these agree on the dominant M1 amplitude but differ on smaller components such as E2 excitation. Isolating the component associated with the Δ requires a further decomposition of these I=3/2 multipoles into resonant and background components. This decomposition requires a model, and model dependences enter the analysis of π-production and Compton scattering in different ways. These two branches have different E2 sensitivities and both are under study at LEGS.

The $p(\vec{\gamma},\pi^o)$ and $p(\vec{\gamma},\gamma)$ reactions were separated by detecting photons in a high resolution NaI(Tl) spectrometer, together with the recoil protons whose trajectories were tracked through wire (drift) chambers and whose energies were measured, both by energy deposition and by time of flight in an array of plastic scintillators. The π^o decay photons closest in energy to Compton scattering are accompanied by low energy photons traveling in nearly the opposite direction. These were detected in additional NaI crystals placed opposite the large high-energy γ-ray spectrometer to enhance the separation of the two channels.

For π-production, in addition to the unpolarized cross section, there are 3 single- and 12 double-polarization observables. Of all of these, the observable most sensitive to an E2 component is the cross section, $\sigma_{\|}$, for π^o production by linearly polarized photons whose electric vector is oriented parallel to the reaction plane. The corresponding cross section for the perpendicular orientation, $\sigma_{\perp}$, is completely insensitive to E2 excitation at all but extreme angles. Thus, the ratio $\sigma_{\|}/\sigma_{\perp}$ maximizes E2 sensitivity, while dividing out systematic uncertainties. The first results from LEGS (Exp. L2) provided high-statistics data on this ratio at a single angle[6], and comparisons with model calculations suggested an E2/M1 mixing ratio between -3% and -5%[7,8].

The parameters of models that are used to extract the resonant part of the E2 transition strength are obtained by fitting predictions of the models to π-production data. The agreement with the full data base (mostly unpolarized measurements) has been far from perfect, and this is at least partly due to the large number of experiments contributing to the data base, each with different systematic uncertainties. This problem is best addressed by a new experiment in which a large number of different observables are measured simultaneously, thus locking them together with a common systematic error. In Experiment L7, polarized cross sections were measured to a high accuracy for both the $p(\vec{\gamma},\pi^o p)$ and $p(\vec{\gamma},\pi^+)$ channels over a wide range of angles and energies.

A sample of the new $p(\vec{\gamma},\pi^o p)$ results[9] is plotted as the solid circles in **Figure 3**, together with previously published data (open symbols) where available[10,11]. There are a large variety of calculations available in the literature to which one may compare such data. In **Figure 3** we plot curves generated with the code of Davidson, Mukhopadhyay and Wittman (DMW)[12], since this model seems to be able to give the most accurate reproduction of $(\vec{\gamma},\pi)$ data. In the DMW model, π-photoproduction is

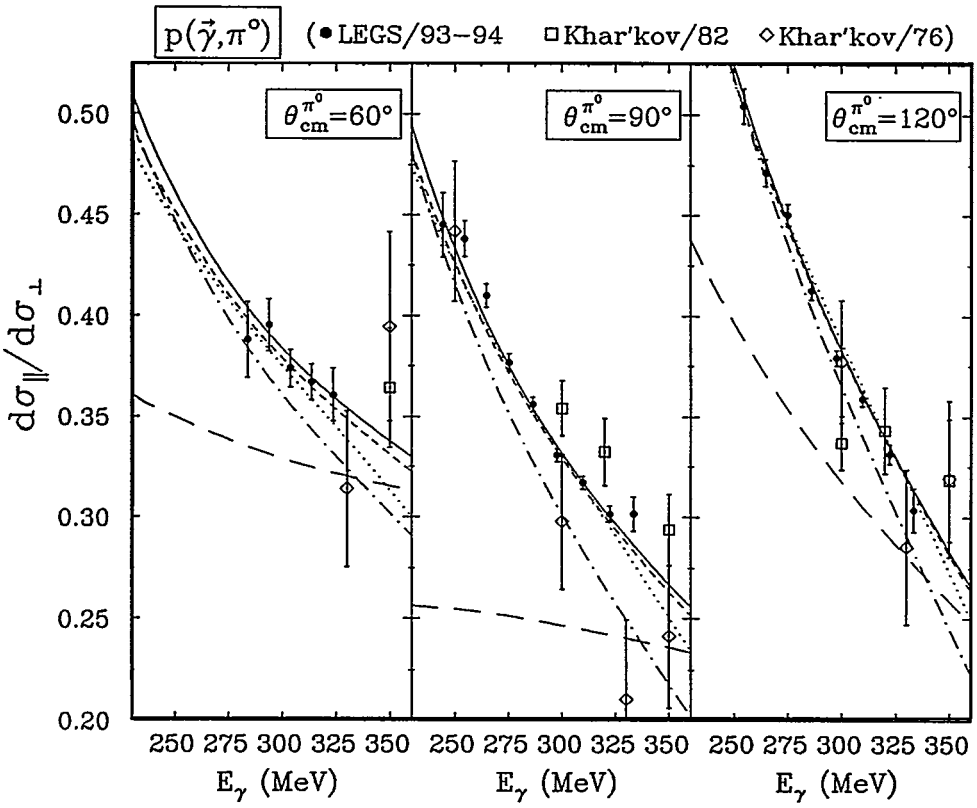


Figure 3 X5: The E2-sensitive observable / for the reaction. New results from Experiment L7 are plotted as the solid circles[9] and compared with previous measurements from Khar'kov[10,11]. The curves are calculations using the model of DMW[12]. The long-dashed curves are produced by setting the total E2 to 0, while the dashed-dot curves correspond to E2($N\rightarrow\Delta$)=0. The solid, short-dashed and dotted curves are the full calculations using the *Olsson*, *K-matrix* and *Noelle* decompositions of the amplitudes into resonant+background components (see text and **Table 1**).

evaluated in terms of effective Lagrangians. Amplitudes are calculated at the tree level and π-loops are effectively included through a unitarization procedure. The model contains five free parameters, G_E and G_M, the electric and magnetic coupling constants at the $\gamma N\Delta$ vertex, and three constants parameterizing the off-shell behavior. With these 5 parameters adjusted to reproduce π-photoproduction, the resonant part of the E2/M1 mixing ratio is given by $-G_E/G_M$.

The long-dashed curves in Figure 3 are obtained by *turning off all of the E2 strength*. The differences between these curves and the new $\sigma_{\parallel}/\sigma_{\perp}$ data are very large. However, most of this E2-signal results from interferences with E2 components of the Born amplitudes, and is quite uninteresting. The dashed-dot curves are obtained by including the full Born contribution while setting the resonant part of the E2 strength to zero ($G_E = 0$). It is the differences between these dashed-dot curves and the data that represents the E2 signal of interest, and the sensitivity is maximal at 90° CM. Modeling the $N\rightarrow\Delta$ transition requires a decomposition of each of the amplitudes into resonant+background terms, and this decomposition is not unique. Three choices for this decomposition have been discussed by DMW[12]: *Olsson's* method, in which the background part of the T-matrix is made separately unitary; a *K-matrix* method, in which the decomposition is made in terms of K-matrix elements; and *Noelle's* method, in which the decomposition is made in the πN phase shifts and carried through to photoproduction via unitarity. We have refitted the parameters of the DMW model to our new polarization data. Since all of the analysis is not yet complete, we have included previously measured unpolarized data from other laboratories. The results are shown in Figure 3 as the solid (*Olsson*), short-dashed (*K-matrix*) and dotted (*Noelle*) curves, respectively. All three are equally good representations of the $\sigma_{\parallel}/\sigma_{\perp}$ π^0 data. Compared to other observables, the *Olsson* and *K-matrix* results are essentially equivalent, while the *Noelle* predictions are somewhat worse for the π^+ asymmetry. The resonant E2/M1 extracted from these fits are summarized in Table 1. The dependence upon the method for the resonant+background decomposition is

Table 1: The resonant part of the E2/M1 mixing ratio, as extracted from comparisons between the new LEGS data and calculations using the DMW code of ref. [12], with three different prescriptions for decomposing the amplitudes into resonance+background components.

$N \rightarrow \Delta$ Decomposition Method	E2/M1($N \rightarrow \Delta$)
Olsson	-2.60 %
K-matrix	-2.71 %
Noelle	-2.82 %

rather minimal and, from this analysis, we would conclude E2/M1($N \rightarrow \Delta$) = -2.7±0.1%. This procedure will be repeated when the analysis of the full data set has been completed. The use of a single data set in the determination of the model parameters will minimize the effects of propagating systematic errors.

The unitarization procedures of the DMW model inherently include the effects of the pion field. As a result, the E2/M1($N \rightarrow \Delta$) values of Table 1 represent a ratio of dressed $\gamma N\Delta$ couplings - dressed by the proton's pion cloud. This is roughly consistent with the Skyrme model of the Nucleon but somewhat larger than Chiral-bag Model predictions. Comparison with the constituent quark model requires a further separation of E2 excitation of the bare Δ from the effects of the pion cloud. In principal, the model of Nozawa, Blankleider and Lee[14] should be able to accomplish this separation, although as yet their calculations are not able to reproduce the E2-sensitive observables. There are speculations as to why this is the case[7], and these are currently under investigation[14].

THE *N*→Δ TRANSITION FROM POLARIZED COMPTON SCATTERING (EXP. L8)

In Experiment L7, the $\Delta \rightarrow \pi N$ decay branch was studied and polarization was used to enhance E2 signals relative to the backgrounds. Compton scattering of polarized photons offers a potentially interesting alternative in which polarization differences can be used to directly cancel many background components[15]. Such measurements are technically demanding, because of the large background of photons from π^0-decay. In addition, there have been long standing speculations, based on the limited published data, that the real part of the scattering amplitude is negligible in the vicinity of the Δ resonance and a large variety of models have been proposed to accommodate this peculiar situation[16-18].

During Experiment L8, the cross sections and beam polarization asymmetries for the $p(\vec{\gamma},\gamma p)$ reaction were measured at angles from 55° to 130° CM and over energies spanning 220 to 330 MeV. Data were collected simultaneously with the π-production measurements of Experiment L7 and Compton scattered photons were clearly resolved from π^0 production. Results for the 90° linearly-polarized-beam asymmetry, $\Sigma = (\sigma_{\parallel}-\sigma_{\perp})/(\sigma_{\parallel}+\sigma_{\perp})$, are

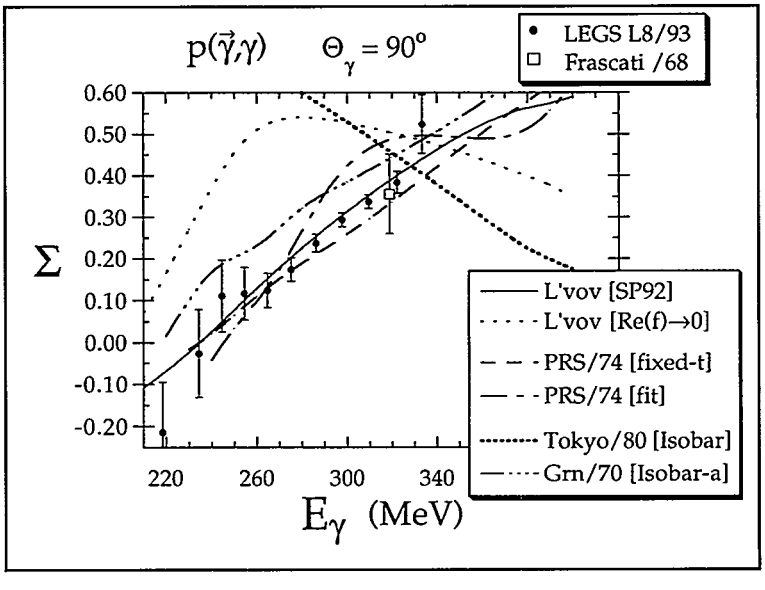


Figure 4 X5: The polarization asymmetry of Compton scattering from the proton [9,19], together with the only published datum (from Frascati)[20]. For the curves labeled as L'vov, the real parts of the scattering amplitudes have been calculated with the code described in ref. [21], while the PRS/74 predictions use the multipoles of ref. [16]. The Isobar predictions of Tokyo/80 and Grn/70 are from refs. [17] and [22], respectively.

shown in Figure 4 (solid points)[9,19], along with the only published datum for this observable (open diamond)[20]. The excitation of the Δ resonance is dominated by magnetic dipole transitions. However, if only M1 scattering contributed, the asymmetry would simply reduce to the value of 3/7, independent of energy. This is clearly not the case, which implies significant contributions from other multipoles.

The predictions of a number of models are shown in the figure. By design, all cross near the one published Frascati/68 point. The corresponding predictions for the unpolarized cross section are relatively close to one another, but their separation in the asymmetry is quite dramatic. The imaginary parts of the Compton scattering amplitude are derivable from π-production via Unitarity, assuming that the π-production multipoles are known with sufficient accuracy. Dispersion relations can be used to calculate the real parts, although there is a fair amount of freedom which comes in through the choice of the subtraction functions that can accompany the dispersion integrals. The result of using (γ,π) multipoles and Unitarity to calculate the imaginary part of the Compton amplitudes, while leaving the real parts set to zero, is shown as the light-dotted curve in the figure. The real parts are clearly important. The curves labeled L'vov[SP92] and PRS/74[fixed-t] have been calculated using Compton amplitudes derived from π-production multipoles - in the case of L'vov[21], from the SP92 solution by Arndt & Workman[23], and in the case of PRS/74,[16] from the Bonn multipole analysis of Pfeil and Schwella[24]. The L'vov[SP92] predictions are closest to the data. There has only been one analysis which included published Compton scattering measurements into a (γ,γ) multipole decomposition, using scattering to fix the real parts of the amplitudes, while their imaginary parts were constrained by π-production. The result (PRS/74[fit] curve in Figure 4) is quite far from these new data. Alternatively, the Tokyo/80 and Grn/70 calculations attempt to incorporate the structure of N* resonances into a fit of unpolarized Compton scattering data. These are completely ruled out by the new Experiment L8 data.

POLARIZED PHOTON SCATTERING FROM ^{4}He AND THE Δ-HOLE INTERACTION (EXP. L16)

The Δ-hole model has been relatively successful in accounting for a large body of π-N scattering data. The expectations for describing photo-reaction data were quite high, since the coupling of the photon to the nucleon is known to a potentially much higher accuracy. However, Δ-hole model calculations have failed to reproduce recent measurements of scattering with unpolarized photons[26], particularly at energies below the peak of the Δ, where non-resonant contributions are expected to be large. In contrast, calculations of quasi-free scattering have succeeded in reproducing the main features of the unpolarized data. The cross section for nuclear Compton scattering is generally written in terms of two structure functions, W_T and W_{TT}. The first can be determined with unpolarized photons, but the second requires a polarized beam. It is expected that the simultaneous determination of both will significantly constrain the reaction mechanisms that are involved, and ^{4}He is a particularly interesting target since rather complete microscopic calculations can be carried out for the mass-4 system. In Experiment L16, Compton scattered photons were detected in the 19" x 19" NaI spectrometer. Isolation of the Compton events was enhanced by another NaI array surrounding the target which was used to veto π°-decays. Analysis of $^4\mathrm{He}(\vec{\gamma},\gamma)$ data from this experiment is underway.

POLARIZED PHOTON SCATTERING FROM ^{16}O AND THE Δ-HOLE INTERACTION (EXP. L14)

Although the Δ-hole description may have difficulty modeling the scattering from ^{4}He, this type of particle-hole description may be better suited to nuclei with a more completely developed mean field. For this, ^{16}O provides an excellent testing ground since accurate wavefunctions are available. Detailed predictions for Compton scattering of polarized photons from ^{16}O have been published by Vesper, Drechsel and Ohtsuka (VDO)[27]. Medium effects were found to be important, and the polarized structure function, W_{TT}, was found to be particularly sensitive to model parameters. Measurements of $^{16}O(\vec{\gamma},\gamma)$ have been made using the same arrangement of detectors as in Experiment L16. A preliminary analysis of the new asymmetry data is largely consistent with the VDO calculations near the peak of the Δ, but deviates significantly at lower energies. This analysis is continuing.

THE E1/E2 PUZZLE IN $^4\mathrm{He}(\vec{\gamma},dd)$ BREAKUP (EXP. L15)

Polarization observables in the $^2\mathrm{H}(\mathrm{d},\gamma)^4\mathrm{He}$ reaction, and its inverse $^4\mathrm{He}(\gamma,\mathrm{d})\mathrm{d}$, provided the first evidence that the ground state of ^{4}He contains a D-state component. These reactions are particularly interesting because symmetry requires the d-d state to obey Bose-Einstein statistics. Assuming central forces, this forbids isovector E1 radiative transitions. Both the capture and the photodisintegration reactions have been measured several times

and in the 200 MeV region the reported cross sections vary by more than a factor of 100. Even more disturbing is the fact that the two most recent published works reported angular distributions that peaked at 90° CM[28,29], which is consistent with E1 radiation, and a variety of complicated two-step meson-exchange processes have been suggested to account for this.

In Experiment L15, the reaction was unambiguously identified by detecting both decay deuterons in coincidence. The polarization asymmetry is particularly important in separating the various contributing multipole transitions. Preliminary analyses show a deep minimum in the cross section near 90°, consistent with E2 radiation.



References:

[1] LEGS Collaboration, G.S. Blanpied *et al.*, Phys. Rev. Lett. **67**, 1206 (1991).
[2] J. Arends *et al.*, Nucl. Phys. **A412**, 509 (1984).
[3] V.G. Gorbenko *et al.*, Nucl. Phys. **A381**, 330 (1982).
[4] C. Ruth *et al.*, Phys. Rev. Lett. **71**, 617 (1994);
[5] D. Tedeschi *et al.*, Phys. Rev. Lett. (in press).
[6] LEGS Collaboration, G.S. Blanpied *et al.*, Phys. Rev. Lett. **69**, 1880 (1992).
[7] R. Davidson and N. Mukhopadhyay, Phys. Rev. Lett. **70**, 3834 (1993).
[8] A.M. Sandorfi and M. Khandaker, Phys. Rev. Lett. **70**, 3835 (1993).
[9] Some preliminary results have been reported in
LEGS Collaboration, M. Khandaker *et al.*, pN-Newsletter 9 (1993);
LEGS Collaboration, A.M. Sandorfi *et al.*, Few-Body Systems, Suppl. **7**, 317 (1994);
[10] V.B. Ganenko *et al.*, Sov. J. Nucl. Phys. **23**, 162 (1976).
[11] A.A. Belyaev *et al.*, Sov. J. Nucl. Phys. **35**, 401 (1982).
[12] R. Davidson, N. Mukhopadhyay and R. Wittman, Phys. Rev. **D43**, 71 (1991).
[13] S. Nozawa, B. Blankleider and T.-S.H. Lee, Nucl. Phys. **A513**, 459 (1990).
[14] T.-S.H. Lee, private communication.
[15] A.M. Sandorfi *et al.*, Topical Workshop on Excited Baryons-1988, Troy NY (ed. by G. Adams, N. Mukhopadhyay and P. Stoler), World Scientific, Singapore, 256 (1989).
[16] W. Pfeil, H. Rollnik and S. Stankowski, Nucl. Phys. **B73**, 166 (1974).
[17] T. Ishii *et al.*, Nucl. Phys. **B165**, 189 (1980).
[18] M. Benmerrouche and N. Mukhopadhyay, Phys. Rev. **D46**, 101 (1992).
[19] Some preliminary results have been reported in LEGS Collaboration, A.M. Sandorfi *et al.*, Proc. Particles and Nuclei Int. Conf. PANIC-XIII, Perugia 1993; (ed. C. Schaerf) World Scientific, Singapore (in press).
[20] G. Barbiellini *et al.*, Phys. Rev. **174**, 1665 (1968).
[21] A.I. L'vov, Sov. J. Nucl. Phys. **34(4)**, 597 (1981).
[22] G.K. Greenhut, Phys. Rev. **D1**, 1341 (1970).
[23] R.A. Arndt, *et al.*, Phys. Rev. **D42**, 1853 (1990); SP92 multipoles calculated with SAID.
[24] W. Pfeil and D. Schwela, Nucl. Phys. **B45**, 379 (1972).
[25] A.M. Sandorfi, C. Molinari and M. Khandaker, to be published.
[26] E.J. Austin *et al.*, Phys. Rev. Lett. **57**, 972 (1986); E.J. Austin et al., Phys. Rev. Lett. **61**, 1922 (1988); D. Delli Carpini *et al.*, Phys. Rev. **C43**, 1525 (1991).
[27] J. Vesper, D. Drechsel and N. Ohtsuka, Nucl. Phys. **A466**, 652 (1987).
[28] J. Arends *et al.*, Phys. Lett. **62B**, 411 (1976);
[29] B.H. Silverman *et al.*, Phys. Rev. **C29**, 35 (1984).

Supported by the US Department of Energy under contract # DE-AC02-76CH00016.

TIME RESOLVED SPECTROSCOPY

Jim Long
Naval Research Lab
Jon Levin
University of Tennessee

I. INTRODUCTION

The promise of using the pulsed nature of synchrotron radiation (SR) for time-resolved investigations, envisaged since the inception of dedicated storage rings, is being fulfilled by a growing community of users at the NSLS. A wide variety of experiments, encompassing the full range of available photon energies, from far-infrared to hard x-ray, is presently being carried out on gases, liquids, solids, and surfaces. The time domain ranges from subnanosecond, limited by the synchrotron pulse duration, to hundreds of nanoseconds, limited by the synchrotron interpulse period. These parameters, listed in **Table 1**, depend on which of the two rings at the NSLS, the X-Ray or the VUV, is employed.

Most pulsed, time-resolved studies require that only one electron bunch circulate in the X-Ray/VUV Ring rather than the usual 25/7. The need for only one bunch depends on the experiment. For example, the longer time window available between synchrotron radiation pulses in single-bunch fills (see **Table 1**) may be necessary to record long time decays. Similarly, a long time window circumvents overlapping photoion time-of-flight spectra. Finally, the number of photons per pulse increases in single-bunch operations, by factors of ~3 on the VUV Ring and ~10 on the X-Ray Ring, with a concomitant improvement in signal for experiments with duty-factor limitations imposed by detectors or, in the case of some pump-probe studies, by low pump-laser repetition rates. The single-bunch fills are scheduled for only limited periods to ameliorate the impact on other users caused by the reduced lifetime and injected current. The X-Ray Ring is formally scheduled for 18 days of single-bunch operations per year. Timing operations on the VUV Ring are scheduled with less formality: 8 or 14 hour shifts, dependent on day of week, are requested a week in advance.

Highlights of work performed on each ring are presented below.

II. X-RAY RING

During single-bunch operations, at least six research groups conducted timing experiments on as many beamlines during 1994, with several groups working on more than one line. Historically, some beamlines have

Table 1: NSLS Storage-ring characteristics relevant to time-resolved experiments.

	Radio Frequency (RF)	Maximum number of bunches	Minimum interpulse period	Maximum interpulse period (single bunch)	Nominal pulse duration (FWHM)
VUV Ring	53 MHz	9	19 ns	170 ns	1.5 ns (a)
X-Ray Ring	53 MHz	30	19 ns	566 ns	0.6 ns (b)

(a) With 4th harmonic cavity powered, trapezoidal profile. Pulse lengths of 200 ps (calculated) expected in future special operations.
(b) Single bunch, 90 mA beam current.

been used extensively during single-bunch operations, and have even become oversubscribed. The result is that some groups perform experiments on several beamlines in order to obtain access to the relatively limited single-bunch time.

X13A

A time-resolved x-ray intensity interferometry experiment was conducted at the X13A beamline in 1994 by Ian McNulty and collaborators of the Advanced Photon Source at Argonne National Laboratory, with help from E. Johnson and J. Safranek of the NSLS staff. Unlike conventional (amplitude) interferometers which rely on two interfering waves to form a fringe pattern, with the coherence of the incident beam being inferred from the fringe visibility, an intensity interferometer measures the degree of coherence by electronically correlating the intensity fluctuations in the beam. Its chief advantage is insensitivity to phase variations caused by optical imperfections and path-length mismatches. Intensity interferometry, invented in 1956 by Hanbury Brown and Twiss and used by them to measure the angular diameters of stars, is historically significant for marking the birth of quantum optics [R. Hanbury Brown and R.Q. Twiss, *Nature* 177, 27 (1956)]. Although it has not yet been demonstrated with x-rays, intensity interferometry may be useful for measurement of the beam coherence and source size of high brightness undulators at third-generation storage rings.

The Argonne team began an intensive construction effort at the end of 1993 to "get their feet wet" on this subject, and to capitalize on a one-year window that was available to make use of the X13 soft x-ray undulator [E. Gluskin, I. McNulty, L. Yang, K.J. Randall, Z. Xu, and E.D. Johnson, *Nucl. Instr. Meth.* A347, 177 (1994)]. X13A, a soft x-ray beamline using a spherical grating monochromator, was commissioned in 1994. First light from the X13A beamline was obtained in February, and a prototype soft x-ray intensity interferometer was tested with undulator radiation at X13A in the following months. The interferometer uses a grazing incidence beamsplitter, microchannel plate detectors, and a fast correlator circuit. Tests at X13A showed that the optics were satisfactory and that the interferometer bandwidth approached 1 GHz.

Correlation measurements of the mini-undulator beam with the interferometer were begun in June and continued until the end of the project in November, 1994. One aspect of the experiment involved varying the vertical source size by changing the horizontal to vertical coupling in the storage ring while monitoring the correlation rate. However to date, despite best efforts to minimize the system noise, a correlation depending solely on the beam coherence has not been observed. Because the effect expected at X13A is quite small, the available source brightness is most likely the limiting factor. In addition, the pulsed nature of the synchrotron radiation itself introduces a strong correlation, which demands considerable dynamic range of the correlator. The data are currently being analyzed for more deeply buried results and to set limits on the experimental uncertainties.

X17C

Of fundamental interest to radiation chemistry are the processes that follow the absorption of ionizing radiation in liquids. Jack Preses and Dick Holroyd (BNL-Chemistry) have used both the UV and X-Ray Rings in the past to study these processes in liquid hydrocarbons. Because a fluorescent excited state is created in liquid alkanes along the tracks of photoelectrons ejected by photon absorption events, time-resolved fluorescence is used to probe the disposition of absorbed energy at the molecular scale.

Pressure is predicted to be an important parameter in the response of liquids to ionizing radiation but has so far remained completely unexplored. A unique experimental capability to apply pressure during the fluorescent measurement is therefore under development and was recently tested on X17C during single bunch operations. A primary motivation for applying pressure is to extend past measurements to small molecules, e.g. ethane, which are much more amenable to theoretical description. At atmospheric pressure, the experiments have proven impractical for molecules smaller than decalin (room temperature) or butane (low temperature) because the fluorescent efficiency falls below detectability as molecular size decreases. Since molecules spawn small, weakly fluorescent fragments after the ionization event, the experiments could be extended if a means of preventing fragmentation were obtained. High pressure affords such a means since liquids under high pressure are less likely to fragment.

X24A

Many calculations have been performed to understand measured photoion charge distributions which result from the vacancy cascade following the creation of a deep inner-shell vacancy in a heavy atom. A broad distribution of charges can be produced, resulting from a superposition of distributions arising from several competing Auger or radiative channels. Theory has been reasonably successful for vacancies created in the "sudden" limit, i.e., with photon energies far in excess of the binding energy of the electron ionized. Here, a photoelectron is ejected with high energy and atomic de-excitation

can be considered decoupled from ionization.

The situation is greatly complicated when the incident photon has energy comparable to the binding energy of an inner-shell electron, and when the photon energy has been monochromatized to a width less than the natural width of the level. In this case, photoion charge distributions show marked photon-energy dependence not visible far from threshold because atomic relaxation occurs while the low-energy photoelectron is still close to the residual ion. Excitation and de-excitation must be considered as a single higher-order process. Detailed understanding of such distributions requires treatment of resonant excitation and post-collision interaction.

Yoshiro Azuma (KEK Photon Factory, Japan) and collaborators have made new measurements which illustrate these features near the K absorption edges of potassium and argon. Data for argon are illustrated in an abstract for beamline X24A.

The many-body problem is pervasive in all of physics. In fact, it is not too much of an exaggeration to say that the lack of an exact solution to even the three-body problem is at the root of most theoretical attempts at understanding physical phenomena.

Helium is the simplest atomic three-body system, and therefore the simplest which can exhibit electron-electron correlation. As a result, photoionization of helium has long been used as a testing ground for understanding correlation phenomena, such as autoionization, correlation-satellite production (shakeup) and double photoionization. At higher photon energies, Compton scattering can produce single or double ionization of helium with a cross section which dominates that of photoionization. Theoretical prediction of the energy dependence of the double photo- or Compton ionization of helium is a fundamental problem in atomic physics which requires solution of the Coulomb three-body problem.

Despite the fundamental importance of the problem, theoretical predictions of the ratio of double-to-single ionization of helium by high-energy photons have not converged (they vary by a factor of two). Jon Levin (U. of Tennessee) and collaborators have conducted an ongoing program of research aimed at elucidating the roles of photoionization and Compton ionization in the 4-6 keV region. Single-bunch operations are critical for these measurements, which use the ring timing signal to differentiate between singly and doubly charged helium by time-of-flight methods. Time-of-flight techniques which require detection of an ejected electron can introduce systematic biases, and pulsing of extraction fields produces broad ion time-of-flight peaks, making discrimination against large cross section electron-impact ionization difficult.

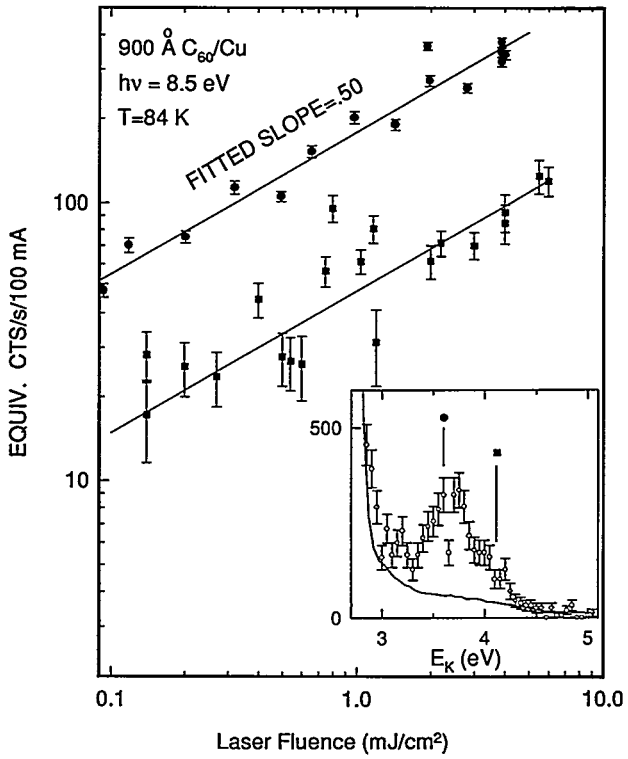


Figure 1 X24C: (Inset) Photoelectron spectrum of excitons excited in a film of C_{60} by a 5-ns copper-vapor laser pulse and probed by a time-overlapped synchrotron pulse. The contributions are marked from triplet excitons (filled circle) and shorter lived singlets (filled square) from which the triplets derive. Solid line shows background in absence of laser irradiation. **(Main part of figure)** Dependence on laser fluence of the singlet and triplet densities as measured by their amplitude in the photoemission spectrum. That a square root dependence, indicative of bimolecular decay, is seen for both species shows them to be tightly coupled at these densities (~10^{18} cm^{-3}) and times (1.5 ns into the laser pulse). (B. S. Itchkawitz, J. P. Long, T. Schedel-Niedrig, W. R. Hunter, R. Schoegl, A. M. Bradshaw, and M. N. Kabler).

X24C

Photoelectron spectroscopy may be extended from a probe of the ground state to a probe of the photoexcited state through pump-probe photoemission. In this tech-

nique, a laser pulse first excites electrons into normally unoccupied levels, and a second UV pulse, incident with controlled delay after the laser pulse, photoemits from the excited electron population. In this way the energies, k vectors, and population dynamics of excited states are directly accessible. The technique is most often practiced with laser-based UV sources but Jim Long (Naval Research Lab) and co-workers have expanded it to include the use of synchrotron radiation.

Figure 1 displays recent results obtained from films of the fullerene C_{60} during single-bunch operations. The inset gives the photoelectron spectrum of excitons excited in the film by a copper-vapor laser pulse ($h\nu$ =2.43 eV, 5 ns FWHM) which was overlapped with the synchrotron pulse ($h\nu$ =8.5 eV, 0.6 ns FWHM). The energy of the excitons lies well below the band gap of solid C_{60}, reflecting the energetics of exciton binding, lattice relaxation, and, possibly, trapping at defects. At least two components can be identified in the spectrum, indicated by vertical lines, and are attributable to short-lived singlet excitons (squares) and long-lived, less energetic triplets (circles) into which the singlets decay. The dependence of exciton signal on pump-laser intensity, seen in the main portion of Figure 1, provides clues into the recombination dynamics of the exciton populations. The square root dependence shows that bimolecular recombination, i.e., annihilation resulting from the collision of two excited species, is operating for both singlets and triplets.

X12A and X25

Rare gases physisorbed on graphite continues to be a problem of considerable experimental and theoretical interest. These systems have quite complicated phase diagrams due to the competing periodicities of the adsorbate and substrate lattices. For example, nominal monolayer krypton (Kr) films undergo a commensurate-incommensurate (C-IC) transition as the monolayer capacity of the commensurate $\sqrt{3}x\sqrt{3}$ R 30° structure is reached. Another feature in the phase diagram is a re-entrant fluid phase that intervenes between two solid (C and IC) phases. Most investigations of this system have concentrated on the static structure of the films, while the dynamic nature (i.e., thermal fluctuation effects) of phase transitions occurring in them has been largely ignored.

Mössbauer spectroscopy (MS) has been used extensively to investigate hyperfine interactions and lattice dynamics in solids for over 30 years. Coherent nuclear forward-scattering of synchrotron radiation (NFS), a technique pioneered in 1990 by a group led by J. Hastings and D.P. Siddons, is the time-analog to the conventional Mössbauer spectrum. Over the past year a group of researchers consisting of D. Johnson (Old Dominion University), J. Hastings and D.P. Siddons (NSLS), and J.Z. Larese (BNL Chemistry) have used NFS from ^{83}Kr to investigate portions of the Kr-on-graphite phase diagram through measurements of the Lamb-Mössbauer factor (f_{LM}) or so-called recoil-free fraction. The Lamb-Mössbauer factor is a quantity related to the time-averaged mean-square displacement of the atomic nucleus from its equilibrium position.

There are a few advantages to the NFS technique over conventional x-ray diffraction and inelastic scattering methods. Firstly, the forward-scattering geometry is insensitive to changes in the static order of the atoms in the sample studied. Thus any changes in the forward-scattered signal arise only from thermal fluctuation effects. Secondly, as f_{LM} represents an integral over the phonon density of states in the solid, one is not restricted to the use of single-crystal substrates — high-specific area substrates such as exfoliated graphite can be used to increase the effective size of the signal and remove much of the UHV restrictions associated with single crystal substrates and inelastic scattering measurements. Finally, as NFS is a

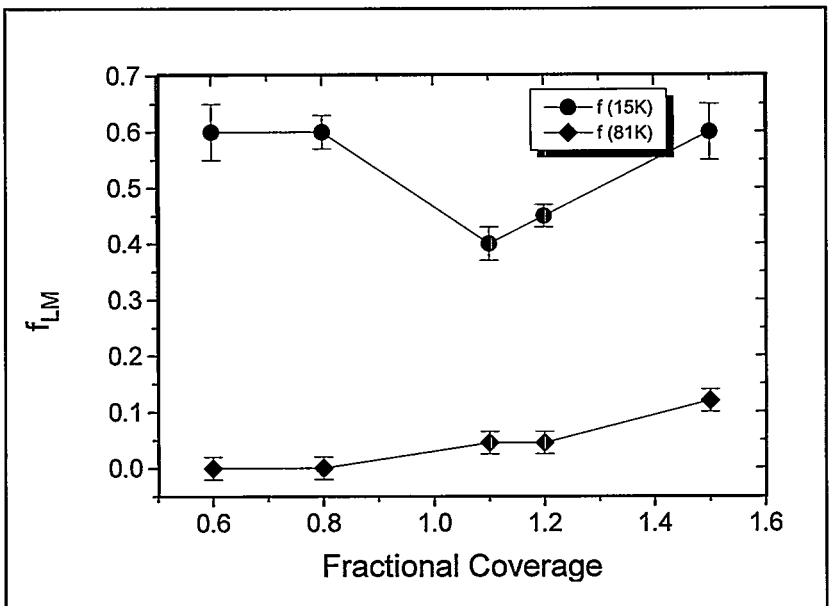


Figure 2 X12A: Time-differential and time-integrated measurements of the NFS intensity taken on Kr films with increasing coverages.

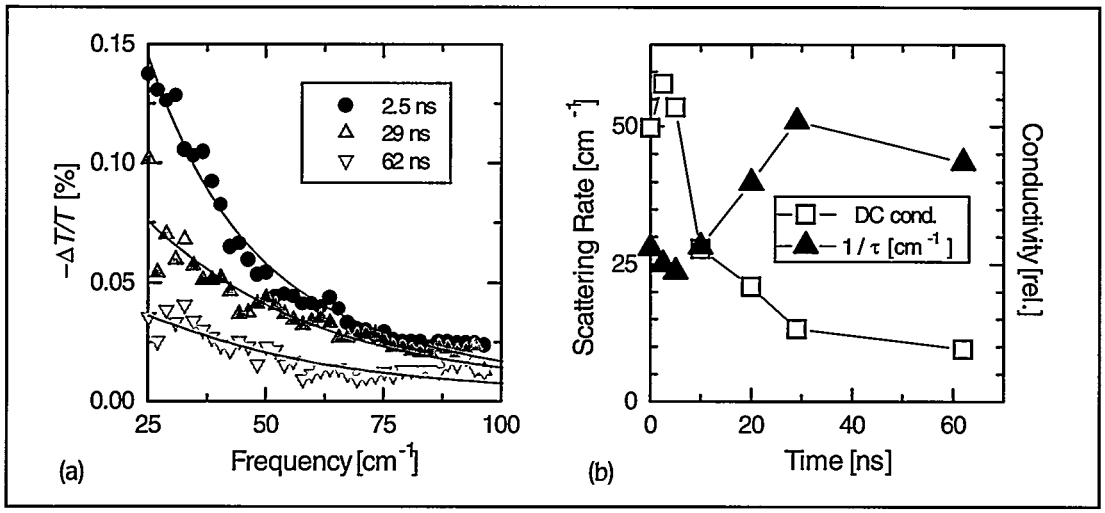


Figure 3 U4IR: (a) Changes in the far infrared absorption spectrum of semi-insulating GaAs induced by a 1 ns pulse of 845 nm laser light, plotted for various synchrotron IR probe times after the laser pulse. The absorption increases (i.e., the transmission, the plotted and measured quantity, decreases) after the laser pulse because free carriers promoted across the forbidden gap are now free to absorb the IR radiation. (b) Decay of the photoinduced DC electrical conductivity and the phonon-mediated momentum scattering time of carriers inferred from a Drude analysis of the time-resolved absorption spectra of the right panel. (G. L. Carr, Grumman Aerospace & Electronics)

scattering process occurring on the time-scale of the excited nuclear state (212 ns), the resonant signal from the adsorbate is easily differentiated from the non-resonant signal of the substrate.

Most recently, an investigation of the C-IC transition was performed. Kr films ranging from 0.6 to 1.5 layers were prepared on an exfoliated graphite substrate using a vapor pressure isotherm apparatus. The Kr was 75% enriched in ^{83}Kr. As the Kr coverage was increased, time-differential and time-integrated measurements of the NFS intensity were taken. Each of these measurements was performed at two temperatures, 15 and 81 K (just below the melting point of < 1.0 layer thick films). Values of f_{LM} were obtained by fits to the data. These values of f_{LM} are shown in **Figure 2**. From the 15 K data, one clearly sees that thermal fluctuations play a role in the C-IC transition and it is not connected solely with static disorder in the adsorbate. From the 81 K data, one sees that at low coverages (where the melting point is nearly 81 K), the film is fluid-like and no NFS is seen. As the coverage is increased to >1.0 layer, where the melting point is higher, one sees a discernible NFS signal indicating the presence of solid. Note that the solid lines in the graph are only guides to the eye.

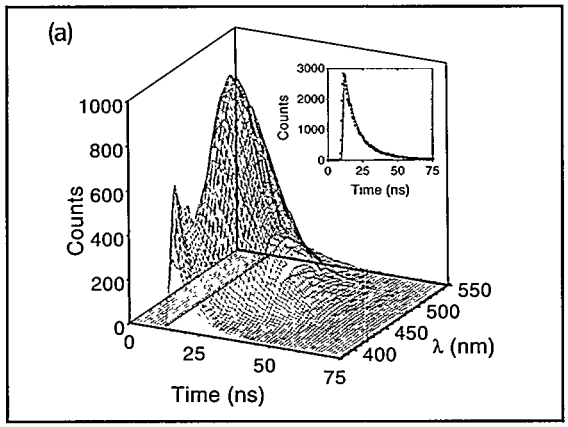
Further experiments are planned, with particular emphasis on the re-entrant fluid and commensurate solid phase mentioned earlier.

III. VUV RING

U4IR

Before the development of infrared (IR) beam lines, nanosecond time-resolved measurements relying on wide IR tunability were not feasible for lack of suitable pulsed sources. Larry Carr (Grumman) and co-workers employ IR absorption spectroscopy to study the dynamics of pulsed-laser-pumped electronic excitations in semiconductors and superconductors. Recently, they have introduced laser diodes synchronized to the ring for their pump-laser source. Laser diodes provide a compact, inexpensive alternative and new wavelengths compared to the Nd:YAG laser used in past experiments.

Figure 3 illustrates the unique transport measurements made possible by a broadly tunable, pulsed source. Here, a sample of semi-insulating GaAs is pumped at 845 nm (1.47 eV) by the laser pulse at 0 time and probed with an IR synchrotron pulse after a controllable delay, given in the inset to **Figure 3(a)**. Pump-induced changes in the far-IR transmission spectrum originate from the population of free electron-hole pairs generated by the laser pulse. This population absorbs IR directly through intraband transitions (free-carrier absorption). The frequency-dependent absorptive losses, plotted in **Figure 3(a)** as the relative change in transmission through the sample, amounts to a measurement of the frequency-dependent electrical conductivity $\sigma(\omega)$. The decrease of



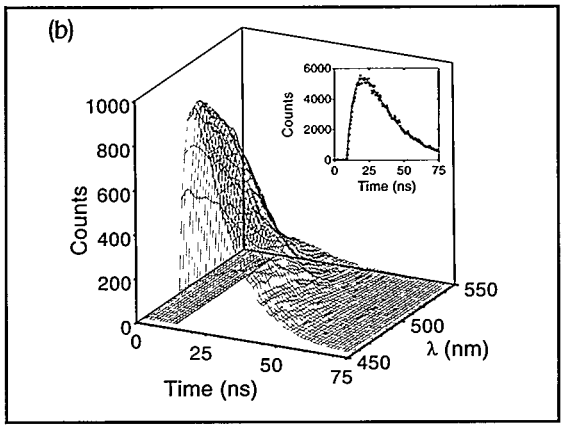


Figure 4 U9B: (a) Example of the simultaneous measurement of both the time decay and the wavelength of synchrotron-excited fluorescence obtained with the new fluorimeter on U9B. The sample is pyrene dissolved in ethanol, a model system used to test the performance of the instrument and chosen for its complex dynamics. Rapid decay of the molecular singlet states initially excited by the 1.5 ns synchrotron pulse is evident in the short wavelength portion of the spectrum.

(b) Emphasized here is the longer wavelength portion of the spectrum, which probes the creation and decay of the excited state molecules (excimers) formed between photoexcited pyrene molecules and their stabilizing ground-state partners. The efficient data rates from the instrument will provide detailed dynamical information on biological molecules. [Lisa A. Kelly, John G. Trunk, Krzysztof Polewski, and John C. Sutherland, *Rev. Sci. Instrum.* **66**, 1 (1995)]

σ with time reflects the decay of current carriers and any changes in the carrier's momentum scattering time τ . In ordinary time-resolved transport measurements, τ is inaccessible. Here, however, τ is extractable since the decrease of σ with ω, the celebrated Drude tail seen in Figure 3(a) depends in a known way on $\omega\tau$. The time dependence of the momentum scattering rate τ^{-1}, reported here as characterizing compositely the electron-hole population, is plotted in Figure 3(b) along with the conductivity. Note that the decay time of tens of ns necessitated the use of single bunch operations (see Table 1).

U9B

The fluorescent emission from biological molecules excited by pulsed UV reveals important information on their photophysical and structural properties and can be carried out in natural aqueous environments for photon energies less than the 7 eV water cutoff. John Sutherland (BNL-Biology) and co-workers have been examining biological molecules such as peptides (protein building blocks) for some time using a fluorimeter capable of measuring the time decay of fluorescence and its polarization at preselected fluorescent wavelengths.

Until now, mapping out the wavelength dependence of the fluorescence decay time required time-consuming accumulations for each discrete wavelength, leading to inevitable gaps in emission wavelength and often necessitating that spectral resolution be compromised in order to reduce the time for each accumulation. This is no longer the case with the completion of a major new fluorimeter, capable of measuring the time decay spectrum *simultaneously* with an entire emission spectrum. The instrument uses a two-dimensional histogramming memory to associate the time of arrival of a fluorescent photon, detected with a microchannel plate (MCP)at the output of the fluorescence spectrometer, with the photon's position, detected with a position-sensitive anode placed after the MCP and over which the emission spectrum is dispersed. (See abstract under U9B for further details.)

Figure 4 illustrates, for the model system of pyrene dissolved in ethanol, the level of detail now available with the new instrument. Emission intensity is plotted versus both the emission wavelength and also the time after excitation by a 375 nm synchrotron pulse. In Figure 4(a), the decay of the initially excited singlet is apparent from the fluorescent decay at shorter wavelengths. Figure 4(b) emphasizes the behavior at longer wavelengths. Here, emission is predominantly from pyrene excimers, which are transient molecules comprising an excited pyrene molecule and its ground-state partner. The growth and subsequent decay of the excimer population can be followed in detail and modelled with rate equations coupled to those describing the singlet population. Such detailed dynamic information is available after only 10 to 30 minutes of averaging, releasing time for the experimentalist to explore additional parameters such as pH, temperature, or concentration. The improved data rate is especially important if limited single bunch operations are required to map out decays exceeding 19 ns, as was the case in this example.

UV Photoemission and Surface Science

Steven Hulbert
Chi-Chang Kao
NSLS

VALENCE BAND PHOTOEMISSION

Angle-resolved photoemission remains the tool of choice to study Fermiology, and near-Fermiology, of clean (U4A, U3C) and adsorbate-covered (U12B) surfaces. Angle-integrated photoemission studies emphasize density-of-states issues (U4A), sometimes at a photon energy which resonantly enhances one of the atomic constituents (U4B).

Over the past few years, K.E. Smith (Boston U.) has established a program to study one-dimensional electronic structure in solids. Specifically, he and his coworkers (K. Breuer, Boston U. and W. McCarroll and M. Greenblatt, Rutgers) have studied the quasi-one dimensional ternary transition metal oxides known as molybdenum bronzes using beamlines U4A and U13UA. These oxides display many unusual phenomena including quasi-1D electrical conductivity, metal-insulator transitions, periodic lattice distortions, and charge density waves (CDW). Importantly, large, stoichiometric single crystals of these oxides can be grown (McCarroll, Greenblatt). The structure of the Fermi surface in these oxides is of particular interest since it controls the lattice stability. Figure 1 presents the first measurement of a quasi-1D Fermi surface for a solid, in this case for $Li_{0.9}Mo_6O_{17}$ [*Phys. Rev. Lett.* 70, 3772 (1993)], measured using angle-resolved photoemission to determine the dispersion of the Mo 4d states across the Fermi level. This Fermi surface agrees well with theory, and allows these authors to predict the existence of significant phonon mode softening and/or a Peierls transition with a displacement vector of q = 0.7 Å^{-1}. These workers have also investigated the electronic structure of defects in the quasi-1D conductor $K_{0.3}MoO_3$, which are of interest since they are known to pin CDWs, but their nature is highly ambiguous. Defects in this material, created using photon stimulated desorption and inert gas ion bombardment, have led to the discovery of a metal/non-metal/metal transition as a function of defect type and density [see *J. Vac. Sci. Technol.* A12, 2196 (1994)].

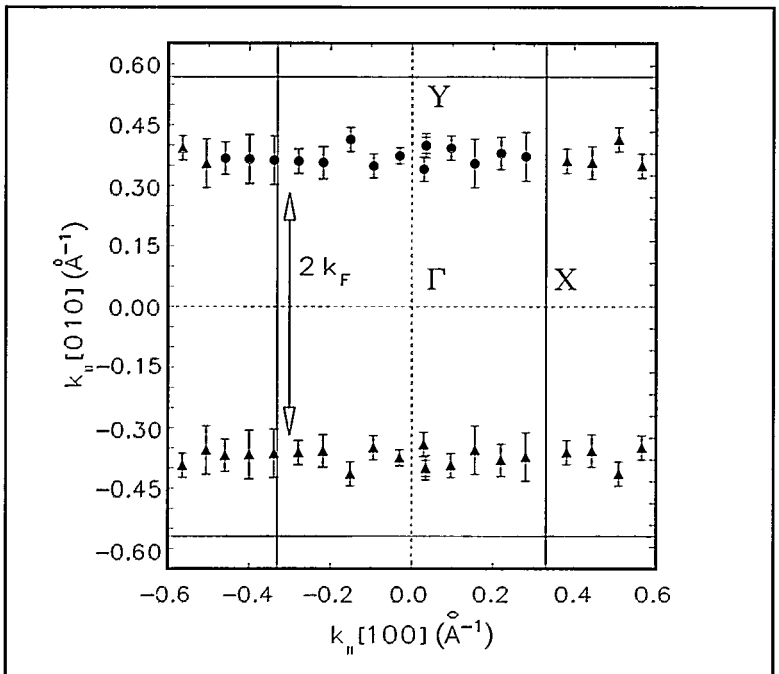


Figure 1 U4A: Quasi-1D Fermi surface for $Li_{0.9}Mo_6O_{17}$(001). $2k_F$=0.7± 0.05Å^{-1}. {dots}=measured data, {triangles}=symmetry points. [*Phys. Rev. Lett.* **70**, 3772 (1993)]

J. Chen (U. Penn.), H.H. Weitering (U. Tenn.), and N.J. DiNardo (Drexel) have performed an angle-resolved photoemission study of Cs adsorption on the Si(111) ($\sqrt{3}$x$\sqrt{3}$)R30°-B surface at beamline U12B. Cs induces formation of an interface state just below the Fermi level which disperses upward and across the Fermi level as the Cs coverage increases. Since this metallic transition is not observed for lighter alkali, it is concluded that the size of the adsorbate atom is crucial in determining the ground state properties of these interfaces. However, this transition cannot be a Mott transition because the saturation coverage of Cs on this surface at room temperature (6.65 Angstroms) is well below the critical density of a Mott transition.

A series of angle-resolved valence band

photoemission studies of single crystal heavy fermion compounds were conducted by the Los Alamos group (U3C). Along high symmetry directions, a modulation of the 4f intensity commensurate with the lattice periodicity was observed in $CeBe_{13}$ and $CePt_{2+x}$ (**Figure 2**). The variation in intensity is attributed to dispersion of the 4f states toward the Fermi level. In the case of $CePt_{2+x}$, the measured 4f dispersion is much larger than that expected for a periodic lattice of impurities.

G.K. Wertheim, J.E. Rowe, D.N.E. Buchanan, and P.H. Citrin (AT&T) have performed a systematic study to determine the valence band width and phonon width of twelve alkali halides. Using photoemission data, taken in their lab and at beamline U4A, and a fairly simple two-part theoretical analysis, the authors have been successful in extracting band widths and phonon widths which are in good agreement with various existing band structure calculations for these materials, and significantly smaller than the values obtained previously by other workers (Figure 3). The phonon widths obtained agree with a calculation due to Mahan, and indicate that the valence hole wave functions are quite localized.

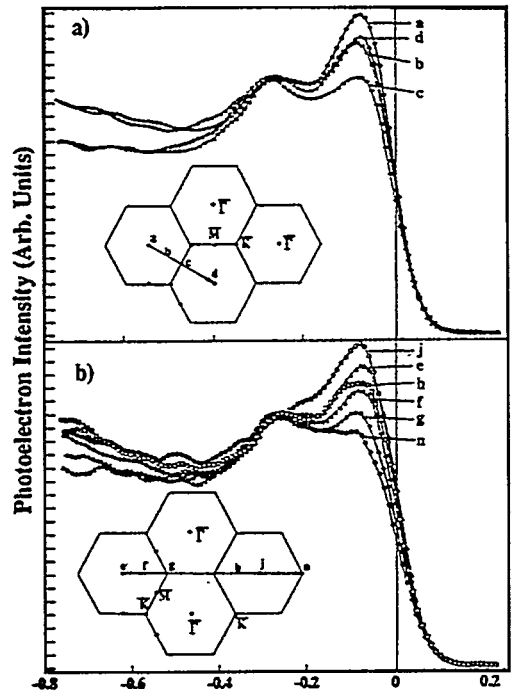


Figure 2 U3C: Angle-resolved photoemission scans from the Ce heavy fermion compound $CePt_{2+x}$ ($0 \le x \le 1$) at the indicated points along the high symmetry lines: (a) $\overline{\Gamma}$-$\overline{M}$ (spectra a-d) and (b) $\overline{\Gamma}$-$\overline{K}$ (spectra e-j). These scans reveal amplitude variations which match the lattice periodicity: The intensity near E_F is strongest at the $\overline{\Gamma}$ and $\overline{M}$ points (as far as the third zone) and decrease toward the zone boundaries.

CORE LEVEL PHOTOEMISSION

As in past years, core-level photoemission, both low and high resolution, was used to study a wide variety of systems, ranging from surface core level shifts in alkali halides (U4A) to surface reaction kinetics (U13UA, U7A).

D. R. Mullins and D. R. Huntley (ORNL) used the high flux × (resolving power) product at U13UA to study

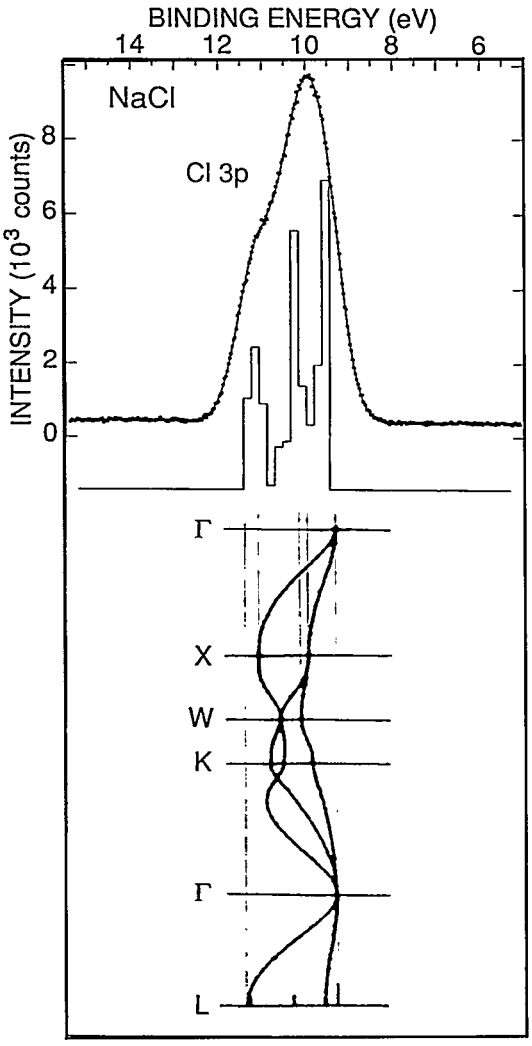


Figure 3 U4A: Top: Angle-integrated Cl 3p photoemission spectrum from NaCl. Middle: density-of-states (DOS) histogram obtained from the experimental data using least-square methods in which the phonon width, which is convoluted with the histogram, and the amplitude of each bin are varied, for fixed energy origin and fixed bin width. Bottom: NaCl band structure calculated by Erwin and Lin [*J. Phys.* **C21**, 4285, (1988)]. The agreement between the optimum histogram and the calculated DOS is very good, except for the weak contribution from states near the Γ point.

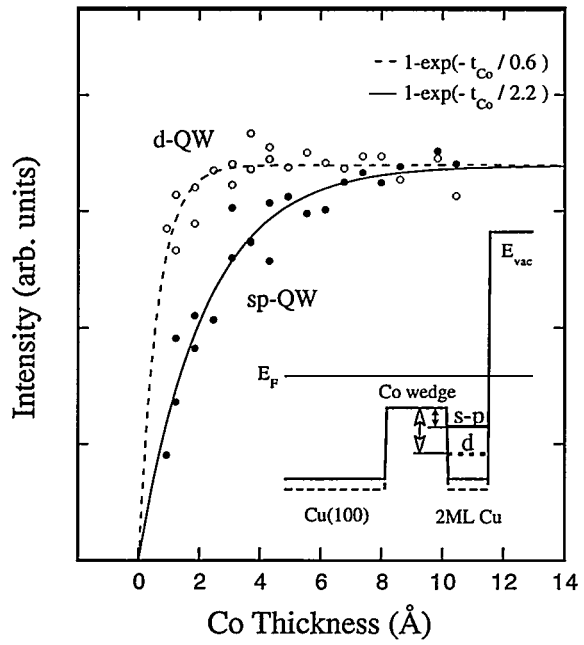


Figure 4 U5U: Peak intensities of the *sp*-derived quantum well (*sp*-QW) state at 1.6 eV binding energy (solid circles) and the *d*-QW state at 2.4 eV binding (open circles; normalized to the same saturation intensity as the *sp*-state) indicating a more pronounced quantum confinement by the Co barrier for the *d*-QW state. Solid and dashed curves represent the experimental fits as indicated in the upper right, where t_{Co} is the Co thickness. Inset: minority spin electron energy potentials experienced by *sp*-(thick solid line) and *d*- (thick dashed line) electrons based on the bulk band structures. The energies for the two QW states of two monolayers of Cu (thin solid and dashed lines) and their energy differences from the top of the corresponding energy barriers (arrows) are also indicated.

the adsorption and reaction kinetics of sulfur-containing molecules (e.g. methylthiolate and thiolate intermediates) on Ni(111) as a function of coverage, temperature, and time. They are able to determine, for example, the activation energy for intramolecular (e.g. carbon-sulfur) bond scission, molecule-molecule interactions (crowding), and interactions along domain boundaries.

The development and understanding of a novel dielectric thin film deposition technique using UV and soft x-ray induced reaction, described in the 1993 Activity Report, has continued at full strength by J.F. Moore, S. Chaturvedi, D.R. Strongin (SUNY-Stony Brook), M. Strongin, and M.W. Ruckman (BNL-Physics) using beamlines U7A and U13UA. The technique involves condensing a reactive mixture of gases (e.g. tetramethylsilane + water or borane + ammonia) onto a substrate at low temperature (80 K), and subsequently exposing the reactants to either white or monochromatic radiation in order to convert them into dielectric films (silica or boron nitride, respectively). The unreacted materials or volatile products are then desorbed by warming the substrate to ambient temperature. In order to better understand the reaction mechanism, this group also studied a simpler system: the formation of deuterated water by white-light irradiation of mixtures of deuterium and oxygen on a silver substrate at low temperature (4 K). They conclude that the reaction is selectively photo-induced rather than via a thermal mechanism.

SPIN-POLARIZED PHOTOEMISSION

Much progress continues to be made in the experimentally-challenging field of spin-polarized photoemission, where the surfaces under study are generally quite reactive and the spin detectors are, to date, relatively inefficient and require their own "care and feeding".

The U5U spin-polarized photoemission beamline continues to operate at the forefront of the valence-band spin-polarized photoemission field. During FY 1994, the U5U program concentrated on two interesting problems: (1) quantum well states in magnetic multilayers and (2) temperature dependence of the exchange splitting of the 5d states of gadolinium. A group consisting of P.D. Johnson, K. Garrison (BNL-Physics), Q.-Y. Dong (NSLS), N.V. Smith (ALS, LBL), D. Li, J.E. Mattson, J. Pearson, and S.D. Bader (ANL) used angle-resolved spin-polarized photoemission to measure the effective mass of the quantum well states in thin Cu films deposited on a Co(001) substrate. Their work reveals that hybridization in the Cu/Co interface leads to a large increase in the in-plane effective mass of the electrons in the very thin (≤6 monolayers) Cu films. This in turn has implications for theories of exchange coupling in this system, because the Fermi surface of the ultrathin Cu layer is different from that of bulk Cu. Members of this group (Li, Pearson, Mattson, Bader, and Johnson) also studied a complementary system consisting of a thin Co wedge sandwiched between a thin (2 monolayer) Cu film and a bulk Cu(100) substrate. For thick (>8 Angstroms) Co in this system, they observe *d*-band derived (2.4 eV binding energy) quantum well states (*d*-QW) in addition to the well known *sp*-band derived (1.6 eV binding energy) quantum well states (*sp*-QW). As shown in **Figure 4**, the intensities of both of these QW states increase rapidly with Co thickness. The intensity vs. Co thickness curves indicate stronger confinement of the *d*-QW state than the *sp*-QW state, in semiquantative agreement with a tight-binding slab calculation. Spin-polarized photoemission was also used to investigate the temperature dependence (130-350 K) of the exchange splitting of Gd(0001) for both the surface

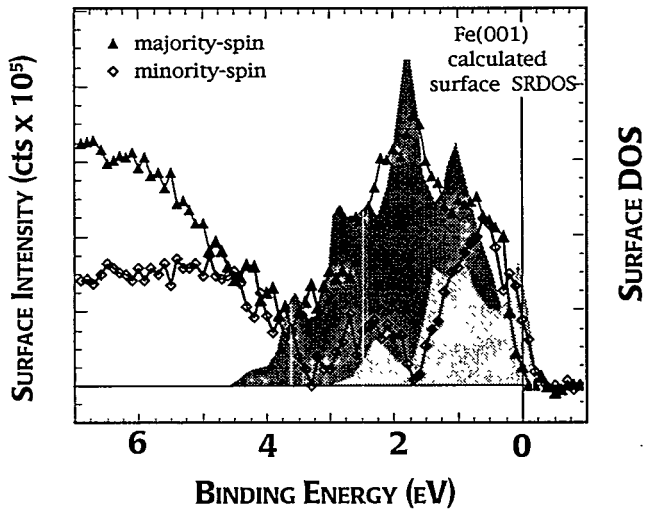


Figure 5 U13UA: Spin-polarized soft x-ray (hυ=260 eV) valence band photoemission, a good experimental determination of the total density-of-states (DOS), was performed on a polycrystalline Fe film in order to compare with calculation. Data points: majority-spin (filled up triangles) and minority-spin (open diamonds) difference spectra obtained by subtracting calculated Fe *bulk* density-of-states (DOS) from the measured spin-resolved photoelectron spectra. Shading: Calculated [S. Onishi, A.J. Freeman, and M. Weinert, *Phys. Rev.* **B28**, 6741 (1993)] *surface* Fe(001)majority (dark shading) and minority (light shading) DOS. Inset: deduced surface spin polarization as a function of electron mean free path. The deduced surface spin polarization of 40±3% is 20±10% greater than that of bulk Fe at room temperature, which is in qualitative agreement with the enhanced surface magnetization predicted for both Fe(001) and Fe(110) surfaces.

state near the Fermi level and the 5d bulk band at 1-2 eV binding energy. Whereas the temperature dependence of the exchange splitting of the 5d states is Stoner-like (proportional to the bulk magnetization), the surface state components do not shift with temperature. In addition, the intensity of the majority surface component is constant vs. temperature and the spin polarization decreases dramatically at the surface Curie temperature. Thus, the polarization changes of the surface state do not originate from collapse of its exchange splitting, but instead, follow the spin mixing behavior expected for a disordered local-moment model of the spatially localized surface state. This difference in behavior is all a manifestation of the different degree of itineracy of the 5d electrons in bulk vs. surface states.

In addition, the two angle-integrated spin-polarized photoemission experimental chambers, which were commissioned during FY 1993 (see the 1993 Activity Report), are now both producing high quality soft x-ray spin polarized photoemission data, at beamlines U13UA, X1B, and U4B. These new experimental stations, combined with the high resolution spherical grating monochromators at these beamlines, make it possible to study the 2p core levels of the 3d transition metals and their compounds, thereby contributing to the understanding of the origin of spin polarization in core-level photoemission.

The NYU spin-polarized photoemission station developed by Boris Sinkovic and his group at NYU was dedicated to studies of iron thin films during FY 1994. One set of experiments by this group was performed on thick (50 Angstroms) polycrystalline iron films evaporated on a polished aluminum substrate. In one experiment, spin-polarized valence band photoemission using 260 eV soft x-ray photons was shown to provide a good experimental determination of the spin-resolved density of states (SRDOS) of iron. The most interesting aspect of this experiment is that the differences between these spectra and calculated bulk iron SRDOS are extremely well accounted for by the calculated *surface* iron SRDOS (**Figure 5**). That is, the SRDOS of just the surface layer of iron has been experimentally determined, for the first time. Another experiment on thin iron films studied the spin polarization of the iron LVV Auger spectrum, both on and off the iron 2p-to-3d resonance.

The BNL Physics Department spin-polarized photoemission station developed by J. Xu and P.D. Johnson (BNL-Physics) is now in operation: during FY 1994, it was used for experiments at beamlines X1B and U4B. The spin-polarized program at X1B has concentrated on studies of the 3s and 3p core levels of the elemental materials Fe, Co and Ni. The reason for this is that although core levels offer the important possibility of obtaining site-specific magnetic information, it still remains unclear as to exactly how the observed polarization in the core level relates to the local magnetic moment. A study of the Fe 3s level (X1B) clearly resolves the different spin dependent components of the 3s multiplet for the first time and confirms a picture where the excitation process is dominated by atomic configuration interactions. A team consisting of Z. Xu, Y. Liu, P. D. Johnson (BNL-Physics), B. Itchkawitz, J. Feldhaus, A. Bradshaw (Fritz-Haber Institut, Berlin), and K. Randall (APS, ANL) has measured a binding energy separation of 3.4 eV between high spin and low spin ionic states, which is smaller than previously measured but in closer agreement with calculation. Line shape fitting (**Figure 6**) provides

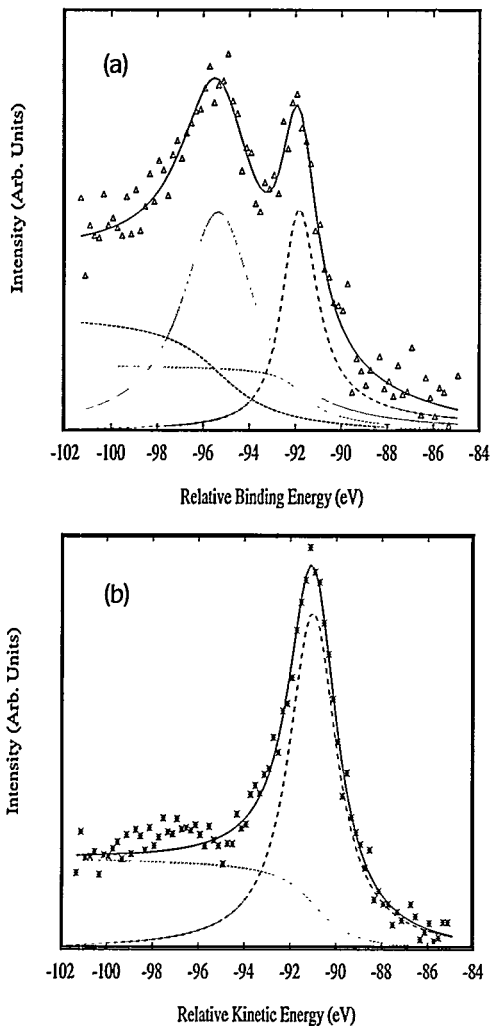


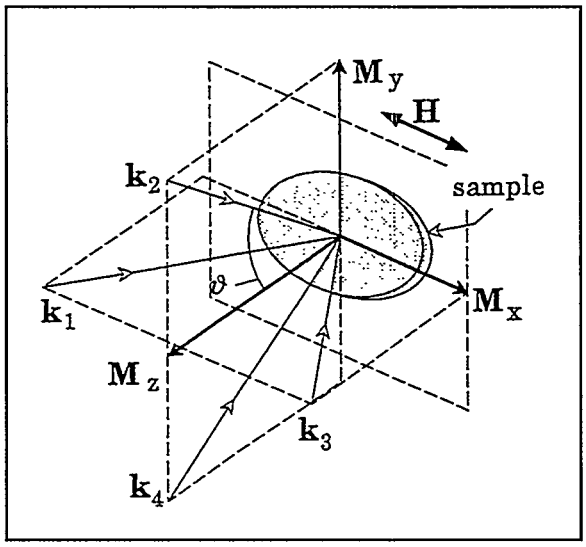
Figure 6 X1B: Soft x-ray core level spin-polarized photoemission of the Fe 3s level in a thin Fe film clearly resolves the different spin dependent components of the 3s multiplet for the first time. The binding energy separation between high spin and low spin ionic states is 3.4 eV, which is smaller than previously measured but in closer agreement with calculation. Line shape fitting provides evidence that the individual peak widths reflect the total spin of the ionic final state rather than the spin of the core hole. (a) Line shape fitting for the majority spin spectrum. Each peak is fitted with a Doniach-Sunjic lineshape and individual bacgrounds. The solid line through the experimental points indicates the integrated fit. (b) As in (a), but for the minority spin channel.

evidence that the individual peak widths reflect the total spin of the ionic final state rather than the spin of the core hole. These widths may reflect the coupling of the different atomic states to the conduction bands, i.e. a solid state effect. Thus, the low spin state would be broader because it is derived from more atomic configurations. A study of the Ni 3p core level (X1B) has provided important insight into the interplay between the spin-orbit coupling, exchange interaction and hybridization in this relatively shallow core level. For the first time, Y. Liu, Z. Xu, P. D. Johnson (BNL-Physics) and G. van der Laan (Daresbury) have been able to show clearly the role of the d^9 configuration in both the main line and the satellites. Their new analysis reverses some of the earlier theoretical assignments in the "spin-orbit split" main peak. In particular, they find that the main peak's leading edge has predominantly ($3p^5,3d^9$) character whereas a shoulder at higher binding energy reflecting the spin-orbit interaction has predominantly ($3p^5,3d^{10}$) character.

K. Starke, E.E. Chaban, C.T. Chen (AT&T), Y. Liu, P.D. Johnson (BNL-Physics), and V. Chakarian (NRL) have performed the "complete" polarization-sensitive photoemission experiment by using the BNL Physics spin-polarized photoemission station at beamline U4B. Using circularly polarized soft x-rays from U4B and spin-polarized photoelectron detection, they were able to examine the spin polarization of the 4f core level photoelectrons in non-magnetic tungsten. This observation, a proof-of-principle experiment, opens new perspectives for spin-dependent diffraction and inelastic scattering experiments, a field which is especially relevant in view of the wide use of tungsten as a substrate for ferromagnetic rare earth and transition metal overlayers.

SOFT X-RAY MAGNETIC CIRCULAR DICHROISM (MCD)

The AT&T U4B Dragon beamline continues to be the hotbed in the development of soft x-ray magnetic circular dichroism. One of the important issues in MCD is the validity and applicability of the sum rules [see B.T. Thole, *et al.*, *Phys. Rev. Lett.* **68**, 1943 (1992) and P. Carra, *et al.*, *Phys. Rev. Lett.* **70**, 694 (1993)] which, in principle, can provide element-specific spin and orbital moments of the sample without relying on model-dependent theoretical analysis of the spectral lineshape. However, rigorous testing of these sum rules has been hampered by many subtle experimental artifacts that can dramatically affect the outcome of the sum rule analysis. To overcome these problems, the AT&T and NRL collaborators have made new transmission MCD measurements on a number of 3d transition metals in which the transmitted photon intensity was used to derive the absorption coefficient. From these new results, the ratio of orbital moment to spin moment in Fe and Co were derived, and found to agree with results from gyromagnetic ratio (GMR) measurements to within a few percent. In addition, by using 3d occupation numbers from first principle band structure calculations and a parameter-free background re-



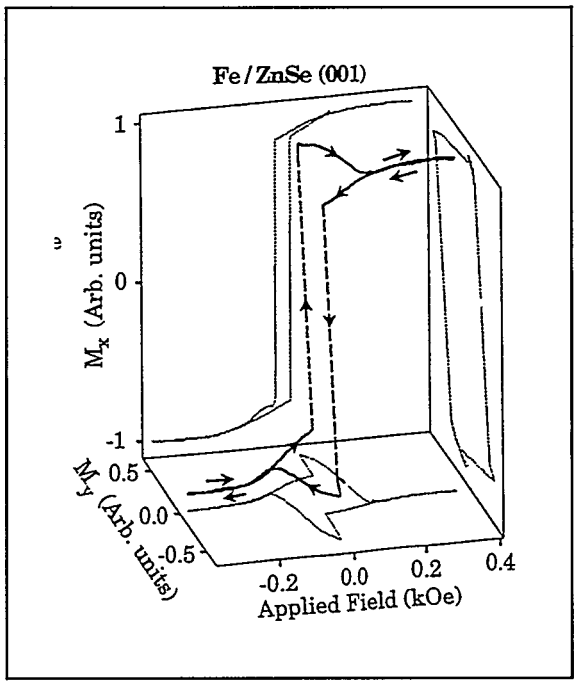


Figure 7 U4B: (a) Experimental arrangement for the use of soft x-ray magnetic circular dichroism (SX-MCD) as a tool for element-specific, 2D and 3D vector magnetometry of magnetic thin films and multilayers. The applied field is provided by a switchable UHV-compatible electromagnet assembly. Hysteresis curves taken at 90 degree intervals of azimuthal rotation of the magnetization direction permit unique determination of the individual components of the magnetization vector (V. Chakarian, *et al.*, to be published).

(b) 3D view of the two dimensional rotation of the measured magnetization vector $\vec{M}$ for a 30 Å Fe(001) single-crystal thin film supported on ZnSe(001) substrate. Note that this film exhibits only in-plane magnetization, i.e. $M_z = 0$.

moval, the spin and orbital moments were determined independently from the data, and found to agree with the GMR results to within 10%. These new findings are clearly important first steps in establishing MCD as a reliable technique in determining element-specific orbital and spin moments.

Novel applications of MCD also continue to be developed at the Dragon beamline. One notable example is the development of element-specific vector magnetometry for magnetic thin films and multilayers by the NRL and AT&T collaboration. In vector magnetometry, the trajectory of individual components of the magnetization vector $\vec{M}$ are traced out in the hysteresis loop measurement. Since the magnitude of the MCD effect is proportional to the projection of the photon wave vector onto the magnetization vector, the components of the magnetization can in principle be determined by measuring hysteresis loops using the MCD effect at several selected combinations of incident photon angles and applied field ($\vec{H}$) directions. Experimentally, the combinations are achieved through an UHV compatible electro-magnet assembly, which allows, for any given incident photon angle, arbitrary selection of applied field direction in the azimuthal plane. Figure 7a shows a schematic of the experimental configuration.

As an example, the magnetization behavior of a 30 Å Fe(001) single-crystal thin film was measured. In this system, $\vec{M}$ is restricted to rotate in the plane of the film, and the lack of an M_z component was verified directly by measuring a null hysteresis signal when the photon beam is incident normal to the thin film. The two in-plane components were then determined by making measurements along k_1 and k_2 (or alternately, k_3 and k_4, see Figure 7a). A 3D view of the two dimensional rotation of the measured $\vec{M}$ is shown in Figure 7b. In this view, the M_x, M_y and M_x vs. M_y curves are all visible as projections on the back, bottom, and right planes, respectively. This information can then be used to model in detail the magnetization reversal process. More importantly, the MCD effect adds element specificity to vector magnetometry, so that it can provide valuable new information to the study of the magnetization process of many heteromagnetic systems.

There are also new developments in resonant magnetic scattering using either linear or circularly polarized soft x-rays. For example, the superlattice magnetic Bragg peak from a Ag/Ni multilayer with antiferromagnetic coupling between the Ni layers was observed by the

CNRS, NSLS, and AT&T collaboration. The magnetic scattering cross section is dramatically enhanced by tuning the photon energy through the $L_{2,3}$ edge of Ni. The intensity of the magnetic reflection is on the order of five percent of that of the charge peak, and a detailed analysis shows that the magnetic scattering amplitude is as high as 8 r_o per Ni atom (J.M. Tonnerre, *et al.*, First European Conference on Synchrotron Radiation in Materials Science, Chester, 3-8 July 1994, to be published in *Nucl. Instrum. and Methods B*).

NEAR EDGE SOFT X-RAY ABSORPTION FINE STRUCTURE

Near edge absorption fine structure (NEXAFS) using linear polarized soft x-rays, especially polarization dependent measurement and fluorescent detection, continues to find new applications in solving materials problems. For example, a combination of fluorescent-yield and polarization dependent Carbon K edge absorption spectroscopy was used to study the nature of the bonding at buried metal/polymer interfaces in order to optimize adhesion at the interfaces in new generation multilayer interconnect devices (NIST, U. Michigan, and Dow Chemical collaboration at U1). Polarization anisotropy was also used to correlate the orientation of a self-assembled monolayer of hexadecylsilane on silicon oxide with the wettability of the resulting surface (NIST, Lehigh, and Dow groups at U1). The goal of this study is to control interfacial interaction by chemically modifying a substrate surface through the adsorption of a self-assembled monolayer. Finally, researchers from Exxon at U1 also used NEXAFS extensively in their effort to understand the electronic and catalytic properties of early transition metal carbides.

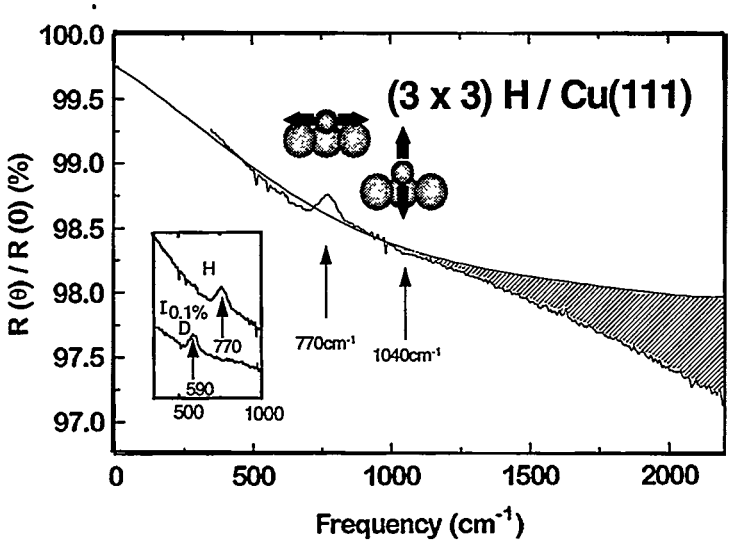


Figure 8 U4IR: Far infrared (FIR) differential reflectivity measurement of an ordered (3 x 3) overlayer of hydrogen on a Cu(111) surface. The data were taken using an f/10 FIR beam incident at 3 degree grazing angle of incidence. The smooth curve is a calculation due to B.N.J. Persson, *et al.* [*Phys. Rev.* **B44**, 3277 (1991) and *Surface Science* **310**, 314 (1994)]. Inset: anti-absorption peaks associated with dipole forbidden parallel vibrational modes for H (770 cm^{-1}) and D (590 cm^{-1}) in three-fold hollow sites on Cu(111). The perpendicular vibrational mode at 1040 cm^{-1} for H in 2-fold bridge sites reported by McCash, *et al.* [*Surface Science* **215**, 363 (1989)] is not observed in the present measurements, implying that all H atoms sit in three-fold hollow sites.

FAR INFRARED SPECTROSCOPY

In the subfield of surface vibrational spectroscopy, there were two major developments involving the measurement of vibrational modes of atoms/molecules other than hydrogen on a metal surface. The first of these is the observation of the vibrational modes of oxygen on the Cu(100) surface: the mode corresponding to oxygen vibrating perpendicular to the surface was at 350 cm^{-1}, caused a reflectivity change of less than 0.1%, and had a width of 75 cm^{-1}. An accompanying broadband change indicates that the dynamics involve electron-hole pair creation. This measurement was made possible by the use of a new Michelson interferometer. This interferometer was also used to investigate, for the first time, the bonding vibrational modes for isotopic mixtures of CO on Cu(111) and Cu(100). Such an experiment allows dipole-dipole and other coupling interactions between molecules on surfaces to be separated from chemical or bonding effects.

Another experiment, involving atomic hydrogen on Cu(111), helped to clarify a new theory of low frequency surface dynamics. A strong dipole-forbidden anti-absorption resonance was observed for this system in the presence of a broadband background change (Figure 8). The anti-resonance corresponds to the parallel vibrational mode as confirmed by measurements on deuterium.

X-Ray Absorption Spectroscopy

Lars Furenlid
NSLS

X-ray absorption spectroscopy (XAS) continues to flourish as a research tool at the NSLS, and 1994 continued a trend of steady productivity among the beamlines carrying out XAS at the facility. There are now eight beamlines on the X-Ray Ring and two on the UV Ring which perform absorption spectroscopy on at least a half-time basis. These include U1, U16B, X6A and B, X9B, X10C, X11A, X18B, X19A, X23A2, and X23B. In addition, specialized XAS experiments are being performed on the microscope at X1A, the microprobe on X26A, and on the very intense insertion device beamline X25. U4B is used for circular dichroism studies, and several other of the UV beamlines are occasionally used for NEXAFS studies. The science reported in the abstracts from these beamlines covers a wide range of scientific fields, but they may be broadly classified into a limited set of categories as either catalysis, biology, surfaces/thin films, solid state/materials science, or technique development. Presented below are some selected highlights from FY 1994 research activities in each of these fields.

The extended x-ray absorption fine structure (EXAFS) technique is a powerful tool for determining structural aspects of sample systems which lack long-range order and are unsuitable for x-ray diffraction studies. These include solutions, clusters, amorphous powders, heterogeneous mixtures, and thin films. It can provide coordination numbers and bond lengths about a selected central atom for neighbors up to 5 Å away. X-ray absorption near-edge spectroscopy (XANES) provides complementary information about elements' oxidation states and geometries. Samples can be solid, liquid, or even gaseous; at any temperature and any pressure. This versatility has resulted in the application of XAS to a vast range of problems. The literature now contains some 9000 papers which list one of the XAS acronyms (XAS, EXAFS, and XANES) among its key words. Materials science (including semi- and super-conductor physics) is the largest single field contributing to this list, but virtually all the physical and life sciences sooner or later find a use for XAS or related techniques.

The sophistication of the average experiment is continually rising, both in terms of the measurement techniques employed and in the conditions to which the samples are subjected. For example, more and more experiments utilize the polarization characteristics of the beam, both linear and elliptic.

CATALYSIS

Many of the industrial beamline developers and PRT members at the NSLS have research in the area of catalysts among their top priorities for their synchrotron science. Much of the most interesting work presumably remains proprietary, of course, but there are a number of reported experiments which give a flavor for the way XAS is employed in catalysis research. For example, J.A. McCaulley (Hoechst Celanese) and F.W. Lytle (The EXAFS Co.) report work at X11A on a carbon supported palladium catalyst system over a range of temperatures while under an ethylene/hydrogen gas mixture. As evi-

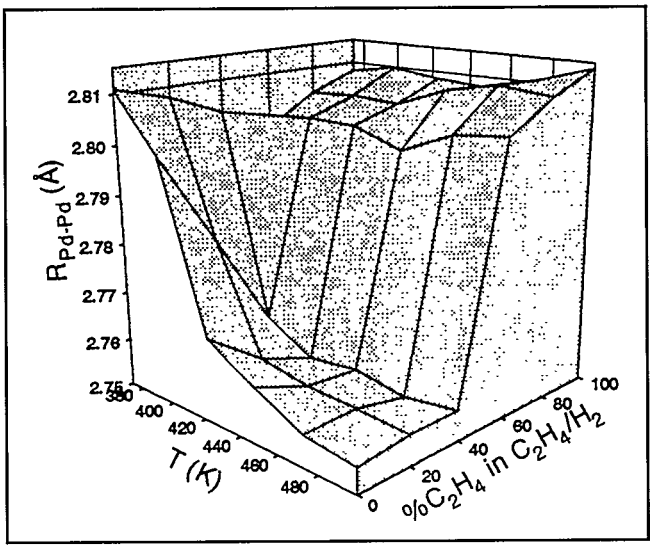


Figure 1 X11A: Dependence of the nearest-neighbor Pd-Pd distance on temperature and composition in C_2H_4/H_2 mixtures.

dent in Figure 1, they find a complex pattern of Pd lattice expansion as determined by the increase in Pd-Pd distance as the temperature is varied over the range of 373-498 K and the ethylene content is varied between 0 and 100%. The resulting three-d plot is a kind of phase diagram, with a Pd-H_x phase at one end and a Pd-C_x phase at the other.

Working on X18B, J.E. Tabora and R.J. Davis (U. of Virginia) have investigated sulfated zirconia systems which catalyze the isomerization of butane. Extending previous x-ray diffraction work by studying nano- and non-crystalline material, they find evidence from Zr EXAFS measurements that the average bond lengths for the first shell oxygens and outer shell Zr-Zr are consistent with all samples being in a strictly tetragonal geometry, regardless of composition as varied by the addition of Fe or Mn. The lack of a Fe-Zr contribution is taken as evidence that Fe ions do not directly substitute into the zirconia structure.

D.-J. Liu and H.J. Robota (AlliedSignal) have reported on the development of an *in situ* system for catalysis research over a number of years. In work on X18B in the past year, they studied Cu-ZSM-5, a candidate system for the decomposition of NO generated during combustion into nitrogen and oxygen gas. The researchers found with a combination of XANES and EXAFS measurements that in freshly prepared catalyst, the Cu is in the +2 oxidation state and has an average coordination of about five oxygens, originating from both zeolite and adsorbed water. Upon calcination in dry air at 500°C, the water ligands are lost, but the copper remains divalent. Upon He gas flow at elevated temperatures, the Cu is reduced to Cu(I) with a coordination number of two. A greatly enhanced 1s-4p peak is observed, as is consistent with formation of a linear Cu(I) complex.

S.R. Wasserman (ANL), F.W. Lytle (The EXAFS Co.), S.L. Suib (U. of Connecticut), and R.E. Winans, K.A. Carrado, S.E. Yuchs, and R.L. McBeth (ANL) investigated manganese oxide photocatalysts on X23A2. Comparing the near-edge and EXAFS spectra of several synthesized catalysts with the natural minerals cryptomelane and todorokite, the researchers conclude that one of their two OMS (octahedral molecular sieves) samples has manganese in a chemical environment essentially identical to that in cryptomelane. However, the second OMS sample has a lower average oxidation state than the corresponding todorokite mineral.

S.R. Bare, L.N. Ito, and M. Cisneros (Dow Chemical) studied carbon supported bimetallic Pt/Cu catalysts on X23A2 as part of a program to fully characterize catalysts which may assist in the conversion of halogenated hydrocarbons into products with higher value.

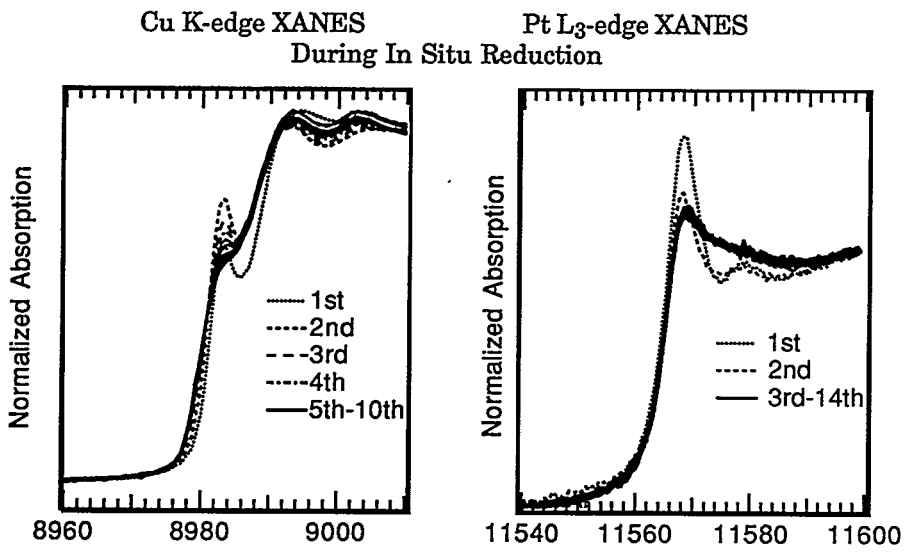


Figure 2 X23A2: XANES spectra at the Cu K-edge (left) and Pt L_3-edge (right) during *in situ* reduction of a carbon supported bimetallic Pt/Cu catalyst.

They measured the Cu K-edge and Pt L_3-edge XANES during *in situ* reduction, reaction, and re-reduction. Shown in Figure 2 are the metal edges during a reduction step. Analysis of the subsequent EXAFS data shows that true bimetallic particles do indeed exist after reduction.

BIOLOGY

The importance of XAS as a tool for structural studies of biological molecules was recognized early on in the modern era of synchrotron science. The large number of atoms in typical metalloproteins makes spectroscopy in the conventional energy domains, for example visible or

infra-red, virtually impossible to interpret. Since the metals in metalloproteins are often the site of the "action", the elemental specificity of XAS provides a great benefit in the study of enzyme-substrate interactions. However, biological EXAFS experiments seem to always involve dilute systems and the potential for x-ray damage, so they are require great care.

M.J. Nelson, B.A. Brennan, J.G. Cummings (DuPont) and S. Rehman, J. Kindt, and R.C. Scarrow (Haverford College) report studying nitrile hydratases on X9B. Two classes of these enzymes, which catalyze the hydration of nitrile groups to amides, are differentiated by containing either iron or cobalt. In previous work, the researchers have shown that the iron form has six fold coordination with three nitrogens, two sulfurs, and one oxygen. In current work on the cobalt analog, the data in Figure 3 suggests that the cobalt has a similar coordination environment. This would be the first report of a Co-S metalloprotein, though confirmation requires further experiments.

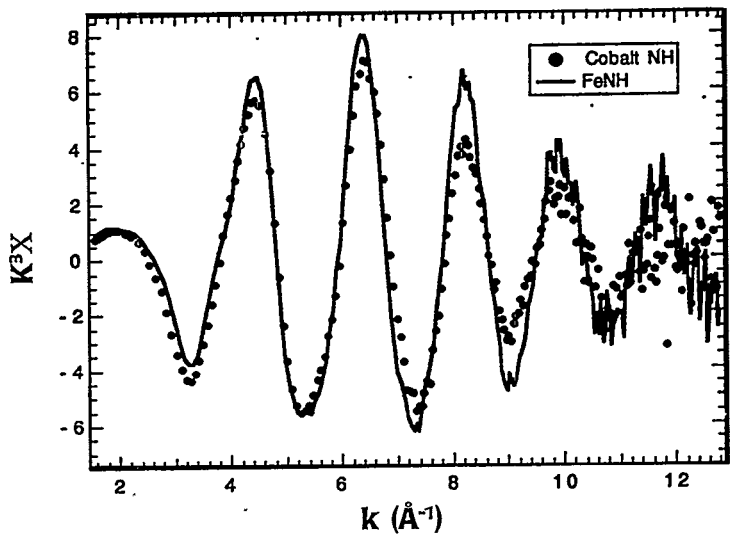


Figure 3 X9B: K^3 weighted experimental EXAFS spectra of iron-containing and cobalt-containing nitrile hydratase.

C.Y. Ralston, B.J. Weiss, J.H. Christiansen, D. Le and S.P. Cramer (U. of California - Davis), and M. Kumar and S.W. Ragsdale (U. of Nebraska - Lincoln) report work on carbon monoxide dehydrogenase on beamline X10C. This nickel and iron containing enzyme catalyzes two different reactions, the oxidation of CO to CO_2 and the synthesis of acetyl CoA, at two different sites. In these experiments, metalloenzyme isolated from *Clostridium Thermoaceticum* bacteria were investigated after treatment with phenanthroline (which removes nickel from one site) and reconstitution with cobalt. The cobalt EXAFS was interpreted to result from 2 S at 2.27 Å and 2-3 N/O at 2.06 Å and a long Co-Fe interaction at 3.01 Å. This might be similar to the native Ni coordination in the same site.

D.L. Tierney and J.E. Penner-Hahn (U. of Michigan) and L.M. Walrath and J.M. Berg (Johns Hopkins U.) performed an unusual experiment in measuring the Zn K-edge spectra of zebra fish eggs on X19A. Measuring eggs in different stages of their development: before fertilization, shortly after fertilization, and after embryo development is well underway, the researchers found significant changes. EXAFS measurements on the unfertilized eggs were most consistent with a largely ZnS coordination environment

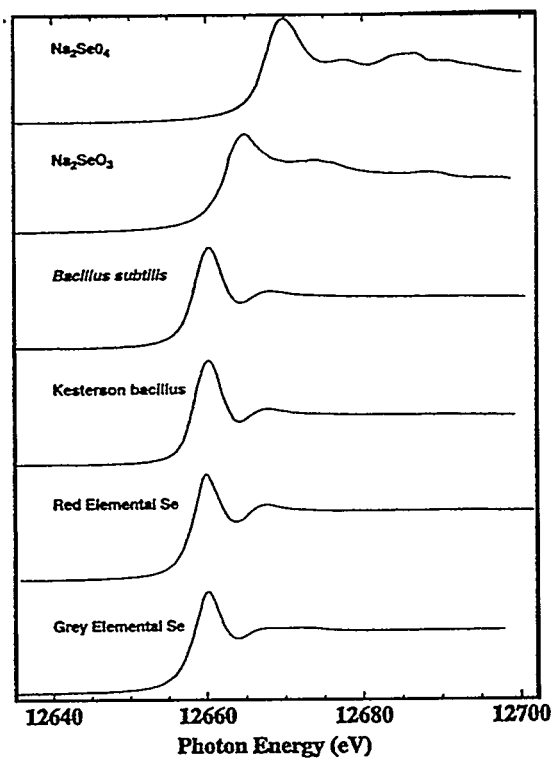


Figure 4 X23A2: The Se K-edge XANES spectra of bacteria after uptake from a selenate solution and comparison to Se reference materials.

which has been suggested to result from sequestering in some sort of storage site. The zinc then presumably ends up in a more heterogeneous mixture of sites during later development and activation of regulatory proteins involved in growth. More experiments are planned to fully characterize these changes.

The bioremediation of selenium by microbes was studied on X23A2 by the following research team: B. Buchanan (U. of California - Berkeley), J. Bucher (LBL), D. Carlson (UCB), N. Edelstein (LBL), E. Hudson (LLNL), N. Kalstoyannis (LBL), T. Leighton (UCB), W. Lukens (LBL), H. Nitsche and T. Reich (Forschungszentrum Rossendorf e.V.), K. Roberts, D.K. Shuh, P. Torretto (LBL), J. Woicik (NIST), W-S. Yang (Jackson State U.), A. Yee (LBL) and B.C. Yee (UCB). XANES measurements were taken on aerobic soil bacteria which incorporate selenium when exposed to ions in aqueous solution. Comparison of the edge spectra of the Se in the bacilla with standard selenium containing models shows that the microbes reduce the selenium ions to the red form of elemental selenium. This makes bioremediation a potentially viable strategy for cleanup of some selected contaminated sites. The XANES spectra in **Figure 4** clearly display the change in oxidation state from Se(VI) and Se(IV) to Se(0).

Another highly toxic element is chromium when it is in the +6 oxidation state. B.L. Illman (Forest Products Laboratory, U. of Wisconsin), D.G. Schultz (Purdue U.), and S. Bajt and S.R. Sutton (U. of Chicago) studied the XANES spectra of chromium in Chromated-Copper-Arsenate treated lumber, commonly called pressure treated wood. In experiments on the microprobe beamline X26A, *in situ* scans of treated southern yellow pine clearly demonstrate that the chromium in Cr(VI)-CCA is reduced to Cr(III) upon contact with the lumber. The Cr was found to remain in the stable Cr(III) form both on the surface and in the interior of the wood two years after treatment.

SURFACE SCIENCE / THIN FILMS

The high intensity of the vuv and x-ray beams at a synchrotron source permit the investigation of materials only a few atoms or less in thickness, such as surfaces, thin films, and interfaces. Since chemical reactions on heterogeneous catalysts, corrosion, semiconductor production, and magnetic multilayer production all depend on detailed knowledge of surface or interface interactions, this is a very active field of research for both XAS and surface scattering/diffraction.

For example, in studies on U1A, B.M. Dekoven (Dow Chemical), D.A. Fischer (NIST), D.H. Parker, J.J. Curphy, and G.E. Mitchell (Dow Chemical), J.L. Gland

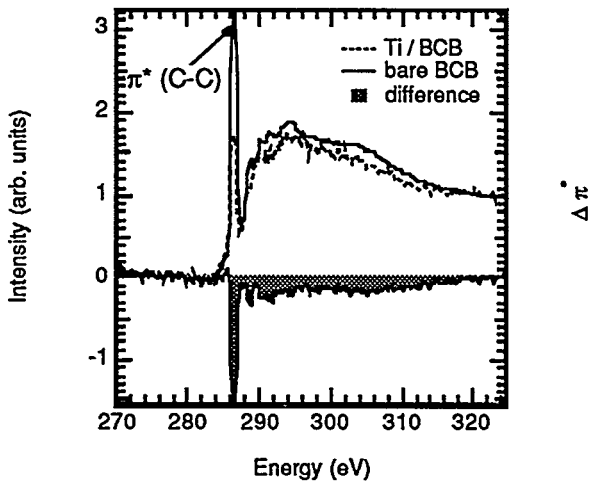


Figure 5 U1A: Carbon K-edge fluorescence yield NEXAFS spectra of benzocyclobutene polymer (BCB) on titanium metal versus pure polymer.

(U. of Michigan), and C.A. Wedelstaedt and S.J. Babinec (Dow Chemical) investigated the interface between metal connects and benzocyclobutene (BCB) polymer. This material combination is used in multilayer interconnects between multichip devices. Using C K-edge NEXAFS measurements on a variety of sample metals, the research team was able to identify changes in the aromatic content of the polymer, maximized when combined with Ti metal. This could be due to bond formation involving donation of charge to the π^* orbitals of the aromatic groups. The difference spectra as revealed in **Figure 5** show the clear attenuation in the π^* peak. As the thickness of the polymer layer is increased, the degree of attenuation is decreased.

J.G. Chen, B.D. DeVries, B. Frühberger, and M.S. Touvelle (Exxon) investigated carbide films formed on transition metals with NEXAFS measurements on U1. These metal carbides offer advantageous catalytic properties over their parent metals and are thus important research objects. For a vanadium metal sample, NEXAFS measurements were made at a fixed energy as further carbon was added to the surface via exposure to ethylene. In contrast to auger electron spectroscopy, which quickly reaches a saturation level due to its limited sampling depth, the fluorescence measurement demonstrates that carbide film growth continues until a V-C film of at least 10 Å is produced. The stoichiometry of these films is confirmed to be VC.

Y. Dao, R.J. Nemanich, and D.E. Sayers (NCSU) are

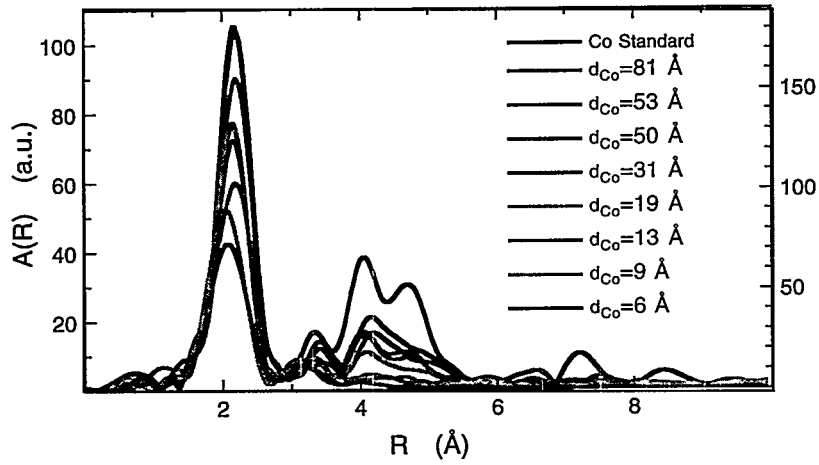


Figure 6 X23A2: Fourier transformed Co EXAFS data for (Ag,Co)-multilayers with different Co film thicknesses.

continuing a program of experiments on fundamental properties of materials important to the semiconductor industry. In previous experiments on X11A, they have characterized the properties of $TiSi_2$, an excellent material for contacts and interconnects in VLSI technology due to low resistivity and high thermal stability. In recent experiments, the researchers have grown $(Ti_{1-x}Zr_x)Si_2$ films on Si substrates and carried out EXAFS experiments to examine the local structure of the Ti and Zr atoms. They find that the Zr-Si bondlengths are shorter in the alloy film than in a pure $ZrSi_2$ film. The alloy film is also more ordered than a pure $TiSi_2$ film. There is some anisotropy in the ordering between the in- and out-of- plane directions.

A. Bartos and J.C. Woicik (NIST) performed experiments on X23A2 to investigate the local environment around Ag and Co atoms in (Ag,Co)-multilayer structures, of interest because of the observation of giant magnetoresistance. Working with 20-50 layer thick samples prepared on float glass via ion deposition techniques, the researchers were able to correlate trends in Co-Co bondlengths with deposition conditions and the Co layer thicknesses. As shown in **Figure 6**, the systematic variation in nearest-neighbor and next-nearest-neighbor amplitudes are quite dramatic.

V.G. Harris, N.C. Koon, and W.T. Elam (Naval Research Laboratory) have been studying iron-terbium films as part of an effort to fully understand these important commercial magnetic materials. In recent investigations on X23B, the researchers have studied the annealing properties of $Tb_{33}Fe_{66}$ amorphous films at various temperatures. By examining the Fe K-edge outer shell EXAFS amplitudes at 4.5 Å as an indicator of the degree of ordering, the team was able to conclude that not until the annealing temperature reaches 623 K is there a significant conversion to a crystallization product.

SOLID STATE AND MATERIALS SCIENCE

As mentioned in the introduction, the materials science field makes perhaps the heaviest use of synchrotron based XAS techniques. The *in situ* style experiments are becoming more and more prevalent, particularly when combined with electrochemistry. And the push for faster semiconductor materials motivate many studies of GaAs.

J.M. Bai (ANL/Brooklyn Coll.), S. Sivananthan (U. of Illinois), and P.A. Montano (ANL/U. of Illinois) investigated the ZnSe/GaAs interface on samples grown with molecular beam epitaxy techniques on X6B and X18B. They find that in comparison to pure GaAs, the interface Ga has a shorter nearest neighbor distance. However, the average As distance remains the same. The researchers conclude from consideration of this and other studies that a (Ga,Se) compound may form preferentially at the ZnSe/GaAs interface.

The area of battery technology is very active at this time, and a major change is taking place in the commercial marketplace as metal hydride electrodes are replacing cadmium in rechargeable alkaline nickel batteries. S. Mukerjee, J. McBreen, J.J. Reilly, G. Adzic, and J.R. Johnson (BNL) have been studying alloys suitable as such electrodes on X11A and X23A2. Many candidate materials are unstable to cycling, as a result of corrosion, and complex materials with as many as nine components are used. In recent studies on a $La_{0.8}Ce_{0.2}Ni_{4.8}Sn_{0.2}$ alloy, EXAFS and XANES results, as presented in **Figure 7**, indicate that after cycling 25 times there is evidence for $Ni(OH)_2$ formation. Quantitative analysis permitted the determination that approximately 6-7% of the Ni in the alloy has degraded.

In experiments on X11A, Q. Lu, B.A. Bunker, H. Luo, A.J. Kropf, S.H. Xin, J.K. Furdyna, and K.M Kemner (U. of Notre Dame) have explored the structure of II-VI semiconductors. Less studied than the III-V

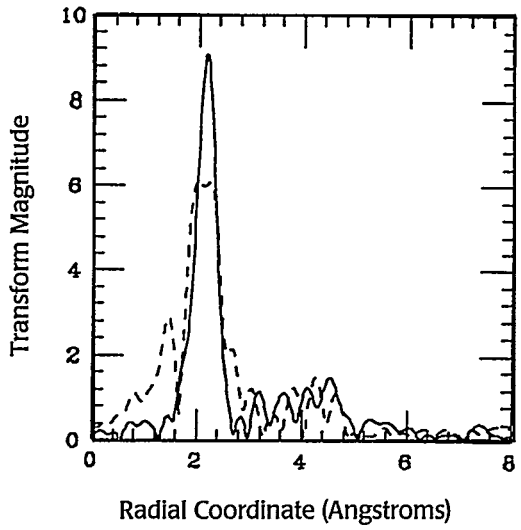
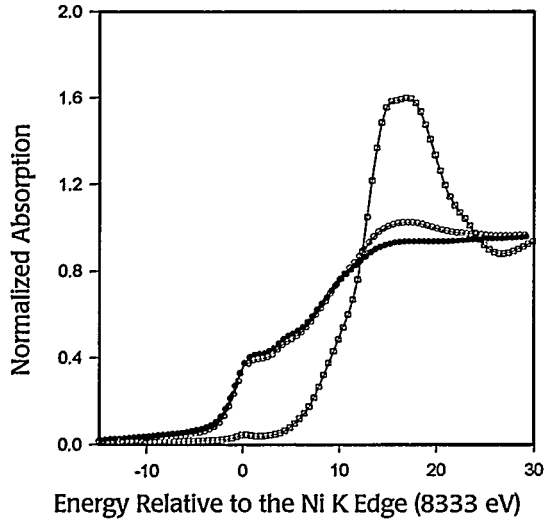


Figure 7 X11A: (top) Fourier transforms of Ni EXAFS for $La_{0.8}Ce_{0.2}Ni_{4.8}Sn_{0.2}$ battery electrodes uncycled (——), after 25 charge/discharge cycles (- - -).



(bottom) Ni edge XANES of same electrode, uncycled (o), after 25 cycles (O), and for $Ni(OH)_2$ (□).

semiconductor class, II-VI semiconductors have drawn increased attention as a result of their successful use in blue-green laser diodes. EXAFS measurements on a $Zn_{0.5}Cd_{0.5}Se_{0.5}Te_{0.5}$ alloy grown by MBE on a GaAs substrate shows that there are approximately 2.6 Zn-Se bonds and 1.4 Cd-Se bonds on average, rather than the 2.2 expected for a random alloy. The observed preference for Zn-Se over Cd-Se bonds agrees with previous work.

In one of the first XANES experiments reported from X11B, G. Frank of Hoechst AG and J.A. McCaulley of Hoechst Celanese investigated a system cited earlier in related C spectroscopy on U1: PdC. By measuring the Pd L_3-edge, the investigators were able to monitor the changes in Pd charge density as a PdC layer formed upon the exposure of Pd metal to ethylene. Upon carbide formation, the edge shifts to higher energy by approximately 1.2 eV (Figure 8).

Another hot area of materials research is glasses, partly for their potential applications in communications and optical computing. J.M. Lee, D.S. Yang, C.U. Segre, and T.I. Morrison (Illinois Institute of Technology) and K. Zhang (U. of Chicago) studied the degree of ordering and local structure around yttrium in Y/Si glasses grown by e-beam evaporation on X23A2. The EXAFS of films on float glass of various compositions of the empirical formula $Y_{1-x}Si_xO_y$ were measured as deposited and after annealing. The researchers found that whereas Y_2O_3 crystallizes upon annealing at 500°C, $Y_{97}Si_3O_y$ remains in a glassy structure (as evident from the attenuation of structure beyond the first shell). At a critical composition level of $Y_{0.54}Si_{0.46}O_y$, the annealing produces a significant structural rearrangement, with a 0.05 Å increase in the average Y-O bondlength.

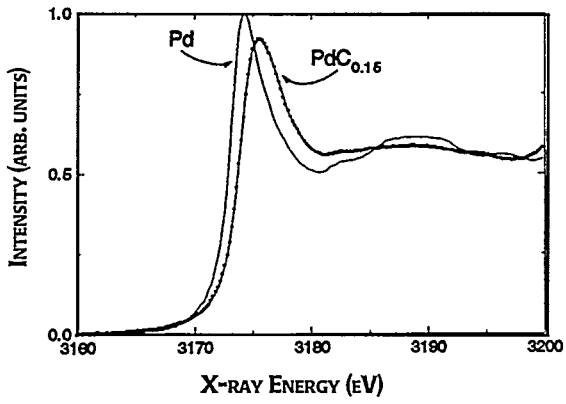


Figure 8 X11B: Pd L_3-edge fluorescence excitation spectra of 2000 Å Pd and $PdC_{0.15}$ films.

TECHNIQUES DEVELOPMENT

A few years ago, a new technique call Diffraction Anomalous Fine Structure (DAFS) emerged which is a hybrid between absorption spectroscopy and diffraction. The advantage of this technique is that it permits the selective measurement of the spectroscopy of an element based on its contribution to the intensity of a diffraction peak, for example permitting the separate measurement of the two copper atom sites in 123 superconductors. P.L. Lee, M.A. Beno, G.S. Knapp, and G. Jennings (ANL) have developed a new technique they term Continuous Energy Diffraction Spectroscopy. Making use of the polychromator on X6A and a CCD area detector (see Figure 9), the researchers have combined a dispersive EXAFS geometry with a diffraction measurement. The advantage is that the entire energy range is determined in one exposure, permitting much faster data collection than in conventional DAFS experiments. Only a single angle rotation of the sample is required to generate the data which contains the full DAFS signal.

M.R. Chance, R. Fischetti, Y. Hai, and C. Lu (Albert Einstein College of Medicine) have developed a replacement high speed amplifier for the germanium solid state detector on X9B. The relatively long shaping times of the current commercial amplifiers limits the total count rate per channel to some 50,000 counts per second before pathological dead time effects set in. The new amplifier can function at 200,000 counts per second, but with a penalty in the achieved energy resolution.

Circular dichroism is another area of intense interest because of the great commercial value of magnetic materials for recording media and read heads. While most of the work at the NSLS in this area has been carried out in the soft x-ray domain on U4B, there have been a few hard x-ray experiments on the X-Ray Ring. J. Chen, A. Young, M. Grush, L. Furenlid (NSLS), and S.P. Cramer (U. of California at Davis) performed such circular dichroism measurements on a sample model system on X19A. It was found that the mirror optics which normally accomplish collimation of vertical divergence and focussing can be adjusted together with an incident white beam slit to deliver below-plane circularly polarized light into the hutch with minimal realignment of the beamline components, a major advantage for beamlines which spend most of their time in linearly polarized mode. Using a superconducting magnet in the hutch, high quality Gd L_2-edge data were acquired in +2 and -2 Tesla fields.

CONCLUSION

X-ray absorption spectroscopy is in a healthy state at the National Synchrotron Light Source. Nonetheless, this is an appropriate time to plan for the long term support of this scientific tool and formulate strategies for furthering developments in experimental techniques, detectors, and data collection. A committee of EXAFS beamline representatives and NSLS staff is starting that job now to ensure that the NSLS remains a forefront facility for XAS research.

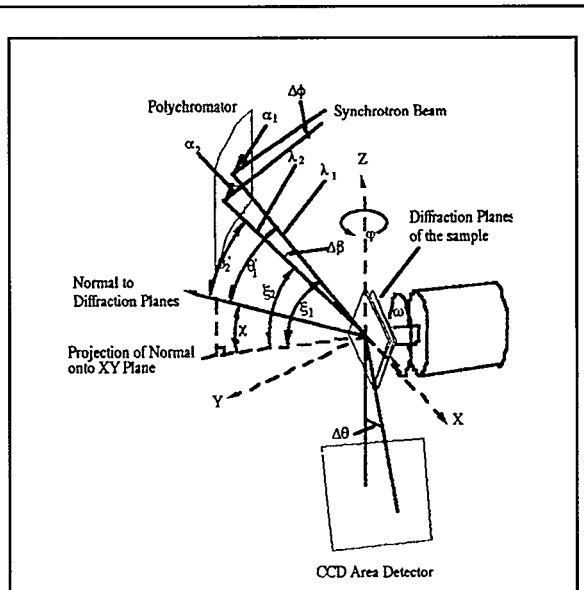
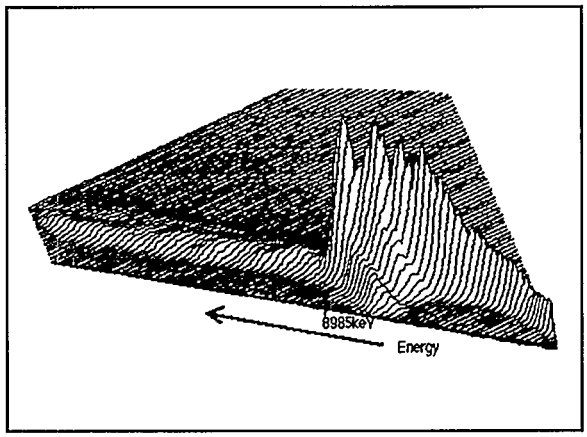


Figure 9 X6A: (top) General diffraction geometry and components for Continuous Energy Diffraction Spectroscopy (CEDS) experiments.



(bottom) CEDS data for a $CuSO_4 \cdot 5H_2O$ crystal produced by a 20 second, 1 degree ω angle rotation.

X-RAY EMISSION SPECTROSCOPY

Ken Miyano
Brooklyn College

EMISSION SPECTROSCOPIES AT CORE EXCITATION THRESHOLDS

Studies of fluorescent x-ray and electron emission near core excitation thresholds have continued at beamline X24A. These studies encompass a range of phenomena, including radiative and nonradiative resonant Raman scattering, post-collision interaction, and coherence effects.

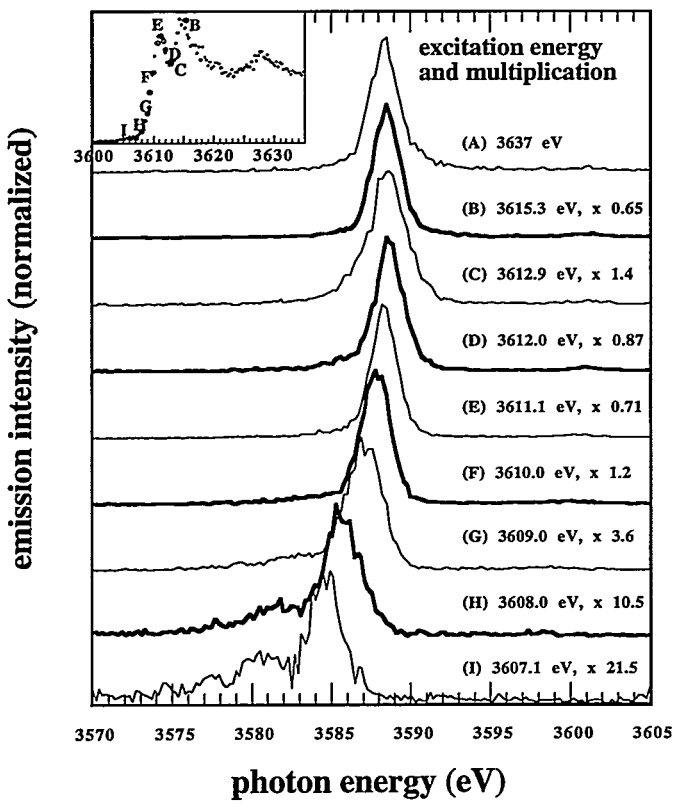


Figure 1 X24A: Potassium K_β emission spectra are plotted for different excitation energies. The inset shows where the excitation energies lie along the measured absorption profile (K. E. Miyano, Y. Ma, S. H. Southworth, P. L. Cowan, and B. A. Karlin, to be published).

Figure 1 shows radiative resonant Raman scattering in the potassium K_β emission from KCl. These spectra exhibit subthreshold energy shifts characteristic of resonant Raman phenomena. The two peaks seen for the lowest excitation energies are associated with the two strong peaks in the absorption spectra (inset). All of the emission spectra, both above and below threshold, are directly interpreted in terms of the absorption spectra. The potassium K emission satellite traditionally labeled K_β' (not visible on the scale of Figure 1), attributed to the Cl 3p to K 1s cross transition, also exhibits resonant Raman shifts for subthreshold excitation energies. Analogous Cl K_β emission and absorption spectra have also been measured.

Figure 2 shows for InP the evolution of the P KLL nonradiative resonant Raman scattering into Auger electron emission across the P K threshold. The sharp feature indicated with arrows, which disperses with excitation energy, is again associated with a strong excitation feature at the K threshold. The overall evolution is found to be in accordance with time-independent resonant scattering theory of inner-shell threshold phenomena.

Another feature that influences the lineshape of electron emission spectra near threshold is the post-collision interaction (PCI), an interaction between the outgoing Auger and photoelectrons. Coincidence techniques were used to compare the photoelectron spectra influenced by the PCI with unaffected spectra. The undistorted spectra were measured in coincidence with the fluorescence which takes place instead of Auger decay following 12% of the photoemission events. Figure 3 demonstrates that with the PCI, there is a transfer of kinetic energy from the photoelectron to the Auger electron, as shown by the peak shifts and asymmetries. This

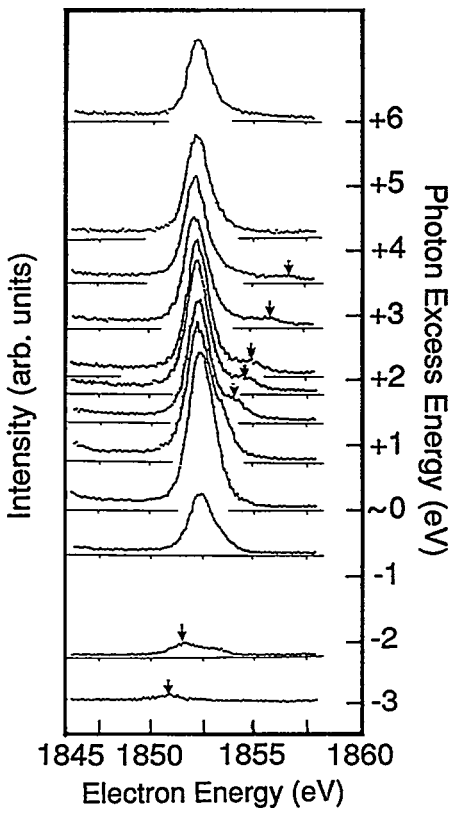


Figure 2 X24A: Plotted here is the $PK\text{-}L_{23}L_{23}\,^1D_2$ resonant Raman scattering into the corresponding Auger line. Arrows indicate the positions of some resonant Raman peaks in spectra measured at various photon excess energies [H. Wang, J. C. Woicik, T. Åberg, M. H. Chen, Alberto Herrera-Gomez, T. Kendelewicz, A. Mäntykenttä, K. E. Miyano, S. Southworth, and B. Crasemann, *Phys. Rev. A*, **50**, 1359 (1994)].

effect is substantially stronger at 10 eV above threshold than at 60 eV above threshold. Detailed Auger emission spectra, demonstrating radiationless resonant Raman effects, have also been recorded.

The scattering formalism which is used to interpret resonant Raman features has been extended to explain certain threshold phenomena observed in valence emission spectra of solid-state samples. In the Activity Reports from the last two years, Yanjun Ma described how core-valence x-ray emission excited near the core threshold exhibits dramatic changes with excitation energy that must be interpreted in terms of inelastic x-ray scattering. These changes are seen in valence emission spectra because of conservation constraints on the crystal and photon momenta. These constraints led to the anticipation of anisotropy in the x-ray emission from systems with cubic symmetry for x-rays with momenta comparable to the Brillouin zone dimensions, and indeed such anisotropy has been measured for Si K-valence emission near threshold. This anisotropy demonstrates that the absorption and emission processes are coherent, both spatially and temporally.

Thus measurement of secondary emission spectra near core excitation threshold has continued to be an active area of research at the NSLS. Understanding and characterization of these threshold phenomena are yielding practical extensions such as the measurement of emission and absorption spectra unbroadened by inner shell lifetimes and the measurement of momentum-resolved energy band structures through detailed characterization of their absorption and emission spectra.

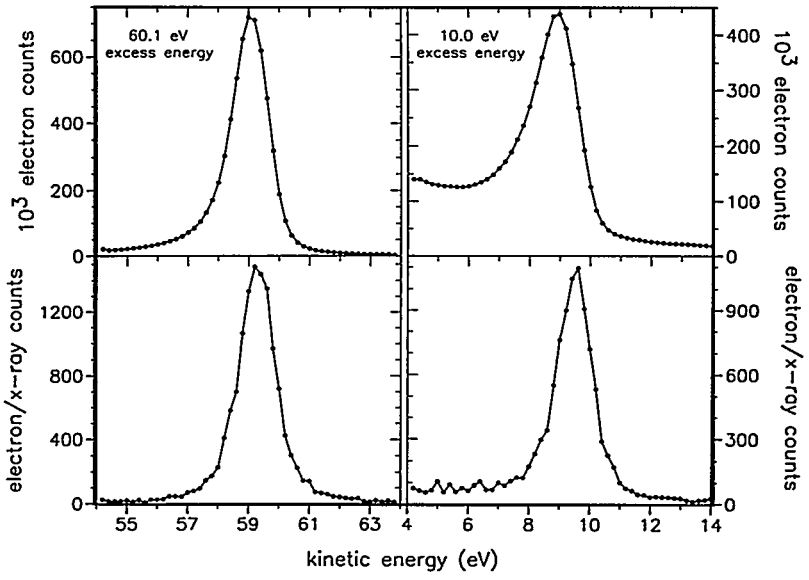


Figure 3 X24A: Plotted here are Ar 1s photoelectron spectra (upper panels) and coincidence spectra between photoelectrons and K fluorescence (lower panels). Results are shown for 10 and 60.1 eV excess energies (S. H. Southworth, M. A. McDonald, T. LeBrun, Y. Azuma, and J. W. Cooper).

X-Ray Scattering and Crystallography

Lonny Berman
D. Peter Siddons
NSLS

SURFACE STUDIES

Highlighting surface x-ray diffraction was the determination of an induced (3x1) reconstruction of the Si(111) surface covered with up to one-third of a monolayer of CaF_2, by C.A. Lucas, G.C.L. Wong, D. Loretto, A.P. Payne, and P.H. Fuoss at X16A [*Phys. Rev. Lett.* 73, 991 (1994)]. The reconstruction (top view shown in **Figure 1a**, side view in **Figure 1b**) consists of a parallel array of zig-zag Si adatom chains oriented along one of the <110> directions in the surface, alternating with a parallel array of CaF_2 chains oriented along the same direction. The Si chain reconstruction is reminiscent of the π-bonded Si chains of the clean (2x1)-reconstructed Si(111) surface, and leaves no dangling bonds at the surface. This reconstruction may be similar to other low-adsorbate-coverage-induced (3x1) reconstructions of this surface, in which the adsorbate might saturate rows of dangling bonds spaced three primitive (1x1) unit cells apart, and the Si reconstructing in between to remove the remaining dangling bonds.

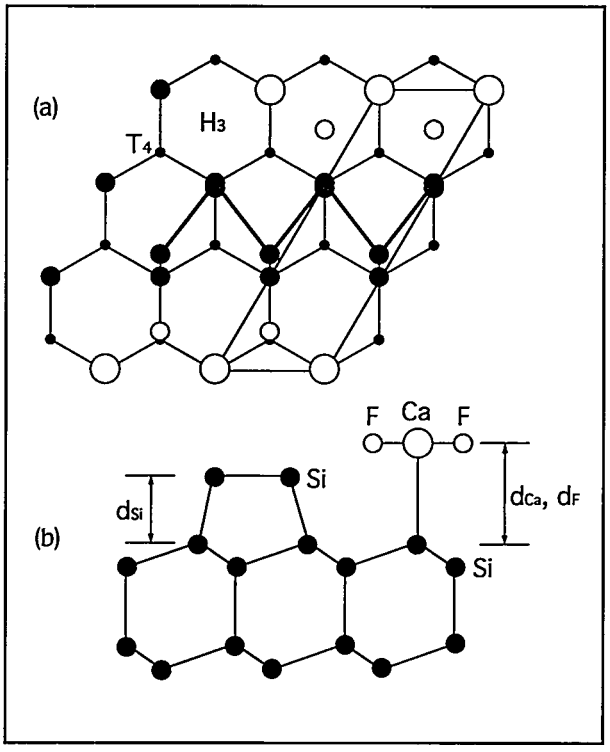


Figure 1 X16A: (a) Top view of the double fluorine model: the single fluorine model is obtained by removal of the double-hatched F atoms. The Si-Si distance on the chains is 2.67± 0.09 Å. The average Ca-F distance if 2.47 ± 0.10 Å (natural bond length: 2.37 Å). The fitted value of the Debye-Waller parameter for the adsorbed Ca and F atoms is 0.75 Å². (b) <1$\bar{1}$0> projection of the final model: The fit parameters from the (1 0 *l*) rod are as follows: $d_{Si} = 2.0 \pm 0.1$ Å, $d_{Ca} = 3.0 \pm 0.1$ Å, $d_F = 3.1 \pm 0.1$ Å. Schematic sp_z orbitals are also depicted.

DIFFUSE SCATTERING

Anomalous x-ray thermal diffuse scattering (TDS), as a function of temperature, has been measured from a paraelectric $BaTiO_3$ crystal by N. Takesue, M. Maglione, and H. Chen at X18A [to be published in *Phys. Rev. B* 51 (1995)]. The origin of the observed TDS intensities is attributed to soft on-(100) transverse acoustic (TA) lattice vibration modes and an overdamped [010] transverse optical (TO) mode for reduced wavevectors q>0.25 and q<0.25 respectively (see **Figure 2**). The distribution and temperature dependencies of the diffuse intensities agree with the results of earlier neutron inelastic scattering measurements. As the temperature is decreased toward the Curie point, the TO contribution near the Brillouin zone center increases. The phonon dispersion curves for the on-(100) TA modes were found to be highly anisotropic. These results support the notion of one-dimensionally-correlated optic motion of ions in paraelectric $BaTiO_3$.

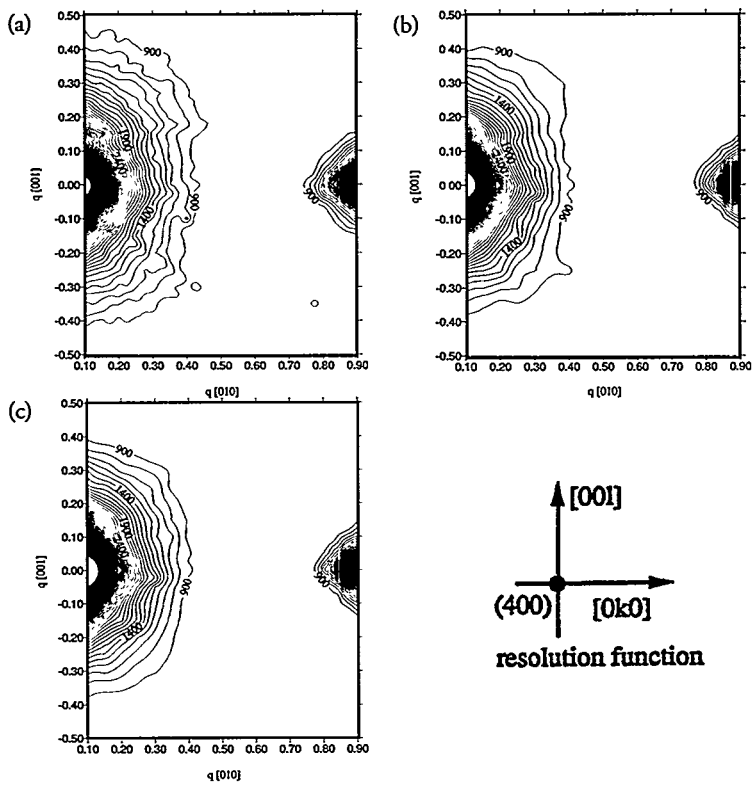


Figure 2 X18A: Equi-intensity contour maps of x-ray diffuse scattering intensities from $BaTiO_3$ on the (100) plane near the (400) reflection at (a) 200, (b) 150 and (c) 135 °C. An approximate resolution function at the (400) reflection is indicated by a round-shaped mark in the lower right corner. The reduced wavevector scales are relative to (400).

MAGNETIC SCATTERING

Magnetic scattering with polarization analysis was used at X25 by B.A. Everitt, M.B. Salamon, B.J. Park, C.P. Flynn, T. Thurston, and D. Gibbs (work submitted to *Phys. Rev. Lett.*) to determine the presence of an induced magnetic moment in normally non-magnetic Lu in a $Dy_{0.6}Lu_{0.4}$ thin film alloy crystal. **Figure 3** shows the first-order magnetic satellite above the bulk (002) reflection, measured using a polarimeter to select the σ-to-π rotated component of the magnetically-diffracted intensity and to suppress the background due to charge scattering. These data were collected in the vicinity of the Lu L_{III} absorption edge and show a resonant enhancement of the Bragg peak at that photon energy, confirming the induced Lu moment origin. The moment, induced in the 5d band of Lu by the ordered 4f moments in the Dy, is estimated to be just a few hundredths of a Bohr magneton per Lu atom. This is the first experimental observation, using resonant-enhanced magnetic scattering, of an induced polarization of a non-magnetic element.

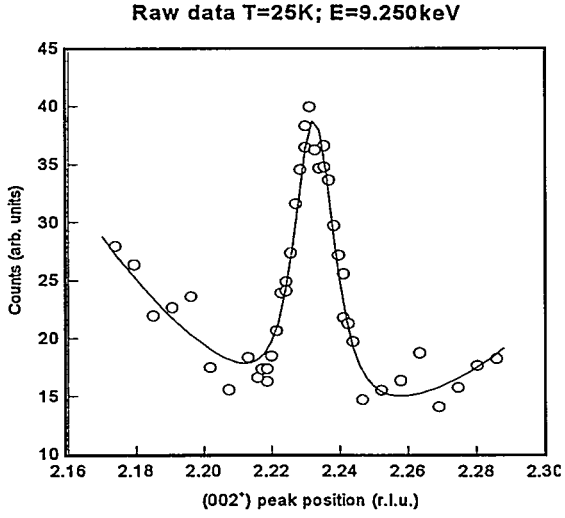


Figure 3 X25: Intensity vs. c* (r.l.u.) Raw data taken near the Lu L_{III} edge; E=9.250keV. The peak fit is to a Lorentzian squared, with a quadratic background.

COHERENT BEAM DIFFRACTION

Time correlations in the small-angle scattering of a coherent x-ray beam from a gold colloid dispersed in glycerol were measured by S.B. Dierker, R. Pindak, R.M. Fleming, I.K. Robinson, and L.E. Berman at X25 (work submitted to *Phys. Rev. Lett.*). Intensity fluctuations in the scattered coherent beam, arising from the Brownian motion of the gold colloid particles, were measured using a two-dimensional CCD area detector. Data from a subset of pixels corresponding to a small range of q were binned and autocorrelated; the resulting time autocorrelation function is shown in **Figure 4**. A single exponential fit to the data reveals a particle diffusion characteristic relaxation time of 9.5 seconds. This experiment illustrates the extension of photon correlation spectroscopy, to probe the dynamics of disordered materials, into a length scale regime that is inaccessible to visible light, and for materials that are optically opaque.

INELASTIC SCATTERING

Resonant inelastic scattering was used at X21 by M. Krisch, C. Kao, F. Sette, W. Caliebe, K. Hämäläinen, and J. Hastings (work submitted to *Phys. Rev. Lett.*) to determine the nature of the electronic transitions of the Gd^{3+} ion in $Gd_3Ga_5O_{12}$ in the vicinity of the Gd L_{III} edge. A high-resolution spectrometer was used to monitor the intensities of scattering from different excited states in the presence of the Gd 2p core hole as functions of incident photon energy. Three different multiplet families were identified, and are shown in **Figure 5**. Multiplet feature A, appearing at the lowest incident energies, is assigned to scattering from the $3d^94f^{n+1}5d^0Gd^{3+}$ ion final state which is enhanced at the energy of the quadrupolar transition of a 2p electron to a 4f orbital. Feature B is assigned to scattering from the $3d^94f^n5d^1$ final state, enhanced at the energy of the dipolar transition of a 2p electron to a 5d orbital, and feature C to scattering from a continuum final state, also associated with a dipolar transition. In a conventional x-ray near-edge absorption or low-resolution emission measurement of this sample, the 2p core hole broadening and different intensity contributions of these transitions to the white line at the L_{III} edge make it impossible to decompose these excitations. The overall energy transfer resolution was about 1.3 eV, with the incident energies around 7.25 keV and the scattered energies around 6.05 keV.

PROTEIN CRYSTALLOGRAPHY

The structure of a photolyzed form of carbonmonoxy (CO) myoglobin has been determined from data measured at X12C by I. Schlichting, J. Berendzen, R.M. Sweet, and G. Phillips from crystals held at 20 K [*Nature* 371, 808 (1994)]. **Figure 6** (see section divider for Chapter 6) shows three states of the oxygen-binding protein myoglobin. The three figures depicting electron density show the same view of the molecule, with the oxygen-binding site in the upper-central portion of the image, and the oxygen-binding porphyrin moiety shown edge-on at the bottom. In the upper left image, one can see de-oxy myoglobin: the active site is empty. In the upper right, the oxygen site is filled with carbon monoxide, which binds very strongly to the iron atom at the center of the porphyrin ring. Both of these structures were determined at a temperature of approximately 120 K. Finally, in the lower left is shown carbonmonoxy myoglobin held in a quite unusual state: in the first place, the crystal had been held at a temperature of only 20 K to freeze out nearly all molecular motion in the molecule. In the second, the specimen had been illuminated strongly with visible light. The effect of this illumination was to photolyze the bond between the iron atom and the CO molecule. This molecule was unable to leave the binding pocket because of the low temperature, but instead it is found nestled in the back of the pocket, resting against an

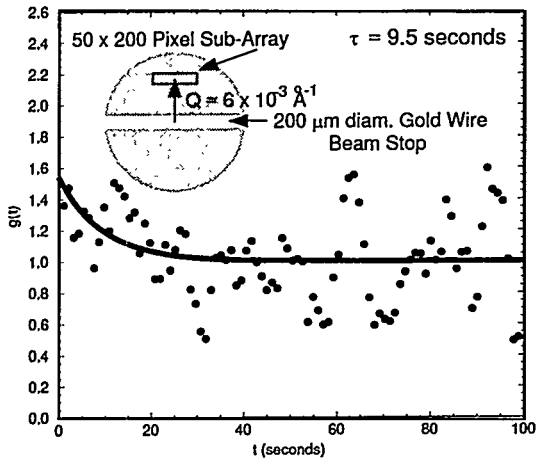


Figure 4 X25: Autocorrelation function of colloid scattering intensity as collected with CCD camera. The inset schematically depicts the scattering "halo", the beam stop, and the sub-array which was ensemble averaged over.

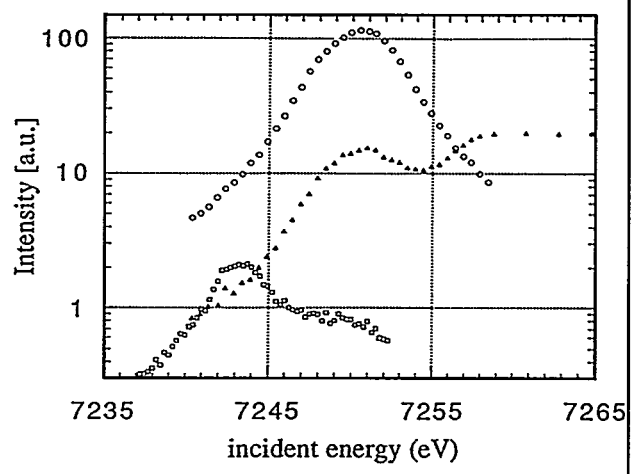


Figure 5 X21: Constant energy transfer scan for three different energy transfers: feature A (cubes): 1191 eV, feature B (circles): 1198.5 eV and feature C (triangles): 1207 eV. The spectra are corrected for self absorption effects.

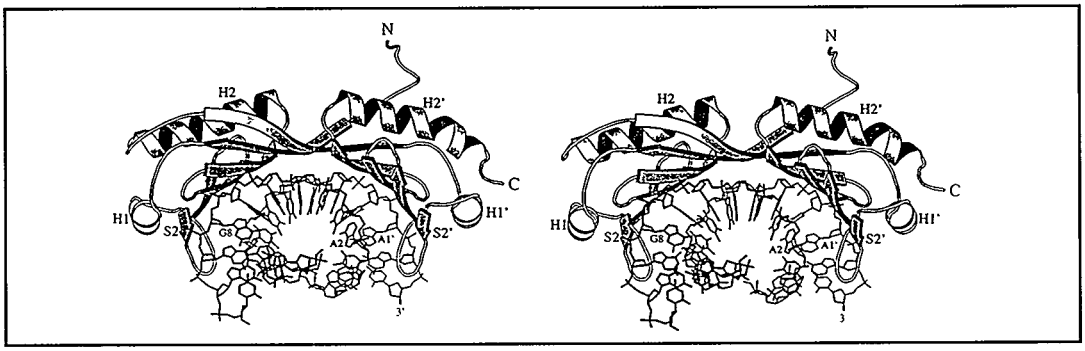
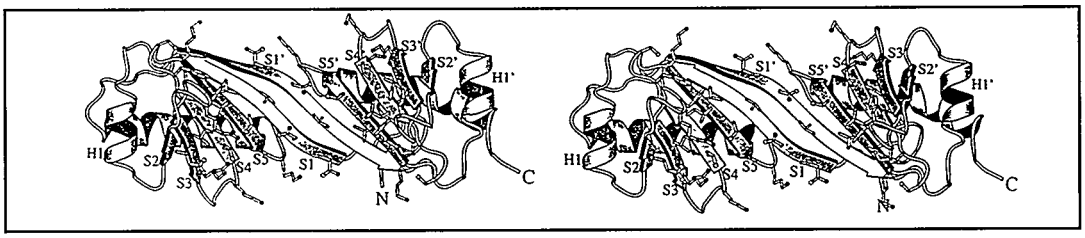


Figure 7 X25: Stereoviews of the TBP-TATA box complex. (a) Molscript drawing viewed perpendicular to the approximate two-fold axis of the complex. TBP is displayed as a ribbon and DNA as stick. The coding strand of the DNA is drawn in black and the noncoding strand in gray. The 5' end of the TATA box enters from the right and interacts with the second direct repeat of TBP, whose secondary structural elements are denoted with a '. The last base pair of the DNA has been removed for clarity.



(b) View along the approximate intramolecular two-fold axis of TBP, looking at the concave DNA binding surface of the protein. Amino acid side chains involved in direct and water-mediated interactions with the DNA are displayed in ball-and-stick representation, with nitrogen atoms shaed black and oxygen atoms white.

aliphatic isoleucine side chain. The figure at lower right is a composite, meant to show the motion of all the atoms involved. This structure is the best view available of this transient state in the release of ligands from myoglobin.

The three-dimensional structure of a TATA box-binding protein (TBP) complexed with a 14-base-pair DNA sequence (TATA element) was refined to 1.9 Å resolution, using oscillation data collected at X25 by J.L. Kim, G. Patikoglou, and S.K. Burley [*Nature Struct. Biol.* 1, 638 (1994)]. This high-resolution structure has been refined to a crystallographic R-factor of 19.4% (stereo views are shown in **Figure 7**), and represents the first refinement of its kind. TBP is the DNA-binding subunit of an RNA polymerase, and is responsible for correct positioning of the polymerase with respect to a DNA sequence in initiating gene transcription. Binding of this saddle-shaped protein induces a conformational change in the DNA. This structural study, and those of TBP complexed with variants of the TATA element, have helped to explain how TBP recognizes and directs transcription initiation from different DNA sequences. The high

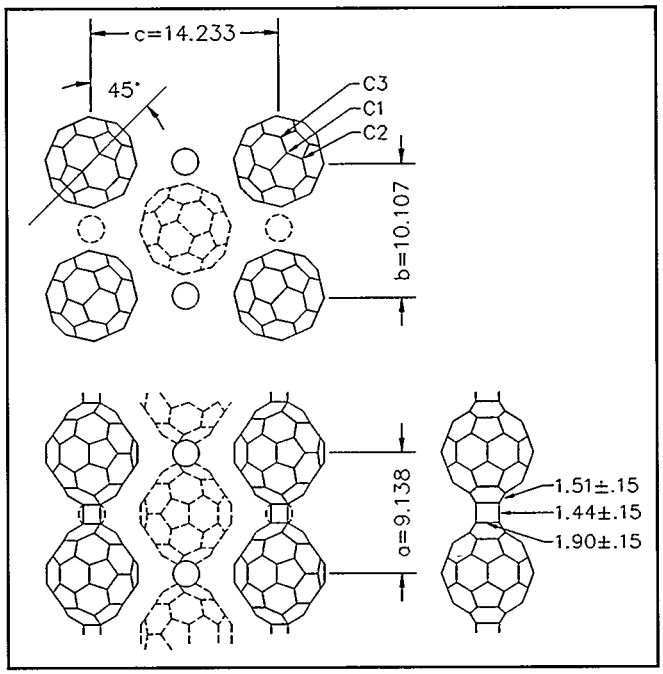


Figure 8 X3B1: Two views of the structure of the fullerene-based conducting polymer Rb_1C_{60}. The 9.1Å lattice translation is unusually short for a fullerene compound, because the molecules are covalently bonded into chains.

Table 1: Results of the macrostress analysis on a mesoscopic scale of doped tungsten wire with 10% deformation after a surface layer removal of (1) 9 μm and (2) 18 μm (2nd set). Wire Radius = radius of the wire specimen after surface layer removal.

Wire Radius [μm]	σ_{11}[MPa]	σ_{12}[MPa]	σ_{13}[MPa]	σ_{22}[MPa]	σ_{23}[MPa]	σ_{33}[MPa]
81	66±23	78±67	-20±20	-241±247	0±14	0
72	27±16	58±41	-6±11	-93±35	-6±7	0
63	7±14	27±30	-8±5	-36±21	5±4	0

x-ray intensity available at X25, and excellent signal-to-background afforded with image plate data collection, permitted the high resolution limit and large number of observations required to refine this structure to such precision.

POWDER DIFFRACTION

Powder diffraction at NSLS continues to expand, with many interesting programs underway. The work on C-60 phases has occupied a significant place in the work at X3B1 and X7A. P. Stephens (SUNY - Stony Brook) at X3B1 has shown that a new phase involving polymer-like bonding of 1-D chains of C_{60} molecules occurs under certain conditions (Figure 8). This phase is a one-dimensional metal, and is the first C_{60} polymer to be studied. D. Cox (BNL-Physics) and collaborators have worked extensively on alkali-metal intercalation compounds of C-60 at elevated temperatures and pressures, discovering a wealth of new phases.

A novel application of powder diffraction was demonstrated at X7A by the Sylvania group, in which strains in a 160 μm diameter tungsten wire due to drawing were mapped. The measurements were used as a check on a finite-element model of the wire-drawing process. Table 1 shows the stress-tensor components as a function of radius.

At X7B, a new position sensitive detector was used to study in real time a variety of synthesis reactions. The rapid data acquisition made possible by this setup allowed Christensen (U. of Aarhus, Denmark) and co-workers to study the rate of reaction in the MgO-H_2O and MgO-$MgCl_2$-H_2O systems (Sorel Cements). Figure 9 shows the evolution of the powder diffraction profile as a function of time. This is only one of a series of experiments by various experimenters at this line studying phase changes and reaction processes using this capability.

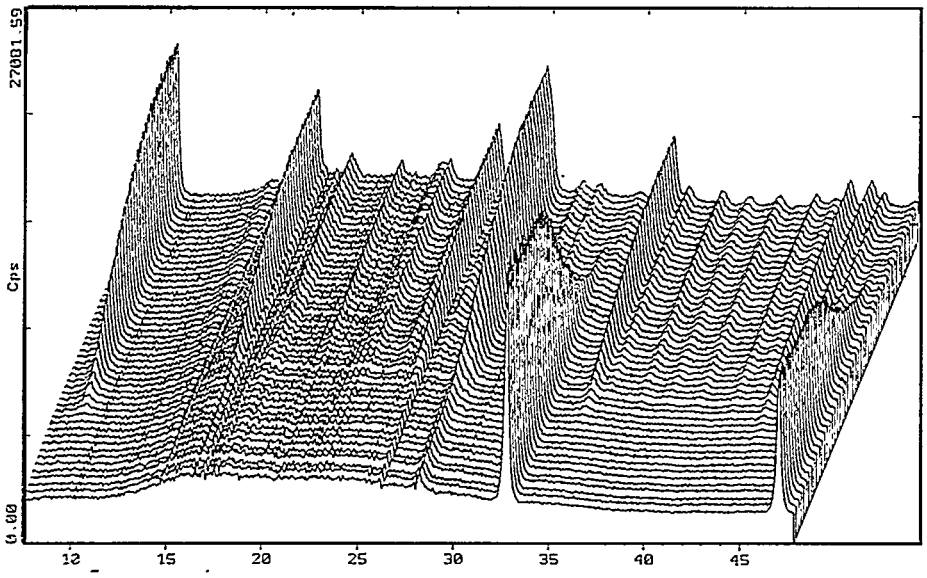


Figure 9 X7B: Bragg reflections of MgO decrease and those of the reaction product increase during the reaction.

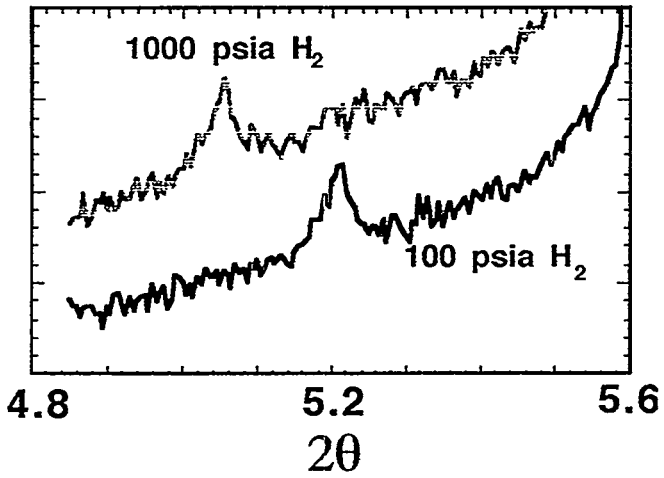


Figure 10 X17B1: Diffraction pattern of a 1% Pd/C supported catalyst loaded in 1/8" stainless-steel tubes using 60.5 keV x-rays. The shift in the Pd(111) peak toward lower angles illustrates the conversion of palladium metal (100 psi H_2) to palladium hydride (1000 psi H_2) at 240° C.

The high-energy capabilities of the X17 superconducting wiggler were used to good effect in an experiment to study the structure of hydrated Pd catalysts under realistic working conditions. The samples were contained in thick-walled stainless-steel capillaries under pressure. The high-energy x-rays (~60keV) available at X17 were able to penetrate this environment and sample the contents. These initial experiments were encouraging, in that diffraction lines from the sample components could be readily distinguished from the stainless enclosure. Figure 10 shows the Pd (111) Bragg peak position changing as a function of hydrogen pressure, indicating the formation of Palladium Hydride. Future work will include the high-temperature stage so that complete simulation of the operating environment will be possible.

An interesting application was made at beamline X14A, by McGuire (The Dow Chemical Company) *et al.*, which probed the residual strain in epoxy-encapsulated copper lines such as those used as interconnects in multi-chip electronic modules. They were able to study strain levels and anisotropy through the epoxy overcoat. Figure 11 gives some of their results.

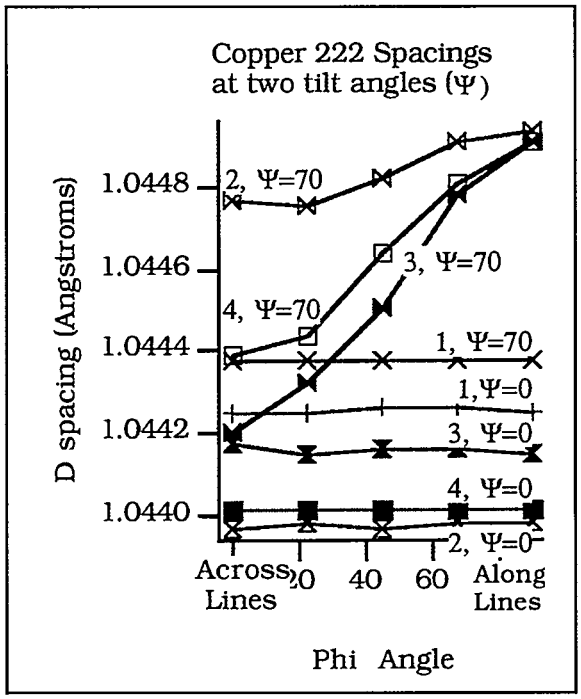


Figure 11 X14A: Synchrotron x-ray diffraction was used to measure residual strain in three orthogonal directions for several arrays of parallel copper lines, each line approximately 18 mm long x 8 μm wide. Approximately three weeks elapsed between fabrication of samples and the residual strain measurements. After the initial measurements were complete, two of the samples were heated under typical curing conditions and re-measured immediately after cooling to room temperature. Preliminary analysis of the data suggest that slightly higher strains are present in these immediately-cured samples.

SAXS

Beamline X3 has recently commissioned a CCD detector for SAXS, giving them a real-time capability which Chu (SUNY - Stony Brook) and collaborators have begun to use for studying properties of polymers under tensile stress. They are able to extract information about changes in crystallinity and texture as a function of strain. Figure 12 shows the output of the CCD detector and stress-strain curves for several different PET fibers.

Small-angle scattering from supercooled water has attracted some attention lately, as evidenced by an experiment performed by Ludwig *et al.* at X20C. They were able to provide evidence against the existence of a spinodal point, and suggest that their measurements support a model involving cluster formation rather than increasing long-range order.

Schaefer *et al.*, using beamline X23A3, investigated the heat-treatment of sol-gel-produced silica aerogels using the ultra-small-angle scattering instrument. They discovered the development of large scale porosity which had been missed in previous SAXS studies, and was made observable in this work by virtue of the increased Q-range provided by this instrument.

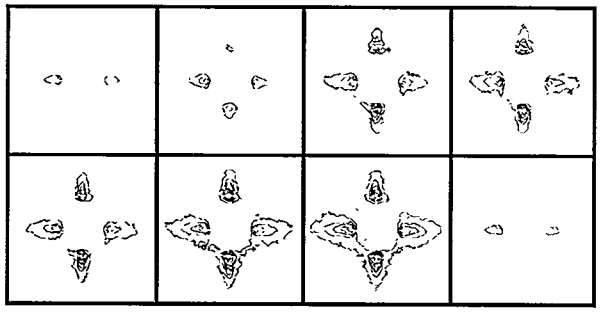
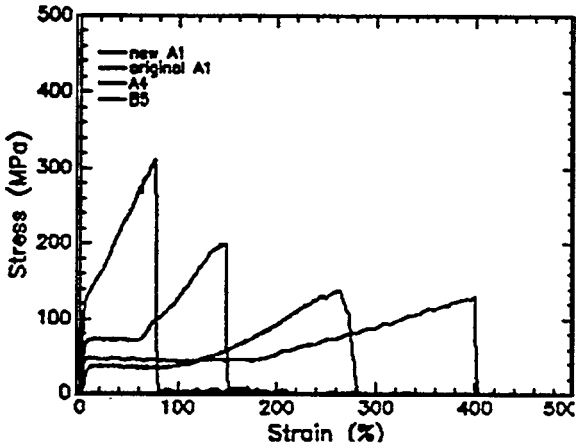


Figure 12 X3A2: (a) Time resolved SAXS for sample A1 (amorphous). Observation time was 45 sec over intervals of 22% strain.



(b) Stress-strain curves for various PET fibers. A1 was spun at 1600 ypm, A4 at 3500 ypm, and B5 at 4500 ypm (most crystalline).

X-Ray Topography

Michael Dudley
SUNY at Stony Brook

This report outlines significant scientific results obtained by X19C and X23A3, the two beamlines mainly comprising the NSLS X-Ray Topography Special Interest Group.

A broad range of experiments has been carried out on X19C in the last year. In a program funded by NASA, D. Larson of Grumman Corporate Research Center and M. Dudley, J. Wu and H. Chung of Stony Brook have been comparing defect structures in CdZnTe crystals grown on earth to those grown in a microgravity environment on Shuttle Mission STS-50. White beam topography has been used to examine as-grown boules as well as slices cut from the boules. An example of a reflection topograph recorded from a slice cut from an as-grown boule is shown in Figure 1, while Figure 2 shows an example of a transmission topograph recorded from a slice cut from a different boule. Dislocation densities appear to be two to three orders of magnitude lower than in ground-based samples.

L.K. Cheng and J. Bierlein of DuPont, in a collaborative program with M. Dudley and H. Chung of Stony Brook, have been using white beam topography to investigate growth defect structures in KTA and KTP crystals, both of which have interesting optical properties. Dislocations, growth sector boundaries, inversion twin lamellae and ferroelectric domains have been observed and characterized. An example of a transmission topograph showing the growth sector boundaries is shown in Figure 3. The influence of these defect structures on optical properties is being investigated.

In a project funded by Army Research Office, C. Fazi of Army Research Laboratory (Adelphi) and M. Dudley,

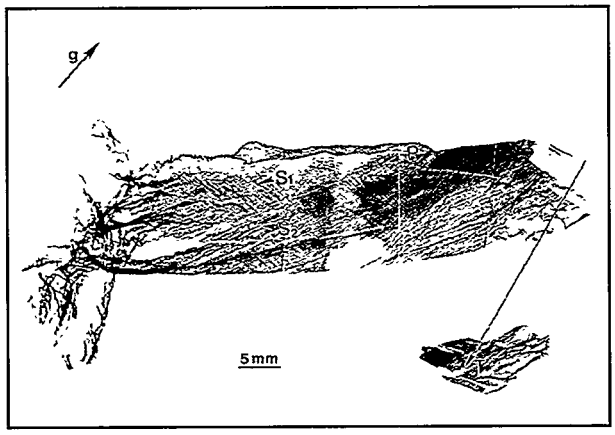


Figure 1 X19C: White beam reflection topograph ($g=0\bar{4}4$, $\lambda=0.982$Å) recorded from a wafer sliced from the CdZnTe flight sample number 1 grown by D. Larson Jr. of Northrop-Grumman CRC on Shuttle Mission STS-50 showing slip bands (S_1 and S_2) belonging to the $[\bar{1}10]/(11\bar{1})$ and $[0\bar{1}1]/(1\bar{1}1)$ slip systems, respectively, precipitates (P) and a 180° rotation twin(T). Research funded by NASA contracts NAS8-38147 and NCC8-48.

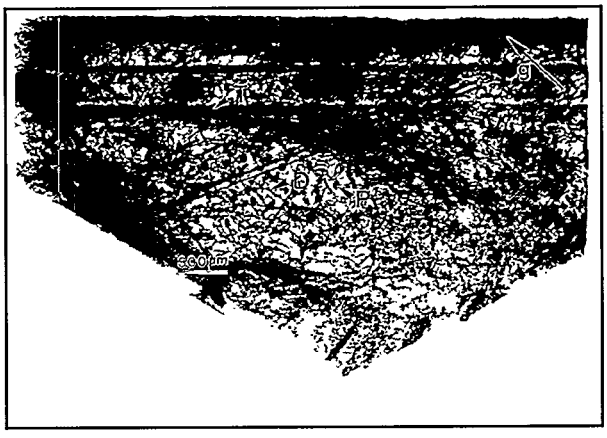


Figure 2 X19C: White beam transmission topograph ($g=\bar{1}\bar{1}3$, $\lambda=0.42$Å) recorded from a 180μm thick CdZnTe wafer sliced from flight sample number 2 grown by D. Larson Jr. of Northrop-Grumman CRC on Shuttle Mission STS-50 showing individual dislocations, (D), Te precipitates, (P), and 180° rotation twins (T). Research funded by NASA contracts NAS8-38147 and NCC8-48.

S. Wang and W. Huang of Stony Brook have continued to make excellent progress in their joint project investigating the influence of defects on the performance of SiC devices. In a collaborative effort with Drs. J.A. Powell and P. Neudeck of NASA Lewis Research Center, Synchrotron White Beam X-Ray Topography has been used to determine the depth distribution of polytypes within epilayers grown on 6H-SiC substrates. An example of a diffraction pattern recorded from a wafer comprising several 3C and 6H device regions is shown in Figure 4, along with the simu-

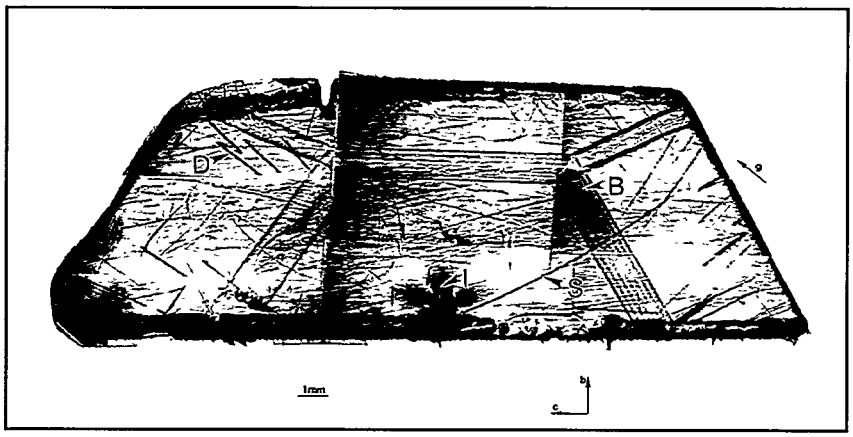


Figure 3 X19C: White beam x-ray topograph (g=101, λ=0.55Å) recorded in transmission geometry from a flux grown KTP single crystal showing growth sector boundaries revealed by fringe contrast (**B**), dislocations (**D**), inclusions (**I**) and surface scratches (**S**). The fringe contrast associated with the growth sector boundaries indicates that the boundaries are faulted and may only have a very low level of lattice strain associated with them. Research funded by DuPont.

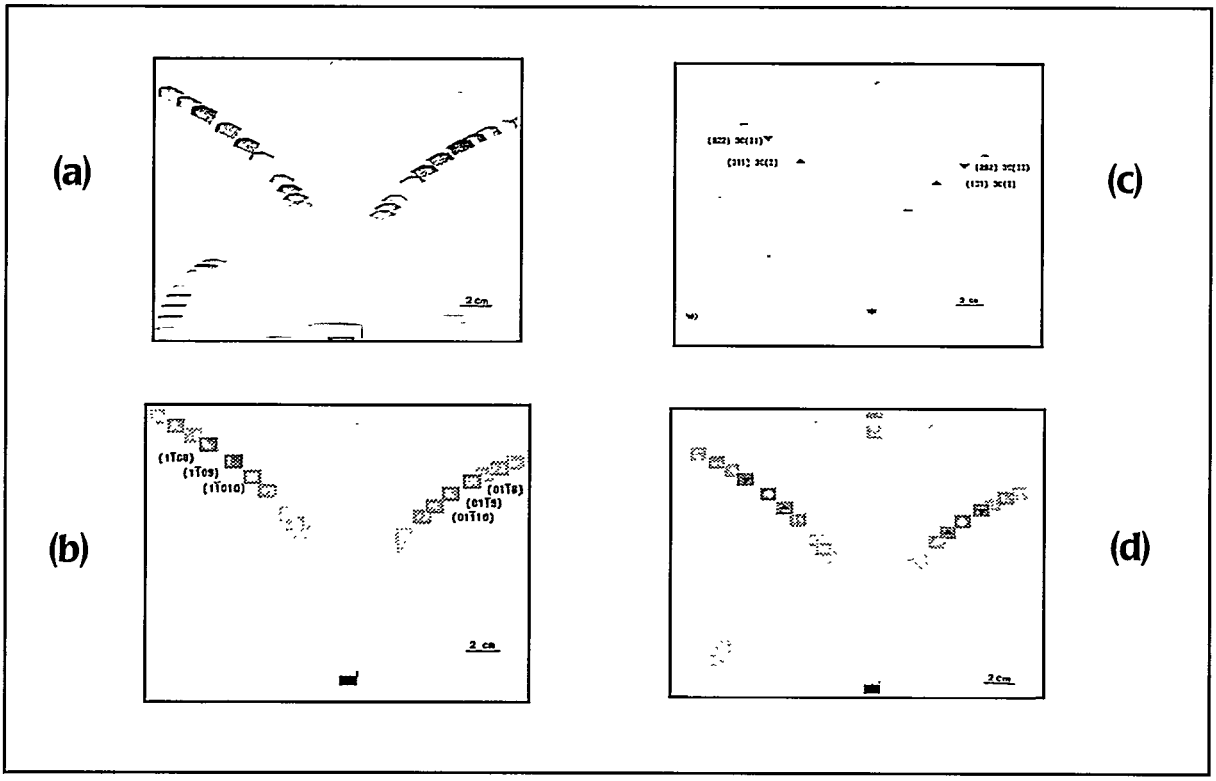


Figure 4 X19C: (a) Synchrotron white beam diffraction pattern recorded in reflection geometry from a wafer comprising several mixed 3C and 6H device regions. (b) Computer generated diffraction pattern for the 6H-SiC structure in the same geometry. (c) Computer generated diffraction pattern of 3C-SiC structure in the same geometry. The upwardly pointing triangles, labeled as 3C(I), represent the diffraction pattern for one of the double positioning twins of the 3C structure and the downwardly pointing triangles, labeled as 3C(II), represent that of the other one. (d) Superimposition of the simulated 6H and 3C diffraction patterns. Research funded by ARO, contract monitor Dr. J. Prater, under contracts DAAL04-94-G-0091 and DAAL04-94-G-0121.

lated diffraction pattern. The recording of similar diffraction patterns with different grazing incidence angles, followed by comparison with the simulations, enables the depth information to be obtained.

In a project funded by Cree Research Inc. via the NIST ATP program, C. Carter and D. Asbury of Cree Research Inc. have joined us in a joint venture investigating defect structures in very high quality SiC crystals grown at Cree. An example showing images recorded in transmission and reflection geometry from the same region of a 6H-SiC wafer is shown in **Figure 5**. Note the basal plane dislocations, B, and the superscrew dislocations S. **Figure 6** shows an image recorded from a wafer cut parallel to the growth axis clearly showing the superscrew dislocations.

I. Baker and F. Liu of Dartmouth College, jointly with M. Dudley, have been using white beam topography to investigate the role of grain boundaries in the plastic deformation of large grain, polycrystalline ice. Recently, deformation processes in ice bicrystals were investigated. **Figures 7 and 8** comprise an example of a sequence of images recorded in transmission geometry from an ice bicrystal showing dislocation structures created at grain boundary facets through grain boundary sliding during in situ compressive deformation.

In a joint project with D. Bliss of Rome Laboratory (Hanscom Airforce Base) and V. Prasad of Stony Brook, M. Dudley, J. Wu and H. Chung of Stony Brook have been examining growth defects in InP single crystals. An example of a reflection image recorded from InP, showing individual dislocations, is shown in **Figure 9**.

A real-time study of dislocation motion in HCl-doped single-crystals of ice has been undertaken at X23A3 in collaboration with Fuping Liu, Xiaohong Hu and Ian Baker of Dartmouth College. It was found that at a concentration of ~1 x 10^{-6}M the dislocation mobility is essentially the same as in pure ice. However, the velocity of dislocations in heavily HCl-doped (1 x 10^{-4}M) ice was found to be at least 2.6 times larger than that previously measured in pure ice. This suggests that the softening effect produced by HCl-doping might be due to a higher bond re-orientation rate at the dislocation core compared to the bulk. In lightly doped crystals the concentration of point defects maybe too low to have significant defects at dislocation cores.

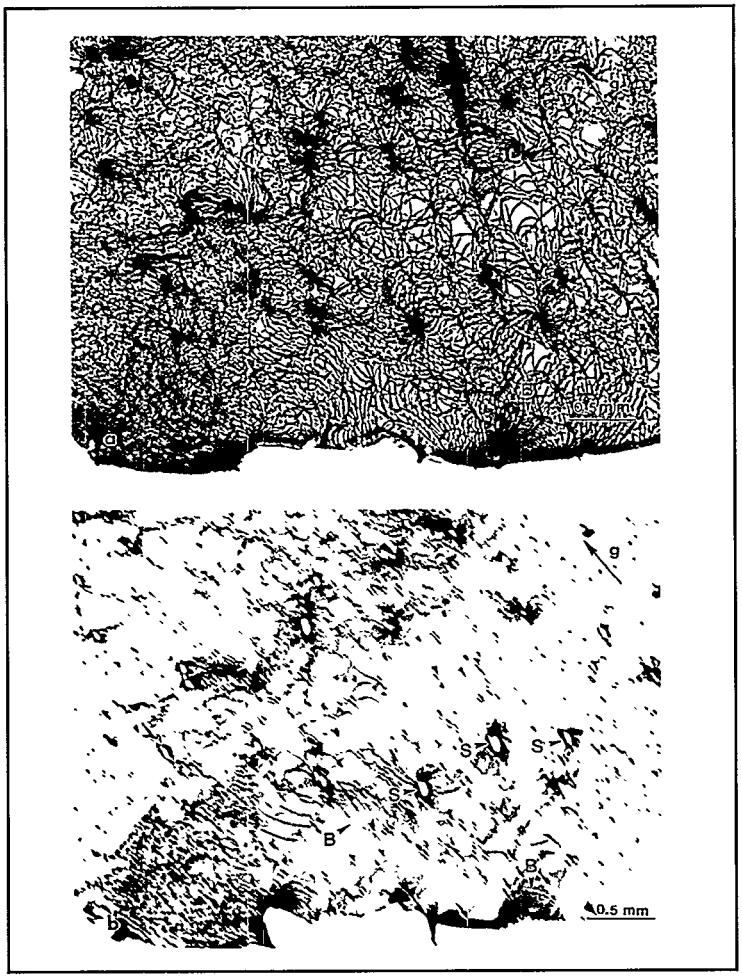


Figure 5 X19C: (top) White beam transmission topograph (g=$1\bar{1}01$, λ=0.89Å) of a 6H-SiC crystal grown by Cree Research Inc., showing basal plane dislocations (B) connecting superscrew dislocations (S). **(bottom)** white beam reflection topograph (g=1126, λ=0.69Å) recorded from the same region of wafer showing superscrew dislocations of varying Burgers vector magnitude and sign (the white circular features of different diameter), and faint images of basal plane dislocations. For details see S. Wang, M. Dudley, C. Carter, Jr., D. Asbury, and C. Fazi, Mat. Res. Soc. Symp. Proc. **307**, 249 (1993); S. Wang, M. Dudley, C. Carter, Jr., and H.S. Kong, Mat. Res. Soc. Symp. Proc. **339**, 735 (1994). Research funded by Cree Research Inc.

The question of the influence that synchrotron radiation may have on the measured mechanical behavior of ice has also been addressed. Uniaxial tensile tests were carried out on pure ice single crystals at -13°C under conditions of continuous illumination by monochromatic x-radiation, and in the lab on identical samples with no x-ray radiation. It was found that the behavior of the crystal is the same with or without x-radiation, which agrees with the results of Shearwood and Whitworth [Shearwood and Whitworth, Phil Mag A, 65, 85, (1992)]. Therefore, the dislocation mobility measured by x-ray diffraction imaging represents the intrinsic properties of ice.

David Black and Harold Burdette of NIST and Gene Cantwell of Eagle-Picher Research Laboratory have used x-ray diffraction imaging to record the defect microstructure of ZnSe crystals grown by physical vapor transport. Surface reflection images show a "texture" in the microstructure which is directly related to the bulk defect density (a more coarse texture resulting from more defects). Defects such as subgrains, inclusions, inhomogeneous strain and residual subsurface damage were also observed. The subsurface damage, observed from as-polished crystals with nearly mirror-smooth surfaces, results from the processing of wafers from the as-grown boule, the major component being the remnants of scratches not removed by polishing.

The spatially enlarged, nearly parallel and monochromatic x-ray beam prepared at X23A3 provides high sensitivity to residual inhomogeneous strain over large sample areas (up to 5 x 5 cm). The observation of inhomogeneous strain in the diffraction images from ZnSe crystals correlates well with measurements of the rocking curve width. The advantage of diffraction imaging is that the distribution of strain is observed over the

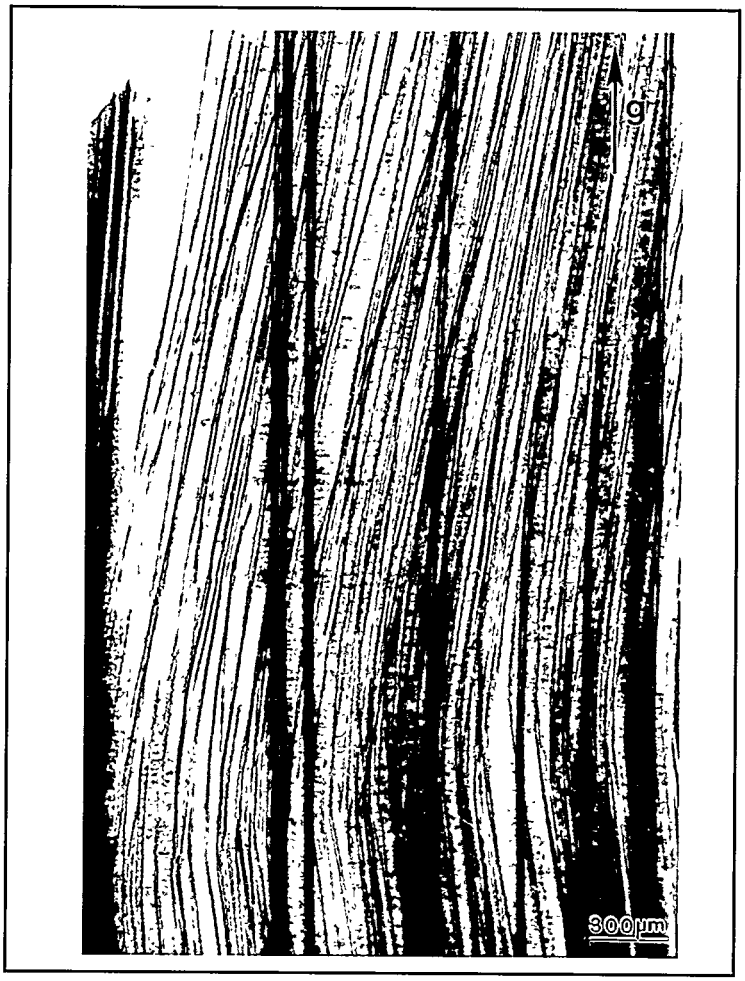
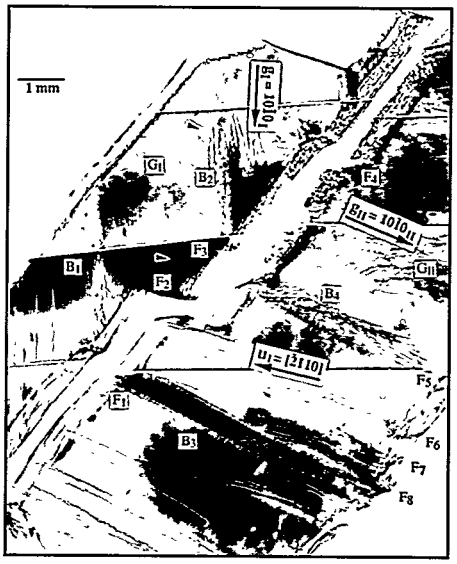


Figure 6 X19C: White beam transmission topograph (g=0006, λ=0.89Å) recorded from a SiC wafer cut parallel to the growth axis showing superscrew dislocations of various sign and magnitude of Burgers vector. Research funded by Cree Research, Inc.

Figure 7 X19C: Transmission topograph recorded from an ice bicrystal prior to applied compressive deformation. Note the dislocation structures which have been generated from facets F_i.



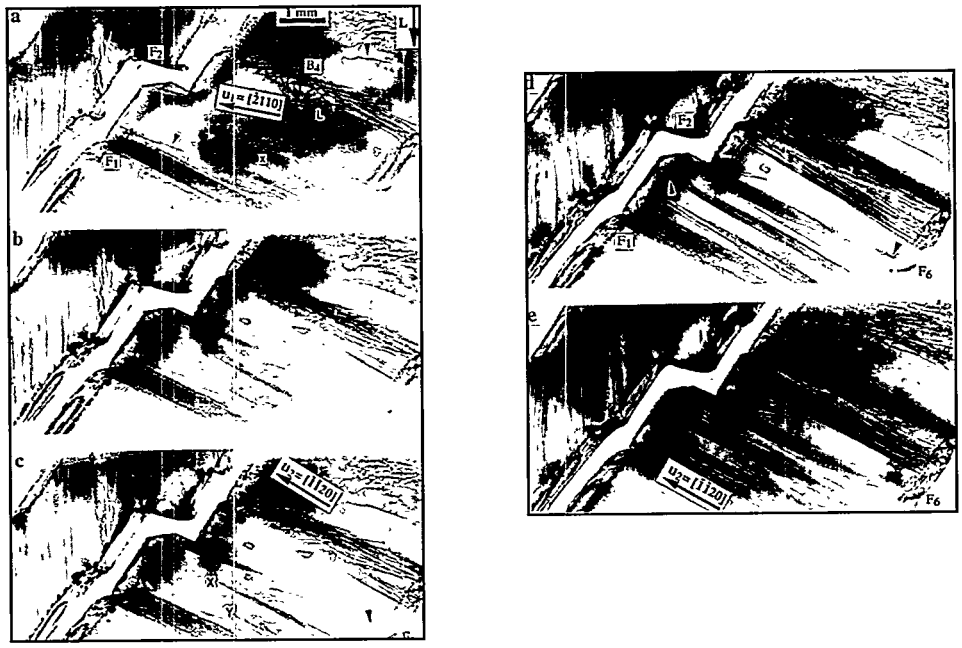


Figure 8 X19C: Sequence of images recorded from the central region of crystal shown in **Figure 7** showing dislocation structures generated during *in situ* compressive deformation. **(a)** following loading of 0.1 MPa for 5 minutes; **(b)** after further loading of 0.2 MPa for 10 minutes; **(c)** recorded five minutes later without loading; **(d)** after further loading of 0.2 MPa for 20 minutes; **(e)** after further loading of 0.2 MPa for 25 minutes. Of particular note are the dislocations generated at the facet F_7 by grain boundary sliding. For details see F. Liu, I. Baker and M. Dudley, *Phil. Mag. A* **71**, 1 (1995); F. Liu, I. Baker, and M. Dudley, *Phil. Mag. A* **71**, 16 (1995). Research funded by ARO grants DAAL03-92-G-0319 and DAAH04-93-G-006 and by the donors of the Petroleum Research Fund, administered by the American Chemical Society.

entire area of the sample rather than over a limited spot size. By rotating the sample Bragg angle while observing the diffraction image in real time, the variation in the magnitude of the strain has been observed and recorded. We have examined several crystals with large, nearly strain-free areas that also have substantial strain in the remaining areas.

We have observed anomalous transmission images from several ZnSe crystals, indicating the high quality of these crystals. The observed dislocation network of ZnSe is very similar to the characteristic microstructure of other II-VI compounds. Enlarged images, see Figure 10, from the best crystal examined to date allowed us to quantify the defect density by count-

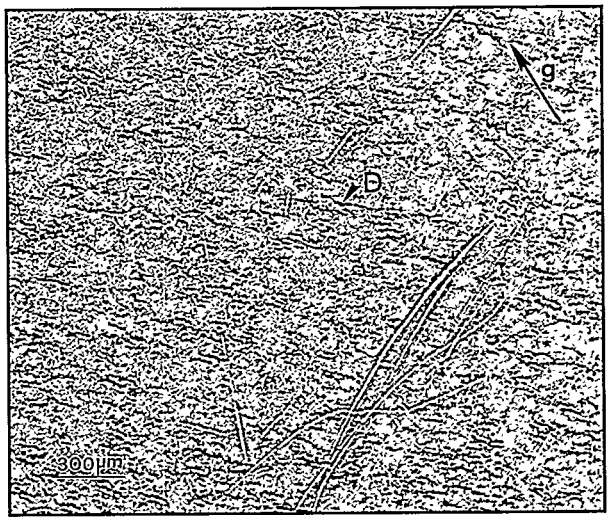


Figure 9 X19C: Synchrotron white beam x-ray topograph ($\mathbf{g}=\bar{3}1\bar{3}$, λ=0.87Å) recorded in reflection geometry from a InP single crystal showing individual dislocations (**D**). Research funded by the Department of Defense, Multidisciplinary Research Program URI.

ing individual dislocations. The measured density compares favorably with other compound semiconducting materials.

Strain induced microcracks in Bi2223/Ag high temperature superconductor composite tapes (i.e. flat wires) have been imaged by microradiography at a resolution of about 2 μm, using the asymmetric Bragg diffraction microscope on beamline X23A3, by R. Spal, C.K. Chiang (NIST), G. Riley and A. Otto (American Superconductor Corp.). As a non-destructive technique using penetrating radiation (24.4 keV), microradiography allowed observation through the Ag matrix of crack initiation and growth in the Bi2223 filaments under progressively increasing applied stress. The goal of the project is to correlate stress induced damage with the strain dependence of critical current, particularly its sharp decline at about 0.5% strain, in order to understand and perhaps enhance the strain tolerance of tapes.

Figure 11 contains microradiographs of a 5-filament tape examined at four strains from 0 to 0.95%. The filament axes and strain direction are vertical, and the filament axes are aligned with each other horizontally (i.e. the filaments completely overlap). Many microcracks, all nearly perpendicular to the strain direction, initially appear at 0.29% strain. At greater strain, they widen (in the strain direction) and new ones appear. The microcracks are concentrated in bands nearly perpendicular to the strain direction, one of which appears in Figure 11.

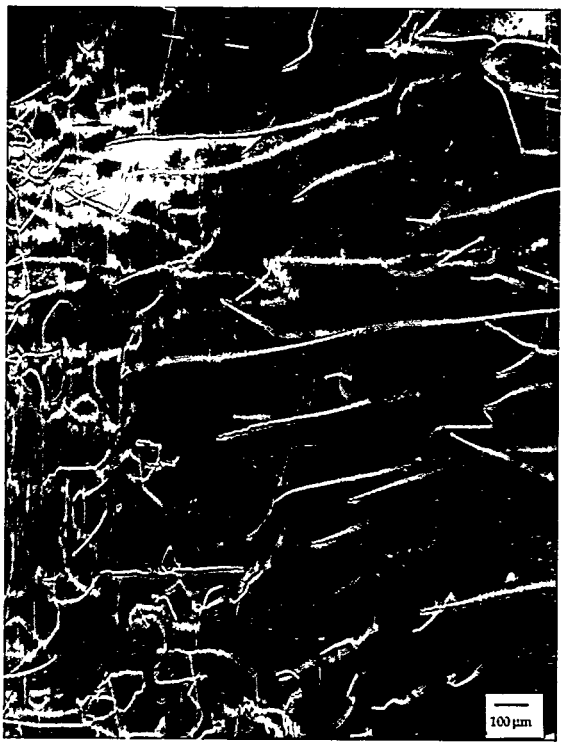


Figure 10 X23A3: An enlargement of part of a (220) symmetric transmission image from a ZnSe single crystal taken with 9.5 keV x-rays.

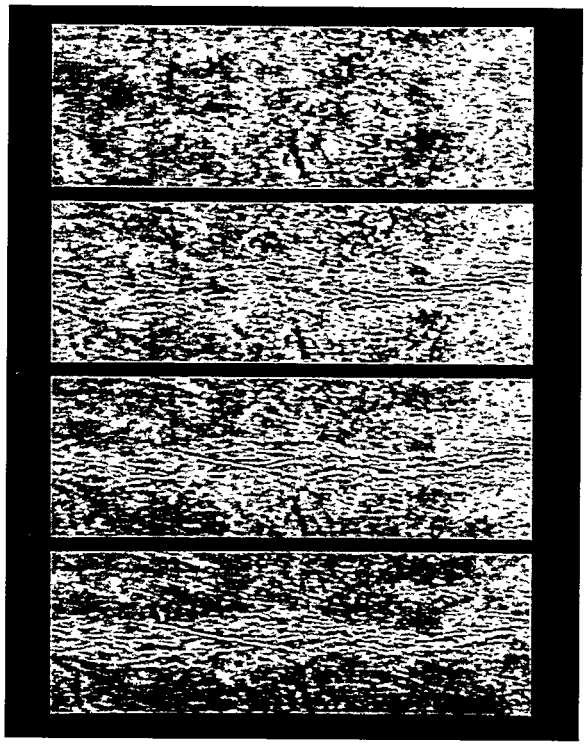
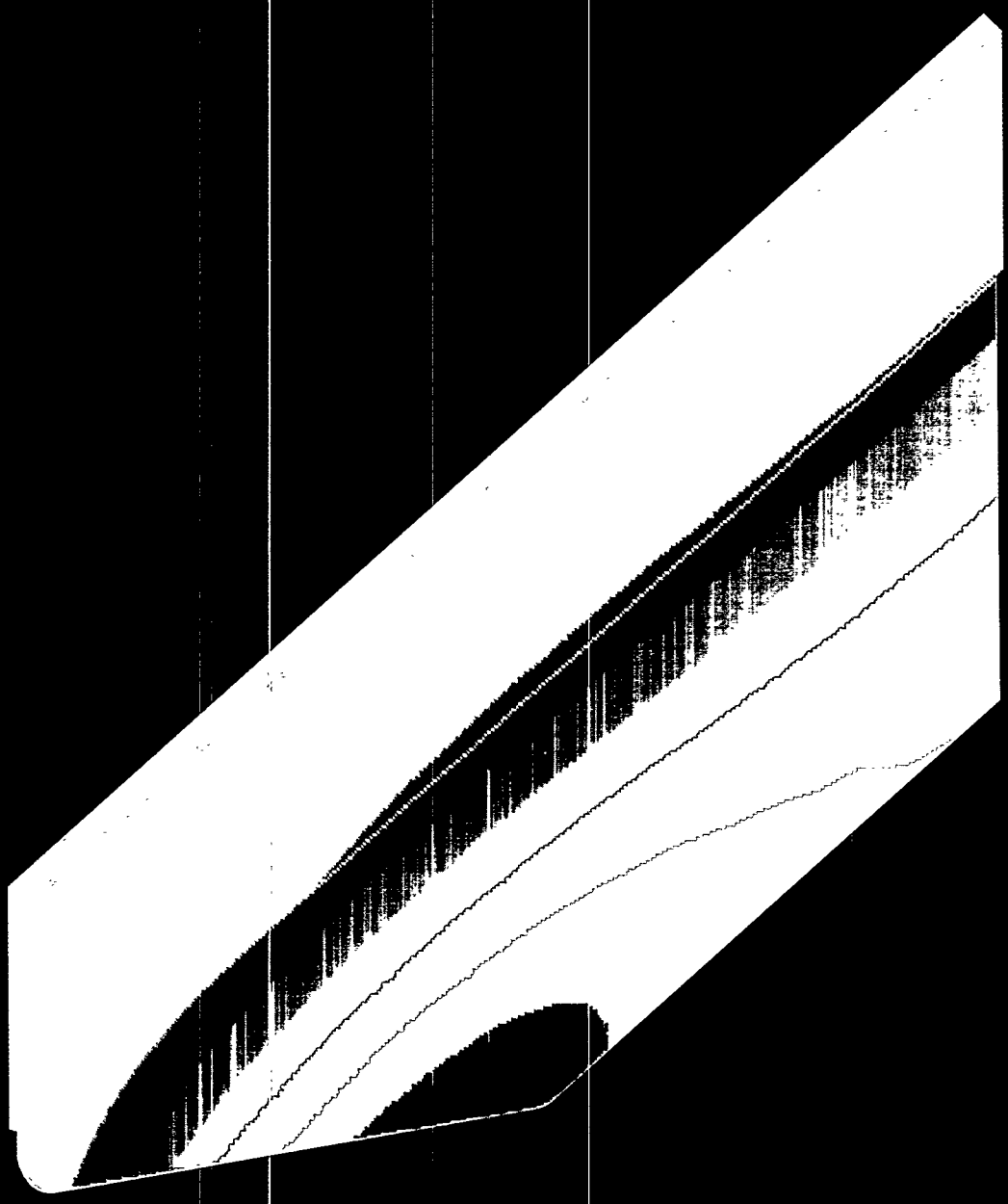
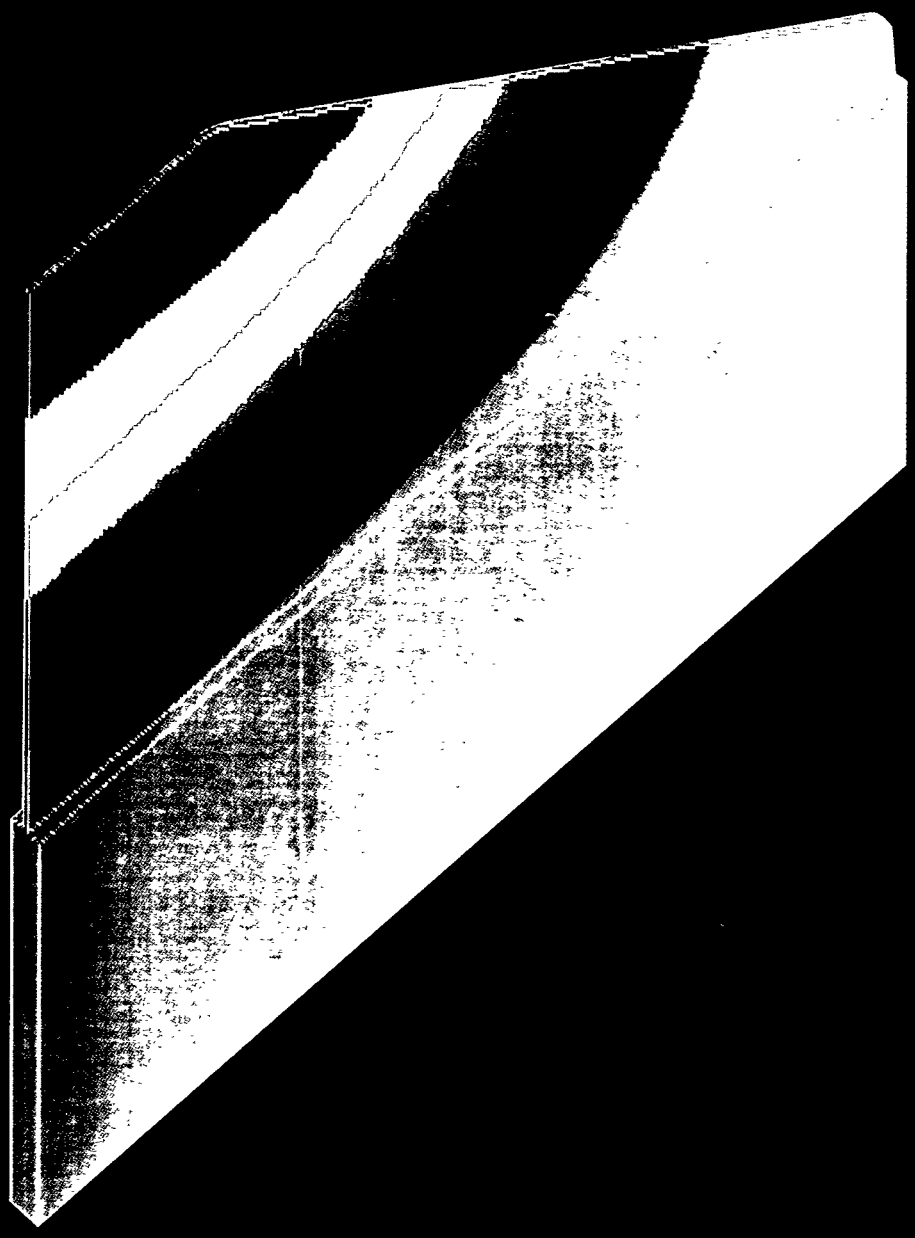


Figure 11 X23A3: Microradiographs of tape at 0, 0.29, 0.64 and 0.95% strain, from top to bottom; each field of view is 262 X 89 μm².



In anticipation of increasing the X-Ray Ring current beyond 250 mA, NSLS Engineers D. Lynch and P. Montanez have used finite element analysis methods to map out thermal and stress distributions in components that could be struck by synchrotron radiation. Shown here are temperature contours in position monitor blades, one style used at X17 (left) and the other at X21 and X25 (right). In normal operation, the thin blade, made of a molybdenum-based alloy and cooled by an external heat sink, skims an edge of the photon beam. The photo-current induced in the blade varies with the beam position. The contours shown here result when the full-power wiggler beam, under 2.5 GeV, 500 mA operating conditions, undergoes a worst-case excursion resulting in a larger interception cross-section with the blade. While the total power absorbed in each of these two cases is about 65-70 W, the X21/X25 blade on the right has a significantly higher maximum temperature (grey = 376° F through red = 3440° F) than the X17 blade (grey = 400° F through red = 1932 °F). Modellings performed by P. Montanez.

THREE
MEETINGS & WORKSHOPS



5TH INTERNATIONAL SYNCHROTRON RADIATION INSTRUMENTATION CONFERENCE: SRI '94

J.B. Hastings
NSLS R&D Section Head
SRI'94 Program Committee Chair



(left to right): Alain Fontaine (LURE), Yves Petroff (Director General of ESRF) and Denis McWhan (Conference Chairman and Chairman of NSLS), at one of the many SRI'94 poster sessions.

Synchrotron Radiation Instrumentation '94 (SRI'94), hosted by the National Synchrotron Light Source, was held at the State University of New York at Stony Brook, Stony Brook, New York, USA, July 18-22, 1994. This was the fifth such meeting in the series which began in 1982 in Hamburg, Germany. The size and breadth of the community has steadily increased over this period. This is reflected in the more than 550 participants from nearly twenty countries, dominated by the host with approximately 300 participants while the remainder were almost equally distributed between Europe and Asia. The highlight of the meeting was the scientific program, while mother nature's influence was certainly present as we suffered through a not atypical week of July weather.

The SRI'94 conference spawned a significant number of workshops as has become the standard for large international meetings. These took place both before and after the main meeting. The Advanced Photon Source and the European Synchrotron Radiation Facility hosted a workshop on high heat load optics at Argonne National Laboratory prior to the main meeting. The bulk of the workshops were held at SUNY Stony Brook on the Saturday before the meeting and these were hosted by the National Synchrotron Light Source Users' Executive Committee. Following the conference a workshop on polarization was held at Cornell's CHESS facility in Ithaca, New York. All of these workshops contributed significantly to the success of the SRI'94 meeting as a large international gathering.

The format of the scientific program of the main meeting was altered with respect to the previous SRI conferences to reflect the evolution in the utilization of synchrotron based science. When the field was in its infancy, any new instrument put into operation led to



(left to right): Sam Krinsky (NSLS Deputy Chairman) and Efrim Gluskin (ANL), meet for a discussion during a coffee break.

new experiments. With the rapid growth of sources more and more purpose-built instruments, tailored to specific experiments, have been constructed. The program reflected this with the plenary talks of the first two days which emphasized the science which has driven new instrumentation. There was an unexpected benefit to this format in the increased quality and participation of the poster sessions which were matched to these general scientific topics.

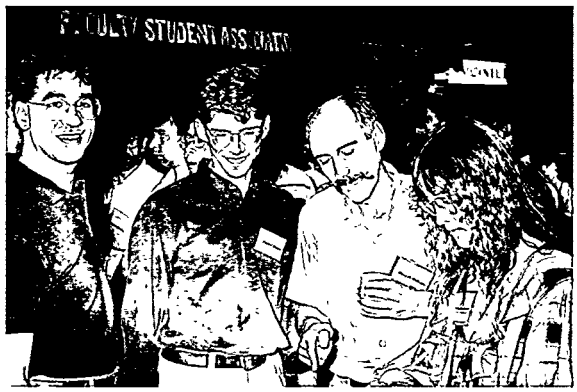
The lead off speaker on Monday morning was Prof. T. Blundell, the Chief Executive of the Biotechnology and Biological Sciences Research Council, United Kingdom. He spoke about the role of x-ray scattering research in bioscience and technology with a particular emphasis on protein crystallography. This is one of the most rapidly growing fields at synchrotron sources world-wide and could easily represent more than one third of their use by the turn of the century.

This talk was followed by a presentation from Dr. S.K. Sinha of Exxon Research and Engineering on synchrotron radiation in materials characterization. This is an important and growing field for the synchrotron community and will lead to a growth in the more applied uses of photons which are relevant to the industrial environment.

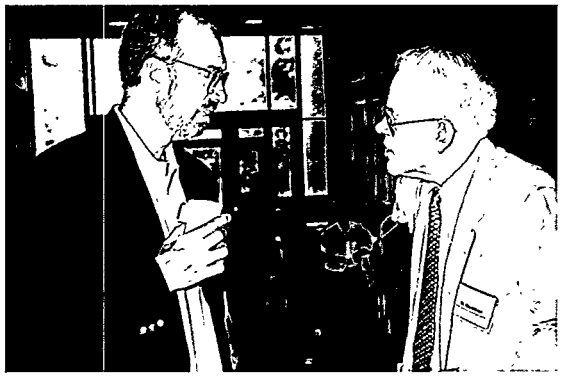
Tuesday's plenary speakers, Prof. R.J. Birgeneau and Prof. G.A. Sawatzky focused on current problems in condensed matter physics from the scattering and spectroscopic viewpoints respectively. In the invited sessions following the talks there was particular emphasis on the polarization properties of the beam, i.e. how to achieve arbitrary polarizations and how to measure them. This is a clear indication of the current trend. As the detailed understanding of the science evolves and the source quality improves, experimenters are gaining confidence in their ability to control more and more properties of the incident beam.

The last three days of invited talks on sources, optics, and detectors purposely did not involve parallel sessions. One of the highlights of the Wednesday sessions was the elegant presentation of the physics of accelerator based photon sources by Dr. A. Hofmann of CERN. Another bright spot was the presentation of Dr. Kitamura from KEK and the SPring-8 Project in Japan on developments of insertion devices. He showed some interesting possibilities, in particular small gap undulator devices on high energy rings to get high energy photons. In Dr. Kitamura's view, if successful these new magnets would make wigglers "dinosaurs".

On Thursday morning the topic was optics, where the challenge provided by the new sources may be the greatest. The significant enhancements in brightness will open up new areas of research using small (submicron) photon beams throughout the x-ray spectrum. This was discussed by Dr. D. Bilderback of CHESS, Cornell University, Ithaca, NY and Dr. A. Snigerev of ESRF, Grenoble, France. Another interesting development is in



(left to right): Lonny Berman (NSLS), Stephan Brauer (IBM), Gwyn Williams (NSLS, SRI'94 Local Organizing Committee Chair) and Jean Jordan-Sweet (IBM, NSLS Users' Executive Committee Chair)



(left to right): David Moncton (ANL Associate Laboratory Director) and Denis McWhan (NSLS Chairman and SRI'94 Conference Chairman).

the area of adaptive optics described by Dr. J. Susini of ESRF where he is developing adjustable optics using piezoelectric bilayers with central electrodes and opposite biasing of the two piezo plates leading to optics with variable radii of curvature at the turn of a knob.

The end of the beamline was saved for the end of the meeting. The Friday morning session concentrated on detectors. All of the presentations were reviews in nature. Looking back to the first talk on Monday emphasizing the SR growth industry (protein crystallography), two talks on the present competing detector technologies of image plates and CCD detectors were presented. Dr. A. Harrison of Edinburgh University, United Kingdom discussed imaging plates, and CCD detectors were described by Prof. S. Gruner of Princeton University USA. Dr Harrison discussed some of the physics of image plates that lead to insights into their true strengths and weaknesses. Dr. Gruner presented the state-of-the-art in CCD detectors and held out the possibilities of large "mosaic" blocks of individual detectors as the wave of the future, what one might call "CCD Wallpaper".

In addition to the scientific program a full program of social events was organized. These included a concert, a play, an afternoon visit to the NSLS, a banquet and daily events for companions. There was also a large vendor show, involving thirty-seven manufacturers, including four from Europe and one from Japan, which took place during the first three days of the conference.

On the last day there were the thank you's to the staff that organized the meeting, to which, as a participant in all the previous meetings, I add mine and note the good humor of the people at Stony Brook and the NSLS in light of the adversity of the weather. Finally, it was announced that SRI'97 will be held in Japan and hosted by the SPring-8 Project team.



Nick Gmur (far left) and Linda Feierabend (NSLS), organizers of the Vendor Exhibit, with Dennis Mills (Argonne National Laboratory) and Dave Rognlie (Blake Industries).

SRI '94

Jean Jordan-Sweet, IBM
SRI'94 Organizing Committee

On Sunday, July 17, five workshops were held in the Student Union and Department of Earth and Space Sciences at SUNY Stony Brook in conjunction with SRI'94. The rooms were packed with a total of over 220 speakers and attenders, and in spite of the hot weather and World Cup Soccer Final, an exciting full day of talks, posters, and discussions was enjoyed by all. Reports on these five workshops follow. Two additional satellite meetings were held on the weekends before and after SRI'94. One, held at the APS, addressed Thermal Management of Optical Components for Synchrotron Radiation, and was organized by Denny Mills, Andreas Freund, and Tetsuya Ishikawa. The second, a workshop on X-Ray Science with Polarized Radiation, was held at CHESS and was organized by Qun Shen and Ken Finkelstein. Reports on these two satellite meetings can be found in Synchrotron Radiation News. Thanks are owed to the NSLS Users' Executive Committee for providing some travel money for speakers at the five workshops held at Stony Brook.

Applications of X-Ray Standing Waves in Studies of Surfaces, Films, and Bulk Materials

David Heskett (University of Rhode Island) and Lonny Berman (NSLS)

The workshop began with introductory talks presented by Bob Batterman (Cornell/CHESS) and Michael Bedzyk (Northwestern University/ANL). Prof. Batterman described some of the basic theory and provided some insights into dynamical diffraction and phase shifts in x-ray scattering. Prof. Bedzyk described x-ray standing wave studies of Langmuir-Blodgett films and special optical effects using a total external reflection geometry to generate the standing wave field.

In the late morning session, Hiroshi Kawata (Photon Factory) presented Magnetic XANES and Compton scattering measurements under a standing wave field which was generated by circularly polarized radiation from an elliptical wiggler at the KEK Laboratory in Japan. Michail Kovalchuk (Institute of Crystallography, Moscow) summarized the activities of his group using the XSW technique to study the amorphization of semiconductor surfaces, impurities in semiconductors, and long period multilayers. The last talk of the morning session, which was held jointly with the XAFS workshop, was a description by Fabio Comin (ESRF) of his beamline for XSW and SEXAFS which is currently under construction at the ESRF in Grenoble, France.

In the afternoon session, Jorg Zegenhagen (Max Planck Institute, Stuttgart) presented some more theory of x-ray standing waves from his recent review article, then continued with a description of a combined XSW/STM investigation of different coverages of Ga on Ge(111). Jim Patel (AT&T) followed with a talk on his studies of the vibrational amplitudes as a function of temperature of overlayers of Ga, As, and Ge on Si(111) and Si(100) obtained by using the XSW technique. Joe Woicik (NIST) presented his results on the structure of clean InP(110), Sb overlayers on III-V(110) semiconductors surfaces, and In on Si(111), the latter involving a combined XSW/SEXAFS study. His work was distinct from the previous talks in that he made use of the back-reflection geometry in his XSW studies.

In the final session of the workshop, seven shorter contributed talks were presented, followed by closing remarks by Lonny Berman. The workshop had approximately fifty attendees and most of the currently active x-ray standing wave groups were represented.

X-Ray Microbeam Techniques and Applications

Slade Cargill (Colombia University) and
Don Bilderback (Cornell University)

This workshop brought scientists together for discussions on techniques of microbeam focussing optics.

Steve Hoffman (Northwestern University) highlighted the work at CHESS where monocapillaries have been observed to make beam sizes down to 50 nm dimension.

Per Engström (ESRF) spoke about the importance of having capillaries with an ellipsoidal rather than a conical (linear) taper for improved efficiency. One current puzzle in tests being made at the ESRF is why so little gain is being obtained with capillaries on an undulator line compared to the excellent prior tests at a HASYLAB bending magnet.

Hyde Kim (University of Washington) spoke about the potential advantages of capillary focussing over ellipsoidal mirror focussing (ten times more intensity) for APS in creating a 1 micron diameter beam.

Dan Thiel (Cornell University) spoke about x-ray tracing design of capillary optics and the question "What shape of real optics is most tolerant of fabrication errors?".

Andrew Peele (University of Melbourne) spoke about x-ray astronomy applications with square and round hole arrays made by etching techniques.

Keith Jones (BNL) talked about imaging and fluorescence microprobe applications with femtogram sensitivity.

Slade Cargill (Columbia University) discussed mapping out microstructure, stress, and composition in polycrystalline materials on a micron scale.

Anatoly Snigirev (ESRF) spoke about x-ray microprobe and micro imaging techniques based on Bragg-Fresnel zone plates with beam sizes down to 0.8 micron.

Barry Lai (ANL) spoke about making microbeams with phase zone plates. Recent tests at the NSLS have produced a resolution of 0.6 micron. He showed an application where one zone plate was used to make a microbeam and a second zone plate was employed to enlarge it in size to better match to the image size of a CCD area detector.

Eliot Specht (ORNL) spoke about microdiffraction analysis of orientational correlations in TI-1223 films. If the tilt boundaries have less than 12 degrees of misorientation, then they are good superconductors.

Kazumasa Ohsumi (Photon Factory) described crystallography studies on submicron-sized grains of aluminum and olivine, emphasizing the successful measurement of many structure factors.

Henry Chapman (SUNY - Stony Brook) described a technique called Wigner deconvolution to obtain phase and amplitude maps of soft x-ray images in order to increase their resolution.

Yasushi Kagoshina (Photon Factory) showed images of magnetic domains analyzed with one micron spatial resolution and circularly polarized light.

Al Thompson (Advanced Light Source) concluded the session with a talk on Kirkpatrick-Baez optics for microfluorescence application at the ALS with two micron resolution.

This workshop had the largest attendance of those held at SRI'94, with over seventy persons. With the arrival of third-generation sources and the current developments underway in optics, this is a very exciting period indeed.



Synchrotron Radiation at High Pressure

Donald J. Weidner
Director of CHiPR at SUNY Stony Brook

X-ray studies at high pressure and temperature continue to be a challenge, limited by instrumentation and data analysis. The workshop on high pressure synchrotron studies, which was sponsored by the SRI'94 organization, the Center for High Pressure Research (CHiPR), and associated with the IUCr, focussed on these issues with twelve presentations and related discussions.

Third-generation synchrotrons offer the possibility of using monochromatic radiation with angle dispersive detection. This allows a better data base for defining crystal structure at elevated pressure and formed the central theme of several of the presentations. Wright (U. of Edinburgh) illustrated the use of 2-D detectors to help eliminate the effects of sample granularity. Svensson (ESRF) discussed methods to eliminate detection errors in imaging plate and CCD detectors. Parise (SUNY - Stony Brook) demonstrated Rietveld refinements from a high pressure angle dispersive study of $NaMgF_3$. Itie (U. Pierre et Marie Curie) demonstrated the power of combining diffraction and absorption techniques to define the structural evolution of $GaAsO_4$ with pressure. The utility of EXAFS for structure analysis at high and low temperature was illustrated with a sample of Ge. Ruoff (Cornell U.) discussed the results of a compression study on CsH to 253 GPa. The sample undergoes a phase transition at 17.5 GPa to a phase that persists throughout the remaining pressure interval, where the fractional volume is reduced to 0.26.

With synchrotron sources it is now possible to define not only pressure, but also deviatoric stress in the sample. Besson (U. Pierre et Marie Curie) demonstrated the homogeneity of the stress field in a compact toroidal anvil system using the ESRF synchrotron where he could observe up to 20 diffraction peaks in NaCl (200 keV). Weidner (SUNY - Stony Brook) analyzed microscopic deviatoric stress as expressed by broadening of the diffraction lines in a polycrystalline diamond sample. On the one hand, these measurements demonstrate the possibility of determining yield strength of samples at high pressure and temperature, while on the other hand they suggest annealing techniques that can help alleviate stress induced peak broadening. Mao (Geophysical Laboratory) demonstrated the role of deviatoric stress in a high pressure phase transition in wustite.

As x-ray systems continue to open new possibilities, so do high pressure, high temperature apparatus. Utsumi (SUNY - Stony Brook) emphasized how the use of sintered diamond anvils has expanded the pressure capabilities of large volume systems. Fiquet (Sciences de la Terre ENS. Lyon) provided diffraction results of a new room pressure/high temperature cell for a $CaTiO_3$ (to 1900K) and MgO and Al_2O_3 (to 2500K). A new experimental station with a CO_2 laser heated diamond anvil cell was presented along with discussion of pressure and temperature calibration.

Hausermann and Shimomura gave updated information concerning high pressure facilities at ESRF and the Photon Factory, respectively. Light limiting experiments on H and He at high pressure are proceeding and will benefit from new focussing optics and a wiggler source. Shimomura presented angle dispersive data obtained with an imaging plate for samples in MAX80 and MAX90, the cubic anvil apparatus at the Photon Factory. The signal to noise ratio is greatly enhanced with a radial slit system. Recently MAX80 has been used as the first of a two stage (so called 6/8 type) apparatus. The second stage consisted of eight sintered diamond cubes, which are also used as the x-ray window to the sample.

Technique and Experimental Method for X-Ray Absorption Fine-structure Spectroscopy

Geraldine Lamble (NCSU)

Over fifty international scientists participated in what was a very interactive and fruitful workshop. A trio of varied overview talks made up the morning session. Steve Heald (PNL) began with a talk on the new XAFS experiments which will be made possible by the third-generation high brilliance machines. These included new opportunities provided by high flux microfocussing, such as single crystal studies on natural grains, microprobe studies of grain boundaries, and time resolved reflectivity and reflexafs. He also considered the benefits to some of the XAFS-related techniques such as DAFS and x-ray energy loss experiments.

The second talk was on Soft X-ray Spectroscopy of Metalloproteins by Steve Cramer (UCLA @ Davis), who discussed work on the L-edges of the transition metals in proteins. He also related the experimental difficulties encountered in working with these liquid samples at such low energies, with path lengths of less than a micron. A partial solution is to minimize window absorbance in detectors, sample cells and chamber. Information-rich spectra make this effort worth-while. X-ray Magnetic Circular Dichroism Spectroscopy (MCD) was discussed along with its experimental challenges. New sample instrumentation for the ALS includes a low inductance rapid field switching magnet and a dilution refrigerator for sample temperatures as low as 0.1K.

The third speaker was Fabio Comin (ESRF), who addressed a joint session of the XAFS and Standing Wave workshops. He discussed some sophisticated instrumentation for the SEXAFS and standing wave beamline currently being commissioned at the ESRF. Emphasis of the beamline design goals was on experimental flexibility, to satisfy the wide range of experiment-specific technical requirements. For instance, the resolution required for the standing wave measurements exceed that for SEXAFS. Here, the additional requirements are met by the availability of a second monochromator for the Standing Wave measurements. Particularly interesting features were a cryogenically cooled sagittally focussing scanning monochromator and scanning support mechanisms with active positional feedback. The latter were based on an old concept for flight simulators.

The afternoon began with an extended poster session. Many interesting presentations were made in a variety of categories. Work related to soft x-ray measurements included that by Joe Wong *et al.* on new opportunities for measurements in the 1-2 keV region with a YB_{66} monochromator; Mark Antonio's phosphorus K-edge measurements represented soft x-ray measurements done on a hard x-ray beamline; Inho Song demonstrated an *in situ* total electron yield detector with sulphur K-edge results on tarnish oxidation/sulfidation products, and fluorescence detection for structural determination of low Z elements (C, N, O, and F) was presented by Danny Fischer. Other presentations on detectors were on: an array of spherically bent germanium crystals for high resolution fluorescence measurements by Jeffrey Moore *et al.*; a wavelength dispersive fluorescence detector using capillary optics by Johnny Kirkland *et al.*; a low temperature total electron yield detector by Ken Kemner *et al.*; CdTe photoconductor array by Pedro Montano *et al.*; a fast amplifier for dead time reduction by Mark Chance *et al.* Presentations related to time resolution measurements included: a critical assessment of the QEXAFS method by Joe Wong *et al.*; a presentation of the instrumentation used on the ANL dispersive XAFS beamline at the NSLS by Peter Lee *et al.*; developments with the dispersive XAFS spectrometer at LURE by Alain Fontaine *et al.*; ideas on the geometry for time resolved fluorescence measurements by Fulong Lu and a demonstration of time resolved XAS for probing the structural dynamics of ligand binding to Myoglobin by Lisa Miller *et al.* Johnny Kirkland *et al.* presented their plans for the redesign of the NRL beamline X23B at the NSLS, including a two mirror system for collimation/focus and a fixed exit double crystal monochromator; Geraldine Lamble presented

design and results of operation of a single/double bounce harmonic rejection mirror; Bob Mayanovik *et al.* showed fluid inclusion measurements using micro-XAFS; Doug Pease *et al.* presented their design for an enhanced intensity DAFS spectrometer; Jim McBreen *et al.* described a sample cell for *in situ* battery and fuel cell materials. A poster from Derrick Mancini and Adam Hitchcock described a network database of core edge excitation spectra of gas phase atoms and molecules, available on the World Wide Web; and Dave Adler *et al.* presented a design for a sagittal focussing crystal bending mechanism, including a hugely popular exhibit of the device in action.

The people who were able to resist the temptation of leaving to watch Brazil playing Italy in the World Cup Final stayed to discuss other subjects of possible interest to the XAFS community in a session chaired by Dale Sayers (NCSU) and Tim Elam (NRL). Topics included the status of the International XAFS Society (IXS). Reports were given by the database subcommittee chairman Bruce Bunker (U. of Notre Dame) and the education subcommittee chairman Tim Morrison (Illinois Inst. of Tech.). Protracted discussion ensued on both these issues and on suggestions for modifications to the "Standards and Criteria" guidelines for publications generated by the IXS in an attempt to control the quality of published XAFS work. These discussions are expected to continue at the International XAFS Conference in Berlin, August 1994. The workshop concluded late in the afternoon, after a very stimulating and enjoyable day.

Computed Microtomography: Techniques and Applications

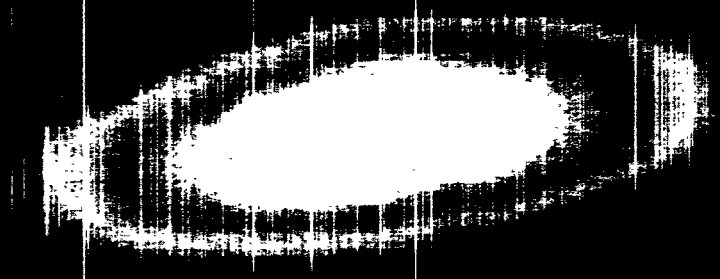
Keith W. Jones and Per Spanne (BNL-DAS)

The field of computed microtomography has developed rapidly in the time following the advent of second-generation synchrotron x-ray sources. Further development of the field can be expected from use of insertion devices at third-generation sources. Advances in the technology of detectors combined with improved reconstruction and display techniques made possible by improved computer technology should lead to further major developments in microtomography in the immediate future. Talks given at this workshop examined some of the major instrumentation questions of importance and examined several applications of the instrumentation.

The present status of charge-coupled devices for x-ray detection was discussed by S. Naday (ANL). The performance of these devices is of interest since times necessary for data accumulation and data read-out determine the rate at which tomographic sections can be acquired. Hans Pfister (SUNY - Stony Brook) discussed computer architectures and their application to high-speed visualization of three-dimensional tomographic data sets. P. Spanne (BNL) and R. Pahl (Cornell University) discussed existing tomographic systems in use at BNL and at Hamburg. The approaches included use of first- and third-generation type apparatus. Applications of computed microtomography were presented by both speakers. Spanne described studies of reservoir rock, catalysts in polyethylene polymerization particles, and plasma-spray coatings of W-Co used in jet engines. Pahl included examples of work with metal matrix composites, supported catalysts, and osteoporotic bone.

I. McNulty (ANL) and E. Haddad (LLNL) discussed tomography experiments based on the use of sub-micrometer beams produced using zone plate optics. These first experiments explore one promising approach for development of ultra-high resolution measurements.

M. Coles (Mobil Research and Development Corp.) presented a discussion of applications of CMT to reservoir rocks. Mobil is using the CMT results to aid in the statistical description of rock/pore systems, calculation of transport properties, and pore level visualization of endpoint fluid saturations in order to develop improved reservoir management tools. The need in instrumentation for this work is to provide larger data sets at high spatial resolution at high acquisition rates in order to facilitate study of fluid flow in larger samples.



These images of the stored electron beam in the X-Ray Ring were taken using a pinhole camera which is under development at beamline X28C. They illustrate the reduction in the X-Ray Ring vertical beam size achieved with a new system of 17 skew quadrupole magnets. The right image shows the beam profile with the new skew quadrupoles, while the image above shows the smallest beam profile previously achievable . Using the new system, the vertical emittance of the X-Ray Ring was reduced by a factor of six to below 2 Å. [J. Safranek and S. Krinsky, "Coupling Correction Using Closed Orbit Measurements," AIP Conference Proceedings 315, 163 (1993)]

FOUO
OPERATIONS



VUV MACHINE

Stephen Kramer
VUV Ring Manager



Stephen Kramer, VUV Ring Manager

The monthly breakdown of the VUV Ring performance statistics is shown in the accompanying **Figures 1** to 6. The VUV Ring reliability remained high during FY 1994 with the users able to rely on the beam being available greater than 98% of the scheduled time. The steady increase of the integrated current delivered to the users over the past several years has taken a slight down turn by about 4%. Most of this decrease was the result of the reduced number of hours scheduled for operations, resulting from the two extended downtime periods in Fall'93 and Spring'94. Although little work was scheduled for the VUV Ring during these periods, the injection system upgrade required these long periods for the installation of new major systems. Improvement in the injection statistics does not appear in this year's data since this improvement program will not be completed until FY 1995. The reduction of the injection rate following the Fall'93 shutdown was partly the result of operators having to learn to tune for changes in the injection system and partly the result of a change in vertical tune of the VUV Ring (described below). It is expected that when the injection system upgrade is completed the higher rates observed in October and November 1993 will become more routine. However, in keeping with the ALARA Order, this rate may not continue to increase in the future as the injection efficiency improves, since the booster current may be reduced in order to reduce the radiation rate during injection. A better method of operation may be to keep the total injection time around five minutes, which is a reasonable time to allow temperature control systems to track these large changes of ring current without causing oscillations.

Prior to the Fall'93 shutdown, the powered 4th harmonic RF system was commissioned and approved for operations by the users. Following this shutdown a combination of problems caused beam intensity fluctuations for the users. Solving these problems required intense effort from the RF and Power Supply Groups to eliminate these fluctuations and to re-commission the 4th harmonic RF system. Although these problems could have been avoided, the pressures of reduced operations staff and the need to continue improvements to the NSLS accelerators and storage rings reduced the resources available for the

maintenance studies that could have identified these problems beforehand. The lessons learned from this difficult period will help reduce their reoccurrence in the future. By the Spring'94 shutdown the powered 4th harmonic RF system was working as it had in November 1993. This RF system, while providing only a modest 10% increase in lifetime at 500 mA over the passive 4th harmonic RF system, increases the lifetime more than 60% at 200 mA and also provides a more constant bunch length and shape at all currents (a useful property for timing experiments). Work will continue on both RF systems to better understand their properties and their effects on the beam current distribution. Significant improvement has already been made on reducing the noise signals in the RF power sources and the fluctuations they induce on the beam. Although most users do not see these fast fluctuations, the new state-of-the-art infrared beamlines see them as noise in their energy spectra which limits their sensitivity for small signals. An additional feature of this powered 4th harmonic RF system that has been studied, was the controlled shortening of the bunches to counter the natural bunch lengthening that occurs as the bunch current increases. Although this will reduce the lifetime, the shorter bunches will be useful for timing experiments, where bunches less than 100 psec are desirable.

Considerable studies were carried out to understand the source of fluctuations in vertical beam size and lifetime during the beam decay of a fill. The source was determined to be the occurrence of several high order coupling resonances near the betatron tune working point. As the beam current decayed, the vertical tune shift would cause the tune to pass through one of these resonances, resulting in an increase in the vertical emittance and lifetime. After the Spring'94 shutdown the vertical tune was increased to avoid passing through these resonances during the beam decay. This eliminated the emittance increase between 600 and 450 mA and is partly the reason the lifetime improvement from the powered 4th harmonic RF system

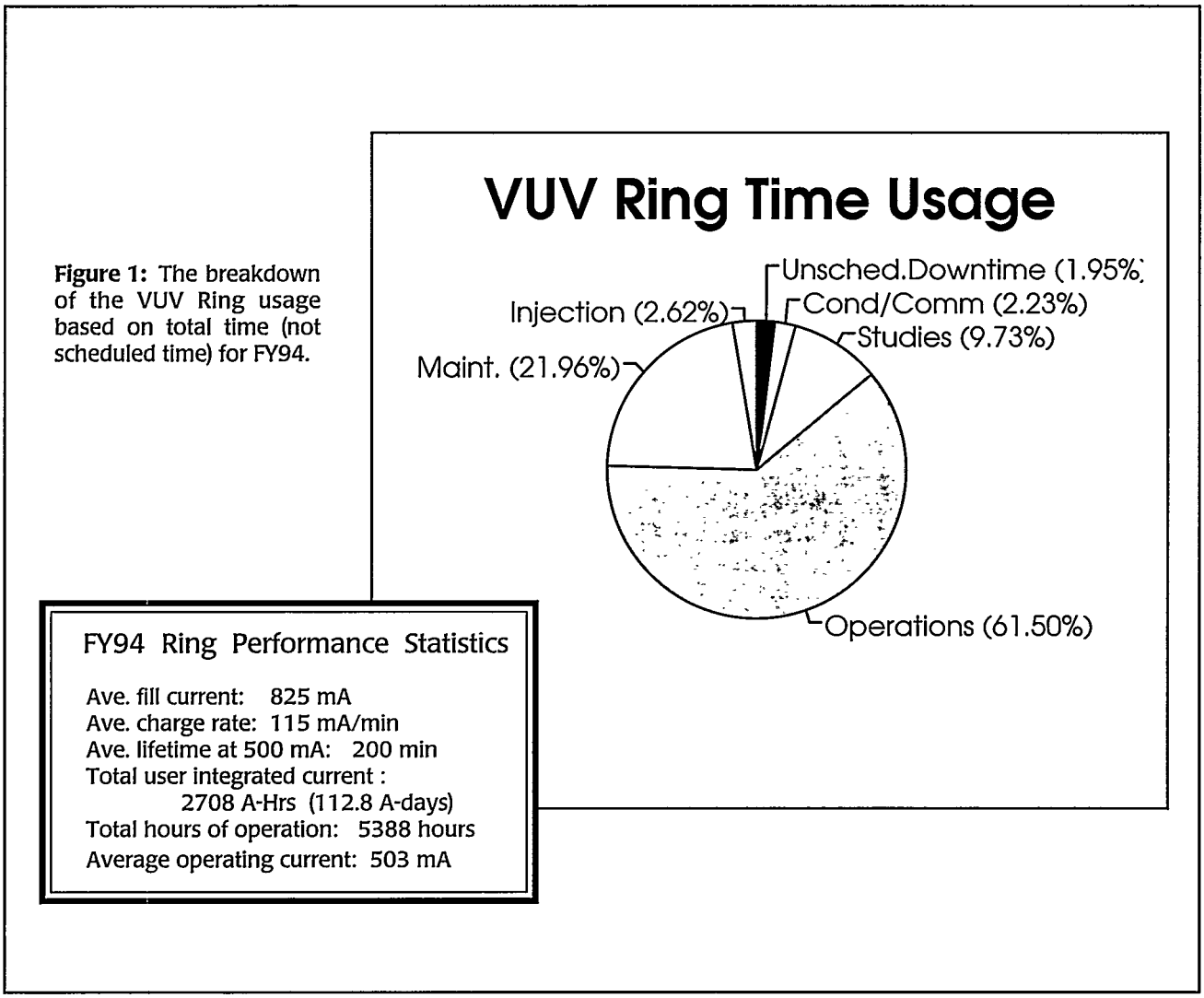


Figure 1: The breakdown of the VUV Ring usage based on total time (not scheduled time) for FY94.

VUV Ring Performance

FY 1994

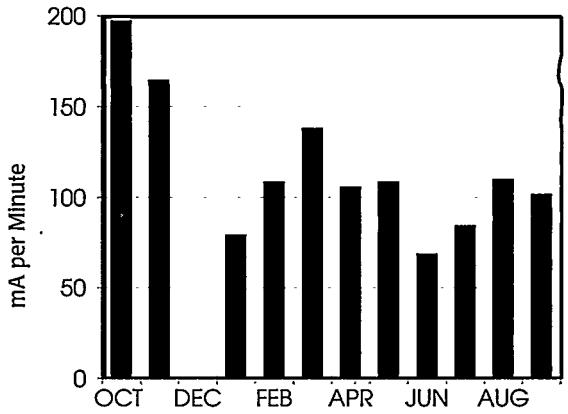


Figure 2: The VUV Ring injection charge rate averaged over all fills in each month.

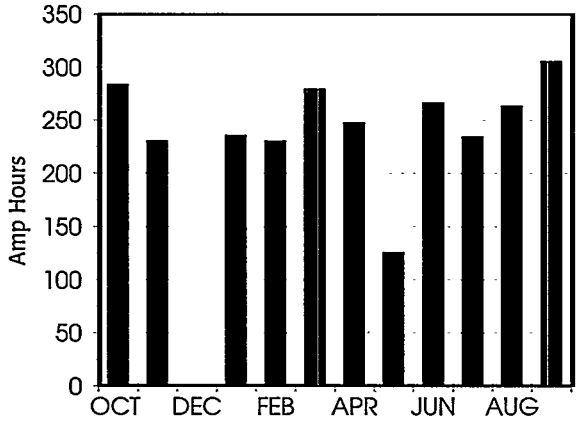


Figure 3: The total integrated current for the VUV Ring accumulated each month.

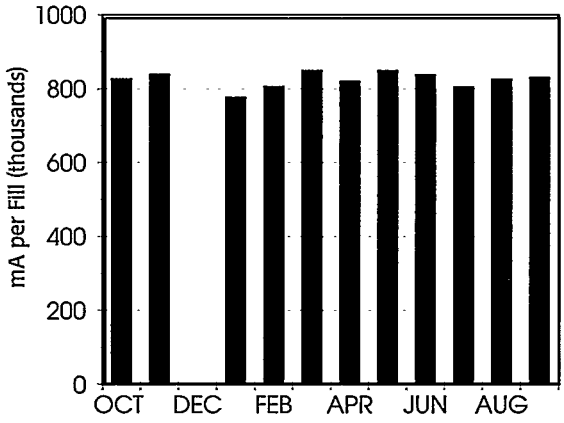


Figure 4: The injection current averaged over all fills in a month for the VUV Ring.

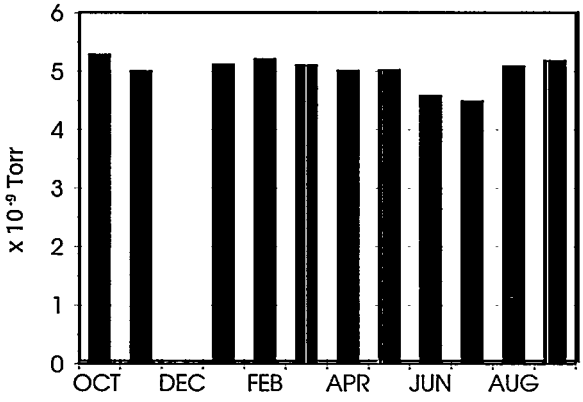


Figure 5: The VUV Ring vacuum pressure at 500 mA beam current averaged over each month.

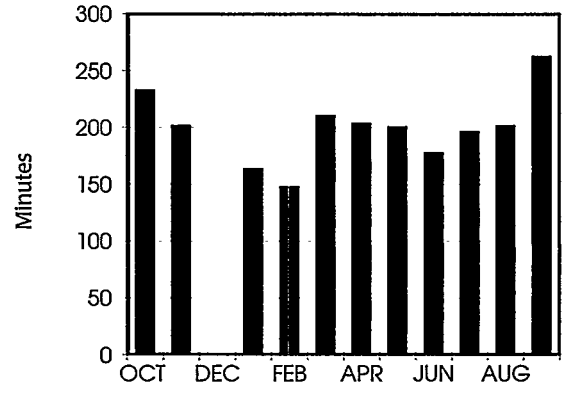


Figure 6: The VUV Ring exponential beam lifetime at 500 mA beam current (seven bunch operation only) averaged over each month.

is not reflected in the average lifetime statistic. However, this variation in photon beam flux, observed by the users, was reduced and the average photon beam brilliance increased. Other sources of photon beam flux changes have been identified as coming from temperature changes in the NSLS water cooling system, which induce electron beam orbit motion. The largest and most frequent of these comes from a beam dump in the X-Ray Ring, which is the major heat load on the water cooling system. Although the Global Orbit Feedback System reduces the rms beam orbit motion to less than 90 microns horizontally and less than 30 microns vertically, the resulting photon flux change is significant for the high resolution beamlines. The NSLS water system will have major improvements during FY 1995, which should greatly reduce these water temperature driven beam orbit motions.

During FY 1994 all magnets have had high resolution Hall probes installed. These devices are read by the NSLS control system and have allowed for the tracking of beam orbit motions caused by changes in the magnetic fields of the dipole and quadrupole magnets. Several unusual glitches have been observed that explain changes in beam flux for the users. The reason for these changes is being studied but since they occur at a very low rate it may be some time before their sources are fully understood.

FY 1994 saw the approval of an upgraded Safety Analysis Report (SAR), that will permit the VUV Ring to operate at electron beam energies greater than 744 MeV. Some initial studies found that the beam could operate up to 825 MeV, but that a change in the dipole power supply would be necessary to go safely above 800 MeV. These changes will be made in FY 1995 and the studies will continue to explore the maximum safe operating energy for the ring. However, studies at 800 MeV have already shown a 70% increase in lifetime for the same vertical emittance as at 744 MeV. It is expected that during FY 1995 the operating energy will be increased to greater than 800 MeV. At that point the VUV user community will need to determine whether to accept all of the increased lifetime or whether to operate at higher brilliance and similar lifetime. The availability of the new Hall probes in the magnets will make operations at these higher energies more reproducible, since the magnets must be ramped between the booster injection energy and the VUV operating energy. Another improvement in lifetime was studied during FY 1994, that of filling all nine bunches in the ring. Previously a large coupled bunch instability was observed at currents above 600 mA, but this instability was absent during the latter half of FY 1994. Although the vertical beam size was observed to have a non-Gaussian component when all bunches were equally filled, a small charge imbalance in one bunch appeared to counter this effect. Next year these studies will continue in order to understand the properties of the beam with all bunches filled, and with the hopes of providing another option for yielding increased lifetime or brilliance.

In conclusion, FY 1994 yielded considerable new insight into the beam properties of the VUV Ring and with the new systems becoming operational the VUV user community will have a difficult decision to make: increased current with the same lifetimes, increased lifetime at the same currents, increased brilliance, or some combination of all three. Along with these options will come a reduction in beam orbit motion to less than 10 microns from the improved water cooling system and the ability to track and correct magnetic field changes. Like most teenagers, the VUV Ring continues to grow in potential and has a number of surprises that will continue to provide improved photon beam properties to the many beamlines already in operation.

VUV Storage Ring Parameters as of November 1994

Normal Operating Energy	0.745 GeV
Peak Operating Current (multibunch ops.)	0.85 amp (0.9×10^{12} e$^-$)
Circumference	51.0 meters
Number of Beam Ports on Dipoles	17
Number of Insertion Devices	2
Maximum Length of Insertion Devices	~ 2.5 meters
$\lambda_c(E_c)$	25.3 Å (486 eV)
$B(\rho)$	1.28 Tesla (1.91 meters)
Electron Orbital Period	170.2 nanoseconds
Damping Times	$\tau_x = \tau_y = 17$ msec; $\tau_\epsilon = 9$ msec
Lifetime @ 200 mA with 52 MHz	200 min
(with 211 MHz Bunch Lengthening)	(350 min)
Lattice Structure (Chasman-Green)	Separated Function, Quad, Doublets
Number of Superperiods	4
Magnet Complement	8 Bending (1.5 meters each) 24 Quadrupole (0.3 meters each) 12 Sextupole (0.2 meters each)
Nominal Tunes (ν_x, ν_y)	3.14, 1.24
Momentum Compaction	0.023
RF Frequency	52.887 MHz
Radiated Power	14.7 kW/amp of Beam
RF Peak Voltage with 52 MHz (with 211 MHz)	80 kV (20 kV)
Design RF Power with 52 MHz (with 211 MHz)	50 kW (10 kW)
Synchrotron Tune (ν_s)	0.002
Natural Energy Spread (σ_e/E)	4.7×10^{-4}, $I_b < 20$ mA
Bunch Length (2σ)	9.7 cm ($I_b < 20$ mA)
($2I_{rms}$ with 211 MHz Bunch Lengthening)	(25)
Number of RF Buckets	9
Typical Bunch Mode	7
Horizontal Damped Emittance (ε_x)	1.38×10^{-7} meter-radian
Vertical Damped Emittance (ε_y)	$\geq 3.5 \times 10^{-10}$ meter-radian (2.8×10^{-9} in normal ops.) *
Power per Horizontal milliradian (1A)	2.3 Watts

Arc Source Parameters

Betatron Function (β_x,β_y)	1.18 to 2.25 m, 10.26 to 14.21 m
Dispersion Function (η_x, η_x)	0.500 to 0.062 m, 0.743 to 0.093 m
$\alpha_{x,y} = -\beta'_{x,y}/2$	-0.046 to 1.087, 3.18 to -0.96
$\gamma_{x,y} = (1 + \alpha_{x,y})/\beta_{x,y}$	0.738 to 0.970 m^{-1}, 1.083 to 0.135 m^{-1}
Source Size (σ_x, σ_y)	536 to 568 μm, >60 to >70 μm (170-200 μm in normal ops.) *
Source Divergence ($\sigma_{x'}$,$\sigma_{y'}$)	686 to 373 μrad, 19.5 to 6.9 μrad (55-20 μrad in normal ops.) *

Insertion Device Parameters

Betatron Function (β_x, β_y)	11.1 m, 5.84 m
Source Size (σ_x, σ_y)	1240 μm, >45 μm (130 μm in normal ops.) *
Source Divergence ($\sigma_{x'}$, $\sigma_{y'}$)	112 μrad, >7.7 μrad (22 μrad in normal ops.) *

* ε_y is adjustable

VUV BEAMLINES

Roger Klaffky
VUV Operations Manager

During FY 1994 there were 163 different experiments performed as determined from a count of NSLS Safety Approval Forms. The institutional breakdown of scientists participating on these experiments was 38% from universities, 22% from industry, 18% from BNL, 10% from other DOE labs, 9% from abroad and 3% from government laboratories.

There were a number of technical beamline improvements. At U2B a Nicolet Magna Michelson interferometer was installed. This instrument has a KBr beamsplitter and a dynamic alignment capability for the stationary mirror. The absolute position of the moving interferometer mirror is measured permitting the correlation of scans of strongly absorbing samples. A second beamline was installed at U2B, bringing a collimated beam into the former IBM clean room. A modified Spectra-Tech IRμs infrared microspectrometer, covering the 800 cm^{-1} to 4000 cm^{-1} range with diffraction-limited spatial resolution, was installed and commissioned on this line.

Reconfiguration of U3A continued in 1994 with the installation of new shielding and an interlock system protecting against power and vacuum losses. The interlock system also permits U3A and U3C to operate independently through a common upstream mirror chamber. Commissioning of the monochromator continued with the partial implementation of computer control. Four pairs of multilayer gratings were purchased for the monochromator and their reflectivities were measured.

At U4IR the main Michelson interferometer was replaced by a Nicolet Impact 400 model modified to operate in vacuum. Using a silicon beamsplitter, this instrument operates over the range 10 to 3500 cm^{-1} with a maximum resolution of 1 cm^{-1} and a repeatability of approximately 0.02% in 100 seconds for frequencies below 1000 cm^{-1}, the region of primary interest on the beamline.

On U4A there was development work done on a new data acquisition system based on an NCR 486 PC running the LINUX operating system.

The upgrade of the U5U monochromator from a moderate energy resolution TGM to a high resolution SGM began in FY 1994. This upgrade will result in an increase in sample intensity by a factor of approximately 100 as a result of the decreased spot size in the SGM design. The collecting/focusing (M0) and refocusing (M1) mirrors were ordered, fabricated, received and checked. The four spherical gratings were ordered and bids were solicited for the grating chamber.

All of the components required to upgrade the U7A monochromator to a high resolution SGM were either fabricated or acquired from outside. This upgrade will enable high energy resolution spectroscopies such as photoabsorption and photoemission (angle-integrated and angle-resolved) to be performed. A refocusing mirror, mirror tank and stand were also designed and ordered.

A new spectrometer for non-vacuum time-resolved fluorescence spectroscopy (wavelengths greater than 180 nm) was commissioned on U9B. The use of all-reflection collection optics eliminated the problems associated with chromatic aberration of luminescence, and improved sample access.

An NSLS angle-resolved photoemission apparatus to achieve ultra-high energy resolution was used to demonstrate that the U11 beamline is appropriate for angle-resolved photoemission measurements at the 10 meV energy resolution level. A number of items were added to the beamline including a windowed gate valve and adapter to facilitate chamber alignment, an IBM PS/2 Server 95 560 computer for data acquisition, and a Gateway 2000 for data analysis. A UHV sample chamber for time-resolved fluorescence measurements was assembled and tested on U11. It was also demonstrated that circular dichroism can be measured to 130 nm with high signal-to-noise using a calcium fluoride photoelastic modulator.

On U13UB, end stations for testing complete EUV imaging systems to an accuracy of 1/4 wave at 14 nm wavelength and for carrying out EUV lithography at 14 nm were installed. A 1X Offner camera operating at 13 nm was partially installed. This device will be able to expose wafers over a large (several square mm) area. It will also be used as a mask inspection tool.

The three soft x-ray gratings (300,600 and 1200 line/mm) on the U13UA high flux, high resolution hybrid wiggler/undulator 6 degree branch line were in use during

all of FY 1994. A 20 degree VUV (30-120 eV) U13UA branch line was installed during FY 1994. When commissioned, this line will utilize two plane mirrors to deflect diffracted light through the moveable exit slit and into the sample chamber of the 6 degree line. In this way, the entire 30 to 1000 eV energy range will be available in the sample chamber. The high resolution, low energy (5-30 eV) U13UB zero degree beamline was specified and components ordered.

A significant renovation of the U15 beamline was completed during this year. The length of the beamline was reduced, and electronic racks and other accessories were rearranged to provide more space for experimental chambers. Vacuum valves and the contamination barrier window were replaced to restore reliability. Electrical power distribution was upgraded for convenience and safety.



X-Ray Machine

Norman Fewell
X-Ray Ring Manager

X-Ray Ring operations for FY 1994 have followed a similar scheduling format developed for FY 1993. The usage diagram (**Figure 1**) and the integrated ring current (Amp Hours on **Figure 2**) are virtually the same as those achieved in the past year. This high level of beam availability has been maintained with a minimum of unscheduled downtime (2.6%). Improvements to the Linac/Booster and faster active interlock test and orbit correction programs have significantly reduced the beam-dump/beam-available turnaround time. Installing the fourth RF system and upgrading RF systems 1 and 2 with Eimac electron tubes has resulted in improved reliability as well as the potential for improved beam-current/energy performance. Increased machine reliability led to user-requested scheduled fills of 12 hour duration when the LEGS experiment is running, and 16 hour duration fills when LEGS is off.

Increases in photon flux await the results of the Vacuum Chamber Task Force, which will probably conclude its findings in the spring of 1995. In anticipation of higher current operations, the Controls and Diagnostics Group is preparing active interlock systems for the insertion devices at X1 and X13. In addition, the PUE RF receivers are being modified to operate over an increased dynamic range. Changes in the circuitry and sampling time have resulted in a much improved receiver that operates from 3 mA to 500 mA. Initially the active interlock and feedback receivers will be upgraded but eventually all the receivers must be changed to the new version.



Norman Fewell, X-Ray Ring Manager

Improvements to beam quality continue; decoupling of the local and global feedback systems and increased system bandwidth have resulted in an orbit stability of a few microns. Low frequency noise reduction up to 100 Hz is shown in **Figure 3**. This shows horizontal orbit motion reduction with the feedback system on; especially noticeable is the reduction of orbit motion caused by Booster operation. Installation of skew-quadrupoles and their power supplies has enabled the normal 25 bunch operational beam brightness to be increased by a factor of two. The slight reduction in integrated current during a fill, caused by reduced lifetime as the result of the tighter beam, has been made up for by the increased ma-

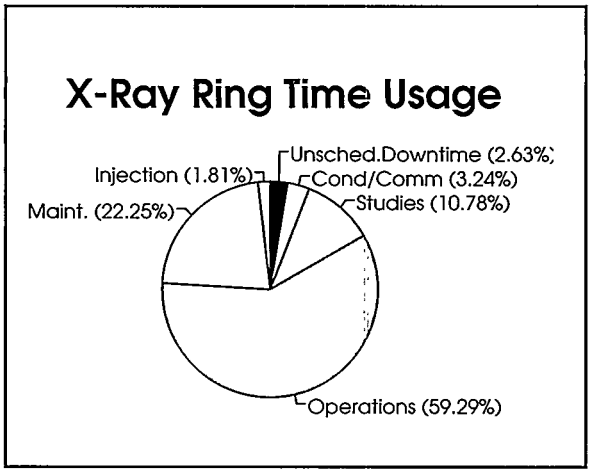


Figure 1: The Breakdown of the X-Ray Ring usage based on total time (not scheduled time) for FY93.

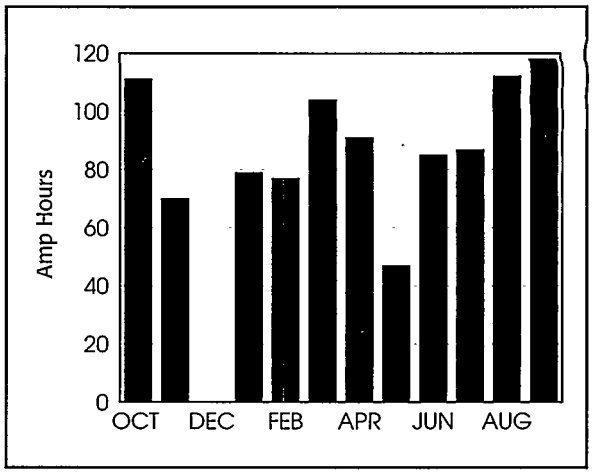


Figure 2: The total integrated current for the X-Ray Ring accumulated each month for FY93.

chine reliability and reduced beam turn-around time. Five bunch runs operate with the previous beam size, and single bunch runs have the beam size increased to achieve a longer lifetime.

The NSLS Prototype Small Gap Undulator was installed in the X13 straight section during the Spring'94 shutdown. Output energy spectra were taken with an electron beam aperture of 3.8 mm. Operation of the undulator at this aperture had no noticeable effect on the performance of the X-Ray Ring. The undulator will be removed during the Fall'94 shutdown for mechanical modifications that will allow the aperture to be reduced further. Studies have indicated that it may be possible to operate the undulator with beam apertures as low as 2.8 mm. Also during the fall shutdown we will install in the same straight section a Circular Polarized Wiggler now being tested at Argonne National Laboratory.

Power feeder upgrades have allowed the main magnet power supplies to operate reliably at 2.8 GeV levels. Operations at this energy are now awaiting the retrofit of additional beamline shielding. We now look forward to operations during 1995 of either 2.8 GeV at 220 mA or 2.584 GeV at currents up to 430 mA.

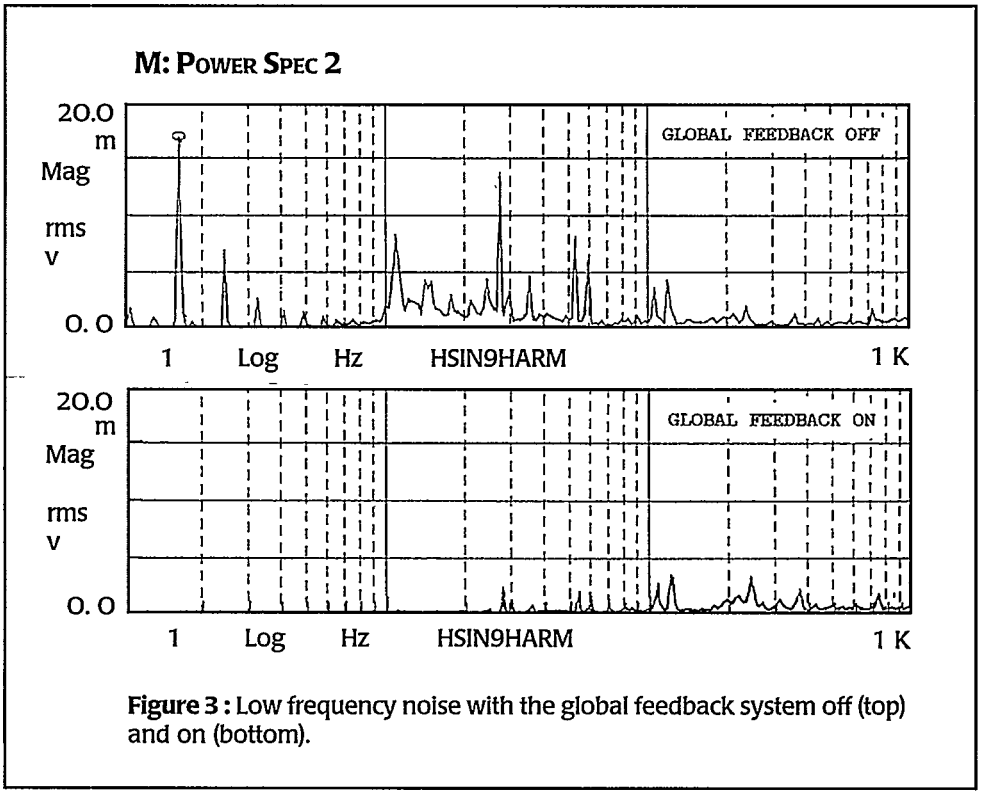


Figure 3: Low frequency noise with the global feedback system off (top) and on (bottom).

X-Ray Beamlines

Roger Klaffky
X-Ray Operations Manager

During FY 1994 there were 1032 different experiments performed as determined from a count of NSLS Safety Approval Forms. The institutional breakdown of scientists participating on these experiments was 43% from universities, 18% from industry, 15% from BNL, 10% from other DOE labs, 8% from abroad and 6% from government labs.

PRTs and the NSLS made a substantial number of beamline technical improvements. New gratings were acquired for the X1B beamline to extend the available photon energy to allow studies on 3-d transition element L-edges. Also, the feasibility of using soft x-ray inelastic scattering as a means of determining band structures was demonstrated. The final X2A beamline layout, design details, vendor selection and assembly procedures were completed, and orders for major components were placed. The hutch installation, utilities, safety system and primary vacuum system were also completed. Initial alignment with x-rays occurred and mirror and monochromator assembly and installation neared completion. On X2B a video-intensified camera was installed to allow real time radiographic measurements. A new 512x512 CCD sensor was also installed for clear image acquisition. A MacIntosh Quadra running IP-Lab was also put into operation to provide a user friendly environment for data acquisition.

On X3A a new monochromator system serving the X3A1 and X3A2 stations was installed. It consists of two monochromators enclosed in a single vessel- the first unit is a double crystal assembly with vertical focusing by the first crystal and sagittal focusing by the second crystal; the second unit consists of three interchangeable triangular crystals mounted on a rotary holder, each crystal reflecting radiation 6 degrees sideways at a different energy. Also a new anti-scatter device was constructed for use with a closed-cycle helium cryostat. Using this device and new imaging plate software, a full set of accurate low temperature synchrotron data was collected. On X3A2 a pinhole small angle SAXS instrument was constructed and installed. A Bonse-Hart ultrasmall SAXS instrument operating at 18.86 KeV was tested on X3A1.

X4A was brought into full operations during FY 1994. Major enhancements to the beamline included the commissioning of focusing mirrors, automated entrance slits, automated diffractometer table control, and a comprehensive automation for anomalous diffraction (MAD) experiments. The X4C monochromator design was completed and construction nearly finished. The mirror and bender assembly were constructed and the experimental table system designed.

Installation of a double focusing mirror at the X6B beamline led to higher intensity and resolution for scattering and spectroscopy experiments. A collimating mirror was installed upstream of the X7B monochromator, and a mirror bender was installed to provide vertical focusing after the monochromator. An image-plate scanner was jointly purchased with beam line X3 to permit rapid acquisition of single crystal and powder diffraction data.

Slit systems were added to the X8A reflectometer test station to improve the accuracy of reflectivity measurements. The test station was also upgraded to provide a $10^{(-8)}$ Torr operational vacuum and a sample interchange chamber to prevent exposure of samples to air.

Beamline construction of X9A continued. On X9B there were a number of technology development projects. These consisted of: 1)freeze quench x-ray spectroscopy, 2)optical pump, x-ray probe spectroscopy, 3)dynamically focusing sagittal monochromator, 4)fast amplifiers for fast pulse processing in conjunction with solid state detectors, and 5)development of optical monitoring devices to be used simultaneously with x-ray data collection. The fast amplifier project demonstrated that the pulse processing rate of the solid state detectors could be increased by a factor of 8-10 with only a twofold loss of resolution.

On X10A a 2D image plate was implemented to further enhance the SAXS measurement capability. Using this new detector, a research program on mechanical properties of polymers was initiated. A 5:1 gear reducer was installed on X11A to solve microstepping problems the line had been experiencing. Plans for a major X11A hutch expansion were made. X11B continued in a testing and commissioning stage. The double-bounce harmonic rejection mirror was fully mounted and characterized. The soft x-ray back end neared completion.

On X12B a robotic fluid sample changer was designed and built which has a 30 sample capacity for 100 microliter samples. To enhance the ability to carry out macromolecular crystallography experiments, a number of improvements were made. A precision rotation stage mount was built to permit rotation crystallography measurements. The air gap between the crystal and downstream end of the collimation system was minimized; collimation down to 100-200 microns was achieved by adding precision steering of the collimator and a more stable floor mount; an in-line image plate detector system, time shared with the X25 Biology Department crystallographic program, was acquired; and extensive changes to data flow and analytical software systems took place. Also a replacement mirror with improved figure and roughness was ordered, to provide significant improvement in usable flux. An image plate detector was installed on X12C. A refocusing mirror was ordered which should provide 3-5 times greater intensity at the specimen.

A spherical grating instrument was completed on X13A and was used for a coherence characterization experiment. With the installation of the Prototype Small Gap Undulator (PSGU) in the X13 insertion straight section, an experiment was carried out to characterize the radiation on the B-line and a white light hutch was installed on X13B for hard x-ray experiments.



Roger Klaffky, Beamline Operations Manager

At X15A there were a number of upgrades. An open-air 2 circle diffractometer was commissioned, a Macintosh Quadra 650 was added for data analysis and the LINUX OS was installed on the data collection PC486 computer. The spherically-bent Al collimating mirror upstream of the X15B monochromator was replaced with a Glidcop (Cu alloyed with Si) mirror. The toroidally-bent Al focusing mirror downstream of the monochromator was also replaced with a ULE (ultra-low expansion fused silica) mirror. These new mirrors have surface roughnesses less than 5 Å resulting in substantially brighter and more intense beams, particularly at higher energies.

After the completion of a number of major technical changes, X16C became a fully functional beamline for x-ray diffraction and absorption work. A Kappa-geometry diffractometer was designed and installed. The diffractometer has a removable stand, which allows for relatively simple installation and removal. A UHV chamber for x-ray absorption studies was fabricated. The beamline has also been modified to allow for lower energy operations. The monochromator was replaced with a sagittally-focusing monochromator which uses a conically- bent Si(111) wafer to focus the full 3.5 mrad beam onto the sample. The monochromator scans the bend and cone angles as the beam energy is changed, to maintain a constant beam spot. The data acquisition computer was upgraded to a PC486 computer.

On the X17B1 Material Sciences beamline, a second

generation monolithic Laue-Bragg monochromator was installed which provides a stable, intense 20-90 keV beam. On the X17B2 angiography/MECT(multiple energy computed tomography) beamline a new single-bent Laue crystal monochromator with enhanced flux and spatial resolution was used for imaging patients. A new monochromator hutch and a new patient chair with computer control of all translations and rotations were also installed.

The X18B monochromator ion pump was replaced with a turbopump to provide quick sample turnarounds. The X19A front collimating mirror was installed and the focusing mirror was mounted in its bender and surveyed into position. The hutch optical table was motorized to provide two translational and three rotational degrees of freedom for accurate alignment. A laser alignment system significantly reduced the experimental setup time. A high stability scanning stage was designed and implemented on the white beam topography camera on X19C. This stage enables scanned images of very large single crystals (for example, six inch diameter wafers) to be recorded in a single exposure. An experimental liquid surface/interface spectrometer was constructed which is capable of measuring x-ray reflection, grazing- incidence diffraction and fluorescence, surface diffuse scattering and anomalous reflection.

Improvements to the X20 beamlines in FY 1994 included an update in computer hardware and data acquisition programs, a change in the X20C crystal mount to obtain lower x-ray energies, and the installation of kinematic pads on the X20C hutch floor.

The X21 IDT started their experimental programs in FY 1994. New spherically-bent back scattering analyzers were tested and commissioned. Construction of phase II monochromators and a focusing mirror was also underway.

Fabrication of the X22A beamline, installation of the spectrometer and all associated electronics were completed and the first monochromatic beam was observed. The range of accessible momentum transfers of the X22B liquid metal spectrometer was extended from 0.8 to 2.5 reciprocal Å. On X22C an "out-of-plane" detector was added for x-ray surface scattering experiments and the polarization analyzer was upgraded for x-ray magnetic scattering experiments.

On X23A2, upgrades included the construction of a sealed Kr ion chamber and the reduction of vibration problems at higher energies. These upgrades allowed high quality transmission data to be collected above 25 keV.

A major improvement was made in the optics of the X23B beamline. The first collimating mirror was replaced with a new silicon mirror, dramatically improving the energy resolution (1.7 eV at 5.8 keV).

Computer software and hardware were upgraded and a visual display added for the X24A gate valve and vacuum safety control system. There was also progress in using a diamond-like coating on the Sb(111) first monochromator crystal to spread out the heat load.

On X25 a soft x-ray operating mode was implemented to provide monochromatic x-rays to slightly lower than 3 keV. This was accomplished by removing some of the upstream graphite filters to improve transmission at lower energies, and simultaneously lowering the wiggler field to reduce the total radiated power, predominantly from the high-energy portion of the spectrum.
Reconstruction of X28A, B and C was completed and all three beamlines were operational. The prototype pinhole for the pinhole camera was installed for initial tests on X28C. A flexible data acquisition and control system to support photon-based monitor and detector development at X28 was designed and its assembly begun.



X-Ray Storage Ring Parameters as of November 1994

Normal Operating Energy	2.584 GeV
Maximum Operating Current	0.25 amp (10^{12} e$^-$)
Lifetime	~20 hours
Circumference	170.1 meters
Number of Beam Ports on Dipoles	30
Number of Insertion Devices	5
Maximum Length of Insertion Devices	< 4.50 meters
$\lambda_c(E_c)$ at 1.25 T (B)	2.23 Å (5.6 keV)
$\lambda_c(E_c)$ at 5.0 T (W)	0.56 Å (22.2 keV)
B(ρ)	1.25 Tesla (6.875 meters)
Electron Orbital Period	567.2 nanoseconds
Damping Times (2.584 GeV)	$\tau_x = \tau_y = 6$ msec; $\tau_\varepsilon = 3$ msec
Touschek (2.584 GeV, 0.25A)	≥27 hrs ($V_{RF} = 700$ kV)
Lattice Structure (Chasman-Green)	Separated Function, Quad Triplets
Number of Superperiods	8
Magnet Complement	16 Bending (2.7 meters each) 40 Quadrupole (0.45 meters each) 16 Quadrupole (0.80 meters each)
32 Sextupole	(0.20 meters each)
Nominal Tunes (ν_x, ν_y)	9.15, 6.20
Momentum Compaction	0.0056
R.F. Frequency	52.88 MHz
Radiated Power for Bending Magnets	144 kW/0.25 amp of Beam
R.F. Peak Voltage	1000 kV
Design R.F. Power	400 kW
ν_s (Synchrotron tune)	0.002
Natural Energy Spread (σ_e/E)	8.6×10^{-4}
Natural Bunch Length (2σ)	10.5 cm
Number of RF Buckets	30
Typical Bunch Mode	25
Horizontal Damped Emittance (ε_x)	1.1×10^{-7} meter-radian
Vertical Damped Emittance (ε_y)	2×10^{-10} meter-radian
Power per Horizontal milliradian (0.25A)	23 watts

Arc Source Parameters

Betatron function (β_x,β_y)	1.0 to 3.8 m, 7.9 to 26.5 m
Dispersion function (η_x,η_x)	0.47 to -0.11, -0.39 to 0.22
$\alpha_{x,y} = -\beta'_{x,y}/2$	-0.49 to 1.62, -3.4 to 4.5
$\gamma_{x,y} = (1 + \alpha_{x,y}^2)/\beta_{x,y}$	0.952 to 0.962 m^{-1}, 0.81 to 0.52 m^{-1}
Source size (σ_x,σ_y)	371 to 565 μm, 38 to 69 μm
Source divergence ($\sigma_{x'}$,$\sigma_{y'}$)	439 to 324 μrad, 12 to 10 μrad

Insertion Device Parameters

Betatron function (β_x,β_y)	1.60 m, 0.35 m
Source divergence ($\sigma_{x'}$,$\sigma_{y'}$)	260 μrad, 50 μrad

INJECTION SYSTEM UPGRADE

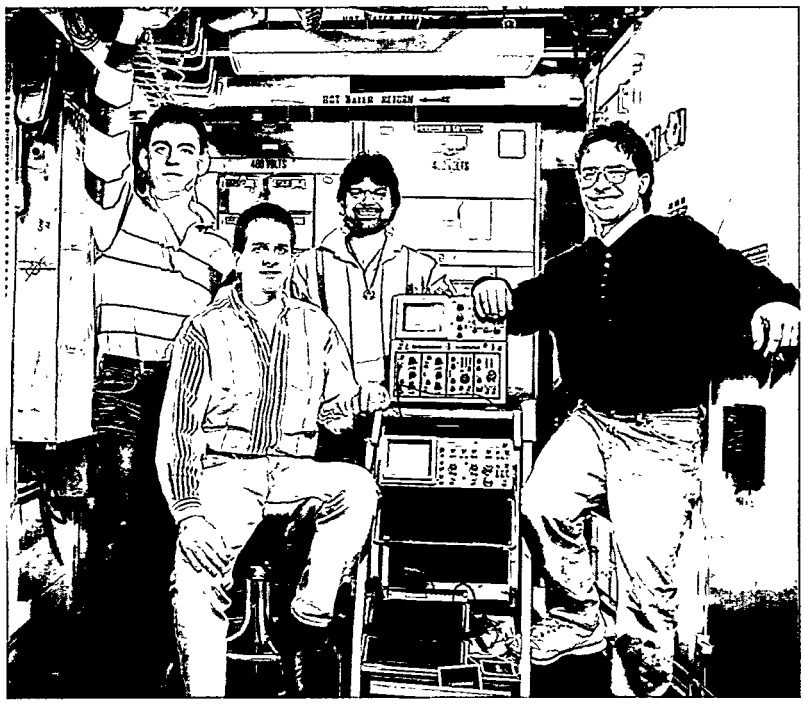
Eric Blum
NSLS Injection System Manager

A program has been underway since 1990 to upgrade the NSLS injection system, consisting of a 120 MeV linear accelerator and a 750 MeV booster synchrotron, by increasing the number electrons accelerated per pulse, reducing the cycle time, and improving reliability. At the beginning of the project, we expected to increase the filling rates in the storage rings by a factor of 7 to 8, largely by increasing the repetition rate from $^2/_3$ to 2 Hz and by improving the stability of the booster from one cycle to the next. Only a small gain was expected in the peak current accelerated. As the project progressed we have been able to double the current accelerated in the booster and have already met our goal for injection rate improvement even though the repetition rate is still less than 1 Hz. We expect to increase the filling rate by another factor of 1.7 when we finally achieve the 2 Hz repetition rate next year.

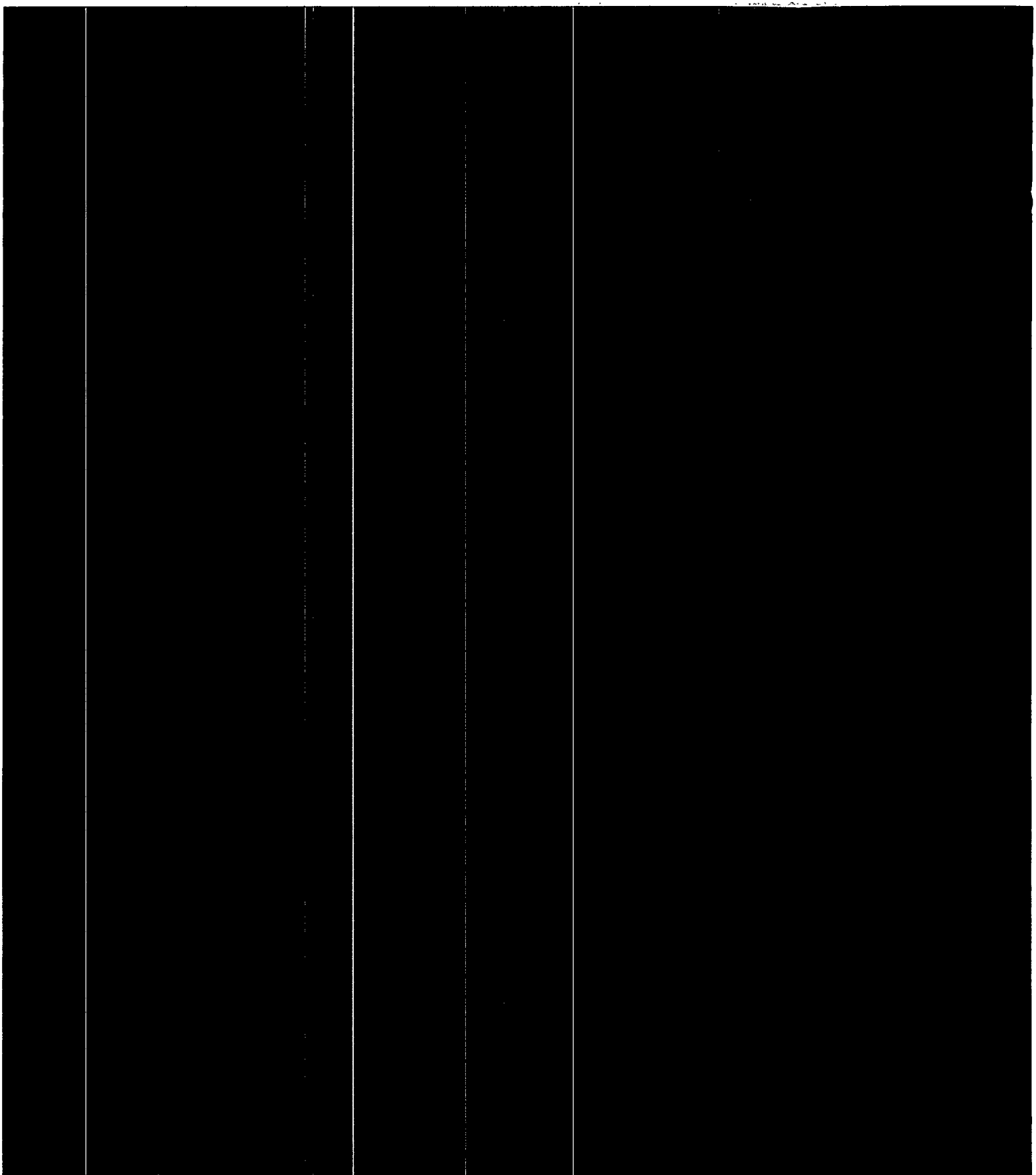
In previous years we increased the energy of the beam from the linear accelerator from 80 to 120 MeV by adding a third accelerating section, stabilized the booster dipole power supply with a digital feedforward circuit, and added instrumentation to track the position and tune of the booster beam. Our major accomplishment in FY 1994 was completing the new booster quadrupole and sextupole power supplies. The supplies, developed by Rolf Olsen and the NSLS Power Supply Group, can provide over twice as much power as the old ones. Together with the dipole supply that will enter service next year, they will allow us to meet our goal of 2 Hz injection. They will be better regulated and more reliable than the old power supplies as well.

Another important achievement in FY 1994 was construction of two new modulators for the linear accelerator. The original modulators were built in the early 1960's and have become unreliable. They have been a significant contributor to accelerator downtime. We expect to install the new modulators during the Fall '94 shutdown that will begin in November, 1994.

During FY 1994 we also installed ferrite phase shifters on the RF system of the linear accelerator. The fine control that they permit over the electron energy played an important part in doubling the booster current. We have finished the final prototypes for a position monitoring system for the linear accelerator, booster and transfer lines and expect to install the completed system next year. We have also begun the improvements to the pulsed injection magnets that will be needed for 2 Hz operation.

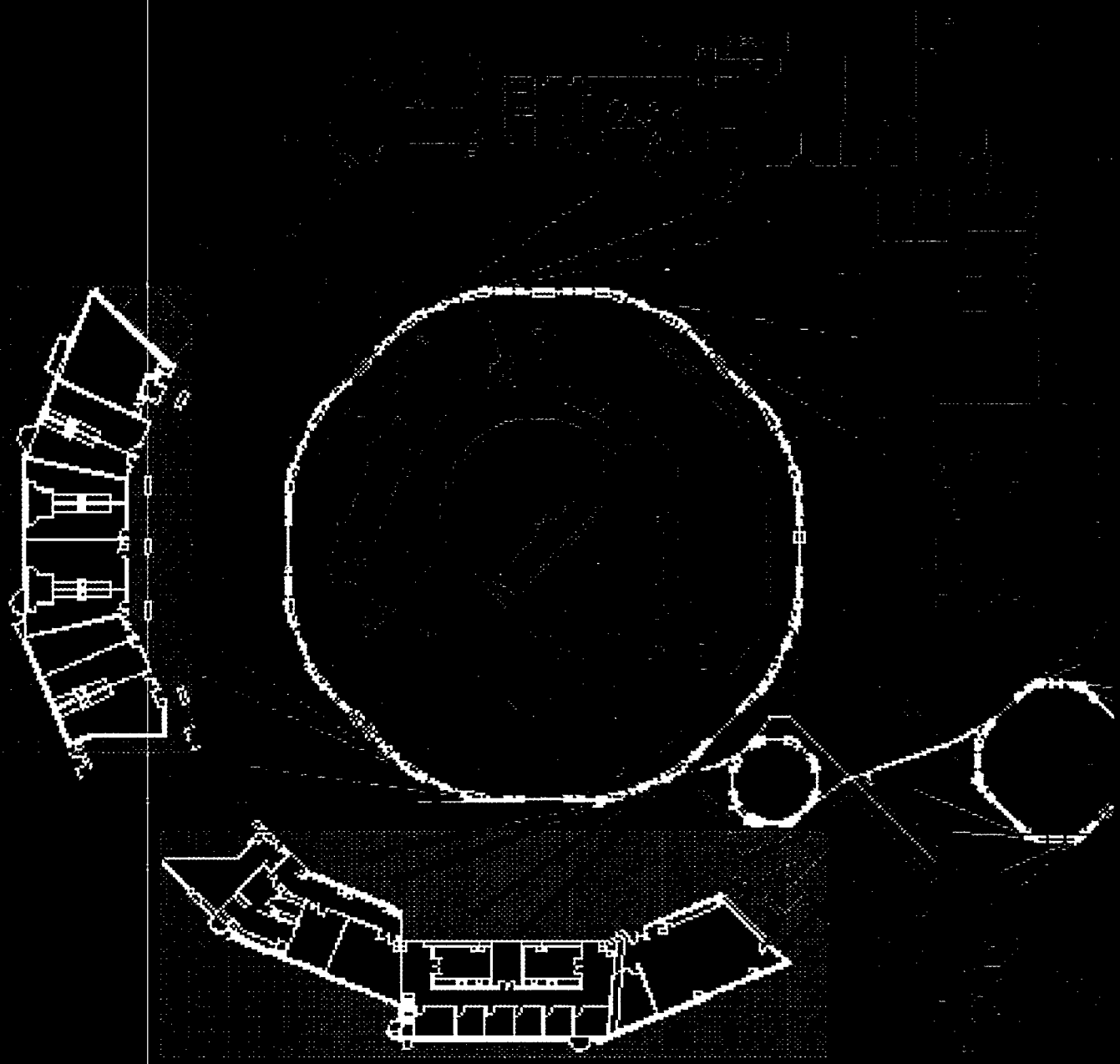


NSLS Power Supply Group (from left to right): Mike Fulkerson, Scott Buda, Pooran Singh, and Thomas McDonald.



Schematic of the X-Ray Ring portion of the NSLS experimental floor. Existing walls are depicted in magenta, and the booster and part of the VUV Ring are visible as light circles in the lower right. The blue box on the left highlights the Structural Biology expansion, while the box at the bottom shows the Control Room expansion. Despite the proximity of the beamlines to the construction areas (radiating green lines) there was minimal disruption to operations. Ground breaking on this construction project took place in April of 1994 and completion is scheduled for March of 1995.

FIVE PROJECTS



THE NSLS SOURCE DEVELOPMENT LABORATORY (SDL): A CONFLUENCE OF OPPORTUNITIES

Ilan Ben-Zvi
Eric Blum
Erik D. Johnson
Sam Krinsky
James B. Murphy
Li-Hua Yu

To maintain its position at the forefront of synchrotron radiation based research, the NSLS has initiated an ambitious project to develop fourth-generation radiation sources. This effort, dubbed the Source Development Laboratory (SDL), is really a consolidation of several projects, and a response to recent developments within the DOE and the synchrotron users community. The SDL is comprised of three major programs:

- 100μm Compressed Bunch Experiments
- μ-Ring Compact Storage Ring with High Frequency RF
- Ultraviolet Project Free Electron Laser (UP-FEL)

For those who have followed the NSLS annual reports and newsletters over the last several years, the seeds of the Source Development Lab were already evident. For the benefit of those not familiar with the program, the motivation and historical development are outlined below, and followed by an overview of the current SDL design.

HISTORICAL DEVELOPMENT

The NSLS has been engaged in the development of proposals for a Free Electron Laser user oriented facility operating in the ultra-violet for more than five years. The Deep Ultra-Violet Free Electron Laser (DUV-FEL) conceptual design report was released in January of 1993. It details the scientific motivation, and describes a user facility designed to meet those needs. The DUV-FEL could produce picosecond pulses of UV radiation at wavelengths as short as 75 nm and peak power of several hundred megawatts. An extension of this technology would operate in a chirped pulse mode which could produce 4 femtosecond pulses at 88 nm with peak power of 100 GW.

As work progressed at the NSLS, a general awakening within the community had occurred which emphasized the need for source development. One element of this perspective is the realization that, even as they are coming on line, the third-generation synchrotrons are inadequate for certain types of experiments. These include non-linear effects and dilute systems where higher peak power is required, or many types of intensity correlation studies where spatial coherence beyond the capabilities of existing sources is beneficial. A second driving force in the recent FEL renaissance has been the advances in many aspects of the accelerator physics.

Experiments conducted at the BNL Accelerator Test Facility (ATF) and other laboratories have demonstrated dramatic improvements in electron beam brightness in the last several years. The current state of development is such that short wavelength FELs can be realistically considered. The theoretical description of the FEL process has also advanced significantly, yielding innovative FEL designs such as the sub-harmonically seeded amplifier.

Recognizing the significance of these developments, the DOE commissioned the National Research Council to perform a study of Free Electron Lasers and Other Coherent Sources of Radiation to aid in evaluating their role in DOE programs. Released in August of 1994, the report recommends establishing a FEL user facility in the far-infrared and supporting the use of existing laser technology in the near-infrared and visible (located in individual investigators' laboratories). In the VUV and x-ray regions, the report recommends pursuing proof of principle experiments at existing synchrotron sources, and supporting the development of technology for FELs in these wavelength regions.

LOOKING AHEAD

Anticipating the outcome of the report, the NSLS initiated several activities during the last year known collectively as the Ultraviolet Project. One component of this work has been supporting a major share of the operation of U11 and the construction of the U13U low energy branch line as sites for proof of principle experiments in UV science which might later be performed at an FEL facility. In this respect, the program seeds the science, and can serve as a focal point for UV based research at BNL. A second major activity has been the development of a collaboration to pursue UV-FEL R&D at Brookhaven utilizing components from other projects at BNL and elsewhere. The kernel of the collaboration was suggested in a workshop "Towards Short Wavelength Free-Electron Lasers" held at BNL in May of 1993.

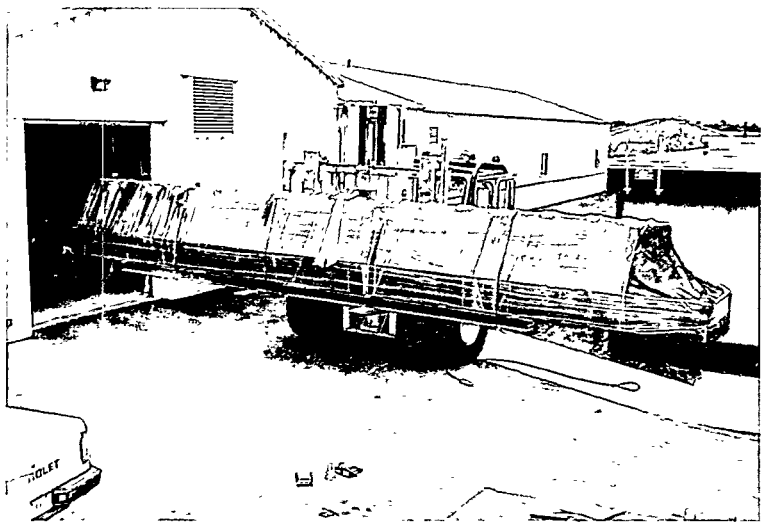


Figure 1: The NISUS undulator (under cover) being transferred to building 729. For scale, its support structure is an optical table 40 feet long!

One of the projects it proposed was utilizing the ARPA linac at BNL (built originally for the SXLS project) with an undulator known as NISUS (Near Infrared Scaleable Undulator System). The 10 meter long NISUS undulator was built by STI Optronics, at a cost of over 8 million dollars, for Boeing Space and Defense in Seattle as part of a contract with the U.S. Army Space & Strategic Defense Commands Directed Energy Weapons Program. On loan to BNL, NISUS arrived in December 1994 (Figure 1) and is currently undergoing modification for use in FEL experiments ultimately leading to a ultraviolet FEL. The Ultraviolet Project FEL (UP-FEL) does not have all of the features designed into the DUV-FEL proposal, but will ultimately provide radiation comparable in peak power and wavelength to the DUV-FEL. Although meant to be an R&D machine, the UP-FEL should provide an opportunity to explore applications (and foibles) of this type of source for research. Experience gained on this machine will be invaluable in the design of a user oriented facility.

This element of the SDL, while sited at BNL, is part of a broad based collaboration involving many institutions in a program of FEL amplifier R&D leading to the development of short wavelength FEL technology, as recommended by the NRC report. Apart from BNL, this effort includes other DOE laboratories (CEBAF, LBL, LANL, SLAC), industrial partners (Boeing, Grumman, STI-Optronics), and universities (Duke, UCLA). This program would build on the established strengths and capabilities of the participating institutions in an effort to pursue the development of what will become the "Fourth-Generation" source for research.

One goal of the larger collaboration is the development of techniques to produce extremely short (compressed) bunches to achieve very high peak currents. In pursuing this development, it became clear that the 100 μm electron bunches could be a useful tool independent of any "down-stream" accelerator. One proposed experiment is to study the response of dielectric materials to electromagnetic stimulation. The realization of the experiment is to pump a dielectric target with electrons from the accelerator, and probe it with transition radiation produced by a second electron bunch impinging on a metal foil. The delay can be varied to measure the response as a function of time after excitation. Time dependent properties of the scattered radiation such as intensity, polarization, angular distribution, and spectrum can thus be measured.

In another parallel activity, the potential of extremely short length bunches was realized as a source of coherent synchrotron radiation. One proposal described the modification of the existing compact storage ring to include a 3 GHz RF system. These modifications would result in stored electron bunches of 300 μm in length. The synchrotron radiation produced by this beam would be coherently enhanced at millimeter and longer wavelengths.

The development of this alternative to FEL technology could potentially address some of the recommendations of the NRC study in the far infra-red. It became clear that each of the source development projects described above could be pursued utilizing many common, and in many instances recycled, components.

SDL OVERVIEW

Figure 2 shows a layout of the Source Development Laboratory located in building 729, across Railroad Street from the NSLS. As currently designed, the SDL accelerator system will consist of a high brightness short pulse linac, a station for coherent synchrotron and transition radiation experiments, a short bunch storage ring, and an ultra-violet free electron laser utilizing the NISUS wiggler. The electrons are provided by a laser photocathode gun of the type developed at the ATF. It feeds the 210 MeV ARPA linac which will be modified to include magnetic bunch compression after the first linac section at approximately 80 MeV, and to provide for the addition of a fifth acceleration section. With the bunch compressor operating, electron bunches as short as 100 μm with 1 nC charge can be generated for pump-probe experiments utilizing coherent radiation. This radiation also serves as a diagnostic of the electron beam quality produced by the accelerator. The electron beam can also be injected into the modified XLS storage ring. Fitted with a superconducting S-band RF cavity, the ring will be a source of millimeter wave *coherent* synchrotron radiation. The linac is also the driver for the UP-FEL, which is designed to allow the study of various aspects of single pass amplifiers.

The initial phase of FEL development involves self-amplified spontaneous emission (SASE) at wavelengths down to 900 nm, and seeded beam operation utilizing only the NISUS wiggler. Sub-harmonic seeding experiments will be possible with the addition of a energy modulation wiggler and a dispersive section upstream of NISUS. The feasibility of utilizing the original UV ring FEL undulator (λ_u=6.5 cm, 38 periods, $B_0 \approx 0.55$ T @1.5 cm gap) for the energy modulation wiggler is currently under study. Chirped pulse amplification (CPA) operation will also be studied, assuming a suitable laser system is available, and a planned energy upgrade (by powering a fifth linac section) to 310 MeV will extend the wavelength range of the FEL to below 100 nm.

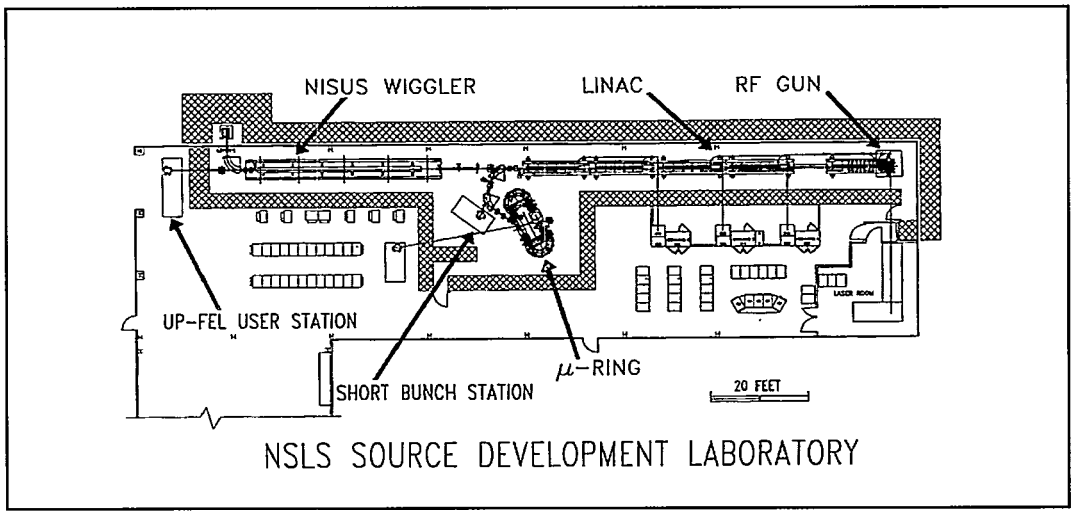


Figure 2: The layout of the Source Development Laboratory located in building 729, across Railroad Street from the NSLS.

CONCLUSION

All of this activity occurs against the backdrop of difficult times for the funding of research in the United States, and difficult choices for the operation of its large research facilities. For BNL, one of these decisions has been to pursue source development. The same motivations that led to the creation of the NSLS drive this effort: to provide the users of its facilities the best possible sources of radiation for their research. Hopefully this new initiative at BNL will meet with the same degree of success the NSLS has enjoyed, and form the basis for the "next generation" user science. Look for a progress update in the 1995 NSLS Activity Report!

THE ACCELERATOR TEST FACILITY

Ilan Ben-Zvi
Ken Batchelor

The Accelerator Test Facility (ATF) is a user facility for accelerator and beam physicists, operated by the NSLS and the BNL Center for Accelerator Physics. The high brightness electron beam of the ATF, produced by a laser-photocathode RF gun, makes it an ideal site for R&D on Free-Electron Lasers (FELs). A number of FEL experiments are being conducted at the ATF. A few of them are centered about ATF beam line #3, where a microundulator oscillator experiment is nearing operation.

A superconducting 68 period micro-undulator (with a period of 0.88 cm and 0.5 Tesla peak field at a gap of 0.44 cm) has been developed at the NSLS. Prototypes of this undulator (up to 23 periods long) were built and performed extremely well in superconducting tests. The field errors of the undulator were very low as constructed, making this perhaps the first undulator that will require no trimming after manufacture. The FEL experiment makes use of the short period of the undulator and the low emittance beam generated by the RF photocathode gun to operate at 500 nm with a 50 MeV electron beam. Since the ATF electron beam energy is currently at about 70 MeV, lasing at below 250 nm should be possible.

An MIT group is carrying out a test of a pulsed microundulator. This undulator, which is currently installed on the beam line, has parameters that are very similar to those of the superferric undulator. Spontaneous emission has already been observed from this device and preparations are under way to get lasing in the near future. A third user group is from Columbia University. They will be using the oscillator experiment for studies of spiking and optical guiding in FELs.

The high-gain harmonic-generation experiment will be located on beam line #2. This experiment is carried out by a NSLS group headed by Li-Hua Yu. The experiment is done in collaboration with Northrop - Grumman, which is providing many components of the undulator for the experiment. This undulator is a derivative of the superconducting micro-undulator of the visible FEL oscillator. It uses the same principle of a continuous yoke but has parabolic pole faces for two-axis focusing and four distinct regions: a prebunching undulator, a dispersive section, an exponential growth section, and a tapered section. This experiment emulates the FEL physics of the NSLS approach to VUV FELs. This approach is based on single pass, seeded FEL amplifiers driven by Ti:sapphire lasers. The final stage of harmonic generation is being done in the FEL. The principle of high-gain-harmonic-generation will be tested and characterized in these experiments, as well as the superconducting undulator, the undulator diagnostics, error and alignment studies and tapering control.

The electron gun of the ATF generates its high current, low emittance beam by irradiating a high-quantum-efficiency metal-cathode in the presence of very high intensity RF electric fields. The generation and careful manipulation of such beams are areas of intense activity in accelerator physics, being the key to short wavelength FELs. A new magnesium photocathode has demonstrated an order-of-magnitude increase in quantum efficiency with a (so far) unlimited lifetime. A new RF gun is currently under development at the ATF in collaboration with SLAC and UCLA. The objectives of this collaboration are to develop a gun boasting low-cost, higher brightness as well as an improved cathode replacement system.

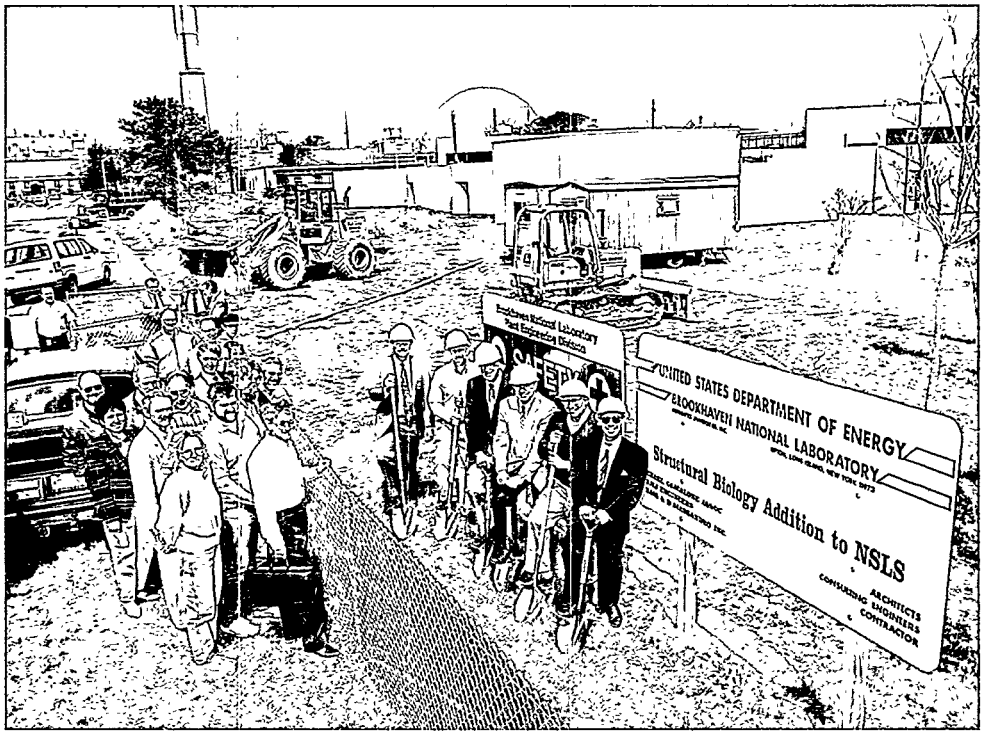
Besides the FEL R&D, many other experiments are taking place at the ATF. These include a Smith-Purcell radiation experiment (initiated by a Dartmouth group), an Inverse FEL experiment (BNL and Yale), an Inverse Cerenkov Laser Accelerator experiment (STI Optronics) and others. Additional research activities include the development of advanced electron beam diagnostics, compact high power lasers (the latest being the development of a compact picosecond pulse terawatt CO_2 laser) and more. So far, seven graduate students have finished their thesis at the ATF and seven more are currently doing thesis research at this facility.

NSLS Facility Improvements

Bill Foyt
NSLS

FY 1994 saw considerable construction activity in and around the NSLS. While most of the projects were small in comparison to the major addition to the south and west sides of the NSLS building they all had a common purpose; that is, to improve the environment for research. Among the projects were:

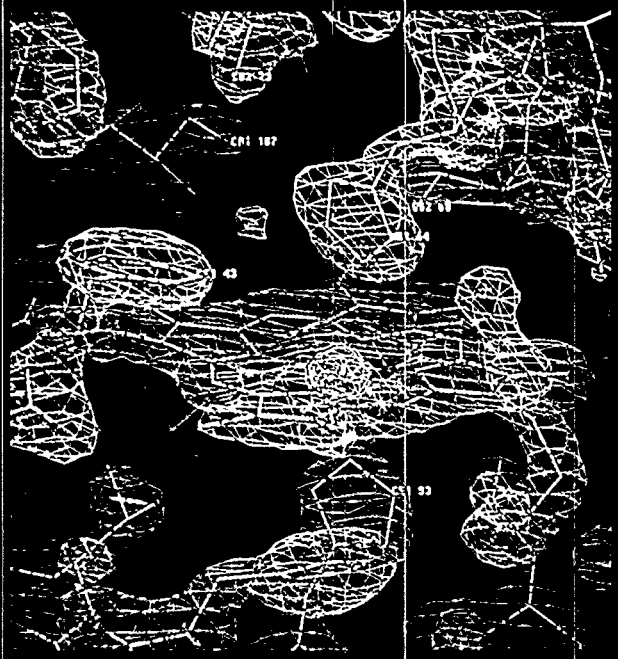
- The Central Chilled Water Hook-Up, which removed dependence on aged cooling towers, now provides both machine and comfort cooling from a stable centrally regulated source.
- A new electric feeder and transformer switch gear assures power that is no longer subject to disruptions from deteriorating equipment.
- The modernization of the building's fire detection and alarm system will provide more specifics when an alarm is sounded.
- A gas nitrogen manifold was connected to the main liquid nitrogen storage vessel, thus eliminating the need for portable Dewars for a number of beamlines.
- Sound absorbing panels that were installed in the VUV experimental area have served to dampen the background noise considerably.

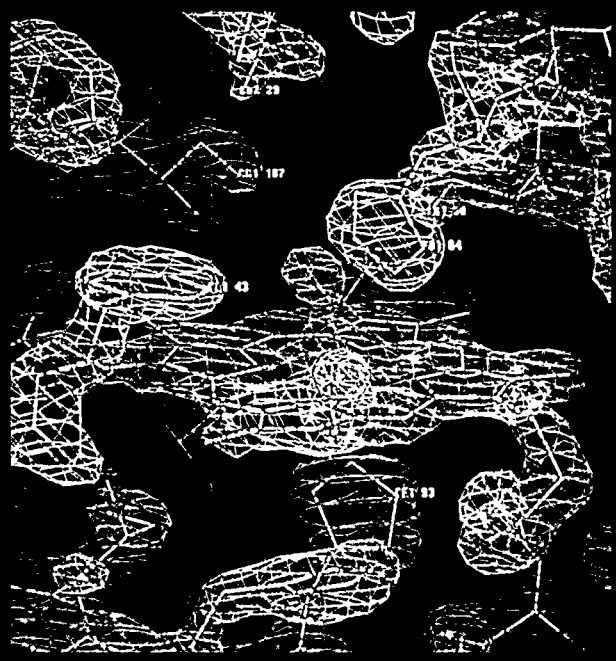


NSLS users and staff attended the NSLS expansion ground breaking on April 14, 1994. Ceremonial shovels were wielded by (left to right): Ove Dyling (Plant Engineering Division), Johnny Kirkland (Naval Research Laboratory/ SFA, Inc. and UEC Chairman), Denis McWhan (Chairman, NSLS Department), Martin Blume (BNL Deputy Director), William Studier (Chairman, BNL Biology Department), and Robert J. Bass (Bass & D'Alessandro).

The major construction activity during FY 1994 was the addition of 6,100 square feet of floor space in the X1 to X4 region (Experimental Floor Space Addition) and 6,300 square feet in the X5 to X12 region (Structural Biology Addition). Contributions by Exxon, Howard Hughes Medical Institute, and the State University of New York @ Stony Brook will allow a complete outfitting of the X1 to X4 region that will result in a new control room, three laboratories (one with a cold room), two lockable storage/set-up areas, six offices, and one mechanical equipment room. The Structural Biology Addition will provide eight laboratories (four with direct access to cold rooms), one conference and one mechanical equipment room. The completion of these projects is now scheduled for Spring 1995. The diagram on the section divider for Chapter 5 shows the layout of these two new areas. In addition, movement of personnel into the Experimental Floor Space area will free up approximately 1,000 square feet in the X20 to X21 region that will be re-assigned to the user community.

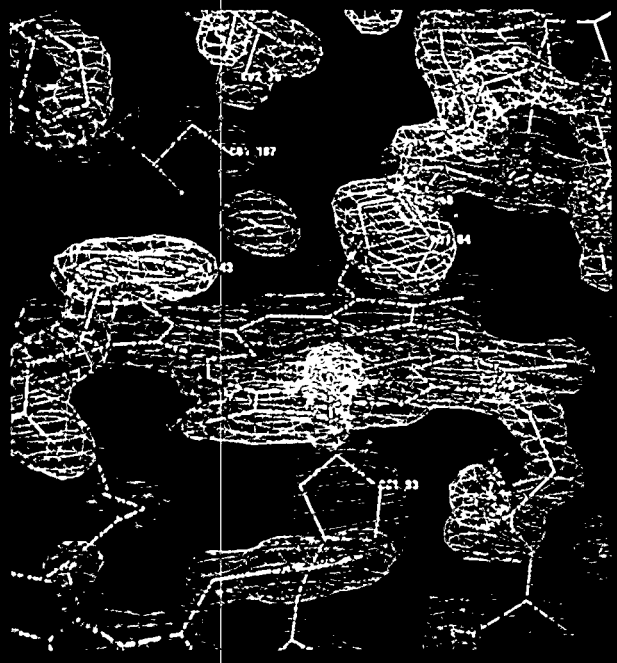
The above listed projects and other miscellaneous facility improvements are examples of the NSLS's commitment to providing the best research environment possible within the resources available.

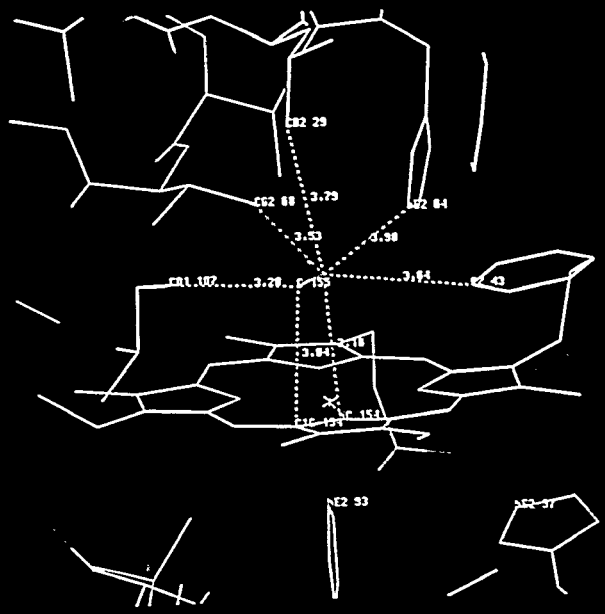




Beamline X12C: The structure of a photolyzed form of carbonmonoxy (CO) myoglobin determined from crystals held at 20 K. The figures depict electron density for three states of the oxygen-binding protein myoglobin. The same view of the molecule is shown, with the oxygen-binding site in the upper-central portion of the image, and the oxygen-binding porphyrin moiety shown edge-on at the bottom. FAR LEFT: The de-oxy myoglobin can be seen: the active site is empty (120 K). LEFT: The oxygen site is filled with carbon monoxide, which binds very strongly to the iron atom at the center of the porphyrin ring (120 K). RIGHT: Carbonmonoxy myoglobin held in an unusual state: the crystal had been held at a temperature of only 20 K to freeze out nearly all molecular motion in the molecule. Furthermore, the specimen had been illuminated strongly with visible light, which caused the photolyzation of the bond between the iron atom and the CO molecule. This molecule was unable to leave the binding pocket because of the low temperature; instead, it is found nestled in the back of the pocket, resting against an aliphatic isoleucine side chain. FAR RIGHT: A composite showing the motion of all the atoms involved. [I. Schlichting, J. Berendzen, R.M. Sweet, and G. Phillips, in *Nature* 371, 808 (1994)]

SIX
ORGANIZATION





NSLS Advisory Committees

1994-1995
Users' Executive Committee

The Users' Executive Committee (UEC) provides for organized discussions among the user community, NSLS administration, and laboratory directorate. It aims to communicate current and future needs, concerns, trends within the user community to NSLS staff and management, and to disseminate to the users information about NSLS and BNL plans. Members were:

Chairperson: Jean Jordan-Sweet, IBM
Vice-Chairperson: Paul Zschack, ORNL
Past -Chairperson: Johnny Kirkland, NRL
Secretary: Paul Lyman, Northwestern U. /ANL
Dan Fischer, NIST
Geraldine Lamble, NSLS/NCSU
Kevin Smith, Boston U.
Robert Sweet, BNL-Biology

Special Interest Group Representatives

Special interest groups in areas of common concern communicate with NSLS management through the UEC. Group representatives were:

Atomic and Molecular Science	David Hanson, SUNY- Stony Brook
Energy Dispersive Diffraction	Syed Qadri, Naval Research Lab
Lithography, Microscopy, Tomography, X-Ray Fluorescence	Sue Wirick, SUNY- Stony Brook
Nuclear Physics	Craig Thorn, BNL-Physics
Students and Post Docs	David Johnson, Old Dominion U./NSLS
Time Resolved Spectroscopy	Peter Siddons, NSLS
Topography	Michael Dudley, SUNY-Stony Brook
UV Photoemission, Surface Science	Boris Sinkovic, NYU
XAFS	Ke Zhang, U. City Science Center
X-Ray Scattering , Crystallography	Stephan Ginell, ANL

Science Advisory Committee

The Science Advisory Committee (SAC) evaluates the science programs at the NSLS and makes recommendations to the Chairman. The SAC met in March and September of 1994 and its members were:

B. Batterman, CHESS, Cornell U.
Gene Dresselhaus, National Magnet Laboratory, MIT
Richard Martin, Department of Physics, U. of Illinois
Yves Petrof, ESRF
David Shirley, Penn State University
Janet Smith, Department of Biological Science, Perdue U.
Chandra Varma, AT&T Bell Laboratories

General User Proposal Study Panels

The Proposal Study Panels met in November 1993, March 1994, and July 1994 to review and rate General User research proposals for the FY 1994 cycles. PSP members are drawn from the scientific community and usually serve a two year term. Members during FY 1994 were:

UV Panel

Steve Hulbert	NSLS
Gunther Wertheim	AT&T
Roger Stockbauer	Louisiana State U.
John Sutherland	BNL-Biology
Cliff Olson	Ames Laboratory

X-Ray Imaging/Other Panel

Harold Ade	NCSU
Bruce Steiner	NIST
Ed Westbrook	ANL
Paul Cowan	ANL

X-Ray Biology

Stephen Burley	Rockefeller U.
Keith Watenpaugh	The Upjohn Co.

*Temporary Member

X-Ray Spectroscopy Panel

*Lars Furenlid	NSLS
*Hugh Isaacs	BNL-DAS
Bruce Gates	U. of California @ Davis
Mark Antonio	ANL
Ronald Felton	Georgia Inst. of Tech.
Gerry Huffman	U. of Kentucky
Ed Stern	U. of Washington
Bruce Bunker	U. of Notre Dame
Dale Sayers	NCSU

X-Ray Scattering Panel

Charles Prewitt	Geophysical Lab
*Theo Siegrist	AT&T
David Sayre	Self-Employed
Peter Eng	AT&T
Glen Held	IBM
Ben Chu	SUNY - Stony Brook
Simon Moss	U. of Houston

General User Oversight Committee

The General User Oversight Committe (GUOC) met in November 1993, March 1994, and July 1994 to allocate time on beamlines to each General User proposal for the FY 1994 cycles. GUOC members are drawn from the scientific community and usually serve a two year term. Members during FY 1994 were:

UV Members

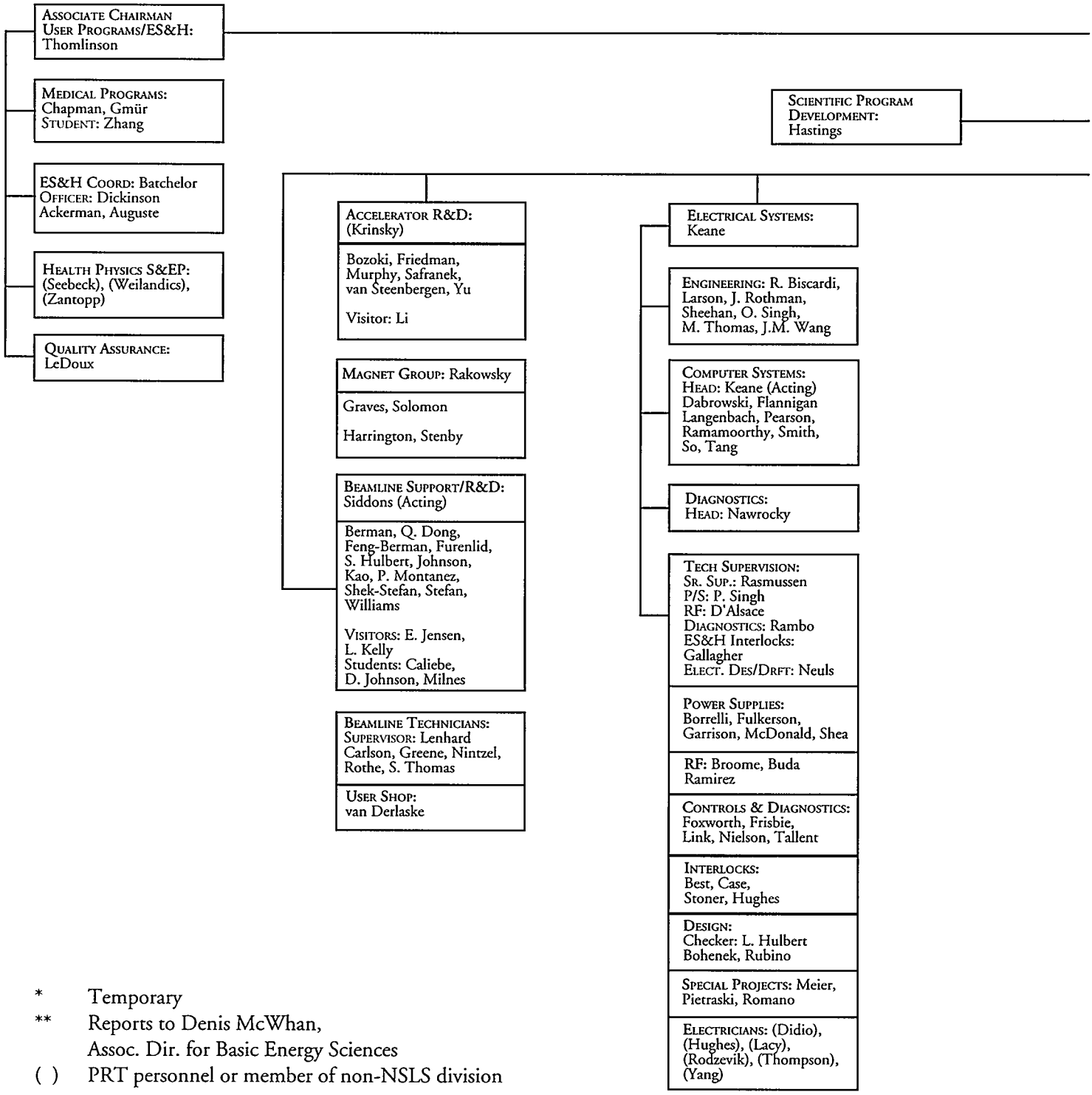
Roger Bartlett	LANL
C.T. Chen	AT&T
*George Meigs	AT&T
Boris Sinkovic	NYU
Paul Stevens	Exxon

*Temporary Member

X-Ray Members

Sean Brennan	SLAC
Geraldine Lamble	NCSU/NSLS
Fulong Lu	U. of Kentucky
Simon Mochrie	MIT
William O'Grady	NRL
Peter Stephens	SUNY-Stony Brook
Joseph Woicik	NIST

NSLS Staff

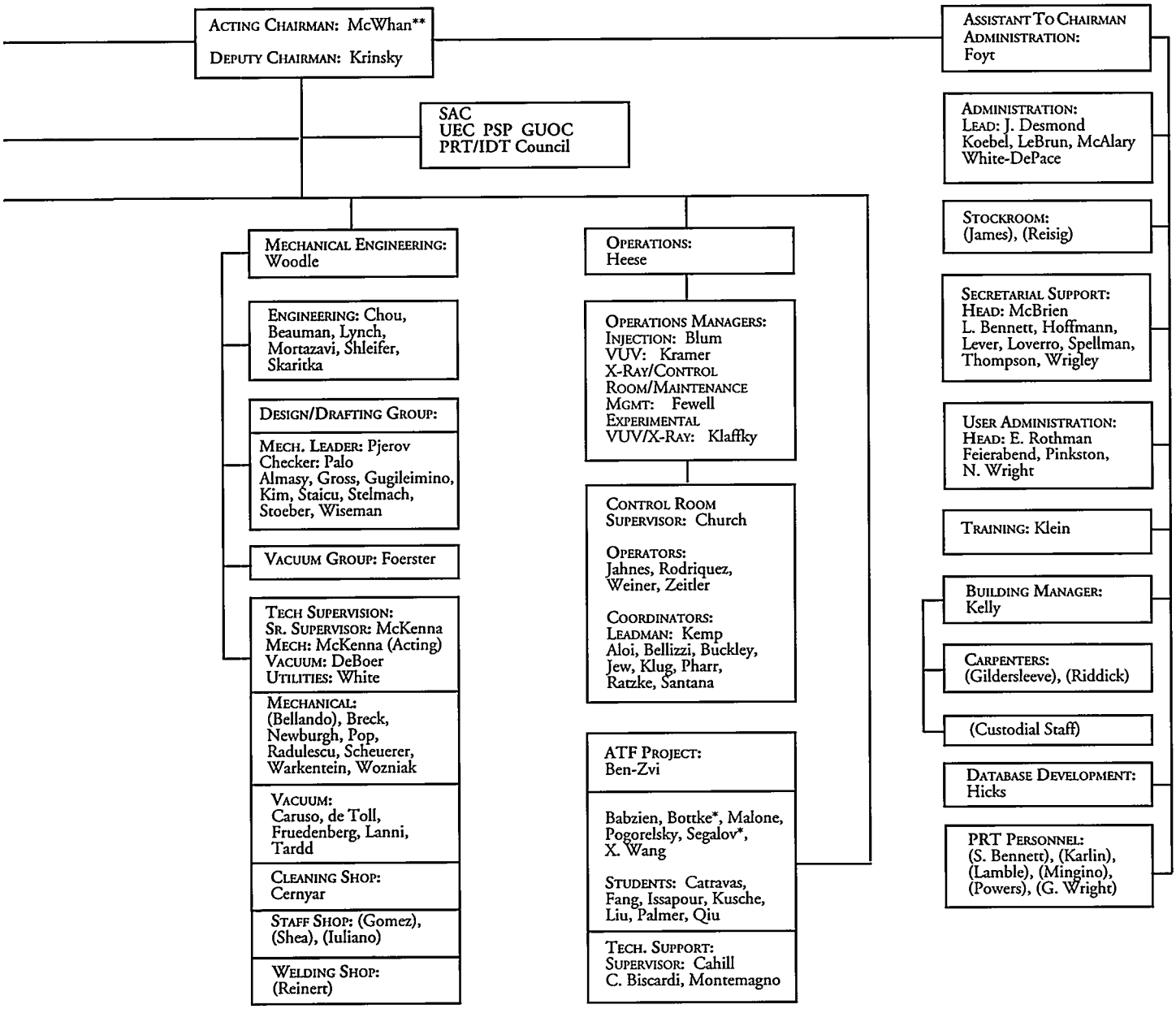


* Temporary

** Reports to Denis McWhan,
Assoc. Dir. for Basic Energy Sciences

( ) PRT personnel or member of non-NSLS division

NSLS STAFF



(signed) **Denis McWhan, Chairman**

January 1, 1995

NSLS Beamline Guide

October 1994

This table lists the abbreviations appearing in the Beamline Guides.

ARUPS	=	Angle-Resolved Ultraviolet Photoemission Spectroscopy
CD	=	Circular Diachroism
C-T	=	Czerney-Turner
ERG	=	Extended Range Grasshopper
EXAFS	=	Extended X-ray Absorption Fine Structure
IR	=	Infared
LEGS	=	Laser Electron Gamma Source
MCD	=	Magnetic CD
MI	=	Michelson Interferometer
NEXAFS	=	Near Edge X-ray Absorption Fine Structure
NIM	=	Normal Incidence Monochromator
PGM	=	Plane Grating Monochromator
SEXAFS	=	Surface EXAFS
SGM	=	Spherical Grating Monochromator
S-N	=	Seya-Namioka
SXES	=	Soft X-ray Emission Spectroscopy
TGM	=	Toroidal Grating Monochromator
TOK	=	Transverse Optical Krystron
UPS	=	Ultraviolet Photemission Spectroscopy
WB	=	White Beam
WDI	=	Wavefront Dividing Interferometer
XPS	=	X-ray Photoemission Spectroscopy
XAS	=	X-ray Absorption Spectroscopy

VUV Beamline Guide

Beam line	Research Program	Mono.	Affiliation	Local Contact	Spokesperson
U1A	SEXAFS, ARUPS, XPS	ERG	Exxon	B DeVries 516-282-4828 516-282-5206	J Chen 516-282-5501 516-282-2738
U1B	(Conceptual)	TGM	Exxon	B DeVries 516-282-4828 516-282-5206	P Stevens 516-282-4828 908-730-2584
U2A	(Unassigned)				
U2B	High pressure, pump-probe, high Tc abs., IR microscopy	MI	SUNY@SB BNL-NSLS Grumman Carnegie Inst of Was	G Williams 516-282-7529 516-282-3634	G Carr 516-282-5502 516-346-9073
U3A	Time-resolved and DC radiometry; reflectometry for optical constants	ERG	Los Alamos Natl Lab Smiths Astro Obs EG&G Energy Meas	W Towell 516-282-2838 516-282-7245	R Blake 516-282-5521 505-983-9683
U3B	(Conceptual)				
U3C	Photoelectron spect.; exp. system and detector calibrations	ERG	Los Alamos Natl Lab Sandia Natl Lab	A Andrews 516-282-4751 516-282-5503 W Towell 516-282-5521 516-282-7245	A Arko 505-665-0758 R Bartlett 516-282-5708 505-667-5923
U4A	ARUPS of solids,surfaces; hi res. core level photo-emission; total yield absorption	TGM	AT&T BNL - NSLS	M Shek 516-282-5930 516-282-5504 J Rowe 908-582-5878	G Wertheim 908-582-4958
U4B	Soft x-ray photoemission spectroscopy; NEXAFS; SXMCD	SGM	AT&T Naval Res Lab	G Meigs 516-282-7290 908-582-3863 C Chen 516-282-7290	C Chen 516-282-7290 908-582-6030

Beam line	Research Program	Mono.	Affiliation	Local Contact	Spokesperson
U4IR	Vibr. spectr of molecules on surfaces; abs of hi Tc superconductors; hi res gas abs.; fast detectors	MI,WDI	BNL-NSLS AT&T Fairleigh Dickinson Exxon	G Williams 516-282-3634 516-282-7529	G Williams 516-282-3634 516-282-7529
U5	Diagnostics		BNL-NSLS	R Nawrocky 516-282-4449	R Nawrocky 516-282-4449
U5U	Spin polarized angle-resolved ultraviolet photoemission	TGM	BNL-Physics	S Hulbert 516-282-7570	P Johnson 516-282-3705
U6	Lithography	WB	IBM	J Silverman 914-945-2099 516-282-5506	J Silverman 914-945-2099
U7A	Photoemission; SEXAFS; Fluorescence yield spectroscopy	TGM	BNL-NSLS BNL-Physics BNL-Chemistry Dow Chemical NIST	Q Dong 516-282-5507 516-282-5358	S Hulbert 516-282-7570
U7B	Photoemission; SEXAFS	PGM	BNL-Physics SUNY@SB	F Loeb 516-282-5507 516-282-2092 M Ruckman 516-282-3515	M Strongin 516-282-3763
U8A	ARUPS NEXAFS	TGM	IBM	R McFeely 516-282-5508 914-945-2068	R McFeely 516-282-5508 914-945-2068
U8B	ARUPS NEXAFS	TGM	IBM	R McFeely 516-282-5508 914-945-2068	R McFeely 516-282-5508 914-945-2068
U8C	Zone plate monochr evaluation; reflectivity measurements of thin films and multilayers	ZONE PL.	IBM	R McFeely 516-282-5508 914-945-2068	R McFeely 516-282-5508 914-945-2068
U8D	(Conceptual) Scanning soft x-ray microscopy		IBM	R McFeely 516-282-5508 914-945-2068	R McFeely 516-282-5508 914-945-2068
U9A	(Planned) Lithography				

Beam line	Research Program	Mono.	Affiliation	Local Contact	Spokesperson
U9B	CD; MCD; time-resolved fluorescence (lifetimes)	C-T	BNL-NSLS BNL-Biology	J Sutherland 516-282-5509 516-282-3406	J Sutherland 516-282-5509 516-282-3406
U10A	(Unassigned)				
U10B	PSD - general vacuum R&D	WB	BNL-NSLS Grumman	C Foerster 516-282-5510 516-282-4754 C Lanni 516-282-4100	C Foerster 516-282-5510 516-282-4754
U11	Gas phase photo-ionization and Spectroscopy	NIM	BNL-NSLS BNL-Biology U of New Mexico BNL-DAS Brandeis U	S Hulbert 516-282-5511 516-282-7570 L Kelly 516-282-2091	E Jenson 617-736-2865 E Johnson 516-282-4603
U12A	High resolution core level spectroscopy (construction)	TGM	Oak Ridge Natl Lab U of Tennessee	P Lyman 516-282-5512 516-282-5615	E Plummer 615-974-2288 D Zehner 615-574-6291
U12B	Angle-resolved photoemission	TGM	Oak Ridge Natl Lab U of Tennessee	P Lyman 516-282-5512 516-282-7395	D Zehner 516-282-5512 615-574-6291 E Plummer 615-974-2288
U13UA	High res. VUV/soft XAS and electron spectroscopy (incl. spin-pol photoem.)	SGM	BNL-NSLS Drexel U U of Wisconsin Brandeis U Rutgers U AT&T NYU	S Hulbert 516-282-5913 516-282-7570	S Hulbert 516-282-7570 E Jensen 617-736-2865
U13UB	Optical metrology for extreme ultraviolet projection lithography	WB	AT&T Sandia Natl Lab BNL-Instrum Naval Res Lab	A MacDowell 516-282-5513 516-282-5334	R Freeman 908-949-9500
U14A	Solid state photoemissions studies	PGM	BNL-NSLS	M Shek 516-282-5514 516-282-5930	M Shek 516-282-5514 516-282-5930

Beam line	Research Program	Mono.	Affiliation	Local Contact	Spokesperson
U14B	Detector Research and Development	WB	BNL-NSLS	J Hastings 516-282-3930	J Hastings 516-282-3930
U15	Soft x-ray spectroscopy (solids and gases)	TGM	BNL-NSLS SUNY@SB SUNY@Buff	D Hanson 516-282-5515 516-632-7917	D Hanson 516-282-5515 516-632-7917
U16A	(Unassigned)				
U16B	ARUPS; XPS; SEXAFS; stimulated desorption; NEXAFS	ERG	Cornell U Sandia Natl Lab	S Woronick 516-282-5516	R Merrill 607-255-9857

X-Ray Beamline Guide

Beam line	Research Program	Energy (keV)	Affiliation	Local Contact	Spokesperson
X1A	Soft x-ray imaging	10-80 Å	BNL-NSLS SUNY@SB LBL NCSU ANL	S Wirick 516-282-4723 516-632-8095	J Kirz 516-282-4723 516-632-8106
X1B	Soft x-ray spectroscopy	10-50 Å	BNL-NSLS BNL-Physics FA - Juelich Fritz-Haber-Inst	P Johnson 516-282-5701 516-282-3705	P Johnson 516-282-3705
X2A	Small angle scattering		Exxon	M Sansone 516-282-5602 201-730-3388	K Liang 908-730-3032
X2B	X-ray microtomography	6.5-30, WB	Exxon	K Mohanty 516-282-5602 516-282-5644	D Noh 908-730-2598
X3A1	Short wavelength crystallography, diffration and scattering	14, 19, 31	SUNY@SB SUNY@Buff	A Darovsky 516-282-5603 516-282-3770	P Coppens 716-645-6800 ext. 2217
X3A2	Diffractometry; x-ray spectroscopy; scattering; crystallography; small angle scattering	3-31	SUNY@SB SUNY@Buff	A Darovsky 516-282-5603 516-282-3770	P Coppens 716-645-6800 ext. 2217
X3B1	X-ray spectroscopy; powder diffraction	4.6-40	SUNY@SB SUNY@Buff	P Stephens 516-282-5603 516-632-8156 R Dinnebier 516-282-5687	P Coppens 716-645-6800 ext. 2217
X3B2	Surface science	4-20	SUNY@SB SUNY@Buff	P Stephens 516-282-5603 516-632-8156	P Stephens 516-282-5634 516-632-8156
X4A	Multiwavelength anomalous diffraction analysis of crystalline biological macromolecules	4-30	Howard Hughes Med In	C Ogata 516-282-5604 516-282-4938	W Hendrickson 516-282-4938 212-305-3456

Beam line	Research Program	Energy (keV)	Affiliation	Local Contact	Spokesperson
X4B	(Conceptual)				
X4C	Diffraction measurements from biological macromolecules	7-20	Howard Hughes Med In	C Ogata 516-282-5585 516-282-4938	W Hendrickson 516-282-4938 212-305-3456
X5	Laser Electron Gamma Source (LEGS); medium energy nuclear physics	80-400 MeV	BNL-Physics	C Thorn 516-282-5605 516-282-7798	A Sandorfi 516-282-7951
X6A	Time and space resolved dispersive x-ray spectroscopy	6.5-20	ANL	P Lee 516-282-5706 516-282-5934	P Montano 708-252-6239
X6B	X-ray scattering	2.4-21.0	ANL Temple U Northwestern U BP	K Huang 516-282-5706 516-282-5498	P Montano 708-252-6239
X7A	Structural char. through powder diffraction	5-45, WB	BNL-NSLS BNL-Physics Carnegie Inst of Was E I DuPont Mobil UOP Air Products Corp	D Cox 516-282-5607 516-282-3818 Q Zhu 516-282-5065 516-282-3818	D Cox 516-282-3808 516-282-3818
X7B	Crystallography; wide angle scattering	5-21	BNL-Chemistry Swedish Nat Res Coun U of Pittsburgh U of Helsinki	J Hanson 516-282-5707 516-282-4381	T Koetzle 516-282-4384
X8A	Photoionization cross-sections; photoelectron spectr; mirror reflect.; detector calib.; spectr.	0.26-5.9	Los Alamos Natl Lab Smiths Astro Obs EG&G Energy Meas	M Sagurton 516-282-5708	R Blake 516-282-5521 505-983-9683
X8C	Diffraction from biological macromolecules and detector calibrations	5-20	Los Alamos Natl Lab Sandia Natl Lab LLNL ANL	R Alkire 516-282-5608 516-282-5025	G Idzorek 516-282-7245 505-667-8848 E Westbrook 708-252-3983
X9A	XAS	3.4-18.6	U City Sci Center	M Sullivan 516-282-3800 Y Hai 516-282-3800	R Fischetti 516-282-3800 215-386-1912

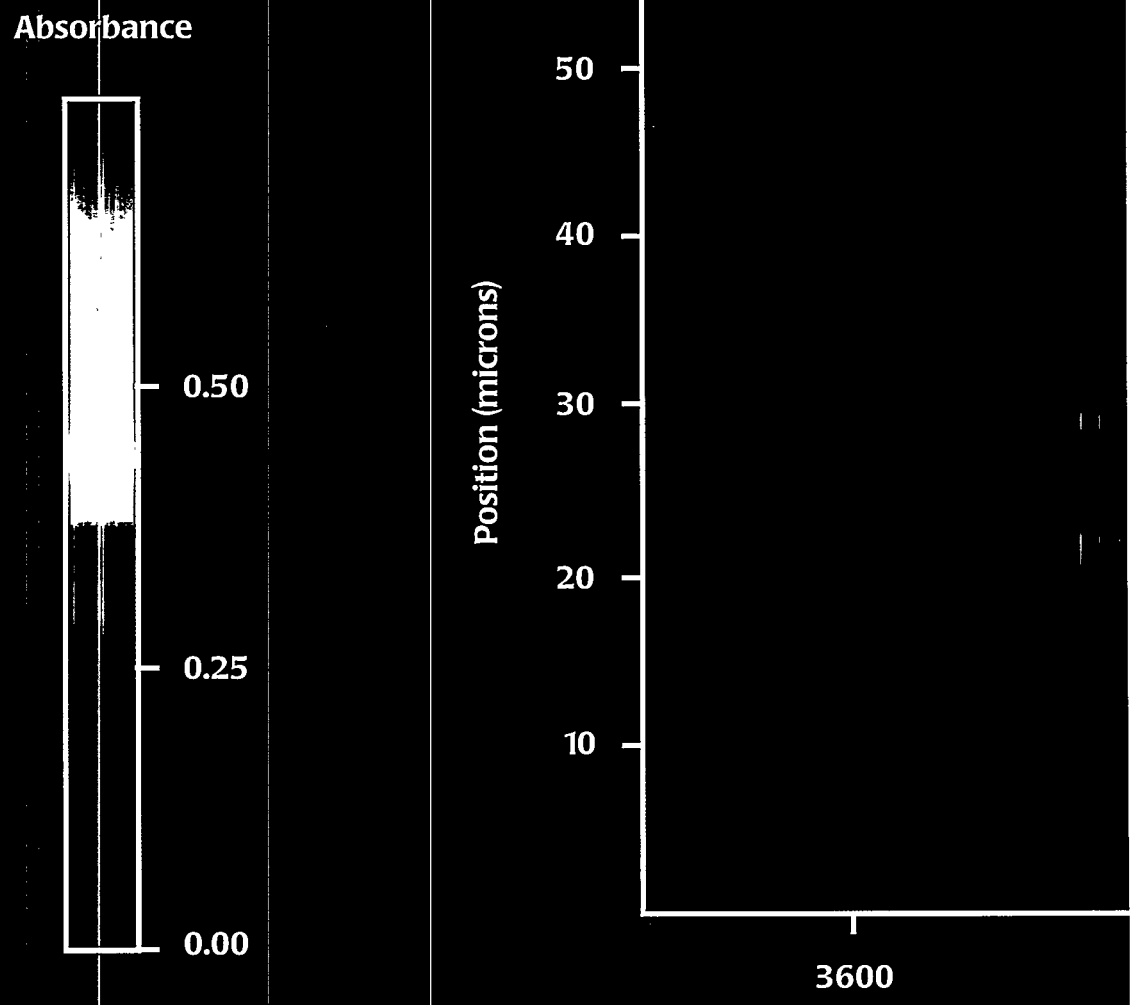
Beam line	Research Program	Energy (keV)	Affiliation	Local Contact	Spokesperson
X9B	Time resolved x-ray spectroscopy; scattering; diffraction; XAS	3.2-18.8	Albert Einstein College of Med	Y Hai 516-282-5609 M Sullivan 516-282-3800	M Chance 516-282-3800 718-430-2894 718-430-3591
X10A	Diffraction; small angle scattering; crystallography; scattering	6-15.2	Exxon	E Sirota 516-282-5610 908-730-3407	K Mohanty 516-282-5644
X10B	Scattering; crystallography	8, 12	Exxon	D Noh 516-282-5710 908-730-2598	B Zhang 516-282-3553
X10C	EXAFS	3.5-24.7	Exxon	M Sansone 516-282-3265 201-730-3388	P Stevens 516-282-4828 908-730-2584
X11A	EXAFS	4.5-35	No Carolina St U U of Connecticut BNL-NSLS Naval Res Lab Mobil E I DuPont Hoechst Celanese Case Western U IL Inst of Tech LLNL Georgia Tech U U of Washington Notre Dame U	G Lamble 516-282-5611 516-282-7734	D Sayers 516-282-7731 919-515-4453
X11B	EXAFS	1.7-8	No Carolina St U U of Connecticut BNL-NSLS Mobil E I DuPont Naval Res Lab Hoechst Celanese Case Western U IL Inst of Tech LLNL Georgia Tech U U of Washington Notre Dame U	G Lamble 516-282-5611 516-282-7734	D Sayers 516-282-7731 919-515-4453
X12A	Instrument development		BNL-NSLS	P Siddons 516-282-2738 516-282-5627	P Siddons 516-282-2738 516-282-5627
X12B	Time-resolved and static x-ray diffr. of macromol. systems in both wide and small angle regimes	6-15	BNL-NSLS BNL-Biology	M Capel 516-282-5712 516-282-5234	M Capel 516-282-5712 516-282-5234

Beam line	Research Program	Energy (keV)	Affiliation	Local Contact	Spokesperson
X12C	Protein crystallography	7.8-13.6	BNL-Biology	R Sweet 516-282-3401 516-282-5712	R Sweet 516-282-3401 516-282-5712
X13	R&D optics development; soft x-ray utilization		BNL-NSLS	E Johnson 516-282-4603 516-282-5613	E Johnson 516-282-4603 516-282-5613
X14A	Scattering; crystallography; spectroscopy	3.5-40	Oak Ridge Natl Lab Dow Chem U of Illinois	P Zschack 516-282-5614 516-282-2583	P Zschack 516-282-5614 516-282-2583
X14B	(Conceptual) X-ray microprobe; x-ray micro-focussing; micro-diffraction	WHITE	Oak Ridge Natl Lab Dow Chem IBM AT&T	P Zschack 516-282-5614 516-282-2583	P Zschack 516-282-2583 516-282-5614
X15A	X-ray standing waves	3-20, WB	ANL Northwestern U Harvard U	P Lyman 516-282-5615	M Bedzyk 516-282-7395 708-252-7763
X15B	SEXAFS EXAFS NEXAFS	1.5-15	AT&T	S Schuppler 516-282-3565 908-582-5275 A MacDowell 516-282-5334	P Citrin 908-582-5275
X16A	Surface diffraction	4-12	AT&T U of Illinois	K Evans-Lutterodt 516-282-5616 516-282-2154	K Evans-Lutterodt 908-582-2154
X16B	Diffraction	7.85	AT&T	A MacDowell 516-282-5716 516-282-5334	E Isaacs 908-582-7261
X16C	Novel spectroscopy; diffraction	3-16	ATT U of Illinois	D Adler 516-282-5716 516-282-2686	W Brown 908-582-3941
X17B1	Chemical crystallography; hi P physics; tomography; x-ray scattering; x-ray fluorescence microprobe	10-100, WB	BNL-NSLS	DP Siddons 516-282-5717 516-282-2738	J Hastings 516-282-3930

Beam line	Research Program	Energy (keV)	Affiliation	Local Contact	Spokesperson
X17B2	Medical research: Angiography; computed tomography; radiotherapy	33.02,33.3	BNL-NSLS SSRL Stanford U No Shore U Hosp LBL BNL-Medical SUNY@SB Austr Nucl Sci & Tech Org ESRF Palo Alto Vetr Admin Hosp	N Gmür 516-282-5617 516-282-2490	W Thomlinson 516-282-3937
X17C	Hi P research; energy dispersive diffraction from microscopic sample volumes	10-100, WB	Naval Res Lab Carnegie Inst of Was Los Alamos Natl Lab AT&T SUNY@SB U of Hawaii LLNL Cornell U U CA of Berkeley U of Washington U of Chicago	J Hu 516-282-5917 202-686-2410	E Skelton 202-767-3014 H Mao 202-686-2410 ext 2467
X18A	Diffuse and surface scattering	4-20	Purdue U Northwestern U U of Illinois U of Missouri	S Ehrlich 516-282-5618 516-282-7862 J Schwanof 516-282-5635 516-282-5618	G Liedl 317-494-4100
X18B	EXAFS; optics char.; reflectivity measurements	4-26	ANL AlliedSignal UOP Chevron	S Khalid 516-282-7597 516-282-5718	P Montano 708-252-6239
X19A	XAS; EXAFS XANES	2.1-25.6	BNL-NSLS UCA@Davis U of Kentucky U of Michigan BNL-DAS Rutgers U	F Lu 516-282-5619 516-282-2338 L Furenlid 516-282-5699	L Furenlid 516-282-5699
X19C	Topography; liquid surface scattering	4-25, WB	BNL-NSLS SUNY@SB Johns Hopkins U Army Research Lab Adelphi U U of Chicago U of ILL at Chicago	M Dudley 516-632-8500 516-282-5719	M Dudley 516-632-8500 516-282-5719

Beam line	Research Program	Energy (keV)	Affiliation	Local Contact	Spokesperson
X20A	Scattering (hi Q-res)	5.6-12	IBM MIT	J Jordan-Sweet 516-282-5720 914-945-3322	B Stephenson 914-945-3008
X20B	Scattering at fixed energy	17.36	IBM MIT	J Jordan-Sweet 516-282-5720 914-945-3322	B Stephenson 914-945-3008
X20C	Scattering (hi and low Q res)	4-11	IBM MIT	J Jordan-Sweet 516-282-5720 914-945-3322	B Stephenson 914-945-3008
X21	High energy resolution inelastic scattering	> 4	BNL-NSLS AT&T BNL-Physics SUNY @ Stony Brook ESRF ANL U of Helsinki	C Kao 516-282-5721 516-282-4494 W Caliebe 516-282-4795 516-282-3930	C Kao 516-282-4494
X22A	In-plane diffr. & refl. studies of surfaces under electro-chem. cond., and thin films and multilayer	10 Nom.	BNL-Physics BNL-DAS	D Gibbs 516-282-5622 516-282-4608 B Ocko 516-282-4299	D Gibbs 516-282-4608
X22B	High resolution x-ray diffraction	5-10	BNL-Physics Harvard U	B Ocko 516-282-5622 516-282-4299	D Gibbs 516-282-4608
X22C	Diffraction studies of magnetic and structural phase transformations; surface scattering	3-12	BNL-Physics	D Gibbs 516-282-5622 516-282-4608	D Gibbs 516-282-4608
X23A2	EXAFS	5.4-30	NIST	J Woicik 516-282-5823 S Chu 301-975-5975	J Woicik 516-282-5236 516-282-5823
X23A3	Topography; small-angle scattering	5-30, WB	NIST	D Fischer 516-282-5623 516-282-5177	G Long 301-975-5975
X23B	EXAFS; scattering; crystallography	3-11	Naval Res Lab	J Kirkland 516-282-5723 516-282-2258	T Elam 202-767-3014
X24A	Atomic, molecular, and optical physics with x-rays	1.8-5.0	NIST ANL	B Karlin 516-282-5624 S Southworth 301-975-4850	R Deslattes 301-975-4841

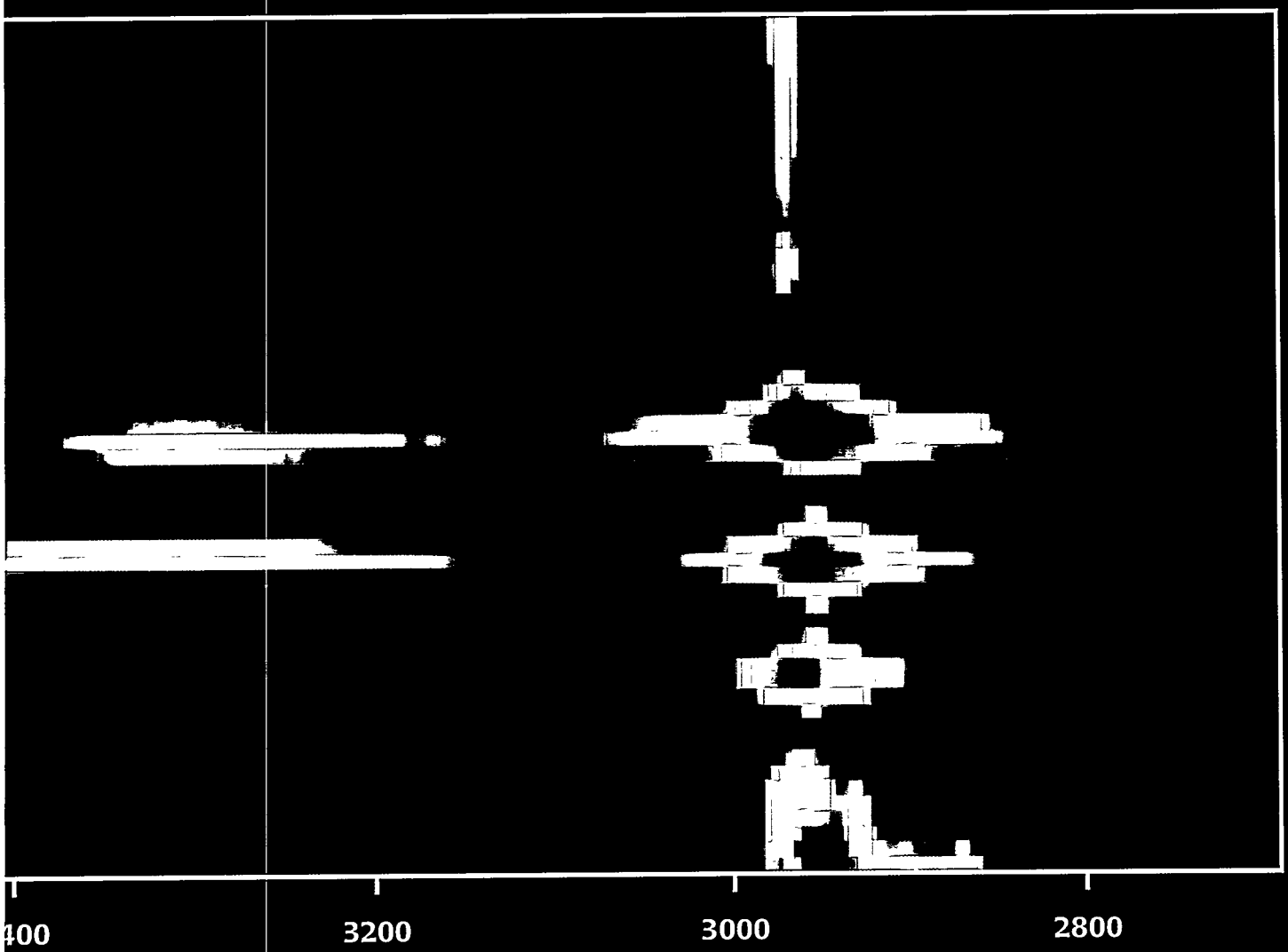
Beam line	Research Program	Energy (keV)	Affiliation	Local Contact	Spokesperson
X24C	Photoemission and reflectance spectroscopy	2-1500 eV	Naval Res Lab	J Rife 516-282-5724 202-767-4654	M Kabler 202-767-2223
X25	High Q-resolution elastic scattering	> 3	BNL-NSLS	L Berman 516-282-5625 516-282-5333	L Berman 516-282-5625 516-282-5333
X26A	Dev. and application of analytical techniques (e.g. microprobe)	4-20, WB	BNL-DAS U of Chicago	S Bajt 516-282-5626 516-282-5596	S Sutton 312-702-9506
X26C	Dev. and applic. of x-ray microscopy techniques; Laue diffraction protein crystallography	4-30, WB	BNL-DAS U of Chicago BNL-Biology	G Shea-McCarthy 516-282-5726	S Sutton 312-702-9506
X27A	Instrument development		BNL-NSLS	P Siddons 516-282-2738 516-282-5627	P Siddons 516-282-2738 516-282-5627
X27B	Instrument development		BNL-NSLS	E Johnson 516-282-4603 516-282-5627	E Johnson 516-282-4603 516-282-5627
X27C	Instrument development		BNL-NSLS	P Siddons 516-282-2738 516-282-5627	P Siddons 516-282-2738 516-282-5627
X28A	Instrument development; vacuum research		BNL-NSLS	P Stefan 516-282-2117 516-282-5728	P Stefan 516-282-2117 516-282-5728
X28B	Photon-based diagnostics and detector development		BNL-NSLS	P Stefan 516-282-2117 516-282-5728	P Stefan 516-282-2117 516-282-5728
X28C	Photon-based diagnostics and detector development		BNL-NSLS	P Stefan 516-282-2117 516-282-5728	P Stefan 516-282-2117 516-282-5728
X29A	(Unassigned)				
X29B	(Unassigned)				
X30	Diagnostic				



Beamline U2B: The modified Spectra-Tech IRμs scanning microspectrometer with a built-in Michelson interferometer takes a full infrared spectrum at each point on a sample with a spatial resolution at the diffraction limit (for 1/f optics, approximately equal to the wavelength). Samples are scanned to produce maps. The figure shows a linear map of a laminate structure in which features as small as 3 microns are distinguished. (C. Zimba, Polaroid Corporation)

APPENDICES

ABSTRACTS & PUBLICATIONS



From the Editor

This year's Activity Report represents another milestone in publishing at the NSLS. The 1993 edition was redesigned and created at the NSLS, allowing the eventual electronic storage and dissemination of the book, on CD ROM, for example. This year, we have conquered the final frontier: the abstract section. Traditionally received on paper and laboriously pasted down and reduced, the abstracts this year were entered via the new Electronic Submission System (ESS). The ESS takes information entered by authors through the Forms function on World Wide Web and stores it in a database optimized for document handling. Composition routines then perform the integration of text and figures and output our choice of PostScript file (for the author to view and also to go to the printer), SGML file (Standard Generalized Markup Language) for electronic publishing, and HTML (Hyper Text Markup Language) for dissemination on World Wide Web. Furthermore, the ESS allows full storage and retrieval of the abstracts, sorted by beamline, any authors, or any word in the text, and available on World Wide Web two to three months before the printed product is released.

Operating as a prototype this year, the ESS is being fine-tuned and will be exclusively used for all future abstract submissions beginning with the 1995 Activity Report. The submissions will be accepted year-round, with abstracts received before the publication cut-off date included in the upcoming Activity Report and those received after the cut-off date rolled over into the next Report. To access the ESS on the World Wide Web, select "Open URL" from the Mosaic File Menu, and enter "http://www.nsls.bnl.gov" to get to the NSLS Home Page. Choose "Electronic Submissions"; all instructions are provided in both viewable and downloadable format.

The NSLS wishes to thank Peggy Sutherland for her oversight of the ESS project, and the BNL Technical Information Division (now part of the new Information Services Division) for their high caliber of expertise and assistance.

ABSTRACTS

VUV Beamlines

Beamline U1A

Determination of the oxidation states of vanadium compounds from the vanadium L-edge peak positions A-8
J. G. Chen, B. D. DeVries, B. Frühberger (Exxon), and C. M. Kim (Kyungpook Nat. Univ., Taegu, South Korea)

A NEXAFS determination of the average stoichiometry and thickness of thin carbide films on a vanadium (110) surface A-8
J. G. Chen, B. D. DeVries, B. Frühberger, and M. S. Touvelle (Exxon)

A comparative investigation of the electronic and catalytic properties of VC/V(110) model surface and VC powder materials A-9
J. G. Chen, B. Fruhberger, B. D. DeVries (Exxon), R. Kapoor, and S. T. Oyama (Virginia Tech.)

A study of the oxidation of iron thin films by NEXAFS: determination of the oxidation state A-9
M. L. Colaianni and F. M. Hoffmann (Exxon)

Investigation of self assembled monolayers using x-ray absorption spectroscopy A-10
B. M. DeKoven, D. A. Fischer (NIST), M. Chaudhury (Lehigh Univ.), J. Curphy, and T. Chritz (all other from the Dow Chemical Company)

Observing bond chemistry at the buried metal / benzocyclobutene (BCB) polymer interface using NEXAFS A-10
B. M. DeKoven (Dow), D. A. Fischer (NIST), D. H. Paker, J. J. Curphy, G. E. Mitchell (Dow), J. L. Gland (Univ. of Michigan), C. A. Wedelstaedt, S. J. Babinec (Dow)

Orientation studies of copper benzotriazole at the carbon, nitrogen, oxygen and copper K-edges using polarised, ultra-soft NEXAFS spectroscopy A-11
E. S. Ferrari, J. Johnstone, C. A. E. Peacock, K. J. Roberts (Univ. of Strathclyde, Glasgow, UK), and B. D. DeVries (Exxon)

An investigation into the orientations and surface melting characteristics of thin films of n-alkanes on Si (111) using synchrotron, polarised, ultra-soft NEXAFS spectroscopy A-11
E. S. Ferrari, J. Johnstone, K. J. Roberts (Univ. of Strathclyde, Glasgow, UK), and B. D. DeVries (Exxon)

In Situ x-ray absorption of diamond (100) surface modified by low energy neonions A-12
Liji Huang, Igor Bello, and Leo W.M. Lau (UWO, Canada); S.-Tong Lee (Kodak), Paul A. Stevens, and Brian D. DeVries

NEXAFS study of the mechanism of the CH_3I + C_6F_5 / Cu(100) reaction to form toluene A-12
P. W. Kash, M. X. Yang, D.-H. Sun, J. Eng Jr., G. W. Flynn, and B. E. Bent (Columbia Univ.)

A NEXAFS study of degradation of vinyl halides on Cu(100) A-13
M. X. Yang, P. W. Kash, J. Eng, Jr., and B. E. Bent (Columbia Univ.)

Beamlines U2B and U4IR

Asphaltene adsorption on kaolinite: characterization by infrared microscopy A-13
J.-L. Bantignies, C. Cartier dit Moulin, H. Dexpert, A.-M. Flank (LURE Université Paris-Sud, France), and G. P. Williams (NSLS)

Infrared microspectroscopy study of oxygen defects in silicon A-14
G. L. Carr (Grumman Aerospace & Electronics)

Nanosecond time resolved far-infrared spectroscopy of photocarriers in GaAs A-14
G. L. Carr (Grumman)

Adsorbate-substrate motion and broadband reflectance change for oxygen adsorbed on Cu(100) ... A-15
P. Dumas (LURE and LASIR-Orsay-France), K. Lin, R. G. Tobin (Michigan State Univ.), and G. P. Williams (NSLS)

Observation of a charge density wave for K on Ag(111) A-15
P. Dumas (LURE and LASIR-Orsay, France), P. Rudolf (LISE, Belgium), F. M. Hoffmann (Exxon), and G. P. Williams (NSLS)

Far-IR mixed isotope feasibility study for CO/Cu(111) A-16
C. J. Hirschmugl and G. P. Williams (NSLS)

Investigation of the superconducting energy gap in Rb_3C_{60} A-16
Dan Koller, Michael C. Martin, and Laszlo Mihaly (SUNY Stony Brook)

Dynamics of atomic adsorbates: - hydrogen on Cu(111) A-17
C. L. A. Lamont (Univ. of Huddersfield, UK), B. N. J. Persson (Inst. fur Festkörperforschung, Germany), and G. P. Williams (NSLS)

Synchrotron infrared spectroscopy and phase diagram of hydrogen at high pressure A-17
M. Ming Li, A. F. Goncharov, R. J. Hemley, and H. K. Mao (Carnegie Inst. of Washington)

"In situ" synchrotron infrared spectroscopy of the electrochemical interface A-18
C. A. Melendres (ANL), B. Beden (Univ. de Poitiers, France), and G. A. Bowmaker (Univ. of Auckland, New Zealand)

Charge transfer and electron-phonon couplings for C_6O deposited on clean and alkali covered Ag(111) A-18
P. Rudolf (LISE-Namur, Belgium), P. Dumas (LURE and LASIR, Orsay, France), L. Struck, Y. J. Chabal (AT&T Bell Labs.), and G. P. Williams (NSLS)

Using far-infrared synchrotron radiation to study collective motions of proteins A-19
A. Xie, L. M. Miller, E. M. Scheuring, B. Sclavi, M. R. Chance (Albert Einstein College of Medicine)

Beamline U3C

Different bulk and surface valences in $YbBe_{13}$ A-19
A. B. Andrews, R. I. R. Blyth, J. J. Joyce, A. J. Arko, and Z. Fisk (LANL)

UPS and XAS study of the Kondo insulator $Ce_3Bi_4Pt_3$ A-20
A. B. Andrews, J. J. Joyce (LANL), A. J. Arko (LANL), and P. C.Canfield (Ames Lab)

ARUPS study of strongly mixed-valent $CeBe_{13}$ A-20
A. B. Andrews, J. J. Joyce, A. J. Arko, and Z. Fisk (LANL)

A Reexamination of the heavy fermion superconductor UPt_3 ..... A-21
A. B. Andrews, J. J. Joyce, A. J. Arko (LANL), and B. Maples (Univ. California, San Diego)

4f bands in the Ce heavy fermions compound $CePt_{2+x}$ A-21
A. B. Andrews (LANL), J. J. Joyce (LANL), A. J. Arko (LANL), J. Tang (Univ. of Irvine), J. M. Lawrence (Univ. of Irvine)

Beamline U4A

Alkali adsorption on quasi-one-dimensional oxides A-22
Klaus Breuer, Kevin E. Smith (Boston Univ.), Martha Greenblatt, and William McCarroll (Rutgers Univ.)

Surface-ion core-level shift in alkali halides A-22
G. K. Wertheim, D. N. E. Buchanan, J. E. Rowe, and P. H. Citrin (AT&T Bell Lab.)

Alkali halide valence band density of states A-23
G. K. Wertheim and J. E. Rowe (AT&T Bell Lab.)

Interatomic Auger rates in sodium halides A-23
G. K. Wertheim, J. E. Rowe, and P.H. Citrin (AT&T Bell Labs)

Beamline U4B

Circularly polarized soft x-ray resonant magnetic scattering from multilayers A-24
V. Chakarian (NRL), Y. U. Idzerda (NRL), C.-C. Kao (NSLS), J.-H. Park (AT&T Bell Lab.), G. Meigs (AT&T Bell Lab.), E. Johnson (NSLS), G. A. Prinz (NRL), and C. T. Chen (AT&T Bell Lab.)

2D element specific vector magnetometry of heteromagnetic multilayers A-24
V. Chakarian (NRL), H.-J. Lin (AT&T Bell Lab.), Y.U. Idzerda (NRL), E.E. Chaban, G. Meigs, J.-H. Park (AT&T Bell Lab.). G.A. Prinz (NRL), and C.T. Chen (AT&T Bell Lab.)

Element specific vector magnetometry via SX-MCD A-25
V. Chakarian (NRL), H.-J. Lin (AT&T Bell Labs.), Y. U. Idzerda (NRL), E. E. Chaban (AT&T Labs.), G. Meigs (AT&T Bell Labs.), J.-H. Park (AT&T Labs.), G. A. Prinz (NRL), and C. T. Chen (AT&T Bell Labs.)

Applicability of the orbital and spin x-ray magnetic circular dichroism sum-rules A-25
C. T. Chen (AT&T Bell Lab.), Y. U. Idzerda (NRL), H.-J. Lin, N. V. Smith, G. Meigs, E. E. Chaban (AT&T Bell Lab.), G. H. Ho (Univ. of Penn.), E. Pellegrin, and F. Sette (AT&T Bell Labs)

Extraction of the coefficient of giant magnetoresistance A-26
Y. U. Idzerda (NRL), C. T. Chen (AT&T Bell Lab.), S.-F. Cheng (NSWC), W. Vavra (NRL), G. A. Prinz (NRL), G. Meigs (AT&T Bell Lab.), and H.-J. Lin (AT&T Bell Lab.)

Electron spectroscopy study of doping dependence in $La_{1-x}Ca_xMnO_3$ A-26
J.-H. Park, W. Bao (AT&T Bell Lab. and Johns Hopkins Univ.), S.-W. Cheong (AT&T Bell Lab.), V. Chakarian (NRL), G. Meigs, and C. T. Chen (AT&T Bell Lab.)

Orbital characters of holes in $Y_{2-x}Ca_xBaNiO_5$, a doped haldane chain compound A-27
J.-H. Park, C. T. Chen, S.-W. Cheong, J. F. Ditusa, G. Aeppli (AT&T Bell Lab.), and C. Broholm (Johns Hopkins Univ. and NIST)

Dopant states in Zn_{1-x}(Co, Fe, Mn)$_x$Se A-27
J.-H. Park (AT&T Bell Lab.), K.-H. Cho, S.-J. Oh (Seoul Natl. Univ.), Y. D. Kim (Kyunghee Univ.), M. S. Han (Seoul City Univ.), J.-S. Kim (Sookmyung Women's Univ.), V. Chakarian, B.T. Jonker (NRL), G. Meigs, and C. T. Chen (AT&T Bell Lab.)

Electronic structure study of RNi_2B_2C (R = rare-earth) compounds by x-ray absorption spectroscopy A-28
E. Pellegrin (Kernforschungszentrum Karlsruhe, Institut fur Nukleare Festkörperphysik, Germany), G. Meigs, C. T. Chen, R. J. Cava, J. J. Krajewski, and W. F. Peck, Jr. (AT&T Bell Labs.)

X-ray magnetic circular dichroism study the spin 1/2 proteins A-28
G. Peng (Univ. California, Davis), J. H. Christiansen (Univ. California, Davis), A. T. Young (LBL), and S. P. Cramer (Univ. California, Davis and LBL)

Spin-polarization in 4f-photoemission from tungsten A-29
K. Starke (AT&T Bell Lab.), Y. Liu, P. D. Johnson (BNL), V. Chakarian (NRL),E. E. Chaban, G. Meigs, C. T. Chen (AT&T Bell Lab.)

Soft x-ray magnetic circular dichroism in Co/Sm/Co A-29
K. Starke, J.-H. Park (AT&T Bell Lab.), V. Chakarian (NRL), E. E. Chaban, G. Meigs, and C. T. Chen (AT&T Bell Lab.)

Beamline U5U

Hybridization and the effective mass of quantum well states in magnetic multilayers A-30
P. D. Johnson, K. Garrison, Q. Dong (BNL), N. V. Smith (LBL), Dongqi Li, J. Mattson,J. Pearson, and S. D. Bader (ANL)

Exchange splitting of Gd 5d states at finite temperature: Stoner-like or not? A-30
Dongqi Li, J. Pearson, S. D. Bader (ANL), D. N. McIlroy, C. Waldfried, P. A. Dowben (Univ. of Nebraska), D. J. Huang, and P. D. Johnson (BNL)

Photoemission study of quantum confinement by a finite barrier: Cu/Co(wedge)/Cu(100) A-31
Dongqi Li, J. Pearson, J. E. Mattson,Present address: Motorola, Inc. Schaumburg,IL 60196 S. D. Bader (ANL), P. D. Johnson (BNL)

Beamline U7A

Photoelectron spectroscopy and NEXAFS investigation of metal poly(*p*-phenylene vinylene) interface formation A-31
E. Ettedgui, H. Razafitrimo, and Y. Gao (Univ. of Rochester), and M. W. Ruckman (BNL)

Photon stimulated desorption studies of mixed molecular solids A-32
J. F. Moore, D. R. Strongin (SUNY Stony Brook), E. D. Johnson (NSLS), and F. M. Jacobsen (BNL)

New developments in the deposition of silica from condensed reactants A-32
J. F. Moore, D. R. Strongin (SUNY Stony Brook), and M. W. Ruckman (BNL)

Water formation 4k from deuterium and oxygen mixtures excited by soft x-rays A-33
J. F. Moore, D. R. Strongin (SUNY Stony Brook), M. W. Ruckman, and Myron Strongin (BNL)

Beamline U7B

Determination of the water adsorption site on NiAl and FeAl(110) by photoemission spectroscopy A-33
N. R. Gleason, S. Chaturvedi, D. R. Strongin (SUNY Stony Brook), and M. W. Ruckman (BNL)

The quantum nature of oxidation A-34
F. M. Jacobsen, M. W. Ruckman, and M. Strongin (BNL)

The reaction of Cl_2 with GaAs(110) at elevated temperature A-34
W. C. Simpson (Univ. Calif., Riverside and LBL), W. M. Tong (LBL), C. B. Weare (Univ.Calif., Riverside and LBL), D. K. Shuh (LBL), and J. A. Yarmoff (Univ. Calif., Riverside and LBL (Univ.Calif., Riverside and LBL)

Beamline U8A

An SXPS Study of the Reaction of GaAs with XeF_2 ..... A-35
W.C. Simpson, P.R. Varekamp and J.A. Yarmoff (UCR)

F^+ PSD from LaF_3/Si(111) A-35
W. C. Simpson, C. B. Weare, and J. A. Yarmoff (Univ. of Calif., Riverside and LBL)

Beamline U9B

Examination of the domain structure of *E. coli* chaperone DnaJ A-36
John Flanagan (BNL)

Simultaneous resolution of spectral and temporal properties of uv and visible fluorescence using single-photon counting with a position-sensitive detector A-36
Lisa A. Kelly (NSLS, BIO), John G. Trunk (BIO), Krzysztof Polewski (Agricultural U., Poz nan, Poland), and John C. Sutherland (BIO)

Structural analysis of Locusta migratoria diuretic hormone A-37
Thomas Nittoli and Scott McN. Sieburth(SUNY at Stony Brook)

Beamline U11

A discharge flow-photoionization mass spectrometric study of FCO (X^2A') A-37
Thomas J. Buckley, Russell D. Johnson, III, Robert E. Huie (NIST), Szu-Cherng Kuo, Zhengyu Zhang, R. Bruce Klemm (BNL)

Electronic spectroscopy of matrix isolated nucleic acid bases at 12 K A-38
Lisa A. Kelly (NSLS, BIO), Krzysztof Polewski (Agricultural Univ., Poznan, Poland), Eri k D. Johnson (NSLS), John G. Trunk, Denise C. Monteleone, John C. Sutherland (BIO)

A discharge flow-photoionization mass spectrometric study of the $NO_3(^2A_2')$ radical: photoionization spectrum, adiabatic ionization energy and ground state symmetry A-38
P. S. Monks, L. J. Stief (NASA/Goddard), M. Krauss (NIST), S. C. Kuo, Z. Zhang, and R. B. Klemm (BNL)

Structural analysis of Locusta migratoria diuretic hormone A-37
Thomas Nittoli and Scott McN. Sieburth(SUNY at Stony Brook)

Vacuum ultraviolet circular dichroism of biopolymers A-39
J. Trunk, D. Monteleone, and J. Sutherland (BNL), and E. Stevens (SUNY Binghampton)

A discharge flow-photoionization mass spectrometric study of the $FO(X^2\Pi_i)$ radical: photoionization efficiency spectrum and ionization energy A-39
Zhengyu Zhang, Szu-Cherng Kuo, R. Bruce Klemm (BNL), Paul S. Monks, and Louis J. Stief (NASA/Goddard)

Beamline U12B

Angle-resolved photoemission study of the Cs/Si(111)($\sqrt{3} \times \sqrt{3}$)R30°-B interface A-40
J. Chen (Univ. of Pennsylvania), H. H. Weitering (Univ. of Tennessee), and N. J. DiNardo (Drexel Univ.)

Angle-resolved photoemission study of the Si(111)3×1-Li surface reconstruction A-40
Xiaorong Shi (Univ. of Tennessee), Hanno H. Weitering (Univ. of Tennessee and ORNL)

Beamline U13UA

High resolution XPS study of the electronic structure of defects in the quasi-one dimensional conductor $K_{0.3}MoO_3$ A-41
Klaus Breuer, Kevin E. Smith (Boston Univ.), Martha Greenblatt, William McCarroll (Rutgers Univ.), and Steve L. Hulbert (NSLS)

Fluorescence yield x-ray absorption near edge structure (XANES) spectroscopy at the nitrogen and oxygen k-edges with a parallel plate proportional counter A-41
T. Crowder and H. Ade (North Caroline State Univ.)

The XANES spectroscopy of biological calcium phosphates using the high resolving power U13UA beamline A-42
C. J. Buckley, S. J. Bellamy (King's College London), X. Zhang (SUNY Stony Brook), G. Dermody (King's College London), and S. Hulbert (BNL)

Zero kinetic energy electron spectra of core excited Ar, N_2, O_2, and N_2Obased on a transverse velocity discrimination technique A-42
K. Lee, D. M. Hanson (SUNY Stony Brook), S. L. Hulbert (NSLS), and P. Kuiper (BNL)

Auger, zero-energy photoelectron coincidence spectroscopy (Azepeco): chemical-site-selectiveauger electron spectroscopy A-43
K. Lee (SRRC, SUNY Stony Brook), S. L. Hulbert (NSLS), P. Kuiper (BNL), D. Ji,and D. M. Hanson (SUNY Stony Brook)

Monoenergetic soft x-ray driven growth of boron nitride films on silicon A-43
J. F. Moore, Sanjay Chaturvedi, D. R. Strongin (SUNY Stony Brook), and Myron Strongin (BNL)

Adsorption and reaction of methylthiolate on Ni(111) A-44
D. R. Mullins and D. R. Huntley (ORNL)

Reaction kinetics of thiolate intermediates on Ni(111) A-44
D. R. Mullins and D. R. Huntley (ORNL)

Spin Resolved Iron Surface Density of States A-45
B. Sinkovic and E. Shekel (NYU), S. Hulbert (NSLS)

Extreme ultraviolet projection lithography A-45
R. Freeman, J. Bjorkholm, L. Eichner, L. Fetter, M. Himel, B. LaFontaine, A. MacDowell, Z. Tan, D. Taylor, D. tennant, S. Vaidya, W. Waskiewicz, D. White, D. Windt, O. Wood II (AT&T Bell Labs.), S. Spector (Stony Brook), T. Jewell (TJ Optics), J. Kortright (LBL)

Beamline U15

Atomic-site-selective solid-state photochemistry in matrix isolated N_2O using monochromatic soft x-rays A-46
S. Sambasivan, J. Glatthaar, S. Y. Chiang, S. L. Anderson, and D. M. Hanson (SUNY Stony Brook)

Determination of the oxidation states of vanadium compounds from the vanadium L-edge peak positions — U1A

J. G. Chen, B. D. DeVries, B. Frühberger (Exxon), and C. M. Kim (Kyungpook Nat. Univ., Taegu, South Korea)

The oxidation states of various vanadium compounds can be estimated from the NEXAFS peak positions of the L_{III} and L_{II} transitions. As shown in Figure 1, the peak positions of vanadium L-edge features depend strongly on the oxidation states of vanadium. From V^0 (atomically-clean vanadium) to V^{5+} (V_2O_5), the L_{III} feature increases from 515.5 eV to 519.0 eV, and the L_{II} feature increases from 522.5 eV to 525.5 eV. Such a relationship of peak positions vs. oxidation state is shown more clearly in Figure 2, where the peak positions of vanadium L-edge features are plotted as a function of oxidation states. The NEXAFS data points (squares) could be readily fitted by a linear function for both L_{III} and L_{II} features, and the slopes of these two linear fits give rise to an average value of 0.68±0.03 eV/per oxidation state for the various vanadium compounds.

By using the calibration curves in Figure 2 we are able to determine the oxidation state of several important vanadium-containing model systems. For example, the oxidation state of the thin oxide layer on V(110) is estimated to be 2.0, suggesting a stoichiometry of VO. In addition, the oxidation state of a thin vanadium carbide film is determined to be approximately 1.0, indicating that the direction of charge transfer is from vanadium to carbon. The latter observation is very important in understanding of the overall bonding configurations in VC/V(110), which has been used as a model system in our investigations of the electronic and catalytic properties of early transition metal carbides.

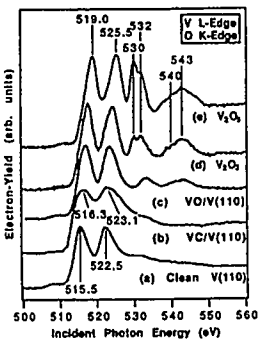


Figure 1

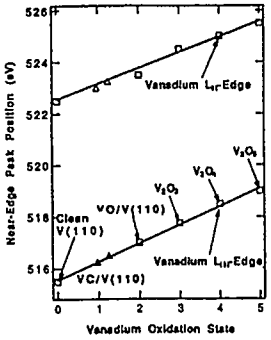


Figure 2

A NEXAFS determination of the average stoichiometry and thickness of thin carbide films on a vanadium (110) surface — U1A

J. G. Chen, B. D. DeVries, B. Frühberger, and M. S. Touvelle (Exxon)

A detailed understanding of the properties of early transition metal carbides is of practical importance because they often demonstrate unique catalytic advantages over their parent metals in activity, selectivity and resistance to poisoning. In an attempt to understand the fundamental aspects related to the electronic and catalytic properties of this important class of catalytic materials, we have chosen vanadium carbide films, produced on a vanadium (110) single crystal surface, as model systems for our experimental investigations.

Well-characterized vanadium carbide thin films can be prepared by exposing a clean V(110) surface to ethylene at 600 K. As shown in Figure 1, the formation of vanadium carbide, rather than other forms of carbon-containing species such as graphite or carbonaceous overlayers, was confirmed by the characteristic AES C(KLL) transition. The average stoichiometry and average thickness of the thin carbide films can be estimated by comparing the uptake curves from the AES and NEXAFS measurements, as shown in Figure 2. The AES results in Figure 2 (solid circles) are plotted in the form of carbon/vanadium atomic ratios; the NEXAFS data in Figure 2 (open circles) were recorded by measuring the fluorescence-yield of carbon K-edge feature at 285.5 eV. The most noticeable difference between the bulk-sensitive fluorescence-yield NEXAFS results and the relatively surface-sensitive AES data is observed at ethylene exposures above 140 L. Unlike the AES measurements, the fluorescence-yield of the carbon K-edge feature continues to increase at higher ethylene exposures, indicating the additional uptake of carbon by the surface. It is likely that the AES measurements are limited by the escape depth of the Auger electrons; the mean free paths for the C(KLL) and V(LMM) Auger electrons are approximately 10 Å. On the other hand, the detection limit of the fluorescence-yield NEXAFS is significantly deeper; the mean free path of the carbon K_α X-ray photon is estimated to be 1500 Å. The comparison in Figure 2 therefore indicates that, at ethylene exposures above 140 L, the average thickness of the carbide films is at least 10 Å and the stoichiometry of these films is VC.

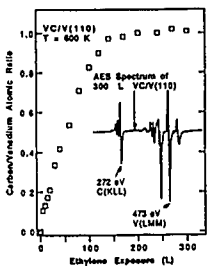


Figure 1

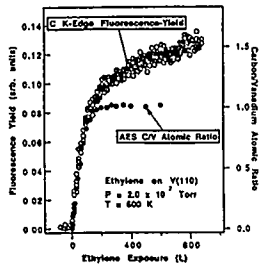


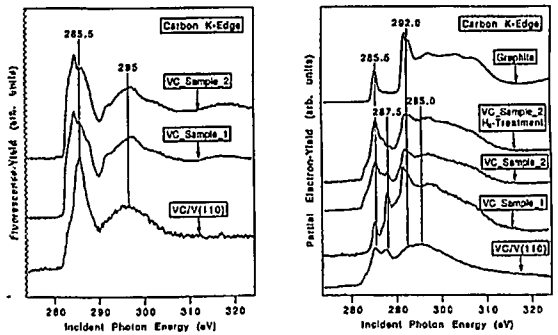
Figure 2

A comparative investigation of the electronic and catalytic properties of VC/V(110) model surface and VC powder materials — U1A

J. G. Chen, B. Fruhberger, B. D. DeVries (Exxon), R. Kapoor, and S. T. Oyama (Virginia Tech.)

In an attempt to understand the fundamental aspects related to the electronic and catalytic properties of early transition metal carbides, we have chosen vanadium carbide films on a V(110) single crystal surface as model systems for our experimental investigations. One of the main advantages of using the single crystal surface is that it enables one to apply powerful surface science spectroscopies to determine the electronic and catalytic modifications resulting directly from the formation of carbide. Another advantage is related to the fact that early transition metals are very reactive, which makes it very difficult to obtain atomically-clean metals or metal carbides in the form of powder materials.

Obviously, it is also very important to extend the fundamental information, obtained on the single crystal model surfaces, to the more realistic powder materials. Figure 2 and 2 show a comparison of the build and surface properties of VCV(110) and VC powders. As shown in Figure 1, the fluorescence-yield spectra of both VC/V(11) and VC powders are characterized by a relatively sharp feature at 285.5 eV and a broad peak at 295.0 eV. Such a comparison suggests that the bulk composition of VC/V(110) is very similar to the two VC powder materials, as features. The main noticeable difference is that the 285.5 eV peak of the VC powder materials is broader than that of VC/V(110), and may consist of two individual peaks for the powder materials. This may suggest the presence of VC units with different phases or orientations in the powder materials, Although the electron-yield NEXAFS data (Figure 2) suggests the presence of a small amount of graphite on the surface, the major surface component of the powder materials is also similar to the vanadium carbide films produced on the V(110) surface.



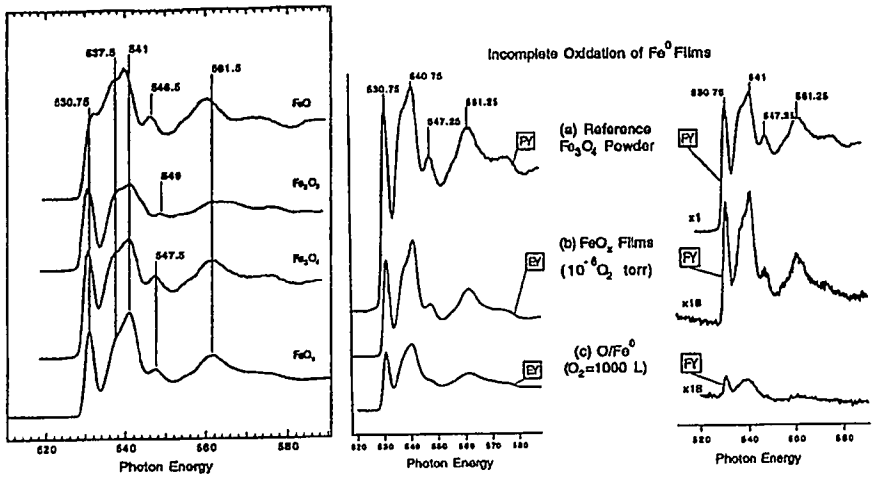
A study of the oxidation of iron thin films by NEXAFS: determination of the oxidation state — U1

M. L. Colaianni and F. M. Hoffmann (Exxon)

NEXAFS analysis of the oxidation of iron thin films (~ 20–30 Å) have been undertaken in an effort to prepare a model iron oxide surface for use in corrosion-related studies. These iron oxide films have been prepared by two methods: 1) Elemental iron was vapor deposited under ultrahigh vacuum conditions followed by post-adsorption of up to 1000L oxygen; and 2) Iron oxide films were prepared directly by vapor deposition of iron in a backing pressor of O_2. Two important questions to be resolved are the oxidation states and the chemical integrity of the oxide films. To address these questions, we have utilized partial-electron-yield NEXAFS, which is a surface sensitive technique, and FYNES which supplies information on the bulk properties of materials.

The oxidation state of our films can be determined by comparing our iron oxide FYNES spectra to reference iron oxide powders, namely, FeO, Fe_2O_3, and Fe_3O_4 (Fig. 1). We see in Fig. 1 that of the three states of iron oxide, the iron oxide prepared by vapor deposition of iron in $1\times10_{-6}$ torr O_2 most closely resembles stoichiometric Fe_3O_4. Further we find that the electron-yield and the photon-yield spectra for this layer [Fig. 2(b)] are very similar, suggesting that the surface and bulk stoichiometry are homogeneous. Contrasted to this, we find that post exposing 1000 L O_2 onto the metallic iron film at room temperature does not produce a homogeneous oxide film [Fig. 3(c)]. While the surface of this oxide resembles Fe_3O_4, it is clear from the intensity and lineshape of the bulk sensitive photon-yield spectrum [Fig. 2(c)] that oxygen has not penetrated into the ~25 Åiron film to form a stoichiometric oxide.

Further studies of iron oxidation, and its interaction with H_2S are in progress.



Investigation of self assembled monolayers using x-ray absorption spectroscopy	U1A

B. M. DeKoven, D. A. Fischer (NIST), M. Chaudhury (Lehigh Univ.), J. Curphy, and T. Chritz (all other from the Dow Chemical Company)

Self assembled monolayers (SAMs) are materials that can effectively be used to chemically modify oxide and metal surfaces and hence control their subsequent interfacial interactions. The chemical and molecular specificity of NEXAFS makes it a unique method for examining the film interface formed between the SAM and its environment. This technique is particularly sensitive to the nature of carbon bonding and molecular bond / chain orientation.

In order to understand the fundamental interactions between the monolayer chains, we have examined films of hexadecylsiline $(O_3)Si(CH_2)_{15}CH_3$ on silicon oxide surfaces as a function of relative surface coverage. As shown in Figure 1 we have found that the surface structure chain orientation obtained from the polarization anisotropy of the electron yield NEXAFS correlates directly with the degree of surface wettability obtained from advancing contact angles of water and hexadecane (not shown) liquid drops. This clearly demonstrates for the first time a direct correlation of surface structure / order with a macroscopic probe of wettability. By using NEXAFS polarization difference spectra shown in Figure 2, the C_{16} chains are oriented at 14°, 44°, and 57° w.r.t. the surface normal for the relative coverages of 1.0, 0.62, and 0.38, respectively. This shows for the first time that the differences in wettability are directly related to significant differences in the structure of the film.

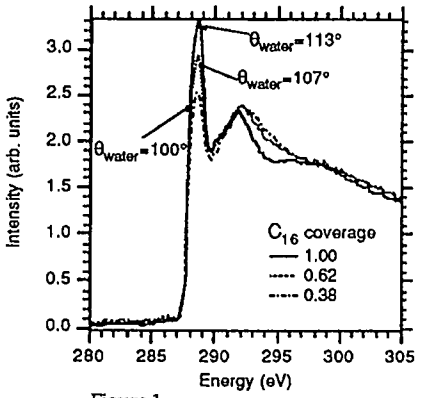


Figure 1.

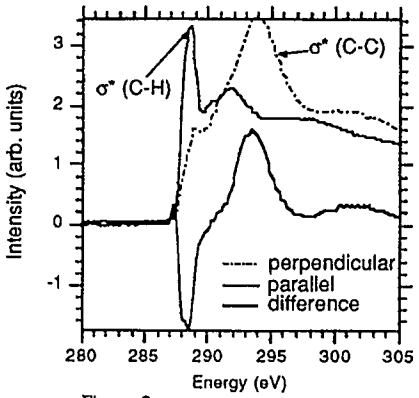


Figure 2.

Observing bond chemistry at the buried metal / benzocyclobutene (BCB) polymer interface using NEXAFS	U1A

B. M. DeKoven (Dow), D. A. Fischer (NIST), D. H. Paker, J. J. Curphy, G. E. Mitchell (Dow), J. L. Gland (Univ. of Michigan), C. A. Wedelstaedt, S. J. Babinec (Dow)

Benzocyclobutene (BCB) polymers are used for dielectric layers in new generation multilayer interconnect devices (multichip modules). In this metal/polymer application it is important to understand the nature of the bonding and complexing which occurs at the metal/polymer interface in order to optimize adhesion. The depth sensitivity (~200 nm) and the nondestructive nature of our fluorescence yield NEXAFS technique are particularly useful in studying the buried metal / BCB interface.

We have observed the relative chemistry of polymer functional groups in several buried metal [Al, Ti, Cu, and Au (10-100 nm thick)] / BCB polymer interfaces using the bond specific carbon K fluorescence yield NEXAFS. NEXAFS spectra in Figure 1 shows an observed decrease in aromatic content at the Ti buried interface perhaps due to bond formation / complexing via donation of electrons from metal d-orbitals to π^* orbitals in BCB.

In Figure 2 the aromatic content of BCB appears to undergo a dramatic change after the formation of the metal polymer interface for Au, Al, Ti, and Cu overlayers compared to free standing BCB surfaces. These preliminary results highlight the use of fluorescence yield NEXAFS as a probe of chemical structure at buried interfaces.

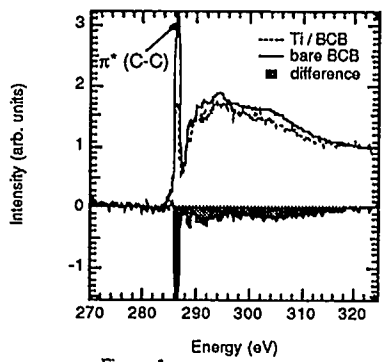


Figure 1.

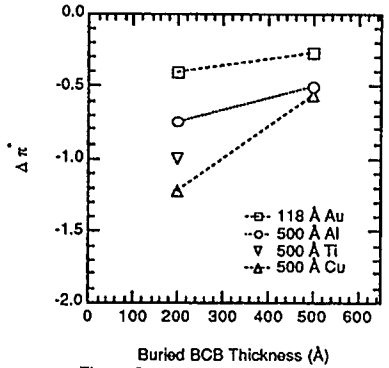


Figure 2.

Orientation studies of copper benzotriazole at the carbon, nitrogen, oxygen and copper K-edges using polarised, ultra-soft NEXAFS spectroscopy	U1A

E. S. Ferrari, J. Johnstone, C. A. E. Peacock, K. J. Roberts (Univ. of Strathclyde, Glasgow, UK), and B. D. DeVries (Exxon)

Benzotriazole has been established as a corrosion inhibitor for copper and copper alloys for many years to prevent tarnishing in the packaging, storage and transport industries, and as an additive in antifreezes, detergents, lubricants etc. However, the mechanism by which it operates and the interfacial chemistry involved has been the subject of continuing debate.

Thin films, of various thicknesses, of copper and silver were deposited by thermal evaporation onto float glass substrates. These samples were then immersed in a solution of benzotriazole such that the benzotriazole molecules should bond, in an ordered fashion on the surface of the copper. Samples were also prepared in solutions of indazole, indole, methyl benzotriazole and benzimidazole for comparison.

In order to determine the orientation and bonding of the benzotriazole molecule on a copper substrate, the oxidation state of the copper and the involvement of the copper oxide layer the samples were scanned at the carbon, nitrogen and oxygen K-edges and at the Copper L_3 and L_2 edges as appropriate. Electron yield detection was used and the angle of incidence of the X-ray beam was varied from glancing (10°) to normal (90°) incidence in order to determine the orientations of the bonds.

The carbon and nitrogen data will be used to determine the ring orientations of the benzotriazole, the copper and nitrogen data may indicate the nature of the bonding between sample and substrate, and the oxygen data will help to identify the role of copper oxide in the bonding and therefore, in the inhibition of corrosion of copper.

An investigation into the orientations and surface melting characteristics of thin films of n-alkanes on Si (111) using synchrotron, polarised, ultra-soft NEXAFS spectroscopy	U1A

E. S. Ferrari, J. Johnstone, K. J. Roberts (Univ. of Strathclyde, Glasgow, UK), and B. D. DeVries (Exxon)

The n-alkanes, form the basis of many more complex materials and thus can be used as simple models for e.g. oils, lipids, surfactants, etc. The molecular orientations of such molecules at interfaces is of particular importance, however, due to experimental difficulties, this is an area which has been poorly studied. It has been suggested that thin films of n-alkanes evaporated onto certain substrates exhibit a change in molecular orientation from lateral to normal upon annealing. NEXAFS spectroscopy can be used to examine the orientations of molecules containing low atomic number elements at surfaces. The aim of our experiments was to determine the precise orientations of a series of n-alkanes using polarised, ultra-soft synchrotron NEXAFS spectroscopy.

Thin films of a series of n-alkanes oriented onto silicon (111) substrates were scanned at the carbon K-edge. Orientation scans were obtained by varying the angle of x-ray incidence from glancing incidence (10°) to normal incidence (90°) in increments of 10°. By this means, it is possible to estimate the tilt angle of the alkane with respect to the substrate. Data for the shorter chain alkanes (C_{22} and C_{24}), which evaporate under the usual vacuum conditions, were obtained by backfilling the sample chamber with Krypton gas. From the tilt angles obtained there from, it will be possible to associate the n-alkanes with a crystalline structure.

Temperature studies were carried out on the longer n-alkanes to observe their surface melting characteristics. The temperature was raised in small increments through the melting point and then lowered to room temperature. The samples were observed in both electron yield and fluorescence yield modes. The electron yield method is sensitive to the topmost layers of the sample (about 2Å), while fluorescence yield, due to the deeper escape depth of the photons, can probe to a depth of about 2000Å, and hence for our purpose is a "bulk" technique. Comparison of the two sets of data shows that, for the chain lengths C_{46} and over, surface melting occurs a few degrees above the bulk melting point and reorientation occurs on cooling, while for the shorter alkanes, surface and bulk melting occurs simultaneously and no reorientation is observed.

In Situ x-ray absorption of diamond (100) surface modified by low energy neon ions *	U1A

Liji Huang, Igor Bello, and Leo W.M. Lau (UWO, Canada); S.-Tong Lee (Kodak); PaulA. Stevens, and Brian D. DeVries

In situ x-ray absorption near-edge structure (XANES) spectroscopy of the surface defect structure of diamond (100) surfaces modified by 500 eV neon ion bombardment and by subsequent vacuum annealing were performed at the Exxon Beamline U-1A. Extended x-ray absorption fine structure using 250 to 800 eV synchrotron radiation, low energy electron diffraction and *ex situ* x-ray photoemission spectroscopy (XPS) were also used to measure the near surface defect structure. The grating monochromator was calibrated against the graphit C $1s \rightarrow \pi^*$ transition (285.4 eV). The energy resolution at 290 eV was about 0.1 eV. Significant changes in the XANES spectra were identified for the defects induced by ion bombardment and subsequent annealing. The diamond discrete exciton absorption at 289.0 eV was clearly suppressed even at the lowest ion fluence used in this study, i.e., $3\times10^{14}/cm^2$, and no such exciton could be observed after the surface was bombarded to an ion fluence of $7\times10^{14}/cm^2$. However, the changes in the multi-maxima shape-resonance absorption structure in the range of 290 to 310 eV indicated that a loss of the diamond long range order required a fluence of $1\times10^{15}/\mathrm{cm}^2$. The structural changes were also manifested by the transformation of gap state absorption typical of clean (2×1) surfaces to the π^* absorption typical of amorphous carbon. XPS showed that the defective layer was about 2 nm thick. Both the XANES and XPS data also indicated that phase transformation from defective layers to graphite was not dominated in the present study even after annealing to a temperature of 1100°C.

1. L.J. Huang, I. Bello, W.M. Lau, S.T. Lee, P.A. Stevens, and B.D. Devries, J. Appl. Phys. 76, 7483(1994).

* This work is supported by Canadian Natural Science and Engineering Council and Exxon Research and Engineering Company.

NEXAFS study of the mechanism of the CH_3I + C_6F_5 / Cu(100) reaction to form toluene	U1A

P. W. Kash, M. X. Yang, D.-H. Sun, J. Eng Jr., G. W. Flynn, and B. E. Bent (Columbia Univ.)

Previous studies of the reaction of CH_3I co-adsorbed with phenyl groups on Cu(100), which find that methyl plus phenyl coupling to form toluene occurs below 160 K near the CH_3-I bond dissociation temperature, suggest a reaction mechanism involving CH_3 radicals which have not accommodated with or bonded to the Cu surface. Unambiguous proof of this radical mechanism, however, requires demonstrating that the C-I bond in isolated CH_3I on Cu(100) dissociates at the same temperature as the C-I bond in CH_3I, which is co-adsorbed with phenyl groups on Cu(100). We have utilized carbon K edge near edge X-ray absorption fine structure spectroscopy measurements, as a function of Cu surface temperature, to precisely determine the CH_3-I dissociation temperature under these two conditions.

Fig. 1 below shows the NEXAFS spectrum obtained after CH_3I is co-adsorbed with C_6F_5 groups at 105 K on Cu(100). The spectrum shows that the $n(C_{1s})\rightarrow \sigma^*$(C-I) transition at 286 eV is easily resolved from the $n(C-1s) \rightarrow \pi^*$(C-C) transition at 288 eV.

Fig. 2 below shows the intensity of the $n(C_{1s}) \rightarrow \sigma^*$(C-I) transition in the NEXAFS spectrum obtained after CH_3I and co-adsorbed C_6F_5 groups on Cu(100) are annealed to the temperature indicated on the x axis. In addition, fig. 2 also overlays the $n(C_{1s}) \rightarrow \sigma^*$(C-I) transition intensity in the NEXAFS spectrum obtained after isolated CH_3I adsorbed on Cu(100) is annealed to the indicated temperature. The $n(C_{1s})\rightarrow \sigma^*$(C-I) transition intensity is directly proportional to the coverage of undissociated CH_3I molecules on the surface. The decrease in the $n(C_{1s}) \rightarrow \sigma^*(C-I)$ transition intensity as the surface is annealed to successively higher temperatures results from dissociation of the CH_3-I bonds. As fig. 2 demonstrates, the C-I bond dissociation temperature in CH_3I co-adsorbed with C_6F_5 groups is identical within experimental uncertainty to the C-I bond dissociation temperature when CH_3I alone is adsorbed on Cu(100). These identical C-I bond dissociation temperatures indicate that the presence of co-adsorbed phenyl groups does not perturb the CH_3-I bond dissociation kinetics. In addition, these results confirm that the reaction of co-adsorbed CH3I and phenyl groups on Cu(100) to produce toluene occurs by a mechanism involving CH3 radicals, produced in CH_3-I bond dissociation, which have not accommodated to the Cu surface.

Fig. 1

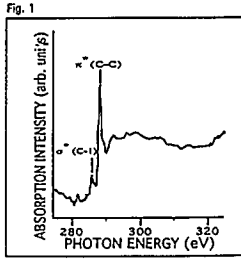
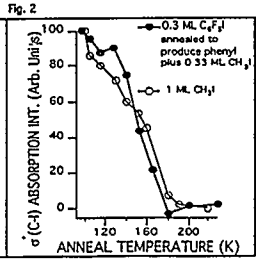


Fig. 2



A NEXAFS study of degradation of vinyl halides on Cu(100) | U1A

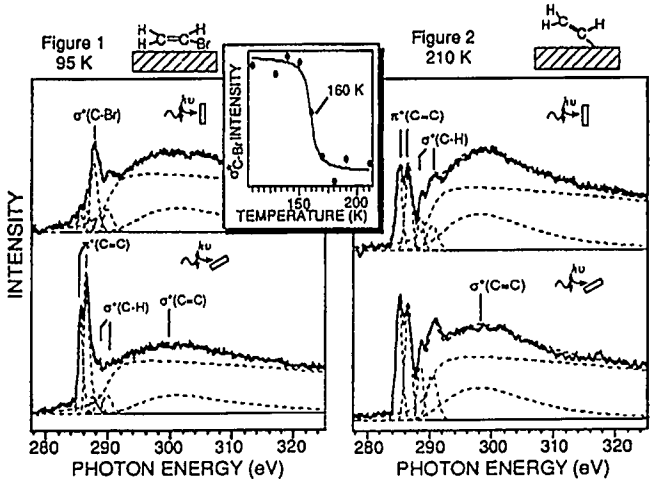
M. X. Yang, P. W. Kash, J. Eng, Jr., and B. E. Bent (Columbia Univ.)

Halogenated hydrocarbons are hazardous to both the environment and the human health. A search for their efficient degradation is therefore of paramount importance. The system under investigation is the decomposition of vinyl bromide (C_2H_3Br) on copper surfaces. Previous studies have shown that vinyl bromide dissociates at low temperatures on copper surfaces to produce 1,3-butadiene, which is liberated from the surface at ~250 K. We have performed near carbon K-edge X-ray absorption fine structure measurements (NEXAFS) to probe the electronic structure and binding geometry of the parent molecule (C_2H_3Br), to monitor its dissociation kinetics and to identify the surface intermediate in the dehalogenation process.

Figure 1 presents the NEXAFS spectra obtained after ~0.8 monolayer of C_2H_3Br is adsorbed on Cu(100) at 95 K. The observation of the $n(C_{1s})\rightarrow\sigma^*(C\text{-}Br)$ transition indicates that the molecule remains intact on the surface at 95 K. Two $n(C_{1s})\rightarrow\pi^*(C{=}C)$ resonances are observed, reflecting a carbon 1s energy level shift caused by the presence of the bromine atom. The polarization dependence of $n(C_{1s})\rightarrow\pi^*(C{=}C)$ and $n(C_{1s})\rightarrow\sigma^*(C\text{-}Br)$ resonances indicates that the C=C bond of the molecule is parallel to the surface.

Figure 2 presents the NEXAFS spectra obtained after annealing a 0.8 monolayer of C_2H_3Br on Cu(100) to 210 K. The disappearance of $n(C_{1s})\rightarrow\sigma^*(C\text{-}Br)$ transition indicates that the C–Br bond has dissociated by this temperature. The surface intermediate is assigned to vinyl group (C_2H_3-), which has its C=C bond significantly tilted away from the surface.

The kinetics of C–Br bond dissociation was studied by monitoring $n(C_{1s})\rightarrow\sigma^*(C\text{-}Br)$ resonance as a function of surface temperature with the incident light propagating from surface normal. The results, which are shown in the inset, indicate a C–Br bond dissociation temperature of ~160 K.



Asphaltene adsorption on kaolinite: characterization by infrared microscopy * | U2B

J.-L. Bantignies, C. Cartier dit Moulin, H. Dexpert, A.-M. Flank (LURE UniversitéParis-Sud, France), and G. P. Williams (NSLS)

An improved knowledge of rock wettability is of primary importance in estimating the amount of crude oil in underground resources. The Institut Francais du Pétrole has observed that the trapping of oils in sedimentary rocks is largely correllated to the presence of kaolinite clays in the intergranular space of the rocks. FTIR microscopy of the hydroxyl group vibrational region from 3550 to 3750 cm^{-1} and from 900 to 1000 cm^{-1} was carried out on a kaolinite (Ploemur, France) before and after contact with asphaltene (Safaniya, Saudi Arabia). The measurements, when combined with XAFS data, show that oil modifies the local environment of the aluminum in this material and more precisely the Al-OH linkage. For the measurements a 10 μm beam size was used.

At the top (of the figure) we show the structure of kaolinite which is composed of a tetrahedral(SiO_4)and an octahedral sheet (AlO_6). Below we show transmission spectra of the O-H stretching region before and after contact with asphaltene. The relative intensities of the bands indicate high crystallinity. Strong modifications to the 3700 cm^{-1} surface band both in terms of its strength and position show that the asphaltenes act on the surface OH. The decrease in intensity is possibly due to a re-orientation of the dipole. Additional work on other bands supports this conclusion.

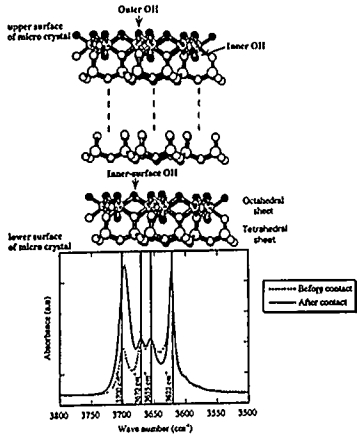


Figure 1.

* We are extremely grateful to Larry Carr, Grumman Corporation, and John Reffner of Spectra-Tech for invaluableassistance and the loan of equipment. The NSLS is supported by the U.S. DOE under contract DE-AC02-76CH00016.

Infrared microspectroscopy study of oxygen defects in silicon * — U2B

G. L. Carr (Grumman Aerospace Electronics)

During the summer of 1994, an infrared microspectrometer system was adapted to the midinfrared beamline at port U2B, and a program of test measurements was begun to quantify the performance advantages of the infrared synchrotron source. The microspectrometer system proved capable of diffraction-limited performance, resolving material variations less than 10 microns apart. One of the proposed applications of the U2B infrared microspectrometer is the analysis of defects in semiconductor electronic materials. An important case is silicon, for which oxygen is an impurity that adversely affects electronic device performance. Like many low mass impurities, the presence of oxygen can be distinguished through two infrared features. One is an absorption near $\lambda = 9\mu$m (1100 cm^{-1}), that is due to the vibration of oxygen atoms occupying interstitial sites. The other occurs near $\lambda = 8\mu$m (1250cm^{-1}), caused by oxygen bonded to silicon; i.e., an oxide. Infrared spectroscopy is therefore capable of locating the presence of oxygen, and differentiating interstitials from oxide precipitates. To illustrate this, scanning infrared microspectroscopy was performed on a silicon wafer region measuring 500 μm long by 300 μm wide, in 25 μm steps. The spatial variations of the absorbance at three wavelengths are shown in the figures below, with darker regions corresponding to greater absorption. Figure 1 represents the overall (non-wavelength specific) absorbance, presumably due to a mechanical defect within the wafer situated primarily near the point (0,0). Figure 2 is an absorbance map for the oxygen interstitials (9 μm) and figure 3 shows the distribution of oxides (8 μm). The absorbance maps demonstrate the ability of scanning infrared microspectroscopy to spatially locate two types of oxygen impurities.

Fig. 1

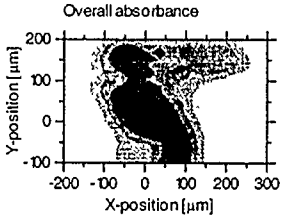


Fig. 2

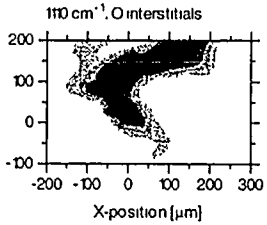
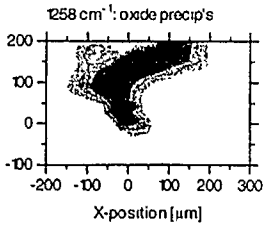


Fig. 3



* Grumman research supported by IR&D funds. The NSLS is funded by DOE through contract DE-AC02-76CH00016.

Nanosecond time resolved far-infrared spectroscopy of photocarriers in GaAs * — U4IR

G. L. Carr (Grumman Aerospace + Electronics, R and D Center)

The relaxation of photoexcited electrons and holes in GaAs was investigated by nanosecond time-resolved, far-infrared spectroscopy. A pump-probe spectroscopic technique was employed, making use of a GaAs/$Al_{1-x}Ga_xAs$ pulsed laser diode synchronized to the NSLS VUV ring's far-infrared pulses. Far-infrared spectroscopy can sense both electrons and holes through their free carrier (intraband)absorption, which appears as an absorption peak at zero frequency with a width determined by phonon scattering. Figure 1 (below) shows the measured (symbols) photo-induced absorption at selected times following the excitation pulse, along with fits to free carrier absorption (solid curves). The data is presented as $-\Delta T/T$, following photo-induced spectroscopy convention. The fit results are presented in figure 2, indicating a rapid decay in photoconductivity during the first 10 ns, followed by a much slower decay component. Simultaneously, the effective carrier scattering rate increases from 25 cm^{-1} to 50 cm^{-1}. Noting that these values are in agreement with the scattering of electrons and holes (respectively) from phonons, one concludes that the electron lifetime is approximately 10 ns whereas the hole lifetime is about an order of magnitude longer. This may be due to surface states that are more effective in trapping electrons.

Fig. 1

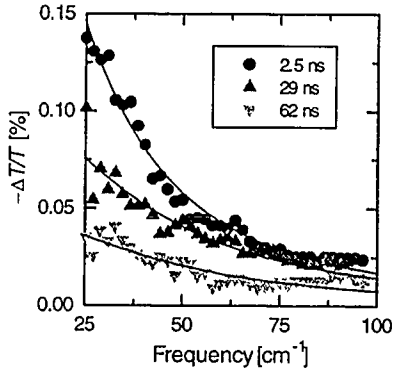
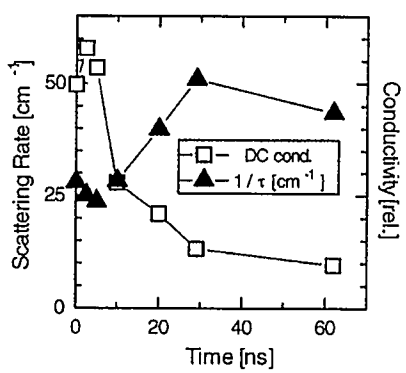


Fig. 2



* Grumman research supported by IR&D funds. The NSLS is funded by DOE through contract DE-AC02-76CH00016.

Adsorbate-substrate motion and broadband reflectance change for oxygen adsorbed on Cu(100) *	U4IR

P. Dumas (LURE and LASIR-Orsay-France), K. Lin, R. G. Tobin (Michigan State Univ.), and G. P. Williams (NSLS)

We report the first infra-red observation of the vibrational mode of an atom, other than hydrogen, on a metal surface. The system measured was oxygen on Cu(100). The Cu-atomic oxygen stretch mode has been reported for this system by M. Wuttig, R. Franchy, and H. Ibach (Surf. Sci. 213, 103, 1989) using HREELS. The present IR work represents an improvement over previous IR work on this system by K. Lin, R.G. Tobin, P. Dumas, C.J. Hirschmugl, and G.P. Williams, Phys. Rev. B48, 2791, 1993. The signal to noise available at the U4IR beamline has recently been greatly improved by the installation of a Nicolet Impact 400 interferometer. The same instrument also allows the frequency range to be extended down to about 40 cm^{-1}. The figure below shows co-added reflectance spectra from 4 separate runs, ratioed to the spectra for clean Cu. One clearly sees the (previously reported) background change upon adsorption of oxygen at room temperature, but with the extended low frequency data one can get a better estimate of the reflectivity change at zero frequency which is critical to the theoretical understanding (B.N.J. Persson, private comm.). From the present data we estimate this value to be 100±0.05.

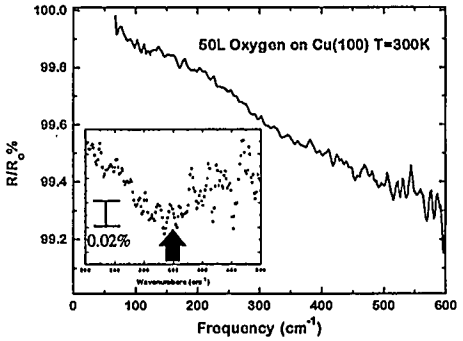


Figure 1. In the inset we show the effect of subtracting the background change from the data. The Cu-O stretch mode is then clearly seen. The large width of the band (FWHM=70-80 cm^{-1}), and the low strength of the mode, yielding a reflectance change of only ~0.04%, makes it clear why it was not observed previously when the noise was a factor of 5 higher. The width is probably attributable to inhomogeneities, although one cannot rule out the possibility of the feature being composed of 2 bands at 340 cm-

* The NSLS is supported by the US DOE under contract DE-AC02-76CH00016. We thank the NSF/CNRS for a collaborative award INT- 9016771.

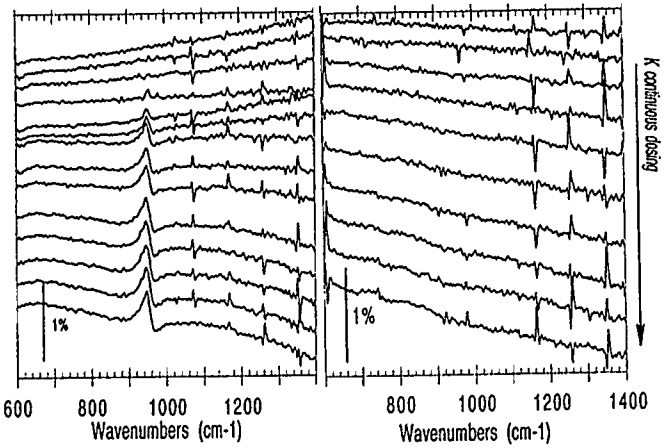
Observation of a charge density wave for K on Ag(111) *	U4IR

P. Dumas (LURE and LASIR-Orsay, France), P. Rudolf (LISE, Belgium), F. M. Hoffmann(Exxon), and G. P. Williams (NSLS)

We have previously reported antiabsorption resonances for K and Na on Cu(111) [1] measured with reflection-absorption infrared spectroscopy. We now report similar antiabsorption resonant behavior for K on Ag(111). In the case of Ag(111) the resonance occurs at a slightly higher energy (950 cm^{-1} than the 850 cm^{-1} value obtained on the Cu(111) surface. The measurements were made at grazing incidence from sputtered and annealed Ag surfaces in ultra-high vacuum. The conditions for the experiment were identical to those described in Ref. 1.

The left side of the figure shows the evolution of the 950 cm−1 antiabsorption resonance with K coverage for a mechanically polished Ag(111) surface. Here we have plotted the change in the reflectivity caused by the addition of the alkali, and have offset successive spectra for clarity. The fact that the charge density wave requires pinning sites due to surface defects is demonstrated by the absence of the resonance on the chemically etched surface shown on the right. The sharper spikes in the data are an artifact due to 60 Hz sidebands on the synchrotron r-f system and can be identified by changing the mirror velocity in the rapid-scan Michelson interferometer.

[1] F.M. Hoffmann, B.N.J. Persson, W. Walter, D.A. King, C.J. Hirschmugl and G.P. Williams, Phs. Rev. Letts. 72, 1256(1994).



* The NSLS is supported by the U.S. DOE under contract DE-AC02-76CH00016. We thank the NSF/CNRS for a collaborative award INT-9016771.

Far-IR mixed isotope feasibility study for CO/Cu(111) * | U4IR

C. J. Hirschmugl and G. P. Williams (NSLS)

Molecules adsorbed on surfaces will interact both with each other and with the substrate, resulting in frequency shifts of the vibrational modes. These shifts can be caused by dipole-dipole coupling and also to changes in bonding with the surface. The use of mixed isotopes allows these 2 terms to be separated. For example there will be no intermolecular dipolar coupling for a different isotope diluted in a matrix of natural CO. Such studies have been made for intra-molecular modes, but not for bonding modes, with the exception of hydrogen. The bonding modes are in the mid to far IR. The present study was made for mixtures of natural CO and $^{13}C^{18}O$.

In the figure we show grazing incidence reflectivity spectra for CO and various mixtures of CO and $^{13}C^{18}O$ on a clean Cu(111) surface. For all the spectra shown the ratios to the clean surface are shown, highlighting the changes induced by the adsorbates. It can be seen that indeed the signal to noise is sufficiently good to resolve 4 modes when they occur. The spectra were taken at 1 cm-1 resolution in less than 2 minutes each. Thus we can analyze the frequency shifts and determine both the chemical and the dipole-dipole coupling terms for this system for comparison with theoretical calculations. Further details of the experiment are discussed in C.J. Hirschmugl, Y.J. Chabal, F.M. Hoffmann and G.P. Williams, J. Vac. Sci. Technol. A12 2229 (1994).

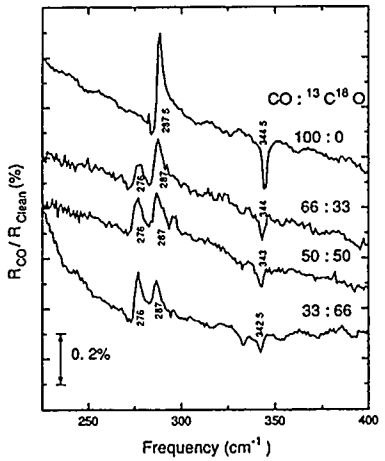


Figure 1. Frequency (cm^{-1})

* We thank G. Nintzel, D. Carlson and T. Lenhard for technical assistance. The sample holder was made by Ed Chaban. The NSLS is supported by the U.S. DOE under contract DE-AC02-76CH00016.

Investigation of the superconducting energy gap in Rb_3C_{60} | U4IR

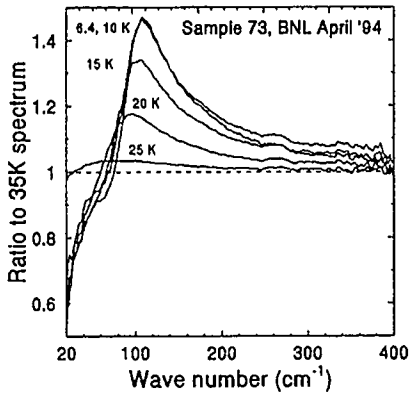
Dan Koller, Michael C. Martin, and Laszlo Mihaly (SUNY Stony Brook)

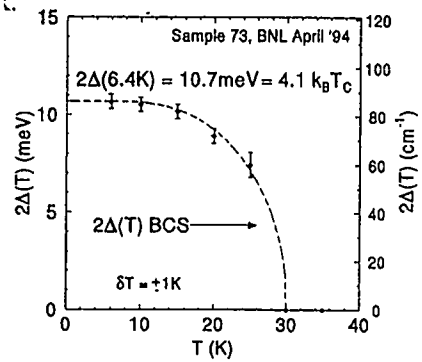
The superconducting energy gap of doped fullerenes [1] with composition A_3C_{60} (A: alkali metal) has been studied by tunneling [2], optical transmission [3], and reflectivity [4] measurements. The absence of general agreement between these works calls for further investigations. Here we report the preliminary results of IR transmission studies performed on thin film samples of Rb_3C_{60}. The samples were made and characterized at Stony Brook [5,6].

Doped C_{60} films of about 1 μm thickness were prepared in a sealed environment [5] on Si substrates. The sample chamber was mounted on a He-flow refrigerator, and the temperature dependence of the transmission was recorded. Figure 1 shows the results below the superconducting transition temperature. The transmission curves are normalilzed to the normal state transmission obtained at 30K.

Figure 2 shows the temperature dependence of the gap, evaluated by fitting a modified BCS conductivity to the measurements. Note that the critical temperature is not a fitting parameter, but it was independently determined from the resistivity of the same film. For good quality fits we had to assume that a significant fraction of the film stays in the normal state. Apparently, the samples were not homogeneously doped. The results unambiguously indicate the presence of the superconducting gap with $2\Delta/k_BT_c = 4.1 \pm 0.3$. This observation is in sharp contrast with measurements on high temperature superconductors [7] (also done at U4IR), where the IR signature of the s-wave gap was notoriously absent.

[1] A.F. Hebard et al. Nature, 350, 600 (1992).
[2] Z. Zhang et al. Nature, 353, 333 (1991).
[3] S.A. FitzGerald et al. Phys. Rev. B 45, 10165 (1992).
[4] L. Degiorgi et al., Phys. Rev. Letters, 69, 2987 (1992).
[5] D. Koller et al. Rev. Sci. Instrum. 65, 760(1994).
[6] Dan Koller, Ph.D. Thesis Stony Brook, 1994.
[7] L. Forro et al. Phys. Rev. Lett. 65, 1941 (1990).



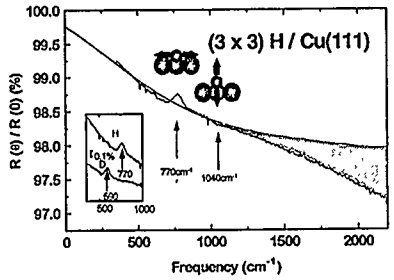


Dynamics of atomic adsorbates: - hydrogen on Cu(111) * | U4IR

C. L. A. Lamont (Univ. of Huddersfield, UK), B. N. J. Persson (Inst. fur Festkörperforschung, Germany), and G. P. Williams (NSLS)

Low frequency dynamics at surfaces, particularly in the region of adsorbate-substrate vibrational modes is of fundamental importance in areas as varied as sliding fraction, catalysis, corrosion and epitaxial growth. We have measured the absolute changes induced in the far infrared reflectivity by H and D atoms adsorbed on Cu(111). For this system no surface reconstruction occurs and an ordered (3 x 3) structure is formed at saturation coverage. The H atoms were previously thought to occupy two-fold bridge sites[1]. The present work, however, shows that all of the H atoms occupy 3-fold hollow sites. The strongest features in the spectra are the dipole forbidden parallel vibrational modes which give rise to anti-absorption peaks with an intensity almost 10 times higher than that of the dipole allowed perpendicular modes. The dynamics can be explained by excitation of electron-hole pairs in the substrate[2]. The energy relaxation of the parallel vibration is 1 ps, but the linewidth is larger by a factor of 10 probably due to lateral tunneling of the adsorbates. The infrared measurements were made at a grazing incidence angle of 87° with an f/10 incident beam and are shown below. In all cases the reflectivity of the H or D covered surface was ratioed to that of the clean surface, the dosing being done in situ. The measuring time for each spectrum was 80 seconds. The smooth curve is a calculation and the shaded area shows the discrepancy between theory and expt. at higher freqs. but the agreement is good at lower freqs. We have indicated on the plot the position of the 60 cm^{-1} wide perpendicular vibrational mode at 1040 cm^{-1} reported by McCash et al.[1] This mode has a peak absorption of only 0.02% and therefore is just on the detection limit of the present measurements, as U4IR is really optimized for the region below 800 cm^{-1}. In the inset we show the corresponding spectrum from D atoms which also show a similar broadband absorption an an anti-absorption peak at 590 cm^{-1}.

[1] E.M. McCash, S.F. Parker, J. Pritchard and M.A. Chester, Surface Science 215 363 (1989); [2] B.N.J. Persson, Phys. Rev. B44 3277 (1991); B.N.J. Persson and A.I. Volokitin, Surface Science 310 314 (1994).



* We thank G. Nintzel, D. Carlson and T. Lenhard for technical assistance. The sample holder was made by Ed Chaban. The NSLS is supported by the U.S. DOE under contract DE-AC02-CH7600016.

Synchrotron infrared spectroscopy and phase diagram of hydrogen at high pressure | U2B

M. Ming Li, A. F. Goncharov, R. J. Hemley, and H. K. Mao (Carnegie Inst. of Washington)

We have investigated infrared absorption spectra of solid molecular hydrogen as a function of temperature from 85 to 295 K to a pressure of 170 GPa. Pure vibron, vibron-roton, and vibron-phonon bands have been studied. The experimental results reveal two phases (II and III) in solid hydrogen under pressure.[1] At ~ 110 GPa and 80 K, a new sharp vibron (v2) has been observed in addition to the broader vibron (v1) similar to that in phase I.[2] The appearance of the sharp vibron is diagnostic of the transition to phase II. Figure 1 shows the temperature behavior of the two vibrons. The intensity of v2 decreases with increasing temperature and diminishes at the I-II phase boundary. However, the intensity of v1 increases with increasing temperature within phase II, and it shows small negative temperature dependence after hydrogen enters phase I. By studying the two vibrons as functions of pressure and temperature, we have been able to map out the I-II phase boundary. Above 150 GPa, a dramatic increase in oscillator strength of the vibron is observed.[2] This change is the characteristic feature of phase III and is indicative of charge transfer in the molecular solid. Figure 2 shows the newly determined I-II phase boundary and phase line of III. The I-II phase boundary has small positive slope, it intercepts phase III boundary forming a triple point.

[1] H.K. Mao and R.J. Hemley, Rev. Mod. Phys. 66, 671 (1994)
[2] M. Hanfland, R.J. Hemley, and H.K. Mao, Phys. Rev. Lett. 70, 3760 (1993).

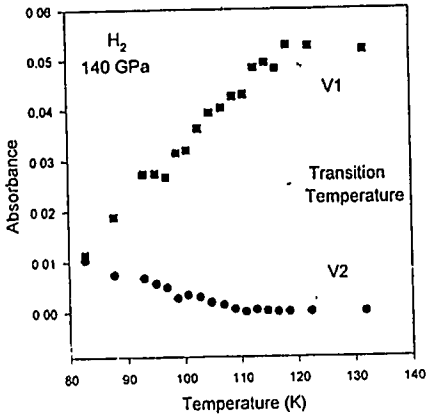


Figure 1. Temperature dependence of sharp vibron and broad vibron at 140 GPa

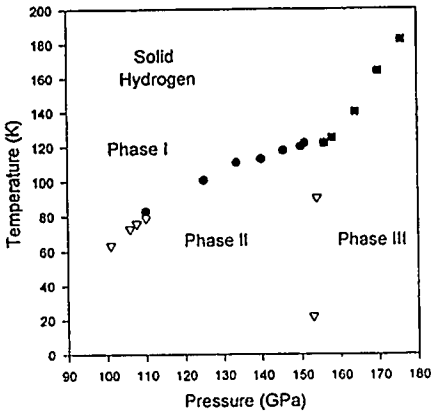


Figure 2. Phase diagram of solid hydrogen. Open triangles represent data obtained from Raman measurements.

"In situ" synchrotron infrared spectroscopy of the electrochemical interface *	U4IR

C. A. Melendres (ANL), B. Beden (Univ. de Poitiers, France), and G. A. Bowmaker (Univ. of Auckland, New Zealand)

The objective of this program is to elucidate the structure of the electrode/solution interface, as well as those of electrochemically formed surface films and absorbed layers. Far infrared measurements were carried out "in situ" in 0.5 M $HClO_4$ in order to examine the adsorption of CO and SCN^- on a platinum electrode as a function of applied electrical potential. While we have been unable to observe the Pt-CO vibration as yet, we found that the anodic oxidation of Pt leads to a surface species which is best described as $Pt(OH)_4$. The far IR spectra measured are shown in Fig. 1. The broad band at about 370 cm^{-1} is assigned to the hydroxylated species and is consistent with published mid IR data. The adsorption of SCN^- on Pt. in 0.1 M $NaClO_4$ has also been detected and manifests itself by the appearance of bands at about 250 and 480 cm^{-1}.

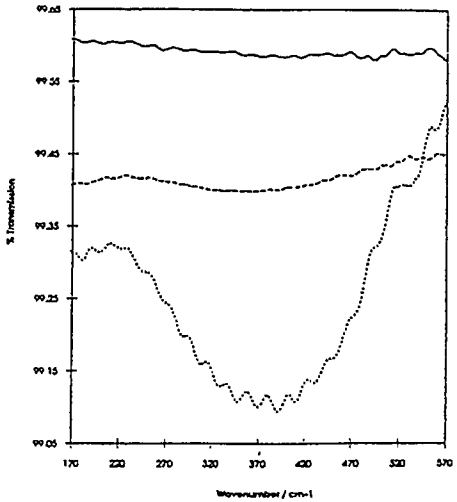


Figure 1. Far IR spectra of a Pt electrode in 0.5 M $HClO_4$ at various potentials(referenced to 0 V): (a) 0.45 V, (b) 1.20 V, (c) 1.20 V following a brief excursion to 1.65V.

* Work supported by the Division of Materials Science, Office of Basic Energy Sciences, U.S. Department of Energy under contract W-31-109-ENG-38.

Charge transfer and electron-phonon couplings for C_6O deposited on clean and alkali covered Ag(111)	U4IR

P. Rudolf (LISE-Namur, Belgium), P. Dumas (LURE and LASIR, Orsay, France), L. Struck, Y. J. Chabal (AT&T Bell Labs.), and G. P. Williams (NSLS)

We report synchrotron infrared spectroscopy of fullerenes adsorbed on clean and alkali covered Ag(111). Fig. 1 shows 2 frequency regions for C_{60}/Ag(111) for increasing coverage up to 1 monolayer. Plotted are the grazing incidence reflectivity changes induced by the adsorbate. The lower frequency mode, the t1u mode corresponds to a vibration in which the pentagons are more deformed than the hexagons, it should therefore stiffen with charge transfer [1]. This is exactly what one sees in Fig. 1 where the mode is stiffer for low coverages than for the higher ones. In fact, C_{60} is known to decorate the steps in the initial phase of adsorption on Ag(111) [2], that is to bind to atoms which can transfer more charge to the molecule than the atoms on the flat terrace, and only later to fill up the terrace sites. The right panel in Fig. 1 shows instead the effect of symmetry breaking at the surface on the vibrational modes of the adsorbed C_{60}: a mode at 1440 cm^{-1} becomes dipole-active. This cannot be the 4th. t1u mode because it is at higher frequency than in bulk C60 while the 4th. t1u should soften with charge transfer. This new mode might be the ag Raman-active pentagonal pinch mode seen to become dipole-active at the surface of K_3C_{60} [3]. When C60 is deposited on 1 monolayer of K on Ag(111), markedly different infrared spectra are observed. Fig. 2 shows the high frequency region, where an anti-absorption band is detected at 1450cm^{-1}. This antiabsorption band originate from an electron-phonon coupling mechanism which involves excitations in the partly filled t1u*-derived band and the ag Raman mode of C_{60}. Similar observations have been made for C_{70}, adsorbed both on bare and K- or Rb-covered Ag(111).

[1] J. Kohanoff, W. Andreoni and M. Parinello, Chem. Phys. Lett. 198, 472 (1992)

[2] E.I. Altman and R.J. Colton, Surf. Sci. 295, 13 (1993)

[3] see for example T. Pichler, M. Matus and H. Kuzmany, Solid State Commun. 86, 221 (1993)

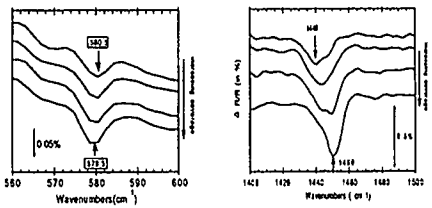


Figure 1.

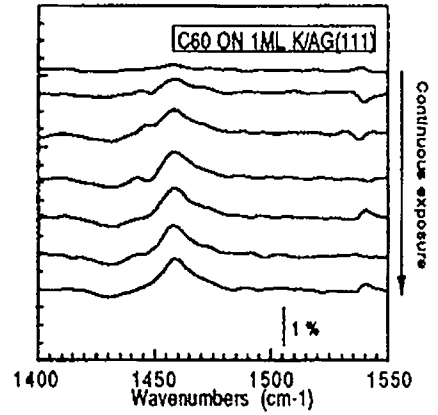


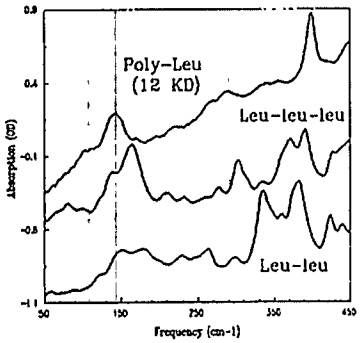
Figure 2.

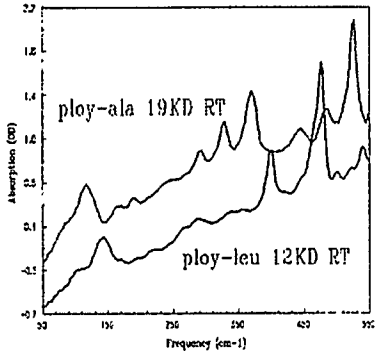
Using far-infrared synchrotron radiation to study collective motions of proteins * | U4IR

A. Xie, L. M. Miller, E. M. Scheuring, B. Sclavi, M. R. Chance (Albert Einstein-College of Medicine)

Recently, a number of theoretical and experimental interests have been focused onto how proteins use collective motions to carry out their biological functions, including electron tunneling in energy transduction, and proton transfers in enzyme reactions. To establish correlations between collective motions of proteins and their reactivities, we have studied far-infrared (FIR) absorption spectra of dried, hydrated, and deuterated purple membrane (pm) and met myoglobin (Mb) films, and a number of amino acid (aa) monomers and polymers. FIR spectra of dried pm and Mb are very different, while those of hydrated pm and Mb exhibit two similar bands at 164 and 230 cm^{-1}, related to water absorption. The number of bands in an aa polymer is much less than those in the corresponding monomer. Furthermore, no common bands were found between L-Leu and poly-L-Leu, and between L-Ala and poly-L-ALa from 50 to 400 cm^{-1}, indicating negligible contributions of side chain absorption to the observed FIR bands of these polymers. Also the observed bands from poly-L-Ala and poly-L-Leu are different (although the overall spectra are similar), suggesting none of them arising from localized motions of polypeptide backbone, but associated to collective motions of polymers.

These studies will provide insight into the nature of collective motions and their roles in protein reactivities.





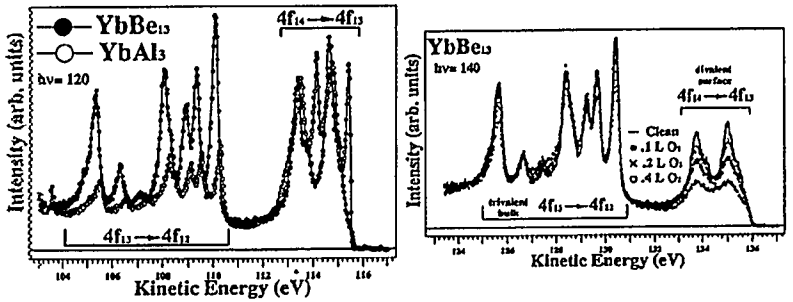
* This work is supported by NIH grants HL-45892 and the Regional Center for Time-Resolved X-Ray Spectroscopy under NIH grant RR-01633.

Different bulk and surface valences in $YbBe_{13}$ | U3C

A. B. Andrews, R. I. R. Blyth, J. J. Joyce, A. J. Arko, and Z. Fisk (LANL)

Many rare earth alloys exhibit surface induced valence changes which reflect the decrease in cohesive energy due to reduced coordination at the surface. Yb heavy fermion compounds typically exhibit anomalously broad divalent surface core levels[1], with energy shifts Δ_{sb}~-.82 eV from the bulk spin-orbit doublet (Fig. 1). We have conjectured that this is because the crystals do not fracture along a well defined plane but rather expose several low index faces. In the nearly trivalent intermetallic compound $YbBe_{13}$($NaZn_{13}$ structure with a = 10.195Å), we have established - by varying the escape depth ($h\nu$), comparing grazing and normal incidence and dosing with O_2 (Fig. 2) - that the surface core level shift is composed of at least two divalent $4f^{13}$ components from the first surface layer alone, with binding energies Δ_{s1}~0.54 and Δ_{s2}~0.91 eV. The relative weight of these two is highly cleave dependent. Thus the broad surface lineshape observed in other Yb compounds is most likely the result of a distribution of surface shifted levels within the first layer, and is due to faceting and surface roughness rather than subsurface emission. There is no detectable surface core level shift for the $4f^{12}$ multiplet, so we conclude that the surface layer is purely divalent.

[1] R.I.R. Blyth et al., PRB 48, 9497 (1993); E. Cho et al., PRB 47 (1993).

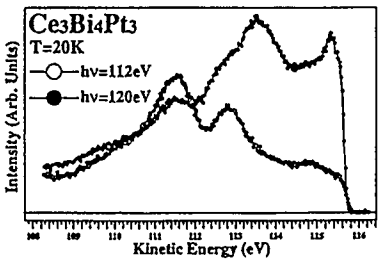


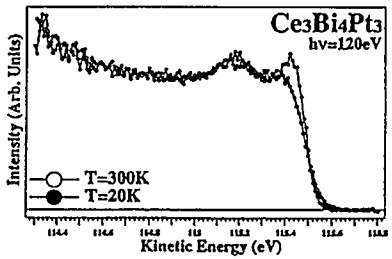
UPS and XAS study of the Kondo insulator $Ce_3Bi_4Pt_3$ | U3C

A. B. Andrews, J. J. Joyce (LANL), A. J. Arko (LANL), and P. C.Canfield (Ames Lab)

$Ce_3Bi_4Pt_3$ belongs to the class of recently discovered heavy fermion compounds known as Kondo insulators. Transport, optical conductivity and neutron scattering measurements all indicate gaps on the order of 100K or $\sim$ 10 meV comparable to a small gap semi-conductor [1], however at higher temperatures the properties are similar to metallic mixed-valent compounds, i.e., the susceptibility, thermal expansion and specific heat exhibit maxima at $\sim$ 80K corresponding to a Kondo temperature of $\sim$300K, and the resistivity increases with decreasing temperature. Band calculations predict a gap of $\sim$ 30 meV [2], but the energy gap in LDA is usually smaller than the measured one to inadequate treatment of the exchange-correlation potential. We made a direct measurement of the gap using high-resolution ARPES at the Ce 4d resonance of 120 eV and 90 meV resolution. We find a shift in the Fermi energy which corresponds to a gap size of 20 $\pm$5 meV, a value somewhat larger than obtained by other techniques. In view of our discovery of one electron effects in other heavy fermion systems, the larger than expected gap in our angle resolved measurements may reflect gap variations with momentum, although we cannot make that claim unambiguously. Since the LDA calculations predict a gap of this magnitude, it is also possible that the measured gap is not intrinsic, but is caused by extrinsic effects which pin the Fermi level closer to the top of the valence band.

[1] P.C. Canfield, et. al., J. Mag. Mag. Mat. 108, 217 (1992).
[2] K. Takegahara, et. al., J. Phys. Soc. Jap. 62, 2103, (1993).





ARUPS study of strongly mixed-valent $CeBe_{13}$ | U3C

A. B. Andrews, J. J. Joyce, A. J. Arko, and Z. Fisk (LANL)

$CeBe_{13}$ (cubic $NaZn_{13}$ structure, a = 5.1 Å), has a spin-fluctuation temperature T_K = 300K. In Fig. 1 single crystal EDC's taken at 10° and 15° show that the 4f states exhibit periodic amplitude modulations which can be produced by the Fermi level cutoff i.e., dispersion toward E_F ($\approx$ 30 meV). This is not observed in polycrystalline samples of $CeAl_3$ and $CeSi_2$, so it cannot be due to an artifact of our experimental method. We are convinced that it is not due to d- states at E_F, since these constitute <20% of the spectral weight of E_F with only broad (>0.5eV) features present which would not selectively affect the Fermi level peak. The temperature dependent energy shift (Fig. 2) is consistent with the estimated dispersion from the angular scans i.e., $\sim$30 meV, except an additional broadening of $\sim$50 meV in addition to the Fermi function is present which can be ascribed to phonons. In the single impurity model the Kondo temperature T_K is a thermodynamic quantity which has no k-dependence by construction (since to calculate the spectral weight requires integration over all conduction electrons). So one must consider instead a periodic lattice of impurities, for which the expected width of the states is $k_B T_K \sim$ 25 meV.

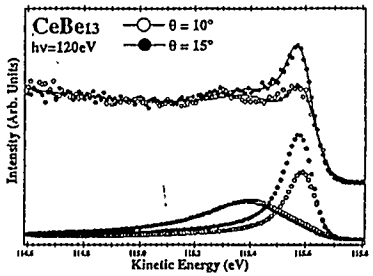


Figure 1.

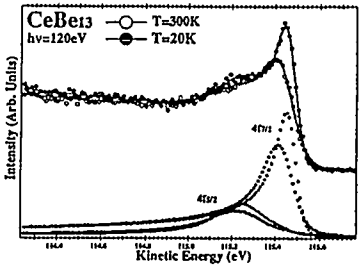


Figure 2.

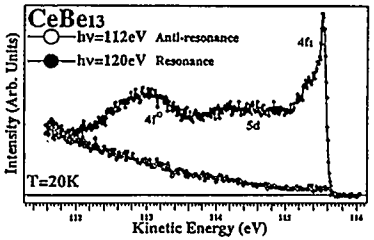


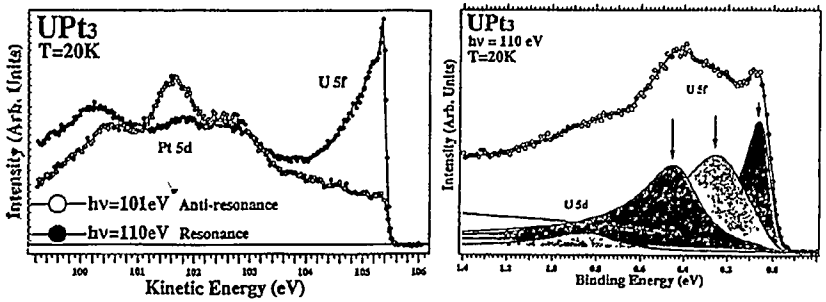
Figure 3.

A Reexamination of the heavy fermion superconductor UPt_3 | U3C

A. B. Andrews, J. J. Joyce, A. J. Arko (LANL), and B. Maples (Univ. California, San Diego)

The interpretation of photoemission data for actinides compounds has been much more problematic than for lanthanides, in part because it is far more difficult to assess the importance of correlation effects in U compounds than say in Ce. Since it is recognized that U 5f's are more bandlike than Ce 4f's and the Coulomb correlation U_{ff} is much smaller (~2eV), deviations from a one electron description are expected to be much smaller. On the other hand, earlier UPS data[1] taken at lower photon energies showed a bandwidth of 2-3 times as large as the LDA derived DOS calculated using one electron band theory[2]; Efforts to explain this have focused on satellites in the valence band (as in Ce). However, the large mass enhancements implied by the specific heat measurements require an even narrower 4f DOS than the LDA results; Hence an attempt to reconcile these discrepancies has also been made with the Anderson Hamiltonian[3], but due to technical difficulties with this approach, this problem has never been resolved satisfactorily. New data at the 5d resonance shows that the f-manifold has a significantly narrower bandwidth than previously measured, ~.5 eV (Fig. 1), much closer to the LDA derived results. We find three f bands in the photoelectron spectrum (Fig. 2), which coincide with structures in the $4f_{5/2}$ PDOS. This supports recent LDA calculations[4] which treat the on-site correlations via a perturbation technique and correctly predict the mass enhancement factors in a number of U compounds.

[1] A.J. Arko et al., PRL 53, 2050 (1984).
[2] R.C. Albers et al., PRB 33, 8116 (1986).
[3] J.W. Allen et al., PRL 54, 2635 (1985).
[4] M.M. Steiner et al., PRL 72, 2923 (1994).

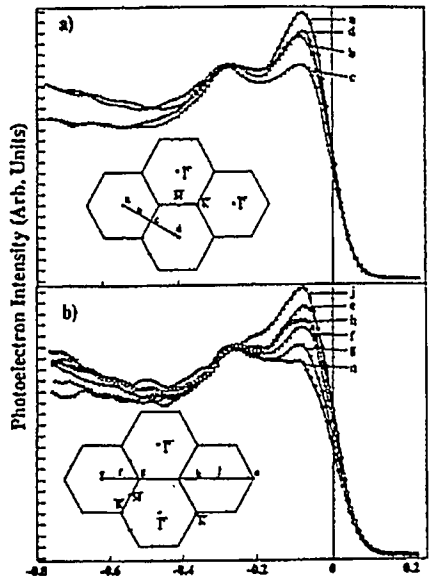


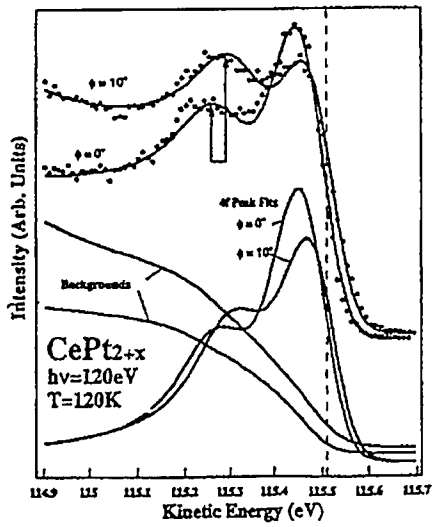
4f bands in the Ce heavy fermions compound $CePt_{2+x}$ | U3C

A. B. Andrews, J. J. Joyce, A. J. Arko (LANL), J. Tang (Univ. of Irvine), J. M. Lawrence (Univ. of Irvine)

The compound $CePt_{2+x}$ ($0 \leq x \leq 1$) grows in the $C_{15}MgCu_2$ Laves phase with a lattice parameter $a_o \approx 7.7$ Å as determined from LEED. Scans along the high symmetry directions Γ-M and Γ- K reveal amplitude variations which match the lattice periodicity i.e., the intensity near E_F is strongest at the Γ points (as far as the third zone), and decreases toward the zone boundaries (Fig. 1). Fig. 2 shows fits at Γ and M using a Doniach-Sunjuic lineshape with a integral background and a Fermi level cutoff. The reduction in amplitude between 0° to 10° can be explained by the dispersion of the 4f states toward E_F ($\approx$ 30 meV) so that the Fermi level cutoff produces the modulation. Renormalized quasiparticle bands exist only below a characteristic coherence temperature $T^{coh} \ll T_K$; above T_K the phase coherence is lost and localization is restored. Here, the magnitude of the estimated energy dispersion is roughly a factor of ~10 greater than what is expected from the Kondo Lattice in a renormalized band description. Since $CePt_{2+x}$ is a low-T_K material (T_K <20K) the KR should be of negligible intensity at the measurement temperature T^{meas}= 120 K. This may indicate that the 4f bands observed in de Haas-van Alphen measurements with a Fermi surface in agreement with LDA calculations, condense out of conventional bands. Our results indicate that in-situ preparation will benefit any UPS study of Ce intermetallics. They also show that the width of the 4f 'bands' is larger than that expected for a periodic lattice of impurities.

[1] N. d'Ambrumenil and P. Fulde, J. Magn. Magn. Mat. 47 & 48, 1 (1985).





Alkali adsorption on quasi-one dimensional oxides * | U4A

K. Breuer, K. E. Smith (Boston Univ.), M. Greenblatt, and W. McCarroll (Rutgers Univ.)

Transition metal oxide bronzes are inorganic quasi-low dimensional solids that are ideal prototypical systems for spectroscopic studies of the physical properties of one dimensional (1D) solids due to the size and quality of available crystals [1,2]. In the course of studying these and other quasi-1D systems, it has been noted that the photoemission intensity close to E_F is very low, despite the metallic nature of these solids. This has been interpreted as evidence for a Luttinger liquid ground state, rather than a Fermi liquid. The Luttinger liquid is the expected state for a true 1D system, and it is characterized by a shift of spectral intensity away from single particle excitations at E_F towards collective excitations at higher binding energies. While the angle resolved photoemission (ARP) spectral intensity at E_F is indeed low in these materials (see the spectrum for the cleaved surface in Fig. 1), it is neither negligible, nor is a Luttinger liquid ground state the only explanation. For example, we have shown that defects can result in a shift of the Mo 4d states away from E_F and thus lead to a reduces spectral intensity at E_F in $K_{0.3}MoO_3$ [1,3,4]. Furthermore, correlation effects in narrow band transition metal oxides often result in alow spectral intensity at E_F irrespective of the dimensionality. Thus it is important to determine what exactly is being measured by ARP for these quasi-1D systems, particularly since the issue of the Luttinger liquid ground state is hotly debated in the area of high T_c superconductors. An approach we have taken recently is to systematically add charge to a quasi-1D conductor, and examine how the electronic structure is modified. In particular, we are looking for any changes in the spectra as the excess charge pushes the bottom of the Mo 4d band away from E_F. The addition of charge to the system was accomplished by dosing the surface of the quasi-1D conductor $K_{0.3}MoO_3$ with a small quantity of Cs. Figure 1 shows preliminary results from these experiments, indicating a shift of the 1D band to higher binding energies, and a reduction of spectral intensity at E_F. This indicates that excess charge on the surface (from, for example, non-stoichiometric cleaves) may also lead to reduced emission at E_F. The data in Fig. 1 can be explained using conventional quasiparticle theories of ARP, and do not indicate a Luttinger liquid ground state. Further experiments examining the controlled addition of charge to a 1D band are planned.

[1] K.E. Smith, Ann. Rep. Prog. Chem. C 90 (in press); [2] K.E. Smith, K. Breuer, M. Greenblatt, and W. McCarroll, Phys. Rev. Lett. 70, 3772 (1993); [3] K. Breuer, K.E. Smith, M. Greenblatt, and W. McCarroll, J. Vac. Sci. Technol. A 12, 2196 (1994); [4] K. Breuer, K.E. Smith, M. Greenblatt, W. McCarroll, and S.L. Hulbert, Phys. Rev. B (submitted).

Figure 1. Normal emission spectra ($h\nu$= 18 eV) from cleaved and submonolayer Cs dosed $K_{0.3}MoO_3$. [Figure unavailable due to space constraints.]

* Work supported in part by the Petroleum Research Fund, administered by the ACS.

Surface-ion core-level shift in alkali halides * | U4A

G. K. Wertheim, D. N. E. Buchanan, J. E. Rowe, and P. H. Citrin (AT&T Bell Lab.)

The surface-ion core-level shift (SCS) of NaF, NaCl, and NaBr has been obtained from photoemission data taken on thin evaporated film of these alkali halides. This extends an earlier study in which first detection of the SCS was reported based on He I data for the chlorides, bromides, and iodides of K, Rb, and Cs [1]. The SCS in these insulators is not apparent by inspection like the surface-atom core-level shift in the alkali metals, because here the phonon broadening is larger than the shift. The SCS, which manifests itself only as an asymmetrical broadening of the photoemission spectrum, is readily determined by fitting the data with symmetrical Voigt function line shapes. The new data, which extend the earlier work to compounds with smaller lattice constant, allow a critical test of the theoretical interpretation proposed earlier. The SCS in these insulators is believed arise from two effects: (1) an initial-state contribution due to the difference between the Madelung potentials in the bulk and at the surface, and (2) a final-state contribution due to the difference in core-hole screening in bulk and surface. The Madelung contribution has been calculated for the close-packed, nonpolar surface of the NaCl structure by R. E. Watson et al. [2]. It is positive and proportional to the reciprocal of the lattice constant. The screening contribution is due to the smaller number of anion near neighbors for cations in the surface layer. A crude estimate of this contribution is obtained by assuming the polarization energy to be proportional to the number of near neighbors. At the (100) surface of the NaCl structure, the surface change in polarization energy is then positive and equal to 1/6 of the bulk polarization energy, which is close to 1.5 eV for the alkali halides considered here [3]. The SCS's of nine NaCl-structure compounds are plotted against the reciprocal of the lattice constant in Fig. 1 [unavailable due to space constraints]. The solid line is a linear least-squares fit to the data. The intercept of the fit in Fig. 1 gives the average reduction in screening-energy at the surface for these compounds. The value of 0.17 eV is in agreement with earlier estimates [1]. It corresponds to an average bulk screening energy of 1.0 eV, which is significantly smaller than typical values in Ref. [3]. This indicates that the simple estimate for the reduction at the surface based on the number of near neighbors is inadequate and suggests that in the absence of one neighbor the remaining five provide additional screening. The slope of the fitted line is 1.91 eV Å, in very close agreement with the theoretical value of 1.9 eVÅ[2]. This confirms that there is no significant surface reconstruction and that the fully ionic model assumed in the calculation of the Madelung potential is appropriate.

[1] G.K. Wertheim, et al., Surf. Sci. Lett (in press); [2] R.E. Watson et al., Phys. Rev. B 24, 1791 (1981); [3] P.H. Citrin and T.D. Thomas, J. Chem. Phys. 57, 4446 (1972).

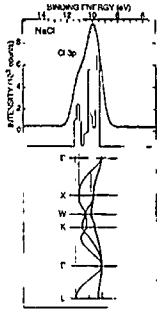
* Work supported by AT&T BellLaboratories.

Alkali halide valence band density of states * | U4A

G. K. Wertheim and J. E. Rowe (AT&T Bell Lab.)

During the past twenty years it has been repeatedly noted that photoemission spectra from the valence band of the alkali halides are significantly broader than indicated by band structure calculations. Encouraged by the finding that spectra of the shallow core levels from thin evaporated films of these materials are fully explained by a combination of lifetime and phonon broadening and the surface-ion core level shift, we have attempted an interpretation of the valence band spectra obtained by the same method. In the past the comparisons with theory have been based on estimates of the full width or the width at half amplitude, measures which do not take proper account of the phonon broadening. Since the lifetime width in the valence band should be negligible, the observed spectrum can be represented by a convolution of the density of states with a Gaussian representing the phonon width. Lacking densities of states derived from band structure calculations, we determine an experimental density of states from the photoemission spectrum and compare it with the published band structure. To carry out this analysis we set up a histogram with fixed energy origin and fixed bin width and adjust the content of the bins so as to optimize the agreement with the data after convolution with the phonon width. This procedure converges rapidly provided the bin width is not made too small and the bin content is constrainted to be positive or zero. Using standard least-squares methods, the content of the bins and the phonon width can be treated as free parameters. The result obtained from data for NaCl at 450 K taken with 75 eV radiation are shown below. For comparison the bands calculated by Erwin and Lin [1] are shown below the density of states histogram obtained from the experimental data. The agreement is very good. Only the weak contribution from states near the Γ point is not reproduced by the analysis. Surface ion shifts are apparently small compared to the phonon width. The phonon width is 0.97 eV, compared to a theoretical value of 1.10 eV calculated for core level excitation [2]. This indicates that the valence band hole is sufficiently well localized to excite the lattice much like a core hole.

[1] S.C. Erwin and C.C. Lin, J. Phys. C 21, 4285 (1988); [2] G.D. Mahan, Phys. Rev. B 21, 4791 (1980).



* Work supported by AT&T BellLaboratories.

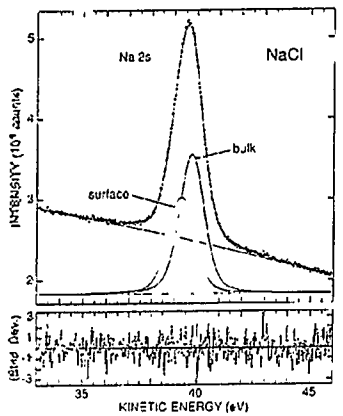
Interatomic Auger rates in sodium halides * | U4A

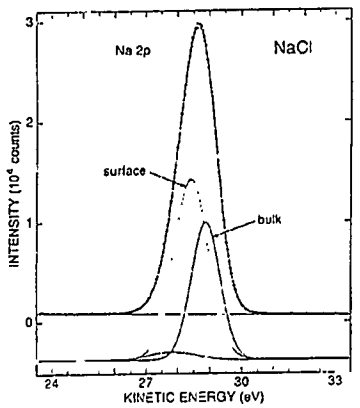
G. K. Wertheim, J. E. Rowe, and P.H. Citrin (AT&T Bell Labs)

In ionic compounds of sodium a hole in the 2p shell can be filled only by an electron from the anion valence band. The dominant decay process is an interatomic Auger process of the type $L_{2,3}$ VV, in which both Auger electrons come from neighboring atoms. For a hole in the deeper Na 2s shell, the super-Coster- Kronig decay, L_1 $L_{2,3}L_{2,3}$, is energetically forbidden, but the interatomic Coster-Kronig decay, L_1 $L_{2,3}$ V, is allowed. The existence of such interatomic processes has been previously verified by the observation of the Auger electrons. The decay rates for a 2s hole in NaCl and NaF and a 2p hole in NaF have been calculated [1,2].

We have measured the lifetime width of these states by photoemission. The samples were prepared by the deposition of the alkali halide vapor onto a Si(111) or Si(100) substrate in a preparation chamber attached to the photoelectron spectrometer. Alkali halide films are not stable when exposed to synchrotron radiation because of the photon stimulated desorption of the halide ions. This changes the surface stoichiometry, generates F-center, and eventually makes alkali metal appear on the surface. We used two approaches to minimize this problem, either limiting the time during which a fresh surface was used or heating the surface to a temperature where it was continually renewed by sublimation. Data for NaCl 2s and 2p, taken with the sample heated to ~500 K, are shown below. In each case bulk and surface components, with a surface-ion core-level shift of ~0.45 eV, were required to fit the data. The phonon width is close to 1 eV at this elevated temperature. The lifetime width for Na 2s is 0.45 ± 0.10 eV, compared to a calculated value of 0.79 eV [1]. The lifetime width of the 2p level is too small to be reliably determined in the presence of the much large phonon width, but a limit of 0.06 eV was established. Similar results have also been obtained for NaF and NaBr.

[1] Y. Yafet and R. E. Watson, Phys. Rev. B 16, 895 (1977).
[2] T.A. Green and D.R. Jennison, Phys. Rev. B 36, 6112(1987).





* Work supported by ATT Bell Laboratories.

Circularly polarized soft x-ray resonant magnetic scattering from multilayers	U4B

V. Chakarian (NRL), Y. U. Idzerda (NRL), C.-C. Kao (NSLS), J.-H. Park (AT&T Bell Lab.), G. Meigs (ATT Bell Lab.), E. Johnson (NSLS), G. A. Prinz (NRL), and C. T. Chen (ATT Bell Lab.)

Circularly polarized soft x-ray resonant magnetic scattering is a technique which combines the structural sensitivity of x-ray scattering and the magnetic sensitivity of soft x-ray magnetic circular dichroism. It offers the possibility of determining layer thickness, interface quality, and the magnetization of a heteromagnetic multilayer in an element- and layer specific manner. As a demonstration of the technique, angle ($\theta - 2\theta$) and energy scans were collected near the L-edges of Fe, Co, and Mn, for a heteromagnetic trilayer: $Fe_{0.3}Co_{0.7}$(106Å/Mn (8.7Å)/ $Fe_{0.3}Co_{0.7}$(106Å). Representative spectra for Fe and Co are shown below. The intriguing interference characteristics seen in the data can be modeled using electromagnetic theory of layered media.

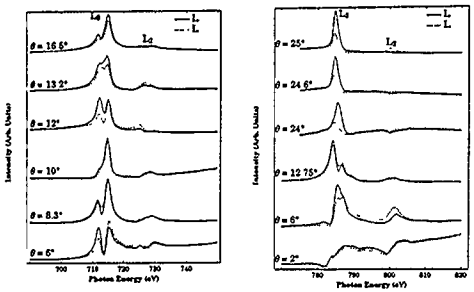


Figure 1. Energy scans along various incidence angles inteh Fe (left) and Co (right) L-edge regions.

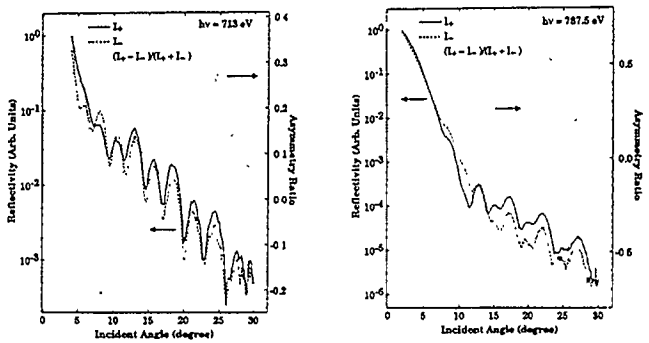


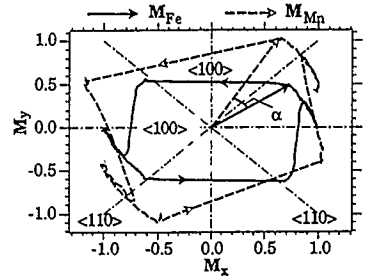
Figure 2. Representative $\theta - 2\theta$ scans at the Fe (left)and Co (right) L_3 white lines.

2D element specific vector magnetometry of heteromagnetic multilayers	U4B

V. Chakarian (NRL), H.-J. Lin (AT&T Bell Lab.), Y.U. Idzerda (NRL), E.E. Chaban, G. Meigs, J.-H. Park (AT&T Bell Lab.), G.A. Prinz (NRL), and C.T. Chen (AT&T Bell Lab.)

Conventional methods for studying magnetization reversal processes, such as vibrating sample magnetometry, magnetization loopers, magneto-optic Kerr effect, magnetoresistance, superconducting quantum interference device susceptometry and Lorentz electron microscopy are often used to determine the magnitude and/or the orientation of only a single component of the magnetic moment vector (typically parallel to the applied magnetic field). Furthermore, in the case of heteromagnetic systems, none of the aforementioned methods discriminate among the various constituent elements of the magnetic material studied, nor do they allow the determination of the magnetization change in three dimensions. As a result, the information obtained by these conventional methods, while valuable, is often limited and incomplete. In this work, magnetic hysteresis curves for Fe, Co and Mn of a $Fe_{0.3}Co_{0.7}$ (106Å)/ Mn (8.7Å)/$Fe_{0.3}Co_{0.7}$ (106Å) trilayer system are measured via soft x-ray magnetic circular dichroism (SXMCD) in x-ray fluorescence yield mode (see our article in this year's report for more details). One of the major conclusions of this work is that Mn has a net moment in this trilayer structure. It should be emphasized that SXMCD is the only method that allows the determination of a Mn moment. Furthermore, a comparison of the switching fields for Fe and Mn moments (not shown) indicates that Mn moment is coupled strongly to the enclosing FeCo layers [1]. 2D parametric representations of M for Fe and Mn are shown below (the Co magnetization curve is identical to that of Fe). Also shown in the figure are the principal crystallographic directions present in the (001) plane. Note that, due to large probing depth of the fluorescence yield measurements, the Fe magnetization curve shown in the figure represents the rotation of the average M, $\langle M \rangle$, and not the individual moments of the two FeCo films. The arrows indicate increasing and decreasing magnetic field. The data indicate that the average Mn moment is rotated from that of Fe and Co by about 25°. As the moments of the FeCo layers rotate in the plane of the film, the associated Mn moments follow and this 25° angle is largely preserved. These 2D parametric loops of $\langle M \rangle$ for Fe and Mn can be used to model the rotation of the magnetic moments of each layer as a function of the applied field [1].

[1] V. Chakarian et al., to be published.



Element specific vector magnetometry via SX-MCD	U4B

V. Chakarian (NRL), H.-J. Lin (AT&T Bell Labs.), Y. U. Idzerda (NRL), E. E. Chaban (AT&T Labs.), G. Meigs (AT&T Bell Labs.), J.-H. Park (AT&T Labs.), G. A. Prinz (NRL), and C. T. Chen (AT&T Bell Labs.)

The use of soft x-ray magnetic circular dichroism (SW-MCD) as tool for element-specific, 2D and 3D vector magnetometry of magnetic thin films and multilayers is demonstrated. Element-specific magnetic hysteresis curves are recorded by monitoring the L_3 white line fluorescence yield intensity of the relevant elements with a solid-state germanium detector as a function of the applied field. An illustration of the experimental arrangement is shown on the left panel. A UHV compatible electromagnet assembly, has been developed which allows one to change the direction of the magnetization relative to the incident photon beam direction. The measured hysteresis curves are proportional to k_i . M, where k_i is the photon momentum (direction of incident photon beam) and M is the magnetization vector ($M = M_x \hat{x} + M_y \hat{y} + M_z \hat{z}$). The azimuthal rotation of the magnetization direction successively by 90° results in a photon momenta to be along one of the k_i (i = 1,2,3,4) shown in the figure. The individual components of the magnetization vector can then be obtained uniquely by forming arithmetic sums and differences of the measured hysteresis curves.[1]

As a demonstration of the technique the magnetization behavior of a 30 Å Fe (001) single-crystal thin film was measured. In this system, M is restricted to rotate in the plane of the film. The lack of an M_z component was verified directly by measuring a null hysteresis signal for photon beam incident normal to the film plane. Note that, for thin films that display only in-plane magnetizations, $M_z = 0$ so that measurements along k_1 and k_2 (or alternately, k_3 and k_4) are sufficient for obtaining M_x and M_y. A 3D view of the two dimensional rotation of the measured M is shown on the right panel. In this view, the M_x, M_y and M_x vs. M_y curves are all visible as projections on the back, bottom and right planes, respectively. A detailed analysis of these results allows the modeling of the magnetization reversal process.[1]

[1] V. Chakarian, et al., to be published.

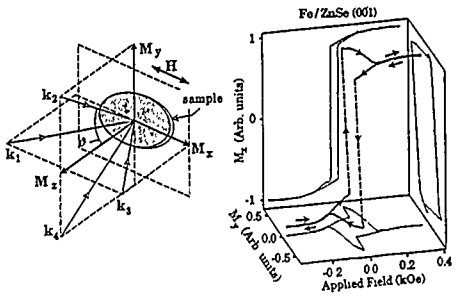


Figure 1.

Applicability of the orbital and spin x-ray magnetic circular dichroism sum-rules	U4B

C. T. Chen (AT&T Bell Lab.), Y. U. Idzerda (NRL), H.-J. Lin, N. V. Smith, G. Meigs, E. E. Chaban (AT&T Bell Lab.), G. H. Ho (Univ. of Penn.), E. Pellegrin, and F. Sette (AT&T Bell Labs)

In order to verify the applicability of the individual orbital andspin x-ray magnetic circular dichroism sum-rules, we have further analyzed our earlier $L_{2,3}$-edges transmission MCD data of Fe and Co (see the NSLS 1993 Annual Report). The figures show the MCD (μ_+-μ_-) (solid curves) as well as their integration (dashed curves) spectra of Fe (figure 1) and Co (figure 2). The orbital to spin relative moments deduced from the MCD integrals ("p" & "q") accordingto the relative sum-rule are 0.043 for Fe and 0.095 for Co, in excellent agreement (within 3%) with the values of 0.044 for Fe and 0.097 for Co obtained by gyromagnetic ration measurements. Interestingly, we also found, by using 3d occupation numbers obtained from first principle band structure calculations (6.61 for Fe & 7.51 for Co) and a no-free-parameter two-step-like function for the XAS edge-jump removal(dotted lines), that the orbital and spin individual moments (in units of μ_B/atom) determined from both the MCD and XAS integrals is ("p", "q", & "r") are 0.085 and 1.98 for Fe, and 0.154 and 1.62for Co, in good agreement (within 9%) with the gyromagnetic results of 0.092 and 2.08 for Fe, and 0.147 and 1.52 for Co. Although further verification of the sum-rules on other magnetic systems, and of the universality of the two-step-like function adopted here, are needed, their success with two of the most important magnetic elements strongly supports the optimism for developing soft-x-ray MCD into a reliable technique for determining element-specific orbital and spin magnetic moments.

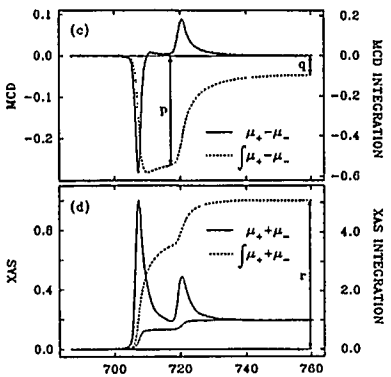


Figure 1.

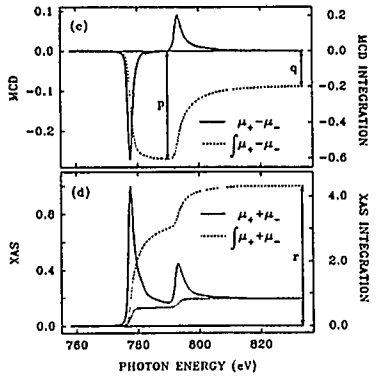


Figure 2.

Extraction of the coefficient of giant magnetoresistance * | U4B

Y. U. Idzerda (NRL), C. T. Chen (AT&T Bell Lab.), S.-F. Cheng (NSWC), W. Vavra(NRL), G. A. Prinz (NRL), G. Meigs (ATT Bell Lab.), and H.-J. Lin (ATT Bell Lab.)

Element specific magnetic hysteresis (ESMH) loops [1] have been used in conjunction with measured magnetoresistance curves to extract the coefficient of giant magnetoresistance (GMR) which is the maximum achievable value of the GMR independent of magnetic domain effects [2]. The conventional, total magnetic hysteresis behavior of a sputtered Fe/Cu/Co trilayer structure (inset of figure below) is shown in the top panel. In the middle panel are the normalized ESMG loops obtained by separately measuring the Fe and CO L_3 absorption intensity by fluorescence yield for right-circularly polarized light. The summed spectra, displayed as the dotted line, gives good agreement with the VSM spectra. The lower figure shows the measured GMR curves for comparison with two calculated GMR curves obtained from the ESMH loops assuming either a single-domain X-Y Heisenberg micro-magnetic behavior or a multidomain Ising behavior. The two vertical axes are displayed in normalized MR values and vividly demonstrate the effects of the incomplete alignment. It is clear from these spectra that these films are best described by a multi-domain Ising model (Which is consistent with the polycrystalline nature of these films). From the value of the maximum measured GMR of 2.1%, we can extract a coefficient of GMR of 3.1%, and increase of almost 50%.

[1] C.T. Chen, Y.U Idzerda, H.-J. Lin, G. Meigs, A. Chaiken, G.A. Prinz, and G.H. Ho, Phys. Rev. B 48, 642 (1993).

[2] Y.U. Idzerda, C.T. Chen, S.-F. Chang, W. Vavra, G.A. Prinz, G. Meigs, H.-J. Lin, and G.H. Ho; Appl. Phys. Lett. 64, 3503 (1994).

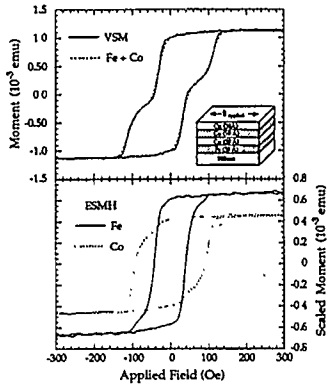


Figure 1.

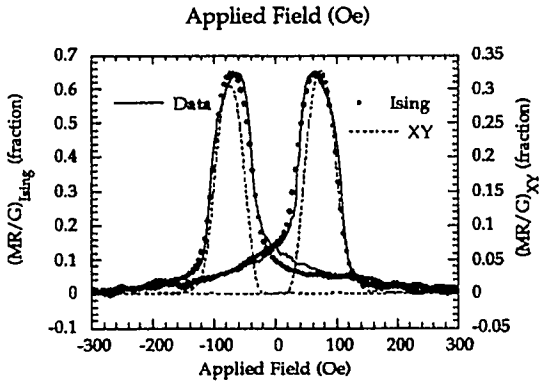


Figure 2.

* This work is partially supported by the Office of Naval Research.

Electron spectroscopy study of doping dependence in $La_{1-x}Ca_xMnO_3$ | U4B

J.-H. Park, W. Bao (AT&T Bell Lab. and Johns Hopkins Univ.), S.-W. Cheong (AT&T Bell Lab.), V. Chakarian (NRL), G. Meigs, and C. T. Chen (AT&T Bell Lab.)

$La_{1-x}Ca_xMnO_3$ is a highly correlated system which exhibits intriguing magnetic and electronic behavior as a function of Ca concentration and of temperature. To help understand its electronic structure, we have measured X-ray absorption spectroscopy (XAS), high resolution valence band photoemission spectroscopy (PES), and resonant photoemission spectroscopy data of $La_{1-x}Ca_xMnO_3$. The PES spectra and O 1s XAS spectra for different Ca concentrations, taken with respective experimental resolutions of 600 meV and of 200 meV, are shown below. The binding energy shown in figure (a) refers to the chemical potential of a clean Pt which was in electrical contact with the samples. These spectra have been scaled to make the O 2s peaks the same height. The binding energies of La 3d, Ca 3p, and O 2s core levels were found to decrease linearly, and a systematic change was observed in valence band region, with increasing x, showing a chemical potential shift with Ca concentration. Figure (b) shows the valence band region of Fig. (a), but with their energy scales shifted to align their core levels. Figure (c) shows the O 1s XAS spectra which reflect the unoccupied states. Interestingly, we found that the spectra of intermediate Ca concentration can be explained by a linear combination of those of $LaMnO_3$ and $CaMnO_3$. This strongly suggests that $La_{1-x}Ca_xMnO_3$ does not behave as a simple hole doping system, but rather, a "dynamic phase separation" system.

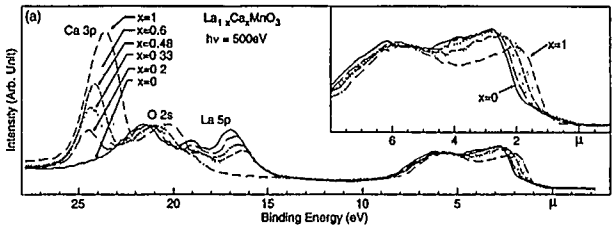


Figure 1.

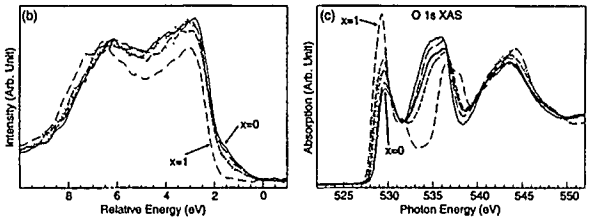


Figure 2.

Orbital characters of holes in $Y_{2-x}Ca_xBaNiO_5$, a doped haldane chain compound

U4B

J.-H. Park, C. T. Chen, S.-W. Cheong, J. F. Ditusa, G. Aeppli (AT&T Bell Lab.), and C. Broholm (Johns Hopkins Univ. and NIST)

Y_2BaNiO_5 is a charge transfer insulator which contains Ni^{2+} (S=1) chains with a quantum disordered Haldane ground state. To help reveal its electronic structure responsible the 1D nature of its conduction, we have measured high resolution polarized x-ray absorption spectra for this system. Figures (a) and (b) show the O K-edge and Ni L_3-edge regions, respectively, of the XAS spectra of two $Y_{2-x}Ca_xBaNiO_5$ single crystals taken with two polarization geometries, i.e., E||a and E||b, where a is alone the Ni-O-Ni chain direction. It is evident form the O K-edge spectra that doping induced holes (prepeak A) reside mainly in the O $2p_x$ orbital of the chains (here we use z, x, and y to denote the a, b, and c crystal axis, respectively). A spectral weight transfer from prepeak B to A is also observed in the E||a spectra, similar to what is observed in other doped charge transfer insulator such as $La_{2-x}Sr_xCuO_4$. Both O K-edge and Ni L-edge spectra show strong doping-induced spectral changes for orbitals along the chain direction (i.e. O $2p_z$ and Ni $3d_{3z^2-r^2}$; see the E||a spectra, but almost no effects for those perpendicular to it (i.e. O $2p_{x,y}$ and Ni $3d_{x^2-y^2,xy}$; see the E||b spectra). These spectroscopic results provide a microscopic understanding for the transport data and demonstrate conclusively that this system is the first 1D analog of doped 2D transition metal oxides. However, in contrast to the latter system, undoped Y_2BaNiO_5 is not an antiferromagnet, but rather a compound with a quantum disordered ground state and a Haldane gap in the magnetic excitation spectrum. Therefore, it represents thus far the only quantum spin liquid in any dimension into which carriers can be introduced.

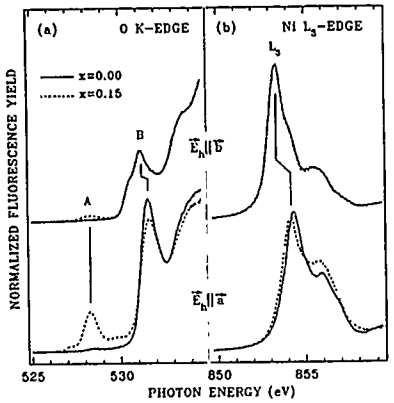


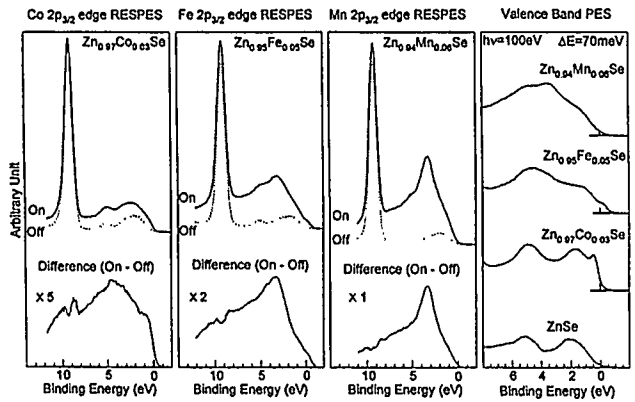
Figure 1.

Dopant states in Zn_{1-x}(Co, Fe, Mn)$_x$Se

U4B

J.-H. Park (AT&T Bell Lab.), K.-H. Cho, S.-J. Oh (Seoul Natl. Univ.), Y. D. Kim (Kyunghee Univ.), M. S. Han (Seoul City Univ.), J.-S. Kim (Sookmyung Women's Univ.), V. Chakarian,B. T. Jonker (NRL), G. Meigs, and C. T. Chen (AT&T Bell Lab.)

Dopant states of diluted magnetic semiconductors, Zn_{1-x}(Co, Fe, Mn)$_x$Se, have been studied by using resonant photoemission spectroscopy (RESPES) and x-ray absorption spectroscopy (XAS) at Co 2p, Fe 2p, and Mn 2p edges, respectively. Even with small dopant concentrations, giant resonant enhancements at the transition metal 2p→3d edges reveal the transition metal dopant 3d states in the photoemission valence band spectra. The samples were grown on GaAs substrates, and the clean surface was prepared by chemical etching and by annealing in situ. After the surface cleaning, only negligible intensities of O 1s and C 1s peaks were detected. The left three figures show the on- and off-resonance valence band spectra and the difference spectra of $Zn_{0.97}Co_{0.03}Se$, $Zn_{0.95}Fe_{0.05}Se$, and $Zn_{0.94}Mn_{0.06}Se$ at Co $2p_{3/2}$, Fe $2p_{3/2}$, and Mn $2p_{3/2}$ edges, respectively. The binding energy refers to the top of the ZnSe valence band. For all three cases, the dopant 3d states obtained from the difference spectra are spread over 10 eV. These results can only be understood in terms of a many-body approach which takes into account the correlation effects and the dopant 3d - Se 4p hybridization explicitly. The other figure shows the high resolution valence band photoemission spectra taken at hv = 100 eV with ΔE = 60 meV overall experimental resolution. Interestingly, some Fe 3d states appear in the Se 4p-Zn 4s bonding-antibonding gap, while the Co 3d states exhibit a sharp peak at 0.5 eV binding energy.



Electronic structure study of RNi_2B_2C (R = rare-earth) compounds by x-ray absorption spectroscopy * — U4B

E. Pellegrin (Kernforschungszentrum Karlsruhe, Institut fur Nukleare Festkörperphysik, Germany), G. Meigs, C. T. Chen, R. J. Cava, J. J. Krajewski, and W. F. Peck, Jr. (AT&T Bell Labs.)

X-ray absorption spectroscopy measurements have been performed on the Ni2p and B1s absorption edges of polycrystalline RNi_2B_2C (R=Y, Sm, Tb, Ho, Er, Tm, Lu). We find evidence for a constant Ni3d electron count close to that of Ni metal and for a unchanged unoccupied Ni3d density of states throughout the whole sample series. A slight decrease is observed in the B2p-derived intensity in the B1s absorption edges close to E_F between 4 and 7 eV above E_F which may be due to structural changes when going from the late to the early rare-earth compounds. We also get direct evidence for the strong covalent bonding between the Ni3d and B2p orbitals. A comparison with results from band structure calculations shows, first, that the unoccupied part of the predicted Ni3d dominated maximum in the density of states is suppressed and shifted to higher energies. Second, the calculations put the B/C2p-related bands at higher energies too high above the Fermi level.

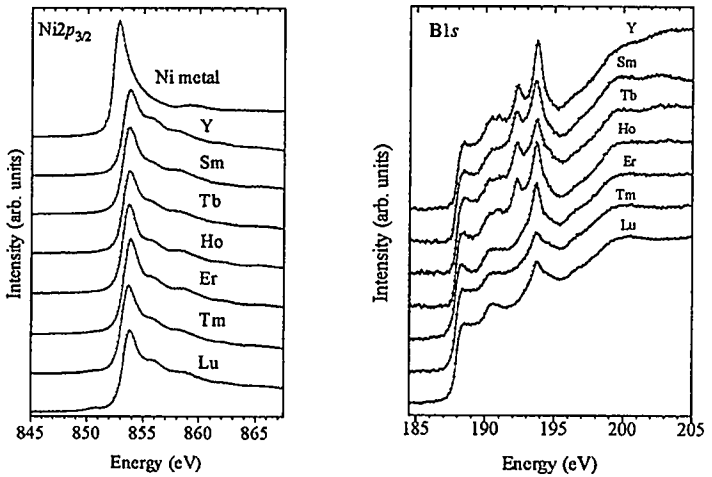


Figure 1. $Ni2p_{3/2}$ and B1s x-ray absorption edges of Ni metal and RNi_2B_2C (R=Y, Sm, Tb, Ho, Er, Tm, Lu). The spectra labeled by their rare-earth constituent.

* Work was supported by the HSPII program of the German Academic Exchange Service (DAAD).

X-ray magnetic circular dichroism study the spin 1/2 proteins — U4B

G. Peng (Univ. California, Davis), J. H. Christiansen (Univ. California, Davis), A. T. Young (LBL), and S. P. Cramer (Univ. California, Davis and LBL)

Using a ^{3}He cryostat which can attain a temperature of 700 mK, we measured the soft X-ray magnetic circular dichroism (XMCD) effects on Fe L-edges of myoglobin incubation with azide and on the Cu L-edge of a blue copper protein. The myoglobin is a heme protein with isolated low spin Fe^{3+} in the azide bound form. The blue copper protein contains a Cu^{2+} with spin 1/2. The spin 1/2 systems are simple systems with only two m_s state available. The XMCD experiment provides insight into the magnetization behavior and electronic structure of the spin 1/2 systems, forming the basis for the understanding of the magnetization behavior of more complicated protein systems that may contain several [nFe-mS] clusters or many different Cu sites. The difficulty of measuring the MCD effect of a spin 1/2 system comes from the small energy gap between the -1/2 and +1/2 m_s states, which causes both states to be populated. Extremely low temperature (< 4 K) and/or extremely high field (>5 Tesla) are required in order to maximize the population in the ground m_s state and to observe the strongest MCD effects. By comparison with the theoretical magnetization curve, the MCD experiment for the spin 1/2 system will also help to establish the exact sample temperature (not the ^{3}He cryostat temperature).

In the figure at the left, the spectra with right and left circular light for myoglobin-azide are shown at the top and the MCD spectrum is at the bottom. The temperature of the cryostat, 700 mK, is measured by a Ge sensor while the sample temperature is estimated at 3K from the comparison of the experimental and theoretical MCD effect for this system. The figure at the right shows the spectra of right and left circular light for the blue copper protein at different fields and temperatures of the ^{3}He cryostat. It clearly shows the importance of low temperature: the higher measurement temperature requires an increased magnetic field that results in weaker spectra and higher noise. Improvements to the thermal condition of the sample are being undertaken to lower the sample temperature down to the milli-kelvin range.

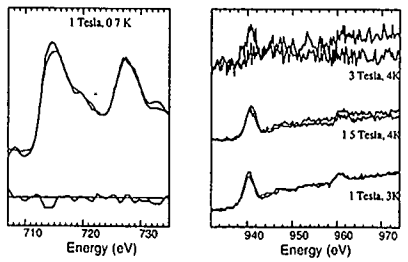


Figure 1.

Spin-polarization in 4f-photoemission from tungsten | U4B

K. Starke (AT&T Bell Lab.), Y. Liu, P. D. Johnson (BNL), V. Chakarian (NRL),E. E. Chaban, G. Meigs, C. T. Chen (AT&T Bell Lab.)

In a 'complete' photoemission (PE) experiment circularly polarized x-rays and electron spin analysis were used to examine the spin-polarization of 4f core-level photoelectrons from W(110). For the spin-orbit split $4f_{7/2}$- and $4f_{5/2}$-photoemission (PE) lines, the electron spin-polarization vector lies in the interaction plane of light incidence and electron- emission direction and it points parallel and antiparallel to the photon angular momentum, respectively.

This spin polarization in core-level PE from a non-ferromagnetic solid is a consequence of the Fano effect and can be quantitatively described in a simple atomic model. Our finding is complementary to the recently reported case of core-level spin-polarization perpendicular to the interaction plane, using linear light [1]. The present observation of spin polarization in the intense 4f-PE lines from W(110) opens new perspectives for spin-dependent diffraction and inelastic scattering experiments, in view of the wide use of W(110) as substrate for ferromagnetic rare earth and transition metal overlayers.

[1] C. Roth et al., Phys. Rev. Lett. 73, 1963 (94).

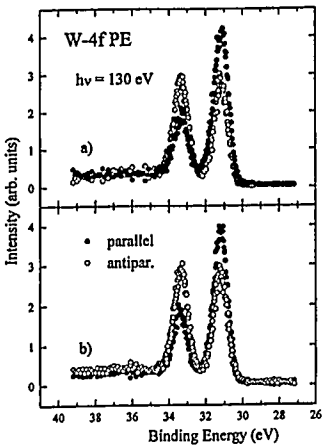


Figure 1. Spin- and helicity-resolved PE spectra from the 4f spin-orbit doublet of W. Byusing (a) right circularly polarized and (b) left circularly polarized light, $4f_{7/2}$-($4f_{5/2}$-)photoelectrons are spin-polarized parallel (antiparallel) to the projection of the photon angular momentum.

Soft x-ray magnetic circular dichroism in Co/Sm/Co | U4B

K. Starke, J.-H. Park (AT&T Bell Lab.), V. Chakarian (NRL), E. E. Chaban, G. Meigs, and C. T. Chen (AT&T Bell Lab.)

Transition metal (TM) super-lattices with antiferromagnetic coupling across non-magnetic Tm-spacer layers have received considerable attention due to their large magnetoresistance. Similarly, antiferromagnetic interlayer coupling is also observed in rare earth (RE) superlattices [1], where magnetic correlations are mediated coherently via non-magnetic RE spacer layers.

In a first exploratory study of exchange coupling of ferromagnetic TM layers across RE spacer layers, Co/Sm/Co-trilayers were investigated. Using the transmission x-ray absorption technique and in-situ grown thin films deposited on semi-transparent 1 μm thick parylene windows [2], element specific magnetic hysteresis-loops were recorded by MCD at the Co $L_{2,3}$- and the Sm $M_{4,5}$-edges (upper Fig.). For a Sm layer thickness below 25 Å identical rectangular shaped hysteresis loops were found for both elements, indicative of ferromagnetic coupling.

By contrast, for 30 to 35 Å Sm spacer thickness the Co hystereses (lower Fig.) show a two step magnetization reversal, which can be interpreted as antiferromagnetic coupling in the presence of large coercivity at the Co/Sm interfaces. Yet, for a unique identification, future studies with variable spacer material and coercivity are planned.

[1] C.F. Majkrzak et al., J. Appl. Phys. 63, 3447 (1988).
[2] C.T. Chen et al., NSLS Activity Rep., A-18 (1993).

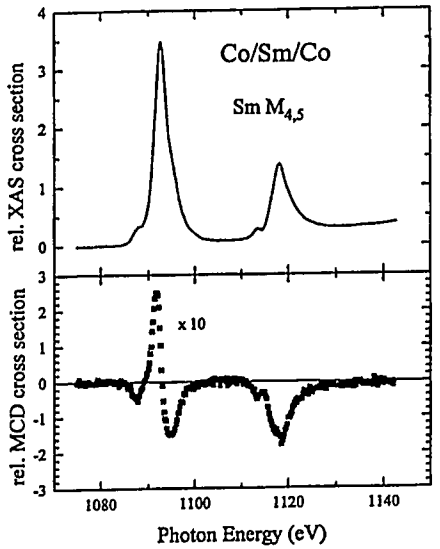


Figure 1.

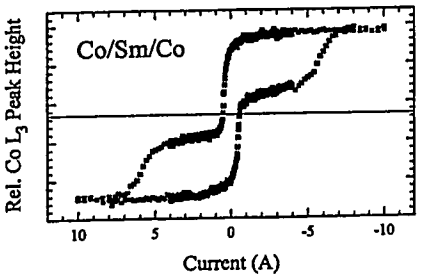


Figure 2.

Hybridization and the effective mass of quantum well states in magnetic multilayers * — U5U

P. D. Johnson, K. Garrison, Q. Dong (BNL), N. V. Smith (LBL), Dongqi Li, J. Mattson,J. Pearson, and S. D. Bader (ANL)

Theories of the oscillatory exchange coupling in the magnetic multilayers frequently predict more than one period of oscillation for the coupling, particularly where Fermi surface spanning vectors away from the center of the zone are invoked as in the case of the short period oscillation in the Co/Cu(001) multilayers. In this study we have used angle resolved photoemission to examine the dispersion away from the center of the zone of the quantum well states in copper thin films deposited on a Co(001) substrate. As shown in fig. 1 our studies reveal that hybridization in the interface leads to a large increase in the in-plane effective mass of the electrons in the very thin films. This observation has implications for theories of the exchange coupling because in the ultrathin regime the Fermi surface of the non-magnetic copper layer will be modified.

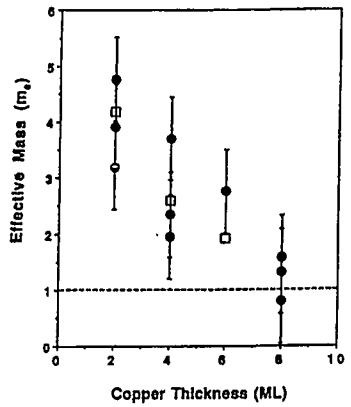


Figure 1. Plot of the fitted effective masses of the quantum well states as a function of the copper film thickness in atomic layers (AL). The solid circles indicate the fits to the experimental data; the open squares indicate the results of tight-binding calculations of the effective masses. The dashed line represents the free electron mass.

* Work supported in part by the Department of Energy under contract numbers DE-AC02-76CH00016, DE-AC03-76SF00098and W-31-109-ENG-38 and in part by the Office of Naval Research under contract number N-00014-94-F-0085.

Exchange splitting of Gd 5d states at finite temperature: Stoner-like or not? * — U5U

Dongqi Li, J. Pearson, S. D. Bader (ANL), D. N. McIlroy, C. Waldfried, P. A. Dowben (Univ. of Nebraska), D. J. Huang, and P. D. Johnson (BNL)

Spin-polarized photoemission was employed to investigate the temperature dependence of the exchange splitting of Gd(0001) for both the surface state near E_F and the 5d bulk bands at 1-2 eV below E_F at 130 - 350K. The bulk bands show two peaks with opposite spin polarization that shift toward each other as the temperature increases, as marked in Fig. 1. This behavior is Stoner-like in that the exchange splitting of the itinerant 5d electrons varies with the bulk magnetization. In contrast, however, the surface state with majority spin character maintains both constant binding energy and constant normalized intensity over the entire temperature range, as shown in Fig. 2, while its spin polarization decreases dramatically at the surface Curie temperature (Fig. 1). Thus, the polarization changes of the surface state do not originate from the collapse of its exchange splitting, but, instead, follow the spin mixing behavior expected for a disordered local-moment model of the spatially localized surface state. The data, therefore, tells us that the difference between the bulk band and the surface state is due to the degree of itinerancy of the 5d electrons in the two states.

Fig. 1

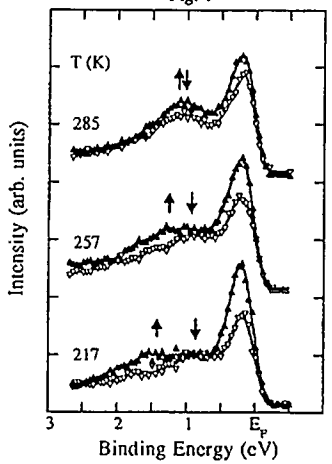
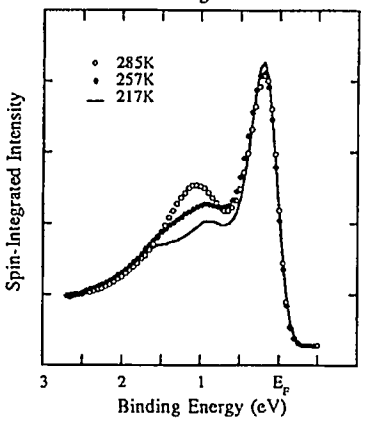


Fig. 2



* Work at Argonne is supported by DOE BES-MS under W-31-109-ENG-38; Nebraska by NSF grant DMR-92-21655.

Photoemission study of quantum confinement by a finite barrier: Cu/Co(wedge)/Cu(100) *	U5U

Dongqi Li, J. Pearson, J. E. Mattson, S. D. Bader (ANL), P. D. Johnson (BNL)

Quantum confinement is studied with angle- and spin-resolved photoemission in ultrathin Cu films. An epitaxial wedge of Co(100) (0-11Å) serves as a finite barrier that separates a Cu overlayer from a Cu(100) substrate. For thick (¿8Å) Co, in addition to the well-known sp-band derived quantum-well (QW) states, d-band derived QW states are observed for 1-3 monolayers (ML) of Cu. For 2ML of Cu, the photoemission intensities of the sp-QW states at 1.6 eV binding energy and the corresponding d-QW state at 2.4 eV increase rapidly with the thickness of the Co barrier, and indicate stronger confinement of the d-QW state than of the sp-state as shown in Fig. 1. These results can be understood in the context of the energy potentials in the layered structure based on bulk band structure, and semiquantitatively agree with a tight-binding slab calculation. The results provide the value of the minimum barrier thickness needed to establish QW states. By implication, this would also be the minimum Co thickness needed to sustain AF coupling in this giant magnetoresistance material. In addition, the successful use of a wedge technique in photoemission is promising for a broad range of experiments at synchrotrons.

Fig. 1. Peak intensities of the sp-QW state at 1.6 eV (solid circles) and d-QW state at 2.4 eV (open circles; normalized to the same saturation intensity as the sp-state) indicating a more pronounced quantum confinement by the Co barrier for the d-QW state. Solid and dashed curves represent the experimental fits as indicated in the figure, where t_{Co} is the Co thickness. Inset: minority spin electron energy potentials experienced by sp- (thick solid line) and d- (thick dashed line) electrons based on the bulk band structures. The energies for the two QW states of 2ML Cu (thin solid and dashed lines) and their energy differences from the top of the corresponding energy barriers (arrows) are also indicated.

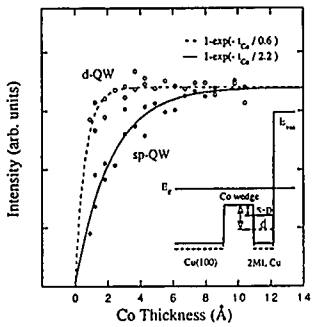


Figure 1.

* Work supported by DOE BES-MS under W-31-109-ENG- 38 and ONR N-00014-94-F-0085; BNL by DOEDE-AC02-76CH00016.

Photoelectron spectroscopy and NEXAFS investigation of metal poly(*p*-phenylene vinylene) interface formation *	U7A

E. Ettedgui, H. Razafitrimo, and Y. Gao (Univ. of Rochester), and M. W. Ruckman (BNL)

The discovery of electroluminescence in π-conjugated polymers has stimulated interest in these materials because of their potential applications in novel light emitting devices. Polymer-based light emitting diodes (LEDS) are prepared by spin coating a conjugated polymer such as poly(p-phenylene vinylene) (PPV), onto a conducting substrate followed by the deposition of a metallic cathode. Proposed mechanisms to account for light emission in PPV invoke the delocalization of electrons in the p_z orbital, giving rise to a band gap across which injected charges recombine. In these models, the theoretical efficiency of PPV-based LEDs is 25%. Experimental investigation has shown photon production efficiencies to be generally lower than 1% and to depend strongly on the type of metal used, with metals of lower work function leading to more efficient light production. These results call for a thorough investigation of the interface formation between the metal cathodes and the π-conjugated polymers.

Our previous x-ray photoemission spectroscopy (XPS) studies of the deposition of metals on PPV have showed changes reminiscent of Schottky barrier formation in semiconductors. Thus, we have found a rigid shift in the binding energies of the C 1s photoelectrons. Unlike in the case of traditional semiconductors, however, Schottky barrier formation in polymers is a slow process that requires the deposition of several angstroms of metal before the binding energy stabilizes. Synchrotron radiation photoelectron spectroscopy allowed us to carefully study the valence band energy levels, which are not as readily accessible by XPS. Making further use of the capabilities of the synchrotron, we collected carbon K edge NEXAFS data to evaluation changes in the band gap of PPV.

The results obtained from the synchrotron radiation studies of metal/polymer interace formation confirm our previous assertion about band bending. In addition, in our study of the valence band spectra, we note an increase in the density of electronic states near the leading edge. This suggests the formation of new electronic states within the band gap of the polymer. Finally, the NEXAFS data indicate by the appearance of additional resonances, the formation of new states as a result of metal deposition. A detailed comparison of the precise interaction following the deposition of different metals on the polymers may help to explain why electroluminescence efficiency varies with the metal used and how to optimize the injection of charge into the material.

* EE, HR and YG were supported, in part, by the NSF Grant No. DMR-9303019 and the NSLS Faculty-Student Research Support Program. MWR was supported by USDOE Division of Materials Sciences under Contract DE-AC02-76CH00016

Photon stimulated desorption studies of mixed molecular solids * | U7A

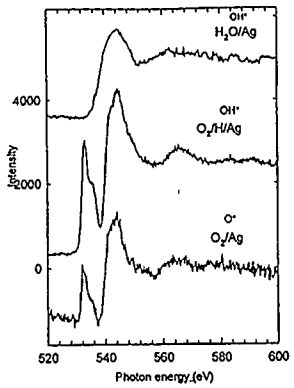
J. F. Moore, D. R. Strongin (SUNY Stony Brook), E. D. Johnson (NSLS), and F. M. Jacobsen (BNL)

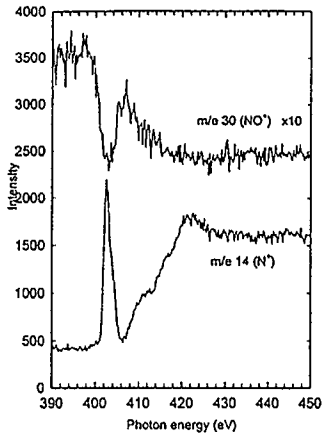
In this study we have investigated the photon-energy dependence of ion desorption from various mixtures of condensed species. Of particular interest were mixtures of hydrogen and oxygen (H and O_2), and oxygen and nitrogen (O_2 and N_2).

A hydrogen (H) covered silver surface at 4K was exposed to O_2 sufficient to generate O^+ ion signals in the time-of-flight detector. This detector consisted of a 2 cm drift tube terminating in a pair of microchannel plates. The drift tube was typically biased at -2kV with respect to sample ground, and its front mesh was positioned about 5mm from the sample surface. This arrangement allowed spectra to be collected with the VUV ring in single bunch operations. The flight time for H^+ was typically 65ns.

In the top figure, ion yield is shown as a function of photon energy for three systems: O^+ from O_2 and H on silver (bottom), OH^+ from the same surface (middle), and OH^+ from water-covered silver (top). This data clearly shows that the initial state of the ion in the mixed layer (O_2 + H) is the molecular oxygen, and that a concerted photoinduced reaction followed by desorption, is taking place.

Another fascinating result is seen when a multilayer mixture of N_2 and O_2 is studied by PSD. In the second figure, the N_2 desorption profile (bottom) follows the expected x-ray absorption profile in this energy range. However, the NO^+ yield (top) is seen to mirror the N_2^+, which can be explained if the N_2^+ yield becomes dominant above the K-edge absorption. It should be noted that the resolution in the top spectrum was considerably lower than the bottom, and the normalized intensity of N_2^+/NO^+ was about 50:1.





* This research is supported by the US Department of Energy under Contract number DE-AC02–76CH00016.

New developments in the deposition of silica from condensed reactants * | U7A, U7B

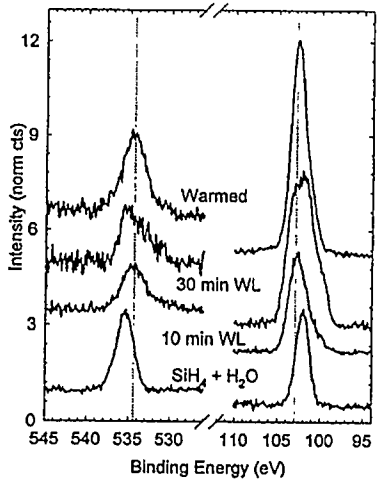
J. F. Moore, D. R. Strongin (SUNY Stony Brook), and M. W. Ruckman (BNL)

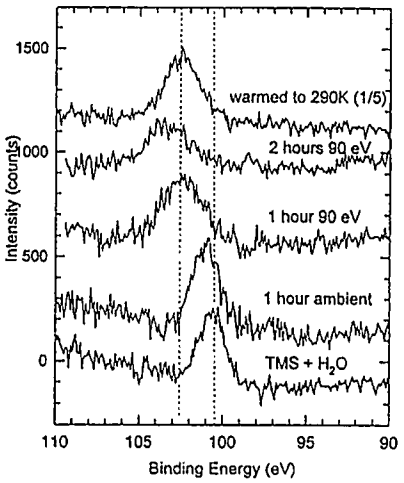
This work represents an extension of our research into the deposition of SiO_x and SiO_xH_y materials from molecular precursors that are excited by synchrotron radiation (SR). The current study demonstrates that condensed mixtures of silane (SiH_4) and water can be excited by zero-order SR (150<E<700eV) to form silica. We also show evidence for the formation of silica from tetramethylsilane and water mixtures exposed to monoenergetic (90eV) SR.

In all experiments, a clean silver film was evaporated onto a cooled cryostat (78K) in ultrahigh vacuum. The silver surface was then covered with multilayers of water mixed with either SiH_4 or TMS. The resulting sample was characterized with photoelectron spectroscopy and near-edge x-ray absorption fine structure (NEXAFS), followed by exposure to zero-order (SiH_4 case) or 90 eV (TMS case) SR. The samples were again characterized after warming to at least 200K to desorb unreacted material.

The left figure shows the mixture of SiH_4 and H_2O (bottom), and its exposure to 10 and 30 minutes of zero-order SR. In the left figure, the silicon 2p feature is seen to have shifted to 103eV binding energy, and the peak area ratio is close to SiO_2.

The right figure shows the progression of the Si 2p feature for the mixture of TMS and H_2O (bottom curve) during exposure to 90 eV SR from the U7B monochromator (~$5x10^{10}$ photons/cm^2 sec). After two hours exposure and a return to 300K, it is clear that an oxidized silicon solid has been formed. It is possible that in this case, the reaction is driven by photoelectrons from the silver valence band.





* This research is supported by the US Department of Energy under Contract Number DE-AC02- 76CH00016.

Water formation 4k from deuterium and oxygen mixtures excited by soft x-rays *	U7A

J. F. Moore, D. R. Strongin (SUNY Stony Brook), M. W. Ruckman, and Myron Strongin (BNL)

This research program is directed toward the study of reactions between mixed molecular species excited by the soft x-ray beam from the synchrotron. We have previously demonstrated growth of dielectric films at low temperature using these techniques, and this study was designed to clarify the mechanism of reaction using a simple system. Deuterium and oxygen were simultaneously dosed onto a clean silver surface at 4K, resulting in the growth of condensed solid D_2 and O_2. The first figure shows photoelectron spectra from this mixture before (bottom), and after exposures to the zerio order beam (10^{13} ph/cm^{2}sec) for the indicated times (upper three). The shift in binding energy for the O 1s peak indicates that the O_2 is being converted to D_2O. Two interesting points can be made based on these spectra; first, the reaction can apparently be driven selectively by the radiation, which suggests that there is not sufficient thermal energy to form products immediately upon irradiation. Second, there appears to be a steady state condition reached between 3.5 and 8.5 minutes. This may be due to decomposition of D_2O by the photons. In the second figure, the near-edge x-ray absorption fine structure (NEXAFS) spectra are shown for the same system as above. It is clear that the $\pi \rightarrow \pi^*$ resonance (first peak, bottom) becomes reduced upon irradiation, and the Rydberg-related features also change shape. The top curve shows the NEXAFS for a pure H_2O sample for comparison.

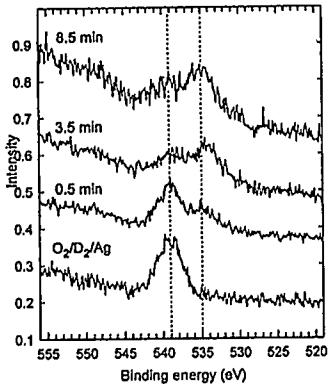


Figure 1.

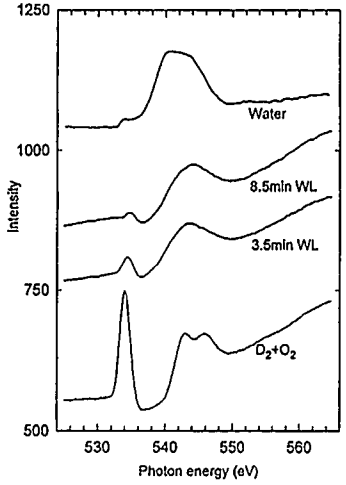


Figure 2.

* This research is supported by the US Department of Energy under Contract Number DE-AC02-76CH00016.

Determination of the water adsorption site on NiAl and FeAl(110) by photoemission spectroscopy. *	U7B

N. R. Gleason, S. Chaturvedi, D. R. Strongin (SUNY Stony Brook), and M. W. Ruckman (BNL)

This experiment is part of a study investigating the interaction of water with transition metal aluminides. The systems based on Fe and Ni are potential candidates as structural materials due to their high melting points and strength to weight ratios; however, these alloys are extremely brittle at room temperature. It is known that the FeAl system lacks ductility due to detrimental effects of H_2O in the environment. The overall goal of the study is to learn how water adsorbs and thermally decomposes on the (110) and (100) surfaces of NiAl and FeAl, while the objective of this experiment is to probe the affinity of H_2O for the Al or transition metal component at 120 K. Fig. 1a and 1b show the Al (2p) core level of NiAl and FeAl (110), respectively, after H_2O adsorption at 120 K and subsequent annealing while Fig. 2 shows the NI (3p) core levels for the same treatments. The most obvious result is that H_2O bonds to the Al component at 120 K, since the Ni core level shows no change while a new feature develops at high binding energy on the Al (2p) core level in each alloy. From work done at Stony Brook, it is known that H_2O adsorption is primarily dissociative on FeAl but is predominantly molecular on NiAl at 120K. This difference in the predominant species on the two surfaces at 120 K may account for the difference in the dosed spectrum in each panel of Fig. 1, since the induced shift on FeAl is larger than on NiAl. For each surface, heating to 173 K produces a new feature at ~75 eV, which is most likely due atomic oxygen on the surface or in the near sub- surface region, although the predominant species on the surface is $OH_{(ad)}$ as determined by vibrational spectroscopy. The feature at 73.5 eV observed on the FeAl surface at 173 K may be due to $OH_{(ad)}$, since this binding energy falls within the range observed for Al-hydroxides. There is no oxidation of the transition metal component, even after thermal treatment to 700 K.

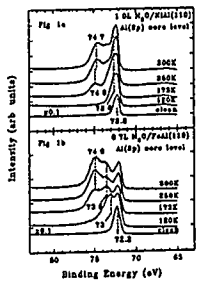


Figure 1.

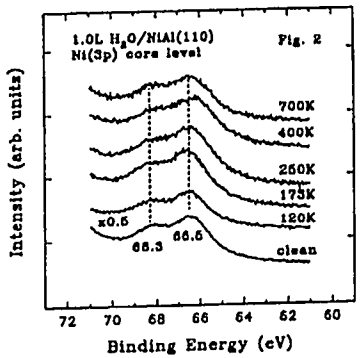


Figure 2.

* Work is supported in part by the National Science Foundation (grant DMR-9258544)

The quantum nature of oxidation — U7B

F. M. Jacobsen, M. W. Ruckman, and M. Strongin (BNL)

Low temperature oxidation and the limited growth of the oxide are well known phenomena. The best known example is probably aluminum on which the oxide can grow to a thickness of about 30 Å in air at 300 K. The present work was initiated in order to test an old theory by Mott on low temperature oxidation.

According to this theory once the first layer (sub-) oxide has been for further oxidation is promoted by electron tunneling from the metal to form oxygen ions on the initial oxide surface. This set up an electric field, E, which assists atomic motion at low temperatures. In the early stages of the oxidation process (the so-called fast oxidation regime) E is a local field related to the image potential and may be the driving force for place exchange of O^- ions with the underlying metal atom. In the later stage of the oxidation the oxygen ions reside on the oxide surface for sufficiently long time so that a collective potential, V, builds up across the oxide and lowers the activation energy for diffusion.

Fig. 1 shows photoemission spectra for clean Ta at 15 K and after various exposure to O_2. These results demonstrate clearly the development of distinct oxide species concluding with the formation of Ta_2O_5 (peak e) at a temperature where there is no thermal activation. In addition the Mott potential was observed to build up. The build up of this potential depends strongly on temperature and pressure. Fig. 2 shows that under similar conditions there is more oxidation at 77 K that at 300 K which is consistent with a Mott potential at 77 K, but not at 300 K. In this case we arrive at the somewhat strange conclusion that to speed up this chemical reaction the temperature should be lowered.

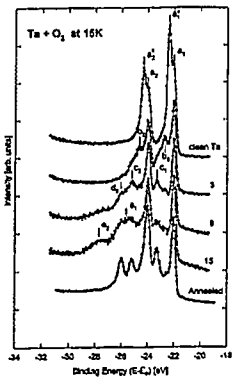


Figure 1.

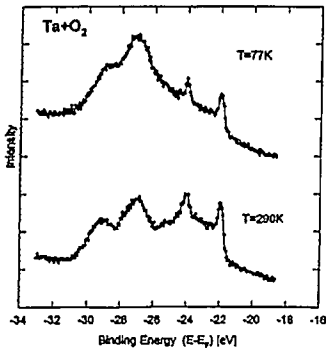


Figure 2.

The reaction of Cl_2 with GaAs(110) at elevated temperature — U8A

W. C. Simpson (Univ. Calif., Riverside and LBL), W. M. Tong (LBL), C. B. Weare (Univ.Calif., Riverside and LBL), D. K. Shuh (LBL), and J. A. Yarmoff (Univ. Calif., Riverside and LBL (Univ.Calif., Riverside and LBL)

The role of substrate temperature in the etching reaction of Cl_2 with GaAs(110) surfaces is studied with soft x-ray photoelectron spectroscopy (SXPS). Chlorine-based etchants are commonly used in the processing of GaAs-based devices, so it is important to understand the fundamental Cl-GaAs interaction. Previous work has shown that the surface can be etched by Cl_2 over a large temperature range. In this experiment, the surface product distribution is measured as a function of substrate temperature by collecting both core-level and valence band (VB) spectra from GaAs(110) wafers exposed to Cl_2 at various temperatures. Four representative VB spectra are shown below. The VB spectrum collected from a sample reacted at 300 K has a feature at $\sim$ 3.5 eV which is due to the presence of Cl on the surface. Following reaction at 500 K, a new VB feature is seen at $\sim$ 2.5 eV, and is tentatively identified as being due to elemental As adsorbed on the surface. The VB spectrum collected after reaction at 650 K is similar to that for the clean surface, showing no evidence of either Cl nor free As, despite the fact that the surface has been heavily etched. These results indicate that various etching reaction mechanisms are operative in the different temperature regimes.

[1] Chemical Science Division, Lawrence Berkeley Laboratory, Berkeley CA 94720.

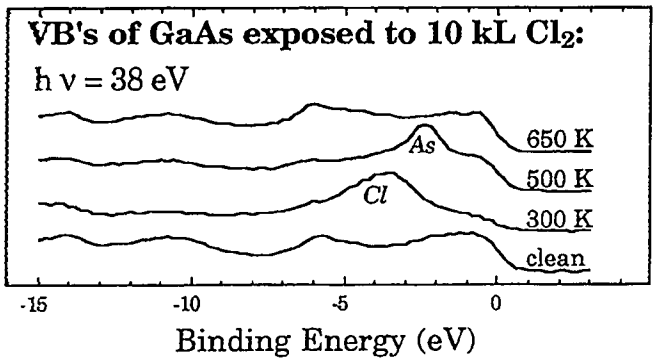


Figure 1.

An SXPS Study of the Reaction of GaAs with XeF_2 | U8A

W.C. Simpson, P.R. Varekamp and J.A. Yarmoff (UCR)

The reaction of atomic F (via XeF_2) with GaAs(110) wafers at room-temperature is studied with soft x-ray photoelectron spectroscopy (SXPS). In this reaction, both film growth and etching occur simultaneously in that the GaAs substrate is consumed to form a GaF_3 film while excess As is removed from the surface. The intermediate reaction products GaF, AsF and/or elemental As, as well as tricoordinate Ga and As atoms, are present at the GaF_3GaAs interface throughout the film growth process. The figures below show the Ga3d and As3d core levels collected from a 4 thick GaF_3 film grown on a GaAs(110) wafer via reaction with XeF_2. Note that the Binding Energy is given with respect to the substrate $3d_{5/2}$ component. The filled circles represent the background-subtracted raw data and the dashed lines are the chemically shifted components that contribute to the core-level intensity, as determined via numerical fitting.

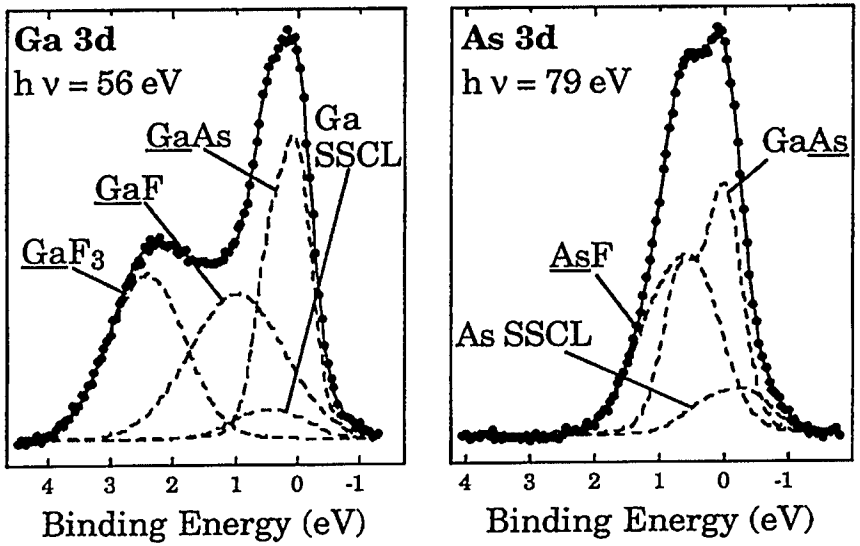


Figure 1.

F^+ PSD from LaF_3/Si(111) * | U8A

W. C. Simpson, C. B. Weare, and J. A. Yarmoff (Univ. of Calif., Riverside and LBL)

LaF_3 films are grown on Si(111) surfaces and studied with soft x-ray photoelectron spectroscopy (SXPS) and photon stimulated desorption (PSD) as part of an ongoing study of the role of bond ionicity in the stimulated desorption of positive halogen ions. Previous studies have shown that the degree of ionicity of the halogen-substrate bond is an important factor in determining whether cation or anion excitation leads to positive ion desorption via an Auger mechanism.[1] In covalently bonded systems, only anion excitations lead to direct ion desorption. For a system with highly ionic bonds, only cation excitations are found to cause direct ion desorption. Interestingly, both cation and anion excitations lead to direct ion desorption in systems of intermediate bond ionicity. LaF_3 films grown on Si(111) appear to fall into this category. A PSD spectrum collected from a thin film of LaF_3 grown on Si(111) is shown below, along with a total electron yield (TEY) spectrum collected from the same sample. Preliminary analysis of this and similar data suggests that, as in the case of F/Si and GaF_3/GaAs, both cation and anion excitation lead to F^+ desorption in this system.

[1] J.A. Yarmoff, V. Chakarian, T.D. Durbin, C.W. Lo, D.K. Shuh, W.C. Simpson, and P.R. Varekamp, in Proceedings of DIET-VI, Nucl. Instrum. Methods, in press.

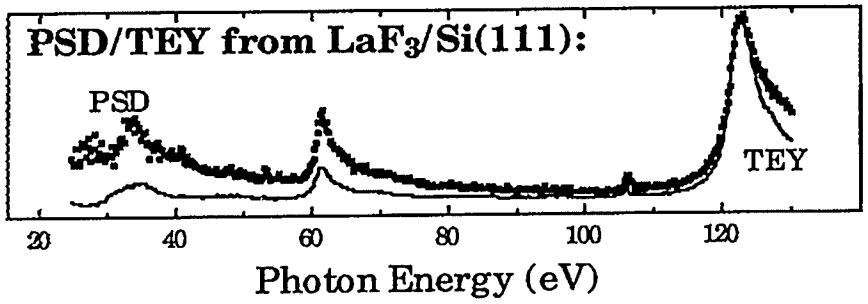


Figure 1.

* Acknowledgement is made to the Donors of the Petroleum Research Fund, administered by the American Chemical Society, for partial support of this research.

Examination of the domain structure of *E. coli* chaperone DnaJ * — U9B

John Flanagan (BNL)

The *E. coli* chaperone DnaJ appears to be a modular enzyme, containing at least three distinct structural and functional domains. To understand the structure and functional organization of DnaJ the protein has been genetically dissected into multiple overlapping fragments that can be expressed independently. Studies are currently underway to characterize the activity of each of these fragments. Structural studies are also being conducted, one component of which is the characterization of the structure and stability of each of the fragments by far UV-Circular Dichroism using the U9-beamline. An illustration of this is given in Figure 1, where the CD spectra DnaJΔ79 and DnaJΔ104 are shown. DnaJΔ79 corresponds to the so called DnaJ homology domain and is thought to play a role in the interaction between DnaK and DnaJ. DnaJΔ104 contains the DnaJ-homology domain and a C-terminal extension that has been shown to be important for the stimulation of the ATPase activity of DnaK by DnaJ. It is clear from Figure 1 that DnaJΔ104 contains some additional structure compared with DnaJΔ79 which may be important for the functional interaction between DnaJ and DnaK. The CD analysis when combined with additional structural and functional studies of DnaJ and fragments thereof may provide useful insight into the action of this chaperone protein.

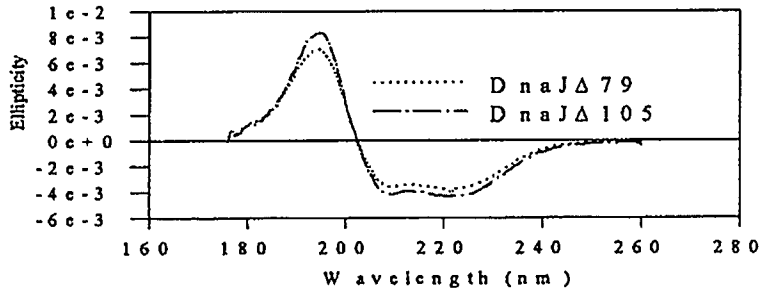


Figure 1. Comparison of the CD-spectra of DnaJΔ79 and DnaJΔ104 on a per-residue basis.

* This work is supported by the BNL Directed Research and Development Program No. 93-32.

Simultaneous resolution of spectral and temporal properties of uv and visible fluorescence using single-photon counting with a position-sensitive detector * — U9B

Lisa A. Kelly (NSLS, BIO), John G. Trunk (BIO), Krzysztof Polewski (Agricultural U., Poznan, Poland), and John C. Sutherland (BIO)

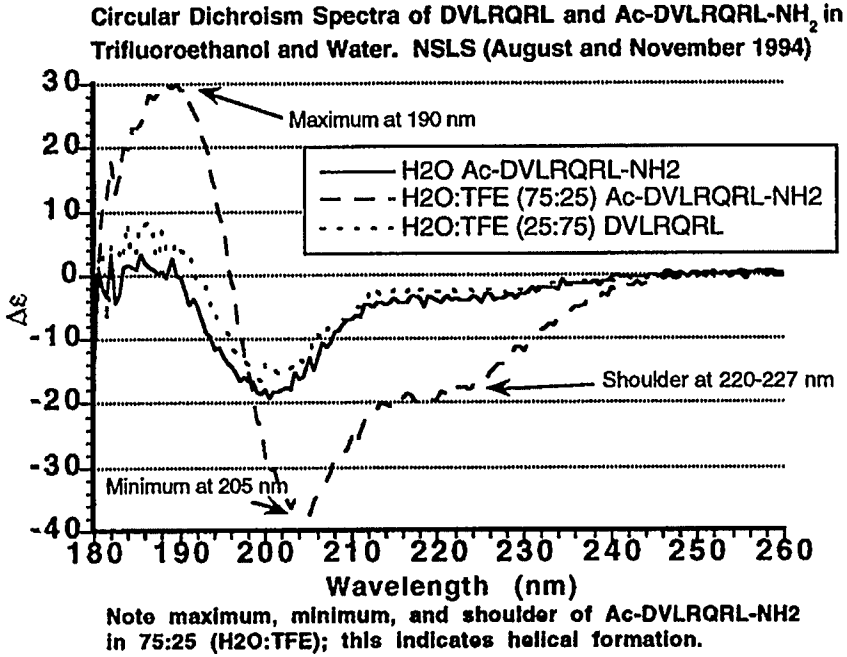
A new fluorescence spectrometer has been assembled at the U9B beamline of the National Synchrotron Light Source to allow simultaneous multi-wavelength and time-resolved fluorescence detection, as well as spatial imaging of the sample fluorescence. The spectrometer employs monochromatized, tunable UV and visible excitation light from a synchrotron bending magnet and an imaging spectrograph equipped with a single-photon sensitive emission detector. The detector is comprised of microchannel plates in series, with a resistive anode for encoding the position of the photon-derived current. The centroid position of the photon-induced electron cascade is derived in a position analyzer from the four signals measured at the corners of the resistive anode. Spectral information is obtained by dispersing the fluorescence spectrum across one dimension of the detector photocathode. Timing information is simultaneously obtained by monitoring the voltage divider circuit at the last MCP detector. The signal from the MCP is used as a "start" signal to perform a time-correlated single photon counting experiment. The analog signal representing the position, and hence wavelength, is digitized concomitantly with the start/stop time difference and stored in the two-dimensional histogramming memory of a multi-parameter analyzer.

* This work was supported by the U.S. Department of Energy, Office of Health and Environmental Research, and the Office of Energy Research. L.A.K. acknowledges the DOE Distinguished Post-Doctoral Fellowship Program, administered by the Oak Ridge Institute for Science and Education, for support.

Structural analysis of *Locusta migratoria* diuretic hormone *	U9B, U11

Thomas Nittoli and Scott McN. Sieburth(SUNY at Stony Brook)

Insect water balance, mediated by diuretic hormone, is a potential target for novel pest control methods. Peptide sequences for several diuretic hormones from insects have been determined and show a significant level of homology. The 46 amino acid sequence for the Locusta migratoria hormone has been compared to sequences in the Brookhaven Protein Databank. Several regions of the hormone have closely related sequences in the Databank and these were analyzed for their secondary structure. This analysis suggests that the hormone contains at least one region of an α-helix. This analysis was supported by the synthesis and study of this region of the hormone by circular dichroism (see Figure 1) and NMR.



* This research was made possible by a grant from the Herman Frasch Foundation (305-HF92).

A discharge flow-photoionization mass spectrometric study of FCO (X^2A') *	U11

T. J. Buckley, R. D. Johnson, III, R. E. Huie (NIST), S.-C. Kuo, Z. Zhang, R. B. Klemm (BNL)

Photoion efficiency (PIE) spectra were obtained for FCO radicals (Fig. 1) using discharge flow-photoionization mass spectrometry (PIMS). Fluorooxomethyl radicals were generated in the flow tube via the reaction sequence: $O+C_2F_4 \rightarrow CF_2O+CF_2$; $O+CF_2 \rightarrow FCO+F$. While small Franck-Condon factors prevented accurate determination of the first adiabatic ionization energy (IE) of FCO, the onset of the PIE spectrum at 127.80 nm (9.70 eV) reduced the upper limit of IE(FCO) substantially below the value of 10.47 eV reported in an earlier photoelectron spectroscopy (PES) study (Dyke et al., J. Chem. Soc. Faraday Trans. 2 77, 667, 1981); see Fig. 2. The vertical IE(FCO) evaluated from the PIE spectrum, however, is in good agreement with the PES value of about 11.2 eV. Calculations performed at the QCISD(T)/G-311+G(3df) level of theory yield the adiabatic IE(FCO) = 9.3 eV and the difference between vertical and adiabatic IE's of 1.85 eV; this leads to a calculated value for the vertical IE (11.15 eV). The latter is in good agreement with the experimental value (11.2 eV) and thus it provides a measure of confidence in the calulated value for the adiabatic IE (9.3 eV). This value for the IE(FCO) is slightly larger than previous theoretical results of 9.0eV (Sung and Lee, Bull. Korean Chem. Soc. 11, 511, 1990) and 8.98 eV (Krossner et al., J. Chem. Phys. 101, 3981, 1994); and it is substantially different from the value of 8.76 eV from the PES study, which was derived by extrapolation using observed and computed vibrational envelopes.

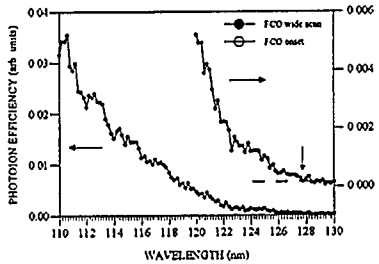


Figure 1. Photoion efficiency spectra of FCO in the wavelength range λ= 110–130 nm (solid circle) and in the onset region (open circle). Vertical arrow indicates the onset at 127.80 nm (9.70 eV). photoion efficiency is ion counts divided by light intensity in arbitrary units.

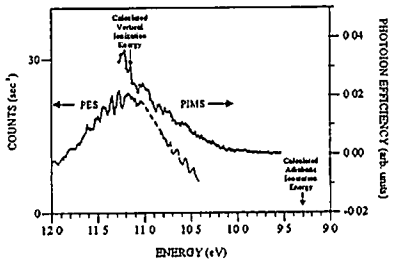


Figure 2. PIMS (this work) and PES (Dyke et al.) spectra of FCO. Vertical arrows indicate the calculated vertical ionization energy (11.2 eV) and the calculated adiabatic ionization energy (9.3 eV).

* This work was supported by the Division of Chemical Sciences, U.S. DOE, Washington, DC under contract No. DE-AC02-76CH00016.

Electronic spectroscopy of matrix isolated nucleic acid bases at 12 K *	U11

Lisa A. Kelly (NSLS, BIO), Krzysztof Polewski (Agricultural Univ., Poznan, Poland), Erik D. Johnson (NSLS), John G. Trunk, Denise C. Monteleone, John C. Sutherland (BNL)

The nucleic acid bases guanine and adenine, isolated in argon matrices at 12 K, were studied by absorption and fluorescence spectroscopy. Excited singlet state dynamics of the isolated bases were probed by time-correlated single-photon counting fluorescence. Emission and excitation spectra of the bases suggest that, in the low temperature noble gas matrices, multiple emitting electronically excited states are populated. Vibrational fine structure has been resolved in the lowest energy excitation band of matrix isolated guanine. The results represent enhancements in signal-to-noise ratio and spectral range (λ_{min} = 110 nm), as well as improved resolution in the excitation spectra, from the previously reported matrix-isolated guanine data.[1] The emission spectrum of matrix isolated adenine is shown to depend dramatically on excitation energy. Irradiation into the blue (267) nm) and red (285 nm) edge of the lowest energy absorption band produces electronically excited triplet and single states, respectively. The phosphorescence, excited by 267 nm, shows the characteristic structure observed in H_2O:ethylene glycol frozen glasses of adenine.[2] Alternatively, excitation at 170, 200, 220, and 285 nm produces a broad, structureless emission (λ_{max} = 445 nm), along with the characteristic fluorescence (λ_{max} = 330 nm). The emission from the former state was "delayed" with respect to the excitation pulse, and thus assigned to be an additional phosphorescence band. The singlet state lifetime of adenine was measured to be ca. 1.8 ns in the condensed matrix.

[1] Polewski, K.; Zinger, D.; Trunk, J.; Monteleone, D.C.; Sutherland, J.C., J. Photochem. Photobiol. B. 1994, 24, 169.

[2] Longworth, J.W.; Rahn, R.O.; Schulman, R.G., J. Chem. Phys. 1966, 45, 2930.

* This work was supported by the U.S. Department of Energy, Office of Health and Environmental Research, and the Office of Energy Research. L.A.K. acknowledges the DOE Distinguished Post-Doctoral Fellowship Program, administered by the Oak Ridge Institute for Science and Education, for support.

A discharge flow-photoionization mass spectrometric study of the $NO_3(^2A_2')$ radical: photoionization spectrum, adiabatic ionization energy and ground state symmetry *	U11

P. S. Monks, L. J. Stief (NASA/Goddard), M. Krauss (NIST), S. C. Kuo, Z. Zhang, and R. B. Klemm (BNL)

The photoion efficiency spectrum of NO_3 was measured over the region λ = 90-104 nm (Fig. 1). The nitrate radical was generated by the reaction F + HNO_3. The adiabatic ionization energy of NO_3, IE(NO_3), is determined to be (12.57±0.03) eV by the average of eight independent threshold measurements (Fig. 2A), corresponding to the $NO_3^+(^1A_1')$←$NO_3(^2A_2')$ transition, from maxima of energy derivative spectra (Fig. 2B). These direct ionization measurements are the first to be reported for NO_3. $\triangle_f H^\circ_{298}(NO_3^+)$ and proton affinity of NO_3 are derived using the ionization result from this work and literature values. CAS-MCSCF calculations were performed to optimize equilibrium D_{3h} and C_{2v} geometries for NO_3 ground state and three NO_3^+ states. The combined experimental and theoretical evidence suggests that the NO_3 ground state is in D_{3h} symmetry: (1) the intense, steep rise at threshold with no evidence of significant structure indicates that neutral and cation share the same symmetry; (2) calculations show unambiguously that the cation symmetry is D_{3h}.

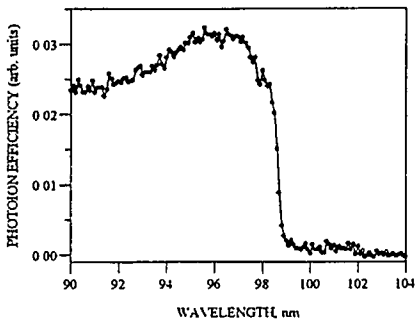


Figure 1. Photoion efficiency spectrum of NO_3 (m/z = 62) at a nominal resolution of 0.23 nm and 0.1 nm steps. Photoion efficiency is ion counts divided by light intesity in arbitrary units

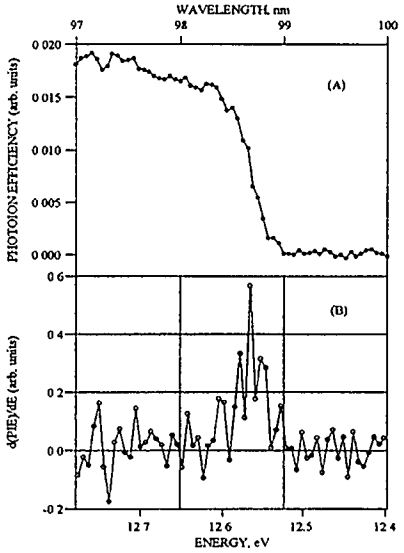


Figure 2. (A) photoion threshold region of NO_3 at a nominal resolution of 0.14 nm and 0.05 nm steps; (B) Energy derivative of (A). The maximum at λ =98.67_5 nm yields IE(NO_3)=12.56_5 eV.

* This work was supported by the Division of Chemical Sciences, U.S. Department of Energy, Washington, DC, under contract No. DE-AC02-76CH00016.

Vacuum ultraviolet circular dichroism of biopolymers * | U11

J. Trunk, D. Monteleone, and J. Sutherland (BNL), and E. Stevens (SUNY Binghampton)

We have adapted beamline U11 for the measurement of circular dichroism (CD) down to about 130 nm in the vacuum UV and measured the CD of a series of biopolymers supported on CaF_2 plates. These supports and the photoelastic modulator used in these experiments limited the spectral range to λ >130 nm. As a test of the ability of U11 to measure vuv CD, we recorded the spectrum of a film of heptamers of the amino acid norvaline cast from trifluoroethanol, as shown below. The analog time constants and digital integration periods used to record this spectrum are shown in the table.

These results indicate that CD experiments can be performed quickly and routinely on U11 down to about 130 nm, hence greatly facilitating the measurement of the CD of biologically important materials in the vuv.

starting λ (nm)	ending λ (nm)	analog time constant. (sec.)	digital period (sec.)
250	160	1	3
160	140	3	10
140	135	10	30

Figure 1.

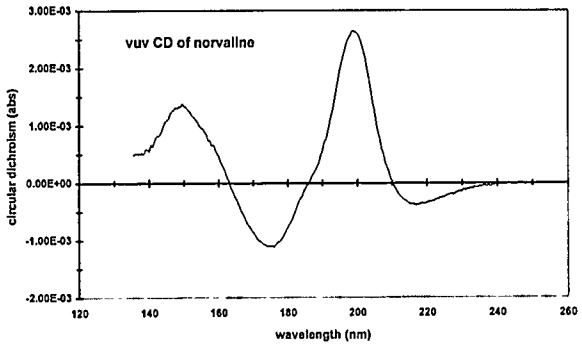


Figure 2.

* Supported by the Office of Health and Environmental Research, US DOE.

A discharge flow-photoionization mass spectrometric study of the $FO(X^2\Pi_i)$ radical: photoionization efficiency spectrum and ionization energy * | U11

Zhengyu Zhang, Szu-Cherng Kuo, R. Bruce Klemm (BNL), Paul S. Monks, and Louis J. Stief (NASA/Goddard)

Photoionization efficiency spectra of FO were measured over the wavelength range λ=80.0-100.0 nm (Fig. 1) using a discharge flow-photoionization mass spectrometer apparatus. FO was generated by the reaction $F(^2P) + NO_3$ and via a F_2/O_2 discharge. The adiabatic ionization energy of FO, IE(FO), was determined to be (12.78±0.03) eV from the photoion threshold (Fig. 2), corresponding to $FO^+(X^3\Sigma^-) \leftarrow FO(X^2\Pi_i)$, based on the average of ten independent measurements. This result, which is the first to be obtained by direct photoionization measurements, corroborates that of a photoelectron spectroscopy (PES) study, however, the spectra from which the present IE(FO) is derived are free from interferences due to other species which complicated the PES measurement. Using the results of this study and of a previous appearance energy measurement, $\Delta_f H^\circ_{298}(FO)$ was calculated to be 109.5±8.0 kJ mol^{-1}. A value for the proton affinity of FO, 511.5±10.0 kJ mol^{-1}, was also computed.

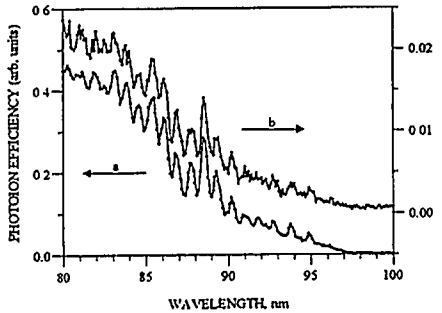


Figure 1. Photoion efficiency spectrum of FO (m/z =35) at a resolution of 0.23 nm and 0.1 nm steps. Photoion efficiency is ion counts divided by light intensity in arbitrary units. The FO radical was produced in (a) by F+NO_3 and in (b) by F_2/O_2 discharge.

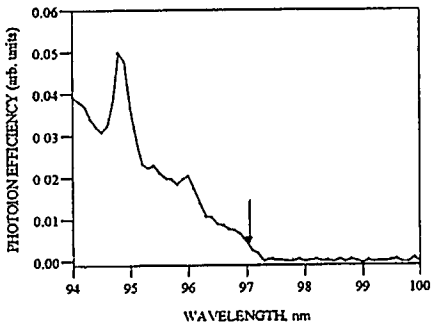


Figure 2. Photoion threshold region of FO at a resolution of 0.14 nm and 0.1 nm steps. The onset of ionization (indicated by arrow) at λ=97.05 nm yields IE(FO)=12.78±0.02 eV.

* This work was supported by the Division of Chemical Sciences, U.S. DOE, Washington, D.C., under contract No. DE-AC02-76CH00016.

Angle-resolved photoemission study of the Cs/Si(111)($\sqrt{3} \times \sqrt{3}$)R30°-B interface *	U12B

J. Chen (Univ. of Pennsylvania), H. H. Weitering (Univ. of Tennessee), and N. J. DiNardo (Drexel Univ.)

Our previous photoemission studies of the K/Si(111) ($\sqrt{3} \times \sqrt{3}$)R30°-B interface have shown that this interface is nonmetallic at room temperature (RT) saturation coverage [1]. A very prominent dispersionless surface state at ~0.7 eV below E_F was identified as the lower Hubbard band of a two-dimensional Mott-Hubbard system. This suggests that the interface might undergo a Mott transition if K would be replaced by a larger adatom.

Angle-resolved photoemission spectra were recorded at beam line U12B of the NSLS. Coverage dependent normal emission spectra of the Cs/Si(111)($\sqrt{3} \times \sqrt{3}$)R30°-B interface are shown in Fig. 1. Upon Cs deposition, an interface state shows up just below the Fermi energy. This state does not cross E_F until the work function Φ reaches a minimum.

Upon further Cs deposition at RT, this state crosses E_F and the interface becomes metallic. This observation is consistent with the appearance of a Doniach-Sunjic lineshape in the Cs 4d core-level spectra and with the disappearance of the excitation gap in the EELS [2]. Even though our results indicate that the size of the adsorbate atom is a crucial parameter in determining the ground state properties of these interfaces, the Cs–Cs distance at RT saturation coverage is 6.65 Å which is well below the critical density of a Mott transition [3].

[1] H.H. Weitering, J. Chen, N.J. DiNardo, and E.W. Plummer, Phys Rev. B 48, 8119(1993).
[2] J. Chen, H.H. Weitering, and N.J. DiNardo, to be published.
[3] A. Ferraz, N.H. March, and F. Flores, J. Phys. Chem. Solids, 45, 627 (1984).

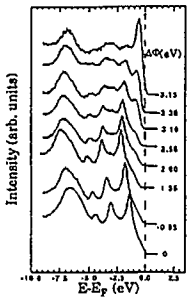


Figure 1. Normal emission spectra as a function of Cs coverage. $\Delta\Phi$is the corresponding work function change.

* This work was supported by the Division of Materials Sciences, U.S. DOE, under contract DE-AC05-84OR21400 with Martin Marietta Energy Systems, Inc.

Angle-resolved photoemission study of the Si(111)3×1-Li surface reconstruction *	U12B

Xiaorong Shi (Univ. of Tennessee), Hanno H. Weitering (Univ. of Tennessee and ORNL)

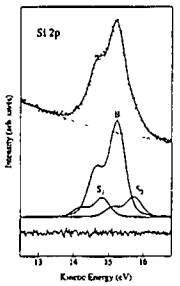
The alkalil metal-induced Si(111)3×1 reconstruction has received much attention recently. This surface reconstruction exhibits an extraordinarily large surface band gap of ~1 eV and is chemically passivated [1]. Recently, we proposed a structural model for this surface reconstruction [2]. A key ingredient of this model is the presence of fivefold Si rings, constituting quasi one-dimensional π-bonded chains along the [110] direction. These chains are separated by channels that can accommodate up to 1/3 monolayer of metal atoms.

Angle-resolved photoemission spectra of a single-domain Si(111)3×1-Li reconstruction were recorded at beamline U12B of the NSLS. Valence band spectra reveal the presence of a Li-induced surface state that disperses downward for wavevectors approaching the zone boundaries. The reconstructed surface is clearly nonmetallic.

Si 2p core-level spectra were recorded using a photon energy of 115 eV. To increase the surface sensitivity, spectra were collected at grazing exit angles. The Si 2p spectrum can be fit with one bulk (B) and two surface components (S_1 and S_2; see figure). The surface components have equal intensity. This result fully agrees with a recent high resolution Si 2p core-level study of the related Si(111)3×1-Na interface[3].

The dispersion of the filled surface state and the Si 2p core-level spectrum are very similar to that of the clean Si(111)2×1 surface [4,5] which is also a π-bonded chain reconstruction. We tentatively conclude that the present data are qualitatively consistent with the recently proposed π bonded chain model of the Si(111)3×1 reconstruction [2].

[1] D. Jeon et al, Phys. Rev. LEtt. 69, 1419(1992); [2] H.H. Weitering et al. Phys. Rev B 49, 16837 (1994); Rapid Communication; [3] J.J. Paggel et al., J. Vac. Sci Technol. B11, 1439 (1993); [4] R.I.G. Uhrberg et al., Phys Rev. Lett 48, 1031 (1982); [5] F. J. Himpsel et al., in Photoemission and Absorption Spectroscopy of Solids and Interfaces with Synchrotron Radiation, Proceedings of the Enrico Fermi School, Ed. M. Campagna and R. Rosei (North Holland, Amsterdam, 1990), p. 203.



* This work was supported by the Division of Materials Sciences, US DOE, under contract DE-AC05-84OR21400 with Martin Marietta Energy Systems, Inc.

High resolution XPS study of the electronic structure of defects in the quasi-one dimensional conductor $K_{0.3}MoO_3$ *	U13UA

Klaus Breuer, Kevin E. Smith, Martha Greenblatt, William McCarroll and Steve L. Hulbert

The goal of our research is to understand the electronic properties of quasi-one dimensional (1D) oxide conductors [1]. These are ternary transition metal oxides that exhibit 1D physical phenomena including charge density waves (CDW) and Peierls transitions. We have undertaken both ARP and core level measurements of the energies. This is due to the transition of the surface to electronic structure of these oxides [2]. Current efforts are aimed at measuring electronic structure changes during the Peierls transition, and $K_{0.3}MoO_3$ is the first oxide studied since the transition occurs at an accessible 180 K. We have discovered that $K_{0.3}MoO_3$ is extremely sensitive to defects produced by photon stimulated desorption (PSD) and ion bombardment [3]. PSD creates only O vacancies, while ion bombardment leads to both K and O vacancies. The latter mechanism results in the initial removal of K atoms, causing the surface to become less metallic, with the subsequent removal of O atoms reducing the surface, and causing it to become more metallic. Investigating the role of defects in modifying Fermi surfaces and charge density wave transport in these systems is a major thrust of our program since a low density of defects pins the CDW and alters the temperature of the Peierls transition, while a large density of defects destroys the CDW state entirely. Fig. 1 presents high resolution core level spectra of the Mo 3d emission from a) cleaved $K_{0.3}MoO_3$, b) a low defect density surface, and c) a high defect density surface [4]. Defects were created by Ar^+ ion bombardment. As is clear, a low density of defects causes a shift of the emission to higher binding energies. This is due to the transition of the surface to a less metallic phase following the removal of K atoms, since the metallic screening of the emission is reduced. This explanation for the shift is supported by a reduction in the asymmetric line shape associated with metallic screening (Doniach-Sunjic). As O vacancies are created, the surface becomes metallic again, and Fig 1c shows a shift to lower binding energies and the reappearance of the metallic screening asymmetry due to a reduction of the surface to almost MoO_2. The metallic screening is entirely due to electron-hole pairs at E_F, which must reside in the quasi-1D Mo 4d states. Thus analysis of the screening of the Mo 3d emission will allow us to probe the electronic structure at E_F in a manner complimentary to our ARP measurements.

[1] K.E. Smith, Ann. Rep. Prog. Chem. C 90 (in press). [2] K.E. Smith, K. Breuer, M. Greenblatt, and W. McCarroll, Phys. Rev. Lett. 70, 3772 (1993). [3] K. Breuer, K.E. Smith, M. Greenblatt, and W. McCarroll, J. Vac. Sci. Technol. A 12, 2196 (1994). [4] K. Breuer, K.E. Smith, M. Greenblatt, W. McCarroll, and S.L. Hulbert, Phys. Rev. B (submitted).

Figure 1. Mo 3d emission from $K_{0.3}MoO_3$. a), cleaved, b)low defect density, c) high defect density. [Figure unavailable due to space constraints.]

* Work supported in part by the Petroleum Research Fund, administered by the ACS.

The XANES spectroscopy of biological calcium phosphates using the high resolving power U13UA beamline	U13UA

C. J. Buckley, S. J. Bellamy (King's College London), X. Zhang (SUNY Stony Brook), G. Dermody (King's College London), and S. Hulbert (BNL)

The absorption cross-section of a number of biological calcium salts has been assessed at the calcium L edge by measuring the total electron yield (TEY) at the high resolving power ($\approx$ 4000) NSLS U13UA beamline[1]. The TEY signal was used because of distortions introduced to spectra by instrumentation when using the transmitted signal. The TEY signal was normalised to the incident beam using the signal from a new silicon nitride foil beam monitor shown schematically in figure 1. This beam monitor was calibrated, by simultaneously measuring its signal and that from a solid state diode[2].

Samples were mounted on copper tape and the absorption spectra were taken for calcium fluoride (CaF_2), calcium hydroxy apatite ($Ca_{10}.(PO_4)_6.(OH)_2$, calcium pyrophosphate ($Ca_2.P_2.O_7$. $2(H_2O)$), and calcium whitlockite ($Ca_3.(PO_4)_2$) - which may contain up to 10%Mg.

The latter two calcium salts were chosen for study because calcium pyrophosphate is the mineral phase responsible for the break up of cartilage in the osteo-arthritis disease, and calcium whitlockite is a mineral phase found in healthy and diseased cartilage which may be a precursor to the onset of osteo-arthritis[3]. Differences were observed in the vicinity of the minor peaks located around 348.1 eV and 351.4 eV[3]. This suggests that imaging a cartilage specimen containing both of these mineral phases at these and adjacent energies in a scanning x-ray microscope could lead to the spatial differentiation of the two phases. This may add valuable information to the study of the initiation and development of the disease. Future experiments will repeat these measurements with an improved signal to noise ratio.

[1] C. Buckley et al., Rev. Sci. Inst. due for publication in Feb. 95.
[2] The diode used for I_o calibration was an IRD AXUV-100 absolute silicon photodiode.
[3] C.A. Scotchford et al., J. Anat. 181, 293-300, (1992)

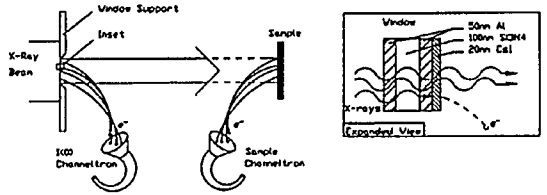


Figure 1. Schematic of the incident flux monitor installed on U13UA

Fluorescence yield x-ray absorption near edge structure (XANES) spectroscopy at the nitrogen and oxygen k-edges with a parallel plate proportional counter *	U13UA

T. Crowder and H. Ade (North Carolina State Univ.)

We designed and commissioned a parallel plate proportional counter for the detection of fluorescent photons. The parallel plate design allows operation at higher count rates than the traditional single wire counter, which can be an important consideration at high flux beamlines. Previous proportional counters[1] have utilized stretched polypropylene windows in a differentially pumped arrangement. We have utilized a silicon nitride membrane as a window, due to its heigh transmission to nitrogen fluorescent photons as well as for the simplicity it lends to the vacuum requirements. The window can support a pressure differential of one atmosphere and has very low gas leakage. A fluorescence yield x-ray absorption experiment has been performed to test the capabilities of the detector. While the detector is not yet optimized, it is already capable of acquiring usable XANES spectra at a fraction of the capital cost of an electronic detector. For a PMDA-ODA polyimide sample with a 22:2:5 atomic ratio of C:N:O, the detector has presently a signal to background ratio of 1.5, and 15 at the nitrogen (Fig. 1) and oxygen edges (Fig. 2), respectively. The angular dependence of the resonances observed will allow us to determine and correlate the orientation of PMDA and ODA group in the bulk and at the surface by monitoring the fluorescent and electron yield, respectively.

[1] D.A. Fischer, J. Colbert, J.L. Gland, Rev. Sci. Instrum. 60,1696(1989). [2] J.L. Jordan, J.F. Morar, G. Hughes, R.A. Pollack, and F. J. Hipsel, NSLS Annual Report, BNL 984, 125.

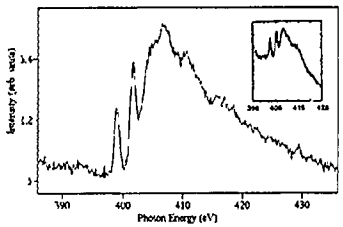


Figure 1. Nitrogen K-edge XANES spectrum for polyimide. The inset shows an electron yield spectrum [2] for comparison. The first two peaks are transitions from the nitrogen 1s to the π^*system of the ODA rings. Total acquisition time was 11 min. Entrance and exit slits were set to 10μm each, which could have been opened significantly for more flux.

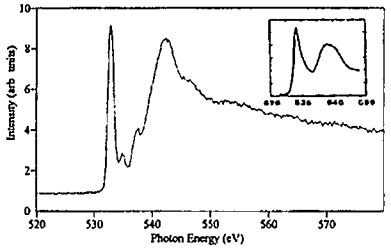


Figure 2. Oxygen K-edge XANES spectrum for polyimide. The inset shows an electron yield spectrum of a spin deposited sample from Jordan et al.[2] The first peak is the π^* resonance of the carbonyl group in the PMDA ring. The second two peaks are π^* resonances from transitions of the ether oxygen in the ODA ring to the ODA π^* system.

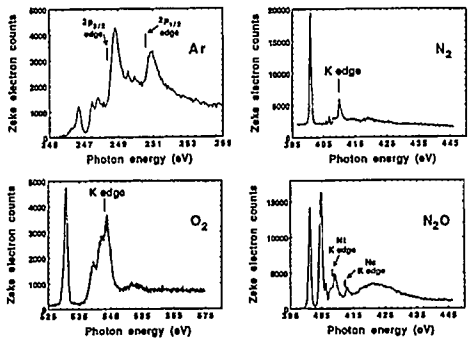
* We gratefully acknowledge S. Hulbert, E. Johnson and G. Smith for their assistance.

Zero kinetic energy electron spectra of core excited Ar, N_2, O_2, and N_2O based on a transverse velocity discrimination technique *	U13UA

K. Lee, D. M. Hanson (SUNY Stony Brook), S. L. Hulbert (NSLS), and P. Kuiper (BNL)

Core excitation zero kinetic energy (ZEKE) electron spectroscopy in the literatures so far has resorted to the time-of-flight technique to isolate the zero energy electrons. When using a storage ring x-ray source, this approach generally requires that the experiment be performed in the single bunch mode to avoid the overlap of electrons from different pulses, resulting in a reduced acquisition rate. In this report a transverse velocity filter consisting of an array of collimating holes sandwiched by two grids was adopted to obtain the ZEKE electron spectra. This kind of spatial filter obviates the need of the single bunch mode operation, hence fully utilizing the available duty cycle of the storage ring.

The ZEKE electron spectra of Ar in its L edge, and N_2, O_2, and N_2O in their K edges are presented below. In general, below the K (or L) edges, the ZEKE spectra mimic the absorption spectra, and above the K (or L) edges, the ZEKE spectra extend far into the continua. In each of these, the landscape is composed of ZEKE electrons deriving from assorted excitation and decay processes, such as threshold photoelectrons, electrons resulting from double photoionization, and electrons from multiple or cascade Auger/Coster-Kronig decays.



* Research supported by the National Science Foundation (CHE-8921729) and the U.S. Department of Energy (DE-AC02-76CH00016)

Auger, zero-energy photoelectron coincidence spectroscopy (Azepeco): chemical-site-selective auger electron spectroscopy *	U13UA

K. Lee (SRRC, SUNY Stony Brook), S. L. Hulbert (NSLS), P. Kuiper (BNL), D. Ji, and D. M. Hanson (SUNY Stony Brook)

The Auger electron spectrum associated with decay of a core-hole on the terminal nitrogen and that associated with the central nitrogen of nitrous oxide, N_2O, are obtained individually through the use of a coincidence technique. Specifically, each of the two Auger electron spectra is obtained by detection of Auger electrons in coincidence with near zero energy (threshold) photoelectrons at their peak close to the respective K shell ionization thresholds. These zero energy electrons serve to identify the core-ionization continuum associated with the different Auger electrons. In each of the two sets of spectra below, the top panel is the ordinary (non-coincidence and composite) Auger electron spectrum, whereas the lower panel displays the true coincidence Auger electron spectrum (with error bars) and a simulated spectrum (smooth curve) based on the theoretical calculations of Larkins [1], with which the salient features of the experimental spectra are in good agreement. These data are believed to be the first examples of chemical-site-selective molecular Auger spectra.

[1] F.P. Larkins, J. Chem. Phys. 86, 3239(1987).

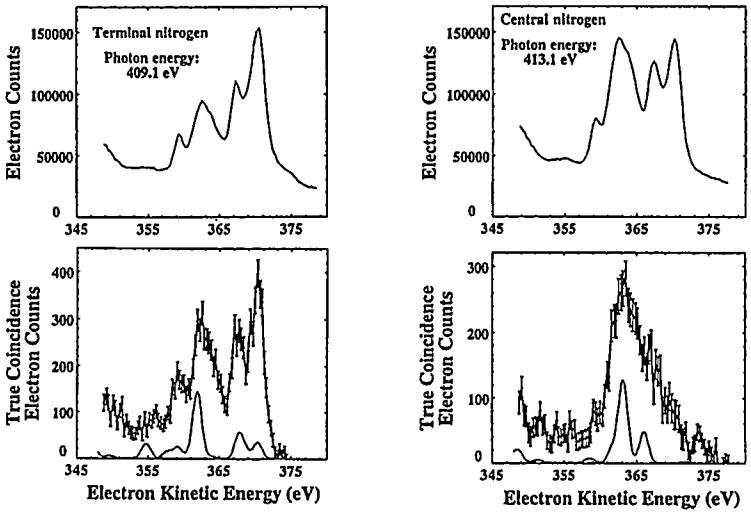


Figure 1.

* Research support by the National Science Foundation (CHE-8921729) and the U.S. Department of Energy (DE-AC02- 76CH00016).

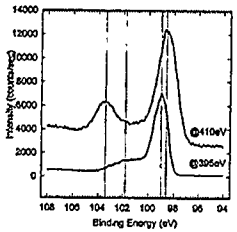
Monoenergetic soft x-ray driven growth of boron nitride films on silicon *	U13UA

J. F. Moore, Sanjay Chaturvedi, D. R. Strongin (SUNY Stony Brook), and Myron Strongin (BNL)

The growth of ultrathin BN films from condensed mixtures of B_2H_6 and NH_3 on silver was previously demonstrated with the zero-order beam from a bending-magnet beamline (U7A). In the current study, BN films were grown on silicon using various energies (90<420 eV) from the U13UA monochromators. One goal of this work is to observe the effect of electron yield changes in the growth rate, particularly around absorption edges in the substrate. We are also interested in the effect of different growth conditions (that is, direct photon excitation versus substrate-electron mediated excitation) on the properties of the deposited materials.

A silicon wafer was sputtered and annealed to provide a clean substrate with a sharply-defined L_{II-III} edge. This was then cooled in a UHV environment to 80K and exposed to a gaseous mixture of B_2H_6 and NH_3 sufficient to condense 100Å onto the Si. Once the near-surface region was characterized with photoelectron spectroscopy (using minimal flux from U13UA), the sample was exposed to about $2x10^{12}$ photons/cm^2 sec for 30 minutes to excite the reaction between the two species that leads to film growth. Although there were some differences in growth found at different energies, it was not possible to exclude changes in dosing reproducibility (ratio of reactants, thickness) between the experiments. Preliminary results suggest, however, that valence excitation of either the reactants or the substrate may be the most significant pathway to growth under these conditions.

The figure shows a considerable change in the interface structure when photons of energy below and above the nitrogen K- edge are used. In the bottom curve, the silicon at the interface of a BN film grown using 395eV is predominantly elemental (99eV), with a weak feature at 102eV indicating some Si-N or Si-B bond formation. The top curve shows the corresponding spectrum for an interface grown at 410eV, where there may be some localized excitation at the N atoms. In this case, there is a strong feature at 103.5, which is the position for fully nitrided silicon, Si_3N_4. We believe that the above-edge excitation may be breaking up residual N-H bonds and causing the desorption of hydrogen. This would then free the N terminated species to form a bond with the Si surface.



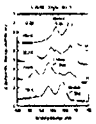
* This research is supported by the US Department of Energy under Contract Number DE-AC02-76CH00016. We thank S. Hulbert for assistance in using U13UA.

Adsorption and reaction of methylthiolate on Ni(111) * | U13UA

D. R. Mullins and D. R. Huntley (ORNL)

Methanethiol (CH_3SH) and dimethyldisulfide (CH_3S-SCH_3) react with Ni(111) at 100 K to form methylthiolate (CH_3S-). The S 2p core level spectra from 0.25 ML of methylthiolate changes as the temperature is increased. At 150 K only one S 2p doublet is observed which is assigned to methylthiolate adsorbed in a two-fold bridge site. At 250 K there is a decrease in the intensity at the original methylthiolate position accompanied by the appearance of two states at lower binding energy and one state at higher binding energy. The two lower binding energy states are assigned to emission from atomic sulfur and indicate cleavage of the C-S bond. The relative intensity of the higher binding energy atomic S state correlates with the amount of atomic C on the surface as observed in the C 1s spectrum. The highest binding energy S 2p state is assigned to methylthiolate that has moved from a two-fold bridge site to a three-fold hollow site. This assignment is based upon an apparent correlation between binding energy and adsorption site that we have observed on other surfaces and is consistent with vibrational spectra [1] and theoretical calculations [2]. The methylthiolate in the high coordination site is much more stable than the low coordination site species and decomposes near 300 K. The spectrum at 400 K is dominated by atomic S influenced by atomic C. Three distinct methylthiolate states can be identified in the S 2p spectra at 100 K as a function of methylthiolate coverage. A single state occurs below 0.1 ML and is joined by a second state at lower binding energy when the coverage reaches 0.15 ML. At 0.25 ML the low coverage state disappears. A third state at a still lower binding energy is evident at 0.30 ML. The methylthiolate observed at the lowest coverage decomposes at a lower temperature than the species observed at higher coverages. All of these states are believed to result from thiolates in bridge adsorption sites. Their binding energies are much lower than the binding energy of the high coordination state that is formed near 250 K. Because the transition between these states occurs as a function of coverage and not temperature, crowding may be influencing the peak position. At the lowest coverage the methylthiolate adsorbates are able to spread out. As the coverage increases the adsorbate density also increases and thiolate-thiolate interactions may become important. Interactions along domain boundaries and the orientation of the C-S bond must also be considered.

[1] T. S. Rufael, D. R. Mullins, J. L. Gland and D. R. Huntley, J. Phys. Chem., Submitted. [2] H. Yang, T. C. Caves, J. L. Whitten and D. R. Huntley, J. Am. Chem. Soc. 116 (1994) 8200.



* Research sponsored bythe Division of Chemical Sciences, Office of Basic Energy Sciences, U.S. Department of Energy under contract DE-AC05-84OR21400 with Martin Marietta Energy Systems, Inc.

Reaction kinetics of thiolate intermediates on Ni(111) * | U13UA

D. R. Mullins and D. R. Huntley (ORNL)

Methanethiol, CH_3SH, and Benzenethiol, C_6H_5SH, react with Ni(111) at 100 K to form thiolate intermediates, RS-, which undergo C - S bond scission leading to desorbed hydrocarbons (methane or benzene) or total decomposition producing S, C and desorbed H_2. The cleavage of the C - S bond can be monitored through the intensity of peak associated with atomic S in the S 2p core level photoemission spectrum. Methylthiolate exhibits an additional reaction pathway not observed in the decomposition of benzenethiol. The thiolate produced at 100 K can convert from a bridge adsorption site to a hollow adsorption site. This process can also be monitored in the S 2p spectrum through a peak associated with the thiolate in the hollow site. The intensities of these two reaction products, atomic S and methyl thiolate in a hollow site, have been recorded as the sample temperature is increased at 1 K/sec. The signal from the thiolate in the hollow site starts to increase around 200 K, peaks around 260 K and then drops back to its initial level by 340 K. The atomic S signal starts to increase around 240 K, levels off around 260 K and increases again around 290 K. The first increase in atomic S results from the cleavage of the C - S bond in the bridge - bonded thiolate. The second increase stems from decomposition of the hollow site thiolate. At a lower coverage of CH_3S- (<.1 ML), the atomic S signal starts to increase at ca. 150 K, indicating a coverage dependence in rate of C-S bond cleavage. There is very little hollow site thiolate formed.

The S 2p intensity can also be monitored as a function of time at constant temperature as shown in order to determine the rate of decomposition at different temperatures. The decomposition of C_6H_5S- is modeled better using a second order rate law than a first order rate law implying that adsorbed H may be involved in the reaction mechanism. An Arrhenius plot of the rate constants indicates that the activation energy for C - S bond scission is on the order of 10 kcal / mole which is lower than one might expect for surface reactions occurring near 250 K. A similar analysis of the decomposition of $CH3_S$- has not yielded reasonable results, possibly due to the complexity resulting from competing reaction pathways.

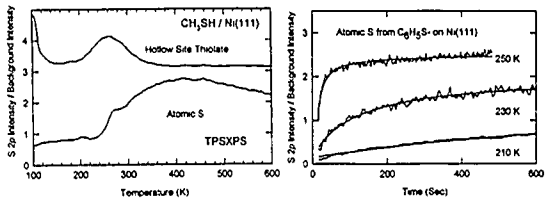


Figure 1.

* Research sponsored by the Division of Chemical Sciences, Office of Basic Energy Sciences, U.S. Department of Energy undercontract DE-AC05-84OR21400 with Martin Marietta Energy Systems, Inc.

Spin Resolved Iron Surface Density of States *	U13UA

B. Sinkovic and E. Shekel (NYU), S. Hulbert (NSLS)

We have performed the first angle-integrated spin polarized valence band photoemission from a ferromagnet in order to measure directly Spin Resolved Density of States (SRDOS). The full Brillouin zone averaging in photoemission was achieved by employing soft X-ray radiation and a well-characterized polycrystalline sample. The experiments were carried out using a newly constructed electron energy and spin analyzer employing a version of the NIST low-energy spin detector mounted on the exit lens of a commercial (100mm radius) hemispherical analyzer with $\pm 6°$ angular acceptance cone. Linearly polarized soft x-ray light was provided by the U13UA wiggler beamline. The overall energy resolution was 0.75 eV. Fig. 1 shows valence band Spin-Resolved Photoemission Spectra (SPPES) of a polycrystalline Fe film taken at 260eV photon energy. The majority-spin spectrum exhibits larger spectral weight than the minority-spin spectrum and an average exchange splitting of $\approx$2.0 eV. These spectra agree qualitatively with the calculated SRDOS of ferromagnetic bcc Fe, also shown in Fig. 1, indicating the angle-integrated photoemission experiments are capable of measuring the true SRDOS. However, small quantitative differences between SRDOS and SPPES exist, which cannot be reconciled by any photoemission effect (instrumental broadening, matrix elements, lifetime broadening) or sample condition. They are, on the other hand, well accounted for by the contribution of surface DOS to the photoemission spectra. Simple subtraction of bulk SRDOS from the SPPES spectra yields surface SPPES "spectra" (see Fig. 2) which are consistent with the main features of the calculated surface SRDOS of both Fe(001) (see Fig. 2) and Fe(110) surfaces. The deduced surface spin polarization of $40\pm3\%$ represents $20\pm10\%$ enhancement compared to bulk values at room temperature, which is in qualitative agreement with enhanced surface magnetization predicted for both Fe(001) and Fe(110) surfaces.

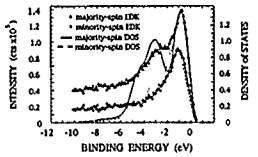


Figure 1. Majority-spin ($\triangle$) and minority-spin ($\diamond$) Fe valence band photoemission spectra (hv=260 eV) from a polycrystalline Fe film, and calculated majority-spin (—) and minority-spin (- - -) densities of states of ferromagnetic bcc Fe. The DOS have been convoluted with a 1.0 eV FWHM Gaussian representing the experimental resolution and are scale

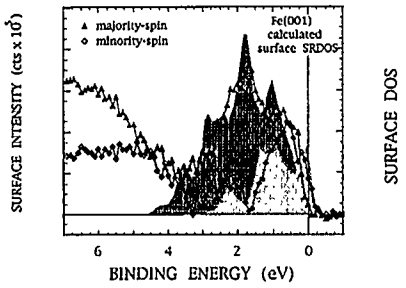


Figure 2. Majority-spin ($\triangle$) and minority-spin ($\diamond$) difference spectra obtained by subtracting the calculated Fe bulk DOS from the measured photoelectron spectra (Fig. 1). Calculated surface Fe(001) majority (dark shading) and minority (light shading) DOS.

* NYU Research Challenge Grant No. 5-201-396 and Div. of Mater. Sci., U.S. DOE, contract # DE-AC02-76CH00016.

Extreme ultraviolet projection lithography *	U13UB

R. Freeman, J. Bjorkholm, L. Eichner, L. Fetter, M. Himel, B. LaFontaine, A. MacDowell, Z. Tan, D. Taylor, D. tennant, S. Vaidya, W. Waskiewicz, D. White, D. Windt, O. Wood II (AT&T Bell Labs.), S. Spector (Stony Brook), T. Jewell (TJ Optics), J. Kortright (LBL)

The goal of this project is to evaluate the feasibility of extreme ultraviolet projection lithography (EUVL) at the sub tenth micron level. Recent results include the following.

1. Demonstrated sub-micron real time spatial imaging of patterned 14nm radiation using a commercially available doped yttrium aluminum garnet (YAG) single phosphor crystal. This class of phosphors emit visible light. Being a single crystal the light is not scattered which is the case for phosphor powders. The light can be collected by a visible light microscope objective and relayed to CCD detector for real time viewing on a TV monitor. The figure below shows the EUV image at the image plane of our 20× Schwarzschild camera operating at 14nm. The image is tht of fluorescent visible light from a doped YAG type single crystal placed at the image plane of the camera. Groups of single lines of dimensions 0.5μm, 0.3μm, 0.1μm, 0.2μm and 0.4μm are resolved, although the 0.1 μm line is only resolved to a resolution of 0.2μm as limited by the Raleigh criterion of the visible light optics of the microscope. The bright area to the left of the image is a tear in the Silicon membrane mask. We note that the YAG phosphor appears to work when illuminated with x-rays of shorter wavelength and could provide the basis for sub-micron imaging in the harder x-ray regime.

2. Established single level resist exposure simulations for wavelengths of 37.5nm, 13.9nm, and 6.8nm. This work is based on resist exposures at these wavelengths where the measured resist sidewalls were 19, 60, and 87 degrees respectively for the above wavelengths. The resist sidewall angle is related to the photon absorption depth, the lower the photon absorption the steeper are the resist side walls. Near vertical resist side walls are required in order to achieve critical dimension control of features to be printed in lithography. This work indicates that a single layer resist scheme is unlikely to work at 13.9nm due tot he sloping resist sidewalls. Continuing to operate at 13.9 nm will require the development of a multilevel resist scheme.

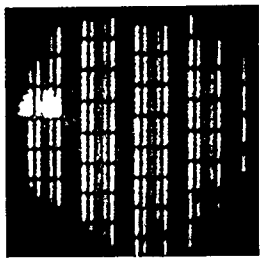


Figure 1.

* Supported in part by AT&T and NIST under ATP Coop Agreement No. 70NANB1H115.

Atomic-site-selective solid-state photochemistry in matrix isolated N_2O using monochromatic soft x-rays	U15

S. Sambasivan, J. Glatthaar, S. Y. Chiang, S. L. Anderson, and D. M. Hanson (SUNY Stony Brook)

Atomic-site selective photochemistry of N_2O, benzaldehyde, and cyanobenzene in Ne and D_2 matrices was studied. The photochemistry induced following the excitation or ionization of the 1s core electrons of N and O in the target molecules was monitored in situ by Fourier transform infrared spectroscopy (resolution 1 cm^{-1}). We were able to examine the effects of the atomic core-hole site, x-ray energy, and matrix environment on the radiolysis efficiency and decomposition pathways. For instance entirely different photoproduct distribution were obtained for N_2O isolated in D_2 compared to Ne matrices, see figure. In the Ne matrix, large amounts of nitrogen oxides and ozone formation were observed; whereas, in the D_2 matrix formation of D_2O and OD complexes were seen predominantly. The ratios of photoproducts show effects of atomic excitation site (i.e. N or O) and an X-ray energy dependence, see figure. We observed no photoproduct formation in irradiating the N_2O at 380 eV, which is below the nitrogen core electron resonances.

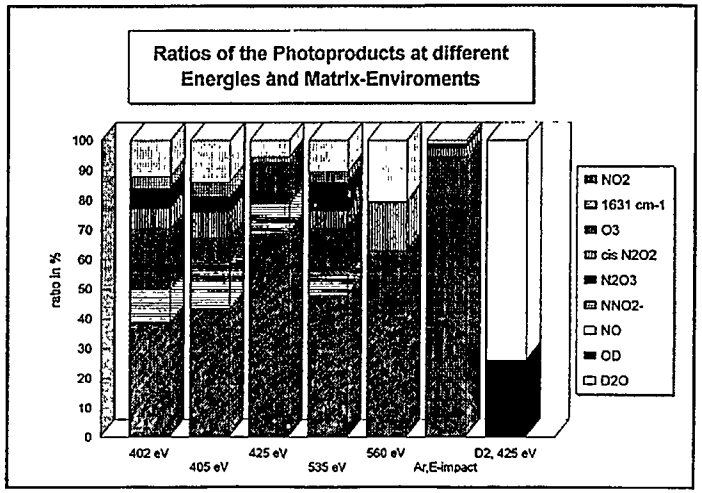


Figure 1.

ABSTRACTS

X-Ray Beamlines

Beamline X1A

Characterization of an aromatic liquid crystalline polyester B-22
H. Ade (North Carolina State Univ.), B. Wood, and I. Plotzker (Du Pont)

Quantitative mapping of calcium using XANES and continuum spectral features B-22
C. J. Buckley

Imaging of immunogold-labelled cells by dark-field scanning transmission x-ray microscopy B-23
Henry N. Chapman, Chris Jacobsen, Jenny Fu (SUNY at Stony Brook), and Shawn Williams (Howard Hughes Medical Institute, Yale).

Photochemical alteration of organic matter detected via C-NEXAFS B-23
G. D. Cody (ANL), H. Ade (NCSU), S. Wirick (SUNY), A. Davis, and G. Mitchell (PSU)

C-NEXAFS microanalysis of "pure components" in organic rich rocks B-24
G. D. Cody, R. E. Botto (ANL), H. Ade (NCSU), S. Behal, M. Disko (ERE), S. Wirick (SUNY)

First results with the second generation scanning photoemission microscope B-24
Cheng-Hao Ko, Janos Kirz (SUNY Stony Brook), Harald Ade (NCSU), Erik Johnson, Steve Hulbert (NSLS) and Erik Anderson (LBL)

X-ray Gabor holography B-25
Steve Lindaas and Malcolm Howells (ALS/LBL), Chris Jacobsen and Alex Kalinovsky (Physics Dept/SUNY Stony Brook)

Determination of degree of radial ordering in kevlar fibers using x-ray linear dichroism microscopy . B-25
A. P. Smith, H. Ade (North Caroline State Univ.), B. Hsiao, and S. Subramoney (Du Pont)

Mapping and measuring DNA and proteins in sperm using the scanning transmission x-ray microscope B-26
X. Zhang (SUNY Stony Brook), R. Balhorne (Lawrence Livermore Natl. Lab.), J. Kirz (SUNY Stony Brook), and S. Williams (Howard Hughes Med. Inst., Yale Univ.)

Beamline X1B

Electronic structure of buried α-$FeSi_2$ and β-$FeSi_2$ layers: Soft x-ray emission and absorption studies compared to band structure calculations B-26
S. Eisebitt, J.-E. Rubensson, M. Nicodemus, T. Böske, S. Blügel, W. Eberhardt (IFF, KFA Jülich), G. Bihlmayer (Univ. Wien), K. Radermacher, and S. Mantl (ISI, KFA Jülich)

Absolute photoabsorption cross section measurements of simple molecules in the core level region .. B-27
B. S. Itchkawitz, B. Kempgens, H. M. Köppe, J. Feldhaus, A. M. Bradshaw (Fritz-Haber-Institut), and W. B. Peatman (BESSY)

High resolution photoemission study of C_2H_4 at the C K-Edge B-27
H. M. Köppe, M. Schmidbauer, B. S. Itchkawitz, A. L. D. Kilcoyne, J. Feldhaus, and A. M. Bradshaw (Fritz-Haber-Institute, Berlin)

Spin-orbit coupling, exchange interaction and hybridization in the photo-excitation of the Ni 3p core level B-28
Y. Liu, Z. Xu, P. D. Johnson (BNL), G. van der Laan (Daresbury Laboratory, United Kingdom)

Selectively Excited Core-to-Core Fluorescence of Potassium Halides B-28
J. Lüning, J.-E. Rubensson, S. Eisebitt, and W. Eberhardt (IFF, KFA-Jülich, Germany)

Beamline X2B

X-ray microtomography B-29
J. H. Dunsmuir, J. H. Hardenbergh, and B. P. Flannery (Exxon)

Beamline X3A1

Construction of a high energy Bonse-Hart ultrasmall-angle x-ray scattering instrument B-29
B. Chu, F. Yeh, Y. Li, P. J. Harney, J. Rousseau (SUNY Stony Brook), A. Darovsky (SUNY, NSLS, BNL), and D. P. Siddons (NSLS, BNL)

Development of the use of imaging plates in accurate crystallographic data collection at synchrotron sources B-30
P. Coppens, R. Bolotovsky, and A. Darovsky (SUNY Buffalo and BNL)

The use of high energy synchrotron radiation in charge density studies B-30
Philip Coppens, Robert Bolotovsky, Ruiming Li and Alex Darovsky (SUNY at Buffalo, BNL)

An anti-scatter device for low-temperature crystallographic experiments with imaging plates B-31
A. Darovsky, R. Bolotovsky, and P. Coppens (SUNY Buffalo and BNL)

Synchrotron structure determination of bis(4,4′-bromophenyl)-61,61,diyl methanofullerene C_{60} at room temperature and at 25k B-31
B. Iversen (Aarhus Univ., Denmark), R. Bolotovsky (SUNY Buffalo and BNL), A. Darovsky (SUNY Buffalo and BNL), F. Wudl (UCSB) and P. Coppens (SUNY Buffalo and BNL)

A novel microporous sulfide: TEA·Ge_2CuS_5 ..... B-32
K. Tan, J. B. Parise (SUNY Stony Brook), and A. Darovsky (BNL)

Beamline X3A2

Time resolved SAXS of pet monofiber deformation B-32
B. Chu, P. Harney (SUNY Stony Brook), and B. Hsiao (Du Pont)

Development of the use of imaging plates in accurate crystallographic data collection at synchrotron sources B-30
P. Coppens, R. Bolotovsky, and A. Darovsky (SUNY Buffalo and BNL)

An anti-scatter device for low-temperature crystallographic experiments with imaging plates B-31
A. Darovsky, R. Bolotovsky, and P. Coppens (SUNY Buffalo and BNL)

Beamline X3B1

Low temperature structure of the linear chain cuprate Sr_2CuO_3 ..... B-33
T. Ami (Sony), M. Crawford, and R. Harlow (Du Pont)

Powder diffraction structure of $[Ru_2(\mu_2;\eta^2\text{-}O_2PMe_2)_2(CO)_4]_n$ B-33
Christopher M. Barnes (Univ. of Wyoming), D. Scott Bohle (Univ. of Wyoming), Robert E. Dinnebier (SUNY Stony Brook), Sara K. Madsen (Univ. of Wyoming), and Peter W. Stephens (SUNY Stony Brook)

Structural investigation of Hg and Cu superconducting cuprates B-34
P. Bordet, M. Anne, C. Chaillout, J.J. Capponi, M. Marezio (CNRS Grenoble), E. Antipov, E. Kopnine (Moscow State Univ.)

Powder diffraction structure of triclinic $C_{60}Br_{24}(Br_2)_2$ B-34
R. E. Dinnebier, P. W. Stephens (SUNY Stony Brook), J. K. Carter, A. N. Lommen,P. A. Heiney, A. R. McGhie, L. Brard, A. B. Smith, III (Univ. of Pennsylvania)

Powder diffraction structure of Cd_3SiO_5 ..... B-35
R. E. Dinnebier, P. S. Stephens (SUNY Stony Brook), W. Eysel (Univ. of Heidelberg FRG)

Powder diffraction structures of Bi_2CdGeO_6 ..... B-35
R. E. Dinnebier, P. W. Stephens (SUNY Stony Brook), S. Wies, and W. Eysel (Univ. of Heidelberg, FRG)

Analysis of the amorphous phase in hydroxyapatite coatings B-36
K. A. Gross, C. C. Berndt, P. Stephens, and R. Dinnebier (SUNY Stony Brook)

Sr_2IrO_4: A new two-dimensional spin 1/2 canted antiferromagnet B-36
R. Harlow, M. Crawford, and M. Subramanian (Du Pont)

Ab initio structure determination of a new ammonium aluminum fluoride phase from powder diffraction data: β-NH_4AlF_4 ..... B-37
R. Harlow, N. Herron, and D. Thorn (Du Pont)

The crystal structure of yet another new form of AlF_3 as determined from its synchrotron powder-diffraction pattern B-37
Richard L. Harlow, Norman Herron, and David L. Thorn (Du Pont)

Barium yttrium fluorides B-38
J. A. Kaduk, J. Faber, S. Pei, R. H. Jarman, and A. P. Wilkinson (AMOCO)

Cation site occupancies and crystallinity of NH_4-exchanged FAU B-38
J. A. Kaduk, J. T. Miller, P. D. Hopkins, and J. Faber (AMOCO)

Determination of the crystal structure of $K_2Al_2B_2O_7$ ab initio using synchrotron powder diffraction data B-39
J. A. Kaduk and L. C. Satek (AMOCO)

Crystal structure of cubic $CsTiAsO_5$ and $CsTiPO_5$ B-39
M. Kunz, R. Dinnebier (SUNY Stony Brook), D. E. Cox (BNL), L. K. Cheng, E. M. McCarron, J. Calabrese (Du Pont), J. B. Parise, P. W. Stephens (SUNY Stony Brook)

Roughness scaling and strain in lattice mismatched $Si_{0.4}Ge_{0.6}$ thin films on Si B-40
Z. H. Ming, S. Huang, Y. L. Soo, Y. H. Kao (SUNY Buffalo), T. Carns and K. L. Wang (UCLA)

Thickness modulation of InGaAs/GaAs superlattices studied by large angle x-ray scattering B-40
Z. H. Ming, Y. L. Soo, S. Huang, Y. H. Kao (SUNY Buffalo), K. Stair, G. Devane, and C. Choi-Feng (AMOCO)

Interfacial microstructures of ultrathin Ge layers on Si probed by x-ray fluorescence yield B-41
Z. H. Ming, Y. L. Soo, S. Huang, Y. H. Kao (SUNY Buffalo), J. C. Tsang, and S. S. Iyer (IBM T. J. Watson Research Center)

Local environment surrounding Mn atoms in $In_{1-x}Mn_xAs$ diluted magnetic semiconductors B-41
Y. L. Soo, S. Huang, Z. H. Ming, Y. H. Kao (SUNY Buffalo), H. Munekata (Tokyo Institute of Technology, Japan), and L. L. Chang (Univ. of Science and Technology, Hong Kong)

Local structures around Mn luminescent centers in Mn-doped nanocrystals of ZnS B-42
Y. L. Soo, Z. H. Ming, S. W. Huang, Y. H. Kao (SUNY Buffalo), R. N. Bhargava (Nanocrystals Technology), and D. Gallagher (Philips Laboratories)

Polymer and dimer phases of Rb_1C_{60} and K_1C_{60} B-42
Peter W. Stephens (SUNY Stony Brook), G. Oszlanyi (Research Inst. for Solid StatePhysics, Budapest and Ecole Poly. Federal de Lausanne), G. Bortel, G. Faigel, M. Tegze (Research Inst.for Solid State Physics), A. Jánossy (Research Inst. for Solid State Physics Budapest and Tech. Univ.Budapest), S. Pekker (Research Inst. for Solid State Physics, Budapest), D. Koller, M. C. Martin, L. Mihály, R. Dinnebier, G. Bendele (SUNY Stony Brook), O. Chauvet, and L. Forró (Ecole Poly. Federald e Lausanne)

Fulleride superconductors and orientational order: T_c vs. lattice constant in $Na_2Rb_xCs_{1-x}C_{60}$ B-43
T. Yilidrim, J. E. Fischer, R. Dinnebier, P. W. Stephens, and C. L. Lin (Univ. of Penn., SUNY Stony Brook, and Temple Univ.)

Beamline X3B2

In-situ investigation on film growth for Ag/Ag(111) B-43
W. C. Elliott (Univ. of Missouri, Columbia), T. Tse, P. W. Stephens (SUNY Stony Brook), P. F. Miceli (Univ. of Missouri, Columbia)

Beamline X4A

Crystal structure determination of carboxymuconate laconizing enzyme (CMLE) from *Neurospora crassa* B-44
T. Glumoff, S. Helin, T. Salminen, and A. Goldman (Turku Univ., Finland)

X-ray Data Collection of Cytochrome Reductase Crystals B-44
J. W. Lee, T. V. Law, and B. K. Jap (LBL)

Beamline X6A

In situ dispersive XAS of vanadium phosphate catalysts during butane oxidation B-45
Simon R. Bare (Dow), George Coulston, Richard Harlow (Du Pont), Harold Kung, Kari E. Birkeland, Greg Bethke (Northwestern Univ.), Peter L. Lee (ANL), P. Joe Georgopoulos, and John Quintana(DND-CAT)

X-ray magnetic circular dichroism B-45
K. J. Gofron (Northern Illinois Univ. and ANL), C. Kimball (Northern Illinois Univ.), S. Mini (Northern Illinois Univ. and ANL), G. Jennings, P. Lee (ANL), P. A. Montano (ANL and Univ. Illinois, Chicago)

Application of the energy dispersive instrument in structural studies of surfaces,interfaces, and thin films B-46
K. G. Huang, P. Lee, M. A. Beno, M. Ramanathan, G. Jennings, G. S. Knapp, and P.A. Montano

Continuous energy diffraction spectroscopy (CEDS) B-46
P. L. Lee, M. A. Beno, G. S. Knapp, and G. Jennings (ANL)

Beamline X6B

Resonant reflectivity measurements on Fe/Cr multilayers B-X47
J. M. Bai (Brooklyn College of CUNY, ANL), E. Fullerton (ANL), and P. A. Montano (ANL, Univ. Illinois, Chicago)

EXAFS study of the ZnSe/GaAs interface B-47
J. M. Bai (Brooklyn College of CUNY) (ANL), S. Sivananthan (Univ. Illinois, Chicago), and P. A. Montano (ANL) (Univ. Illinois, Chicago)

Transparent non-diffracting polarization rotation regime (TNDPR) B-48
M. A. Baysal and J. M. Bloch (Temple Univ.)

Application of the energy dispersive instrument in structural studies of surfaces,interfaces, and thin films B-46
K. G. Huang, P. Lee, M. A. Beno, M. Ramanathan, G. Jennings, G. S. Knapp, and P.A. Montano

Structural properties of siloxene films on Si(111) B-48
K. G. Huang (ANL), M. Rosenbauer, and J. Zegenhagen (Max-Planck-Institut fur Festkorperforschung,Germany)

Diffraction studies of self-assembled azobenzenealkanethiol monolayers on gold surfaces B-49
A. Malik, W. B. Caldwell, B. R. Herr, M. K. Durbin, C. A. Mirkin, and P. Dutta (Northwestern Univ.) and K. G. Huang (ANL)

Evolution of structure in multilayer Langmuir-Blodgett films B-49
A. Malik, M. K. Durbin and P. Dutta (Northwestern Univ.), and K. G. Huang (ANL)

Time evolution of specular and off-specular reflectivity during sputter deposition of platinum film . B-50
G. Rue, H. K. Kim (Pusan Natl. Univ., Korea), K. G. Huang (ANL), K. B. Lee (Pohang Inst. Sci. Technol., Korea), R. T. Kampwirth, and H. You (ANL)

Total-electron-yield measurement of sulfur K-edge XAFS of SO_2-containing humid atmosphere B-50
I. Song, B. I. Rickett, P. Janavicius, J. H. Payer (Case Western Reserve Univ.), and M. R. Antonio (ANL)

Concentration of synchrotron beams by means of polycapillary x-ray optics B-51
J. B. Ullrich (Univ. at Albany), K. G. Huang (ANL), S. M. Owens, D. C. Aloisi, F. A. Hofmann, N. Gao, I. L. Klotzko, W. M. Gibson (Univ. at Albany)

Spin-dependent EXAFS in magnetized polycrystals of $[Fe(\alpha\text{-picolylamine})_3]Cl_2 \cdot EtOH$ B-51
Z. Wang, C. Kimball (Northern Illinois Univ.), L. X. Chen, J. R. Norris, K. G. Huang, and P. A. Montano (ANL)

Beamline X7A

Structure and behavior of zintl ions in restricted geometries B-52
P. Armand, L. Iton, D. L. Price, and M-L. Saboungi (ANL)

Investigation of the low-temperature structure of Fe_3O_4 ..... B-52
P. Bordet,J.D. Sullivan,M. Marezio (CNRS Grenoble), D.E. Cox (BNL)

Deformation induced bond orientational order in metallic glasses B-53
T. Egami, W. Dmowski, P. Kosmetatos, M. Boord (U. Penn.), T. Tomida (Sumitomo Metal Industries), E. Oikawa and A. Inoue (Tohuku U.)

Interfacial structures of giant magnetoresistance Fe-Cr multilayers B-53
T. Egami, W. Dmowski, D. Louca (U. Penn), D. Kelly, I. Schuller (U.C. San Diego)

Sr-doped $La_{2-y}RE_yCuO_4$ superconductors: suppression of Tc at 1/8-hole doping is independent of rare earth B-54
R. Harlow, M. Crawford and E. McCarron (Du Pont)

Residual stress measurements of KSiAl - doped tungsten wires B-54
F. Hepp (Univ. of Freiberg, GER), A. Hilscher (Osram, Schwabmünchen, GER), and J. H. Selverian (Osram Sylvania)

Crystal structure of cubic $CsTiAsO_5$ and $CsTiPO_5$ B-39
M. Kunz, R. Dinnebier (SUNY Stony Brook), D. E. Cox (BNL), L. K. Cheng, E. M. McCarron, J. Calabrese (Du Pont), J. B. Parise, P. W. Stephens (SUNY Stony Brook)

Structural changes upon sorption and desorption of Xe from Cd-exchanged zeolite rho: a real-time synchrotron x-ray powder diffraction study B-55
J. B. Parise (SUNY Stony Brook), D. R. Corbin, L. Abrams (Du Pont)

Structural studies of novel high-pressure perovskite-related phases on the join $CaTiO_3$-$FeTiO_3$ B-55
J. B. Parise (SUNY Stony Brook), K. Leinenweber (ASU, Tempe)

Structure of $CaAu_2O_4$: a novel high pressure aurate with corner linked square planar Au^{3+} B-56
J. B. Parise, J. Park, and M. Kunz (SUNY Stony Brook)

Search for copper on the mercury site in $HgBa_2CuO_{4+\delta}$ by x-ray anomalous diffraction B-56
P. G. Radaelli, M. Marezio (CNRS), and D. Cox (BNL)

Cation siting determination in CaLSX by combined x-ray/neutron Rietveld Refinement B-57
Brian H. Toby, James E. MacDougall, and Charles G. Coe (Air Products and Chemicals Corporation)

Beamline X7B

Study of KTiOPO4 (KTP) on modulation by an applied electric field B-57
J. Albertsson, R. J. Bolt (CTH, Sweden), J. Hanson, M. C. Nelson (BNL), K. Ståhl (Lund Univ., Sweden), and G. Svensson (CTH, Sweden)

In situ powder diffraction studies of ion exchange; molten salt ion exchange of analcime with ammonium nitrate B-58
E. Krogh Andersen, I. G. Krogh Andersen (Univ. of Odense, Denmark), P. Norby, and J. C. Hanson (BNL)

In situ powder diffraction study of solid state syntheses; formation of lanthanum manganate(III)(IV), $LaMnO_{3+\delta}$ B-58
E. Krogh Andersen, I. G. Krogh Andersen (Univ. of Odense, Denmark), P. Norby, and J. C. Hanson (BNL)

In situ studies of the dehydration process in the natural zeolite stilbite B-59
G. Artioli (Univ. di Milano, Italy), G. Cruciani (Univ. di Ferrara, Italy), A. Gualtieri (Univ. di Modena, Italy), K. Ståhl (Univ. of Lund, Sweden), and J. C. Hanson (BNL)

In situ studies of the dehydration process in the natural zeolite yugawaralite B-59
G. Artioli (Univ. di Milano, Italy), G. Cruciani (Univ. di Ferrara, Italy), A. Gualtieri (Univ. di Modena, Italy), K. Stahl (Univ. of Lund, Sweden), and J. C. Hanson (BNL)

Characterization of thick film resistor devices by grazing incidence powder diffraction B-60
G. Artioli (Univ. di Milano, Italy), A. Gualtieri, S. Goretti, B. Morten, M. Prudenziati (Univ. di Modena, Italy), and J. C. Hanson (BNL)

Powder diffraction study of the phase transitions in KNO_3 ..... B-60
A.N. Christensen (Univ. of Aarhus, Denmark), P. Norby, and J. C. Hanson (BNL)
Time resolved powder diffraction; Sorel cements B-61
Axel Nørlund Christensen (Univ. of Aarhus, Denmark), Poul Norby, and Jonathan C.Hanson (BNL)
Position sensitive detectors for powder diffraction; a comparison between INEL CPS120 and CPS90 ..... B-61
Poul Norby and Jonathan C. Hanson (BNL)
Powder diffraction using imaging plates; structure determination and Rietveld refinement B-62
Poul Norby and Jonathan C. Hanson (BNL)
In situ synchrotron powder diffraction studies of syntheses of layered α-Ti- and α-Zr-phosphates ... B-62
Poul Norby, Jonathan C. Hanson (BNL), and Anne Marie Krogh Andersen (Univ. of Odense, Denmark)
Time resolved powder diffraction of oxidation/reduction of $Sr_xLa_{1-x}MnO_{3+\delta}$ at high temperature .. B-63
Poul Norby, Jonathan C. Hanson (BNL), E. Krogh Andersen, and I. G. Krogh Andersen (Univ. of Odense, Denmark)
Powder diffraction study of the phase transitions in $Na_4Ge_7O_{16}{\cdot}nH_2O$ B-63
Poul Norby, Ping Wu, and Jonathan C. Hanson (BNL)
The structure refinement of a new high pressure silicate, $Na_2CaSi_6O_{14}$ B-64
J. B. Parise, K. Tan, M. Kunz, T. Gasparik (SUNY Stony Brook), and J. Hriljac (BNL)
The influence of composition on polymorphism in Tl-2201 ..... B-64
C. Ström, S. G. Eriksson (Inorganic Chem. GU), J. Albertsson (CTH), J. Hanson (BNL)

Beamline X9B

X-ray diffraction studies of tethered protein monolayers and ultrathin organic monolayer/multilayer films B-65
J. K. Blasie, S. Xu, M. Murphy, J. Chupa, and R. Fischetti (Univ. of Pennsylvania & Biostructures Institute)
Kinetics and mechanism of lipid phase transitions B-65
M. Caffrey (Ohio State Univ.)
Fast pulse processing for solid state detectors B-66
M. R. Chance, R. Fischetti, Y. Hai, and C. Lu (Albert Einstein College of Medicine)
Time-resolved x-ray absorption spectroscopy: novel methods applied to examining the structure of the myoglobin-CO photoproduct B-66
M. R. Chance, A. Xie, L. M. Miller, E. M. Scheuring, Y. Hai, and Y. Lu (Albert Einstein College of Medicine)
The ambiguities in ZnS_nX_{4-n} EXAFS B-67
Kimber Clark, David Tierney, James Penner-Hahn (Univ. of Michigan), Kumar Govindaswamy, Eric Gruff, and Stephen A. Koch (SUNY Stony Brook)
Dynamical focusing for a sagittal monochromator B-67
R. Fischetti and M. Sullivan (Albert Einstein College of Medicine)
Structural studies of discotic liquid crystals B-68
P. Heiney (Univ. of Pennsylvania), H. Ringsdorf, T. Plesnivy, and P. Schuhmacher (Institute für Organische Chemie, Germany)
Structural and electronic factors that influence oxygen affinities: a spectroscopic comparison of ferrous and cobaltous myoglobin B-68
L. M. Miller and M. R. Chance (Albert Einstein College of Medicine)
EXAFS and XANES studies of Co^{3+} in nitrile hydratase B-69
Mark J. Nelson, Bridget A. Brennan, John G. Cummings (Du Pont), Saqib Rehman, James Kindt, and Robert C. Scarrow (Haverford College)
Mediation of Co-C bond cleavage by cobalamin dependent enzymes B-69
E. M. Scheuring and M. R. Chance (Albert Einstein College of Medicine)

Thiol ligation of zinc in isoleucine t-RNA synthetase B-70
D. L. Tierney, J. E. Penner-Hahn (Univ. of Michigan), J. A. Landro, E. Schmidt, and P. Schimmel (MIT)

Beamlines X10A and X10B

Epitaxial growth of otavite on calcite B-70
R. P. Chiarello and Neil C. Sturchio (ANL)

Surface structure and dissolution dynamics of calcite in water B-71
R. P. Chiarello and N. C. Sturchio (ANL)

Real time x-ray scattering of sputtering growth of TiN films B-71
J. H. Je (Exxon and Pohang Univ., Korea), D. Y. Noh (Exxon), H. K. Kim (Pusan Univ., Korea), and K. S. Liang (Exxon)

Interfacial structure of thin Au films on GaAs B-72
D. Y. Noh (Exxon), Y. Hwu (Academia Sinica, Taipei, Taiwan), H. K. Kim (Pusan Nat. Univ., Korea), and M. Hong (AT&T)

Time-resolved x-ray scattering study of the normal alkanes B-72
H. H. Shao, H. E. King Jr., E. B. Sirota (Exxon)

Rotator phase behavior in binary mixtures of the normal alkanes B-73
H. H. Shao, H. E. King Jr., E. B. Sirota, and D. M. Singer (Exxon)

Thin films on "rough" surfaces: an x-ray study B-73
M. Tolan (Inst. fur Exp. Phys. Uni Kiel),M.T. is indebted to the Exxon Research Labs for financial support of his visit. G. Vacca, S. K. Sinha (Exxon), Z. Li, M. Rafailovich, J. Sokolov (SUNY Stony Brook), H. Lorenz, and J. P. Kotthaus (S ek. Phys. LMU Munchen)

X-ray diffraction from mesoscopic systems: thin films on "rough" surfaces B-74
M. Tolan (Institut für Experimentalphysik der Universitat Kiel, Germany), G.Vacca, S. K. Sinha (Exxon), Z. Li, M. Rafailovich, J. Sokolov (SUNY Stony Brook), H. Lorenz, J. P.Kotthaus Lufwig-Maximilians (Universitat Munchen, Germany)

Powder x-ray diffraction studies of the phase transformation in calcined MFI zeolite B-74
Baoshan Zhang, Harry W. Deckman, Keng S. Liang, E. W. Corcoran, Jim McHenry (Exxon Corporate Research), and J. P. Verduign (Exxon Chemical Europe Inc.)

Beamline X10C

Structural modification in the active site of arthropod hemocyanin in response to heterotropic effectors as detected by x-ray absorption spectroscopy B-75
L. Bubacco, M. D. Wirt, R. S. Magliozzo, J. Peisach (A. Einstein Coll. of Med.), and L. Powers (Utah State U.)

In situ x-ray absorption study of the structure of the passive oxide film on iron B-75
Alison J. Davenport (BNL) and Michael Sansone (Exxon)

K-edge EXAFS study of carbon monoxide dehydrogenase from clostridium thermoaceticum B-76
C. Y. Ralston, B. J. Weiss, J. H. Christiansen, D. Le, and S. P. Cramer (Univ. California, Davis), M. Kumar, and S. W. Ragsdale (Univ. Nebraska, Lincoln)

Reflectivity study at the sulphur k-edge of the lubricating oil additive B-76
M. Sansone (Exxon), E. S. Ferrari, C. A. E. Peacock, and K. J. Roberts (Univ. of Strathclyde, Glasgow, UK)

Beamline X11A

Site occupancy of ternary dopants in β phase transition metal aluminides B-77
M. Balasubramanian, D. Pease, J. Budnick, T. Manzur, and D. Brewe (Univ. of Connecticut)

Local environment of Fe in nanostructured M50 type steel samples B-77
M. Balasubramanian, Y. Zhang, J. Budnick, and D. Pease (Univ. of Connecticut)

Local structure, phase stability and surface morphology studies of $(Ti_{1-x}Zr_x)Si_2$thin films on Si(100) and Si(111) B-78
Yuan Dao, R. J. Nemanich, and D. E. Sayers (North Carolina State Univ.)

Charge distribution effects in $BaZrO_3$ by XAFS B-78
D. Haskel, E. A. Stern, B. Ravel, M. Newville (Univ. of Washington) and S. Heald (Pacific Northwest Laboratories)

An XAFS study of the oxidation of structural iron in biotite mica by solutions containing Br_2 or H_2O_2 ..... B-79
S. M. Heald, J. E. Amonette, G. D. Turner (PNL), and J. D. Scott (Iowa St. Univ.)

X-ray absorption studies on the metal environments in $Ti_{1-x}Nb_xS_2$ phase B-79
Geraldine Lamble (BNL), Sigrid Furuseth (Univ. of Oslo, Norway), and David Nicholson (Univ. of Trondheim, Norway)

XAFS studies of atomic correlation in II-VI quaternary semiconductor alloys B-80
Q. Lu, B. A. Bunker, H. Luo, A. J. Kropf, S. H. Xin, J. K. Furdyna, and K. M. Kemner (Univ. of Notre Dame)

Glancing angle EXAFS studies of GE "pre-melting" at the Ge/C interface B-80
Q. Lu, B. A. Bunker (Notre Dame), R. A. Mayonovic (Southwest Missouri State Univ.), A. J. Kropf, S. T. Ruggiero (Notre Dame), J. R. Buschert (Goshen College)

Atomic structure of sputtered amorphous $Al_{100-2x}Co_xCe_x$ (x=8, 9 and 10) and $Al_{80}Fe_{10}Ce_{10}$ alloys B-81
A. N. Mansour (Naval Surface Warfare Center)

A study of the structure of passive oxide films on amorphous Al-Fe-Ce alloys B-81
A. N. Mansour (Naval Surface Warfare Center) and C. A. Melendres (ANL)

In situ XAFS study of the structure of oxides formed on Ni thin film electrodes in KOH solution .. B-82
A. N. Mansour (Naval Surface Warfare Center) and C. A. Melendres (ANL)

XAFS investigation of the structure and valency of nickel in some oxycompounds B-82
A. N. Mansour (Naval Surface Warfare Center) and C. A. Melendres (ANL)

Phase stability diagram of a carbon-supported palladium catalyst in C_2H_4/H_2 mixtures at T = 373-498 K B-83
J. A. McCaulley (Hoechst Celanese Research) and F. W. Lytle (The EXAFS Company)

XAS studies of the corrosion of metal hydride electrodes B-83
S. Mukerjee, J. McBreen, J. J. Reilly, G. Adzic, and J. R. Johnson (BNL)

Local thermodynamic measurements of Ag-based alloys using XAFS B-84
Matthew Newville and Edward A. Stern (Univ. of Washington)

A method of performing DAFS fluorescence corrections: basis of an enhanced intensitydesign B-84
Douglas Pease, Mahalingham Balasubramanian, Dale Brewe, and Joseph Budnick (Univ. of Connecticut)

EXAFS and XRD studies of the phase formation of Co-SiGe reaction B-85
Z. Wang, R. J. Nemanich, and D. E. Sayers (North Carolina State Univ.)

Mineralization of ferritin depends on conserved glutamic acid side chains B-85
Z. Wang, G. S. Waldo, D. E. Sayers, and E. A. Theil (North Carolina State Univ.)

The structure of denatured cytochrome C B-86
Y. Zhang and E. A. Stern (Univ. of Washington)

Beamline X11B

Spectroscopic studies of a palladium carbide phase B-86
G. Frank (Hoechst AG, Germany) and J. A. McCaulley (Hoechst Celanese Res. Div., New Jersey)

X-ray diffraction anomalous fine structure study of a supported Pt catalyst B-87
Qing Ma (North Carolina State Univ.), Jyh-Fu Lee (BNL), and D. E. Sayers (North Carolina State Univ.)

Beamline X12B

Real-time x-ray scattering of binary polymer blends:poly(butylene terephthalate)/polycarbonate B-87
Mark V. Brillhart (MIT), Peggy Cebe (MIT), and Malcolm Capel (NSLS)

Crystallization study of liquid crystalline polycarbonates using real-time small angle x-ray scattering B-88
Yao-Yi Cheng, Peggy Cebe (MIT), Heidi Schreuder-Gibson (U. S. Army Natick RD&E Center), Malcolm Capel (NSLS)

X-ray Scattering Studies of Motor Proteins B-88
S. Fujiwara, D. Stone (UCSF), M. Capel (BNL), and R. Mendelson (UCSF)

Small angle x-ray scattering study of new-TPI thermoplastic polyimide B-89
Sharon Xin Lu (MIT), Peggy Cebe (MIT), and Malcolm Capel (NSLS)

Beamline X12C

Structural studies of human protein tyrosine phosphatase 1B B-89
D. Barford (Cold Spring Harbor Lab.)

Crystal structure of yeast TATA-binding protein at 2.3Å resolution B-90
D. Chasman and P. Sharp (MIT)

Crystallization and preliminary x-ray analysis of a 1:1 complex of Ospa and Fab184.1 ..... B-90
Hong Li and Catherine L. Lawson (BNL)

Crystal structure of phosphoenolpyruvate carboxykinase from *E. coli* B-91
A. Matte, H. Goldie (Univ. of Saskatchewan), R. M. Sweet (NSLS), and L. T. J. Delbaere (Univ. of Saskatchewan)

Structure of monoclonal Fab fragment of Jel42 specific for HPr B-91
L. Prasad, M. Vandonselaar, J. S. Lee (Univ. of Saskatchewan), R. M. Sweet (NSLS), and L. T. J. Delbaere (Univ. of Saskatchewan)

Preliminary structure studies of Soybean l-3 lipoxygenase B-92
J. Steczko, W. Minor, B. Axelrod (Purdue Univ.), V. Stojanoff (BNL)

Structure analysis of Torpedo californica acetylcholinesterase-ligand complexes B-92
Joel L. Sussman, Michal Harel, Mia L. Raves (Weizmann Inst. of Science, Israel),Raimond B. G. Ravelli (Lab. Crystall. and Struct. Chem., The Netherlands), Helen Kycia, Vivian Stojanoff, Israel Silman (Weizmann Inst. of Science, Israel)

Crystal structure of casein kinase-1, a phosphate-directed protein kinase B-93
Rui-Ming Xu (CSHL), Gilles Carmel (Molecular Geriatrics Corp.), Robert M. Sweet (BNL), Jeff Kuret (Molecular Geriatrics Corp.), and Xiaodong Cheng (CSHL)

Beamline X14A

C_{60}/Ge(100) boundary structure B-93
R. D. Aburano, Hawoong Hong, K. Chung, M. C. Nelson, H. Chen, T.-C. Chiang (Univ. of Illinois, Urbana-Champaign), and P. Zschack (ORISE)

Atmospheric durability of a (4×4) C_{60} monolayer on Cu(111) B-94
R. D. Aburano, Hawoong Hong, M. C. Nelson, T. Miller, T.-C. Chiang (Univ. of Illinois, Urbana-Champaign) and P. Zschack (ORISE)

Au/Si(111) anomalous truncation rods B-94
R. D. Aburano, J. M. Roesler, Hawoong Hong, T.-C. Chiang (Univ. of Illinois, Urbana-Champaign), and P. Zschack (ORISE)

Diffraction from a lipid monolayer along an isobar B-95
M. K. Durbin, A. Malik, R. Ghaskhadvi, A. Richter, P. Dutta (Northwestern Univ.), and P. Zschack (ORNL)

Suppression of the magnetic moment in superconducting UPt_3 ..... B-95
E. D. Isaacs, A. P. Ramirez, G. Aeppli, C. Oglesby and E. Bucher (AT&T), P. Zschack(ORISE), C. L. Broholm (Johns Hopkins Univ.), C. Burns (W. Michigan Univ.), R. Erwin (NIST)

Local atomic arrangements in $Fe_{46.5}Ni_{53.5}$ B-96
X. Jiang, G. E. Ice, C. J. Sparks, and P. Zschack (Oak Ridge National Laboratory)

Triaxial residual stress measurement for copper microcircuitry packaged in polymer B-96
N.K. McGuire, C.E. Crowder. M.J. Radler (Dow Chemical, MI), C.G. Barnes (Dow Chemical, LA), and B. Rogers (MCNC)

Atomic short-range order and static displacements in an $Fe_{62.3}Ni_{36.8}$ invar alloy B-97
J. L. Robertson, C. J. Sparks, G. E. Ice, X. Jiang (ORNL), S. Lefebvre (Univ. Paris-Sud), F. Bley (Univ. de Grenoble, France), P. Zschack (ORISE)

The effect of colony microstructure on superconductivity B-97
E. D. Specht, A. Goyal, D. M. Kroeger (Oak Ridge National Lab.), J. E. Tkaczyk, and J. A. DeLuca (General Electric)

Ordered structure of Si_xGe_{1-x} alloy thin films B-98
J. Z. Tischler, J. D. Budai, D. E. Jesson, G. Eres, and P. Zschack (ORNL), J.-M.Baribeau, and D. C. Houghton (Inst. for Microstructural Sci., Canada)

Preferred domain orientation in ordered SiGe films grown on miscut Si (001) B-98
J. Z. Tischler, J. D. Budai (ORNL), P. Zschack (ORISE), J.-M. Baribeau, and D.C. Houghton (NRC, Canada)

Beamline X15A

Microscopic structure of the hexagonal and striped discommensurate phases of Ge(111)In B-99
M. Boehringer (Max-Planck-Institut, Germany), P. F. Lyman (Northwestern Univ.), and J. Zegenhagen (Max-Planck-Institut, Germany)

Microscopic structure of the discommensurate phase of Ge(111)/Cu B-99
P. F. Lyman (Northwestern Univ.), M. Boehringer, and J. Zegenhagen (Max-Planck-Institut,Germany)

Structure and substrate relaxation of the Sb/Si(001)-(2×1) surface B-100
Paul F. Lyman (Northwestern Univ.), Y. Qian, and M. J. Bedzyk (Northwestern Univ.and ANL)

X-ray standing wave investigation of the thermal vibrational amplitude of Ad-atoms on Ga/Si(001) B-100
Y. Qian and M. J. Bedzyk (ANL and Northwestern Univ.)

Resolving ad-dimer locations and orientations on the Ga/Si(001)-2×2 surface B-101
Y. Qian, M. J. Bedzyk (ANL and Northwestern Univ.), G. E. Franklin (HarvardUniv.), S. Tang and A. J. Freeman (Northwestern Univ.)

Precise lattice location of trace elements within minerals and at their surfaces with x-ray standing waves B-101
Y. Qian, N. C. Sturchio, R. P. Chiarello, P. F. Lyman, T. Lee, and M. J. Bedzyk (ANL and Northwestern Univ.)

Structure and thermal characterization of membrane bound and surface adsorbed protein B-102
Jin Wang, Martin Caffrey (OSU), Carmichael J. A. Wallace (Dalhousie Univ.), and Ian Clark-Lewis (Univ. of British Columbia)

Structure characterization of membrane bound and surface adsorbed cytochrome c B-102
Zhijian Yin, Jin Wang, Stephan Kirchner, and Martin Caffrey (OSU)

Beamline X16A

Initial stages of nickel silicide formation on Si(111) B-103
P. Bennett, (Physics - ASU.), R. Schuster, A. Ghosh, and I. K. Robinson (U. of Illinois)

Symmetry of the 7×7 Si(111) surface: p6mm or p3m1? B-103
A. Ghosh, R. Schuster, and I. K. Robinson (Univ. of Illinois, Urbana)

Parallel adatom chains on Si(111): a chemisorption-induced surface reconstruction B-104
C. A. Lucas, G. C. L. Wong, D. Loretto (LBL), A. P. Payne, and P. H. Fuoss (AT&T Bell Lab.)

Scaling of island distributions during growth of Cu on Cu(110) B-104
I. K. Robinson, K. L. Whiteaker, and R. Schuster (Univ. of Illinois, Urbana)

Relaxations in uniaxial reconstructions of the Cu(110) surface B-105
R. Schuster, P. J. Eng, and I. K. Robinson (University of Illinois)

Beamline X16C

Electrocompression of a Pb monolayer on Cu(111) B-105
Y.Chu and I. K. Robinson (Univ. of Illinois)

Interfacial morphology of graded-temperature rare earth superlattices B-106
K. A. Ritley, C. P. Flynn, and I. K. Robinson (Univ. Illinois, Urbana)

DAFS measurements of CoSi films on Si(111) B-106
R. Schuster, A. Ghosh, D. L. Adler, I. K. Robinson (University of Illinois), N. Onda, and H. von Känel (Eidgenössische Technische Hochschule Zürich)

Beamline X17B1

Single-energy images for preclinical MECT research B-107
F. A. Dilmanian, X. Y. Wu, J. F. Coderre, J. Kress, B. Ren, D. N. Slatkin (BNL),D.Chapman, M. Shleifer, W. C. Thomlinson, Z. Zhong (NSLS), T. M. Button, F. Giron, C. T. Roque (SUNY StonyBrook), M. H. Miller, H. Weedon (Analogic Corp.), D. J. Krus, L. Perna (Bicron), and K. Yamamoto(Hamamatsu)

In situ determination of the olivine, beta and spinel phase boundaries for CO_2SiO_4at high pressures and temperatures B-107
L. Galoisy (U. P6, P7 and IPGP), J. Zhang (CHiPR, ESS, SUNY Stony Brook), S. Rossano (U. P6, P7, and IPGP), R. C. Liebermann, F. Guyot, and I. Martinez (CHiPR, ESS, SUNY Stony Brook)

Measurements and theoretical calculations of the pressure-volume-temperature relations in olivines B-108
F. Guyot, Y. Wang (SUNY Stony Brook), and Ph Gillet (ENS Lyon, France)

Catalyst characterization with high-energy x-ray diffraction B-108
R. Harlow, G. Coulston, F. Herkes, and G. Jones (Du Pont)

Characterization of Pd/C catalyst by x-ray diffraction under commercial hydrogenation pressures: in situ for the masses B-109
R. Harlow, G. Coulston, S. Ziemecki, F. Herkes, and G. Jones (Du Pont)

Phase transition of portlandite [$Ca(OH)_2$] at high pressure B-109
M. Kunz, D. J. Weidner, M. Vaughan, J. B. Parise, Y. Wang, and K. Leinenweber (SUNY Stony Brook)

In-situ x-ray diffraction at high pressure and temperature of aragonite and dolomite. Evidence for dolomite breakdown to aragonite and magnesite B-110
I. Martinez, J. Zhang, R. J. Reeder, and G. Symmes (SUNY Stony Brook)

Two- and three-dimension microbeam radiation therapy (MRT) of malignant brain tumors in rats B-110
D. N. Slatkin, S. M. Cole, F. A. Dilmanian, D. D. Joel, P. L. Micca, M. M. Nawrocky,X.-Y.Wu (BNL), P. Spanne (Groupe d'Imagerie, ESRF, France), J.-O. Gebbers (Institut de Pathologie, Hopital Cantonal, Lucerne, Suisse), and J. A. Laissue (Insti tut de Pathologie de l'Universite, Berne Suisse)

Thermal equation of state of $CaSiO_3$ perovskite B-111
Yanbin Wang, Francois Guyot, and Donald J. Weidner (CHiPR, SUNY Stony Brook)

Performance of the low-energy section of the MECT monochromator B-111
X. Y. Wu, F. A. Dilmanian, Z. Chen, J. Kress, B. Ren (BNL),
M. Shleifer, D. Chapman,A.Lenhard, M. Radulescu, W. Thomlinson, M. Woodle, and Z. Zhong (NSLS)

In situ x-ray diffraction study on magnesite at high pressure and temperature B-112
J. Zhang, I. Martinez, F. Guyot (CHiPR and SUNY Stony Brook), P. Gillet (ENS Lyon), and S. K. Saxena (Uppsala Univ., Sweden)

Beamline X17B2

Comparing transvenous coronary angiography images using 0.5mm and 0.25mm resolution detectors B-112
D. Chapman, W. Thomlinson, N. Gmur (NSLS), J. Dervan, T. Stavola (SUNY), E. Rubenstein, J. Giacomini, H. Gordon (Stanford U.), W. Lavender (SSRL), C. Schulze, and B. Bertrand (ESRF)

Comparing transvenous coronary angiography images using 3.0T and 4.0T superconducting wiggler fields B-113
D. Chapman, W. Thomlinson, N. Gmur (NSLS), J. Dervan, T. Stavola (SUNY), E. Rubenstein, J. Giacomini, H. Gordon (Stanford Univ.), W. Lavender (SSRL), C. Schulze, B. Bertrand (ESRF)

Beamline X18A

Multiple x-ray diffraction studies of decagonal quasicrystals B-113
R. Eisenhower, R. Colella (Purdue Univ.), and B. Grushko (Institut fur Feskorperforschung, Forchungszentrum Julich, Germany)

Effect of Dopants on Arsenic Precipitation in GaAs Deposited at Low Temperatures B-114
V. Mahadev, M.R. Melloch, J.M. Woodall, N.Otsuka, and G. L. Liedl (Purdue University)

Quasiepitaxial growth model for n-alkane films B-114
Z. Wu, B. Bolon (Univ. of Missouri-Columbia), S. N. Ehrlich (Purdue Univ.), B. Matthies,K. W. Herwig (Univ. of Missouri-Columbia), H.-S. Youn (Postech, Pohang, Korea), and H. Taub (Univ. of Missouri-Columbia)

Properties of $NiS_{2-x}Se_x$ (x = 0.51, 0.55, 0.63) B-115
X. Yao, S. N. Ehrlich, G. L. Liedl, and J. M. Honig (Purdue Univ.)

Beamline X18B

Surface EXAFS study of Fe/Cr multilayers B-115
J. M. Bai (Brooklyn College of CUNY) (ANL), E. Fullerton (ANL), and P. A. Montano(ANL) (Univ. Illinois, Chicago)

EXAFS study of the ZnSe/GaAs interface B-47
J. M. Bai (Brooklyn College of CUNY) (ANL), S. Sivananthan (Univ. Illinois, Chicago), and P. A. Montano (ANL) (Univ. Illinois, Chicago)

Monitoring lead reduction on the surface of titanium dioxide by x-ray absorption B-116
L. X. Chen (ANL), Z. Y. Wang (NIU), T. Rajh, A. Ostafin, D. M. Tiede, M. C. Thurnauer, P. A. Montano, J. R. Norris (ANL)

Structural characterization of quantized TiO_2 particles B-116
L. X. Chen (ANL), Z. Wang (NIU), T. Rajh, A. Ostafin, D. M. Tiede, M. C. Thurnauer,P. A. Montano, J. R. Norris (ANL)

X-ray absorption spectroscopic study of a commercial heat stabilized nylon during heat-aging process B-117
Di-Jia Liu (Allied Signal)

X-ray absorption spectroscopic study of Cu in Cu-ZSM-5 during NO catalytic decomposition B-117
Di-Jia Liu and Heinz J. Robota (Allied Signal)

On the nature of methyltrioxorhenium(VII) occluded in zeolite Y B-118
Andrzej Malek and Geoffrey Ozin (Univ. of Toronto)

EXAFS investigations of lanthanide ion hydration in concentrated electrolyte solutions B-118
B. Stout, B. Helmer, E. Conover, D. Peterman (Univ. Cincinnati), S. Clark, and A. Bryce (SREL)

Evaluation of zirconia-based superacid catalysts by EXAFS B-119
José E. Tábora and Robert J. Davis (Univ. of Virginia)

In situ x-ray absorption fine structure measurements of $LaNi_5$ electrodes in alkaline electrolytes .. B-119
D. A. Tryk, I. T. Bae, S. Kim, Y. Hu, D. A. Scherson (Case Western Univ.), M. A.Antonio (ANL), V. Leger, and G. E. Blomgren (Eveready Battery Co.)

The electrochemical insertion of lithium into pyrite from non-aqueous electrolytes at room temperature: an *in situ* Fe K-edge x-ray absorption fine structure study B-120
D. A. Tryk, S. Kim, Y. Hu, W. Xing, D. A. Scherson (Case Western Reserve Univ.),M. A. Antonio (ANL), V. Leger, and G. E. Blomgren (Eveready Battery Co.)

Beamline X19A

Surface structures of supported molybdenum oxide catalysts: characterization by *in situ* Raman and Mo $L_{2,3}$-edge XANES B-120
Simon R. Bare (Dow Chemical Co.), Hangchun Hu and Israel E. Wachs (Lehigh Univ.)

Structures of organocuprate-substrate intermediates B-121
T. M. Barnhart and J. E. Penner-Hahn (Univ. of Michigan)

A quick conversion for x-ray magnetic circular dichroism experiments at X19A beamline B-121
J. Chen (UCD), A. Young, (LBL), M. Grush (UCD), L. Furenlid (BNL), and S. P. Cramer (UCD and LBL)

The fate of bulk zinc in the development of zebra fish B-122
D. L. Tierney, J. E. Penner-Hahn (Univ. of Michigan), L. M. Walrath, and J. M. Berg (John Hopkins Univ.)

Beamline X19C

Imaging GaN thin film on (0001) sapphire substrates by synchrotron white beam x-ray topography B-122
H. Chung and M. Dudley (SUNY Stony Brook)

Characterization of basal plane dislocations in sapphire crystals by synchrotron white beam x-ray topography B-123
H. Chung, M. Dudley (SUNY Stony Brook), D. Larson, Jr., D. Dimarzio, and L. Carr (Grumman)

Imaging of crystal defects in sapphire crystals by synchrotron white beam x-ray topography B-123
H. Chung, M. Dudley (SUNY Stony Brook), D. Larson, Jr., D. Dimarzio, and L. Carr (Grumman)

Studies of elastic strains associated with 180° ferroelectric domain walls in KTP single crystals by synchrotron white beam x-ray topography B-124
H. Chung, S. Wang, and M. Dudley (SUNY Stony Brook), L. K. Cheng, J. D. Bierlein, and W. Bindloss (Du Pont)

The analysis of displacement vectors of 180° ferroelectric domain walls in KTP single crystals by synchrotron white beam x-ray topography B-124
H. Chung, S. Wang, M. Dudley (SUNY Stony Brook), L. K. Cheng, J. D. Bierlein, and W. Bindloss (Du Pont)

Characterization of growth defects in a ultra-thin CdZnTe single crystal by synchrotron white beam x-ray transmission topography B-125
H. Chung, J. Wu, M. Dudley (SUNY Stony Brook), and D. Larson, Jr. (Grumman)

Imaging large CdZnTe single crystals by synchrotron white beam x-ray topography B-125
H. Chung, J. Wu, M. Dudley (SUNY Stony Brook), and D. Larson, Jr. (Grumman)

Synchrotron white beam x-ray topographic investigation of microgravity grown CdZnTe single crystals B-126
H. Chung, J. Wu, M. Dudley (SUNY Stony Brook), and D. Larson, Jr. (Grumman)

Computer aided synchrotron white beam topography B-126
W. Huang, S. Wang, and M. Dudley (SUNY Stony Brook)

Influence of structural defects on electrical properties of SiC devices B-127
W. Huang, S. Wang, M. Dudley (SUNY Stony Brook), C. Fazi (U.S. Army Research Laboratory,Adelphi, MD)

Assessment of damage accompanying the electrical breakdown of GaAs devices B-127
W. Huang, S. Wang, M. Dudley (SUNY Stony Brook), C. Fazi, R. Kaul (U.S. Army Research Laboratory, Adelphi, MD), and J. H. McAdoo (Mission Research Corporation)

Synchrotron white beam investigation of depth distribution of electrical damage in GaAs devices . B-128
W. Huang, S. Wang, M. Dudley (SUNY Stony Brook), C. Fazi, R. Kaul (U.S. Army Research Laboratory, Adelphi, MD), and J. H. McAdoo (Mission Research Corporation)

Characterization of polytypes in SiC devices by synchrotron white beam x-ray topography B-128
W. Huang, S. Wang, M. Dudley (SUNY Stony Brook), J. A. Powell, P. Neudeck (NASA Lewis Research Center), C. Fazi (U.S. Army Research Laboratory)

Comparison of defect structures in PVT and lely SiC devices B-129
W. Huang, S. Wang, M. Dudley (SUNY Stony Brook), J. A. Powell, P. Neudeck (NASA Lewis Research Center), C. Fazi (U.S. Army Research Laboratory)

Depth profiling analysis of polytypes and stacking faults in SiC devices using synchrotron white beam x-ray topography B-129
W. Huang, S. Wang, M. Dudley (SUNY Stony Brook), J. A. Powell, P. Neudeck (NASA Lewis Research Center), C. Fazi (U.S. Army Research Laboratory)

Influence of surface morphology on SiC epitaxial growth through CVD technique B-130
W. Huang, S. Wang, M. Dudley (SUNY Stony Brook), J. A. Powell, P. Neudeck (NASA Lewis Research Center), C. Fazi (U.S. Army Research Laboratory)

Observation of DPBs in SiC devices by synchrotron white beam x-ray topography B-130
W. Huang, S. Wang, M. Dudley (SUNY Stony Brook), J. A. Powell, P. Neudeck (NASA Lewis Research Center), C. Fazi (U.S. Army Research Laboratory)

Synchrotron white beam characterization of defect structures in LELY SiC platelets B-131
W. Huang, S. Wang, M. Dudley (SUNY Stony Brook), J. A. Powell, P. Neudeck (NASA Lewis Research Center), C. Fazi (U.S. Army Research Laboratory)

Molecular orientation of a water-supported langmuir monolayer of n-$C_{18}H_{37}C_{12}F_{25}$studied by x-ray scattering B-131
Z. Huang (James Franck Institute), M. L. Schlossman (James Franck Inst. and Univ. of Chicago), A. A. Acero, N. Lei (James Franck Institute), Z. Zhang (Univ. of Illinois, Chicago),S. A. Rice (James Franck Institute)

X-ray topographic studies of K_2SO_4 crystals with dye inclusions B-132
M.P. Kelley, B. Kahr (Purdue Univ.), and M. Dudley (SUNY Stony Brook)

Investigation of the role of grain boundaries in the plastic deformation of ice: I. Predeformation microstructure B-132
F. Liu, I. Baker (Dartmouth College), and M. Dudley (SUNY Stony Brook)

Investigation of the role of grain boundaries in the plastic deformation of ice: II. *In situ* straining B-133
F. Liu and I. Baker (Dartmouth College), and M. Dudley (SUNY Stony Brook)

Investigation of the role of grain boundaries in the plastic deformation of ice: III. In situ annealing B-133
F. Liu, I. Baker (Dartmouth College), and M. Dudley (SUNY Stony Brook)

A new spectrometer for studying liquid surfaces and interfaces B-134
M. L. Schlossman (James Franck Inst. and Univ. of Chicago), D. J. Synal, G. Shea-McCarthy (Univ. of Chicago), Z. Huang, Y. Guan (James Franck Inst.), M. Meron (Univ. of Chicago), S. A. Rice (James Franck Inst.)

A new method for time-resolved "footprinting" of macromolecules B-134
B. Sclavi, M. R. Chance, and M. Brenowitz (Albert Einstein College of Medicine)

X-ray topography of thin films prepared from longitudinal cut 6H-SiC wafers B-135
W. M. Vetter, M. Dudley (SUNY Stony Brook)

Analysis of synchrotron topographic contrast from super screw dislocations in PVT 6H-SiC single crystals B-135
S. Wang and M. Dudley (SUNY Stony Brook), C. H. Carter, Jr. (Cree Research, Inc.)

Hollow core screw dislocations in PVT 6H-SiC single crystals revealed by synchrotron topography and SEM B-136
S. Wang and M. Dudley (SUNY Stony Brook), C. H. Carter, Jr. (Cree Research, Inc.)

Super screw dislocations in PVT 6H-SiC single crystals revealed by synchrotron topography B-136
S. Wang and M. Dudley (SUNY Stony Brook), C. H. Carter, Jr. (Cree Research, Inc.)

Synchrotron back-reflection topography for imaging super screw dislocation in PVT6H-SiC single crystals B-137
S. Wang and M. Dudley (SUNY Stony Brook), C. H. Carter, Jr. (Cree Research, Inc.)

Characterization of dislocation structures in PVT 6H-SiC crystal wafers by synchrotron white beam topography B-137
S. Wang and M. Dudley (SUNY Stony Brook), C. H. Carter, Jr. and V. Tsvetkov (Cree Research, Inc.)

Comparison of super screw dislocations in PVT 4H-SiC and 6H-SiC single crystals revealed by synchrotron back-reflection topography B-138
W. Wang, and M. Dudley (SUNY Stony Brook), C. Fazi (U.S. Army Research Laboratory,Adelphi, Md) and R. Rupp (Siemens, Germany)

Defect structures in PVT 4H-SiC single crystals revealed by synchrotron topography B-138
S. Wang and M. Dudley (SUNY Stony Brook), C. Fazi (U.S. Army Research Laboratory, Adelphi, MD) and R. Rupp (Siemens, Germany)

Investigation of structural defects in ZnSe single crystals by synchrotron x-ray topography B-139
W. Zhou, H. Chung, M. Dudley (SUNY Stony Brook), C. H. Su, M. P. Volz, D. C. Gillies, F. R. Szofran, and S. L. Lehoczky (NASA Marshall Space Flight Center, Alabama)

Beamline X20A

Magnetic X-ray Scattering Study of the Random Field Ising Model $Fe_{0.5}Zn_{0.5}F_2$ at X20A B-139
Q. Feng, Q.J. Harris, R.J. Birgeneau (MIT)

Magnetic x-ray scattering study of competing anisotropies in $Fe_xCo_{1-x}TiO_3$ B-140
Q. J. Harris, Q. Feng, R. J. Birgeneau (MIT), A. Ito (Ochanomizu University, Japan)

Critical behavior at the spin-peierls transition in $CuGeO_3$ B-140
Q. J. Harris, Q. Feng, R. J. Birgeneau (MIT), K. Kakurai, J. E. Lorenzo, G. Shirane (BNL), M. Hase, K. Uchinokura (University of Tokyo, Japan), H. Kojima, I. Tanaka, and Y. Shibuya (Yamanashi University, Japan)

Tricriticality in the phase diagram of stepped Si(113) surfaces B-179
S. Song and S. G. J. Mochrie (MIT)

Beamline X21

Inelastic x-ray scattering study of LiF B-141
Wolfgang Caliebe (NSLS), Chi-Chang Kao (NSLS), Michael Krisch (ESRF, France), Jerry Hastings (NSLS)

Resonant Raman Scattering Spectroscopy from Er B-141
K. Hamalainen (Univ. of Helsinki, Finland) C.-C. Kao, W.Caliebe and J.B. Hastings (NSLS), M. Krisch and F. Sette (ESRF, France)

High resolution Compton scattering study of beryllium B-142
K. Hamalainen, S. Manninen (Univ. of Helsinki, Finland), C.-C. Kao, W. Caliebe, J. B. Hastings (NSLS), A. Bansil, and S. Kaprzyk (Northeastern Univ.), P. Platzman (AT&T Bell Lab.)

Dynamic structure factor of solid and liquid metals B-142
J. P. Hill, C. C. Kao, J. B. Hastings, and Doon Gibbs (BNL)

Inelastic x-ray scattering study of $Li_{1-x}Mg_x$ alloys B-143
J. P. Hill, C. C. Kao, J. B. Hastings, and Doon Gibbs (BNL)

Inelastic x-ray scattering and the mit in V_2O_3 ..... B-143
E. D. Isaacs, P. M. Platzman (AT&T), C. C. Kao (NSLS), P. Metcalf, J. Honig (Purdue Univ.)

Inelastic x-ray scattering study of diamond B-144
C.-C. Kao, W. Caliebe (NSLS), M. Krisch (ESRF, France), K. Hamalainen (Univ. of Helsinki, Finland), J. Hastings (NSLS)

Evidence for quadrupolar contribution to the absorption cross section at the L_{III} edge of gadolinium gallium garnet B-144
M. Krisch (ESRF), C.-C. Kao (NSLS), F. Sette (ESRF), W. Caliebe (NSLS), K. Hamalainen (Univ. Helsinki), and J. Hastings (NSLS)

Inelastic x-ray scattering from 6H-SiC B-145
A. T. Macrander, V. I. Kushnir, R. C. Blasdell, P. A. Montano (ANL), and C.C. Kao (BNL)

Inelastic x-ray scattering investigation of oxide insulators B-145
Peter W. Stephens (SUNY Stony Brook), Chi-Chang Kao (NSLS), Wolfgang Caliebe (NSLS), and Jerry Hastings (NSLS)

Beamline X22A

X-ray studies of the hydrogen charging and discharging behavior of thin Nb films B-146
N. M. Jisrawi, T. R. Thurston, M. W. Ruckman, and Myron Strongin (BNL)

Beamline X22B

Langmuir monolayer phases of hexadecanoic acid ($CH_3(CH_2)_{14}COOH$) from crystallites B-146
M. Bommarito, W. J. Foster and P. S. Pershan (Harvard)

Grazing x-ray diffraction study of a monolayer of methyl arachidate at the air/water interface B-147
W. J. Foster, M. Shih, and P. S. Pershan (Harvard University)

X-ray reflectivity study of Si-based MOS devices B-147
S. D. Kosowsky, P. S. Pershan (Harvard), J. Bevk, and P. K. Roy (AT&T)

Surface structure of liquid mercury B-148
O. M. Magnussen, B. M. Ocko (BNL), M. Deutsch (Bar-Ilan Univ., Israel), M. Regan, and P. S. Pershan (Harvard)

Chloride and bromide adlayers on Au(111) and Ag(111) electrodes B-148
O. M. Magnussen, B. M. Ocko, J. X. Wang, and R. R. Adzic (BNL)

Observation of charge density waves in thin epitaxial Cr-films B-149
P. Sonntag, P. Bödeker, W. Donner (Ruhr-Universität Bochum), J. P. Hill, G.Helgesen, T. R. Thurston, D. Gibbs (BNL), and H. Zabel (Ruhr-Universität Bochum)

Electroepitaxy of Tl on Ag(001) and Au(001) B-149
J. X. Wang, R. R. Adzic, O. M. Magnussen, and B. M. Octo (BNL)

Beamline X22C

Antiferromagnetic layer formation in UAs B-150
N. Bernhoeft, A. Stunault, C. Vettier, F. De Bergevin (ESRF, CNRS), Doon Gibbs, T. R. Thurston, S. M. Shapiro, J. B. Hasings (BNL), P. Dalmas (CEA), G. Helgesen (BNL, Institutt Energiteknikk), O. Vogt (ETH)

Scaling of higher harmonic satellites near the magnetic phase transition of thulium B-150
G. Helgesen, J. P. Hill, T. R. Thurston, and Doon Gibbs (BNL)

Element specific magnetic scattering from a Ho-Pr thin film alloy B-151
J. P. Hill, G. Helgesen, Doon Gibbs (BNL), D. F. McMorrow (Riso), and R. A. Cowley (Oxford Univ.)

X-ray scattering study of the cubic-to-tetragonal transition and its precursor phenomenain V_3Si .. B-151
K. Hirota, Doon Gibbs, L. Rebelsky, G. Shirane (BNL), and S. J. Williamson (NYU)

Magnetic x-ray scattering from uranium antimonide B-152
S. C. Perry, W. J. Nuttall, W. G. Stirling (University of Keele, UK), G. H. Lander (E.I.T.U., Germany), and Doon Gibbs (BNL)

X-ray scattering characterization of high temperature superconducting wires B-152
T. R. Thurston, U. Wildgruber, T. Vogt, P. Siddons, J. Hastings, M. Suenaga, T.Wang (BNL), and P. Haldar (IGC Corporation)

Magnetic x-ray diffraction from neodymium B-153
D. Watson, E. M. Forgan, and D. Fort (Univ. of Birmingham, UK), W. J. Nuttall, andW. G. Stirling (Univ. of Keele, UK)

Surface magnetic scattering: UO_2 (001) B-153
G. M. Watson and Doon Gibbs (BNL), B. D. Gaulin (McMaster U.), and G. H. Lander (European Commission, Institute for Transuranium Elements)

Dynamics of phase separation on stepped Pt(001) surfaces B-154
G. M. Watson and Doon Gibbs (BNL), M. Yoon and S. G. J. Mochrie (MIT), and D. M. Zehner (ORNL)

Beamline X23A2

Bond length relaxation in $Si_{1-x}Ge_x$ alloys B-154
D. B. Aldrich, R. J. Nemanich, and D. E. Sayers (North Carolina State Univ.)

In situ EXAFS/XANES study of carbon-supported bimetallic Pt/Cu catalysts B-155
Simon R. Bare, Larry N. Ito, and M. Cisneros (Dow Chemical Co.)

EXAFS characterization of (Ag,Co)-multilayer structures B-155
Axel Bartos and Joseph C. Woicik (NIST)

Bioremediation of selenium by microbial action B-156
B. Buchanan (UCB), J. Bucher (LBL), D. Carlson (UCB), N. Edelstein (LBL), E. Hudson LLNL), N. Kaltsoyannis (LBL), T. Leighton (UCB), W. Lukens (LBL), H. Nitsche and T. Reich (Forschungszentrum Rossendorf e. V.), K. Roberts (LBL), D. K. Shuh (LB L), P. Torretto (LBL), J. Woicik (NIST), W-S. Yang(Jackson State U.), A. Yee (LBL), and B. C. Yee (LBL)

XAS study of Fe/Si and Fe/{FeSi} multilayers B-156
C. L. Foiles, M. Franklin and R. Loloee (MSU)

Performance of the ALS double-crystal monochromator B-157
G. Jones, S. Ryce, R. C. C. Perera (LBL), D. W. Lindle (UNLV), B. A. Karlin (NSLS), and J. C. Woicik (NIST)

XAS studies of Br^- aza complexes in non-aqueous electrolytes B-157
H. S. Lee, X. Q. Yang, and J. McBreen (BNL)

EXAFS study of ionic glassy Y_2O_3 and Y:Si:O B-158
J. M. Lee, D. S. Yang, C. U. Segre, and T. I. Morrison (Illinois Inst. of Technology),K. Zhang (U. of Chicago)

XAFS studies of atomic correlation in II-VI quaternary semiconductor alloys B-80
Q. Lu, B. A. Bunker, H. Luo, A. J. Kropf, S. H. Xin, J. K. Furdyna, and K. M. Kemner (Univ. of Notre Dame)

Glancing angle EXAFS studies of GE "pre-melting" at the Ge/C interface B-80
Q. Lu, B. A. Bunker (Notre Dame), R. A. Mayonovic (Southwest Missouri State Univ.),A. J. Kropf, S. T. Ruggiero (Notre Dame), J. R. Buschert (Goshen College)

In situ XAS studies of metal hydride electrodes B-158
J. McBreen, S. Mukerjee, J. J. Reilly, G. Adzic, and J. R. Johnson (BNL)

XAS studies of mixed salt $CoBr_2$/LiBr-PEO complexes B-159
J. McBreen, X. Q. Yang and H. S. Lee (BNL)

X-ray absorption studies of copper in copper-silicates II B-159
David A. McKeown (Howard University)

Role of structural and electronic properties of Pt and Pt alloys on electrocatalysis of oxygen reduction: an in-situ XANES and EXAFS investigation. B-160
S. Mukerjee and J. McBreen (BNL)

X-ray absorption spectroelectrochemistry B-160
Robert O. Rigney, Jie Yuan, Yingping Deng, Bella Helmer-Chudnovsky, William R.Heineman, and R. C. Elder (Univ. of Cincinnati)

Tb oxidation state and hybridization in $Y_{0.9}Tb_{0.1}Ba_2Cu_3O_{7-\delta}$($\delta$=0.02, 0.84) and $Pb_2Sr_2TbCu_3O_8$ B-161
U. Staub, Mark R. Antonio, and L. Soderholm (ANL)

Ex situ XANES study of anodic oxide film growth on zirconium thin films in boratesolution B-161
Carissima M. Vitus and Hugh S. Isaacs (BNL)

X-ray absorption studies of manganese oxide octahedral molecular sieves, clays, and coals B-162
S. R. Wasserman (ANL), F. W. Lytle (The EXAFS Co.), S. L. Suib (U. of Conn.), R.E. Winans (ANL), K. A. Carrado (ANL), S. E. Yuchs (ANL), and R. L. McBeth

Beamline X23A3

Microstructure control in nanophase zirconia B-162
A. J. Allen, S. Krueger, and G. G. Long (NIST), G. Skandan (Rutgers U.) and J.Parker (Nanophase Technology, Inc.)

Effect of x-radiation on ice B-163
Xiaohong Hu, Fuping Liu, Ian Baker (Dartmouth College), and David Black (NIST)

Structural characteristics of agarose gels studied by USAXS B-163
S. Krueger (NIST) and R. Nossal (National Institutes of Health)

Small-angle scattering studies of the microstructure of silicon nitride during processing B-164
G. G. Long, A. J. Allen, S. Krueger (NIST), and C. J. Hwang (Dow)

Microradiograpy of strained high-T_c superconductor composite tapes B-164
R. D. Spal, C. K. Chiang (NIST), G. N. Riley and A. Otto (American Superconductor Corp.)

Initial observation of [001] Domains in Czochralski-grown strontium barium niobate B-165
Bruce Steiner (NIST), Gerard Fogarty and Mark Cronin-Golomb (Tufts), Robert Uhrin, Mark Garrett, and John Martin (Deltronic Crystal Ind.), and Uri Laor (NRC-Negev)

Uniformity of strontium barium niobate, czochralski-grown for holographic storage B-165
Bruce Steiner (NIST), Gerard Fogart and Mark Cronin-Golomb (Tufts), Robert Uhrin,Mark Garret, and John Martin (Deltronic Crystal Ind.), and Uri Laor (NRC-Negev)

Beamline X23B

EXAFS studies of the decomposition of heat-treated fcc-$Fe_{50}Cu_{50}$ powders B-166
V. G. Harris, K. M. Kemner (NRL), P. Crespo, A. Hernando (Instituto de MagnetismoAplicado, Madrid, Spain), A. Garcia Escorial (CENIM-CSIC, Madrid, Spain)

Thermal stability and crystallization of amorphous $Tb_{33}Fe_{66}$ films B-166
V. G. Harris, N. C. Koon and W. T. Elam (NRL)

Crystallization studies of thin Fe-B films using EXAFS B-167
V. G. Harris (NRL), S. A. Oliver (Northeastern Univ.), J. D. Ayers, and N. C. Koon (NRL)

Local structure and interface properties of fcc Fe on diamond B-167
V. G. Harris (NRL), D. Pappas (Virginia Commonwealth Univ.), and G. A. Prinz (NRL)

Direct measurement of octahedral and tetrahedral site environments in NiZn-ferrites B-168
V. G. Harris (NRL), C. M. Williams (Morgan Sate Univ.), M. Abe, and Q. Zhang (Tokyo Institute of Technology, Japan)

EXAFS studies of CsX-dibenzo-18-crown-6 ether solutions B-168
K.M. Kemner, W.T. Elam (NRL), D.B. Hunter, and P.M. Bertsch (Savannah River Ecology Lab.)

Wavelength-dispersive x-ray fluorescence detector B-169
J.P. Kirkland (SFA Inc.), V.E. Kovantsev (X-Ray Optical Systems, Inc.), C.M. Dozier (NRL), J.V. Gilfrich (SFA Inc.), W.M. Gibson (SUNY Albany), Qi-Fan Xiao (X-Ray Optical Systems, Inc.), and K. Umezawa (SUNY Albany)

Beamline X24A

Attenuation of photon in helium B-169
Y. Azuma, H. G. Berry, D. S. Gemmell, J. Suleiman (ANL), M. Westerlind, I. A. Sellin (U. Tennessee), J. C. Woicik (NIST), J. P. Kirkland (SFA/NRL)

Alkali absorption spectra B-170
Y. Azuma, J. Suleiman, H. G.Berry, P. L. Cowan, D. S. Gemmell (ANL), M. Westerlind (U. Tennessee)

Argon and potassium ion time-of-flight spectra near the k-edge B-170
Y. Azuma, J. Suleiman, H. G. Berry, P. L. Cowan, D. S. Gemmell, T. LeBrun (ANL)

Threshold dependence of x-ray emission from Ag metal B-171
A. Bartos and S. H. Southworth (NIST)

Electron/x-ray coincidence spectroscopy B-171
T. LeBrun (ANL), U. Arp, S. H. Southworth (NIST), M. A. MacDonald (Daresbury)

Threshold K-LL auger spectra of P in InP B-172
Honghong Wang (Univ. of Oregon), Joseph C. Woicik (NIST), Teijo Aberg (Helsinki Univ. Technol.), Mau Hsiung Chen (Lawrence Livermore Natl. Lab.), Alberto Herrera-Gomez, Tom Kendelewicz (Stanford Univ.), Anna Mantykentta (Univ. Oulu), Ken E. Miyano (Brooklyn College), Stephen Southworth (NIST), Bernd Crasemann (Univ. of Oregon)

Accomodation of strain in ultra-thin InAs/GaAs films B-172
J. C. Woicik, J. G. Pellegrino, S. H. Southworth, P. S. Shaw, B. A. Karlin (NIST),K. E. Miyano (Brooklyn College)

Beamline X24C

VUV spectroscopic study of lithium triborate crystal B-173
T. J. Chen (Southern Illinois U.), W. R. Hunter (Sachs Freeman Assoc.), M. Chen,R. Zitter, R. Tao (SIU), L. Song (Perking U.), J. C. Rife (Naval Research Center)

Beamline X25

A transmission-bragg phase plate for circular dichroism and x-ray raman scattering B-173
W. A. Caliebe, C.-C. Kao (NSLS), M. Krisch, F. Sette (ESRF, France), L.E. Berman, and J. B. Hastings (NSLS)

X-ray photon correlation spectroscopy study of brownian motion of gold colloids in glycerol B-174
S. B. Dierker (Univ. Michigan), R. Pindak, R. M. Fleming (AT&T), I. K. Robinson (Univ. Illinois), and L. Berman (NSLS)

Temperature dependent x-ray diffuse scattering from single crystals of La-Sr-Cu-O B-174
W. Dmowski, R. J. McQueeney, T. Egami (Univ. Penn), Y. P. Feng, and S. K. Sinha (Exxon)

Magnetic scattering from Dy and Lu in Dy/Lu alloys B-175
B. A. Everitt, M. D. Salamon, B. J. Park, C. P. Flynn (UIUC), T. Thurston, and D.Gibbs (NSLS)

Site selective EXAFS spectroscopy B-175
M. M. Grush (UC Davis), A. G. Froeschner (UC Davis), C. R. Randall (UC Davis/LBL),G. Christou (Indiana U.), and S. P. Cramer (UC Davis/LBL)

Structural studies of the NFκB transcription factor B-176
Stephen C. Harrison (HHMI/Harvard University)

The geometric structure of Rb/Cu(111) investigated with x-ray standing waves: Rb coverage dependence B-176
D. Heskett, P. Xu (Univ. of Rhode Island) L. Berman, C.-C. Kao (NSLS), and M. J. Bedzyk(Northwestern Univ. and Argonne MSD)

X-ray crystallographic studies of TBP recognizing DNA B-177
J. L. Kim (Howard Hughes Medical Institute), G. Patikoglou (Rockefeller Univ.), and S. K. Burley (Rockefeller Univ.) (Howard Hughes Medical Institute)

X-ray standing wave structural study of Pb-sorbed natural calcite ($10\underline{1}4$) surface B-177
Y. Qian, P. F. Lyman, M. J. Bedzyk (ANL and Northwestern Univ.), R. P. Chiarello, N. C. Sturchio (ANL), and L. E. Berman (BNL)

Site-selective EXAFS spectroscopy-II. High-resolution K_β emission and XANES spectra of nickel(II) complexes. High-resolution K'_β emission spectrum of Ni(II)-substituted rubredoxin B-178
C. Randall (LBL/UC Davis), A. Froeschner (UC Davis), M. Grush (UC Davis) and S.Cramer (LBL/UC Davis)

Transmitting beam position monitor and profiler tests B-178
D. Shu, J. Barraza, Y. Li, and T. M. Kuzay (ANL)

Tricriticality in the phase diagram of stepped Si(113) surfaces B-179
S. Song and S. G. J. Mochrie (MIT)

Beamline X26A

$Cr^{2+}/(Cr^{2+}+Cr^{3+})$ Measurements of Fe and Cr in Synthetic Olivine and Coexisting Glass as a Function of Oxygen Fugacity using Synchrotron micro-XANES B-179
S. Bajt, S. R. Sutton (U. of Chicago and CARS), G. McKay (NASA/JSC), T. Mikouchi (U. of Tokyo), and J. S. Delaney (Rutgers U.)

Assessment of the uncertainties and limitations of quantitative elemental analysis of individual fluid inclusions using synchrotron x-ray fluorescence B-180
R. J. Bodnar, R. J. Mavrogenes, A. J. Anderson (Virginia Tech.), S. Bajt, M. L. Rivers, and S. R. Sutton (Univ. of Chicago)

Synchrotron x-ray fluorescence and laser ablation ICP-MS microprobes: useful instruments for analysis of experimental run products and other small samples B-180
Claude Dalpé and Don R. Baker (McGill Univ., Canada), and Steve R. Sutton (Univ. of Chicago)

X-ray microprobe investigation of composition thresholds in the passivation of Fe-Cr alloys B-181
A. J. Davenport (BNL), M. Simmonds, M. Ryan, R. Newman (UMIST), S. R. Sutton, and S. Bajt (Univ. of Chicago)

Synchrotron x-ray fluorescence trace element measurements on interplanetary dust particles as a method to infer their sources and interrelationships B-181
George J. Flynn (SUNY Plattsburgh), Stephen R. Sutton, and Saša Bajt (Univ. of Chicago)

Iodine oxidation states in contact with minerals B-182
M. Fuhrmann (BNL/DAT) and S. Bajt (Univ. of Chicago)

Investigation of the pre-edge absorption XANES structure B-182
Albert L. Hanson (BNL), and Saša Bajt (Univ. of Chicago)

Micro-XANES analysis of chromium in wood treated with chromated-copper-arensate (CCA) B-183
B. L. Illman (Univ. of Wisconsin), S. Bajt, and S. R. Sutton (Univ. of Chicago)

Manganese detection in wood using x-ray absorption near edge structure B-183
B. L. Illman (Univ. of Wisconsin), D. G. Schulze (Purdue Univ.), S. Bajt, S. R.Sutton (Univ. of Chicago)

Structure determinations on fluid inclusions in quartz using XAFS and micro-beam techniques ... B-184
R. A. Mayanovic (Southwest Missouri State Univ.), A. J. Anderson (St. Francis Xavier Univ.), and S. Bajt (Univ. of Chicago)

Intracrystalline trace element partitioning relative to surface structure: sectoral and intrasectoral zoning in topaz B-184
Paul A. Northrup and Richard J. Reeder (SUNY Stony Brook)

Differential incorporation of Trace elements during growth of grossular and apatite: intrasectoral zoning vs. Dissymmetrization B-185
John Rakovan and Richard J. Reeder (SUNY Stony Brook)

Surface-controlled distributions of trace elements studied by synchrotron x-ray fluorescence microanalysis B-185
Richard J. Reeder (SUNY Stony Brook)

Synchrotron XRF analysis of trace elements in zoned garnets from metasomatic contact metamorphic aureoles, SE Alaska B-186
C. K. Ridgway, H. H. Stowell (Univ. of Alabama), S. Bajt (Univ. of Chicago), P. Nuessle (Univ. of Georgia)

Manganese oxidation states in *Gauemannomyces* infested wheat rhizospheres probed by micro XANES spectroscopy B-186
Darrell G. Schulze, Tina McCay-Buis, Don M. Huber (Purdue Univ.), and Stephen R. Sutton (Univ. of Chicago)

Determination of manganese oxidation state in soils using x-ray absorption near-edge structure (XANES) spectroscopy B-187
Darrell G. Schulze (Purdue Univ.), Stephen R. Sutton, and Saša Bajt (Univ. of Chicago)

X-ray microprobe tests of models for selenium and chromium heterogeneities in contaminated sediments B-187
Tetsu K. Tokunaga (LBL), Stephen R. Sutton, Saša Bajt (Univ. of Chicago), Al Thompson, and Karen Chapman (LBL)

Zerovalent metal solubility in silicate melts B-188
Shaoxiong Wen, Hanna Nekvasil (SUNY Stony Brook), and Saša Bajt (Univ. of Chicago)

Beamline X26C

X-ray topography of protein crystals B-188
V. Stojanoff and D. P. Siddons (BNL)

Preliminary Laue diffraction studies on acetylcholinesterase B-189
Joel L. Sussman, Raimond B. G. Ravelli (Lab. Crystallography and Structural Chemistry), Paul Singer, Bob Sweet, Mia L. Raves (Weizmann Inst. of Science), Joseph Nachman, Israel Silman (Weizmann Inst. of Science)

Beamline X27C

Critical fluctuations in $RbCaF_3$ studied in reflection and transmission geometries B-189
J. P. Hill, D. P. Siddons, J. B. Hastings (BNL), J-M. C. Gillet (Univ. Marne laVallee, France), D. McMorrow (Riso, Denmark), and A. Gibaud (Univ. Maine, France)

X-ray Focusing with a Dynamically Bent multilayer B-190
M. Krisch (ESRF, France), W. Caliebe, and P. Siddons (NSLS)

X-ray scattering characterization of high temperature superconducting wires B-152
T. R. Thurston, U. Wildgruber, T. Vogt, P. Siddons, J. Hastings, M. Suenaga, T.Wang (BNL), and P. Haldar (IGC Corporation)

Characterization of an aromatic liquid crystalline polyester | X1A

H. Ade (North Carolina State Univ.), B. Wood, and I. Plotzker (Du Pont)

We have investigated the phase morphology of a liquid crystalline polyester based on several aromatic monomers. Electron microscopy and differential scanning calorimetry indicated the existence of phase separation in materials based on this polyester, but these techniques could not determine whether the phases are chemically distinct, and if so how many phases there are, or whether the observed phase separation is solely due to differences in crystallinity. We therefore employed the chemical sensitivity of XANES microscopy[1] to investigate these materials and compared a melt-screened and un-screened sample. We found that the un-screened sample had four chemically distinct phases. As an illustration we show micrographs acquired at 285.0 eV and 286.8 eV in Figs. 1A and B, respectively. The former emphasizes aromatic content and a discontinuous phase with domains smaller then 100 nm, as well as continuous phases with dimensions of a few microns are clearly discernible. Fig. 1B reverses the contrast between the continuous phases, while there is virtually no contrast between the small features. This demonstrates the different chemical character of these domains (We assume that there are no orientational differences[2] for which we did not test explicitly). The phase morphology observed in the un-screened sample was completely absent in the screened sample, which illuminates and illustrates the structural dependence of the materials on the processing route.

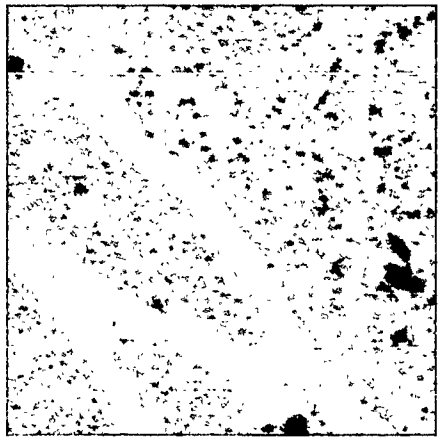


Figure 1. Micrographs of the same region of a thin section of an aromatic liquid crystalline polyester imaged at (A) 285.0 and (B) 286.8 eV. Field of view is 9 x 9 μm.

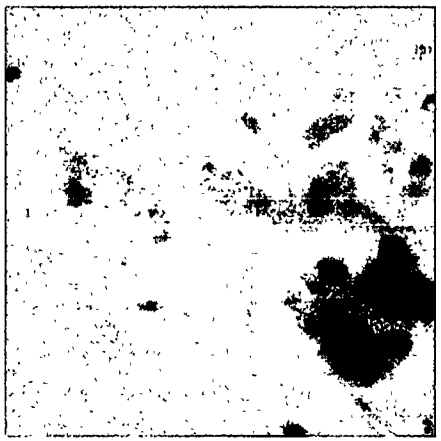


Figure 2.

Quantitative mapping of calcium using XANES and continuum spectral features * | X1A

C. J. Buckley

A technique for quantitatively mapping calcium in embedded and sectioned mineralised tissues has been developed and employed using the scanning transmission x-ray microscope (STXM) at the X1a beamline. Elemental mapping can be performed using just two images, one at a XANES peak and another at a pre-ionisation edge energy. However, the results are non-linear (due to monochromator band-pass effects) and give only an indication of the relative distribution of calcium in the specimen. By imaging across the absorption edge proper (where band-pass distortions are vanishingly small), and correcting for the organic content of the specimen by imaging across the carbon K-edge, it is possible to form a quantitative concentration map. The resulting map though quantitative, is rather noisy. However, this map can be used to scale the non-linear, high signal to noise image formed using a XANES peak, to produce a high signal to noise, quantitative calcium concentration map. An example of such a map is shown in figure 1.

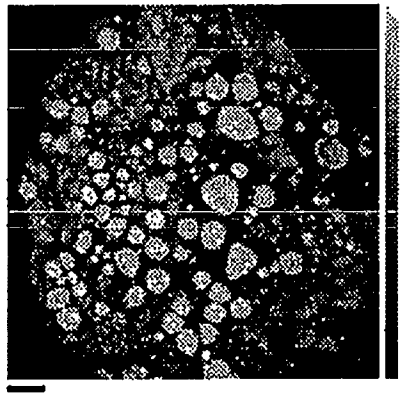


Figure 1. Quantitative calcium map of "tendonitis" human shoulder tendon section. This image was computed from five images taken at342.8eV, 350.4eV, 357.6eV(Ca L edge), and 278.6eV and 295.2eV(C K edge). The calcium concentration has been mapped in this 0.1 micron thick section, to show the distribution and density of the pathogenic mineral deposits in order to study the possible processes responsible for isolating the calcification in rounded islands. The scale bar is 20 micros, and the peak brightness represents a calcium concentration of 5.5 micro grams per cm^2.

* This work was aided by some fruitful discussions with Xiaodong Zhang of the Physics department of SUSB.

Imaging of immunogold-labelled cells by dark-field scanning transmission x-ray microscopy *	X1A

Henry N. Chapman, Chris Jacobsen, Jenny Fu (SUNY at Stony Brook), and Shawn Williams (Howard Hughes Medical Institute, Yale).

At the scanning transmission x-ray microscope (STXM), operated at the beamline X-1A, dark-field (DF) images have been obtained by blocking the undeviated transmitted photons so that only x rays scattered by the specimen are detected [1]. The method offers much higher contrast of small features then does bright-field (BF) and the possibility of detecting small features with higher signal to noise for the same incident x-ray flux. One important application of DF x-ray microscopy is the imaging of immunogold-labelled biological specimens. This unites the advantages of x-ray microscopy (the ability of imaging thick biological objects, low radiation dose) with those of gold labelling (specific-site or specific-protein labelling, well documented protocols).

DF images were acquired either by placing a circular stop, matched to the outside diameter of the zone-plate diffraction pattern, between the sample and the detector; or by collecting a series of microdiffraction patterns (one for each point in a two-dimensional scan) with a CCD detector and then extracting the DF and BF signals simultaneously by appropriate masking and integration of each frame.

Comparison of TEM and DF STXM images of a sample consisting of 30-nm-diameter gold spheres on a formvar film have shown that individual spheres can be detected easily in DF. Calculations have predicted that the signal to noise ratio (SNR) of a DF image of a single 30-nm sphere should be about 2.5 times that of a BF image, which has been experimentally verified using the CCD data. Images of a sperm cell labelled with 20-nm immunogold are shown in Fig. 1, Such images can be used for the study of the distribution of individual chromosomes and chromosome domains in sperm cells.

[1] G. R. Morrison and M. T. Browne, Rev. Sci. Instrum. 63, 611[-]614 (1992).

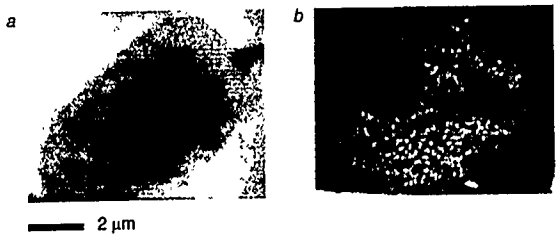


Figure 1. (a) STXM BF image, and (b) STXM DF image, of a sperm-cell labelled with 20-nm immunogold, attached by in-situ hybridisation to the telomere sequences of the chromosomes. The BF image isa map of the absorption, due mostly to carbon, whereas the DF image is a mapof the scattering, primarily from the gold.

* Supported by the NSF (Grant No. BIR-9316594) and the DoE (Grant No. DE-FG02-89ER60858).

Photochemical alteration of organic matter detected via C-NEXAFS *	X1A

G. D. Cody (ANL), H. Ade (NCSU), S. Wirick (SUNY), A. Davis, and G. Mitchell (PSU)

The vast majority of organic matter on earth is recycled through oxidative weathering. Important intermediate products of this oxidation are humic acids. The chemistry of humic acid formation is crucial to the establishing a relationship between the production of biomass and flux of carbon into rivers and ultimately into the oceans. In a related situation, fossilized organics (kerogens), exhumed during the weathering of sedimentary rocks may either be oxidized or re-entrained in sediments.

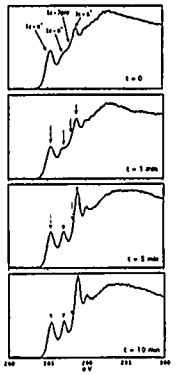
The extent to which any continental derived organic matter is recycled or preserved is clearly a function of a number of factors. An assessment of the contribution of oxidation kinetics and chemistris difficult as oxidation is surface phenomenon and kerogens are microheterogenous materials. We have set out to assess the chemistry of photochemical oxidation of a type III kerogen (woody tissue derived organic matter) using the microfocusing capabilities and energy scanning capabilities of STXM.

Figure 1 shows the time resolved photochemical alteration of kerogen's carbon edge spectrum. Oxidation was initiated via irradiation with blue light (450nm) under ambient atmospheric conditions. In the unaltered spectrum, absorption bands associated with aromatic, hydroxylated aromatic, methyl/methylene carbon, and carboxylic carbon are present. With irradiation the average number of hydroxyls and carboxyls per ring increases while the number of methyl/methylene groups decreases. The oxidation chemistry results from the parallel reactions,

$Ph\text{-}CH_3 \rightarrow PH\text{-}COOH$

$Ph \rightarrow PH\text{-}(OH)_n$

where both reactions are pseudo-first order in kinetics. These results constitute an important first step in understanding the oxidation chemistry of kerogens. An extension of this analysis to other types of otherwise resistant organic matter is in progress.



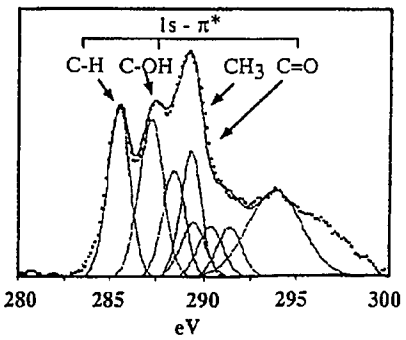
* Work supported by the Office of Basic Energy Sciences, Division of Chemical Science, US DOE Contract No. W-31-109-38

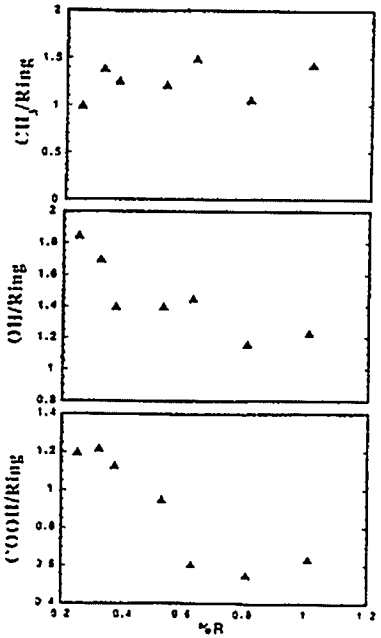
C-NEXAFS microanalysis of "pure components" in organic rich rocks | X1A

G. D. Cody, R. E. Botto (ANL), H. Ade (NCSU), S. Behal, M. Disko (ERE), S. Wirick (SUNY)

A high degree of compositional heterogeneity exists within organic (kerogen) rich sedimentary rocks which confounds most attempts to characterize the evolution of kerogen's molecular structure with increases in thermal maturity. Recently, we have employed the microimaging and analytic capabilities of the scanning transmission X-ray microscope (STXM) at X1A to address a variety of fundamental questions in organic geochemistry. The high degree of spatial resolution coupled with the energy scanning capabilities of the STXM provides information on the organic structure unattainable using any other analytical technique. By focusing on the evolution of a "pure component" we hope to better elucidate the trends in specific functional group concentration and constrain the various reaction mechanisms.

Figure 1 shows a representative carbon spectrum of a type III (woody tissue derived) kerogen. A number of absorption bands are present corresponding to aromatic carbon, hydroxylated aromatic carbon, aliphatic carbon, and carboxylate carbon. Figure 2 shows the concentration of methyl, hydroxyl, and carboxyl groups, all on a "per aromatic ring" basis plotted against the rank parameter % R (the reflectivity of vitrinite measured in oil). In terms of an average chemical structure for these kerogens, the kerogen evolves from a dihydric to monohydric aromatic system, with a nearly 50% reduction in carboxylic groups, and essentially no change in the concentration of methyl (and/or methylene) carbon. Current efforts are focusing on the thermal evolution of other kerogen types.





First results with the second generation scanning photoemission microscope * | X1A

Cheng-Hao Ko, Janos Kirz (SUNY Stony Brook), Harald Ade (NCSU), Erik Johnson, Steve Hulbert (NSLS) and Erik Anderson (LBL)

For the past few years we have been developing an instrument - the X1A Second Generation Scanning Photoelectron Microscope (X1A SPEM II) - that combines the techniques of X-ray Photoelectron Spectroscopy (XPS) and Zone Plate (ZP) microfocusing to perform spectromicroscopy. The X1A undulator provides a bright photon source (a requirement for microscopy) in the soft x-ray range with a high degree of transverse coherence for ZP focusing. Photon energy can be selected with the SGM (280-800 eV). A Fresnel ZP focuses the monochromatic beam to form a microprobe (with the current ZP, the spatial resolution is about 0.2 μm). Photoelectron spectra are acquired from the small irradiated area by a Hemispherical Sector Analyzer (HSA) with a multi-channel detector. With the beam focused on the sample and the energy window of the analyzer tuned to a specific photopeak, element-specific images are obtained by mechanically scanning the sample. Sample current (related to total electron yield) as well as other signals (up to 16 input signals) can be monitored simultaneously to form images.

In order to fully utilize the photon energy range (280 to 800 eV), the X1A SPEM II is equipped with an advanced positioning device for the focusing elements, which allows the position of the ZP to be readjusted when different photon energy is used (the focal length of a ZP is proportional to the photon energy). The multi-channel detector of the HSA enables simultaneous acquisition of multiple photoelectron images with each image corresponding to an equally spaced kinetic energy with a certain energy bandwidth (the bandwidth and energy separation between channels are set by the pass energy of the HSA). With this parallel detection scheme, different core level shifts peak at different channels in the multi-channel detector. This technique - Parallel Imaging for Chemical State Mapping (PICSM) - is a unique feature of our spectromicroscope. With the PICSM technique, image drifting due to repeated scans is eliminated by mapping the chemical shifts with one single scan.

Fig. 1 [unavailable due to space constraints] shows a fine resolution photoelectron image (tuned to the Nb 3d photopeak) of a Nb circuit. Image size is 120 pixels by 120 pixels with a pixel size of 0.25 μm and a dwell time of 220 ms. The shadowing effect is caused by topological features on the surface. Fig. 2 [unavailable due to space constraints] is a sample current image acquired simultaneously with the photoelectron image. Fig. 3 [unavailable due to space constraints] shows XPS spectra taken at two different locations on the surface.

* Work at the NSLS is supported in part by the DOE under contract DE-AC-02-76CH00016. The Center of X-ray Optics is supported by the DOE under contract DE-AC-03-76SF00098.

X-ray Gabor holography | X1A

Steve Lindaas and Malcolm Howells (ALS/LBL), Chris Jacobsen and Alex Kalinovsky (Physics Dept/SUNY Stony Brook)

Soft x-ray microscopy offers an approach to transmission imaging of wet, micron-thick biological objects at a resolution superior to that of optical microscopes. Gabor holography has unique characteristics which make it particularly well suited for certain investigations: it requires no prefocussing, it is compatible with flash x-ray sources, and it is able to use the whole footprint of multimode sources. Work at X1A serves to refine the technique in anticipation of the development of suitable flash sources (such as x-ray lasers) and to develop cryo capabilities with which to reduce specimen damage. Our primary emphasis has been on biological imaging so we use x-rays in the water window (between the O-K and C-K absorption edges) with which we record holograms in vacuum or in air. The hologram is recorded on a high resolution recording medium; our work employs the photoresist poly(methylmethacrylate) (PMMA). The developed photoresist records hologram fringes as surface topography; we have therefore developed a custom atomic force microscope[1] with a highly linear ($\sim 0.05\%$) scanning stage for hologram readout. We reconstruct numerically with a computer, obtaining both the magnitude and phase of the reconstructed image. With this approach we imaged dry diatoms at sub 45 nm resolution [2] (the best obtained by an x-ray holographic technique to date). We have also reconstructed holograms of latex spheres (an organic object) recorded in air and in an aqueous environment. We show a subimage from a reconstructed image of a critical point dried NIL cell. An image from a visible light microscope (100× N.A.=0.9) of the same region is shown for comparison. Small subcellular features as well as a tendril are observed in the x-ray image that are not resolved in the visible light micrograph. We are continuing to refine X-ray Gabor holography for the examination of biological specimens.

[1] S. Lindaas, C. Jacobsen, M. Howells, and K. Frank, "Development of a linear scanning force microscope for x-ray Gabor hologram readout" [Proc. SPIE 1741, pp. 213–222 (1992).

[2] S. Lindaas, X-ray Gabor Holography using a Scanning Force Microscope, PhD thesis, Department of Physics, SUNY at Stony Brook (April 1994).

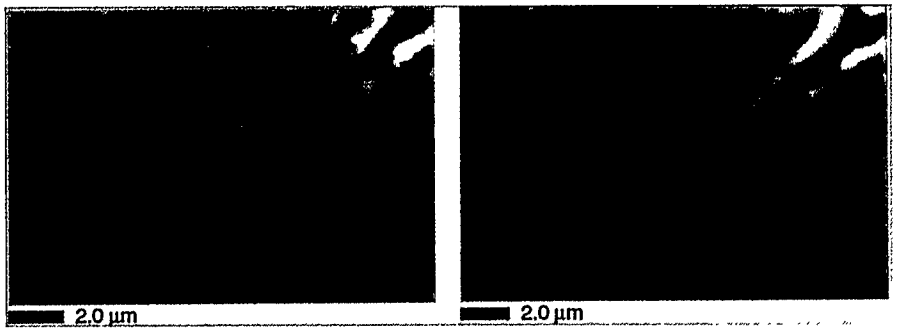


Figure 1. (Right) Reconstructed Gabor hologram. Figure 2. (Left) Visible light micrograph.

Determination of degree of radial ordering in kevlar fibers using x-ray linear dichroism microscopy * | X1A

A. P. Smith, H. Ade (North Caroline State Univ.), B. Hsiao, and S. Subramoney (Du Pont)

We are in the process of utilizing x-ray linear dichroism microscopy[1] to quantitatively determine the degree of radial order in poly(p-phenylene terephthalamide) (Kevlar^{TM}) fibers. Micrographs of thin sectioned fibers cut at 45° exhibit a "butterfly pattern when imaged at a specific photon energy. This pattern is strongest for Kevlar 149, intermediate for Kevlar 49, and weakest for Kevlar 29. By analyzing pairs of images obtained at 285.5 eV and 283.0 eV respectively, we will be able to quantitatively determine the degree of ordering of the aromatic groups in the various fiber grades. By obtaining NEXAFS spectra in the more transparent (horizontal) and more absorbing (vertical) directions of the fibers as exhibited in the micrographs, an independent measure of the degree of order can be obtained. The difference between the grades is illustrated by the spectra in figure 1. The relative change in peak heights between the horizontal and vertical locations and between the two grades of fibers is most apparent for the carbonyl π^* resonance (288.1 eV) and the sigma resonances (296 and 304 eV). By extracting these peak heights and their changes through a spectral fitting procedure, we will obtain quantitative information for the degree of radial ordering in these fibers.

[1] H. Ade and B. Hsiao, Science 262, 1427 (1993).

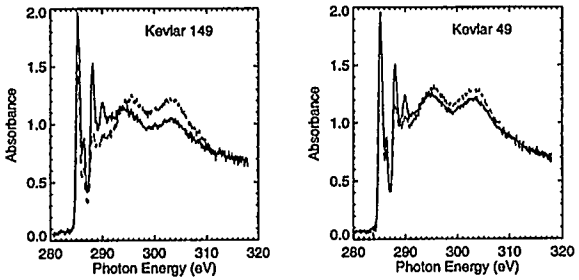


Figure 1. Spectra of Kevlar 149 and Kevlar 49 fibers obtained from the relative transparentareas (dash) and relative absorbing areas (solid) of an image acquired at 285.5 eV. The differences in the peak intensities is an indication of the degree of radial order in the fiber. Note, that the peak intensity differences are much smaller in Kevlar 49 than in Kevlar 149. By fitting the intensities of these spectral differences, quantitative information of the degree of order can be obtained.

* Work supported by NSF, under grant DMR-9458060

Mapping and measuring DNA and proteins in sperm using the scanning transmission x-ray microscope	X1A

X. Zhang (SUNY Stony Brook), R. Balhorne (Lawrence Livermore Natl. Lab.), J. Kirz (SUNY Stony Brook), and S. Williams (Howard Hughes Med. Inst., Yale Univ.)

X-ray absorption near-edge structure spectra have been used in STXM to show chemical contrast in polymer blends and to map proteins and DNA in Chinese hamster ovarian cells at beamline X1A. Figure 1 shows the x-ray absorption fine structure spectra at the carbon absorption edge from DNA and bovine serum albumin (BSA, a typical protein) taken using the STXM. Differences between the spectra of these two biologically important molecules have been used to distinguish DNA and proteins. By images taken at the spectral peaks, and by further numerical image processing, the protein and DNA distribution can be separated. Recently, this method has been applied to map DNA and protein in sperms from five different species and to measure total protein and DNA amounts in the sperm heads.

Potamine 1 and protamine 2 are two basic proteins involved in DNA packing in sperm heads. Studies have shown that sperm from different species have a different protamine 2 content. The problem we are attempting to solve with this method is to determine whether the DNA to protein ratio in different sperm, which have different amounts of protamine 2, is constant. This will allow us to determine whether there is a constant amount of protamine 1 in the sperm of all species, or if the total protamine content is constant, and protamine 2 replaces an equivalent amount of protamine 1. Male infertility is also believed to be linked to the lack of protamine 2. Previous work by chemical analysis methods yielded averaged results from a large pool of sperm. Here we are attempting to measure the protein amount in individual sperm to investigate whether all infertile sperm lack protamine 2 or just some do. Figure 2 shows DNA and protein distributions in an individual bull sperm head. The DNA distribution is quite uniform inside the head, while the protein distribution varies along the head showing a pronounced equatorial band. Preliminary results also show that the DNA to protein ratio in bull, stallion, hamster and mouse sperm is a constant. Further analysis is needed to draw a firm conclusion.

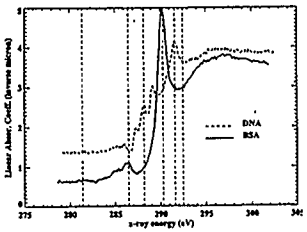


Figure 1. X-ray absorption near-edge fine structure spectra of DNA and BSA at the carbon absorption edge. These differences are used to separate DNA and protein.

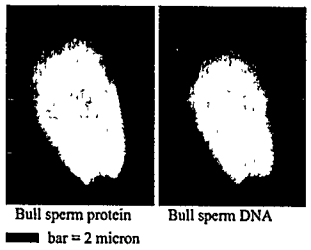


Figure 2. Distribution of DNA and protein in a bull sperm head. The DNA distribution in the sperm head is quite uniform while the protein distribution has significant variation.

Electronic structure of buried α-$FeSi_2$ and β-$FeSi_2$ layers: Soft x-ray emission and absorption studies compared to band structure calculations	X1B

S. Eisebitt, J.-E. Rubensson, M. Nicodemus, T. Böske, S. Blügel, W. Eberhardt (IFF, KFA Jülich), G. Bihlmayer (Univ. Wien), K. Radermacher, and S. Mantl (ISI, KFA Jülich)

We have studied the electronic structure of $FeSi_2$ layers buried by means of ion-beam-synthesis in Si wafers. $FeSi_2$ exists in two thermodynamically stable (bulk-) phases, as tetragonal, metallic α-$FeSi_2$ and as orthorhombic, semiconducting β-$FeSi_2$. This phase in particular has lately attracted interest because of its potential in optoelectronics. Using fluorescence spectroscopies, we were able to investigate the silicide layers, which are buried below a 600 Å Si cap layer, in situ. Fe L_3 soft x-ray emission (SXE) spectra for both $FeSi_2$ phases are presented in Fig.1. They reflect the occupied local Fe d density of states (except in the region above 0 eV, where correlation effects in the nonbonding states influence the spectral shape) and and are in good agreement with our ab-initio band structure calculation. The high energy cut-off in the spectra is located at lower energy in β-$FeSi_2$ than in α-$FeSi_2$, indicating the metallic to semiconducting transition in the two phases. The unoccupied Fe d density of states was probed by soft-x-ray absortion (SXA) spectra, recorded in the fluorescence-yield (FY) mode at the same Fe L_3 edge. The inclusion of the core hole potential was found to be crucial in order to compare the band structure calculations with the experiment (Fig.2). The absorption edge in the β phase is shifted to higher energy, again reflecting the formation of the bandgap. By combining the two experiments, the bandgap in the electronic states of d-symmetry locally at the Fe atoms of β-$FeSi_2$ was found to be 0.8 ± 0.2 eV, in agreement with our calculation (0.78 eV).

[1] S. Eisebitt, J.-E. Rubensson, M. Nicodemus, T. Böske, S. Blügel, W. Ebehardt, K. Radermacher, S. Mantl, and G. Bihlmayer , Phys. Rev. B 50, 18330 (1994)

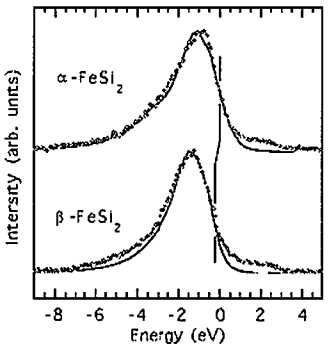


Figure 1. SXE spectra (circles) of buried layers of α-$FeSi_2$ (top) and β-$FeSi_2$ (bottom) referred to the Fermi energy.

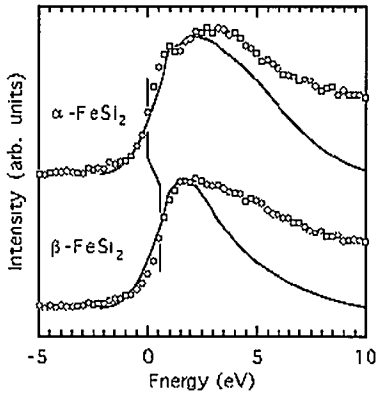
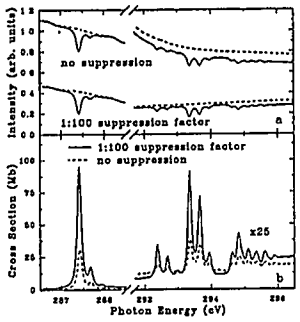


Figure 2. FY-SXA spectra (circles) for buried layers of α-$FeSi_2$ (top)and β-$FeSi_2$ (bottom) recorded at the Fe L_3 absorption edge.

Absolute photoabsorption cross section measurements of simple molecules in the core level region *	X1B

B. S. Itchkawitz, B. Kempgens, H. M. Köppe, J. Feldhaus, A. M. Bradshaw (Fritz-Haber-Institut), and W. B. Peatman (BESSY)

Absolute inner-shell photoabsorption cross section measurements were obtained from a variety of simple gas-phase molecules containing low Z elements (C, N, O, F), independent of the effects of stray light, high order light, and photoabsorption from the various optical elements. The experimental apparatus consisted of a compact high order light suppressor (HOLS), which uses two plane mirror reflections at grazing angles to suppress the high order radiation from the monochromator while yielding a reasonable transmission of light of the desired energy, and a gas-phase absorption system which measures the photon flux before and after a gas cell, to produce absorption spectra independent of the contributions from absorption of the various optical elements, response functions of the photon detectors used, and variations of the photon flux during the scans. The subsequent absolute photoabsorption cross section measurements can be made in a straightforward way, without the background subtraction, kinematic correction, and scaling procedures necessary in the inner-shell electron energy loss measurements. The effect of high order light on photoabsorption spectra is apparent by comparing the C-1s threshold region of CO measured with and without high order suppression. Figure 1a show the normalized transmission through the filled (solid line) and empty (dashed line) gas cell without high order suppression and with a suppression of R2(600 eV): R2(300 eV) = 1:100. Figure 1b show the resulting photoabsorption cross section with 1:100 suppression (solid line) and with no suppression (dashed line). For the CO C-1s→ π^* and C-1s→ Rydberg resonances, the high order light reduces the apparent resonance cross sections and changes the background. The absorption of CO of the second order light (574-600 eV) is small and does not have any structure, so the existence of the high order light reduces the percentage of the light apparently absorbed by the gas. In general though, for spectra taken without the HOLS, structure in the high order absorption of the sample would appear as additional structure in the measured first order photoabsorption.



* This work is supported by the German Minister for Research and Technology.

High resolution photoemission study of C_2H_4 at the C K-Edge	X1B

H. M. Köppe, M. Schmidbauer, B. S. Itchkawitz, A. L. D. Kilcoyne, J. Feldhaus, and A. M. Bradshaw (Fritz-Haber-Institute, Berlin)

Recent high resolution photoemission studies on the C 1s level of CO have revealed a wealth of additional information on the vibrational fine structure and the shake-up satellites [1,2]. As a further example we have studied the C 1s photoelectron spectrum of C_2H_4 in the threshold region where a strong shape resonance is found at a photon energy of ~298 eV[3]. Two typical C 1s spectra are shown in Fig. 1, one near the maximum of the shape resonance (a), the other one at higher photon energy (b). The influence of the resonance on the vibrational structure is evident from the spectra. In contrast to the C $1s^{-1}\pi^*$ excitation leading to vibronic coupling and to the excitation of non-to-tally symmetric vibrational modes, the photoelectron spectra can probably be explained by the excitation of just the two totally symmetric C-H and C=C stretching modes ν_1 and ν_2. Since the shape resonance is located on the C=C bond the two vibrational progressions should be affected in a different way in this energy region. A preliminary analysis gives 415 meV and 190 meV for ν_1 and ν_2, respectively, suggesting a strengthening of the C-H bond and a weakening of the C=C bond in the core ionized molecule. For the lifetime broadening we find a value of 90 ± 10 meV. These values are the result of a least squares fit using asymmetric line profiles characteristic for post-collision-interaction (PCI).

[1] K.J. Randall, A.L.D. Kilcoyne, H.M. Köppe, J. Feldhaus, A.M. Bradshaw, J.-E Rubensson, W. Eberhardt, Z. Xu, P.D. Johnson, Y. Ma, Phys. Rev. Lett. 71, 1156 (1993).

[2] T. Reich, P.A. Heimann, B.L. Petersen, E. Hudson, Z. Hussain, D.A. Shirley, Phys. Rev. A 49, 4570 (1994)

[3] A.L.D. Kilcoyne, M. Schmidbauer, A. Koch, K.J. Randall, J. Feldhaus, J.Chem. Phys. 98, 6735 (1993).

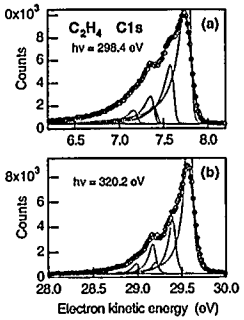


Figure 1. The C 1s photoelectron spectrum of C_2H_4 measured on the shape resonance (a) and at higher photon energy(b). The open circles are data points. The full line is the result of a least squares fit convoluting PCI line shapes (shown as dashed lines) with the instrumental profiles of the electron spectrometer and the monochromator.

Spin-orbit coupling, exchange interaction and hybridization in the photo-excitation of the Ni 3p core level * | X1B

Y. Liu, Z. Xu, P. D. Johnson (BNL), G. van der Laan (Daresbury Laboratory, UnitedKingdom)

Shown in fig. 1, a spin polarized photoemission study of the Ni 3p core level reveals the spin polarization of the main line and the satellites. The incident photon energy for these studies is 250 eV. The satellite D at 14 eV binding energy with respect to the main peak is predominantly majority spin, that at 6 eV, C, is a mix of majority and minority spin. A detailed comparison with calculation confirms earlier assignments that these satellites have d^9 character. However the measurement also reveals the role of spin-orbit and exchange interactions in determining the spin polarization of the main peak. In particular the main peak's leading edge, A, is found to have predominantly $\underline{c}3d^9$ character where $\underline{c}$ represents the core hole in the final state. The shoulder at higher binding energy, B, reflecting the spin-orbit interaction has predominantly $\underline{c}3d^{10}$ character. These assignments reflect the strong hybridization of the d^9 and d^{10} configurations.

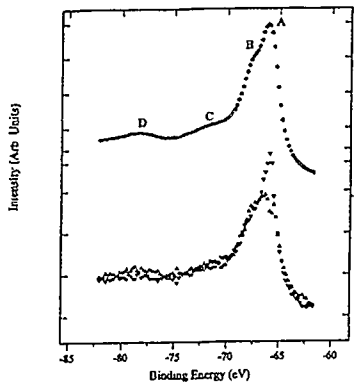


Figure 1. Spin integrated (upper spectrum) and spin resolved (lower spectra) photoemission spectra of the Ni 3p core level. A-B indicate "spin-orbit derived features in the main line and C andD indicate satellite features. In the lower panel the minority spin electrons are indicated by the opentriangles and the majority spin electrons are indicated by the filled triangles. The incident photon energy is 242 eV.

* Work supported in part by the Department of Energy under contract number DE-AC02-76CH00016.

Selectively Excited Core-to-Core Fluorescence of Potassium Halides * | X1B

J. Lüning, J.-E. Rubensson, S. Eisebitt, and W. Eberhardt (IFF, KFA-Jülich, Germany)

Potassium salts are to a first approximation atomic-like systems with closed shells. In threshold excited core-to-core fluorescence states are populated that cannot be reached in a single absorption process due to the dipole selection rule, e.g., the K $3s^{-1}3d$ states. The quasi-atomic interactions and the influence of solid state effects in these states can be investigated. This method was applied earlier by Rubensson et al. [1] to CaF_2. In Fig. 1 the K $L_{2,3}$ absorption of KF is shown. In a simplifying picture [2] the four absorption resonances are assigned to transitions from the spin-orbit split K 2p levels to the crystal field split $3d$ levels (the K 3d orbitals are split in states of t_{2g} and e_g symmetry directed in-between and towards the halide atoms, respectively). Due to the positive charge of the K 2p core hole the 3d orbitals are contracted towards the K core and the 3d electrons are bound in an excitonic state to the core hole. These excitation are located below the ionization limit, as determined from photoemission and optical band gap data. The absorption peaks A, A', B, and B' are within this simplified picture assigned to $2p_{3/2}t_{2g}$, $2p_{3/2}e_g$, $2p_{1/2}t_{2g}$, and $2p_{1/2}e_g$ states, respectively. The emission spectra in Fig. 2 were excited high above the ionization threshold and at the absorption resonances, as indicated in the figures. The high energy excited spectrum shows two peaks corresponding to the K $2p_{3/2}^{-1} \rightarrow 3s^{-1}$ and $2p_{1/2}^{-1} \rightarrow 3s^{-1}$ transitions. Compared to these the resonantly excited spectra A and B show emission structures that are broadened and shifted towards lower emission energy. These peaks are due to spectator transitions of the excited K $2p^{-1}t_{2g}$ excitons into the K $3s^{-1}t_{2g}$ final state which is split by the exchange interaction. The low intensity of one of the components in the case of the e_g excited spectra (A' and B') indicates that transitions of ionized K core holes contribute to these spectra. Thus, well-below the ionization threshold determined from photoemission and optical band gap data the excited 3d electron seems to be able to delocalize. For further details we refer to our publication submitted to Physical Review B.

[1] J.-E. Rubensson et al., Phys. Rev. B 50, 9035 (1994)
[2] F.M.F. de Groot et al., Phys. Rev. B 41, 928 (1990)

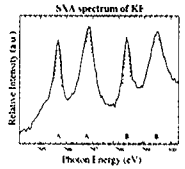


Figure 1. Dotted lines are the 'excitation functions' (absorption spectra multiplied bythe different monochromator functions) for SXE spectra in Fig. 2.

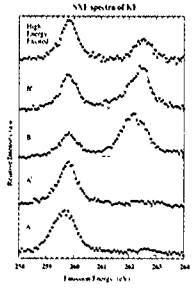


Figure 2. The notation refers to the excitation functions of Fig. 1.Dotted lines give single peak contributions as resulting from a line shape analysis

* S.E. is supported by the DAAD (HSPII)

X-ray microtomography	X2B

J. H. Dunsmuir, J. H. Hardenbergh, and B. P. Flannery (Exxon)

During this year, we at Exxon have used X-ray microtomography (XMT) to characterize porous media and in particular, oil reservoir rocks. XMT produces three dimensional X-ray opacity information from 1-5 millimeter sized objects with 1-10 micron resolution. The pore geometries obtained using XMT of a representative group of reservoir rocks have been imported into geometric and diffusive transport models and used to calculate rock properties such as porosity, permeability and formation factor. We continue to obtain good agreement between model calculations and laboratory measurements of rock properties for rack types with simple structure.

A preliminary study with David Sarnoff Research Center (DSRC) to evaluate the use of XMT and real time digital subtraction microradiography (DSR) for the characterization of micromachines has resulted in a joint proposal to ARPA. We propose to apply DSRC's imaging and parallel computing technology to microtomography data acquisition, processing, analysis and visualization to significantly advance the capabilities of X2B.

In a collaborative effort with the Mayo Foundation we have successfully demonstrated the ability of microtomography to measure the micro structure of several specimens of biological interest. Three dimensional data sets of rodent organs include the cardio-vascular tree, the liver vascular and bilary duct systems, bone haversian network and the structure of the lung. Whole rodent organs are scanned using a conventional X-ray source and small portions of these specimens are scanned at high resolution at X2B using region of interest reconstruction techniques. The Mayo Foundation has been awarded NIH and NSF funding for a three year research program to continue this work.

We have done an initial study of the structure and properties of concrete specimens before and after sulphate attack with researchers from NIST. X-ray microtomography shows the three dimensional aggregate and mortar distribution as well as internal cracks and small crystal formation due to the sulphate attack. Structural relationships obtained from XMT data are to be used to compare calculated with measured mechanical properties.

Construction of a high energy Bonse-Hart ultrasmall-angle x-ray scattering instrument *	X3A1

B. Chu, F. Yeh, Y. Li, P. J. Harney, J. Rousseau (SUNY Stony Brook), A. Darovsky (SUNY, NSLS, BNL), and D. P. Siddons (NSLS, BNL)

A Bonse-Hart ultrasmall-angle X-ray scattering (USAXS) instrument, employing a synchrotron X-ray source at an energy of 18.86 keV (wavelength $\lambda = 0.06573$ nm), has been designed, constructed and tested. The HWFM is 3.6 arc second which is close to the theoretical value, 2.9 arc second of Si(111). Solid as well as suspensions of polystyrene and poly(chlorostyrene) latex spheres were used as reference standards in order to demonstrate the range of this instrument. The USAXS results measured at $\lambda = 0.06573$ nm were compared with those from a calibrated Bonse-Hart instrument operating at $\lambda = 0.154$ nm. It can achieve a lower q value than when working at $\lambda = 0.154$ nm. It can achieve a lower q value than working at $\lambda =$ 0.154 nm because of the smaller HWFM. The crystals were supported by super Invar mechanical elements, making the high temperature experiments feasible. Moreover, the higher-energy synchrotron X-rays permit us to study absorbing and/or opaque materials having long range inhomogeneities of the order of microns. Furthermore, for many polymer systems the optimal sample thickness at $\lambda = 0.066$ nm is increased to ~10 mm and thin-walled glass windows become acceptable. Thus, both USAXS and LLS could measure the same sample by using a cylindrical glass cell with a wall thickness of 0.3 nm.

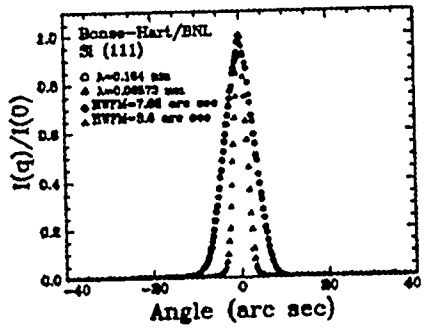


Figure 1. Rocking curve of Bonse-Hart USAXS.

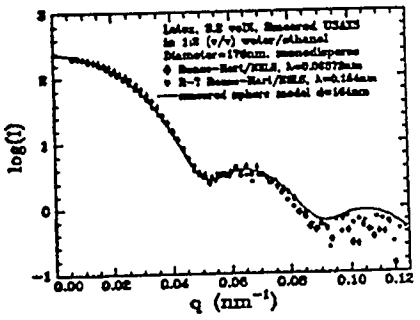


Figure 2. USAXS profile of PS latex suspension (3.2 vol %).

* The SUNY X3 beamline at NSLS is supported by the Division of Basic Energy Sciences of the US Department of Energy (DE-FG02-86ER45231). Support of this work by the US department of Energy is gratefully acknowledged (DE-FG02-86ER45237.)

Development of the use of imaging plates in accurate crystallographic data collection at synchrotron sources *	X3A1, X3A2

P. Coppens, R. Bolotovsky, and A. Darovsky (SUNY Buffalo and BNL)

An improved dynamic mask procedure for the integration of imaging plate diffraction maxima has been developed. A peak mask is identified that grows from a seed until the skewness of the intensity distribution outside the mask is minimized. This "seed-skewness" method provides a much more reliable estimate of the intensity of weak peaks than the standard box method and does not require any a priori information about the peak shape or the background distribution in the box. The improved performance of the method in providing accurate intensity data is demonstrated for a set of synchrotron diffraction intensities on sodium nitroprusside, $Na_2Fe(NO)(CN)_5 \cdot 2H_2O$, and a substituted fullerene derivative, Bis(4,4′-bromophenyl-61,61,diyl methanofullerene C_{60}. The comparison is illustrated in Figure 1. The improvement for the weak reflections is quite dramatic. Lower R-factors are also obtained in the structure factor least-squares refinement.

For a third set of data collected at a rotating anode source, we have reached agreement factors between repeated measurements of 0.5%, which is comparable with the best data obtained with conventional methods.

[1] R. Bolotovskyh, M.A. White, A. Darovsky and P. Coppens, J. Appl. Cryst. In Press.

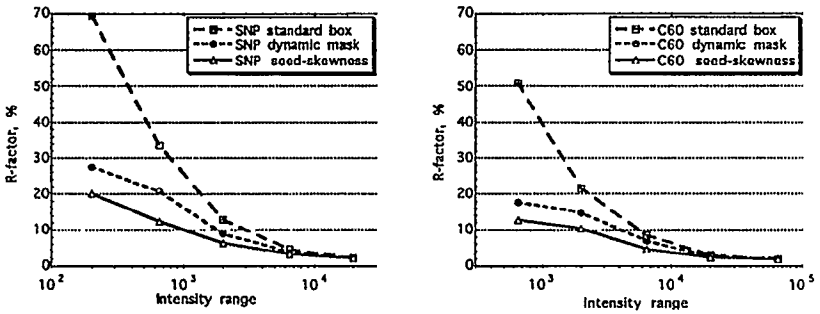


Figure 1. Agreement factor between equivalent reflections vs.intensity for data sets on sodium nitroprusside and bis (4,4′-bromophenyl)-61,61, diyl methanofullerene C_{60} processed by difference integration methods.

* The SUNY X3 beamline at NSLS is supported by the Division of Basic Energy Sciences of the US Department of Energy (DE-FG02- 86ER45231). We would also like to acknowledge the National Science Foundation for support of the work (CHE9308086).

The use of high energy synchrotron radiation in charge density studies *	X3A1

Philip Coppens, Robert Bolotovsky, Ruiming Li and Alex Darovsky (SUNY at Buffalo, BNL)

We have performed the first charge density study at NSLS, using imaging plates and a CT201 Displex cryostat equipped with the newly designed anti-scatter device at the fixed-angle X3A1 station. The results on sodium nitroprusside dihydrate, $Na_2[Fe(CN)_5NO] \cdot 2H_2O$, show that reliable data can be obtained with this configuration. A wavelength of 0.65Å from a Si(111) monochromator was used. To further reduce absorption and extinction effects a shorter wavelength is desirable. The newly installed sideways monochromator assembly on the X3A1 station allows use of a number of different wavelengths at this fixed- angle station by interchange of the monochromating crystals, which are mounted on a revolving crystal holder. With a Si(220)) crystal, a wavelength of 0.50Åavailable. We find that even at this bending magnet station, beam intensity is more than adequate with crystals of 200 μ maximum dimension. At 25K, diffraction spots are observed to at least $\sin\theta\lambda = 1.6\text{Å}^{-1}$, indicating that significant improvements in resolution are achievable.

* The SUNY X3 beamline at NSLS is supported by the Division of Basic Energy Sciences of the US Department of Energy (DE-FG02-86ER45231). We would like to acknowledge the National Science Foundation for partial support of the work (CHE9308086).

An anti-scatter device for low-temperature crystallographic experiments with imaging plates *	X3A1, X3A2

A. Darovsky, R. Bolotovsky, and P. Coppens (SUNY Buffalo and BNL)

The use of area detectors in low-temperature crystallographic data collection requires new methods for elimination of scattering cy cryostat chambers, because diffracted beam collimators cannot be employed when a large aperture area detector is sued as the recording device. A novel anti-scatter device was constructed for use with a closed-cycle helim cryostat (DISPLEX CT 201) (Figure 1). The device is mounted on a circular bearing inside the vacuum chamber. It is kept stationary during sample rotation by the use of a magnetic clamkp mounted outside the cryostat chamber. The apparatus has been successfully used in the collection of data sets on both conventional and synchrotron sources [1]. It is being used in low-temperature structure determination and in accurate low temperature measurements for charge density studies.

1. A. Darovsky, R. Bolotovsky and P. Coppens, J. Appl. Cryst., (1194) In Press.

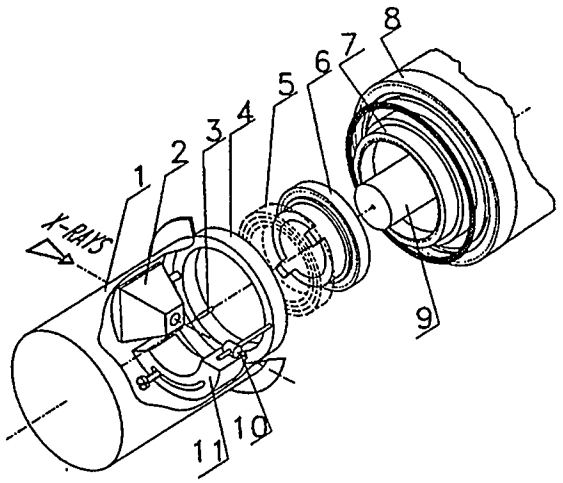


Figure 1. Radiation shielding assembly. (1) vacuum chamber, (2)incident beam tunnel, (3) pin for crystal mounting, (4) steelring, (5) outer ring of bearing, (6) mounting ring, (7) holding ring, (8) cryostat vacuum sleeve, (9) cold finger, (10) beamstop,(11) counter weight.

* The SUNY X3 beamline at NSLS is supported by the Division of Basic Energy Sciences of the US Department of Energy (DE-FG02-86ER45231). We would like to acknowledge the National Science Foundation for partial support of the work (CHE9308086).

Synchrotron structure determination of bis(4,4′-bromophenyl)-61,61,diyl methanofullerene C_{60} at room temperature and at 25k *	X3A1

B. Iversen (Aarhus Univ., Denmark), R. Bolotovsky (SUNY Buffalo and BNL), A. Darovsky (SUNY Buffalo and BNL), F. Wudl (UCSB) and P. Coppens (SUNY Buffalo and BNL)

This work represents the first determination of a methanofullerence crystal structure, and the first structure determination performed on the X3A1 beamline station. The analysis is made possible but the use of imaging plate methods, which we find to be much less sensitive to beam instabilities than sequential data collection techniques.

Initially it was suggested that all adducts prepared by reaction with diazomethance have the ring-opened structure 1, but more recently the assignment was revised [1] to structure 2 on the basis of a thorough NMR structural analysis and energy minimization calculations.

The X-ray structure shows that the critical transannular distance is bis(4,4/*prime*-bromophenyl)-61,61,diyl methanofullerene C_{60} in the figure) is 0.2Å longer than expected for a single bond and essentially of the same length as in 11,11- dimethylmethano[10] annulene 6, and thus supports structure 1 rather than 2. The solid state structure is more densely packed than C_{60}, at least in the a direction (9.913Å). Tough the molecules are not expected to rotate in the solid state as freely as C_{60} or $C_{61}h_2$, they show large amplitude librations around an axis running through the bridge carbon and the opposite pole of the fullerence.

25K data were collected to improve the precision of the experimental geometry through reduction in the quite pronounced thermal motion.

[1] M. Prato, V. Lucchini, M. Maggini, E. Stimpfi, G. Scorrano, M. Eiermann, T. Suzuki, and F. Wudl (1993) J. Am. Chem. Soc. 115, 8479.

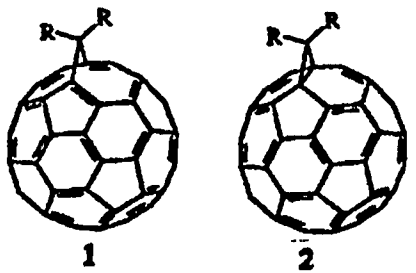


Figure 1.

* The SUNY X3 beamline at NSLS is supported by the Division of Basic Energy Sciences of the US Department of Energy (DE-FG02-86ER45231).

A novel microporous sulfide: TEA·Ge_2CuS_5. * | X3A1

K. Tan, J. B. Parise (SUNY Stony Brook), and A. Darovsky (BNL)

Hydrothermal treatment of amorphous GeS_2 in the presence of tetraethylammonium (TEA) hydrogen carbonate and cupric acetate at 150°C produces a novel three-dimensional open structure, TEA·Ge_2CuS_5. Because of the low density of these microporous sulfides (typical values of D_∞ range from 2 to 3 g/cm^3) and the small size single crystals produced in the synthetic runs (0.02×0.02×0.10 mm), synchrotron x-ray diffraction was used to collect data for structural determination and refinement.

Three sets of imaging plate data with different exposure times were collected at 16K. An oscillation angle of 10 degrees, with 2 degree overlap between consecutive frames, was used for the data collection. The compound, $TEAGe_2CuS_5$, crystallized in the space group I4, with a=b=17448 Å and c= 11.012 Å. The structure consists of the adamantine-like secondary building units $Ge_4S_{10}^{4-}$, four-connected by reduced Cu(I). The organic template, TEA^+ resides in the holes within the structure.

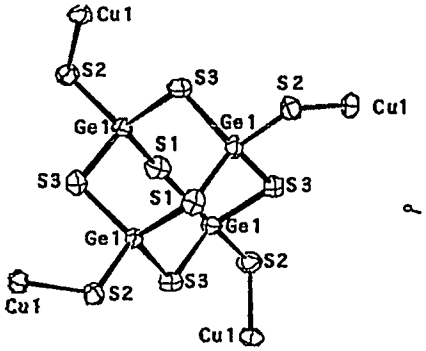


Figure 1. One of two crystallographically unique like $Ge_4S_{10}^{4-}$ building units.

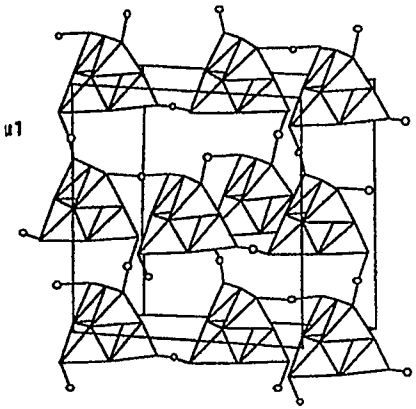


Figure 2. Ge-S polyhedra and frame-adamantine-work topology. Templates are omitted for clarity.

* The SUNY X beamline is supported by the Division of Basic Energy Sciences of the U.S. Department of Energy (DE-FG02-86ER45231). The National Science Foundation is gratefully acknowledged (DMR-9024249)

Time resolved SAXS of pet monofiber deformation * | X3A2

B. Chu, P. Harney (SUNY Stony Brook), and B. Hsiao (Du Pont)

A pre-aligned pinhole small angle x-ray scattering camera has been automated for more efficient use with synchrotron x-rays. Small angles below 2 mrad can be achieved with an alignment time of about 3 hours. An on-line deformation study of poly(ethylene terphthalate) PET monofibers has been undertaken. A modified Instron stretching device has been developed to deform thin films or fibers and permit irradiation with synchrotron x-rays. Automated control of stress, strain, and temperature facilitates morphological studies on many polymer systems. Initial studies of PET monofibers have shown a cross pattern typical of craze microstructure formation. Models for craze microstructure have been based on thin film studies until now. Initial results from time resolved deformation experiments are shown below. Preliminary morphological studies have also been performed. However, a sacrifice in the time resolution is made because of the low intensity from the small scattering volume.

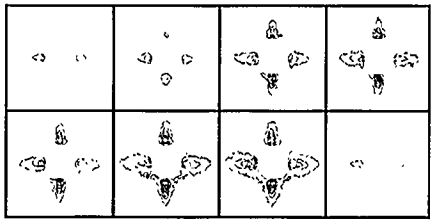


Figure 1. Time resolved SAXS for sample A1 (amorphous). Observation time was 45 sec over intervals of 22%strain.

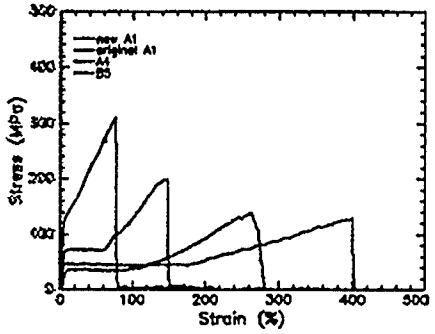


Figure 2. Stress-strain curves for various PET fibers. A1 was spun at 1600 ypm, A4 at 3500 ypm, and B5 at 4500 ypm (most crystalline).

* The SUNY X3 beamline at NSLS is supported by the Division of Basic Energy Sciences of the U.S. Department of Energy (DE-FG02-86ER45231). Support of this work by the U.S. DOE DE-FG02-86ER45237i is gratefully acknowledged

Low temperature structure of the linear chain cuprate Sr_2CuO_3 | X3B1

T. Ami (Sony), M. Crawford, and R. Harlow (Du Pont)

The report of superconductivity in $Sr_2CuO_{3+\delta}$ has raised important questions concerning the minimum magnetic and electronic dimensionalities which will support high T_c since the parent insulating phase for these superconductors, Sr_2CuO_3, has a crystal structure which is characterized by one- dimensional chains parallel to the a axis, very different from the 2-dimensional CuO_2 sheets of all known systems with $T_c > 40K$. The structure of the parent phase is known to have 14/mmm symmetry: except for the in-plane oxygen vacancies, the structure is very similar to that of the high temperature form of La_2CuO_4. A lower temperatures, La_2CuO_4 undergoes a phase change to an orthorhombic phase with Bmab symmetry in which the CuO_6 octahedra tilt out of the ab plane. Since similar distortions could affect the magnetic properties of the parent Sr_2CuO_3 and ultimately the superconducting properties of the oxygen-doped phases, we decided to investigate the structure of Sr_2CuO_3 at 12K. A close inspection of the powder pattern (below) clearly shows that no phase transition occurs. All of the peaks can indeed be accounted for with the simple I4/mmm cell.

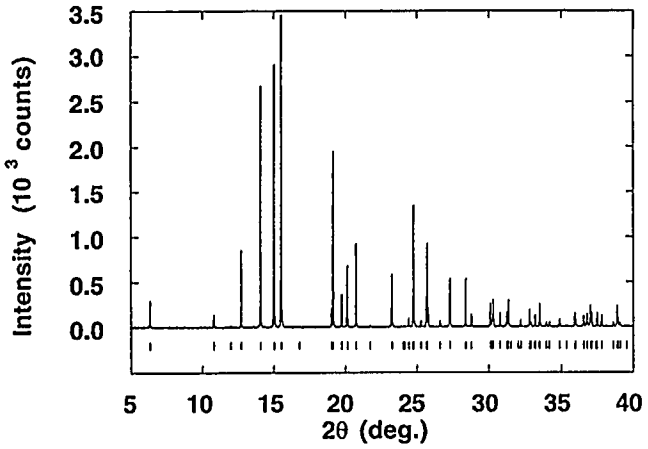


Figure 1.

Powder diffraction structure of $[Ru_2(\mu_2;\eta^2\text{-}O_2PMe_2)_2(CO)_4]_n$ * | X3B1

Christopher M. Barnes (Univ. of Wyoming), D. Scott Bohle (Univ. of Wyoming), Robert E. Dinnebier (SUNY Stony Brook), Sara K. Madsen (Univ. of Wyoming), and Peter W. Stephens (SUNY Stony Brook)

The ruthenium(I) "sawhorse" dimers $[Ru_2(\mu_2;\eta^2\text{-}X_2)_2(CO)_4]_n$ (X = oxoanions such as carboxylate, phosphinate, sulfinate, or bisulfate) are an extensive class of compounds which are readily prepared by the oxidative addition of monoprotic acids to $Ru_3(CO)_{12}$ under mild conditions. Although some of these are useful precursors for a variety of homogenous catalysts, we have very little structural information about these materials due to their insolubility and their tendency to crystallize as needles too small for single crystal diffraction experiments. Using powder diffraction, we have determined the structure of one of these polymers prepared from dimethylphosphinic acid.

At room temperature, the unit cell is monoclinic, space group C2/c, with lattice parameters a=18.095Å, b=9.074Å, c=10.037Å, β=112.04°. Using a combination of direct methods and molecular modeling, we obtained a set of atomic coordinates which could be used as a starting point for refinement of the structure illustrated below. The chains extend along the a axis. The final crystallographic weighted R factor is 10.6

At 240K, the unit cell distorts into a triclinic phase, a=9.902Å, b=9.862Å, c=8.935Å, α=92.00°m β=115.07°. Direct methods and Patterson maps were unable to locate the molecule in the triclinic cell, and so we used a grid search of the location of the fragment determined from the room temperature phase. The chains (running along b) are more kinked. This structure is illustrated.

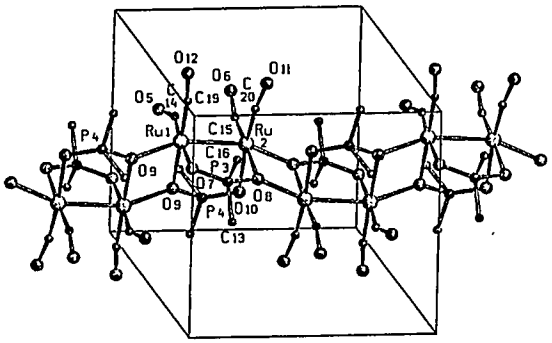


Figure 1.

* Work at the SUNY X3 beamline is supported by the Division of Basic Energy Sciences, U.S. Dept. of Energy (DE- FG0286-ER45231). Work at UW supported by the Research Corporation of the UW Research Office. Partial support was provided by the NSLS faculty-student travel fund.

Structural investigation of Hg and Cu superconducting cuprates | X3B1

P. Bordet, M. Anne, C. Chaillout, J.J. Capponi, M. Marezio (CNRS Grenoble), E. Antipov, E. Kopnine (Moscow State Univ.)

Two new series of high Tc superconducting cuprates have been recently discovered in our laboratory. The chemical formula of the compounds belonging to these series are $HgBa_2Ca_{n-1}Cu_nO_{2n+2+x}$ and $(Cu,C)Ba_2Ca_{n-1}Cu_nO_x$, respectively, (0¡6). We have used synchrotron x-ray powder diffraction at the X3B1 beam line to gain insight into several structural problems involving these highly interesting new materials. Data were collected with the flat-plate geometry at a 1.149A wavelength using a Si(111) double-crystal monochromator and a Ge(111) analyzer.

The structure of the Hg-cuprates has been studied by several authors, including us, using neutron powder diffraction. In most of these studies, low occupancy factors for the Hg site at the origin of the unit cell have been obtained. They were tentatively attributed by different authors to Hg vacancies or substitution of Hg by Cu or CO3 groups. In Grenoble, we have started a systematic study of the effects of synthesis procedure on the physical and structural properties of these compounds. As part of this program, we have investigated during the present experiment the diffraction spectra of two Hg-1223 samples prepared by using the same high pressure synthesis procedure, but starting from either oxide precursors (sample 1) or carbonate mixture (sample 2). Sample 2 obtained from carbonates was multiphasic, had a lower Tc (80K) than sample 1 (133K) and different cell parameters. Refinements carried out using the GSAS program yielded a 0.7 occupancy factor for Hg in sample 2. Furthermore, the apparent Hg-O distance along the c axis decreased from 1.96A in sample 1 to 1.75A in sample 2. This very short latter distance can be attributed to an average between Hg-O and C-O distances due to disordered substitution. Although the position of the CO3 groups could not be refined due to the multiphasic nature of the sample, the results of these refinements, together with our previous knowledge of these samples, strongly indicate that carbonate groups substitute for Hg in our high pressure synthesized samples.

Since the recent discovery of superconducting (Cu,C) cuprates, most of the structural work has been restrained to electron microscopy technique, due to the lack of pure bulk samples. Using this technique, we have proposed a structure similar to that of Hg-cuprates, were Hg would be replaced by a mixture of copper and carbonate cations. The presence of carbonate groups was demonstrated by EELS measurements. A superstructure involving the doubling of the a and c axes has been observed and attributed to the ordering between Cu and C in the basal plane of the structure. We have collected powder diffraction data on a multiphasic sample of the (Cu,C)-1234 compound (Tc=118K). Refinement of these data allowed us to obtain a confirmation of the general structural arrangement. Moreover, superstructure reflexions have been observed for the first time on a bulk sample. The widths of these reflexions being similar to those of the subcell ones, the ordering responsible for the superstructure is long range. However, due to the small number of superstructure peaks detected, the refinement including a model of the superstructure has not benn attempted.

Powder diffraction structure of triclinic $C_{60}Br_{24}(Br_2)_2$ * | X3B1

R. E. Dinnebier, P. W. Stephens (SUNY Stony Brook), J. K. Carter, A. N. Lommen,P. A. Heiney, A. R. McGhie, L. Brard, A. B. Smith, III (Univ. of Pennsylvania)

The crystal structure of the triclinic low temperature ($P\bar{1}$ phase of $C_{60}Br_{24}(Br_2)_2$ has been solved. The lattice constants at 35K are a = 14.291Å, b = 12.469Å, c = 12.850Å, $\alpha = 62.77°$, $\beta = 93.45°$, $\gamma = 57.10°$. A high temperature phase ($R\bar{3}$) of $C_{60}Br_{24}(Br_2)_x$ (x = 0.5-2) is previously known from single crystal work by Tebbe et al. (1992).

X-ray powder diffraction patterns were recorded at several temperatures at the SUNY X3A2 and X3B1 beamlines, using 1.19825Å X-rays from double Si(111) monochromator and Ge(111) analyzer. The minimum FWHM was 0.035° 2Θ.

The structure with 132 positional parameters may be described as distorted fcc lattices of brominated fullerene, with excess bromine in the octahedral voids. The known coordinates of the highly symmetrical ($Pm\bar{3}$) $C_{60}Br_{24}$ molecule were used as a starting point for the structure determination. A grid search of rigid body rotation with the requirement that the minimum Br-Br distance is at least 3.5Å. yields only one possible solution of the orientation of the $C_{60}Br_{24}$ molecule.

The position and number of the free bromine molecules could then be found by using difference Fourier methods and consecutive Rietveld refinements. The final crystallographic R-factors are R-p = 10.4%, R-wp = 13.3%, Rbragg = 9.1%, x^2 = 1.4.

[1] Tebbe, F.N. et al., Science, 256, p. 822-825, (1992)

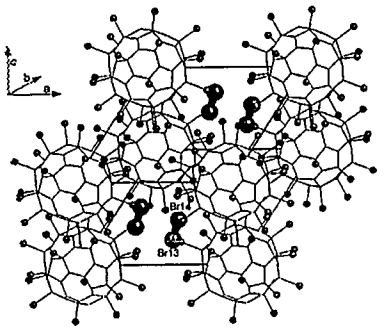


Figure 1.

* Work at the SUNY X3 beamline is supported by the Division of Basic Energy Sciences, U.S. Dept. of Energy (DE-FG0286-ER45231). Research at SUNY was supported by the NSF under grant DMR-92-02529. Research at UPENN was supported by the NSF Grant under DMR-MRL-92-20668 and by the Donors of the Petroleum Research Fund, admin. by the Americ. Chem. Soc.

Powder diffraction structure of Cd_3SiO_5 *	X3B1

R. E. Dinnebier, P. S. Stephens (SUNY Stony Brook), W. Eysel (Univ. of Heidelberg FRG)

The crystal structure of tetragonal (P4/ n m m) has been confirmed and refined. The lattice constants are a = 6.8376(2)Å, c = 4.9551d(3)Å. Structure proposals were published earlier by Glasser Glasser (1964) and Eysel (1970).

X-ray powder diffraction patterns were recorded using 1.14891Åfrom double Si(111) monochromator and Ge(111) analyzer. The minimum FWHM was o.046 2Θ.

After extracting integrated intensities we were able to locate all atoms in the asymmetric unit with direct methods. The solution found is identical to the suggested one. The Rietveld technique was used to refine the structure. The structure is pheudo-rhombohedral layered and contains two types of anion-polyhedra.

The actual Rietveld plot with 151 reflections up to $90°2\theta$ yields to R-p = 12.116.0peak shapes, which is an indication for stacking faults. TEM pictures and structural considerations confirm this assumption.

Dent Glasser, L.S. Glasser, F.P., Inorg. Chem., 1964, 3, 1228-1230.
Eysel, W., N. Jb. Miner. Mh., 1970, 12, 534-547.

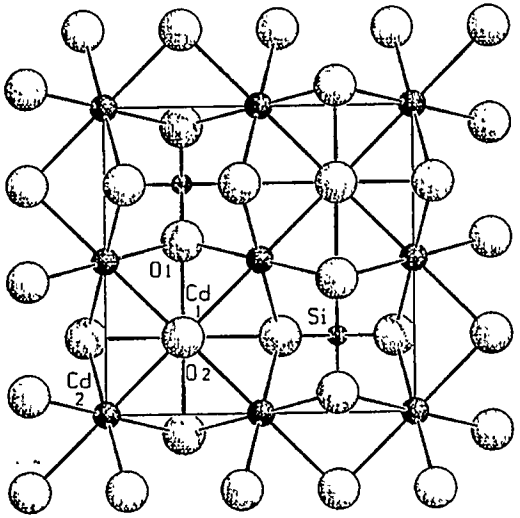


Figure 1.

* Work at the SUNY X3 beamline is supported by the Division of Basic Energy Sciences, U.S. Dept. of Energy (DE-FG0286-ER45231). Research at UHB was supported by the DRG and ICDD.

Powder diffraction structures of Bi_2CdGeO_6 *	X3B1

R. E. Dinnebier, P. W. Stephens (SUNY Stony Brook), S. Wies, and W. Eysel (Univ.of Heidelberg, FRG)

The crystal structures of the orthorhombic (Pbcn) high and the monoclinic ($P2_1/n$) low temperature phases of Bi_2CdGeO_6 have been solved ab initio. The lattice constants area = 10.497(1)Å, b = 10.0926(6)Å, c = 5.6063(4)Å for the high temperature phase (Wies, 1993) and a = 10.4827(1)Å, b = 10.0702(2)Å, c = 5.6000(1)Å, β = 90.378(1)° for the low temperature phase at 25K. The phase transition occurs during cooling below 270K and shows hysteresis after heating.

X-ray powder diffraction patterns were recorded using 1.15Å from double Si(111) monochromator and Ge(111)analyzer. The minimum FWHM was 0.033° 2Θ.

After extracting 265 integrated intensities up to 65°2Θ we were able to find the position of all atoms in the high temperature structure by using direct methods. The difference Fourier method and consecutive Rietveld refinements were used to confirm and refine both structures. The structures are layered and contain three types of anion-polyhedra: regular $[GeO_4]$-tetrahedra, distorted $[CdO_6]$-antiprism and distorted $[BiO_{4+2}]$-pyramids.

The actual Rietveld plot of the high temperature phase with 553 reflections up to 88°2Θyields to R-p = 13.5%, R-wp = 19.8%, R-Bragg = 6.0%, R-F = 4.2%, x^2 = 2.9. The R-factors for the low temperature structure are similar. Some peaks in both phases show strong anisotropical strain broadening which is not yet refined. The high temperature structure is shown.

Wies, S., Dissertation, University of Heidelberg, 1993, ISBN 3-89257-064-1.

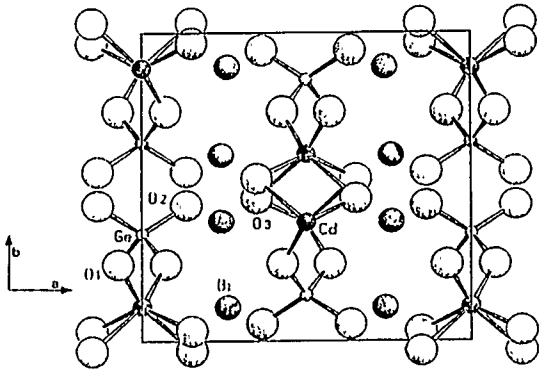


Figure 1.

* Work at the SUNY X3 beamline is supported by the Division of Basic Energy Sciences, U.S. Dept. of Energy (DE-FG0286-ER45231). Research at SUNY was supported by the NSF under grant DMR-92-02529. Research at UHB was supported by the DFG andICDD.

Analysis of the amorphous phase in hydroxyapatite coatings * | X3B1

K. A. Gross, C. C. Berndt, P. Stephens, and R. Dinnebier (SUNY Stony Brook)

The amorphous phase is usually found to accompany the crystalline apatite in hydroxyapatite coatings. The last synchrotron study was focused at the analysis of the crystalline hydroxyapatite component. Findings showed that after the plasma spraying operation, the surface layer becomes hydroxylated however the layers underneath remain in a dehydroxylated condition. The use of synchrotron radiation made it possible to analyze the underlying layers without subjecting it to a change of environment. This has an implication to the solubility of this coating when it is used in the form of a coating on a dental or orthopedic prosthesis.

This present study addresses the use of synchrotron radiation to examine crystallinity variations within the coating, in particular, variations with depth. The two coating assemblies were analyzed using x-rays at different energies (8, 14, 20, and 30 keV, which gave penetration depths of 10, 15, 25, and 45 microns respectively for Q=2. The penetration of the x-rays at energies of 8 and 14 keV were expected to be within the surface layer and the higher x-ray energies had sufficient penetration power to reach the second layer. The x-ray diffraction spectra showed that an increase in crystallinity with depth is more easily detected as depicted in the figure. This is due to difficulty in detection further from the coating surface. It was found that the sensitivity of this technique is limited, and the change in crystallinity cannot be monitored very accurately. Presently these coatings are being analyzed with other techniques such as micro-raman spectroscopy for comparison with the synchrotron data.

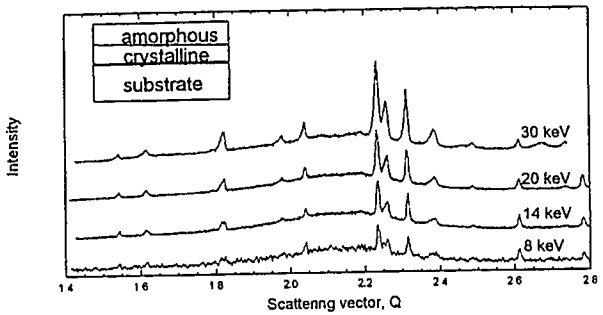


Figure 1.

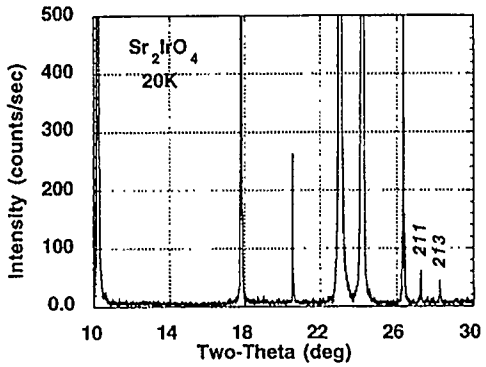
* Work at the SUNYX3 beamline is supported by the Division of Basic Energy Sciences, U.S. Department of Energy under grant DE-FG02-86ER45231.

Sr_2IrO_4: A new two-dimensional spin 1/2 canted antiferromagnet | X3B1, X3B2

R. Harlow, M. Crawford, and M. Subramanian (Du Pont)

Previous work on doped-$LaCuO_4$ superconductors has shown that their structures distort from the ideal tetragonal, I4/mmm K_2NiF_4 structure. These distortions take the form of tilts of the CuO_6 octahedra out of the ab plane and have a negative impact on Tc which may, in part, be a consequence of changes in the magnetic interactions between the spin 1/2 Cu atoms. In an effort to better understand the magnetic properties of the cuprates, we have begun to investigate other spin 1/2, K_2NiF_4-type compounds. Sr_2IrO_4, for example, was reported[1] to have the idealized K_2NiF_4 structure with a =3.89 and c=12.92. Magnetic studies of this material, however, showed that it has a distinct magnetic transition at approximately 200K with significant magnetic hysteresis below this temperature. This weak ferromagnetic (canted antiferromagnetic) behavior strongly suggested that the structure below 200K was distorted. In-house x-ray patterns failed to show any splittings or superlattice lines which would have been indicative of a distorted structure. Room temperature and low-temperature synchrotron powder diffraction patterns, however, clearly showed the presence of superlattice lines (figure below) which could only be indexed with a cell which was 4x larger in volume than the idealized cell with $a' = \sqrt{2}a$, $c' = 2c$. A similar superlattice pattern and unit cell had been reported [2] for Ca_2MnO_4 where it was determined that the MnO_6 octahedra had rotated about the c-axis by some 10°. Because the superlattice lines were so weak in the x-ray pattern, neutron powder diffraction data was ultimately used to refine the structure and to confirm the presence of a cooperative rotational distortion (of the IrO_6 octahedra) in Sr_2IrO_4.

[1] Randall, Katz, and Ward, JACS 79, 266 (1957).
[2] Leonowicz, Poeppelmeier, and Longo, J. Solid State Chem. 59, 71 (1985).



Ab initio structure determination of a new ammonium aluminum fluoride phase from powder diffraction data: β-NH_4AlF_4	X3B1, X3B2

R. Harlow, N. Herron, and D. Thorn (Du Pont)

As part of program to synthesize new compounds as catalysts and catalyst supports for the production of chlorofluorocarbon substitutes, a new phase of NH_4AlF_4, now designated as the beta form, was synthesized when a solution of $HAlF_4$ in formamide was heated briefly to 200°C. The unit cell was determined (TREOR) to be tetragonal with systematic absences which suggested space group I4/mcm: a=11.6390(1) and c=12.6602(3). Intensity data were abstracted and the structure was solved by direct methods (SHELX). The structure was refined by the Rietveld technique (GSAS) and converged at R=0.133. The nitrogen atoms behaved anomalously, apparently assuming some of the scattering from the hydrogen atoms which could not be seen in difference maps and which were thus not included in the refinement.

The structure is composed of two layers of corner-sharing aluminum fluoride octahedra separated by a layer of ammonium ions. In this sense, the beta structure is identical to the alpha form. The two forms are distinguished, however, by the different ring structures which each possesses: the alpha form contains only 4-membered rings while the beta forms contains 3- ,4- and 5-membered rings (counting Al atoms only). The two aluminum fluoride layers which make up the beta structure are related by the body centering operation; while the 4-membered rings sit on top of each other, the 5-membered rings sit on top of the 3-membered rings so that no 5-ring channel develops. One aluminum fluoride layer is shown below (the isolated spheres are the nitrogen atoms of the NH_4+ ions which sit above and below the plane of the layer.

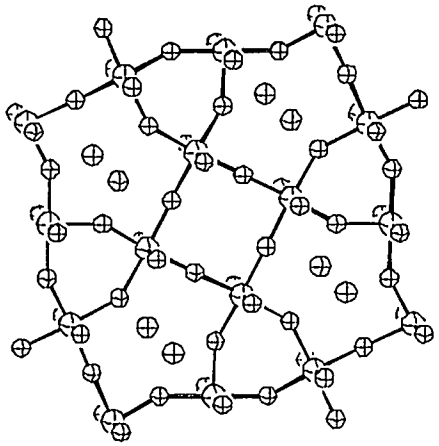


Figure 1.

The crystal structure of yet another new form of AlF_3 as determined from its synchrotron powder-diffraction pattern	X3B1

Richard L. Harlow, Norman Herron, and David L. Thorn (Du Pont)

Aluminum fluoride phases are established catalysts in many classes of fluorocarbontransformations. While exploring new routes to synthesize specific AlF_3 phases, it was discovered that β-NH_4AlF_4 when heated decomposed to yield another new phase of AlF_3 which we have designated as the kappa phase. Although the peaks in its powder diffraction pattern were somewhat broad, indicating the presence of very small crystallites, the structure was solved in an ab initio fashion without any apparent difficulties: tetragonal, P4/mbm with a=11.4060(4) and c=3.5443(2) Å. The structure is very similar to that of its parent, β-NH_4AlF_4: the individual layers are, in fact, exactly the same. The extraction of the ammonium ions and half of the out-of-plane fluorine atoms causes the layers to collapse onto one another. The reaction is not truly topotactic since adjacent layers in the parent compound have alternating orientations while all of the layers in the kappa phase are in identical orientations. The structure of the kappa phase, shown below, contains 3-, 4- and 5-ring channels which run parallel to the unique axis.

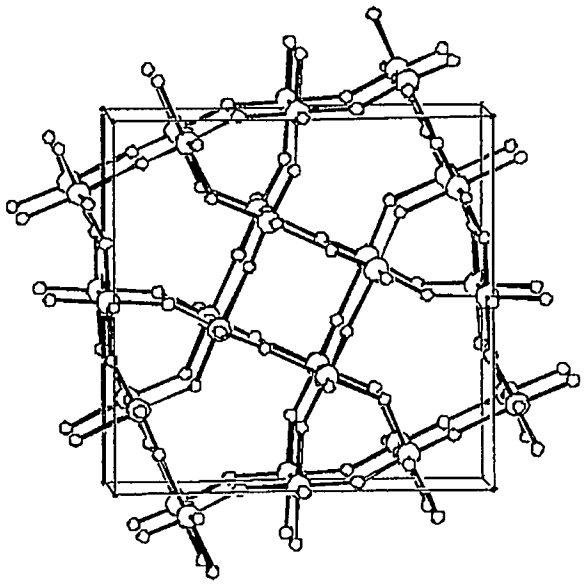


Figure 1.

Barium yttrium fluorides * | X3B1

J. A. Kaduk, J. Faber, S. Pei, R. H. Jarman, and A. P. Wilkinson (AMOCO)

The crystal structure of BaY_2F_8 has been refined using powder diffraction data collected on X3B1. The only published reference to this structure type [1] contains unreasonable (negative) displacement coefficients. Accurate structural parameters are important to understand the subtle structural changes which lead to improved optical properties in doped materials. Special pains had to be taken to ensure a true powder sample, and to model the reflection profiles accurately.

The crystal structure (C2/m, a = 6.97862(3), b = 10.51164(5), c = 4.26118(2) Å, β = 99.6751a(4° at 27°C, Z = 2) contains 12-coordinate Ba and 8-coordinate Y, joined through Y-F-Ba bridges. The Y coordination is best described as square antiprismatic. The Y-F distances fall within the normal range. The Y sites are linked in a pseudohexagonal network perpendicular to c by sharing edges of coordination polyhedra. These layers are joined into a 3-dimensional network by corner- sharing parallel to c. the tetracapped square prismatic Ba reside in cavities formed by the Y network.

The lattice parameters of Ba $(Y_{1/2}Yb_{1/2})_2F_8$ are significantly smaller than those of BaY_2F_8, consistent with the difference in ionic radii. The Ba coordination spheres are identical in the two compounds, but the Yb substitution results in a small shift of the metal position in the F_8 coordination sphere. [1] O.E. Izotova and V.B. Aleksandrov, Dokl. Akad. Nauk. SSR, 192, 1037-1039 (1970).

* The SUNY X3 beamline at NSLS is supported by the Division of Basic Energy Sciences of the US Department of Energy (DE-FG02-86ER45231).

Cation site occupancies and crystallinity of NH_4-exchanged FAU * | X3B1

J. A. Kaduk, J. T. Miller, P. D. Hopkins, and J. Faber (AMOCO)

The crystal structure of hydrated Na-Y (LZ-Y52) and three ammonium-exchanged sieves have been determined by applying Rietveld techniques to synchrotron powder diffraction data collected on X3B1. In LZ-Y52, sites I′,II, and II′ are occupied—I′ and II by Na, and II′ by a mixture of Na and water molecules. In the ammonium-exchanged sieves, the Na at sites I′ and II are replaced by NH_4 ions. Sodium ions occupy site II′, and are the last to be removed in the ion exchange. Ammonium ions exhibit a slight preference for site II in the supercages, while Na ions tend to occur in the sodalite cages. Apparent anomalously-high crystallinities of the exchanged materials obtained by the standard faujasite analysis are completely explained by the structural variations, which affect the relative intensities of the diffraction lines.

* The SUNY X3 beamline at NSLS is supported by the Division of Basic Energy Sciences of the U.S. Department of Energy(DE-FG02-86ER45231).

Determination of the crystal structure of $K_2Al_2B_2O_7$ ab initio using synchrotron powder diffraction data *	X3B1

J. A. Kaduk and L. C. Satek (AMOCO)

The crystal structure of $K_2Al_2B_2O_7$ has been solved ab initio and refined using synchrotron powder diffraction data collected on beamline X3B1. The compound crystallizes in the trigonal space group P321, with a = 8.55800(2) and c = 8.45576(3) Å at 27°C, and Z=3. The structure was solved originally in space group P3, and additional symmetry was found relating the 19 atoms in the asymmetric unit in this space group. In P321, there are 11 atoms in the asymmetric unit.

The structure is composed of 3-dimensional network of corner-sharing planar BO_3 and tetrahedral AlO_4 share corners to form Al_2O_7 "pillars" between planes perpendicular to the BO_3 units along the c-axis. There are two different Al_2O_7 units: one is nearly "eclipsed" and the other "staggered". There are twice as many staggered pillars as eclipsed, and the density of pillars alternates between high and low along the c-axis. There are two independent K ions, one 7-coordinate, and the other 8-coordinate, which reside in channels parallel to c. The topology of the structure is that of $Rb_2Be_2Si_2O_7$. It can be considered analogous to that of tridymite if half of the Si_2O_7 units are replaced by trigonal BO_3 and the other half of Al_2O_7. The crystal structure provides insight into the mechanism of ionic conductivity of the black semiconducting amorphous solid formed in its vicinity in the K_2O-Al_2O_3-B_2O_3 phase digram.

* The SUNY X3 beamline at NSLS is supported by the Division of Basic Energy Sciences of the US Department of Energy (DE-FG02- 86ER45231).

Crystal structure of cubic $CsTiAsO_5$ and $CsTiPO_5$ *	X3B1, X7A

M. Kunz, R. Dinnebier (SUNY Stony Brook), D. E. Cox (BNL), L. K. Cheng, E. M. McCarron,J. Calabrese (Du Pont), J. B. Parise, P. W. Stephens (SUNY Stony Brook)

$CsTiAsO_5$ (CTA) is the high temperature (> 963°C) phase of the orthorhombic $CsTiOAsO_4$ which exhibits strong nonlinear optical properties. $CsTiPO_5$ (CTP) has the same structure, down to room temperature. Due to strong twinning parallel to {111}, the structure of these compounds could not be solved using single-crystal-ray data.

The structures of the two compounds were solved by direct methods and refined by the Rietveld profile technique from high resolution powder data collected on X3B1 (CTA) and X7A (CTP). The structures are cubic, space group Fd $\bar{3}$m, with a=10.2328Å(CTA) and a=10.0872Å(CTP). The Ti and As (resp. P) atoms are disordered, occupying the same crystallographic site. We cannot fit the oxygens to full occupancy of any site, and so our interpretation of the structure is that of an unusual framework consisting of randomly disordered TiO_6 and $AsO_4(PO_4)$ polyhedra. The local disorder between the two polyhedra is spatially averaged in an X-ray diffraction experiment. This cubic structure is related to the orthorhombic $KTiOPO_4$-type structure (shared by CTA) in that the latter can be derived from the former by a particular ordering of the TiO_6 octahedra and the $AsO_4(PO_4)$ tetrahedra.

* Work supported by DuPont Company and by NSF through Grant DMR-90242249 to JBP. The SUNY X3 beamline is supported by the Division of Basic Energy Sciences, US DOE Grant DE-FG02-86ER45231.

Roughness scaling and strain in lattice mismatched $Si_{0.4}Ge_{0.6}$ thin films on Si *	X3B1

Z. H. Ming, S. Huang, Y. L. Soo, Y. H. Kao (SUNY Buffalo), T. Carns and K. L. Wang (UCLA)

Interfacial roughness between lattice mismatched materials is one of the factors limiting the performance of modern semiconductor electronic and optoelectronic devices. We are studying the variation of interfacial roughness in multilayer semiconductors prepared under different conditions. The interfacial microstructures are closely related to the strain arising from the lattice mismatch. Measuring the lattice strain in the layers by X-ray diffraction and the interfacial roughness by grazing-incidence X-ray scattering (GIXS) techniques, we have obtained insight into the changes of interfacial microstructures as a function of film thickness during epitaxial growth. A new scaling-law behavior can be compared with recent dynamic scaling theoretical models.

The surface and buried interfacial roughness in a series of thin Si -0.4Ge $_{0.6}$ films grown on Si(100) by molecular beam epitaxy were measured. The strain in the layer and the critical thickness of the film were measured by analysis of the Si(004) reflection. The roughness parameters fit a scaling-law with an exponent $\beta = 0.71$ for both the surface and interfacial roughness. As the film thickness changes from below the critical thickness to above, the scaling behavior shows significant deviation, indicating a large change in the morphology of surface and interface microstructures. Physical understanding of such a scaling behavior is especially useful for predicting the interfacial roughness as a function of the epilayer thickness between lattice mismatched material systems.

Typical results are shown below. (a) Specular reflectivity for $Si_{0.4}Ge_{0.6}$ films on Si(100). Solid lines are theoretical calculations. (b) Surface roughness (squares) and buried interfacial roughness (circles) as function of layer thickness. Solid and dashed lines are theoretical fits to the measured surface and interfacial roughness, respectively, by a scaling-law with $\beta = 0.71$.

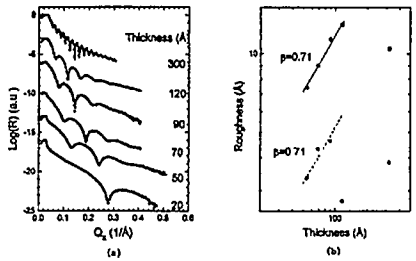


Figure 1.

* Research supported by DOE (DE-FG02-87ER45283). The SUNY X3 beamline at NSLS is supported by the Division of Basic Energy Sciences of the US DOE (DE-FG02-86ER45231).

Thickness modulation of InGaAs/GaAs superlattices studied by large angle x-ray scattering *	X3B1

Z. H. Ming, Y. L. Soo, S. Huang, Y. H. Kao(SUNY Buffalo), K. Stair, G. Devane, and C. Choi-Feng (AMOCO)

Superlattices of 100-period $In_xGa_{1-x}As$ (15 Å) / GaAs (100 Å) grown on GaAs (100) substrates by molecular beam epitaxy were studied by using large angle X-ray scattering techniques. In addition to the usual superlattice satellite peaks corresponding to structural periodicity along the growth direction, unusual satellite peaks in the lateral direction parallel to the sample surface were observed in a sample with x = 0.535 grown at 480°C, indicating an in-plane ordering. This result is confirmed by high resolution transmission electron microscopy observations that thickness modulation in the $In_xGa_{1-x}As$ layers gives rise to long-range lateral periodic arrays of cluster-like microstructures with spacing on the order of a few hundred Å. This thickness modulation is found to occur only in the [110] direction, thus the material can be viewed as a somewhat disordered array of grown-in parallel quantum wires.

* TheSUNY X3 beamline at NSLS is supported by the Division of Basic Energy Sciences of the US Department of Energy (DE-FG02-86ER45231).

Interfacial microstructures of ultrathin Ge layers on Si probed by x-ray fluorescence yield *	X3B1

Z. H. Ming, Y. L. Soo, S. Huang, Y. H. Kao (SUNY Buffalo), J. C. Tsang, and S. S. Iyer (IBM T. J. Watson Research Center)

Characterization of interfacial microstructures in multilayer materials is important for the fabrication of synthetic superlattice devices. Recently $Si_{1-x}Ge_x$and short range Si_mGe_n superlattices have become important candidates for new Si-based optoelectronic devices, as in these systems the normally forbidden indirect optical transitions in bulk Si and Ge can become weakly allowed; this effect is crucial to the efficiency of some practical devices such as the Si-based light emitting diodes. For a physical understanding of the effects of interface, it is essential to investigate the changes in the interfacial roughness as a function of thin Ge epilayers grown on Si. In this project, we have applied the techniques of grazing incidence x-ray scattering (GIXS) and GeDα fluorescence yield (FY) to a study of buried ultrathin Ge layers grown on bulk Si(100) substrate. Results obtained with three samples having different Ge layer thickness were compared. The thickness of the Gelayers, rms interfacial roughness as well as the lateral and cross correlation lengths of the roughness were obtained. Some results are summarized in Figure 1.

Our results also indicate that the interfacial roughness at neighboring interfaces is highly correlated. Significant changes of microstructures in the Ge epilayer were found as the layer thickness approached the critical thickness. We have also carried out a similar x-ray investigation of $Si_{1-x}Ge_x/Si$ heterostructures [Phys. Rev. B 47, 16373 (1993)]. We thus demonstrated that x-ray scattering technique is convenient for probing partial lattice relaxation in multilayers of compound semiconductors.

Results of this investigation have been published [Appl. Phys. Lett. 65, 1382(1994)].

Sample	D_{Si}	D_{Ge}	σ_0	$\sigma_{Si/Ge}$	$\sigma_{Ge/Si}$	h	$\xi_{\parallel}$	$\xi_{\perp}$
A	57	4.5	11	4	11	0.55	1240	-
B	48±1	11±1	7±1	0.1±1	4±2	0.51	1460	50
C	76±1	18±1	8±1	3±1	6±2	0.95	4680	80

Figure 1. Structural parameters of thin Ge Layers. D_{Si}(Å) andD_{Ge} (Å)denote the thickness of the Si and Ge epilayer,respectively; σ_0(Å), $\sigma_{Si/Ge}$(Å)and $\sigma_{Ge/Si}$ denote the rms roughness for the top surface, Si/Ge and Ge/Si interface, respectively;h is the texture coefficient; $\xi_{\parallel}$ (å) and $\xi_{\perp}$ (Å) denote the lateral and cross-correlationlength, respectively.

*The SUNY X3 Beamline at NSLS is supported by the Division of Basic Energy Sciences of the U.S. Department of Energy (DE-FG02-86ER45231). Research supported by DOE undergrant DE-FG02-87ER45283.

Local environment surrounding Mn atoms in $In_{1-x}Mn_xAs$ diluted magnetic semiconductors *	X3B1

Y. L. Soo, S. Huang, Z. H. Ming, Y. H. Kao (SUNY Buffalo), H. Munekata (Tokyo Institute of Technology, Japan), and L. L. Chang (Univ. of Science and Technology, Hog Kong)

Incorporation of controllable large amounts of Mn impurities into a III-V semiconductor InAs was first accomplished using molecular-beam-epitaxy (MBE) techniques [1]. This demonstrated that it is possible to synthesize III-V diluted magnetic semiconductors(DMS) under proper MBE processing conditions. In view of the difficulties in the control of magnetic impurities in II-VI compounds, doping of transition-metal elements into III-V semiconductors could provide unprecedented opportunities for making new magnetic materials.

The physical properties of the DMS are closely related to the local short-range structures around the magnetic impurity atoms. While conventional diffraction techniques are not useful for this investigation, EXAFS is uniquely suited for probing the local structures. In this project we applied EXAFS techniques to investigate various $In_{1-x}Mn_xAs$ films supplied by Munekata et al. in order to clarify the local structures and interpret observed magnetic properties.

Our results have shown that for samples grown at low substrate temperatures (near 200°C) or with a low Mn concentration (about 1 atomic %), the Mn atoms can substitute forIn in the InAs host, thus indicating that III-V diluted magnetic semiconductors can indeed be prepared by substitutional doping of magnetic impurities. On the other hand, substitution does not take place in high Mn concentration samples (above 10%) or in samples grown at high substrate temperatures (around 300°C); these samples contain a large amount of MnAs clusters and become ferromagnetic. In addition, the local environment surrounding Mn impurity atoms usually show some disorder and lattice distortion. Mn can become amphoteric, depending on the local arrangement of neighboring atoms. These results are very useful for the interpretation of the observed magnetic properties of this new class of magnetic semiconductors.

Preliminary results have been published [Phys. Rev. B 47, 7187(1993)].

[1] H. Munekata et al., Phys. Rev. Lett. 63, 1849 (1989).

* The SUNY X3 beamline at NSLS is supported by the Division of Basic Energy Sciences of the US Department of Energy (DE-FG02-86ER45231).

Local structures around Mn luminescent centers in Mn-doped nanocrystals of ZnS * | X3B1

Y. L. Soo, Z. H. Ming, S. W. Huang, Y. H. Kao (SUNY Buffalo), R. N. Bhargava (Nanocrystals Technology), and D. Gallagher(Philips Laboratories)

Recently there has been considerable interest in the study of compound semiconductors with dimensions on the nanometer scale. This class of new materials has not only provided many unique opportunities for studying physics in low dimensions, but also exhibited novel optical and transport properties which are potentially useful for technological applications. Of special interest is the advent of doped semiconductor nanocrystals (e.g. ZnS:Mn). High photoluminescent quantum efficiency and greatly enhanced transition rates associated with Mn luminescent centers have recently been observed in Mn-doped ZnS nanocrystals of sizes ranging from 70 to 30 Å. The luminescent decay time was found to decrease with the particle size and was at least five orders of magnitude faster than the corresponding Mn^{2+} radiative transition in the bulk crystals.

The drastic changes in optical properties in the doped nanocrystals are clearly related to the nature and local structure of the luminescent center in the material. Because of the small size of the system, a single impurity center can give rise to significant changes in the physical properties as a result of symmetry-breaking, crystal field distortion, size quantization, and hybridization of s-p states in the host with d-orbitals of Mn, etc. The enhanced transition probability as well as the decay rate of the Mn ion should therefore be closely related to the local structure around the Mn ions resulting from the ionic size difference and valence mismatch between the dopant and the host cations.

The present work is aimed at a quantitative determination of the local structures in nanocrystals of ZnS:Mn of different size distributions by means of XAFS. Because the impurities in the nanocrystals do not have long range structural order, conventional X-ray diffraction method is not useful for this purpose. On the other hand, the short-range-structure-probing technique of XAFS is uniquely suited for this task.

Two ZnS:Mn nanocrystal materials with different size distributions ranging from 30–35 Å to 50–55 Å, as well as a bulk ZnS:Mn sample were studied. The interatomic distances between Mn and neighboring atoms, coordination number, local disorder, and effective valency determined for the nanocrystals are compared with those in bulk Mn-doped ZnS. The Mn ions are found to substitute for the Zn sites in the host ZnS but with significant size-dependent local structural changes. The questions of Mn-cluster formation and presence of Mn impurities on the surface of the nanocrystals are addressed. Near edge X-ray absorption fine structure (NEXAFS) indicates that the effective valency of Mn ions in the nanocrystals is close to +2 with a weak size dependence. These local structures are believed to be closely related to the novel optical properties observed in this new class of semiconductors.

Fee details of the results, see Phys. Rev. B50, 7602 (1994).

* The SUNY X3 beamline at NSLS is supported by the Division of Basic Energy Sciences of the US Department of Energy (DE-FG02-86ER45231).

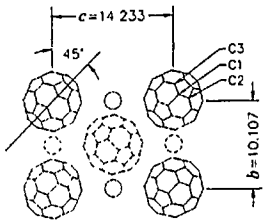
Polymer and dimer phases of Rb_1C_{60} and K_1C_{60} * | X3B1

Peter W. Stephens (SUNY Stony Brook), G. Oszlanyi (Research Inst. for Solid StatePhysics, Budapest and Ecole Poly. Federal de Lausanne), G. Bortel, G. Faigel, M. Tegze (Research Inst.for Solid State Physics), A. Jánossy (Research Inst. for Solid State Physics Budapest and Tech. Univ.Budapest), S. Pekker (Research Inst. for Solid State Physics, Budapest), D. Koller, M. C. Martin, L. Mihály, R. Dinnebier, G. Bendele (SUNY Stony Brook), O. Chauvet, and L. Forró (Ecole Poly. Federalde Lausanne)

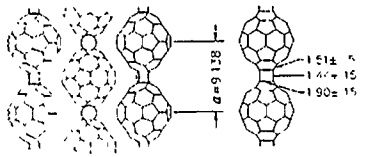
Nearly all of the molecular crystals containing C_{60} formed at ambient pressure have inter-fullerene separations of the order of 10Å. The sole exceptions are room temperature and quenched low-temperature phases of A_1C_{60} (A = K, Rb, and Cs). The room temperature phases are orthorhombic, formed by a reversible transformation from high temperature (> 150°C) fcc phases. The fullerenes are linked into chains with 9.1Å repeat distance by a [2+2] cycloaddition reaction in the solid state [1]. This phase is an electrical conductor, and is unique among the fullerides in being stable upon exposure to air [2].

When quenched from the fcc phase to below 0°C, an insulator with a different orthorhombic structure appears [3]. Here, the C_{60} molecules are covalently bonded into dimers, although we have not been able to give a structural solution at the same level of detail as for the polymer phase.

[1] P.W. Stephens et al., Nature 370, 637 (1994).
[2] D. Koller et al., submitted to Appl. Phys. Letters.
[3] G. Oszlanyi et al., submitted to Phys. Rev. B.



* Supported by US NSF grant DMR-9202528, Hungarian OKTA 2943, and Copernicus program of the EEC under contract 2943. Work at the SUNY X3 beamline is supported by the Division of Basic Energy Sciences, U.S. Dept. of Energy under grant DE-FG02-86ER45231.



Fulleride superconductors and orientational order: T_c vs. lattice constant in $Na_2Rb_xCs_{1-x}C_{60}$ *	X3B1

T. Yildrim, J. E. Fischer, R. Dinnebier, P. W. Stephens, and C. L. Lin (Univ.of Penn., SUNY Stony Brook, and Temple Univ.)

The effect of orientational order on fulleride superconductivity was studied by performing high-resolution x-ray diffraction and SQUID magnetometry on the title quaternary phases. These are all simple cubic, $Pa\bar{3}$ space group, with the same molecular orientational order as occurs in the low temperature phase of C_{60}. The T_c vs. lattice constant (a) correlation shown below is much steeper than is found for the merohedrally disordered $Fm\bar{3}m$ phases, implying the possibility of large T_c enhancements with only minor additional dilation of the sc lattice. We interpret these results as arising from a narrower conduction band in the orientationally ordered state.

[1] T. Yildrim et al. Solid State Commun. (in press)

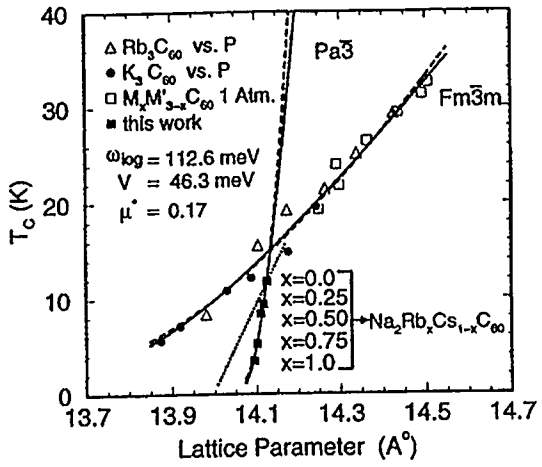


Figure 1. T_c vs. a for $Fm\bar{3}m$ (from the literature) and $Pa\bar{3}$ (present work)superconducting fullerides. Solid and dashed lines are results of fits to McMillan's formula forsuperconducting T_c under two different assumptions of the form of the density of states vs.a.

* Supported by NSF grants DMR91-20668 and DMR92-02528. Work at the SUNY X3 beamline is supported by the Division of Basic Energy Sciences, U.S. Dept. of Energy under grant DE-FG02-86ER45231.

In-situ investigation on film growth for Ag/Ag(111) *	X3B2

W. C. Elliott (Univ. of Missouri, Columbia), T. Tse, P. W. Stephens (SUNY Stony Brook), P. F. Miceli (Univ. of Missouri, Columbia)

We have begun an experimental program to study, in situ, the homoepitaxial growth of Ag(111). Through these studies we hope to gain insight to the microscopic mechanisms that control the behavior of a growing surface at both high and low temperatures - the later regime is expected to exhibit dynamic scaling of the surface roughness. Ag offers a number of excellent advantages for these studies, including the absence of surface reconstructions, high resistance to surface contamination, and ease of surface preparation for repeated measurements.

The experiments so far have focused on the specular reflectivity which gives the rms surface roughness, as shown in the figure where the reflectivity is measured around the (111). A pronounced temperature dependence of the roughness is observed. However, at low temperature we find scaling behavior well over two decades of film thickness, as shown in the inset. Future studies will look at surface diffuse scattering which reveals the spatial correlations during growth.

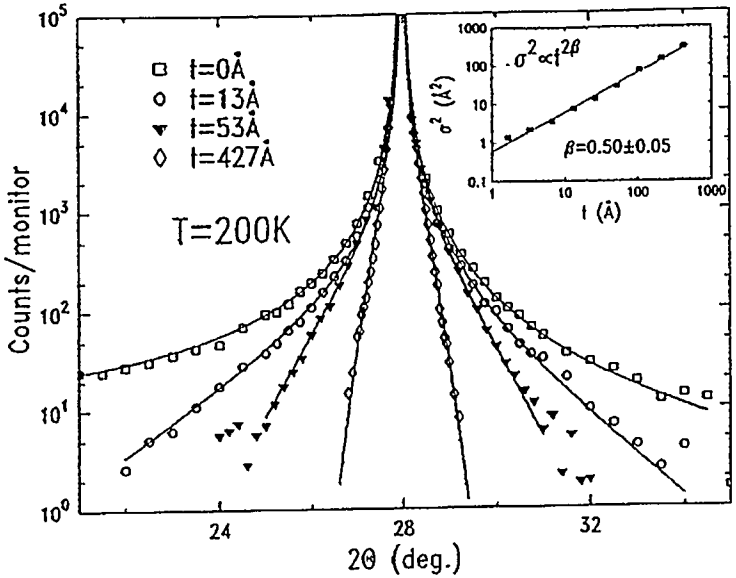


Figure 1.

* Supported by NSF grant DMR-9202528. Work at the SUNY X3 beamline is supported by the Division of Basic Energy Sciences, U.S.Dept. of Energy under grant DE-FG02-86ER45231.

Crystal structure determination of carboxymuconate laconizing enzyme (CMLE) from Neurospora crassa *	X4A

T. Glumoff, S. Helin, T. Salminen and A. Goldman (Turku Univ., Finland)

Single crystal X-ray diffraction experiments were conducted on crystals of 3-Carboxy-cis,cis-Muconate Lactonizing Enzyme from Neurospora crassa. The crystals are orthorhombic and belong to the space group $P2_12_12_1$ with unit cell dimensions of a=92.2 Å, b=160.0 Å, c=236.1 Å. The crystallized molecule is a tetramer of 41 kDa subunits.

The crystals were flash-frozen to 100K after incubation in a cryo-protectant solution. This was needed because of the tendency of the crystals to lose their diffraction power very rapidly upon exposure to the X-ray beam. When frozen, the crystals maintained their diffraction quality throughout the experimental time.

Oscillation method was used for the data collection. One-degree shots of 60 to 90 seconds each were taken on Fuji image plates. Only one crystal was needed for each data set. The following data sets were collected: native crystals, three heavy atom derivatives, one substrate complex and one inhibitor complex. The beam energy was 12800 keV and the wavelength used was 0.96875 Å.

The experimental setup could not be optimized in the course of the session, becasue processing of the raw data was not possible. Evaluation of the data is in progress. However, considerable improvement is to be expected compared to the results obtained with a conventional X-ray source at the home laboratory. This is in part due to the ability to use very small crystals (down to 0.2mm × 0.15mm × 0.02 mm), which appear to be better ordered than bigger crystals used with conventional X-ray sources. A nominal resolution of up to 1.7 Åcould be achieved with fairly complete data sets to about 2.5 Åresolution to be expected. Corresponding figures for data collected at the home laboratory are 2.1 Åand 3.2 Å, respectively.

* Supported by the Academy of Finland.

X-ray Data Collection of Cytochrome Reductase Crystals *	X4A

J. W. Lee, T. V. Law, and B. K. Jap (LBL)

Ubiquinol-cytochrome c reductase, also known as the bc_1 complex, was studied by single crystal X-ray crystallography. This large membrane protein composed of eleven subunits (ca 240 kD) forms three-dimensional crystals of hexagonal bipyramidal shape under the proper mixture of lipid and detergent. These crystals, when mounted in a glass capillary, had previously diffracted X-rays to a resolution of 3.5 Åat SSRL. Unfortunately, the lifetime of these sensitive crystals in the synchrotron beam near room temperature is rather short, rendering a full data set from a single crystal rather difficult to obtain.

During this reporting visit to beamline X4 of NSLS, we successfully cooled crystals of the bc_1 complex down to 100 K. The 20 x 25 cm imaging plates were placed at 400 mm for 6 minute exposures using 0.5 degree oscillations. The crystals retained their diffractability at 100 K, giving rise to a maximum resolution of 3.4 Å. The cooled crystals did not suffer noticeable damage during the span of over two days of data collection. A full data set (to 90 degrees) was thereby collected from a single cryo-cooled crystal. The preliminary results from autoindexing using Denzo gave an I-centered tetragonal unit cell of a = b = 154 Å, c = 602 Å.

This experiment demonstrated for the first time that a large membrane protein can in fact be studied at cryogenic temperatures. A manuscript describing the details of this experiment is in preparation.

* This investigation was supported by the Office of Health and Environmental Research, US Department of Energy, under contract DE-AC03-76SF00098, and by NIH grant GM51487.

In situ dispersive XAS of vanadium phosphate catalysts during butane oxidation	X6A

Simon R. Bare (Dow), George Coulston, Richard Harlow (Du Pont), Harold Kung, Kari E. Birkeland, Greg Bethke (Northwestern Univ.), Peter L. Lee (ANL), P. Joe Georgopoulos, and John Quintana(DND-CAT)

There is currently a thrust world-wide in the chemical industry to replace alkene feedstocks with much cheaper alkanes in processes for making partially oxygenated hydrocarbons. The transition has been slow because catalysts have not yet been found which are capable of converting the alkanes without fully combusting them. The only exception is vanadium pyrophosphate, $(VO)_2P_2O_7$, which is used in the commercial scale process to convert butane to maleic anhydride. The DuPont company is currently commercializing such a process which makes use of the ability of $(VO)_2P_2O_7$ to supply oxygen to butane by a process that results in vanadium reduction. The catalyst is subsequently reoxidized in a separate vessel and then recycled back to the reactor. In order to understand how this catalyst works one needs detailed information about how the vanadium oxidation state changes with gas composition. We have, therefore, made use of the facilities at NSLS X6A to study in situ the transient response of VPO compounds to cyclic changes in gas composition.

In a typical experiment, a 150μm wafer of catalyst is placed in a micro-reactor with 2μm thick Be windows. The reactor exit is in-line with a mass spectrometer so the production of maleic anhydride can be followed during the experiment. A polychromatic X-ray beam is focused onto the sample by a bent Si(111) crystal and the transmitted beam is dispersed onto a one dimensional photodiode array detector. With this configuration, the complete XAS spectrum can be collected with adequate S/N in $\leq$1 sec. This allows for data such as that shown in Figure 1 to be collected as the gas composition is cycled from 20% O_2/He to butane. These are the first experiments to show the transient evolution of the catalyst while it is used during unsteady-state conditions. The transformation of the vanadium from V^{5+} to V^{4+} caused by butane is clearly evidenced by the changes in both the $1s \rightarrow t_{2g}$ absorption feature and the shift in the K-edge position.

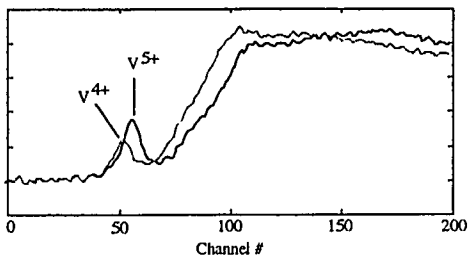


Figure 1. Channel No.

X-ray magnetic circular dichroism *	X6A

K. J. Gofron (Northern Illinois Univ. and ANL), C. Kimball (Northern Illinois Univ.),S. Mini (Northern Illinois Univ. and ANL), G. Jennings, P. Lee (ANL), P. A. Montano (ANL and Univ.Illinois, Chicago)

We have evaluated the energy dispersive beamline for studies of X-ray Magnetic Circular Dichroism (X-MCD) in 6 keV-25 keV energy range. Preliminary measurements in Fe/Ni alloy have been attempted as a test of the system. Requirements for stabilities of the detector system have been determined. The detector shielding was redesigned. The technique of X-MCD studies unoccupied magnetic density of states. The MCD signal is the difference between absorption when the magnetic moment and the incident photon (right-handed) point in the same direction minus the case when magnetic moment and photon are in the opposite direction. The consequences are important for understanding of magnetism in materials.

The XANES spectra are collected using 1024 channel Linear Diode Array detector. The energy dispersive beamline allows data collection of whole near edge in one step with pixel separation of about 140 meV. The degree of circular polarization was measured using x-ray polarimeter by measuring degree of linear polarization present in the radiation incident at the sample, and using known properties of synchrotron radiation. The polarimeter operates on the basis of the angular dependence of Compton (Thomson) scattering of x-rays. In the plane of the orbit the number of photon is $3.7*10^{10}$ photons/100 mA/ s using 600 μm slits. The beamline provides $4.87*10^{9}$ right circularly polarized photons per 100 mA in ring per second in energy window of about 1 keV centered at 7112 eV. We used right circularly polarized photons at 0.26 mrad below the plane of the orbit emitted into 600 μm slit placed at 10 m from the source. These photons were measured to have better than 95% right circular polarization. The beamline stability was improved by separating sample stage (requiring motion) from detector and goniometer stages (fixed during measurement).

A preliminary spectrum for Fe K edge X-MCD is shown in Fig. 1.

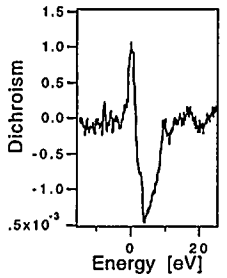


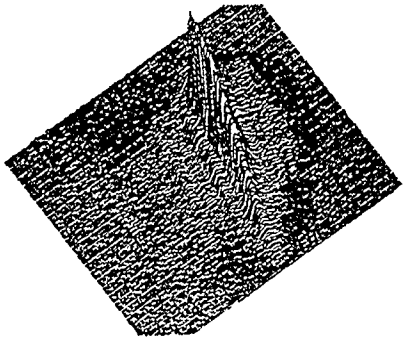
Figure 1.

* This work is supported by Department of Energy under contract W-31-109-Eng-38 and NIU-HECA/ State of Illinois.

Application of the energy dispersive instrument in structural studies of surfaces,interfaces, and thin films *	X6A, X6B

K. G. Huang, P. Lee, M. A. Beno, M. Ramanathan, G. Jennings, G. S. Knapp, and P.A. Montano (ANL)

New synchrotron x-ray techniques are being developed using the energy dispersive instrument at beamline X6A. These techniques make use of the energy dispersity to measure anomalous reflectivity, diffraction, and diffuse scattering from surfaces, interfaces, and thin films for real-time structural studies. Preliminary results obtained at X6A from thin films show the potential of these techniques and high quality data taken at X6B with conventional x-ray optics on the same samples demonstrate the power of these techniques. As an example, a continuous energy anomalous reflectivity (CEAR) measurement of a 3000 Å YBCO film epitaxially grown on $SrTiO_3$2(001) is briefly described. The curved Si(220) polychromator diffracts a divergent white beam from the source, and focus the beam horizontally to a narrow 100 μm line. The polychromatic beam has a 1000 eV bandpass and a convergent angle of a few mrads. In the CEAR experiment, such a beam is incident to the thin film sample at a small angle (reflection geometry). The intensity pattern of the reflected beam was recorded by a 2D Charge-Couple-Device (CCD) detector. Fig. 1 shows a 3D plot of scattering intensities versus the x-ray energies near the Cu K-edge (8.979 keV, center), and the reflection angle. Along the peak, the x-ray energy varies due to the dispersity. The intensity profile along the peak is, in fact, a continuous energy anomalous reflectivity (near a constant Q) taken simultaneously. The same sample was measured at X6B with focused monochromatic beam in an E- scan at a fixed Q (0.35 $Å^{-1}$). Fig. 2 shows the data with clear features due to anomalous effect. Continuous anomalous reflectivity and diffuse scattering measurements using energy dispersive instrument could be useful for studies of dynamic behaviors of interface growth.



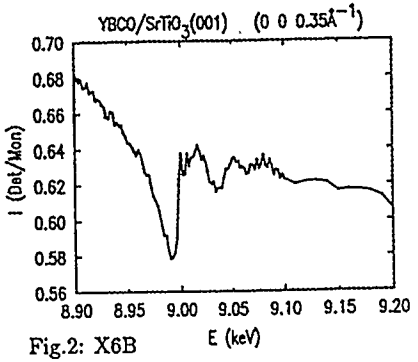


Fig.2: X6B

* Work supported by the U.S. DOE, BES-MS, under contract number W-31-109-ENG-38

Continuous energy diffraction spectroscopy (CEDS) *	X6A

P. L. Lee, M. A. Beno, G. S. Knapp, and G. Jennings (ANL)

We have developed a new technique, Continuous Energy Diffraction Spectroscopy (CEDS), for diffraction experiments using a synchrotron energy dispersive polychromatic beamline. Such a beamline uses a polychromator crystal to focus a range of X-ray energies (bandwidth ~1 keV) into a small (100-120 μm) line image. With a sample at this image point, using an area detector, we are able to measure diffracted intensities for the entire energy range of the incident beam simultaneously with limited or no motion of the sample. This method allows the collection of anomalous scattering intensity data and facilities doing DAFS experiments faster and more accurately. It also creates a new and better option for time resolve diffraction and phase transition studies. Furthermore, various types of samples including single crystal, powder and thin films can be studied with this technique. This technique provides new data collection strategies and promises many new experimental opportunities.

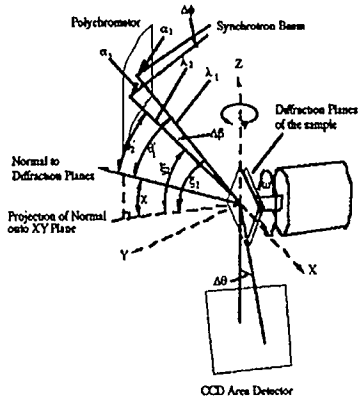


Figure 1. General diffraction geometry and components for the experiment. $\Delta\alpha = \alpha_2 - \alpha_1$. λ_1 and λ_2 are the first and last wavelength of the incident beam. Θ_1' and Θ_2'are the angles between the normal of the sample diffraction planes for λ_1 and λ_2. $\xi_1$and ξ_2 are

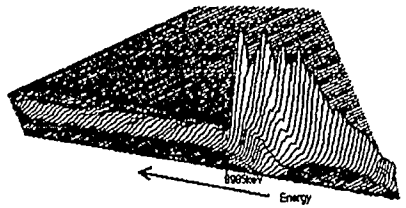


Figure 2. Image of a reflection for a $CuSO_4 \cdot 5H_2O$ crystal produced by a 20 second, 1 degree ω angle rotation. A DAFS spectrum can be derived from this data. The energy at the absorption edge was determined by an EXAFS measurement.

* Work at Argonne National Laboratory is sponsored by the US Department of Energy, Office of Basic Energy Sciences, Division of Materials Sciences, under contract W-31-109-ENG-38.

Resonant reflectivity measurements on Fe/Cr multilayers * | X6B

J. M. Bai (Brooklyn College of CUNY, ANL), E. Fullerton (ANL), and P. A. Montano(ANL, Univ. Illinois, Chicago)

Resonant reflectivity measurement are carried out by making use of the energy dependence of the density (ρ) and linear absorption coefficient (μ) of the materials (see Fig. 1). The ρ and μ show significant contrast between the Cr and Fe layers and the MgO substrate. It varies as the energy of incident x-ray changes. The reflectivity measured at selected energies then shows different features and gives more information on the composition profile of the multilayers. The samples were produced by epitaxial sputtering on MgO substrates. Sample A is on MgO (100) and B on MgO (110). For both samples, twenty bilayers of Fe (20 angstrom) /Cr (11 angstrom) were grown on the top of a 100 angstrom Cr buffer layer on MgO substrates.

Fig. 2 shows the reflectivity curves measured at E = 6.1 KeV (a), 6.94 KeV (b), 7.16 KeV (c) and 7.3 KeV (d). The drastic change of the line shape reflects the energy dependence of the electron density and the linear absorption of iron and chromium. For example, at E = 7.3 KeV, the ρ and μ contrast between Cr and Fe layers is minimized, hence the multilayers Bragg peaks almost disappear. It is also interesting to compare the 6.1 KeV and 7.16 KeV curves, as the electron density contrast is inverted. Detailed analysis will be followed to give a detailed quantitative description of the composition structures of the multilayers.

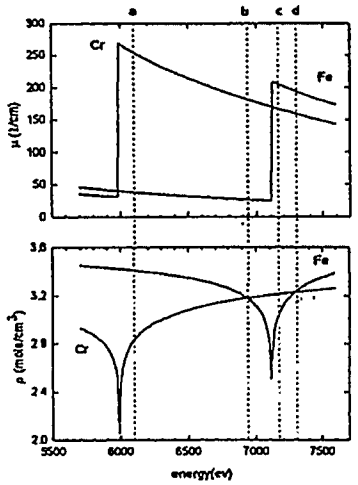


Figure 1. The Energy dependence of the electron density and linear absorption of Cr and Fe.

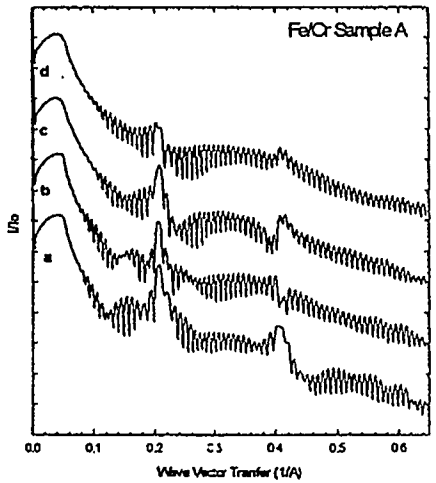


Figure 2. The resonant reflectivity measurements of Fe/Cr multilayer.

* This work is supported by U.S. DOE BES No. W-31-109-ENG-38.

EXAFS study of the ZnSe/GaAs interface * | X6B, X18B

J. M. Bai (Brooklyn College of CUNY) (ANL), S. Sivananthan (Univ. Illinois, Chicago),and P. A. Montano (ANL) (Univ. Illinois, Chicago)

We measured the fluorescence EXAFS spectra at the K-edges of Ga and As in a ZnSe/GaAs structure. The samples were grown by MBE techniques on GaAs (111) substrate. The epitaxially grown ZnSe samples thickness varied between 1.5 to 13 microns. We observed that the first shell radius of Ga at the ZnSe/GaAs interface is smaller than that of pure GaAs. However, the first shell radius of As remains the same as in bulk GaAs. A typical EXAFS fit at the Ga K-edge for the first shell in a 1.5 micron sample is shown in figure 1.

According to Ref. 1, GaAs and ZnSe form a continuous series of solid solutions and the lattice period correspond approximately to Vegard's law. In that case, the first shell radius of Ga and As at the ZnSe/GaAs interface should be the same and should increase with increasing amounts of ZnSe at the interfacial layer. On the other hand, Y.H. Wang and S.S. Li (Ref. 2) pointed out that the out-diffusion of As atoms in ZnSe is smaller than that of Ga atoms. That means there are more Ga atoms in the interfacial layer than As atoms. So the interface may not be a simple ZnSe/GaAs layer. D.W. Tu and A. Kahn (Ref. 3) suggested the formation of (Ga,Se) compound at the ZnSe/GaAs heteroepitaxial interface.

One of the stable phases of (Ga,Se) compounds, Ga_2Se_3, is known to have zincblende structure, and one third of Ga sites are left as structural vacancies. As a result of these structural vacancies, the lattice parameter of Ge_2Se_3 is about 5was supported by J. Qiu and coworkers in their Dark field TEM analysis. (Ref. 4) So our surface EXAFS result is another evidence to the formation of (Ga,Se) compounds at the ZnSe/GaAs interface. The first Shell radius of $''a$ is actually the inter atomic distance between Ga and Se in the (Ga,Se) compound and the first shell radius of As is the Ag-As inter atomic distance in GaAs.

[1] N.A. Goryunova and N.N. Fedorova, Soviet Phys. Solid State, 1, 307 (1959).
[2] Y.H. Wang and S.S. Li, J. Appl. Phys. 68(5) 2535 (1990).
[3] D.W. Tu and A. Kahn, J. Vac. Sci. Technol. A3, 992 (1985).
[4] J. Qiu, Q.-D. Qian, M. Kobayashi, R.L. Gunshor, D.R. Menke and D. Li and N. Otsuka, J. Vac. Sci. Technol. B8 (4) 701 (1990).

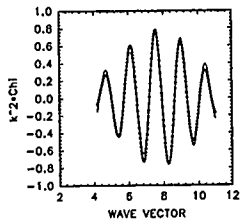


Figure 1.

* This work is supported by the DOE undercontract W-31-109-Eng-38.

Transparent non-diffracting polarization rotation regime (TNDPR) | X6B

M. A. Baysal and J. M. Bloch (Temple Univ.)

We investigated the previously unexplored TNDPR regime in which the linear polarization direction is rotated or converted into a circular one. The previous investigations studied the polarization rotation due to birefringing in Si crystals with small transparency values and only at the exact Bragg condition. To reach the TNDPR regime, it is crucial to choose a dynamically diffracting crystal with the smallest absorption to diffraction ratio and with geometry in which diffraction width is the narrowest. Therefore a 300 μm thick diamond [400] crystal in the non-symmetrical geometry was utilized.

We obtained a highly transparent polarization rotation outside the diffraction regime using the following method: The beam was oriented with an incident angle $\alpha = 30^\circ$ and polarization parallel to the sample surface. The sample was then rotated around an axis normal to the surface (ω) until an inclined plane enters into the diffraction condition. The transmitted and also the polarized beam intensities, diffracted from a second diamond [220] crystal (polarizer) at $2\theta_{[220]} \approx 90^\circ$, were measured. The rocking curves of the full and polarized transmissions of the [111] plane are given in (I) and (II) of Fig. 1 respectively.

Our experimental results were consistent with the theoretical predictions (Fig. 1). Pure linear rotation ($\Psi = \pm\pi$) and maximally circular beam ($\Psi = \pm\pi/2$) occurred outside the diffraction regime. The absolute value for the form factor of diffractions were also derived from this TNDPR experiment without resorting to measure the diffracted intensities. The misfit parameter $a = (2\vec{K}\cdot\vec{h} + h^2)/2K^2$ is found to be proportional to the square of the form factor by the expression $\Delta a(\pm\Psi) = -[\ln T/(2\Psi\chi^{(o)}_{[imag]})](|\ \chi^{(h)}\ |\ \sin 2\theta)^2$ where T: the transparency, Ψ: the relative phase between the S-P beams. From $\Delta\omega_2$ ($\Psi = \pm\pi$) in Fig. 1, the scattering factor was evaluated to be $\chi^{[111]} = -1.23 \times 10^{-5}$ ($\chi^{[220]} = -1.02 \times 10^{-5}$) at E = 6.953 keV. The TNDPR technique proposed here yields efficiencies superior to the simultaneous polarization rotation-diffraction configuration reported previously. Thus it promises to be of significance to the applications requiring an intensive X-ray beam with tunable polarization. Any desired linear rotation and fully circular beam with high transparencies can be achieved by a proper choice of the crystal thickness, orientation and energy resolution.

Figure 1. Scan around the diamond [111] diffraction at 6.9530 keV. The circles are the experimental data points and the fitting curves are calculated from the S-P Coupled Dynamical Theory with 16 internal waves. Curve (III) gives the rotation in linear polarization angle and curve (IV) is (minor/major axis)^2 of the polarization ellipse. The top three curves were integrated over an energy dispersion of 0.6 eV. [Figure not available due to space constraints.]

Structural properties of siloxene films on Si(111) * | X6B

K. G. Huang (ANL), M. Rosenbauer, and J. Zegenhagen (Max-Planck-Institut fur Festkorperforschung,Germany)

The atomic structure of siloxene [$Si_6H_3(OH)_3$] films prepared on Si(111) surfaces was studied using x-ray scattering in order to understand its luminescence mechanisms. The siloxene film of μm thickness was made by deposition of Ca vapor (550°C) onto a hot Si(111) substrate (740°C) where Ca reacts with Si to grow $CaSi_2$ layers epitaxially, followed by reaction with 37% HCl at 0°C. The photoluminescence of these siloxene films is peaked near 550 nm.

X-ray specular reflectivity measurements of the siloxene/Si(111) sample reveal a siloxene peak in the Si(111) direction (solid line in Fig. 1: a hexagonal coordinate system is used to index the reciprocal space) indicating that the siloxene film has a layered structure parallel to the Si(111) surface with a d-spacing of about 6.30 Å. The formation of siloxene from $CaSi_2$ powder was known to be topotactic, with Si layers remaining intact. However, it is remarkable that the film prepared in such a chemical procedure exhibits a good layered structure of $Si_6H_3(OH)_3$ which align to Si(111) planes within a few degrees. A 2θ scan at grazing incidence (Fig. 2) was made to investigate the in-plane structure of the film. The characteristic of the scan profile is independent of the sample azimuthal orientation. The broad peak centered around 28° was due to scattering from the basal plane structure of the Si-rings in siloxene. The observation of Si(111) and Si (220) powder peaks suggests the existence of small Si particles embedded in teh siloxene film. After annealing the sample at about 400°C for about 10 min, the layered structure was completely destroyed (dashed line in Fig. 1) while the powder peaks of Si nanoparticles remain. A detailed analysis is underway to understand whether these Si nano-crystals play a role in the luminescence of siloxene.

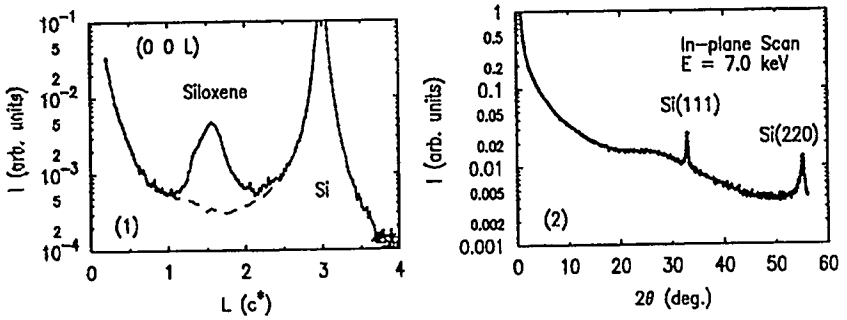


Figure 1.

* Work supported by the U.S.Doe, BES-MS, under contract number W-31-109-ENG-38.

Diffraction studies of self-assembled azobenzenealkanethiol monolayers on gold surfaces *	X6B

A. Malik, W. B. Caldwell, B. R. Herr, M. K. Durbin, C. A. Mirkin, and P. Dutta (Northwestern Univ.) and K. G. Huang (ANL)

Self-assembly of monolayer films has been demonstrated for a wide range of adsorbate functional groups and substrates; however, experimental studies (including x-ray scattering) have focussed primarily on "simple" straight-chain molecules. We have studied self-assembled monolayers of molecules containing an azobenzene segment, an alkane chain, and a thiol head group attached to Au(111) substrates. We find (Fig. 1, top) a monolayer peak that is incommensurate with the gold surface (a $\sqrt{3}$x$\sqrt{3}$R30 structure would give a diffraction peak at 1.5Å^{-1}). However, the rocking curve (Fig. 1, bottom shows that the lattice is rotated 30° with respect to the Au(111) surface.

We propose that the thiols are in fact attached to the gold surface at the $\sqrt{3}$x$\sqrt{3}$R30 sites, as previously reported. [1] However, the azobenzenes take advantage of the flexibility of the alkane chains to form, at the monolayer-air interface, a slightly compressed and thus incommensurate structure. Even though the structure is incommensurate, it is most likely to be aligned in the R30 direction because this alignment requires the least amount of alkane chain distortion.

We have also studied the diffraction peak as a function of temperature (Fig. 1, top). The peak becomes weaker as a function of temperature; upon cooling, the maximum is at about the same place in K_{xy} but has shifted to lower K_z. In other works, the azobenzene are originally tilted, but move towards the vertical upon annealing.

[1] E.g., P. Fenter, P. Eisenberger, and K.S. Liang, Phys. Rev. Lett 70, 2447 (1993).

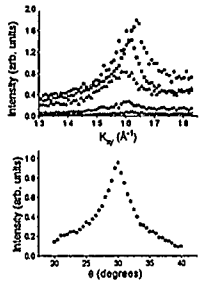


Figure 1. TOP: Radial diffraction scans at: room temperature, K_z=0.45Å^{-1} (square); 108°C, K_z=0.45 Å^{-1} (triangle); 118°C,K_z =0.45Å^{-1} (circles); 128°C, K_z = 0.45Å^{-1} (×);back to room temperature, K_z = 0.1Å^{-1} (stars). BOTTOM: rocking curve at room temperature (the origin is the direction of the Au(11) peak

* Submitted to J. Am. Chem. Soc. This work was supported by the Materials Research Center, Northwestern Univ. (NSF-MRL). Beamline X6B is supported by the US Department of Energy under contract W-31-109-ENG-38 (ANL).

Evolution of structure in multilayer Langmuir-Blodgett films *	X6B

A. Malik, M. K. Durbin and P. Dutta (Northwestern Univ.), and K. G. Huang (ANL)

There are experimental indications that the structure of a monolayer Langmuir-Blodgett (LB) film is different from the structure of an LB film with a large number of layers. To study how the structure evolves, we have looked at 1-, 3- and 5-layer LB films of lead stearate. (Films with even numbers of layers are not stable except under water.) Each film shows a diffraction peak at ~1.52Å^{-1} (Fig. 1, left: the monolayer peak is weaker because there are fewer layers, but it is statistically unambiguous). The 3-layer and 5-layer films show two peaks, with the second at ~1.72Å^{-1} (Fig. 1, center). In other words the first layer is hexagonal (as we have previously reported [1]) but the structure becomes distorted hexagonal as soon as there are three layers.

"Rod" scans are shown in Fig. 1 (right). The monolayer rod scan shows no features (none are expected). The difference between the 3-layer and 5-layer rod scans are noticeable, however: the 5-layer scan shows an additional set of maxima between the more intense maxima common to both multilayers. these peaks are from the lead planes (the distance between lead planes is twice the distance between monolayers). The absence of such peaks in the three-layer film suggests that the first layer retains its hexagonal structure even in a multilayer film. [1] A. Malik, M.K. Durbin, K.G. Huang, and P. Dutta, submitted to Langmuir.

[2] M.C. Shih, J.B. Peng, K.G. Huang, and P. Dutta, Langmuir 9, 776(1993).

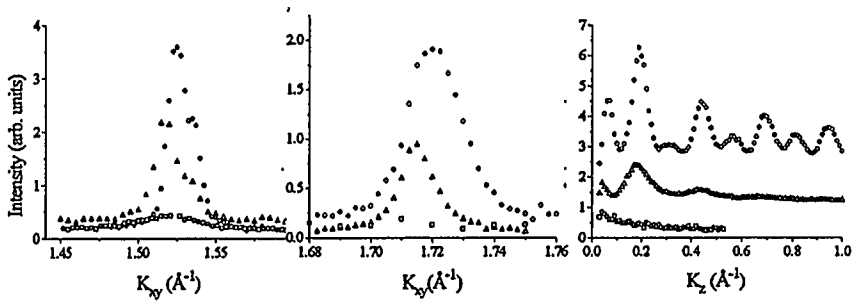


Figure 1. Radial scans in the film plane (showing the two observed peaks), and "rod' scans for monolayer (open square), three-layer (△) and five-layer (o) Langmuir-Blodgett films of lead stearate. Two of the rod scans (right) have been shifted vertically for clarity.

* This work was supported by US Dept. of Energy grant No. DE-FG02-84ER45125, and by US Department of Energy contract no. W-31-109-ENG-38 (ANL)

Time evolution of specular and off-specular reflectivity during sputter deposition of platinum film *	X6B

G. Rue, H. K. Kim (Pusan Natl. Univ., Korea), K. G. Huang (ANL), K. B. Lee (Pohang Inst. Sci. Technol., Korea), R. T. Kampwirth, and H. You (ANL)

Dynamic evolution of vacuum/platinum-film interface during growth is studied by x-ray specular and off-specular reflectivity measurements. Platinum was deposited on polished silicon substrates in a sputtering chamber with a mylar x-ray-transparent window. The chamber is based on off-axis deposition from a faced-magnetron assembly and redesigned from the chamber previously used for the Au/Si experiments [1]. One of the main improvement is the shape of the window which allows x-rays to scatter in-plane over the range of $\pm 8°$. Measurements were made for the temperature range from room temperature of 400°C and for the argon-pressure range from 1 to 50 mTorr. A series of specular scans and a series of off-specular scans were made in a similar deposition condition for direct comparison. An example set of the specular and off-specular scans are shown in Fig. 1. These scans were made in a deposition condition of 110°C substrate temperature and 10 mTorr of argon pressure. In the specular scans (lower panel) the critical angle of platinum is clearly visible for a deposition of <100Å. The oscillation period, which is inversely proportional to the film thickness, becomes smaller and smaller until it disappears around at 10 minute deposition (at the deposition rate of ~1Å/sec). At higher deposition the oscillation is no longer visible and the reflectivity is similar to that from two in-coherent interfaces [1]. In the upper panel a series of off-specular reflectivity measured during deposition in a similar condition. A series of ψ scans were made at Q_z=0.2Å^{-1}. The diffuse part of the scattering evolves for the initial 5 min deposition but saturates to an almost steady state form while the intensity of specular peak continuously decreases. It indicates that the surface morphology in a length scale that x-rays probe does not rapidly evolve after a few hundreds Å deposition. The films grown at 400°C or igher show a significant amount of clustering at the interface. The clustering is inferred from reflectivity scans with a modulated oscillatory behavior and non-uniform increase of the film thickness. The mobility of platinum atoms is sufficiently high to form clusters at this temperature. Data analysis is in progress.

[1] H. You, R.P. Chiarello, H.K. Kim, and K.G. Vandervoort, Phys. Rev. Lett. 70 2900 (1993).

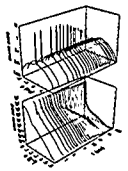


Figure 1. Specular and off-specular reflectivity measured from Pt film during growth.

* This work was supported by Korean Science Foundation & RCDAMP (PNU), by US DOE under contract W-31-109-ENG-38 (ANL), and by Pohang Light Source (Postech).

Total-electron-yield measurement of sulfur K-edge XAFS of SO_2-containing humid atmosphere *	X6B

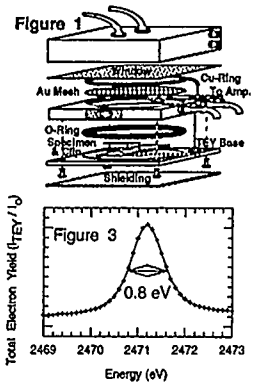
I. Song, B. I. Rickett, P. Janavicius, J. H. Payer (Case Western Reserve Univ.), and M. R. Antonio (ANL)

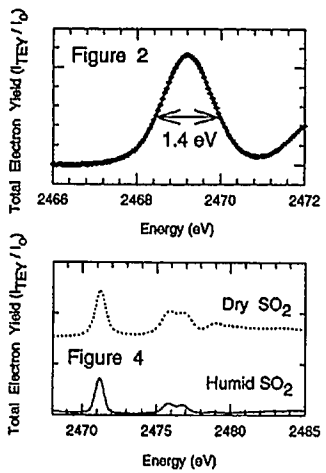
A total-electron-yield (TEY) detector shown in Figure 1 was constructed for in situ XAFS measurements of the sulfur-containing species in a humid atmosphere containing SO_2. Using the detector, gas phase XAFS spectra were collected for both dry and humid SO_2 atmospheres. Presented are the examples of the sulfur K-edge spectra collected during the study. In the solid state XANES data for $Na_2S_2O_3 \cdot 5H_2O$ (Figure 2) taken to verify the detector performance, a spectral broadening by approximately 140% was indicated by the FWHM of the first sulfur absorption peak (1s-a_1). [1] This is interpreted as the effect of the final state bandwidth of the solid state specimen in conjunction with the experimental broadening. In constrast, the first sulfur absorption peak (1s-$\pi^*(3b_1)$) in the XANES of gaseous SO_2

(Figure 3) was resolved with a total spectral broadening of approximately 40%. [2] This agrees with the estimated experimental resolution, 0.53 eV, at sulfur K-edge. The XANES data of gas phase SO_2 shown in Figure 4 indicated that the structure (C_{2v}) and the chemistry (IV+) of dry SO_2 did not change with the introduction of gaseous H_2O (88% relative humidity) at room temperature. It was possible to record a sulfur K-edge TEY signal from a simulated atmospheric condition, namely 20% O_2 in helium at 90% relative humidity.

[1] H. Sekiyama, N. Kosugi, H. Kuroda and T. Ohta, Bull. Chem. Soc. Jpn. 59 (1986) 575.

[2] S. Bodeur and J.M. Esteva, Chem. Phys. 100 (1985) 415.





* This work was supported by IBM/CWRU SUR(No. 1314) and NSF (No. DMR-9015475).

Concentration of synchrotron beams by means of polycapillary x-ray optics *	X6B

J. B. Ullrich (Univ. at Albany), K. G. Huang (ANL), S. M. Owens, D. C. Aloisi, F. A. Hofmann, N. Gao, I. L. Klotzko, W. M. Gibson (Univ. at Albany)

Polycapillary optics have been shown to be powerful tools in the manipulation of x-ray beams, specifically in the case of concentrating synchrotron beams for high flux experiments. Most of the previous work has been done on single tapered capillaries, or polycapillaries of very small diameter, but they suffer from the problems of low transmission efficiencies, small effective capture areas, and are quite fragile. The optics examined here, known as monolithic optics, eliminate some of these problems, being stronger and more stable due to their close-packed geometry. Earlier work shows the high potential gain expected from such an optic, and here we report on the characterisation and use of four such lenses with beamline X6B at the NSLS.

A general sketch of the optics is shown in figure 1. The geometry of some of the prototypes tested is listed in table 1. The optics represent a cross section of prototype optics that were available at the time. All optics were evaluated before hand using a point source. The width of the input beam was made comparable to but smaller than the input diameter of the lenses using the toroidal mirrors in X6B. This was proven by knife-edge scans and by exposing photographic paper in front of and behind the lens. The intensity of the beam was monitored in front of and behind the lens simultaneously with different ion chambers. The ion chambers were calibrated without lens several times.

A significant gain in intensity of the beam was achieved using these optics as compared to the normal beam. This gain, however, should be compared to conventional focussing mirrors. For mirrors, higher gains are possible since larger efficiencies are possible while achieving smaller spot sizes. The special advantages of monolithic optics are: i) they can be mounted in experimental hutch outside the vacuum due to the extremely short focal length, ii) the optics are much easier to handle and align than focusing mirrors, and iii) the spot size and shape of the focused beam is not as severely energy dependent as when using focusing mirrors. Over the course of the experiment, radiation damage of the lenses was observed. The lenses showed visible discoloration after being exposed for a few seconds, but the damage did not significantly reduce transmission until much larger doses were absorbed. For the lens used in the radiation damage experiment, transmission degraded from 45% down to 38% over the course of 5 hours. This damage is larger than seen for single capillaries.

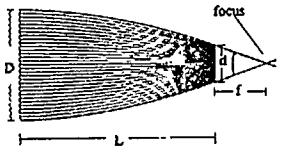


Figure 1: Sketch of a polycapillary optic.

Lens #	Length (mm)	Input Dia. (mm)	Output Dia. (mm)
5.5.2	119.5	6.5	1.9
19483A	67.8	4.3	3.3

Table 1: Geometry of used prototypes.

Lens #	Energy (keV)	Transmission (%)	focal length (mm)	focus size FWHM (mm)
5.5.2	8	0.5	15	0.13
19483A	8	45	135	0.43

Table 2: Summary of results.

* This work was supported under NASA contract NAS8-39926.

Spin-dependent EXAFS in magnetized polycrystals of [Fe(α-picolylamine)$_3$]Cl$_2$·EtOH *	X6B

Z. Wang, C. Kimball (Northern Illinois Univ.), L. X. Chen, J. R. Norris, K. G. Huang, and P. A. Montano (ANL)

Spin-dependent x-ray absorption using synchrotron radiation is a young technique for magnetic structure studies. It has been shown recently that the x-ray absorption of circularly polarized x-rays in magnetized targets depends on the spin polarization of the photons relative to the spin polarization of the magnetic electrons in the absorber [1,2]. The interesting effect was interpreted in terms of the transfer of a spin-polarized photoelectrons from a unpolarized initial core state into the magnetized neighbors. The experimental procedure is relatively simple, and since the initial electron state, 1s level, has non spin density or spin-orbit coupling, the spin-dependent absorption depends only on the differences of the spin densities of the final state, which is a simplification for the theoretical interpretations. Therefore, the spin-polarized EXAFS (SPEXAFS) may become a useful method for the investigations of various magnetic materials.

Here we report our first experimental attempts for a spin-dependent EXAFS experiment on magnetized polycrystals of [Fe(α-picolylamine)$_3$]Cl$_{-2}$·EtOH. In the sample preparation, the crystals were deposited on a mylar substrate by very slow evaporation of EtOH under reduced pressure, and the system was placed in an applied magnetic field of 1kG. Thus the magnetic moment of the molecules was aligned along the magnetic field direction within the substrate plane. Linearly polarized x-rays from the beam center were used in the measurement at transmission geometry. Absorption spectra were taken with the magnetic moment of sample molecules parallel and perpendicular to the direction of x-ray polarization, respectively (Fig. 1). It is clear that at near edge region, the outgoing photoelectrons in the parallel mode has a larger transition cross section than that in the perpendicular mode. This may be understood qualitatively in terms of the exchange potential between the polarized outgoing photoelectrons and the magnetic electrons in the absorber. Further data analysis and more complete experiments are underway.

[1] G. Schutz, W. Wagner, W. Wilhelm, P. Kienle, R. Zeller, R. Franham, and G. Materlik, Phys. Rev. Lett. 58, 737 (1987).

[2] G. Schutz, R. Frahm, P. Mautner, R. Wienke, W. Wagner, W. Wilhelm, and P. Keinle, Phys. Rev. Lett. 62, 2620 (1989).

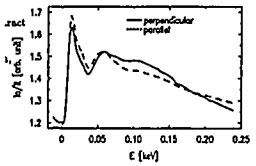


Figure 1.

* This work was supported by NIU-HECA/CARS and by DOE under contract W-31-109-ENG-38 (ANL).

Structure and behavior of zintl ions in restricted geometries | X7A

P. Armand, L. Iton, D. L. Price, and M-L. Saboungi (ANL)

Alloying of alkali metals with polyvalent metals in Group IV, V and VI of the periodic table produces alloys with remarkable structural, electronic and thermodynamic properties. Roughly speaking, these can be rationalized in terms of transfer of an electron from the alkali to the polyvalent metal, leading to charged polyvalent metal ions which have behavior characteristic of element shifted one column to the right in the periodic table. They tend to form covalent bonds with a number of similar ions, leading to ionic complexes ("Zintl ions") which are readily seen in diffraction measurements.

Both X-ray diffraction and anomalous X-ray scattering measurements around the Se and Rb K edges were carried out, at room temperature, to determine the structure of Se and RbSe loaded in Nd-exchanged Y-type zeolite.

The diffraction data were analyzed by the Rietveld method. For the two samples, no electron density positions could be attributed to selenium or rubidium atoms. These results suggest that the element or the alloy is distributed "out of registry" into the supercages of the zeolite. The differential radial distribution functions, obtained by Fourier transform of the corresponding structure factors, allowed us to get partial information on the nature of the loading elements. For illustration, $\Delta_{Se}T(r)$ for Se/NdY and RbSe/NdY are shown in Figs. 1 and 2 respectively.

The curve fitting analysis for Se confined in Y zeolite reveals that the twofold coordinated structure of selenium is preserved, with an average bonding-distance of 2.32 Å. The second neighbor shell centered at 3.62 Å, contains 2.7 selenium atoms. These results suggest that the helical-chain structure of selenium still remains into the supercages of the zeolite.

Concerning RbSe-loaded into Y zeolite, the area of the Gaussian function, centered at 2.40 Å in $\Delta_{Se}T(r)$, corresponds to one Se atom. On the other hand T(r) of this same sample, obtained around the Rb K edge (Rb-Rb, Rb-Se...interactions) doesn't show any peak at this distance. These remarks tend to confirm the formation of Se_2^{2-} ionic dimers, known as "Zintl ions", as expected for this alloys, even in restricted geometry.

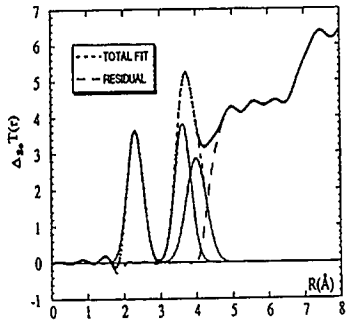


Figure 1. T(r) obtained for Se/NdY around Se K edge.

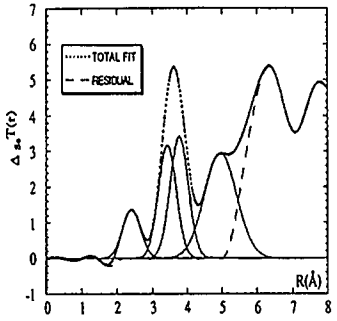


Figure 2. T(r) for RbSe/NdY zeolite around Se K edge.

Investigation of the low-temperature structure of Fe_3O_4 | X7A

P. Bordet,J.D. Sullivan,M. Marezio (CNRS Grenoble), D.E. Cox (bnl)

We carry on a detailed characterization by high resolution synchrotron x-ray powder diffraction of the structural distortion and Fe2+/Fe3+ charge ordering occurring in magnetite below the Verwey transition temperature (Tv=123K). During preceding experiments carried out with flat-plate geometry, reflexion splitting and superstructure peaks were observed, indicating that the transition was accompanied by a symmetry change from cubic (Fm3m spinel, as=8.4A) to C-centered monoclinic (a=asV2, b=asV2, c=2cs, beta=90.26). However, these data were not sufficient to envisage a structural refinement, since only parts of the diffraction spectrum had been measured.

The present experiments were dedicated to full data collection with the most well adapted experimental setup. In order to eliminate problems due to a somewhat erratic evolution of peak widths with Bragg angle observed previously, we first chose after several room temperature tests to work with capillaries at a 0.85A wavelength. This led to more consistent peak widths, but superstructure peaks could no longer be observed due to increased background and decreased diffracting volume with this geometry.

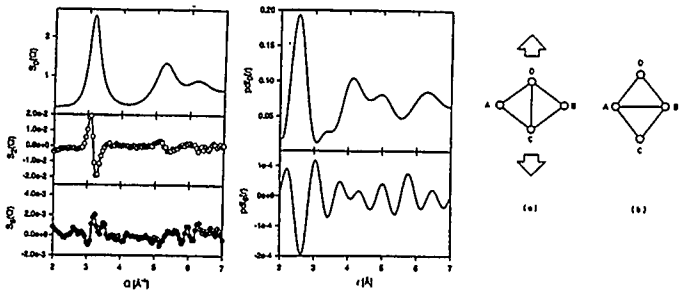
In a second attempt, we used flat-plate geometry again, and took extreme care in sample preparation : the powder was prepared by gently grinding a single crystal and then sieved between 270 and 400 mesh sieves (about 35 microns grain size) Powder diffraction data were collected at 0.85A with a Si(111) channel-cut monochromator and a Ge(220) analyzer up to 40 deg. Bragg angle. Higher angle data could not be measured due to synchrotron beam dump.

Preliminary inspection of the data indicates that the superstructure reflexions corresponding to the above monoclinic cell are indeed observed. However, most of the superstructure intensity is concentrated in reflexions indexable with the (as/V2,as/V2,as) monoclinic subcell. We are presently attempting to refine the data within models based on this subcell. Neutron powder diffraction data have been collected with the same sample at the BNL high flux reactor. Joint refinement of the synchrotron and neutron data should allow us to gain insight into the understanding of this very complex and subtle structural phase transition.

Deformation induced bond orientational order in metallic glasses * | X7A

T. Egami, W. Dmowski, P. Kosmetatos, M. Boord (U. Penn.), T. Tomida (Sumitomo Metal Industries), E. Oikawa and A. Inoue (Tohuku U.)

Topological description, for example in terms of local clusters such as icosahedra, has been widely used to characterize the structure and explain the properties of metallic glasses. Experimental verification has, however not been as vigorous as the theoretical and modelling effort. The object of the research reported here is to demonstrate the validity of the network concept in describing the structure of metallic glass, by demonstrating the existence of sixfold bond orientational order induced by anelastic deformation. A ribbon of $Fe_{81}B_{12}S_4C_2$ metallic glass of thickness 30 μm and width 30 mm was annealed in vacuum under a 100 kg/mm^2 stress at 300°C for 30 mins to induce anelastic deformation. The sample was then examined in beamline X7A at NSLS using a position sensitive detector(PSD) of 10cm length. A si(111) monochromator was used to set the beam energy at 15 KeV. The PSD was scanned over 2θ to cover a wide range of angles. The scattered intensity was normalized by the Fe Fluorescence signal from the sample. Measurements were performed lin transmission geometry with the diffraction vector Q kept in the plane of the ribbon. The direction of the anelastic deformation stress was assigned to be the z-axis; the sample was rotated away from this axis by an angle χ reaching up to $\pm 90°$ so as to cover all the 2-Dsample plane with the Q vector. The intensity data thus collected as a function of θ and χ were used to determine the anisotropic structure factor $S(Q)= \sum_{l,m} S_l^m(q)Y_l^m(Q/Q)$, expanded by means of spherical harmonics. In our particular case, m=0 since the sample has cylindrical symmetry. Fig. 1 shows S_0^0, S_2^0 and S_6^0. Furthermore the anisotropic pair distribution function (PDF), $\rho_l^m(r) = [(i)^l/2\pi^2] \int S_l^m(Q)\mathcal{J}_l(Qr)Q^2 dQ$ was calculated (see Fig. 2). All are in excellent agreement with theoretical predictions and existing simulations. these predict that the sixth order component will be dominant; this is because during deformation bond exchanges (see fig. 3) will result in a 30° rotation of triangles. The sixth order component calculated by our analysis is indeed sizeable, however it is also much lower in magnitude than what we may have expected. That may be due to the fact that the glass we examined is multicomponent, whereas the simulations were performed having a monoaatomic specimen in mind. Size differences between various elements involved in the real glass may give rise to disorder, hence obscuring the simplified picture of the ideal simulation environment.



* Support provided by NSF through grants DMR93-00728 and DMR91-20668

Interfacial structures of giant magnetoresistance Fe-Cr multilayers * | X7A

T. Egami, W. Dmowski, D. Louca (U. Penn), D. Kelly, I. Schuller (U.C. San Diego)

Fe-Cr multilayers exhibit giant magnetoresistance effect which can be utilized in magnetic recording. There are many studies indicating the role of the interfacial structure on the magnetoresistance effect. To elucidate this point we have performed x-ray diffraction study of three $[Fe(30A)/Cr(12A)]_{10}$ superlattices which had been sputtered in 4, 7, and 10 mTorr of Ar. We used position sensitive detector in horizontal setup to collect simultaneously specular scattering intensity (Q_z perpendicular to the film) and off-specular intensity of Q_y parallel to the plane of the sample. This technique [1] allows to study the effect of the in-plane disorder such as interface roughness or defects. In conventional low angle diffraction analysis the off-specular intensity which can be created by the interfacial roughness is neglected. It is known that the intensity of the superlattice diffraction peaks is reduced by the roughness of the interfaces (correlated or uncorrelated) and by the atomic interdiffusion. Our technique allows to evaluate correlation effects and (by integration over Q in plane) to eliminate the effect of the in-plane disorder and separate the effect of the interdiffusion. From the Fourier transform of the intensity distribution the interfacial height fluctuation function can be obtained. The three samples have the same modulation wavelength but different roughness. The width of the superlattice peaks in $Q_{y,z}$ direction indicates significant amount of the in-plane disorder. Figure 1 presents off-specular intensity in z-y plane for 7 mTorr sample.

[1] X. Yan and T. Egami, Phys. Rev. B 47, 2362 (1993).

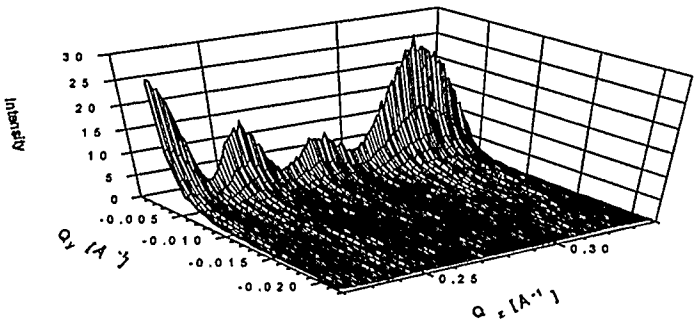


Figure 1.

* The work at University of Pennsylvania was supported by the NSF Grant DMR91 20688.

Sr-doped $La_{2-y}RE_yCuO_4$ superconductors: suppression of Tc at 1/8-hole doping is independent of rare earth	X7A

R. Harlow, M. Crawford and E. McCarron (Du Pont)

La_2CuO_4 exists in a high-temperature tetragonal form (HTT,I4/mmm) in which the copper-oxygen sheets are, on average, perfectly planar and in a low-temperature orthorhombic form (LTO1,Bmab) in which the copper-oxygen octahedra tilt around one diagonal, (110), of the HTT cell by a few degrees. In previous experiments, we have noted that partial substitution of La with Nd leads to one or two additional phase transitions at low temperatures: LTO1 → (LTO2,Pccn)→(LTT,$P4_2$/ncm). In the LTO2 and LTT forms, the octahedra tilt by unequal and equal amounts, respectively, about both diagonals of the HTT cell. We have also examined the effects of smaller rare-earth elements on these transitions in the insulated materials, $La_{2-y}RE_yCuO_4$, and have shown that the smaller rare earths are more effective in promoting these phase transitions. We have now extended our studies to the Sr-doped superconductors to see what effect the presence of smaller rare earth ions has on the anomalous suppression of Tc at 1/8-hole doping. The figure is a comparison of the phase diagrams and Tc's for compounds which contain $Nd_{0.4}$ and $Sm_{0.2}$, respectively. As can be seen, the suppression of Tc at a concentration of $Sr_{0.125}$ is independent of the rare earth.

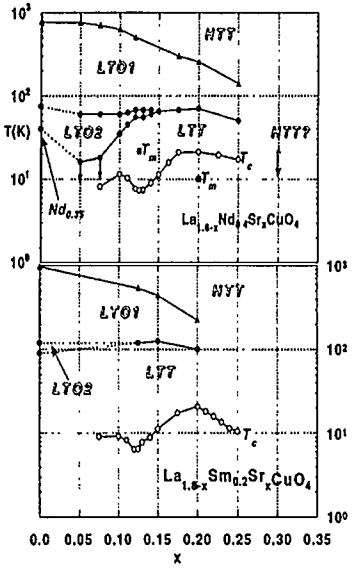


Figure 1.

Residual stress measurements of KSiAl - doped tungsten wires *	X7A

F. Hepp (Univ. of Freiberg, GER), A. Hilscher (Osram, Schwabmünchen, GER), and J. H. Selverian (Osram Sylvania)

Internal stress measurements were performed on KSiAl-doped tungsten wires with different degrees of deformation. The aim is to improve the wire drawing process by measuring internal stresses and by comparing the results with predictions from finite element modeling. Deformed specimens were used for the X-ray measurements; 10% deformation/162m diameter/771 MPa drawing force; 13% deformation/156μm diameter/889 MPa drawing force; 17% deformation/150μm diameter/1144 MPa drawing force. The mean values of the drawing forces give an impression of the forces used in the drawing process. The stress measurements were with a Huber θ-2θ goniometer, choosing the wavelength of 0.11504 nm, a compromise between reasonable flux and working at a high Bragg- angle. For the macrostress analysis the sin2Ψ - method which is described in /1/ was used. The stress measurements were performed on the surface of the wire at three different spots, and through the thickness by electrolytically removing material twice. The thickness of the removed surface layer was 9μm. The maximum depth of the incident beam was 3.2 μm. For the X-ray elastic constants the values $s_1 = 0.77\ 10^{-7}$ MPa^{-1} and $1/2s_2 = 3.06\ 10^{-6}$ MPa^{-1} of Prümmer and Macherauch /2/ were used. The calculated results are presented in Figs. 1 and 2. The results in Fig. 1 show a decrease of tensile stresses with increasing deformation. Higher drawing forces lead to a more homogeneous deformation of the material than lower drawing forces.

[1] H. Doelle, V. Hauk, HTM 31 (1976)3, 165-168.
[2] R. Prümmer, E. Macherauch, J. Soc. Mat. Sci., Jap. 15, (1966), 845

Deformation	σ_{11}[MPa]	σ_{12}[MPa]	σ_{13}[MPa]	σ_{22}[MPa]	σ_{23}[MPa]	σ_{33}[MPa]
10%	66±23	78±67	-20±20	-241±247	0±14	-8±35
13%	30±15	-65±30	-27±11	412±203	-19±17	-33±24
17%	23±1	-45±23	-26±8	417±168	-39±9	-34±27

Figure 1. Results of the macrostress analysis of doped tungsten wires with different deformation states on a mesoscopic scale (1st set). σij = the components of the stress tensorσ_{11} is the axial, σ_{22} is the tangential, σ_{33} is the radial component.

Wire Radius [μm]	σ_{11}[MPa]	σ_{12}[MPa]	σ_{13}[MPa]	σ_{22}[MPa]	σ_{23}[MPa]	σ_{33}[MPa]
81	66±23	78±67	-20±20	-241±247	0±14	0
72	27±16	58±41	-6±11	-93±35	-6±7	0
63	7±14	27±30	-8±5	-36±21	5±4	0

Figure 2. Results of the macrostress analysis on a mesoscopic scale of doped tungsten wire with10% deformation after a surface layer removal of (1) 9 μm and (2) 18 μm (2nd set). Wire Radius = radius of the wire specimen after surface layer removal.

* This research was carried out at Brookhaven National Laboratory and supported by the U.S. Department of Energy.

Structural changes upon sorption and desorption of Xe from Cd-exchanged zeolite rho: a real-time synchrotron x-ray powder diffraction study *	X7A

J. B. Parise (SUNY Stony Brook), D. R. Corbin, L. Abrams (Du Pont)

We have recently described a novel mechanism for the entrapment of Xe in Cd-exchanged zeolite rhu [1]. Following exposure to the atmosphere at room temperature the powder diffraction pattern for the fully loaded Cd-rho(Xe), shown in Fig. 1 as phase A′, changes rapidly. These changes occur in three stages and have been followed in real-time using a PSD. The first stage involves loss of Xe from phase A′ to form phase B. The loss is from the 8-ring sites with the total Xe in the S6R-sites remaining constant or increasing a little. This initial loss is apparently not accompanied by a great deal of hydration since the lattice parameter for phase B, 14.3321 (5)Å, is smaller than for the fully loaded sample [1] and close to that expected from previous studies of dehydrated Cd-rho [1,3]. The partitioning of the remaining Xe over the S6R-sites also changes; there is an almost equal distribution between the two sites in phase B with a total of 1.6Xe occupying these sites. This value is remarkably consistent with the 1.7Xe/unit cell obtained from the TG/MS analysis [1]. We ventured (reference 1) that exposure to the atmosphere might be implicated in a loss of Xe from the sample prior to loading into the TG/MS apparatus, and that this led to a lower than expected weight loss attributable to Xe. The analysis using the real-time diffraction data is consistent with this speculation.

[1] Corbin et al., J. Chem. Soc., Chem. Comm 1993, 1027
[2] Corbin et al., J. Amer. Chem. Soc. 1990, 112, 4821
[3] Parise, J.B.; Liu, X.; Corbin, D.R.; J.C.S. Chem. Commun, 1991, 3, 162

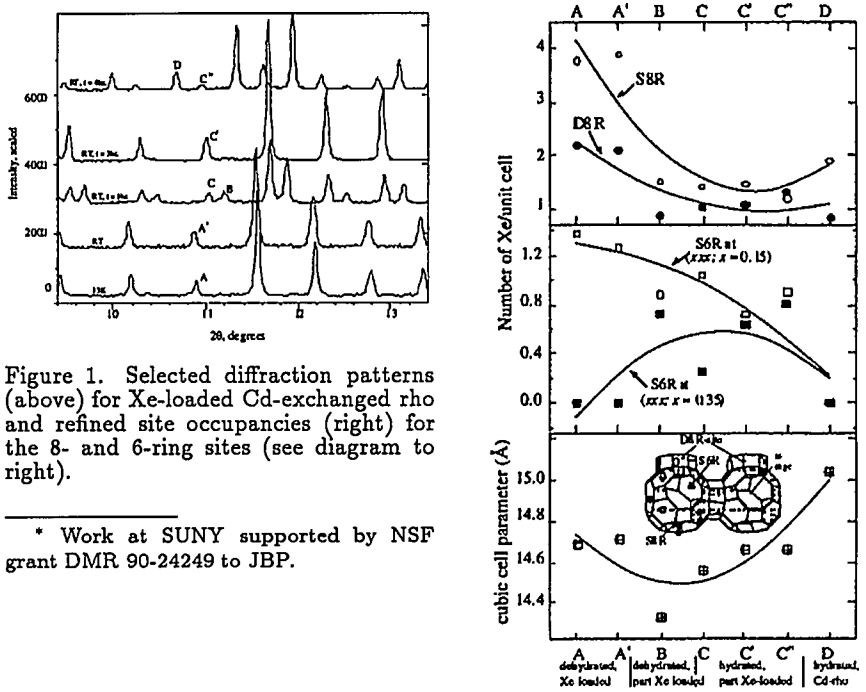


Figure 1. Selected diffraction patterns (above) for Xe-loaded Cd-exchanged rho and refined site occupancies (right) for the 8- and 6-ring sites (see diagram to right).

* Work at SUNY supported by NSF grant DMR 90-24249 to JBP.

Structural studies of novel high-pressure perovskite-related phases on the join $CaTiO_3$-$FeTiO_3$ *	X7A

J. B. Parise (SUNY Stony Brook), K. Leinenweber (ASU, Tempe)

An exploratory high-pressure study of the join $CaTiO_3$-$FeTiO_3$ in the split-sphere device at SUNY Stony Brook has uncovered two new high-pressure ordered perovskites. Because of the size of samples produced from these runs, typically less than 0.04 mm^3, synchrotron x-ray powder diffraction must be employed to obtain data suitable for structural refinement. One of the compounds, $CaFe_3Ti_4O_{12}$, is isostructural with $NaMn_7O_{12}$. Rietveld refinement of the structure confirmed the space group $Im\bar{3}$, with a = 7.4672 Å. Iron is at the center of a slightly distorted square of oxygens (Fe-O = 2.042(3) Å) with a rectangle in a plane perpendicular to the square at Fe-O = 2.780(6) Å. Calcium is in a distorted icosahedron with Ca-O = 2.635(5) Å. Rietveld refinement was also performed for the previously known perovskite-related form of $FeTiO_3$ recovered from high pressure (lithium niobate type). This compound is trigonal, R3c, with a= 5.1233(1) and c=13.7602(2)Å.

The second compound has the composition $CaFeTi_2O_6$, midway along the join. This material is tetragonal, space group $P4_2/nmc$, with a = 7.5157(2) and c= 7.5548(2). Calcium and 2 iron atoms are ordered on 3 different A sites, with calcium in approximately 10-fold coordination, one iron atom in tetrahedral coordination (Fe-O = 2.084(2)Å), and the other iron atom in square-planar coordination (Fe-O=2.097(2)Å). The system of octahedral tilts which this compound adopts has not been observed previously in a perovskite. The tilt system was described in a theoretical treatment of perovskites [$a^+a^+c^-$ in the notation of Glazer [1]] and was (incorrectly) assigned space group Pmmn.

[1] A. M. Glazer, Acta Crystallog. B28, 3384 (1972).

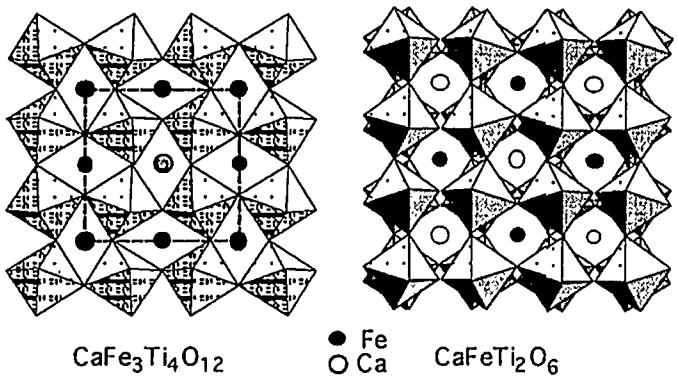


Figure 1.

* Work at SUNY supported by NSF grant DMR 90-24249 to J.B.P.

Structure of $CaAu_2O_4$: a novel high pressure aurate with corner linked square planar Au^{3+} *	X7A

J. B. Parise, J. Park, and M. Kunz (SUNY Stony Brook)

Classic solid state synthetic techniques are generally unsuited for the synthesis of ternary gold oxides; in the case of Au^{3+}-compounds decomposition often occurs before sufficient activation of the reaction. In such situations, synthesis at very high pressures is a viable route to novel aurates. The phase $CaAu_2O_4$ was synthesized during exploratory high- pressure studies of the Au_2O_3-CaO system in the split-sphere device at SUNY Stony Brook. The sample was contained in an Au capsule and heated to 1300°C at 15 Gpa. microprobe analysis of small crystals confirmed the metal stoichiometry. Synchrotron x-ray powder diffraction data were collected using the conditions given in Fig. 1. The structure (a = 5.9912(3), c = 10.0500(5), $I4_1/a$) consists of AuO_4 square planes corner-linked to form a framework containing the Ca^{2+} cations; this is depicted in the stereo pair below.

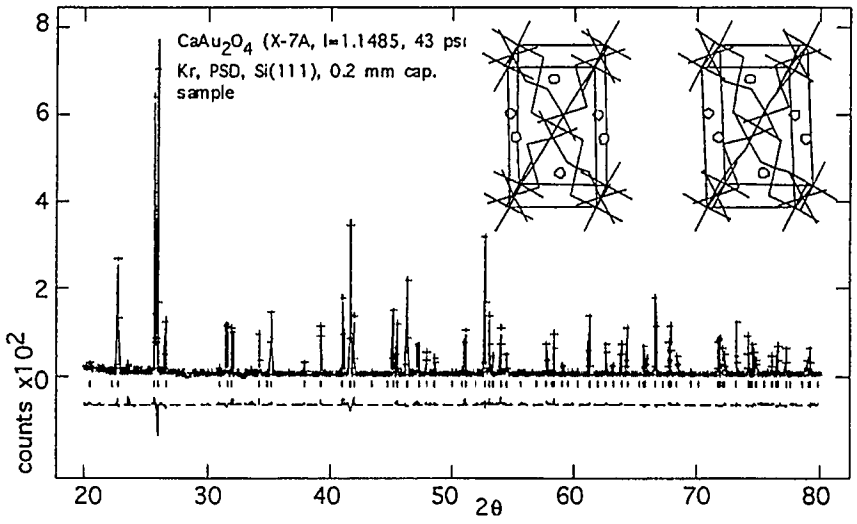


Figure 1. Observed and calculated (continuous line) data for $CaAu_2O_4$; the difference curve below is plotted on the same scale. A stereo representation of the structure is given in the upper right hand corner; circles represent the sites for Ca in this drawing.

* Work at SUNY supported by NSF grant DMR 90-24249 to JBP.

Search for copper on the mercury site in $HgBa_2CuO_{4+\delta}$ by x-ray anomalous diffraction	X7A

P. G. Radaelli, M. Marezio (CNRS), and D. Cox (BNL)

We studied a $HgBa_2CuO_{2+\delta}$ sample with $T_c \sim 40K$, prepared by high-pressure synthesis. This technique allows the synthesis of high-quality samples in the "over-doped" region of the phase diagram, hence with reduced or even suppressed superconducting transitions. X-ray diffraction data were collected at 2 wavelengths (λ_1=1.05036 Å, λ_2=1.37247 Å) in the Debye-Scherrer configuration. The two data sets were corrected for absorption and simultaneously analyzed by the Rietveld method using the GSAS program (the Rietveld plot at λ_1=1.05036 Å is shown in the figure). Electron density maps of the unit cell were obtained by the maximum entropy technique.

Close inspection of the Bragg reflections reveals the existence of two well-defined isostructural phases, probably associated with two different concentrations of oxygen. Independent refinements of the Hg and Cu occupancies on the 0,0,0 site ruled out the possibility of either Cu or light element substitutions for Hg in this sample. Electron density maps confirmed the presence of a single interstitial oxygen site O3 at 1/2,1/2,0 (n(03)=0.12(2) from the Rietveld analysis), and evidenced the existence of a large displacement field in the ab plane for the "apical" oxygen atoms. It is likely that this displacement field, which is much larger than that measured for samples with lower oxygen contents, is the result of a static distortion of the unit cells where O3 is occupied.

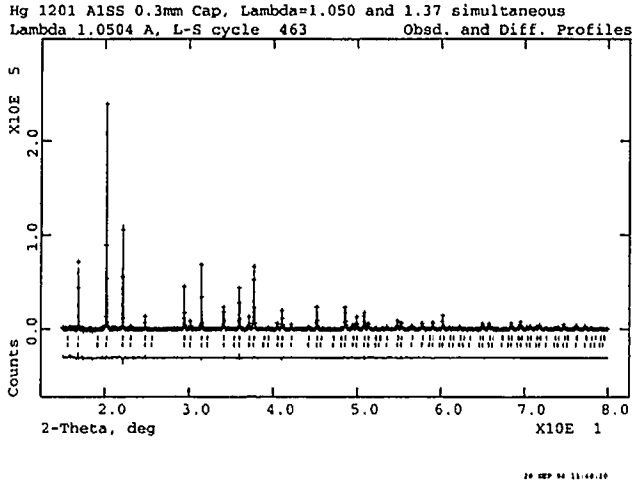


Figure 1.

Cation siting determination in CaLSX by combined x-ray/neutron Rietveld Refinement	X7A

Brian H. Toby, James E. MacDougall, and Charles G. Coe (Air Products and Chemicals Corporation)

Low silica X (LSX) zeolite is the Al-rich end-member of the faujasite zeolite family with a Si:Al ratio of 1.0 and thus has the highest possible density of cation sites. The faujasite family of molecular sieves are used for a variety of industrial processes including catalysis and separation technologies. Understanding these processes requires detailed knowledge of the zeolite framework topology and particularly the siting of the charge-compensating cations.

Diffraction data for dehydrated CaLSX were collected at room-temperature using synchrotron x-ray radiation at the X7A beamline at the NSLS and using CW neutrons using the 32-detector BT-1 diffractometer at NIST. The crystal structure was refined using the Rietveld method in cubic space group Fd3 in a combined x-ray/neutron refinement using the GSAS software package. The majority of the Ca is found in site I, a six-coordinate site at the center of the hexagonal prism and at site II, a three- coordinate site in the plane of the six-ring on the wall of the supercage. If these two sites were at full occupancy, this would account for the stoichiometric amount of Ca, however the occupancy of each site is below unity. A small amount of Ca is found in site I′, a three-coordinate site in the face of the hexagonal prism.

It is useful to contrast the information provided by each data set to the structure. As expected, a refinement using the x-ray dataset alone provided significant detail of the Ca siting, to the level of demonstrating significant anisotropic thermal parameters of Ca in site II. However, the x-ray only refinement was insensitive to the zeolite framework and bond-length constraints were needed to prevent divergence or oscillation. In contrast, the neutron-only refinement was more sensitive to the framework structure, but was less conclusive with respect to Ca siting. In both cases, significant correlation was noted between background parameters, thermal parameters and cation occupancies. In both refinements, extensive restraints on background or thermal parameters were required to obtain a model that refined in a stable manner. In the combined refinement, it was possible to refine background, thermal parameters, and occupancies without any constraints. A single constraint was added in the final stages of refinement on the total amount of Ca present, to insure that the model was consistent with its chemical composition. This work demonstrates the significant advantages that can be obtained from a joint x-ray and neutron refinement.

Study of KTiOPO4 (KTP) on modulation by an applied electric field *	X7B

J. Albertsson, R. J. Bolt (CTH, Sweden), J. Hanson, M. C. Nelson (BNL), K. Ståhl (Lund Univ., Sweden), and G. Svensson (CTH, Sweden)

Potassium titanyl phosphate, $KTiOPO_4$, (KTP) is a non-linear optical material. It crystallizes in space group $Pn2_1a$ with cell dimensions a = 12.819(3), b = 10.584(2) and c = 6.399(1) Å at room temperatures.[1] Single crystals of pure and scandium doped KTP have been prepared with the top seeded solution growth technique out of a three-zone furnace.[2] Fluxes were $K_6P_4O_{13}$ or 99.8% $K_6P_4O_{13}$, 0.2% Sc_2O_3. Crystals were cut, ground and polished to plates with tabular b habit and a thickness $\leq$ 1 mm. KTP is subject to electrolytic decomposition in a dc field because of charge carrier transport [3] an effect which can be decreased by low temperature and doping with trivalent cations.

The electric field experiments were made at the NSLS crystallography station X7B in a setup similar to the one used by Ståhl, Kvick & Abrahams.[4] The crystal plate was mounted on the cold finger of a Displex closed-cycle refrigerator within an evacuated beryllium can. This addition was made since the ferroelectric hysteresis curve of KTP can be detected only at low temperatures. [5] When mounted in the cryostat, the crystal could be polarized by a square-wave variable voltage 100–1500 V alternatingly applied to each side of the crystal at 5-200 Hz. A scaler and a clock were gated to each of the two square waves. Reflections $0k0$ were measured at λ = 0.9341 Å and temperatures 15, 100 and 150 K. With scandium doped (231 ppm) KTP a peak split could be observed between the two field directions, Fig. 1. Typical early results, for reflection 0 10 0 at 50 Hz, are shown in Fig. 2.

The 15 and 150 K data indicate a maximum in the $\Delta\omega$ split at 1100 V, i.e., near the coercive field strength, 1.5 MV m^{-1}. Besides electrostriction and charge carrier transport, domain inversion could be the cause of the effect, mixing $0k0$ with $0-k0$ at a frequency equal to the frequency of the square wave.

[1] Thomas, P.A. Glazer, A.M. & Watts, B.E. Acta Cryst. B46, 333, 1990.
[2] Bolt, R.J., van der Mooren, M.H. & de Haas, H.J. Crystal Growth 114, 141, 1991.
[3] Sebastian, M.T., Klapper, H. & Bolt, R.J. J. Appl. Cryst. 25, 274, 1992.
[4] Ståhl, K., Kvick, Å. & Abrahams, S.C. Acta Cryst. A46, 478, 1990.
[5] Shaldin, Yu. V. & Poprawski, R.J. Phys. Chem. Solids 51, 101, 1990.

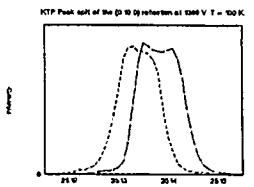


Figure 1.

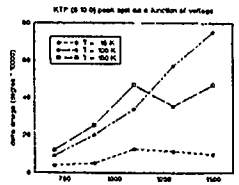


Figure 2.

* Work at BNL was supported under contract AC02-76CH00016 with DOE by its Division of Chemical Sciences, Office of Basic Energy Sciences, and by the Swedish Natural Science Research Council (NFR).

In situ powder diffraction studies of ion exchange; molten salt ion exchange of analcime with ammonium nitrate *	X7B

E. Krogh Andersen, I. G. Krogh Andersen (Univ. of Odense, Denmark), P. Norby, and J. C. Hanson (BNL)

In a preliminary investigation of the use of in-situ powder diffraction in studying ion exchange, the natural zeolite analcime (sodium-form) was ion exchanged to the ammonium form from molten ammonium nitrate at 165°C. A ratio of 1:5 in weight between analcime and NH_4NO_3 was used. The samples were contained in 0.5 mm quartz capillaries and mounted in a ferrule to allow the sample to be under pressure (8 atm.). They were heated in a stream of hot air from an Enraf Nonius heater gun. A position sensitive detector (INEL CPS90) was used to collect powder diffraction data using a wavelength of 1.3771Å.

Figure 1 is a small part of the diffraction patterns, and shows how the ion exchange proceeded. During ion exchange two distinct phases are visible. The solubility of ammonium in the sodium analcime is low as is the solubility of sodium in the ammonium form. In Figure 2 the intensities of the 400 reflection of NH_4-analcime and the 332 reflection of Na-analcime are shown as function of time. The sodium analcime used in the experiment was nearly cubic. By ion exchange to the ammonium form it becomes tetragonal[1]. The results show that in-situ powder diffraction can be a suitable tool for studying ion exchange reactions.

[1] E. Krogh Andersen and I.G. Krogh Andersen, in preparation.

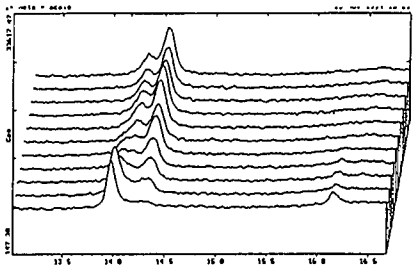


Figure 1. Diffraction patterns during ion exchange.

* This work was supported by contract DE-AC02-76CH00016 with the US Department of Energy by its Division of Chemical Sciences, Office of Basic Energy Sciences and by the Danish Natural Science Research Council.

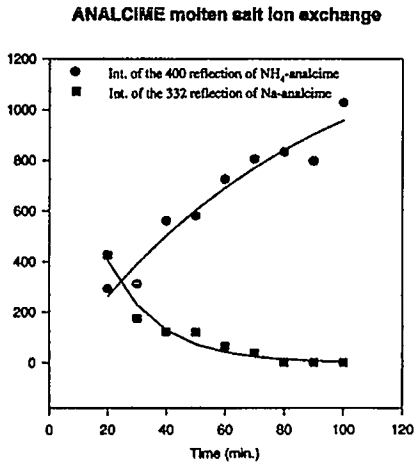


Figure 2. Integrated intensities vs. time.

In situ powder diffraction study of solid state syntheses; formation of lanthanum manganate(III)(IV), $LaMnO_{3+\delta}$ *	X7B

E. Krogh Andersen, I. G. Krogh Andersen (Univ. of Odense, Denmark), P. Norby, and J. C. Hanson (BNL)

n to study the solid state syntheses of $LaMnO_3$.

The samples were contained in 0.5 mm quartz capillaries. The sample was heated using a stream of hot air from an Enraf Nonius heater gun. A position sensitive detector (INEL CPS120) was used to collect powder diffraction data using a wavelength of 1.3771Å

The amorphous starting material was prepared from lanthanum acetate and manganese acetate, which were thoroughly mixed and heated to 350°C as described in ref. 1. The material was heated to different temperatures and the crystallization was followed.

Figure 1 shows the crystallization as the material was heated to 825°C and kept at that temperature. The crystallization of $LaMnO_3$ is preceded by the appearance and disappearance of an unknown phase with a few, weak reflections. The amount of crystalline material was estimated by taking the integrated intensity of some of the diffraction peaks. Growth of the crystallites could be followed by looking at the width of the diffraction peaks.

[1] I.G. Krogh Andersen, E. Krogh Andersen, P. Norby and E. Skou, J. Solid State Chem. In press, 1994.

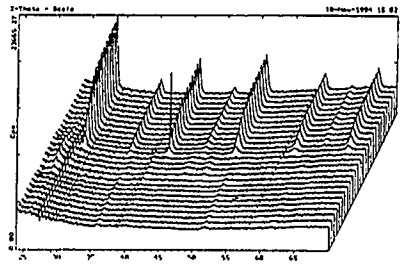


Figure 1. Crystallization of $LaMnO_{3+\delta}$

* This work was supported by contract DE-AC02-76CH00016 with the US Department of Energy by its Division of Chemical Sciences, Office of Basic Energy Sciences, by the Danish Natural Science Research Council and by the Danish Ministry of Energy and ELSAM with the program DK-SOFC 1993-1996.

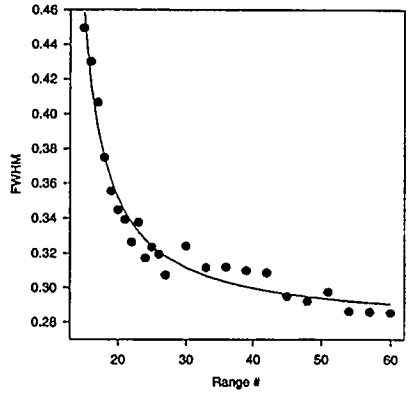


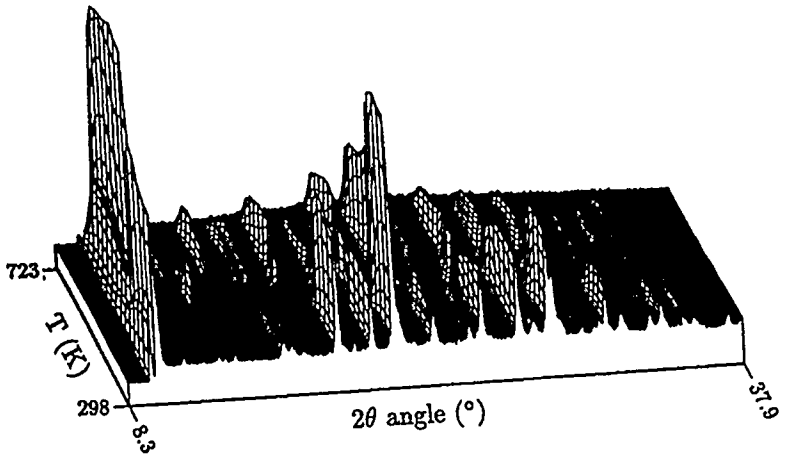
Figure 2. Variation of peak width during crystallization

In situ studies of the dehydration process in the natural zeolite stilbite	X7B

G. Artioli (Univ. di Milano, Italy), G. Cruciani (Univ. di Ferrara, Italy), A. Gualtieri (Univ. di Modena, Italy), K. St(Univ. of Lund, Sweden), and J. C. Hanson (BNL)

The dehydration process of the natural zeolite stilbite upon heating in air has been studied in situ using powder diffraction data collected at beam line X7B. The powder specimen was loaded in a 0.3 mm capillary and axially spinned during data collection. The profile data were recorded using a position sensitive detector covering a range of 120 °2θ (CPS120 by INEL), each histogram was accumulated for 5 min, and the temperature was increased by intermittent heating in step of 6 K. The powder pattern resolution is suitable for structure refinement by Rietveld profile techniques. Diffraction data were collected at a wavelength of 1.488 Å in the temperature range 298–723 K. Figure 1 shows the variation of the low 2θ region of the powder profile with temperature.

The starting stilbite phase ($NaCa_4Al_9Si_{27}O_{72}\cdot 30H_2O$) is monoclinic C2/m, and is commonly described by a pseudo-orthorhombic F2/m cell: a=13.636(1), b=18.243(1), c=17.844(1) Å, β=90.33(°). It is commonly referred to as the A-phase. At least two phase transitions are present in the explored temperature region. The first one occurs at about 420 K and leads to the so-called B-phase, related to the barrerite structure: probable space group Amma, cell parameters are a=13.695(1), b=17.890(1), c=17.606(1) Å. Before the phase transition the chain of 4-4-1units forming the stilbite topology undergo a rapid distortion, which is the driving mechanism for the symmetry change. The other phase change is above 500 K, and the newly formed high temperature phase (C-phase) is at present under study.



In situ studies of the dehydration process in the natural zeolite yugawaralite *	X7B

G. Artioli (Univ. di Milano, Italy), G. Cruciani (Univ. di Ferrara, Italy), A. Gualtieri (Univ. di Modena, Italy), K. Stahl (Univ. of Lund, Sweden), and J. C. Hanson (BNL)

The dehydration process of the natural zeolite yugawaralite upon heating in air has been studied in situ using powder diffraction data collected at beam line X7B. The experimental setting included: 0.3 mm capillary specimen mount, resistance intermittent heating, and a position sensitive detector covering a range of 120 °2θ (CPS120 by INEL). The setup allowed recording of the complete powder pattern with a time discrimination of 5 min and resolution suitable for structure refinement by Rietveld profile techniques. Diffraction data were collected at a wavelength of 1.488 Å, with temperature steps of about 5 K, from room temperature to 780 K.

There is an evident major phase change at a temperature of about 700 K, which is related to the shift of the Ca cation position in the cavity and to the connected framework distortion. The Ca coordination changes from eight at room temperature (4 framework oxygens [FO] and 4 water molecules [OW]) to seven (4 FO and 3 OW) at about 380 K, then to six (4 FO and 2 OW) at about 500 K, then at about 700 K another water molecule is released and the Ca atom maintains six coordination by increasing the number of bonded framework oxygen atoms (5 FO and 1 OW). The latter transition is related to a dramatic framework distortion, the change in space group symmetry from Pc to Pn, and the doubling of the a cell parameter. Figure 1 shows the variation of the low 2θ region of the powder profile with temperature.

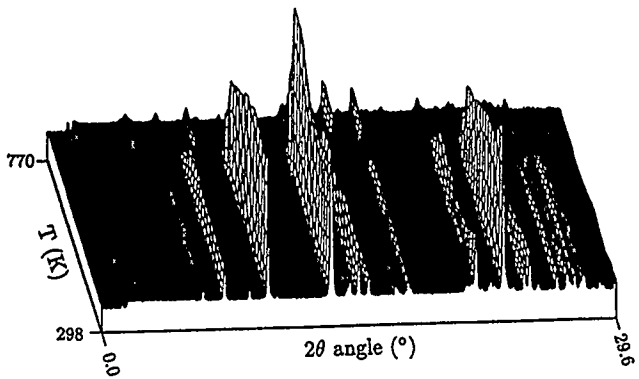


Figure 1.

* The work at BNL was carried out under contract DE-AC02-76CH00016 with the US Department of Energy and supported by its Division of Chemical Sciences, Office of Basic Energy Sciences.

Characterization of thick film resistor devices by grazing incidence powder diffraction * | X7B

G. Artioli (Univ. di Milano, Italy), A. Gualtieri, S. Goretti, B. Morten, M. Prudenziati (Univ. di Modena, Italy), and J. C. Hanson (BNL)

Thick film resistors are commonly used as piezoresistors for sensors and as components for hybrid microelectronics. They are obtained by screen-printing and firing inks on alumina substrates. The inks are prepared by mixing RuO_2 and glass powders with an organic vehicle. Firing temperatures are in the range 750-1000°C. The final thickness of the resistor films ranges from 8 to 30 μm. The composition of the glass matrix of the samples used in the present study is: PbO 66.2, SiO_2 30.5, and Al_2O_3 1.35 wt%. RuO_2 powder with surface area 0.5 m^2/g was added to the matrix as 15 wt% of the total. They were fired at 750, 800, 850 900, 950 and 1000°C. Electrical measurements and microstructural analysis (SEM, TEM, EDX, and conventional XRPD) were carried out in order to elucidate the conduction mechanism in the resistor films. Preliminary results by absorption spectroscopy (EXAFS) on the Pb L_{III} edge were interpreted on the basis of newly formed crystalline phases in the matrix during the firing process: proposed phases should have the pyrochlore structure and a variable composition in the range $Pb_{(2+x)}Ru_{(2-x)}O_{6.5}$ with $0 < x < 1$. The aim of the present study in the determination of the crystal phases formed during the heat cycle.

The samples were characterized by grazing incidence powder diffraction on the crystallographic beam line X7B. The grazing incidence angle for each experiment depends on the film thickness and it was therefore optimized for each sample by maximizing the signal ratio between the (110) reflection of the RuO_2 in the film and the (012) reflection of the Al_2O_3 substrate. Diffraction data were collected at fixed incidence angle with wavelength 0.889 Å.

Preliminary analysis of the diffraction data shows that: (1)there is no (Pb,Ru) oxide in the matrix with the proposed pyrochlore structure; (2) there are newly formed phases, yet to be identified, and these crystalline phases depend on the temperature of the firing process; and (3) there are surprising and yet unreported broadening and splitting of the RuO_2 diffraction peaks, which might indicate the presence of structure defects and possibly a space group symmetry lower than the expected $P4_2/mnm$ space group.

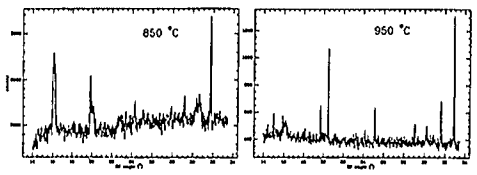


Figure 1.

* The work at BNL was carried out under contract DE-AC02-76CH00016 with the US Department of Energy and supported by its Division of Chemical Sciences, Office of Basic Energy Sciences.

Powder diffraction study of the phase transitions in KNO_3 | X7B

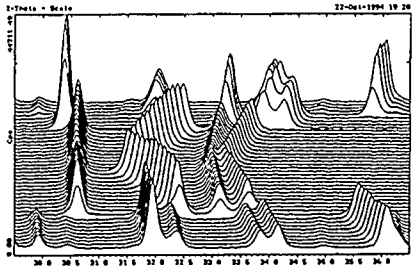
A.N. Christensen (Univ. of Aarhus, Denmark), P. Norby, and J. C. Hanson (BNL)

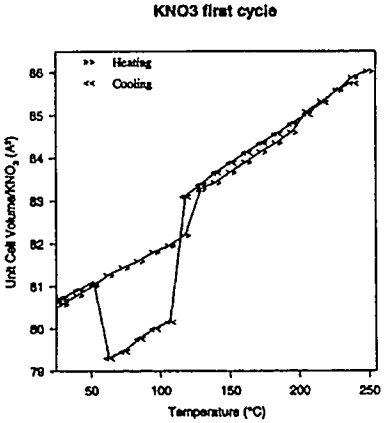
Potassium nitrate exists in different modifications depending on pressure and temperature. At atmospheric pressure orthorhombic α-KNO_3 transforms into trigonal β-KNO_3 at approx. 128°C. Upon cooling an intermediate trigonal phase, γ-KNO_3, exists in a short temperature interval. The precise temperature of transformation depends on the thermal history of the sample[1].

Acoustic emission was used[2] to study thermally induced phase transformations in KNO_3. Acoustic emission is generated in crystals when mechanical events such as formation of cracks or movement of dislocations take place. Strong acoustic signals were observed at the phase transformations and weaker signals were observed at temperatures prior to the phase transition.

We used temperature resolved powder diffraction to study the relation between the phase transitions in KNO_3 and the thermal history of the sample. A position sensitive detector covering 120° in 2θ (INEL CPS 120) was used to record the diffraction patterns. The sample was contained in a 0.3 mm quartz capillary and heated using a hot air stream[3]. The heating cycles used was: RT-250°C-RT-200°C-RT-250°C-RT. Unit cell parameters for the 116 obtained diagrams were refined, and it was found that the temperature interval in which γ-KNO_3 exists is decreasing with the number of thermal cycles. The figures below show the diagrams obtained in the first heating and cooling cycle and the related unit cell volumes.

[1] J.K. Nimmo and B.W. Lucas, Acta Crystallogr. B32 1968 (1976). [2] S. Shimada, Y. Katsuda and M. Inagaki, J. Phys. Chem. 97, 8803 (1993). [3] P. Norby, A. N. Christensen and J.C. Hanson, in "Studies in Surface Science and Catalysis", Vol. 84. Weitkamp, H.G. Karge, H. Pfeifer and W. Hölderich (eds.) Elsevier, Amsterdam 1994 p. 179.





Time resolved powder diffraction; Sorel cements *	X7B

Axel Nørlund Christensen (Univ. of Aarhus, Denmark), Poul Norby, and Jonathan C.Hanson (BNL)

Time resolved X-ray powder diffraction can be used to study the rate of chemical reactions in heterogeneous mixtures. In case of reactions between a solid and water the sample can be a paste of the components kept in a capillary. The rate of the reactions may be studied from a series of diffraction patterns if the speed of recording a pattern is at least an order of magnitude faster than the velocity of the chemical reaction to reach an equilibrium. Intensities of selected Bragg reflections of the phases identified in the powder pattern will be proportional to the quantities of the crystalline phases in the reaction mixture.

Synchrotron X-ray powder diffraction was used to study reactions in the systems MgO- H_2O and MgO-$MgCl_2$-H_2O[1]. The powder patterns were measured at 1.0, 2.5, 5.0 and 10.0 minute intervals on a Huber diffractometer at the beam line X7B at NSLS, BNL. A curved INEL position sensitive detector of type CPS120 was mounted on the θ-arm of the diffractometer. The wavelengths used were λ=1.1895 and 1.2097 Å. The patterns are plotted in a display so that the evolution in time of the patterns can be observed.

The main crystalline products in the investigated temperature range up to 100°C were $Mg(OH)_2$, $MgCl_2 \cdot 5Mg(OH)_2 \cdot 8H_2O$, $MgCl_2 \cdot 9Mg(OH)_2 \cdot 5H_2O$, $MgCl_2 \cdot 2Mg(OH)_2 \cdot 4H_2O$. Fig. 1 displays X-ray powder diffraction diagrams of a mixture of MgO and 4.5M $MgCl_2$ solution at 45°C recorded at 5 min. intervals. The reaction product is $MgCl_2 \cdot 5Mg(OH)_2 \cdot 8H_2O$.

[1] A. N. Christensen, P. Norby and J.C. Hanson, J. Solid State Chem. 1994, In press.

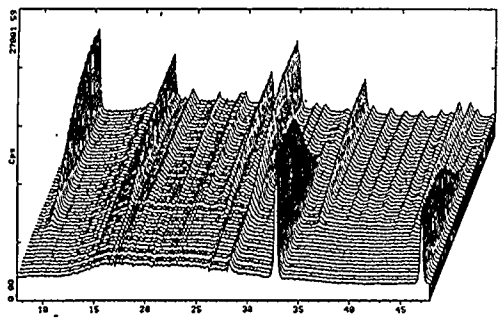


Figure 1. Bragg reflections of MgO decrease and those of the reaction product increase during the reaction.

* This work was supported by contract DE-AC02-76CH00016 with the US Department of Energy by its Division of Chemical Sciences, Officeof Basic Energy Sciences and by the Danish Natural Science Research Council.

Position sensitive detectors for powder diffraction; a comparison between INEL CPS120 and CPS90 *	X7B

Poul Norby and Jonathan C. Hanson (BNL)

We have used position sensitive detectors for time and temperature resolved powder diffraction. Good resolution is important when structural details of the phases present are investigated. However, in order to obtain fast data collection, intensity is crucial.

The curved position sensitive detector CPS120 from INEL covers 120° in 2θ and has a radius of 250mm. The CPS90 detector covers only 90° in 2θ, but the radius is 500mm. In Debye Sherrer geometry using capillaries the doubled radius means that the instrumental peak widths will decrease by a factor of two. The "step width", given by the multi channel analyzer, decreased by 25%. However, as the horizontal width of the two detectors is the same, the intensity of the diffraction pattern decreases by a factor of two. The increased absorption in air must also be considered but by using a helium path the effect may be diminished.

In order to determine the resolution function for the two detectors a sample of LaB_6 (NIST 660) in a 0.2 mm capillary was measured using a wavelength of 1.3771Å.

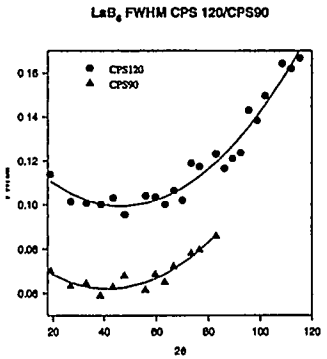


Figure 1. A comparison between the Full Width at Half Maximum (FWHM) for LaB_6using the two detectors. The decrease in FWHM is approx. 40%.

* This work was supported by contract DE-AC02-76CH00016 with the US Department of Energy by its Division of Chemical Sciences, Office of Basic Energy Sciences and by the Danish Natural Science Research Council

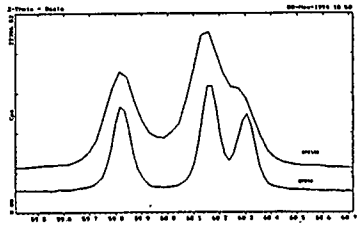


Figure 2. A small part of the diffraction pattern of α-quartz measured with CPS120and CPS90 respectively. The resolution of the "quartz triplet" is clearly increased when using the CPS90 detector. The resolution is determined mainly by the size of the capillary and the distance to the detector.

Powder diffraction using imaging plates; structure determination and Rietveld refinement	X7B

Poul Norby and Jonathan C. Hanson (BNL)

In connection with time resolved powder diffraction experiments we are interested in Rietveld refinement of Imaging Plate powder diffraction data using short exposure times.

The sample chosen for the test experiment was a new tetragonal 3-dimensional zirconium hydrogen phosphate, $Zr(HPO_4)_2$, the structure of which was recently solved from powder diffraction data[1]. The space group is $I4_1cd$ and the unit cell axes are a=11.253 and c=10.765 Å.

The sample was contained in a 0.3 mm glass capillary. A Fuji Imaging Plate system with flat plates was used. The wavelength was 0.9356 Å.

Using a 30 seconds exposure it was demonstrated possible to solve and refine the crystal structure from Imaging Plate powder diffraction data. The profile fitting program ALLHKL was modified to accept non-equal step length and individual intensities were extracted from the powder data. The intensity data were used as input for Sirpow-92. All the atoms (except H) were found using direct methods. A modified version of XRS-82 was used for subsequent Rietveld refinement.

[1] A.M. Krogh Andersen and P. Norby. In preparation.

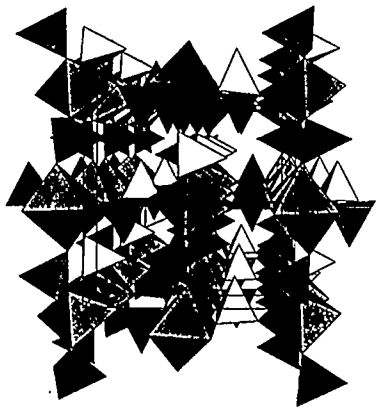


Figure 1. The structure of $Zr(HPO_4)_2$ seen along c.

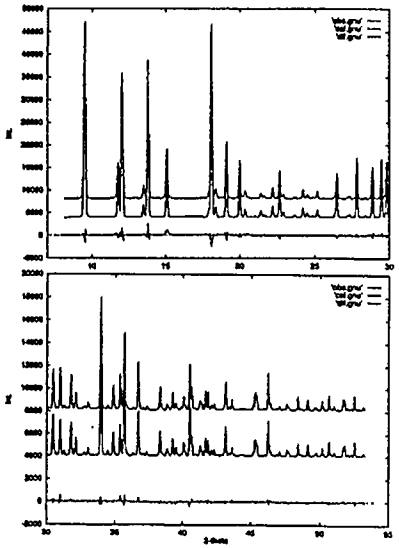


Figure 2. Observed, calculated and difference profiles.

In situ synchrotron powder diffraction studies of syntheses of layered α-Ti- and α-Zr-phosphates *	X7B

Poul Norby, Jonathan C. Hanson (BNL), and Anne Marie Krogh Andersen (Univ. of Odense, Denmark)

Layered Ti- and Zr-phosphates are of interest as intercalation materials. We have studied the syntheses of layered phosphates using on-line synchrotron powder diffraction. The samples were kept in sealed quartz capillaries and a position sensitive detector (INEL CPS120) was used, enabling fast data collection. When syntheses above 100°C were performed, an external pressure was applied. Full diffraction patterns were obtained in 30-60 s allowing studies of even quite fast chemical reactions and syntheses.

The starting materials for the syntheses were amorphous Ti- and Zr-phosphate and phosphoric acid. Syntheses were performed at temperatures from 50-200°C. The amount of crystalline material was estimated from integrated intensities of reflections in the diffraction pattern.

Crystallization of α-TiP, $Ti(HPO_4)_2\ H_2O$, starts at approx. 50°C and the crystallization kinetics could be followed up to 130°C. Figure 1 shows diffraction patterns recorded during crystallization of α-TiP at 90°C. The crystallization curves were fitted using a first order rate expression. When plotting ln(k) against 1000/T in an Arrhenius plot two straight lines are observed, which would indicate two different crystallization processes. We are planning further experiments to determine if this is indeed the case or if it is an artifact imposed by the experimental setup.

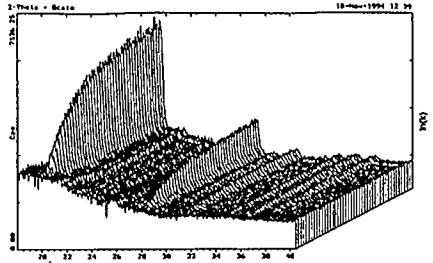


Figure 1. Crystallization of α-TiP at 90°C. Diffractions patterns obtained every 60s.

* This work was supported under contract DE-AC02-76CH00016 with the US Dept. of Energy by its Division of Chemical Sciences, Office of Basic Energy Sciences and by the Danish Natural Science Research Council.

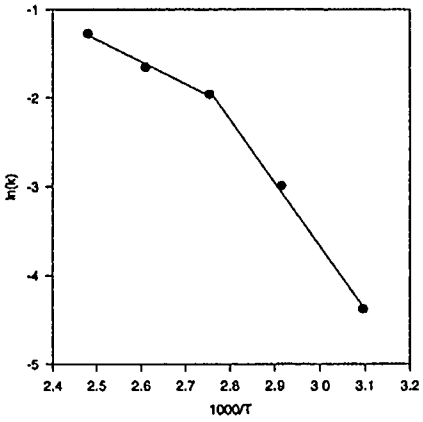


Figure 2. Arrhenius plot for crystallization of α-TiP. ln(k) plotted against 1000/T.

Time resolved powder diffraction of oxidation/reduction of $Sr_xLa_{1-x}MnO_{3+\delta}$ at high temperature *	X7B

Poul Norby, Jonathan C. Hanson (BNL), E. Krogh Andersen, and I. G. Krogh Andersen(Univ. of Odense, Denmark)

Strontium substituted lanthanum manganates(III)(IV) are of interest as cathode materials for high temperature fuel cells. In-situ powder diffraction was used to obtain structural and kinetic information concerning the material at actual operating conditions.

The samples were contained in 0.5 mm quartz capillaries and mounted in a ferrule to allow a flow of gas with a controlled oxygen partial pressure. The gas flow was controlled using flowmeters, and by using two separate strings it was possible to change the oxygen partial pressure during the experiment (Figure 1). The sample was heated up to 875°C using a stream of hot air from an Enraf Nonius heater gun. Position sensitive detectors (INEL CPS120 and CPS90) were used to collect time resolved powder diffraction data using sampling times down to 30s.

By switching between e.g. air and N_2, the kinetics of oxygen diffusion during oxidation and reduction of $Sr_xLa_{1-x}MNO_{3+\delta}$ was studied. Figure 2 shows a small part of the diffraction pattern of $LaMnO_{3+\delta}$ at 825°C when changing from air → N_2 → air. Figure 3 shows the corresponding unit cell volumes for the first 20 diagrams after changing from air to nitrogen. Oxygen/reduction reactions were studied for different oxygen partial pressures, temperatures and degrees of Sr-substitution.

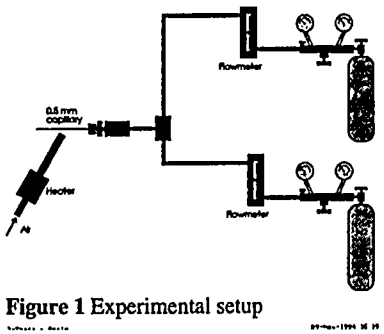


Figure 1 Experimental setup

Figure 1. Experimental setup

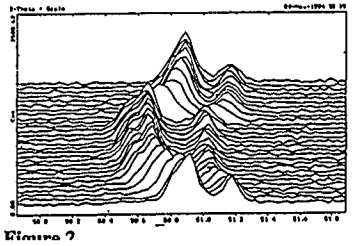


Figure 2.

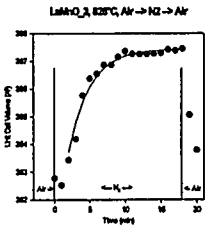


Figure 3. Unit cell volumes during reduction at 825°C.

* This work was supported by contract DE-AC02-76CH00016 with the US Departmentof Energy by its Division of Chemical Sciences, Office of Basic Energy Sciences, by the Danish Natural Science Research Council and by the Danish Ministry of Energy and ELSAM within the program DK-SOFC 1993-1996.

Powder diffraction study of the phase transitions in $Na_4Ge_7O_{16}{\cdot}nH_2O$ *	X7B

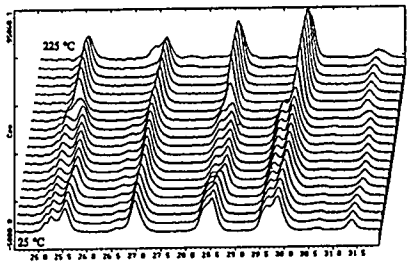
Poul Norby, Ping Wu, and Jonathan C. Hanson (BNL)

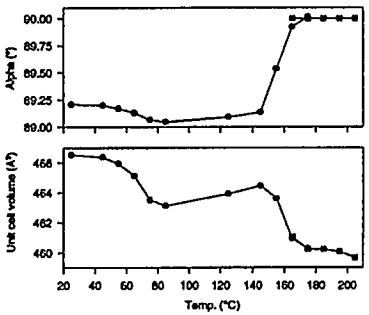
Microporous germanates with general formula $M_4Ge_7O_{16}{\cdot}nH_2O$ have been known for a long time[1]. Recently they have been studied for their ionic conducting properties.[2] These compounds possess framework structures consisted of both four- and six-coordinated germanium atoms. While most members of this series were reported to have a cubic structure, we found that $Na_4Ge_7O_{16}{\cdot}nH_2O$ synthesized by hydrothermal reaction exhibits a rhombohedral distortion. Furthermore, this compound undergoes several thermal transformations before decomposition.

We used temperature resolved powder diffraction to study the phase transitions in $Na_4Ge_7O_{16}{\cdot}nH_2O$. A position sensitive detector covering 120° in 2θ (INEL CPS120) was used to record the diffraction patterns. The sample was contained in a 0.2 mm glass capillary and heated using a hot air stream[3]. The counting time per diagram was 2.5 min, and the sample was heated at a constant rate of 4°C/min. The figures below show a portion of the diagrams obtained during heating and the refined unit cell dimensions.

The rhombohedral unit cell contracted between 60 and 80°C, probably because of partial dehydration. Between 150-180°C, the sample transformed into a cubic phase. At higher temperature, a new phase formed, indicating a substantial change of the framework structure. These results are consistent with those from thermogravimetric analysis.

[1] A. Wittmann, Fortschr. Miner. 43, 230 (1965).
[2] S. Feng, M. Tsai and M. Greenblatt, Chem. Mater. 4, 388 (1992).
[3] P. Norby, A. Nørlund Christensen and J.C. Hanson, in "Studies in Surface Science and Catalysis", Vol. 84. Weitkamp, H.G. Karge, H. Pfeifer and W. Hölderich (eds.) Elsevier, Amsterdam 1994 p. 179.





* This work was supported by contract DE-AC02-76CH00016 with the US Department of Energy by its Division of Chemical Sciences, Office of Basic Energy Sciences and by the Danish Natural Science Research Council.

The structure refinement of a new high pressure silicate, $Na_2CaSi_6O_{14}$ * | X7B

J. B. Parise, K. Tan, M. Kunz, T. Gasparik (SUNY Stony Brook), and J. Hriljac (BNL)

In the Na_2O-CaO-SiO_2 system, at pressures between 8 - 14 GPa, a new phase was found to be stable. It has an ideal formula of $Na_2CaSi_6O_{14}$ as determined from x-ray diffraction studies. The compound crystallizes in space group P321 with a = 7.903(8) and c = 4.595(4)Å. The structure consists of layers in (001); one centered at z = 0 contains the (CaNa)- and ^{VI}Si-sites the other centered at z = 1/2 consists of corner linked^{IV} Si-tetrahedra (Figs. 1 and 2). The latter structural unit is constructed from open branched crankshaft vierer chains linked via tetrahedra to form the sheet. The structure was refined using room temperature data of comparable resolution (0.63Å) collected in house at Stony Brook and with an imaging plate at X7B. The later set of data were processed using the "seed-skewness" method [1]. Fig. 2 is a half-normal probability plot [2] for the positional parameters derived from structure refinements using the two data sets. The distribution of points shows there is no obvious systematic bias between the laboratory and synchrotron derived positional parameters.

[1] Bolotovsky, White, Darovsky and Coppens (submitted). [2] Abrahams and Keve (1971) Acta Crystallog., A27, 157.

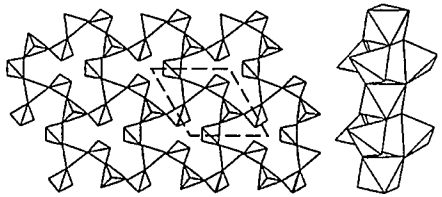


Figure 1. The tetrahedral sheet (left) composed of open-branched crankshaft chains. These sheets are linked along the c-axial direction by octahedrally coordinated Si (right), which resides at the origin of the unit cell.

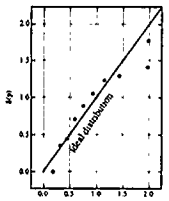


Figure 2. Half-normal probability plot of 10 δp_i derived from refinements of the structure of $Na_2CaSi_6O_{14}$.

* Supported by NSF grant DMR 90-24249 to JBP

The influence of composition on polymorphism in Tl-2201 * | X7B

C. Ström, S. G. Eriksson (Inorganic Chem. GU), J. Albertsson (CTH), J. Hanson (BNL)

Structural and superconducting variations caused by a change in the stoichiometry in Tl-12201 have been studied. All samples have been prepared by a method with the possibility to control thallium losses[1,2]. The effects of changing thallium and oxygen content, substituting the Ba site with Sr and La, partly replace Cu with Co or, Fe as well as effects of moderate heat treatments have been investigated. The phase transition between orthorhombic and tetragonal form of Tl-2201 have been induced by changing the oxygen and/or thallium stoichiometry and by substitution of the Ba site with strontium. The structural changes observed strontium substituted materials and changes in T_c are consistent with an increase in charge carrier concentration in the CuO_2 plane. The mechanism for the redistribution of charge involves the overlap of Tl 6s and Cu 3d bands. Close to the O-T transition an abrupt redistribution of charge occurs. This is reflected in a marked decrease in T_c and the observed structural changes can be rationalized in terms of a redistribution of charge[1-4].

The aim of this experiment was to carefully study the O-T phase transition i Tl-2201 by use of high resolution X-ray powder diffraction. Figure 1 shows the changes in cell parameters as a function of Sr substitution. X-ray powder data were collected at beamline X7B, NSLS. Figure 2 shows the coexistence of orthorhombic and tetragonal phase in $Tl_2Ba_{1.47}Sr_{0.53}Cu_{6-d}$. Between the (200) and (020) peaks from the orthorhombic phase the (110) peak from the tetragonal phase appears.

[1] C. Ström, Thesis, University of Goteborg, 1993.
[2] C. Ström, S. -G. Eriksson, L. -G. Johansson, A. Simon, Hj. Mattausch and R. K. Kremer JSSC, 1994, 109, p. 321.
[3] C. Ström , S. -G. Eriksson Submitted to Physica C.
[4] C. Ström, S. -E. Eriksson, J. Albertsson and N. Winzek, Accepted for publication in Physica C.

Figure 1.

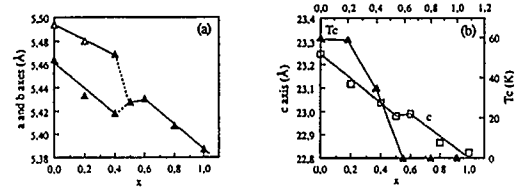
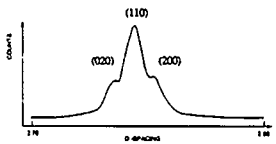


Figure 2.



* Work at BNL was supported under contract AC02-76CH00016 with DOE by its Division of Chemical Sciences, Office of Basic Energy Sciences, and by the Swedish National Research Council (NFR).

X-ray diffraction studies of tethered protein monolayers and ultrathin organic monolayer/multilayer films *	X9B

J. K. Blasie, S. Xu, M. Murphy, J. Chupa, and R. Fischetti (Univ. of Pennsylvania& Biostructures Institute)

Protein can be tethered to the surface of inorganic substrates via bifunctional organic chain molecules possessing one endgroup specific for one or more residues on the protein's surface and one endgroup specific for the inorganic surface. Such tethering can provide a single, vectorially-oriented monolayer of the fully-functional protein of the surface of the substrate suitable for both structural and functional studies. It is important to understand the structure and dynamics of the self-assembled monolayer of organic chain molecules on the inorganic surface in order to understand their resulting effect on producing vectorial orientation and in-plane ordering in the tethered protein monolayer. More recently, we have studied the effect thermal annealing on both the profile and in-plane structures of the "most simple" methyl-terminatedalkylsiloxane self-assembled monolayers on silicon substrates. Results to date have directly demonstrated that considerable structural reorganization occurs upon thermal annealing within both the silicon oxide surface of the substrate and the organic monolayer; both the siloxyl and methyl ends of the chains are much better ordered in the monolayer profile structure and the in-plane intermolecular correlation lengths are substantially increased. These results have important implications for the fabrication of well-ordered organic self assembled monolayers possessing more "bulky" chemical endgroups (eg. -SH, -NH_{3+}, -COO, etc.) specific for protein surface residues. In addition, resonance x-ray diffraction data about the FeK-edge have recently been collected from vectorially-oriented, tethered monolayers of cytochrome oxidase employing amino terminated self-assembled monolayers for tethering the oxidase via their mimicking the arginine and lysine residues of cytochrome c involved in its interaction with the oxidase. Analysis of these data currently underway should uniquely determine the positions of the cytochrome oxidase heme a and heme a_3 iron atoms within the protein's profile structure to a precision of $\pm$ 1 Å.

* Supported by: NIH grants HL18708, GM33525 & RR01633 and NSF/DSF grant 88-19885.

Kinetics and mechanism of lipid phase transitions *	X9B

M. Caffrey (Ohio State Univ.)

We have developed an x-ray diffraction compatible pressure oscillation calorimeter and have used it to study the lamellar gel/lamellar liquid crystalline transition in 1,2-dimyristoyi-sn-glycero-3-phosphocholine (DMPC)/60% (w/w) water. The position (2θ) of the lamellar (001) reflection was monitored as a measure of the degree of phase structural transformation in response to a pressure oscillation. The heat absorbed and released during the oscillation was monitored by recording the temperature change by means of a small thermistor positioned in the lipid sample. The structural and thermal response amplitude and relative to the driving pressure oscillation were analyzed with respect to perturbation frequency and mean pressure. By measuring the temperature response amplitude at a fixed temperature and at a series of fixed oscillation frequencies while varying the mean pressure, we determined the frequency-dependent heat capacity as a function of pressure. The structure response spectrum was obtained at a mean pressure value where the temperature response was maximal. At this point in the transition, the structure and temperature responses are linear up to oscillation amplitudes of at least +3 bar. The data are consistent with a transition best described by the Kolmogorov-Avrami kinetic model (Ye et al., Biophys. J. 60: 1002–1007 (1991)) having an effective dimensionality of one and a structural relaxation time of 1.0±0.2s. This analysis has been extended to the $L\alpha/L\beta$ phase transition in hydrated monoelaidin.

* This work is supported by the NIH, grant DK45295.

Fast pulse processing for solid state detectors | X9B

M. R. Chance, R. Fischetti, Y. Hai, and C. Lu (Albert Einstein College of Medicine)

A major stumbling block in the collection of high quality x-ray absorption spectroscopy data is the limited count rate that can be accessed by solid state detectors. Due to the use of the dynamical focusing monochromator on beamline X9B, even experiments on dilute samples experience total count rates of the individual channels that result in saturation of the detector capability.

We have built a single channel prototype amplifier that is designed for multipurpose testing of both pulsed optical and resistive feedback type pre-amplifiers. In tests with the 13 element detector at NSLS (equipped with pulsed optical preamplifiers), the amplifier shows output pulses of 300 ns fwhm (compared to 2000 ns for the Canberra output pulses). The performance of the amplifier is extremely good, as evidenced by the dead time of 500 ns. The noise level is higher than desirable, as evidenced by the resolution of 575 eV.

In Figure 1, we show the side by side performance of the Canberra and fast amplifiers for a concentrated cobalt acetate sample (20 mM). These spectra were recorded simultaneously on geometrically adjacent and comparably performing channels of the 13 element detector. The Canberra and fast amplifiers record adequate data at 50,000 counts per second total count rate (ICR) but the Canberra dead time reduces its edge jump at these rates. The poorer resolution of the fast amplifier can be seen in the pre-edge baseline. Figure 3 shows the two amplifiers at 200,000 counts per second total count rate. The data from the fast amplifier is improved by the expected factor of two, while the Canberra amplifier is paralyzed. Additional tests on the fast amplifier were performed at ICR values up to 600,000 counts per second. The amplifier still records valid data at these count rates but begins to suffer dead time losses.

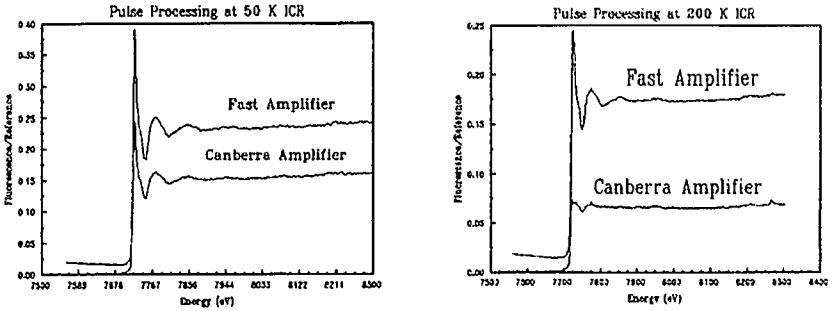


Figure 1.

Time-resolved x-ray absorption spectroscopy: novel methods applied to examining the structure of the myoglobin-CO photoproduct * | X9B

M. R. Chance, A. Xie, L. M. Miller, E. M. Scheuring, Y. Hai, and Y. Lu (Albert Einstein College of Medicine)

X-ray absorption spectroscopy (XAS) gives very accurate distance and geometric information on metalloproteins. We have developed a data acquisition system that currently provides x-ray edge data on microsecond time scales and EXAFS data on millisecond timescales. Ultimately, beamline improvements will allow EXAFS data on microsecond time scales and edge data on sub-microsecond time scales. We have shown x-ray kinetic data that probes the relaxation of the iron atom in myoglobin, subsequent to photolysis, at a range of temperatures. The structures observed at liquid helium temperatures and above the glass transition (where relaxation of the heme iron comes into play) have been compared to crystallographic data to contrast the strengths and limitations of the two methods.

In the first figure, we show the x-ray kinetics of myoglobin rebinding after a laser flash (at 20 Hz repetition rate). The monochromator was set to an energy where the ground state and photoproduct have the greatest differences (an increase in fluorescence yield with photolysis), the time solution was 5 μs and the data is plotted on a log time scale to show the geminate and solution rebinding phases. The rebinding event (which is accompanied by a decrease in x-ray counts) includes two processes, the structural conversion from deoxy to the liganded state with the movement of iron into the heme plane and the relaxation of the initial photoproduct to the deoxy state with the change in barrier that is known to occur. Comparison of the x-ray kinetics to optical kinetics taken under the same conditions reveals the relaxation rate of the iron atom, a controlling feature of the kinetic phases.

The second figure shows a proof-of principle EXAFS spectrum on a 1mM myoglobin sample with 10 ms time resolution defining the conditions that are reasonable for acquiring a time-resolved EXAFS spectrum. The total data acquisition time was 2 hours.

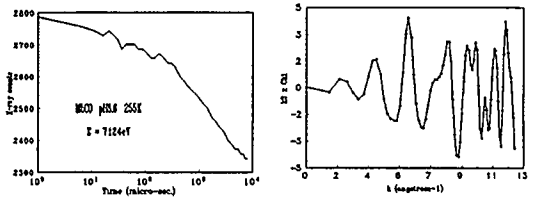


Figure 1.

* This work is supported by NIH grant HL- 45892, NSF grant BIR-9303830, and the Regional Center for Time-Resolved X-ray Spectroscopy through NIH grant RR-01633.

The ambiguities in ZnS_nX_{4-n} EXAFS | X9B

Kimber Clark, David Tierney, James Penner-Hahn (Univ. of Michigan), Kumar Govindaswamy, Eric Gruff, and Stephen A. Koch (SUNY Stony Brook)

The majority of zinc environments in proteins are four coordinate with roughly tetrahedral geometries. Because zinc is intermediate between hard and soft acids, it shows little preference for hard bases (e.g., oxygen) over soft bases (e.g. sulfur) [1]. As a consequence of this, the zinc environments in proteins are likely to contain ligands such as histidine or aspartate in addition to (or in place of) cysteine residues. It thus becomes important to establish the conditions under which EXAFS can be used to distinguish between the possible ligation types. In principal it is a simple matter to determine whether a two shell fit is better than a one shell (S only) fit. In practice, however, a two shell S+N fit will always be better than a one shell sulfur only fit simply as a result of the increase in the number of variables being used to fit the data. Care must be taken to distinguish between an improvement due to the presence of additional scatterers and the improvement which results simply from an increase in the number of free variables. We performed a series of fits for models having ZnS_4, ZnS_3N and ZnS_2N_2 structures. The coordination number was fixed at four, while the number of sulfur scatterers was varied from zero to four in 0.25 increments. The percent improvement in the goodness of fit for the i^{th} fit, P_i, was calculated as $P_i = [(F_{4S} - F_i)/F_{4s}] \times 100$, where F_{4S} and F_i are the mean-square goodness of fit obtained for a single shell fit using four sulfurs and for the i^{th} fit, respectively. A large value for P_i thus represents a fit that is significantly better than the single shell 4S fit. The percent improvement in the goodness of fit as a function of the percent sulfur in the ligation sphere is shown in Fig. 1. For each plot, the P_i value corresponding to a two-shell, all-sulfur fit is shown as a horizontal line. This is an upper limit, or ceiling, representing the amount of improvement to be expected simply as a result of increasing the number of variable parameters. The P_i for the ZnS_4 model does not cross this ceiling. In other words, the N+S fits are always worse than the S+S fit, as expected for a ZNS_4 structure. It is important to note, however, that the S_3N fit is better than the one shell, S-only fit. This is characteristic of all of the ZnS_4 models we have studied. If care were not taken to control the number of variable parameters, this could lead to the erroneous conclusion that the ZnS_4 model has a ZnS_3N structure. In contrast, the P_i values for the ZnS_3N and ZnS_2N_2 models cross the 2S+2S ceiling by a significant amount and, more importantly, these plots have maxima corresponding (within 10%) to the true % sulfur in the complex. We are now using this analysis protocol to determine the Zn ligation environment in Zn-MerR and in a variety of other Zn metalloproteins.

[1] Huheey, J.E. Inorganic Chemistry; 3rd ed.; Harper & Row: New York, 1983, pp 314. [2] E.S. Gruff and S.A. Koch, J. Am. Chem. Soc. 1989, 111, 8762-8763. [3] Corwin, D.T.; Koch, S.A. Inorg. Chem. 1988, 27, 493-496.

Figure 1. Percent sulfur calibration curves for the zinc models. Circles: ZnS2N2. Diamonds: ZnS3N. Triangles: ZnS4. The horizontal lines represent the 2S + 2S ceiling(see text). [Figure unavailable due to space constraints.]

Dynamical focusing for a sagittal monochromator * | X9B

R. Fischetti and M. Sullivan (Albert Einstein College of Medicine)

The sagittal focusing monochromator on beamline X9B has performed quite well producing horizontal beam sizes on the order of 0.5 mm or less. This has been achieved by replacing the normally flat, second crystal of the double crystal monochromator with a thin crystal that is mounted in a bending stage and bent to a cylindrical cross section. For a given X-ray energy the source to crystal distance and the radius of curvature determine the crystal focus distance. Thus, different energies will have different focal lengths unless the radius of curvature is changed. This is not a problem for diffraction experiments that are performed at one X-ray energy. However, for an XAS experiment the focal position will move further downstream with increasing energy. Ideally the position and width of the focused beam would remain constant during a scan. In order to achieve this, the radius of curvature of the crystal must decrease with increasing energy. Briefly, the focusing is controlled by a motor which drives a pair of linear translators and vacuum feedthroughs to provide vertical positioning of a rail that runs parallel to the trolley rails in the vacuum chamber. The bending stage is mounted on the trolley, which translates the second crystal in order to maintain a constant exit beam height. As the trolley moves the bender, a cam follower running along the rail transmits the motor position to the bending stage. Normally, the rail is level, and thus the curvature radius remains constant as the energy and trolley position are scanned.

Figure 1 shows the results of initial tests of this modification in January of 1984. The energy was scanned from 6.80 to 8.05 keV in 100 eV increments. At each energy the horizontal intensity distribution was recorded by scanning a 25 micron slit through the beam and recording the intensity with a PIN diode. Except for the first few energies the full width at half maximum of the beam width was maintained at less than 0.5 mm. The mirror was focusing in the vertical direction so the beam size was $<0.5 \times 0.5$ mm^2.

Figure 2 shows the reproducibility of the I_0 scans for three different energy regions (Fe-, Cu- and Zn-XAS regions). This procedure provides good reproducibility in determining the piezo calibration curve.

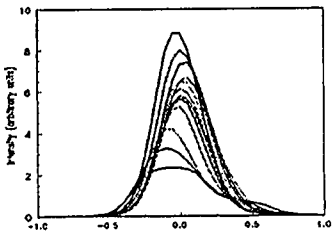


Figure 1.

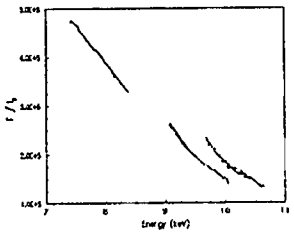


Figure 2.

* This work is supported be the Regional Center for Time-Resolved X-ray Spectroscopy under NIH grant RR-01633.

Structural studies of discotic liquid crystals *	X9B

P. Heiney (Univ. of Pennsylvania), H. Ringsdorf, T. Plesnivy, and P. Schuhmacher(Institute für Organische Chemie, Germany)

We have used X-ray diffraction at grazing incidence (GID) to study ultra-thin films of a new class of amphiphilic material. Superdisks are star shaped oligomeric compounds composed of mesogenic subunits. In the bulk, they typically form hexagonal columnar liquid crystals. At the air-water interface, they undergo a conformational change such that the triphenylene substituents sit perpendicular to, and the core lies parallel to, the interface. The conformation is preserved upon transfer to a solid substrate and the triphenylene subunits are organized in columns aligned along the direction of deposition with an intercolumn spacing $\approx$ 20 A. GID confirms the structural anisotropy in the plane of the film with a mosaic spread of 40° about the direction of deposition, in agreement with earlier atomic force microscopy investigations.



Figure 1.

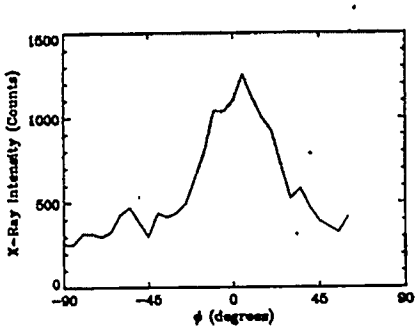


Figure 2.

* This research is supported by the National Science Foundation, Grants DMR-MRL-92-20668 and DMR-89-01219.

Structural and electronic factors that influence oxygen affinities: a spectroscopic comparison of ferrous and cobaltous myoglobin *	X9B

L. M. Miller and M. R. Chance (Albert Einstein College of Medicine)

The role of iron in oxygen binding and release in myoglobin has been studied by addressing various structural and electronic factors that result in similar rates of oxygen association (k_{on}) and differing rates of oxygen dissociation (k_{off}) for ferrous (FeMb) and cobaltous (CoMb) myoglobin. Comparable values of k_{on} in CoMb and FeMb imply similar barriers to oxygen binding in myoglobin. Structurally, the magnitude of this barrier is influenced by the metal displacement from the heme plane of the oxy and/or deoxy species. The ratio of peaks in the ligand field indicator region (Figure 1) of an x-ray absorption near edge spectrum (XANES) has been correlated to the spin state and iron out-of-plane distance in ferryl, ferric, and ferrous hemeproteins by calibration of spectral changes to known crystallographic data (Figure 2). XANES is better suited than crystallography for determining metal-heme displacements of photolysis intermediates in which the quantum yield is less than unity (like $CoMbO_2$ and $FeMbO_2$, which have photoproduct yields of 0.5) since the necessary difference techniques are straightforward. The XANES of CoMb and FeMb reveal similar metal-heme displacements for the deoxy, oxy, and low temperature photoproduct states of CoMb and FeMb, supporting similar barriers to oxygen binding.

Lower values of k_{off} for $FeMbO_2$ versus $CoMbO_2$ imply a higher barrier to oxygen release in $FeMbO_2$. Electronically, x-ray edge positions (Figure 1) of CoMb and FeMb indicate a substantial transfer of electron density from the metal to the ligand upon oxygenation. More electron density is transferred from iron than from cobalt indicated by a 3 eV versus and 2 eV shift to higher energy from the respective deoxy values. This difference is reflected in a weaker Co-O bond when compared to Fe-O and a weaker colbaltous dioxygen bond in heme protein models which lack a hydrogen bond to the distal histidine. The $FeMbO_2$ and $CoMbO_2$, this hydrogen bond is present; however, in $CoMbO_2$, the dioxygen stretching frequency is closer to that of heme protein models lacking this hydrogen bond, suggesting a weaker hydrogen bond to the distal histidine. Thus, less electron density transfer from cobalt to the dioxygen moiety translates into important differences in the distal pocket environments of $CoMbO_2$ and $FeMbO_2$, resulting in different barriers to oxygen release.

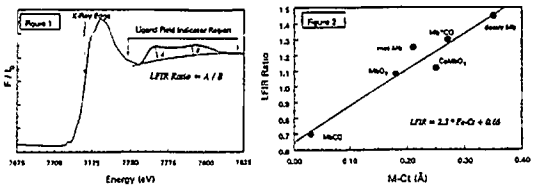


Figure 1.

* This work was supported by the NIH grant HL-45892.

EXAFS and XANES studies of Co^{3+} in nitrile hydratase | X9B

Mark J. Nelson, Bridget A. Brennan, John G. Cummings (Du Pont), Saqib Rehman, James Kindt, and Robert C. Scarrow (Haverford College)

Nitrile hydratases are metalloenzymes that catalyze the hydration of nitriles to amides. Two classes have been identified - those that contain low-spin Fe^{3+} and those that contain low-spin Co^{3+}. We are studying the metal coordination environments of these enzymes as part of a program to elucidate their mechanism. We have shown previously that the iron nitrile hydratase has a biologically novel N_3S_2O coordination. From amino acid sequence homology we expect the cobalt enzyme to have a similar coordination - if confirmed this would make this enzyme the first described cobalt-sulfur protein. In our first attempt to collect x-ray data on the cobalt enzyme we found that the EXAFS data ($k^3\chi$ vs. k) are similar to those from the iron enzyme, supporting our hypothesis. More precise interpretation awaits analysis of data from a more extensive collection of model compounds.

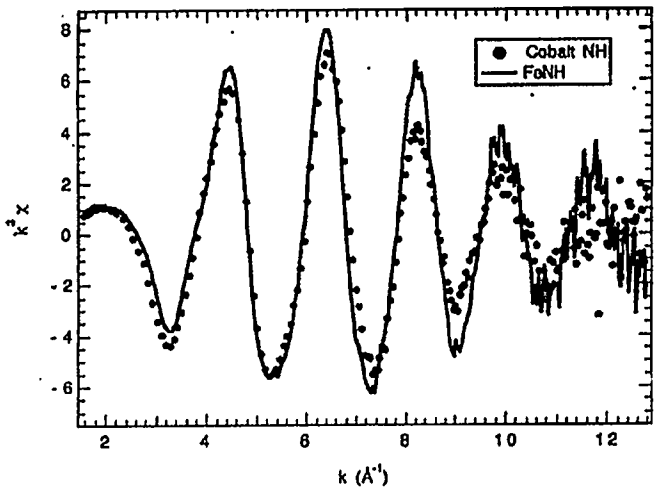


Figure 1.

Mediation of Co-C bond cleavage by cobalamin dependent enzymes * | X9B

E. M. Scheuring and M. R. Chance (Albert Einstein College of Medicine)

Cobalamin dependent enzymes participate in a number of carbon skeleton rearrangement reactions as well as methylation reactions essential to all mammals. The key step in all of these reactions is the breakage of the Co-C bond. We have been intensively studying different forms of the free cobalamins and also the enzyme bound complexes by X-ray absorption spectroscopy (XAS) to answer the question how the enzyme accelerates the Co-C bond cleavage. The 5,6-dimethylbenzimidazole group (DMB or "base"), connected to the Co atom on the opposite side of the Co-C bond, has a significant role modulating the Co-C bond cleavage. The "base-on/base-off" configuration has a proven effect on favoring homolytic versus heterolytic cleavage. An interesting hypothesis concerns the possible replacement of the DMB ligand with ligand from the enzyme. This is not the case for the cobalamin transport protein cobalophilin (Frisbie, S.M. and Chance, M.R. Biochemistry, 1993, 32, 13886). Recent crystallographic data from Rowena Matthews (University of Michigan) and collaborators shows that in the 27K proteolytic fragment of methionine synthase, a methylcobalamin dependent enzyme, the DMB ligand of the cofactor is replaced by a histidine group of the enzyme. We have recently collected EXAFS data on the native methionine synthase provided by Dr. Matthews' group. We analyzed the data in combination with ab initio X-ray Absorption Fine Structure (XAFS) calculations using FEFF 6. Comparison of Fourier-transform data of methylcobalamin and the enzyme bound complex shows differences inconsistent with methylcobalamin presence in its free form in the enzyme. For the FEFF calculations we took the crystallographic coordinates of methylcobalamin, replaced the 5,6- dimethylbenzimidazole group with a histidine adjusting the Co-N bond distance between 2.0-2.2 Åand performed ab initio XAFS calculations up to 5.0 Å away from the Co atom. We compared the Fourier-transform data of the FEFF simulation and the experimental data. The experimental data of the enzyme bound cofactor gives a better match with the FEFF simulation of the modified cobalamin. EXAFS data analysis is currently in progress but or FEFF calculations support the histidine replacement of the DMB base but at a shorter distance than it is shown in the X-ray crystallographic data.

* This work is supported by NRICGP/CSRS/USDA Program in Human Nutrients 91-6180-6798 and the Regional Center for Time-ResolvedX-ray Spectroscopy under NIH grant RR-01633.

Thiol ligation of zinc in isoleucine t-RNA synthetase * | X9B

D. L. Tierney, J. E. Penner-Hahn (Univ. of Michigan), J. A. Landro, E. Schmidt,and P. Schimmel (MIT)

Class I t-RNA synthetases generally contain a characteristic N-terminal catalytic core joined to a C-terminal domain that is idiosynchratic to the enzyme. The closely related class I E. coli methionyl- and isoleucyl-tRNA synthetases each have a single zinc atom coordinated to ligands found in the catalytic domain. Isoleucyl-tRNA synthetase has a second, functionally essential zinc bound to ligands at the C-terminal end of the protein. Recent evidence suggested this structure curls back and interacts directly or indirectly with the active site. Recent studies on a cobalt substituted enzyme [1] have suggested that substrate causes a perturbation in the active site structure. We have examined E. coli isoleucyl-tRNA synthetase (IleRS) with and without substrate in an effort to determine the ligation of the two zinc atoms and to characterize the interaction of the enzyme with substrate. There is no dramatic change in the zinc XANES spectra for IleRS on addition of substrate, implying that isoleucine does not significantly alter the average zinc coordination sphere. In addition, there is no detectable change in the observed EXAFS. These results suggest that, at most, isoleucine causes a small geometric rearrangement of the zinc site structure without binding directly to the metal. The Fourier transforms (FTs) of the EXAFS for IleRS with and without substrate are shown in Figure 1. The FTs show no clear evidence for an interaction between the two metal atoms such as that seen for GAL 4. While the absence of an obvious interaction does not preclude its existence, the present data show that any such interaction must be extremely weak. Quantitative curve fitting analyses are consistent with an average coordination sphere that is predominantly sulfur with an average Zn-S bond length of 2.33 Å. Employing the method of Clark, et al. [2], we conclude that the two zinc atoms in IleRS are bound to 7 ± 1 cysteine thiolates. Though we cannot rule out an average of 3.5 sulfurs per zinc, the data are most consistent with an average environment of ZnS_4.

[1] Landro, J.A.; Schmidt, E.; Schimmel, P.; Tierney, D.L.; Penner-Hahn, Biochemistry, in press. [2] Clark, K.; Tierney, D.L.; Govindaswamy, K.; Gruff, E.; Kim, C.W.; Berg, J.M.; Koch, S.A.; Penner-Hahn, J.E., manuscript in preparation.

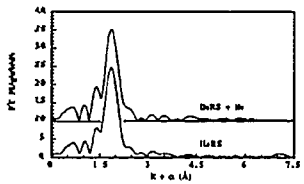


Figure 1. Fourier transforms of IleRS EXAFS with and without isoleucine.

* The National Synchrotron Light Source is supported by the US Department of Energy and Beamline X9 is supported by the NIH Division of Research Resources.

Epitaxial growth of otavite on calcite * | X10C

R. P. Chiarello and Neil C. Sturchio (ANL)

In response to the need for accurate experimental data regarding mineral precipitation and growth rates, we have performed a preliminary experiment to evaluate the feasibility of in situ measurements of these parameters using synchrotron X-ray scattering techniques. We chose to examine the growth of otavite on calcite because the calcite $(10\bar{1}4)$ cleavage surface provides an ideal single crystal substrate for X-ray reflectivity studies, calcite can be prepared in large enough samples to take advantage of the entire incident X-ray beam without microfocusing, and otavite can be easily grown on the calcite cleavage surface from aqueous solution.

Synchrotron X-ray Reflectivity (XR) and X-ray diffraction (XD) techniques were used to characterize and otavite ($CdCO_3$) over-growth during its precipitation from an aqueous solution onto a calcite $(10\bar{1}4)$ cleavage surface. XR was used to measure the otavite thickness and the roughness of the calcite/otavite and otavite/fluid interfaces. Specular and off-specular XD were used to measure the crystallographic orientation and long-range atomic order of the otavite over-growth. The otavite grew coherently with $(10\bar{1}4)$ growth plane oriented parallel to the calcite $(10\bar{1}4)$ cleavage surface. The average growth rate of the otavite for the first nine hours was 15 Å·h^{-1}. During the early growth stage (< 50 Å), the otavite $(10\bar{1}4)$ d-spacing was compressed by as much 2.2% in the direction perpendicular to the calcite cleavage surface (see Figure inset). As the otavite thickness (L) increased, this d-spacing approached that of bulk otavite. At a thickness of 443 Å, the otavite was determined to be of single crystal quality (0.4° mosaic) and epitaxial with calcite. These results indicate that synchrotron X-ray scattering is a powerful approach for elucidating the rates and mechanisms of reactions occurring at mineral-fluid interfaces.

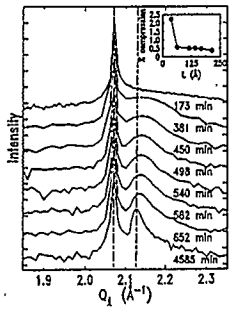


Figure 1. Diffracted intensity (logarithmic scale) vs. perpendicular momentum transfer. The vertical dashed lines at $Q_\perp = 2.07$ and 2.13 Å^{-1} indicate the calcite and otavite $(10\bar{1}4)$reflections, respectively.

* Work Supported by the Geosciences Research Program OBES/DOE under contract W-31-109-ENG-38 to Argonne National Laboratory.

Surface structure and dissolution dynamics of calcite in water * | X10C

R. P. Chiarello and N. C. Sturchio (ANL)

The crystal truncation rod (CTR) of the calcite $(10\bar{1}4)$ cleavage surface was measured during experiments performed in both static and flow-through reaction cells. In the static cell, calcite was allowed to approach equilibrium by free drift with deionized water and dilute nitric acid solutions. In the flow-through cell, calcite was reacted with a dilute ground-water like solution and the solution pH was controlled by autotitration. The CTR in both experimental systems could be modeled using a stepped-surface model[1] with steps having average heights of one or two monomolecular layers. There was no evidence of surface reconstruction, relaxation, or for the presence of a disordered hydrated layer (Figure 1).

Time-resolved glancing-incidence measurements made in the flow-through cell were used to investigate dissolution dynamics (Figure 2). At dissolution rates between 1.2 x 10^{-7} and 1.5 x 10^{-7} mmol·cm^2·sec^{-1} evidence was found for layer-by-layer dissolution by monomolecular step retreat. At dissolution rates between 1.5 x 10^{-7} and 2.7 x 10^{-7} mmol·cm^{-2}·sec^{-1} surface roughness was proportional to dissolution rate and approached a steady state maximum. The observed increase in surface roughness at dissolution rates greater than 1.5 x 10^{-7} mmol·cm^{-2}·sec^{-1} may be explained by spontaneous nucleation and growth of etch features. These results further demonstrate the viability of synchrotron-based X-ray scattering techniques for in situ investigations of fundamental mineral-fluid interface processes.

[1] H. You and Z. Nagy, Current Topics in Electrochemistry 2, 21 (1993).

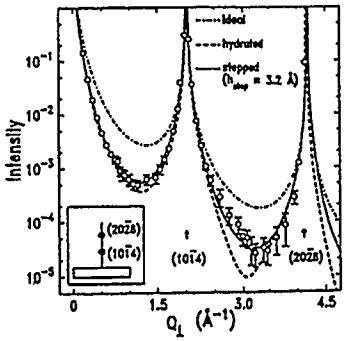


Figure 1. Calcite $(10\bar{1}4)$ CTR (open circles) measured in static reaction cell. Dashed line is expected CTR for a 3 Å thick hydrated surface phase at the calcite-fluid interface.

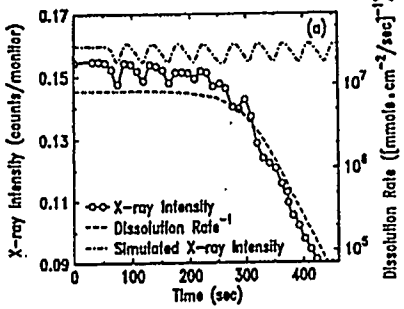


Figure 2. Time-dependent X-ray intensity at $Q_\perp = 0.1$ Å^{-1} (open circles) in the flow-through cell.

* Supported by the Geosciences Research Program, OBES/DOE under contract W-31-109-ENG-38 to Argonne National Laboratory.

Real time x-ray scattering of sputtering growth of TiN films | X10A, X10B

J. H. Je (Exxon and Pohang Univ., Korea), D. Y. Noh (Exxon), H. K. Kim (Pusan Univ., Korea), and K. S. Liang (Exxon)

Sputter growth of TiN films has been extensively studied for the interest of surface protective coating. Based on our previous in-house results suggesting the change of growth direction from the ⟨002⟩ (early stage) to the ⟨111⟩ direction (late stage), we have carried out a real-time x-ray scattering experiment using a newly constructed x-ray cell. Our results reveal a quite different and interesting picture of the TiN growth.

The experiment was carried out by measuring the diffraction profile in real time as we grow a TiN film on Si(001) substrates by RF sputtering. Figure 1 shows a typical intensity variation of the TiN (002) and the (111) peaks measured in powder scans along the surface normal as a function of time (expressed in film thickness). The data show an orientation crossover similar to the in-house results. However, the detailed growth mechanism indicated by a rocking curve shown in figure 2, was quite different from the naive crossover from the ⟨002⟩ to the ⟨111⟩ direction. Based on figure 2 and other measurements we believe that the crystallites at late stage still grow in the ⟨002⟩ direction that was preferably tilted 60° away from the surface normal. Consequently, the (111) axis is 5° from the surface normal as shown in figure 2. The observed crossover may be understood by noting that the (002) face has the lowest surface energy and therefore, is the easy growth direction. In later stage, the (002) plane tilts away from the surface normal to provide a favorable morphology for strain release.

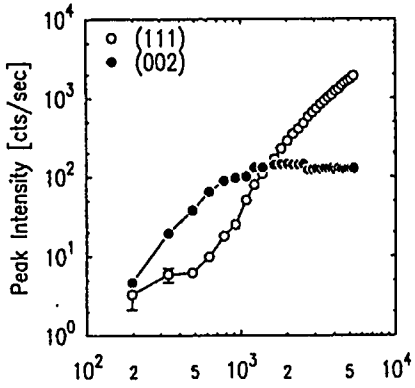


Fig 1. Peak Intensity of TiN film.

Figure 1.

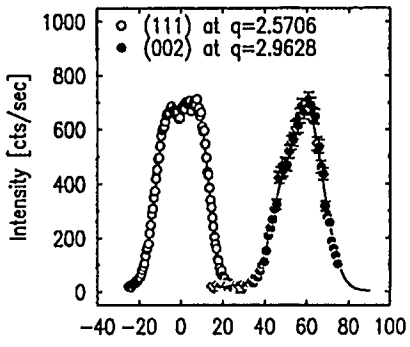


Fig 2. Chi scans of TiN film.

Figure 2.

Interfacial structure of thin Au films on GaAs	X10A, X10B

D. Y. Noh (Exxon), Y. Hwu (Academia Sinica, Taipei, Taiwan), H. K. Kim (Pusan Nat. Univ., Korea), and M. Hong (AT&T)

We present results of an ex-ray reflectivity measurement on a Au film, 1000 Åthick, in-situ epitaxially grown on GaAs by molecular beam epitaxy (MBE). The specular reflectivity curve shown in Figure 1 was analyzed to obtain the roughness of the buried Au/GaAs interface (5Å) and the Air/Au interface (8Å). The well-defined Au/GaAs interface indicated that the interdiffusion was minimal at room temperature. The regular intensity oscillations suggested that the film thickness was uniform in atomic scale across the whole illuminated area. The height fluctuations of the interfaces were highly correlated as illustrated by the regular intensity oscillations in the longitudinal diffuse profile. We obtained the correlated height fluctuations, $G_{12}(r\rightarrow)=\langle(h_1(r\rightarrow)\text{-}h-2(0))^2\rangle$quantitatively by comparing the diffuse profile at the crest of a oscillation to that at the valley. The correlated height fluctuations were also manifested by the newly discovered satellite peaks at low incident angles. The satellite peaks were consistently explained by the dynamic scattering effects and the intensity oscillations in the diffuse scattering due to the correlated roughness.

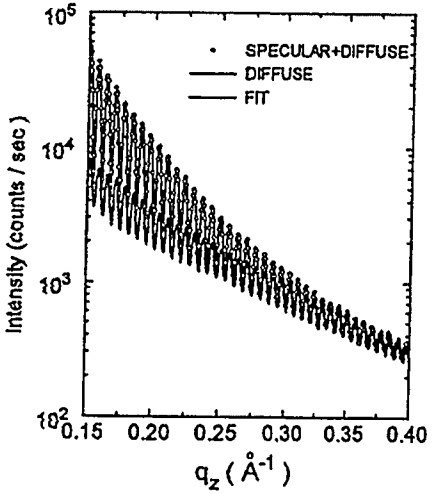


Figure 1. Specular reflectivity and the longitudinal diffuse scattering

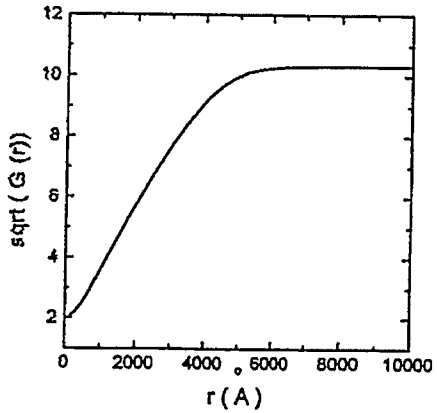


Figure 2. Square Root of the Height Correlation Function

Time-resolved x-ray scattering study of the normal alkanes	X10A, X10B

H. H. Shao, H. E. King Jr., E. B. Sirota (Exxon)

Unlike conventional crystals, normal alkanes do not directly enter a fully-ordered crystal state upon cooling from the melt. Rather, they order into a series of plastic-crystal phases commonly referred to as rotator phases. Although the rotator and crystal phase behaviors of normal alkane are well understood,[1] the kinetics of these phase transitions is still unclear. Here we present our recent study trying to understand nucleation and growth of these n-alkanes. The samples were prepared by fractionating of polydisperse emulsion. The n- alkane used are n-C16, n-C15 and n-C16/n-C17 mixtures with a surfactant, SDS. The sizes range from 0.2 - 2 micros diameter. The time resolved synchrotron x-ray scattering is carried out on NSLS X10A. The Position Sensitive Detector is used to monitor the kinetics when the samples are quenched through liquid-solid transition. We found that no crystals are formed in the duration of experiment, 12 hours for the quench step less than 13°C. The nucleation rate for deeper quench seems to follow the growth law predicted by Turnbull[2].

[1] J. Chem. Phys., 98, 5809 (1993).
[2] J. Chem. Phys., 34, 820 (1961).

Rotator phase behavior in binary mixtures of the normal alkanes | X10A, X10B

H. H. Shao, H. E. King Jr., E. B. Sirota, and D. M. Singer (Exxon)

Normal alkanes are an important basic organic series and form the building blocks for surfactants, lipids and liquid crystals. Based on our previous work on pure normal alkanes[1], we carried out high resolution synchrotron powder x-ray scattering as well as differential scanning calorimetry on several normal alkane binary mixtures. Our main aims were to define the stability ranges of the phases and measure the temperature dependence of their order parameters, such as lattice distortion and molecular tilt. The binary mixtures have a similar phase behavior, $R_{II} \rightarrow R_I \rightarrow R_V \rightarrow$crystal, as the pure alkanes, but the temperature stability range of the rotator phases is expanded. The hexagonal R_{II} phase is favored over the other rotators but shows evidence for structural frustration–Bragg scattering gradually disappears upon cooling. The R_{II}-to-R_I transformation is shifted down by about 2°C relative to the single-chain value, but the distortion-order-parameter jump at the transition is essentially equal to that in the pure alkanes. The tilted rotator phase R_V is destabilized by mixed chain lengths. Its stability range narrows and/or disappears near 50:50 weight fraction.

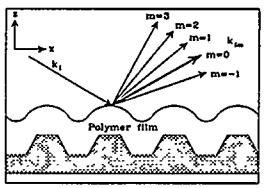
[1] J. Chem. Phys., 98, 5809 (1993)

Thin films on "rough" surfaces: an x-ray study * | X10B

M. Tolan (Inst. fur Exp. Phys. Uni Kiel), G. Vacca, S. K. Sinha (Exxon), Z. Li, M. Rafailovich, J. Sokolov (SUNY Stony Brook), H. Lorenz, and J. P. Kotthaus (Sek. Phys. LMU Munchen)

The morphology on thin films deposited on rough surfaces is of great interest, both in basic research and in materials science. In particular, the question how the roughness propagates from a substrate through a thin film to the surface is important for investigations concerning the growth of films and multilayers. In the present work we concentrate on the growth of polystyrene (PS) films on laterally structured surfaces (i.e. surface gratings, see figure 1). These substrates can be regarded as a special kind of "roughness" with only a few enhanced Fourier-components in the wave-number spectrum which may be damped by an absorbed film. Andelmann, Joanny and Robbins [1] have theoretically investigated a system with van der Waals interactions between the rough substrate and a thin film. Our PS films on top of surface gratings with a lateral spacing d = 9800 Å and a height of h $\approx$ 130 Å are a model system with dominating van der Waals interactions between the substrate and the PS chains and render it ideal for an investigation of the aforementioned theory. Our experiments were performed using (a) x-ray scattering in the region of small incidence angles to investigate the layer thicknesses and structures of the interfaces grating/PS and PS/air, and (b) Atomic Force Microscopy (AFM) to look directly at the topmost surface. The x-ray experiments were carried out at the beamline X10B (Exxon) and the AFM-measurements were performed at the Materials Science Department in Stony Brook (commercial Nanoscope III Instrument). The figure 2 shows transverse q_x-scans for film thicknesses of l = 275, ..., 695Å. A detailed analysis of the data is in progress. Preliminary results of fits of the data give strong hints that the theory of Andelmann, Joanny and Robbins does not explain the data quantitatively if simple van der Waals interactions between the PS layer and the substrate are assumed.

[1] D. Andelmann, J.-F. Joanny, M.O. Robbins; Europhys. Lett. 7, 731 (1988); M.O. Robbins, D. Andelmann, J.-F. Joanny, Phys. Rev. A, 43, 4344 (1991).



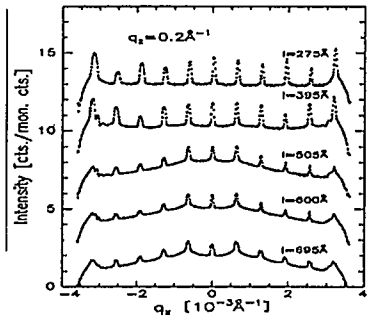


Figure 2. Transverse scans along q_x for fixed q_z = 0.20 Å^{-1} and five different PS films ! - V with the thickness l = 275 Å, 395 Å,505 Å, 600 Å, and 695 Å.

* M.T. is indebted to the Exxon Research Labs for financial support of his visit.

X-ray diffraction from mesoscopic systems: thin films on "rough" surfaces *	X10A, X10B

M. Tolan (Institut für Experimentalphysik der Universitat Kiel, Germany), G.Vacca, S. K. Sinha (Exxon), Z. Li, M. Rafailovich, J. Sokolov (SUNY Stony Brook), H. Lorenz, J. P.Kotthaus Lufwig-Maximilians (Universitat Munchen, Germany)

In this work x-ray diffraction measurements on thin polystyrene films deposited on laterally structure surfaces are reported. The experiments were performed in the region of small incidence and exit angles, respectively. The x-ray data are compared with the results of AFM investigations, both performed to obtain the morphology of the polymer film on top of the surface grating. Our results do not confirm existing theoretical predictions assuming pure van der Waals interactions between the substrate and the film.

[1] D. Andelmann, J. F. Joanny et al., Europhys. Lett. 7 731(1988).

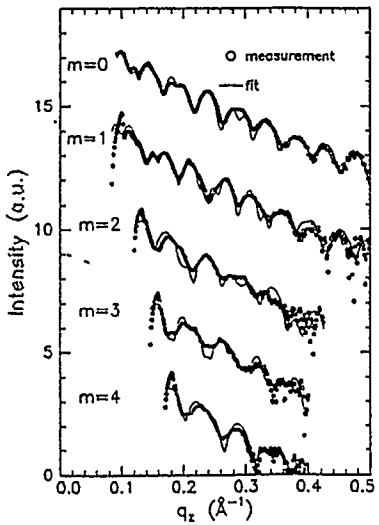


Figure 1. The figure shows the datum and fits of the reflectivity and the first four diffraction orders (m=1,...,4) for film with the thickness l_3=270Å. Due to the Born approximation,the first part of the curves of the diffraction orders can not be explained. Curves are shifted for clarity.

* Worksupported by NSF-DOE etc.

Powder x-ray diffraction studies of the phase transformation in calcined MFI zeolite	X10A, X10B

Baoshan Zhang, Harry W. Deckman, Keng S. Liang, E. W. Corcoran, Jim McHenry (Exxon Corporate Research), and J. P. Verduign (Exxon Chemical Europe Inc.)

Recently, we have succeeded in preparing calcined silicate MFI zeolite of quite uniform sizes ranging from a few hundred Angstroms to a few microns. Using these mono-size powders, we have carried out powder x-ray diffraction measurements to study their structure and phase transformation. A typical set of x-ray scans taken from 6 micron powders on beamline X-10B is shown in Fig. 1, which covers temperature from 25 to 240°C. All measurements have been done under the Ar gas flow, and the sample was heated up to 200°C for 3 hours to release the water molecules. A structure transformation from a monoclinic (tilt angle β=90.516°) to a orthorhombic phase was identified. Fig. 2 plots the (200) peak position as a function of temperature which indicates the transition temperature is about 65°C. We note that this transformation is similar to what was observed in ZSM-5[1]. We analyzed our powder diffraction profiles using the Thompson- Cox-Hastings pseodu-Voight functions[2]. The results as shown in Fig. 3 indicate that the (200) peak width of Lorentzian part remains constant through the structure transformation. The results, therefore, imply that no significant twin boundaries are created in the transformation along the [200] direction, the channel direction. Fig. 2 shows that the Gaussian part of the (200) peak has slight increases. The reason is not clear. One possible reason may come from the movement of the remain atoms inside channels during this transformation. Both Lorentzian and Gaussian parts remain constants along other two directions through this transformation. We also found the following phenomena. For the Monoclinic phase, the tilt angle increases to β=90.583° when the samples expose to water vapor at room temperature. For the orthorhombic phase, the thermal expansion coefficient is negative along the sin-channel [020] direction, the absorption coefficient decreases when the temperature goes up.

[1] H. Van Koningsveld, J. C. Jansen and H. Van Bekkum, Zeolites, Vol. 10, 235-242 (1990)

[2] P. Thompson, D. E. Cox, and J. M. Hastings, J. Appl. Crystallogr., Vol. 20, 79-83 (1987)

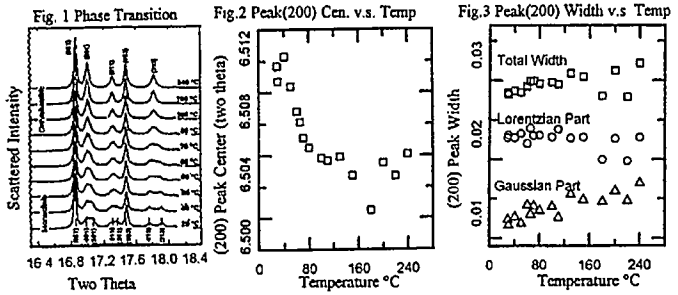


Figure 1. Phase Transition

Structural modification in the active site of arthropod hemocyanin in response to heterotropic effectors as detected by x-ray absorption spectroscopy	X10C

L. Bubacco, M. D. Wirt, R. S. Magliozzo, J. Peisach (A. Einstein Coll. of Med.), and L. Powers (Utah State U.)

Hemocyanin (Hc) is a multisubunit copper protein whose physiological function is the reversible binding of oxygen as a μ-η^2:η^2 peroxo bridge[1] at a binuclear copper active site. Changes in oxygen affinity are induced by heterotropic effectors.[2] In this study, k-edge x-ray absorption spectroscopy was used to investigate the effect of protons and chloride on the coordination geometry of Cu(I) in Panulirus interruptus and subunit II of Limulus polyphemus deoxy- HC.

Based on the k-edge absorption properties of several Cu(I) model complexes Blackburn et al.[3] identified a correlation between the intensity of the $1s \rightarrow 4p_z$(8982.5 eV) transition and the coordination geometry of the metal ion. In trigonal-planar (D_{3h}) complexes this transition has a high intensity. However, as the Cu(I) ion is moved out of the plane defined by the three equatorial ligands toward a pseudotetrahedral symmetry (C_{3v}) the intensity of this transition decreases. This feature was used to investigate the structure of the active site of Arthropod Hc. The analysis of k-edge data collected for Hc under different solution conditions, (which from the oxygen binding experiments are known to induce changes in affinity) allowed for the identification of the coordination geometry of the metal in the active site corresponding to high and low oxygen affinity forms of the protein. In deoxy-Hc changes from psuedotetrahedral to a more trigonal geometry either by raising pH or by addition of chloride were observed. Since high pH and the presence of chloride produce opposite changes in O_2 affinity [2], it is suggested that oxygen affinity may not be uniquely governed by Cu(I) coordination geometry.

[1] Magnus, K., Hoa, T.T., Carpenter, J.E., In "Bioinorganic Chemistry of Copper"; Karlin, K.D. and Tyeklar, Z., eds. (Chapman & Hall, 1993); pp. 143-150.

[2] Brenowitz, M., Bonaventura, C., Bonaventura, J., Arch. Biochem. Biophys. 1984, 230, 238-249.

[3] Blackburn, N.J., Strange, R.W., Reedijk, J., Volbeda, A., Farooq, A., Karlin, K.D., Zubieta, J., Inorg. Chem. 1989, 28, 1349-1357.

In situ x-ray absorption study of the structure of the passive oxide film on iron *	X10C

Alison J. Davenport (BNL) and Michael Sansone (Exxon)

The nature of the passive film grown electrochemically on iron in pH 8.4 borate buffer at a high potential (+0.4V(MSE)) was investigated with high resolution *insitu* XANES. Details of the pre-edge peak at the base of the Fe K edge were resolved by using the (333) reflection from the Si(111) monochromator crystals. For oxides and oxyhydroxides such as α-Fe_2O_3, α-FeOOH and γ-FeOOH which contain iron that is entirely octahedrally co-ordinated to oxygen, the pre-edge peak is split into two components due to crystal field effects. Conversely, oxides with the spinel structure, γ- Fe_2O_3/Fe_3O_4 (in which 1/3 of the iron ions are tetrahedrally co-ordinated), give a single pre-edge peak. The single peak from the passive film is consistent either with the spinel structure, γ-Fe_2O_3/Fe_3O_4, that has been proposed in the literature, or with a disordered structure with distorted co-ordination polyhedra [1].

[1] A.J .Davenport and M. Sansone, "High Resolution *InSitu* XANES Investigation of the Nature of the Passive Film on Iron in a pH 8.4 Borate Buffer", J. Electrochem. Soc., (in press).

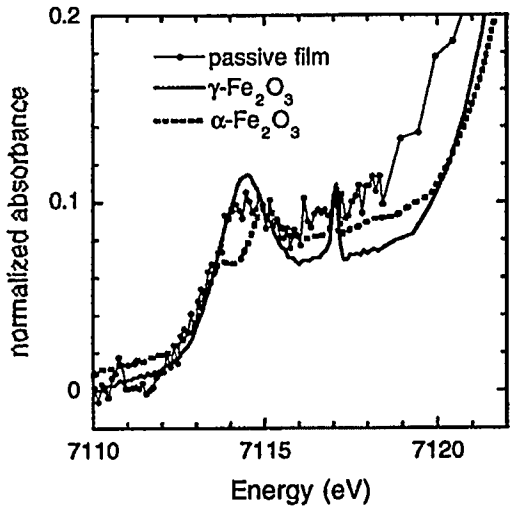


Figure 1. Detail of the pre-edge peak at the base of the Fe K edge for γ-Fe_2O_3, α-$Fe_2O_3$and the passive film on iron grown at +0.4V(MSE).

* Work supported in part by the US DOE Contract DE-AC02-76CH00016.

K-edge EXAFS study of carbon monoxide dehydrogenase from clostridium thermoaceticum	X10C

C. Y. Ralston, B. J. Weiss, J. H. Christiansen, D. Le, and S. P. Cramer (Univ. California, Davis), M. Kumar, and S. W. Ragsdale (Univ. Nebraska, Lincoln)

Carbon monoxide dehydrogenase from Clostridium Thermoaceticum (Ct-CODH) is responsible for the oxidation of CO to CO_2 and for the synthesis of acetyl CoA. These two functions occur at different Ni-Fe sites within the enzyme [1], termed site A (acetyl CoA synthesis) and site C (CO oxidation).

It was recently reported that treatment of Ct-CODH with 1,10-phenanthroline (phen) eliminates the acetyl-CoA activity while not affecting the CO oxidation activity of the enzyme [2]. It is therefore thought that phen treatment selectively removes the Ni from site A. The phen treated enzyme can be reconstituted with Co, which results in 40% regained acetyl-CoA synthesis activity.

We have collected EXAFS data at the Ni edge of native Ct-CODH and at the Co edge of phen treated and Co reconstituted Ct-CODH. Preliminary data analysis of the Co EXAFS suggests that the Co is coordinated by 2 S at 2.27 Å and 2-3 N/O at 2.06 Å, with a long Co-Fe interaction at 3.01 Å. Although the local structure of Co in site A may differ from the native Ni in site A, the EXAFS analysis is consistent with the proposed Ni-X-Fe structure [3], and will help elucidate the mechanism of acetyl Co-A synthesis in Ct-CODH.

[1] M Kumar et al., J. M. Am. Chem Soc., 115, 11646-11647(1993).
[2] W. Shin et al., J. Am. Chem. Soc., 115, 5522-5526 (1993).
[3] C. Fan et al., Biochem., 30, 431-435(1991).

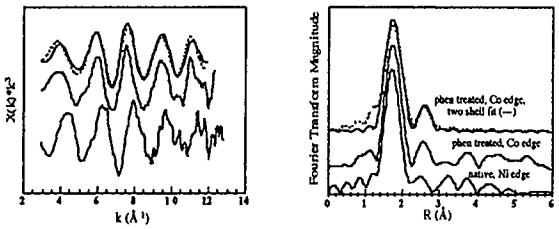


Figure 1.

Reflectivity study at the sulphur k-edge of the lubricating oil additive	X10C

M. Sansone (Exxon), E. S. Ferrari, C. A. E. Peacock, and K. J. Roberts (Univ. of Strathclyde, Glasgow, UK)

Surface modification additives, such as Zinc Dialkyldithiophosphates (ZZDPs), have long been used in the formulation of lubricating oils because they significantly improve the wear resistance of metal engine parts. However the exact mode of operation of many of these additives is poorly understood. Thus the structure of the liquid/solid interface formed between lubricating oils and steel has been investigated by X-ray based surface analysis techniques, such as EXAFS and ReflEXAFS at the K-edge of each of the atoms involved in the anti-wear process (namely Zn, Fe, P and S atoms).

The in-situ decomposition of a sample of formulation oil, from room temperature up to 150°C, has been studied at the O K-edge and Fe, P, S L-edges on station U1A at Brookhaven NSLS during the summer of 1993. The results taken at these edges showed that the intensity of the peak corresponding to the Fe L-edges increases with the temperature, whereas the intensity of the Zn L-edge peak decreases going from room temperature to 135°C. It was also possible to establish that the reaction between the ZDDP and the iron at the steel surface is reversible below 75°C. Once the system has been heated at 135°C and the decomposition of ZDDP took place the reaction becomes irreversible.

During the summer 1994, the same in-situ decomposition study of ZDDP using the ReflEXAFS techniques has been carried out at the S K-edge. A sample of formulation oil has been decomposed using a furnace, built at Strathclyde University, which has been mounted onto the diffractometer available on station X10C at Brookhaven, NSLS. The angles of incidence chosen for the incoming beam were 1.2 and 1.8 degrees. This experimental set-up enabled us to study a thin layer of the interface formed between the steel and the lubricating oil containing the ZDDP. The fluorescence signal from the surface was recorded by a 13 elements solid state detector.

We plan to continue this work during the next year investigating different additive systems, to be studied not only at the S K-edge but also at the Zn Fe and Cu K-edges.

Site occupancy of ternary dopants in β phase transition metal aluminides *	X11A

M. Balasubramanian, D. Pease, J. Budnick, T. Manzur, and D. Brewe (Univ. of Connecticut)

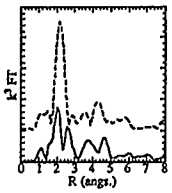
Darolia et al. [1] demonstrated that Fe doped transition metal (TM) rich NiAl single crystals exhibit significant ductility enhancement for small additions of Fe. Further, a much weaker ductilization was found for Co and Mo dopants. We have earlier reported that in TM rich, $Fe_xNi_{50}Al_{50-x}$, the added Fe dopants occupy the available Al type sites exclusively [2]. We have now investigated, using XAFS, the environments of various other dopants in NiAl and other related β phase systems. We find that, (1) In TM rich $Fe_2Co_{50}Al_{48}$, Fe dopants occupy the available Al type sites exclusively. (2) In Al rich $Co_2Ni_{46}Al_{52}$, Co atoms occupy the available TM type sites as expected. (3) In TM rich $Co_xNi_{50}Al_{50-x}$, Co atoms predominantly occupy the TM sublattice. Further, a systematic study shows that in such systems both Ni and Co atoms are found in the Al sublattice, with a greater preference for such occupation by Co relative to Ni, (4) In $Mo_2Ni_{50}Al_{48}$, Mo exists as small precipitates of bcc Mo.

Our findings are consistent with a simple model based on the relative heats of formation of binary TM aluminides. As the magnitude of the heat of formation of FeAl is much less than NiAl and CoAl, Fe atoms in $Fe_x(Ni/Co)_{50}Al_{50-x}$ are driven to Al type sites by Ni/Co. On the other hand, the heats of formation of NiAl and CoAl are similar and hence, both Ni and Co atoms occupy the Al sublattice.

Our findings also indicate that there appears to be a relationship between site occupancy and ductility enhancement. In other words, Fe dopants driven to Al type sites in TM rich NiAl seem to produce more ductility than Co and Mo dopants in similar system.

Figure shows the k^3 FT magnitude of Fe in $Fe_2Co_{50}Al_{48}$ (Dashed) and of Co in $Co_2Ni_{50}Al_{48}$ (Solid). We note that the FT of Fe dopants is similar to the FT of Fe in $Fe_1Ni_{50}Al_{49}$ (2) and that of the Co dopants is similar to the FT of TM (Ni, Co, Fe) in the corresponding binary TMAl (2). Hence, using the FT as a fingerprint one can immediately see that in $Fe_2Co_{50}Al_{48}$ Fe atoms occupy Al sublattice; while in $Co_2Ni_{50}Al_{48}$ the Co atoms occupy the TM type sites predominantly.

[1] R. Darolia, D. Lahrman, and R. Field, Scripta Metall. 26, 1007 (1992).
[2] P. Chartier, M. Balasubramanian, D. Brewe, T. Manzur, D. Pease, J. Budnick, L. Huang, C. Law, S. Russell, and C. Kimball, J. Appl. Phys. 75 (8), 3842 (1994).



* Supported by the U.S. DOE under contract Nos. DE-A505-80-ER-10742, DE-F602-90ER4524, and DE-FG05-89ER45384.

Local environment of Fe in nanostructured M50-type steel samples *	X11A

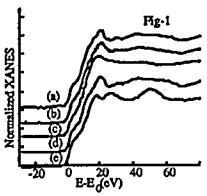
M. Balasubramanian, Y. Zhang, J. Budnick, and D. Pease (Univ. of Connecticut)

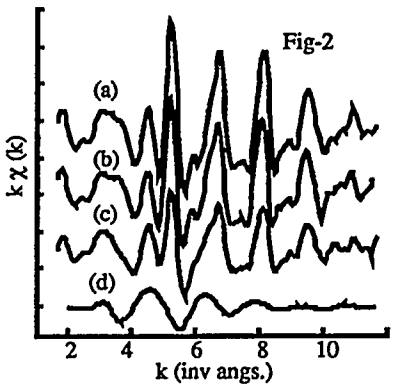
We have utilized XAFS and "zero-field" nuclear magnetic resonance (NMR) in the investigation of the local structure and magnetic properties of Fe in nanostructured M50 type steel. Nanostructured M50 type powders were prepared using a chemical route,[1] namely, either by the thermal decomposition of organometallic precursors or by the coprecipitation of metallic halides. A portion of the as-synthesized powders was consolidated. The average crystallite size of the consolidated specimen, calculated from x-ray broadening analysis, was about 45 nm for the powders obtained by the decomposition of organometallic precursors (hereafter, referred to as "sample O") and about 70 nm for powders obtained from the coprecipitation of the halide (hereafter, referred to as "sample H"). Our NMR results on the as-synthesized M50 type steel powders indicate that this material has a highly disordered phase(s) and some α-Fe. The NMR measurements further reveal that the particles are ferromagnetic in nature. XANES and EXAFS measurements show that the as-synthesized powder sample lacks long-range crystalline order and that the immediate near neighbor shells around Fe are not like bcc or fcc Fe (See figures). On the other hand, XAFS experiments on the consolidated samples clearly show that Fe in the sample is predominantly in the form of α-Fe with good long range crystalline order. However, the EXAFS amplitude (and the corresponding FT) of sample O is drastically reduced. This reduction cannot be attributed to particle size effects. Although the actual cause of the reduction in amplitude of the EXAFS oscillations in Sample O is not yet completely understood, we believe that some reduction might be due to the presence of micro-voids in the sample. Detailed data analysis and further experiments are in progress. We note that the XANES and EXAFS of as-synthesized M50 is different from bcc Fe. The XANES and EXAFS of sam. H and sam. O are similar. However the EXAFS amplitude of sam. O is reduced relative to bcc Fe.

Figure 1 below: XANES of Fe in (a) sam. H., (b) sam. O, (c) as-synthesized M50 powders, (d) bcc Fe,and that of (e) fcc Ni (Fcc Ni used to represent fcc Fe).

Figure 2 below: $k\chi(k)$ of Fe in (a) bcc Fe, (b) sam. H, (c) sam. O, (d) as-synthesized M50 powders.

[1] K. E. Gonsalves, et al., Nanostructured Mat., Vol. 4 (2), 139, (1994).





* Research supported by the U.S. DOE under contract Nos. DE-F602-90ER45424, DE-A505-80ER10742, and DE-FG05-89ER45384 and by the Precision Manufacturing Center, U. of Connecticut.

Local structure, phase stability and surface morphology studies of $(Ti_{1-x}Zr_x)Si_2$thin films on Si(100) and Si(111) *	X11A

Yuan Dao, R. J. Nemanich, and D. E. Sayers (North Carolina State Univ.)

$TiSi_2$ thin films are often considered to be the optimal choice for contacts and inter-connections in Very Large Scale Integrated (VLSI) circuits because of their low resistivity and high temperature stability. $TiSi_2$ has two different phases, a stable C54 phase with an orthorhombic face-centered structure and a metastable C49 phase with an orthorhombic base-centered structure. On the other hand, $ZrSi_2$ has only one stable phase: C49. Previous studies have shown that after annealing at high temperatures (700°C- 900°C), Ti films react with the silicon substrates and form the C54 phase of $TiSi_2$. However, the C54 phase films are prone to islanding due to their high surface free energy. Thus, the sheet resistance of the C54 $TiSi_2$ thin film increases as the surface roughness becomes larger at high annealing temperature (> 800°C). In order to grow a smoother $TiSi_2$ film, which has larger areal coverage of the film on the Si substrate after high temperature annealing (>700°C), we previously have grown $(Ti_{1-x}Zr_x)$ Si_2 thin films on Si(111) wafers. The alloy silicide thin films stay in the C49 phase at up at least 900°C. The C49 phase of $TiSi_2$ is stabilized with the presence of Zr atoms. Recently, we have grown $(Ti_{1-x}Zr_x)Si_2$ on Si(100) substrates. The Raman experiment results show that the 200Å thick alloy silicide thin films have the C49 phase at up to at lease 1000°C. The atomic force microscope (AFM) experiments showed that these alloy thin films have lower RMS surface roughness. $TiSi_2$ and $ZrSi_2$ phase segregation is not observed, since X-ray diffraction experiments showed that the d-spacing of (151) plane increases linearly with the Zr composition in the alloy film increases. X-ray absorption experiments were carried out at the beamline X-11A at NSLS to study the local structure of these alloy silicide thin films. To examine the local atomic structure around Ti and Zr, Ti K-edge and Zr K-edge EXAFS experiments were performed. To examine crystal orientation effects, data was collected with the sample surface oriented both parallel and perpendicular to the polarization of the incident X-rays. EXAFS fitting results show that the Zr-Si bond lengths in the C49 alloy films are shorter compared to the standard $ZrSi_2$ film. (As shown in figure 1.) The C49 alloy films annealed at high temperatures (~810°C) are more ordered than the C49 $TiSi_2$ films (~600°C). In addition, the C49 alloy films are more ordered in the perpendicular direction to the sample surface than the parallel direction.

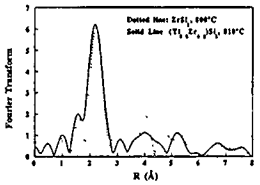


Figure 1. Fourier transforms of the k^3-weighted Zr K-edge EXAFS from 2.75 Å to 10.5 Å of C49 $ZrSi_2$ and $(Ti_{0.8}Zr_{0.2})Si_2$.

* This work is supported by the Division of Materials Science of the Department of Energy under contract DE-AS05- 80ER10742.

Charge distribution effects in $BaZrO_3$ by XAFS *	X11A

D. Haskel, E. A. Stern, B. Ravel, M. Newville (Univ. of Washington) and S. Heald(Pacific Northwest Laboratories)

A comparison between theory and experiment is made for hte XAFS of the Zr and Ba K-edges in $BaZrO_3$. $BaZrO_3$ is chosen because of its simple and well understood structure but combines metallic atoms with oxygens making its chemistry rich at the valence level. The theoretical XAFS was calculated using the FEFF5 code [1]. Experimental data at 10, 100, and 200 K was fitted in r-space through the fourth shell, including multiple scattering contributions. it is found that adding phase corrections to the theoretical XAFs calculated by FEFF5 significantly improves the accuracy of th structural parameters. These corrections are changes in the core electron threshold energy E_0 for each single scattering path involving a different type of backscattering atom.

The XAFs phase shifts are calculated by FEFF5 based on an overlapping relativistic atom muffin tin potential model. This model uses a constant interstitial charge density for the whole cluster of atoms which is certainly not true fo highly covalent materials where the charge density is bigger along the bonds. it also neglects charge transfer since it uses a sum of neutral atomic potentials. these chemical effects can be approximately compensated for by a change in the energy reference for each path, since both affect the XAFS phase mainly at low k. This together with the fact that no corrections were needed for pure metal Cu, suggests that the phase corrections needed are due to charge distribution effects which are neglected in the theory.

[1] J.J. Rehr, J. Mustre de Leon, S. Sabinsky, and C. Albers, J. Am. Chem. Soc 113, 5135 (1991).

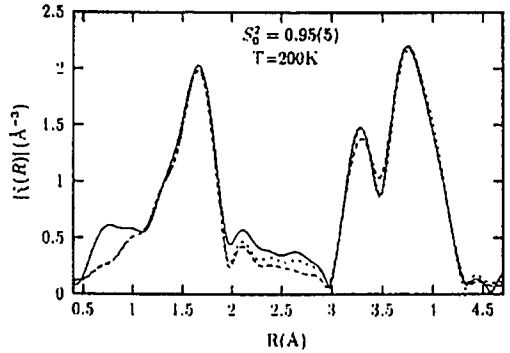


Figure 1. Fitting results for the Zr K edge. Solid line, data; long dashes, theory using overall ΔE_0; short dashes, theory using $\Delta E_0(i)$.

* This research has been supported by DOE grant No. DE-FG06-90ER45425.

An XAFS study of the oxidation of structural iron in biotite mica by solutions containing Br_2 or H_2O_2 *	X11A

S. M. Heald, J. E. Amonette, G. D. Turner (PNL), and J. D. Scott (Iowa St. Univ.)

Biotites, as Fe(II)-rich micas, have structures similar to (and serve as precursors for) clay-sized layer-silicate minerals such as smectites and vermiculites that dominate the chemistry of soils and sediments. To accommodate the charge imbalance created in these minerals by structural Fe(II) oxidation, several other changes, including ejection of structural cations, are known to occur. This abstract reports the first stage in a set of experiments aimed at understanding the changes in the Fe environment in micas undergoing oxidation. EXAFS measurements have been made on the Fe edge for a series of biotite micas oxidized to different extents by solutions containing either Br_2 or H_2O_2. The Fe in the Br_2-treated sample is nearly completely oxidized to Fe(III), while the H_2O_2 -treated samples showed an intermediate degree of oxidization. Both the near-edge and EXAFS for the H_2O_2 samples could be fit well by a linear combination of the untreated and Br_2-treated samples. The figure below shows the EXAFS result. The results of these fits were in good agreement with chemical analysis for the Fe(II) to Fe(III) ratio. This indicates that the partially oxidized samples have the two forms of Fe in distinct sites. Detailed analysis gave for the oxidized site a coordination of 5.7±0.5 with a Fe-O distance of 1.99 $\AA$. This is the expected result for Fe(III). More detailed analysis of the more distant shells is continuing to determine if the Fe remains in its original site.

* Pacific Northwest Laboratory is operated for the U.S. Department of Energy by Battelle Memorial Institute under Contract No. DE-AC06-76RL01830. Beamline X11 is supported by the U.S. DOE under Contract No. DE-AS05-80-ER10742.

X-ray absorption studies on the metal environments in $Ti_{1-x}Nb_xS_2$ phase	X11A

Geraldine Lamble (BNL), Sigrid Furuseth (Univ. of Oslo, Norway), and David Nicholson (Univ. of Trondheim, Norway)

The local environments about both metal atoms in a series of four compounds belonging to the $Ti_{1-x}Nb_xS_2$ phase ($0 < x < 0.98$), which crystallizes as golden, hexagonal platelets with the CdI2-type structure are known from x-ray diffraction. In these structures the metal atoms are sandwiched in layers, each being octahedrally coordinated to the sulphur atoms. These compounds constitute a graduated series of reference compounds for an x-ray absorption spectroscopic investigation on a closely related series of five compounds. The latter differ from the former in that the additional metal atoms are distributed over a given fraction of the interlayer positions. The coordination about these metal atoms is also octahedral. Questions to be addressed concerning structural; features of the latter include the identity of the interlayer atoms. These compounds have attracted extensive interest because of their anisotropic physical properties and their ability to serve as hosts in intercalation reactions. Whereas the reference compounds with the (Ti,Nb): S ratio or 1:2 are viable hosts the metal-rich series is of interest because the interlayer occupancy of metal atoms hampers corresponding intercalation reactions.

XAFS studies of atomic correlation in II-VI quaternary semiconductor alloys	X11A, X23

Q. Lu, B. A. Bunker, H. Luo, A. J. Kropf, S. H. Xin, J. K. Furdyna, and K. M. Kemner(Univ. of Notre Dame)

Recently developments in II-VI semiconductors have drawn a great deal of attention due to their success in blue-green laser diodes. In order to fully exploit these materials, detailed studies of their structural properties have become more important. II-VI alloys have not been as thoroughly studied as III-V alloys. In an attempt to study their structure properties, XAFS measurements were performed at liquid nitrogen temperature to study the local atomic correlations in the II-VI quaternary alloy $Zn_xCd_{(1-x)}$ $Se_yTe_{(1-y)}$. where x=y=0.5. Samples were grown by molecular beam epitaxy (MBE) on (100)B GaAs substrates, 4 degrees miscut towards the (111) direction. The Se edge fitted results, as shown in the figure below, show there are 2.6±0.3 Zn-Se bonds and 1.4±0.3 Cd-Se bonds on average, instead of the 2,2 as expected for a random alloy. This preference for Zn-Se bonds instead of Cd-Se bonds is consistent with XAFS studies of interfaces in ZnTe/CdSe superlattice.[1]

[1] K. M. Kemner, B. A. Bunker, H. Luo, N. Samarth, J. K. Furdyna, M. R. Weidmann, and K. E. Newman, Phys. Rev. B (Rapid Comm,) 46, 7272 (1992); and Phys. Rev. B, in press.

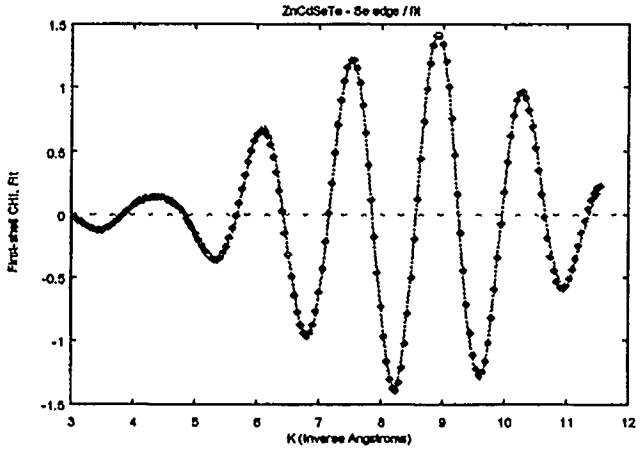


Figure 1. Fitted Se edge data for $Zn_{.5}Cd_{.5}Se_{.5}Te_{.5}$. Points are experimental data, the solid line is the computer generated fit.

Glancing angle EXAFS studies of GE "pre-melting" at the Ge/C interface	X11A, X23

Q. Lu, B. A. Bunker (Notre Dame), R. A. Mayonovic (Southwest Missouri State Univ.),A. J. Kropf, S. T. Ruggiero (Notre Dame), J. R. Buschert (Goshen College)

Melting is one of the fundamental phase transitions. Although recently a number of experiments have shown that surfaces play an important role in melting, "premelting" near internal interfaces has not been nearly as well studied. These concepts are important not only for understanding the basic melting process, but also in technologies such as power metallurgy, crystal growth, and advanced composite materials. XAFS with glancing-angle x-ray reflectivity is performed to study the "premelting" behavior of single crystal Ge (110) and (111) at buried interfaces in Ge/C and other systems. The sample was fabricated by RF sputtering 1000A graphite on one half of a two inch diameter Ge single crystal wafer at 10^{-6} torr. The goal of this experiment is to study the magnitude and anistropy of vibrational amplitudes as a function of temperature below the melting point. XAFS measurements were performed with the x-ray polarization parallel and perpendicular to the interface at various temperatures. By varying the angle of incidence, it is possible to obtain depth-dependent structural information with the sampling depth varying from 10A to 50A. From these experiments the effect of the top several layers near the interface is expected. Results for the (110) and (111) orientation will be compared. Further data analysis on these measurement is underway.

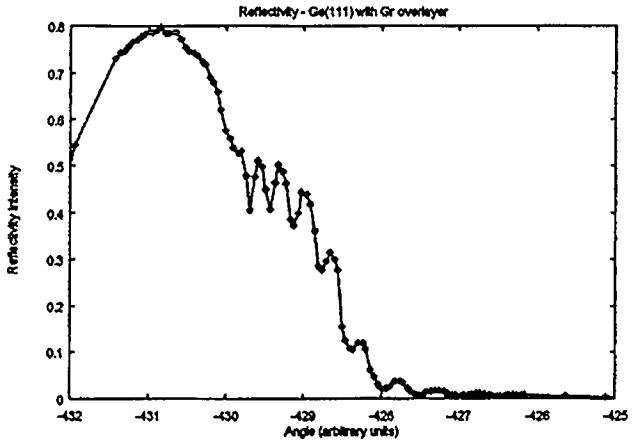


Figure 1. X-ray reflectivity measured at room temperature, 11.403 KeV, with the x-ray polarization perpendicular to interface

Atomic structure of sputtered amorphous $Al_{100-2x}Co_xCe_x$ (x=8, 9 and 10) and $Al_{80}Fe_{10}Ce_{10}$ alloys *	X11A

A. N. Mansour (Naval Surface Warfare Center)

Aluminum based metallic glasses with remarkably high Al content are relatively new materials. These amorphous alloys can be prepared with extremely high aluminum content either by vapor quenching using dc magnetron sputtering method or rapid solidification from the liquid phases using the melt-spinning method. The amorphous phase is formed with an Al content as high as 84 atomic percent for samples prepared by the magnetron sputtering process and as high as 90 atomic percent for samples prepared by the melt-spinning process. These materials are truly non-crystalline alloys which combine the properties of a metal with the short range order of a glass. They are very homogenous and lack the defects such as grain boundaries and dislocations typical of a crystalline material. The homogeneity and the lack of grain boundaries have led to a number of remarkable mechanical and magnetic properties.

A fundamental understanding of the effects of preparation methods and composition on the ease of glass formability through determination of the local atomic structure is necessary so that preparation conditions can be tailored to produce alloys with high stability. Hence, we report on the local atomic structure in the vicinity of Fe and Ce in magnetron sputtered $Al_{100-2x}Co_xCe_x$)x = 8, 9 and 10) and $Al_{80}Fe_{10}Ce_{10}$ amorphous alloys as determined by XAFS spectroscopy.

From analysis of the XAFS data at the K-edges of Co and Fe and the L_3-edge of Ce, the following conclusions with regard to local structure are made. The first coordination sphere of Co in $Al_{1---2x}Co_xCe_x$ (x = 8, 9 and 10) consists of 5.8 to 6.4 Al atoms at a distance of 2.44 Å. The local coordination sphere for Fe in $Al_{80}Fe_{10}Ce_{10}$ consists of 6.4 Al atoms at a distance of 2.47 Å. Ce in both systems appears to be coordinated with roughly 5 and 9 Al atoms at distances of 2.95 and 3.15 Å, respectively. These results are discussed in light of the dense random packing (DRP) of hard spheres model. Both Co-Al and Fe-Al bond lengths are anomalously short (9anomalously low coordination numbers (45using the metallic state radii. These anomalous changes indicated a strong interaction between Co or Fe atoms and the Al atoms which perhaps may be a result of a covalently bonded environment. The Ce-Al distance in both the Al-Co-Ce and Al-Fe-Ce systems, on the other hand, is smaller by only 0.17 Å(a contraction of only 5from expected values based on the DRP model. The contraction in the distance and reduction in the coordination number for Ce are much smaller than those values for Co or Fe and, hence, the local bonding for Ce is likely to be metallic in character. In addition, we show that the composition of the glass forming region of these magnetron sputtered alloys strictly follows the theoretical limit calculated on the basis of the atomic size criterion.

* This work was supported by the Independent Research (IR) Program of the Naval Surface Warfare Center. We also acknowledge the support of the U.S. DOE under contract Number DE-AS05-80-ER10742 for its role in the development and operation of Beamline X11A.

A study of the structure of passive oxide films on amorphous Al-Fe-Ce alloys *	X11A

A. N. Mansour (Naval Surface Warfare Center) and C. A. Melendres (ANL)

Aluminum based metallic glasses are of technological importance due to their high strength, and low density. Due to lack of grain boundaries, it is expected that this material will have high resistance to corrosion. Amorphous samples in the form of 25 micron thick ribbons with nominal composition, $Al_{90}Fe_xCe_{10-x}$ (x = 3, 5 and 7), were prepared by rapid solidification from the liquid phase using the melt-spinning method. Passive films were formed in 0.9 wtanodizing below the pitting potential for 60 minutes. The 0.9 wtacidic with a pH equal to 5.1. The passivated samples were then removed from the solution and dried in a stream of nitrogen gas. The effect of sample rinsing with copious amounts of deionized H_2O on the chemistry and structure of passive films was also investigated.

XAFS spectra of the Ce L_3-edge and Fe K-edge data for the alloys were obtained using transmission, fluorescence and total electron yield detection modes. The fluorescence and total electron yield data were obtained using a specialized fluorescence ion chamber detector and total electron yield detector, respectively. Due to surface sensitivity of the electron yield data and, hence, enhanced sensitivity to the passive film structure, only results from the electron yield spectra for the passivated alloys will be discussed.

Analysis of Fe K-edge XANES data reveals that iron in the passive film for the three alloys appears to be present as in Fe_3O_4 and γ-Fe_2O_3. The Ce L_3-edge XANES spectrum for passivated $Al_{90}Fe_7Ce_3$ resemble more closely that of $Ce(NO_3)_3$ while that of passivated $Al_{90}Fe_3Ce_7$ is identical to that of CeO_2. The spectrum for passivated $Al_{90}Fe_5Ce_5$ is intermediate between those of $Ce(NO_3)_3$ and CeO_2. Based on these results we conclude that the oxidation state of Ce in the passive film of $Al_{90}Fe_7Ce_3$ is mainly +3. For $Al_{90}Fe_3Ce_7$, Ce in the passive film is present only in the +4 oxidation state. Ce in the passive film of $Al_{90}Fe_5Ce_5$ is present in both the +3 and +4 oxidation states. This indicates that the fraction of Ce in the +4 oxidation state increases with increase in the Ce content of the alloy. XANES spectra of passivated alloys rinsed with copious amounts of deionized H_2O show that the fraction of Ce in the +3 oxidation state decreased relative to that characteristic of passivated samples dried in a stream of nitrogen gas. Thus, the effect of H_2O rinsing on the chemistry of Ce in the passive film region is to oxidize a fraction of Ce present in the +3 state to Ce in the +4 state. No change in the chemistry in the chemistry of Fe is observed in samples rinsed with copious amounts of deionized H_2O vis. samples dried in a stream of dry nitrogen gas.

* This work was supported by the Independent Research Program (IR) of NSWC (ANM), and the U.S. DOE (CAM). We are grateful to Professor S.J. Poon, Dr. Y. He, and Professor G.J. Shiflet of the University of Virginia, Charlottesville, VA 22903-2458 for providing the samples used in this investigation.

In situ XAFS study of the structure of oxides formed on Ni thin film electrodes in KOH solution *	X11A

A. N. Mansour (Naval Surface Warfare Center) and C. A. Melendres (ANL)

We have used XAFS spectroscopy for "in-situ" structural determinations of oxides formed on a 200 Å Ni thin film electrode. The anodization of Ni was made in 5M KOH solution as a function of the applied potential using cyclic voltammetry in an electrochemical cell specially designed for in situ XAFS measurements. Room temperature XAFS spectra of the Ni K-edge were measured in the fluorescence mode. Figures 1 and 2 show in situ Ni K-edge XANES and Fourier transforms of k-weighted EXAFS spectra, respectively, where a): reference spectrum of a 4 μm thick Ni foil, b): 200 Å Ni thin film electrode mounted in the electrochemical cell with no KOH, c): 200 Å Ni film mounted in the electrochemical cell filled with 5M OH and held at open circuit potential (OCP) of 0.37 V, d): cycled electrode, 5 cycles, -0.5 to -1.10 V, 10 mV/sec, held at -0.70 V, (Ni^{2+} region), e): d)+20 cycles, -1.10 to -0.50 V, 10 mV/sec, held at -0.66 V f): e)+100 cycles, -1.10 to -0.50 V, 100 mV/sec held at OCP, g): f)+1 cycle, -1.10 to +0.50V, 10 mV/sec, held at +0.4 V (Ni^{3+} region), h): g)+held at -0.5 V. Preliminary analysis of spectra indicates that, under the conditions of our experiment, oxidation of only a fraction of Ni has been achieved. At most only 60% of Ni has been oxidized. Distinct features are observed in curves d) and g) corresponding to anodization in the potential range of -1.10 to -0.5and -1.10 to +0.5 V, respectively.

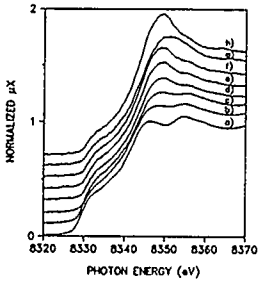


Figure 1. In situ XANES spectra of Ni K-edge for a 200 Å Ni film cycled in 5M KOH.

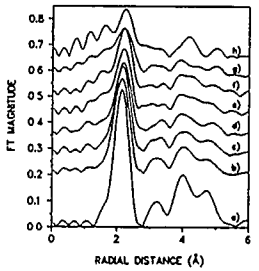


Figure 2. Fourier transforms of in situ Ni K-edge $k_x(k)$ for a 200 Å Ni film cycled in 5M KOH.

* This work is supported by ONR and the IR Program of NSWC (ANM) and by the U.S. DOE(CAM). We also acknowledge the support of the U.S. DOE for beamline X11A.

XAFS investigation of the structure and valency of nickel in some oxycompounds *	X11A

A. N. Mansour (Naval Surface Warfare Center) and C. A. Melendres (ANL)

We have examined the valency and local atomic structure of Ni in chemically prepared (CP) NiO, α-$Ni(OH)_2$, β-$Ni(OH)_2$, $Ni_2O_3 \bullet 6H_2O$, $Ni_3O_2(OH)_4$, β- NiOOH, γ-NiOOH, NiO_2 and $NiKIO_6$ and electrochemically prepared (ECP γ-NiOOH. Most of the compounds investigated were prepared by chemical synthesis following procedures established in the literature; others were purchased from commercial sources. Room temperature XAFS spectra of the Ni K-edge were measured in the transmission mode.

Analysis of the XANES data (not shown here) reveals, as expected, that the Ni K-edge energy shifts to higher energies as the oxidation state increases from Ni° (metallic Ni) to Ni^{2+} (NiO) to $Ni^{4+}$$NiKIO_6$. The observed shifts suggest that the average valency of Ni increases in the order α-$Ni(OH)_2$, $Ni_2O_3 \bullet 6H_2O$, NiO_2, $Ni_3O_2(OH)_4$, β-NiOOH, ECP γ-NiOOH, CPγ-NiOOH and $NiKIO_6$. The shift in edge energy, measured at half-height of the edge step, is roughly 2 eV per unit change in nickel valency taking the average valency of Ni in γ-NiOOH as +3. The pre-edge structure due to the transition from the 1s core level to unoccupied d-states has an intensity of roughly 3.5edge step and shifts at a rate of 1 eV per unit change in oxidation state of nickel.

Figure 1 shows comparison of Fourier transforms of Ni K-edge k^3-weighted EXAFS spectra in some oxycompounds (Δk of 2.6-16.1 $Å^{-1}$). The data were fitted using theoretical standards calculated with the FEFF Code (version 4.06). The local structure parameters for β-$Ni(OH)_2$ are consistent with the brucite C6 type structure. The $NiKIO_6$ first shell distance of 1.89 Åis consistent with what one expects for Ni^{4+}. The first shell for all other samples except NiO consist of a short and long distances characteristic of Ni^{4+} and Ni^{2+} local coordination, respectively, with varying fractions depending on preparation methods.

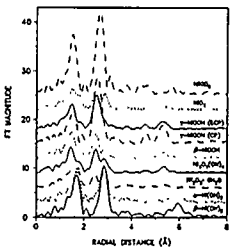


Figure 1. Fourier transforms of Ni K-edge k^3-weighted EXAFS data for some oxycompounds.

* This work is supported by ONR and the IR Program of NSWC (ANM) and by the U.S. DOE (CAM). We also Acknowledge the support of the DOE for beamline X11A.

Phase stability diagram of a carbon-supported palladium catalyst in C_2H_4/H_2mixtures at T = 373-498 K *	X11A

J. A. McCaulley (Hoechst Celanese Research) and F. W. Lytle (The EXAFS Company)

Pd K-edge x-ray absorption fine structure (XAFS) was used to characterize Pd-containing phases in a 5% Pd/C catalyst over the temperature range 373-498 K in C_2H_4/H_2 mixtures. Dilation of the Pd lattice, detected via the Pd-Pd nearest neighbor distance R_{Pd-Pd}, signals the presence of an interstitial solid solution, either a hydride (PdH_x), carbide (PdC_x), or ternary (PdC_xH_y phase. Although XAFS cannot directly distinguish between these phases, the topography of a 3-D plot of R_{Pd-Pd} vs T and composition reveals regions of stability of interstitial PdC_x and PdH_x phases. These plateaus are separated by ternary compositions in a miscibility gap between low- and high-occupation interstitial solutions.

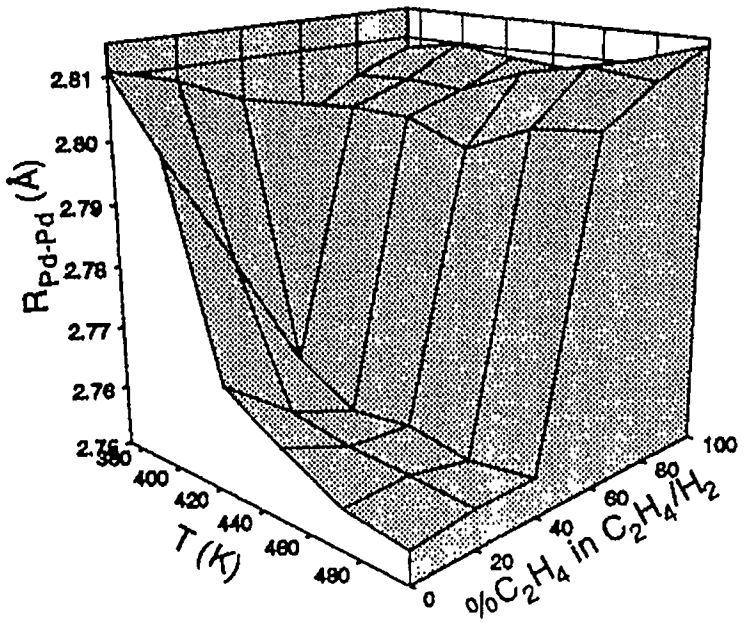


Figure 1. Dependence of the nearest-neighbor Pd-PdDistance on temperature and composition in C_2H_4/H_2

* This work was supported by the U.S. DOE under DE-FG05-89ER45384.

XAS studies of the corrosion of metal hydride electrodes *	X11A

S. Mukerjee, J. McBreen, J. J. Reilly, G. Adzic, and J. R. Johnson (BNL)

Metal hydride electrodes are rapidly replacing cadmium as the anode in rechargeable alkaline nickel batteries. The electrodes are either AB_2 or AB_5 alloys. The prototype AB_5 alloy, $LaNi_5$, is not stable with cycling. However, the stability of the electrode on cycling can be greatly improved by the addition of other alloying elements. In batteries there can be as many as nine components in the alloy. Degradation of the alloy with cycling is caused by corrosion. XAS is an ideal method for the study of alloy hydride electrodes because it is element specific and permits study of corrosion of individual components. XASat the Ni K edge was used to study Ni corrosion in a $La_{0.8}Ce_{0.2}Ni_{4.8}Sn_{0.2}$ alloy. Figure 1 shows Fourier transforms of the EXAFS for an unused electrode and an electrode that had been cycled 25 times in a battery. In the cycled material there is a peak at 1.5 Å, indicating the presence of $Ni(OH)_2$, the corrosion product of Ni. Analysis of the data for this peak yielded a Ni-O coordination number of 0.36. In $Ni(OH)_2$ the Ni-O coordination number is six. This indicates corrosion of about 6% of the Ni in the alloy. Figure 2 shows a comparison of the Ni XANES for an uncycled electrode, an electrode after 25 cycles, and a $Ni(OH)_2$ standard. In the cycled electrode there is indication of a white line. Comparison of the while line area with that for $Ni(OH)_2$ indicates corrosion of about 7% of the Ni. Thus the results from the XANES and EXAFS are consistent. The results demonstrate the power of XAS in corrosion studies of these complex materials.

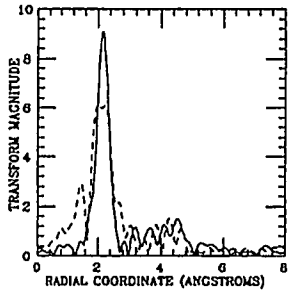


Figure 1. Fourier transforms of Ni EXAFS for $La_{0.8}Ce_{0.2}Ni_{4.8}Sn_{0.2}$ electrodes(a) uncycled (—), (b) after 25 cycles (- - -).

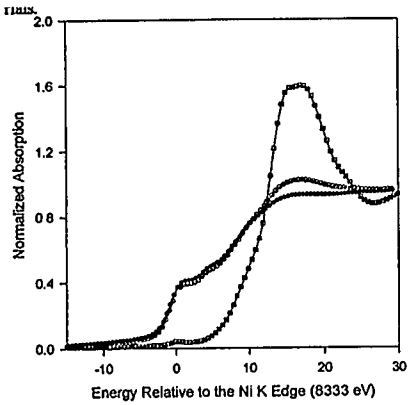


Figure 2. Ni XANES for $La_{0.8}Ce_{0.2}Ni_{4.8}Sn_{0.2}$ (a) uncycled(•),(b) after 25 cycles (o), and (c) for $Ni(OH)_2$ (open square).

* Work supported by the U.S. DOE under Contract No. DE-AC02-76H00016.

Local thermodynamic measurements of Ag-based alloys using XAFS *	X11A

Matthew Newville and Edward A. Stern (Univ. of Washington)

XAFS measurements over a temperature range of 200K to 900K have been made for pure Ag and for the minority components in the alloys Ga_xAg_{1-x}, and Au_xAg_{1-x} for $x = 0.05$. The temperature dependence of the partial pair distribution function for the Ag near-neighbor, $\rho_{Ag}(r)$ is found from the analysis of the XAFS data. The temperature dependence of these $\rho_{Ag}(r)$ are used to determine the effective one-dimensional anharmonic potential for the interatomic bond, using a form $V(r) = \frac{1}{2}ar^2 + br^3 + cr^4$. The three force constants a, b, and c have been determined for each bond and are shown in the Table.

This description of the interatomic bonds gives unique local information about the thermodynamic parameters of the systems. For example, the thermal expansion coefficient α can be found from the ratio of force constants b and a. The vibrational entropy can also be determined from these force constants. The table lists values for both α and $S_{vib}(T = 1200\,K)$ for the three systems. The value for α for pure Ag can be compared to bulk measurements, and agrees with the bulk value.

Bond	ΔR (Å)	a (eV/Å^2)	b (eV/Å^3)	c (eV/Å^4)	$\alpha\,(10^{-6})$	$S_{vib}\,(k_B)$
Ag-Ag	-0.005(3)	2.98(4)	-1.50(7)	0.84(12)	15(2)	2.99(4)
Ga-Ag	-0.037(8)	1.74(5)	-0.75(6)	0.58(15)	23(2)	3.11(4)
Au-Ag	-0.008(12)	3.11(6)	-1.53(11)	1.41(24)	14(4)	3.05(5)

Figure 1. Parameters of an anharmonic potential for Ag-Ag, Ga-Ag, and Au-Ag bonds found by XAFS. ΔR is the change in bondlength from the 300-K Ag-Ag bond length found by XRD. α is the coefficient of linear thermal expansion. Vibrational entropy values S_{vib} are given at T = 1200 K.

* This work has been supported by D.O.E grant #DE-FG06-90ER45425

A method of performing DAFS fluorescence corrections: basis of an enhanced intensitydesign *	X11A

Douglas Pease, Mahalingham Balasubramanian, Dale Brewe, and Joseph Budnick (Univ.of Connecticut)

Diffraction anomalous fine structure spectroscopy (DAFS) is a newly developing technique for obtaining x-ray absorption fine structure (XAFS) information for inequivalent sites of thesame element within a given sample[1,2]. One needs to use samples with a small absorption length for the element studied in order to minimize bulk absorption; however, for polycrystalline materials one mustthen deal a weak signal and consequent interfering fluorescence fine structure. We demonstrate the useof a simple subtraction technique which can be to large detector area more readily and inexpensivelythan enery dispersive detection [2]. Fig. 1 shows our results for a 3000 Angstrom film of polycrystallinecopper, (111) reflection, in which the fluorescence correction consists of subtracting the results ofa scan just off the (111) from a scan just on the (111) peak. Here we use a conventional Bragg - Brentanodiffractometer design.

We are constructing a DAFS spectrometer which will use two annular slits, one on and one just off a Braggpeak, to obtain fluorescence corrected DAFS in a similar manner to that used in the present case; however,the much larger collection angle should yield greatly enhanced intensities for polycrystalline samples. During a scan, the Bragg peak condition will be maintained by use of a precision translation stage.

[1] H. Stragier, J. O. Cross, J. J. Rehr, L. Sorensen, C. E. Bouldin, and J. C. Woicik, Phys. Rev. Lett.69, 1992, 3064.

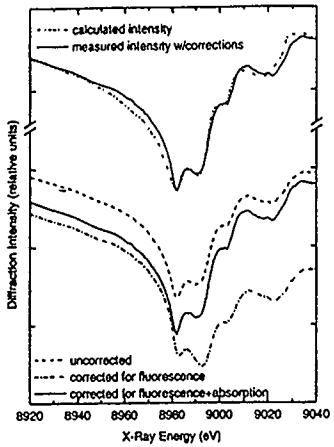


Figure 1.

* Supported by DOE contracts DEA505-80ER10742, DE-F602-90ER45424, and DE-FG05-89ER45384.

EXAFS and XRD studies of the phase formation of Co-SiGe reaction *	X11A

Z. Wang, R. J. Nemanich, and D. E. Sayers (North Carolina State Univ.)

Knowledge about reactions between thin metal films and epitaxial SiGe is essential for applications with SiGe devices.. We have investigated the phase formation of Co with SiGe alloys under different annealing processes. $Si_{0.80}Ge_{0.20}$ alloys of 800 Åin thickness were used for the study of Co-SiGe reactions under UHV annealing conditions. For each sample, a 200 Å Colayer was deposited onto room temperature substrates. The mettallized sample was then annealed in in-situ at a specific temperature ranging from 300°C to 700°C for 20 minutes.

We have reported our preliminary results last year that the Co k-edge EXAFS spectrum of samples annealed for 400°C to 600°C were similar to that of CoSi. Our fitting results show that the coordination numberi=s of first shell Si and second shell Co increases as the annealing temperature increases and the DW factors of Co-Si and Co-Co bonds decrease. No statistically significant Co-Ge number of bonds were found from fitting. These EXAFS data were taken with E parallel to the sample surface. X-ray diffract (XRD) pattern of these sample show same features as those of CoSi. However, the peak positions have shifted to lower angles in comparison with those of CoSi. This shift can be associated with an expansion of interplanar spacing. There are two possible explanations: (a) the formed compounds are $Co(Si_{1-y}Ge_y)$ or (b) the reacted layer is strained CoSi. To clarify if the thin films formed around 500 °C are strained, we have also measured EXAFS of the 500°C annealed sample with E perpendicular to the sample surface. Our fitting results show no difference between these two orientations. This indicates that the formed thin films are strained. Therefore, the line shifts in the X-ray diffraction patterns are caused by the formation of $Co(Si_{1-y}Ge_y)$. From their X-ray diffraction peak position, it is found that Ge composition y is 12% for the 400°C ample for 8% for the 600C sample.

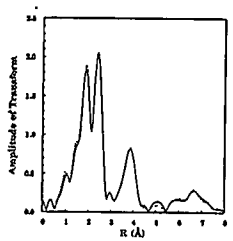


Figure 1. The Fourier transforms of k^{2-} weighted EXAFS oscillations from $3Å_{-1}$ to $12Å_{-1}$ of the 500°C annealed sample obtained with E parallel (solid line) and perpendicular(dashed line) to the sample surface.

* Work supported by US DOE Contract DE-FG05-89ER45384 and NSF Grant DMR 8717816.

Mineralization of ferritin depends on conserved glutamic acid side chains *	X11A

Z. Wang, G. S. Waldo, D. E. Sayers, and E. A. Theil (North Carolina State Univ.)

Ferritin is aprotein which concentrates iron billions of times above the solubility of the free iron. The purpose is to make ferric ions available to cells in a dioxygen environment, for use in respiration, photosynthesis and nitrogen fixation. To study the role of the protein in guiding the mineralization process, which has analogies to rust formation, cloned cDNA encoding ferritin subunits ere engineered to replace conserved glutamic acid residues (carboxylate side chains) with alanines (methyl side chains). Earlier EXAFS studies had indicated that carboxylates coordinated to small Fe(III)-oxo clusters with a functional role of nucleation sites. Genetically engineered with alanine in place of glutamic acid form minerals, but more slowly than the native sequence. EXAFS showed that only the natural sequence could have the Fe environment (Fe-Fe = 30 A) of the small clusters, while the protein with the alanine replacement had the Fe environment of the bulk mineral (Fe-Fe = 3.0 and 3.4 A) even though only a small number of iron atoms were added. Clearly the mutated residues were crucial for nucleation of the iron mineral inside ferritin.

* This research has been supported by NIH grant DK-20251 and DOE grant No. DeFG06-90ER45425.

The structure of denatured cytochrome C * | X11A

Y. Zhang and E. A. Stern (Univ. of Washington)

X-ray absorption fine structure (XAFS) measurements were made of native cytochrome c, denatured cytochrome c and its CO-bonded form. Our results show that the local structure around the heme site in denatured ferrous cytochrome c is not significantly different from the one in native ferrous cytochrome c. However, significant difference is found between the native ferric cytochrome c and denatured ferric cytochrome c. This difference is determined as a N or an O replacing S ligand of Fe in the heme site of denatured ferric cytochrome c. Our results also indicate that when CO binds to denatured ferrous cytochrome c, CO takes place of the S ligand, unfolding the denatured ferrous cytochrome c further.

* Research supported in part by the D.O.E Grant No. DE-FG06-90ER45425.

Spectroscopic studies of a palladium carbide phase * | X11B

G. Frank (Hoechst AG, Germany) and J. A. McCaulley (Hoechst Celanese Res. Div.,New Jersey)

When supported Pd catalysts are exposed to carbon-containing gases (e.g. ethylene) at high temperature, an interstitial carbide phase (PdC_x, x, ~0.15 may be formed. To facilitate identification of carbide phases in supported Pd and Pd-containing bimetallic catalysts, we have used a variety of spectroscopic techniques, including XPS, UPS, and XAFS to characterize "bulk" $PdC_{0.15}$. XPS analysis yielded a near-surface carbon concentration, 15.6±1.5 atom in $PdC_{0.15}$ are shifted 0.6 eV higher in binding energy than in bulk Pd metal. The asymmetry of the Pd 3d core levels is reduced, as is the intensity of core level and valence band satellites. Interstitial carbon in $PdC_{0.15}$ has a C 1s binding energy, 284.6 ±0.1eV, revealing the covalent nature of C bonding in the Pd lattice. XPS valence band spectra and He I and He II UPS spectra reveal a decreased density of occupied states near the Fermi level, E_F. The low DOS near E_F is responsible for the reduced asymmetry of the Pd 3d core levels and weak core level and valence band satellites. There is a weak peak ~6 eV below E_F in valence band spectra of $PdC_{0.15}$ that may be attributable to Pd-C bonding levels. Pd L_3-edge XAFS (see Figure 1) spectra reveal a shift of the white line maximum by 12 eV, decreased white line intensity, and decreased density of unoccupied states near E_F. No peak attributable to Pd-C antibonding levels was observed.

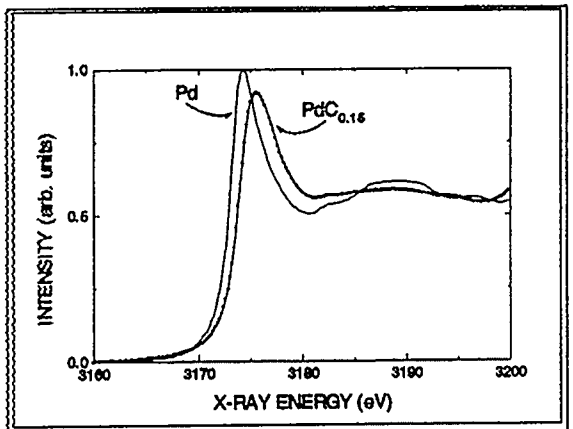


Figure 1. Pd L_3-edge fluorescence excitation spectra of 2000 Å Pd and $PdC_{0.15}$ films.

Figure 1.

* Work supported by the US DOE contract DE-FG04-89ER45384.

X-ray diffraction anomalous fine structure study of a supported Pt catalyst *	X11B

Qing Ma (North Carolina State Univ.), Jyh-Fu Lee (BNL), and D. E. Sayers (North Carolina State Univ.)

Diffraction Anomalous Fine Structure (DAFS) measurements were attempted on an as-prepared Pt catalyst ($Pt(NH_3)_4$/ZSM-5). The experiment was performed in the vicinity of the Pt L_{III} absorption edge using the x-ray beam delivered from the X11B line. For metal supported catalysts, it is important to know whether the location of the metal is on or in the support. Since DAFS is able to provide more selective information, such as the atomic structure around a specific site, our interest is to investigate the site occupancy of Pt in the catalyst and more importantly to test if the DAFS technique is suitable for structural studies of catalysts. The powder sample of the as-prepared catalyst was pressed into a disk of ~2 cm in diameter and with a thickness of about 300μm, which allowed a simultaneous measurement of scattering in reflection mode and absorption in transmission mode. Double Si(111) crystals were used to select the beam energy. The incident x-ray beam was monitored by an ion chamber. A Si:Li solid state detector was used to measure scattering. A second ion chamber was used to measure the x-ray transmittance. Two slits were used to define the incident beam size to 0.3×10 mm^2. A vertical slit with an aperture of 10×2 mm^2 was used in front of the Si:Li detector in order to include the energy dependent shift of the diffraction peak in the energy range of 600 eV.

Preliminary results suggested that for the as-prepared sample, all the Pt atomes appeared to exist in the tetramine complex. Further studies of this sample and of the treated samples using the DAFS technique are planned.

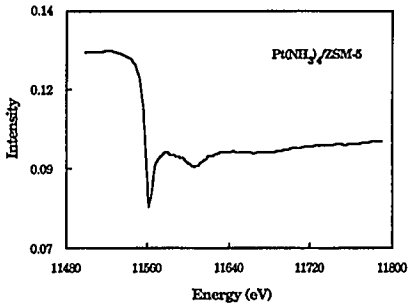


Figure 1. A typical scan measured at X11B that shows the intensity variation of a Bragg peak with energy around the PtL_{III} edge.

* This work is supported in part by the Mobil Research and Development Corporation. We would like to thank RickWood, Larry Fareria, and Gerry Lamble for their technical support.

Real-time x-ray scattering of binary polymer blends: poly(butylene terephthalate)/polycarbonate *	X12B

Mark V. Brillhart (MIT), Peggy Cebe (MIT), and Malcolm Capel (NSLS)

Our group has been studying crystallization kinetics and microstructure development in binary polymer blends [1-4] using real-time small angle X-ray scattering (SAXS). Here we describe our research on blends of a crystallizable polymer, poly(butylene terephtalate)[1], PBT, with an amorphous polymer, poly(carbonate), PC. PBT/PC blends are not believed to be miscible in the melt. This study was undertaken to determine whether the PBT crystallization kinetics were affected by the presence of low molecular weight PC. PBT and PC homopolymer and blend pellets were obtained from General Electric Corp. We report results from high molecular weigh PBT (M_W=108,000g/mol) blended with low molecular weight PC (M_W=19,100g/mol). Blend composition is specified by weight fraction and by molecular weight: 80H/20L refers to 80% high M_W PBT blended with 20Crystallized samples were prepared by cooling from the melt at 250°C and holding at 205°C, for 1 hr. Real-time SAXS experiments were performed at NSLS at elevated temperature. A Mettler hot stage was used to provide temperature control. The detection system was a 10cm × 10cm two dimensional position sensitive histogramming detector. The sample to detector distance was about 120cm and the X-ray wave-length was λ=1.28Å. Data were taken as a function of time during isothermal crystallization at 205°C. Due to the isotropic nature of our sample, circular integration of the diffracted intensity was used to increase the signal to noise ratio. Intensities were corrected for background, changes in incident beam intensity, sample absorption, and thermal density fluctuation. For 80H/20L, the long period begins to develop at about the 10^{th} time slice, or 150 seconds after equilibration at the crystallization temperature. The time development of the long period is much slower in 40H/60L. Here L does not develop until 500 seconds into the crystallization process. While the kinetics were affected by blend composition, other parameters were not. At the end of crystallization, the long period was about the same in the two blends, about 176Å. The lamellar thickness and linear crystallinity also did not vary. According to thermal and wide angle X-ray scattering analyses, total mass fraction crystallinity is reduced as the PC content of the blend increases. From real-time X-ray studies the rate of nucleation and rate of crystallization are reduced in blends with larger proportion of PC. However, after crystallization is completed, within the lamellar stacks, the linear crystallinity, long period and lamellar thickness remain about the same in 80H/20L as in 40H/60L. These results suggest that there may be partial miscibility in this blend.

[1] P. Huo, P. Cebe, and M. Capel. J. Polym. Sci., Polym. Phys. Ed., 30, 1459 (1992). [2] P. Huo, and P. Cebe. Macromol., 26, 5561 (1993). [3] P. Huo, P. Cebe, and M. Capel. Macromol., 26, 4275 (1993). [4] P. Huo, P. Cebe. Macromol., 26, 3127 (1993).

* Research was supported by U.S. Army Contract DAAH04-94-G-0317.

Crystallization study of liquid crystalline polycarbonates using real-time small angle x-ray scattering *	X12B

Yao-Yi Cheng, Peggy Cebe (MIT), Heidi Schreuder-Gibson (U. S. Army Natick RD&ECenter), Malcolm Capel (NSLS)

We report on crystallization and melting studies of recently synthesized monotropic liquid crystalline polycarbonates [1] based on aα-methyl stilbene and methylene-containing flexible spacer using real-time small angle x-ray scattering (SAXS). The flexible spacer number ranges from n=4–10,12. Crystallization behavior has been studied for these polycarbonates using differential scanning calorimetry and wide angle x-ray scattering [2].

SAXS experiments were done in transmission mode. A gas-filled two dimensional histogramming wire detector was used. All samples studied here were isotropic, so circular integration of the intensity was used to enhance the signal to noise ratio. The beam profile was treated according to pinhole geometry. The sample to detector distance was in the range from 1.46 m to 1.85 m, and was calibrated by cholesterol meristate and collogen fiber. X-ray wavelength was 1.49 Åor 1.53 Å. Data collection times range from 10 to 120 seconds.

SAXS data were taken at room temperature for HMS-4 to 10 crystallized by cooling at 5°C/min from the melt. HMS polycarbonates have alamellar structure in which stacks of lamellae alternate with amorphous material. Therefore, the one-dimensional electron density correlation function can be used to obtain long period, lamellar thickness, and linear crystallinity. Lamellar thickness and linear crystallinity show an odd-even effect for HMS-4 to 10. The even members of the series have systematically higher values of lamellar thickness and linear crystallinity.

SAXS data were also taken in real time during heating at 5°C/min. HMS-5 to 9 all show similar melting behavior during the heating scan, except that HMS-9 has lower melting temperature. Taking HMS-6 as an example, below 100°C, almost no melting occurs as seen from the nearly constant long period. But the linear crystallinity and lamellar thickness increase slightly due to further crystallization of the sample. However, between 100–135°C there is slight melting, which causes a slight increase of long period. The linear crystallinity and lamellar thickness still increase slightly, which suggest crystal reorganization during the heating scan. After 135°, major meltin occurs, which causes a drastic decrease of the invariant linear crystallinity and lamellar thickness, and a significant increase of long period.

[1] Bluhm, A.L.; Cebe, P.; Schreuder-Gibson, H.L.; Stapler, J.T.; Yeomans, W., Mol. Cryst. Liq. Crys. 239, 123(1994).

[2] Cheng, Y.-Y.; Cebe, P.; Schreuder-Gibson, H.L.; Bluhm, A.L.; Yeomans, W., Macromolecules 27, 5440(1994).

* Research was supported by U.S. Army Contract DAAL03-G-91-0134 and DAAH04-93-G-0347.

X-ray Scattering Studies of Motor Proteins	X12B

S. Fujiwara, D. Stone (UCSF), M. Capel (BNL), and R. Mendelson (UCSF)

Muscle contraction occurs through interactions between proteins called actin and myosin. We have been doing X-ray scattering experiments to obtain structural information of these motor proteins in solution under various conditions. The head region of the myosin molecule called S1 is particularly important because this head region interacts with actin. As a part of ongoing projects, we have measured scattering curves from S1. Since crystal structure of myosin S1 was solved recently, it will soon be possible to compare the crystal structure with the solution scattering curves. In order to do this, the scattering curve measured to high- angles is required. We measured the scattering curve from S1 at a concentration of 45 mg/ml. The curve was measured up to 0.35 nm^{-1} (see Figure).

It is important to investigate other motor proteins because they may have different mechanisms from the acto-myosin system. We have obtained scattering curves from a kinesin-related microtubule-based motor protein called "ncd" (nonclaret disjunctional protein). Analysis of these curves is underway.

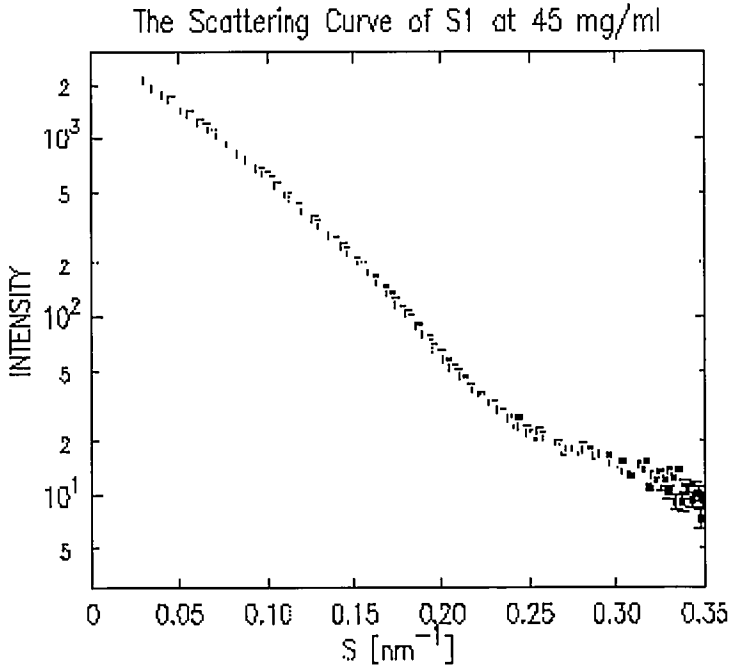


Figure 1.

Small angle x-ray scattering study of new-TPI thermoplastic polyimide *	X12B

Sharon Xin Lu (MIT), Peggy Cebe (MIT), and Malcolm Capel (NSLS)

We have used small angle X-ray scattering (SAXS) to investigate the crystal structure and crystallization behavior of NEW-TPI thermoplastic polyimide. Static and real-time SAXS have been employed to study both isothermal and non-isothermal cold crystallization of NEW-TPI from the rubbery amorphous state. Amorphous NEW-TPI sample was used directly for real-time SAXS. For static SAXS experiments, the amorphous samples were cold crystallized from 300 °C to 360°C until the completion of crystallization, as determined from our prior experiment [1]. The samples were then air-quenched to room temperature for the static SAXS measurements. SAXS experiments were done in transmission mode with a wavelength of 1.54 Å. Sample-to-detector distance was about 1.8m, calibrated using cholesteral meristate. The beam profile at the detector was treated according to a pinhole geometry. NEW-TPI sample was inserted into a Mettler hot stage, and the heating profile was controlled by computer. The isotropic SAXS intensity. The background and thermal density fluctuation was subtracted from the normalized scattering intensity. The one-dimensional electron density correlation function, Kz, was then calculated to obtain long period (L), lamellar thickness (l_c), crystallinity (χ_c) and interphase thickness of NEW-TPI. From the static SAXS experiments, we have observed that both L and l_c increase as a function of the cold crystallization temperature. A slope change in L has been observed at the temperature where NEW-TPI has the fastest crystallization rate, while no such change is found in l_c. Relatively more amorphous phase is included in between the lamellar stacks as the cold crystallization temperature increases. A slight decrease is observed for χ_c obtained from the correlation function. However, within experimental error, the change can be considered minimal. The interphase thickness has also been calculated and an average value of 22 Åis found for all the cold crystallization temperatures. Real-time SAXS study of non-isothermal cold crystallization of amorphous NEW-TPI has been carried out from 250°C to 350°C at a heating rate of 5°C/min. No scattering peak develops until the temperature reaches 300°C. From our SAXS analysis L shows a significant drop from 245 Åaround 305°C and levels off at ~203 Å when temperature reaches 322.5°C. l_c increases from 42 Å to 60 Å as temperature increases from 305°C to 315°C, then levels off up to 350°C. χ_c increases from 0.05 to 0.30 as temperature increases to 320°C and remains constant until 350°C. These observations can be explained using the lamellar insertion mechanism. The interphase thickness increases as a function of temperature from 300°C to 320°C, and then maintains a constant value of 25 Åup to 350°C. This interphase thickness is approximately one monomer repeat unit of NEW-TPI.

[1] P.P. Huo, J.B. Friler and P. Cebe, Polymer, 34, 4387(1993).

* Work supported by Electric Power Research Institute contract RP:8007-13.

Structural studies of human protein tyrosine phosphatase 1B *	X12C

D. Barford (Cold Spring Harbor Lab.)

Protein tyrosine phosphatases are signal transducing enzymes that catalyse the dephosphorylation of phosphotyrosine containing peptides and proteins. The structure of the complex of protein tyrosine phosphatase 1B with the substrate phosphotyrosine was determined. The crystals were obtained by replacing an essential catalytic site cysteine residue with serine. The mutant protein was crystallized and soaked phosphotyrosine. Data were collected on beamline X12C using the newly installed 30 cm MAR research image plate system. Al data were collected from a single crystal frozen using the Oxford Cryostream device. Data were collected to 2.3 Å resolution and the final scaling R-factor was 0.039.

The structure was determined using the existing structure of protein tyrosine phosphatase 1B that had been refined to 2.8 Åresolution. The new data allowed the positioning of the phosphotyrosine residue at the catalytic site of the protein and the identification of 246 water molecules. The tyrosyl moiety of the phosphotyrosine interacts with hydrophobic residues at the catalytic site of the protein and the structure explains the enzyme's specificity for phosphotyrosine containing substrates. The structure has been refined to give a crystallographic R-factor of 0.172 to 2.3Å resolution using all data.

* Work supported by Cold Spring Harbor Laboratory.

Crystal structure of yeast TATA-binding protein at 2.3Å resolution *	X12C

D. Chasman and P. Sharp (MIT)

We had determined previously the structure of the TATA-Binding Protein from yeast at 2.6Å resolution by molecular replacement from crystals diffracting to a maximum resolution of 1.7Å. A new data set was obtained having useful data extending to 2.3Å with the FAST detector on beamline X12C at the NSLS. The resolution of data collection was primarily limited by decay of the crystals during exposure to X-rays. The previous model was refined against the new data by positional refinement in XPLOR with shells of data representing resolution ranges of 20-60Å, 20.0-2.6Å, 6.0-2.6Å, and 6.0-2.3Å sequentially. Additional refinement of the model was performed by simulated annealing followed by tightly restrained refinement of B factors for individual atoms. The current R-factor for the model to 2.3Å resolution is 23.3%. Omit electron density maps define the model in regions which were unresolved by the previous data at 2.6Å resolution. Displayed below is electron density from a simulated annealing omit map calculated at 2.3Å resolution and circumscribing the omitted peptide backbone and valine residue.

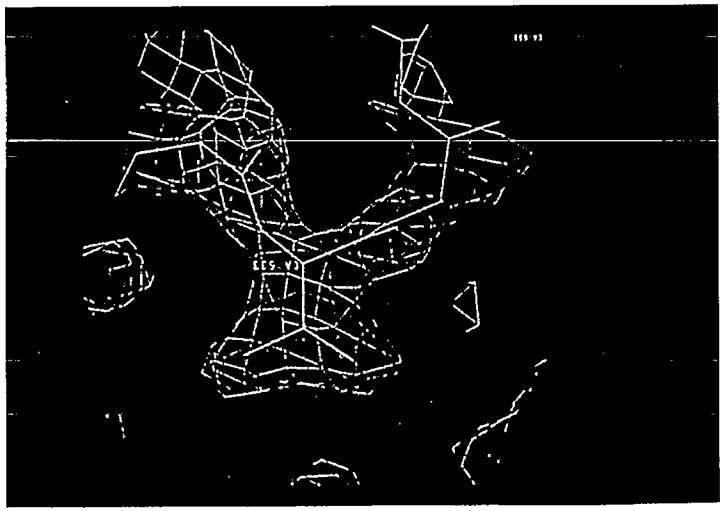


Figure 1.

* Work sponsored by grants DRG-1112 and P01-CA14051 from the Daymon Runyon-Walter Winchell Cancer Fund (D.C.)and the National Institutes of Health (P.S), respectively.

Crystallization and preliminary x-ray analysis of a 1:1 complex of Ospa and Fab184.1 *	X12C

Hong Li and Catherine L. Lawson (BNL)

Borrelia burgdorferi is the organism responsible for Lyme disease on Long Island. OspA is an abundant surface protein of Borrelia burgdorferi that has been found to trigger immunopathological processes. As an effort to aid in the vaccine development for Lyme disease, the crystal structure of OspA and its complex with the Fab fragment of a monoclonal antibody (Fab 184.1) will be determined.

Crystals of the OspA-Fab 184.1 complex (0.02 mm × 0.02 mm × 0.5 mm) were obtained from protein solutions containing a 1:1 ratio of the purified Fab 184.1 and OspA. The crystallization conditions are 50 mM Tris-HCl (pH 8.5), 80 mM $MgCl_2$, 4% glycerol and 6-12% polyethylene glycol 3.7 K. A native data set was collected at 4 °C at the X12C beamline of the NSLS. The OspA-Fab 184.1 crystals diffracted to a minimum d-spacing of 2.8Åat the synchrotron x-beam. However, crystals suffered from radiation damage and the initial data set yielded useful data only to 3.8Å. The R_{merge} on intensities is 12% and the completeness is 83%. The lattice type is primitive orthorhombic cell parameters of a=89.4Å, b=91.6Åand c=103.1 Å. Assuming the asymmetric unit cell contains one complex molecule, i.e., one OspA and one Fab184.1 molecule, the V_m value was calculated to be 2.64 $Å^3$/Da, indicating solvent content of approximately 56% [1]. Known structures of Fab fragments were used as models in the molecular replacement method to locate the orientation and the position of the OspA-Fab184.1 complex in its crystal lattice. A best solution was found when using only the constant region of a lysozyme antibody Fab fragment (HyHEL5). The crystallographic residual R is 46% for data between 10-4 Å when the entire HyHEL5 molecule is positioned according to the molecular replacement solution. Investigation of the correctness of the solution is underway.

[1] Matthews, B.W. (1968). Solvent content of protein crystals. J. Mol. Biol. 33:491–497.

* This research was supported by the U.S.Department of Energy Office of Health and Environmental Research.

Crystal structure of phosphoenolpyruvate carboxykinase from *E. coli* *	X12C

A. Matte, H. Goldie (Univ. of Saskatchewan), R. M. Sweet (NSLS), and L. T. J. Delbaere(Univ. of Saskatchewan)

The crystal structure of the enzyme phosphoenolpyruvate carboxykinase (PCK) from E. coli has been determined using multiple isomorphous replacement, and refined to a conventional R-index of 22.9% to 2.14 angstrom resolution. This enzyme catalyzes the decarboxylation and phosphorylation of oxaloacetate by ATP to form phosphoenolpyruvate and ADP, the first committed step in gluconeogenesis. This work represents the first crystal structure determination of this enzyme.

X-ray intensity data for a single crystal of PCK (0.125 x 0.275 x 1.0 mm) have been collected at ambient temperature on beam line X12C using a MAR image plate scanner. A total of 262,295 measurements were recorded yielding 46,961 unique reflections in the resolution range 50-1.9 Å. These data were 89% complete with | 3sigma| with an R_{sym}=8.9%. The PCK model is currently being refined against these data using simulated annealing in the program XPLOR 3.1, and so far has been refined to 2.14 angstroms yielding a conventional R-factor of 22.9%, and a R-free of 28.8%. The present model includes 530 residues consisting of 4912 protein atoms. The model has excellent geometry, with r.m.s. deviations of 0.007 angstroms in bond lengths, and 1.49 degrees in bond angles. A total of 88% of the residues fall within the most-favoured region of the Ramachandran plot. Refinement will be extended to 1.9 A in the near future and ordered solvent incorporated into the model.

PCK folds into one larger N-terminal domain, and a smaller C-terminal domain. The active site is located in a deep crevice between the two domains. The overall folding is that of a mixed, open-faced, twisted alpha/beta structure, similar to several other proteins which bind mono- and dinucleotides. Several amino acid residues possibly involved in substrate-binding or catalysis have been identified to date, including Arg-65, Lys-212, Lys-213, Lys-254, Arg-332, and His-232. PCK contains a consensus sequence for mononucleotide binding, Gly-X-X-Gly-X-Gly-Lys-Thr, part of which is seen as a glycine-rich "P-loop" motif in the crystal structure. Crystals of PCK grown in the presence of 2 mM ATP, 5 mM Mg^{2+} have recently become available, and will be used to determine precisely which residues interact with bound substrate. Other substrate complexes of the enzyme are also being prepared for structural analysis.

* Supportedby an Operating Grant to L.T.J.D. from the Medical Research Council of Canada.

Structure of monoclonal Fab fragment of Jel42 specific for HPr *	X12C

L. Prasad, M. Vandonselaar, J. S. Lee (Univ. of Saskatchewan), R. M. Sweet (NSLS), and L. T. J. Delbaere (Univ. of Saskatchewan)

The crystal structure of the Fab fragment of Jel42 has been determined by molecular replacement methods and refined to an R-factor of 24% at 2.5Åresolution. Jel42 is a monoclonal antibody specific for the histidine-containing protein HPr, a small phospho-carrier protein required for sugar transport in E. coli.

X-ray intensity data for this Fab fragment were measured using a crystal grown in microgravity during the space shuttle mission STS-62, at room temperature and at low temperature by flash freezing, on beamline X12C using a MAR image plate scanner. The protein crystallizes in space group $P2_1$ with two molecules in the asymmetric unit. The cell dimensions at low temperature are a=65.68, b=64.83, c=102.0Å, $\beta = 96.53°$. A total of 28500 unique reflections was measured with an Rsym of 0.09. The structure was solved using this data and the coordinates of the Fab fragment complexed with HPr, using the routine AMORE in the CCP4 package of programs. The structure was refined by simulated annealing using XPLOR.

The two independent molecules in the asymmetric unit have approximately the same orientation in the unit cell. However, there was no non-crystallographic symmetry between the two molecules and they have different elbow angles; 165.9° for molecule 1 and 169.7° for molecule 2. The two independent Fab fragments also interact with each other. There are extensive hydrogen bonds and van der Waals contacts between the hypervariable loops of the two fragments. Further refinement of the structure is in progress.

* Work supported by a grant from the Medical Research Council of Canada and a contract with the Canadian Space Agency to L.T.J.D.

Preliminary structure studies of Soybean l-3 lipoxygenase * | X12C

J. Steczko, W. Minor, B. Axelrod (Purdue Univ.), V. Stojanoff (BNL)

The primary objective of this research is to elucidate the structure-function relationship existing in lipoxygenases. lipoxygenases are non heme iron dioxygenases catalyzing the region- and stereo-selective oxygenation of fatty acids containing one or more 1(Z),4(Z)-pentadiene systems to form fatty acid hydroperoxides. Lipoxygenases are responsible for an important fraction of polyunsaturated fatty acid metabolism in both plants and animals. In mammalian tissues, lipoxygenases are involved in the initial steps of the biosynthesis of the leukotrienes and lipoxins. Leukotrienes are powerful leukocyte chemo-attractants and induce smooth muschle contraction, among many other postulated functions. Lipoxins appear to have a role in the preventing natural kiler cells from inhibiting the proliferation of certain types of cancers cells. Finally, the fatty acid hydroperoxides generated by lipoxygenases are thought to contribute significantly to the creation of atherosclerotic lesions.

From the many sequences now available it appears that the plant and animal enzymes are related. Several motifs in primary structure are retained in all 26 plant and animal enzymes examined. In addition, a number of single amino acid residues are invariant throughout this group. The degree of similarity among the sequences indicates that there may be common aspects of the structure which are related to the catalytic mechanism.

The monoclinic L-3 isozyme crystals belong to space group C2 with the unit cell parameters a=111.9 Å, b= 136.4 Åand c= 61.6 Åand =95.7°. Crystals diffracted to approximately 3.0 A on X12C station at Brookhaven. The L-3 structure is highly homologous to the structure of Soybean L-1 Lipoxygenase solved previously to 1.4 A. The function of the protein although is a different one. The Molecular Replacement solution has been already found. The ultimate solution fo the structure is under way.

[1] Minor, W., Steczko, J., Bolin, J.T., Otwinowski, Z., and Axelrod, B. Crystallographic determination of the active site iron and its ligands in soybean lipoxygenalse L-1, Biochemistry 32:6320-6323, 1993.

[2] Minor, W. Steczko, J. Bolin, J.T., Axelrod, B., and Otwinowski, Z. The crystal structure of L-1 isozyme of soybean lipoxygenase, XVI Congress and General Assembly International Union of Crystallography, Beijing (China), 1993.

* Support: NFS grant 9304565-MCB.

Structure analysis of Torpedo californica acetylcholinesterase-ligand complexes * | X12C

Joel L. Sussman, Michal Harel, Mia L. Raves (Weizmann Inst. of Science, Israel),Raimond B. G. Ravelli (Lab. Crystall. and Struct. Chem., The Netherlands), Helen Kycia, Vivian Stojanoff, Israel Silman (Weizmann Inst. of Science, Israel)

The inhibition of acetylcholinesterase (AChE), the enzyme that cleaves the neurotransmitter acetylcholine at the cholinergic synapse, is of great interest to clinicians and toxicologists, since anticholinesterase compounds are under active consideration for the management of Alzheimer's disease, and AChE is the principal target of organophosphate nerve agents. In addition, many commonly used insecticides belong to either the organophosphate or carbamate families of AChE inhibitors.

We have successfully soaked various inhibitors, including two organophosphate compounds, into trigonal crystals of native Torpedo californica AChE and determined their structure. The complex with paraoxon (p-nitrophenyl diethylphosphate), an insecticide, diffracted to 2.6 Å, and the complex with diisopropyl fluorophosphate (DFP) to 2.5 Å. Inhibition is known to occur as a result of covalent attachment of the organophosphoryl moiety or $O\ \gamma$ of the active-site serine, Ser200, and in both structures this attachment can be clearly visualized.

In the trigonal native crystals it was known that the entrance to the gorge that leads to the active site is actually blocked by a symmetry-related molecule. Despite this fact, long or bulky inhibitors (M.W. ca. 500) still have access to the active site, as evidenced by the crystal structures of the complexes. We have studied and orthorhombic crystal form which displays a similar packing arrangement. The asymmetric unit in this space group ($P2_12_12_1$) contains a dimer in which the monomers are related by a non-crystallographic two-fold axis.

We have cocrystallized Torpedo AChE with fasciculin 1, a neurotoxin that is found in the venom of the green mamba snake, Dendroaspis angusticeps, which exerts it toxic action by complexing tightly with AChE in the neuromuscular synaptic cleft. Crystals of the complex diffracted to 3.5 Å: a data set of 97% completeness with R_{sym}+8 solution with molecular replacement (using the AMORE program package). Further refinement of the structure is ongoing.

* Work supported by Netherlands Foundation for Chemical Research and Netherlands Organization for Scientific Research.

Crystal structure of casein kinase-1, a phosphate-directed protein kinase	X12C

Rui-Ming Xu (CSHL), Gilles Carmel (Molecular Geriatrics Corp.), Robert M. Sweet(BNL), Jeff Kuret (Molecular Geriatrics Corp.), and Xiaodong Cheng (CSHL)

Casein kinase-1 (CK1) is a family of protein kinases common to all eukaryotic cells. These enzymes phosphorylate many proteins in vitro, including SV40 T-antigen, glycogen synthase, the transcriptional regulators CREM, and p53. CK1 phosphorylation alters the activity of each of these substrates.

The structure of a truncated variant of casein kinase-1 from Schizosaccharomyces pombe, has been determined in complex with MgATP at 2.0Å resolution. The model of the 298-residue catalytic core resembles the "closed", ATP-bound conformations of the cyclin-dependent kinase 2 and the cAMP-dependent protein kinase, with clear differences in the structure of surface loops that impart unique features to casein kinase-1. The structure is of unphosphorylated, active conformation of casein kinase-1 and thee peptide-binding site is fully accessible to substrate. The proteinfolds into a small N-terminal lobe and a large C-terminal lobe. The cleft lying between the two lobes binds nucleotide substrate.

Trigonal crystals were subjected to X-ray diffraction on an Enraf-Nonius FAST television area detector at beamline X12-C of the National Synchrotron Light Source of Brookhaven National Laboratory. The wavelength was 1.0 Å for native crystals. When collecting mercurial derivative datasets, the incident energy was adjusted to 90 eV above the Hg L_{III} absorption edge (12.286 keV) to enhance anomalous signals (i.e., λ=1.0012 Å). Anomalous differences were determined from Bijvoet pairs that were measured simultaneously by aligning the crystals with the c-axis parallel to the rotation axis. Derivatization of the crystals was monitored prior to data collection by assaying the Hg L_{III} absorption edge through X-ray fluorescence measurements.

C_{60}/Ge(100) boundary structure *	X14A

R. D. Aburano, Hawoong Hong, K. Chung, M. C. Nelson, H. Chen, T.-C. Chiang (Univ. of Illinois, Urbana-Champaign), and P. Zschack (ORISE)

C_{60} films deposited on Si(111) and Si(100) substrates preserve the clean surface reconstructions. On one hand, this would not seem to be surprising since a C_{60} film is a van der Waals solid and should only weakly interact with an underlying substrate, thereby minimally disturbing the substrate reconstruction. However, studies have shown the interaction between C_{60} and various substrates including both above mentioned faces of Si, is beyond merely van der Waals bonding. This is especially true for metal substrates and metal induced semiconductor reconstructions where C_{60} lifts the reconstruction. One then has to wonder if the characteristics of Si make it an isolated and unique case. To determine this, we examined the boundary structure of a C_{60} capped Ge(100)- (2×1) surface.

This interface retains a Ge(100)-(2×1) periodicity at the boundary. We collected 28 symmetry inequivalent in-plane half-order and integer-order reflections. In addition, the surface (1/2 0), (3/2 0) and (1/2 1) half-order rods and the (1 0 L) integer-order rod were also measured. Preliminary comparison to UHV x-ray diffraction data of the clean Ge(100)-(2×1) surface show excellent overall qualitative agreement. Evaluation of our data sets with both theoretical and experimental clean Ge(100)-(2×1) structural models is underway.

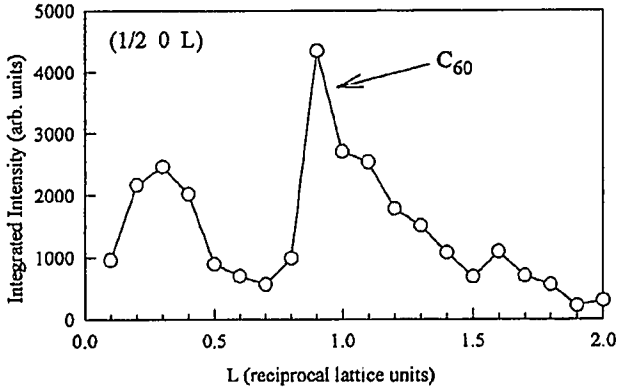


Figure 1. The (1/2 0 L) superstructure rod for the C_{60}/Ge(100)-(2×1) interface. The overall shape away from the C_{60} peak mimics the UHV clean surface rod.

* This work was supported by U.S. D.O.E. grant DE-FG02-91ER45439 (T.-C.C.) and contract DE-AC05-84OR21400 with Martin Marietta Energy Systems Inc. (P.Z.).

Atmospheric durability of a (4×4) C_{60} monolayer on Cu(111) * | X14A

R. D. Aburano, Hawoong Hong, M. C. Nelson, T. Miller, T.-C. Chiang (Univ. of Illinois, Urbana-Champaign) and P. Zschack (ORISE)

There is a strong interaction between C_{60} overlayers and metal substrates. Altman and Colton have shown deposition of C_{60} onto Au(111) substrates removes the surface reconstruction.[1] From STM studies, it appears a possibly even stronger interaction between C_{60} and a Cu(111) substrate exists.[2] In addition, numerous groups, including ours, have found Herculean efforts are necessary to remove the last monolayer (ML) of C_{60} from various surfaces. These facts coupled with the near invulnerability of C_{60} lead us to suspect the (4×4) overlayer structure of a single ML of C_{60} on a Cu(111) substrate would be preserved after exposure to the ambient atmosphere. This stability to atmospheric exposure was investigated with reflection high energy electron diffraction (RHEED) and grazing-incidence x-ray diffraction (GIXD).

For the GIXD experiment, a hexagonal surface coordinate system was used. We performed a number of in-plane reciprocal space line scans. The relative intensity between the 1/4- and 1/2-order peaks are consistent with the RHEED pictures from a vacuum annealed atmosphere exposed sample. A non-powder peak originating from the surface is also observed at the h=0.71 position, this corresponds to a d-spacing of 4.28Å. So far, we have been unsuccessful in identifying the cause of this peak.

The results of this GIXD experiment and the accompanying RHEED experiment have found the C_{60}/Cu(111)-(4×4) structure to be partially preserved under the atmospheric adsorbed layer. However, this (4×4) structural remnant was metastable and had a limited lifetime. These results are consistent with previous findings, and yield a clue as to the durability of C_{60} ML structures.

[1] E. I. Altman and R. J. Colton, Surf. Sci. 279, 49 (1992).
[2] T. Hashizume *et al.*, Phys. Rev. Lett. 71, 2959 (1993).

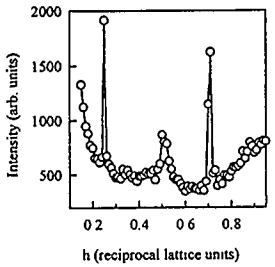


Figure 1. A reciprocal space line scan along the [h 0] direction. The (4×4) overlayer structure peaks are observed at the 1/4- and 1/2-order positions.

* This work was supported by U.S. D.O.E. grant DE-FG02-91ER45439 (T.-C.C.) and contract DE-AC05-84OR21400 with Martin Marietta Energy Systems Inc. (P.Z.).

Au/Si(111) anomalous truncation rods * | X14A

R. D. Aburano, J. M. Roesler, Hawoong Hong, T.-C. Chiang (Univ. of Illinois, Urbana-Champaign), and P. Zschack (ORISE)

The structure of the metal/semiconductor interface is a subject of continued interest in gaining a greater fundamental understanding of these systems. The confirmed correlation between macroscopic effects and the atomic structure at an interface only further enhances this interest. Following and paralleling our studies of the structure of Ag/Si(111) interfaces, we examined the Au/Si(111) interface.

We deposited a Au film on a room temperature Si(111)-(7×7) substrate. This interface, unlike the corresponding room temperature Ag/Si(111) interface, does not retain the (7×7) periodicity. In-plane k-space scans indicate the resulting periodicity is (1×1). The Si(1 0 L) truncation rod profile is markedly different from both the room temperature deposited Ag/Si(111)-(7×7) interface and a post-deposition annealed room temperature grown Ag/Si(111)-(1×1) interface. These differences may arise since the Au/Si(111) interface is known to be not as abrupt as the Ag/Si(111) interface and is in fact believed by a number of researchers to be diffusive. So in order to determine the role of Au at the interface, we measured the Si(1 0 L) rod profile at two separate energies below the Au L-III absorption edge. Further data reduction and structural modeling are currently underway.

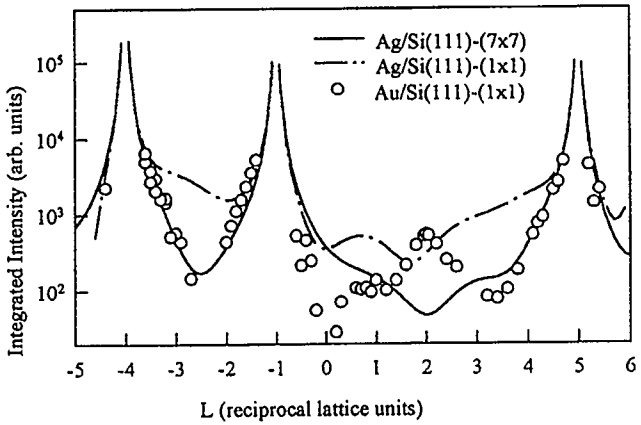


Figure 1. This figure shows the Si(1 0 L) truncation rod for Au/Si(111)-(1×1)along with current models of the Si(1 0 L) truncation rod profiles for the Ag/Si(111)-(7×7) and Ag/Si(111)-(1×1) systems. The intensities for the rod profiles are matched near the bulk Si Bragg peaks.

* This work was supported by U.S. D.O.E. grant DE-FG02-91ER45439 (T.-C.C.) and contract DE-AC05-84OR21400 with Martin Marietta Energy Systems Inc. (P.Z.).

Diffraction from a lipid monolayer along an isobar * | X14A

M. K. Durbin, A. Malik, R. Ghaskhadvi, A. Richter, P. Dutta (Northwestern Univ.),and P. Zschack (ORNL)

We used X-ray diffraction to study monolayers of nonadecanoic (C_{19} acid and arachidic (C_{20}) acid along a 15 dyn/cm isobar from very low temperature (0.5°C) to relatively high temperatures (50°C) near the melting point of the C_{19} monolayer. According to recent literature [1,2] this isobar should pass through at least three phase transitions. At the highest temperatures, we expect the monolayer to be in a distorted hexagonal (DH) lattice with the long chains of the molecules tilted towards their next- nearest neighbors. At even lower temperatures, we expected to see a transition between a DH lattice with chains tilted towards nearest neighbors (NN tilt) to a DH lattice with NNN tilt. Instead we found a transition from the NN phase to a phase with three strong first order diffraction peaks, similar to the phase Peterson et al observed at much higher temperatures. An example of the diffraction data from this phase shown below.

The fact that three peaks appear at these low temperature explains the commonly observed trend that the peak widths at low temperatures become asymmetric. Although only two peaks are observed from T=20°C to T=3°C, the width of the off-plane peak increases with decreasing temperature, until the point where three peaks are observed. We conclude that the wide second peak at low temperatures can be fit with two narrower peaks, which separate as temperatures is decreased.

[1] M.K. Durbin, A. Malik, R. Ghaskhadvi, M.C. Shih, P. Zschack, and P. Dutta, J. Phys. Chem., 98, 1753, (1994).

[2] I. R. Peterson, R.M. Kenn, A. Goudot, P. Fontaine, F. Rondelez, W.G. Bouwman, and K. Kjaer, submitted to Nature.

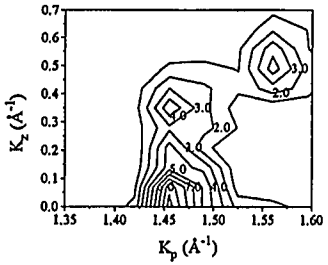


Figure 1. Contour plot of diffraction data from an arachidic acid monolayer at 1°Cand 15 dynes/cm, showing three strong first order peaks, Data are plotted as K_p/K_zcontours, where K_p is the magnitude of the diffraction vector in the horizontal plane, and K_z is the magnitude in the vertical direction. K_p cannot be broken up into component

* Works supported by USDOE grant DEFG02-84ER45125

Suppression of the magnetic moment in superconducting UPt_3 | X14A

E. D. Isaacs, A. P. Ramirez, G. Aeppli, C. Oglesby and E. Bucher (AT&T), P. Zschack(ORISE), C. L. Broholm (Johns Hopkins Univ.), C. Burns (W. Michigan Univ.), R. Erwin (NIST)

UPt_3 has been clearly established as a non-s-wave superconductor. Convincingevidence for such unconventional superconductivity was the discovery of a splitting of the superconducting transition in zero magnetic field observed in the specific heat. [1] It has been suggested, in analogy to the B phase in superfluid ^{3}He, that the splitting in zero field arises from the coupling of a superconducting order parameter with internal degrees of freedom (i.e., spin or orbital) angular momentum) to another symmetry-breaking field in the system. The most likely candidate for such a symmetry-breaking field is the weak antiferromagnetic order (μ_{ord}=0.02 μ_B, T_N = 5 K), which imposes an orthorhombic symmetry on the hexagonal lattice. Neutron scattering studies have indeed shown that the antiferromagnetic order parameter is affected as superconductivity develops below $T_c \sim$0.5 K, [2] but until now little has been known about how it is affected.

Therefore, we have used resonant magnetic x-ray to study the interplay of antiferromagnetism with superconductivity. The figure shows the magnetic x-ray scattering results from beamline X14A. Here we show that the superconducting order parameter brings about the same 10% reduction in the magnetic scattering at Q=(1/2,0,2) for two different scattering geometries - i) with the (h,0,1)-plane normal to the scattering plane (upper panel)and ii) with the (h,0,1)- plane in the scattering plane (lower panel). Similar results are obtained with neutron scattering. This unambiguously demonstrates that the supression in scattering intensity is due to a reduction in the staggered magnetization with no change in the symmetry of the antiferromagnetic order parameter. Our result is important because it establishes the form of the coupling term between antiferromagnetism and superconductivity in a phenomenological Ginzburg-Landau free energy functional.

[1] R. Fisher et al., PRL 62, 1311 (1989).

[2] G. Aeppli et al., PRL 63, 676 (1989).

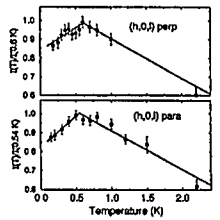


Figure 1. Resonant magnetic scattering in UPt_3 at Q=(1/2,0,2) for two different scattering geometries. Upper panel - (h,0,1)-plane normal to the scattering plane; Lower panel - (h,0,1)-plane in the scattering plane.

Local atomic arrangements in $Fe_{46.5}Ni_{53.5}$ * | X14A

X. Jiang, G. E. Ice, C. J. Sparks, and P. Zschack (Oak Ridge National Laboratory)

Many properties of crystalline solid solutions depend on the "atomic size" difference between alloying elements, and theorists are beginning to recognize the need to include displacements to resolve discrepancies between their calculations and experimental observations. We are using resonant (anomalous) scattering techniques to separate the individual pair displacements in a series of binary Fe-Ni, Fe-Cr, and Cr-Ni alloys. Previously we reported on the $Fe_{22.5}Ni_{77.5}$ composition. A more robust mathematical procedure has been developed to analyze the diffuse X-ray scattering from these crystalline solid solutions taken at three x-ray energies, the 3λ method [1]. This mathematical procedure makes use of the fact that a change in the X-ray energy changes only the X-ray atomic scattering factors while the atomic arrangements of the sample remain fixed. This permits writing two difference expressions for the 3λ's which are solved by nonlinear least squares. Though similar to the differential anomalous scattering DAS technique,[2] this method gives both chemical and interatomic distances for the three kinds of atom pairs in a crystalline binary solid solution out to ten or more neighbors. In Figure 1 below, we give the recovered first nearest neighbor displacements and interatomic distances between the three kinds of atom pairs in $Fe_{46.5}Ni_{53.5}$ compared with $Fe_{22.5}Ni_{77.5}$. These displacements are averaged over all the 10^{18} pairs of atoms illuminated by the X-ray beam. With increasing iron additions, the lattice parameter increases and we note that the Fe-Fe [110] distance remains rather constant near 2.564 Å while both the Ni-Ni and Fe-Ni first neighbor distances expand.[3] The hard sphere model is shown to be a poor approximation.

[1] G. E. Ice, C. J. Sparks, A. Habenschuss and L.B. Shaffer, Phys. Rev. Lett. 68, 863, (1992).

[2] P. H. Fuoss, P. Eisenberger, W.K. Warburton, and A.I. Bienenstock, Phys. Rev. Lett., 45, 1537, (1981).

[3] X. Jiang, G.E. Ice, C.J. Sparks, and P. Zschack, to be submitted to Phys. Rev. B.

	a_0(Å)	Average d_{110}(Å)	δ^{Fe-Fe}_{110} Å	Fe-Fe Pairs d_{110}Å	δ^{Ni-Ni}_{110} Å	Ni-Ni Pairs d_{110}(Å)	δ^{Ni-Fe}_{110} Å	Ni-Fe Pairs d_{110} (Å)
$Ni_{53.5}Fe_{46.5}$	3.5811(3)	2.5322(3)	0.0305(10)	2.5627	0.0011(3)	2.5333	-0.0117(8)	2.5205
$Ni_{77.5}Fe_{22.5}$	3.5512(5)	2.5111(4)	0.0539(17)	2.5650	-0.0006(3)	2.5105	-0.0034(9)	2.5077
Hard-sphere								
Pure Ni	3.5236(3)	2.4916(2)				2.4916		2.5107
Pure Fe	3.5776(5)	2.5298(3)		2.5298				

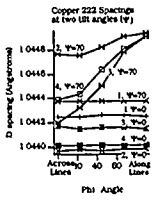
Figure 1. Average interatomic distances between first neighbor {110} pairs in NiFe alloys. The distances are the summation of the measured pairwise displacements and the lattice constant. Listed in the bottom two rows are the atomic distance calculated with the hard-sphere model which assumes that the atoms touch along the close packed direction. The atomic sizes for the hard sphere model are derived from pure Ni and fcc Fe corrected for thermal expansion to 300K.

* This research sponsored in part by the Division of Materials Sciences, US DOE Contract DE-AC05-84OR21400 with Martin Marietta Energy Systems, Inc.

Triaxial residual stress measurement for copper microcircuitry packaged in polymer | X14A

N.K. McGuire, C.E. Crowder, M.J. Radler (Dow Chemical, MI), C.G. Barnes (Dow Chemical, LA), and B. Rogers (MCNC)

The development of high density interconnection technology in multichip modules has necessitated the evaluation of stresses produced during manufacturing. Polymeric films insulate and separate layers of metallic circuitry supported on a rigid substrate such as a silicon wafer. During manufacture, the polymer is applied to the wafer as a viscous liquid, then cured at temperatures in the vicinity of 250°C. Upon colling, differences in coefficients of thermal expansion for the polymer, metallic interconnects, and the substrate produce residual stresses in the system. It is essential that these stresses be understood to engineer reliable designs for multichip modules. Synchrotron x-ray diffraction was used to measure residual strain in three orthogonal directions for several arrays of parallel copper lines, each line approximately 18 mm long $\times 8\mu$ wide. Two wavelengths of incident radiation were selected so as to position the x-ray diffraction peaks as far as possible into the back-reflection region, in order to maximize sensitivity to small changes in strain. The ability to select from a continuous spectrum of x-ray wavelengths is unique to synchrotron sources. Copper lines were patterned onto silicon wafers in the configurations shown in the table below (results for samples 1–4 illustrated in the figure below). Continuous films of copper were measured for each of the above configurations to obtain an unstressed lattice spacing for copper using the Haulk method. Since the lateral dimensions of the copper films were large compared to the thickness of the polymer layers, the stress in these samples is strictly planar. Approximately three weeks elapsed between fabrication of samples and the residual strain measurements. After the initial measurements were complete, two of the samples were heated under typical curing conditions and remeasured immediately after cooling to room temperature. Preliminary analysis of the data suggest that slightly higher strains are present in these immediately-cured samples. The main limitation to the quality of the data was the small number of metal grains exposed to the x-ray beam. This is a result of the very small angle of beam divergence at Beamline X14. Several measurements were repeated using an oscillating stage to expose a larger area of the sample to the beam. This produced a noticeable improvement in counting statistics.



	Copper thickness	Polymer underlayer	Polymer overlayer
1	2 µm	0 µm	0 µm
2	2	0	10
3	2	10	0
4	2	10	10
5	4	0	0
6	4	0	10
7	4	10	0
8	4	10	10

Atomic short-range order and static displacements in an $Fe_{62.3}Ni_{36.8}$ invar alloy * | X14A

J. L. Robertson, C. J. Sparks, G. E. Ice, X. Jiang (ORNL), S. Lefebvre (Univ. Paris-Sud),F. Bley (Univ. de Grenoble, France), P. Zschack (ORISE)

The most interesting physical properties of Invar alloys are the variation of the thermal expansion, magnetism and elastic modulus with external parameters such as temperature, pressure, composition and applied magnetic field. These properties have motivated extensive research on Invar alloys since their discovery around the turn of the century. Though the bulk properties of these alloys have been well characterized, [1] little is known about the local atomic environments so important to understanding these properties

Using anomalous X-ray scattering with X-ray energies 20eV below the Fe (7092eV) and Ni (8313eV) K edges as well as at 8725eV (which gives the minimum scattering contrast between Fe and Ni), we measured the diffuse scattering in a repeat volume of reciprocal space defined by the cubic symmetry reciprocal lattice vectors at two temperatures, 300K and 60K. Data we converted to absolute units (electron units) and reduced data containing only the Laue dependent scattering sets were obtained by subtracting the minimum contrast data (E=8725eV, scaled to the average scattering for the other contrasts). These data sets were then used in a nonlinear least- squares fit to determine the Warren-Cowley short-range order parameters and the first-order static displacements at the two temperatures.

The alloy shows only a slight preference for unlike first and like second nearest neighbors with the occupation probabilities becoming essentially random beyond the first three neighbor shells. As expected there was no observable change in the short range order between the 300K and the 60K data. Scattering from the first order static displacements or size effect shows a strong temperature dependence, see Figure. All atom pair (Ni-Fe, Ni-Ni and Fe-Fe) first and second neighbors move further from the average interatomic distance on cooling. Pairs closer than the average (Ni-Fe and Ni-Ni) become even closer on cooling while Fe-Fe pairs become even further apart. Further analysis may lead to a better understanding of the role local atomic structure on the physical (bulk) properties associated with Invar alloys.

[1] E.F. Wasserman,"Invar: Moment-Volume Instabilities in Transition Metals and Alloys" in Ferromagnetic Materials 5, edited by K.H.J. Buschow and E.P. Wohlfarth, Elsevier Scientific Publishers.

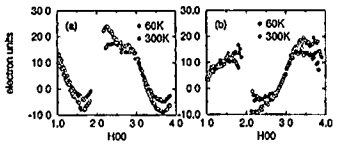


Figure 1. Contrast dependent scattering along the 100 direction for the (a) Fe-edge and (b)Ni-edge data. Note the contrast reversal between the Fe-edge and Ni-edge data.

* Work supported by the US DOE Contract DE-AC05-84OR21400 with Martin Marietta Energy SystemsInc.

The effect of colony microstructure on superconductivity * | X14A

E. D. Specht, A. Goyal, D. M. Kroeger (Oak Ridge National Lab.), J. E. Tkaczyk,and J. A. DeLuca (General Electric)

Thick $Tl_1Ba_2Ca_2Cu_3O_x$ superconducting films have been deposited on polycrystalline substrates by a spray process with potential for scale-up to useful lengths. While these films carry high currents, even in magnetic fields, the critical current within a film can vary by an order of magnitude. X-ray microdiffraction was used to map grain orientation over areas as large as $20mm^2$ with 0.1mm resolution. While the [001] axes of the tetragonal grains were aligned normal to the films, the overall [100] orientation was random. However, "colonies" of aligned grains were evident. Each colony contains some 10^4 grains with [100] axes aligned to within $\sim 10°$. Colony size ranges up to 1mm. In the map shown below, each cross corresponds to the most common orientation of the [100] axes at that point.

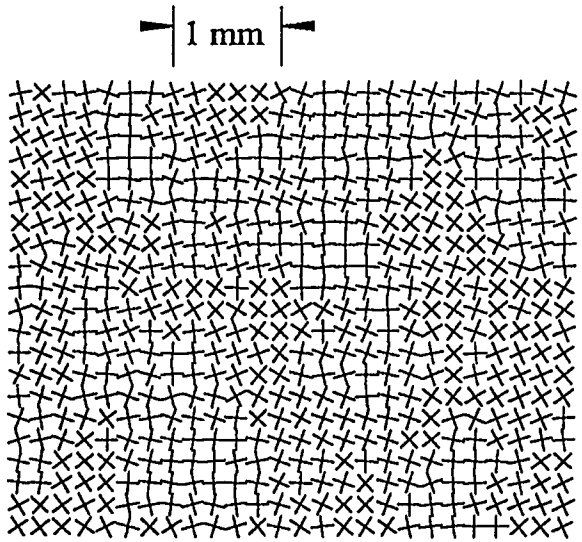


Figure 1. Using the known dependence of critical current on grain alignment, we have simulated the critical current for different portions of this film. We find that the variation in the simulated current agrees well with the observed variation.

* Work supported bythe US DOE Office of Advanced Utility Concepts—Superconducting Technology Program and Division of MaterialScience under Contract DE-AC05-84OR21400 with Martin Marietta Energy Systems, Inc.

Ordered structure of Si_xGe_{1-x} alloy thin films * | X14A

J. Z. Tischler, J. D. Budai, D. E. Jesson, G. Eres, and P. Zschack (ORNL), J.-M.Baribeau, and D. C. Houghton (Inst. for Microstructural Sci., Canada)

Ordering of $Si_{.5}Ge_{.5}$ alloy films grown epitaxially on Si (001) substrates was investigated by x-ray diffraction. Thin film alloy samples 3000 Å and 50 Å thick grown by MBE, as well as a 50 Å thick sample grown by pulsed CVD were measured, and half integral reflections arising from doubling of the conventional cubic unit cell were observed in all samples. The measured half-integral structure factors are compared to the calculated structure factors of three models in Fig. 1. The measured structure factors (including a non-zero 002 reflection) agree with the predictions of a bilayer step-flow model with ordering at kinks (the RS3 model) [1], and rule out the other proposed models, which are labeled RS1 and MS1 in Fig. 1. Only the RS3 model produces oscillations in phase with the measurements. In addition to the half integral reflections, other weak reflections of integral hkl that are forbidden in the diamond structure lattice were also measured. These reflections are explained by a secondary structure similar to ordered CuAu-I, but with the ordered planes perpendicular to the surface.

[1] D.E. Jesson, S.J. Pennycook, J. Z.Tischler, J.D. Budai, J.-M. Baribeau, and D.C. Houghton, Phys. Rev. Lett., 70, 2293, (1993).

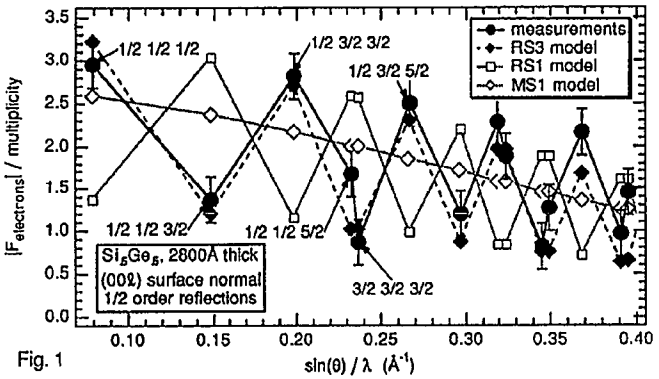


Figure 1.

* Work Supported by US DOE Contract DE-AC05-84OR21400with Martin Marietta Energy Systems, Inc.

Preferred domain orientation in ordered SiGe films grown on miscut Si (001) * | X14A

J. Z. Tischler, J. D. Budai (ORNL), P. Zschack (ORISE), J.-M. Baribeau, and D.C. Houghton (NRC, Canada)

When $Si_{0.5}Ge_{0.5}$ alloy films are grown on Si(001) substrates by either MBE or MOCVD at temperatures near 400° C, they show compositional ordering which manifests itself as Bragg reflections with half-integral hkl (as well as lattice-forbidden hkl reflections); We have previously observed two distinct types of ordering in $Si_{0.5}Ge_{0.5}$ films, the RS3 ordering and a weaker CuAu-I type ordering [1]. The RS3 ordered structure has alternating Si rich bilayers and Ge rich bilayers along one of the four ⟨111⟩ directions, and is the source of the observed half-integral reflections. The CuAu-I type ordering has Si bilayers and Ge bilayers along an in-plane ⟨100⟩ direction, and this structure produces the observed integral hkl lattice-forbidden reflections. For both of these structures there are four symmetry equivalent domain orientations for growth on a [001] surface.

X-ray measurements of the relative domain populations were made on $Si_{0.5}Ge_{0.5}$ MBE films grown on 4° miscut Si (001) substrates. These measurements show that the domains grow preferentially with the ordering direction in the direction of miscut. This result is demonstrated in the figure where the two strong peaks are equally distant from the [100] miscut direction. This observation holds true for both the half-integral reflections from the RS3 structure and for the integral lattice-forbidden reflections from the CuAu-I type structure.

By means of radial reciprocal-space scans through various reflections we have also determined that the RS3 ordered regions grow largest in the ordering direction, to a length of ~1200 Å, while in the perpendicular directions the ordered length is approximately one third as great. Thus the RS3 ordered domains form prolate ellipsoids that are three times longer than wide with their long axis along a ⟨111⟩ type direction.

[1] D.E. Jesson, S.J. Pennycook, J.Z. Tischler, J.D. Budai, J.-M. Baribeau, and D.C. Houghton, Phys. Rev. Lett., 70, 2293, (1993).

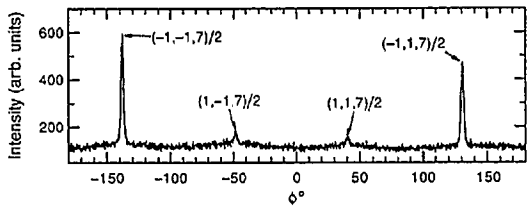


Figure 1. A phi scan for a sample miscut toward the [100] direction. It shows two strong domains and two weak domains.

* Work Supported by US DOE Contract DE-AC05-84OR21400 and with Martin Marietta Energy Systems, Inc.

Microscopic structure of the hexagonal and striped discommensurate phases of Ge(111)In	X15A

M. Boehringer (Max-Planck-Institut, Germany), P. F. Lyman (Northwestern Univ.), and J. Zegenhagen (Max-Planck-Institut, Germany)

The clean Ge(111) surface in equilibrium adopts the well known c(2x8) reconstruction which breaks the threefold symmetry of the bulk-truncated (111) surface. The c(2x8) reconstruction can be viewed as stripes of Ge adatoms (on T4 sites) in a 2x2 arrangement, separated by c(4x2) antiphase domain walls. After deposition of 1/100 ML amounts of In, STM shows that the Ge adatoms rearrange in hexagonal 2x2 domains , separated by a c(4x2) domain boundaries. Increasing the coverage beyond 0.1 ML, STM reveals a new striped phase on the surface. However, the width of the stripes, which are undoubtedly made of rows of Ge adatoms in 2x2 arrangement, fluctuates in width. The In must be located in dark stripes, separating Ge adatom rows, where is STM, however, cannot resolve the atomic structure. Increasing the In coverage further, the width of the Ge adatom rows decreases to a minimum and this discommensurate striped phase becomes almost commensurate (8x2). Above 0.3 ML the surface undergoes a phase transition and a hexagonal $4x\sqrt{3}$ reconstruction is revealed by STM.[1]

Using XSW, we have investigated the adsorption site of In in the striped and hexagonal, $4x\sqrt{3}$ phases. XSW scans are shown below. The analysis shows that In substitutes for Ge in the (111) top surface double layer in both phases. However, in the $4x\sqrt{3}$ phase In occupies positions in regular and reversed (stacking fault) positions. Most likely because of differences in surface strain, the vertical position (normal (111)) of the In is about 0.05Å higher in the striped phase.

[1] M. Boehringer, J. Zegenhagen, annual report Max-Planck- Institut-FKF, 1993, and Surf. Sci. to be published.

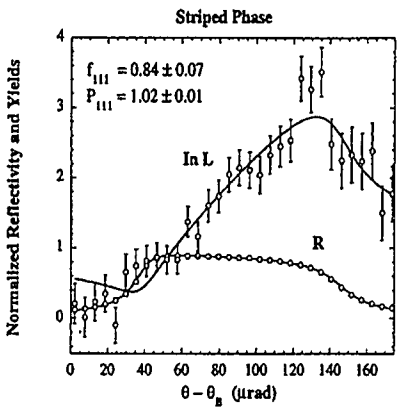


Figure 1.

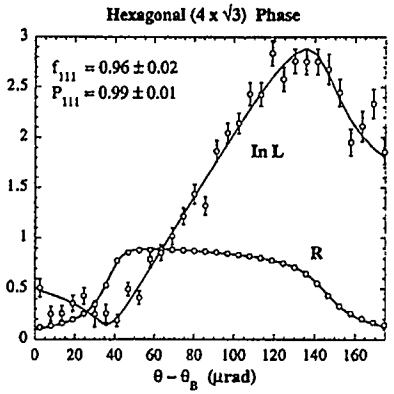


Figure 2.

Microscopic structure of the discommensurate phase of Ge(111)/Cu	X15A

P. F. Lyman (Northwestern Univ.), M. Boehringer, and J. Zegenhagen (Max-Planck-Institut,Germany)

On Ge(111), Cu induces a discommensurate phase which appears in STM topographs as almost periodic, hexagonal domain superstructure with a periodicity of about 36 Å. This structure forms at relatively low temperatures (about 100C) and exhibits a saturation coverage of 0.7ML. At room-temperature, the interior of the domains cannot be imaged with atomic resolution. However, at 50K a hexagonal arrangement of protrusions with a surface lattice constant about 5% larger than of the substrate (4 Å) can be resolved.[1] XSW measurements acquired after a 200C anneal revealed that Cu occupies a substitutional lattice site in this reconstruction in a regular and reversed stacking (stacking fault). This is evidenced not only by the coherent positions, but also by the moderately high coherent fraction found in the (111) scan, but the low coherent fraction in the off-normal (11-1) scan. Increasing the annealing temperature above 300C, the x-ray measurements prove that Cu starts to diffuse into the Ge bulk. STM shows that in parallel 3D islands of epitaxial Cu or Cu germanide start to grow causing the discommensurate superlattice eventually to disappear and leaving increasing areas of the Ge(111) surface with the native c(2x8) reconstruction.

[1] M.Boehringer, R.Berndt, W.-D.Schnedier, and J.Zegenhagen, to be publ.

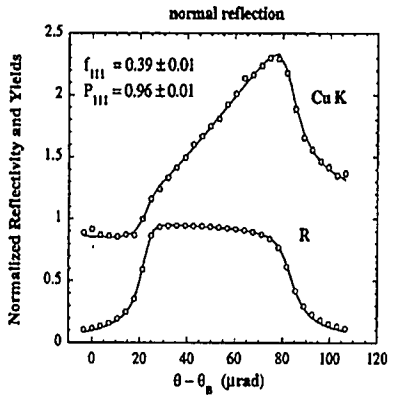


Figure 1.

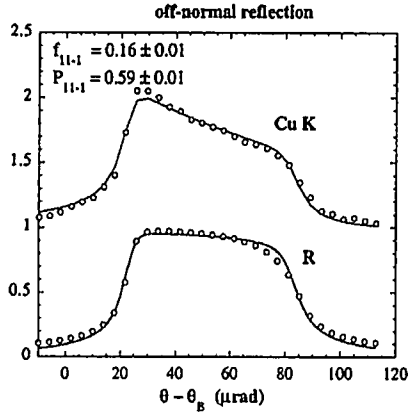


Figure 2.

Structure and substrate relaxation of the Sb/Si(001)-(2×1) surface *	X15A

Paul F. Lyman (Northwestern Univ.), Y. Qian, and M. J. Bedzyk (Northwestern Univ.and ANL)

The structure of the 1 ML Sb/Si(001)-(2x1) surface was determined using the x-ray standing wave (XSW) technique, and the relaxation of the subsurface Si was obtained by combining our results with previous measurements of the bond lengths. The Sb-terminated surface was created by MBE deposition of Sb onto the clean Si(001)-(2×) held at 550°C. The XSW measurements, which were carried out at beamline X15A of the NSLS, were made by monitoring the Sb L fluorescence while scanning through the Si(004) and Si(002) Bragg reflections. The theoretical and experimental angular dependence for the x ray reflectivity and the Sb fluorescence is shown in Figs. 1(a) and 1(b). Our results indicate that the Sb ad-dimer is located 1.64 ±0.01 Å above the bulk-extrapolated Si(004) atomic layer and that the Sb ad-dimer bond length is 2.81 ± 0.09 Å. While these results are largely consistent with the previously reported symmetric ad-dimer model, they indicate that the Sb-Sb bond is shorter than previously believed. When combined with previous SEXAFS measurements of the bond lengths, we can conclude that the top Si surface layer is contracted inward by 0.10 Å.

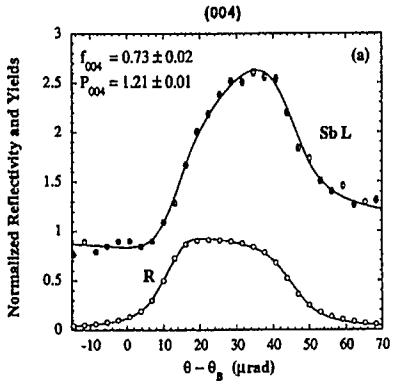


Figure 1.

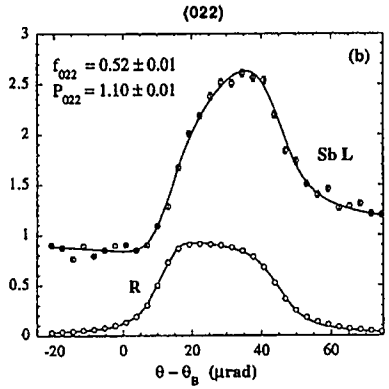


Figure 2.

* Work sponsored by the U.S. Department of Energy, Office of Basic Energy Sciences, Division of Materials Sciences,under contracts W-31-109-ENG-38 to Argonne National Laboratory and DE-AC02-76CH00016 to the NSLS.

X-ray standing wave investigation of the thermal vibrational amplitude of Ad-atomson Ga/Si(001) *	X15A

Y. Qian and M. J. Bedzyk (ANL and Northwestern Univ.)

We have used x-ray standing wave (XSW) techniques to perform a direct measurement of the thermal vibrational amplitude of Ga ad-atom on the SI(001) 2x1 surface at room temperature. For a 0.3 ML Ga coverage, both fundamental Si(004) and second-order Si(008) measurements were conducted on the Ga/Si(001) surface at room temperature. The incident photon energy was tuned at 12 keV, which is above the Ga K-edge. The (004) and (008) Si reflectivity and Ga Kα fluorescence yield data and fits to the dynamical theory of the x-ray diffraction are illustrated by Fig. 1 and Fig. 2. Measured coherent fractions and coherent positions are listed in Table 1. At room temperature, we found that the thermal vibrational amplitude of Ga ad-atom on the Si(001) surface is 0.135±0.01 Å. This represents the first direct measurement of the thermal vibrational amplitude on the Si(001) surface. This result also improved the accuracy of the Ga ad-dimer bondlength measurement when we combined the (022) measurement performed on the same surface. The Ga dimer bondlength is found to be 2.58 ± 0.04 Å, agrees very well with the predicted value from the previous theoretical calculation.

Table 1

	f	P
(004)	0.61 ± 0.01	0.77 ± 0.01
(008)	0.34 ± 0.02	0.58 ± 0.01
(002)	0.35 ± 0.01	0.91 ± 0.01

Figure 1.

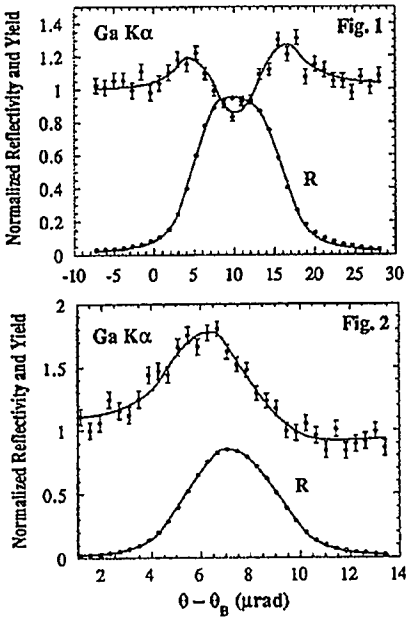


Figure 2.

* Work was sponsored by the U.S. De partment of Energy, Office of Basic En ergy Sciences,Division of Materials Sciences under contract W-31-109-ENG-38 and DE AC02-76CH00016 to the NSLS.

Resolving ad-dimer locations and orientations on the Ga/Si(001)-2×2 surface *	X15A

Y. Qian, M. J. Bedzyk (ANL and Northwestern Univ.), G. E. Franklin (HarvardUniv.), S. Tang and A. J. Freeman (Northwestern Univ.)

The atomic structure of Ga chemisorbed on the Si(100) 2x1 surface at low coverage has been studied by a combination of X-ray standing wave (XSW) measurements and molecular cluster total energy calculation. For various Ga coverages below 1/2 ML, the Ga ad- dimer is found to be 1.03 ± 0.01 Å above the Si (400) diffraction plane. The measured Ga ad-dimer bond length is 2.50 ± 0.06 Å, which matches the covalent bond length of gallium. By comparing experimental results with the theoretical calculation, we conclude that the Ga ad-dimers are oriented parallel to the underlying Si dimers, which is consistent with a previous total-energy calculation. This parallel dimer geometry is in contrast to the orthogonal dimer model proposed by previous LEED, AES, and STM studies. Our measurement is the first experimental confirmation of this parallel Ga ad-dimer model.

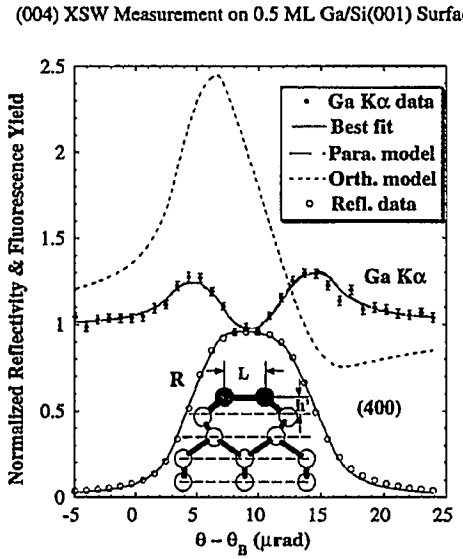


Figure 1.

* Work sponsored by the U.S. Department of Energy, Office of Basic Energy Sciences, Division of Materials Sciences,under contract W-31-109-ENG-38 and DE-AC02- 76CH00016 to the NSLS.

Precise lattice location of trace elements within minerals and at their surfaces with x-ray standing waves *	X15A

Y. Qian, N. C. Sturchio, R. P. Chiarello, P. F. Lyman, T. Lee, and M. J. Bedzyk (ANL and Northwestern Univ.)

Using x-ray standing waves (XSW) generated by dynamical Bragg diffraction, we have precisely measured lattice locations of trace elements within and at the surface of mineral single crystals. Natural calcite samples were cleaved along the (10$\bar{1}$4) plane to obtain pristine surfaces. After cleavage, some samples were reacted with a dilute aqueous Pb solution to obtain Pb-sorbed surfaces. XSW measurements were then performed on both unreacted and reacted samples using the calcite (10$\bar{1}$4) Bragg reflection. On these samples, we observed a nearly ideal fit of the experimental reflectivity curve to the dynamical diffraction theory curve. Our XSW measurements show that the naturally occurring trace element Mn substitutes for Ca. On the Pb-reacted calcite sample, Pb was located on the calcite (10$\bar{1}$4) lattice plane where Ca atoms also reside. To our knowledge, no other atomic scale structural measurements exist for this system. Our measurements clearly demonstrate a new and powerful application of synchrotron radiation in earth and environmental sciences to provide element-specific atomic-scale structural information within and at the surface of minerals. The XSW measurements were made at the NSLS X15A beamline.

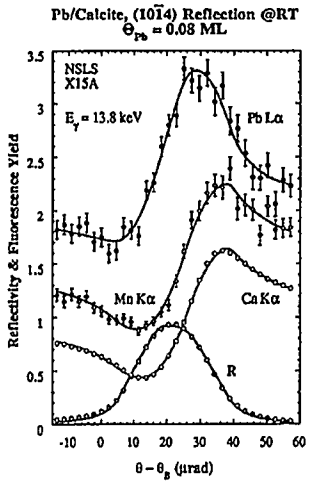


Figure 1.

* Work was sponsored by the U.S. Department of Energy, Office of Basic Energy Sciences, Division of Materials Sciences, under contract W-31-109-ENG-38 and DE-AC02-76CH00016 to the NSLS.

Structure and thermal characterization of membrane bound and surface adsorbed protein *	X15A

Jin Wang, Martin Caffrey (OSU), Carmichael J. A. Wallace (Dalhousie Univ.), and Ian Clark-Lewis (Univ. of British Columbia)

The x-ray standing wave (XSW) method has been used to study the topology of the protein, cytochrome c, bound to a negatively charged model lipid membrane and adsorbed at a metal surface. At the metal surface, cytochrome c forms an hexagonally close-packed monolayer. A similar packing arrangement is observed at the surface of a self-assembled lipid monolayer on silver. In the case of a Langmuir-Blodgett (LB) film, protein multilayers are formed. The data suggest that cytochrome c maintains its native globular structure upon surface binding and subsequent storage for an extended period. Further, the data are consistent with a protein docking mechanism wherein the heme plane is oriented perpendicular to and with its exposed edge facing the surface. The XSW measurement has also been used to show that the surface bound cytochrome c monolayer on a silver mirror surface undergoes a thermal melting transition starting at ca. 50°C. Unlike the unfolding transition of cytochrome c in aqueous buffer solution, this melting transition is not reversible upon cooling to room temperature. This study demonstrates the utility of the XSW method as a new and powerful structural tool for investigating membrane- and surface-protein interactions.

* Supported by NIH DK45295.

Structure characterization of membrane bound and surface adsorbed cytochrome c *	X15A

Zhijian Yin, Jin Wang, Stephan Kirchner, and Martin Caffrey (OSU)

Our initial x-ray standing wave (XSW) study of the membrane and solid substrate (silver mirror) bound topology of horse heart cytochrome c made use of a singly selenomethionine (Se-Met80) labeled form of the protein (Wang, et al., J. Mol. Biol., 237: 1-4, 1994). This XSW measurement gave a selenium-to-silver mirror surface distance that eliminated many possible orientations for the bound protein. However, with a single distance measurement, several other orientations were possible. To further refine the protein orientation, use was made of a doubly labeled protein incorporating Se-Met at position 80 and bromotyrosine (Br-Tyr) at position 97 (Se-Br-cytochrome c). On a bare silver mirror, the Br- and Se-to-mirror surface distances are 4 Å and 11 Å, respectively. On a w-thiolun decanoic acid (wTUA) coated mirror, the corresponding distances are 26.5 Å and 18.5 Å. Assuming that the protein adopts the same 3-D structure in the surface bound state as it does in the crystal form, these distances are consistent with cytochrome c binding to the bare silver mirror via a docking plane formed by four lysine side chains corresponding to residue numbers 7, 8, 25, and 27. A distinctly different orientation is assumed by the protein on the wTUA coated surface. Parenthetically, we note that the Se:Br mole ratio, determined by x-ray fluorescence (after mirror background Br fluorescence has been subtracted from the total Br fluorescence signal), is consistent with a 1:1 to 1:2 labeling of the bound Se-Br- cytochrome c.

* Supported by NIH DK45295

Initial stages of nickel silicide formation on Si(111) * | X16A

P. Bennett, (Physics - ASU.), R. Schuster, A. Ghosh, and I. K. Robinson (U. of Illinois)

We have studied the reaction of Ni on Si(111)-7×7 at room temperature using x-ray diffraction. We find that an ordered, epitaxial structure forms, contrary to all previous work in the literature for Ni/Si and related silicide systems. the crystal truncation rod profile shon in Fig. 1 (5 Å dose at RT) clearly shows adsorption induced features near L=-4 and -2, and also less clearly near L= +2 and +4. The latter are mixed coherently with the bulk Si peaks at L= +1 and +4. The overlayer seems to be Ni2Si-theta, a hexagonal phase with a good lattice match to Si(111). Intensity oscillations occur during deposition, signifying a layerwise etching of the substrate, similar to the Pd/Si system, which we described earlier [1]. the skewed shape of rod features suggests a highly faulted overlayer. Annealing to 200°C improves the Ni2Si structure, giving stronger and more narrow (ΔL) features. Annealing to 500C produces B-type NiSi2, with peaks at L=-4 and -1, and well defined "wiggles" signifying a sharp interface structure.

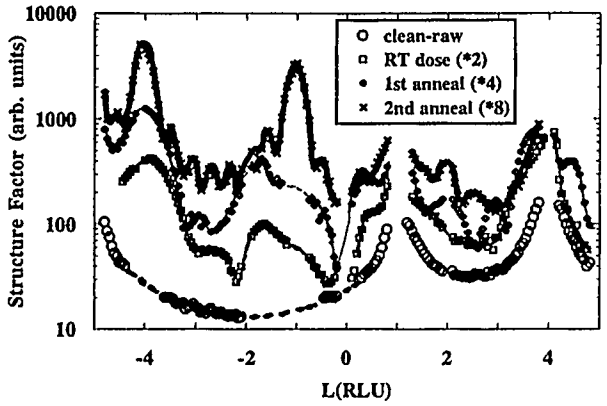


Figure 1.

* Work supported in part (P.A.B.) by the NSF (DMR9221201).

Symmetry of the 7×7 Si(111) surface: p6mm or p3m1? | X16A

A. Ghosh, R. Schuster, and I. K. Robinson (Univ. of Illinois, Urbana)

This experiment was conducted to probe the symmetry and the structure of the 7×7 reconstruction of the Si(111) surface. The existing picture for the 7×7 reconstruction describes the structure by a dimer-adatom-stacking fault (DAS) model. The DAS model assumes a p6mm symmetry for the reconstructed surface, which implies an even higher symmetry than the underlying bulk crystal (p3m1). This X-ray diffraction experiment was done to investigate this above mentioned discrepancy.

Fig. 1 shows the diffraction pattern of the 7×7 reconstruction (using the LEED convention of the 1×1 surface for the directions) at $q_\perp \cong 0$. At $q_\perp \cong 0$ in the reciprocal space both the symmetries, i.e. p3m1 and p6mm, are degenerate and give rise to the same symmetry of the diffraction pattern. The 6 fold symmetry of the reflections in Fig. 1 is consistent with both p6mm and p3m1 symmetry. However, as we go towards large $q_\perp$ in reciprocal space p3m1 and p6mm should result in different symmetries of the diffraction pattern: In Fig. 2 ($q_\perp = 2.8$) one can see that the reflection pattern no longer includes the dashed line relating the upper and the lower halves, which shows that the structure of the 7×7 reconstructed Si(111) surface is p3m1 not p6mm. This is probably due to vertical displacements in the 7×7 reconstruction, which reflect the p3m1 symmetry of the underlying substrate. The symmetry breaking is small, with the displacements of order 0.1Å. The detailed refinement is in progress. Our results show the importance of accurate out-of-plane crystallographic measurements in determining the symmetry of the surface structure.

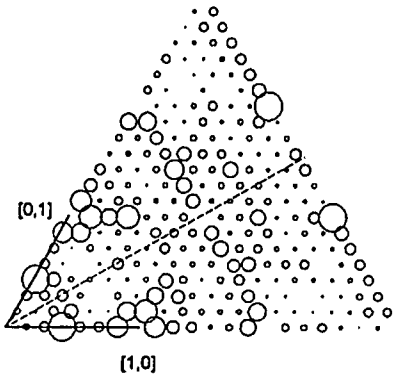


Fig 1 ($q_\perp = 0$)

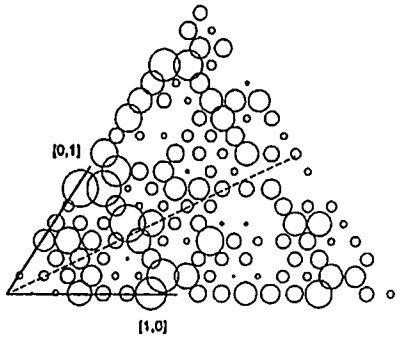


Fig 2 ($q_\perp = 2.8$)

Parallel adatom chains on Si(111): a chemisorption-induced surface reconstruction * | X16A

C. A. Lucas, G. C. L. Wong, D. Loretto (LBL), A. P. Payne, and P. H. Fuoss (AT&T Bell Lab.)

There are three known large scale Si(111) surface reconstructions, the (2X1) π-bonded chain structure native to cleaved surfaces, the commonly observed (7x7) dimeradatom-stacking-fault (DAS) structure, and a metastable ($\sqrt{3}$x$\sqrt{3}$)- R30° structure. Recent work has shown that reconstructions with a (3x1) symmetry can also be generated on Si(111) by a variety of adsorbates, such as CaF_2, Ag, and the alkali metals. We have determined the atomic structure of a chemisorption-induced, large scale (3x1) Si reconstruction using in-situ x-ray scattering. CaF_2 is an ionic insulator with a similar fcc-type structure and lattice constant to Si, and has been observed to form a series of ordered reconstructions on Si(111)-7x7 with increasing submonolayer coverages. The first of these is a (3x1) phase, which forms at coverages from as low as ~1/10 monolayer (ML), and as high as ~1/3 ML. We studied this reconstruction by measuring the superlattice Bragg reflections, specific to the (3x1) phase, as well as the (10l) bulk crystal truncation rod. We find that the CaF_2/Si(111)-(3x1) reconstruction is primarily a Si reconstruction, with a parallel array of zig-zag Si adatom chains oriented along $\langle 1\bar{1}0 \rangle$. The basic structural unit, the adatom chain, forms a 5-member ring in $\langle 1\bar{1}0 \rangle$ projection. The domain size of the (3x1) phase is comparable to that of the original Si(111)-(7x7) reconstruction on our samples. The structure is shown schematically in the figure, (a) top view and (b) $\langle 1\bar{1}0 \rangle$ projection. The Si-Si distance on the chains is 2.67 ± .09 Å. The average Ca-F distance is 2.47 ± .10 Å (natural bond length: 2.37 Å). The fitted value of the Debye-Waller parameter for the adsorbed Ca and F atoms is 0.75 Å^2. The fit parameters from the (1 0 /) rod are as follows: $d_{Si} = 2.0 \pm .1$ Å, $d_{Ca} = 3.0 \pm .1$ Å, $d_F = 3.1 \pm .1$ Å. Schematic sp_z orbitals are also depicted. This surface structure, with no dangling bonds at only 1/3 monolayer adsorbate coverage, may explain the occurrence of (3x1) reconstructions among a diverse range of Si-adsorbate systems.

[1] G.C.L. Wong, C.A. Lucas, D. Loretto, A.P. Payne and P.H. Fuoss, Phys. Rev. Lett. 73, 991 (1994).

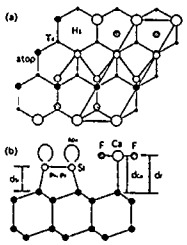


Figure 1.

* Work supported by U.S. Department of Energy under contract No. AC03- 76SF00981.

Scaling of island distributions during growth of Cu on Cu(110) * | X16A

I. K. Robinson, K. L. Whiteaker, and R. Schuster (Univ. of Illinois, Urbana)

This experiment was designed to probe the distribution of islands that form by the diffusion of evaporated species on a surface. The anisotropic (110) surface was chosen because the diffusion is expected to be much faster in one direction than the other, so should result in highly elongated island shapes. Therefore the surface diffraction becomes diffuse in just one surface direction, and is therefore detectable with NSLS flux levels.

The left figure shows the cross section of one of the CTRs of our crystal in the slow diffusion direction (bulk 100). The diffraction was found to have a ridge-shape which was always sharp in the fast-diffusion direction (bulk 110). Each set of data was taken during growth after about 0.5 monolayers at the same deposition rate (about 1ML per 20 minutes), but with different samples temperatures, as indicated. The clear side peaks correspond to a roughly regular array of islands with a spacing that varies with temperature. The peak positions were found also to change with time and growth rate.

The shape of the peak is related to the detailed distribution of island sizes. In order to demonstrate an invariant distribution function, we have rescaled the data on both the intensity and momentum transfer axes in the right figure. The close matching of the three sets of dta demonstrates this scaling property in the Cu/Cu(110) system.

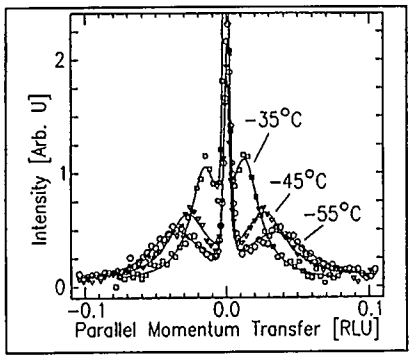


Figure 1.

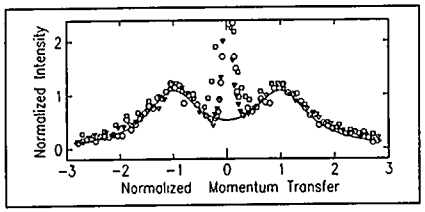


Figure 2.

* This work was sponsored by the NSF under award DMR93-15691.

Relaxations in uniaxial reconstructions of the Cu(110) surface | X16A

R. Schuster, P. J. Eng, and I. K. Robinson (University of Illinois)

We studied uniaxial reconstructions on Cu(110), induced by Cs adsorption, with surface x-ray diffraction. Particular effort was taken to determine the relaxations of the metal surface in these reconstructions.

A low Cs coverage ($\theta_{Cs} \sim 0.15$ML) our structure determination revealed a (1x3) missing-row structure, where every third close packed [1$\bar{1}$0] row of Cu-atoms has been removed. The lower panel of the figure shows a sideview of this structure. Grey circles mark the atoms of the surface unit cell. In agreement with former studies, increasing the Cs coverage led to a (1x2) structure with every second row missing and a high coverage (1x3) structure with two neighboring missing rows in the top layer (see figure).

The graph shows the contraction of the top-layer distance of the metal for the different structures as determined by measuring at least 8 different crystal-truncation and superstructure rods for each structure and fitting a model, allowing vertical and in plane relaxations down to the fourth metal layer. The inclusion of the alkali metal in the model was necessary to account for the data.

The contraction of the top-layer distance increases considerably with more extensive reconstruction. Closer inspection of the displacements of deeper-layer atoms reveals that the surface is more or less reacting as an elastic medium: the stress, caused by the reconstruction is passed on by the atoms and released gradually within a range of several lattice constraints. As the coordination of the top-layer atoms towards their Cu neighbors does not change among the considered structures, such arguments cannot explain the observed trend of the distortions. The contraction of the top-layer in the (1x2) structure decreases with increasing alkali coverage. This trend has also been observed for Cs/Ag(110) and can be rationalized in the effective medium picture: Additional alkali metal in the (1X2) structure increases the charge density in the surface and increases the effective coordination of the neighboring Cu atoms.

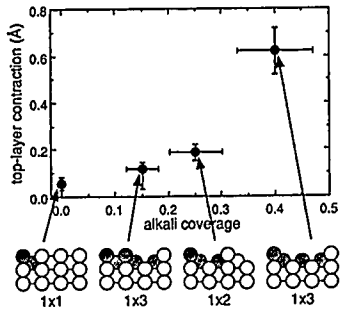


Figure 1.

Electrocompression of a Pb monolayer on Cu(111) * | X16C

Y. Chu and I. K. Robinson (Univ. of Illinois)

Using the new sagittal-focussing monochromator on beamline X16C, we have succeeded in observing the diffraction from an electrochemically deposited monolayer. Pb undergoes underpotential deposition (UPD) on Cu(111) at a potential of approximately -0.24V relative to Ag/AgCl, and bulk deposition at a potential of -0.44V in 0.1M $HClO_4$ and 2mM Pb^{++}. This means that the monolayer phase is stable between these potentials. Diffraction measurements of electrochemical monolayers on Cu surfaces have not previously been reported, partly because of the extreme sensitivity of such surfaces to oxidation or contamination by halides.

The figure shows our measurements of a Pb monolayer held in-situ at two potentials near the ends of the UPD range. A clear diffraction peak is seen near the position (0.75, 0, 0.2) using surface diffraction nomenclature; the smaller peak is a powder ring from the polypropylene film membrane containing the electrolyte in our cell. A large intensity is obtained, appropriate for a close-packed monolayer of Pb; the spacing corresponds to about 2% less than the nearest neighbor distance in bulk Pb. the peak shifts distinctly with potential, from h=0.743 to 0/757 RLU. Interestingly, it shows no tendency to lock-in at the commensurate position h= 0.75.

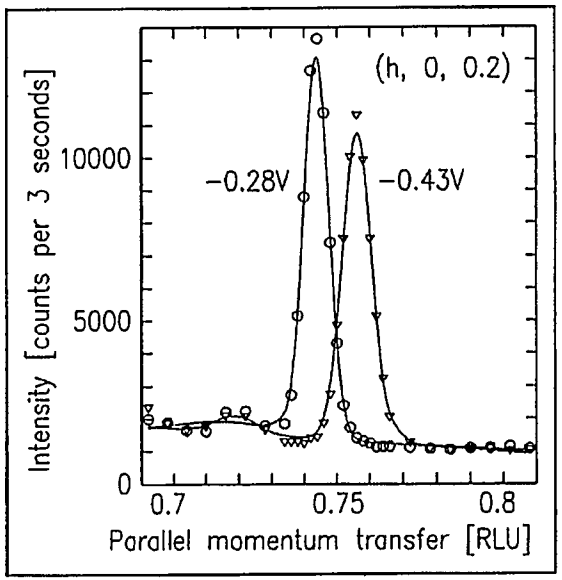


Figure 1.

* The work was supported by the Illinois MRL under DEFG02-91ER45439.

Interfacial morphology of graded-temperature rare earth superlattices *	X16C

K. A. Ritley, C. P. Flynn, and I. K. Robinson (Univ. Illinois, Urbana)

Understanding the role of growth temperature in the preparation of superlattices by molecular beam epitaxy (MBE) is important for refining the structural quality of these systems. The growth temperature is expected to have significant effects in these inherently nonequilibrium structures: for temperatures too low, the interfaces are expected to be rough; for temperatures too high, the interfaces are expected to be interdiffused.

An improved growth technique has been developed, in which up to five samples can be simultaneously prepared, such that the growth temperature of each is different, but that the samples are identical in all other respects.

A diffraction experiment performed at NSLS beamline X16C on these samples is providing important insight into the interfacial morphology of these systems. An interesting overlap of scattering intensity of the superlattice (large ripples in figure 2) and extended scattering from surface of the underlying Al_2O_3 substrate (narrow streak in figure 2) has been observed. It is expected that this will contribute important information about the starting template upon which the superlattice is grown.

The damping of the Fourier components of the superlattice periodicity, (extracted from the integrated intensity ratio of the superlattice harmonics to the fundamental) observed in scans in radial direction and as shown in the figure above, suggests there may be an optimal growth temperature of 400°C. Further analysis of the intensity distribution is expected to contribute information about in-plane roughness and correlation in these systems.

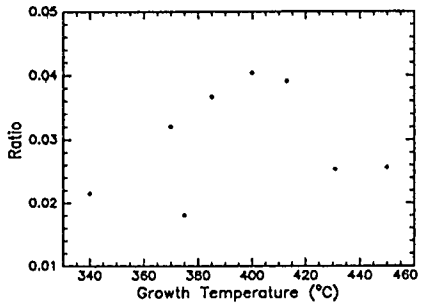


Figure 1.

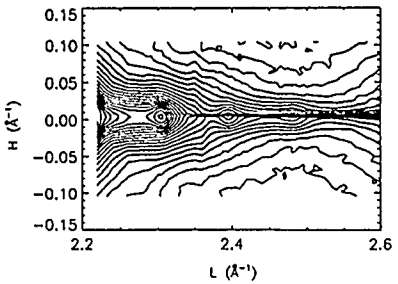


Figure 2.

* Work supported in part by NSF-DM-91-21888.

DAFS measurements of CoSi films on Si(111) *	X16C

R. Schuster, A. Ghosh, D. L. Adler, I. K. Robinson (University of Illinois), N. Onda, and H. von Känel (Eidgenössische Technische Hochschule Zürich)

We investigated the structure of grown CoSi films on Si(111) by x-ray diffraction, using the new Kappa diffractometer on beamline X16C. Cobalt silicides attract a lot of attention because they form smooth, epitaxial interfaces on Si, making them particularly suited for contacting Si-devices. Beside the well studied $CoSi_2$ also other cobalt silicides gain importance because of the hope to design their structural and electronic properties according to their particular applications.

The measurement of the structure factors of the film peaks of a CoSi film of ≈10 layer thickness revealed a well ordered CsCl structure. In plane the lattice grows epitaxial to the Si(111) substrate, whereas out of plane the lattice is expanded by about 5%.

The figure shows the measured structure factors for two qualitatively different film peaks, the (-1,0,3.92) and the (1,0,1.96) peak, as a function of the x-ray energy. For the notation of the reciprocal lattice vectors the LEED convention is used. These peaks represent the two sets of reciprocal lattice vectors of the CsCl structure, whose structure factors are given by (f_{Co}-f_{Si}) and (f_{Co}+f_{Si}), respectively. The anomalous scattering of the Co close to the binding energy of its 1s electrons at 7.709 keV leads to a considerable reduction of the structure factor, which is naturally more pronounced for the difference peak at (1,0,1.96). Above the K-binding energy, oscillations of the structure factor with energy are seen. These are closely related to the oscillations in the x-ray adsorption, employed in EXAFS (extended x-ray absorption fine structure) to determine the local environment of the atoms, i.e. neighbor distances and coordination. Even though the structure of the CoSi in the above problem is already known from the measured structure factors, the figure proves the capability of the present equipment of X16C to carry out DAFS (diffraction absorption fine structure) measurements. The signal to noise ratio in the DAFS signal is substantially enhanced by the structure factor cancellation. The DAFS analysis is in progress.

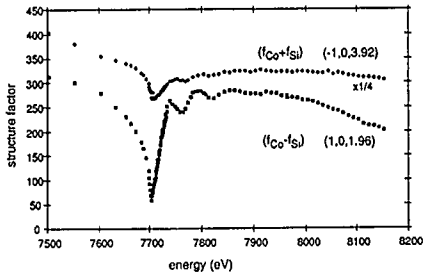


Figure 1.

* This work was supported by DOE DEFG02-91ER45439 and the DFG

Single-energy images for preclinical MECT research *	X17B1

F. A. Dilmanian, X. Y. Wu, J. F. Coderre, J. Kress, B. Ren, D. N. Slatkin (BNL),D.Chapman, M. Shleifer, W. C. Thomlinson, Z. Zhong (NSLS), T. M. Button, F. Giron, C. T. Roque (SUNY StonyBrook), M. H. Miller, H. Weedon (Analogic Corp.), D. J. Krus, L. Perna (Bicron), and K. Yamamoto(Hamamatsu)

First results from the second phase of the multiple energy computed tomography [MECT] system development are presented. MECT is being developed for imaging the human head and neck. Its new components, which were used for acquiring images of phantoms and live rabbits, are the following: (a) Monochromator: The low-energy section of MECT's two-section Laue-Laue monochromator, with an energy range of 24.5 - 51.2 keV, was commissioned recently and installed in the X17 transport hutch (Wu et al., this report). (b) Detector : MECT's new scintillator/diode detector is a seamless, modular, linear array device, comprised of $CdWO_4$ scintillators (Bicron, Solon, OH) and PIN-diode arrays (Hamamatsu, Bridgewater, NJ). Each module has 32 elements with 0.5 mm center-to-center spacing, 6 mm height, and 3.5 mm scintillator thickness. (c) Data acquisition system [DAS]. The DAS (upgraded 4/94) has a fast interface designed by us, which allows data transfer from its front end (Analogic, Peabody, MA) to a DEC Alpha 3000 Model 400 computer at 1.4 Mbytes/s for as long as the disk allows. Images were obtained at 33 keV. The other parameters were as follows: (a) slice height: 2 mm; (b) viewing rate: 1440 Hz; (c) subject rotation: 180° in 18 s; (d) detuning of the monochromator: 15% of the peak beam; (e) average ring current: 150 mA; (f)beam filter: none, and none, an: none, and 3.2 mm Al. Data were obtained for each image ($\approx$ 0.3 mm resolution) from two positions of the rotation axis separated by 0.25 mm. The entrance absorbed dose was estimated to be $\approx$ 0.05 Gy. Figs. 1 and 2 show a transaxial slice of an anesthetized rabbit using separate gray scales for soft tissue and bone, respectively; Figs. 3 and 4 show a plastic phantom (9.5 cm diam.) with 4 mm-deep concentric grooves (outer groove: 0.35 mm-wide) reconstructed with two frequency-cutoff sinc filters. The lower-frequency filter (Fig. 4), used in Figs. 1 and 2 to remove breathing artifacts, degraded the resolution. The image noise for tissue/plastic is $\sigma = 0.3\%$, compared to $\approx 0.5\%$ in conventional computed tomography for the same dose and slice thickness. Human studies are expected to begin in Room X17B2 during 1996 or 1997.

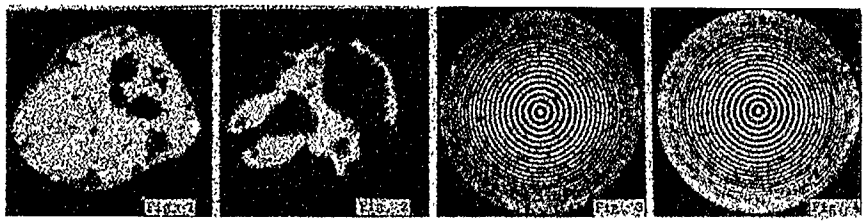


Figure 1. – Figure 4.

* We thank J.B. Hastingsand D.P. Siddons for their contribution to the optical design of the monochromator, and Z. Chen and P.Spanne for their help with image reconstruction. Research supported by U.S. DOE under contract DE-AC02-76CH0006.

In situ determination of the olivine, beta and spinel phase boundaries for CO_2SiO_4at high pressures and temperatures *	X17B1

L. Galoisy (U. P6, P7 and IPGP), J. Zhang (CHiPR, ESS, SUNY Stony Brook), S. Rossano(U. P6, P7, and IPGP), R. C. Liebermann, F. Guyot, and I. Martinez (CHiPR, ESS, SUNY Stony Brook)

Phase transformations amongst the olivine, beta and spinel polymorphs of Co_2SiO_4have been studied using in situ X-ray diffraction and a DIA-type cubic-anvil high-pressure apparatus (SAM 85) at the superconducting wiggler beamline at the National Synchrotron Light Source (NSLS). Starting materials were powders of the olivine or spinel phases synthesized previously. Samples contained in BN capsules were compressed at room temperature 7 to 10 GPa and then heated along P-T paths which crossed the spinel-olivine and spinel-beta phase boundaries at temperatures between 900 and 1220°C. The transformations between the olivine, beta and spinel phases were identified by observation of the growth of the peaks corresponding to the different polymorphs. The beta phase which grows from spinel has strong preferred orientation as indicated by the systematic absences of certain peaks in the diffraction patterns. This suggests that the transformation from spinel to the beta phase is crystallographically-controlled and that topotactic relationships exist between the spinel and the beta phases. All of the transformations appear to be highly kinetically controlled, presumably because all of the P-T conditions in our experiments are very close to the equilibrium phase boundaries. These in situ experiments demonstrate the feasibility of determining the phase boundaries and the olivine-beta-spinel triple point more precisely than has been possible from quench-type studies (Akimoto and Sato, 1968; Remsberg and Liebermann, 1991), as well as studying the kinetic rates of reactions amongst the polymorphs of Co_2SiO_4.

[1] Akimoto, S., and Y. Sato, Phys. Earth Planet. Interiors, 1, 498.
[2] Remsberg, A.R., and R.C. Liebermann, Phys. Chem. Minearal, 18, 161.

* This work was supported by the NSF Center for High PressureResearch (CHiPr)

Measurements and theoretical calculations of the pressure-volume-temperature relations in olivines *	X17B1

F. Guyot, Y. Wang (SUNY Stony Brook), and Ph Gillet (ENS Lyon, France)

The molar volumes of synthetic forsterite and natural olivine (Fo10 from San Carols,Arizona) have been precisely measured in situ at high pressure and temperature up to 8 GPa and 1200 K in a DIA-type multi-anvil high-pressure apparatus (SAM 85), using energy-dispersive powder X-ray diffraction at the superconducting wiggler beamline at the National Synchrotron Light Source (NSLS, X17B). Both materials were present in the same high-pressure cell, together with NaCl used as a pressure standard. Temperatures were measured with a thermocouple and nonhydrostatic stress components in the cell were evaluated from the NaCl spectra following the method of Weidner et al (1992). A good correlation was found between the measured deviatoric stress and the width of the diffraction lines. Deviatoric stresses were annealed out in samples heated at temperatures exceeding 1000 K. Then, spectra taken on cooling remained of good quality and only such deviatoric-stress free spectra were used to extract quantitative equation of state data. High-pressure room-temperature data points showing nonhydrostatic stress were observed to be inconsistent with ultrasonic data. This clearly shows that only deviatoric-stress-free data should be used to discuss the equations of state of mantle minerals.

Spectroscopic models have been used to calculate the Pressure-Volume-Temperature (P-V-T) relations in forsterite and olivines. In these models, the thermal pressure is calculated by combining neutron, Raman, infrared and acoustic data to construct the vibrational density of state and also mode Gruneisen parameters measured by Chopelas (1990). Such models successfully reproduce both P-V-T and calorimetric data, in a more quantitative way than a Debye's model, and they are used to derive a full set of thermodynamic parameters for olivine at high pressure and temperature.

[1] D.J. Weidner et al. in High Pressure Research pp 13-17 Syono and Manghnani editors TERRAPUB/AGU, 1992.

[2] A. Chopelas Phys. Chem. Miner., 17, 149-156, 1990.

* This work was supported by the NSF Center for High Pressure Research (CHiPR).

Catalyst characterization with high-energy x-ray diffraction *	X17B1

R. Harlow, G. Coulston, F. Herkes, and G. Jones (Du Pont)

In situ characterization of catalysts using traditional x-ray diffraction techniques has generally been limited to one atmosphere or less because laboratory x-rays lack the energy (8-17 Kev)necessary to penetrate a thick-walled reaction vessel. X17B1, however, has reasonable intensities even at 100 Kev which makes it theoretically possible to study catalysts under full in situ conditions. To explore this possibility, we have completed a successful feasibility study of Pd and other hydrogenation catalysts sealed in 1/8" and 1/16" stainless steel reaction tubes.

Although our proposal called for the use of energies in the neighborhood of 60 Kev, we were only able to attain patterns at 42.2 and 49.7 Kev because the main monochromator developed a cooling water leak and had to be taken offline. Nonetheless, the data collected on a Pd sample in a hydrogen-gas atmosphere clearly demonstrated that it was possible to obtain high-resolution diffraction patterns in which both Pd metal and Pd hydride peaks could be seen.

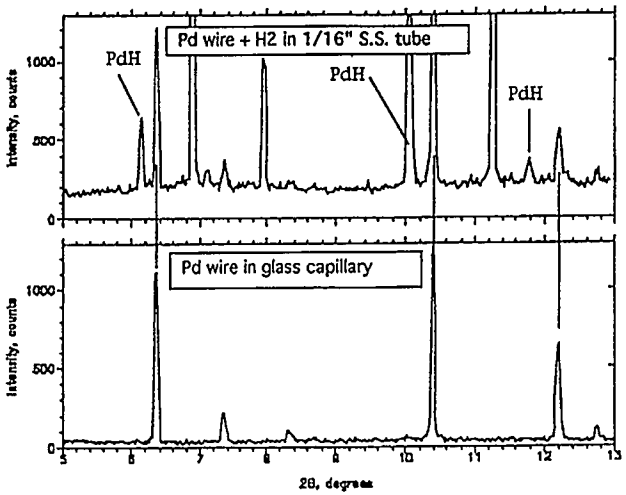


Figure 1.

* With thanks to N. Lazarz, D. Chapman, J. Hastings, and P. Siddons (NSLS).

Characterization of Pd/C catalyst by x-ray diffraction under commercial hydrogenation pressures: in situ for the masses *	X17B1

R. Harlow, G. Coulston, S. Ziemecki, F. Herkes, and G. Jones (Du Pont)

In situ characterization of catalysts using traditional x-ray diffraction techniques has generally been limited to pressures of one atmosphere or less because laboratory x-rays lack the energy (8-17 Kev) necessary to penetrate a thick-walled reaction vessel. We had demonstrated earlier, however, that it was possible to observe diffraction patterns for materials encased in a 1/16" stainless-steel tube if higher energy x-rays were used. In particular, palladium hydride was shown to form when Pd wire placed inside the tube was pressurized with hydrogen gas. We have now successfully extended these studies to a 1% Pd/C supported catalyst loaded in 1/8" stainless-steel tubes using 60.5 kev x-rays under conditions which mimic commercial operations. The shift in the Pd(111) peak toward lower angles in the diffraction patterns below illustrates the conversion of palladium metal (100 psi H_2) to palladium hydride (1000 psi H_2) at 240° C. In addition, we have mapped out the complete PT phase diagram for this catalyst and determined that the small particles of Pd in the catalyst behave in a fashion similar to bulk palladium.

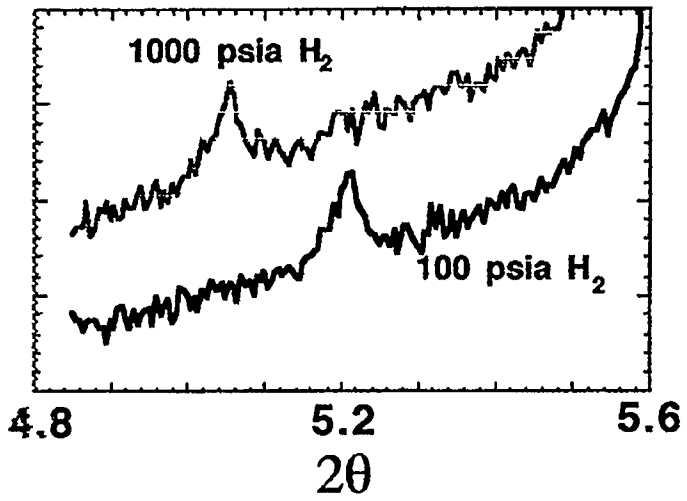


Figure 1. new

* With thanks to N.Lazarz, J. Hastings, P. Siddons (NSLS)

Phase transition of portlandite [$Ca(OH)_2$] at high pressure *	X17B1

M. Kunz, D. J. Weidner, M. Vaughan, J. B. Parise, Y. Wang, and K. Leinenweber (SUNYStony Brook)

High pressure in situ synchrotron x-ray powder diffraction collected in both, energy-dispersive and angle-dispersive mode, were used to investigate the non-quenchable phase transition of Portlandite ($Ca(OH)_2$) reported by Leinenweber (1993). The phase transition was bracketed at 500°C to about 56.5 kbar ± 4 kbar. The onset of the high-pressure phase during compression occurred at 60.7 kbar whereas its disappearance on decompression was found at 52.7 kbar. The phase transition was not observed when compressing at room temperature. It is not clear yet whether this represents a real property of the phase diagram or is rather due to low kinetics at low temperatures.

Very low intensity peaks at low angles together with low peak to background ratio hampered various attempts to find a cell for the high pressure phase using customary programs. We therefore attempted to find a cell by structural modeling. this was done assuming that the most important structural changes occur in the stacking arrangement of the $(001)_{hex}$ layers. This simple approach led to a tentative unit cell based on the orthorhomic pseudo-cell of the low-temperature phase. The main difference of the proposed high-pressure unit cell relative to the hexagonal Portlandite cell is a shift of the layers relative to each other by 1/3 $[110]_{hex}$ leading to a tripling of the c-axis. the proposed unit cell is monoclinic, possibly triclinic, and relates in the following way to the hexagonal Portlandite cell: $a_{hp} \approx 3 \cdot a_{hex}$; $b_{hp} \approx \sqrt{} \cdot a_{hex}$; $c_{hp} \approx 3 \cdot c_{hex}$. The monoclinic angle β_{hp} is around 92°.

[1] Leinenweber, Kurt (1993): NSLS Annual Report 1993 B-128.

* This work was supported by the NSF under a grant to the Center for High Pressure Research.

In-situ x-ray diffraction at high pressure and temperature of aragonite and dolomite. Evidence for dolomite breakdown to aragonite and magnesite *	X17B1

I. Martinez, J. Zhang, R. J. Reeder, and G. Symmes (SUNY Stony Brook)

Aragonite, $CaCO_3$, and dolomite, $CaMg(CO_3)_2$, have been studied in situat high pressure and temperature in a DIA-type multi-anvil high-pressure apparatus (SAM 85), using energy-dispersive X-ray diffraction at the superconducting wiggler beamline at the National Synchrotron Light Source (NSLS,X17B). Starting materials were natural single crystals from Eugui (Spain), ground into fine powder. Temperatures were measured with a thermocouple, whereas pressures were derived from the NaCl internal standard. The cell parameters and cell volumes of aragonite and dolomite have been measured up to 8 GPaand 1300 K, and up to 5 GPa and 1100 K, respectively. Only deviatoric-stress-free spectra were used to extract quantitative data.

Aragonite undergoes no decarbonation or phase change up to the maximum pressures and temperatures reached in this study, whereas at pressures exceeding 6 GPa, dolomite breaks down forming aragonite and magnesite.Assuming a constant value of 4 K_0', the following parameters have been derived for aragonite and dolomite, respectively: $K_0 = 67.7\ (\pm 3)$ and 88 (± 7) GPa, $\alpha_{298-1000}K = 7.36^{*}10^{-5}$and $4.03^{*}10^{-5}$ K^{-1}, $\alpha K = 6.46^{*}10^{-3}$ and $3.95^{*}10^{-3}$ GPa/K, dK/dT= -0.0236 and -0.025 GPa/K.

In addition to literature data for enthalpies and entropies, we used the P-V-T relations measured in this study for aragonite and dolomite, as well as that for magnesite, to calculate the free energy of the three phases at high pressure and temperature as well as the pressure-temperature conditions of thermodynamic equilibrium for the reaction dolomite → aragonite+magnesite. This breakdown reaction is potentially very important for the ultra-high pressure metamorphism of carbonates.

* This work was supported by the NSF Center for High Pressure Research (CHiPR).

Two- and three-dimension microbeam radiation therapy (MRT) of malignant brain tumors in rats	X17B1

D. N. Slatkin, S. M. Cole, F. A. Dilmanian, D. D. Joel, P. L. Micca, M. M. Nawrocky,X.-Y.Wu (BNL), P. Spanne (Groupe d'Imagerie, ESRF, France), J.-O. Gebbers (Institut de Pathologie, Hopital Cantonal, Lucerne, Suisse), and J. A. Laissue (Institut de Pathologie de l'Universite, Berne Suisse)

Brain 9L gliosarcomas [1] weighing ≈ 40 or ≈ 60 mg were irradiated in prone rats from three directions using either 2- or 3-dimension [D] MRT either 14 or 15 d post initiation [PIN], respectively, in the right striatum by injection of 10^4 tumor cells in 1 μl of in vitro culture fluid 4 mm lateral to the bregma and 4–5 mm deep to the calvaria (the isocenter). From each direction, 2D MRT (7/26/94) yielded an array of 100 parallel, 12 mm-high × 25 μm-wide microplanar zones of directly exposed tissue, 100 μm on center. The arrays converged horizontally around the isocenter at 60° intervals and yielded skin-entrance absorbed doses [SEDs] of 221 or 312 Gy [2]. The 3D MRT (11/12/94) arrays and SEDs were identical except that convergence was orthogonal from the anteroposterior [AP], 45° left superolateral [LS] and 45° right superolateral [RS] directions, and that the anesthetized rats were held in a flat-bottomed holder by rubber bands. The 13-mm high "guard-rails" did not prevent several degrees of rat swivel (yaw) during the 45° rolls required for the LS and RS exposures, even using bolsters, and neither extra stepping motors nor extra television monitors were positioned to correct the resultant misalignments as they were observed at the control console.

Median PIN survivals of unirradiated control rats were 21d (range 18–27; n =9) and 20.5d (range 17–26d; n =10) during the 2D and 3D studies, respectively. Morbidity/mortality indices [3] [MMIs] were defined as % weight loss since 7d post irradiation antemortem or 500+ the number of days postmortem. Although 11/16 3D- vs. 27/27 2D MRT rats were alive at PIN 34, judged by pairwise Wilcoxon tests of MMIs this early palliation was as good by 3D- as by 2D-MRT using 312 Gy (but not using 221 Gy) SEDs despite the inaccurate 3D exposures of ≈30% larger (PIN 15 vs. 14) tumors. Thus we postulate that properly implemented 3D MRT will prove advantageous. We suggest that, after extensive preclinical tests and with obligatory physical refinements [4,5] of MRT, infants and toddlers with otherwise intractable brain tumors may undergo 3D MRT while supine or prone, under anesthesia.

[1] J.A. Coderre, T. M. Button, P.L. Micca, C. Fisher, M.M. Nawrocky, H.B. Liu. Int. J. Radiat. Oncol. Biol. Phys. 30, 643–652 (1994).

[2] D.N. Slatkin, M. Miura, P. Spanne. in LDRD Annual Report, Eds. Ogeka, G.J., and Romano, A.J., December 1994, BNL-52351; in press, 1995.

[3] J.A. Coderre, D.N. Slatkin, P.L. Micca, J.R. Ciallela. Radiat. Res. 128, 177–185 (1991).

[4] D.N. Slatkin, P. Spanne, F.A. Dilmanian, M.M. Nawrocky, J.-O. Gebbers, J.A. Laissue. NSLS Activity Report 1993, Ed. Rothman, E.Z., BNL-52415, Brookhaven National Laboratory, Upton, NY (1994), p. B132.

[5] D.N. Slatkin, F.A. Dilmanian, M.M. Nawrocky, P. Spanne, J.-O. Gebbers, D.W. Archer, and J.A. Laissue. Rev. Sci. Instr. 66, 1459-1460, 1995.

Thermal equation of state of $CaSiO_3$ perovskite *	X17B1

Yanbin Wang, Francois Guyot, and Donald J. Weidner (CHiPR, SUNY Stony Brook)

It is well known that $CaSiO_3$ perovskite is unstable at ambient conditions;this non-quenchable nature makes it difficult to study the P-V-T behavior of this material. We use a DIA-type cubic-anvil apparatus (SAM-85) to synthesize $CaSiO_3$ perovskite and measure the pressure-temperature-volume (P-V-T) relations by synchrotron X-ray diffraction. Starting material is wollastonite and the sample is embedded in NaCl which serves as the pressure standard. Sample synthesis is carried out prior to P-V-T measurement and the perovskite phase is identified in situ by X-rays. A comprehensive P-V-T data set has been obtained in pressure and temperature ranges up to 14 GPa and 1600 K, allowing isothermal, isobaric, as well as isochoric measurements on the thermoelastic properties. Special care has been taken to minimize effects of non-hydrostatic stress on these measurements. We take the advantage of the high temperature capability in SAM-85 to reduce the effects of non-hydrostatic stress on the volume measurement by heating to 1000K. At a constant load, data above 700 K and immediately after the cooling cycle from above that temperature are the least affected by the non-hydrostatic stress, as the strength of the surrounding NaCl diminishes. Our isothermal data are fit by a high-temperature Birch-Murnaghan equation of state at various temperatures, allowing a direct measurement on $(\delta K_T/\delta T)_p$. The isobaric data are analyzed to obtain thermal expansion (α) within the stability field of $CaSiO_3$ perovskite. Isochoric data between 4 and 12 GPa indicate that $(\alpha K_T)_V$ is nearly constant with increasing temperatures up to 973K. These results, in combination with previous data obtained using similar technique [1], give an average $(\delta K_T/\delta T)_p$ = -0.03(5) GPa/K over the pressure and temperature range of the experiments.

[1] Wang, Y. and D. J. Weidner, Thermoelasticity of $CaSiO_3$ perovskite and implications for the lower mantle. Geophys. Res. Lett., 21, 895–898, 1994.

* This work was supported by the NSF under a grant to the Center for High Pressure Research (CHiPR).

Performance of the low-energy section of the MECT monochromator *	X17B1

X. Y. Wu, F. A. Dilmanian, Z. Chen, J. Kress, B. Ren (BNL), M. Shleifer, D. Chapman,A.Lenhard, M. Radulescu, W. Thomlinson, M. Woodle, and Z. Zhong (NSLS)

The low-energy section of the monochromator for the Multiple Energy Computed Tomography [MECT] program was tested before and after its installation in the X17 transport hutch. The monochromator, a flat Laue-Laue device employing Si ⟨111⟩ crystals, has an energy range of 24.5 - 51.2 keV [1]. The complete MECT monochromator will include two such sections in tandem, and will be used for dual photon absorptiometry CT (e.g. at 40 and 100 keV) with a 2 s energy switching time, using a shutter that opens one beam at a time [2]. The highlight of the monochromator's mechanical design is that it employs independent, mechanically driven spindles with a double-gimbal mechanism for precise angular positioning of each crystal in the Bragg and the tilt directions [1]. An angular resolution of 0.04 arcsec is achieved by using a linear motion of 0.1 μm (Klinger stages) on a lever arm of 48.4 cm. The vertical beam offset is 15 mm.

The two Laue crystals were 12 cm wide, 6 mm high, and 1 mm thick. The first crystal was water- cooled. Both crystals were supported from below, without clamps, by three metallic half-spheres, 1 mm (1st) and 2.5 mm (2nd) in diameter.

Preliminary tests were carried out at the X26C and X27C beamlines. The X17B1 test were carried out a 33 keV, under vacuum, with a beam size of 99 mm x 2 mm using no filter and a 3.2 mm Al filter. The results were the following: (a) the monochromator was very stable, except for a transient heat-loading effect with a time constant of $\approx$ 10 min. A small amount of change in the horizontal beam profile was observed transiently, which disappeared with temperature equilibration and with fine adjustment of the tilt angle. (b) The minimum width of the rocking curve (obtained with $\approx 0.5^\circ$ tilt adjustment) was about 3.0 arcsec. This is only 40% larger than the expected value of 2.2 arcsec (obtained from Darwin width of 1.7 arcsec, convoluted for the Laue-Laue configuration). The horizontal and vertical beam profiles were uniform. These results indicate that crystal distortion was negligible. (c) Beam intensity fluctuations were $\approx$ 5% (tuned beam) and $\approx$ 30% (half-maximum detuned). The frequency range was 0 - 170 Hz, with a Fourier spectrum similar to that of the accelerometer- measured stand vibrations. Insertion of Iso-Mode pads under the stand reduced the Fourier components above 80 Hz. The effect was removed from the data, using unattenuated edges of the fan beam as references. (d) The monochromator's backlash was $\approx$ 0.5 μm (i.e. 0.21 arcsec), the source of which is presently unknown. It is, however, apparently inconsequential since active beam tuning was not necessary because of the monochromator's stability.

The results indicate that the performance is adequate for clinical MECT.

[1] M. Shleifer, F.A. Dilmanian, F.A. Staicu, and M.H. Woodle, Nucl. Instr. and Meth. A 347 (1994) 356.

[2] Optical design of the monochromator was developed with the help of J.B. Hastings and D.P. Siddons, to whom the authors are indebted.

* The authors thank L.E.Berman,C. Brite, W. deBoer, E. Gaudet, R. Greene, E. McKenna, S. Pjerov, S. Pop, R. Scheurer, and F.A.Staicufor their contribution to this work. Research supported by U.S. DOE under contract DE-AC02-76CH0006.

In situ x-ray diffraction study on magnesite at high pressure and temperature *	X17B1

J. Zhang, I. Martinez, F. Guyot (CHiPR and SUNY Stony Brook), P. Gillet (ENS Lyon),and S. K. Saxena (Uppsala Univ., Sweden)

The P-V-T data on magnesite constrain the temperature and pressure dependences of the bulk modulus and thermal expansion and are important in understanding the stability of magnesite in the mantle and its role as a store-house of CO_2. Using the DIA-type, cubic anvil apparatus (SAM-85) in conjunction with in situ X-ray diffraction at the X-17B1 beamline of the National Synchrotron Light Source (NSLS), we have measured the unit cell volume of magnesite at pressure and temperature up to 9 GPa and 1300 K. Synthetic polycrystalline magnesite was used as the starting material and NaCl as a pressure standard.

By fitting the experimental P-V-T data to the third-order high-temperature Birch Murnaghan equation of state, we obtain the following parameters for magesite: $K_o = 107(3)$ Gpa, $K_o' = 2.37(1.02)$, $(dK/dT)_p$=-0.014(1) Gpa/K, and $\alpha = 3.10(14)\text{x}10^{-5} + 1.78(24)\text{x}10^{-8}(\text{T-}298)\ K^{-1}$. These results are in good agreement with the single-crystal measurements reported by Ross (1994), who performed the compression study at room temperature, and by Markgraf and Reeder (1985), who refined the structure of magnesite up to 500 °C at 1 bar. The product of αK for magnesite is independent of temperature, even below the Debye temperature. We also find out that the present P-V-T data on magnesite can be successfully predicted by the spectroscopic models, in which the thermal pressure is calculated by combining Raman, infrared and acoustic data to construct the vibrational density of state.

[1] Markgraf, S.A. and R.J. Reeder, High temperature structure refinements of calcite and magnesite, Am. Mineral., 70,590-600, 1985.

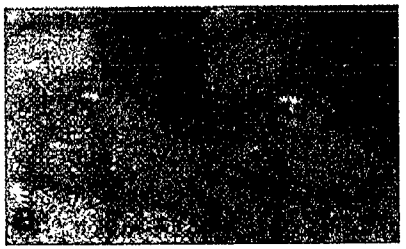
[[2] Ross, N.L., Magnesite at high pressure, Terra Abstract Supplement to Terra Nova, 6, 40, 1994.

* Work supported by the NSF under a grant to the CHiPR.

Comparing transvenous coronary angiography images using 0.5mm and 0.25mm resolution detectors *	X17B2

D. Chapman, W. Thomlinson, N. Gmur (NSLS), J. Dervan, T. Stavola (SUNY), E. Rubenstein,J. Giacomini, H. Gordon (Stanford U.), W. Lavender (SSRL), C. Schulze, and B. Bertrand (ESRF)

A major goal of the transvenous coronary angiography project is to develop an imaging technique for acquiring high quality coronary angiograms with reduced risk to the patient. The risk reduction is derived from the use of venous (as opposed to arterial) catheterization and should allow long term serial imaging of patients subsequent to medical intervention. During the history of angiography research at the NSLS, 16 patients have been imaged using either a) a 600 element, 0.5mm resolution detector (9 patients; 10/5/90 - 11/13/92), or b) a 1200 element, 0.25mm resolution detector (7 patients; 3/4/93 - 10/22/93). In anticipation of a beamline equipment upgrade and the need to resolve detector/imaging issues, a decision had to be made whether to continue research with either existing 0.5 or 0.25mm resolution detector or to develop a new detector with an intermediate resolution. Data to make this decision were obtained in two ways: a)imaging a highly characterized phantom which allowed a detailed analysis of the spatial resolution of the detector; and b) imaging a human patient which incorporated the complexity of the human anatomy and lent itself to diagnostic analysis. Both procedures used the two existing detectors. The detector's ability to resolve spatially varying features is characterized by the Modulation Transfer Function (MTF). The MTF for each detector was measured under the same conditions and compared. At 1 line-pair/mm (the resolution limit for a 0.5mm pitch detector) the MTF for the 0.5mm pitch detector was 0.6 while the 0.25mm pitch detector's MTF was 0.8; a 20% improvement. While one patient had already been imaged on two separate occasions (2/12/91 and 9/24/93) using the 0.5 and 0.25mm detectors, respectively, the answer to the current question required imaging the same patient in the same orientation during the same imaging session. This was accomplished on 10/21/93 when a patient was imaged in a LAO 30 degree projection. The 600 element - 0.5mm pitch detector image is shown on the left (a) and the 1200 element - 0.25mm pitch detector is in the right (b). These are sections of the original images showing the distal right coronary artery along the bottom with part of the left ventricle and aorta in the upper right. Upon close inspection of the images, smaller and sharper features are visible in the 1200 element image. Based on these results the decision was made to construct a new 1200 - 0.25mm pitch detector.



* Work funded by DOE Contract No. DE-AC02-76CH00016(BNL), DOE Contract No. DE-FG03-87ER60527and NIH Account No. NIH 5R01 HL 39253-04(Rubenstein.)

Comparing transvenous coronry angiography images using 3.0T and 4.0T superconducting wiggler fields *	X17B2

D. Chapman, W. Thomlinson, N. Gmur (NSLS); J. Dervan, T. Stavola (SUNY), E. Rubenstein, J. Giacomini, H. Gordon (Stanford Univ.), W. Lavender (SSRL), C. Schulze, B. Bertrand (ESRF)

As a corollary to the detector study outlined in the accompanying abstract, a further set of tests were undertaken in which phantoms and a human patient were imaged using the 1200–0.25 mm pitch detector at two superconducting wiggler fields— 3.0T and 4.0T.

A problem associated with producing 33keV imaging x-rays using a monochromator crystal is that significant intensities of harmonics (esp. the 2nd harmonic at 99keV) may be produced. This condition is exacerbated by the fact that such an x-ray beam is hardened as it passes through human tissue, the 33keV xrays being preferentially absorbed compared to the 99keV x rays. The harmonic signal adds a background component to the hgih and low image which degrades the ration or iodine image if no attempt is made to correct for its presence.

At the two wiggler fields used, the expected amount of flux at 99keV relative to the 33keV fundamental is 0.45% at 4T and 0.10% at 3T. When these beams traverse 20cm of water (a nominal equivalent to the patient thickness) the relative harmonic content is enhanced to 9.6% at 4.0T and 2.2% at 3T. The primary effect of the enhanced harmonic content is to create an error in the ability to determine the iodine content in the image (which will also degrade the image quality and appearance). The calculated error in determining an iodine areal mass density of 10mg/cm^2 (coronary arteries typiclly have values of $\approx$2–5mg/cm^2) through 20cm of water is -3.4% at 4T and -0.8% at 3T.

Measurements were made of iodine containing phantoms of known areal mass density with varying amounts of water absorptin and the results compared with calculations. This comparison is shown in the figure which shows the error in determining iodine areal mass density of 10mg/cm^2 at varioous water absorber thicknesses. The solid line shows the calculated 3.0T iodine error and the dashed the equivalent for 4.0T. The measurements at 3.0T are shown as boxes and the 4.0T measurements as crosses. The agreement with the calculations is reasonably good.

A patient image set was taken with the same projection at the two fields (3.0T and 4.0T). No visible differences were seend in the images (presumably because the harmonic content at 4.0T and 3.0T is so low in both cases). At present the most compelling reason to operate at the reduced 3.0T field is to obtain slightly better iodine values.



Figure 1.

* Work funded by DOE Contract No. DE-AC02-76CH00016 (BNL); DOE Contract No. DE-FG03-87ER60527 and NIH Account No. NIH 5R01 HL 39253-04 (Rubenstein)

Multiple x-ray diffraction studies of decagonal quasicrystals	X18A

R. Eisenhower, R. Colella (Purdue Univ.), and B. Grushko (Institut fur Feskorperforschung, Forchungszentrum Julich, Germany)

Multiple diffraction of x-rays makes it possible to determine phases of Bragg reflections. (R. Colella, "P.P. Ewald and his Dynamical Theory of X-ray Diffraction," edited by D.W.J. Cruickshank, H. J. Juretschke and N. Kato. Oxford University Press, 1993). A convenient technique consists in spinning a small crystal mounted on a four-circle diffractometer around the scattering vector of a weak reflection and monitor its intensity as a function of the azimuthal angle ψ called "azimuthal plot", typically exhibits well pronounced peaks when other strong reflections are excited simultaneously. The wings of such peaks often exhibit asymmetric features, from which phases of Bragg reflections can be determined. The only allowed phase values for centrosymmetric structures are 0° or 180°. Several three- beam experiments have been performed on $Al_{88}Cu_{11}Co_{21}$ does not possess a center of inversion symmetry. Similar results have been obtained on $Al_{70}Cu_{\Upsilon}Co_{30-\Upsilon}$ (Υ = 4,6,8,10 and 12) by electron diffraction. (K. Saitoh, et al., Mater. Sci. Eng. A181/A182 805-810 (1194). Phase values consistent with non-centrosymmetric structures have also been obtained in the icosahedral phases of Al-Cu-Fe (H. Lee, et al., Acta Cryst. A49, 600-605 (1993) and Al-Pd-Mn (H. Lee Ph.D Thesis Purdue University, 1993. Unpublished).

Effect of Dopants on Arsenic Precipitation in GaAs Deposited at Low Temperatures * | X18A

V. Mahadev, M.R. Melloch, J.M. Woodall, N.Otsuka, and G. L. Liedl (Purdue University)

High resolution x-ray diffraction using synchrotron radiation was used to characterize GaAs grown by MBE at low temperatures (LT-GaAs). LT-GaAs grown at 225 C is stoichiometric and exhibits a 0.15along the growth direction. Annealing LT-GaAs results in arsenic clusters with a well-defined orientation relationship with the GaAs matrix and a relaxation of the LT-GaAs lattice. The arsenic precipitation corresponds to a classical case of diffusion controlled nucleation and growth followed by coarsening. While the rates of growth and coarsening in the n-doped and the p-doped samples are observed to be identical, the effects of the superlattice seem to accelerate the precipitation kinetics in the p-n superlattice sample.

The enhanced coarsening in the p-n superlattice sample is consistent with a previously proposed model involving interaction between charged precipitate and arsenic defects.

* Work sponsored by DOE under grant (DE-FG02-85ER45813) and AFOSR grants (F49620-93-1-0031 and F49620-93-1-0388).

Quasiepitaxial growth model for n-alkane films * | X18A

Z. Wu, B. Bolon (Univ. of Missouri-Columbia), S. N. Ehrlich (Purdue Univ.), B. Matthies,K. W. Herwig (Univ. of Missouri-Columbia), H.-S. Youn (Postech, Pohang, Korea), and H. Taub (Univ.of Missouri-Columbia)

Synchrotron x-ray and neutron diffraction have been used to study the growth mode of hexane (n-C_6D_{14}) and butane (n-C_6D_{10}) adsorbed on Ag(111) and graphite (0001) surfaces. The monolayer unit cell of n-hexane/Ag(111) and both films on graphite is rectangular with a herringbone arrangement of the molecules.[1] For both films on Ag(111) and n-butane/graphite[2], we find that the solid n-alkane film incompletely wets the substrate; i.e., above $\approx$ 2 layers, solid bulk particles nucleate with their densest-packed plane parallel to the surface. Use of the single-crystal Ag(111) substrate eliminates capillary condensation effects and allows precise determination of the orientation of the bulk particles.

In the figure, we show x-ray specular reflectivity scans as a function of coverage for (a) hexane and (b) butane on the Ag(111) substrate. Our preliminary interpretation is that both have a two-component structure with a sharp peak of the well-oriented bulk particles superimposed on the smoothly varying contribution from the film. For hexane, the peak results from the (101) plane of the bulk triclinic structure being aligned parallel to the surface whereas for butane it is the (100) plane of the bulk monoclinic phase.

We suggest that the alkane molecules' rod-like shape is responsible for both the incomplete wetting of the film and the preferential orientation of the bulk phase. Thus we expect this quasiepitaxial growth mode to apply to a large class of films consisting of molecules with similar steric properties.

[1] H. Taub, in The Time Domain in Surface and Structural Dynamics, NATO ASI, Vol. 228, Ser. C (Kluwer, Dordrecht, 1988), p. 467.

[2] K. W. Herwig, J. C. Newton, and H. Taub, Phys. Rev. B, 15 November 1994.

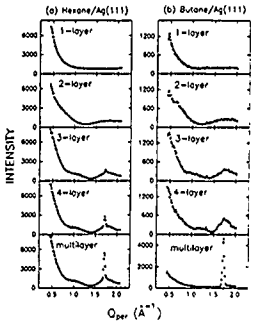


Figure 1.

* Supported by NSF Grant Nos.DMR-9011069 and DMR-9314235 and DOE Grant No. DE-FG02-85ER45183 of the MATRIX PRT at the NSLS.

Properties of $NiS_{2-x}Se_x$ (x = 0.51, 0.55, 0.63) * — X18A

X. Yao, S. N. Ehrlich, G. L. Liedl, and J. M. Honig (Purdue Univ.)

The electrical, magnetic and structural properties of $NiS_{2-x}Se_x$ have been investigated as a function of temperature. For x = 0.51 and 0.55 a broad electrical and corresponding magnetic anomaly was encountered above T = 40K for the single crystal samples; the sample with x = 0.63 remained a poor metal. X-ray powder diffraction patterns were taken at T = 20K, 60K, 80K, 90K, 150K and 298K for the x = 0.51 sample and at T = 50K, 150K, 180K, 200K, 235K and 298K for the x = 0.55 sample. Careful examination of these patterns shows no discernible change in the location of the diffraction peaks, nor is any broadening or splitting of these peaks immediately apparent. Only the heights of many of the peaks fluctuate with temperature. These observations are compatible with a structure that remains essentially unaltered as the material passes through a temperature range of the electrical anomaly. The intensity changes may reflect slight rearrangements of the atoms in a manner that preserves the overall symmetry of the lattice. These matters are to be resolved by Rietveld refinement of the diffraction patterns. However, this is not likely to affect the principal conclusion that there is no major change in structure as $NiS_{2-x}Se_x$ passes through the temperature range under investigation.

The figure below shows a diffraction pattern for the sample with x = 0.51 and T = 60K. The resistivity vs. temperature data for the same sample is shown in the inset.

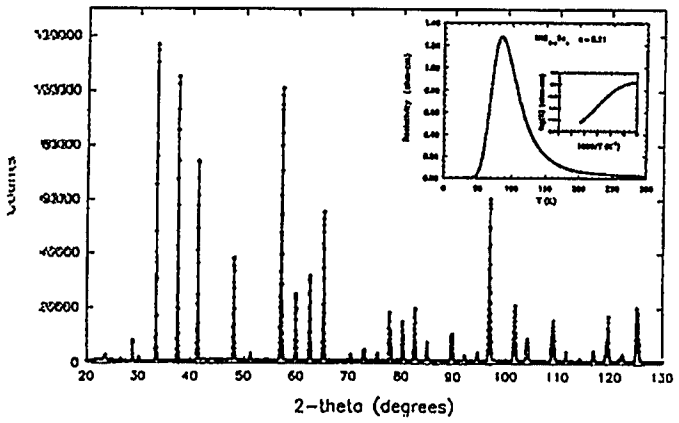


Figure 1.

* Work supported by NSFgrant DMR 92-22986 and DOE grant DE-FG02-85ER45183.

Surface EXAFS study of Fe/Cr multilayers * — X18B

J. M. Bai (Brooklyn College of CUNY) (ANL), E. Fullerton (ANL), and P. A. Montano(ANL) (Univ. Illinois, Chicago)

We have used surface fluorescence EXAFS to determine the interface composition of two Fe/Cr multilayer samples (A and B). The samples were measured at different angles of x-ray incidence. The samples were produced by epitaxial sputtering on MgO substrates. Sample A is on MgO (100) and B on MgO (110). For both samples, twenty bilayers of Fe (20 angstrom) /Cr (11 angstrom) were grown on the top of a 100 angstrom Cr buffer layer on MgO substrates.

Fig. 1 shows the Cr K-edge fluorescence EXAFS measurements on sample A at two incident angles (0.4 and 0.4745 deg.) below the critical angle. The fluorescence signal comes mainly from the Cr thin layers and the EXAFS are quite different from that at large incident angle. This means that the structure of the Cr thin layer in the Fe/Cr multilayers are significantly different from that of the Cr buffer layers for sample A. In contrast, Fig. 2 shows the EXAFS measurements of sample B. The EXAFS at small angle (0.3 deg.) is not much different from that at large angles. This experiment shows the dependence of multilayer structures on the orientation of the substrate crystal. Similar measurements were carried out at the Fe K-edge. A full analysis of the data is in progress.

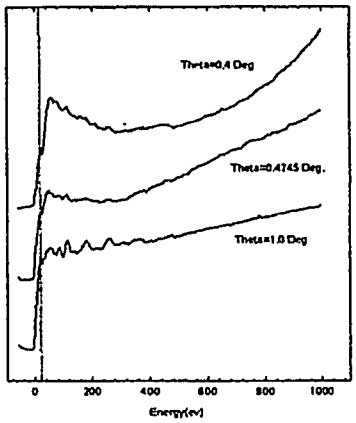


Figure 1. Surface EXAFS of Fe/Cr multilayer sample A (MgO (100) substrate).

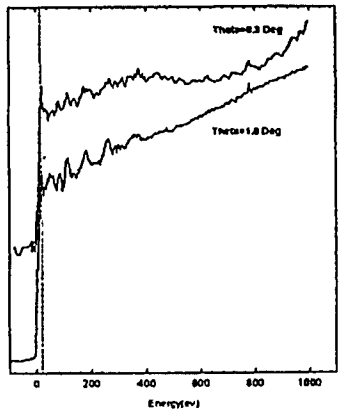


Figure 2. Surface EXAFS of Fe/Cr multilayer sample B (MgO (110) substrate).

* This work is supported by the U.S.DOE DESW-31-109-ENG-38.

Monitoring lead reduction on the surface of titanium dioxide by x-ray absorption *	X18B

L. X. Chen (ANL), Z. Y. Wang (NIU), T. Rajh, A. Ostafin, D. M. Tiede, M. C. Thurnauer, P. A. Montano, J. R. Norris (ANL)

Photoinduced charge separation in TiO_2 particles act as electron donors for the reduction of heavy ions, such Pb^{2+} and Hg^{2+}, in solutions. The reaction efficiency is increased by binding some surface reagent molecules of the TiO_2 surface. However, it is not clear how the heavy metal ions interact with the TiO_2 surface in the presence or absence of the surface reagents. We intended to monitor the process through x-ray absorption spectra of lead L_{III} edge for various lead complexes. Analyses of the XAS spectra for Pb^{2+} in aqueous solution, with surface reagent cysteine, and with TiO_2 particles are in progress.

During our experiments, we have found that Pb^{2+} can be unexpectedly reduced by TiO_2 under synchrotron X-ray irradiation at 30K without additional UV illumination as conducted in the laboratory. The reduction was not observed at room temperature after overnight exposure of the X-ray for the same sample. Figure 1 shows the lead reduction in a period of 90 min. illumination of X-ray beam while XAS spectra were collected at 30K. The top two curves show the characteristics XANES spectra of lead metal and Pb^{2+} in aqueous solution. The bottom spectra show the evolution of the XANES spectra from the first scan to the forth scan at 30K for the sample with Pb^{2+}, cysteine, and TiO_2. Similar spectral evolution was also observed for the sample containing Pb^{2+} and TiO_2 particles. Clearly the spectral features change from those for Pb^{2+} to Pb^0. This observation might be due to cascade transitions of the bonded electrons as a consequence of the excitations of th core electron, which may emit photons to induce the charge separation in TiO_2 particles. An increased trapped electron lifetime in TiO_2 at a low temperature may stabilize the efficiency of the metal reduction. However, a more conclusive statement can only be made after a more complete investigation. We plan to conduct a time-resolved experiment to monitor the process with energy dispersive XAS in the future.

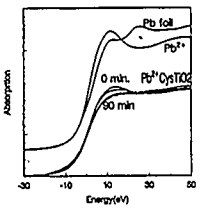


Figure 1. XANES spectra of Pb containing compounds (see text).

* This work is supported by the Department of Energy under contract W-31-109-Eng-38. We thank Dr. S. Khalid for his assistance during beamline operations.

Structural characterization of quantized TiO_2 particles	X18B

L. X. Chen (ANL), Z. Wang (NIU), T. Rajh, A. Ostafin, D. M. Tiede, M. C. Thurnauer,P. A. Montano, J. R. Norris (ANL)

Photoirradiation on semiconductor particles, such as TiO_2, creates charge separation on the particle surface. This photoinduced charge separation in the semiconductor particles present different electronic properties than those of the bulk material. Although many important photocatalytic reactions, such as reduction of heavy metal ions and oxidation of halogenated aromatics/aliphatics, occur on irradiated TiO_2 surface, the surface structures of the TiO_2 particles and changes of the s urface structure due to irradiation have not been well characterized. It is important to establish the correlations of surface structures and catalytic reactivities. As the first step towards characterization of the surface structure, we intended to characterize the structures for the interior and surface TiO_2 respectively by comparing the EXAFS spectra of TiO_2particles of different sizes. Figure 1 shows the X ANES spectra of TiO_2 particles with different sizes and preparation conditions. The preedge triplet features $A_{1,2,3}$, the shoulder B at the rising edge, and the peaks C and D above the threshold are characteristics of different structures with var ions degrees of distortion from the octahedral coordination found in normal anatase structure. The preedge features are weak in an octahedral coordination, and are enhanced in tetrahedral coordination. Thus,the relative intensities of these preedge peaks to the maximum peak C above the edge are the indication of the distortion of the structure. The XANES spectra of Degussa powder which ha s mainly anatase structure and particles of 320Å diameter are very similar with relatively weak preedge structures indicating the octahedral coordination. The preedge features for the particles of 45Ådiameter show an enhancement of the A_2 peak s uggesting a distortion from the octahedral coordination. This distortion can be from the surface structure,which 27% of TiO_2 possess, or from the distortion of the entire particle indicated by the enhancement of the preedge features in amorphous TiO_2. The shoulder B in the middle of the rising edge is very distinct in ordered crystalline TiO_2 as in Degussa and 320 Å particles, but virtually invisible in 45 Åparticles at room temperature. In amorphous TiO_2, feature B moves to a higher energy and becomes broader than in the crystalline TiO_2. Features C and D are sharp and have complicated fine structures in the crystalline TiO_2, but become broad and have no fine features. A structural change indicated by these spectral features has been found in 45 Åparticles when the sample was kept at 30K for a few hours. We have also conducted experiments on TiO_2 particles with surface reagents and under light illumination. A complete understanding and quantitative theoretical modeling of these features is in progress with the goal of characterizing the surface structure of neat TiO_2 particles, of particles with surface reagents, and of particles with light illumination.

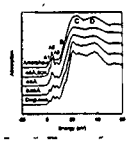


Figure 1. XANES spectra of different TiO_2 samples (see text).

X-ray absorption spectroscopic study of a commercial heat stabilized nylon during heat-aging process	X18B

Di-Jia Liu (Allied Signal)

Copper halide, when properly dispersed, could enhance the heat stabilization properties of Nylon. It is suggested that thermo-oxidative degradation of Nylon is caused by peroxide formation which is initiated by heat or light. The propagation of peroxide radicals induces Nylon chain scission thus weakening the mechanical properties. Cuprous ion, on the other hand, acts as a catalytic center which transfers electrons between halide ions and peroxide radicals and consequently terminates the propagation process. A proposed mechanism includes a redox cycle in which Cu(I) by taking an electron from halide ion X^-. If this cycle is interrupted, Cu(I) will be exhausted gradually by oxidizing species and converted to cupric ion, Cu(I). The anti-aging activity will thus stop.

To verify the redox mechanism experimentally poses a significant challenge for the conventional analytical techniques because the copper level is less than 100 ppm in commercial heat stabilized Nylon. Furthermore, there is no long range structure to be studied by conventional XRD or Microscopy methods.

Recently, we studied the oxidation state and coordination chemistry of Cu in commercial heat stabilized Nylon during the molding and heat-aging process using EXAFS and XANES spectroscopic methods. We observed a change of copper oxidation state from Cu(I) (Fig. 1), accompanied with local structural change. Furthermore, the variation of cuprous concentration correlates well with Nylon tensile strength. This study confirmed the hypothesis that Cu(I) plays a pivotal role in a redox mechanism by relaying the electrons from halide ions to peroxy radical to neutralize nylon chain scission.

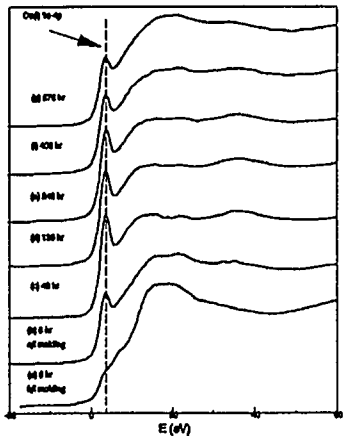


Figure 1.

X-ray absorption spectroscopic study of Cu in Cu-ZSM-5 during NO catalytic decomposition	X18B

Di-Jia Liu and Heinz J. Robota (Allied Signal)

Nitric oxide, NO, is one of the major pollutants generated by high temperature combustion devices such as automotive engines and industrial boilers. Under catalytic reaction conditions, NO can be decomposed directly to nitrogen and oxygen. There has been limited success in finding suitable catalysts to accomplish this task. One of the candidates is Cu-XSM-5 [1] system. As an industrial research and development effort, it is crucial to understand the mechanism of NO decomposition, therefore providing suggestions for next stage of catalyst development.

Reported here is our recent in situ investigation of Cu in Cu-ZSM-5 by XANES and EXAFS methods at X18B of NSLS. We designed an in situ reactor system for NO decomposition with which we can pretreat the catalyst and measure the relative NO conversion level while taking EXAFS and XANES spectra under the catalytic reaction conditions [2]. We observed that Cu in freshly prepared Cu-ZSM-5is fully oxidized as Cu(II) (Fig. 1a) and coordinated with an average of 4.8 O atoms (Fig. 2a) from both adsorbed water and zeolite framework. After calcination in dry air at 500°C, Cu lost the water ligands and is re-anchored to ZSM-5 framework with a clear higher shell structure while remaining in Cu(II) state, as is shown in Fig. 1b and 2b. Cu in Cu-ZSM-5 can be auto-reduced to Cu(I) in inert gas flow at elevated temperature. As is shown in Fig. 1c, a narrow, intense peak which is assigned to the 1s-→4p electronic transition of Cu(I) appears after Cu-ZSM-5 is activated in pure He. Accompanying the auto-reduction, the number of O coordination also decreases from 4 to 2, indicating change in Cu local geometry in ZSM-5 framework. Both the oxidation state and local structural information generated from this study are extremely important to interpret our XANES and EXAFS spectra obtained during the actual catalytic reaction [2].

[1] For example, M. Iwamoto, N. Mizuno and H. Yahiro, Sekiyu Gakkaishi, 34, 375(1991) and the references therein.

[2] D.J. Liu, and H.J. Robota, Catal. Lett. 1993, 21, 291.

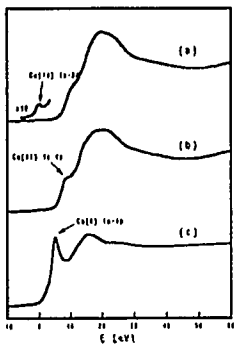


Figure 1. XANES spectra of Cu-ZSM-5 after different treatment.

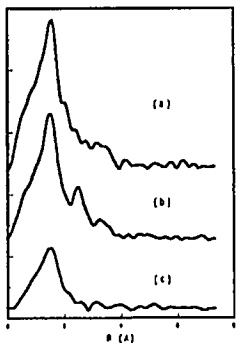


Figure 2. RDF of Cu in Cu-ZSM-5 after different treatment conditions.

On the nature of methyltrioxorhenium(VII) occluded in zeolite Y | X18B

Andrzej Malek and Geoffrey Ozin (Univ. of Toronto)

The adsorption of gaseous molecular methyltrioxorhenium(VII), CH_3ReO_3 (denoted MTO) into zeolite Y hosts, is the subject of an in situ Mid-IR, UV-Vis, XPS, EXAFS, PXRD, and Gravimetry multianalytical technique investigation, aimed at elucidating the identity, anchoring details, thermal stability and chemical reactivity of the occluded guests. The combined results of this study demonstrate that, at room temperature, a maximum of four intact MTO molecules can either hydrogen-bond to Bronsted acit sites or attach to extraframework cationic sites, in the supercages of $M_{56}Y$, where M= H, Na, Rb. The favoured anchoring interaction is found to be CH_3ReO_3...MOZ, in which the oxygen-end of the oxorhenium bond in MTO, binds preferentially to supercage cation or proton sites. Minimum energy universal force field calculations indicate tht in fully loaded $(MTO)_{32}M_{56}Y$, groups of four MTO guests associate through Re=O...Re interactions. These aggregates of MTO are induced to form as a consequence of the high Lewis and Bronsted acidity and intense electric fields associated with the anchoring cation or proton sites, and are believed to be responsible for the visible optical absorption that is observed to develop in these materials. Adsorbed water causes de-aggregation of these groupings of MTO guests. Thermal treatment of these materials around 120° is found to yield CH_4 and H_2O together with the formation of an intrazeolite cluster species containing ReRe bonds.

EXAFS investigations of lanthanide ion hydration in concentrated electrolyte solutions * | X18B

B. Stout, B. Helmer, E. Conover, D. Peterman (Univ. Cincinnati), S. Clark, and A. Bryce (SREL)

Questions concerning the hydration of lanthanide ions in aqueous solutions and the presence or absence of anions in the primary coordination sphere have persisted, despite the number of techniques which have been brought to bear on this area of research. Though data exist for dilute solutions, plans for the disposal of actinide waste in salt mines at the Waste Isolation Pilot Project site in New Mexico have prompted an examination of actinide speciation in concentrated salt systems. Lanthanide ions have a stable trivaleent oxidation state and serve as convenient nonradioactive models for the actinide (III) ions present in radioactive waste. EXAFS spectra of solution of Eu_{3+} and Tb_{3+} in dilute (0.7 M) and concentrated (9.7 M) HL and $HClO_4$ were collected at room temperature. The fluorescence spectra of the L_{III} absorption edge of Tb and EU were measured.

Terbium. The average Tb-O (from inner sphere H_2O) distance in either Tb_{3+} solution was found to be 2.41 Å. The concentrated $HClO_4$ solution showed a greater disorder in the inner sphere compared to the dilute, indicated by a 30% decrease in the amplitude of the Tb-O peak. This same Tb-O peak was virtually identical in amplitude in the concentrated and dilute HCl solution at ca. 3.2 Å. Thi sis much longer than the 2.77 ÅTb-(inner sphere) Cl distance found in the model compound. Also, there was another peak n the spectrum of the concentrated solution at 5.8 Å, again evidence of more outer sphere chloride ions. Both outer sphere chloride peaks were identified by backtransforming these peaks and fitting the EXAFS with theoretical Cl FEFF backscattering amplitudes and phase functions for O and Cl. Cl gave the best fit in both cases.

Europium. A decrease in the amplitude of the Eu-O peak was seen in concentrated $HClO_4$ solutions, similar to that found for Tb-O. No evidence ofCl^- or ClO_4^- ions in the inner sphere were found. Outer sphere Cl^- and ClO_4^- if present, were sufficiently small in number that they were undetectable by EXAFS. A small increase in the Eu-O distance was observed in both the concentrated acid systems. There is no thermodynamically consistent explanation for this, though it persists even if a slightly larger k-space is used for the Fourier transformation.

* The authors would like to acknowledge the NSLS Faculty Student Research Support Program for funding these experiments.

Evaluation of zirconia-based superacid catalysts by EXAFS *	X18B

José E. Tábora and Robert J. Davis(Univ. of Virginia)

An Fe, Mn promoted sulfated zirconia catalyst was two orders of magnitude more active than an unpromoted catalyst for butane isomerization at low temperature [1]. In this work, the bulk structures of the unpromoted and promoted superacid catalysts were investigated using x-ray absorption spectroscopy at the Zr and Fe K-edges. Analysis of the XRD patterns of these materials revealed that the primary crystalline phase of ZrO_2 is tetragonal; however, x-ray diffraction does not detect any nanocrystalline and non-crystalline components in the material. Therefore, we used x-ray absorption spectroscopy to evaluate local structural parameters of all domains of the material, both crystalline and non-crystalline. The Zr-O EXAFS from the superacids were fit with two shells at 2.10 and 2.34Å. Close examination of the EXAFS results of Li, et al. [2] for zirconia polymorphs indicates that tetragonal zirconia has Zr-O contributions at 2.10 and 2.33 Å, which are the same as the oxygen distances in the superacids, within experimental error. We also found that a single Zr-Zr distance of 3.62 Å can account for the large peaks in the Fourier transforms of both superacid samples. This interatomic distance is the same as that reported by Li, et al. For tetragonal zirconia, whereas the Zr-Zr distances for other zirconia polymorphs are completely different. Thus, the Zr-O and Zr-Zr interatomic distances derived from EXAFS indicated that both zirconia catalysts were exclusively tetragonal regardless of composition. The radial structure function from Fe EXAFS of the promoted superacid shows an oxygen distance at 2.02 Å which is very similar to the Fe-O distance in hematite (2.03 Å) and much shorter than the Zr-O distances in tetragonal zirconia (2.10, 2.34 Å). Since no Fe- Zr contribution was detected by EXAFS, direct substitution of Fe ions into the tetragonal zirconia structure did not occur.

[1] Hsu, C.-Y., Heimbuch, C.R., Armes, C.T., and Gates, B.C., J. Chem. Soc., Chem. Commun. 1645 (1992).

[2] Li, P., Chen, I.-W., and Penner-Hahn, J.E., Phys. Rev. B 48, 10063 (1993).

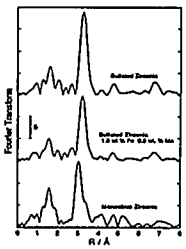


Figure 1. Fourier transforms of the Zr K-edge EXAFS data for the zirconia-based superacids and monoclinic zirconia.

* This work was fundedby a NSF Young Investigator Award CTS-9257306.

In situ x-ray absorption fine structure measurements of $LaNi_5$ electrodes in alkaline electrolytes *	X18B

D. A. Tryk, I. T. Bae, S. Kim, Y. Hu, D. A. Scherson (Case Western Univ.), M. A.Antonio (ANL), V. Leger, and G. E. Blomgren (Eveready Battery Co.)

In situ Ni K-edge and La L_{III}-edge x-ray absorption fine structure (XAFS)measurements of $LaNi_5$ electrodes supported on hydrophobic carbon black-PTFE layers were carried out in strongly alkaline electrolytes as a function of the state of charge. The Ni K-edge x-ray absorption near edge structure (XANES) for the material in the discharged (and uncharged) and charged states were essentially identical to those reported earlier for crystalline $LaNi_5$ before and after exposure to gas phase hydrogen, respectively, Also consistent with gas-phase results was the FT analysis of the Ni K-edge extended x-ray absorption fine structure (EXAFS), which was characterized by a single major peak containing contributions from at least two Ni neighbors. Curve fitting of the FT back-transforms for the uncharged, charged and discharged materials revealed an increase in the weighted average nearest neighbor distance for the charged (2.52 +/- 0.02 Å) compared to the discharged and uncharged electrodes, which yielded in both cases a value of 2.47 +/- 0.02 Å. This observation is in agreement with the partial conversion of the hydride from the α to the β form. In addition, the white line of the La L_{III}-edge XANES was found to be significantly more intense from the charged than for the uncharged $LaNi_5$. This effect is consistent with published band structure calculations, which predict an increase in the density of empty d-like states just above the Fermi level due to a hydrogen-induced shift of the Fermi level from a point below the La d-band to a point within the band.

* Work supported by the U.S. Department of Energy, Basic Energy Science and Eveready Battery Company, Westlake, OH.

The electrochemical insertion of lithium into pyrite from non-aqueous electrolytes at room temperature: an in situ Fe K-edge x-ray absorption fine structure study *	X18B

D. A. Tryk, S. Kim, Y. Hu, W. Xing, D. A. Scherson (Case Western Reserve Univ.),M. A. Antonio (ANL), V. Leger, and G. E. Blomgren (Eveready Battery Co.)

The effects of lithium ion insertion on the structural and electronic properties of FeS_2 (pyrite) have been examined in situ by Fe K-edge x-ray absorption fine structure (XAFS) using electrodes and electrolytes similar to those found in conventional, ambient temperature, primary Li/FeS_2 batteries. A substantial reduction in the amplitudes of the Fe-S and Fe-Fe backscattering was observed as the amount of intercalated lithium in the FeS_2 lattice was increased from 0 to 2 Li^+ equivalents, $(Li^+)_{eq}$. After the insertion of two $(Li^+)_{eq}$, the second shell Fe-S interaction and the distant Fe-Fe interactions were no longer discernible in the FT data. Curve fitting analysis of the $k^3\chi(k)$ extended x-ray absorption fine structure for this latter material yielded an average Fe-S distance, d(Fe-S) = 2.31 +/-0.02 Å, which is about 0.05 Å longer than d(Fe-S) in crystalline pyrite. In addition, the x-ray absorption near edge structure revealed a rounding of the otherwise highly structured edge of the FeS_2 as the amount of inserted lithium was increased. This behavior is consistent with the formation of $Fe_{1-x}S$ and thus support the assignment made on the basis of in situ ^{57}Fe Mossbauer effect spectroscopy of the same system.

* Work supported by the U.S. Department of Energy, Basic Energy Science and Eveready Battery Company, Westlake, OH.

Surface structures of supported molybdenum oxide catalysts: characterization by in situ Raman and Mo $L_{2,3}$-edge XANES	X19A

Simon R. Bare (Dow Chemical Co.), Hangchun Hu and Israel E. Wachs (Lehigh Univ.)

We have continued our investigation of the application of in situ XANES at the Mo $L_{2,3}$- edges to the characterization of highly dispersed TiO^2-, SiO^2- and Al^2O^3-supported molybdenum oxide catalysts [1]. We make use of the splitting of the white line at the $L_{2,3}$- edges to determine the local symmetry of the supported molybdenum oxide species [2]. In this series of experiments we have shown that by combining the XANES measurements with Raman spectroscopy a powerful combination of techniques results. Under ambient conditions, the structures of the hydrated surface molybdenum oxide species are controlled by the net surface pH at the point of zero charge. Under dehydrated conditions, the structures of the surface molybdenum oxide species depend on both the specific oxide support as well as surface coverage. At low coverages of MoO_3 on Al_2O_3 and TiO_2, the primary species is isolated and tetrahedral coordinated. At high surface coverages for TiO_2 the primary species is polymerized and octahedral coordinated, but for Al_2O_3 there is a mixture of tetrahedral and octahedral coordinated species. The surface molybdenum oxide species on SiO_2 is isolated and appears to possess a coordination that is between tetrahedral and octahedral. Monolayer coverage was achieved at the same surface density of molybdenum oxide on the different oxide supports with the exception of SiO_2.

[1] H. Hu, I.E. Wachs and S.R. Bare, J. Phys. Chem. (submitted).
[2] S.R. Bare, G.E. Mitchell, J.J. Maj, G.E. Vrieland, J.L. Gland, J. Phys. Chem., 97, 6048, (1993).

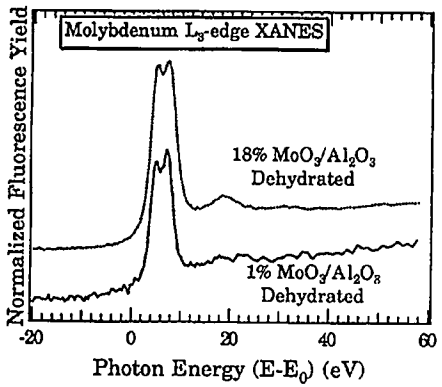


Figure 1. new

Structures of organocuprate-substrate intermediates *	X19A

T. M. Barnhart and J. E. Penner-Hahn (Univ. of Michigan)

Organocopper compounds (R_2CuLi, where R= alkyl, aryl, etc.) are among the most veratile organometallic reagents for forming new carbon-carbon bonds. Although their synthetic utility is well established, the structures of both the cuprate and the putative substrate bound intermediate remain largely unexplored. Molecular weight determinations suggest that R_2CuLi exists as a dimer or oligomer in THF (Fig. 1). NMR studies show that additions of enone substrate to solutions of R_2CuLi cause large chemical shift differences that are consistent with formation of a Cu-alkalene π-bond. This observation supports the proposed mechanism for cuprate-mediated 1,4 addition reactions which involves a cuprate-enone π-complex intermediate on the reaction path. We have measured EXAFS spectra for several preparations of dimethyl cuprates. In all cases, the EXAFS are dominated by the nearest neighbor scattering from a shell of two carbons with R_{Cu-C}=1.95Å. For some preparations, this is the only detectable EXAFS feature; however, other preparations display an outer shell attributable to a Cu–Cu intereaction at 2.45Å(see Fig. 2). This is consistent with the Cu–Cu distances of 2.4–3.1 Åseen in crystallographically characterized oligomers (e.g., Fig. 1, left). This variability in the EXAFS suggests that dimerization of Me_2CuLi may be very sensitive to preparative methods, but not vital to reactivity (vide infra).

EXAFS was also used to characterize these same samples after addition of the enone substrate trans-cinnamate methyl ester. It is noteworthy that the EXAFS spectra of the cuprate+enone solutions were identical, regardless of the starting preparation. If a Cu–Cu intereaction was present in the initial cuprate, it was disrupted on addition of the enone. In addition, these data show an increase in first shell bond length from 1.95 to 1.99 Å. This is consistent with a change in the copper coordination number from 2 to 3 (counting a π bond as a single ligand). This structural change is also relected in the 1s-4p transition which decreases in intensity on addition of cinnamate. Finally, the apparent number of first shell scatterers increases from 2 to 4 with addition of cinnamate. These data provide the first direct structural evidence for formation of a π complex between he enone and the copper center.

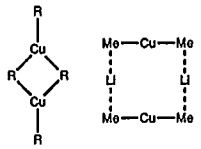


Figure 1. Two of several limiting structures for $[Me_2CuLi]_2$ dimers insolution. Structure on right is consistent with both EXAFS andebulliometry data if Cu-Cu distance is sufficiently large.

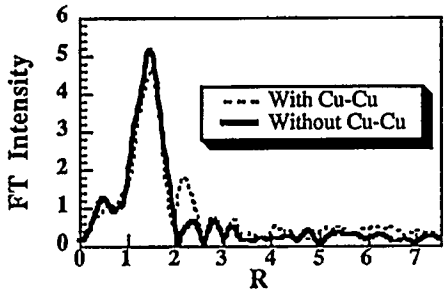


Figure 2. Ft of EXAFS of solutions of Me_2CuLi with andwithout Cu-Cu intereaction at 2.45 Å.

* Supported in part by the Alfred P. Sloan and the Henry and Margaret Sokol Foundations.

A quick conversion for x-ray magnetic circular dichroism experiments at X19A beamline *	X19A

J. Chen (UCD), A. Young, (LBL), M. Grush (UCD), L. Furenlid (BNL), and S. P. Cramer (UCD and LBL)

The x-ray magnetic circular dichroism (XMCD) has attracted much attention recently because of its unique capabilities for investigating the magnetic structure of transition metal and rare earth compounds. In here, we report a simple setup at X19A beamline can change linear polarized light to circular polarized light within a few minutes. The idea is to collect the off plane synchrotron radiation by moving the front slit and realign the beam optics using newly installed mirrors. The optic path of the setup is displayed in Figure 1. S1, S2, M1, and M2 are front slit, beam aperture slit, front collecting mirror, and refocus mirror, respectively.

As a test case, we have measured the MXCD spectra of Gd L_2-edge using normal transmission mode. The spectra were taken by moving dawn the front slit 0.11 mR and flip the magnetic field from 2 Tesla to -2 Tesla. the measured XMCD spectra are very similar to the published data by Schütz group [1] (Figure 1), but with much better signal to noise ratio. The observed MCD effect is 6%, which is larger than early reported 4%. This may be due to the more complete magnetization for our sample. We noticed that the field strength used in early experiment is 0.08 Tesla. This result demonstrated that XMCD experiments can be done at the X19A beamline, and one can easily convert linear polarized light to circular polarized light by adjusting the front slit and mirrors. The future goal will be to use two collecting mirrors and do left- and right-circular polarized measurement simultaneously.

[1] G. Schütz et al., Z. Phys. B 73, 67 (1988).

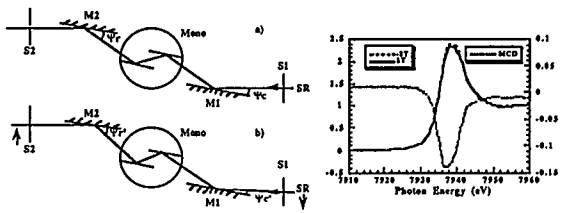


Figure 1. (Left) The optics for linear (a) and circular (b)polarized photons (Right) The XMCD spectra of Gd L_2-edge taking at +2 Tesla (solid line) and -2 Tesla field (dash).

* This work was supported by National Science Foundation through grants DIR-9105323 and DMB-9107312, the National Insitutes of Health through GM-44380.

The fate of bulk zinc in the development of zebra fish | X19A

D. L. Tierney, J. E. Penner-Hahn (Univ. of Michigan), L. M. Walrath, and J. M. Berg (John Hopkins Univ.)

The role of zinc as a biological co-factor has only recently come under study. In the past several years, the importance of zinc-fingers in regulatory biology has been well established. Zinc-fingers and many other since proteins play a major role in transcription and gene regulation. The presence of zinc in high concentration in the unfertilized eggs of zebra fish has recently been demonstrated and this concentration is apparently maintained throughout the early stages of embryo development [1]. We have used XAS to examine the zinc environment(s) in zebra fish eggs, and to characterize the time dependence of the zinc structure in early development.

Preliminary EXAFS data on the unfertilized eggs are consistent with the average zinc ligation being primarily sulfur. The ability to observe EXAFS oscillations suggests the bulk zinc must be in a fairly ordered environment. However, the data are not of sufficiently high quality to rule out the presence of low-Z scatterers or to definitively assign the coordination number. The average Zn-S bond length of 2.28 Åis typical of those seen for four coordinate zinc complexes.

Figure 1 shows the normalized XANES spectra for zebra fish eggs before fertilization, shortly (¡6 h) after fertilization, and after the developing embryo begins to envelop its egg sack (mid-blastula transition, MBT). From the spectra it is clear that there is a time dependent change in the average zinc environment. The XANES spectrum for the unfertilized eggs is most consistent with that observed for a ZnS_3N or ZnS_4 site [2]. Together with the EXAFS, this suggests that the bulk of the zinc present in the unfertilized egg is sequestered in some form of a storage site. The time dependent changes after fertilization suggest that zinc may be released and then re-sequestered as the embryo develops, possibly during the activation of regulatory proteins involved in growth. Further experiments are in process in order to better characterize the changes in the since structure.

[1] Walrath, L.M. and Berg, J.M., manuscript in prepartion.
[2] Clark, K.; Tierney, D.L.; Govindaswamy, K.; Gruff, E.; Kim, C.W.; Berg, J.M.; Koch, S.A.; Penner-Hahn, J.E., manuscript in preparation.

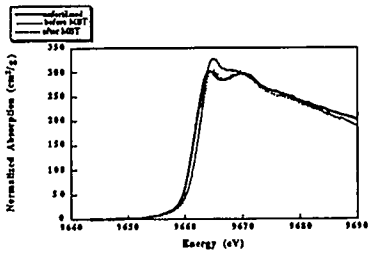


Figure 1. Normalized zinc XANES spectra for zebra fish eggs.

Imaging GaN thin film on (0001) sapphire substrates by synchrotron white beam x-ray topography * | X19C

H. Chung and M. Dudley (SUNY Stony Brook)

GaN, with its direct-band-gap energy corresponding to the blue/ultraviolet region of the optical spectrum, is one of the most promising materials for the applications as light emitting devices in the blue, violet, and near-ultraviolet spectra. Moreover, its excellent thermal conductivity and saturation velocity make it the prime candidate for high temperature, high frequency, and higher power devices. however, the application of GaN is hindered by its poor crystal quality. In this work, a GaN thin film ($\approx 10\mu$m in thickness grown on a (0001) sapphire substrate is imaged by synchrotron white beam x-ray reflection topography as shown in Fig. 1. The upper part of the topograph is the image of GaN thin film and the lower part is the image of substrate. Although many reflections have been investigated, no features related to the defect structure in the GaN thin film can be resolved from these blurred images. This most likely results from the poor quality of the GaN thin film.

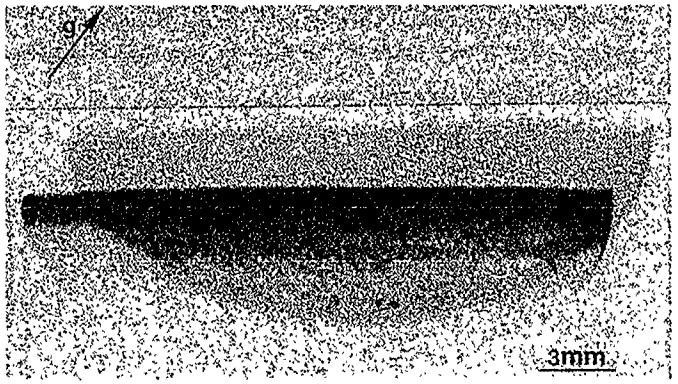


Figure 1. Experimental setup and schematic of x-ray fluorescence detector.

* Acknowledgements: Work performed on the Synchrotron Topography Project Beamline X19C.

Characterization of basal plane dislocations in sapphire crystals by synchrotron white beam x-ray topography *	X19C

H. Chung, M. Dudley (SUNY Stony Brook), D. Larson, Jr., D. Dimarzio, and L. Carr(Grumman)

Dislocations in a (0001) sapphire single crystal have been imaged by Synchrotron White Beam X-ray Topography (SWBXT). One of the advantages of using white X-rays is that we can obtain high quality topographs from several diffractions simultaneously, therefore abundant information about defect structure can be obtained in a single exposure so that we can effectively investigate the defect structure in detail. In sapphire crystals, the accumulation of individual dislocations possessing several different Burgers vectors in tangles leads to the complication in interpreting the dislocation configuration. To acquire more information about these dislocations, SWBXT is the best technique of choice. Figure 1 is a topography recorded from to $(2\bar{1}\bar{1}0)$ reflection. The basal plane dislocations labeled by (D_1), (D_2), and (D_3) are out of contrast on the $(30\bar{3}0)$ reflection as shown in Figure 2. By applying the $g \cdot b = 0$ criterion, the Bergers vector of these dislocations is determined to be parallel to the $[1\bar{2}10]$ direction. On the other hand, the extinction of basal plane dislocations are also observed on the $(\bar{3}330)$ and $(0\bar{3}30)$ reflections suggesting the existence of Burgers vectors parallel to the $[11\bar{2}0]$ and $[\bar{2}110]$ directions. Therefore, three sets of basal plane dislocations with Burgers vectors parallel to the $(11\bar{2}0)$ directions are characterized. Although Kronberg according to his theoretical studies proposed the existence of basal plane partial dislocations with Burgers vectors of $1/3\langle 0110\rangle$ types [1], no partial dislocations were observed in the present work.

[1] M. L. Kronberg, Acta. Cryst., 5, 507(1957)



Figure 1.



Figure 2.

* Acknowledgements: Work performed on the Synchrotron Topography Project-Beamline X19C.

Imaging of crystal defects in sapphire crystals by synchrotron white beam x-ray topography *	X19C

H. Chung, M. Dudley (SUNY Stony Brook), D. Larson, Jr., D. Dimarzio, and L. Carr(Grumman)

Crystal defects in sapphire single crystals has been studied by many investigators using different methods over a period of many years. For high quality sapphire crystals, X-ray topography is the most suitable method for this purpose. In this study, the defect structure of a large (0001) sapphire single crystal is observed by X-ray transmission topography. Figure 1 ($g = \bar{2}110$),$\lambda = 0.5$Å) is a topograph of the crystal in which the overall defect structure is revealed. The most prominent crystal defects are basal plane dislocations (D) which are highly curved and tangle together. Other defects such as inclusions (I) which cover all over the crystal are also imaged. Analyses of the Burgers vectors of basal plane dislocations revealed by X-ray topographs suggest the existence of the Burgers vectors parallel to the $\langle 11\bar{2}0\rangle$ directions, which confirms the theoretical study and experiment investigation carried out by Kronberg and Caslavsky [1,2]. More detailed studies of the basal plane dislocations are still underway.

[1] M. L. Kronberg, Acta Cryst., 5, 507, (1957)
[2] J. L. Caslavsky, C. P. Gazzara, and R. M. Middleton, Phi. Mag., 25, 35 (1972).

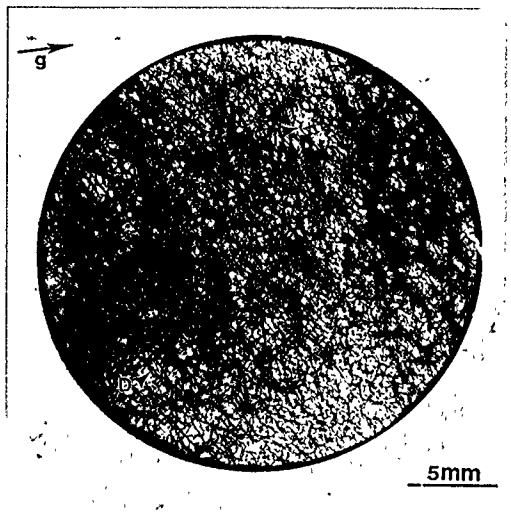


Figure 1.

* Acknowledgement:Work performed on the Synchrotron Topography Project Beamline X-19C.

Studies of elastic strains associated with 180° ferroelectric domain walls in KTP single crystals by synchrotron white beam x-ray topography *	X19C

H. Chung, S. Wang, and M. Dudley (SUNY Stony Brook), L. K. Cheng, J. D. Bierlein,and W. Bindloss (Du Pont)

180° ferroelectric domain walls in $KTiOPO_4$ single crystals have been imaged by synchrotron white beam X-ray topography [1]. The character and structure of 180° ferroelectric domain walls can be determined by analyzing the contrast of domain walls on X-ray topographs. Figure 1 (g=(221), $\lambda = 0.5$Å is a topograph of a (010) hydrothermally grown KTP single crystal in which the 180° ferroelectric domain walls (W) are revealed by fringe contrast. The presence of this fringe contrast suggests that there is a relative lattice displacement between the regions with opposite polarities. In X-ray topography, the displacement vectors associated with domain walls can be determined by observing the fringe contrast variations in different reflections [2]. In Figure 2 (g=(101), λ=0.7 Å), the kinematical contrast of the walls is imaged. The presence of kinematical contrast due to strain concentrations along the walls indicates the existence of a local deformation of the crystal in a volume of substantial thickness near the wall plane. Such strains are believed to be due to the curvature of the domain walls [3]. By analyzing strain contrast variations of the walls, one can find that the strain contrast of domain walls is weak when the diffraction vector g is parallel to the wall plane while it becomes strong when g is normal to the wall plane. Thus, it is determined that the displacement vector arising from the lattice deformation associated with the walls is perpendicular to the wall plane.

[1] S. Wang, M. Dudley, L. K. Cheng and J. D. Bierlein, Mat. Res. Soc. Symp. Proc., 307, 243 (1993).

[2] H. Klapper, Proc. Cryst. Growth and Charact., 14, 367 (1987).

[3] S. S. Jiang, M. Surowiec, B. K. Tanner, J. Appl. Cryst., 21, 145 (1988).

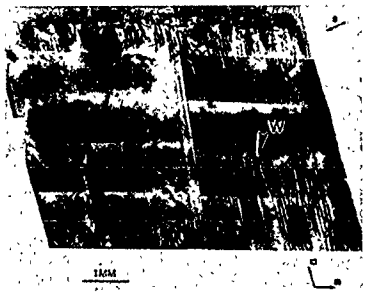


Figure 1.

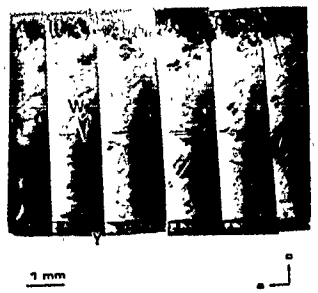


Figure 2.

* Work performed on the Synchrotron Topography Project Beamline X-19C, and supported by E. I. duPont de Nemours & Company, Inc.

The analysis of displacement vectors of 180° ferroelectric domain walls in KTP single crystals by synchrotron white beam x-ray topography *	X19C

H. Chung, S. Wang, M. Dudley (SUNY Stony Brook), L. K. Cheng, J. D. Bierlein,and W. Bindloss (Du Pont)

180° ferroelectric domain walls are planar defects that can be treated as inversion twin boundaries. The phase shift of X-ray wavefields due to the ferroelectric domain walls is, therefore, given by $\delta_{hkl} = 2\pi \mathbf{g} \cdot \mathbf{u} + 2\alpha_{hkl}$ where g is the diffraction vector, u is the displacement vector due to a relative lattice displacement associated with the walls, and α_{hkl} is the phase angle of a structure factor. 180° ferroelectric domain walls (W) are usually revealed on X-ray topographs by fringe contrast a shown in Figure 1. Extinction of this fringe contrast can be achieved when the total phase shift is equal to 0 or $2n\pi$, where n is an integer. An example is shown in Figure 2 in which the (004) reflection is used. The displacement vector associated with a ferroelectric domain wall can be deduced by observing fringe contrast variations of the wall in a sufficient number of reflections. This can be conveniently carried out using synchrotron white beam X-ray topography. Observing the fringe contrast variations of the walls in the {h01}-type reflections, one can find that fringes are out of contrast on reflections such as (004), (103), (10$\bar{3}$), etc, in which h +1 = even number. Since the phase angle, α_{h0l}, of these reflections is always zero, the value of U and V components of the displacement vectors u = (UVW) can easily be deduced as U = $\pm 1/2$ and W = $\pm 1/2$. On the other hand, only very weak fringe contrast can be imaged on the (210), (410), (411) and (212) reflections, which suggests that the V component can be $\pm 1/2$. Thus, the displacement vectors of the domain walls are determined as u = $\pm 1/2$[111].

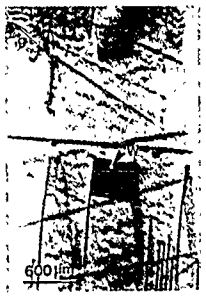


Figure 1.



Figure 2.

* Work performed on the Synchrotron Topography Project Beamline X-19C, and supported by E. I. duPont de Nemours & Company,Inc.

Characterization of growth defects in a ultra-thin CdZnTe single crystal by synchrotron white beam x-ray transmission topography *	X19C

H. Chung, J. Wu, M. Dudley (SUNY Stony Brook), and D. Larson, Jr. (Grumman)

A (111) CZT flight sample cut from a boule grown by the seeded Bridgman-Stockbarger method has been thinned down to the thickness of 180 μm and characterized by transmission X-ray topography. Figure 1 is a topograph recorded using the $(\bar{1}\bar{1}3)$ reflection. Dislocations (D) lying on the (111) plane are imaged as discrete line segments, which indicates that the dislocations are low in density. It is also worth noting that some of dislocations are invisible on the $(3\bar{1}\bar{1})$ reflection as shown in Figure 2. It indicates that the Burgers vector of these dislocations is parallel to the $[0\bar{1}1]$ or $[01\bar{1}]$ direction. In addition, extinction of dislocation images is also observed on the $(2\bar{2}0)$ and $(20\bar{2})$ reflections suggesting the existence of Burgers vectors parallel to the [110] and [101] directions, respectively. To determine the Burgers vectors of these dislocations with accuracy, more reflections will be investigated. Other features shown in Figure 1 such as the singular dark spots which can be found everywhere in the sample are thought to be Te precipitates. The straight lines running along the $[\bar{1}11]$ direction are characterized as 180° rotational twins (T). Twin orientation contrast is observed on the $(\bar{3}1\bar{3})$, $(\bar{3}31)$, and $(13\bar{3})$ reflections, whereas no orientation contrast is observed on the $(\bar{2}22)$, $(\bar{1}\bar{1}3)$, and $(\bar{1}3\bar{1})$ reflections. Through detailed analyses of orientation contrast revealed on transmission X-ray topographs, the twinning is characterized to be 180° rotation type about the $[\bar{1}11]$ axis.

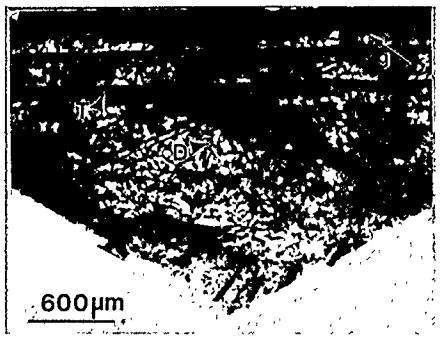


Figure 1.

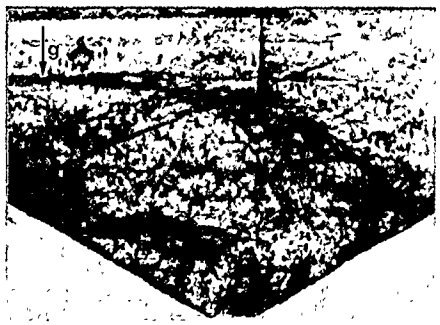


Figure 2.

* Work performed on the Synchrotron Topography Project BeamlineX-19C, and supported in part by NASA under contract No. NAS8-38147.

Imaging large CdZnTe single crystals by synchrotron white beam x-ray topography *	X19C

H. Chung, J. Wu, M. Dudley (SUNY Stony Brook), and D. Larson, Jr. (Grumman)

CZT is an important member of the family of II-VI compounds semiconductors. The most important application for the crystal is as substrates for the epitaxial growth of HgCdTe infrared detector material. The requirements for large-area, high performance infrared device stimulate the demands for high quality, large CZT substrates. To date, up to 40mm diameter boules can be grown by vertical and horizontal Bridgman methods. To characterize structural defects in large crystals, the new technique, a scanning mechanism associated with a specific Bragg reflection geometry, is developed. Advantages of the technique include increasing the speed of topographic experiment, eliminating image inhomogeneity resulting from the uneven source intensity, and reducing the intensity of background which can become very strong and can reduce the contrasts of crystal defects when a large-size incident beam is used. Figure 1 is the scanned image of a CZT substrate recorded using the (335) reflection. Three sets of dislocations (D_1), (D_2), and (D_3) lying along the [110], [101], and [011] directions respectively are imaged. Other defects such as a mosaic structure of cells (C), precipitates (P), and a subgrain boundary (SB) revealed by orientation contrast are also imaged. Figure 2 is a high magnification topograph of Figure 1 showing the configuration of dislocations in the substrate. The similar configuration of dislocations are also observed in a CZT flight sample.

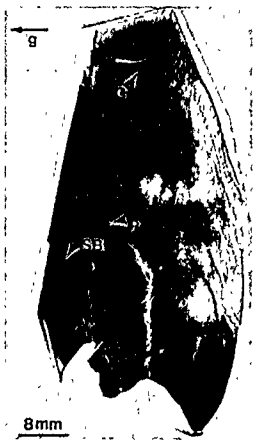


Figure 1.

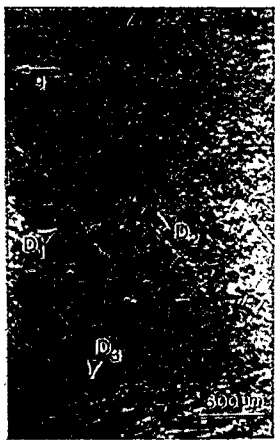


Figure 2. new

* Work performed on the Synchrotron Topography Project Beamline X-19C.

Synchrotron white beam x-ray topographic investigation of microgravity grown CdZnTesingle crystals *	X19C

H. Chung, J. Wu, M. Dudley (SUNY Stony Brook), and D. Larson, Jr. (Grumman)

A specific Bragg reflection diffraction geometry has been developed to screen the quality of CdZnTe substrate wafers. The Bragg reflection geometry developed fully utilizes the broad wavelength range of the synchrotron X-ray source to produce high quality topographic images in a single exposure. The multiple topographic images obtained from single exposure cover X-ray penetration depths ranging from 0.5 micrometers to 10.3 micrometers and diffraction rocking curve widths ranging from 0.7 arc seconds to 17 arc seconds. Therefore, defect information from different depth and at different strain sensitivities can be obtained on single exposure and compared to get a more detailed understanding of the defect content present in the wafers examined. Recently, this specific geometry has been applied to characterize the quality of a microgravity grown CZT sample and high quality topographic images are obtained. Figure 1 is a (202) reflection topograph in which the structural defects of this crystal are revealed. Two sets of parallel lines denoted as (L_1) and (L_2) respectively lying along the [$\bar{1}$] and [$0\bar{1}1$] directions are dislocations. A few 180^0 rotational twins are revealed by orientation contrast. The twinned regions are close to the seed and macroscopic in size. The white circles lying on the upper right region of the topograph are the images of precipitates (P). In addition, the diffusive, intense strain contrast shown at left-hand side- of the image reveals that high lattice strain is associated with the crystal in that area. The wavy contrast denoted by (B) lying in the central region of the topograph are thought to be growth bands. The formation of these bands is of great interest, and will be investigated in the near future.

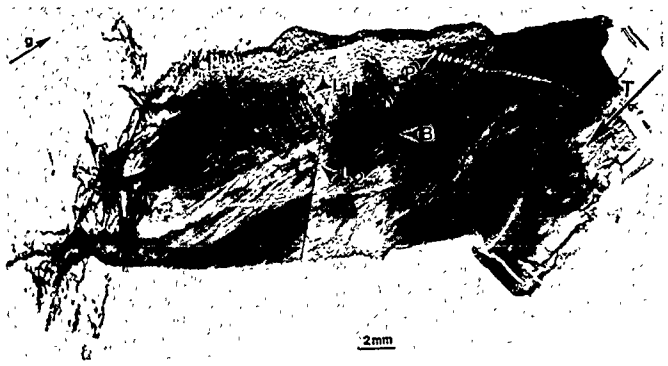


Figure 1. .

* Acknowledgements: Work performed on the Synchrotron Topography Project BeamlineX-19C, and supported in part by NASA under contract No. NAS8-38147.

Computer aided synchrotron white beam topography *	X19C

W. Huang, S. Wang, and M. Dudley (SUNY Stony Brook)

Indexing synchrotron white beam X-ray diffraction patterns can be a time-consuming, labor-intensive and experience-dependent process. When complicated diffraction patterns from mixed structures present on a single x-ray film, it is almost impossible to index them manually. Therefore software for unambiguous and automatic indexing has been developed. Although the indexing scheme is similar to that of others previously available, this program is more convenient to use. Simulated diffraction patterns of various kinds of materials and their combination in any diffraction geometry, such as transmission, reflection, grazing Bragg-Laue reflection and backreflection, can be generated with this program. All kinds of rotation options of the crystal as well as the detector are considered. The simulated pattern shows not only the location of each diffraction spot, but also the relative intensity of each image calculated by incorporating the source spectrum, structure factors, absorption and harmonic contamination. Such simulated patterns can be viewed on a computer screen and printed using a laser printer with the same size as a real x-ray film and with a gray scale of up to 256 levels. For example, figure 1(a) is a diffraction pattern recorded with a 6H-SiC wafer, while figure 1(b) is the corresponding simulated diffraction pattern assuming 6H-SiC structure. Good agreement is evident for this case, as in the case for other structures and geometries. In addition to the general data calculated including diffraction vectors g, intensity and wavelength, the x-ray penetration depth and rocking curve width is calculated simultaneously through input of the relevant geometric parameters. With the aid of this computer program, one can index the recorded diffraction pattern instantaneously so that the efficiency of the research work can be greatly improved by saving a lot of time and x-ray film in finding the best crystal orientation. Mixed structures within a single wafer can be easily identified and complex or unknown structures are readily analyzed with this software. Automatic and more accurate control of the rotation of goniometer and digital image processing can be achieved by the special design of this program. This is ongoing on beamline X19C.

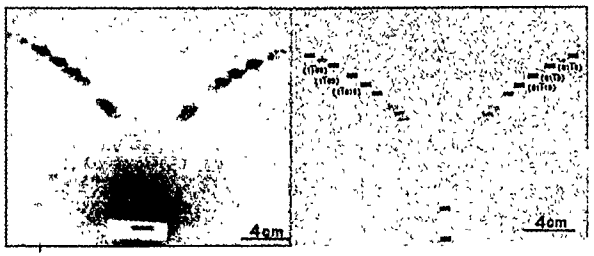


Figure 1.

* Work performed on the Synchrotron Topography Project Beamline X19C, supported by U.S. Army Research Laboratory under Grant No. DAAL02-92-R-9147/2FE425and U.S. Army Research Office under Grant No.s DAAL04-94-G-0091 and DAAL04-94-G- 0121.

Influence of structural defects on electrical properties of SiC devices *	X19C

W. Huang, S. Wang, M. Dudley (SUNY Stony Brook), C. Fazi (U.S. Army Research Laboratory,Adelphi, MD)

Synchrotron white beam x-ray topography has been employed in the investigation of influence of structural defects on electrical properties of SiC devices. Figure 1 is an optical micrograph of a pn junction fabricated on a (0001) 6H-SiC wafer. Figures 2, 3 and 4 are reflection topographs(g=01$\bar{1}$9, λ=0.82 Å) recorded from similar devices. Super-screw dislocations, indicated by S, and small angle grain boundaries, indicated by B, are found in these devices. Electrical testing showed that the values of leakage current of the devices showing in Figure 2,3 and 4 are - 7.39E-8 (A), -5.56E-8 (A) and -1.72E-10 (A), respectively. It can be seen that dislocations of large Burgers vectors, especially those located near the device working areas, as shown in Figure 2, seriously damage the devices. Small angle grain boundaries, as shown in Figure 3, also detrimentally affect the electrical properties. Improving the quality of the SiC wafers by decreasing the density of large Burgers vector dislocations and small angle grain boundaries is expected to reduce the leakage current by about 100 to 1000 times.

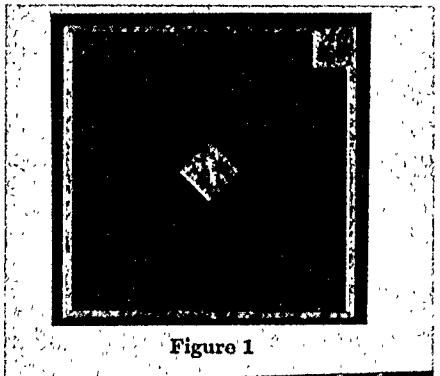


Figure 1

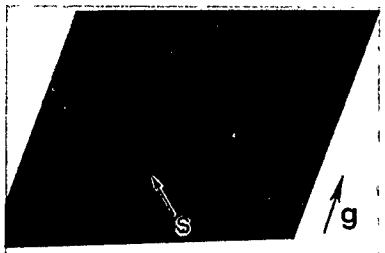


Figure 2

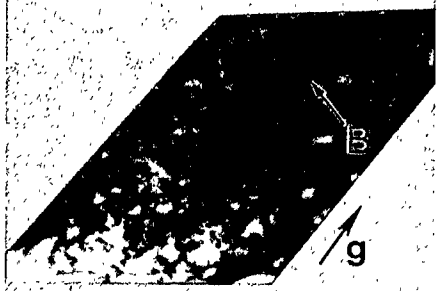


Figure 3

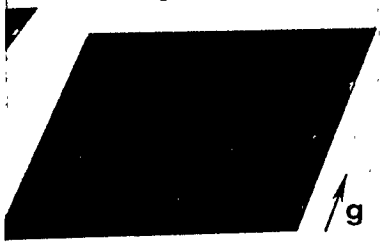


Figure 4

Assessment of damage accompanying the electrical breakdown of GaAs devices *	X19C

W. Huang, S. Wang, M. Dudley (SUNY Stony Brook), C. Fazi, R. Kaul (U.S. Army Research Laboratory, Adelphi, MD), and J. H. McAdoo (Mission Research Corporation)

Synchrotron white beam x-ray topographic imaging has been proved to be a powerful technique for the assessment of the structural damage resulting from electrical breakdown in semiconductor devices. In this work, this technique is applied to the investigation of the damage in GaAs devices induced during breakdown. Figure 1 is an optical micrograph of a device, in which the light areas correspond to the metallization regions and the dark areas correspond to the GaAs substrate. These features are visible on the X-ray topograph (g=51$\bar{1}$, λ=0.74 Å) shown in Figure 2, through a combination of differential absorption and strain contrast associate with the presence of the metallization lines. The white lines on the topograph correspond to the metallization lines because the high absorption of the metallization leads to low diffracted beam intensity. The strained regions are able to diffract x-rays that would not normally be diffracted by the near-perfect matrix, leading to a local increase in diffracted beam intensity. Figure 3 shows the topograph (g=51$\bar{1}$, λ=0.74 Å) recorded from a device which is electrically damaged. There are new contrast features, indicated by S, with enhanced X-ray intensity superimposed on the original contrast features. They are indicative of the presence of an additional strain field induced by the electrical breakdown process.

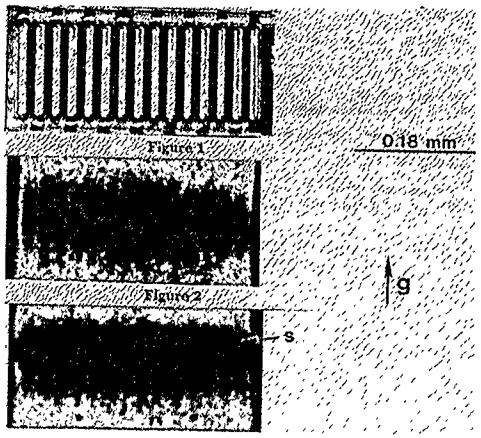


Figure 1.

* Work performed on the Synchrotron Topography Project Beamline X19C, supported by U.S. Army Research Laboratory under Grant No. DAAL02-92-R-9147/2FE425 and U.S. Army Research Office under Grant Nos. DAAL04-94-G-0091and DAAL04-94-G-0121.

Synchrotron white beam investigation of depth distribution of electrical damage in GaAs devices *	X19C

W. Huang, S. Wang, M. Dudley (SUNY Stony Brook), C. Fazi, R. Kaul (U.S. Army Research Laboratory, Adelphi, MD), and J. H. McAdoo (Mission Research Corporation)

Grazing Bragg-Laue white beam topographic imaging has been used to determine the distribution of damage as a function of depth, resulting from the electrical breakdown in GaAs devices. Figure 1 (a), (b), (c) and (d) are a series of details taken from grazing Bragg-Laue images (g=$51\bar{1}$), recorded with increasing penetration depth from 0.24 μm to 0.29 μm, showing the damage accompanying complete breakdown of the GaAs device. The white and dark lines correspond to the metallization lines and the GaAs substrates respectively, while the contrast features showing enhanced x-ray intensity, indicated by S, represent the strain field induced by the breakdown process. The largest and strongest strain field can be found near the area 0.27 μm in depth, which is characteristic of the fact that the greatest distortion is located in this region. The variation in the extent of distortion field generated by electrical operation as a function of depth, defined by the ratio of the total metallization area, is showing schematically in Figure 2. This information may shed light on the failure mechanism of such devices and help to suggest ways to improve their survivability.

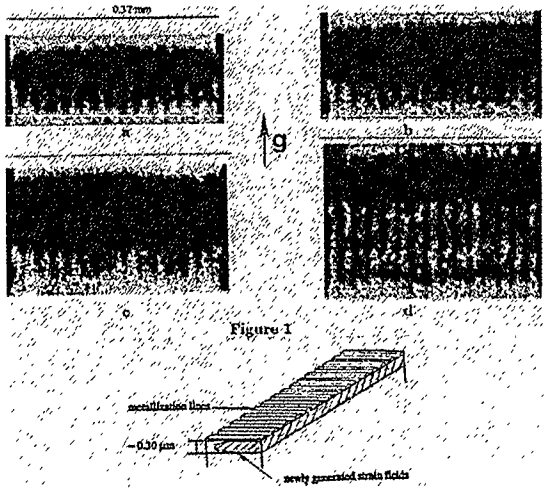


Figure 1.

* Work performed on the Synchrotron Topography Project Beamline X19C, supported by U.S.Army Research Laboratory under Grant No. DAAL02-92-R-9147/2FE425 and U.S. Army Research Office under Grant Nos. DAAL04-94-G-0091 and DAAL04-94-G-0121.

Characterization of polytypes in SiC devices by synchrotron white beam x-ray topography *	X19C

W. Huang, S. Wang, M. Dudley (SUNY Stony Brook), J. A. Powell, P. Neudeck (NASA Lewis Research Center), C. Fazi (U.S. Army Research Laboratory)

Synchrotron white beam x-ray topography is particularly useful for revealing the configurations of mixed polytypes since each polytype structure has a characteristic diffraction pattern for white radiation and where several polytypes are present a superimposition of each characteristic pattern occurs. With the aid of computer simulation, the polytype structures can be revealed by indexing and assigning each topograph to a particular polytype. Even polytype configurations in epitaxial layers of only several microns in thickness can be identified by using grazing incidence Bragg-Laue reflection geometry. An example is shown in Figure 1, which is a topograph recorded using grazing incidence reflection geometry from a sample consisting of (0001) 6H-SiC substrate, grown by Lely technique, with 1 mm^2 regions of epilayer, nominally consisting of (111) 3C, or (0001) 6H, distributed over the surface. Analysis shows that the regions with enhanced intensity are those which are nominally of 3C structure (g=022, λ = 0.934 Å), while the other areas correspond to 6H regions (g=$1\bar{1}08$, λ=0.932 Å). The lower relative intensity in some of the 6H regions shows the existence of another kind of 3C structure (double positioning twins). There is a slight difference between the positions of 6H images and the 3C images due to the small difference in lattice parameter. The distribution of defects with reference to the polytype configurations can be established simultaneously.

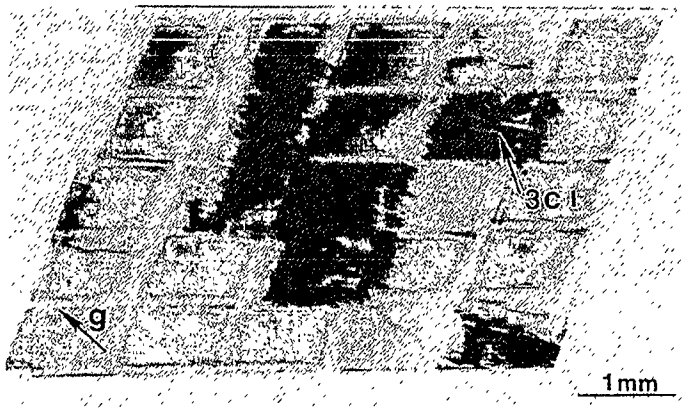


Figure 1.

* Work performed on the Synchrotron Topography Project Beamline X19C, supported by U.S. Army Research Laboratory under Grant No. DAAL02-92-R-9147/2FE425 and U.S. Army Research Office under Grant Nos. DAAL04-94-G-0091and DAAL04-94-G-0121

Comparison of defect structures in PVT and lely SiC devices * | X19C

W. Huang, S. Wang, M. Dudley (SUNY Stony Brook), J. A. Powell, P. Neudeck (NASALewis Research Center), C. Fazi (U.S. Army Research Laboratory)

Lely and Physical Vapor Transport (PVT) are the most common techniques used to grow 6H-SiC crystals. SiC devices have been fabricated by growing 6H or 3C epitaxial layers on the wafers produced by these two methods. The defect structures in these devices have been investigated by synchrotron white beam x-ray topographic imaging. Figures 1 and 2 are reflection topographs recorded from SiC devices fabricated on Lely and PVT 6H-SiC (0001) substrates, respectively. Grooves were cut in the growth surface of the substrates, producing 1 mm^2 mesas on which 3C-SiC (111) and 6H-SiC (0001) epilayers were grown via CVD. The squares with 3C and 6H epilayers are indicated accordingly. For 6H/6H epitaxy, replication of the defects from the substrates to the epilayers is expected. Therefore the quality of the 6H epilayers grown on the lower defect density Lely platelet substrates might be expected to be higher than those grown on the higher defect density PVT grown substrates. This is borne out by the observations of Figures 1 and 2. The 6H epilayer is essentially defect free in the case of Lely wafer substrate while super-screw dislocations, indicated by S, are observed in the film on the PVT grown substrate. This is due to the replication of the superscrew dislocations in the subsequently grown epilayers from the PVT substrate. These super-screw dislocations were not present in the Lely platelet substrates and so were not observed in the epilayers. The quality of the 3C/6H epilayer, however, is influenced by many factors such as growth conditions, other substrate defects and the substrate surface orientation. It can be seen that the general quality of the 3C/6H epilayer in both Lely and PVT wafer is relatively poor. In the Lely wafer, the existence of linear defects in the mixed regions close to the substrate/epilayer interface, indicated by L, are revealed. More DPBs, indicated by D, are observed in the 3C regions in the PVT wafer than in the Lely wafer.

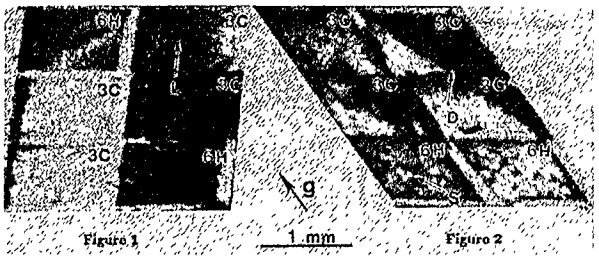


Figure 1.

* Work performed on the Synchrotron Topography Project Beamline X19C, supported by U.S. Army Research Laboratory under Grant No. DAAL02-92-R-9147/2FE425 and U.S. Army Research Office under Grant Nos. DAAL04-94-G-0091 andDAAL04-94-G-0121.

Depth profiling analysis of polytypes and stacking faults in SiC devices using synchrotron white beam x-ray topography * | X19C

W. Huang, S. Wang, M. Dudley (SUNY Stony Brook), J. A. Powell, P. Neudeck (NASA Lewis Research Center), C. Fazi (U.S. Army Research Laboratory)

X-ray depth profiling techniques in the grazing incidence Bragg-Laue reflection geometry utilizing synchrotron white radiation have been employed to investigate the polytype configurations as well as crystallographic defect structures in epitaxial layers on 6H-SiC substrates. Using the highly surface sensitive grazing incidence Bragg-Laue reflection geometry, images from different layers near the surface region can be obtained by changing x-ray absorption depth t_{pk}. Figure 1(a) is a grazing incidence reflection topograph of 6H-SiC devices (g=$1\bar{1}09$, λ=0.72Å, t_{tk}=8.6μm). 3 mm^2 mesas were produced in the 6H substrate on which 6H epilayers of about 10 μm in thickness were grown. 3C-SiC polytype, indicated by P, and some stacking faults, indicated by S are observed in the region near the grooves. Figure 1(b) is a topograph recorded from the same wafer with a smaller penetration depth (g=$1\bar{1}09$, λ=0.78 Å, t_{pk}=1.5 μm). Comparison of these two images shows that the stacking faults exist in the regions close to the substrate/epilayer interface while the 3C polytype structure mainly on the surface.

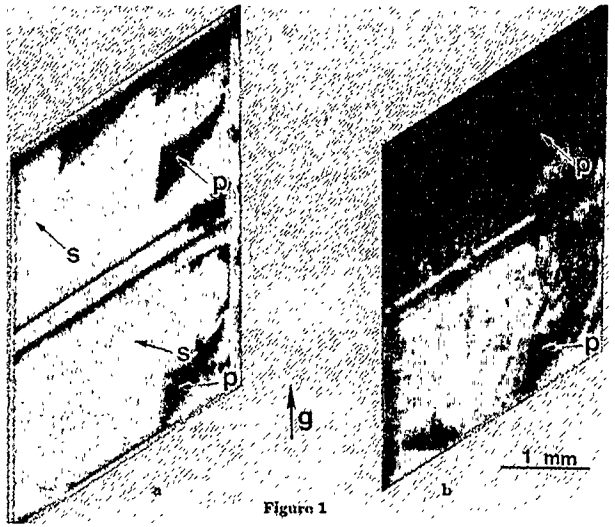


Figure 1.

* Work performed on the Synchrotron Topography Project Beamline X19C,supported by U.S. Army Research Laboratory under Grant No. DAAL02-92-R-9147/2FE425 and U.S. Army Research Office under Grant Nos. DAAL04-94-G-0091 and DAAL04-94-G-0121.

Influence of surface morphology on SiC epitaxial growth through CVD technique *	X19C

W. Huang, S. Wang, M. Dudley (SUNY Stony Brook), J. A. Powell, P. Neudeck (NASALewis Research Center), C. Fazi (U.S. Army Research Laboratory)

SiC is known as a classical polytypic substance that exists in more than 250 modifications or polytypes[1]. Since the common polytypes, 6H, 15R, 4H and 3C, coexist over a wide range of temperatures[2], obtaining single crystals containing only a single desired polytype is often difficult. The similar problem is encountered in epitaxial growth by chemical vapor deposition (CVD), which is a key process in the fabrication of semiconductor devices. Factors that control the polytype formation of CVD-grown SiC films on (0001) 6H-SiC substrates include the tilt angle of the substrate and the defects on the growth surface. At small tilt angles, defects in substrate surface regions are the dominant factor which is responsible for polytype nucleation[3]. Figure 1 is a synchrotron white beam x-ray topograph (g=$1\bar{1}09$, λ=0.74Å) recorded from a (0001) Lely 6H-SiC crystal. The substrate was divided into 3 mm^2 mesas by grooves. On each mesa epilayers of nominally 6H-SiC were grown via CVD. Polytype 3C structures, indicated by P, are found to be present in the regions near the grooves, while high quality 6H epilayer was grown on the rest of the mesas. This indicates that the presence of grooves in the surface and their associated stress fields have a significant effect on inducing 3C structure in the epilayer. The formation of stacking faults, indicated by S, near the grooves are also observed.

[1] S. Din and M. Suleman, Materials Letters, 17, 241 (1993).
[2] W.F. Knippenberg, Pilips Res. Repts., 18, 161 (1963).
[3] J.A. Powell, D.J. Larkin, J.B. Petit, and J.H. Edgar, Springer Proceedings in Physics, Amorphous and Crystalline Silicon Carbide IV, 71, 23 (1992).

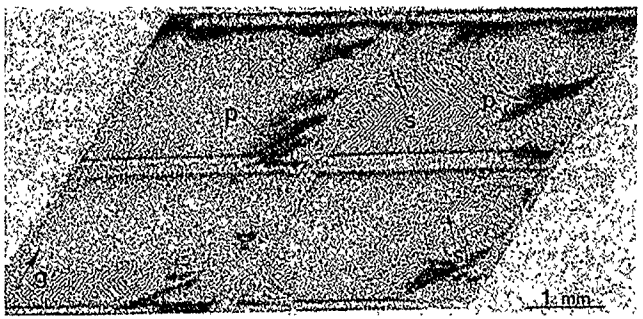


Figure 1.

* Workperformed on the Synchrotron Topography Project Beamline X19C, supported by U.S. Army Research Laboratoryunder grant number DAAL02-92-R-9147/2FE425 and U.S. Army Research Office under grant numbers DAAL04-94-G-0091and DAAL04-94-G-0121.

Observation of DPBs in SiC devices by synchrotron white beam x-ray topography *	X19C

W. Huang, S. Wang, M. Dudley (SUNY Stony Brook), J. A. Powell, P. Neudeck (NASA Lewis Research Center), C. Fazi (U.S. Army Research Laboratory)

It is known that the growth of 3C-SiC or 15R-SiC structures can be accompanied by 180o twining, which is often referred to as double positioning twinning. 6H-SiC has a zigzag sequence ABCACB and there are two possible configurations of 3C or 15R grown (at terraces) on this kind of substrate, those with ABCABC or ACBACB stacking sequences of 3C, for example. These two kinds of structure can be clearly revealed through synchrotron white beam x-ray topographs. Figure 1(a) and (b) are topographs recorded from a crystal consisting of 6H-SiC substrate with mixed 6H-, 3C- and 15R-SiC epilayer regions. The epilayers were grown on 1 mm^2 mesas and arrays of circular (25 to 200 μm in diameter) or square (25 to 200 μm on edge) topology diodes (with metallization) were fabricated in the epilayers. The mixed regions are the dark areas, indicated by M, while the other regions are exclusively 6H. Two kinds of 3C and 15R structures are revealed on Figure 1(a) ($g_{(6H)}$=$01\bar{1}14$, $\lambda_{(6H)}$=0.66 Å; $g_{(3C_I)}$=313, λ_{3C_I})=0.66 Å; $g_{(15R_{II})}$=$01\bar{1}35$, $\lambda_{(15R_{II})}$=0.66 Å) and (b) ($g_{(6H)}$=$1\bar{1}014$, $\lambda_{(6H)}$=0.66 Å; $g_{(3C_{II})}$=133, $\lambda_{(3C_{II})}$=0.66 Å; $g_{(15RI)}$=$1\bar{1}035$, $\lambda_{(15RI)}$=0.66 Å), respectively. Double positioning boundaries (DPBs), indicated by DPB, can be seen through the comparison of these two topographs. These DPBs, along with the super-screw dislocations, indicated by S, will strongly affect the performance of these devices. The round features, indicated by p, are due to the strains associated with the diode topology.

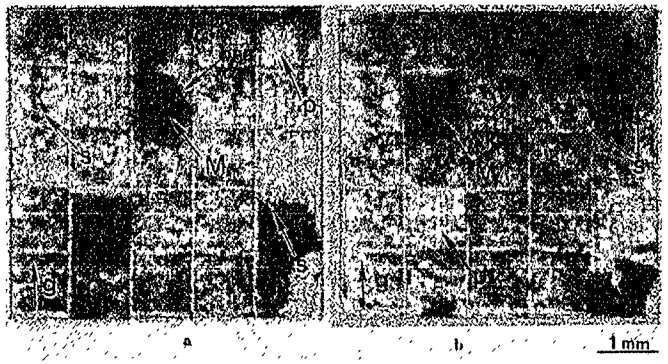


Figure 1.

* Work performed on the Synchrotron Topography Project Beamline X19C, supported by U.S. Army Research Laboratory under Grant No. DAAL02-92-R-9147/2FE425 and U.S. Army Research Office under Grant Nos. DAAL04-94-G-0091and DAAL04-94- G-0121.

Synchrotron white beam characterization of defect structures in LELY SiC platelets *	X19C

W. Huang, S. Wang, M. Dudley (SUNY Stony Brook), J. A. Powell, P. Neudeck (NASA Lewis Research Center), C. Fazi (U.S. Army Research Laboratory)

SiC has been known for several decades to have excellent physical and electronic properties which enables production of electronic devices that can operate at high temperature, emit radiation throughout the visible spectrum or photogenerate power in the UV range. The growth of large size single crystals of SiC with high quality has been the objective of many laboratories throughout the world, in fact has become somewhat of an international contest[1][2]. The Lely method has been used to grow SiC for many years[3]. However, Lely 6H-SiC single crystals used to be small in size (3 to 5 mm diameter on average). Recent developments in the Lely method have led to the advent of high quality and relatively large size 6H-SiC single crystal platelets. Examples are shown in figures 1 and 2, which are synchrotron white beam x-ray transmission topographs recorded from Lely 6H-SiC plates about 12 mm across and 0.5 mm thick. No super-screw dislocations with giant Burgers vectors were found in these wafers. In fact these wafers are essentially defect free except for some stacking faults, indicated by S, in the crystal shown in Figure 1 (a) (g=$\bar{1}011$, λ=1.05Å), and basal plane dislocations, indicated by D, in the crystal shown in figure 2 (g=$\bar{1}101$, λ=1.05Å). These stacking faults and dislocations are located near the as-grown edges, which indicates that they were probably formed in the late stage of crystal growth or post-growth cooling. Both wafers are of sufficient crystalline perfection for device fabrication.

[1] J.A. Edmond, H.S. Kong, C.H. Carter, Jr., J. Physica B, 185, 453 (1993).
[2] H. Posen and J.A. Bruce, Proceedings of the Third International Conference on Silicon Carbide, 238 (1973).
[3] J.A. Lely, Ber Deut. Keram, Ges., 28, 229 (1955).

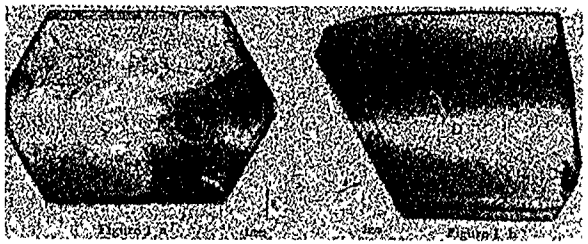


Figure 1.

* Work performed on the Synchrotron Topography Project Beamline X19C, supported by U.S. Army Research Laboratory under Grant No. DAAL02-92-R-9147/2FE425 and U.S. Army Research Office under grant numbers DAAL04-94-G-0091and DAAL04-94-G-0121.

Molecular orientation of a water-supported langmuir monolayer of n-$C_{18}H_{37}C_{12}F_{25}$studied by x-ray scattering	X19C

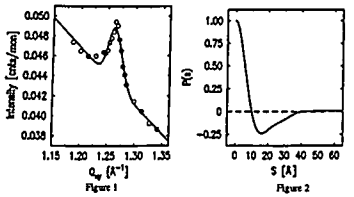
Z. Huang (James Franck Institute), M. L. Schlossman (James Franck Inst. and Univ. of Chicago), A. A. Acero, N. Lei (James Franck Institute), Z. Zhang (Univ. of Illinois, Chicago),S. A. Rice (James Franck Institute)

Molecules that form stable monolayers on water surface typically have a hydrophilichead group and a hydrophobic tail. A recent study [2] of perfluoro-n-eicosane, however, showed that this non-polar, long-chain molecule also forms an ordered monolayer on water, even though it does not contains hydrophilic head group. We report here our latest experimental data suggesting that a partially fluorinated alkane, n-$C_{18}H_{37}C_{12}F_{25}$, also forms an ordered monolayer on water surface, with the hydrocarbon part in contact with water and the fluorinated part pointing away from water.

Characterization of the n-$C_{18}H_{37}C_{12}F_{25}$ monolayers was first carried out by studying their isotherms on water surface. At T = 4 - 30°C the isotherms exhibit a sharp pressure rise at surface densities of approximately 33 Å^2/molecule. The collapse pressure ranges from 15 to 25dyne/cm, which over a period of a few hours decays to and stabilizes at 5 - 10 dyne/cm. Grazing-incidence-ray diffraction measurements on n-$C_{18}H_{37}C_{12}F_{25}$ monolayers at T = 5 - 24°Cshow an in-plane peak at 1.26Å^{-1} (Fig 1; fitted with a Gaussian), which is consistent with a monolayer structure in which the fluorinated part assumes hexagonal close packing. The peak position is independent of temperature and surface pressure to within our experimental errors.

X-ray reflectivity measurements had different values from different regions of the monolayer film, indicating that macroscopic inhomogeneities were present. Shown below (Fig. 2) is the Patterson function, P(s), of a set of reflectivity data measured from one part of a sample at a surface pressure of 3 dynes/cm, T =4.9°C, and an average surface density of 34.5 Å^2/molecule. As previously shown, the Patterson function is the autocorrelation function of the gradient of the electron density normal to the surface[2]. P(s), as shown, indicates that the highest electron density is at the vapor interface and it then decays (not necessarily monotonically) to the value for bulk water. This result places the fluorocarbonpart of the chain adjacent to the vapor and the hydrocarbon part on the water. Preliminary fitting with a real space model for the electron density confirms these results.

[1] M. Li, A.A. Acero, Z. Huang and S.A. Rice, Nature 367, 151-153 (1994).
[2] M.L. Schlossman, D.K. Schwartz, E.H. Kawamoto, G.J. Kellogg, P.S. Pershan, M.W. Kim, and T.C. Chung,J. Phys. Chem. 6628 (1991).

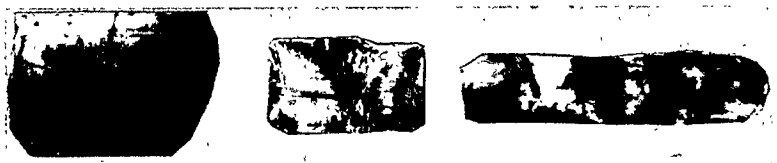


X-ray topographic studies of K_2SO_4 crystals with dye inclusions * | X19C

M.P. Kelley, B. Kahr (Purdue Univ.), and M. Dudley (SUNY Stony Brook)

The growth of crystals of simple ionic salts from aqueous solution may be influenced by the presence of certain organic dyes, which can modify the habit of the salts and become included in specific host growth sectors [1]. Crystals of K_2SO_4 grown in the presence of the dye acid fuchsin form single crystals of high quality with particularly well-defined 110 growth sectors. We have had the occasion to examine such crystals and thos grown from solutions containing a related triarylmethane dye in which two phenyl hydrogen atoms have been replaced by methyl groups. the corresponding topographs (g=(100), λ=1.12Å) are shown in Figure 1 and Figure 2, respectively [Figures unavailable]. The quality of the crystals including the two related dyes, as evidenced by x-ray topography, are comparable. Both these dyes (ca. 200μM) were found to have little effect on the crystallinity of K_2SO4. However, K_2SO_4 crystals grown in slightly basic and neutral solutions of the laser dye pyranine, which includes through the 110 and 010 growth sectors [2] were of poorer quality. Figure 3 [figue unavailable] shows a topograph of such a crystal, indicating that although it appeared unblemished optically, it was composed of several slightly misoriented regions of poor crystallinity.

[1] H.E. Buckley, "Crystal Growth," John Wiley, New York (1951).
[2] M.P. Kelley, B. Janssens, B. Kahr, W.M. Vetter, J. Am. Chem. Soc. 116, 5519 (1994).



* Work performed at the Synchrotron Topography Project, Beamline X19C.

Investigation of the role of grain boundaries in the plastic deformation of ice: I. Predeformation microstructure * | X19C

F. Liu, I. Baker (Dartmouth College), and M. Dudley (SUNY Stony Brook)

Detailed studies have been made of the role of grain boundaries in the plastic deformation of ice. Specimens studied had a grain boundary oriented at 45° to the axis of compressive loading. Samples were deformed in situ in a specially designed compression stage assembled into a cryostat, and several diffraction images were recorded simultaneously. The dislocation structures present in the crystals before loading are shown in figure 1. Most of the dislocations in grains FI and GII lie on the basal plane. Note the facet intersections F1-3, and slip bands B1-4. Clearly B1 and B3 nucleated from F1, and B2 and B4 nucleated from F3.

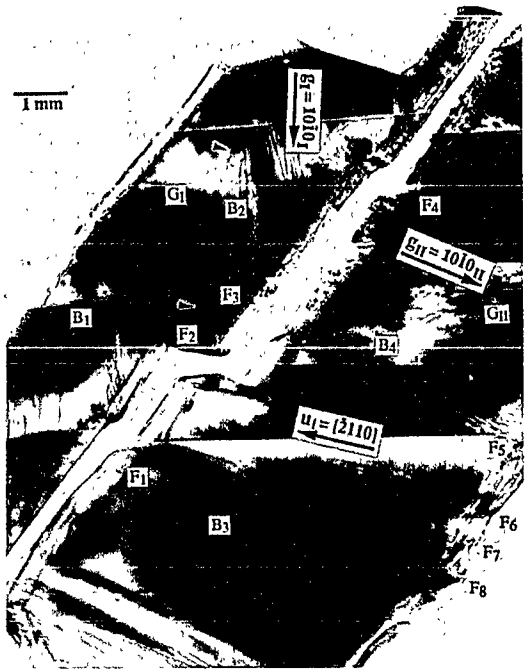


Figure 1.

* Topography work, carried out at the Stony Brook Synchrotron Topography Facility, Beamline X-19C, was supported by NSF grant number DPP-9218386, U.S. Army Research Office grants numbers: DAAL03-92-G-0139 and DAAH04-93-G-006, and in part by the Petroleum Research Fund which is administered by the American Chemical Society. Prof. E.M. Schulson is acknowledged for use of the ice laboratory.

Investigation of the role of grain boundaries in the plastic deformation of ice:II. In situ straining *	X19C

F. Liu and I. Baker (Dartmouth College), and M. Dudley (SUNY Stony Brook)

Figure 1 shows a series of white beam topographs recorded from the middle 5 mm length of the specimen discussed in part I after compression at $-6 \pm 0.1°C$. At the very beginning of straining the grain boundary acted as a dislocation source. For example several dislocations at X were generated from a facet intersection. Simultaneously, several pre-existing dislocations (arrowed) moved noticeably. Figure 1(b) was obtained by giving the x-ray film a double exposure (each of 1 second duration); one before loading and the other immediately after loading. Several dislocations arrowed in figure 1(b) were nucleated from F1 in GI. Dislocation pile-ups are directly observed for the first time in ice. 1(c) was recorded about 5 minutes later. More dislocations, with line direction $[\bar{1}\bar{1}20]$ were generated from F7 and F8. Figure 1(d) shows the microstructure after a prolonged loading of 0.2MPa for 20 minutes. In summary, dislocations always nucleate at facet intersections and stop at grain boundaries. They do not broaden by multiple cross-slip because the main segments cannot cross-slip off the basal plane.

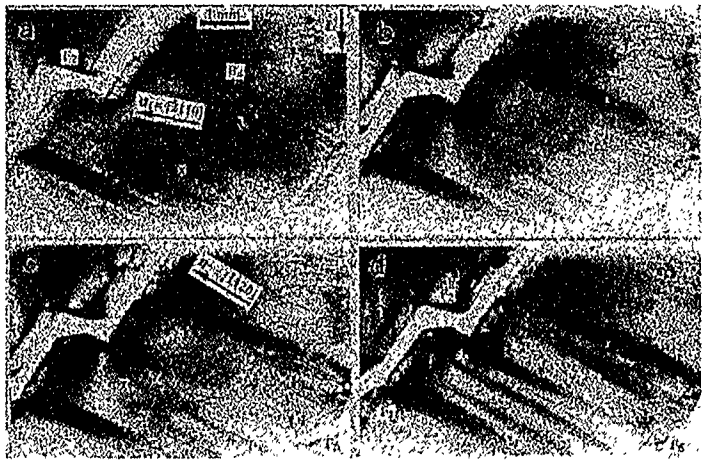


Figure 1.

* Topography work, carried out at the Stony Brook Synchrotron Topography Facility,Beamline X19C, was supported by NSF grant number DPP-9218386, U.S. Army Research Office grants numbers DAAL03-92-G-0319 and DAAH04-93-G-006, and in part by the Petroleum Research Fund, which is administered by the American Chemical Society. Prof. E.M. Schulson is acknowledged for use of the ice laboratory.

Investigation of the role of grain boundaries in the plastic deformation of ice: III. In situ annealing *	X19C

F. Liu, I. Baker (Dartmouth College), and M. Dudley (SUNY Stony Brook)

In order to explore the relaxation of the dislocation structure after unloading, the sample studied in parts I and II was annealed at elevated temperature. The microstructure after annealing at -4.0oC for 30 minutes is shown in figure 1(a). The pile-up observed in part II has relaxed and the dislocations have moved back down their slip plane. The dislocation tips emerging on the rear surface of the sample deviated from their screw orientations, as arrowed. A topograph recorded from a larger area of sample, following an additional anneal at -1.0oC for 30 minutes, is shown in figure 1(b). Further backward motion of the dislocations is observed. The main segments stay on their slip planes, while their tips further deviated from the original orientation. The overall dislocation density in the slip bands has noticeably decreased indicating that there were repulsive forces between the like dislocations.



Figure 1.

* Topography work, carried out at the Stony Brook Synchrotron Topography Facility, Beamline X-19C, supported by NSF grant number DPP 9218386, U.S. Army Research Office grants numbers: DAAL03-92-G-0319 and DAAH04-93-G-006, and by the Petroleum Research Fund, which is administered by the American Chemical Society. Prof. E. M. Schulson is acknowledged for use of the ice laboratory.

A new spectrometer for studying liquid surfaces and interfaces | X19C

M. L. Schlossman (James Franck Inst. and Univ. of Chicago), D. J. Synal, G. Shea-McCarthy(Univ. of Chicago), Z. Huang, Y. Guan (James Franck Inst.), M. Meron (Univ. of Chicago), S. A. Rice (JamesFranck Inst.)

An experimental station whose capabilities are optimized for the use of x-ray surface-sensitive structural techniques in the study of liquid surfaces and interfaces has been constructed at beam line X19C. To accommodate this facility, beam line X19C was completely rebuilt and now includes a doubly focusing mirror and a single bounce monochromator. This optics delivers a focused (0.4 mm × 1 mm, vertical × horizontal) monochromatic x-ray beam that can be projected downward onto a horizontal liquid surface. With a single bounce off a horizontally scattering Si(111) monochromator a photon flux of 4 $\times 10^{11}$ photons/sec (at 8 KeV) is available. A general purpose liquid surface spectrometer has been installed in the experimental hutch and is capable of measuring x-ray reflection, grazing-incidence diffraction and fluorescence, surface diffuse scattering, and anomalous reflection (see photograph). It has the following features: (a) The capacity to use large and heavy sample chambers as are required for high vacuum experiments. (b) Straightforward tuning of the x-ray wavelength which allows for measurement of differential anomalous reflectivity and fluorescence, and grazing incidence anomalous x-ray scattering. (c) Use of a simple optical system, a single crystal monochromator, to monochromate and steer the beam. (d) A sturdy design which allows for precise (and accurate) specification of the Q-vector as well as enhanced sample stability (important for liquid samples).

Preliminary experiments during the present phase of commissioning have included x-ray reflectivity and grazing incidence diffraction studies of surfactant monolayers on the water surface. The companion abstract describes the results of some of these initial studies.

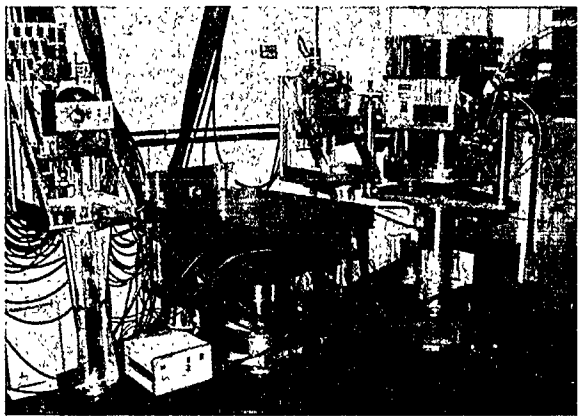


Figure 1.

A new method for time-resolved "footprinting" of macromolecules * | X19C

B. Sclavi, M. R. Chance, and M. Brenowitz (Albert Einstein College of Medicine)

The radiolysis of water by high energy x-rays produces free electrons and hydroxyl radicals. These radicals can abstract a hydrogen from the ribose sugar of DNA causing a strand break. The amount of hydroxyl radicals which can cut DNA can be controlled and used to do footprinting studies of the interactions of DNA with DNA-binding proteins, as well as RNA and protein folding reactions. The high flux from a white synchrotron x-ray beam of X19C at the National Synchrotron Light Source results in a timescale for cutting of the DNA to be extended far beyond previously available techniques, in fact the footprinting can achieved on millisecond timescales, in the range of the deadtime of rapid mixing instruments.

The hydroxyl radicals created by x-rays are highly advantageous for footprinting since their cleavage patterns are insensitive to the sequence of the DNA but are sensitive to the solvent accessibility of the small groove of the helix. This allows single base pair resolution for the examination of the protein DNA interaction. Figure 1 shows the cutting of radiolabeled DNA by a white light synchrotron x-ray beam, cutting times were based on use of the photon shutter. The cutting for one second of exposure cleaved 99attenuators to extrapolate the estimated cutting for shorter timescales. This indicated that 30cutting could be achieved at 12 ms timescales, while only 10results suggest that novel methods to examine the time-resolved structure of protein-DNA complexes are feasible using synchrotron based technology. This method has been validated by examining footprints of both Lac and Gal repressors and can potentially be used to study macromolecular interactions and folding on millisecond timescales.

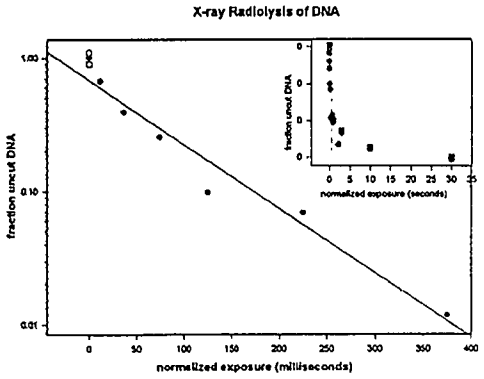


Figure 1.

* This work is supported by the Regional Center for Time-Resolved X-ray Spectroscopy under NIH grant RR- 01633.

X-ray topography of thin films prepared from longitudinal cut 6H-SiC wafers *	X19C

W. M. Vetter, M. Dudley (SUNY Stony Brook)

Dislocation structures in commercial PVT 6H-SiC single crystal wafers have been extensively studied by synchrotron white beam X-ray diffraction topography. The main features identified were super screw dislocations, which have Burgers vectors that are some multiple of the c lattice constant and run roughly parallel to the c-axis and the crystal growth direction, and a network of regular dislocations which lie in and have Burgers vectors parallel to the basal plane. In our topographs we have identified super screw dislocations with very dark contrast presumably with large Burgers vectors and often associated with optically visible hollow cores or "micropipes," and also screw dislocations of less intense contrast, thought to be have Burgers vectors of some single or low multiple of c. Since the presence of hollow cores are deleterious to semiconductor device performance, it is an important questions whether these screw dislocations of small Burgers vector possess hollow cores of an optically invisible diameter. To answer this question as well as to study the dislocations more closely, we have undertaken the reduction of a longitudinal $(10\bar{1}0)$ cut 6H-SiC wafer to thin films for transmission electron microscopy. The wafer was diced into 2.3mm squares which were then angle lapped by several degrees through mechanical grinding with coarse SiC abrasive. The squares were successively thinned and polished to 30μm thickness with graded SiC and diamond abrasives, then finished with 0.25μm diamond paste. The figures below show topographs of one of these samples. Figure 1 shows a reflection in which the super screw dislocations are in strong contrast (g=(0006), λ=0.65Å) and figure 2 shows one where both super screw and basal plane dislocations are in contrast (g=$(11\bar{2}0)$, λ=0.64Å). It is apparent that the final polishing has removed all detectable surface strain, rendering the samples quite suitable for X-ray topography. We intend to continue thinning these samples to 1μm thickness, appropriate for TEM, and then relate TEM observations to the features visible in the topographs obtained in the previous thinning stage.

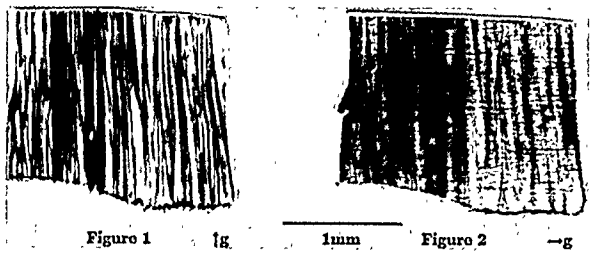


Figure 1.

* Work performed at the Synchrotron Topography Project Station, Beamline X-19C, supported by NIST via Cree Research, Inc.d and by U. S. Army Research Office under grant numbers: DAAL09-94-G-0091 and DAAL04-94-G-0121

Analysis of synchrotron topographic contrast from super screw dislocations in PVT 6H-SiC single crystals *	X19C

S. Wang and M. Dudley (SUNY Stony Brook), C. H. Carter, Jr. (Cree Research, Inc.)

While some comparisons have been drawn between the contrast mechanisms operative in Lang topography with those in synchrotron white beam X-ray topography (SWBXT) [1,2] few systematic attempts have been made to analyze the detailed contrast mechanisms which operate in SWBXT. It is generally assumed for example that the direct image formation mechanism which operates in SWBXT is the same as that in the well-understood Lang technique. However, unlike the case for the Lang technique the angle subtended by the largest source dimension at any point on the specimen in SWBXT is either comparable to or less than the crystal rocking curve. It is apparent that energy dispersion effects play an important role in the formation of direct images of defects in the SWBXT. By taking into account the energy dispersion effect, a new parameter, the deviation parameter [3], which is similar to the well-known Authier's effective misorientation parameter [4], was introduced in order to quantitatively explain the contrast features observed on synchrotron topographs recorded from 6H-SiC single crystals. The effective deviation parameter defines the volume around a defect in the crystal that gives rise to direct images of the defect. By applying the theory to the super screw dislocations in 6H-SiC, one yields that for transmission topographs recorded from longitudinal-cut wafers, bimodal images were predicted, similar to Authier's theory. This agrees well with the experimental results. For back-reflection topographs recorded at Bragg angles at 80 degrees or more, an example or which is shown in figure 1 [figure unavailable due to space constraints], the new theory predicts circular contrast associated with super screw dislocations (e.g. indicated by S), which is in good agreement with the topographic results shown. Such circular contrast associated with super screw dislocations cannot be predicted by Authier's theory. It should be pointed out that the presence of the white circles (absence of intensity) at the centers of the images of the super screw dislocations on the back reflection topographs is due to the angular divergence of the diffracted beams giving rise to the direct image (which appear on the image as a black circle). As a matter of fact, as one approaches the dislocation core, the directions of the diffracted beams from the strained regions deviate by an increasingly greater degree from their perfect crystal counterparts. Therefore, the diffracted beams from regions close to the super screw dislocation core will be integrated with those from regions further from the core because of relatively large specimen-recorder distances used. This gives rise to the overall appearance of the dislocations images, i.e. dark circles surrounding regions devoid of diffracted intensity–the circular white features.

[1] M. Hart, J. Appl. Crystallogr., 9, 436 (1975). [2] B. K. Tanner, et al., J. Appl. Crystallor., 10, 281 (1977). [3] M. Dudley, et al., J. Phys. D, Appl, Phys. (1994) (submitted). [4] A. Authier, J. Phys. Radium, 27, 57 (1966).

* Topography work performed at the Stony Brook Synchrotron Topography Facility, Beamline X-19C, is supported by NIST via Cree Research, Inc. dand by the U.S. Army Research Office under grant numbers: DAAL04-94-G-0091 and DAAL04-94-G-0121.

Hollow core screw dislocations in PVT 6H-SiC single crystals revealed by synchrotron topography and SEM *	X19C

S. Wang and M. Dudley (SUNY Stony Brook), C. H. Carter, Jr. (Cree Research, Inc.)

Linear defects close to being parallel to the [0001] growth axis, often known as "micropipes", are the primary defects found in 6H-SiC single crystals grown by physical vapor transport technique (PVT). In the present study, growth spirals entered at the axis of "micropipes" were observed by Nomarski optical microscopy, as shown on the optical micrograph in figure 1(a), where two groups of multi-spoke growth spirals were imaged, indicating the presence of closely spaced screw dislocations. The centers of the growth spirals were examined and hollow tubes of submicrons to microns in diameter were found, an example of which can be found on the SEM micrographs in figure 1(b) and (c), where a faceted hollow center of about 1μm in diameter is clearly imaged. The transmission synchrotron topograph, shown in figure 1(d), recorded from a longitudinal-cut wafer containing two such "micropipes" shows broad, bimodal images, characteristic of screw dislocations. It is, therefore, concluded that the "micropipes" are indeed hollow core screw dislocations with large Burgers vectors, as predicted by Frank [1].

[1] F. C. Frank, Acts Cryst., 4, 497 (1951).

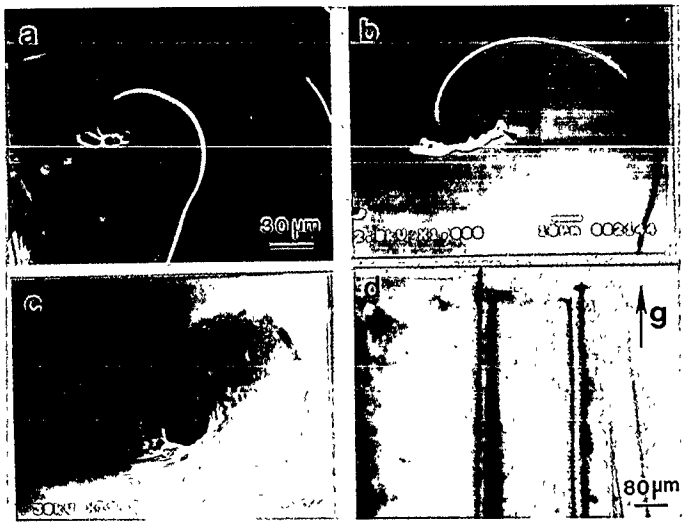


Figure 1.

* Topography work performed at the Stony Brook Synchrotron Topography Facility, Beamline X-19C, is supported by NIST via Cree Research, Inc and by U.S. Army Research Office under grant numbers: DAAL04-94-G-0091 and DAAL04-94-G-0121

Super screw dislocations in PVT 6H-SiC single crystals revealed by synchrotron topography *	X19C

S. Wang and M. Dudley (SUNY Stony Brook), C. H. Carter, Jr. (Cree Research, Inc.)

Optically observable linear defects lying approximately parallel to the [0001] growth axis, often referred to as "micropipes" as shown on the optical micrograph in figure 1(a), are characteristic defects in 6H-SiC single crystals grown on (0001) seeds by physical vapor transport technique (PVT). Efforts have been made to determine the nature of these "micropipes" by using etch-pit techniques [1] and transmission electron microscopy [2] and more recently by synchrotron white beam X-ray topography [3]. Although some such "micropipes" are observed to have growth spirals of apparently large step heights associated with them on the as-grown surfaces of the PVT boules, indicating that they are screw dislocations with large Burgers vectors, the majority of the "micropipes" emerging from the as-grown surfaces with local surface orientations deviating significantly from (0001) have no observable growth spirals associated with them. Therefore, it is necessary to elucidate the nature of these "micropipes" using synchrotron topography. Figure 1(b) is a synchrotron transmission topograph (g=0006, λ=0.89Å) recorded from the same area of the crystal shown in figure 1(a). Apparently, the double-line or bi-modal images, e.g. S, are associated with the "micropipes". The bi-modal images are characteristic of screw dislocations in this diffraction condition and the wide image widths suggest that these "micropipes" are indeed screw dislocations with large Burgers vectors - super screw dislocations, since dislocation image width is proportional to the magnitude of its Burgers vector. It should also be noted that there are many similar, but narrower, bimodal images observed on the topographs that were not revealed by the optical microscopy. They are apparently screw dislocations with smaller Burgers vectors and with no discernible "micropipes". Most of these screw dislocations were determined to possess Burgers vectors equal to the lattice parameter c=15.17Å.

[1] J. Takahashi, M. Kanaya and Fujiwara, J. Cryst. Growth, 135, 61 (1994).
[2] J. Yang, Ph.D. Thesis, Case Western Reserve University, 1993.
[3] S. Wang, M. Dudley, C. H. Carter, Jr., D. Asbury, and C. Fazi, MRS Sumposium proceeding, 307, 249 (1993).

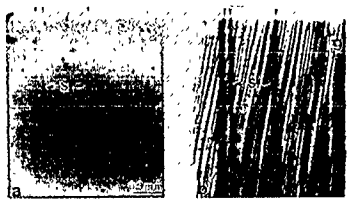


Figure 1.

* Topography work performed at the Stony Brook Synchrotron Topography Facility, Beam X-19C, is supported by NIST via Cree Research, Inc. and by U.S. Army Research Office under grant numbers: DAAL04-94-G-0091 and DAAL04-94-G-0121.

Synchrotron back-reflection topography for imaging super screw dislocation in PVT6H-SiC single crystals *	X19C

S. Wang and M. Dudley (SUNY Stony Brook), C. H. Carter, Jr. (Cree Research, Inc.)

Synchrotron X-ray topographs recorded in back-reflection geometry with Bragg angles of about 80 degrees or more were found to be particularly useful for imaging super screw dislocations, including "micropipes", in PVT 6H-SiC single crystals [1]. An example of such back-reflection topographs recorded from the as-grown surface of a longitudinal-cut wafer is shown in figure 1(a) (g=00024, λ=1.25Å), where the circular white features, e.g. indicated by S1, S2 and S3, are associated with super screw dislocations approximately parallel to the [0001] growth axis. By comparing with the corresponding Nomarski optical micrograph shown in figure 1(b), it is evident that super screw dislocation S1 has a growth spiral with apparently large step heights associated with it, confirming that it is a screw dislocation with large Burgers vector, while super screw dislocation S3 has a growth spiral of very small (faint) step, confirming that it is a screw dislocation with a small Burgers vector. In fact, theoretical calculations based upon an image contrast mechanism model developed for synchrotron white beam topography [2] showed that the magnitude of the Burgers vectors of the super screw dislocations that give rise to the small circular contrast features are equal to the lattice parameter c=15.17Å, while the super screw dislocations that give rise to large circular contrast features, such as S1 and S2, have Burgers vectors 3 to 7 times of the lattice parameter c. The super screw dislocations with large Burgers vectors were observed to have "micropipes" associated with them. The diameter of the hollow cores determined by SEM ranges from one tenth of a micrometer to a few micrometers. Super screw dislocations with Burgers vectors equal to c, which constitute the majority of the super screw dislocations, were found to have no discernible "micropipes" associated with them.

[1] S. Wang, M. Dudley, C.H. Carter, Jr., D. Asbury and C. Fazi, MRS Symposium Proceeding, 307, 249 (1993).

[2] M. Dudley, S. Wang, W. Huang, C.H. Carter, Jr., and C. Fazi, J. Phys. D: Appl. Phys. (submitted) (1994).

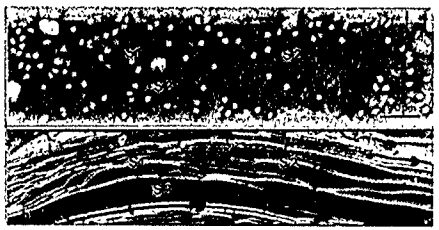


Figure 1.

* Topography work performed at the Stony Brook Synchrotron Topography Facility,Beamline X-19C, is supported by NIST via Cree Research, Inc. and by the U.S. Army Research Office undergrant numbers: DAAL04-94-G-0091 and DAAL04-94-G-0121.

Characterization of dislocation structures in PVT 6H-SiC crystal wafers by synchrotron white beam topography *	X19C

S. Wang and M. Dudley (SUNY Stony Brook), C. H. Carter, Jr. and V. Tsvetkov (CreeResearch, Inc.)

Commercially available (0001) 6H-SiC single crystal wafers grown by the sublimation physical vapor transport (PVT) technique were examined by synchrotron white beam X-ray diffraction topography. Defect structures, primarily dislocation structures, were characterized and analyzed. There are two kinds of dislocations, basal plane dislocations and super screw dislocations, as revealed by the transmission topograph shown in figure 1(a) where they are indicated by B and S, respectively. The so-called superscrew dislocations are those lying approximately parallel to the [0001] growth axis. Some of the superscrew dislocations, presumably with large Burgers vectors, are associated with optically observable "micropipes" and so are hollow core screw dislocations [1], while others, presumably with smaller Burgers vectors, have no discernible "micropipes" associated with them. The basal plane dislocations appearing in a network structure lying tin the basal plane were determined to have Burgers vectors of mainly $\langle 11\bar{2}0 \rangle$ type. These are perfect dislocations. Such a distribution of basal plane dislocations can be confirmed by the reflection topograph recorded from the same area of the wafer as shown in figure 1(b), where only basal plane dislocations located close to the wafer surface were revealed because the x-ray penetration depth for the reflection topograph is only 20 μm. Also some basal plane dislocations loops are seen to emanate from super screw dislocations, which can be explained by a surface-relaxation dislocation generation mechanism [2].

[1] P. Krishna, S.-S. Jiang and A.R. Lang, J. Cryst. Growth, 71, 41 (1957).

[2] S. Wang, M. Dudley, C.H. Carter, Jr., D. Asbury and C. Fazi, MRS Symposium Proceeding, 307, 249 (1993).

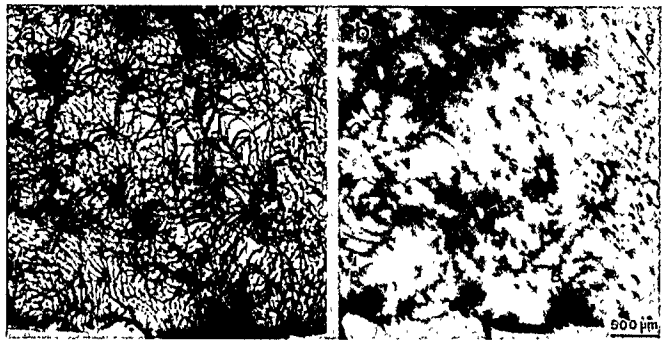


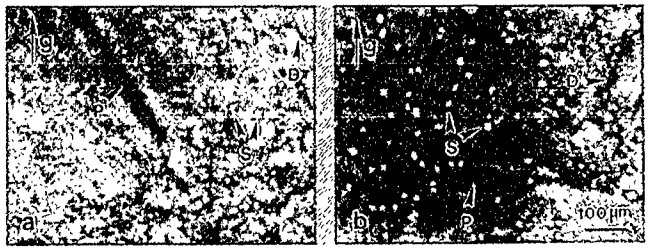
Figure 1.

* Topography work performed at the Stony Brook Synchrotron Topography Facility,Beamline X-19C, is supported by NIST via Cree Research, Inc. and by U.S. Army Research Office under grant numbers: DAAL04-94-G-0091 and DAAL04-94-G-0121.

Comparison of super screw dislocations in PVT 4H-SiC and 6H-SiC single crystals revealed by synchrotron back-reflection topography *	X19C

W. Wang, and M. Dudley (SUNY Stony Brook), C. Fazi (U.S. Army Research Laboratory,Adelphi, Md) and R. Rupp (Siemens, Germany)

Commercially available (0001) 4H-SiC and 6H-SiC single crystal wafers grown on (0001) seeds by physical vapor transport technique (PVT) have been examined by synchrotron topography technique. Among the defects revealed, super screw dislocations approximately parallel to the [0001] growth axis are the most important defects and synchrotron white beam back-reflection topography developed at our beamline was found particularly useful for imaging such super screw dislocations in the standard (0001) wafers polished only on one side. Figure 1(a) and (b) are examples of such back-reflection topographs (g=00024, λ=1.25Å) recorded from a 4H-SiC wafer and a 6H-SiC wafer, respectively, and at the same magnification. Since the x-ray penetration depth is larger than the thickness of the wafers, polishing marks on the back sides of the wafers (e.g. P) were observed but they do not seem to hinder the observation of contrast features from other crystal lattice defects, contrary to the case of transmission topographs, in which contrast from these polishing marks overwhelms that from the lattice defects. The circular white features on both topographs, e.g. indicated by S, are associated with super screw dislocations and the diameter of the features are proportional to the magnitude of the super screw dislocation Burgers vectors. It should be noted that, on either one of the two topographs, the diameters of majority of circular features associated with super screw dislocations are approximately the same and these super screw dislocations were determined to have Burgers vectors equal to the c lattice parameters of 4H and 6H structures, respectively. This is also quite apparent when one compares the smallest circular features on these two back-reflection topographs of the same magnification and realizes the fact that the diameters of the super screw dislocations presumably with unit Burgers vectors in 4H-SiC are considerably smaller than that in the 6H-SiC, simply because the difference of the c lattice parameters of these two structures. In addition, basal plane dislocations, e.g. indicated by D on both topographs, were also revealed as dark lines terminating at or emanating from super screw dislocations.



* Topography work performed at the Stony Brook Synchrotron Topography Facility, Beamline X19C, is supported by U.S. Army Research Office under Grant Nos.: DAAL04-94-G-0091 and DAAL04-94-G-0121. PVT SiC wafers grown by Cree Research, Inc. and provided by Siemens Corporation.

Defect structures in PVT 4H-SiC single crystals revealed by synchrotron topography *	X19C

S. Wang and M. Dudley (SUNY Stony Brook), C. Fazi (U.S. Army Research Laboratory, Adelphi, MD) and R. Rupp (Siemens, Germany)

Commercially available (0001) 4H-SiC single crystal wafers grown on (0001) seeds by physical vapor transport technique (PVT) have been examined by synchrotron topography technique. Figure 1 is a synchrotron reflection topograph recorded from a 4H-SiC wafer of one inch in diameter. The large circular white features are associated with super screw dislocations approximately parallel to the [0001] growth axis. These super screw dislocations, presumably with large Burgers vectors, were observed associated with "micropipes" penetrating the thickness of the wafer by stereo-optical microscopy which are very similar to those observed in PVT 6H-SiC wafers. However, some of the micropipes: in the 4H-SiC wafers tend to line-up along the (10$\bar{1}$0) directions, e.g. the group of "micropipes" indicated by M. The density of the micropipes seem to be less than that in the PVT 6H-SiC. There are also many super screw dislocations, presumably with smaller Burgers vectors, observed on the topograph and they appear as small dark "dots", e.g. indicated by S. Similar to the case of 6H-SiC, the majority of the super screw dislocations with smaller Burgers vectors were determined to possess Burgers vectors equal to the c lattice parameter (10.10Å) of 4H- SiC crystal. In addition, subgrain boundaries appear as white strips (B1) or dark strips (B2) on the topograph, which are believed to be due to planar groups of super screw dislocations. Basal plane dislocations were also observed (refer to another report in this volume).



Figure 1.

* Topography work performed at the Stony Brook Synchrotron Topography Facility, Beamline X-19C, is supported by U.S. Army Research Office under grant numbers: DAAL04-94-G-0091 and DAAL04-94-G-0121. PVT 4H-SiC wafers grown by Cree Research, Inc., and provided by Siemens Corporation

Investigation of structural defects in ZnSe single crystals by synchrotron x-ray topography *	X19C

W. Zhou, H. Chung, M. Dudley (SUNY Stony Brook), C. H. Su, M. P. Volz, D. C. Gillies,F. R. Szofran, and S. L. Lehoczky (NASA Marshall Space Flight Center, Alabama)

ZnSe is isomorphous with ZnTe possessing a zinc blende structure with a lattice parameter of 5.6676Å. In this study, a (110) ZnSe single crystal grown by physical vapor transport (PVT) has been characterized by synchrotron white beam x-ray topography using reflection geometry. The dominant defects observed in the sample are twins (T). Twinning can be revealed by synchrotron x-ray topography through orientation contrast. Figure 1 ($g = (33\bar{1})$, $\lambda = 0.68$ Å) is a topograph showing the twin structure of this sample where the numbers represent the different orientations. By analyzing topography images, all twins are found to be 180° rotation twins along {111} plane normals. In addition, four sets of black, parallel lines lying along ⟨111⟩ directions are characterized as slip bands (S). As shown in Figure 2 ($g = (60\bar{2})$,λ = 0.71Å) the slip bands are actually curved. The bending of the slip bands can be attributed to the long range elastic strains in the crystal.

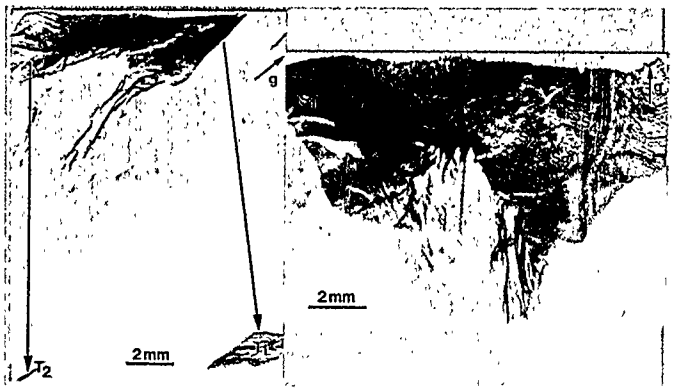


Figure 1.

* Work performed on the Synchrotron Topogrpahy Project Beamline X19C, and supported byNASA Marshall Space Flight Center under Grant No. NAG8-891.

Magnetic X-ray Scattering Study of the Random Field Ising Model $Fe_{0.5}Zn_{0.5}F_2$ at X20A	X20A, X20B, X20C

Q. Feng, Q.J. Harris, R.J. Birgeneau (MIT)

Although the lower critical dimension of the random field Ising model (RFIM) has been theoretically proven to be 2 in equilibrium, neutron scattering studies on 3d diluted antiferromagnets in an applied field (DAFF), which are experimental realizations of 3d RFIM, have observed long range order (LRO) after zero field cooled protocol (ZFC) but only short range order (SRO) after field cooling (FC) in all fields studied. With the advent of the magnetic x-ray scattering technique made possible by synchrotron radiation sources, a FC LRO component has recently been observed in one weakly anisotropic $Mn_{0.75}Zn_{0.25}F_2$ sample and was believed to exist only in the near surface region of the crystal. We report here a study on samples of $Fe_{0.5}Zn_{0.5}F_2$, a strongly anisotropic 3d DAFF. For relatively low applied fields (H<3T), a LRO component was observed in the FC state along with the SRO component arising from the domains (Fig.1). The intensity of this LRO component decreases with increasing external field and becomes unobservable for H>3T. At H=1.5T, line shape studies were carefully performed during FC and field heating (FH) procedures. There is apparent hysteresis for temperatures in the regime t=—1-T/Tc—¡0.1, where both the FH domain sizes and the FH LRO intensity are significantly greater than the FC ones. There is little difference between FH and FC results for t>0.1 (Fig.2). The fact that LRO exists and diminishes with increasing field can be understood phenomenologically as the result of a competition between a certain ordering mechanism, i.e. surface effects, and random fields and random bonds. High resolution neutron scattering experiments at corresponding fields need to be carried out in order to determine whether the LRO exists in the bulk of the crystal or only near the surface.

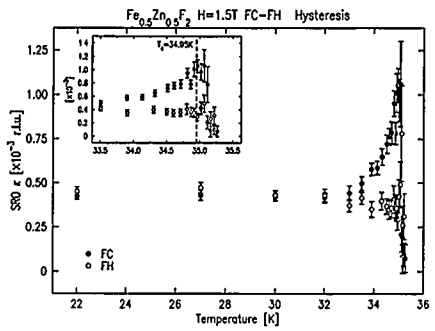


Figure 1.

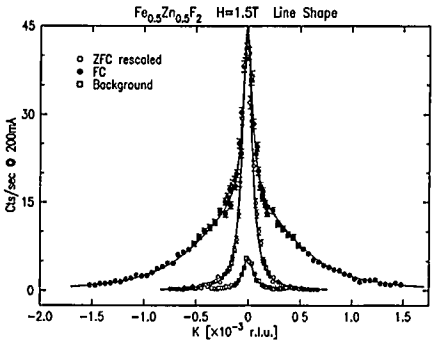


Figure 2.

Magnetic x-ray scattering study of competing anisotropies in $Fe_xCo_{1-x}TiO_3$	X20A

Q. J. Harris, Q. Feng, R. J. Birgeneau (MIT), A. Ito (Ochanomizu University, Japan)

Random magnets have captured wide-spread attention in the past two decades. Amongthem, a solid solution with competing orthogonal spin anisotropies is one of the simplest. Crystalline $Fe_xCo_{1-x}TiO_3$ provides us with an excellent example of that kind. We have carried out high resolution synchrotron x-ray scattering studies of $Fe_xCo_{1-x}TiO_3$ with the composition x=0.75, 0.35 and 0.60, representing respectively the three different regions in the concentration-temperature (x-T) phase diagram, namely, the $\vec{S}_{\parallel}$-ordered phase ($\parallel$ to the hexagonal c-axis), the $\vec{S}_{\perp}$-ordered phase ($\perp$ to the hexagonal c-axis) and the mixed phase, in which both $\vec{S}_{\parallel}$ and $\vec{S}_{\perp}$ are ordered. With high resolution available from the synchrotron x-ray scattering techniques, we have discovered a magnetoelastic effect associated with the $\vec{S}_{\perp}$ ordering, which was not able to be detected previously in the neutron scattering experiments, as illustrated in Fig. 1. The two successive transitions in the mixed region are observed to be coupled, contradictory to the prediction of the theory [1]. The magnetic peak of the lower transition is found to be resolution limited, as shown in Fig. 2, contradictory to the intuition that at the lower transition, the long-range-order of the one of the magnetic components generates random fields for the other [2]. More detailed studies of the mixed phase and effects of an external magnetic field are being planned.

[1] S. Fishman and A. Aharony, PRL 37 1587 (1976); PRB 18 3507 (1978).
[2] P. Wong, P.M. Horn, R.J. Birgeneau and G. Shirane PRB 27 428 (1983).

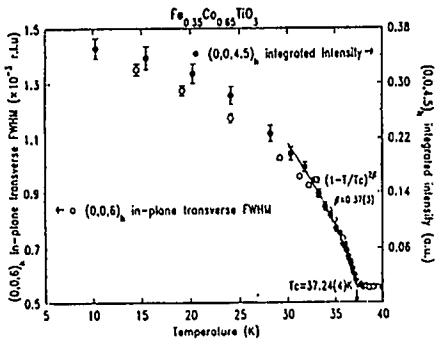


Figure 1. The magnetoelastic effect associated with the $\vec{S}_{\perp}$ ordering.

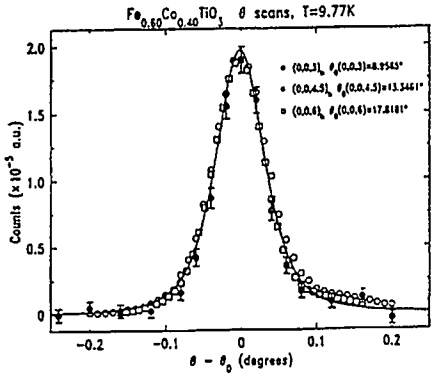


Figure 2. The magnetic peak of the lower transition is resolution limited.

Critical behavior at the spin-peierls transition in $CuGeO_3$	X20A, X20B

Q. J. Harris, Q. Feng, R. J. Birgeneau (MIT), K. Kakurai, J. E. Lorenzo, G. Shirane (BNL), M. Hase, K. Uchinokura (University of Tokyo, Japan), H. Kojima, I. Tanaka, and Y. Shibuya (Yamanashi University, Japan)

We report the results of a synchrotron x-ray-scattering studying of the spin-Peierls transition in the quasi-one-dimensional spin-1/2 antiferromagnetic chain system $CuGeO_3$. Below the transition temperation (T_c), the peak width of the superlattice reflections resulting from the lattice dimerization is independent of temperature and is resolution limited, see Fig. 1. Below (but close to) the transition temperature, the intensity of the superlattice reflection is well described by a simple power law: $I \propto (1-T/T_c)^{2\beta}$, with the exponent β=0.30 $\pm$ 0.05, as illustrated in Fig. 2. Above the transition temperature, the pre-transitional lattice fluctuations, which broaden rapidly and anisotropically with increasing temperature, are observed, as shown in Fig 2. In addition, a spontaneous thermal contraction $\triangle b$ is found to be proportional to the intensity of the superlattice reflections, $\triangle b \propto I$. We confirm that the appearance of this contraction is coupled with the spin-Peierls transition by measuring $\triangle b$ in various magnetic fields. The spin-Peierls transition temperature is depressed by the magnetic field. $\triangle T \equiv T_c(0) - T_c(H)$ scales as H^2, in quantitative agreement with the results of magnetic susceptibility measurements and with theory. [2]

[1] permenant address: Neutron Scattering Laboratory, ISSP, the University of Tokyo, c/o JAREI, Tokai 319-11, Japan.

[2] Q.J. Harris et. al. PRB 50 12606 (1994).

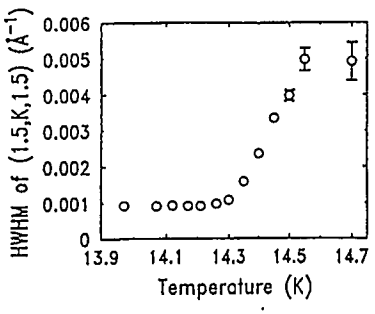


Figure 1. The HWHM of (1.5,K,1.5) evolves with increasing temperature.

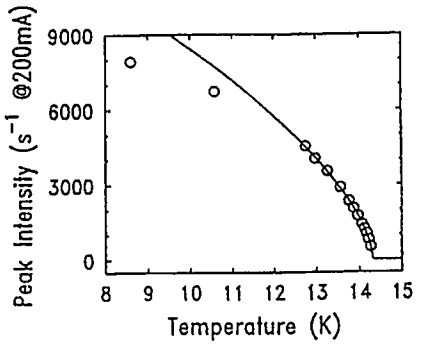


Figure 2. The peak intensity of (1.5,1,1.5) below the transition temperature as a function of temperature.

Inelastic x-ray scattering study of LiF * | X21

Wolfgang Caliebe (NSLS), Chi-Chang Kao (NSLS), Michael Krisch (ESRF, France), Jerry Hastings (NSLS)

Experimental information on electronic band structures of materials is routinely provided by optical spectroscopies, angle-resolved photoemission, and electron energy loss spectroscopy (EELS). Most of these techniques, however, have to be performed in ultrahigh vacuum and depend strongly on the surface conditions of the sample. In the last decade, inelastic X-Ray scattering spectroscopy (IXSS) has been developed as a new experimental probe for the study of electronic band structures, through single-particle interband transitions, as well as various other electronic excitations, such as plasmons, and core-level transitions. In IXSS, the monochromatized and focussed beam (at X21: 0.7 eV bandwidth and 10x0.2mm^2 beamsize at 8 keV) is scattered from the sample and the scattered photons are energy analyzed by a spherically bent analyzer. Usually, the detector and analyzer are kept in a fixed position, and by varying the incident energy the energy loss spectrum is obtained. Also by rotating the sample and/or rotating the analyzer-detector the direction and the magnitude of the momentum transfer can be selected. The double differential cross section can then be related directly to the dynamical structure factor $S(q,\omega)$. Since both the incident and the scattered photons are high energy x-rays, IXSS is essentially a probe of bulk properties and an ultrahigh vacuum environment is not required.

In this work IXSS study of LiF in the (100)-direction with energy transfer between 0 and 70 eV and momentum transfer from close to 0Å^{-1} to 3Å^{-1} was performed. Below 20 eV band structure features are dominating and the different peaks can be assigned to different interband transitions. The peak at 25 eV is the plasmon and at 61 eV the Li 1s-2s transition is clearly visible. These data are very similar to EELS data obtained by Fields et al. [2].

[1] W. Schülke, Inelastic Scattering by Electronic Excitations, in Handbook on Synchrotron Radiation, Vol. 3, edited by G. Brown and D. E. Moncton, Elsevier Science Publishers B .V.,1991

[2] J.R. Fields, P.C. Gibbons and S.E. Schnatterly, Phys. Rev. Lett., 38, 430, (1977)

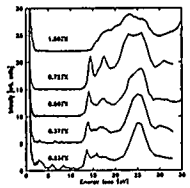


Figure 1. IXSS of LiF at different momentum transfers in the first and second Brillouin-zone

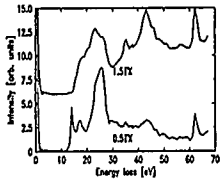


Figure 2. IXSS of LiF at 0.5ΓX and 1.5 ΓX. In both scans the Li-1s-2s transition at 61 eV is clearly visible, the peak at 35 eV in the high-q-data is a transition from the F 2s core state to the Li conduction band.

* Supported by US DOE under contract # DE-AC02-76CH00016.

Resonant Raman Scattering Spectroscopy from Er * | X21

K. Hamalainen (Univ. of Helsinki, Finland) C.-C. Kao, W.Caliebe and J.B. Hastings (NSLS), M. Krisch and F. Sette (ESRF, France)

X-ray absorption spectroscopy is a well established technique, and can provide information on electronic structure and local order. High energy resolution measurements of the fluorescence photon from the core-hole decay can reveal more detailed information on the system. Especially, systematic study of the scattered photon spectrum while scanning the incident energy through an absorption edge can be used to resolve the different electronic transitions and the related states. For example below the absorption edge, in the so called Resonant Raman regime, the quadrupole transitions can be separated and are furthermore enhanced due to the low absorption.

In this work, we have measured the X-ray Resonant Raman scattering spectra from erbium iron garnet close to the L_{III} absorption edge. The figure below shows the two dimensional raw data grid. Several interesting spectral features can easily be identified in the figure: linear dispersion of resonant Raman scattering, strong white line corresponding to 2p → 5d dipole transition and well separated pre-peak corresponding to 2p → 4f quadrupolar transition. This small feature is almost totally invisible in the conventional absorption spectrum due to the 2p lifetime broadening.

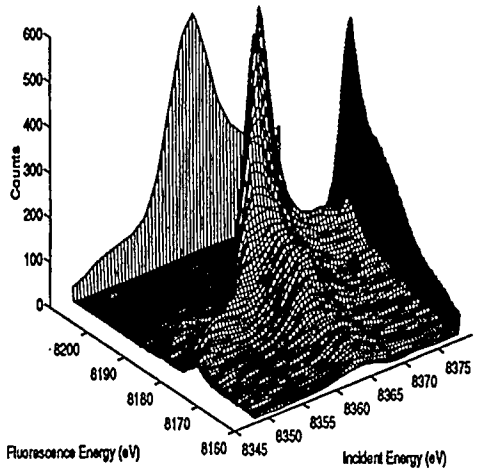


Figure 1. High resolution resonant Raman spectra near the Er L_{III} edge from erbium iron garnet.

* Supported by US DOE under contract# DE-AC02-76CH00016

High resolution Compton scattering study of beryllium * | X21

K. Hamalainen, S. Manninen (Univ. of Helsinki, Finland), C.-C. Kao, W. Caliebe, J. B. Hastings (NSLS), A. Bansil, and S. Kaprzyk (Northeastern Univ.), P. Platzman (AT&T Bell Lab.)

Compton scattering is a unique tool in the study of the valence electron momentum distributions in solids. Using single crystal samples it is possible to study small anisotropies between different crystal directions. However, the obtainable information has been limited by poor momentum resolution of the detection systems. The best momentum resolution demonstrated so far is about 0.1 a.u. [1-3]. At X21, momentum resolution of 0.02 a.u. at 8 keV incident photon energy is achieved by high resolution backscattering spectrometer based on a spherically bent Si(111) analyzer crystal.

Compton profiles from Be single crystal in different crystal directions were measured in this work as a test case to see if new information can be obtained from the improved momentum resolution. For example, the improved momentum resolution may reveal the topology of the Fermi surface. It may also provide a more stringent test on the theory of electron correlation effects. Figure 1 shows the directional Compton profiles from Be in the ⟨00.1⟩ and ⟨11.0⟩ direction. Significant larger anisotropy in the directional profiles was observed. The first derivative of Compton profile around the Fermi surface is also sharper in the new measurement.

[1] G. Loupias, J. Petiau, A. Issolah, M. Schneider, Phys. Stat. Sol. (b) 102 79 (1980)

[2] N. Shiotani, N. Sakai, F. Itoh, M. Sakurai, H. Kawata, Y. Amemiya, M. Ando, Nucl. Instrum. Methods 275, 447 (1989)

[3] Y Sakurai, M. Ito, T. Urai, Y. Tanaka, N. Sakai, T. Iwazumi, H. Kawata, M. Ando, N. Shiotani, Rev. Sci. Instrum. 63, 1190 (1992)

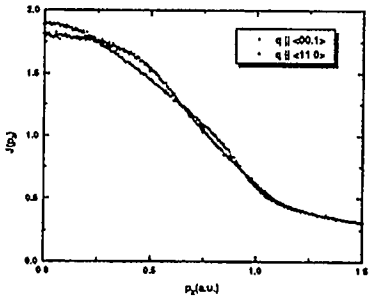


Figure 1. High resolution Compton profiles from Br. Open circle is the Comtponprofile in the ⟨11.0⟩ direction. The incident energy is around 8 keV, and the scattering angle is 160°.

* Supported by US DOE under Contract DE-AC-2-76CH00016.

Dynamic structure factor of solid and liquid metals | X21

J. P. Hill, C. C. Kao, J. B. Hastings, and Doon Gibbs (BNL)

The behavior of electrons in solids is of wide ranging practical importance. Atthe same time, it is of great theoretical interest. The behavior of the electron gas may be summarized in the complex dielectric function. In the past, jellium-like models have been used to approximate the conduction electrons in simple metals, and the dielectric function has been calculated within the Random Phase Approximation. The RPA response function, at small q, consists of a sharp well defined resonance, the plasmon, which disperses to higher energies with increasing q, until it meets the band of allowed particle-hole pair excitations, at which point it broadens to form a featureless bump. Experimentally, the quantity that is measured in a scattering experiment is the dynamic structure factor $S(q,\omega)$ which is intimately related to the dielectric function. Inelastic x-ray scattering offers the advantage over other scattering techniques in that large energy transfers are readily achievable and, because x-rays are a weakly interacting probe, the interpretation of the cross-section is simple, even at large momentum transfers. Early x-ray scattering measurements showed a double peaked hump in the intermediate q regime, which appeared to be common to a number of simple metals and to scale with electron gas parameters. It was argued that this feature was a many body effect and represented the need for higher order corrections to the RPA. An alternative explanation is that the structure arises as a result of new transitions allowed by the periodicity of the lattice. In an attempt to distinguish empirically between the two mechanisms, we have measured the response function of Li and Na in the liquid and solid state. The solid state measurements were performed on polycrystalline samples at room temperature. Energy scans as a function of q for solid Li are shown in Fig. 1. In the liquid state, a similar response was seen. The q=0 plasmon is shifted to lower energies, consistent with the reduction in electron density at the higher temperature, but the dispersion coefficient and the plasmon lifetime remain the same, to within errors. In Fig. 2, detailed scans of the intermediate q response are shown in the solid and liquid state. Qualitatively the two are similar, although the small feature at 20 eV, highlighted in the insets appears to be absent in the liquid state.

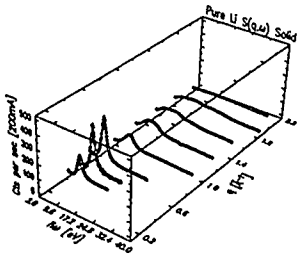


Figure 1.

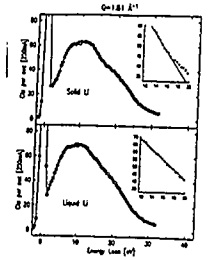


Figure 2.

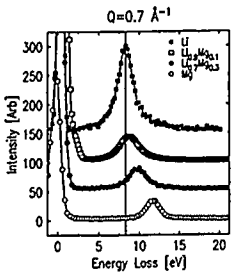
Inelastic x-ray scattering study of $Li_{1-x}Mg_x$ alloys | X21

J. P. Hill, C. C. Kao, J. B. Hastings, and Doon Gibbs (BNL)

The x-ray scattering cross-section is proportional to the dynamic structure factor of the electrons in the probed region. In typical scattering experiments, the energy resolution is poor ($\approx$10eV) and the dynamic information is lost. If the scattering is energy resolved however, the dynamic structure factor S(q,ω) is recovered. This quantity is directly related to the complex dielectric function of the material, which in turn may be calculated theoretically and is of fundamental importance in describing the behavior of the electrons in the solid. This technique offers the advantages of a weak interaction, allowing a simple interpretation of the data, even at high momentum transfers, and the possibility of large energy transfers (on the order of 100 eV).

In the RPA (jellium) picture of simple metals, there is a single variable, the electron density, which determines the important parameters of the electron liquid. As a means of varying the electron density, we have carried out a study of S(q,ω) for a series of $Li_{1-x}Mg_x$ alloys, with 0.0, 0.1, 0.3, 1.0. The samples studied were crystallographic powders which results in an averaging of any band structure effects. In addition, a single crystal of Mg was studied.

The beamline was configured with a miscut Si(220), horizontally focusing monochromator. A spherically bent Si(444) crystal operating in a near-back scattering geometry was used to analyze the scattered beam. Energy scans were typically performed by scanning the incident energy with the exit energy held fixed. All experiments were done in transmission and the overall energy resolution was 0.7 eV FWHM. Energy scans at fixed q=0.7Å^{-1} are shown for the four concentrations in the left figure. The peak at E=0 is the quasi-elastic scattering from the sample and a single peak due to the plasmon resonance is observed at finite energy transfers. A progressive trend is seen towards increasing plasma frequency with increasing conduction electron density (Li to Mg). The data cannot be scaled onto each other by measuring the energy transfer in units of either the appropriate Fermi energy or of the corresponding q=0 plasma frequency. In right figure, the plasmon dispersion is shown along the a and c axes of single crystal Mg. The plasmon dispersion is isotropic. The dispersion follows $\hbar\omega(q) = \hbar\omega(0) + (\hbar^2/m)\alpha q^2$ with $\alpha = 0.30\pm0.04$, lower than the RPA prediction $\alpha_R PA = 0.39$.



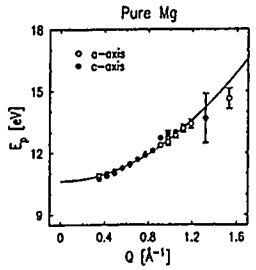


Figure 1.

Inelastic x-ray scattering and the mit in V_2O_3 | X21

E. D. Isaacs, P. M. Platzman (AT&T), C. C. Kao (NSLS), P. Metcalf, J. Honig (Purdue Univ.)

The discovery of high-T_c superconductivity has revitalized the study of the metal-insulator transition (MIT) in highly correlated systems. Of particular interest are the transition-metal charge transfer and Mott-Hubbard insulators, examples of which are the parent high -T_c material La_2CuO_4 and V_2O_3, respectively. La_2CuO_4 is insulationg, but can be made metallic by doping with (Ba,Sr). V_2O_3 is metallic at room temperature and can be made insulationg by either doping with Cr or cooling. This behavior represents a spectacular breakdown of band theory which predicts that these systems should be metallic. There is mounting evidence that the strong electron correlations, not included in conventional band theory, play an essential role in the quantum mechanical delocalization of the carriers. The delocalization process occurs over short distance scales (d$\sim 1/n^{1/3} \sim$10Å).

Therefore, we have used inelastic x-ray scattering spectroscopy to measure the density response function, S(Q,ω), with an energy resolution of $\delta\omega \sim$1 eV at finite-Q ($\sim$1/d) in $V_{1.978}Cr_{0.022}O_3$. We observe three spectral peaks at energy-loss $\Delta E \cong$2.4, 9 and 12 eV. The two lower energy peaks appear only in the low temperature antiferromagnetic insulationg phase below T_{AFI}=173 K. The appearance of these peaks in the insulation phase is most likely due to a shift in spectral weight from the low energies associated with the metal ($\Delta E<1$ eV, i.e., unresolved Drude peak), to ΔE=2.4 eV leaving the Fermi surface in a gap. Thus, V_2O_3 becomes insulationg. In this scenario, the lower energy peak can be associated with an intra d-band transition (e.g., Hubbard bands), while the peak at 9 eV, which is not observed in optical reflectivity measurements (Thomas, et al., PRL73, 1529 (1994)) measurements at Q$\sim$0Å^{-1}, can be associated with a charge transfer excitation from the O2p states well below the Fermi surface (L. Mattheiss, preprint) to the same unoccupied upper d-band. The peak at 12 eV is observed at all temperatures, as well as in the optical data, and is associated with an O2p-V3d charge-transfer excitation.

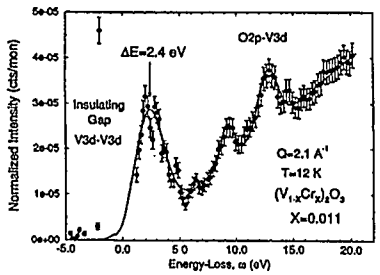


Figure 1. Normalized inelastic x-ray scattering spectrum, S(Q,ω) in $V_{1.978}Cr_{0.022}O_3$ in the AFI phase at T=12 K and Q= 2.1Å^{-1}. Thepeak at ΔE= 2.4 eV appears only for $T<T_{AFI}$ and we ascribe itto a d-d transition between filled (lower)and empty (upper) Hubbard-like bands. The peaks at higher energies are due to O2p-V3d charge transfer excitations.

Inelastic x-ray scattering study of diamond * | X21

C.-C. Kao, W. Caliebe (NSLS), M. Krisch (ESRF, France), K. Hamalainen (Univ. of Helsinki, Finland), J. Hastings (NSLS)

An inelastic x-ray scattering spectroscopy (IXSS) study of diamond was performed. Inelastic scattering spectra along the (001) direction with energy transfer from 0 to 100 eV and momentum transfer from 0.3Å^{-1} to 3.4Å^{-1} were recorded. The measured intensity can be related via the dynamical structure factor $S(Q,\omega)$ to the dielectric function.

A few selected spectra are shown in figure 1. The momentum transfers in the figure are normalized to the distance in reciprocal space between the zone center and X point. At small Q, the spectra are dominated by a loss feature at 33 eV, and is usually assigned to the plasmon. With increasing momentum transfer, several other features appear at the low energy side of the plasmon, with large dispersion in energy and change in intensities.

Figure 2 shows an expanded view of several inelastic scattering spectra around energy transfer comparable to the band gap of diamond. The onset of the scattering intensity can be clearly observed in these spectra. The position of the threshold also shows strong dispersion with momentum transfer, and reaches a minimum of about 5.5 eV at momentum transfer equal to 1.3 ΓX. The minimum energy transfer agrees well with reported indirect band gap og diamond[1].

[1] Clark, C.D., Dean,P.J., Harns, P.V., Proc. R. Soc. London A277 (1964) 312.

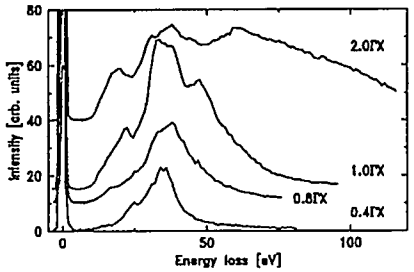


Figure 1. IXSS-data of diamond at q=0.4, 0.8, 1.0, 1.8 and 2 ΓX.

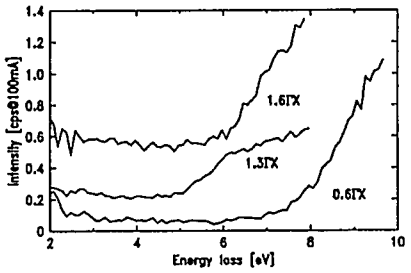


Figure 2. IXSS-data of diamond at q=0.6, 1.3 and 1.6 ΓX.

* Supported by US DOE under contract DE-AC02-76CH00016.

Evidence for quadrupolar contribution to the absorption cross section at the L_{III} edge of gadolinium gallium garnet * | X21

M. Krisch (ESRF), C.-C. Kao (NSLS), F. Sette (ESRF), W. Caliebe (NSLS), K. Hamalainen (Univ. Helsinki), and J. Hastings (NSLS)

The existence and strength of the $2p^5 4f^{n+1}$ quadrupolar transition at the L_{III} edge in $Gd_3Ga_5O_{12}$ is measured by high resolution resonant x-ray inelastic scattering. The $3d^9 4f^{n+1} 5d^0$ and $3d^9 4f^n 5d^1$ families of multiplets, generated by the de-excitation of the 2p core hole, are resonantly enhanced at the $2p^5 4f^{n+1} 5d^0$ and $2p^5 4f^n 5d^1$ resonant intermediate state excitation energies, respectively. The large energy separation between these two multiplet families due to their very different Coulomb integrals, allows the detection of quadrupolar $2p^5 4f^{n+1} 5d^0$ and dipolar $2p^5 4f^n 5d^1$ transitions in spite of the large 2p core hole lifetime broadening.

Supported by US DOE under contract DE-AC02-76CH00016.

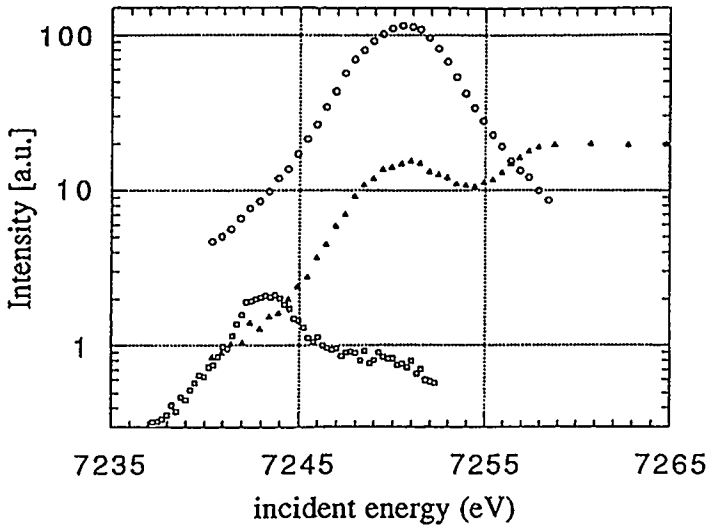


Figure 1. Constant energy transfer scan for three different energy transfers:feature A (cubes): 1191 eV, feature B (circles): 1198.5 eV and feature C (triangles): 1207 eV. The spectra are corrected for self absorption effects.

* Supported by US DOE under Contract DE-AC02-76CH00016.

Inelastic x-ray scattering from 6H-SiC *	X21

A. T. Macrander, V. I. Kushnir, R. C. Blasdell, P. A. Montano (ANL), and C.C. Kao (BNL)

We have studied electronic excitations in 6H-SiC using inelastic x-ray scattering. Inelastic scattering spectra measured at momentum transfers ranging from 0.47 $Å^{-1}$ to 2.00 $Å^{-1}$ along the c-axis, i.e., along [00.1], are shown in the figure. These were compared to spectra obtained for momentum transfers along the [10.0] direction. Comparison of the two sets of data reveals an orientation dependence of the spectra, except for a characteristic peak at 23 eV that occurs for both directions at low Q. This peak has also been observed in electron energy loss spectroscopy studies and is identified as a bulk plasmon. The orientation dependence of the other spectral features indicates that band structure effects must be involved in their origin. This data were obtained suing a Ge(444) analyzer in a near backscattering geometry (1).

[1] A.T. Macrander, V.I. Kushnir, and R.C. Blasdell, Rev. Sci. Instrum., 1994, in press.

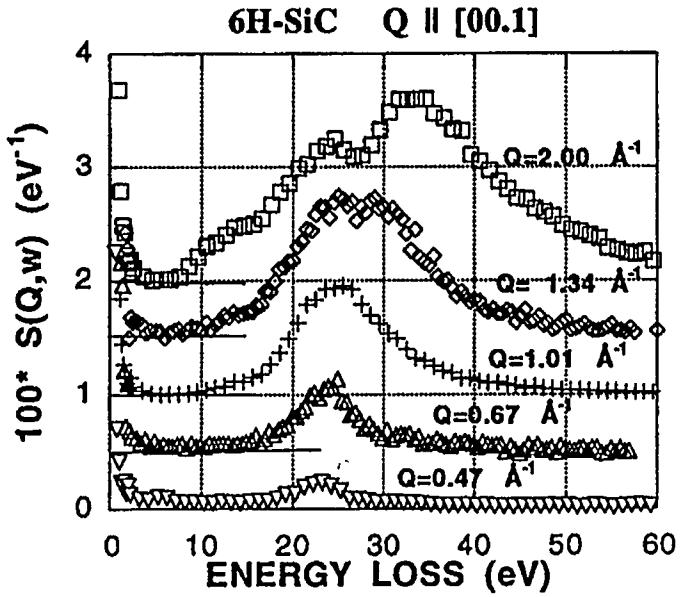


Figure 1.

* Work supported by the U.S. Dept. of Energy, BES-Materials Sciences, under contract no. W-31-109-ENG-38.

Inelastic x-ray scattering investigation of oxide insulators	X21

Peter W. Stephens (SUNY Stony Brook), Chi-Chang Kao (NSLS), Wolfgang Caliebe (NSLS), and Jerry Hastings (NSLS)

We have measured the dynamical structure factor of MgO and Al_2O_3 with an energy resolution of 0.8 eV FWHM. Spectra were taken at constant E_f as a function of E_i, at various scattering angles θ. In this range of parameters, the experiment is principally sensitive to inter-band transitions, and one can see significant variation with the scattering vector Q between different curves. We intend to compare this data to pseudo potential models of band structure and matrix elements, with an eye toward application to more complicated d-band systems.

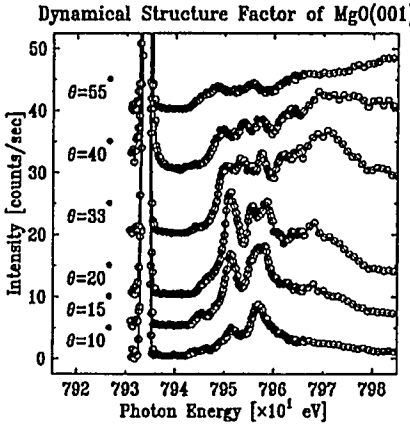


Figure 1.

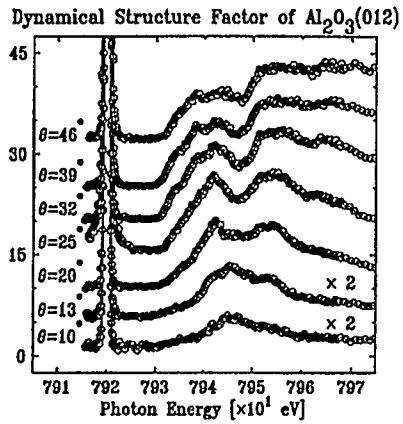
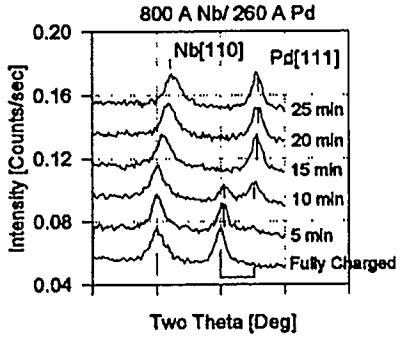


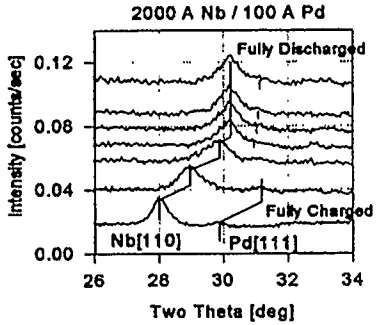
Figure 2.

X-ray studies of the hydrogen charging and discharging behavior of thin Nb films *	X22A

N. M. Jisrawi, T. R. Thurston, M. W. Ruckman, and Myron Strongin (BNL)

We have performed a systematic x-ray study of hydrogen charging and discharging in air of palladium-capped thin Nb films (500 to 2000 Å thick). Hydrogen uptake is enhanced in thin films of Nb when capped with thin layers of Pd. X-ray data (see figures) shows that the intense Nb[110] and Pd[111] lines are shifted in 2θ by up to 2° and 1.2°, respectively, which corresponds to a lattice expansion of about 6.7% for Nb- H and 3.6% for Pd-H phases. The Pd[111] peak shows shifted and unshifted bragg peaks which is a signature of phase segregation, whereas the Nb[110] Bragg peak moves slowly from the shifted position as hydrogen leaves the sample at a rate determined by the thickness of the Nb film and its Pd overlayer. The slow shift of the Nb[110] peak is indicative of the fact that the hydrogen is dissolved in Nb in solid solution. Figure 1 shows the behavior of the Pd[111] x-ray diffraction peak as hydrogen leaves the sample. The peak diminishes quickly at the shifted position while a new peak starts to grow at the [111] peak position of uncharged metallic Pd. The time in minutes after the sample is exposed to air is shown in the figure. The shifted peak at 2θ=30° is therefore attributed to the PdH phase which then dissociates quickly when exposed to air into as evidenced by the quick rise of the metallic peak at 2θ=31.1°. This behavior is contrasted with that of the Nb[110] peak shown in the two figures which moves slowly from the shifted position to that of pure Nb while keeping its relative intensity. The experiment confirms the behavior observed by monitoring the room temperature resistivity of the Nb/Pd bi-layers. It also suggests hydride formation in the case of Pd whereas hydrogen is thought to dissolve in Nb in solid solution. This finding suggests that NbH phase is the α component rather than the β component expected for bulk niobium hydride.





* Work supported by US DOE Division of Materials Sciences under Contract DE-AC02-76CH00016.

Langmuir monolayer phases of hexadecanoic acid ($CH_3(CH_2)_{14}COOH$) from crystallites *	X22B

M. Bommarito, W. J. Foster and P. S. Pershan (Harvard)

Must studies of surfactant films at the water/gas interface are conducted by depositing Langmuir monolayers (LM) of relatively long chain (insoluble) surfactants from a solvent solution. Once the solvent evaporates these LM can remain stable for many hours, or even days. On the other hand it is not clear if the two dimensional phases observed by compressing such LM are in local thermodynamic equilibrium. We attempted to confront his question by forming LM in thermodynamic equilibrium with a 2d gas phase formed by depositing three dimensional crystallites of the fatty acid on the surface of water, without any solvent. Figure 1 is a plot of the observed surface pressure (π) as a function of temperature for LM formed from crystals of hexadecanoic acid ($CH_3(CH_2)_{14}COOH$) from crystallites.

LM do not form for T17°C when the monomer is insoluble in the aqueous subphase. For 34%°CT17°C, the LM is in equilibrium with monomers dissolved in the subphase. It consists of macroscopic domains of an untilted phase with a single GID peak with Q_{xy} = 1.49 Å^{-1}, Q_z= 0. Assuming an untilted hexagonal unit cell this would correspond to an area of 20.4 Å^2/molecule, which is only slightly larger than the area measured for the untilted surface phases of longer chain bulk alkanes. No Bragg peaks are observed T 34%°C. Complementary Brewster angle microscope studies indicate inhomogeneous LM with macroscopic domain structure for 17 T34°C and homogenous LM for T34°C, where the 2-dimensional ordered LM has melted into a homogenous liquid. There is no indication of an pretransition effects and we believe the melting is first order. Specular reflectivity was done for the homogeneous monolayer at T34°C.

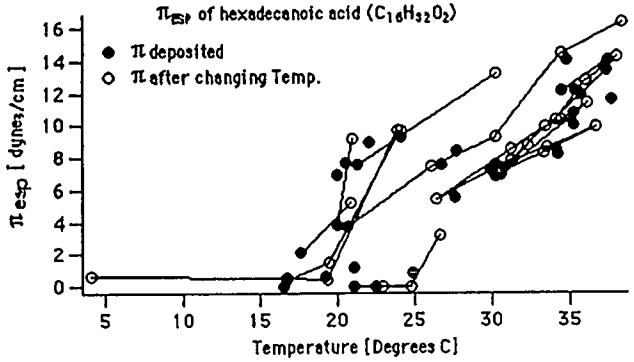


Figure 1.

* This work was supported by the DOE under DE-AC02-76CH00016 (NSLS), by and the NSF under NSF-DMR-91-13782 and NSF-DMR-89-20490.

Grazing x-ray diffraction study of a monolayer of methyl arachidate at the air/water interface *	X22B

W. J. Foster, M. Shih, and P. S. Pershan (Harvard University)

Although recent advancements in techniques for studing the structure of Langmuir monolayers (LM) have yielded new insights about the two-dimensional (2d) LM phases, unambiguous methods by which their thermodynamic equilibrium and the relevant phase transitions are still undeveloped. This is particularly true for the condensed crystalline (or hexatic) two-dimensional phases were grain boundary relaxation can have decay times of hours. [1,2,3] Much experimental work has concentrated on LM of fatty acids; however, there is good reason to suspect that hydrogen bonding effects inhibit the kinetics and we have carried out a combination of Brewster Angle Microscope (BAM) and grazing incidence diffraction studies (GIDS) experiments on Langmuir monolayers of methyl eicosanoate (arachidate) ($CH_3(CH_2)_{18}COOCH_3$).

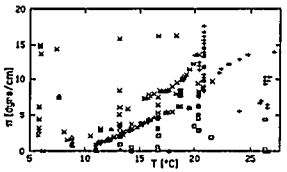
The figure illustrates all of the GIDS peaks observed to date as a function of the surface pressure (π) and temperature (T). For T 10 C and for π 5 dynes GIDS shows a single diffraction peak (indicated by an open square) with maximum intensity at $(Q_{xy}, Q_z) \approx (1.51, 0.25)\text{Å}^{-1}$. This is particularly interesting since the 2d order of these monolayers is typically slightly distorted hexagonal, and out of plane peaks are associated with tilt of the alkane chains. For 2d positional order it is not possible to have only one peak if that peak is out of the plane (i.e. $Q_z \neq 0$) and this data strongly suggests a phase with one dimensional positional order. At higher pressures a single broad peak (+) may represent the untilted versions of the same phase. Other points are the observed positions where there are either two in plane peaks (x), indicative of the untilted 2d crystalline I'(L_2''), or two peaks, one of which is in plane and one is out of plane ($\triangle$), indicative of one of the previously observed 2d tilted LM phases.

For high T and low π BAM studies indicate a birefringent phase with optically observed textures that appear to be consistent with the GIDS measurements. GIDS studies continue into Sept. 1994.

[1] M.L. Schlossman, D.K. Schwartz, P.S. Pershan, E.H. Kawamoto, G.J. Kellogg and S. Lee, Phys. Rev. Let. 66, 1599 (1991).

[2] D.K. Schwartz, M.L. Schlossman and P.S. Pershan, J. Chem. Phys. 96, 2356 (1991).

[3] J.T. Buontempo, S.A. Rice, S. Karaborni and J.I. Slepman, "Differences in the structures of relaxed and unrelaxed Langmuir monolayers of heneicosanol: Dependence of collective molecular tilt on chain conformation", (to appear).



* This work was supported by the DOE under DE-ACO2-76CH00016 (NSLS), by the NSF under NSF-DMR-91-13782and NSF-DMR-89-20490.

X-ray reflectivity study of Si-based MOS devices *	X22B

S. D. Kosowsky, P. S. Pershan (Harvard), J. Bevk, and P. K. Roy (AT&T)

We have performed x-ray specular reflectivity measurements on a series of Si-based MOS structures of interest to device personnel at AT&T Bell Laboratories. The devices were prepared at the AT&T production facility at Allentown, Pa. under different sets of growth conditions with the intention of relating structural properties to processing parameters.

The structures are single crystal Si(001) substrates, with approximately 80Å of SiO_2 grown on top. A 2500 Ålayer of doped polycrystalline Si is then deposited on top of the wafer to form a conductive cap.

Typical reflectivity curves are reproduced below and are currently being analyzed; however, some features of the reflectivity can be interpreted with only preliminary analysis. (1) The rapid oscillations originate from the 80 Å SiO_2 layer sandwiched between the c-Si substrate and the p-Si cap. However, the modulations in the amplitude of the interference fringes are not able to be modeled by this simple two (80 + 2500 Å) layer model. (2) The rapid fall off in the reflectivity data in the range a<.2 Å^{-1} corresponds to a 49Å rms roughness of the p-Si/vacuum interface. For q>.2Å^{-1}, that interface contributes insignificantly to the reflectivity and the oscillations and structure are due to the other layer. (3) Consequently, it is likely that the modulations arise because one or the other of these interfaces for the 80Å layer has a substructure on the order of 5 to 10 Å. The fact that the oscillations appear to vanish at different positions for films prepared by different processing techniques may have practical importance.

This is the first of a series of proposed collaborative experiments between Harvard and AT&T to demonstrate that with x-ray scattering we can characterize structural parameters of deeply buried production quality interfaces. Unfortunately, the principal support for this program was terminated by the Joint Services Electronics Program as of Oct. 1994 and continuation is currently uncertain.

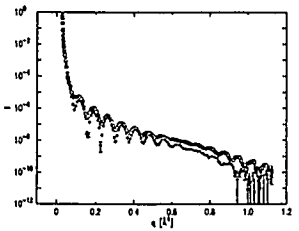


Figure 1. Typical specular reflectivity curves for steam (open box) and thermal (filled box)oxides grown on Si. Both are capped with a 2500Å layer.

* Work supported by the DOD Joint Services Electronics Program under grant N00014-89-J-1023, Harvard Materials Research Laboratory under grant NSF-DMR-89-20490 and by AT&T Bell Laboratories.

Surface structure of liquid mercury | X22B

O. M. Magnussen, B. M. Ocko (BNL), M. Deutsch (Bar-Ilan Univ., Israel), M. Regan,and P. S. Pershan (Harvard)

The surface structure of liquid metals is an important unsolved problem in statistical mechanics and has been subject to extensive theoretical and simulational studies. Unique structural effects such as atomic layering, and enhanced in-plane order at the interface were predicted but could not be unambiguously proven in the few experimental studies of the structure of liquid metal surfaces due to the limited q_z range of these previous measurements.

We have carried out a series of reflectivity measurements on mercury up to $q_z = 2.5\text{Å}^{-1}$ using a special glass cell allowing reflectivity measurements to high q_z in an inert atmosphere. The cell is mounted on an active vibration isolation table, which mounts directly on the Harvard/BNL Liquid Surface diffractometer and effectively eliminates vibration pickup, as shown by the small divergence measured for the reflected beam. Our cell has also been designed to minimize contaminant effects. The measurements indicate that the surface of Hg is kept clean for periods exceeding 24 hours in an inert atmosphere. In Fig. 1 we show our the reflectivity data measured at room temperature under hydrogen, along with the ideal Fresnel curve and the best fit of the data. The slow decrease below the Fresnel curve out to $q_z \cong 1.5\text{Å}^{-1}$,indicates a surface roughness of 1-2Å^{-1} in good agreement with capillary wave theory and measurements on Ga. The broad peak observed at $q_z=2.2\text{Å}^{-1}$, followed by a rapid drop in the reflected intensity, is a clear evidence for surface layering. A preliminary modeling, yields the electron density profile shown in the inset in Fig. 1 with a layer spacing of $\cong$2.8Å and about 4 distinct atomic layerswhich decay with depth. These results are in excellent agreement with theory.

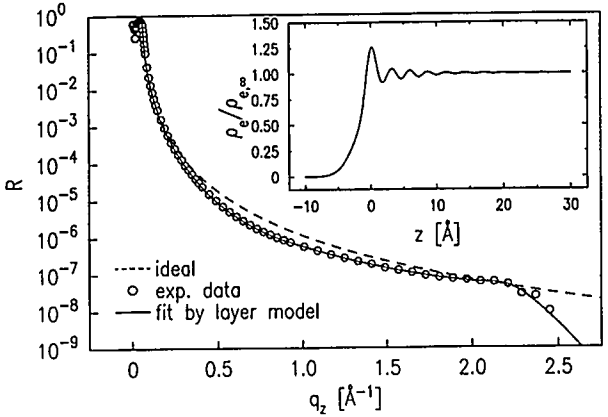


Figure 1.

Chloride and bromide adlayers on Au(111) and Ag(111) electrodes | X22B

O. M. Magnussen, B. M. Ocko, J. X. Wang, and R. R. Adzic (BNL)

In-situ grazing incidence angle x-ray diffraction was utilized to study the structure of halide anions adsorbed on Au(111) and Ag(111) single crystal electrode surfaces. On Au(111) hexagonally arranged in-plane diffraction peaks are observed at positive potentials in solutions containing chloride (Fig. 1) or bromide (Fig. 2) ions. They correspond to the formation of close-packed chloride and bromide monolayers at 0.68V and 0.42V, respectively (in 0.1M solution), which are incommensurate with the underlying lattice. The chloride adlayer is aligned along the $\sqrt{3}$- direction of the Au substrate, the bromide adlayer deviates from the latter by a small potential dependent angle ϕ ($3.3° \leq \phi \leq 4.7°$). With increasing potential the diffraction peaks are shifted negatively, indicating compression of the adlayer. Similar hexagonal chloride and bromide adlayer, albeit in a narrower and more negative potential range, are found on Ag(111). While Cl on Ag(111) is incommensurate and compresses with potential, Br forms a high-order commensurate (7x7)-structure with coverage θ=0.51. Both adlayers are aligned along the Ag substrate axes, in striking contrast to the adlayers on Au. The 3 incommensurate structures exhibit a well defined dependence of the coverage with potential (Fig. 3), is independent of the direction of the potential change. Studies of the concentration dependences yield electrosorption valencies close to -1 indicating that the adsorbed anions are almost completely discharged. The adlayer formation is accompanied by sharp current spikes in the corresponding cyclic voltammetric curves and may be interpreted as an order-disorder transition. From the θ(E)-curves the two-dimensional compressibilities of halide monolayers can be calculated. They range between 4.65$\text{Å}^2\text{eV}^{-1}$ (Cl/Au(111)) and 6.74$\text{Å}^2\text{eV}^{-1}$ (Br/Au(111)), i.e. in between the values found for noble gases and metal monolayers.

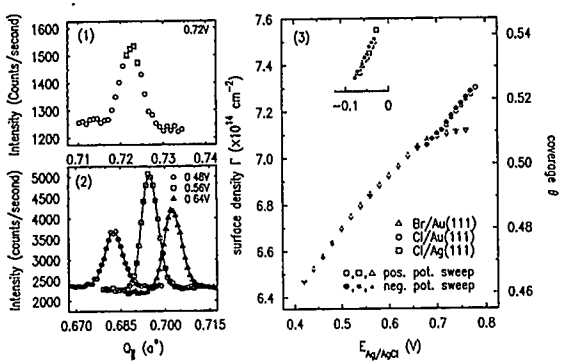


Figure 1.

Observation of charge density waves in thin epitaxial Cr-films | X22B

P. Sonntag, P. Bödeker, W. Donner (Ruhr-Universität Bochum), J. P. Hill, G.Helgesen, T. R. Thurston, D. Gibbs (BNL), and H. Zabel (Ruhr-Universität Bochum)

Bulk chromium is an itinerant antiferromagnet with a bcc chemical structure. An incommensurate spin density wave state forms below ~310K. Knowledge about this SDW and its behavior in thin films is important for understanding the interlayer magnetic coupling in e.g. Co/Cr or Fe/Cr multilayer systems.

By means of Molecular Beam Epitaxy thin epitaxial Cr(110) and Cr(001) films have been grown on sapphire substrates with Nb buffer layers. The film thicknesses range from 50 to 4000 angstroms. These samples are of high crystallographic quality, with mosaics ranging from ~0.25 to ~0.5 degrees HWHM.

Associated with the SDW is a Charge Density Wave (CDW) with wavevector $\vec{q}_{CDW} = 2\vec{q}_{SDW}$. This CDW can be meassured using synchrotron x-ray scattering techniques, as shown in figure below. The scan is around a Cr(220) reflection in a 1000 angstrom thick Cr(110) film with T=140K. The two satellites arise from CDW scattering.

In all of our studies, we only found CDW satellites with a wavevector component perpendicular to the film plane. All possible CDWs with wavevectors in the film plane were not visible. However, in bulk Cr neutron scattering measurements show CDWs with all three possible orientations. [1] Future experiments with samples grown on substrates with different epitaxial strains may provide insights into the origin of this behavior.

Additionally we investigated the temperature dependence of the CDW wavevectors for temperature ranges from 13K to 320K. The figure below shows the absolute value of the wavevector versus temperature in a1000 angstrom thick Cr(001) film. A phase transition occurs at ~310K, and the behavior is comparable to that seen in bulk samples. This confirms that the satellite scattering observed arises from CDWs associated with the SDW.

[1] E. Fawcett, Rev. Mod. Phys. 60, 209 (1988).

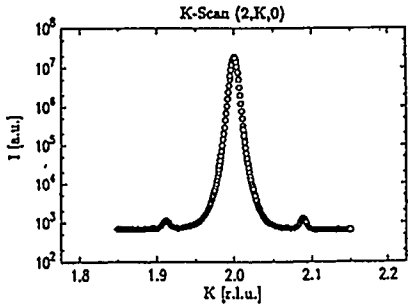


Figure 1.

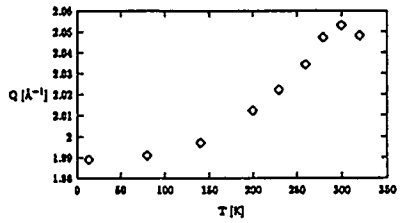


Figure 2.

Electroepitaxy of Tl on Ag(001) and Au(001) | X22B

J. X. Wang, R. R. Adzic, O. M. Magnussen, and B. M. Octo (BNL)

The structure of electrodeposited Tl overlayers on Ag(001) and Au(001)in 0.1 M HCl_4 solution containing 2.5 mM Tl_2SO_4 was determined by surface X-ray scattering techniques. On Ag(001), the underpotential deposition of Tl occurs below -0.1 V in three distinct steps (submonolayer, monolayer, and bilayer) which give rise to the three pairs of current peaks in the voltammetry curve (Fig. 1). A c(px2) close-packed monolayer forms below -0.32 V and compresses uniaxially (p decreases from 1.185 to 1.168) with decreasing potential. Upon the deposition of the second layer at potentials negative of -0.46 V, both layers form a commensurate c(1.2x2) structure. The multilayer deposited at more negative potentials forms an aligned hcp structure on top of the c(1.2x2) bilayer. This gives rise to additional sharp intensity spikes in the (1/p,1/2) and (2/p,0) surface rods (the diffractions of hcp and c(1.2x2) nearly overlaps within the H-K plane) as shown in Fig. 3 and 4, respectively. The Tl layer densities, normalized to the bulk value, are plotted versus potential in Fig. 2. The layer-by-layer or 2D growth mode seems to extend beyond second layer since the in-plane coherence length retains the same value from monolayer to the thin film of over 30 layers. The formation of this well-ordered metal thin film at room temperature is unusual and it does not occur on Au(001) although the Tl monolayer has the same structure and the same maximum layer density as on Ag(001) (see Fig. 2). Further deposition on Au(001) results in the formation of imperfectly-aligned hcp crystallites on top of the c(p×2) monolayer suggesting a 3D growth mode beyond monolayer. The different growth modes, despite of the nearly identical substrate geometry and monolayer structures, demonstrates that epitaxial growth is sensitive to the details of substrate-overlayer interactions.

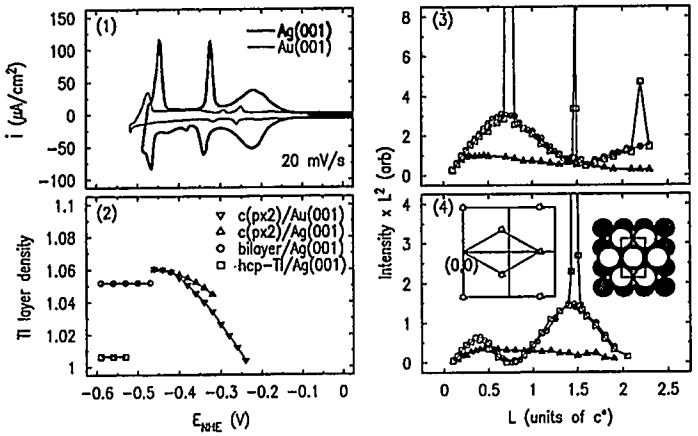


Figure 1.

Antiferromagnetic layer formation in UAs | X22C

N. Bernhoeft, A. Stunault, C. Vettier, F. de Bergevin (ESRF) (CNRS), Doon Gibbs,T. R. Thurston, S. M. Shapiro, J. B. Hastings (BNL), P. Dalmas (CEA), G. Helgesen (BNL) (Institutt Energiteknikk), O. Vogt (ETH)

The nature of the paramagnetic to antiferromagnetic phase transition in the uraniummonopnictides with the NaCl crystal structure continues to be a challenging problem. To this end we have studied the detailed lineshape of diffracted beams from several samples of UAs. In taking advantage of the resonant enhancement of the magnetic X-ray scattering cross-section by tuning the X-ray energy to the uranium M_{iv} absorption edge (3728 eV) we become near surface sensitive and preferentially probe the top 2000Å of the sample. The magnetic phase is characterised by domains where the propagation vector and net magnetic moment lie parallel to the three orthogonal cubic axes (type I). In the chosen scattering geometry $(0,0,\tau)$ we are sensitive to those domains with moments perpendicular to the sample's surface. The effects reported on below have not been observed in those domains with antiferromagnetic correlations parallel to the sample's surface. Typical scans, perpendicular and parallel to the surface, taken at the onset of bulk antiferromagnetism are displayed in Fig. 1. An interpretation of the highly anisotropic broad component of the measured response which exists in the vicinity of T_n is offered in terms of a finite number of (surface) antiferromagnetic layers, the number of which is given by the measured width of the response in momentum space. The analysis is complementary to that given in the study of other magnetic systems which also exhibit both broad and narrow components of scattering intensity in the vicinity of the phase transition [1]. In these examples of second order phase transitions, a global analysis in terms of temperature dependent correlation lengths is given, we simply wish to present a possible microscopic interpretation which maybe applicable in our case.

[1] S. Langridge, W.G. Stirling, G.H. Lander, J. Rebizant, J.C. Spirlet, D. Gibbs, O. Vogt, Europhys.Lett. 25, 137-142 (1994)

[2] K. Hirota, G. Shirane, P.M. Gehring, C.F. Majkrzak, Phys. Rev., B49, 11967-11978 (1994)

[3] T.R. Thurston, G. Helgesen, J.P. Hill, D. Gibbs, B.D. Gaulin, P.J. Simpson, ibid, 15730-15744.

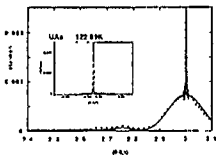


Figure 1. Resonant magnetic X-ray scattering from UAs versus reciprocal lattice vector along the direction $(0,0,\tau)$. The narrow and broad components of the response correspond to the onset of bulk antiferromagnetism and the surface antiferromagnetism respectively. The solid line corresponds toa model calculation with 11 surface and approximately 600 bulk magnetic layers. The insert is a scanalong $(\tau,0,3)$.

Scaling of higher harmonic satellites near the magnetic phase transition of thulium | X22C

G. Helgesen, J. P. Hill, T. R. Thurston, and Doon Gibbs (BNL)

Below the Néel temperature, T_N=56.0 K, the magnetic moments of thulium-metal order in a sinusoidally, c-axis modulated structure. In addition to the primary magnetic satellite, which has an intensity proportional to the square of the order parameter at the transition, x-ray scattering measurements also show higher order harmonic satellites. These satellites which are displaced by 2τ and 4τ along the reciprocal c*-direction relative to the crystalline Bragg reflections, where τ is the magnetic wave vector, reflect a harmonic lattice modulation induced by the magnetic ordering. In the experiments, the photon energy was tuned to the L_{III} absorption edge of Tm (E=8.65 keV) and the integrated intensity I_1 of the resonant magnetic scattering at the primary magnetic satellite was measured as a function of temperature. Near T_N, this intensity shows a power-law behavior of the reduced temperature $t=(T_N-T)/T_N$ with a critical exponent $\beta= 0.49\pm0.08$. Similarily, the intensity I_n of the n'th higher order satellite follows a power-law with exponent β_n in agreement with mean field theory, i.e., $\beta_n=n\beta$. This scaling of the intensity breaks down below $0.7T_N$ as the temperature approaches the transition temperature $T_2=0.48T_N$ of the ferrimagnetic low temperature phase of Tm.

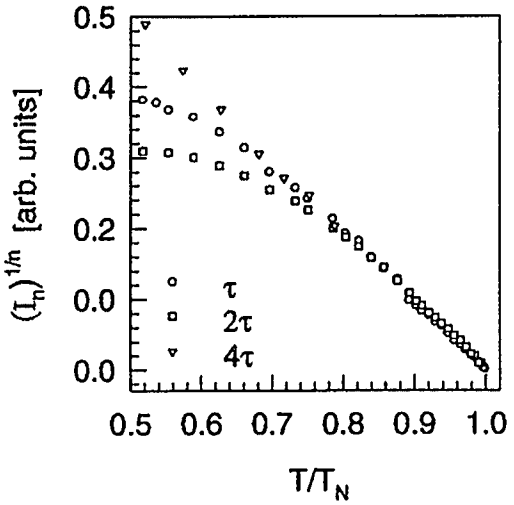
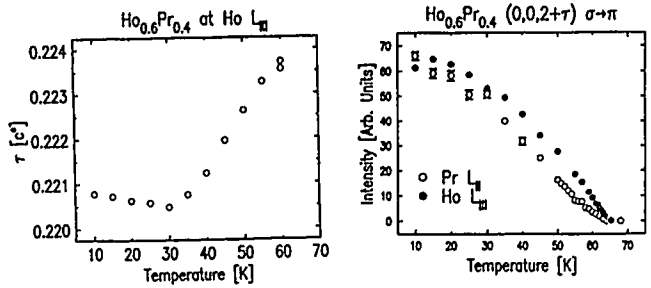


Figure 1. Scaling of the integrated intensity of the principal and higher order satellites at Q= (0,0,2-nτ) (n=1,2, and 4) to a universal scaling function.

Element specific magnetic scattering from a Ho-Pr thin film alloy	X22C

J. P. Hill, G. Helgesen, Doon Gibbs (BNL), D. F. McMorrow (Riso), and R. A. Cowley(Oxford Univ.)

The heavy rare-earth holmium exhibits antiferromagnetic order below T_N=132K, forming a basal plane spiral, with a propagation vector, τ = 0.28c* at T_N, along the c-axis of the hcp structure. In contrast, the light rare-earth praseodymium, crystallizes in the double hcp structure and crystal field effects inhibit ordering until T_N = 0.05 K. The transition temperature may be raised by doping with magnetic impurities and depends on the doping level and the susceptibility. Alternatively, application of uniaxial pressure along the a-axis raises the ordering temperature by lifting the degeneracy of the crystal field. It is an intriguing problem as to what the magnetic phase behavior of a site-random alloy of these two elements might be. Such a system may be viewed as a collection of localized moments interacting through the polarizability of the mediating conduction electrons. It therefore also provides a test of our understanding of the RKKY interaction. X-ray resonant exchange scattering allows the determination of the magnetic wave-vector to high precision, and more importantly by tuning to the appropriate atomic transition, the ordering of each element may be studied independently. A 10,000Å thick $Ho_{0.6}Pr_{0.4}$ film, grown on a yttrium substrate was studied. The mosaic of the film was 0.13° FWHM. Large backgrounds due to surface reflectivity and scattering from the substate were observed in the vicinity of the Bragg peaks. To improve the signal to noise ratio at the magnetic satellites, a polarization analyzer was employed. Here, an analyzer crystal with a Bragg angle of 45° is set to diffract out of the scattering plane. This discriminates against scattering which leaves the horizontal polarization of the incident beam unchanged and preferentially selects scattering that rotates the photon polarization (which is purely magnetic in origin). Gr(006) and Cu(220) crystals were used at the Ho L_{III} and Pr L_{II} edges, respectively. Magnetic Bragg peaks, consistent with a spiral structure, were observed below T_N=65 K, at both edges. Count rates of $\approx$ 1000 s^{-1} at the HO edge and $\approx$ 100 s^{-1} at the Pr edge were observed. The L_{II} enhancement was larger than the L_{III} for Pr, and the converse was true for Ho. In fig. 1, we plot the temperature dependence of the magnetic wave-vector, measured in units of c*. In contrast to pure Ho, it shows very little change. In fig. 2, the Ho and Pr order parameters are shown. The intensities have been normalized to agree at T=10 K. The ordering disappears at the same temperature for both components, but does not have the same temperature dependence.



X-ray scattering study of the cubic-to-tetragonal transition and its precursor phenomenain V_3Si	X22C

K. Hirota, Doon Gibbs, L. Rebelsky, G. Shirane (BNL), and S. J. Williamson (NYU)

As a prototypical system of the A15 compounds, which show relatively high superconducting transition temperatures T_C as well as a martensitic transition at T_{MC}, V_3Si (T_C≈17 K, T_M≈21 K) has been under extensive experimental and theoretical investigations for many years. The structural transition is characterized by a drastic softening of the [110] transverse acoustic phonon near the zone center, [1] changing a cubic phase to a slightly distorted tetragonal phase. [2] We searched for the order parameter of V_3Si below the martensitic transition. As shown in Fig. 1, appearance of the new Bragg peaks at (100) and (300) reflections, which are forbidden in the cubic phase, have been confirmed below T_M, after removing multiple scattering. Temperature dependence of the intensities indicates that the sublattice displacements are linear to the tetragonal strain as is the case with Nb_3Sn. [1] We also found that, even above T_M, there remain intensities at (100) and (300), which gradually decrease with increasing temperature. (See Fig. 2) We speculate that this is a precursor to the martensitic transition.

[1] G. Shirane and J.D. Axe, Phys. Rev. B 4, 2957 (1971).
[2] B.W. Batterman and C.S. Barrett, Phys. Rev. 145, 296 (1966).

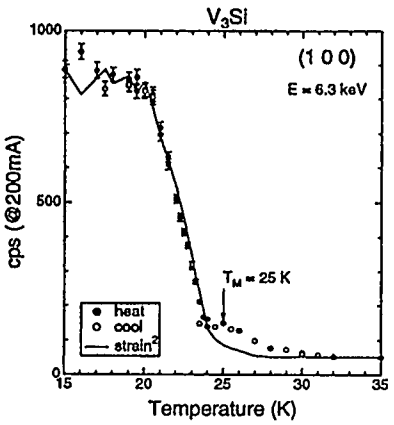


Figure 1.

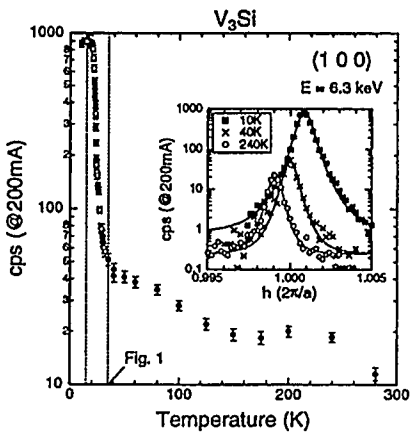


Figure 2.

Magnetic x-ray scattering from uranium antimonide * | X22C

S. C. Perry, W. J. Nuttall, W. G. Stirling (University of Keele, UK), G. H. Lander(E.I.T.U., Germany), and Doon Gibbs (BNL)

As part of a systematic study of actinide compounds, we have recently performed an experiment on X22C to investigate the magnetic critical scattering and ordered-phase structural properties of antiferromagnetic Uranium Antimonide.

Following the work of Langridge et. al. [1] on NpAs, we have used the resonant-enhancement at the M_{IV}-edge of Uranium to study the critical fluctuations of USb above the Neél temperature (T_N). The inherently high wave vector resolution of the x-ray technique means that the range of spatial correlations observed extends beyond that of previous work using neutrons [2]. A study of the charge lattice from deep in the ordered phase to well above T_N was also performed with the diffractometer in a triple-axis configuration,in order to corroborate the results of a neutron powder-diffraction experiment that we have performed.

The (0,0,3) and ($\bar{1}$,0,2) magnetic reflections were measured as a function of temperature in order to determine the sub-lattice magnetisation exponent (β), and T_N. Allowing for differences in thermometry, the values obtained are in agreement with previous results. Measurements were then madeof the scattering arising from fluctuations in the spin system above the ordering temperature about these positions. Examples of critical scattering from the (0,0,3) position are shown in Figure 1 (T_N = 203.37K). In agreement with several other investigations, including such systems as Ho[3], Tb[4], and NpAs[1],we find the data to be consistent with a two length-scale description. The broad component appears tobe of similar width to that determined from neutron studies.

[1] S. Langridge, W.G. Stirling, G.H. Lander, J. Rebizant, J.C. Spirlet, D. Gibbs and O. Vogt, Europhys.Lett. 25 (2), 137 (1994).

[2] G.H. Lander, S.K. Sinha, D.M. Sparlin and O. Vogt, Phys. Rev. Lett. 40, 523 (1978).

[3] K. Hirota et. al., Phys. Rev. B49 11967 (1994).

[4] T.R. Thurston et. al., Phys. Rev. B49 15730 (1994).

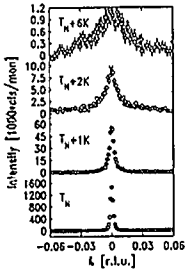


Figure 1. Critical scattering at (0,0,3).

* Supported by UK SERC grant no GR/H56335.

X-ray scattering characterization of high temperature superconducting wires | X22C, X27C

T. R. Thurston, U. Wildgruber, T. Vogt, P. Siddons, J. Hastings, M. Suenaga, T.Wang (BNL), and P. Haldar (IGC Corporation)

Despite the fact that high-temperature superconductors are brittle ceramics, theyhave been wrapped into solenoids and used in magnets and motors for demonstration purposes. Out of the currently known high-temperature superconducting materials, the most technologically promising wires have been made from $Bi_2Sr_2Ca_2Cu_3O_10$ ($T_c \sim$ 110K) and $Bi_2Sr_2CaCu_2O_8$ (T_c ~84K) encased in a silver cladding. Fabricating these materials into commercially viable products is an extremely challenging materials science problem, however; production runs of these wires have not had critical current densities nearly as large as laboratory samples. Ideally, one would like to manufacture a wire under certain conditions, and then characterize it in situ to see what changes should be made in the manufacturing process. Transport and conventional microscopy measurements provide useful characterizations, but they do not give precise structural information in a nondestructive manner. A probe which can give useful structural information without removing the silver cladding is x-ray diffraction. Preliminary x-ray scattering characterization experiments have been performed at beam lines X-22 and X-27 on wires made at BNL-DAS and IGC corporation. In the experiments done at X-22, the x-ray energy was 8keV, and the sample region within ~1 micron of the silver interface was probed. A surprising and interesting new result was found almost immediately in nominally T_c ~110K wires. This is that near the silver interface, the T_c ~110K phase does not form, but rather the T_c ~84K phase only is present. This result has implications with regard to the growth process of the T_c ~110K phase in the wire. At X-27, the x-ray energy was sent at ~25keV, and the experiments were performed in a transmission geometry. Under these conditions, the entire superconductor volume was probed. The mosaic of these textured polycrystalline wires was measured for the first time. The results of this work are shown in figure, where the mosaic is plotted against the current carrying capacity. It is clear that there is some correlation between mosaic and current carrying capacity. This is not surprising, since the critical current is dependent on the grain alignment. The importance of this data is that poor grain alignment can now be separated from other causes for poor current carrying capacity, such as impurity disposition, so the manufacturing conditions can be more easily optimized to ameliorate all of the deleterious effects.

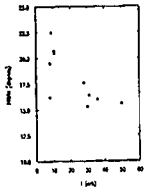


Figure 1.

Magnetic x-ray diffraction from neodymium * | X22C

D. Watson, E. M. Forgan, and D. Fort (Univ. of Birmingham, UK), W. J. Nuttall,andW. G. Stirling (Univ. of Keele, UK)

There have been many neutron investigations of the magnetic ordering of the light rare earth metal neodymium, but there continue to be surprises. It is now clear that the ordering is double-q between about 8 and 19 K, and that at lower temperatures triple- and quadruple-q structures form [1,2]. The modulation wavevectors describing these structures appear to be incommensurate with the lattice, although there have been recent suggestions [3] that some of the structures may be higher-order commensurate, with the magnetic unit cell rotated with respect to the crystal cell. We have performed a magnetic X-ray diffraction study on an excellent single crystal of Nd (mosaic spread of only 0.03o) in the temperature range 10-20K, chosen to include both double-q and single-q structures. Magnetic satellites were observed at all three of the L-absorption edges (L_I, L_II and L_III). Within the volume of the sample illuminated by the X-rays (1mm^2 by a few microns depth), at 11 K we observed a single domain of a double-q structure. When the sample was heated, the single domain double-q structure remained until about 0.1 K from T_N. This observation is in disagreement with previous phase diagrams (accepted until now); Landau theory [4] predicts a region about 1 K wide below T_N where ordering should be single-q. The temperature variation of the vector q_q was investigated in considerable detail. These measurements, typified by Fig. 1, gave very precise values of the q-vectors rather different from those reported elsewhere [3]. There was no sign of any wavevector lockin to commensurate values over the temperature range studied. A publication describing these results is in preparation. We plan to extend these measurements into the lower temperature region, where a futher series of fascinating phase transitions takes place.

[1] McEwen, Forgan et al., Physica 130B 360 (1985).
[2] Forgan et al., Phys. Rev. Lett. 62 470 (1989)
[3] Lebech et al., J. Phys. Cond. Mat. 6, 5201 (1994)
[4] McEwan and Walker, Phys. Rev. B34 1781 (1986)

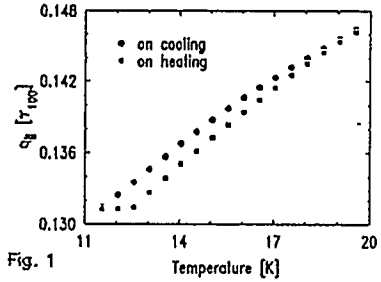


Fig. 1

Figure 1.

* This work supported by the U.K.Engineering and Physical Sciences Research Council.

Surface magnetic scattering: UO_2 (001) * | X22C

G. M. Watson and Doon Gibbs (BNL), B. D. Gaulin (McMaster U.), and G. H. Lander (European Commission, Institute for Transuranium Elements)

In a resonant magnetic x-ray scattering experiment, the incident photon energy is tuned near an adsorption edge. Dramatic enhancements have been observed at the L edges of the rare earths and the M edges of the actinides. In addition to the inherent high resolution of the technique, resonant magnetic x-ray scattering also offers the possibility of studying samples with weak magnetic moments or with small scattering volumes. Here we present the results of an experiment in which we believe we have observed magnetic scattering from a surface. Further resonant magnetic x-ray surface scattering experiments are planned to search for magnetic surface reconstructions and for surface-induced ordering effects.

UO_2 is a semiconductor with the CaF_2 structure, which orders antiferromagnetically below T_N=30.2 K. All data were obtained at the UM_{IV} edge ($\hbar\omega$ = 3.728 keV). For the (001) surface of UO_2 studied, the (011) truncation rod corresponds to a bulk magnetic rod, but not to a bulk charge truncation rod. In Fig. 1, we show inplane scans through the (001) rod obtained at an l of 0.075 c*. Evidently, at a sample temperature of 10 K, a weak peak is observed at the expected position for the magnetic surface peak with a count rate to ~15 cpm. When the sample is warmed to a temperature above T_N (see Fig 1 top), the peak disappears, suggesting that the peak observed at T = 10 K is magnetic in origin.

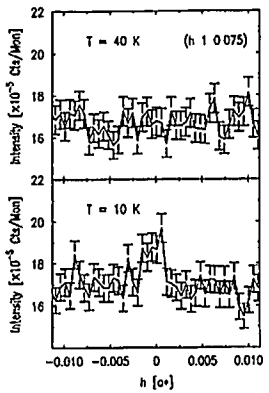


Figure 1. Grazing-incidence resonant x-ray scattering scans at (0 1 0.075) from the (001) surface of UO_2 at a sample temperature of 10 K (bottom) and 40 K (top). T_N is 30.2 K.

* Work is supported at Brookhaven by the U.S. DOE under contract No. DE-AC02-76CH00016.

Dynamics of phase separation on stepped Pt(001) surfaces * | X22C

G. M. Watson and Doon Gibbs (BNL), M. Yoon and S. G. J. Mochrie (MIT), and D. M. Zehner (ORNL)

Steps on the surface of a crystal play an important role in such physical phenomena as catalysis, crystal growth, and epitaxy. We have determined the phase diagram for vicinal Pt(001) surfaces miscut by up to 6o from the ¡001¿direction in the ¡110¿azimuth. [1] We find that above 1820 K, the Pt(001) surface and its ¡110¿vicinals are rough. Below 1820 K, stepped surfaces phase separate to form (001) facets and rough, stepped domains. The tilt angle of the stepped domains exhibits a one-half power-law dependence on reduced temperature consistent with simple theoretical ideas.

In order to study the dynamics of the faceting transformation, we have performed temperature quenches from above 1820 K into the two phase region of the phase diagram. The scattered intensity from the initial rough phase as well as from the two final phases is measured as a function of time. The time scale of the phase separation ranges from approximately 1 second for the deepest quenches studied, to more than 1000 seconds for quench temperatures nearer 1820 K. When normalized to this characteristic time, the time-dependence of the scattered intensity from the (001) facets as well described by a universal form (see Fig. 1).

[1] G.M. Watson et al., Phys. Rev. Lett. 71, 3166 (1993); M. Yoon et al., Phys. Rev. B 49, 16702 (1994).

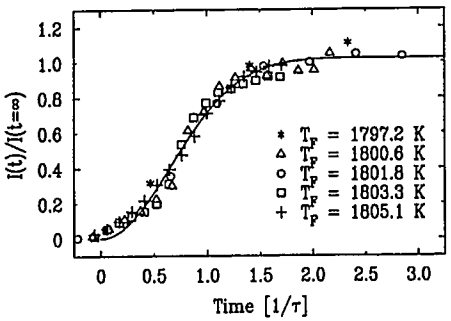


Figure 1. Time evolution of the intensity of x-rays specularly scattered from (001) facets normalized to the final intensity for a number of temperature quenchs to final temperatures T_F. In order to illustrate the universal nature of the kinetics, the x-axis is scaled to the characteristic time describing each quench.

* Work is supported at Brookhaven by the U.S. DOE under contract No. DE-AC02-76CH00016, at MIT by the NSF DMR-9119675, and is sponsored at ORNL by the U.S. DOE under contract No. DE-AC05-84OR21400 with Martin Marietta Energy Systems, Inc.

Bond length relaxation in $Si_{1-x}Ge_x$ alloys * | X23A2

D. B. Aldrich, R. J. Nemanich, and D. E. Sayers (North Carolina State Univ.)

We have measured and quantified the effect of alloy composition on the atomic bonding in relaxed MBE deposited crystalline $Si_{1-x}Ge_x$ alloys. X-ray absorption fine structure (XAFS) and X-ray diffraction (XRD) were used to examine how the atomic bonding in $Si_{1-x}Ge_x$ is affected by changes in alloy composition. XRD was used to measure the strain (due to the substrate) in the $Si_{1-x}Ge_x$ alloys to ensure that the influence of the substrate was minimized. The Ge-Ge and Ge-Si bond lengths were measured using Ge K-edge XAFS and compared with the conflicting results of existing analytical models and previous XAFS studies (Figure 1).

The measured Ge-Ge and Ge-Si bond lengths were found to be in good agreement with the analytical models which predict that the Ge-Ge, Ge-Si, and Si-Si bonds maintain distinctly different lengths which change linearly with alloy composition. The topological rigidity parameter a^{**}=0.63 was used to quantify the linear dependence of the bond lengths on alloy composition and a value of a^{**} was calculated from the measured bond lengths. An extensive XAFS error analysis was performed and the error in the topological rigidity parameter a^{**}=0.63 +0.07/-0.13 was determined. This value of a^{**} which is notably different from 0 or 1 indicates that both the bond lengths and bond angles are distorted by changes in composition. This work has been accepted for publication in Phys. Rev. B 50.

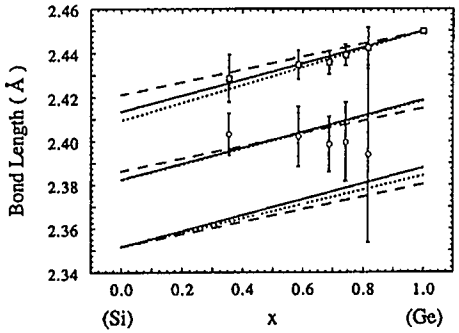


Figure 1. Comparison of measured and predicted Ge-Ge and Ge-Si bond lengths in $Si_{1-x}Ge_x$. The measured Ge-Ge and Ge-Si bond lengths are indicated by the open squares and circles respectively. The solid lines indicate the Ge-Ge, Ge-Si, and Si-Si bond lengths predicted by a^{**}=0.63. The renormalized results of Weidman Newman(Phys. Rev. B45,8388, (1992))

* Work Supported in part by the Division of Materials Science of the Department of Energy under Contract DE-FG05-89ER45385, NSF Grant DMR-9204285, and the National Institute of Standards and Technology

In situ EXAFS/XANES study of carbon-supported bimetallic Pt/Cu catalysts	X23A2

Simon R. Bare, Larry N. Ito, and M. Cisneros (Dow Chemical Co.)

The management of halogenated hydrocarbons is a critical issue in environment chemistry. An enabling technology for processing these compounds is by heterogeneous catalytic transformation. Dow is developing several catalytic processes for the conversion of halogenated compounds to higher value products. The catalysts developed for use in these processes are substantially better than those presently available. We are attempting to develop a full understanding of the activation and deactivation of these catalysts during the reactions by a comprehensive catalyst characterization program using mainly transmission electron microscopy, chemisorption, XPS and X-ray absorption methods. The catalysts comprise Cu and Pt highly dispersed on activated carbon support. We are interested in comparing the structure of different catalyst formulations with their inherent activity in order to develop more active and selective catalysts. We have used XANES to probe the oxidation states of the metals as a function of metals loading during *in situ* reduction, reaction, and re-reduction. We have also followed the oxidation states during different pre-treatments of the catalysts. A full EXAFS analysis shows that the catalysts comprise true bimetallic particles after reduction. The *in* reaction EXAFS data is still being analyzed.

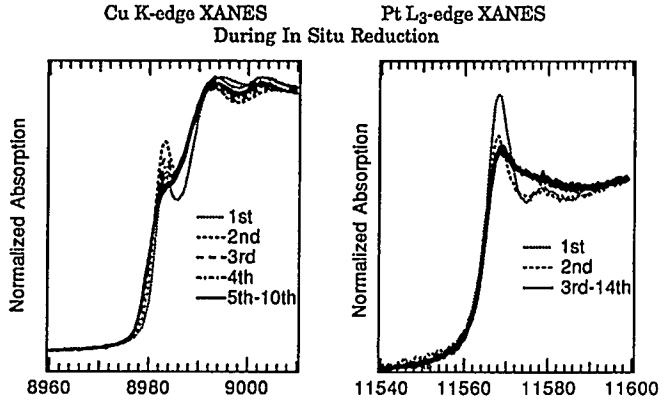


Figure 1. new

EXAFS characterization of (Ag,Co)-multilayer structures *	X23A2

Axel Bartos and Joseph C. Woicik (NIST)

Giant magnetoresistance (GMR) has been observed in a wide range of multilayer structures or granular alloys composed of a ferromagnetic material and a nonmagnetic metal. Today it is assumed that spin-dependent scattering from magnetic states localized at the magnetic/nonmagnetic interface is the origin of the GMR. We have performed Co and Ag EXAFS experiments on (Ag,Co)-multilayers. 20-50 (Ag,Co)-bilayer pairs were deposited on float glass using a Dual Ion Beam Deposition technique covering d-spacings from d=22-91 Åand assist beam energies ranging between V_{Assist}=0-900 V (I_{Assist}=5 mA). Their interface structure was studied by grazing angle X-ray reflectivity measurements. Complementary information on the local layer structure were obtained by in plane EXAFS experiments.

Fig. 1 depicts the Fourier transformed Co EXAFS data for [$Ag_{11-15/AA}$, $Co_{d_{Co}}$ multilayers deposited with an assist voltage of V_{Assist}=100 V and covering Co film thicknesses from d_{Co}=81-6/AA. The data show a significant reduction of the NN amplitude and vanishing NNN amplitudes with decreasing Co film thickness, indicating an increasing disorder of the local Co structure and an enhanced contribution of Ag scattering from the interface. In addition, the Co-Co bond length decreases from d_{Co-Co}=2.50-2.4Å. This reflects the increased signal contribution from the interface, as the Co-Co bondlength is reduced in the surface layer. A dependence is found also for the variation of the assist beam voltage: here, the local structure becomes more defined with increasing V_{Assist}.

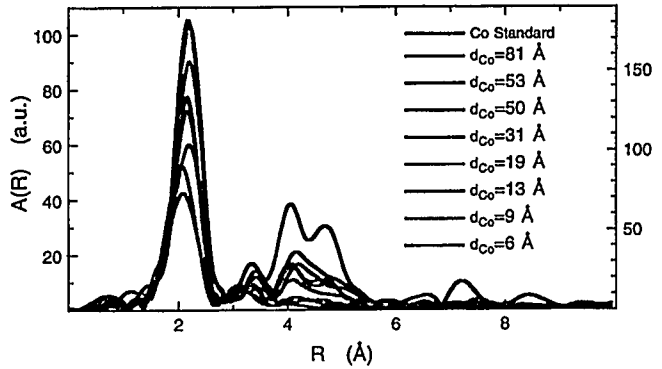


Figure 1. Fourier transformed Co EXAFS data for (Ag,Co)-multilayers with different Co film thicknesses.

* A.B. gratefully acknowledges the financial support by the Alexander von Humboldt foundation.

Bioremediation of selenium by microbial action * | X23A2

B. Buchanan (UCB), J. Bucher (LBL), D. Carlson (UCB), N. Edelstein (LBL), E. Hudson(LLNL), N. Kaltsoyannis (LBL), T. Leighton (UCB), W. Lukens (LBL), H. Nitsche and T. Reich (Forschungszentrum Rossendorf e. V.), K. Roberts (LBL), D. K. Shuh (LBL), P. Torretto (LBL), J. Woicik (NIST), W-S. Yang(Jackson State U.), A. Yee (LBL), and B. C. Yee (LBL)

The concentration and stabilization of hazardous materials by microbial agents offers great potential for use in environmental remediation technologies. The aerobic soil bacterium,Bacillus subtilis is known to incorporate selenium on or within the vegetative cell wall when exposed to a Se(IV) solution, although the exact mechanism of uptake is not fully understood. XANES spectroscopy demonstrates that both B. subtilis and bacillus isolated from selenium rich soil reduce selenite to thered allotrope of elemental selenium. The red and grey forms of selenium are distinguished by their XANES spectra. XAFS show only one absorber-backscatter distance in both red and grey selenium, at 2.43 2.44 Årespectively. Possible future applications of bioremediation technologies are to oil refinery waste streams containing selenite and to the severely selenium-contaminated site at the Kesterson Reservoir in California.

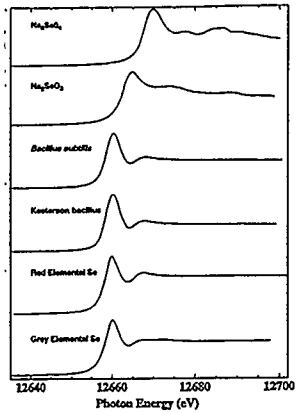


Figure 1. The Se K edge XANES spectra of bacteria after uptake from a selenate solution and comparison to Se reference materials.

* This work was supported in part by the Director, Office of Energy Research, Office of Basic Energy Sciences, Chemical Sciences Division of the US Department of Energy under Contract No. DE-AC03-76SF00098. This work was performed in part at the NSLS and SSRL which are operated by the US Department of Energy, Office of Basic Energy Sciences, Divisions of Chemical Sciences and Materials Science.

XAS study of Fe/Si and Fe/{FeSi} multilayers | X23A2

C. L. Foiles, M. Franklin and R. Loloee (MSU)

Magnetic coupling between Fe layers via Si spacer layers have been reported by several groups for different types of Fe/Si samples. A group at Argonne National Laboratory has done extensive studies on sputtered Fe/Si and Fe/{FeSi} multilayers [1]. {FeSi} denotes a spacer layer performed alternately sputtering 2Å of Fe then 2Å of Si and repeating this pattern until a designated total spacer layer thickness is obtained. The Argonne group found structural coherence in samples showing magnetic coupling; this coherence extended over greater spacer layer thicknesses for {FeSi} samples. Using measurements for a number of microscopic properties they inferred the presence of Fe-silicides. This inference approach led to the suggestion that the silicide could be as much as 30% of the nominal bilayer unit.

We have prepared sputtered Fe/Si multilayers that reproduce both the magnetic coupling and structural coherence reported by the Argonne group. We used transmission electron diffraction as a direct test for the presence of Fe-silicides. No silicide lines were found in the Fe/Si samples; the 10 to 12 observed lines were consistent with BCC Fe [2]. Initial data for Fe/{FeSi} samples gives some evidence of a Fe-silicide but its dominant line coincides with the Fe⟨110⟩. We have begun XAS studies to achieve better structural characterization. Despite limited data and only preliminary analysis, two features are clear. One, a qualitative change in the absorption occurs near the XANES-EXAFS boundary. Figure 1 shows that pure Fe gives a broad bump centered near 7150 eV, dashed curve, while a Fe/{FeSi} sample gives a very little change near that energy.

Two, EXAFS signals for Fe/{FeSi} appear to be a scaled version of Fe signals. Fourier transforms are identical but smaller out to the 4th shell and back transformed fits for the 1st shell give the same distance with a coordination number of 4 rather than 8. We are currently testing structural models in an attempt to produce these two features.

[1] J. A. Mattson, et al., Phys. Rev. Lett. 71, 185 ('93) and citations.
[2] C. L. Foiles, et al., accepted by Phys. Rev. B, Aug. 1994.

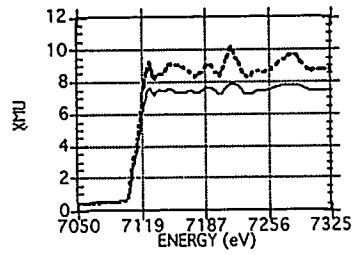


Figure 1. Fe K-shell data. Dotted line is pure Fe data while solid line is Fe 28.7A/{FeSi} 40A data times 10.

Performance of the ALS double-crystal monochromator | X23A2

G. Jones, S. Ryce, R. C. C. Perera (LBL), D. W. Lindle (UNLV), B. A. Karlin (NSLS),and J. C. Woicik (NIST)

A new "Cowan type" ALS double-crystal monochromator was tested on the X23A2 beamline. This monochromator based on the boomerang design used at NSLS Beamline X-24A has been developed for the beamline 9.3.1 at the ALS, a windowless UHV beamline covering the 1–6 keV photon energy range, designed to achieve the goals of high energy resolution, high flux, and high brightness at the sample. We have simplified the mechanical design and included recent improvements in technology. The chromium K absorption spectrum measured without using positional feedback available with piezoelectric devices is shown in figure 1. The deviations in I_0 over this energy range was about 7% (without any feed-back system).

The measured mechanical precision of the monochromator shows significant improvement over existing designs. Such precision is essential because of the high brightness of the radiation and the long distance (12 m) from the source (sample) to the collimating (focusing) mirror. The monochromator will provide a bright, high resolution, and stable x-ray beam for use in the x-ray spectroscopy program at the ALS.

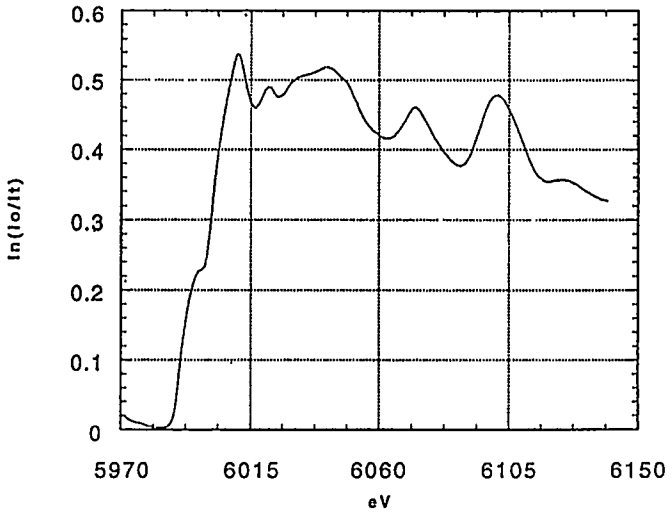


Figure 1. Chromium K absorption spectrum measured without using a positional feedback system.

XAS studies of Br^- aza complexes in non-aqueous electrolytes * | X23A2

H. S. Lee, X. Q. Yang, and J. McBreen (BNL)

Non-aqueous electrolytes consisting of lithium salts dissolved in either organic liquid or polymeric solvents are used in ambient temperature lithium batteries. Unlike aqueous solutions, the lithium salts are not completely dissociated. They exist largely as ion pairs or higher aggregates. This reduces the number of charge carriers and the conductivity of the electrolyte. In the past the addition of cation complexing agents such as crown ethers or crypt ands has been used to enhance ion dissociation. Recently we have synthesized a new family of aza compounds which also greatly increase the electrolyte conductivity. For instance, the conductivity of 0.1 M LiBr in tetrahydrofuran (THF) is increased by two orders of magnitude on the addition of 0.1 M of a cyclic aza compound. The structure of some of these aza compounds is shown in Figure 1. The R groups (CF_3SO_3-) are electron withdrawing and impart some positive charge to the N atoms. It was surmised that these compounds are anion complexing agents. This was confirmed in an extensive Br XANES study of LiBr electrolytes. Figure 2 shows a set of XANES spectra obtained in several electrolytes. With increasing chain length of the aza compound there is an increase in the pre-edge peak in the Br XANES indicating complexing of the anions.

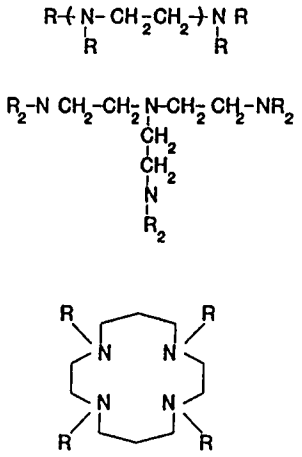


Figure 1. Molecular structure of R-substituted aza compounds. From top: linear, branched and cyclic compounds.

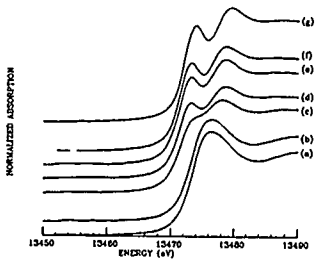


Figure 2. Br XANES spectra for (a) 0.2 M LiBr in THF and for 0.2 M LiBr in THF with additions of 0.2 M of the linear compounds (b) $CH_4{}_3NRCH_2CH_2NRCH_3$, (c) $R_2NCH_2CH_2NR_2$ (d) $R(NRCH_2CH_2)_3NR_2$ (e) $R(NRCH_2CH_2)_5NR_2$, (f) $R(NRCH_2CH_2)_2NR_2$and (g) the branched aza compound in Fig. 1.

* Work supported by the U. S. DOE under Contract No. DE-AC02-76CH00016

EXAFS study of ionic glassy Y_2O_3 and Y:Si:O * | X23A2

J. M. Lee, D. S. Yang, C. U. Segre, and T. I. Morrison (Illinois Inst. of Technology),K. Zhang (U. of Chicago)

Yttrium K-edge fluorescence EXAFS measurements were carried out to investigate the local structural variations for Y-O and Y-O-Y in the presence of Si-O bonds. Electric insulating thin films, $Y_{1-x}Si_xO_y$, were deposited onto glass substrates at room temperature by e-beam evaporation at 2-10 Å/sec and subsequently annealed in an oxygen environment at 500°C. The compositions of these film alloys are prepared as the mixture of different evaporation rates from separate Y_2O_3 and silicon targets. Thus, oxygen deficiency is normally expected as silicon content increases. Compositions are determined by e-beam microprobe techniques, but the oxygen composition (y) is not properly measured and is assumed to be $y = 1.5x < 0.5\ (4 - x)$.

As shown in the EXAFS k^3-weighted FT (Fig. 1), when the samples are annealed, Y_2O_3 is crystallized, forming the second shell (Y-O-Y) ordering, but $Y_{97}Si_3O_y$ is still in the glassy structure. Above all, the first shell is attributed to the ionic tendency of Y-O pair. In the Y:Si:O system, crystallization originated from the ionic tendency (Y-O) is inhibited by the influence of a strong covalent tendency in the Si-O bonds. In. Fig. 2, the first shell (Y-O) coordination and its atomic distance are analyzed for various compositions. The results indicate: (i) For x=0.03-0.32, the coordination number of Y-O (4.8- 5.1) and its atomic distance (2.27-2.28Å) are preserved - not significantly modified - between the deposited and the annealed state. (ii) At x=0.46 (particularly, the case of an excess oxygen deficient state producing a high Si-Si bond concentration), the initial deposited state (N=4.3, R=2.25Å) undergoes significant structural rearrangements into the well- annealed state (N=3.9, R=2.30Å). This result suggests that the relatively weak ionic tendency of Y-O pair can be substituted by a Si-O bond.

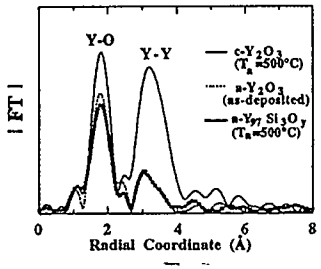


Figure 1. The k^3-weighted Fourier transforms of the chi-data. The parameters chosen for this computation are: K_{min}=2.9, K_{max}=10, dK_{min}=0.3 and dK_{max}=0.5.

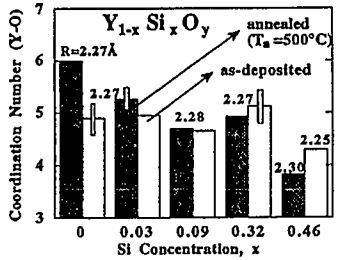


Figure 2. Structural variations of the first shell (Y- pair) between as-deposited and annealed state in Y:Si:O system. Coordination numbers (N's) and atomic distances(R's) are computed by the ratio method at various compositions. When STD > 0.1 in N, error bars are added in the figure.

* Work supported by AmocoCorporation and Illinois Inst. of Tech.

In situ XAS studies of metal hydride electrodes * | X23A2

J. McBreen, S. Mukerjee, J. J. Reilly, G. Adzic, and J. R. Johnson (BNL)

Metal hydride electrodes are rapidly replacing cadmium in rechargeable alkaline batteries. Most of the metal hydrides are based on AB_5 alloys, with $LaNi_5$ as the prototype. However $LaNi_5$ is not stable in batteries. Stability and good performance have been achieved by alloying additions. Alloys in batteries contain as many as nine components. The element specific nature of XAS make it an ideal method to study these materials. In situ XAS studies were done on $La_{0.8}Ce_{0.2}Ni_{4.8}Sn_{0.2}$ electrodes in 6 M KOH. This is the most simple AB_5 alloy that gives good performance and life. XAS measurements were done at the Ni K edge and the La and Ce L_3 edges on dry uncharged electrodes, and in situ, in a spectroelectrochemical cell, on charged (hydrided) and discharged electrodes. Figure 1 shows XANES spectra for a dry uncharged electrode and in situ spectra for a charged and an uncharged electrode. In the uncharged electrode the Ni edge is shifted to lower energies because of mixing of p and d states. Thus transitions can occur from the 1s states into empty Ni d states in the vicinity of the Fermi level. When the electrode is charged these states are pulled below the Fermi level and are not available. So the edge shifts to the Ni edge. Figure 2 shows results at the Ce L_3 edge. In the uncharged alloy the Ce is in a mixed +4/ +3 valence state. On hydriding it reverts to a +3 state.

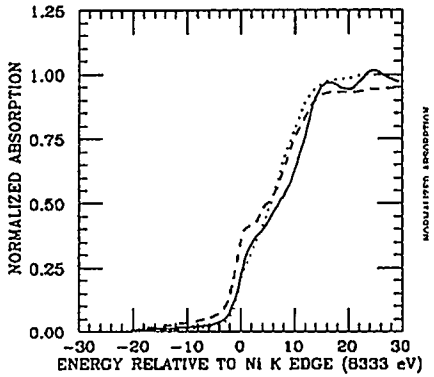


Figure 1. Ni K edge XANES for Ni foil (—), a dry uncharged electrode(- - -), and in situ results for a charged electrode (• • •).

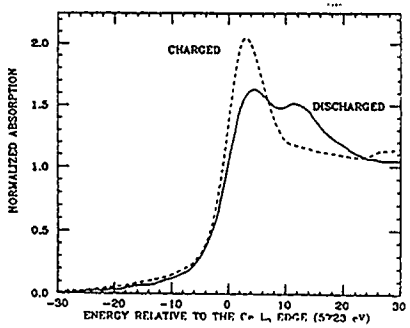


Figure 2. Ce L_3 XANES for a dry uncharged electrode (—) and in situ data for a charged electrode (- - -).

* Work supported by the U. S.DOE under Contract No. DE-AC02-7600016.

XAS studies of mixed salt $CoBr_2$/LiBr-PEO complexes * | X23A2

J. McBreen, X. Q. Yang and H. S. Lee (BNL)

The conductivity of poly(ethylene oxide) (PEO) based electrolytes can be modified by several methods such as the use of salts with a low lattice energy, modification of the polymer host to increase segmental motion, incorporation of polar plasticizers, and by the addition of a second salt. The latter is known as the mixed cation effect. The most remarkable effects have been observed in PEO-based polymer electrolytes containing mixed $CoBr_2$/LiBr salts. The mechanism of the mixed cation effect is not known. One possibility is that the effect is due to complex formation. It is also possible that the second salt modifies the polymer segmental motion and the ion mobility. In an effort to elucidate the mechanism, x-ray absorption (XAS) studies were done at the Co K edge on $CoBr_2(PEO)_{16}$ and $[0.45CoBr_2 + 0.55LiBr](PEO)_{16}$ at 25°C. Figures 1 and 2 show comparisons of the EXAFS and XANES for the two complexes. Analysis of the EXAFS reveals that in $CoBr_2(PEO)_{16}$ the salt consists of mostly undissociated $CoBr_2$ coordinated with six oxygens from the PEO. The respective Co-Br and Co-O bond lengths are 2.36 Å and 2.49 Å. In $[0.45CoBr_2 + 0.55LiBr](PEO)_{16}$ the Co is coordinated with three Br atoms with a bond distance of 2.40 Å and between two and three O atoms with a bond distance of 2.27 Å. Apparently, the bidentate -OCH_2CH_2O- units of the PEO function as a single ligand by forming five membered rings. On the addition of LiBr and Co coordination changes from a mixture of octahedral and tetrahedral species to exclusively tetrahedral coordination. The anomalous conductivity behavior of the mixed salt $CoBr_2$/LiBr-PEO complex is related to the formation of $CoBr_3^-$ complexes and a reduction in crosslinking of the PEO by the $CoBr_2$.

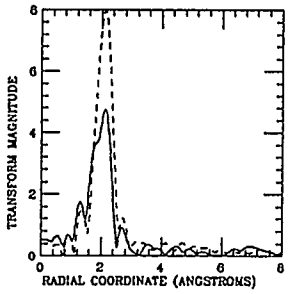


Figure 1. Fourier transforms of the EXAFS for $CoBr_2(PEO)_{16}$ (—) and $[0.45CoBr_2\ 0.55LiBr]\ (PEO)_{16}$ (- - -).

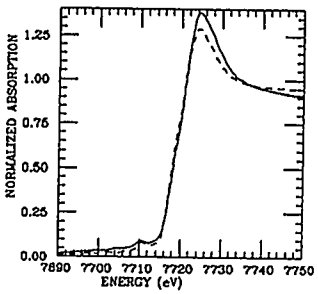


Figure 2. Normalized XANES spectra for $CoBr_2(PEO)_{16}$ (—) and $[0.45CoBr_2\ 0.55LiBr]\ (PEO)_{16}$ (- - -).

* Work supported by the U. S. DOE under Contract No. DE-AC02-76H00016.

X-ray absorption studies of copper in copper-silicates II | X23A2

David A. McKeown (Howard University)

This study concentrates on room temperature XAS data for shattuckite, a crystalline Cu-silicate containing CuO_4 unit strips similar to those proposed for the unknown structure of chrysocolla (amorphous Cu-silicate) and three chrysocolla samples from different locatities having various compositions. Conclusions from an earlier Cu XAS study of crystalline and amorphous Cu-silicates [1] indicate that Cu in chrysocolla is coordinated by four oxygens to form CuO_4 units similar to those in dioptase (crystalline Cu-silicate) and tenorite (crystalline CuO), where each unit is most likely linked to two other CuO_4 units to form strips similar to those in tenorite. These results are contrary to earlier conclusions [2], where it was thought that chrysocolla contains crystalline Cu and Cu-oxide domains. The Fourier transforms for the crystalline samples indicate that interference effects change the second shell features such that the peaks do not necessarily correspond to shells of atoms around the absorbing Cu (Fig. 1). These interference effects are clearly present in the second shell features for shattuckite and tenorite, which both have CuO_4 units arranged in strips; however those strips are linked with each other such that the associated Cu atoms are in symmetrical lattices that create the interference conditions; in these cases, a beating phenomenon for tenorite and destructive interference for shattuckite are observed near 2.7 Å. Fourier transforms for the various chrysocolla samples are nearly identical, indicating little structural variation around Cu, as composition is varied (Fig. 2). EXAFS analyses are in progress for these Cu-silicates at room and liquid nitrogen temperatures.

[1] D. Ad. McKeown, J. Non-Crystalline Solids, in press (1994)
[2] F. V. Chukhrov, B. B. Zvyagin, A. I. Gorshkov, L. P. Ermilova, Am. Min., 54 (1968) 993.

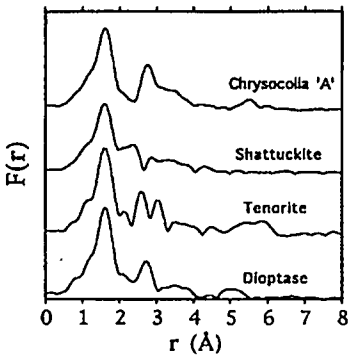


Figure 1. Partial RDFs for the Cu-silicates.

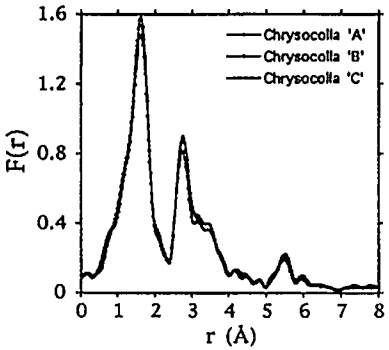
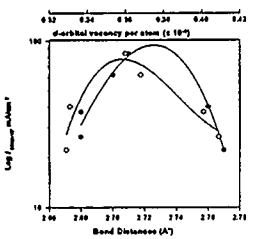


Figure 2. Partial RDFs for the chrysocolla samples.

Role of structural and electronic properties of Pt and Pt alloys on electrocatalysis of oxygen reduction: an in-situ XANES and EXAFS investigation *	X23A2

S. Mukerjee and J. McBreen (BNL)

The electrocatalysis of thee oxygen reduction reaction (ORR) on five binary Pt alloys (PtCr/C), PtMn/C, PtFe/C, PtCo/C and PtNi/C supported on high surface area carbon) in a proton exchange membrane fuel cell was investigated. Electrode kinetic studies on thee Pt alloys at 95°C and 5 atm pressure showed theat the kinetics of oxygen reduction on thee alloys was much faster than on Pt. The increase was between two and three fold withe PtCr/C having the fastest kinetics. In situ EXAFS and XANES at potentials in thee double layer region (0.54 V vs. RHE, a potential where normally notheing is adsorbed on the electrode surface) revealed (i) that all thee alloys possess higher Pt d-band vacancies per atom (with the exception of PtMn/C alloy) relative to Pt/C electrocatalyst (Table I) and (ii) contractions in thee Pt-Pt bond distances, which confirmed results from ex situ XRD analysis. A potential excursion to 0.84 V vs. RHE (a potential which normally marks thee onset of adsorption of OH type species from thee electrolyte) showed that, in contrast to the Pt alloys, the Pt/C electrocatalyst exhibits a significant increase in the Pt d-band vacancies per atom (Table I). This increase, in Pt/C has been rationalized as being due to adsorption of OH species from thee electrolyte. This does not occur on the Pt alloys. Correlation of thee electronic (Pt d-band vacancies) and geometric (Pt-Pt bond distance) factors withe the electrochemical performance characteristics exhibits a volcano type behavior(Fig. 1) with th PtCr/C alloy being at thee top of the curve. The enhanced electrocatalysis by the alloys can theerefore be rationalized on the basis of the interplay between the electronic and geometric factors on one hand and theeir effect on thee chemisorption behavior of OH species from the electrolyte.



Electrocatalyst	D_v^* 0.54 V vs. RHE	D_v^* 0.84 V vs. RHE
Pt/C	0.329	0.370
PtMn/C	0.331	0.344
PtCr/C	0.360	0.358
PtFe/C	0.368	0.370
PtCo/C	0.401	0.390
PtNi/C	0.409	0.404

* D_v is the number of *d* band vacancies per atom

Figure 1. Correlation of oxygen electrode performance of Pt and Pt alloy electrocatalysts withe the Pt-Pt distance (filled circle) and the d orbital vacancy of Pt (open circle).

* This work was supported by the U.S.DOE under contract No. DE-AC02-76H00016.

X-ray absorption spectroelectrochemistry	X23A2

Robert O. Rigney, Jie Yuan, Yingping Deng, Bella Helmer-Chudnovsky, William R.Heineman, and R. C. Elder (Univ. of Cincinnati)

X-ray absorption spectroscopy (XAS) is a powerful tool which may be used to acquire structural information on amorphous materials and solutions. When interfaced with an electrochemical technique, oxidation states of a transition metal may be controlled and redox structural dependent changes probed. We have employed XAS spectroelectrochemistry to investigate the structure in a zinc amalgam. Zinc and mercury ions were codeposited onto a pyrolytic graphite electrode in a thin-layer XAS spectroelectrochemical cell as a homogeneous binary amalgam. X-ray absorption spectra for mercury and zinc in the amalgam were collected along with the spectra of pure metals at room temperature. Figure 1 displays an averaged raw spectrum for mercury collected via fluorescence. In solid metals, strong oscillatory features in the absorption region indicate an ordered internal structure. In this region for mercury, the smooth feature demonstrates high disordering and little or no ordered structure surrounding fluid mercury atoms in the amalgam. Figure 2 displays a pseudo-radial distribution function (PRDF) indicating electron density from an absorbing zinc atom in an amalgam. The PRDF was generated from the Fourier transform of the extended X-ray absorption fine structure (EXAFS) between 3-12 $Å^{-1}$ with a smoothing Gaussian window of 0.1 $Å^{-1}$. When the peak at a $(r + \alpha)$ distance of 2.3 Å was backtransformed, a zinc backscattering shell of atoms was indicated. Thus the amalgam appears to contain zinc-zinc clusters. No zinc-mercury intermetallic compounds were indicated from the zinc PRDF of the amalgam.

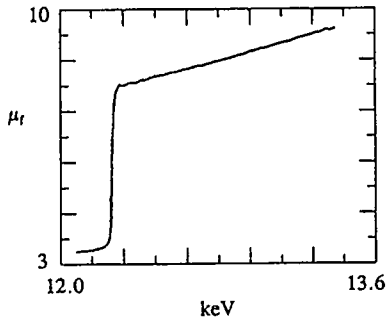


Figure 1. Mercury X-ray absorption spectrum in a in binary zinc amalgam.

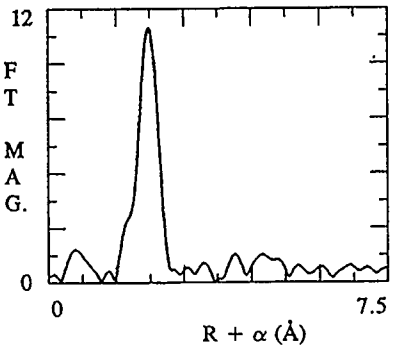


Figure 2. PRDF of zinc in the amalgam (solid) and the pure metal (dotted).

Tb oxidation state and hybridization in $Y_{0.9}Tb_{0.1}Ba_2Cu_3O_{7-\delta}(\delta=0.02, 0.84)$ and $Pb_2Sr_2TbCu_3O_8$ *	X23A2

U. Staub, Mark R. Antonio, and L. Soderholm (ANL)

It is well known that the $RBa_2Cu_3O_7$ (R = Y, rare earth) are superconducting below 92K except when R - Ce, Pr, and Tb. This compound does not form for Rtb, and this was explained by assuming that Tb is tetravalent or intermediate valent. To clarify the valence of Tb in $RBa_2Cu_3O_7$ we collected Tb L_3-edge data on $Y_{0.9}Tb_{0.1}Ba_2Cu_3O_{7-/delta}$ and various Tb^{+3} and Tb^{+4} standards on X23A2 using a Si (311) double monochromator (Figure). The observation of a single, sharp resonance line clearly indicates that Tb is trivalent in this compound. A further line width analysis revealed no significant hybridization between Tb and the CuO_2 bands. [1] These results are in good agreement with the interpretation of susceptibility experiments. [1] L_3-edge experiments on Tb in $Pb_2Sr_2TbCu_3O_8$ have produced similar results. [2]

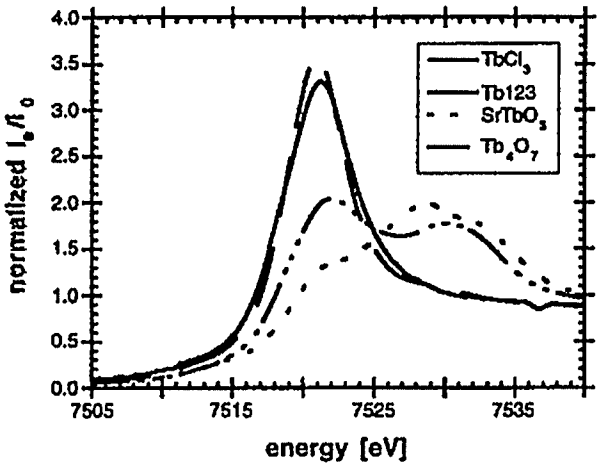


Figure 1. The TB L_e-edge XANES of Tb)$0.1Ba_2Cu_3O-6.98$,$TbC1_3.6H_2O$, Tb_4O_7 and SrTbO−3 obtained through electron-yield detection at ambient temperature.

* This work is supported by the US Department of Energy , Basic Energy Sciences - Chemical Sciences, Contract No. W-31-109-ENG- 38.

Ex situ XANES study of anodic oxide film growth on zirconium thin films in borate solution *	X23A2

Carissima M. Vitus and Hugh S. Isaacs (BNL)

An ex situ x-ray absorption near edge structure (XANES) investigation of anodicoxide film growth under galvanostatic conditions on zirconium thin films was undertaken. Thin Zr films were prepared by magnetron sputtering Zr only clean float glass. Film thickness was determined under galvanostatic conditions at $10mA/cm^2$ in a borate/boric acid buffer solution, pH 8.4, assuming a constant film growth of 27Å/V in neutral borate buffer. The sample face was positioned 45° with respect to the incident radiation and the detector and was fixed so that the same region was investigated throughout the experiment. Fluorescent radiation at the Zr K_α edge was collected using a Lytle detector.

Figure 1 shows a series of spectra taken before oxidation (metal) and after galvanostatic oxidization at $5mA/cm^2$ in pH 8.4 borate buffer to increasing potentials. The metal spectrum has been normalized to unity and all others spectra have been normalized with respect to metal. The flat shape of the spectrum above the edge as well as the edge position of the metal spectrum before oxidation indicate the sputtered film consists mostly of Zr in the metallic state. As the anodic film thickens, the shape of the spectra changes to that of an oxidized species, i.e. the edge shifts higher in energy and the peak shape just above the edge becomes sharp. The spectrum at 90V resembles that of Zr^{+4} in a ZrO_2 powder standard in agreement with literature results which indicate that the oxide which forms on Zr has the structure and composition of ZrO_2[1,2]. The height above the edge yields a quantitative measurement of the amount of Zr (in all valency states) sampled within the beam. Determination of the amount of Zr lost during galvanostatic oxidation is underway.

[1] J. S. L. Leach and B. R. Pearson, Corrosion Sci., 28, 43 (1988).
[2] E. M. Patrito and J. Macagno, J. Electrochem. Soc. 140, 1576 (1993).

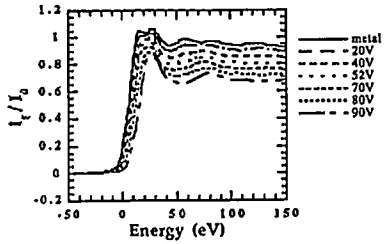


Figure 1. Zirconium thin film, 200 nm on float glass, galvanostatically anodized at 5 mA/cm^2in borate buffer. Corresponding potentials in which anodic films are grown is shown at right.

* Supported by Office of Basic Energy Science under Contract No. DE-AC02-76CH00016.

X-ray absorption studies of manganese oxide octahedral molecular sieves, clays, and coals *	X23A2

S. R. Wasserman (ANL), F. W. Lytle (The EXAFS Co.), S. L. Suib (U. of Conn.), R.E. Winans (ANL), K. A. Carrado (ANL), S. E. Yuchs (ANL), and R. L. McBeth

Manganese K-edge X-ray absorption spectra were taken to examine the average oxidation state and local structure of new synthetic manganese oxide photocatalysts, including the materials known as octahedral molecular sieves (OMS). The structures of these materials were compared to the natural minerals cryptomelane and todorokite.

Transmission and fluorescence manganese K-edge spectra were acquired using a si(311) double crystal monochromator, standard ion chambers, and a Lytle fluorescence detector equipped with a three absorption length chromium filter. The energy calibration was maintained by simultaneously monitoring the maximum at 6539 eV in the derivative of the spectrum of a manganese mesh. The OMS materials were synthesized in the laboratories of S.L. Suib.

The near edge and unfiltered EXAFS data for OMS2 and cryptomelane, which are synthetic and natural versions, respectively, are virtually identical. This means that the Mn in both materials possess the same average oxidation state and local structure, which consists of potassium cations within a 2x2 tunnel of MnO_6 octahedra. All materials containing 3x3 tunnel structures have lower absorption energies than the 2x2 samples. Synthetic OMS1 exhibits a lower average oxidation state than the natural todorokite mineral. The edge energies correlate well with the manganese valency that is deduced from elemental analysis.

An amorphous sample also displays the lower edge energy. The near-edge and EXAFS spectra for the amorphous manganese oxide indicate that the valence and local structure are similar to those in natural todorokite. However, they are also similar to birnessite, a layered manganese oxide, which is consistent with the weak X-ray powder diffraction pattern seen.

During this run, a suite of prophyrins and metalloporphyrins on clays was also studied in order to complete some earlier work. In addition to reproducing this earlier work, we were able to determine that approximately 80clay are complexed by a porphyrin macrocycle upon contact. Therefore, the extent of metallation on a clay surface can be directly monitored. the remaining copper may be left uncomplexed due to steric considerations. Another suite of samples was also run in order to complete an earlier study of iron species in coals. In summary, the division of the iron species into ferrous, ferric and pyritic can be made.

* This work was supported by the Division of Chemical Sciences, Office of Basic Energy Sciences,US Department of Energy, under /Contract No. W-31-109- ENG-38.

Microstructure control in nanophase zirconia	X23A3

A. J. Allen, S. Krueger, and G. G. Long (NIST), G. Skandan (Rutgers U.) and J.Parker (Nanophase Technology, Inc.)

Nanophase ceramic oxides exhibit novel properties including plastic deformation by creep processes at low temperature. They also offer the prospect for combining advanced mechanical properties (e.g., high strength and wear resistance) with good formability during processing into components. In practice, however, it is difficult to obtain high density material without coarsening of the pore/grain microstructure. Therefore, we seek to obtain a better understanding of how the microstructure develops during sintering, and of how sintering parameters and additives can be used to improve the final microstructure.

We have carried out an extensive characterization of nanophase zirconia fabricated either by gas-condensation technique or a continuous-flow technique. Samples have been used in absolute-calibrated small-angle neutron scattering experiments at the NIST reactor and in absolute-calibrated small-angle x-ray scattering experiments at X23A3. Our data have established that, in samples less than 100materials arises from the grain/pore interfaces, not from a supposed low-density disordered grain- boundary phase.

Fig. 1 shows typical absolute-calibrated SANS and SAXS data. The primary scattering features are slightly oblate pores between the grains. From our model, a number of nanophase microstructure parameters can be quantified and followed through the sintering process: grain size and polydispersity, grain/pore surface area, porosity and coarse pore volume fraction, and the fractional closure and disappearance of pores along the grain boundaries. The most important microstructure-determinin material variable is found to be the relative density, as illustrated in Fig. 2.

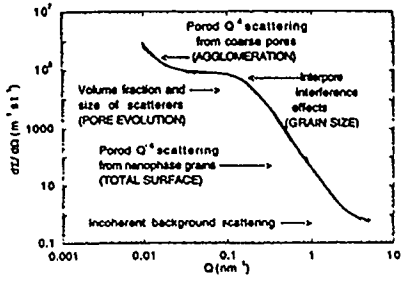


Figure 1. SAXS and SANS data.

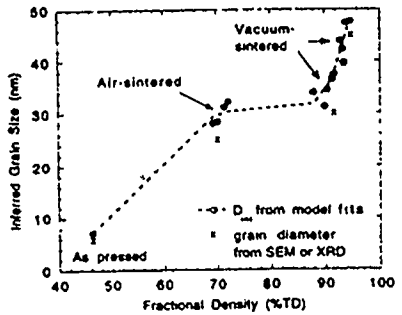


Figure 2. Grain diameter vs. density

Effect of x-radiation on ice *	X23A3

Xiaohong Hu, Fuping Liu, Ian Baker (Dartmouth College), and David Black (NIST)

It has been shown that ice is softened by HCI doping (Nakamura and Jones, Script Metall, 4, 123, 1970). One explanation for this observation is an increase in the number of point defects due to doping. These defects produce a higher probability for reorientation of bonds that are holding up dislocations, resulting in a higher dislocation velocity. However, recent white beam topography results (Shearwood and Whitworth, Phil Mag A, 65, 85, 1992) found no difference in dislocation mobility of HCI doped ice crystals. This raises the question of whether synchrotron radiation has an effect on dislocation mobility or does a different mechanism explain the softening of doped ice. To address this question, uniaxial tensile tests were carried out on pure ice single crystals at - 130°C under conditions of continuous illumination by monochromatic x-radiation, and in the lab on identical samples with no x-ray radiation. One of the measured creep curves is shown below. As can be seen, the behavior of the crystal is the same with or without x-radiation, which agrees with the results of Shearwood and Whitworth. Therefore, the dislocation mobility measured by x-ray diffraction imaging represents the intrinsic properties of ice and a difference mechanism is responsible for softening in doped ice.

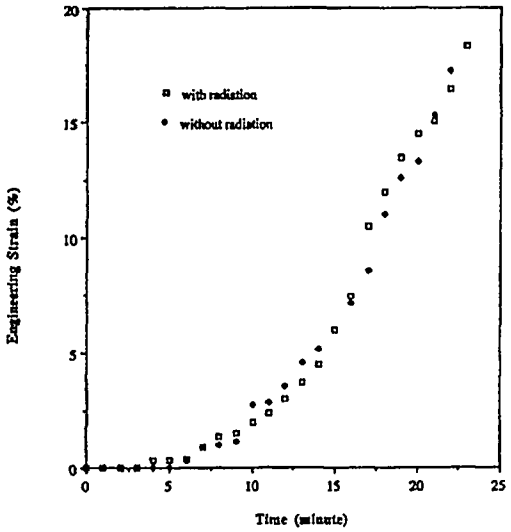


Figure 1.

* This work was sponsored by NSF Grant No. DPP-9218336 and ARO Grant No. DAA HO4-93-G006.

Structural characteristics of agarose gels studied by USAXS	X23A3

S. Krueger (NIST) and R. Nossal (National Institutes of Health)

Although agarose-based pulsed gel electrophoresis is widely used for the separation and analysis of long DNA fragments, relatively little is known about the microstructure of the agarose gel matrix itself. Yet, characteristics such as void size, strand thickness, gel microheterogeneity and correlations in spatial structure can be expected to influence the way macromolecules migrate through the gels. Small-angle neutron scattering (SANS) has been used previously [1] to study the structure of 3% agarose gels in D_2O over a wide range of length scales spanning approximately 2.0 nm to 125 nm. Definite changes in the scattering profiles were observed when the solvent quality was changed by the addition of dimethylsulfoxide (DMSO), which is known to disrupt hydrogen bonding in polysaccharide gels. However, it was not possible to totally separate the scattering due to changes in gel structure from that due to incoherent scattering from hydrogen in the sample. Thus, ultra-small-angle x-ray scattering (USAXS) studies were undertaken not only to extend the largest length scale to greater than 1500 nm but also to avoid ambiguities in the data due to incoherent scattering from hydrogen.

Upon addition of DMSO to the solvent, the USAXS intensity decreases markedly for values of the scattering vector below $Q = 0.02$ nm^{-1}, corresponding to length scales larger than 300 nm. This decrease in USAXS intensity at small Q values occurs concomitantly with an increase in the SANS intensity for $Q \geq 0.8$ nm^{-1}, corresponding to length scales smaller than 8.0 nm. Thus, the addition of DMSO leads to the disruption of hydrogen bonds between agarose strands while enhancing the degrees of freedom of the individual strands themselves.

[1] Krueger, S., Andrews, A.P. & Nossal, R., Biophys. Chem (1994), in press. ??

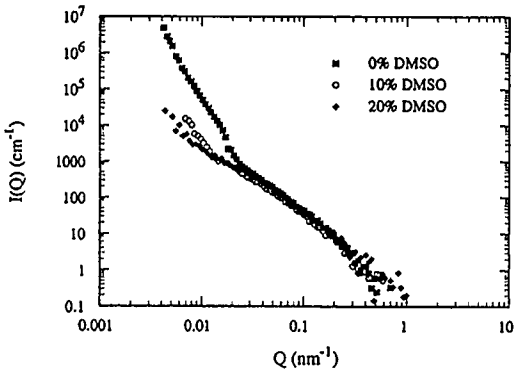


Figure 1. Log-log plot of the scattered USAXS intensity from 3% agarose in D_2Oversus scattering vector Q as a function of DMSO in the solvent.

Small-angle scattering studies of the microstructure of silicon nitride during processing *	X23A3

G. G. Long, A. J. Allen, and S. Krueger (NIST), and C. J. Hwang (Dow)

Silicon nitride is potentially one of the best structural materials for use in high-temperature heat engines. Since its properties depend upon its underlying microstructure, we have been conducting studies to understand and control the microstructure evolution during processing. Using ultra-small-angle x-ray scattering (USAXS) at X23A3 and multiple small-angle neutron scattering (MSANS) at the NIST Reactor, we have characterized Si_3N_4 as a function of processing during non-pressure sintering as a function of time, temperature and sintering-aid.

Both the powder and the sample fabrication were carried out at the Dow Chemical Company in Midland, MI. For sufficiently-dense sample material, and samples thinned to $\approx$ 100 μm, we utilized absolute-calibrated USAXS to determine directly the scattering cross sections $d\Sigma/d\Omega$, as a function of scattering wave vector, Q, in the range Q = 0.008 - 0.03 nm^{-1}. Maximum entropy methods were used to extract the pore-size distributions from the USAXS data. The total volume fractions of pores deduced from USAXS agreed to within 1% with the sample porosities deduced from precision density measurements.

Fig. 1 displays the volume distributions of pores as a function of pore diameter, where the diameters determined from MSANS are also indicated. These results are direct evidence that the average sizes of pores in silicon nitride neither coarsens nor shrinks during final-stage sintering, but rather the quantity of pores at any given diameter decreases as density increases. The sensitivity of these measurements to large pores underscores the great value of USAXS since such pores are frequently considered possible incipient failure points within finished ceramics.

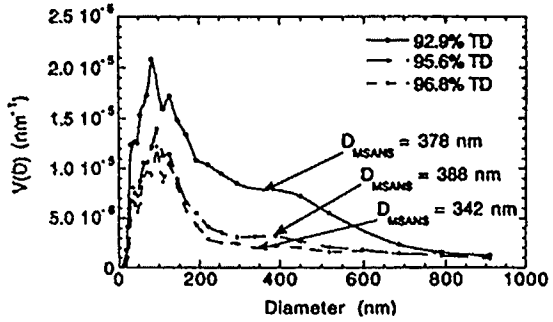


Figure 1. Volume pore-size distributions during final-stage sintering of Si_3N_4. The peak is near 100 nm;the shoulder measured by means of MSANS is also indicated.

* Supported in part through Iowa State University subcontract no. 70NANB2H1230 and in part by the National Science Foundation under agreement no. DMR-9122444.

Microradiograpy of strained high-T_c superconductor composite tapes	X23A3

R. D. Spal, C. K. Chiang (NIST), G. N. Riley and A. Otto (American Superconductor Corp.)

In many applications, high-Tc superconductor wires and tapes require some flexibility and strain tolerance. Quite promising in this regard are composite tapes of Bi2223 filaments in a Ag matrix, fabricated by an oxide-powder-in-tube (OPIT) process. Their critical current is nearly independent of strain up to a critical strain of about 0.5it drops sharply due to cracks in filaments. The goal of this study was to demonstrate that such cracks are observable near the critical strain by microradiography. The radiographs were taken through the matrix without thinning it.

Several 19-filament Bi2223/Ag OPIT tapes, 0.007" thick and 0.1" wide, with different tensile strains along the filament axis, were examined at a resolution of about 2μm, using an asymmetric Bragg diffraction microscope operating at 24.8 keV and 39X magnification. The incident beam was normal to the tape surface, and the transmission factor was abour 15to the hexagonal packing of filaments prior to rolling into tape form, up to five filaments can overlap in a radiograph. Radiographs for three strains are shown in Fig. 1, in which the filament (and strain) axis is vertical. The 0have respectively one and several sharply defined cracks, all perpendicular to the strain axis. The most prominent crack in the 3thickness was computed from the image contrast. the strained tapes also have diffusely defined cracks, which may be diffused because they are narrower than the microscope resolution or have faces oblique to the incident beam. Due to the successful observation of cracks, a more detailed study involving in-situ strain is planned.

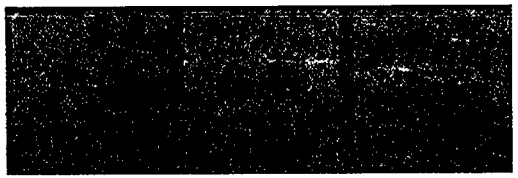


Figure 1. Positive image radiographs of tapes with 0, 0.7, and 3% strain, from left to right; field of view is 0.21 × 0.21 mm^2.

Initial observation of [001] Domains in Czochralski-grown strontium barium niobate. *	X23A3

Bruce Steiner (NIST), Gerard Fogarty and Mark Cronin-Golomb (Tufts), Robert Uhrin,Mark Garrett, and John Martin (Deltronic Crystal Ind.), and Uri Laor (NRC-Negev)

Long thin domain, a few micro-meters in width and several millimeters in length and oriented in the [001] direction (vertical features in Figure 1), have been observed in high resolution monochromatic diffraction images of the large faces of (100) slices and the edges of (001) slices of Czochrasli-grown strontium barium niobate. In other images of the large faces of (001) slices, star-like features are observed with a substantially lower density (Figure 2).

The restriction of these features to these particular orientations, strongly suggests that they are, respectively, side view and end-on views of 180° domains; and this thesis has been verified in subsequent poling experiments. Their greater density close to a surface than in the interior is similar to the occurrence of 180° domains in barium titanate. However, the 180° domains in barium titanate are an order of magnitude or two wide than the domains in Figure 1. The poling of this material can now be optimized.

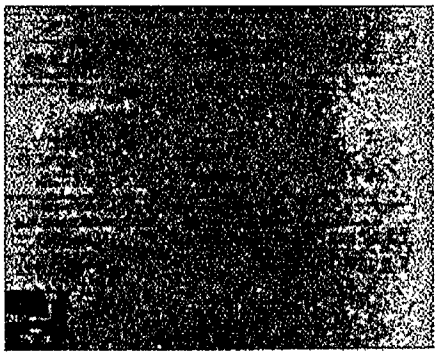


Figure 1. An asymmetric (804) 8 keV monochromatic diffraction image of (001) slice of SBN,cut parallel to the growth direction, in Bragg geometry.

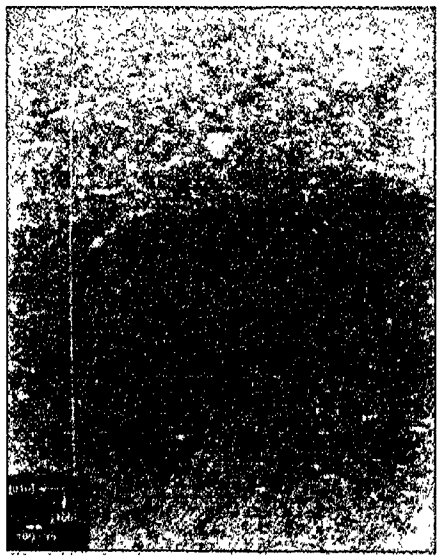


Figure 2. An asymmetric (404) 8 keV monochromatic diffraction image of (001) slice of SBN,cut perpendicular to the growth direction, in Bragg geometry.

* This research was supported by the NIST Advanced Technology Program.

Uniformity of strontium barium niobate, czochralski-grown for holographic storage *	X23A3

Bruce Steiner (NIST), Gerard Fogart and Mark Cronin-Golomb (Tufts), Robert Uhrin,Mark Garret, and John Martin (Deltronic Crystal Ind.), and Uri Laor (NRC-Negev)

The uniformity of Czochralski strontium barium niobate (SBN), recently grown for holographic storage, has been found to be substantially higher than previously observed on a scale from micrometers to millimeters. Figure 1 displays nearly featureless high resolution monochromatic diffraction from a (001) slice. Figure 2 displays similar diffraction from a (100) slice. Only very faint residual striations are observed in the first slice, cut normal to the growth direction. The second slice, cut parallel to the growth direction, displays the prominent striations characteristic of Czochralski-grown material.

The simultaneous diffraction over the entire 1 cm^2 crystal displayed in both images indicates long range chemical uniformity that is remarkable for a non-stoichiometric material. However the striations appear to present a continung challenge for the development of holographic storage.

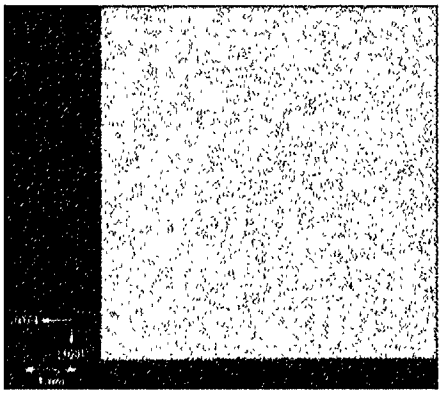


Figure 1. An Assymetric (804) 8 keV monochromatic diffraction image of (001) slice of SBN, cut normal to the growth direction, in Bragg geometry.

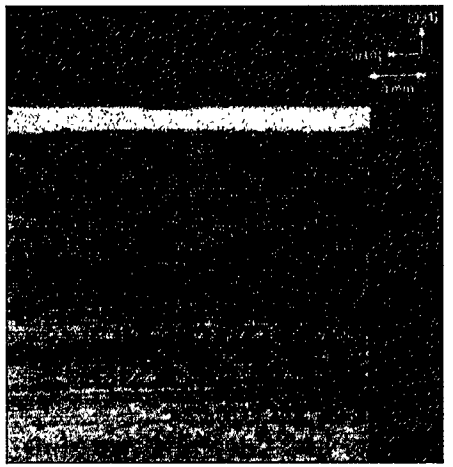


Figure 2. An Assymetric (804) 8 keV monochromatic diffraction image of (100) slice of SBN, cut parallel to the growth direction, in Bragg geometry.

* This research was supported by the NIST Advanced Technology Program.

EXAFS studies of the decomposition of heat-treated fcc-$Fe_{50}Cu_{50}$ powders	X23B

V. G. Harris, K. M. Kemner (NRL), P. Crespo, A. Hernando (Instituto de MagnetismoAplicado, Madrid, Spain), A. Garcia Escorial (CENIM-CSIC, Madrid, Spain)

A ferromagnetic fcc-Fe_{50} Cu_{50} solid solution, obtained by ball milling elemental powders, was heat-treated to induce decomposition. Magnetization values measured at low temperatures for annealed samples deviate from the $T^{3/2}$ law suggesting that the decomposition does not take place via the nucleation and growth mechanism but alternatively by means of spinodal decomposition. In an attempt to elucidate this phenomenon we have studied the structure and chemistry of the short- and long-range-ordering in the alloy before and after heat treatments by means of extended x-ray absorption fine structure (EXAFS) and X-ray diffraction (XRD) measurements, respectively. XRD measurements of samples heat treated at T$\leq$623K illustrate only diffraction features corresponding with a single fcc phase. After anneals at T$\geq$723K diffraction features corresponding with fcc and bcc phased are observed, signaling a phase separation. Fourier transformed Fe EXAFS data for as-milled and annealed samples are depicted in Fig. 1 [figure unavailable due to space constraints] with similar data for an Fe foil which is used as an empirical standard of the bcc structure. These data have been vertically offset to allow a clear inspection of the development of higher order neighbors. In this plot the data corresponding to the as-milled sample closely resembles that of fcc Cu indicating that Fe resides in an fcc lattice. The Fourier features appearing over an r-range of 3- 5Å begin to change with an anneal at 823K. After an anneal at 823K the transform profile looks very much like that of the bcc standard. EXAFS modeling analysis using theoretical standards indicates that the first coordination shell in the as-milled sample is comprised of Fe and Cu atoms whose relative fraction reflects the samples' nominal composition of $Fe_{50}Cu_{50}$. After an anneal at 423K the modeling of the first shell reflects a significant increase in the Fe-Fe and Cu-Cu correlations suggesting a chemical ordering within the fcc structure has taken place. Empirical modeling of the Fourier transformed Fe EXAFS data indicates that 28% of Fe atoms reside in the bcc structure after an anneal at 723K; increasing to 72% after an anneal at 923K. These results are in qualitative agreement with Mossbauer Effect measurements which illustrate a quadruple splitting of the central absorption line in annealed samples indicating the existence of Fe-Fe dimers and trimers in the Cu-rich fcc phase. These results support the interpretation that the deviation of magnetization from the $T^{3/2}$ law in annealed samples is due to the variation of local compositions around the Fe sites brought about by the heat treatments.

Figure 1. Fourier transformed Fe EXAFS data for as-milled and annealed Fe-Cu powder samples. The k-range used in Fourier transforms was 2.5-12.5$Å^{-1}$ with a k^2-weighting. All data sets are vertically offset on the samex-axis to allow improved inspection of the development of higher-order neighbors. [Figure unavailable due to space constraints.]

Thermal stability and crystallization of amorphous $Tb_{33}Fe_{66}$ films	X23B

V. G. Harris, N. C. Koon and W. T. Elam (NRL)

The amorphous-to-crystalline transition in sputter- deposited amorphous TbFe films has been studied using conversion- electron extended X-ray absorption fine structure (EXAFS). A series of 250 nm Fe-rich, TbFe films were ion beam sputter-deposited onto glass substrates under ambientconditions. Films were capped with a 150 Ålayer of Ge to retard oxidation upon removal from the deposition chamber. Samples were then subjected to heat treatments in vacuo at temperatures ranging from 473K to 773K for a period of 60 minutes.

The X-ray absorption coefficient near the Fe K and Tb L_{III} edges were collected on beamline X23B. Following standard EXAFS analysis procedures the fine structure appearing above the edge were isolated and normalized to the edge height and energy. These data were then converted to photoelectron wavevector space and Fourier transformed to radial coordinates. The Fourier transformed Fe EXAFS data for the as-deposited (amorphous) and annealed $Tb_{33}Fe_{66}$ samples are depicted in Figures 1 and 2. Figure 1 contains the Fourier transformed Fe EXAFS data collected from the as-deposited samples and those annealed at 473K, 573K, and 623K. The inset panel to this figure illustrates an expanded view of the 3-5 Åregion of the plot. This is the area of the plot in which evidence for higher-shell ordering is likely to appear. Upon inspection of Fig. 1 (and its inset plot) one sees that not until an anneal at 623K does there appear a peak centered near 4.5 Å. Some peak amplitude changes occur over 3-4 Åin the data for samples annealed at lower temperatures but the physical significance of this unclear. Figure 2 illustrates Fourier transformed Fe EXAFS for samples annealed at 623K, 673K, 723K, and 773K. In these samples we see the first evidence for the order of α-Fe, the primary crystallization product for this composition. The evidence is predominantly the appearance and growth of the peak centered near 4.5 Å. This peak arises from the photoelectron scatter of the body-diagonal site and the neighboring unit cell's body cenered site. The amplitude of this peak is enhanced from the diffraction geometry established between the central, body- centered and body-diagonal sites of the unit cell and is a useful finger-print of the bcc structure.

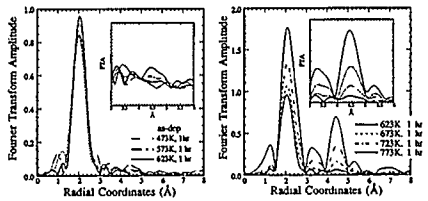


Figure 1. and Figure 2. Fourier transformed Fe EXAFS data collected from as-deposited (amorphous)and annealed Tb_{33} Fe_{66} films. All data have been transformed using k-ranges of 2.3-9.7 $Å^{-1}$and k^{-2}-weighting. Inset plots are expanded regions of the 3-5 Å region of the larger panelsand illustrate the evolution of higher-order neighbors with increased heat-treatment temperatures.

Crystallization studies of thin Fe-B films using EXAFS	X23B

V. G. Harris (NRL), S. A. Oliver (Northeastern Univ.), J. D. Ayers, and N. C. Koon(NRL)

Thin amorphous films (t≈200Å) of $Fe_{80}B_{20}$ were annealed at temperatures ranging from 473K-823K and studies using extended X-ray absorption fine structure (EXAFS) to investigate the evolution of local structure around the Fe atoms with heat treatments. The X-ray absorption coefficient near the Fe K edge was collected in total-electron-yield mode on the X23B beamline. Following standard EXAFS analysis procedures the fine structure appearing above the absorption edge were isolated and normalized to the edge energy and height. These data were then converted to photoelectron wave vector space and Fourier transformed to radial coordinates. Figure 1 is a plot of Fourier transformed Fe EXAFS data for the as-deposited and annealed samples. These data were normalized to the near neighbor (NN) peak height (appearing near 2Å) and vertically offset to allow inspection of the evolution of the higher-order atoms which appear over an r-range of 3-5/AA. In this figure one sees clearly that the higher-order peaks coinciding with higher order atomic shells begin to form in samples annealed at 523K. This is nearly 200K lower than ordering temperatures measured in bulk samples. The drastic decrease in ordering temperature is believed to be due to the increase in nucleation site density coinciding with the dominant role of the sample's surfaces.

Modeling of a broad EXAFS range (0-8 Åin r-space) using empirical standards was employed to determine the relative fraction of the crystalline component in each sample as a function of annealing temperature. Empirical standards used in this study include α-Fe, Fe_3B and Fe_2B. Figure 2 is a plot of the atomic fraction of Fe in each phase present in the annealed samples. In short, the initial crystallization occurs with the co-precipitation of α-Fe and Fe_3B as would be expected with eutectic crystallization. After an anneal at 623K there is no amorphous phase detected but a small amount of the Fe_2B is measured. This forms at the expense of the metastable Fe_3B.

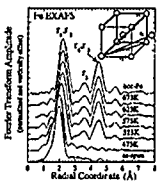


Figure 1. Fourier transformed EXAFS data for as-deposited and annealed $Fe_{80}B_{20}$ samples. All data have been Fourier transformed using a κ-range of2.5-12/AA^{-}1, with a κ^2-weighting. Data have been normalized to the NN peak amplitude and vertically offset using the same baseline to allow improved inspection of the evolution of higher-order n

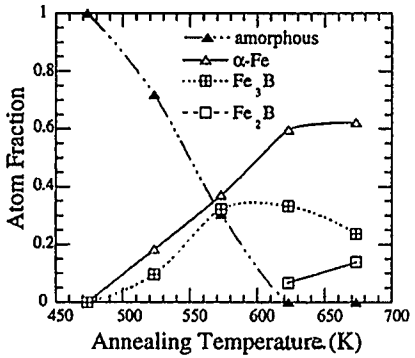


Figure 2. Annealing Temperature (K). Atomic fraction of individual phases present in annealed Fe-B samples determined by empirical EXAFS modeling of the data in Fig. 1.

Local structure and interface properties of fcc Fe on diamond	X23B

V. G. Harris (NRL), D. Pappas (Virginia Commonwealth Univ.), and G. A. Prinz (NRL)

The local atomic structure of four atomic layers of Fe grown on (100) diamond and capped with Cu was investigated using extended x-ray absorption fine structure. Both the film structure and the properties of the two interfaces were determined. X-ray absorption data encompassing the Fe K absorption edge were measured in conversion electron mode on the X23B beamline. The incident beam was aligned normal to the plane of the sample with the electric field vector aligning in-plane, hence the EXAFS data reflects strongly the in-plane structure. Following established EXAFS analysis procedures the fine structure appearing above the absorption edge were isolated and normalized to the edge energy and height. These data were then converted to wave vector space and Fourier transformed to radial coordinates. Figure 1 are Fourier transformed EXAFS data for two Fe/C samples (t_{Fe}=5Å and 18Å) together with similar data collected from bcc Fe (top profile) and fcc Cu (bottom profile) which are provided for comparison.

A qualitative inspection of these data shows that the 5ÅFe/C sample most closely matches the fcc structure of Cu. This can best be seen by comparing the relative distances and amplitudes of the Fourier features appearing over the r-space range of 3- 5Å. In contrast, the data corresponding with the 18Å Fe/C sample matches more closely with the bcc Fe data. These data indicate that very thin thicknesses Fe grows epitaxially on the fcc surface net of (100) diamond, while at higher thicknesses the Fe reverts back to its low-energy bcc structure. Modeling of the near neighbor EXAFS region of the Fourier transformed EXAFS data for the 5Å Fe/C sample using FEFF 3.1 indicates an Fe-Fe bond of 2.50±0.01Åwhich provides an in-plane lattice constant of 3.54Å. The fitting also revealed that the Fe-C and Fe-Cu bond distances in the interfacial regions are 1.84±0.02Å and 2.62±0.02Å, respectively, with little evidence for intermixing of the Cu and C atoms into the Fe film.

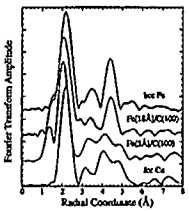


Figure 1. Fourier transformed Fe EXAFS data collected from Fe(5Å)/C(100) samples. k-ranges used in the Fourier transformation were 2.5-11.0Å^{-}1 with a k^2-weighting. Similar data are presented for Fe and Cu foils as empirical standards of the bcc andfcc structures.

Direct measurement of octahedral and tetrahedral site environments in NiZn-ferrites | X23B

V. G. Harris (NRL), C. M. Williams (Morgan Sate Univ.), M. Abe, and Q. Zhang (TokyoInstitute of Technology, Japan)

For many years researchers have studied the effects of substitutional metals in spinel ferrites upon their magnetic and electronic properties. Much of this work has been done empirically because of the difficulties involved with identifying the site that the substitutional metal ions. We have recently illustrated the flexibility of using extended X-ray absorption fine structure (EXAFS) to identify the occupation and chemistry of the substitutional metal ions in NiZn-ferrites.

The films used in this investigation were prepared using a spin-spray, plating process. These films were deposited onto glass substrates and are approximately 1 μm thick with compositions: $Ni_{0.15}Zn_yFe_{2.85-y}O_4$(y=0.16,0.23,0.40,0.60).

X-ray absorption spectra were collected for each sample encompassing the absorption edges of Ni, Zn, and Fe. Fourier transformation of these data to radial coordinates was performed following established procedures. Theoretical partial radial distribution functions were generated to help identify the Fourier features one can expect when the transition metal (TM) is positioned on the octahedral versus the tetrahedral site, or a mix of the two sites. Figure 1 is a plot of the Fourier transformed Fe EXAFS data collected from the four ferrite film samples. These data were treated identically during the analysis procedures leading to the Fourier transformation, hence direct comparisons between these data sets are valid and useful.

The split peak appearing between 2.2 and 3.6 Å is dominated by TM-TM correlations. The lower r peak corresponds to correlations which are greater when the central atom (Fe) resides on the octahedral sites (B) and the higher τ peak corresponds to correlations which are greater when the central atom resides on the tetrahedral sites (A). By comparing the data sets of the four samples one sees that the peak heights over this range systematically change with changes in the samples composition. Because the data in Fig. 1 are Fe EXAFS we can deduce from this that the Fe occupation on the B sites is systematically increasing with increasing Zn content. Using this technique one can correlate the changes in site chemistry and occupation with changes in the sample composition and compare these changes with trends in sample magnetization and anisotrophy fields.

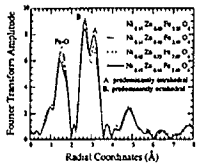
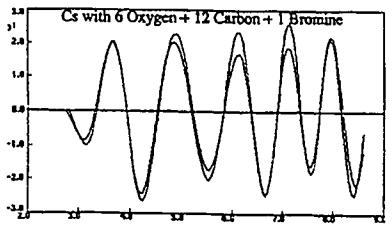


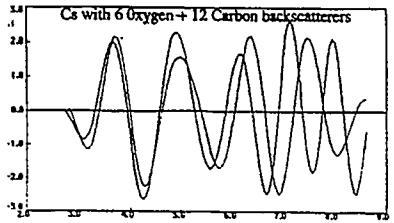
Figure 1. Fourier transformed Fe EXAFS for four NiZn-ferrite films. k-ranges used in Fouriertransformation are 2.3-12.0 $Å^{-1}$ with a k^3-weighting.

EXAFS studies of CsX-dibenzo-18-crown-6 ether solutions | X23B

K.M. Kemner, W.T. Elam (NRL), D.B. Hunter, and P.M. Bertsch (Savannah River Ecology Lab.)

Since the beginning of crown-ether chemistry, it has been recognized that the size of the intramolecular cage, formed by the oxygen atoms of the crown ether, can discriminate in the binding of different cations. Cations whose diameter are closest to the crown ether's intramolecular hole size usually form the most stable complexes. In the past, most structural x-ray studies of these systems have been limited to the solid phases. However, adequate models for predicting the fate of the ions captured within these crown-ethers depends on an accurate understanding of their local chemical environment in both the solid and solution phases. CsX-dibenzo-18-crown-6 ether solutions were prepared by adding 20–40 mM 18-=crown-6 ether to acetonitrile and then adding CsX (where X = F, Cl, or Br) such that the final molar ratio of crown-ether to Cs was 1:1. Previous NMR data has demonstrated that a 1:1 complex exists at this molar ratio. Similarly, stability Constants have shown the ration of CsX in solution to Cs in a crown-ether environment ot be 1:10000. We have made EXAFS measurements at the Cs LIII edge on all three of the above-mentioned solutions in the fluorescence mode utilizing a Sc filter combined with solar slits to reduce the large background signal due to scattered radiation from the solution. We have also made transmission measurements on CsF, CsCl, and CsBr powders. Calculated spectra using FEFF3 were used to simulate first shell backscatterers of F, Cl and Br around Cs and checked with the experimentally obtained transmission data. FEFF3 was then used to simulate oxygen and carbon backscatterers to be used as standards to analyze the crown-ether samples. Unlike results from previous XAFS studies in the solid phase, we find evidence suggesting that, when in solution, the anion remains in contact with the Cs cation even when encircled by the dibenzo-18-crown-6 ether. We also find evidence suggesting there is only one Cs-O shell at ca. 3.03 Å and one Cs-C shell at ca. 3.96 Å. To illustrate the presence of the counter ion, the Fourier filtered first shell data and its best fit, for CsBr in a crown ether solution, are shown in Figs 1 and 2, with and without the inclusion of 1 Br backscatterer.





Wavelength-dispersive x-ray fluorescence detector | X23B

J.P. Kirkland (SFA Inc.), V.E. Kovantsev (X-Ray Optical Systems, Inc.), C.M. Dozier (NRL), J.V. Gilfrich (SFA Inc.), W.M. Gibson (SUNY Albany), Qi-Fan Xiao (X-Ray Optical Systems, Inc.), and K. Umezawa (SUNY Albany)

A wavelength-dispersive x-ray fluorescence detector system has been developed that can be used to discriminate fluorescent photon energies for practically any incident flux. The system uses a Kumakhov polycapillary lens to collimate fluorescent photons from a sample. The collimated photons are transmitted to a crystal-counter combination on a stepping motor driven θ-2θ stage. The stage diffracts the photon wavelength of interest and a photon-counting or current-mode counter is used to measure the photons. The system had a resolution of less than 150eV at 8 keV using the (200) reflection from an abraded and etched LiF crystal, and was easily able to discriminate between Zn K_α (8.620 keV) and Cu K_β (8.905 keV) x-rays emitted from a brass sample. The LiF(400) reflection had a resolution of approximately 50eV, but with ten times less intensity.

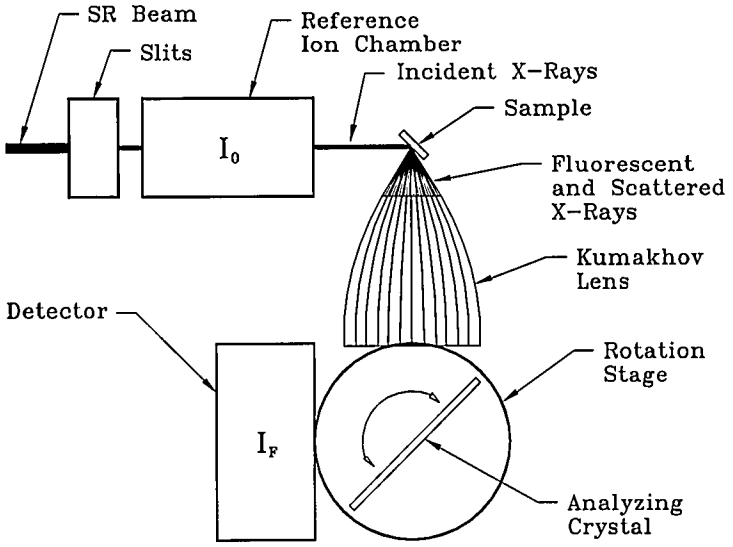


Figure 1. Experimental setup and schematic of x-ray fluorescence detector.

Attenuation of photons in helium | X24A

Y. Azuma, H. G. Berry, D. S. Gemmell, J. Suleiman (ANL), M. Westerlind, I. A. Sellin(U. Tennessee), J. C. Woicik (NIST), J. P. Kirkland (SFA/NRL)

We have measured the total photo-attenuation cross-section of helim for photons in the energy range of 3-5.5 keV at beamline X24A. At these energies, the photoionization cross section is rapidly decreasing, so that Compton scattering becomes important in this energy range. Our measurements verify the dominance of Compton scattering in this energy range and its importance in recent measurements of the ratio of double-to-single photoionization of helium. The measured cross sections, which have a precision of better than 2calculated cross sections for Compton scattering and photoionization, and we are able to distinguish the contributions of the two effects. In this energy range, the attenuation cross section varies between 25 and 2 barns.

The apparatus consisted of a 1.4 m long, 5 cm diameter helim absorption tube, with 75 μm thick, 7 mm diameter kapton windows on each end. The tube is connected to a gas-handling system, and could be filled with helium to a pressure of 10^{6} Pa. The whole system was pumped out initially to better than 3 x 10^{-5} Pa. Pressure and vacuum gauges with electronic readouts allowed us to monitor the absolute pressure to better than 1simultaneously with the photoabsorption measurements. At each photon energy we measured the absorption ratio fo typically 10-15 pressures between 0.1 - 8 x 10^{5} Pa. The measured slope is proportional to the attenuation cross section at the given photon energy.

the figure shows are measured data (filled circles) compared with theory (solid line) and earlir data (triangles and square).

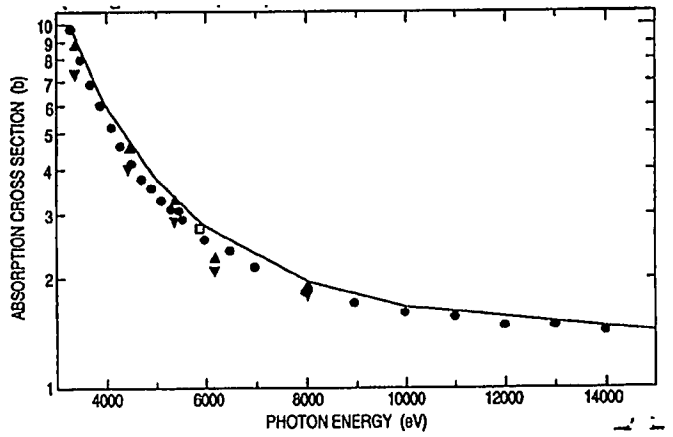


Figure 1.

Alkali absorption spectra | X24A

Y. Azuma, J. Suleiman, H. G.Berry, P. L. Cowan, D. S. Gemmell (ANL), M. Westerlind(U. Tennessee)

We have used a heat-pipe target in a monochromatized x-ray beam at the X24A beamline to obtain photoabsorption spectra of potassium at its K- and Km-edges, in the photon energy range near 3600 eV. We have also obtained first measurements of the L_2 and L_3 edges in cesium. Preliminary identifications of most of the edges and resonance peaks observed are being made using Dirac-Fock calculations. We have compared these results with those obtained previously in closed-shell rare-gas absorption spectra. The absolute energies are in the process of being obtained through an improved calibration of the X24A system using measurements of several metal L-edges in the 3200-5000 eV energy range.

The figure shows our new identifications in the potassium KM region.

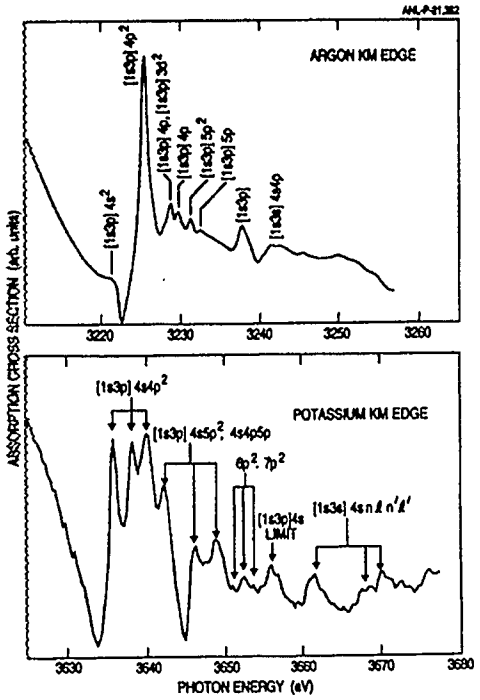


Figure 1.

Argon and potassium ion time-of-flight spectra near the k-edge | X24A

Y. Azuma, J. Suleiman, H. G. Berry, P. L. Cowan, D. S. Gemmell, T. LeBrun (ANL)

We have studied the production of argon and potassium ions near the thresholds of their respective K-edges. It has been shown previously that the average ionic charge is a linearly increasing function of energy just below the K-edge of argon. The normal resonant ionization behavior would produce a Iorentzian with quadratic energy dependence away from the resonance. Amusia has explained the linear energy dependence as due to the formation of a virtual 1s state below the edge with consequent further ionization with a 2s or higher electron vacancy.

We have made more detailed measurements of the charge state productions for argon ions from 100 eV below the K-edge to above the Km resonances, as well as similar initial measurements in potassium. Time-of-flight measurements of the ions were made utilizing the single bunch operating mode at the NSLS. We estimated the effects of differing detection efficiencies of the ions reaching the channel plate detector with differing velocities by comparing results with different time-of-flight voltages. The individual charge state distributions show the 4p resonances strongly, although it is clear that the slowly increasing energy dependence below threshold can be seen in the higher charge state distributions (4-6) below threshold, as shown in the figure.

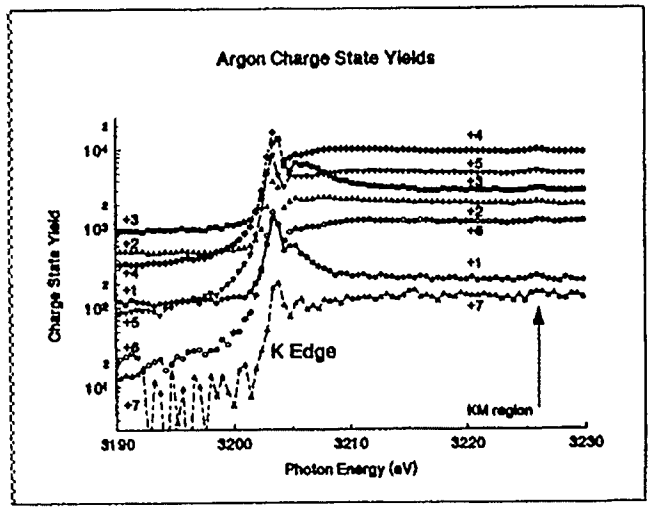
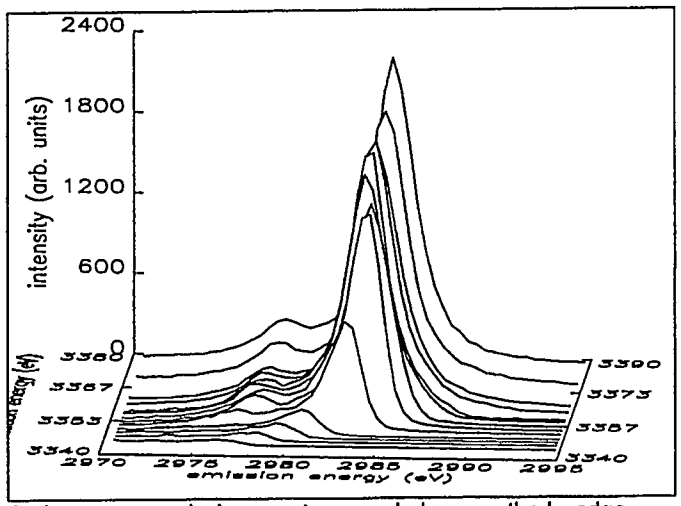


Figure 1.

Threshold dependence of x-ray emission from Ag metal	X24A

A. Bartos and S. H. Southworth (NIST)

We have studies the threshold dependence of Ag $L\alpha_{1,2}$ x-ray emission from polycrystalline Ag as the energy of the incident x-ray beam was scanned across the L_3 edge. Near threshold, strong variations are observed in the positions, intensities, and lineshapes of the x-ray emission spectrum compared with the characteristic spectrum produced using broadband excitation. These effects are similar to those observed in Cu metal and interpreted using the x- ray resonant Raman scattering model [1]. We previously observed similar threshold effects in x-ray emission from atomic Xe [2]. the present data appear to nicely demonstrate the "half-width narrowing effect" [1,3], in which the high- energy side of the emission peak is cut off at excitation energies below threshold, resulting in highly asymmetric lineshapes.



Ag $L\alpha_{1,2}$ x-ray emission spectra recorded across the L_3 edge.

Figure 1.

Electron/x-ray coincidence spectroscopy *	X24A

T. LeBrun (ANL), U. Arp,S. H. Southworth (NIST), M. A. MacDonald (Daresbury)

A new coincidence technique has been used to disentangle the complex processes involved in the decay of the 1s hole in atomic argon following x-ray absorption. After excitation of the 1s shell the atom relaxes rapidly by Auger- electron emission or x-ray fluorescence. Most of these decay processes lead to unstable states which decay further, creating a cascade of decay processes and an array of final charge states, Ar^{1+} to $Ar^{8}+$ [1,2].

The new technique uses coincident detection of x-rays and electrons to select decay pathways that involve emission of both an x-ray photon and electrons. The kinetic energy spectra of photoelectrons and Auger electrons produced in coincidence with fluorescent x-rays are selectively recorded. The instrumentation and experimental methods have been described in Ref. [3].

In a simple demonstration of this technique, the Ar 1s photoelectron spectrum has been selectively recorded in coincidence with x-ray fluorescence to eliminate the asymmetric broadening and shifting of the energy distribution which result due to post-collision interaction with K-Auger electrons [3,4]. We have also applied this technique to the much more complex problem of understanding Auger-electron spectra produced by vacancy cascades following inner-shell excitation. For example, we have previously recorded non-coincident electron spectra of $L_{2,3}MM$ Auger transitions following K-shell excitation of argon [3,4]. Interpretation of these spectra is difficult because they are complicated and consist of many overlapping or unresolved Auger transitions between different ionic states.

However, these vacancy-cascade electron spectra are much more easily understood when measured in coincidence with x-ray fluorescence. In argon, $K\alpha$ fluorescence accounts for $\approx$12state with a single hole in the 2p shell. Recording the $L_{2,3}MM$ Auger spectrum in coincidence with x-ray fluorescence allows the Auger spectrum of the 2p hole produced via initial K- shell excitation to be selectively studied and distinguished from the several other competing processes. The resulting coincidence spectra are relatively simple and straight-forward to interpret. This technique has been particularly informative for the study of states produced following resonant or near-threshold excitation of the K-shell.

[1] T.A. Carlson, and M.O. Krause, Phys. Rev. 1327, A1655 (1965)

[2] J.C. Levin, C. Biedermann, N. Keller, L. Liljeby, C.-S. O, R.T. Short, I.A. Sellin, and D.W. Lindle, Phys. Rev. Lett. 65, 988, (1990)

[3] S.H. Southworth, M.A. Macdonald, T. LeBrun and R.D. Deslattes, Nucl. Instrum. Methods A 347, 499 (1994).

[4] S.H. Southworth, M.A MacDonald, T. LeBrun, Y. Azuma, and J.W.Cooper, in Proceedings of the Workshop on Atomic Physics at Hight Brilliance Synchrotron Sources, Argonne National Laboratory report 1994.

* Alexander von Humboldt/Feodor Lynen Research Associate.

Threshold K-LL auger spectra of P in InP	X24A

Honghong Wang (Univ. of Oregon), Joseph C. Woicik (NIST), Teijo Aberg (Helsinki Univ. Technol.), Mau Hsiung Chen (Lawrence Livermore Natl. Lab.), Alberto Herrera-Gomez, Tom Kendelewicz (Stanford Univ.), Anna Mantykentta (Univ. Oulu), Ken E. Miyano (Brooklyn College), Stephen Southworth (NIST), Bernd Crasemann (Univ. of Oregon)

The evolution of $K - L_{2,3}L_{2,3}\ ^1D_2$ radiationless resonant Raman scattering into Auger-electron emission was studied by tuning synchrotron radiation across the K edge of P in InP. The spectrum can be interpreted in terms of a two-component model that involves excitation of a photoelectron (1) into a discrete excitation state and (2) into continuum; extra-atomic relaxation is taken into account. Auxiliary studies of above-threshold Auger and photoelectron spectra arising from K photoionization were used to identify the dominantly atomic features of these spectra.

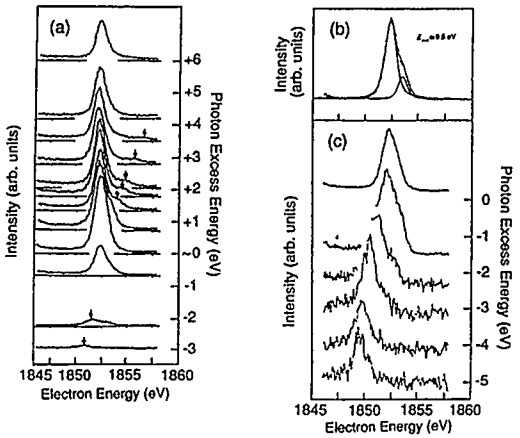


Figure 1. (a) Evolution across the K threshold of P $K - L_{2,3}L_{2,3}\ ^1D_w$ resonant Raman scattering into the corresponding Auger line. Arrows indicate the position of some resonant Raman peaks in spectra measured at various approximate photon excess energies (indicated on the right). (b) Two-component decomposition of the spectrum at $E_{exc} = 0.5$ eV, after subtraction of a linear background. (c) Enlargement of K-$L_{2,3}L_{2,3}\ ^1D_2$ spectra measured with E_{exc} in therange from approximately −5 to +0.2 eV. The sequence shows the asymmetrical shape of the normal Raman peaks which with increasing E_{Eec} evolve into the Auger line.

Accomodation of strain in ultra-thin InAs/GaAs films	X24A

J. C. Woicik, J. G. Pellegrino, S. H. Southworth, P. S. Shaw, B. A. Karlin (NIST),K. E. Miyano (Brooklyn College)

The geometric consequences of strain in a buried ultra- thin (1 monolayer) InAs film grown on GaAs(001) by molecular beam epitaxy have been studied with the x-ray standing wave and extended x-ray absorption fine structure techniques. The perpendicular distance of the In layer from the first GaAs plane is found to be 0.16 ± 0.002 d_{004} GaAs lattice units. As the natural lattice constant of InAs is 7corresponds to a 9direction due to the compression in the (001) plane imposed by the substrate. Surprisingly, this expansion agrees nearly exactly with the prediction of macroscopic elastic theory, but falls short of the prediction of a simple bond angle distortion. This deviation is directly observed as a small, but measurable, compression of 0.04 ± 0.002Åin the In-As near neighbor bond length. A microscopic model is presented which accounts for these as well as distortions in other epitaxial semiconductor systems.

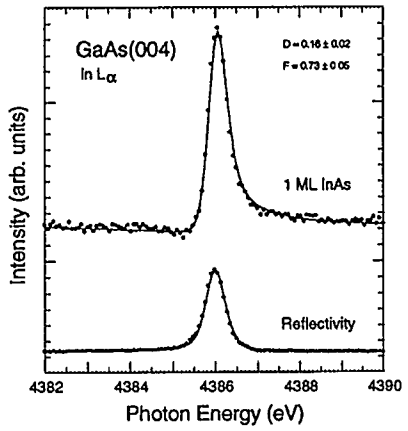


Figure 1. new

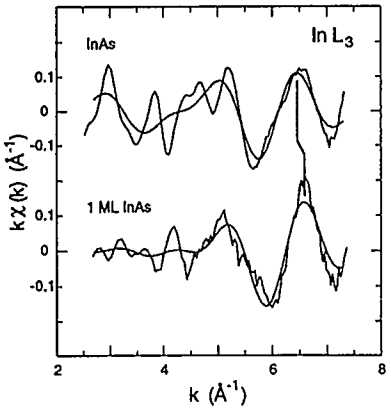


Figure 2. new

VUV spectroscopic study of lithium triborate crystal * | X24C

T. J. Chen (Southern Illinois U.), W. R. Hunter (Sachs Freeman Assoc.), M. Chen,R. Zitter, R. Tao (SIU), L. Song (Perking U.), J. C. Rife (Naval Research Center)

Lithium Triborate crystal (LiB_3O_5, or LBO) is a novel nonlinear optical crystal. Its direct band gap is ~7.8 ev, therefore the VUV spectrum is suitable for study of its band structure. The crystalline structure of LBO is orthohombic, belongs to $Pna2_1$ space group and mm2 point group. We have done the VUV spectroscopic measurement at the NSLS X24C beamline. The crystal used in our experiment is a 2 x 6 x 6mm^3 Z-cut sample and was laser grade polished.

The observed step in 7.8 ev region in reflection spectrum at 30° incidence is consistent with the previous transmission measurement [1]. In addition, a 0.15ev blue shift of the S polarization component relative to the P component was observed in our experiment.

A reflection peak appears at 59.2ev in P polarization spectrum, and the peak shows a strong orientation dependence in terms of the bandwidth and amplitude. The narrowest bandwidth and highest reflectance occurs at 25° incidence (Fig. 1). As the incidence angle increases the peak becomes broader and has less amplitude. At 60° incidence, the peak is even reversed into a dip (Fig. 2). The 63.5 ev peak varies in an almost opposite way. The absorption bands related to the reflection peaks in LBO crystal are mainly due to the absorption of the anionic group of the crystal. The observed orientation dependence contains the information of the orientation of the anionic groups in the crystal and the polarization of the related dipoles.

[1] R. French, Phys. Rev. B44,8496 (1991).

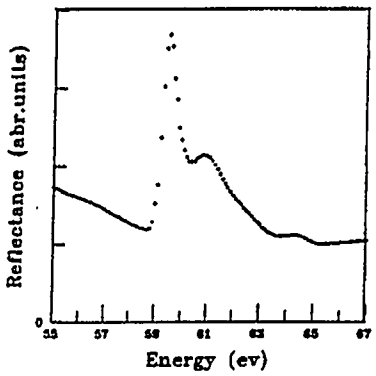


Fig.1

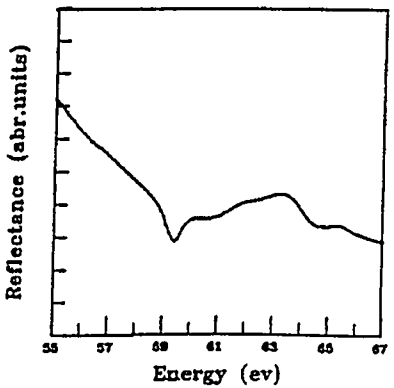


Fig.2

* This work is supported by the Illinois Board of Higher Education.

A transmission-bragg phase plate for circular dichroism and x-ray raman scattering * | X25

W. A. Caliebe, C.-C. Kao (NSLS), M. Krisch, F. Sette (ESRF, France), L.E. Berman, and J. B. Hastings (NSLS)

Over the last decade the utilization of circularly polarized x-rays has increased. In the beginning experiments were performed by using the elliptical polarized radiation from above and below the orbital plane with significant reduction of available photon flux. Recently, crystal optics based x-ray quarter-wave plate (QWP), notably the transmission Bragg phase plate, has been demonstrated to convert linear polarized x-rays into circular polarized x-rays with high efficiency and broad tunability[1-3]. Until now, mostly high quality single crystals like Diamond and Silicon were used. In this work, we present results obtained using a LiF crystal with a mosaicity. In order to determine the performance of the QWP, we measured the Magnetic Circular Dichroism (MCD) of iron near the Fe K absorption edge. The circular dichroism signal (μ_c/μ) is proportional to the difference of the absorption of left and right handed circularly polarized light with the magnetic field pointing in one direction. By switching the magnetic field one reverses the sign of the effect. In fig. 1 we present the two MCD-signals together with the absorption coefficient of Fe at the K edge. These data agree well with earlier MCD results from other groups [4,5]. From the magnitude of the MCD effect, the degree of circular polarization of the x-rays, after transmitted through the LiF phase plate, is estimated to be about 50%, which agrees well with the theoretical calculation based on the vertical and horizontal acceptance of the beamline. The efficiency of the phase plate at 7 keV is a few percent, and should increase to about 10% at 8 keV. The monochromatic and circularly polarized x-rays were then used to excite x-ray Raman scattering from Gd near the Gd L_{III} edge. A high resolution spectrometer was used to analyze the scattered photons, around the energy range of the Gd L_α fluorescence line. Fig. 2 shows the Raman spectrum (solid line) taken at incident energy of 7241 eV, 8 eV below the L_{III} white line, and the asymmetry ratios of the Raman spectrum obtained by changing the helicity of the incident photon to be either parallel or anti-parallel to the magnetization of the sample.

[1] V.A. Belyakov, V.A. Dmitrienko, Sov. Phys. Usp. 32, 697, 1989. [2] K. Hirano et al., Jpn. J. Appl. Phys. 30, L407, 1991. [3] Carlos Giles et al., J. Appl. Cryst., 1993. [4] G. Schütz et al., Phys. Rev. Lett. 58, 737, 1987. [5] M. Hart et al., Rev. Sci. Instr., 1992.

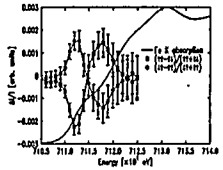


Figure 1. MCD-signal of Iron on top of the Fe K-absorption edge

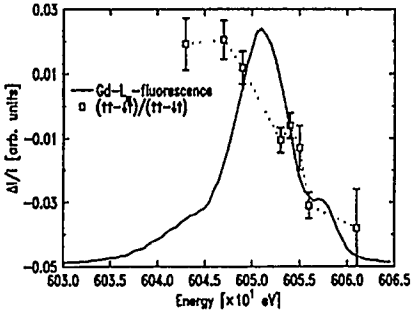


Figure 2. Fluorescence-MCD-signal of Gd

* Supported by US DOE under contract # DE-AC02-76CH00016

X-ray photon correlation spectroscopy study of brownian motion of gold colloids in glycerol *	X25

S. B. Dierker (Univ. Michigan), R. Pindak, R. M. Fleming (AT&T), I. K. Robinson (Univ. Illinois), and L. Berman (NSLS)

frequency dynamics can be probed down to interatomic spacings. Additionally, many of the important problems in the low frequency dynamics of condensed matter systems for which XPCS should be uniquely suited arise in disordered materials, in particular, liquids. In this experiment, we made equilibrium dynamic measurements on a disordered system using XPCS. Specifically, we made small angle x-ray scattering measurements of the static structure factor of a gold colloid dispersed in the viscous liquid glycerol. We also made a determination using XPCS of the dynamic correlation function for the Brownian motion of the colloid particles. The measurements were made with a 2D CCD area detector. Fig. 1 shows the static structure factor, S(q), of the gold colloid in glycerol sample taken under incoherent x-ray conditions. The strongly peaked signal in the center is the main beam and the channel cut is the shadow of a gold wire used as a beam block. The colloid particle radius deduced from S(q) was 270 $\AA$, which agrees well with the as-prepared radius. Fig. 2 shows the time autocorrelation function of the scattered x-rays due to Brownian motion of the gold colloid particles as well as a fit to a single exponential relaxation. The fit gives a characteristic decay time of 9.5 seconds. The nominal expected decay time is 60 seconds, however this would be substantially shortened if the viscosity of the very hygroscopic glycerol were reduced by absorbed water. More measurements are needed to fully understand this point. Note that these measurements were made on an optically opaque sample in a q range inaccessible to visible light. We also gained valuable experience with the promises and pitfalls of using multilayer monochromator and bent crystal focussing optics in coherent scattering experiments which should be of benefit to future coherent x-ray scattering experiments at X25.

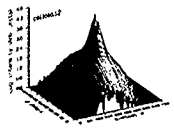


Figure 1. Log plot of incoherent scattering intensity from the colloid collected with the CCD camera.

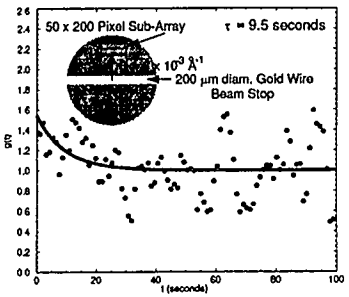


Figure 2. Autocorrelation function of colloid scattering intensity as collected with CCDcamera. The inset schematically depicts the scattering 'halo', the beam stop, and the sub-array which was ensemble averaged over.

* Support under NSF grant No. DMR 92-17956 and also the Donors of the Petroleum Research Fund, administered by the American Chemical Society, for the partial support of this research under grant ACS-PRF No. 26389-AC9. I.K.R. acknowledges support under NSF grant no. DMR 93-15691. The NSLS is supported by the U.S. Department of Energy under Contract No. DE-AC02-76CH00016.

Temperature dependent x-ray diffuse scattering from single crystals of La-Sr-Cu-Os assistance during the measurement. *	X25

W. Dmowski, R. J. McQueeney, T. Egami (Univ. Penn), Y. P. Feng, and S. K. Sinha (Exxon)

X-ray diffuse scattering from single crystals of $La_{2-x}SSr_xCuO_4$ (x=0.10, 0.15, 0.20) was studied in the vicinity of several Bragg peaks near the c*-axis as a function of temperature. In order to separate thermal difuse scattering (TDS) due to phonons from the total scattering intensity, we calculated the TDS intensity using the shall model. Figure 1 [unavailable due to space constraints] presents diffuse scattering intensities measured along (ξ, ξ, 18,2) at 300 K and at 10 K for the x = 0.2 sample. The solid lines represent the calculated TDS intensity plus the Compton scattering intensity given in the electron units per atom. The measured and calculated intensities agree excellently at 300 K. In contrast at 10 K the phonon contribution accounts for only a portion of the measured intensity, and the rest, the non-phonon contribution, is actually dominant. The same is true for other compositions although the amount of the non-phonon intensity is composition dependent. Using perpendicular scans along the two diagonal directions in the $q_x - q_y$ plane we eliminated the 2-fold component from the data. Then the calculated contribution from the TDS and Compton scattering was subtracted and the resulting non-phonon intensity was integrated over $\vec{q}$ (xi, xi, 18 $\pm$ 0.15) from ξ = 0.02 to 0.1. Figure 2 [unavailable due to space constraints] presents the temperature dependence of such an integrated intensity for three compositions. Note that the x = 0,2 sample shows that the integrated intensity particularly strongly depends upon temperature, and is close to zero at room temperature, as indicated by the good agreement between the measured and calculated intensity ties in Fig. 1. The most conspicuous characteristic of the non-phonon diffuse scattering identified in this work is its temperature dependence. The temperature variation is particularly strong in the case of the x = 02 sample as shown in Fig. 2. While the diffuse scattering at room temperature is dominated by phonon scattering, at low temperatures residual non-phonon diffuse scattering is clearly seen. The intensity of the residual non-phonon scattering depends upon temperature and composition in a characteristic manner. It is suggested that the non-phonon scattering is due to local lattice distortions induced by charge carriers in these compounds.

* A part of this work at the University of Pennsylvania was supported by the National Science Foundation through DMR93-000728 and DMR91-20688. The operation of the National Synchrotron Light Source is supported by the Department of Energy, Division of Materials Sciences and of Chemical Sciences. The authors are grateful to D. E. Moncton for various suggestions, in particular regarding the high-resolution scattering. They are thankful also to L. E. Berman of the NSLS beamline X-25 for his selfles

Magnetic scattering from Dy and Lu in Dy/Lu alloys * | X25

B. A. Everitt, M. D. Salamon, B. J. Park, C. P. Flynn (UIUC), T. Thurston, and D.Gibbs (NSLS)

We have observed x-ray resonant enhanced magnetic scattering from both components of a $Dy_{0.6}Lu_{0.4}$ thin film alloy. The alloy, previously studied using neutron diffraction, orders as a basal-plane c-axis helimagnet. Measurements were carried out on the first-order magnetic satellites about the (002), (004) and (006) reflections at the Dy and Lu L_{III} E1 resonances, respectively. Although the Lu, which has a filled 4f shell, is nonmagnetic, it supports an induced spin-density wave in the 5d band due to the ordered 4f moments in the Dy. This is the first experiment to measure the induced polarization of a nonmagnetic element using resonant enhanced x-ray diffraction. Due to the small signal at the Lu resonance, it was necessary to use a polarimeter to increase the signal-to-noise. Using our UIUC-built polarimeter with an MgO(420) analyzer crystal (Bragg angle of 45.4° at the Lu resonance) to detect only the σ-to-π channel of the scattered radiation, we were able to reduce the charge scattered background enough to observe magnetic scattering from the Lu. In this configuration, we were only getting ≈20c/sec at the Lu resonance (Figure 1), underscoring the necessity of running at X25. By comparing the strength of the resonances at both the Dy and Lu L_{III} edges, we estimate that the induced 5d moment is of the order of only a few hundredths of a Bohr magneton per Lu atom.

Measurements of the stronger Dy signal were carried out both with and without the polarimeter in place. The high q-resolution of the synchrotron revealed that, below 60K, the first-order harmonic actually exhibits a two-component lineshape, which was not previously observed with neutron diffraction (inset, Figure 2). This mixed-phase, characterized by two distinct wavevectors, exists throughout the temperature range T≤ 60K in which the wavevectors remain locked-in near the value of 5/21 (0.2381). Above 60K, the ordering is characterized by a single wavevector, which increases continuously with increasing temperature to T_N=120K (Figure 2).

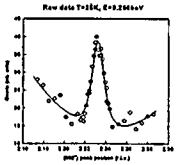


Figure 1. Intensity vs. c* (r.l.u.). Raw data taken near the Lu L_{III} edge; E=9.250keV. The peak fit is to a Lorentzian squared, with a quadratic background.

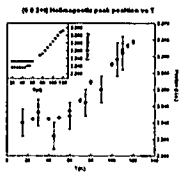


Figure 2. τ vx. T for the (0 0 2 $+\tau$) magnetic peak; x-ray data near the Lu L_{III}edge, E=9.250keV(O), and neutron diffraction data (•). Inset. XRES data taken near the Dy L_{III}edge, E=9.792keV. Below 60K, the helimagnetic turn angle 'locks-in' to two wavevectors. The splitting is not evident in the x-ray data taken at the Lu edge or in the

* Work performed at Brookhavenis supported by the USDOE under contract ED-AC02-76CH00016. University of Illinois research is supported by NSF Grant DMR-91-21888 and DOE Grant DEFG02-91-ER45439.

Site selective EXAFS spectroscopy * | X25

M. M. Grush (UC Davis), A. G. Froeschner (UC Davis), C. R. Randall (UC Davis/LBL),G. Christou (Indiana U.), and S. P. Cramer (UC Davis/LBL)

Using a custom-built Mn spectrometer, we have recorded the first site-selective EXAFS. The sample examined was $Mn_3O(O_2CPh)_6(py)_2(H_2O)$, a Mn$_3$(II,III,III) trimer. This mixed valence complex has a different environment around the Mn(II) compared to the average Mn(III) environment. By setting three Si(440) spectrographs to record the emission energy favorable to either Mn(II) or Mn(III) species, we measured oxidation state selective EXAFS on this compound (Figures 1&2). The isolated EXAFS have been smoothed over a 0.3 eV range and a k range of 2-9$Å^{-1}$ was used for the Fourier transform due to the noise in the raw data above 9$Å^{-1}$.

One of the primary differences in the environment of the Mn(II) and Mn(III) species occurs in the Mn-Mn distances. The two Mn(II)-Mn(III) distances are 3.35Å and 3.38Å, while the Mn(III)-Mn(III) distance is 3.21Å. Qualitatively, the Fourier transform intensity around 3Å(the R values shown here have not been phase shifted which results in an approximately 0.3Åshift to higher energy), due predominately to Mn, is larger in the Mn(II) case, as is expected since Mn(II) would see two homogenous Mn-Mn distances while a Mn(III) would see two different Mn-Mn distances, dampening their contribution. We are further analyzing these spectra to obtain quantitative site selective data on the near neighbors to the Mn.

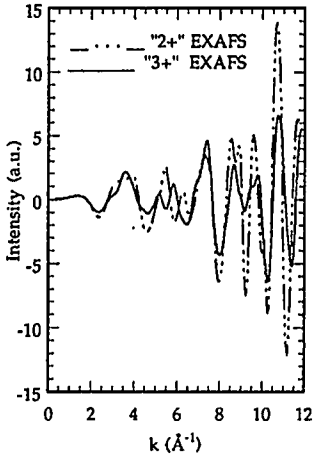


Figure 1.

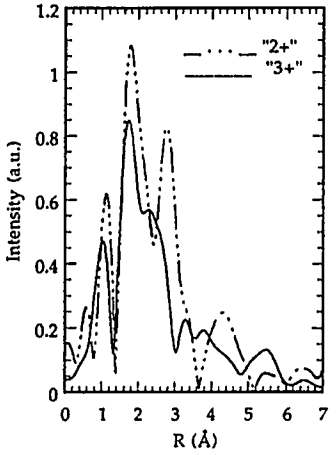


Figure 2.

* Work supported by the National Institute of Health, GM48145-03.

Structural studies of the NFκB transcription factor *	X25

Stephen C. Harrison (HHMI/Harvard University)

We have collected data from crystals of recombinant NFκB p50 in complex with a specific DNA site. The crystals are in space group $P4_12_12$, a = b= 138.4 Å, cc = 57.2 Å. A selenomethionine substituted protein has been used for multiple-wavelength anomalous dispersion (MAD) phasing. These crystals contain a more complex structure than used hitherto in most MAD experiments: data collection at liquid nitrogen temperature was essential for adequate crystal stability. Two MAD data sets were collected (on two different runs) – one at three wavelengths and one at four. Data from crystals with unsubstituted ("native") protein and with iodinated DNA were also collected. The combined MAD and isomorphous phases have yielded an interpretable map, and the structure is being refined using the 2.6 Å resolution native data.

* Work supported by the Howard Hughes Medical Institute.

The geometric structure of Rb/Cu(111) investigated with x-ray standing waves: Rb coverage dependence *	X25

D. Heskett, P. Xu (Univ. of Rhode Island) L. Berman, C.-C. Kao (NSLS), and M. J. Bedzyk(Northwestern Univ. and Argonne MSD)

We have carried out a Back Reflection x-ray Standing Wave (BRXSW) investigation of the geometric structure and degree of ordering of the system Rb/Cu(111) as a function of Rb coverage. In the direction normal to the surface, we observe no change in the relative Rb-Cu(111) Bragg plane spacing as a function of coverage down to coverages of less than θ=0.25 (constant coherent position in the (111) direction—see Figure 1). Furthermore, we find a high degree of ordering of the Rb atoms perpendicular to the surface at all coverages (high coherent fractions in the (111) direction—Figure 1), but a very low degree of order parallel to the Cu(111) surface (low coherent fractions in the (111) direction—Figure 2.

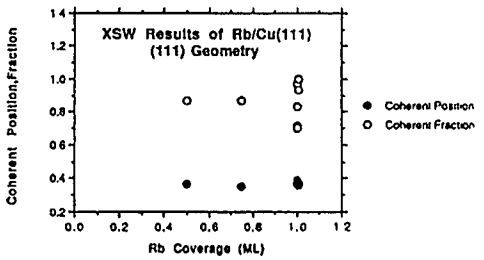


Figure 1.

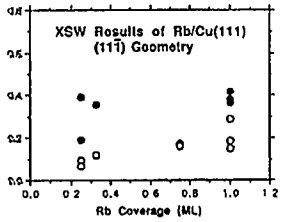


Figure 2.

* For P. Xu and D. Heskett, for partial support of this research, acknowledgement is made to the Donors of The Petroleum Research Fund, administered by the American Chemical Society, and to the URI Council for Research. L. Berman, C.-C. Kao, and the NSLS are supported by the DOE under Grant No. DE-AC02-76CH00016. M. Bedzyk received partial support through ANL under DOE-BES contract No. W-31-109-ENG-38 and through the NSF-MRL program at NU under contract No. DMR-9120521.

X-ray crystallographic studies of TBP recognizing DNA *	X25

J. L. Kim (Howard Hughes Medical Institute), G. Patikoglou (Rockefeller Univ.),and S. K. Burley (Rockefeller Univ.) (Howard Hughes Medical Institute)

The National Synchrotron Light Source X25 beam line was used for high resolution,X-ray diffraction data collection of crystalline preparations of the TATA box-binding protein, a central eukaryotic transcription factor, bound to DNA recognition sequences known as TATA elements.

Initiation of messenger RNA synthesis in eukaryotes begins with the TATA box-binding protein (TBP) recognizing the core promoter, which includes the transcription start site and the TATA consensus sequence. TBP is the DNA-binding subunit of the RNA polymerase II general transcription initiation factor known as transcription factor IID (composed of TBP and tightly-bound proteins known as TBP-associated factors or TAFs), and is primarily responsible for correct positioning of RNA polymerase II at the transcription start site. Sequence comparisons showed that the protein consists of a phylogenetically conserved, 180 amino acid C-terminal portion that contains two imperfect direct repeats. TBP binds to the TATA consensus sequence (TATAa/tAa/t) with high affinity (k_d=2-4x10^9M) and long half-life, recognizing determinants in the minor groove and promoting DNA bending. The N-terminal portion of TBP varies in length, shows little or no conservation among different organisms and is largely unnecessary for transcription in certain yeast strains.

Our earlier X-ray crystallographic studies of TBP have included structures of the apo-protein at a final resolution limit of 2.1Å [1,2], and of TBP complexed with a 14 base pair oligonucleotide (GCTATAAAAGGGCA) derived from the TATA element of the Adenovirus major late promoter, obtained at 2.25Å resolution [3]. Oscillation data collection using the X25 beam line in its focused monochromatic mode enabled us to extend the resolution limit to 1.9Å resolution, and this high-resolution structure has been refined to a crystallographic R-factor of 19.4% [4]. Further work on X25 has included data collection at comparable resolution limits from cocrystals of TBP complexed with variants of the TATA element. These studies have permitted us to make a systematic study of the mechanisms by which TBP recognizes DNA. A detailed comparision of a dozen high-resolution cocrystal structures is in preparation for publication.

[1] Nikolov, D.B., Hu, S.-H, Lin, J., Gasch, A. Hoffmann, A., Horikoshi, M., Chua, N.-H., Roeder, R.G.& Burley, S.K. (1992) Nature 360, 40-46.
[2] Nikolov, D.B. & Burley, S.K. (1994) Nature Structureal Biology 1, 621-636.
[3] Kim, J.L., Nikolov, D.B. & Burley, S.K. (1993) Nature 365, 520-527.
[4] Kim, J.L. & Burley, S.K. (1994) Nature Structural Biology 1, 637-653.

* This work was supported by the Howard Hughes Medical Institute.

X-ray standing wave structural study of Pb-sorbed natural calcite (1014) surface *	X25

Y. Qian, P. F. Lyman, M. J. Bedzyk (ANL and Northwestern Univ.), R. P. Chiarello, N. C. Sturchio (ANL), and L. E. Berman (BNL)

We have utilized x-ray standing waves (XSW) generated by dynamical Bragg diffraction to measure lattice locations of trace elements (Mn and Pb) within and at the surface of mineral calcite single crystals. Natural calcite samples were cleaved along the (10$\bar{1}$4) plane to obtain pristine surfaces. After cleavage, the sample was reacted with a dilute aqueous Pb solution for 92 hours to obtain Pb-sorbed surfaces. XSW measurements were then performed using the calcite (10$\bar{1}$4) Bragg reflection. The incident photon energy was 13.5 keV which is above the Pb L-III absorption edge. The measured coherent fractions (f) and coherent positions (P) are tabulated in Figure 1. Our XSW measurements show that the naturally occurring trace element Mn substitutes for Ca. For the Pb chemi-sorbed on the calcite surface, we found that Pb is also located on the calcite (10$\bar{1}$4) lattice plane where Ca atoms reside.

Table 1. Structural parameters determined by XSW

	f	P
Ca	0.66 ± 0.01	1.00 ± 0.01
Mn	0.57 ± 0.02	1.00 ± 0.01
Pb	0.62 ± 0.04	1.00 ± 0.01

Figure 1.

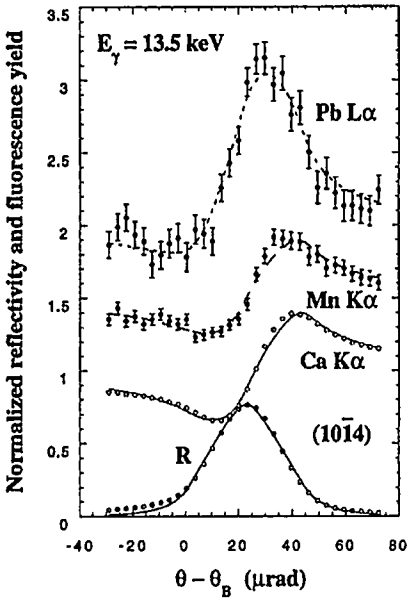


Figure 2.

* Work was sponsored by the U.S. Department of Energy, Office of Basic Energy Sciences, Division of Material Sciences, under contract W-31-109-ENG-38 and DE-AC02- 76CH00016 to the NSLS.

Site-selective EXAFS spectroscopy-II. High-resolution K_β emission and XANES spectra of nickel(II) complexes. High-resolution K'_β emission spectrum of Ni(II)-substituted rubredoxin *	X25

C. Randall (LBL/UC Davis), A. Froeschner (UC Davis), M. Grush (UC Davis) and S.Cramer (LBL/UC Davis)

We recently recorded emission and spin-selective XANES spectra of a variety of nickel-containing complexes, using an array of three spherically bent Ge(642) spectrographs. By monitoring at the K_β and K'_β emission energies, respectively, we were able to record the spin-selective excitation spectra shown in Figure 1. Note that the 1s→3d regions of the two spectra are strikingly different, while the lower energy EXAFS regions from 8380-8400 eV are nearly identical.

We also took the first emission spectrum of a nickel-containing protein (Figure 2). The sample was a 10 mM frozen solution of Ni(II)-substituted rubredoxin at liquid nitrogen temperature. This spectrum, the sum of three scans, shows the feasibility of our technique with protein samples. By optimizing our experimental technique, we will be able to record high-resolution XANES and EXAFS spectra of Ni-containing proteins such as hydrogenase and CO dehydrogenase.

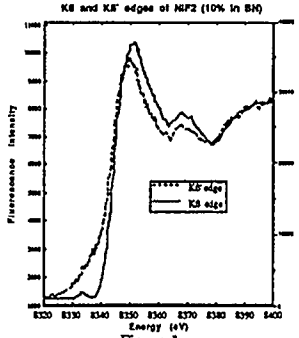


Figure 1.

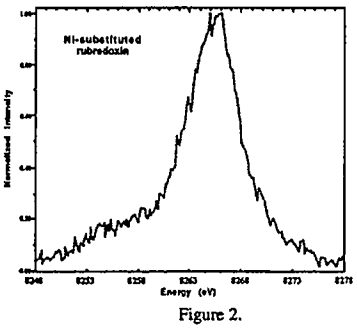


Figure 2.

* Work supported by the Department of Energy, Office of Health and Environmental Research,and by the National Institutes of Health, Grant GM-48145.

Transmitting beam position monitor and profiler tests *	X25

D. Shu, J. Barraza, Y. Li, and T. M. Kuzay (ANL)

Three styles of transmitting X-ray monitors [1] were tested using a focused white beam from a wiggler downstream of a Be window at the NSLS X-25 beamline. The tests were performed on a single 72 × 22 × .125 mm CVD diamond clamped to a cooling base, forming a 72 × 7 mm diamond aperture normal to the X-ray beam. Three sets of aluminum patterns were coated on the diamond to perform three X-ray monitor experiments: (1) a beam profiler, (2) a simulated 4-blade beam position monitor, and (3) a 4-quadrant area beam position monitor.

Using high-precision positioning stages, each pattern was scanned horizontally and vertically across the X-ray beam. The photo-emission signals were measured, indicating the following results.

The beam profile monitor consists of two 100 μm wide coated strips which are perpendicular to each other and cross the X-ray beam at 45 degrees from the horizontal. The signal from the each strip coating provides the integrated X-ray beam profile information. The 4-blade monitor, simulated by two pairs of 125 μm wide strips, performed as well as a typical 4-blade monitor and is extremely sensitive to beam motion fluctuations resulting from low frequency mirror vibrations and other sources. Figure 1 is a plot of the sensitivity data in 5 μm jump steps. The 4-quadrant area monitor, comprised of four aluminum coated areas, exhibited typical performance during a horizontal test scan. The monitor demonstrated high sensitivity in a 1 mm dynamic range. The tests also proved the viability of features for future designs: The 3000 – 4000 Å aluminum coating yields a good photo-emission signal in the microamp range, and the cooling of the CVD diamond was enhanced by clamping directly against the cooling base without additional electrical isolating interface. (This was a first).

In conclusion, these tests demonstrated, once again, the feasibility and the utility of CVD diamond foil used as a transmitting profiler and position monitor for hard X-ray applications.

[1] Patent applied for ANL-IN-92-28, 1992.

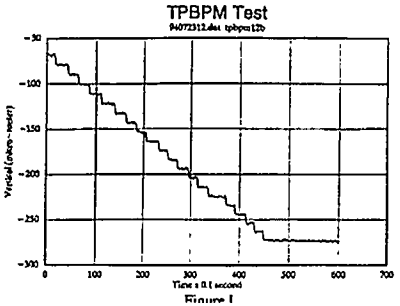


Figure 1.

* Research supported by the Department of Energy under Contract W-31-109-ENG-38.

Tricriticality in the phase diagram of stepped Si(113) surfaces	X25, X20

S. Song and S. G. J. Mochrie (MIT)

A striking change in surface morphology occurs at a faceting transformation, in which an initially uniform surface separathes into regions with different surface orientations. The morphology for a given themperature and orientation may be specified by means of an orientational phase diagram, analogous to the phase diagram of a fluid with the surface orientation (or sthep density) corresponding to the particle density. Attractive intheractions between fluid particles lead to condensation of a liquid in coexisthence with a vapor at the appropriathe temperature and densities. Therefore for attractive interactions between steps, faceting might occur. Such a possibility has been predithed, but has not previously been observed. For a fluid, special interest attaches to the liquid-gas critical point. In the same way that a near-critical fluid exhibits critical apolescence, so might a surface with mutually attracting stheps show step fluctuations that are manifest as a divergent surface roughness. Such a critical behaviour seems remarkable, but is nevertheless uncovered in the experiments reported here.

We studied sthepped Si surfaces miscut from the [113] direction towards [001] [1]. The phase diagram is shown in Fig. 1 [unavailable due to space constraints]. Solid lines indicathe phase boundaries; the dashed line corresponds to a triple point; solid circles and squares represent mesoscopic surface orientations measured for samples with macroscopic misorientations of 2.1° and 3.7°, respectively. Above 1223 K, there is a one-phase region (hatched in Fig. 1), where the surface is uniformly sthepped. We infer a continuous transformation versus orientation between theh stepped phase and the (113) facet above 1223K. Here we find increasing diffuse scatthering with decreasing temperature, which is the result of a corresponding increase in sthep fluctuations. Just as critical scatthering anticipates fluid phase separation, the sthep critical scattering found here precedes faceting. Fig. 2 [unavailable due to space constraints] highlights the sthep critical scattering by showing profiles at fixed surface normal wavevector transfer (L=2) for several thempeatures abote T_i on a log-log scale versus κ. (κ is the wave vector deviation from a specular condition along the surface.) The inset shows power-law behavior versus reduced themperature of the surface stiffness deduced from lineshape fits (solid lines) to the data shown.

Between 1223 and 1130 K, there is a two phase region (unhatched), so that the transformation versus orientation between the sthepped phase and the (113) facet is first order. A point separating a line of continuous phase transformation from a line of first order phase transformation is a tricritical point. Thus T_t=1223 K and zero misorientation angle is a tricritical point (open square in Fig. 1). The range of angles forbidden to the sthepped phase increases continuously versus themperature below T_t, reaching an angle of 6.4° by 1134 K. Below a triple point themperature of $T_3 = 1134 \pm 6$K (dashed line in Fig. 1), coexisthence between (113) and (114) facets, lying 5.7° from the [113] direction, replaces coexisthence between (113) facets and sthepped phase regions.

[1] S. Song and S.G.J. Mochris, Phys. Rev. Lett. 73, 995 (1194).

$Cr^{2+}/(Cr^{2+}+Cr^{3+})$ Measurements of Fe and Cr in Synthetic Olivine and Coexisting Glass as a Function of Oxygen Fugacity using Synchrotron micro-XANES	X26A

S. Bajt, S. R. Sutton (U. of Chicago and CARS), G. McKay (NASA/JSC), T. Mikouchi (U. of Tokyo), and J. S. Delaney (Rutgers U.)

Chromium partitioning between olivine and coexisting basaltic glass at 1400°C was studied as a function of fO_2 for a series of experimental charges synthesized at fO_2 between 4 log units above (IW+4) and 2 log units below (IW-2) the iron-wustite (IW) buffer. $Cr^{2+}/(Cr^{2+}+Cr^{3+})$ ratios in the olivine and glass were determined by measuring the valence-related energy shifts of spectral features in the Cr K XANES using synchrotron x-ray microprobe at beam line X26A. The XANES spectra were calibrated against a series of Cr valence standards (borosilicate glass and synthetic forsterite). Cr^{total} for the areas analysed (20 μm diameter on thin sections of the charges) were between 0.05 and 0.12 wt.%.

The transition of Cr^{3+} to Cr^{2+} occurs from IW+1.3 to IW-2 for olivine and from IW to IW-2 for glass. Thus, the stabilization of Cr^{2+} in olivine occurs at higher oxygen fugacity than in the coexisting glass. Despite this difference between olivine and glass, the partitioning of Cr^{total} remains relatively constant over the fO_2 range studied [1]. These results are unexpected and more experiments are being done to explore the critical region between IW-0.5 and IW-1.5. The variation of Cr^{2+}/Cr^{3+} in the olivine may correlate with variation in Fe content, perhaps indicating that Cr and Fe are swapping electrons to produce both 2+ and 3+ cations of both elements independent of the imposed oxygen fugacity. Measurements of $Fe^{3+}/(Fe^{2+}+Fe^{3+})$ are in progress on these and other samples.

[1] Mikouchi et al., LPSC XXV, 907 (1994).

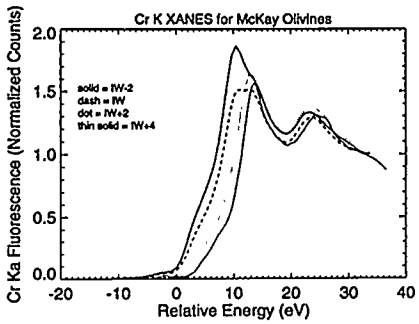


Figure 1. Cr K XANES spectra for four synthetic olivines produced at 1400°C and oxygen fugacities between−2 and +4 log units around the iron wustite buffer.

Assessment of the uncertainties and limitations of quantitative elemental analysis of individual fluid inclusions using synchrotron x-ray fluorescence *	X26A

R. J. Bodnar, R. J. Mavrogenes, A. J. Anderson (Virginia Tech.), S. Bajt, M. L. Rivers, and S. R. Sutton (Univ. of Chicago)

The uncertainties and limitations of synchrotron XRF analysis of individual fluid inclusions have been evaluated by analyzing synthetic fluid inclusions containing known concentrations of strontium chloride aqueous solutions. The geometries (depth below the mineral surface, thickness of inclusion, shape) were determined using a modified spindle stage attached to a petrographic microscope. Compositions of the fluids in inclusions were obtained from freezing point depression measurements of the inclusions and confirmed by atomic absorption analysis of the solution removed from the capsule after forming the inclusions. SXRF analyses were conducted at the National Synchrotron Light Source at the Brookhaven National Laboratory on beamline X26A using an 8 x 12 micron "white" X-ray beam.

Analyses of numerous inclusions from five different samples, each containing a different concentration of strontium chloride, were obtained. The precision of individual analyses is very poor, with a standard deviation of 10–39% of the mean value. However, analyses of a large number of inclusions in one sample provides a "mean" value that is very close to the known concentration in the inclusion. Our results suggest that the largest uncertainty in quantitative analysis of inclusions is associated with errors in determining the inclusion geometry or analytical volume.

Compared to analyses of homogeneous "thick" films, the detection limits for elements in fluid inclusions is orders of magnitude larger. This results because of the relatively small analytical volume of the inclusion, and because of absorption of the X-rays (produced in the inclusions) as they travel through the quartz host to the detector. For strontium, the detection limit in a typical (5-15 micron thick) inclusion approximately 10 microns below the crystal surface is on the order of 2000 ppm Sr. This detection limit is considerably larger than detection limits predicted for homogeneous "thick" films containing strontium.

* Work supported by NSF Grant EAR 9316051.

Synchrotron x-ray fluorescence and laser ablation ICP-MS microprobes: useful instruments for analysis of experimental run products and other small samples	X26A

Claude Dalpé and Don R. Baker (McGill Univ., Canada), and Steve R. Sutton (Univ.of Chicago)

The Synchrotron X-ray Fluorescence Microprobes (SXRFM) and Laser Ablation Microprobe-Inductively Coupled Plasma-Mass Spectrometer (LAM-ICP-MS) have been found to be efficient instruments for the accurate measurement of a large suite of trace elements in natural and synthetic minerals and glasses. The small beam sizes of both instruments (10 and 20μm diameter respectively) permit in situ analysis of samples whose cross-sections are as little as 500 μm^2. These instruments have been used to analyze experimentally produced crystals and glasses, natural minerals in petrogenetic thin sections, and fluid inclusions.

Optimization of both instruments was carried out using two basaltic glass standards. The sensitivity of both instruments behaves linearly at least up to 30 ppm for Rb, 1600 ppm for Sr, 25 ppm for Y, 300 ppm for Zr, and 100 ppm for Nb (the maximum concentrations of these elements in our standards). The lower limits of detection of the SXRFM for Rb, Sr, Y, Zr, and Nb are approximately 4 ppm based upon our standards, and the analyses have a precision of ±20 relative %. Lower limits of detection for the LAM-ICP-MS are approximately 1 ppm; these analyses have a precision ±10 to 15 relative %.

The SXRFM and the LAM-ICP-MS were used to measure concentration ratios (partition coefficients) between a Ti-rich calcic amphibole and a Ti-rich basanitic quenched glass produced in a piston-cylinder apparatus at 1100°C, 1.5 Gpa from a natural starting material. Partition coefficients (D Conc. in Ti-rich calcic amph./Conc. in Ti-rich quenched melt) determined by SXRFM for Sr, Y, and Zr are: DSr 0.32 (±0.04), DY 0.25 (±0.04), DZr 0.12 (±0.07). Partition coefficients determined by LAM-ICP-MS are: DRb 0.22 (±0.04), DSr 0.38 (±0.01), DY 0.33 (±0.03), DZr 0.12 (±0.01), DNb 0.05 (±0.01). Based on one standard deviation applied to each technique, the value of DZr determined by SXRFM and by LAM-ICP-MS is identical. Although not within error, DSr and DY determined by the different techniques are still quite similar. The LAM-ICP-MS was also used to measure partition coefficients for Ba, La, Ce, Nd, Sm, Eu, Hf, and Ta which are: DBa 0.28 (±0.01), DLa 0.04 (±0.005), DCe 0.07 (± 0.005), DNd 0.14 (±0.01), DSm 0.19 (±0.08), DEu 0.35 (±0.02), DHf 0.33 (±0.01), and DTa 0.07 (±0.02).

The main advantages of using the SXRFM rather than the LAM-ICP-MS are its smaller beam size and the fact that the SXRFM is a nondestructive technique. The LAM-ICP-MS ablates material from the specimen, up to a depth of a few hundred microns, resulting in significant destruction of the specimen. The advantage of the LAM-ICP-MS is its ability to analyze a larger suite of trace elements at higher precision and lower detection limits.

X-ray microprobe investigation of composition thresholds in the passivation of Fe-Cr alloys *	X26A

A. J. Davenport (BNL), M. Simmonds, M. Ryan, R. Newman (UMIST), S. R. Sutton, and S. Bajt (Univ. of Chicago)

It has long been known that alloying with chromium protects iron from corrosion. Theoretical work using percolation theory has predicted that there should be a well-defined threshold in the chromium concentration above which loss of iron is prevented by a protective layer of chromium oxide and below which dissolution of iron proceeds unchecked. The existence of such a threshold is presently being investigated with an x-ray microprobe study of compositionally graded thin metal films. These measurements were made possible by the use of a new 13-element Ge detector equipped with electronics capable of collecting and processing full spectra on each detector element allowing time-dependent data to be collected from samples under electrochemical control.

100Å films of Fe-Cr were deposited on Ta-coated (100Å) 6 μm Mylar by sputtering simultaneously from two targets (Fe and Cr) separated in space such that the final films have gradient in composition from 15–25% Cr across the 10cm width of the film. These films were then used to form the window of an electrochemical cell containing a reference electrode (mercury sulfate) and a counter electrode and an acetate buffer. At -1.5V(MSE), where neither metal dissolves, the ratio of counts in the Fe and Cr Kα peaks is a smooth function across the film, reflecting the initial linear composition gradient ((a) in the figure). After the potential is stepped to -0.75V where Fe is soluble and Cr is passive, there is a sharp transition in the Fe/Cr ratio that evolves with time ((b)-(e) in the figure). Above this transition, little dissolution takes place, preserving the Fe/Cr ratio but below it there is substantial dissolution of iron. The transition occurs in the region of 18–19%, consistent with theoretical predictions.

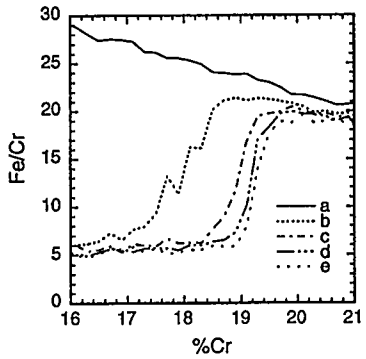


Figure 1.

* This work was supported in part by the U.S. DoE under Contract DE- AC02-76CH00016.

Synchrotron x-ray fluorescence trace element measurements on interplanetary dust particles as a method to infer their sources and interrelationships *	X26A

George J. Flynn (SUNY Plattsburgh), Stephen R. Sutton, and Saša Bajt (Univ. of Chicago)

Interplanetary Dust Particles (IDPs) collected from the Earth's stratosphereare believed to originate principally from asteroids and comets. Some cometary IDPs can be identified because they are heated severely during atmospheric deceleration. The lost of volatile elements on atmospheric entry can be used as an internal thermometer. To calibrate this thermometer we have compared trace element abundances in IDPs known to have been severely heated because of the presence of magnetite rims (formed during entry) and other IDPs which were heated less severely (no magnetite rims). The results indicate that of the elements from Cr to Mo the most extreme loss occurs for Zn, followed by Ge and Br. Trace element contents were also measured in meteorite fragments of composition and size similar to IDPs, the fragments were pulse heated to simulate entry heating, and the trace elements were remeasured. These results demonstrated that Zn loss was the most severe effect, and preliminary results suggest a loss temperature near 1100°C.

The matrix of the Semarkona meteorite, an unusual ordinary chondrite with a hydrated matrix, was examined to test the suggestion that hydrated IDPs (which are mineralogically distinct from most chondrites) might be derived from the Semarkona parent body. The trace element content of Semarkona matrix was distinctly different from that of hydrated IDPs, making a common origin unlikely.

Large micrometeorites (greater than 25 microns in size) are recovered from the polar ices as well as the stratosphere. Collection from the ice provides a much larger mass of sample than aircraft collection from the stratosphere, but the degree of alteration experienced by residence in the ice must be assessed. We compared the element abundances in stratospheric IDPs greater than 35 microns and polar micrometeorites from 50 to 100 microns in size. Much lower abundances of Ni, Ge, and Se in the polar micrometeorites suggest weathering losses, while much higher Pb abundances suggest contamination. Thus the polar micrometeorites, while inherently easier and less costly to collect, appear to suffer more severe terrestrial alteration than the stratospheric IDPs.

* Work Supported by NASA Planetary Materials and Geochemistry Grant NAG-459.

Iodine oxidation states in contact with minerals | X26A

M. Fuhrmann (BNL/DAT) and S. Bajt (Univ. of Chicago)

The environmental fate of iodine (especially ^{129}I) is of interest becauseit is a long-lived radionuclide that is present in radioactive waste and may be released during accidents such as that at Chernobyl. Studying the sorption/desorption processes of iodine in association with natural geologic materials and mineral separates provides basic information on the mobility of iodine under varying conditions.

Sample cells were prepared with Kapton windows and were filled with slurries of the powdered solids and a simulated groundwater containing high concentrations (1000 ppm) of iodine as IO_3^-. XANES analysis of iodine oxidation states was carried out in the fluorescence mode at the L_{III} edge at 4557 eV using the X-26A beamline. Three sets of reference reagents were used to assess our ability to distinguish between I^- and IO_3^-. In addition, elemental iodine was analyzed. Results are given in the table below. There were clear differences between I^- and IO_3^-; with the latter having a pronounced pre-edge structure due to the presence of oxygen, as well as a shift by about +6 eV in the edge. Iodide was distinguishable from elemental iodine by a -1 to -2 eV shift in the edge.

Most minerals tested did not alter the oxidation state of iodine. However one sample, Fithian illite, was a notable exception. Iodine in the water overlying the illite was present as I^-. The XANES scan of the solid phase in the same cell showed that iodine was present as I_2^0. Dramatic changes in concentration and observed staining of the cell indicate that iodine was being released as a vapor. It is unlikely that illite itself is responsible for this reaction.More likely it is the presence of a trace mineral such as pyrite. The implication is that an inorganic process may be important for establishing vapor phase remobilization of iodine contaminants that have been deposited in soils.

XANES ANALYSIS OF IODINE OXIDATION STATES

SAMPLE	EDGE (eV)	PRE-EDGE (eV)	SPECIES	COMMENT
Iodine	0	—	I_2^0	On Tape
$Cu(IO_3)_2$	+6.13	0	I^{+5} (IO_3^{-1})	Pellet
CuI	-1.77	—	I^{-1}	Pellet
$Na(IO_3)$	+6.2	-0.41	I^{+5} (IO_3^{-1})	Pellet
NaI	-2.1	—	I^{-1}	Powder on Tape
$K(IO_3)$	+5.0	+1.0	I^{+5} (IO_3^{-1})	Liquid in Cell
KI	+0.5	—	I^{-1}	Liquid in Cell
Limonite	+7.0	+0.5	I^{+5} (IO_3^{-1})	Liquid in Cell
Limonite	+7.0	+0.5	I^{+5} (IO_3^{-1})	Solid in Cell
Illite	-2.0	—	I^{-1}	Liquid in Cell
Illite	0	—	I_2^0	Solid in Cell
Kaolinite	+7.0	-1	I^{+5} (IO_3^{-1})	Solid in Cell
Biotite	+7.0	-1	I^{+5} (IO_3^{-1})	Solid in Cell

Figure 1.

Investigation of the pre-edge absorption XANES structure | X26A

Albert L. Hanson (BNL), and Saša Bajt (Univ. of Chicago)

The pre-absorption edge structure (XANES) of scattered X-rays is being studied with a high energy resolution wavelength dispersive spectrometer. The purpose of this work is to investigate if information concerning valence states of the scattering atoms can be extracted directly from the spectra taken with the high resolution spectrometer. If a sample contains an element in multiple valence states it is often difficult to use XANES for quantitative purposes and supplemental techniques are desirable. Initial work [1] indicates that at least in chromium, this is feasible using below edge X-ray emission spectra. High resolution spectra from iron compounds are more complicated. Presently an investigation is underway to determine if one can determine upper limits on the concentration of iron in the +0 oxidation state (metallic iron). The investigation has included using standards containing one valence state or a known ratio of two valence states, for example metallic iron and Fe^{2+}. Fe^{2+} and Fe^{3+}, etc.

[1] A.L. Hanson, S. Bajt, B.M. Johnson, M. Meron and M.L. Rivers, Phys. Lett. A184, 143 (1993).

Micro-XANES analysis of chromium in wood treated with chromated-copper-arensate (CCA) *	X26A

B. L. Illman (Univ. of Wisconsin), S. Bajt, and S. R. Sutton (Univ. of Chicago)

Synchrotron X-ray fluorescence spectroscopy (SXRF) is being used to analyze metal redox reactions involved in the mechanism of chromated-copper-arsenate (CCA) wood preservatives. Understanding the mechanism of CCA will help determine leachability of Cr, Cu and As into the environment, decrease the quantity of metal-based preservatives used and develop strategies for recycling and remediation of preservative-treated wood. The SXRF microprobe on beam line X26A at NSLS is being used to detect metals in situ in southern yellow pine lumber that was pressure-treated with CCA. Metal oxidation states are being determined on a small scale of 150 microns by measuring X-ray absorption near-edge structure (XANES). In our initial SXRF experiments, we tested wood for Cr(VI) and Cr(III) using established microXANES techniques [2]. Wood was treated with liquid Cr(VI)-CCA by standard methods [1]. Specimen were taken from the surface or from inner sections (1.3 cm from the surface) of lumber 2 years after CCA-treatment. The XANES spectrum for Cr(VI) has a strong pre-edge feature that is not present in the spectrum for Cr(III). Only the Cr(III) XANES spectra was detected on the surface and in the interior of the wood. The absence of spectra with the Cr(VI) pre-edge peak demonstrates the complete reduction in wood of toxic Cr(VI) to non-toxic Cr(III). It is significant that Cr is in the stable Cr(III) form on the surface and in the interior of wood 2 years after CCA-treatment. This work has shown that microXANES is an excellent, nondestructive technique to measure in situ concentrations of Cr, Cu and As on a small scale in the heterogeneous materials in wood. MicroXANES will be used in future analysis of CCA-treated wood taken from several environments to determine (a) binding of metals to wood components, (b) changes in the oxidation state and subsequent leachability of the metals.

[1] ASTM. 1991. Book of Standards. Am. Wood-Pres. Assoc., Woodstock, MD, USA.

[2] Bajt, S., S. B. Clark, S. R. Sutton, M. L. Rivers, J. V. Smith. 1993 Anal. Chem. 65(13):1800- 1804.

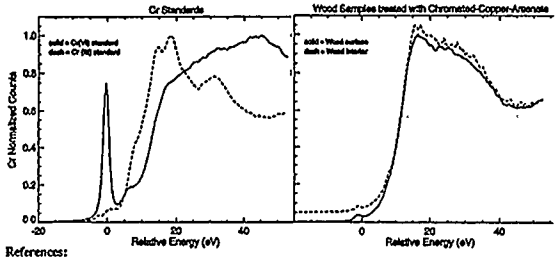


Figure 1.

* This research has been supported by the following grants: USDA 94-37103-1016, DOE DE-FG02-92ER14244, NASANAG9-106 and NSF EAR89-15699.

Manganese detection in wood using x-ray absorption near edge structure *	X26A

B. L. Illman (Univ. of Wisconsin), D. G. Schulze (Purdue Univ.), S. Bajt, S. R.Sutton (Univ. of Chicago)

Fungal degradation of lignocellulose in wood causes economic losses worldwide. Knowledge about fungal mechanisms is needed to develop environmentally compatible strategies to prevent degradation. Manganese redox reactions are involved in fungal mechanisms of lignocellulose degradation, but the role of Mn has not been clearly defined. White-rot fungi secrete a Mn oxidizing enzyme. Brown-rot fungi have a membrane-bound Mn oxidizing enzyme and secrete unknown Mn reductant(s). The synchrotron X-ray fluorescence (SXRF) microprobe at X26A at the National Synchrotron Light Source at Brookhaven National Laboratory is being used to detect and map Mn *in situ* during fungal decay of wood. Hemlock wood from lumber with commercially unacceptable "brown- stain" was scanned for Mn content, demonstrating for the first time that Mn is concentrated in 'stained' yearly rings of the wood. X-ray absorption near edge structure (XANES) was used to detect Mn oxidation states in southern yellow pine lumber during fungal decay. To determine Mn oxidation states in unknown samples, calibration curves were developed for Mn(IV)- birnessite, Mn(III)-acetate, Mn(IV)-oxide, Mn(II)-oxide, Mn(II)-fluoride, Mn(II)-carbonate, and Mn(II)-sulfate in solid and liquid form using parameters established at X26A (Schulze et al, 1994). Micro- XANES were obtained for sound wood and for dark stained, plus adjacent clear, regions of decayed wood. Our results demonstrate that Mn(II) was the primary oxidation state of Mn in southern yellow pine wood. During the early stage of decay by a white-rot fungus, a small amount of Mn(II) had been oxidized to Mn(IV). Brown-rot fungi did not oxidize detectable levels of Mn during early decay.

D.G Schulze, S.R. Sutton, and S. Bajt, Soil Science, 1994, (in press).

* Work supported by the following grants: USDA 94-37103-1016, DOE DEFG02-92ER14244, NASA NAG9-106 and NSF EAR89-15699.

Structure determinations on fluid inclusions in quartz using XAFS and micro-beam techniques	X26A

R. A. Mayanovic (Southwest Missouri State Univ.), A. J. Anderson (St. Francis Xavier Univ.), and S. Bajt (Univ. of Chicago)

Recent developments, principally involving focusing of x-rays, are permitting in situ structure studies of isolated microscopic regions within heterogeneous materials using synchrotron radiation. Structure determinations on fluid phases in inclusions are important for understanding the chemistry of fluid-related processes within the Earth's crust. We have for the first time successfully performed XAFS experiments on single fluid inclusions in quartz. Zn K-edge XAFS spectra were collected in the fluorescence mode, using a 30 mm^2 Si (Li) detector, from fluid inclusions in quartz. Beam line setup included a single Si(111) channel cut monochromator and a 8:1 ellipsoidal Al (Pt coated) focusing mirror, giving a flux of $\sim 1 \times 10^5$ photons/s at 230 mA of stored current.

Fig. 1 shows the XAFS spectrum having the highest signal-to-noise ratio and the two-point averaged data, from a single inclusion located $\sim 5\mu$m below the surface and measuring $\sim 60 \times 30$ μm. Zn Kα x-ray maps indicated a uniform distribution of zinc in the liquid phase of the inclusion: The total number of zinc ions, as estimated from XRF spectra, is $\sim 10^{11}$ - 10^{12}. We found good agreement between the inclusion XAFS data and that obtained from a zinc chloride ($ZnCl-4^{2-}$ aqueous solution (see Fig. 1). The Fourier transforms (Fts) were calculated from k^2 χ data (χ:isolated XAFS), over the 3.0-9.3$Å^{-1}$ range. The spectra used to fit the FT data (see Fig. 2) were generated using FEFF 5 [1]. Using a four-fold coordinated $ZnCl_4^{2-}$ model to fit the FT data in the 1.3–2.6Å range, we obtained the following: a ZnCl bond length of 2.33 $\pm$ 0.01 Å, a coordination number of 4.2 $\pm$ 0.4 atoms, and a mean square relative displacement of the atoms of 0.004 $\pm$ 0.001 $Å^2$. Our results indicate that the zinc complex in the liquid phase of the inclusions at room temperature is $ZnCl_4^{2-}$.

[1] J. Mustre de Leon et al., Phys. Rev. B 44, 4146(1991).

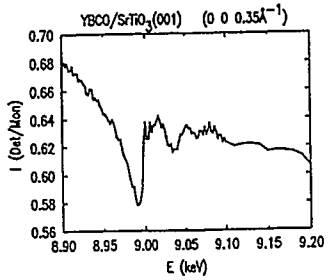


Figure 1. XAFS Spectra

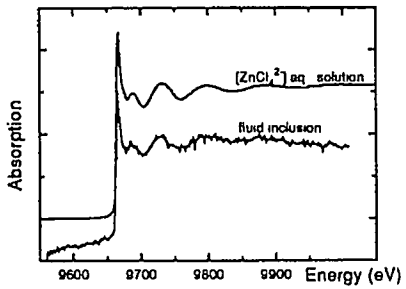


Figure 2. Fourier Transform Data

Intracrystalline trace element partitioning relative to surface structure: sectoral and intrasectoral zoning in topaz *	X26A

Paul A. Northrup and Richard J. Reeder (SUNY Stony Brook)

It has been determined that, during crystal growth, topaz ($Al_2SiO_4(F,OH)_2$) differentially incorporates trace elements into regions of the crystal that formed contemporaneously but under structurally nonequivalent surfaces [1]. Using the X-ray fluorescence microprobe at NSLS beamline X26A, we have measured different concentrations of Fe, Ti, As, Mn, Nb, V, Cr, and Ga in sample sections below nonequivalent crystal faces (sectors), as well as below nonequivalent vicinal faces of spiral-growth hillocks (subsectors). Recent work expanded our earlier findings to include samples from various worldwide sources, showing that such phenomena are common, if not prevalent, in the mineral topaz.

[1] P.A. Northrup and R.J. Reeder, American Mineralogist, 79 (1994).

* Work supported by NSF grant EAR 9204809.

Differential incorporation of trace elements during growth of grossular and apatite:intrasectoral zoning vs. Dissymmetrization	X26A

John Rakovan and Richard J. Reeder (SUNY Stony Brook)

Optically anomalous grossular crystals have been studied for minor-and trace-element distributions. Synchrotron X-ray fluorescence microanalysis line scans taken between coeval portions of adjacent subsectors (regions within a given sector that have grown by incorporation onto different vicinal surfaces) exhibiting different optical orientation show no detectable variation in the concentration of Fe, Mn, or Ga. This result contrasts with studies of apatite where trace element concentrations and optical properties vary between symmetrically nonequivalent subsectors (intrasectoral zoning).

Intrasectoral zoning in minerals is the result of differential incorporation by structural differences along growth steps of different orientation on a crystal face, and is constrained by the plane symmetry of the face, a subgroup of the crystal symmetry. A site in the crystal structure that is exposed along symmetrically different steps will have different surface expressions. Each of these protosites may have different affinities for a given element leading to differential partitioning and intrasectoral zoning. If there is no symmetry element contained within a given step then a site may have different expressions on one step. Such an arrangement is found on 110 of garnet. The surface symmetry of 110 is 2 mm, which constrains the structure of the 4 different growth steps to be equivalent. The step itself contains none of these symmetry elements, however, and along a given step the octahedral site of the structure has several different surface expressions. Differential affinities between protosites on a given step can then lead to ordering, which causes dissymmetrization. This has been suggested as the cause of optical anomalies in these samples. However, because of the symmetry constraints the ordering scheme taken by different steps and their associated subsectors will be equivalent. Therefore, there should be no differential partitioning between subsectors in these samples. Hence, dissymmetrization is found in grossular as in apatite, however, surface symmetry precludes intrasectoral zoning in grossular even after dissymmetrization. Both intrasectoral zoning and dissymmetrization in these samples are caused by differential incorporation between different protosites during growth. The relationships of such protosites to surface growth features and surface symmetry dictate which phenomena can occur.

Surface-controlled distributions of trace elements studied by synchrotron x-ray fluorescence microanalysis *	X26A

Richard J. Reeder (SUNY Stony Brook)

Calcite single crystals grown from low-temperature solutions containing various divalent metal ions (Co^{2+}, Ni^{2+}, Zn^{2+}, and Ba^{2+}) show spatial distributions of trace elements within the calcite that are controlled by the detailed structure of the growth surface. The 10-14 faces of calcite are found to grow by the spiral mechanism and exhibit polygonized growth spirals, or hillocks, composed of four vicinal faces. The vicinal faces are distinguished by the orientation of growth steps on them. The four step orientations, however, are not symmetrically equivalent; rather pairs of steps related by the c-glide symmetry operations are equivalent, giving two nonequivalent step types.

Previous studies have shown that divalent ions Mg^{2+}, Mn^{2+}, and Sr^{2+} are incorporated differentially into the nonequivalent steps during growth. This differential partitioning results in well-defined regions within the 10-14 growth sector that differ in trace element concentrations.

Similar growth experiments involving Co^{2+}, Ni^{2+}, Zn^{2+}, and Ba^{2+} were conducted to evaluate whether surface controlled differential incorporation occurs for these ions also. Suitably prepared sections through the 10-14 growth sector were analyzed by synchrotron X-ray fluorescence microanalysis at beamline X26A at the NSLS. Co^{2+}, Zn^{2+}, and Ba^{2+} were observed to exhibit differential incorporation patterns that were consistent with those previously observed. Difficulties with synthesis prevented analysis of the Ni^{2+} samples.

The findings further confirm the importance of ion size in controlling the step-specific preferences for incorporation. Ba^{2+} and Sr^{2+} show a preference for growth steps that are predicted to contain larger and geometrically less constrained kink sites. On the other hand, smaller ions, such as Co^{2+} and Mn^{2+}, show a preference for the nonequivalent step type containing smaller sites.

These observations emphasize the importance of surface structure - specifically surface incorporation sites - for controlling the incorporation of trace elements in crystals during growth.

* Work supported by NSF grants EAR 9204809 and EAR 9405046

Synchrotron XRF analysis of trace elements in zoned garnets from metasomatic contact metamorphic aureoles, SE Alaska *	X26A

C. K. Ridgway, H. H. Stowell (Univ. of Alabama), S. Bajt (Univ. of Chicago), P. Nuessle (Univ. of Georgia)

Contact metamorphic aureoles around ca. 94 Ma plutons of the Grand Island plutonic complex contain garnet-bearing pelitic schists that experienced multiple metamorphic and metasomatic events. These events are indicated by reaction history and major element compositional zoning determined by electron microprobe analysis (EMPA); garnets show oscillatory zoning in major elements and step-like changes in selected trace elements.

Pelitic garnets may contain tens to hundreds of ppm of trace elements. Understanding the incorporation of trace elements in the garnet lattice may provide constraints on understanding metamorphism and metasomatism during crystal growth and subsequent re-equilibration.

Major element chemistry on sample HS29j was obtained on the JEOL 8600 electron microprobe at the University of Alabama. Trace element concentrations were determined using synchrotron suggests cyclic zoning x-ray fluorescence analysis (SXRFA) on X26A beamline at NSLS. Samples were analyzed using the white x-ray beam with a Si(Li) energy dispersive system, a small detector aperture, an 85 micron Al filter, and a data acquisition time of ten minutes. EMPA analyses were used to calculate garnet densities and Fe concentrations were used for standardization. Zn, Cr, Ar, Y, Yb, Lu, Nd, Sm, and Tm were detected at concentrations of tens to hundreds of ppm using NRLXRF procedures. Analyses were collected along linear traverses and two dimensional grids.

EMPA suggests cyclic zoning in Ca (Fig. 1) and sympathetic zoning in Fe. Preliminary SXRFA indicate that the following trace elements are above detection limits (ppm): Cr 369–747, Zn 27–58, Y 2330–2770, Zr 60–85, and Yb 210–278. These results indicate that zonation of Zr, Y, and Yb correlate with the major element zoning of Ca (fig.1), Mn, and Fe. Future research will address the source of trace elements during garnet growth zoning; for example, trace element-rich metasomatic fluids or a local source episodically diluted by metasomatic fluids.

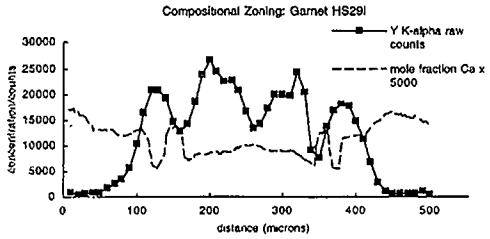


Figure 1.

* This research has been supported by BNL #94-X-878, and the Univ. of Alabama Hooks Fund and Council of Presidents.

Manganese oxidation states in *Gauemannomyces* infested wheat rhizospheres probed by micro XANES spectroscopy *	X26A

Darrell G. Schulze, Tina McCay-Buis, Don M. Huber (Purdue Univ.), and Stephen R. Sutton (Univ. of Chicago)

The take-all disease, caused by *Gaeumannomyces graminis* var. *tritici* (Ggt), is one of the world's major wheat diseases. Fungal oxidation of Mn in the soil surrounding the root prior to invasion of the pathogen has been hypothesized to predispose the plant to infection by compromising the root's defense mechanisms. For the first time, a direct test of this hypothesis has been possible using micro X-ray Absorption Near Edge Structure (XANES) spectroscopy to obtain spatially resolved Mn oxidation state information in and around live wheat roots growing in agar amended with 50 $\mu g\ g^{-1}$ Mn and infected with Ggt. Mn in clear agar occurred only as Mn^{2+}, while Mn around dark roots infected with Ggt was predominately present as Mn^{4+}. The micro-distribution of Mn oxidation state clearly showed the presence of Mn^{4+}-containing precipitates in the interior of a root infected with Ggt. This was consistent with the map of Mn concentration showing a relative accumulation of total Mn in the interior of the root as a result of Ggt catalyzed biomineralization of Mn. Application of this technique to roots growing in soil will make it possible to probe Mn chemistry during pathogenesis under conditions which closely simulate natural soil conditions.

* Work supported by US DOE Grant No. 92ER14244 (SRS).

Determination of manganese oxidation state in soils using x-ray absorption near-edge structure (XANES) spectroscopy *	X26A

Darrell G. Schulze (Purdue Univ.), Stephen R. Sutton, and Saša Bajt (Univ. of Chicago)

The soil-borne pathogen, *Gaeumannomyces graminis var. tritici*, which causes the take-all disease of wheat *(Triticum aestivum L.)*, may catalyze the oxidation of Mn^{2+} to Mn^{4+} in the rhizosphere as part of the infection process. Micro x-ray absorption near-edge structure (XANES) spectroscopy has the potential for studying Mn redox chemistry in the rhizosphere of live wheat plants growing in soil infested with G. graminis. The objective of this study was to develop calibration curves for determining Mn oxidations states in soil samples using micro-XANES spectroscopy. Oxidation state standards were prepared by mixing dry powders of $MnSO_{4}{}_{2}O$ as the Mn^{2+} source and a synthetic Na-birnessite, $Na_4Mn_{14}O27{*}9H_2O$, as the Mn^{4+} source to obtain mixtures with various Mn^{2+} mole fractions, $f(Mn^{2+})$, where $f(Mn^{2+}) = Mn^{2+}/(Mn^{2+}+Mn^{4+})$. Corundum ($\alpha$-$Al_2O_3$) was used as a diluent to prepare mixtures containing 50, 1000, and 100,000 $\mu g\ g^{-1}$ Mn. XANES spectra were obtained using the x-ray fluorescence microprobe on beamline X26A at the National Synchrotron Light Source, Brookhaven National Laboratory, Upton, NY. Quantitative analysis of Mn oxidation state is possible using either the energy of the pre-edge peak at 6540 eV or a ratio based on the intensity of the Mn^{2+} white line peak at 6552.6 eV divided by the intensity of the Mn^{4+} white line peak at 6560.9 eV. The white line intensity ratio is more sensitive, with an estimated lower detection limit of 20 $\mu g\ g^{-1}$ Mn using a 300×300 μm spot. The white line intensity ration predicts $f(Mn^{2+})$ with an accuracy of $\pm$ 0.1 mole fraction (95% confidence interval) over most of its range. The $f(Mn^{2+})$ for 4 air-dried, Indiana surface soils ranged from 0.26±0.1 to 0.44±0.1. Saturation and reduction of the soils for 5 days resulted in complete reduction of Mn in the soil matrix with XANES spectra indicating $f(Mn^{2+}) = 1.08\pm0.1$. Micro XANES spectroscopy shows considerable promise for studying the redox chemistry of Mn in soils under realistic moisture conditions.

* This research has been supported by the following grants: US DOE DE-FG02-92ER14244 (SRS) and DE-AC02-76CH00016 (BNL),and NAG W-3651 (SRS)).

X-ray microprobe tests of models for selenium and chromium heterogeneities in contaminated sediments	X26A

Tetsu K. Tokunaga (LBL), Stephen R. Sutton, Saša Bajt (Univ. of Chicago), Al Thompson, and Karen Chapman (LBL)

Our previous X-ray microprobe (NSLS X26A) studies demonstrated the existence of highly heterogeneous, small-scale distributions of selenium in contaminated sediments collected at Kesterson Reservoir, California. A model based on diffusion of soluble Se(VI) into localize reducing zones of sediments around decomposing plant tissue, where reduction to Se(IV) and Se(0) takes place, was developed. X-ray microprobe maps of total Se distributions in laboratory sediment simulations of the contaminated process were supportive of this model. However, the previous work relying on fluorescence spectra generated with white radiation lacked valence- specific information. Recent runs on X26A using monochromatic beams on similar sediment systems permitted extraction on oxidation state data necessary for more quantitative testing of the model. The valence-dependence of Se K-edge absorption energies was utilized to preferentially detect Se()), Se(IV), Se(VI), and total Se with different monochromatic incident beams. Deconvolution of the data provided maps of relative concentrations of these Se oxidation states in sediments surrounding a decomposing plant root. These micro-XANES maps show accumulation of Se(0) and some Se(IV), at the expense of Se(VI) reduction, in good agreement with model predictions.

Recent X-ray microprobe analyses (conducted at both ALS and the NSLS) of chromium- contaminated sediments showed highly heterogeneous patterns of trace element enrichment, similar to that previously found for Se-contaminated system. In both cases, most of the contamination was localized within a small portion (3 to 10Laboratory experiments on local redox-driven diffusive accumulations of Cr in sediments were analyzed with the X-ray microprobes at both the NSLS and ALS. AT the NSLS X26A, micro- XANES maps of Cr(III), Cr(VI), and total Cr were obtained in real time, tracking both diffusion and localized reduction of Cr(VI), and total Cr were obtained in real time, tracking both diffusion and localized reduction of Cr(VI). The hypothesis that reduction-driven diffusion can generate heterogeneities in small-scale spatial distributions of total Cr was supported by this micro- XANES experiment.

The highly localized nature of the Se and Cr distributions in these sediments may have been important implications on long-term persistence of trace element contaminants. Such localization may limit later reoxidation and transport required for *insitu* removal of trace element contaminants. These X-ray microprobe observations also raise new questions concerning spatial scales to which contaminant concentrations are assigned.

Zerovalent metal solubility in silicate melts | X26A

Shaoxiong Wen, Hanna Nekvasil (SUNY Stony Brook), and Saša Bajt (Univ. of Chicago)

Significant zervalent metal species solubility in silicate melts could explain the long-standing problem of the excess abundance of siderophile elements (Fe, Co, Ni, Cr, etc.) in the earth's mantle (Murthy, 1991). The most modern theories of earth formation suggest that the earth would be molten by the time it had grown to about one-tenth of its present mass (Tonks et al., 1991; Wetherill, 1990; Greenberg et al., 1979). The separation of the core from the mantle in this proto-earth started at this stage. The chemical equilibrium between the metal-rich core and the silicate-rich mantle requires some solubility by defining the activity of the metal species. However, the extent of this solubility remains a critical unknown.

The possibility of direct determination of zerovalent metal species in quenched silicate melts in provided by XANES. Based on the pre-edge features of various minerals, the relative pre-edge peak shift (to magnetite) in Fe K-edge spectra appears not to be significantly matrix dependent and a calibration relation between $Fe^{3+}/(Fe^{3+} + Fe^{2+})$ and relative pre-edge peak shift of Fe in minerals has been established (Bajt etal., in press). In order to extend this calibration is including Fe^0, a series of synthetic mixtures in the compositional space Fe^0 and Fe^{2+}. This initial calibration effort shows that the presence of Fe^0 will result in artificially high $Fe^{3+}/(Fe^{3+} + Fe^{2+})$ ratio if it is not accounted for.

A series of glass samples in system Fe_2SiO_4_$NaAlSi_3O_8$_O_2 synthesized at various temperatures along two fO_2 buffers (IW and MW) have been examined by Fe-XANES of X26A. The preliminary observation indicates that the relative shift trends are contracted in the glasses synthesized at those buffers because of the competing effect of Fe^0 and Fe^{2+}. Upton further calibration, quantitative measurement of Fe^0 looks feasible by combining Fe-XANES with additional analytical techniques such as Mossbauer spectroscopy.

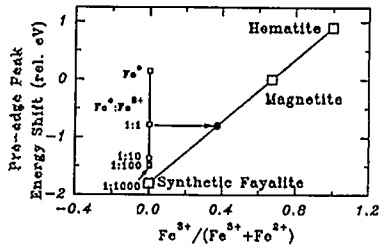


Figure 1. Effect of Fe^0 on calibration of Bajt et al. (in press). Horizontal arrow and filled cricle show the apparent $Fe^{3+}/(Fe^{3+} + Fe^{2+}$ ratio if Fe^0:Fe^{2+} =1:1and no Fe^{3+} is present.

X-ray topography of protein crystals | X26C

V. Stojanoff and D. P. Siddons (BNL)

White beam x-ray topography has been widely used to characterize growth defects in many kind of crystals, providing insight into crystal growth mechanisms. We describe the first application of the technique to the study of protein crystals. White radiation from beamline X26C at the National Synchrotron Light Soruce at Brookhaven National Laboratory was used in preliminary studies. For these studies lysozyme crystals grown by the hanging drop method in different conditions were employed. Results show that growth conditions and handling affected the quality of the crystals. Highly strained regions could be observed in some crystals as well as quite perfect regions with just a few dislocations could be observed in others. After the topography studies one of the crystals was submitted to a monochromatic beam on beamline X12C. The mosaicity measured was the same obtained for a crystal grown under the same conditions but not submitted to white radiation, suggesting that the topography exposure may not be too destructive which would allow systematic studies of the effects o different defect configurations and observed intensities.

[1] J. Miltat, Characterization of crystal growth defects by x-ray methods, ed. B.K. Tanner and D.K. bowen, Plenum Press, (1989), 401.

[2] A. McPherson, Preparation and analysis of protein crystals, R.E. Krieger Publishing Co., Malabar, FL, (1989)

[3] See for example (a) F. Rosenberger et al., J. Crystal Growth 129 (1993), 1; (b) J. Crystal Growth 129 (1993), 465. (b) L.J. De Lucas et al. to be published J. Crystal Growth.

Preliminary Laue diffraction studies on acetylcholinesterase | X26C

Joel L. Sussman, Raimond B. G. Ravelli (Lab. Crystallography and Structural Chemistry), Paul Singer, Bob Sweet, Mia L. Raves (Weizmann Inst. of Science), Joseph Nachman, Israel Silman (Weizmann Inst. of Science)

Acetylcholinesterase (AChE) plays a major role in the process of nerve signal transmission at the cholinergic synapse; by cleaving the neurotransmitter acetylcholine (ACh) at a very high turnover rate ($\approx 25,00\ \mathrm{sec}^{-1}$) it terminates transmission of one nerve impluse and clears the synapse for the next. Electrostatic calculations have indicated that the positively charged quaternary substrate is drawn towards the catalytic site, situated at the bottom of a narrow gorge (lined with aromatic residues), by the strong dipole moment of the enzyme. At the active site, ACh acylates Oγ of the active site serine, Ser200, with concomitant release of choline. Subsequent deacylation results in regeneration of the free enzyme. The fact that one of the raction products, choline, bears the same charge as the substrate, ACh, raises the question of its route of exit from the active site.

In order to attempt to observe the reaction process we have started to utilize Laue diffraction techniques. We have collected six frames of data on orthorhombic crystals of the native enzyme, using white radiation and exposure times of 40–60 msec. The relative unit cell parameters and crystal orientation were determined directly from the Laue pattern. Integration and normalization of the data within a wavelength range of 0.8–1.7 Åyielded 13,813 unique reflections up to a resolution of 2.8 Å, with an I/σ cutoff of 2.0. Initial refinement with this data set, with a completeness of only 37%, gave an R factor of 24% . The maps, though imperfect in some regions, clearly show the position of the catalytic triad residues.

Future studies will involve a trigonal crystal form which is more robust and therefore, should be more suitable for Laue diffraction studies. Our goal is to do time-resolved Laue experiments. These will involve two classes of compounds. The first class, caged derivatives of carbamylcholine, will release carbamylcholine upon photoactivation. This should lead to carbamylation of the active-site serine, with concomitant release of choline, followed by slow decarbamylation. The second class of compounds, being developed by Dr. Maurice Goeldner, at Universite Louis Pasteur in Strasbourg, should release choline upon photoactivation, thus permitting direct monitoring of the fate of this ligand.

Critical fluctuations in $RbCaF_3$ studied in reflection and transmission geometries | X27C

J. P. Hill, D. P. Siddons, J. B. Hastings (BNL), J-M. C. Gillet (Univ. Marne laVallee, France), D. McMorrow (Riso, Denmark), and A. Gibaud (Univ. Maine, France)

In recent years, the phenomena of critical fluctuations exhibiting two length scales has been observed in a variety of solid state systems, including structural transitions in the perovskites, magnetic transitions in some rare-earths and actinide compounds and in some incommensurate density wave systems. Although it is believed that the second length scale is associated with defects, the phenomenon remains poorly understood. In experiments performed with 8 keV x-rays, often only the sharp component is observed. This has led to speculation that it may be an intrinsic surface effect. It is possible, however that the density of defects is simply higher in the near-surface region. Further, resolution effects need to be considered carefully.

In these experiments, we have studied the critical fluctuations of $RbCaF_3$ with two complementary experimental configurations. In the first, experiments were performed in reflection at an incident photon energy of 8333eV for which the near-surface region is probed. The experiment was then repeated at 33332eV in transmission. By use of a mosaic dominated Ge(111) analyzer, the in-plane resolution function remained largely unchanged for these two configurations. Two differences in the data sets warrant comment. First, the temperature dependence of the order parameter is markedly smoother in the 8 keV data. The 33 keV data exhibits an apparent discontinuity (Fig. 1). The transition is believed to be first order and we speculate that the origin of this difference lies in strains present in the near-surface region of the crystal which cause a smearing of the transition. It is possible that it is just such surface strain fields which spawn the second length (longer) length scale in the critical fluctuations. Second, the visibility of the short length scale (i.e. conventional) fluctuations is greatly enhanced in the high energy data, which suggests that the broad component of the scattering exists preferentially in the bulk (Fig. 2). A full deconvolution of the 3D resolution function for each configuration needs to be performed before definitive statements may be made.

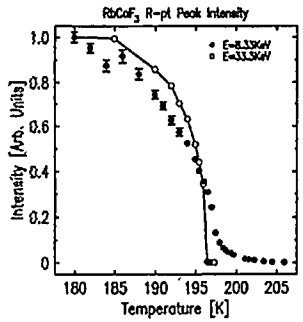


Figure 1.

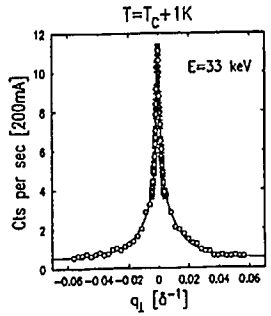
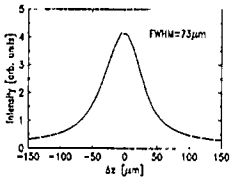


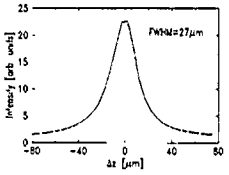
Figure 2.

X-ray Focusing with a Dynamically Bent multilayer * | X27C

M. Krisch (ESRF, France), W. Caliebe, and P. Siddons (NSLS)

Synthetic multilayers are already established optical elements in beamlines dedicated to, for example, x-ray small angle scattering or x-ray microprobe analysis. More generally, an optical scheme consisting of a focusing multilayer with a variable radius of curvature in conjunction with a silicon double-crystal monochromator represents an attractive alternative to a focusing crystal in Rowland circle geometry. We have realized such an setup in order to test the performance of the bending device and the optical scheme in conditions where the source size is strongly demagnified in one direction. The experiment was performed at the X27C station. The incoming x-rays were monochromatized by a Si (1,1,1) channel cut crystal to about 10 keV and the beamsize was limited to 2 mm horizontally and 3 mm vertically. The multi- layer consisted of 200 layers of W and Si with a thickness of 21.5 Å deposited on a flat Zerodur substrate. At 10 keV the Bragg angle is 1.65° and the measured angular acceptance for the flat multilayer was 0.02° The multilayer was mounted in a bending device, designed to provide an adjustable meridional radius between 40 and a few hundred meters with high precision. The x-rays were reflected in the vertical plane and the size of the line focus was measured by scanning a slit of 10 μm through the focal plane. The demagnification M of the source is given by q/p, where p and q are the distances source-multilayer and multilayer-focal plane, respectively. The experiment was performed at two different focal distances (2.3 m and 1 m), corresponding to M = 0.14 and 0.06. Figure 1 a) and b) show the intensity profile in the focal plane. The full-width-half-maxima (FWHM) of the curves are 73 μm and 27 μm, respectively. The results are in good agreement with the expected theoretical demagnification of the source size (about 0.35 to 0.4 mm). The increase of flux density, however, of 38 (in the case of M=0.14) and 10 (in the case of M=0.06) is lower than the expected value. This can be explained by the change of the incidence angle θ on the multilayer along its illuminated length l, which is given by $\Delta\theta = l * \sin(\theta)/2 * (1/q - 1/p)$. In our case $\Delta\theta$ is 0.032° (for M=0.14) and 0.081 (for M=0.06). These values are larger than the intrinsic angular acceptance of the multilayer and lead therefore to the observed decrease in throughput. The efficiency of such an optical scheme could be enhanced by utilizing a multilayer with a d-spacing gradient along the illuminated length. In this way, the variation of the angle of incidence is compensated by the change of the d-spacing. The compensation condition can be formulated as follows: $\Delta d/d = l * \cos(\theta)/2 * (1/q - 1/p)$. Figure 1, below: Intensity as a function of slit position in the focal plane for a) M = 0.14,radius:136 meter and b) M = 0.06, radius: 64 meter





* Supported by US DOE under contract # DE-AC02-76CH00016

PUBLICATIONS

NSLS USERS

Beamline U1

Chen, J.G., DeVries, B.D., Lewandowski, J.T., and Hall, R.B., "Direct Differentiation of Surface and Bulk Compositions of Powder Catalysts: Application of Electron-Yield and Fluorescence-Yield NEXAFS to $Li_xNi_{1-x}O$", *Catalysis Letters*, 23, 25-35, (1994).

Huang, S.X., Fischer, D.A., and Gland J.L., "The Correlation Between the Surface Configurations and Hydrogenolysis-Aniline on the Pt(111) Surface", *J. Of Vac. Sci. And Technol.*, A12/4, 2164-9, (1994).

Moodenbaugh, A.R., and Fischer, D.A., "Hole State Density and Super Conductivity in Oxygen Deficient $La_{2-x}Sr_xCuO_{4-y}$ and $Yba_2Cu_3O_{7-\delta}$" *Physica*, C230, 177-83, (1994).

Rightor, E., Mitchell, G.E., Leapman, R., Urquhart, S., Hitchcock, A., Fischer, D.A., Hunt, J., and Gland, J.L., "Polymer Characterization in the STEM by EELS and Comparison to Synchrotron and Gas Phase EELS Results", *Microbeam Analysis*, 2, 5264-5, (1993).

Schmidt, D.L., Coburn, C.E., DeKoven, B.M., Potter, G.E., Meyers, G.F., and Fischer, D.A., "A Water Based, Non-Stick, Hydrophobic Coating System", *Nature*, 368, 39-41, (1994).

Beamline U2B

Reffner, J., Carr, G.L., Sutton, S., Hemley, R.J., Williams, G.P., "Infrared Microspectroscopy at the NSLS", *Synch. Rad. News.*, 7/2, 30, (1994).

Beamline U3C

Andrews, A.B., Blyth, R.I.R., Arko, A.J., Joyce, J.J., Fisk, Z., Thompson, J.D., Bartlett, R.J.,Canfield, P.C., Olson, C.G., Benning, P., and Riseborough, P.S., "Temperature Dependence of the 4f PES Features and Hole Occupancy in Ytterbium Heavy Fermions", *Physica B*, 199/200, 15, (1994).

Blyth, R.I.R., Andrews, A.B., Arko, A.J., Joyce, J.J., Canfield, P.C., Bennett, B.I., and Weinberger, P., "Valence Band Photoemission and Auger Lineshape Study of Au_xPd_{1-x}", *Phys. Rev.*, B49, 16149, (1994).

Blyth, R.I.R., Andrews, A.B., Arko, A.J., Joyce, J.J., Canfield, P.C., Fisk, Z., Lahiase, U.G.L., and Delong, L., "Effects of Sub-Monolayer Coverages of Oxygen on the 4f Lineshapes of Cerium Compounds", *Surface Review and Letters*, 1, 3, (1994).

Diebold, U., Tao, H.-S., Shinn, N.D., and Madey, T.E., "Electronic Structure of Ultrathin Fe Films on TiO_2(110) Studied with Soft X-ray Photoelectron Spectroscopy and Resonant Photoemission", *Phys. Rev.*, B50, 14474, (1994).

Joyce, J.J., Arko, A.J., Andrews, A.B., and Blyth, R.I.R., "Photoemission and the Lack of a Kondo Scales", *Phys. Rev. Lett.*, 72, 1774, (1994).

Tao, H.-S., Diebold, U., Shinn, N.D., and Madey, T.E., "Surface Chemistry of PH_3, PF_3 and PC1_3 on Ru(0001)", *Surf. Sci.*, 312, 323, (1994).

Veal, B.W., Liu, R., Paulikas, A.P., Shi, H., Downey, J.W., Olson, C.G., Arko, A.J., Joyce, J.J., Blyth, R.I.R., "Electronic Structure Studies of $YBa_2Cu_3O_x$ ($6.2 < x < 6.9$)", *Surface Science Reports*, **19**, 121, (1993).

Beamline U4A

Andrews, A.B., Riffe, D.M., and Wertheim, G.K., "Surface Core-Level Shifts of Ta(110) and W(110) Versus Alkali-Metal-Atom Coverage: Implications for the Alkali-Metal—Substrate Interaction", *Phys. Rev.*, **B49**, 8396, (1994).

Breuer, K., Smith, K.E., Greenblatt, M., and McCarroll, W., "Electronic Structure of Surface Defects in K0.3MoO3", *J. Vac. Sci. Technol.*, **12**, 2196, (1994).

Smith, K.E., Breuer, K., Greenblatt, M., and McCarroll, W., "Fermi Surface of a Quasi-Low Dimensional Oxide Conductor", *Phys. Rev. Lett.*, **70**, 3772, (1993).

Smith, K.V., and Henrich, V.E., "Photoemission Study of Temperature- and Composition-Induced Metal-Insulator Transitions in Cr-Doped V203", *Phys. Rev.*, **B50**, 1382, (1994).

Wertheim, G.K., Riffe, D.M., and Citrin, P.H., "A Harmonic Surface Vibrations in Photoemission from Alkali Metals", *Phys. Rev.*, **B49**, 2277, (1994).

Wertheim, G.K., Riffe, D.M., and Citrin, P.H., "Nature of the Charge Localized Between Alkali Adatoms and Metal Substrates", *Phys. Rev.*, **B49**, 4834, (1994).

Beamline U4B

Chen, C.T., "Recent Advances in Soft-X-ray Absorption Spectroscopy", In X-ray Absorption in Bulk and Surfaces, edited by H.B. Garg, E.A. Stern, and D. Norman, World Scientific Publ., New Jersey, p. 61, (1994).

Idzerda, Y.U., Chen, C.T., Cheng S.F., Vavra, W., Prinz, G.A., Meigs, G., Lin, H. -J., and Ho, G. H., "Extraction of the Coefficient of Giant Magnetoresistance", *Appl. Phys. Lett.*, **64**, 3503, (1994).

Idzerda, Y.U., Gutierrez, C.J., Tjeng, L.H., Lin, H. -J., Meigs, G., and Chen, C.T., "Magnetic Circular Dichroism of Fe_xCo_{1-x} Single Crystal Thin Films", *J. Magn. Mater*, **127**, 109, (1993).

Kao, C.-C., Chen, C.T., Johnson, E.D., Hastings, J.B., Lin, H. -J., Ho., G.H., Meigs, G., Brot, J. -M., Hulbert, S. L., Idzerda, Y.U., and Vettier, C., "Dichroic Interference Effects in Circularly Polarized Soft-X-ray Resonant Magnetic Scattering", *Phys. Rev.*, **B50**, 9599, (1994).

Schirmer, J., Trofimov, A.B., Randall, K.J., Feldhaus, F., Bradshaw, A.M., Ma, Y., Chen, C. T., and Sette, F., "K-Shell Excitation of the Water, Ammonia, and Methane Molecules Using High Resolution Photoabsorption Spectroscopy", *Phys. Rev.*, **A47**, 1136 (1993).

Tjeng, L.H., Chen, C.T., Rudolf, P., Meigs, G., van der Laan, G., and Thole, B.T., "Magnetic Circularly Polarized 2p Resonant Photoemission of Nickel", *Phys. Rev.*, **B48**, 13378, (1993).

van Elp, J., George, S.J., Chen, J., Pang, G., Chen, C.T., Tjeng, L.H., Meigs, G., Lin, H.-J., Zhou, Z.H., Adams, M.W.W., Searle, B.G., and Cramer, S.P., "Soft X-ray Magnetic Circular Dichroism, a New Probe for Studying Paramagnetic Bioinorganic Systems", Proc. Natl. Acad. Sci. USA, **90**, 9664, (1993).

Beamline U4IR

Beden, B., Melendres, C.A., Bowmaker, G., and Moroni, V.A., "The Adsorption of CO and H_2O on Polycrystalline Gold, as Studied by Synchrotron Infrared Spectroscopy", edited by C.A. Melendres and A. Tadjeddine, Synchrotron Techniques in Interfacial Electrochemistry, Kluwer Academic Publishers, Dordrecht, The Netherlands, pp. 433, (1994).

Carr, G.L., Tanner, D.B., Etemad, S., and Inam, A., "Thin YBCO Films as Fast Infrared Detectors: Model Calculations and Experimental Results", *SPIE*, **2159**, 48, (1994).

Hartge, J., Forro, L., Mandrus, D., Martin, M.C., Kenziora, C., and Mihaly, L., "Tunneling and IR Spectroscopy on High T_c Superconductors", *J. Phys. Chem. Solids*, **54**, 1359, (1993).

Hemley, R.J., Soos, Z.G., Hanfland, M., and Mao, H.-K., "Charge Transfer States in Dense Hydrogen", *Nature*, **369**, 384, (1994).

Hirschmugl, C., Dumas, P., Chabal, Y., Hoffmann, F.M., Suhren, M., and Williams, G.P., "Dipole Forbidden Vibrational Modes for NO and CO Observed in the Far IR", *J. Elect. Spect.* **64**, 67, (1993).

Hirschmugl, C.J., Williams, G.P., Persson, B.N.J., and Volokitin, A.I., "Adsorbate Vibrational Dynamics in the Anomalous Skin Effect Region", *Surface Science*, **317**, L1141, (1994).

Hirschmugl, C.J. and Williams, G.P., "The Application of Infrared Synchrotron Radiation to the Study of Interfacial Vibrational Modes", *NATO ASI Series*, **432**, 387, (1994).

Hirschmugl, C.J., Williams, G.P., Chabal, Y.J., and Hoffmann, F.M., "Low Frequency Dynamics of CO/Cu - Breakdown of Born-Oppenheimer Approximation", *J. Vac. Sci. & Tech.*, **A12**, 2229 (1994).

Hoffmann, F.M., Persson, B.N.J., Walter, W., King, D.A., Hirschmugl, C.J., and Williams, G.P., "Anti-Absorption Resonances in Infrared Reflectance Spectroscopy of Alkali-Cu(111) Adsorbate Systems - Is the Ground State a Charge Density Wave Condensate?", *Phys. Rev. Letts.*, **72**, 1256, (1994).

Martin, M.C., Du, X., Kwon, J., and Mihaly, L., "Observation and Assignment of Higher Order Vibrations in the IR Transmission of C60 Crystals", *Phys. Rev.*, **B50**, 173, (1994).

Martin, M.C., Koller, D., Du, X., Stephens, P., and Mihaly, L., "Insulating and Conducting Phases of RbC60", *Phys. Rev.*, **B49**, 10818, (1994).

Martin, M.C., Koller, D., and Mihaly, L., "In-Situ IR Transmission Study of Rb and K Doped Fullerenes", *Phys. Rev.*, **B47**, 14607, (1993).

Meade, C., Reffner, J.A., and Ito, E., "Synchrotron Infrared Absorbency Measurements of Hydrogen in MgSiO3 Perovskite", *Science*, **264**, 1558, (1994).

Melendres, C.A., Beden, B., Bowmaker, G., Liu C., and Maroni, V.A., "Synchrotron Infrared Spectroscopy of H_2O Adsorbed on Polycrystalline Gold", *Langmuir*, **9**, 1980, (1993).

Reffner, J., Carr, G.L., Williams, G.P., Sutton, S., and Hemley, R.J., "Infrared Microspectroscopy at the National Synchrotron Light Source", *Synchrotron Radiation News*, **7/2**, 30, (1994).

Russell, A.E. and O'Grady, W.E., "Far-Infrared Synchrotron Radiation and the Electrochemical Interface", *NATO ASI Series*, **432**, 421, (1994).

Williams, G.P., "Fourier Transform Spectroscopy with Synchrotron Radiation in the Mid and Far Infrared with Extensions to the VUV and Soft X-ray Region", *SPIE,* **2089**, 62, (1993).

Beamline U5U

Garrison, K., Chang, Y., and Johnson, P.D., "On the Spin Polarization of Quantum Well States in Copper Thin Films Deposited on a Co(001) Substrate", *Phys. Rev. Lett.*, 71, 2801, (1993).

Johnson, P.D., Brookes, N.B., Chang, Y., and Garrison, K., "Spin Polarized Photoemission Studies of Quantum Well States in Thin Films", MRS Symp. Proc., **313**, 609, (1993).

Li, D., Zhang, J., Dowben, P.A., Garrison, K., Johnson, P.D., Tang, H., Walker, T.G., Hopster, H., Scott, J.C., Weller, D., and Pappas, D.P., "Canted Magnetic Moments at the Gd(0001) Surface", MRS Symp. Proc., **313**, 451, (1993).

Smith, N.V., Brookes, N.B., Chang, Y., and Johnson, P.D., "Quantum-Well and Tight-Binding Analyses of Spin-Polarized Photoemission from Ag/Fe(001) Overlayers", *Phys. Rev.*, **B49**, 332, (1994).

Smith, N.V., Hulbert, S.L., Johnson, P.D., and Erskine, J.L., "Spherical-Grating Monochromator System with Circular-Polarization Capability for the U5U Undulator at Brookhaven", *Nucl. Instrum. Meth.*, **A347**, 119, (1994).

Wu, S.C., Garrison, K., Begley, A.M., Jona, F., and Johnson, P.D., "Electronic Structure and Magnetism of the Rh {001} Surface", *Phys. Rev.*, **B49**, 14081, (1994).

Beamline U7

Anashin, V.V., Dudnikov, V.G., Malyshev, O.B., Osipov, V.N., Foerster, C.L., Jacobsen, F.M., Ruckman, M.W., Strongin, M., Kersevan, R., Maslennikov, I.L., and Turner, W.C., "Cold Beam Tube Photodesorption Experiments for the SSCL 20 TeV Proton Collider", *J. Vac. Sci. Technol.*, **A12/4**, 1663-1672, (1994).

Kuiper, P., and Dunlap, B. I., "The Absorption Peak at the Oxygen 1s Edge of O_2: Exchange Splitting, Ultrafast Diss., and Atomic-like Auger Spectra", *J. Chem. Phys.*, **100/6** , 4087-4092, (1994).

Moore, J.F., Strongin, D.R., Ruckman, M.W., and Strongin, M., "Deposition of Dielectric Thin Films by Irradiation of Condensed Reactant Mixtures", MRS Symp. Proc., **335**, 81-86, (1994).

Ruckman, M.W., and Strongin, M., "Monolayer Metal Films on Metallic Surfaces: Correlation Between Electronic Structure and Molecular Chemisorption", *Acc. Chem. Res.*, **27/8** , 250-256, (1994).

Ruckman, M.W., Xia, B., and Qui, S.L., "Adsorption of C_{60} on Ta(110): Photoemission and C K-edge Studies", *Phys. Rev.*, **B48/20**, 457-460, (1993).

Xia, B., Ruckman, M.W., and Strongin, M., "Photoelectron Study of Yb/C_{60} Bilayers and the Yb Fullerides formed at the Interfaces", *Phys. Rev.*, **B48/19**, 623-628, (1993).

Beamline U9B

France, L.L., Kieleczawa, J., Dunn, J.J., Luft, B.J., Hind, G., and Sutherland, J.C., "Evidence for an Alpha-Helical Epitope on Outer Surface Protein A from the Lyme Disease Spirochete, *Borrelia burgdorferi:* an Application of Steady-state and Time-resolved fluorescence Quenching Techniques", *Biochemica et Biophysica Acta,* **1202**, 287, (1993).

Polewski, K., Kramer, S.L., Kolber, Z.S., Trunk, J.G., Monteleone, D.C., and Sutherland, J.C., "Time-resolved Fluorescence Using Synchrotron Radiation Excitation: A Powered Fourth-Harmonic Cavity Improves Pulse Stability", *Rev. Sci. Instrum.*, **65**, 2562, (1994).

Suzuki, H., Scintillation Mechanisms of Cerium-Doped Rare Earth Oxyorthosilicates, PhD Thesis, Cal. Tech. University, (1994).

Suzuki, H., Tombrello, T.A., Melcher, C.L., Peterson, C.A., and Schweitzer, J.S., "The Role of Gadolinium in the Scintillation Processed of Cerium-doped Gadolinium Oxyorthosilicate", *Nucl. Instr. And Meth.*, **A346**, 510-521, (1994).

Suzuki, H., Tombrello, T.A., Melcher, C. L., and Schweitzer, J.S., "Energy Transfer From Gd to Ce in $Gd_2(SiO_4)O$:Ce", *J. Luminescence,* **60/61**, 963-966, (1994).

Suzuki, H., Tombrello, T.A., Melcher, C.L., and Schweitzer, J.S., "Energy Transfer Mechanism in $Gd_2(SiO_4)O$:Ce Scintillators", *IEEE Trans. In Nuclear Science*, 41, 681-688, (1994).

Beamline U10

Anashin, V., Malyshev, O., Osipov, V., Foerster, C., Ruckman, M., Strongin, M., Kersevan, A., Maslennikov, I., and Turner, W., "Cold Beam Tube Photodesorption Experiments for the SSCL 20TeV Proton Collider", VT-TUM1, AVS 40th National Symposium, *J. Vac. Sci. Techno.*, **A12/4**, 1663, (1994).

Barletta, W.A., Calderon, M., Foerster, C.L., Halama, H., and Korn, G., "Photo-Desorption from Copper Alloys", XVth. International Conference on High Energy Accel., *Int. J. Mod. Phys.*, **2A**, 358, (1993).

Calderon, M., Holdener, F., Barletta, W., Foerster, C.L., and Petersen, D., "Distributed Ion Pump Testing for PEP-II, Asymmetric B-Factory Collider", Proceedings 1993 IEEE Particle Accelerator Conf., p. 3876, (1993).

Foerster, C.L., Halama, H., and Korn, G., "Photo Desorption from Copper, Beryllium, and Thin Films", *J. Vac. Sci. Technol.*, **A10/4**, 2077, (1992)

Foerster, C.L., Lanni, C., Maslennikov, I., and Turner, W., "Photon Desorption Measurements of Copper and Copper Plated Beam Tubes for SSCL 20 TeV Proton Collider", *J. Vac. Sci. Technol.*, **A12**, 1673, (1994).

Maslennikov, I., Turner, W., Anashin, V., Malyshev, O., Osipov, V., Naxmov, V., Pindyurin, V., Salimov, A., Foerster, C.L., and Lanni, C, "Photodesorption Experiments on SSC Collider Beam Tube Configurations", Proceedings 1993 IEEE Particle Accel. Conf., p. 3876, (1993).

Beamline U11

Clay, J.T., Walters, E.A., Grover, J.R., and Willcox, M.V., "Photoionization of Gas-Phase Bromotrifluoromethane and Its Complexes with Methanol: State Dependence of Intracluster Reactions", *J. Chem. Phys.*, **101**, 2069, (1994).

Grover, J.R.,Cheng, B.-M., Herron, W.J., Coolbaugh M.T., Peifer, W.R., and Garvey, J.F., "Photoionization-induced Intracluster Reactions of Cholorbenzene/Ammonia Mixed Complexes", *J. Phys. Chem.*, **98**, 7479 (1994).

Kuo, S.C., Zhang, Z. Klemm, R.B., Liebman, J.F., Stief, L.J., and Nesbitt, F. L., "Photoionization of Hydroxymethyl (CD_2OH and CD_2OD) and Methoxy (CD_3O) Radicals: Photoion Efficiency Spectra, Ionization Energies, and Thermochemistry", *J. Phys. Chem.*, **98**, 4026, (1994).

Monks, P.S., Stief, L.J., Krauss, M., Kuo, S.C., and Klemm, R.B., "A Discharge Flow-Photoionization Mass Spectrometric Study of HOBr(X^1A'): Photoion Yield Spectrum, Ionization Energy, and Thermochemistry", *J. Chem. Phys.*, **100**, 1902, (1994).

Yencha, A.J., Devinder, K., Donovan, R.J., Kvaran, A., Hopkirk, A., Lefebvre-Brion, H., and Keller, F., "Ion-Pair Formation in the Photodissociation of HCl and DCl", *J. Chem. Phys.*, **99**, 4986, (1993).

Beamline U12B

Lyman, P.F., and Zehner, D.M., "Core-Level Spectroscopy Investigation of the $Mo_{0.75}Re_{0.25}$(100) Surface", Metallic Alloys: Experimental and Theoretical Perspectives, edited by J.S. Fulkner and R.G. Jordan, Kluwer Academic Publishers, Dordrecht, the Netherlands, p. 113, (1994).

Weitering, H.H., Chen, J., Perez-Sandoz, R, and DiNardo, N.J., "Electron Localization and the Nonmetal-to-Metal Transition at Ultrathin Alkali-Metal/Si(111) Interfaces", *Surf. Sci.*, **307**, 978, (1994).

Beamline U13UA

Dermody, G.S., The Development of a Transmission X-ray Flux Monitor for an Undulator Beam Line on a Vacuum-Ultraviolet Synchrotorn Storage Ring, MSC Dissertation, London University, (1994).

Lee, K., Hulbert, S., Kuiper, P., Ji, D, and Hanson, D.M., "Auger, Zero-Energy Photoelectron, Coincidence Spectroscopy (AZEPECO): Chemical-Site-Selective Auger Electron Spectroscopy", *Nuclear Instruments and Methods*, A347, 446, (1994).

Lee, K., Kim, D.Y., Ma, C.I., and Hanson, D.M., "Identification of the Core-Hole Excited States of N2: A Failure of the Equivalent Core Approximation", *J. Chem. Phys.*, **100**, 8550, (1994).

Beamline U13UB

Calvert, J.M., Koloski, T.S., Dressick, W.J., Dulcey, C.S., Peckerar, M.C., Cerrina, F., Taylor, J.W., Suh, D., Wood , II, O.R., and MacDowell, A.A., "Projection X-ray Lithography with Ultrathin Imaging Layers and Selective Electroless Metallization", *Opt. Engineer,* 32, 2437, (1993).

Calvert, J.M., Koloski, T.S., Dressick, W.J., Dulcey, C.S., Peckerar, M.C., Cerrina, F., Taylor, J.W., Suh, D., Wood, II, O.R., MacDowell, A.A. and D'Souza, R. M., "Soft X-ray (14 nm) Lithography with Ultrathin Imaging Layers and Selective Electroless Metallization", SPIE Proc., 1924, 30 , (1993).

Early, K., Tennant, D.M., Jeon, D.Y., Mulgrew, P.P., MacDowell, A.A., Wood, II, O.R., Kubiak, G.D., and Tichenor, D.A, "Characterization of AZ-PN114 Resist for Soft X-ray Projection Lithography", *App. Opt.*, 32, 7044-7049, (1993).

MacDowell, A.A., Bjorkholm, J.E., Early, K., Freeman, R.R., Himel, M., Mulgrew, P.P., Szeto, L. H., Taylor, D.W., Tennant, D.M., Wood, II, O.R., Boker, J., Eichner, L., Jewell, T.E., Silfvast, W.T., Waskiewicz, W.K., White, D.L., Windt, D.L., Wood, II, O.R., D'Souza, R.M., and Zernike, F., "Soft X-ray Projection Lithography Using a 1:1 Ring Field Optic", *App. Opt.,* 32, 7072-7078, (1993).

MacDowell, A.A., Wood, II, O.R., Calvert, J.M., and Koloski, T.S., "A New Surface Imaging Resist Technology for Soft-X-ray Projection Lithography", OSA Proceeding on Soft-X-ray Projection Lithography, edited by A.M. Hawryluk and R.H. Stulen, Optical Society of America, Washington, D.C., 18, 87-93, (1993).

Murphy, J.B., White, D.L., and MacDowell, A.A., "Synchrotron Radiation Sources and Condensers for Projection X-ray Lithography", *App. Opt.*, 32, 6920-6929, (1993).

Tennant, D.M., Fetter, L.A., Harriott, L.R., MacDowell, A. A., Mulgrew, P.P., Pastalan, J.Z., Waskiewicz, W.K., White, D.L., Windt, D.L., and Wood, II, O.R., "Mask Technologies for Soft X-ray Projection Lithography at 13nm", *App. Opt.,* 32, 7007-7011, (1993).

Beamline U14A

Shek, M.L., Miyano, K.E., Dong, Q.-Y., Callcott, T.A., and Ederer, D.L., "Preliminary Soft X-ray Studies of Beta -SiC", *J. Vac. Sci. Technology,* A12, 1079, (1994).

Stadnik, Z.M., Zhang, Z.M., Tsai, A.-P, and Inoue, A., " A Resonant Photoemission Study of the $Al_{65}Cu_{20}Ru_{15}$ Icosahedral Alloy", *J. Phys.: Condens. Matter,* 6, 1, (1994).

Zhang, G.W., Stadnik, Z.M., Tsai, A.-P., and Inoue, A., "Electronic Structure of Icosahedral $Al_{70}Pd_{20}Mn_{10}$", *Phys. Rev.,* B50, 6696, (1994).

Beamline U15

Lee, K., Hulbert, S., Kuiper, P., Ji, D., and Hanson, D.M., "Auger, Zero-Energy Photoelectron, Coincidence Spectroscopy (AZEPECO): Chemical-Site-Selective Auger Electron Spectroscopy", *Nucl. Instrum. and Meth.,* A347, 446, (1994).

Lee, K., Kim, D.Y., Ma, C.I., and Hanson, D.M., "Identification of the Core-Hole Excited States of N_2: A Failure of the Equivalent Core Approximation", *J. Chem. Phys.*, 100, 8550, (1994).

Ma, C.I., Lee, K., Kim, D.Y., and Hanson, D.M., "A Time-of -Flight Spectrometer for Use in Energy-Resolved, Auger-Electron, Multiple-Ion Coincidence Spectrometry", *Nucl. Instrum. and Meth.*, A347, 453, (1994).

Mahalingam, M., Lee, K., Ji, D., and Hanson DM., "High Resolution and High Sensitivity Instrumentation for Detection of Vis-UV Luminescence from Products of Core-Hole Decay", *Nucl. Instrum. and Meth.*, A347, 457, (1994).

Mochiji, K., Lee, K., Ma, C.I., Kim, D.Y., Mahalingam, M., and Hanson, D.M., "Photodissociation of SF_6 Near the F-1s Absorption Edge", *J. Vac. Sci. Technol.*, A12, 216, (1994).

Sambasivan, S., Hintz, P.A., Anderson, S.L., and Hanson, D.M., "An Experimental Approach to Elucidating Selective Solid-State Photochemistry Induced by Monochromatic X-rays", *Nucl. Instrum. and Meth.*, A347, 462, (1994).

Beamline X1A

Ade, H., Jacobsen, C., Kirz, J., Ko, C. -H., Lindaas, S., Williams, S., Zhang, X., Buckley, C., Anderson, E., Gonz, K., and Rothman, S., "Recent Developments in Scanning Soft X-ray Microscopy," Vacuum Ultraviolet Radiation Physics: Proceedings of the Tenth VUV Conference., Edited by F. J. Wuilleumier, Y. Petroff, and I. Nenner , Singapore, World Scientific, 523 - 533, (1993).

Ade, H., and Hsiao, B., "X-ray Linear Dichroism Microscopy", *Science,* **262** , 1427-1429, (1993).

Ade, H., "NEXAFS Microscopy of Polymeric Samples", *Synch. Rad. News* , 7/2 , 11-15, (1994).

Bennett, P.M., Foster, G.F., Buckley, C.J., and Burge, R.E., "The Effect of Soft X-Radiation on Myofibrils", *J. Microscopy* , 172 , 109-119, (1993).

Botto, R.E., Cody, G.D., Kirz, J., Ade, H., Behal, S., and Disko, M., "Selective Chemical Mapping of Coal Microheterogeneity by Scanning Transmission X-ray Microscopy", *Energy & Fuels,* **8** , 151-154, (1994).

Jacobsen, C., Lindaas, S., Williams, S., and Zhang, X., "Scanning Luminescence X-ray Microscopy: Imaging Fluorescence Dyes at Suboptical Resolution", *J. Microscopy* , 172 , 121-129, (1993).

Kirz, J., Ade, H., Anderson, E., Buckley, C., Chapman, H., Howells, M., Jacobsen, C., Ko, C. -H., Lindaas, S., Sare, D., Williams, S., Wirick, S., and Zhang, X., "New Results in Soft X-ray Microscopy", *Nucl. Instrum. and Meth,.* B87, 92-97, (1994).

Beamline X1B

Johnson, P.D., and Ma, Y., "Band Structure and X-ray Resonant Inelastic Scattering", *Phys. Rev.*, B49, 5024, (1994).

Neeb, M., Rubensson, J.-E., Biermann, M., and Eberhardt, W., "Coherent Excitation of Vibrational Wave Functions Observed in Core Hole Decay Spectra of O_2, N_2 and CO", *J. Electron Spectr.*, 67, 261, (1994).

Neeb, M., Rubensson, J.-E., Biermann, M., and Eberhardt, W., "Determination of the Exchange Splitting of the Shape Resonance of O2 Using the Core Hole Decay Spectrum as a Fingerprint", *Phys. Rev. Lett.*, 71, 3091, (1993).

Rubensson, J.-E., Eisebitt, S., Nicodemus, M., Boske, T., and Eberhardt, W., "Electron-Correlation in CaF_2 Studied in Threshold Excited Soft X-ray Fluorescence", *Phys. Rev.*, **B50**, 9035-9045, (1994).

Rubensson, J.-E., Eisebitt, S., Nicodemus, M., Boske, T., and Eberhardt, W., "Exchange-Split Ca $3s^{-1}3d$ states in CaF2 Observed in Threshold Excited Core-to-Core Fluorescence", *Phys. Rev.*, B49, 1507, (1994).

Beamline X2B

Schwartz, L. M., Auzerais, F., Dunsmuir, J., Martys, N., and Torquato, S., "Transport and Diffusion in Three Dimensional Composit Media", *Physica A*, 207, 28-36, (1994).

Beamline X3A2

Ade, H., and Hsiao, B.S., "R Polarization Dependent X-ray Microscopy", *Science*, 262, 1427-1429, (1993).

Ade, H., Hsiao, B.S., Mitchell, G., Cameron, S., and Cosstello, S., "X-ray Microscopy in Polymer Science: Prospects of a New Imaging Technique", Proc. 51St Annual Meeting of Microscopy Society of America, pp. 902, (1993).

Byrne, C.A., Desper, C.R., Schneider, N.S., Chu, B., and Gao, T., "Polyethylene-Based Polyurethane Block Copolymers", *Polymer Preprints*, 34, 602, (1993).

Cheng, S.Z.D., Wu, S.S., Chen, J., Zhuo, Q., Quirk, R.P., VonMeewall, E.D., Hsiao, B.S., Habenschuss, A., and Zschack, P.R., "Isothermal Thickening and Thinning Process in Low Molecular Weight Poly(ethylene Oxide) Fractions. 4. End Group Dependence", *Macromolecules*, 26, 5105-5117, (1993).

Chu, B., Harney, P.J., Li, Y., Linliu, K., Yeh, F., and Hsiao, B.S., "A Laser-Aided Prealigned Pinhole Collimator for Synchrotron X-rays", *Rev. Sci. Instrum.*, 65, 597, (1994).

Crawford, M.K., Harlow, R.L., McCarron, E.M., Farneth, W.E., Herron, N., Chou, H., and Cox, D.E., "Structural Phase Transitions and Interlayer Magnetic Interactions in $La_{2-x}Nd_xCuO_{4+\delta}$, *Phys. Rev.*, B47, 11623-11626, (1993).

deBoissieu, M., Stephens, P.W., Boudard, M., and Janot C., "Is the Al-Pd-Mn Icosahedral Phase Centrosymmetrical?", *J. Phys. Condens. Matter*, 6, 363, (1994).

deBoissieu, M., Stephens, P.W., Boudard, M., Janot, C., Chapman, D., and Audier, M., "Disorder and Complexity in the Atomic Structure of the Perfect Icosahedral Alloy AlPdMn", *Phys. Rev. Letts.*, 72, 3538, (1994).

Desper, C.R., Chu, B., Li, Y., and Byrne, C.A., "Morphology Studies of CHDI Urethane Elastomers by X-ray Diffraction Using Synchrotron Radiation", *Polymer Preprints*, 34, 612, (1993).

Gardner, K.H., Hsiao, B.S., and Faron, K.L., "Diffraction Studies of Polymorphism in Poly(aryl ether ketones)", Crystallization of Polymers, edited by M. Dosiere, Kluwer Academic, Dordrecht, pp. 443-448, (1993), and *ACS Polym. Prep.*, 33/1, 307, (1992).

Hsiao, B.S., and Gardner, K.H., "Time-Resolved X-ray Studies of Crystallization and Melting in Poly(aryl ether ether ketone)", Crystallization of Polymers, edited by M. Dosire, Vol. 405, Kluwer Academic, Dordrecht, the Netherlands, pp. 415-420, (1993).

Hsiao, B.S., Gardner, K.H., Wu, D.Q., and Chu, B., "Time-Resolved X-ray Studies of Poly(aryl ether ether ketone) Crystallization and Melting Behavior, Part 1: Crystallization", *Polymer*, 34, 3986-3995, (1993).

Hsiao, B.S., Gardner, K.H., Wu, D.Q., and Chu, B., "Time-Resolved X-ray Studies of Poly(aryl ether ether ketone) Crystallization and Melting Behavior, Part 2: Melting", *Polymer*, 34, 3996-4003, (1993).

Hsiao, B.S., Gardner, K.H., Wu, d.Q., Liang, B., and Chu, B., "Time-Resolved X-ray Study of Crystallization and Melting in Poly(aryl ether ether ketone)", *ACS Polym. Prep.*, 33/1, 265, (1992).

Hsiao, B.S., Kennedy, A.D., Leach, R.A., Barton, Jr., R., Seifert, S., and Zachmann, H.G., "Structure Development During Fiber Processing via Synchrotron X-ray Measurements", *Polym. Symp. Prep.*, 399-400, (1994).

van Smallen, S., deBoer, J.L., and Coppens, P., "Synchrotron Radiation X-ray Diffraction of Modulated Structures in Charge-Density-Wave Materials. Application to $NbSe_3$", *J. De Physique IV,* C2, 3, 89-96, (1993).

Wu, D.Q., Liang, B., Hsiao, B.S., Li, Y., and Chu, B., "Synchrotron SAXS Studies of NAFION Morphology", *ACS Polym. Prep.*, 33/1, 350, (1992).

Beamline X3B1

Bohle, D.S., Conklin, B.T., Cox, D., Madsen, S.K., Paulson, S., Stephens, P.W., and Yee, G.T., "Structural and Spectroscopic Studies of beta-Hematin the Heme Coordination Polymer in Malaria Pigment", Chapter in Inorganic and Organometallic Polymers II, ACS Symposium Series 572, edited by P. Wisian-Nielson, H.R. Allcock, and K.J. Wynne, ACS, pp. 497-515, (1994).

Chauvet, O., Oszlanyi, G., Forro, L., Stephens, P.W., Tegze, M., Faigel, G., and Janossy, A., "Quasi-One-Dimensional Electronic Structure in Orthorhombic RbC_{60}", *Phys. Rev. Letts.*, 72, 2721, (1994).

Crawford, M.K., Subramanian, M.A., Harlow, R.L., Fernandez-Baca, J.A., Wang, Z.R., and Johnston, D.C., "Structural and Magnetic Studies of Sr_2IrO_4", *Phys. Rev.*, B49, 9198-9201, (1994)

Faigel, G., Bortel, G., Oszlanyi, G., Pekker, S., Tegze, M., Stephens, P.W., and Liu, D., "Low-Temperature Phase Transition in C_{60}-*n*-pentane", *Phys. Rev.*, B49, 9186, (1994).

Kao, Y.H., "Nondestructive Characterization of Interfacial Microstructures in Multilayer Semiconductors Using Synchrotron Radiation Techniques", Proc. First International Symposium on Control of Semiconductor Interfaces,, *Elsevier Science*, p. 333, (1994).

Koller, D, Martin, M.C., Stephens, P.W., and Mihaly, L., "A Chamber for the *in-situ* IR Measurement of C_{60} Thin Films While Doping with Alkali Metals", *Rev. Sci. Instrum.*, 65, 760, (1994).

Krol, A., Soo, Y.L., Huang, S., Ming, Z.H., Kao, Y.H., Munekata, H., and Change, L.L., "Effects of Local Structures on Material Properties: Mn in III-V Diluted Magnetic Semiconductors ",Proc. 21St International Conf. On the Physics of Semiconductors, Beijing, China, 1992, p. 1896, (1994).

Krol, A., Soo, Y.L, Ming, Z.H., Kao, Y.H., Munekata, H., and Chang, L.L., "Formation of Mn-As Clusters in $In_{1-x}Mn_xAs$ diluted Magnetic Semiconductors", *Mat. Res. Soc. Symp.Proc.*, 290, 245, (1993).

Lommen, A., Heiney, P.A., Vaughan, G.B.M., Stephens, P.W., Liu, D., Li, D., Smith, A.L., McGhie, A.R., Strongin, R.M., Brard, L., and Smith, A.B., III, "Structure and Phase Transition of the 6,5-Annulene Isomer of $C_{61}H_2$", *Phys. Rev.*, B49, 12572, (1994).

Martin, M.C., Koller, D., Du, X., Stephens, P.W., and Mihaly, L., "Insulating and Conducting Phases of RbC_{60}", *Phys.Rev.*, B49, 10818, (1994).

Ming, Z.H., Krol, A., Soo, Y.L., Kao, Y.H., Park, J.S., and Wang, K.L., "Microscopic Structures of Interfaces in $Si_{1-x}Ge_x$/Si Heterostructures and Superlattices Probed by X-ray Scattering and Fluorescence", Proc. 21st International Conf. On the Physics of Semiconductors, Beijing, China, 1992, p. 405, (1994).

Munekata, H., Chang, L.L., Krol, A., Soo, Y.L., Huang, S., Ming, Z.H., and Kao, Y.H., "Local Structures in III-V Diluted Magnetic Semiconductor (In,Mn)As", *J. Crystal Growth,* 127, 528, (1993).

Sandford, D., Fendorf, M., Stacy, A.M., Holstein, W.L, and Crawford, M.K., "Observation of Hendricks-Teller Partial Order in a Tetragonal Cuprate Superconductor: $La_{1.68}Nd_{0.14}Na_{0.10}K_{0.082}CuO_4$", *Phys. Rev. B,* **50**, 9419, (1994).

Stephens, P.W., Bortel, G., Faigel, G., Tegze, M., Janossy, A., Pekker, S., Oszlanyik, G., and Forro, L., "Polymeric Fullerene Chains in RbC_{60} and KC_{60}", *Nature,* **370**, 637, (1994).

Beamline X4

Coleman, D.E., Berghuis, A.M., Lee, E., Linder, M.E., Gilman, A.G., Sprang, S.R., "Structures of Active Conformations of $G_{i\alpha}1$ and the Mechanism of GTP Hydrolysis", *Science,* **265**, 1405-1412, (1994).

Fandl, J.L, Tobkes, N.J., McDonald, N.Q., Hendrickson, W.A., Ryan, T.E., Nigam, S., Acheson, M. A., Cudny, H., and Panayotatos, N., "Characterization and Crystallization of Recombinant Human Neurotrophin-4", *J. Biol. Chem* ., **269**, 755-759, (1994).

Hendrickson, W.A., "MAD Phasing for Macromolecular Crystal Structures", in Resonant Anomalous X-ray Scattering: Theory and Applications, edited by G. Materlik, K. Fischer and C.J. Sparks, Elsevier, Amsterdam, p. 159-173, (1994).

Leahy, D.J., Erickson, H.P., Aukhil, I., Joshi, P., and Hendrickson, W.A., "Crystallization of a Fragment of Human Fibronectin: Introduction of Methionine by Site-Directed Mutagenesis to Allow Phasing via Selenomethionine", *Proteins,* **19**, 48-54, (1994).

Martin, L.J., Bardwell, J.C.A., and Kuriyan, J., "Crystal Structure of the DsbA Protein Required for Disulphide Bond Formation *in vivo*", *Nature* , **365**, 464-468, (1993).

Wu, H., Lustbader, J.W., Liu, Y., Canfield, R.E., and Hendrickson, W.A., "Structure of Human Chorionic Gonadotropin at 2.6Å Resolution from MAD Analysis of the Selenomethionyl Protein", *Structure,* **2**, 545-558, (1994).

Beamline X5

Ruth, C., et. al, "First Measurements of the Reaction $^3He(\gamma,p)X$ with Polarized Photons", *Phys. Rev. Letts.,* **71**, 617, (1994).

Sandorfi, A.M., et al., "The E2/M1 Mixing Ratio in the Excitation of the Δ from Polarized Photo-Reactions:", *Few-Body Systems, Suppl.*, 7, 317, (1994).

Sandorfi, A.M., et al., "The E2 $N \rightarrow \Delta$ Transition from Polarized Compton Scattering", Proc. Particles and Nuclei Int. Conf., PANIC-XIII, Perugia, Italy, edited by A. Pascolini, World Scientific, Singapore, pp. 459, (1994).

Tedeschi, D.J., et al, "Exclusive Photodisintegration of ^3He with Polarized Photons", *Phys. Rev. Letts.,* **73**, 408, (1994).

Beamline X6A

Lee, P.L., Beno, M.A., Jennings, G., Ramanathan, M., Knapp, G.S., Huang K., Bai, J., and Montano, P.A., "An Energy Dispersive X-ray Absorption Spectroscopy Beamline, X6A, at NSLS", *Rev. Sci. Instrum.*, 65, 1, (1994).

Lee, P.L., Beno, M.A., Knapp, G.S., and Jennings, G., "Continuous Energy Diffraction Spectroscopy: A New D-Space Matching Technique for Energy Dispersive Synchrotron Radiation Diffraction", *Rev. Sci. Instrum.*, 65, 2206, (1994).

Beamline X6B

Cai, Z. H., Lai, B., Yun, W.B., McNulty, I., Huang, K.G., and Russell, T.P., "Observation of X-ray Speckle by Coherent Scattering at Grazing Incidence", *Phys. Rev. Lett.*, 73, 82, (1994).

Chen, L.X., Bowman, M.K., Wang, Z.Y., Montano, P.A., and Norris, J.R., "Structural Studies of Photo-Induced Intramolecular Electron Transfer in Cyclopentadienyl Nickelnitrosyl", *J. Phys. Chem.*, 98, 9457-64, (1994).

Foiles, C.L., Loloee, R., and Rahman, S., "Diffraction of Co/X (X=Mo, Cu) Multilayers Using Anaomalous Dispersion Enhancement,", MRS Symposium Proceedings, 307, 305, (1993).

Staub, U., Antonio, M.R., Soderholm, L., Guillaume, M., Henggeler, W., and Furrer, A., ""Tb Oxidation State and Hybridization in $Y_{0.9}Tb_{0.1}Ba_2Cu_3O_{7-\delta}$ (δ=0.02, 0.84): An Magnetic Susceptibility and X-ray Absorption Study, *Phys. Rev., B.*, 50, 7085-91, (1994).

Beamline X7A

Clearfield, A., "Crystal Structure Determination From X-ray Powder Diffraction Data", *Rigaku Journal*, 11, 1-3, (1994).

Cox, D.E., and Wilkinson, A.P., "Powder Diffraction Studies Using Anomalous Dispersion", Resonant Anomalous X-ray Scattering, Theory and Applications, edited by G. Materlik, C.J. Sparks and K. Fischer, p.p. 195-219, (1994).

Elder, S.H., DiSalvo, F.J., Parise, J.B., Hriljac, J.A., and Richardson, Jr., J.W., "The Synthesis and Structural Characterization of Na_3WO_3N", *J. Solid State Chem.*, 108, 73-79, (1994).

Fischer, J.E., "Disorder in C_{60} Intercalation Compounds and Implications for Superconductivity", *Mol. Cryst. Liq. Cryst.*, 244, 295-298, (1994).

Fischer, J.E., and Heiney, P.A., "Order and Disorder in Fullerene and Fulleride Solids", *J. Phys. Chem. Solids*, 54, 1725-1757, (1993).

Hriljac, J.A., Moodenbaugh, A.R., and Xu, Y., "Neutron-Diffraction Study of Reduced and Reoxidized $YBa_2(Cu_{0.90}Co_{0.10})_3O_{7-\delta}$, *Physica C*, 219, 315-326, (1993).

Hriljac, J.A., and Torardi, C.C., "Synthesis and Structure of the Novel Layered Oxide $BiMo_2O_7OH2\bullet H_2O$", *Inorg. Chem.*, 32, 6003-6007, (1993).

Jephcoat, A.P., Hriljac, J.A., Finger, L.W., and Cox, D.E., "Pressure-Induced Orientational Order in C_{60} at 300 K", *Europhys. Lett.*, 25, 429-434, (1994).

Kniaz, K., Fischer, J.E., Zhu, Q., Rosseinsky, M.J., Zhou, O. and Murphy, D.W., "C_{60} Orientational Ordering in Superconducting Na_2RbC_{60}", *Solid State Comm.*, 88, 47-50, (1993).

La Placa, S.J., Bringley, J.F., Scott, B.A., and Cox, D.E., "Structure of $La_2Cu_2O_5$ by High Resolution Synchrotron X-ray Diffraction", *Acta Cryst.*, C49, 1415-1417, (1993).

Leonowicz, M.E., Lawton, J.A., Lawton, S.L., and Rubin, M.K., "MCM-22: A Molecular Sieve With Two Independent Multidimensional Channel Systems", *Science*, 264, 1910-1913, (1994).

Lobo, R.F., Pan, M., Chan, I., Li, H.X., Medrud, R.C., Zones, S.I., Crozier, P.A., and Davis, M.E., "SSZ-26 and SSZ-33: Two Molecular Sieves With Intersecting 10- and 12-Ring Pores", *Science*, 262, 1543-1546, (1993).

Marler, B., Deroche, C., Gies, H., Fyfe, C.A., Grondey, H., Kokotailo, G.T., Feng, Y., Ernst, S., Weitkamp, J., and Cox, D.E., "The Structure of Zeolite ZSM-23 (MTT) Refined From Synchrotron X-ray Powder Data", *J. Appl. Cryst.*, 26, 636-644, (1993).

McCusker, L.B., "Advances in Powder Diffraction Methods for Zeolite Structure Analysis", *Stud. Surf. Sci. Catal.*, 84, 341-356, (1994).

Mehta, A., and Heaney, P.J., "Structure of $La_2NiO_{4.18}$", *Phys. Rev.*, B49, 563-571, (1994).

Parise, J.B., Corbin, D.R., Abrams, L., Northrup, P., Rakovan, J., Nenoff, T.M., and Stucky, G.D., "Structural Relationships Among Some BePO-, BeAsO-, and AlSiO-RHO Frameworks", *Zeolites*, 14, 25-34, (1994).

Poojary, D.M., and Clearfield, A., "Structure Refinement of Large-Pore Aluminophosphate Molecular Sieve, H1, by Rietveld Methods", *Zeolites*, 13, 542-548, (1993).

Poojary, D.M., Hu, H.L, Campbell III, F.L., and Clearfield, A., "Determination of Crystal Structures From Limited Powder Data Sets: Crystal Structure of Zirconium Phenylphosphonate", *Acta. Cryst.*, B49, 996-1001, (1993).

Poojary, D.M., Zhang, Y., Cox, D.E., Rudolf, P.R., Cheng, S., and Clearfield, A., "Synthesis and Crystal Structures of Aluminum, and Iron Phosphites", *J. Chem. Cryst.*, 24, 155-163, (1994).

Rosenfeld, H.D., and Egami, T., "A Model of Local Atomic Structure in the Relaxor Ferroelectric $Pb(Mg_{1/3}Nb_{2/3})O_3$", *Ferroelectrics*, 150, 183-197, (1993).

Schirber, J.E., Overmyer, D.L., Bayless, W.R., Rosseinsky, M.J., Murphy, D.W., Zhu, Q., Zhou, O., Kniaz, K., and Fischer, J.E., "Fullerene Superconductors: Phase Stability and Anomalously Low T_c's in Some Ternary Compounds", *J. Phys. Chem. Solids*, 54, 1427-1431, (1993).

Tse, J.S., Klug, D.D., Ripmeester, J.A., Desgreniers, S., and Lagarec, K., "The Role of Non-Deformable Units in Pressure-Induced Reversible Amorphization of Clathrasils", *Nature*, 369, 724-726, (1994).

Vaughan, G.B.M., Heiney, P.A., Cox, D.E., Fischer, J.E., McGhie, A.R., Smith, A.L., Strongin, R.M., Cichy, M.A., and Smith III, A.B., "Structural Phase Transitions and Orientational Ordering in C_{70}", *Chem. Phys.*, 178, 599-613, (1993).

Zhu, Q., Zhou, O., Fischer, J.E., McGhie, A.R., Romanow, W.J., Strogin, R.M., Cichy, M.A., and Smith III, A.B., "Unusual Thermal Stability of Site-Ordered MC_{60} Rocksalt Structure (M=K, Rb, Cs)", *Phys. Rev.*, B47, 13948-13951, (1993).

Zhu, Q., Fischer, J.E., and Cox, D.E., "Is K_3C_{60} a Line Phase?", Springer Series in Solid State Science, edited by H. Kuzmany, and S. Roth, 117, pp. 168-173, (1994).

Beamline X7B

Norby, P., Christensen, A.N., and Hanson, J.C., "In Situ Studies of Zeolite Syntheses Using Powder Diffraction Methods. Crystallization of "Instant Zeolite A" Powder and CoAPO-5", *Studies in Surf. Sci. & Catal.*, 84, 179-186, (1994).

Stahl, K., and Hanson, J., "Real-Time X-ray Synchrotron Powder Diffraction Studies of the Dehydration Process in Scolecite and Mesolite", *J. Appl. Cryst.*, 27, 543-550, (1994).

Beamline X8A

Samson, J.R., He, Z. X., Bartlett, R.J., and Sagurton, M., "Direct Measurements of He^+ Ions Produced by Compton Scattering Between 2.5 and 5.5 KeV", *Phys. Rev. Lett.*, 72, 3329, (1994).

Beamline X8C

Alkire, R.W., Sullivan, E.P., Michaud, F.D., Trela, W.J., Bartlett, R.J., "The X8C Duel Wire Beam Position Monitor", *Nucl. Instrum. And Meth. In Phys. Res.* A350, 13-16, (1994).

Barford, D., Flint A.J., and Tonks, N.K., "Crystal Structure of Human Protein Tyrosine Phosphatase 1B", *Science*, 262, 1397-1404, (1994).

Boles, J.O., Lewinski, K., Kunkle, M., Odom, J.D., Dunlap, R.B., Lebioda, L., and Hatada, M., "Bioincorporation of Telluromethionine into Buried Residues Dihydrofolate Reductase", *Nature Struct. Biol.*, 1, 283, (1994).

Pedersen, L.C., Yee, V.C., von Dasswo, G., Hazeghazam, M., Reeck, G.R., Stenkamp, R.E., and Teller, D.C., "The Corn Inhibitor of Blood Coagulation Factor XIIa, Crystallization and Preliminary Crystallographic Analysis", *J. Mol. Biol.*, 236, 385-387, (1994).

Beamline X9B

Asturias, F.J., Fischetti, R.F., and Blasie, J.K., "Changes in the Profile Structure of the Sarcoplasmic Reticulum Membrane Induced by Phosphorylation of the Ca +2 ATPase Enzyme in the Presence of Terbium: A Time-Resolved X-ray Diffraction Study", *Biophys. J.*, 66, 1653-1664, (1994).

Asturias, F.J., Fischetti, R.F., and Blasie, J.K., "Changes in the Relative Occupancy of Metal-Binding Sites in the Profile Structure of the Sarcoplasmic Reticulum Membrane Induced by Phosphorylation of the Ca +2 ATPase Enzyme in the Presence of Terbium: A Time-Resolved, Resonance X-ray Diffraction Study", *Biophys. J.*, 66, 1665-1677, (1994).

Auld, D.S., "Low-Temperature Stopped Flow Rapid-Scanning Spectroscopy: Performance Tests and Use of Aqueous Salt Cryosolvents", *Methods in Enzymology,* 220, 543-565, (1993).

Blackburn, N. J., Barr, M.E.,Woodruff, W.H.,Van der Ooost, J., and de Vries, S., "Metal-Metal Bonding in Biology: EXAFS Evidence for a 2.5 A Copper-Copper Bond in the Cu_A Center of Cytochrome Oxidase", *Biochemistry,* 33, 10401-10407, (1994).

Briggs, J., and Caffrey, M., "The Temperature-Composition Phase Diagram of Monomyristolein in Water: Equilibrium and Metastability Aspects", *Biophys. J,* 66, 573-587, (1994).

Cheng, A.C., Hogan, J.L., and Caffrey, M., "X-rays Destroy Lamellar Structure of Model Membranes", *J. Mol. Biol,* 229, 291-294, (1993).

Cheng, A., Hummel, B., Menchke, A., and Caffrey, M., "Kinetics and Mechanism of the Barotropic A Lamellar Gel/Lamellar Liquid Crystal Phase Transition in Fully Hydrated DHPE: A Time-Resolved X-ray Diffraction Study Using Pressure-Jump", *Biophys. J.,* 67, 293-303, (1994).

Chung, H., and Caffrey, M., "The Neutral Area Surface of the Cubic Mesophase: Location and Properties", *Biophys. J,* 66, 377-381, (1994).

Chung, H., and Caffrey, M., "The Curvature Elastic-Energy Function of the Lipid-Water Cubic Mesophase", *Nature,* 368, 224-226, (1994).

Chupa, J.A., Xu, S., Fischetti, R.F., Strongin, R.M., McCauley, Jr., J.P., Smith, III, A.B., Blasie, J.K., Peticolas, L.J., and Bean, J.C., "A Monolayer of C 60 Tethered to the Surface on an Inorganic Substrate: Assembly and Structure", *J. Am. Chem. Soc.*, 115, 4383 (1993).

Frisbie, S.M., and Chance, M.R., "Human Cobalophilin: The Structure of Bound Methylcobalamin and a Functional Role in Protecting Methyl Cobalamin from Photolysis", *Biochemistry,* 32, 13886-13892, (1993).

Klein, M.P., Sauer, K., and Yachandra, V.K. , "Perspectives on the Structure of the Photosynthetic Oxygen Evolving Manganese Complex and its Relation to the Kok Cycle", *Photosynth. Res.*, 38, 265-277 (1993).

Liang, W., Latimer, M.J., Dau, H., Roelofs, T.A., Yachandra, V.K., Sauer, K., and Klein, M.P., "Correlation Between Structure and Magnetic Spin State of the Manganese Cluster in the Oxygen-Evolving Complex of Photosystem II in the S_2 State: Determination by X-Ray Absorption Spectroscopy", *Biochemistry,* 33, 4923-4930, (1994).

Murphy, M.A., Blasie, J.K., Peticolas, L.J., and Bean, J.C. , "X-ray Iterferometry/Holography for the Unambiguous Determination of the Profile Structures of Single Langmuir-Blodgett Monolayers", *Langmuir,* 9, 1134-1141, (1993).

Pollock, D.W., Williamson, K.J., Weber, K.S., Lyons, L.J., and Sharpe, L.S., "Ion Pairing and Ionic Conductivity in Amorphous Polymer Electrolytes: A Structural Investigation Employing EXAFS", *Chem. Mater.*, 6/11, 1912, (1994).

Powers, L., "Biomolecular Materials and Design (Molecular Electronics and Molecular Electronic Devices)", *CRC Press,* III, 211-218, (1994).

Powers, L., Sinclair, R., Chance, B., and Reddy, K.S. , "The Structure-Function Relationship of the Active Sites in Haemoprotein Catalysis", *Synch. Rad. Biosciences,* 4/4-7, 302-311, (1994).

Scheuring, E., Sagi, I. , and Chance, M.R., "Sulfur Containing Cobalamins: X-Ray Absorption Spectroscopic (XAS) Characterization", *Biochemistry*, 33, 6310-6415, (1994).

True, A.E., Scarrow, R.C., Randall, C.R., Holz, R.C., and Que, Jr., L., "EXAFS Studies of Uteroferrin and its Anion Complexes", *J. Am. Chem. Soc.*, 115, 4246-4255, (1993).

Vallee, B.L., and Auld, D.S., "Cocatalytic Zinc Motifs in Enzyme Catalysis", *Proc. Natl. Acad. Sci*, 90, 2715-2718, (1993).

Van Elp, J., Peng, G., Searle, B.G., Mitra-Kirtley, S., Huang, Y.H., Johnson, M.K., Zhou, Z.H., Adams, M.W.W., Maroney, M.J., and Cramer, S.P., "Electronic Structure and Symmetry in Nickel L Edge X-ray Absorption Spectroscopy: Application to a Nickel Protein", *J. Am. Chem. Soc.*, 116, 1918-1923, (1994).

Wang, J., Caffrey, M., Bedzyk, M.J., and Penner, T.L., "Structural Changes in Model Membranes Monitored by Variable Period X-ray Standing Waves", *J. Phys. Chem.*, 98, 10957-10968, (1994).

Wang, J., Wallace, C., Clark-Lewis, I., and Caffrey, M., "Structure Characterization of Membrane Bound and Surface Adsorbed Protein", *J. Mol. Biol.*, 237, 1-4, (1994).

Whitehead, J.P., Gurbiel, R.J., Bagyinka, C., Hoffmann, B.M., and Maroney, M.J., "The Hydrogen Binding Site in Hydrogenase: 35-GHz ENDOR and XAS Studies of the Ni-C Active Form and the Ni-L Photoproduct", *J. Am. Chem. Soc.*, 115, 5629-5635, (1993).

Xu, S., Fischetti, R.F., Blasie, J.K., Peticolas, L.J., and Bean, J.C., "Profile Structures of Self-Assembled Monolayers on Ge/Si Multilayer Substrates by X-ray Interferometry/Holography", *J. Phys. Chem.*, 97, 1961-1969.

Yachandra, V.K., DeRose, V.J., Latimer, M.J., Mukerji, I., Sauer, K., Klein, M.P., "A Structural Model for the Photosynthetic Oxygen Evolving Manganese Complex in Research in Photosynthesis", edited by N. Murata, Vol. II, pp. 281-287, Kluwer, Dordrecht, the Netherlands, (1993).

Yachandra, V.K., DeRose, V.J., Latimer, M.J., Mukerji, I., Sauer, K., and Klein, M.P. , "A Structural Model for the Photosynthetic Oxygen Evolving Manganese Complex in Synchrotron Radiation in Biosciences", edited by B. Chance, et. al., pp. 275-283, Oxford University Press, New York, (1994).

Yachandra, V.K., DeRose, V.J., Latimer, M.J., Mukerji, I., Sauer, K., and Klein, M.P., "A Structural Model for the Photosynthetic Oxygen Evolving Manganese Complex", *J. App. Physics*, 1/32, S32-2, 523-526, (1993).

Yachandra, V.K., DeRose, V.J., Latimer, M.J., Mukerji, I., Sauer, K., and Klein, M.P., "Where Plants Make Oxygen: A Structural Model for the Photosynthetic Oxygen Evolving Manganese Cluster", *Science*, 260, 675-679, (1993).

Zang, Y., Pan, G., and Que, Jr., L., "First Diferric Complex with an Fe_2 (u-O) Core. Structure and Reactivity of ({Fe_2(u-O)(u-OH)(6TLA)$_2$}(CIO4)3", *J. Am. Chem. Soc.* , 116, 3653-3654, (1994).

Zhang, K., and Auld, D.S., "XAFS Studies of Carboxypeptidase A: Detection of a Structural Alteration in the Zinc Coordination Sphere Coupled to the Catalytically Important Alkaline pK", *Biochemistry*, 32, 13844-13851, (1993).

Zhu, T., and Caffrey, M., "Thermodynamics, Thermomechanical and Structure Properties of an Asymmetric Phosphatidylcholine", *Biophys. J*, 65, 939-954, (1993).

Beamline X10A

Behal, S.K., Chludzinski, J.J., Disko, M.M., Garner, R.T., Liang, K.S., Lohse, D.J., and Milner, S.T., "Morphology and Miscibility of Miktoarm Styrene-Diene Copolymers and Terpolymers", *Macromolecules,* **26**, 5812, (1993).

Disko, M.M., Liang, K.S., Behal, S.K., Roe, R.J., and Jeon, K.J., "Catenoid-Lamellar Phase in Blends of Styrene-Butadiene Diblock Copolymer and Homopolymer", *Macromolecules,* **26**, 2983, (1993).

Fenter, P., Eberhardt, A., and Eisenberger, P., "Self Assembly of n-Alkyl Thiols as Disulfides on Au(111)", *Science*, **266**, 1216 (1994)

Liu, G.-Y., Fenter, P., Chidsey, C.E.D., Ogletree, D.S., Eisenberger, P., Salmeron, M., "An Unexpected Packing of Fluorinated n-Alkane Thiols on Au(111)", *J. Chem. Phys.* **101**, 4301 (1994)

Liu, Y., Zhao, W., Zheng, X., King, A., Singh, A., Rafailovich, M.H., Sokolov, J., Dai, K.H., Kramer, E.J., Schwarz, S.A., Gebizlioglu, O., and Sinha, S.K., "Surface-Induced Ordering in Asymmetric Block Copolymers", *Macromolecules,* **27**, 4000, (1994).

Shen, Y., Safinya, C.R., Liang, K.S., Ruppert, A.F., and Rothschild, K.J., "Stabilization of the Membrane Protein Bacteriorhodopsin to 140° C in Two-Dimensional Films", *Nature*, **366**, 48, (1993).

Sirota, E.B., Singer, D.M., and King, Jr., H.E., "Structural Effects of High Pressure Gas on the Rotator Phases of Normal Alkanes", *J. Chem. Phys.*, **100**, 1542, (1994).

You, H. and Nagy, Z., "Application of X-ray Techniques for the Study of Electrochemical Interfaces", *Electrochemistry*, **2**, 21, (1993).

You, H. and Nagy, Z., "Oxidation-reduction-induced Roughening of Pt(111) Surface", *Physica B,* **198**, 187 (1994).

Beamline X10C

Davenport, A.J., Sansone, M., Bardwell, J.A., Aldykiewicx, Jr., A.J., Taube, M., and Vitus, C.M., "*In Situ* Multielement XANES Study of Formation and Reduction of the Oxide Film on Stainless Steel", *J. Electrochem. Soc.,* **141**, L6, (1994).

Gea, Y. Model Compound Synthesis and Physical Studies on Enzymes from Molybdenum-Containing Mesophilic and Tungsten-Containing Hyperthermophilic Organisms, Ph.D. Dissertation, State University of New York at Stony Brook, December, (1993).

Gorbaty, M.L., Kelemen, S.R., Vaughn, S.N., Sansone, M., and Kwiatek, P.J., "The Chemistry of Sulfur During Hydropyrolysis of Coals", *ACS Fuel Chem. Div. Preprints*, **39/3**, 757, (1994).

Beamline X11

Barkyoumb, J.H., Mansour, A.N.,Chakrabarti, K., and Mathur, V.K., "EXAFS Study of the Local Environment of the Thalium Ion in $CaSO_4$: Tm Dosimetric Phosphors", *Rad. Protection Dosimetry*, 47, 59 (1993).

Barkigia, K.M., Renner, M.W., Furenlid, L. R., Medforth, C.J., Smith, K.M., and Fajer, J., "Crystallographic and EXAFS Studies of Conformationally Designed Nonpolar Nickel(II) Prophyrins", *J. of Am. Chem. Soc.* 115, 3627 (1993).

Bunker, B.A., Wang, Z., and Islam,Q.,"X-ray Studies of Off-Center Ions and Ferroelectricity in PbS_xTe_{1-x} and $Zn_xCd_{1-x}Te$ Alloys", *Ferroelectrics*, 150, 171 , (1993).

Chartier, P., Balasubramanian, M., Brewe, D., Manzur, T., Pease, D., Budnick, J., Huang, L., Law, C., Russell, S., and Kimball, C., "Site Selectivity in Fe Doped ß Phase NiAl", *J. Appl. Phys.* 75, 8 (1994).

Fendorf, S.E., Lamble, G.M., Stapelton, M.G., Kelley, M.J., and Sparks, D.L., "Mechanisms of Chromium(111) Sorption on Silica. 1. Cr(111) Surface Structure Derived by Extended X-ray Absorption Fine Structure Spectroscopy", *Env. Science and Tech.*, 28, 284 (1994).

Fendorf, S.E., Sparks, D.L., Lamble, G.M., and Kelley, M.J., "Applications of X-ray Absorption Fine Structure Spectroscopy to Soils", *Soil Science Society of America Journal*, 58, 1583-1595, (1994).

Frenkel, A., Stern, E.A., Voronel, A., Qian, M., and Newville, M., "Buckled Crystalline Structure of Mixed Ionic Salts", Phys. Rev. Lett., 71, 34, (1994).

Frenkel, A., Stern, E.A., Voronel, A., Qian, M., and Newville, M., "Solving the Structure of Disordered Mixed Salts", *Phys. Rev.*, B49, 11662, (1994).

Hathaway, K.B., Cheng, S.F., and Mansour, A.N., "Structure and Magnetism of Sputtered Fe/Cu Multilayers", *J. of Mag. and Mag. Materials*, 126, 79 (1993).

Ibidunni, A.O., MaSaitis, R.L., Opila, R.L., Davenport, A.J., Isaacs, H.S., and Taylor, J.A., "Characterization of the Oxidation of Tantalum Nitride", *Surface & Interface Analysis*, 20, 559 (1993).

Kemner, K.M., Bunker, B. A., Luo, H., Samarth, N., Furdyna, J. K., Weidmann, M. R., and Newman, K. E., "X-ray Absorption Spectroscopy Investigations of Atomic Reordering at ZnTe/CdSe Interfaces", in Statics and Dynamics of Alloy Phase Transitions, edited by P.E.A. Turchi and A. Gonis, pg. 203-206, (1993).

Kemner, K.M., Bunker, B. A., Luo, H., Samarth, N., Furdyna, J. K., Weidmann, M. R., and Newman, K. E., "EXAFS Studies of Interfaces in ZnTe/CdSe Superlattices", *Jpn. J. of Appl. Physics*, 32/2, 399, (1993).

Lamble, G., Moen, A., and Nicholson, D.G., "Structure of the Diamminecopper(l) Ion in Solution: An X-ray Absorption Spectroscopic Study", *J. Chem. Soc. Faraday Trans.*, 90, 2211, (1994).

Little, B.I., Wagner, P.A., Hart, K.R., Ray, R.I., Lavoie, D.M., O'Grady W.E., and Trzaskoma, P.P., "Localization and Speciation of Copper Ions in Biofilms on Corroding Copper Surfaces", *CORROSION*, 94, 256, (1994).

Livins, P., Theil, D., Stern, E.A., and Lewis, A., "Structure of Photoexcited Platinum Pop Measured with Microsecond Resolved XAFS", *Jpn. J. of Appl. Physics*, 32/2, 195, (1993).

Mansour, A.N., Melendres, C.A., Pankuch, M., and Brizzolara, R.A., "X-Ray Absorption Fine Structure Spectra and the Oxidation State of Nickel in Some of its Oxycompounds", *J. Electrochem. Soc. Lett,* 141, L69, (1994).

McBreen, J., "EXAFS Studies of Absorbed Copper on Carbon-Supported Platinum", *J. Electoanal. Chem.*, 357, 373, (1993).

McCaulley, J.A., "Temperature Dependence of the Pd K-edge Extended X-ray Absorption Fine Structure of PdC_x (x-0.13)", *Phys. Rev.*, B47, 4873, (1993).

Newville, M., Livins, P., Yacoby, Y., Rehr, J.J., and Stern, E.A., "An Improved Background Removal Method for XAFS", *Jpn. J. of Appl. Physics,* 32/2, 125, (1993).

O'Grady, W.E., and Pandya, K.I., "*in situ* X-ray Absorption Spectroscopy of Nickel Oxide Electrodes", edited by C.A. Melendres and A. Tadjeddine, Synchrotron Techniques in Interfacial Electrochemistry, Kluwer Academic Press, The Netherlands, p. 247, (1994).

Purnell, S.K., Sanchez, K.M., Patrinio, R., Chang, J.-R., and Gates, B.C., "Genesis and Growth of Pt Particles on MgO: Characterization By X-ray Absorption Spectroscopy and Infrared Spectroscopy", *J. of Phys. Chem.* 98, 1205, (1993).

Qian, M., Sarikaya, M., and Stern, E.A., "Exelfs Revisited: An Improved Data Analysis Technique", edited by G.W. Bailey and G.L. Rieder, Proc. 51St Meeting of the Spectroscopy Society of America, p. 578-579, (1994).

Ravel, B., Stern, E.A., Yacoby, Y., and Dogon, F., "Lead Titanate is not a Classic Case of a Displacive Ferroelectric Phase Transition", *Jpn. J. of Appl. Physics,* 32/2, 722, (1993).

Rechav, B., Yacoby, Y., Stern, E.A., and Rehr, J.J., "Local Structure Distortions Below and Above the Anitferrodistrotive Phase Transition", *Phys. Rev. Lett.*, 72, 1352, (1994).

Sarikaya, M., Qian, M., and Stern, E.A., "Acquistion of EELS Spectra for High-resolution Spectroscopy", edited by G.W. Bailey and C.L. Reider, Proc. 51St Meeting of the Spectroscopy of America, p. 578-579, (1994).

Shorrosh, R.S., An X-ray Absorption Fine Structure Study of Semiconductor Nanoclusters, PhD Thesis, Georgia Institute of Technology, (1993).

Sicron, N., Ravel, B., Yacoby, Y., Stern, E.A., Dogon, f., and Rehr, J.J., "Nature of Ferroelectric Phase Transition in PbTiO(3)", *Phys. Rev.*, B50, 13168, (1994).

Stern, E.A., "The Future of XAFS", *Jpn. J. of Appl. Physics,* 32/2, 851, (1993).

Stern, E.A., Qian, M., and Sarikaya, M. "Spatially Resolved Local Atomic Structure from EXELFS", edited by M. Sarikaya *et al.*, MRS Proceedings, Vol. 332, 1-12, (1994).

Stern, E.A., Qian, M., Yacoby, Y., Heald, S.M., and Maeda, H., "Apical Cu-O Bond in $YBa_2Cu_3O_{7-8}$ Superconductors by XAFS", *Jpn. J. of Appl. Physics,* 32/2, 331, (1993).

Voss, K.F., Kim, K.H., Stern, E.A., Briown, F.C., and Heald, S.M., "A Capilla Concentrator for an X-ray Microprobe", *Nucl. Instrum. & Meth. In Phys.*, A347, 390, (1994).

Beamline X12B

McClusky, J.V., Priester, R.D., O'Neill, R.E., Willkomm, W.R., Heaney, M.D., and Capel, M.S., "The Use of FT-IR and Dynamic SAXS to Provide an Improved Understanding of the Matrix Formation and Viscosity Build of Flexible Polyurethane Foams", *Cellular Plastics*, **30**, 4, (1994).

Quantock, A.J., Klinktsworth, G.K., Capel, M.S., and Schanelin, D.J., "Glycosaminoglycans Give Rise to the Unique 4.61Å Macular Corneal-Dystrophy X-ray Reflection", *Investigative Opthamology and Visual Sciences*, **35**, 4, (1994).

Beamline X12C

Cheng, X., Zhang, Z., Pflugrath, J.W., and Studier, F.W., "The Structure of Bacteriophage T7 Lysozyme, A Zinc Amidase and an Inhibitor of RNA Polymerase", *Proc. Natl. Acad. Sci. USA*, **91**, 4034-4038, (1994).

Clancy, L.L.,Finzel, B.C., Yem, A.W., Deibel, Jr., M.R., Strakalaitis, N.A., Brunner, D.P., Sweet, R.M., and Einspahr, H.M., "Initial Crystallographic Analysis of a Recombinant Human Interleukin-1 Receptor Antagonist Protein", *Acta Cryst.*, **D50**, 197-201, (1993).

Klimasauskas, S., Kumar, S., Roberts, R.J., and Cheng, X., "HhaI Methyltransferase Flips its Target Base out of the DNA Helix", *Cell*, **76**, 357-369, (1994).

Lawson, C.L., and Carey, J., "Tandem Binding in Crystals of a *trp* Repressor/Operator Half-Site Complex", *Nature*, **366**, 178-182, (1993).

Skinner, M.W., Zhang, H., Leschnitzer, D.H., Guan, Y., Bellamy, H., Sweet, R.M., Gray, C.W., Konings, R.N.H., Wang, A., H-J., and Terwilliger, T.C., "Structure of the Gene V Protein of Bacteriphage f1 Determined by Miltiwavelength X-ray Diffraction on the Selenomethionyl Protein", *Proc. Nat. Acad. Sci.*, **91**, 2071-2075, (1993).

Xie, X., Harrison, D.H., Schlichting, I., Sweet, R.M., Kalabokis, V.N., Szent-Györgyi, A.G., and Cohen, C., "Structure of the Regulatory Domain of Scallop Myosin at 2.8 Å Resolution", *Nature*, **368**, 306-312, (1994).

Beamline X14A

Beach, R.S. Magnetic and Magnetoelastic Phenomena in Rare-Earth Dy/Lu Superlattices and Thin Films, PhD. Dissertation, Physics Department, University of Illinois, Urbana, IL, (1993).

Cheng, S.Z.D., Wu, S.S., Chen, J., Zhou, Q., Quirk, R.P., von Meerwall, E.D., Hsiao, B.S., Habenschuss, A., and Zschack, P., "Isothermal Thickening and Thinning Processes in Low Molecular Weight Poly(ethylene oxide) Fractions Cyrstallized from the Melt. 4. End Group Dependence", *Macromolecules*, **26/5**, 5105-5117, (1993).

Durbin, M.K., Malik, A., Ghaskadvi, R., Shih, M.C., Zschack, P., and Dutta, P. "X-Ray Diffraction Study of a Recently Identified Phase Transition in Fatty-Acid Langmuir Monolayers", *J. Phys. Chem.*, **98/7**, 1753-1755, (1994).

Feenstra, R., Li, X., Kanai, M., Kawai, T., Kawai, S., Budai, J.D., Jones, E.C., Sun, Y.R., Thompson, J.R., Pennycook, S.J., and Christen, D.K., "Electron-doped and Hole-doped Infinite Layer $Sr_{1-x}CuO_{2-\delta}$ Films grown by Molecular Beam Epitaxy", *Physica C*, 224, 300-316, (1994).

Gaulin, B.D., Gibbs, D., Isaacs, E.D., Lussier, J.G., Reimers, J.N., Schoeder, A., Taillefer, L., and Zschack, P., "Resonant Magnetic X-ray Scattering Study of Phase Transitions in UPd_2Al_3", *Phys. Rev. Lett.*, 73/6, 890-893, (1994).

Gaulin, B.D., Isaacs, E.D., Lussier, J.G., Reimers, J.N., Gibbs, D., Zschack, P., Schroeder, A., Taillefer, T., Garrett, J.D. "Resonant Magnetic X-Ray Scattering Studies of Heavy Fermion Superconductors", *Physica B,* 199, 57-62, (1994).

Hong, H., Aburano, R., Lin, D.-S., Chiang, T.-C., Chen, H., Zschack, P, and Specht, E.D., "Change of the Si (111) Surface Reconstruction under Noble Metal Films", MRS Symposia Proc., 237, 387-392, (1993).

Ice, G.E., and Sparks, C.J., "Conical Geometry for Sagittal Focusing as Applied to X-Rays From Synchrotrons", *J. Opt. Soc. Am.*, A11/4, 1265-1271, (1994).

Ice, G.E., Sparks, C.J., and Shaffer, L.B. "Chemical and Displacement Atomic Pair Correlations in Crystalline Solid Solutions Recovered by Resonant (Anomalous) X-Ray Scattering", edited by G. Materlik, C.J. Sparks, and K. Fischer, Resonant Anomalous X-Ray Scattering Theory and Applications, North-Holland, New York, pp. 265-294, (1994).

Isaacs, E.D., Aeppli, G., Zschack, P., Cheong, S.-W., Williams, H., and Buttrey, D.J., "Diffuse X-Ray Scattering in $La_{2-x}Sr_xNiO_4$ and $La_{2-x}Sr_xCuO_4$", *Phys. Rev. Lett.*, 72/21, 3421-3424, (1994).

Jesson, D.E., Pennycook, S.J., Tischler, J.Z., Budai, J.D., Baribeau, J.-M., and Houghton, D.C., "Interplay Between Evolving Surface Morphology, Atomic-Scale Growth Modes, and Ordering During Si_xGe_{1-x} Epitaxy", *Phys. Rev. Lett.*, 70 /15, 2293-2296, (1993).

Schoenfeld, B., Ice, G.E., Sparks, C.J., Haubold, H.-G., Schweika, W., and Shaffer, L.B. "X-Ray Study of Diffuse Scattering in Ni-20 at% Cr", *Phys. Stat. Sol. (b),* 183, 79, (1994).

Shih, M.C., Durbin, M.K., Malik, A., Zschack, P., and Dutta, P., "Lattice Structures and Molecular Tilts in Langmuir Monolayers of Saturated Fatty Acid-Alcohol Mixtures", *J. Chem. Phys.*, 101, 9132, (1994).

Shih, M.C., Peng, J.B., Huang, K.G., and Dutta, P., "Structures of Fatty Acid Monolayers Transferred to Glass Substrates From Various Langmuir Monolayer Phases", *Langmuir*, 9, 776, (1993).

Specht, E.D., Goyal, A., Kroeger, D.M., DeLuca, J.A., Tkaczyk, J.E., Briant, C.L., and Sutliff, J.A., "X-Ray Micro-diffraction Analysis of mm-Scale Orientational Correlations in Tl-1223 High-Critical-Current, High-Temperature Superconducting Films", *Physica C,* 226, 76 , (1994).

Tischler, J.Z., Larson, B.C., Boatner, L.A., Alp, E., Mooney, T., and Shen, Q. "Development of neV Scattering Spectroscopy using Resonant Nuclear Bragg Scattering", edited by G. Materlik, C.J. Sparks, and K. Fischer, Resonant Anomalous X-Ray Scattering Theory and Applications, , North-Holland, New York, pp. 265-294, (1994).

Walker, F.J. and Specht, E.D. "Anomalous Crystal Truncation Rod Intensity: A Chemical and Structural Probe", edited by G. Materlik, C.J. Sparks, and K. Fischer, Resonant Anomalous X-Ray Scattering Theory and Applications, , North-Holland, New York, pp. 265-294, (1994).

Beamline X15A

Qian, Y., Bedzyk, M.J., Tang, S., Freeman, A.J., and Franklin, G.E., "Resolving the Ga Ad-Dimer Location and Orientation on the Si(100) Surface", *Phys. Rev. Lett.*, 73, 1521, (1994).

Beamline X15B

Adler, D.L., Collins, I.R., Liang, X., Murray, S.J., Leatherman, G.S., Tsuei, K.-D., Chaban, E.E., Chandavarkar, S., McGrath, R., Diehl, R.D., and Citrin, P.H., "Top-site Adsorption for K on Cu(111) and Ni(111) Surfaces", *Phys. Rev.*, B23, 17445, (1993).

Benton, J.L., Eaglesham, D.J., Almonte, M., Citrin, P.H., Marcus, M.A., Adler, D.L., Jacobson, D.C., and Poate, J.M., "Correlation of Electrical, Structural, and Optical Properties of Erbium in Silicon", *Mat. Res. Soc. Symp.*, 298, 447, (1993).

Friedman, S.L., Marcus, M.A., Adler, D.L., Xie, Y.-H., Harris, T.D., and Citrin, P.H., "Unimportance of Siloxene in Luminescent Porous Silicon as Determined by NEXAFS and EXAFS", *Mat. Res. Soc. Symp.*, 298, 295, (1993).

Schuppler, S., Adler, D.L., Pfeiffer, L.N., West, K.W., Chaban, E.E., and Citrin, P.H., "Can Electrical Deactivation of Highly Si-doped GaAs be Explained by Autocompensation?", *Appl. Phys. Lett.*, 63, 2357, (1993).

Schuppler, S., Friedman, S.L., Marcus, M.A., Adler, D.L., Xie, Y.-H., Ross, F.M., Harris, T.D., Brown, W.L., Chabal, Y.J., Brus, L.E., and Citrin, P.H., "Dimensions of Luminescent Oxidized and Porous silicon Structures", *Phys. Rev. Lett.*, 72, 2648, (1994).

Beamline X16A

Green, M.L., Brasen, D., Evans-Lutterodt, K.W., Feldman, L.C., Krisch, K., Lennard, W., Tang, H.T., Manchanda, L., Tang, M.T., "Rapid Thermal Oxidation of Silicon in N20 between 800 and 1200: Incorporated Nitrogen and Interfacial Roughness", *Appl. Phys. Lett.*, 65, 848, (1994).

Meyerheim, H.L., Robinson, I.K., Jahns, V., Eng, P.J., and Moritz, W., "Coverage Dependent Adsorption Sites in the K/Cu(100) System: A Crystal Truncation Rod Analysis", *Zeitschrift fur Kristallographie*, 208, 73-92, (1993).

Meyerheim, H.L., Wever, J., Jahns, V., Moritz, W., Eng, P.J., and Robinson, I.K., "Coverage-dependent Adsorption Sites for K/Cu(001) and Cs/Cu(001) Determined by Surface X-ray Diffraction", *Surface Science*, 304, 267-280, (1994).

Meyerheim, H.L., Wever, J., Jahns, V., Moritz, W., Eng, P.J., and Robinson, I.K., "The Structure of K- and Cs-Monolayers on Cu(100): Diffraction Experiments far from the Bragg Point", *Physica*, B198, 66-69, (1994).

Pietsch, U., Metzger, H., Rugel, S., Jenichen, B., and Robinson, I.K., "Depth-Resolved Measurement of Lattice Relaxation in Ga1-xInxAs/GaAs Strained-layer Superlattices by means of Grazing Incidence X-ray Diffraction", *Journal of Applied Physics*, 74, 2381, (1993).

Robinson, I.K., "Oxidation of Mo(001) Surfaces", in Synchrotron Techniques in Interfacial Electrochemistry,edited by C.A. Melendres and A. Tadjeddine, NATO Advanced Science Institutes, Kluwer Academic Publishers, C432, 171-180, (1994).

Tang, M.T., Evans-Lutterodt, K.W., Green, M.L., Brasen, D., Krisch, K., Manchanda, L., Higashi, G.S., Boone, T., "Growth Temperature Dependence of the Si(001)/Si02 Interface Width", *Appl. Phys. Lett.*, 64, 748, (1994).

Tang, M.T., Evans-Lutterodt, K.W., Higashi, G.S., Boone, T., "A Comparison of the Roughness of Various Si/ Si02 Interfaces using X-ray Diffraction", *Mat. Res. Symp. Proc.*, 315, 399, (1993).

Wong, G.C. L., Lucas, C.A., Loretto, D., Payne, A.P., Fuoss, P.H., "Parallel Adatom Chains on Si(111): A Chemisorption-induced Surface reconstruction", *Phys. Rev. Lett.*, 73, 991, (1994).

Beamline X16B

Gaulin, B.D., Gibbs, D., Isaacs, E.D., Lussier, J.G., Reimers, J.N., Schroeder, A., Taillefer, L., and Zschack, P., "Resonant Magnetic X-ray Scattering Study of Phase Transitions in UPd2A13", *Phys. Rev. Lett.*, 73, 890, (1994).

Gaulin, B.D., Isaacs, E.D., Lussier, J.G., Reimers, J.N., Gibbs, D., Zschack, P., Schroeder, A., Taillefer, L., and Garrett, J.D., "Resonant Magnetic Scattering Studies of Heavy Fermion Superconductors", *Physica*, **B199/200**, 57, (1994).

Isaccs, E.D., Aeppli, P., Zschack, P., Cheong, S.-W., Williams, H., and Buttrey, D.J., "Diffuse X-ray Scattering from $La_{2-x}Sr_xNiO_4$ and $La_{2-y}Sr_YCuO_4$", *Phys. Rev. Lett.*, 72, 3421, (1994).

Isaccs, E.D., Zschack, P., Ramirez, A.P., Oglesby, C.S., and Bucher, E., "Antiferromagnetic Order in Superconducting UPt_3: An X-ray Magnetic Scattering Study", *J. Appl. Phys.*, 76, 6133, (1994).

Beamline X17B1

Guardala, N.A., Price, J.L., Land, D.J., Simons, D.G., Lee, D.H., Johnson, B.M., Glass, G.A., and Brennan, J.G., "Compton-electron Spectroscopy Using High-energy Synchrotron X-rays", *Nuclear Instruments and Methods*, A347, 504, 1994.

Liu, X., and Liebermann, R.C., "X-ray Powder Diffraction Study of $CaTiO_3$ Perovskite at High Temperatures", *Phys. Chem. Minerals*, 20, 171-175, (1993).

Luke, P.N., Pehl, R.H., and Dilmanian, F.A., "A 140-element Ge Detector Fabricated Using Amorphous Ge Blocking Contacts", *IEEE Trans. Nucl. Sci.*, 41, 976-978, (1994).

Meng, Y., Weidner, D.J., Gwanmesia, G.D., Liebermann, R.C., Vaughan, M.T., Wang, Y., Leinenweber, K., Pacalo, R.E., Yeganeh-Haeri, A., and Zhao, Y., "*In situ* P-T X-ray Diffraction Studies on Three Polymorphs (α,β, γ) of Mg_2SiO_4", *J. Geophys, Research*, 98, 22, 199-22, 207, (1993).

Shleifer, M., Dilmanian, F.A., Staicu, F.A., and Woodle, M.H., "Mechanical Design of a High-Resolution Tunable Crystal Monochromator for the Multiple Energy Computed Tomography Project", *Nucl. Instrum. And Meth. In Phys. Res.*, A347, 356-359, (1994).

Slatkin, D.N., Dilmanian, F.A., and Spanne, P., "Method for Microbeam Radiation Therapy", *U.S. Patent*, 5, 339-347, (1994).

Wang, Y., and Weidner, D.J., "Thermoelasticity of $CaSiO_3$ Perovskite and Implications for the Lower Mantle", *Geophys. Res. Lett.*, 21, 895-898, (1994).

Wang, Y., Weidner, D.J., Liebermann, R.C., and Zhoa, Y., "P-V-T Equation of State of (Mg, Fe) SiO3 Perovskite: Constraints on Composition of the Lower Mantle", *Physics of the Earth and Planetary Interiors*, 83, 13-40, (1994).

Weidner, D.J., Wang, Y., and Vaughan, M.T., "Yield Strength at High Pressure and Temperature", *Geophys. Res. Lett.*, 21, 753-756, (1994).

Zhao, Y., and Weidner, D.J., "The Single Crystal Elastic Moduli of Neighborite", *Phys. Chem. Minerals*, 20, 419-424, (1993).

Zhao, Y., Weidner, D.J., Ko, J., Leinenweber, K., Liu, X., Li, B., Meng, Y., Pacalo, R.E.G., Vaughan, M.T., Wang, Y., and Yeganeh-Haeri, A., "Perovskite at High P-T Conditions: An *in situ* Synchrotron X-ray Diffraction Study of $NaMgF_3$ Perovskite", *J. Geophys. Res.*, 99, 2871-2885, (1994).

Beamline X17B2

Chapman, D., and Schulze, C., "Arterial Cross-Section Measurements from Dual Energy Transvenous Coronary Angiography Images", edited by L. Klaisner, IEEE Conference Record, Nuclear Symposium and Medical Imaging Conference, October 31-November 6, 1993, San Francisco, CA., 3, 1528-1532 , (1994).

Gmür, N.F., Chapman, D., Thomlinson, W., Scalia, K., Malloy, N., Mangano, J., and Jacob, J., "NSLS Transvenous Coronary Angiography Project Advanced technology Initiatives", *Synchrotron Rad. News*, 7/5, 34-36, (1994), BNL 60608.

Rubenstein, E., Brown, G.S., Chapman, D., Garrett, R.F., Giacomini, J.C., Gmür, N., Gordon, H.J., Lavender, W.M., Morrison, J., Thomlinson, W., Thompson, A.C., and Zeman, H., "Synchrotron Radiation Coronary Angiography in Humans", edited by B. Chance et al, Synchrotron Radiation in the Biosciences, Oxford University Press, New York, 639-645, (1994), BNL 60609.

Schulze, C., Suortti, P. And Chapman, D., "Test of a Bent Laue Double Crystal Fixed Exit Monochromator", *Synchrotron Rad. News*, 7/3, 8-11, (1994).

Suortti, P., Thomlinson, W., Chapman, D., Gmür, N., Siddons, D.P., and Schulze, C., "A Single Crystal Bent Laue Monochromator for Coronary Angiography", *Nucl. Instr. and Meth. In Physics Res.*, A336, 304-309, (1993), BNL 49127.

Thomlinson, W., "Medical Applications of Synchrotron Radiation at the National Synchrotron Light Source", edited by B. Chance et al., Synchrotron Radiation in the Biosciences, Oxford Unversity Press, New York, pp. 674-680, (1994), BNL 47916.

Thompson, A.C., Lavender, W.M., Chapman, D., Gmür, N., Thomlinson, W., Rosso, V., Schulze, C., Rubenstein, E., Giacomini, J.C., Gordon, H.J., Dervan, J.P., "A 1200 Element Detector System for Synchrotron-Based Coronary Angiography", *Nucl. Instr. and Meth. in Physics Res.*, A347, 545-552, (1994).

Beamline X17C

Duffy, T.S., Vos, W.L., Zha, C.-S., Hemley, R.J., and Mao, H.-K., "Sound Velocities in Dense Hydrogen and the Interior of Jupiter", *Science*, 263, 1590-1593, (1994).

Eggert, J.H., Hu, J.Z., Mao, H.-K., Beauvais, L., Meng, R.L., and Chu, C.W., "Compressibility of the $HgBa_2Ca_{n-1}Cu_nO_{2n+2+\delta}$(N=1,2,3) High-Temperature Superconductors", *Phys. Rev.* B49, 15299-15304, (1994).

Fei, Y., and Mao, H.-K., "Static Compression of $Mg(OH)_2$ to 78 Gpa at High Temperature and Constraints on the Equation of State of Fluid H_2O", *J. Geophys. Res.*, 98, 11875-11884, (1993).

Fei, Y., Mao, H.-K., and Hemley, R.J., "Thermal Expansivity, Bulk Modulus, and Melting Curve of H2O-ice VII to 20 GPa", *J. Chem. Phys.*, 99, 5369-5373, (1993).

Gu, G., Vohra, Y.K., Benedict, U., and Spirlet, J.-C., "Ultrahigh-Pressure Phase Transformations in the CeTh Alloy: Implications for F-Electron Behavior Under Compression, *Phys. Rev.*, B50, 2751, (1994).

Hu, J., Mao, H.-K, Shu, J., and Hemley, R.J., "High Pressure Energy Dispersive X-ray Diffraction Technique with Synchrotron Radiation", edited by S.C. Schmidt, J.W. Shaner, G.A. Samara and M. Ross, *High Pressure Science and Technology*, 1, 441-444, (1994).

Kingma, K.J., Hemley, R.J., Veblen, D.R., and Mao, H.-K., "High Pressure Crystalline Transformations and Amorphization in α-Quartz", edited by S.C. Schmidt, J.W. Shaner, G.A. Samara and M. Ross, *High Pressure Science and Technology*, 1, 39-42, (1994).

Mao, H.-K., and Hemley, R.J., "Ultrahigh-Pressure Transitions in Solid Hydrogen", *Rev. Mod. Phys.*, 66, 671-692, (1994).

Mao, H.-K. And Hemley, R.J., "Material Science at Ultrahigh Pressures" in Advanced Materials '94, Proceeding of ISAM94 International Symposium on Advanced Materials '94, edited by M. Kamo, H. Kanda, Y. Matsui, and T. Sekine, International Comm. Specialist, Inc., Tokyo, p. 229-234, (1994).

Mao, H.-K, Shu, J., Hu, J., and Hemley, R.J., "High-pressure X-ray Diffraction Study of Diaspore", *Solid State Comm.*, 90, 497-500, (1994).

Skelton, E.F., Drews, A.R., Osofsky, M.S., Qadri, S.B., and Hu J.Z., "Direct Observation of Microscopic Inhomogeneities with Energy-Dispersive Diffraction of Synchrotron Produced X-rays", *Science*, 263, 1416-1418, (1994).

Reichlin, R., McMahan, A.K., Ross, M., Martin, S., Hu, J., Hemley, R.J., Mao, H.-K., and Wu, Y., "Optical, X-ray and Band-Structure Studies of Iodine at Pressures of Several Megabars", *Phys. Rev.*, B49, 3725-3733, (1994).

Vos, W.L., Finger, LW., Hemley, R.J., and Mao, H.-K., "Novel H_2-H_2O Clathrate at High Pressures", *Phys. Rev. Lett.*, 71, 3150-3153, (1993).

Vos, W.L., Finger, L.W., Hemley, R.J., Mao, H.-K., and Yoder, H.S., "Phase Behavior of H_2-H_2O at high Pressure", edited by C. Schmidt, J.W. Shaner, G.A. Samara and M. Ross, *High Pressure Science and Technology*, 1, 857-860, (1994).

Zha, C.-S., Duffy, T.S., Mao, H.-K., and Hemley, R.J., "Elasticity of Hydrogen to 24 GPa from Single-Crystal Brillouin Scattering and Synchrotron X-ray Diffraction", *Phys. Rev.*, B48, 9246-9255, (1993).

Zha, C.-S., Duffy, T.S., Mao, H.-K., and Hemley, R.J., "High-Pressure Brillouin Scattering and Elastic Constants of single-Crystal Hydrogen to 24 GPa", edited by S.C. Schmidt, J.W. Shaner, G.A. Samara and M. Ross, *High Pressure Science and Technology*, 1, 873-876, (1994).

Beamline X18A

Anderson, J.P., and Chen H., "Determination of the Short-Range Order Structure of Au-25 At. Pct Fe Using Wide-Angle Diffuse Synchrotron X-Ray Scattering", *Metallurgical and Materials Transactions*, A25, 1561-1573, (1994).

Bessiere, M., Lee, H., Motsch, T., Lefebvre, S., Denoyer, F., and Colella, R., "Feasibility of Phase Determination in Quasicrystals and Microcrystals by Means of Multiple Bragg Scattering", *Zeitschrift für Kristallographie*, 209, 390-394, (1994).

Butler, B.D., and Cohen, J.B., "What the Latest Diffraction Techniques Can Tell us About an Old Material: Steel", *Ultramicroscopy*, 52, 238-242, North-Holland, (1993).

Colella, R., "Enantiomorphism and Multiple Beam X-ray Diffraction", *Acta Cryst.*, A50, 55-57, (1994).

Dai, P., Angot, T., Wang, S.-K., Taub, H., and Ehrlich, S.N., "Structural Perfection in Physisorbed Films: A Synchrotron X-Ray Diffraction Study of Xenon Absorbed on the Ag (111) Surface", *Phys. Rev. Lett.*, 72, 695-698, (1994).

Epperson, J.E., Anderson, J.P. and Chen, H., "The Diffuse-Scattering Method for Investigating Locally Ordered Binary Solid Solutions", *Metallurgical and Materials Transactions A*, A25, 17-35, (1994).

Fullerton, E.E., Mini, S.M., Bommannavar, A.S., Sowers, C.H., Ehrlich, S.N., and Bader, S.D., "Interfacial Structure of Lattice Mismatched bcc(110)/bcc(110) Superlattices of Transition Metals", Mat. Res. Soc. Symposium Proceedings, 307, 131, (1993).

Liu, Z., and Davis R.J., "Investigation of the Structure of Microporous Ti-Si Mixed Oxides by X-ray, UV Reflectance, FT-Raman, and FT-IR Spectroscopies", *J. Phys. Chem.*, 98, 1253-1261, (1994).

Mahadev, V., Mahalingam, K., Liedl, G.L., and Sanders, Jr., T.H., "Very Early Stage of δ' Precipitation in a Binary Al-3.2 Wt % Li Alloy", *Acta. Metall. Mater.*, 42/3, 1039-1043, (1994).

Mahadev, V., Melloch, M.R., Woodall, J.M., Otsuka, N., and Liedl, G.L., "Effect of Dopants on Arsenic Precipitation in GaAs Deposited at Low Temperatures", *Journal of Electronic Materials*, 23/9, 1-13, 1994.

Parrill, J.L., Georgopoulos, P., Chung, Y.-W., and Cohen, J.B., "GISAXS-Glancing Incidence Small Angle X-Ray Scattering", *Journal De Physique IV, Colloque C8, Supplement au Journal de Physique I*, 3, (1993).

Quintana, J.P., and Cohen, J.B., "Local Atomic Structure in $Hg_{0.8}Cd_{0.2}Te$ and $Cd_{0.725}Mn_{0.275}Te$" in Diffusion in Ordered Alloys, edited by B. Fultz, R.W. Cahn, and D. Gupta, The Minerals, Metals & Materials Society, pp. 151-161, (1993).

Wang, S.-K., Dai, P., and Taub, H.J., "Angle Calculations for a Five-circle Diffractometer used in Surface X-Ray Diffraction Experiments", *J. Appl. Cryst.*, 26, 697-705, (1993).

Williams, S.M., Yang., H.Q., and Ketterson, J.B., "A Miniature Multi-target Sputtering System for the *in situ* X-Ray Study of High T_c Multilayer Film Growth", *J. Vac. Sci. And Technol.*, A12, 2, 598-600, (1994).

Beamline X18B

Chen, L.X., Bowman, M.K., Wang, Z.Y., and Montano, P.A., and Norris, J.R., "Structural Studies of Photo-Induced Intramolecular Electron Transfer in Cyclopentadienyl Nickelnitrosyl", *J. Phys. Chem.*, 98, 9457-64, (1994).

Davis, R.J., and Boudart, M., "Structure of Supported PdAu Clusters Determined by X-ray Absorption Spectroscopy", *J. Phys. Chem.*, 98, 5471-5477, (1994).

Liu, D.J., and Robota, H.J., "X-ray Absorption Spectroscopic Study of Cu in Cu-ZSM-5 During NO Catalytic Decomposition", *Cat. Lett.*, 21, 291, (1993).

Yoo, S.S., Wang, K., Montano, P.A., Faurie, J.P., Huang, Q., and Rodricks, B., "Ultrafast Photoconductor CdTe Detectors for Synchrotron X-ray Studies", *Nucl. Instr. And Meth. In Phys. Res.*, A348, 527, (1994).

Beamline X19A

Chen, J., Croft, M., Jeon, Y., Xu, X., Shaheen, S.A., Ansari, P., "XAS Studies of 1:2:2 Transition Metal Compounds", *Sol. State. Comm.*, 85, 291-296, (1993).

Clark, K., Structural Characterization of Zn Sites in Metalloproteins Using X-ray Absorption Spectroscopy, PhD Thesis, Advised by J.E. Penner-Hahn, University of Michigan, 1993.

Coyer, M., Herber, R., Chen, J., Croft, M., and Szu, S.P., "Ligand Isomerism and Stacking in Square Planar Pt(II) Complexes II: Evidence for Mixed-Isomerism in {Pt(4,4'dmdp)(CSN) }", *Inorg. Chem.*, 33, 716, (1994).

Dodge, C.J., Francis, A.J., Lu, F., Hadada, G.P., Kagwade, S.V., and Clayton, C.R., "Speciation of Uranium After Microbial Action by XANES and XPS" *Mat. Res. Soc. Symp. Proc.*, 307, 89-93, (1994).

Feng, Z., Zhao, J., Huggins, F.E., and Huffman, G.P., "Agglomeration and Phase Transition of a Nanophase Iron Oxide Catalyst", *J. Catal.*, 143, 510, (1993).

Francis, A.J., Dodge, C.J., Lu, F., Hadada, G.P., and Clayton, C.R., "XPS and XANES Studies of Uranium Reduction by Clostridium sp", *Environ. Sci. & Tech.*, 28, 636-639, (1994).

Herber, R., Croft, M., Coyer, M., Sahiner, A., and Bilash, B., "Origin of Polychromism of cis-Square Planar Pt(II) Complexes and the Crystal Structure of the Yellow Form of Pt[2,2'bpy(Cl)]", *Inorg. Chem.*, 33, 2422-2426, (1994).

Huffman, G.P., Huggins, F.E., Shah, N., and Zhao, J., "Speciation of Critical Trace Elements in Coal and Combustion as by XAFS Spectroscopy", *Fuel Process Technology*, 39, 47, (1994).

Huffman, G.P., Huggins, F.E., Shah, N., Lu, F., and Zhao, J., "XAFS Studies of Coal", *ACS Div. Fuel Chem.*, 39, 77, (1994).

Huffman, G.P., Huggins, F.E., Shah, N., Lu, F., and Zhao, J., "Sulfur Speciation Studies in Coal and Other Fossil Energy Materials by S K-edge XANES Spectroscopy", *ACS Div. Fuel Chem.*, 38, 369, (1993).

Huggins F.E., Zhao, J., Shah, N., and Huffman, G.P., "Modes of Occurrence of Trace Elements in Coal from XAFS Spectroscopy", *ACS Div. Fuel Chem.*, 39, 504, (1994).

Huggins , F.E., Helble, J.J., Shah, N., Zhao, J., Srinivasachar, S., Morency, J.R., Lu, F., and Huffman, G.P., "Forms of Occurrence of Arsenic in Coal and Their Behavior During Coal Combustion", *ACS Div. Fuel Chem.*, 38, 265, (1993).

Jeon, Y., Chen, J., and Croft, M., "4d/5d Transition Metal-Group III/IV Compounds": Systematic XAS Studies of d-Occupancies", *Phys. Rev.*, B50, 6555, (1994).

Miura, M., Majumder, S.A., Hobbs, J.D., Renner, M.W., Furenlid, L.R., and Shelnutt, J.A., "Synthesis and Spectroscopic Characterization of Octaacetic Acid Tetraphenylporphyrins", *Inorg. Chem.*, 33, 6078, (1994).

Shahiner, A., Peng, J., Croft, M., Zhang, Z., Greenblatt, M., Liang, G., Xu, X., Li, W., Badresingh, D., and Lu, F., "XAS Evidence for Ni-d Hole Variation in Ni-Based Oxides", *Bull. Am. Phys. Soc.*, 39/1, 204, (1994).

Shorrosh, R.A., An X-ray Absorption Fine Structure Study of Semiconductor Nanoclusters, PhD Thesis, advised by R.S., Felton, Georgia Institute of Technology, (1993).

Zhao, J., Huggins, F.E., Feng, Z., Lu, F., Shah, N., and Huffman, G.P., "Structure of a Nanophase Iron Oxide Catalyst", *J. Catal.*, 143, 499, (1993).

Zhao, J., Feng, Z., Huggins, F.E., Shah, N., and Huffman, G.P., "Structure and Phase Transition of an Ultrafine Iron Oxide Catalyst", *ACS Div. Fuel Chem.*, 38, 196, (1993).

Beamline X19C

Baker, I., Liu, F., Dudley, M., and Black, D., "*in situ* Synchrotron X-ray Topographic Studies of Polycrystalline Ice", Proceedings of IAHR Ice Symposium 1994, Trondheim, Norway, pp. 416, (1994).

Casagrande, L.G., Larson, D.J., Jr., DiMarzio, D., Wu, J., and Dudley, M., "Growth of Large-Area, High Quality CdZnTe Substrates by the Computer Controlled Vertical Bridgman Method", edited by H.K. Pollehn and R. Balcerak in Producibility of II-VI Materials and Devices, SPIE Proc., 2228, 21, (1994).

Casagrande, L.G., Larson, D.J., Jr., DiMarzio, D., Wu, J., and Dudley,M., "The Growth and Comparison of Large-Diameter, Vertical Bridgman CdZnTe and CdTe", *J. Crystal Growth*, 137, 195, (1994).

Chiang, F.P., Li, X.M., Wu, J., and Dudley, M., "Experimental Measurement of Crack Tip Strain Field in a Single Crystal", Proceedings of the International Seminar Mecamat '91, edited by C. Teodosiu, J.L. Raphanel, and F. Sidoroff, A.A.Balkema , Rotterdam, NL, p. 143, (1993).

DiMarzio, D., Larson, D.J., Jr., Casagrande, L.G., Wu, J., Dudley, M., Tobin, S.,and Norton, P., "Large Area X-ray Topographic Screening of II-VI Substrates and Epilayers", in Producibility of II-VI Materials and Devices, edited by H.K. Pollehn and R. Balcerak,, SPIE Proc., 2228, 289, (1994).

Dudley, M., "Characterization by X-ray Topography", edited by D. Bloor, R.J. Brook, M.C. Flemings and S. Mahajan, Pergamon, in Encyclopedia of Advanced Materials, 4, 2950, (1994).

Dudley, M., Liu, F., and Baker, I., "Studies of Defect Behavior in Large-Grain, Polycrystalline Ice Using Synchrotron X-ray Topography", *Mol. Cryst. Liq. Cryst.* , 240, 73, (1993).

Dudley, M., Wu, J., Larson, D.J., and DiMarzio, D., "Use of White Beam X-ray Topography to Characterize IR Detector Manufacturing Processes", in Diagnostic Techniques for Semiconductor Materials Processing, edited by O.J. Glembocki, F.H. Pollak, S.W. Pang, G. Larrabee, and G.M. Crean, Mat. Res. Soc. Symp. Proc., 324, 457, (1994).

Fazi, C., Dudley, M., Wang, S., and Ghezzo, M., "Issues Associated with Large Area SiC Diodes with Avalanche Breakdown" in SiC and Related Materials, International Institute of Physics Conference Series Number 137, edited by M.G. Spencer, R.P. Devaty, J.A. Edmond, M. Asif Khan, R. Kaplan, and M. Rahman Institute of Physics Publishing, Bristol and Philadelphia, 487, (1994).

Larson, D.J., Jr., DiMarzio, D., Casagrande, L.G., Carlson, F.M., Lee, T., Steiner, B., Long, G., Seiler, D.G., Wu, J., and Dudley, M., "Producibility Improvements Suggested by a Validated Process Model of Seeded CdZnTe Vertical Bridgman Growth", in Producibility of II-VI Materials and Devices, edited by H.K. Pollehn and R. Balcerak, SPIE Proc., 2228, 11, (1994).

Liu, F., Baker, I., and Dudley, M., "Dislocation/Grain Boundary Interactions in Ice Crystals", *Phil. Mag.*, 71, 15, (1994).

Liu, F.,Baker, I., and Dudley, M.,"Dislocation Grain Boundary Interactions in Ice Under Creep Conditions", Proceedings of IAHR Ice Symposium 1994, Trondheim, Norway, pp. 484, (1994).

Liu, F., Baker, I., and Dudley, M., "Thermally Induced Dislocation Loops and Stacking Faults in Polycrystalline Ice", *Phil. Mag.*, 71, 1, (1994).

Su, C.-H., Sha, Y.-G., Volz, M.P., Gillies, D.C., Szofran, F.R., Lehoczky, S.L., Zhou, W., Dudley, M., Liu, H.-C., Brebrick, R.F., and Wang, J,C., "Ground-Based Research of Crystal Growth of II-VI Compound Semiconductors by Physical Vapor Transport", Reno, NV, 1994, Paper No. AIAA 94-0564, American Institute of Aeronautics and Astronautics, Inc., (1994).

Wang, S., Dudley, M., Carter, C.H., Jr., and Kong, H.S., "X-ray Topographic Studies of Defects in PVT 6H-SiC Substrates and Epitaxial 6H-SiC Thin Films", in Diamond, Silicon Carbide and Nitride Wide-Bandgap Semiconductors, edited by C.H. Carter, Jr., G. Gildenblat, S. Nakamura, and R.J. Nemanich, Mat. Res. Soc. Symp. Proc., 339, 735, (1994).

Wang, S., Dudley, M., Cheng, L.K., Bierlein, J.D., and Bindloss, W., "Imaging of Ferroelectric Domains in $KTiOPO_4$ Single Crystals by Synchrotron X-ray Topography", in Ferroelectric Thin Films III, edited by E.R.Myers, B.A. Tuttle, S.B. Desu, and P.K. Larsen, Mat. Res. Soc. Symp. Proc., 310, 29, (1993).

Zhou, W., Dudley, M., Su, C.-H., Volz, M.P., Gillies, D., Szofran, F.R., and Lehoczky, S.L., "Characterization of Growth Defects in ZnTe Single Crystals", in Infrared Detectors - Materials, Processing, and Devices, edited by A. Applebaum and L.R. Dawson, Mat. Res. Soc. Symp. Proc., 299, 203, (1994).

Zhou, W., Dudley, M., Su, C.-H., Volz, M.P., Gillies, D., Szofran, F.R., and Lehoczky, S.L., "Synchrotron Topography Characterization of ZnTe Single Crystal", *Mater. Sci. & Engin.*, B27,143, (1994).

Beamline X20

Abernathy, D.L., Song, S., Blum, K.I., Birgeneau, R.J., and Mochrie, S.G.J., "Chiral Melting of the Si(113) (3x1) Reconstruction", *Phys. Rev.* , **B49**, 2991, (1994).

Baddorf, A.P., Zehner, D.M., Helgesen, G., Gibbs, D., Sandy, A.R., and Mochrie, S.G.J., "X-ray Scattering Determination of the Cu(110)-(2x3)N Structure", *Phys. Rev. B.*, 48, 9013, (1993).

Berkowitz, S.J., DeObaldia, E., Ludwig, Jr, K.F., Skocpol, W.J., Mankiewich, P.M., Ono, R.H., Beall, J.A., Vale, L.R., Rudman, D.A., O'Malley, M.L., Drabeck, L.M., and Polakos, P.A., "Increased Transition Temperature in *in-situ* Coevaporated $YBa_2Cu_3O_{7-\delta}$ Thin Films by Low Temperature Postannealing", *Appl. Phys. Lett.*, 65, 1587, (1994).

Farrow, R.F.C., Lee, C.H., Marks, R.F., Harp, G.R., Toney, M.F., Rabedeau, T.A., Weller, D., and Brändle, H., "Chemical Ordering and Magnetic Anisotropy in MBE-Grown Co/Pt Multilayers", edited by Farrow, Dieny, Donath, Fert, Hermsmeier, Magnetism and Structure in Systems of Reduced Dimension, NATO ASI Series, **B309**, Plenum, New York, 1993,

Farrow, R.F.C., Harp, G.R., Weller, D., Marks, R.F., Toney, M.F., Cebollada, A., and Rabedeau, T.A., "MBE-Growth of Chemically Ordered Co-Pt and Fe-Pt Alloy Phases", *SPIE*, **2140**, 106, (1994).

Farrow, R.F.C., Marks, R.F., Harp, G.R., Weller, D., Rabedeau, T.A., Toney, M.F., and Parkin, S.S.P., "MBE Growth of Artificially-Layered Magnetic Metal Structures on Semiconductors and Insulators", *Mater. Sci. Eng.*, **R11**, 155, (1993).

Farrow, R.F.C., Weller, D., Toney, M.F., Rabedeau, T.A., Hurst, J., Harp, G.R., Marks, R.F., Geiss, R.H., and Notarys, H., "Microstructure and Chemical Ordering in UHV-Deposited, Polycrystalline CoPt Alloy Films for Magneto-Optic Recording", Materials Research Society Symposium Proceedings ,Vol. 343, 375, (1994).

Fischer, H.E., Brauer, S., Zaluska, Z., Sutton, M., and Ström-Olsen, J.O., and Stephenson, G.B., "Rapid Crystallization of Amorphous Co-Zr and Fe-B Close to Eutectic Compositions", *Mat. Sci. & Eng.*, 179, 396-400, (1994).

Grüebel, G., Gibbs, D., Zehner, D.M., Sandy, A.R., and Mochrie, S.G.J., "Reconstruction of the Pt(111) Surface: X-ray Scattering Measurements", *Phys. Rev. B.*, 48, 18119, (1993).

Harp, G.R., Weller, D., Rabedeau, T.A., Farrow, R.F.C., and Toney, M.F., "Magneto-Optical Kerr Spectroscopy of a New Chemically Ordered Alloy: Co_3Pt", *Phys. Rev. Lett.*, 71, 2493, (1993).

Hill, J.P., Feng, Q, Birgeneau, R.J., and Thurston, T.R., "Loss of Long Range Order in the 3D Random Field Ising Model", *Phys. Rev. Lett.*, 70, 3655, (1993).

Kycia, S.W., Goldman, A.I., Lograsso, T.A., Delaney, D.W., Black, D., Sutton, M., Dufresne, E., Brunig, R., and Rodricks, B., "Dynamical X-ray Diffraction From an Icosehedral Quasicrystal", *Phys. Rev.*, B48, 3544-3547, (1993).

Marks, R.F., Farrow, R.F.C., Harp, G., Parkin, S.S.P., Rabedeau, T.A., Toney, M.F., Cebollada, A., Thangaraj, N., and Krishnan, K.M., "Giant Magnetoresistance and Structure of Phase-Segregated Epitaxial Metals", Materials Research Society Symposium Proceedings, 313, 411, (1993).

McClain, B.R., Lee, D.D., Carvalho, B.L., Mochrie, S.G.J., Chen, S.H., and Litster, J.D., "X-ray Reflectivity Study of an Oil-water Interface in Equilibrium with a Middle-phase Microemulsion", *Phys. Rev. Lett.*, 72, 246, (1994).

Nuttall, W.J., Fahey, K.P., Young, M.J., Keimer, B., Birgeneau, R.J., and Suematsu, H., "A Synchrotron X-ray Diffraction Study of the Structural Phase Behaviour of Mutilayer Xenon on Single-Crystal Graphite", *J. Phys. Condens. Matter*, 5, 8159, (1993).

Nuttall, W.J., Noh, D.Y., Wells, B.O., and Birgeneau, R.J., "Synchrotron X-ray Scattering Study of the Pressure Melting of Near-monolayer Xenon on Single Crystal Graphite at 140K", *Surface Science*, **307/309**, 768, (1994).

Rabedeau, T.A., Toney, M.F., Marks, R.F., Parkin, S.S.P., Farrow, R.F.C., and Harp, G.R., "Giant Magnetoresistance and Co Cluster Structure in Phase-Separated Co-Cu Granular Alloys", *Phys. Rev.*, **B48**, 16810, (1993).

Song, S., and Muchrie, S.G.J., "Tricriticality in the Orientational Phase Diagram of Stepped Si(113) Surfaces", *Phys. Rev. Lett.*, 73, 995, (1994).

Sutton, M., "Time-Resolved X-ray Diffraction Studies of Crystallization in Metallic Glasses", *Mat. Sci. & Eng.*, A178, 265-270, (1994).

Toney, M.F., Gordon, J.G., Borges, G.L., Melroy, O.R., Yee, D., and Sorensen, L.B., "Comment on Superstructures of Pb Monolayers Electrochemically Deposited on Ag(111)", *Phys. Rev.*, **B49**, 7793, (1994).

Toney, M.F., Howard, J.N., Richer, J., Borges, G.L., Gordon, J.G., Melroy, O.R., Wiesler, D.G., Yee, D., and Sorensen, L.B., "Voltage-Dependent Distribution of Water Molecules at the Electrode-Electrolyte Interface", *Nature*, **368**, 444, (1994).

Toney, M.F., and Ocko, B.M., "Atomic Structure at Electrode Interfaces", *Synchrotron Radiation News*, **6/5**, 28, (1993) (special issue on electrochemistry).

Toney, M.F., "Studies of Electrodes by *in situ* X-ray Scattering", Synchrotron Techniques in Interfacial Electrochemistry, edited by C. Melendres and A. Tadjeddine, NATO ASI Series 432, Kluwer Academic, Dordrecht, p. 109, (1994).

Watson, G.M., Gibbs, D., Zehner, D.M., Yoon, M., and Mochrie, S.G.J., "Faceting Transformations of the Stepped Pt(001) Surface", *Phys. Rev. Lett.*, 71, 3166, (1993).

Wiesler, D.G., Toney, M.F., Melroy, O.R., McMillan, C.S., and Smyrl, W.H., "X-ray Diffraction From Anodic TiO_2 Films: *in situ* and *ex situ* Comparison of the Ti (0001) Face", *Surface Science*, **302**, 341 (1994).

Wu, L., Young, M.J., Shao, Y., Garland, C.W., Birgeneau, R.J., and Heppke, G., "Critical Behavior of the Second Harmonic in a Density Wave System", *Phys. Rev. Lett.*, 72, 376, (1994).

Xie, Y., Ludwig, Jr., K.F., Morales, G., Hare, D., and Sorensen, C., "Noncritical Behavior of Density Fluctuations in Supercooled Water", *Phys. Rev. Lett.*, 71, 2050, (1993).

Yoon, M., Mochrie, S.G.J., Zehner, D.M. Watson, G.M., and Gibbs, D., "Faceting and the Orientational Phase Diagram of Stepped Pt(001) Surfaces", *Phys. Rev. B*, 49, 16702, (1994).

Beamline X21

de Groot, F.M.F., Fontaine, A., Kao, C.-C., and Krisch M., "Charge Transfer Multiplet Calculations of the K-beta X-ray Emission Spectra of divalent Nickel Compounds", *J. Phys. Condns. Mat.*, **6**, 6875-6884, (1994).

Peng, G., de Groot, F.M.F., Hämäläinen, K., Morre, J.A., Wang, X., Grush, M.M., Hastings, J.B., Siddons, D.P., Armstring, W.H., Mullins, O.C., and Cramer, S.P., "High-Resolution Manganese X-ray Fluorescence Spectroscopy. Oxidation-State and Spin-State Sensitivity", *J. Am. Chem. Soc.*, **116**, 2914-2920, (1994).

Beamline X22B

Adzic, R.R., Wang, J., Vitus, C., and Ocko, B.M., "The Electrodeposition of *PB* Monolayer on Low Index Surfaces: An X-ray Scattering and Scanning Tunneling Microsocpy Study", *Surface Science*, **293**, L876-83, (1993).

Chen, C.H., Kepler, K.D., Gewirth, A.A., Ocko, B.M.,and Wang, J., "Electrodeposited Bismuth Monolayers on *Au*(111) Electrodes: Comparison of Surface X-ray Scattering, Scanning Tunneling Microscopy and Atomic Force Microscopy Lattice Structures" *J. Phys. Chem.*, **97**, 7290-4, (1993).

Lurio, L.B., Rabedeau, T.A., Pershan, P.S., Silvera, I.F., Deutsch, M., Kosowsky, S.C., and Ocko, B.M., "X-ray Specular-Reflectivity Study of the Liquid-vapor Density Profile of *4He*", *Phys. Rev.*, **B48**, 9644-59, (1993).

Ocko, B.M., Wu, X.Z., Sirota, E.B., Sinha, S.K., and Deutsch, M., " An X-ray Reflectivitiy Study of Thermal Capillary Waves on Liquid Surfaces", *Phys. Rev. Lett.*, 72, 242-6, (1994).

Ocko, B.M., Wang, J., and Watson, G.M., "The Structure and Electrocompression of Electrodeposited Iodine Monolayers on *Au*(111)", *J. Phys. Chem*, **98**, 897-906, (1994).

Pershan, P.S., "X-ray Scattering Studies of Liquid Surfaces", *Physica*, **A200**, 50, (1993).

Pershan, P.S., "Effects of Surface Profile and Interface Correlations on X-ray Reflectivity from Fluid Interfaces", *J. Phys. Condens. Mat.*, **6**, A37, (1994).

Pershan, P.S., "X-ray Studies of the Thickness and Roughness of Thin Adsorbed Fluid Layers", *Ber. Bunsenges, Phys. Chem.*, **98**, 372, (1994).

Polewska, W., Vitus, C.M., Ocko, B.M., and Adzic, R.R., "Direction Observation of the *Au*(100) Reconstruction During the Course of O_2 and HO_2 Reduction in Alkaline Solutions", *J. Electroanl. Chem.*, **364**, 265-9, (1994).

Wang, J., Watson, G.M., and Ocko, B.M., "Uniaxial Incommensurate Phases at the *Au*(111) Electrode", *Physica*, **A200**, 679-87, (1993).

Wang, J., Adzic, R.R., Ocko, B.M., "X-ray Scattering Study of *T1* Adlayers on the *Au*(111) Electrode in Alkaline Solutions: Metal Monolayer, OH^{-1} Coadsorption and Oxide Formation", *J. Phys. Chem.*, **7182**, 7182-90, (1993).

Wu, X.Z., Ocko, B.M., Sirota, E.B., Sinha, S.K., and Deutsch, M., "A New Surface Phase in Liquid Normal-Alkanes", *Physica*, **A200**, 751-8, (1993).

Wu, X.Z., Ocko, B.M., Sirota, E.B., Sinha, S.K., Deutsch, M., Cao, B.H., and Kim, M.W., "Surface Tension Measurements of Surface Freezing in Liquid Normal-alkanes", *Science*, **261**, 1018-21, (1993).

Beamline X22C

Abernathy, D.L., Gibbs, D., Grübel, G., Mochrie, S.G.J., Watson, G.M., Yoon, M., and Zehner, D.M., "Thermal Phase Behavior of Metal Surfaces: X-ray Scattering studies of Pt(001)". In the Proc. Of the Fourth Intl. Conf. On the Structure of Surfaces: The Structure of Surfaces IV, edited by Xide Xie, S.Y. Tong, M.A. Van Hove, World Scientific Publ., p. 157-64, (1994).

Bahr, D., Press, W., Jebasinski , R., and Manel, S., "X-ray Reflectivity and Define Scattering Study on $CoSi_2$ Layers in *Si* Produced by ion beam Synthesis", *Phys. Rev.*, **B48**, 4385, (1993).

Gaulin, B.D., Gibbs, D., Isaacs, E., Lussier, J., Keimers, J., Schroeder, A., Taillefer, L., and Zschack, P., "Resonant Magnetic X-ray Scattering Study of Phase Transitions in UPd_2Al_3", *Phys. Rev. Lett.*, **73**, 890, (1994).

Grübel, G., Huang, K., Gibbs, D., Zehner, D.M., Sandy, A.R., and Mochrie, S.G.J., "Reconstruction of the *Pt*(111) Surface: X-ray Scattering Measurements", *Phys. Rev.*, **B48**, 18117, (1994).

Grübel, G., Gibbs, D., Zehner, D.M., Abernathy, D.L., Sandy, A.R., and Mochrie, S.G., "J. Phase Behavior of *Au* and *Pt* Surfaces", *Sur. Sci.*, **287/8**, 842-6, (1993).

Helgesen, G., Gibbs, D., Baddorf, A.P., Zehner, D.M., and Mochrie, S.G.J., "X-ray reflectivity of the *Cu*(110) Surface", *Phys. Rev.*, **B48**, 15320-5, (1993).

Helgesen, G., Hill, J.P., Thurston, T.R., Gibbs, D., Kwo, J., and Hong, M., "Temperature Dependence of Resonant X-ray Magnetic Scattering in Holmium", *Phys. Rev.*, **B50**, 2990, (1994).

Hueng, K.G., Zegenhagen, J., Phillips, J.M., and Patel, J.R., "Two-dimensional Structural Modulation in Epilaxial CaF_2 Overlayers on *Si*(111)", *Phys. Rev. Lett.*, **72**, 2430, (1994).

Langridge, S., Stirling, W.G., Lander, G.H., Rebizant, J., Spirlet, J.C., Gibbs, D., and Vogt, O., "X-ray Study of the Critical Magnetic Scattering in NpAs", *Europhys. Lett.*, **25**, 137, (1994).

Sanyal, M.K., Gibbs, D., Bohr, J., and Wulff, M., "Resonance Magnetic X-ray Scattering Study of Erbium", *Phys. Rev.*, **B49**, 1079-85, (1994).

Sanyal, M.K., Sinha, S.K., Gibaud, A., Huang, K.G., Carvalho, B.L., Rafailovich, M., Sokolov, J., Zhao, X., and Zhao, W., "Fourier Reconstruction of Density Profile of Thin Films using Anomalous X-ray Reflectivity", *Euro. Phys. Lett.*, **21**, 691-4, (1993).

Thurston, T.R., Helgesen, G., Hill, J.P., Gibbs, D., Gaulin, B., and Simpson, P.J., "X-ray and Neutron Scattering Measurements of two Length Scales in the Magnetic Critical Fluctuations of Holmium", *Phys. Rev.*, **B49**, 15730-44, (1994).

Watson, G.M., Gibbs, D., Zehner, D.M., Yoon, M., and Mochrie, S.G.J., "Faceting Transformations of the Stepped *Pt*(001) Surface", *Phys. Rev. Lett.*, 71, 3166-9, (1993).

Yoon, M., Mochrie, S.G.J., Zehner, D.M., Watson, G.M., and Gibbs, D., "Faceting and the Orientational Phase Diagram of Stepped *Pt*(001) and Surfaces", *Phys. Rev.*, **B49**, 16702, (1994).

Beamline X23A2

Antonio, M.R., Xue, J.S., and Soderholm, L., "The Oxidation State of Cerium in Ce_2MoO_6", *J. Alloys and Cmpds.*, 207/208, 444 (1994).

Bunker, B.A., Wang, Z., Islam, Q., "X-ray Studies of Off-center Ions and Ferroelectricity in PbS_xTe_{1-x} and $Zn_xCd_{1-x}Te$ Alloys", *Ferroelectrics*, 150, 171 (1993).

Conway, B.E., Qu, D., and McBreen, J., "*in situ* and *ex situ* Spectroelectrochemical and X-ray Absorption Studies on Rechargeable, Chemically-modified and other MnO_2 Materials", Synchrotron Techniques in Interfacial Electrochemistry, NATO ASI Series 432, edited by C.A. Melandres and A. Tadjeddine, Kluwer Academic Publishers, Dordrecht, p. 311 (1994).

Elder, R.C., Sharpe, L.R., Igo, D.H., Rigney, R.O., and Heineman, W.R., "EXAFS Studies of Film Coated Electrodes", NATO Advanced Science Institutes Series, C: *Mathematical and Physical Sciences,* 432, 335-348, (1994).

Jentys, A., Englisch, M., Lercher, J.A., and Haller, G.L., "Effects of Adsorbed oxygen containing molecules on the XANES of Pt in supported Pt/SiO_2 catalysts", *Catalysis Letters*, 21, 30 (1993).

Jones, W.B., Elgren , T.E., Morelock, M.M., Elder, R.C., and Wilcox, D.E., "Technetium Metallothionein: A Spectroscopic and EXAFS Study of 99TCO+3 binding in Zn7-Methallothioneins", *Inorganic Chemistry*, 33, 5571-5578, (1994).

Kemner, K.M., Bunker, B.A., Luo, H., Samarth, N., Furdyna, J.K., Weidmann M.R., and Newman, K.E., "X-ray Absorption Spectroscopy Investigations of Atomic Reordering at ZnTe/CdSe Interfaces", in Statics and Dynamics of Alloy Phase Transitions, edited by P.E.A. Turchi and A. Gonis, Plenum, New York, p. 203 (1993).

Merzbacher, C.I., and McKeown, D.A., "X-ray Absorption Studies of Ge and Ga Environments in $BaO\text{-}Ga_2O_3\text{-}GeO_2$ Glasses", *Journal of Non-Crystalline Solids*, 162, 81 (1993).

Morris, Anne-Tabor, Investigations of Structural Ordering in Photo-activated Semiconductors using the Technique of XAFS, PhD Thesis, University of Notre Dame, (1994).

Mukerjee, S., Platinum and Platinum Alloy Electrocatalysts for Oxygen Electrodes in Proton Exchange Membrane FuelCells: Electrochemical and X-ray Absorption Spectroscopic Investigation, PhD Thesis, Texas A&M University, (1994).

Resasco, D.E., Durante, V.A., Kim, J., Larsen, G., and Haller, G.L., "Platinum-Nickel/L-Zeolite Bimetallic Catalysts: Effect of Sulfur Exposure on Metal Particle size and N-hexane Aromatization Activity and Selectivity", Proceed. Intern. Sym. on Zeolites and Microporous Crystals, edited by T. Hattori and T. Yashima, Kodansha Ltd., 83, 321, (1993).

Sachtler, W.M.H., and Haller, G.L., "Catalyst Characterization: Structure/Function", in Advanced Heterogeneous Catalysis for Energy Applications, Catalysis: Key to Clean, Efficient Energy, Research Needs Assessment Vol. II, Consultec Scientific, Inc., Chapter 3 (1994).

Sorensen, L.B., Cross, J.O., Newville, M., Ravel, B., Rehr, J.J., Stragier, H., Bouldin, C.E., and Woicik, J.C., "Diffraction anomalous fine structure: Unifying X-ray Diffraction and X-ray Absorption with DAFS", in Resonant Anomalous X-ray Scattering: Theory and Applications, edited by G. Materlik, C.J. Sparks, and K. Fischer, Elsevier Science B.V., 389 (1994).

Xue, J.S., Antonio, M.R., White, W.T., Soderholm, L., and Kauzlarich, S.M., "The Electronic Properties of Ce in $CeFe_4P_{12}$", *J. Alloys and Cmpds.*, 207/208, 161 (1994).

Beamline X23A3

Allen, A.J., Jemian, P.R., Black, D.R., Burdette, H.E., Spal, R.D., Krueger, S., and Long, G.G., "Ultra-small-angle X-ray Scattering to Bridge the Gap Between Visible Light Scattering and Standard Small-angle-scattering", *Nucl. Inst. & Meth.*, A347, 487-490, (1994).

Black, D.R., Robins, L., Buchan, N., and Henshall, D., "The Defect Microstructure of SiC Single Crystals", *Inst. Phys. Conf. Ser.*, 137/3, 337-340, (1993).

Schaefer, D.W., "Structure of Mesoporous Aerogels", *MRS Bulletin*, 19, 49-53, (1994).

Schaefer, D.W., Olivier, B.J., Ashley, C.S., Beaucage, G., Richter, D., Farago, B., Frick., B., and Fischer, D.A., "Structure and Topology of Silica Aerogels During Densification", *J. Non-Cryst. Sol*, 172/174, 647-655, (1994).

Spal, R.D., "The Effect of A Crystal Monochromator on the Local Angular Divergence of an X-ray Beam", *Acta Crystall.*, A50, 295-301, (1994).

Beamline X23B

Ayers, J.D., Harris, V.G., Sprague, J.A., and Elam, W.T., "On the Role of Cu and Nb in the Formation of Nanocrystals in Amorphous $Fe_{73.5}Nb_3Cu_1Si_{13.5}B_9$", *Appl. Phys. Lett.*, 64/8, 974-976, (1994).

Harris, V.G., Das, B.N., Elam, W.T., and Koon, N.C., "Amorphous-to-crystalline Transition in $Tb_{33}Fe_{66}$ Films Studied Via EXAFS:, Mat. Res. Soc. Symp. Proc., 321, 185-190, (1994).

Harris, V.G., Das, B.N, Rubinstein, M., Goldenberg, J.L., Elam, W.T., Koon, N.C., "Structural Evolution and Magnetoresistance Properties of Heat Treated $Cu_{80}Co_{15}Fe_5$ Ribbons", *IEEE Trans. On Magn.*, 29/6, 2616-2618, (1993).

Harris, V.G., Elam, W.T., and Koon, N.C., "Deposition-Temperature Dependence of Structural Anisotropy in Amorphous Tb-Fe Films", *Phys. Rev. B*, 49/5, 3637-3640, (1994).

Harris, V.G., Kaatz, F.H., Browning, V., Gillespie, D.J., Everett, R.K., Ervin, A.M., Elam, W.T., and Edelstein, A.S., "Structure and Magnetism of Heat-Treated Nanocrystalline $Cu_{80}Co_{20}$ Powders Prepared Via Chemical Means", *J. Appl. Phys.*, 75/10, 6610-6612, (1994).

Robinson, K.M., and O'Grady, W.E., "A Transmission Geometry Electrochemical Cell for *in situ* X-ray Diffraction", *Rev. Sci. Instrum.*, 64/4, 1061-1065, (1993).

Robinson K.M., and O'Grady, W.E., "*In Situ* X-ray Diffraction Studies of the Electrodeposition of Pb Monolayers on Au(100) Single Crystals", Synchrotron Techniques in Interfacial Electrochemsitry, edited by C.A. Melendres and A. Tadjeddine, Kluwer Academic Press, The Netherlands, p. 124, (1994).

Sampath, S., Neiser, R.A., Herman, H., Kirkland, J.P., and Elam, W.T., "A Structural Investigation of a Plasma Sprayed Ni-Cr Based Alloy Coating", *J. Mater. Res.*, 8/1, 78-86, (1993).

Beamline X24A

Cooper, J.W., Southworth, S.H., MacDonald, M.A., and LeBrun, T., "Cascade Effects on the Ar LMM Auger Spectrum", *Phys. Rev.*, A50, 405, (1994).

Herrera-Gomez, A., Kendelewicz, T., Woicik, J.C., Miyano., K.E., Pianetta, P., Southworth, S., Cowan, P.L., Karlin, B.A., and Spicer, W.E., "Geometrical Structure of the Bi/GaP (110) Interface: An X-ray Standing Wave Triangulation Study of a Nonideal System", *J. Vac. Sci. Technol.*, A12, 2473, (1994).

Karlin, B.A., Woicik, J.C., and Cowan, P.L., "Performance of InSb/KDP Monochromator Crystal Pair", *Nucl. Instrum. Methods*, A347, 360, (1994).

Shi, X., Su, C., Heskett, D., Berman, L., Kao, C.C., and Bedzyk, M.J., "Adsorption-Site Investigation of Rb/Cu(111) using the X-ray Standing-Wave Method", *Phys. Rev.*, B49, 14638, (1994).

Southworth, S.H., "Resonance and Threshold Effects in Polarized X-ray Emission from Atoms and Molecules", *Nucl. Instrum. Methods,* B87, 247, (1994).

Southworth, S.H., MacDonald, M.A., LeBrun, T., and Deslattes, R.D., "Electron-Ion-X-ray Spectrometer System", *Nucl. Instrum. Methods*, A347, 499, (1994).

Wang, H., Woicik, J.C., Åberg, T., Chen, M.H., Herrera-Gomez, A., Kendelewicz, T, Mäntykenttä, A., Miyano, K.E., Southworth, S., and Crasemann, B., "Threshold, K-LL Auger spectra of P in InP", *Phys. Rev.*, A50, 1359, (1994).

Beamline X24C

Hunter, W.R., and Long, J.P., "Thin-Film Interference Mirror to Suppress Grating Harmonics in Vacuum-Ultraviolet Radiation", *Appl. Opt.*, 33, 1264, (1994).

Beamline X25

Bergmann, U., Hastings, J.B., and Siddons, D.P., "Time Evolution of Incoherent Nuclear Scattering from ^{57}Fe Excited with Synchrotron Radiation", *Phys. Rev.*, B49, 1513-1516, (1994).

Bergmann, U., Shastri, S.D., Siddons, D.P., Batterman, B.W., and Hastings, J.B., "Temperature Dependence of Nuclear Forward Scattering of Synchrotron Radiation in α-^{57}Fe", *Phys. Rev.*, B50, 5957-5961, (1994).

Berman, L.E. and Hart, M., "Preserving the High Finesse of X-Ray Undulator Beams from Perfect Water-Jet-Cooled Diamond Monochromators", *Nucl. Instrum. Methods Phys. Res.*, A 334, 617-620 (1993).

Egami, T., Dmowski, W., McQueeney, R.J., Sendyka, T.R., Ishihara, S., Tachiki, M., Yamauchi, H., Tanaka, S., Hinatsu, T., and Uchida, S., "Nature of Electron-Lattice Interaction in Superconducting Oxides", *SPIE*, 2158, 27-38 (1994).

Ferré-D'Amaré, A.R., Pognonec, P., Roeder, R.G., and Burley, S.K., "Structure and Function of the b/HLH/Z Domain of USF", *EMBO J.*, 13, 180-189 (1994).

Hamalainen, K., Siddons, D.P., Berman, L.E., Kao, C.-C., and Hastings, J.B., "High Resolution Near Edge X-Ray Spectroscopy", in Resonant Anomalous X-Ray Scattering Theory and Applications, edited by G. Materlik, C.J. Sparks, and K. Fischer, Elsevier Science North-Holland, Amsterdam, pp. 485-493, (1994).

Helgesen, G., Hill, J.P., Thurston, T.R., Gibbs, D., Kwo, J., and Hong, M., "Temperature Dependence of Resonant X-Ray Magnetic Scattering in Holmium", *Phys. Rev.*, **B50**, 2990-3004, (1994).

Isaacs, E.D., Aeppli, G., Zschack, P., Cheong, S.-W., Williams, H., and Buttrey, D.J., "Diffuse X-Ray Scattering from $La_{2-x}Sr_xNiO_4$ and $La_{2-y}Sr_yCuO_4$", *Phys. Rev. Lett.*, 72, 3421-3424, (1994).

Kim, J.L., and Burley, S.K., "1.9 Å Resolution Refined Structure of TBP Recognizing the Minor Groove of TATAAAAG", *Nature Struct. Biol.*, 1, 638-653, (1994).

Lambright, D.G., Noel, J.P., Hamm, H.E., and Sigler, P.B., "Structural Determinants for Activation of the ∝-Subunit of a Heterotrimeric G Protein", *Nature,* 369, 621-628, (1994).

Lee, W.-K. and Mills, D.M. "High Heat Load X-Ray Optics Research and Development at the Advanced Photon Source -- An Overview", *Nucl. Instrum. Methods Phys. Res.,* A 347, 618-626, (1994).

Ocko, B.M. and Wang, J., "Surface Structure at the Au(111) Electrode", in Synchrotron Techniques in Interfacial Electrochemistry", NATO ASI Series Vol. 432, edited by C.A. Melendres and A. Tadjeddine, Kluwer Academic, Dordrecht, The Netherlands, pp. 127-155, (1994).

Peng, G., deGroot, F.M.F., Hamalainen, K., Moore, J.A., Wang, X., Grush, M.M., Hastings, J.B., Siddons, D.P., Armstrong, W.H., Mullins, O.C., and Cramer, S.P., "High-Resolution Manganese X-Ray Fluorescence Spectroscopy: Oxidation-State and Spin-State Sensitivity", *J. Am. Chem. Soc.* , 116, 2914-2920, (1994).

Shu, D., Collins, J.T., Barraza, J., and Kuzay, T.M., "The Advanced Photon Source X-Ray Transmitting Beam-Position-Monitor Tests at the National Synchrotron Light Source X25 Beam Line", *Nucl. Instrum. Methods Phys. Res.*, A 347, 577-580, (1994).

Song, S., and Mochrie, S.G.J., "Tricriticality in the Orientational Phase Diagram of Stepped Si(113) Surfaces", *Phys. Rev. Lett.,* 73, 995-998, (1994).

Thurston, T.R., Helgesen, G., Hill, J.P., Gibbs, D., Gaulin, B.D., and Shirane, G., "X-Ray and Neutron Scattering Studies of Magnetic Critical Fluctuations in Holmium", *Physica,* **B192**, 177-181, (1993).

Thurston, T.R., Helgesen, G., Hill, J.P., Gibbs, D., Gaulin, B.D., and Simpson, P.J., "X-Ray- and Neutron-Scattering Measurements of Two Length Scales in the Magnetic Critical Fluctuations of Holmium", *Phys. Rev.,* B49, 15730-15744 (1994).

Beamline X26A

Bajt, S., Sutton, S.R., and Flynn, G.J., "Iron Oxidation State in an Interplanetary Dust Particle and Semarkona Matrix by Micro-XANES:", *Meteoritics*, 29, 441, (1994).

Bertsch, P.M., Hunter, D.B., Sutton, S.R., Bajt, S., and Rivers, M.L., "*in situ* Chemical Speciation of Uranium in Soils and Sediments by Micro X-ray Absorption Spectroscopy", *Environ, Sci. Tech.*, 28/5, 980-984, (1994).

Carroll, M.R., Sutton, S.R., Rivers, M.L., and Woolum, D., "An Experimental Study of Krypton Diffusion and Solubility in Silicic Glasses", *Chem. Geol.*, 109, 9-28, (1994).

Cline, J.S., Vanko, D.A., Ghazi, A.M., Sutton, S.R., and Roedder, D., "Synchrotron X-ray fluorescence Analysis of Dense Brine and Lower Salinity Inclusions from the Questa Porphyry Molybdenum Deposit, Questa, New Mexico, USA", *Archiwum Mineralogiczne*, 159, 39-41, (1993).

Flynn, G.J., Sutton, S.R., Bajt, S., Klock, W., Thomas, K.L., and Keller, L., "Hydrated Interplanetary Dust Particles: Element Abundances, Mineralogies, and Possible Relationships to Anhydrous IDPs", *Lunar Planet. Sci.*, XXV, 381-2, (1994).

Flynn, G.J., "Cometary Dust: A Thermal Criterion to Identify Cometry Samples Among the Interplanetary Dust Collected from the Stratosphere", in Analysis of Interplanetary Dust, edited by M.E. Zolensky, T.L. Wilson, F.J.M. Reitmeijer, and G.J. Flynn, AIP Conference Proceedings, *American Institute of Physics*, New York, 127-144, (1994).

Flynn, G.J., "Changes to the Composition and Mineralogy of Interplanetary Dust Particles by Terrestrial Encounters", in Analysis of Interplanetary Dust, edited by M.E. Zolensky, T.L. Wilson, F.J.M. Rietmeijer, and G.J. Flynn, AIP Conference Proceedings, *American Institute of Physics*, New York, 127-144, (1994).

Flynn, G.J., Sutton, S.R., Bajt, S., Klöck, W., Thomas, K.L., and Keller, L.P., "Hydrated Interplanetary Dust Particles: Element Abundances, Mineralogies, and Possible Relationships to Anhydrous IDPs", *Lunar Planet. Sci.*, XXV, 381-382, (1994).

Flynn, G.J., Sutton, S.R., Bajt, S., Klöck, W., and Thomas, K.L, "The Trace Element Content of Semarkona Matrix: a Comparsion to Hydrated Interplanetary Dust Particles", *Meteoritics*, 29, 446, (1994).

Hanson, A.L., Bajt, S., Johnson, B.M., Meron, M., and Rivers, M.L., "Below Edge X-ray Emission Structure", *Physics Letters*, A184, 143-147, (1993).

Janssens, K.H., Langevelde, F., Adams, F.C., Vis, R.D., Sutton, S.R., Rivers, M.L., and Jones, K.W., "Comparison of Synchrotron X-ray Microanalysis with Electron and Proton Microscopy for Individual Particle Analysis", *Advances in X-ray Analysis*, 35, 1265, (1994).

Kaplan, D.I., Hunter, D.B., Bertsch, P.M., Bajt, S., and Adriano, D.C., "Application of Synchrotron X-ray Fluorescence Spectroscopy and Energy Dispersive X-ray Analysis to Identify Contaminant Metals on Goundwater Colloids", *Environ, Sci. Tech.*, 28/6, 1186-1189, (1994).

Klöck, W., Flynn, G., Sutton, S., Bajt, S., and Neuking, K., "Heating Experiments Simulating Atmospheric Entry of Micrometeorites", *Lunar Planet. Sci.*, XXV, 713-14, (1994).

Staudt, W.J., Reeder, R.J., and Schoonen, M.A.A., "Surface Structural Controls on Compositional Zoning of SO_4 and SeO_4 in Synthetic Calcite Single Crystals", *Geochimica et Cosmochimica Acta*, 58, 2087-2098, (1994).

Sutton, S.R., "Chemical Compositions of Primitive Solar System Particles, In Analysis of Interplanetary Dust", editing by M. Zolensky, T. Wilson, F. Rietmeijer, and G. Flynn, *Amer. Inst. Physics*, 145-157, (1994).

Sutton, S., Bajt, S., and Delaney, J., "Microanalysis of Iron Oxidation States using X-ray Absorption Spectroscopy", *Lunar Planet. Sci.*, XXV, 1361-2, (1994).

Thomas, K.L., Clemett, S.J., Flynn, G.J., Keller, L.P., McKay, D.A., Messenger, S., Nier, A.O., Schlutter, D.J., Sutton, S.R., Walker, R.M., and Zare, R.N., "Anatomy of a Cluster IDP (ll): Noble Gas Abundances, Trace Element Geochemistry Isotopic Abundances and Trace Organic Chemistry of Several Fragments from L2008#5", *Lunar Planet. Sci.*, XXV, 1391-2, (1994).

Török, Sz., Faigel, G., Jones, K.W., Rivers, M.L., Sutton, S.R., and Bajt, S., "Chemical Characterization of Environmental Particulate Matter using Synchrotron-Radiation", *X-ray Spectrometry*, 23, 3-6, (1994).

Vanko, D.A., Ghazi, A., Sutton, S.R., and Cline, J., "Synchrotron X-ray Fluorescence Microprobe Applied to the Analysis of fluid Inclusions (ECROFI XII- the European Current research on Fluid Inclusions, Warsaw, Poland)", *Archiwum Mineralogiczne*, 159, 230-232, (1993).

Beamline X26C

Chen, Y., Time-resolved X-ray Crystallography and Temperature Jump in Protein Crystals, PhD. Thesis, Cornell University, (1994).

Chen, Y., Srajer, V., Ng, K., LeGrand, A., and Moffat, K., "Optical Monitoring of Protein Crystals in Time-resolved X-ray Experiments", *Rev. Sci. Instrum.*, 65, 1506-1511, (1994).

Getzoff, E.D., Jones, K.W., McRee, D., Moffat, K., Ng, K., Rivers, M.L., Schildkamp, W., Singer, P.T., Spanne, P., Sweet, R.M., Teng, T.-Y., and Westbrook, E.M., "Laue Diffraction Protein Crystallography at the National Synchrotron Light Source", *Nucl. Instrum. and Methods*, B79, 249-255, (1993).

Lee, D.H., Johnson, B.M., Guardala, N.A., Price, J.L, Glass, G.A., Stumborg, M.F., and Jones, K.W., "Ne, Ar, Fe and Cu Auger-electron Production at National Synchrotron Light Source", *Nucl. Instrum. and Methods*, B79, 261, (1993).

NSLS STAFF

Ben-Zvi, I., and Qiu, Xu Z., "High Precision Beam Alignment of Electromagnet Wigglers", Electron Beam Sources of High-Brightness Radiation, SPIE Conference Proc., Vol. 2013, p. 44, (1993), BNL 49730.

Berman, L.E., "High Heat Load Crystal Optics Experiments at the NSLS X25 X-ray Wiggler Beam Line", *Nuclear Instruments and Methods in Phys. Rev.*, A347, 607-608, (1994), BNL 49555.

Blumberg, L.E., "Preliminary Report on the BNL Spallation Neutron Source Design Study", Proc. Twelfth Meeting of the Intl. Collaboration on Advanced Neutron Sources (ICANS-XII), Rutherford Appleton Laboratory, RAL 94-025, Vol. II, A-20, (1994), BNL 49274.

Bozoki, E., and Friedman, A., "Orbit Correction in Accelerators/Storage Rings Using Neural Networks", Simulation of Neural Networks with SNNS Workshop, Stuttgart, Germany, p. 41, September 1993, BNL 49229.

Bozoki, E., and Sagan, D., "On Shaking of Ions in Electron Storage Rings", *Nucl. Instrum. And Meths. In Phys. Res.*, A340, 259-271, (1994), BNL 49525.

Chapman, D., and Schulze, C., "Arterial Cross Section Measurements from Dual Energy Transvenous Coronary Angiography Images", Nuclear Science Symposium and Medical Imaging Conference, 3, 1528, (1993), BNL 60385.

Friedman, A., and Bozoki, E., "Use of Eignevectors in Understanding and Correcting Storage Ring Orbits", *Nucl. Instrum. and Meth. in Phys. Res.* A344., 269, (1994), BNL 49527.

Fisher, A., Gallardo, J., van Steenbergen, A., and Sandweiss, J., "Inverse Free Electron Laser Development", Proc. XVth Intern. Free Electron Laser Conference, The Haag, Netherlands, NIM, A341, p. 111, (1994). BNL 49609.

Fontana, J.R., Kimura, W.D., Steinhauer, L.C., Pogorelsky, I., Design Analysis for a 100 MeV Inverse Cerenkov Laser Accelerator. Proceedings of the 1993 Particle Accelerator Conference, Washington, DC, May 17-20, 1993, p. 2614, February 1994, BNL 60092.

Feng-Berman, S.K., Siddons, D.P., and Berman , L., "NSLS Beam Line Data Acquisition and Analysis Computer System", *Nuclear Instruments and Methods in Phys. Rev.*, A347, 603-606, (1994), BNL 49556

Gmur, G., Chapman, D., Thomlinson, W., Scalia, K., Malloy, K., Mangano, J., and Jacob, J. "NSLS Transvenous Coronary Angiography Project Advanced Technology Initiatives"' *Synchrotron Radiaton News*, 7/5, p. 34-36, BNL 60608.

Hastings, J.B., Bergmann, U., and Siddons, D.P., "Suppression of Charge Scattering in Mossbauer Experiments Using Synchrotron Radiation", edited by G. Materlik, C.J., Sparks, and K. Fischer, Elsevier Science, p. 619, (1994).

Hirschmugl, C., and Williams, G., "The Application of Infrared Synchrotron Radiation to the Study of Interfacial Vibrational Modes", *NATO ASI Series*, 432, 67, (1993), BNL 60419.

Hirschmugl, C., Williams, G.P., Persson, B.N.J., and Volokitin, A.I., "Adsorbate Vibrational Dynamics in the Anomalous Skin Effect Frequency Region", *Surface Science*, 31, L1141, (1994), BNL 60419.

Hirschmugl, C., Williams, G.P., Chabal, Y.J., and Hoffmann, F.M., "Low Frequency Dynamics of CO/Cu-Breakdown of Born-Oppenheimer Approximation", *J. Vac. Sci. And Technol.*, A12, 2229, (1994), BNL 49777.

Hoffmann, F.M., Persson, B.N.J., Walter, W., King, D.A., Hirschmugl, C.J., and Williams, G.P., "Anti-absorption Resonances in Infrared Reflectance Spectroscopy of Alkali-Cu(111) Adsorbate Systems - is the Ground State a Surface Charge Density Wave Condensate?", *Phys. Rev. Letts.*, 72, 1256, (1994), BNL 49775.

Hoffmann, F.M., and Williams, G.P., "Synchrotron Radiation in the Far Infrared: Infrared Reflection Absorption Spectroscopy", Application of Synchrotron Radiation, *Surface Science*, 263, (1994), BNL 48976.

Kao, C.-C., Chen, C.T., Johnson, E.D., Hastings, J.B., Lin, H.J., Ho, G.H., Meigs, G., Brot, J.-M., Hulbert, S.L., Idzerda, Y.U., and Vettier, C., "Dichroic Interference Effects in Circularly Polarized Soft-X-Ray Resonant Magnetic Scattering", *Phys. Rev.*, **B50**, 9599, (1994), BNL 60855, Sept. 1994.

Karlin, B.A., Woicik, J.C. and Cowan, P.L. "Performance of InSb/KDP Monochromator Crystal Pair", *Nucl. Instrum.and Meths.*, 347, 360-363, (1993).

Kimura, W.D. Steinhauer, L.C., Kim, G.H., Tidwell, S.C., Pogorelsky", I., and Kusche, K.P., "Update on the ATF Inverse Cerenkov Laser Acceleration Experiment", Proc. Of the 1993 Particle Accelerator Conf., Washington D.C., p. 2564, (1994), BNL 60093.

Lee, H., Colella, R., and Chapman, L.D., "Phase Determination of X-Ray Reflections in a Quasicrystal", *Acta Cryst.*, A49, 600-605 (1993), BNL 60183, March 1994.

Lee, K., Hulbert, S.L., Kuiper, P., Ji, D., Hanson, D.M., "Auger, Zero-Energy Photoelectron, Coincidence Spectroscopy (AZEPECO): Chemical-Site-Selective Auger Electron Spectroscopy", *Nucl. Instrum. And Meths.*, A347, 446, (1994), BNL 60182.

Leung, K.P., Yu, L.H. and Ben-Zvi, I., "RF Phase Stabilization for RF Photocathode Gun Through Electro-Optical Monitoring", Electron Beam Sources of High-Brightness Radiation, SPIE Conference Proc., Vol. 2013, p.147, (1993), BNL 49729.

McWhan, D.B., "Synchrotron Radiation in the Study of Magnetism", *J. of Synch. Rad.*, 1, 83-90, (1994). BNL 60459.

Murphy, J.B. and Krinsky, K., "Millimeter Wave Coherent Synchrotron Radiation in the SXLS Phase I Electron Storage Ring", *Nucl. Instrum. and Meth. in Phys. Res.*, A346, 571-577, (1994). BNL 49750.

Peng, G., DeGroot, M.F., Hamalainen, K., Moore, J.A., Wang, X., Grush, M.M., Hastings, J.B., Siddons, D.P., Armstrong, W.H., Mullins, O.C., Cramer, S.P., "High-Resolution Manganese Xray Fluorescence Spectroscopy Oxidation-State and Spin-State Sensitivity", *J. Am. Chem. Soc.* 116/7, 2914-2920 (1994), BNL 60891.

Pogorelsky, I., Fischer, J., Fisher, A.S., Srinivasan-Rao, T, Kurnit, N.A., Bigio, I.J., Harrison, R.F., Shimada, T., Kusche, K., and Babzien, M., "10-GW CO_2 Laser System at the Brookhaven Accelerator Test Facility", Proc. Of Internationl Conference, Lasers 1993, p. 647, (1994), BNL 60088.

Reffner, J., Carr, G.L., Williams, G.P., Sutton, S., and Hemley, R.J., "Infrared Microspectroscopy at the National Synchrotron Light Source, Brookhaven National Lab", *Synch. Rad. News*, 7/2, pp. 30-37, BNL 60179, March 1994.

Rubenstein, E., Brown, G.S., Chapman, D., Garrett, R.F., Giacomomini, J.C., Gmur, N., Gordon, H.J., Lavender, W.M., Morrison, J., Thomlinson, W., Thompson, A.C., and Zeman, H. "Synchrotron Radiation Coronary Angiography in Humans", Synchrotron Radiation in the Biosciences, edited by B. Chance, J. Deisenhofer, S. Ebashi, D.T. Goodhead, J.R. Helliwell, H.E. Huxley, T. Iizuka, J. Kirz, T. Mitsui, E. Rubenstein, N. Sakabe, T. Sasaki, G. Schmahl, H.B. Stuhrmann, K. Wuthrich, and G. Zaccai, Oxford University Press, New York, Chapter 8.1, pp. 639-645, (1994), BNL 60609.

Shek, M.L., Miyano, K.E., Dong, Q.-Y., Callcott, T.A., and Ederer, D.L., "Preliminary Soft X-ray Studies of Beta SiC", *J. Vac. Sci. Technol.*, A12, 1079, (1994), BNL 60381.

Shi, X., Su, C., Heskett, D., Berman, L., Kao, C.-C., and Bedzyk, M.J., "Adsorption-Site Investigation of Rb/Cu(111) Using the X-rayStanding-Wave Method", *Phys. Rev. B*, 49(2), 638-642, (1994), BNL 60864.

Shleifer, M., Sharma, S., Woodle, M., Rotela, E., and Brite, C., "Design of a High-Precision Double Crystal Tunable Monochromator", *SPIE*, 1997, 361, (1993), BNL 49661.

Shleifer, M., Dilmanian, F.A., Staicu, F.A., and Woodle, M., "Mechanical Design of a High-Resolution Tunable Crystal Monochromator for the Multiple Energy Computed Tomography Project", *Synch. Rad. Instrum.*, 356, (1993), BNL 49519.

Shulze, C., Suortti, P., and Chapman, D., "Test of a Bent Laue Double Crystal Fixed Exit Monochromator", *Synch. Rad. News*, 7, 3, May 1994. BNL 60418.

Siddons, D.P., Johnson, E.D., and Guckel, H., "Precision Machine Using Hard X-Rays", *Synch. Rad. News*, 7/2, 16-18, (1994), BNL 60178.

Smith, N.V., Hulbert, S.L., Johnson, P.D., and Erskine, J.L., "Spherical-Grating Monochromator System with Circular-Polarization Capability for the U5U Undulator at Brookhaven", *Nucl. Instrum. Methods in Phys. Res.*, A347, 119, (1994), BNL 60858.

Thomlinson, W., "Medical Applications of Synchrotron Radiation at the National Synchrotron Light Source", Synchrotron Radiation in the Biosciences, edited by B. Chance, J. Deisenhofer, S. Ebashi, D.T. Goodhead, J.R. Helliwell, H.E. Huxley, T. Iizuka, J. Kirz, T. Mitsui, E. Rubenstein, N. Sakabe, T. Sasaki, G. Schmahl, H.B. Stuhrmann, K. Wuthrich, and G. Zaccai, Oxford University Press, New York, pp. 674-680, (1994), BNL 60609.

Thompson, A.C., Lavender, W.M., Rosso, V., Shulze, C., Chapman, D., Thomlinson, W., Rubenstein, E., and Giacomini, J.C., "A 1200 Element Detector System for Synchrotron-Based Coronary Angiography", *Nucl. Instr. And Meth. In Phys. Rev.*, A347, 545-552, (1994), BNL 60383.

Yu, L.H., Johnson, E., Li, D., and Umstadter, D., "Femtosecond Free-Electron Laser by Chirped Pulse Amplification" *Phys. Rev. A,* 49, 4480, (1994), BNL 60031.

Murphy, J.B. and Krinsky, K., "Millimeter Wave Coherent Synchrotron Radiation in the SXLS Phase I Electron Storage Ring", *Nucl. Instrum. and Meth. in Phys. Res.*, A346, 571-577, (1994). BNL 49750.

Peng, G., DeGroot, M.F., Hamalainen, K., Moore, J.A., Wang, X., Grush, M.M., Hastings, J.B., Siddons, D.P., Armstrong, W.H., Mullins, O.C., Cramer, S.P., "High-Resolution Manganese Xray Fluorescence Spectroscopy Oxidation-State and Spin-State Sensitivity", *J. Am. Chem. Soc.* 116/7, 2914-2920 (1994), BNL 60891.

Pogorelsky, I., Fischer, J., Fisher, A.S., Srinivasan-Rao, T, Kurnit, N.A., Bigio, I.J., Harrison, R.F., Shimada, T., Kusche, K., and Babzien, M., "10-GW CO_2 Laser System at the Brookhaven Accelerator Test Facility", Proc. Of Internationl Conference, Lasers 1993, p. 647, (1994), BNL 60088.

Reffner, J., Carr, G.L., Williams, G.P., Sutton, S., and Hemley, R.J., "Infrared Microspectroscopy at the National Synchrotron Light Source, Brookhaven National Lab", *Synch. Rad. News*, 7/2, pp. 30-37, BNL 60179, March 1994.

Rubenstein, E., Brown, G.S., Chapman, D., Garrett, R.F., Giacomomini, J.C., Gmur, N., Gordon, H.J., Lavender, W.M., Morrison, J., Thomlinson, W., Thompson, A.C., and Zeman, H. "Synchrotron Radiation Coronary Angiography in Humans", Synchrotron Radiation in the Biosciences, edited by B. Chance, J. Deisenhofer, S. Ebashi, D.T. Goodhead, J.R. Helliwell, H.E. Huxley, T. Iizuka, J. Kirz, T. Mitsui, E. Rubenstein, N. Sakabe, T. Sasaki, G. Schmahl, H.B. Stuhrmann, K. Wuthrich, and G. Zaccai, Oxford University Press, New York, Chapter 8.1, pp. 639-645, (1994), BNL 60609.

Shek, M.L., Miyano, K.E., Dong, Q.-Y., Callcott, T.A., and Ederer, D.L., "Preliminary Soft X-ray Studies of Beta SiC", *J. Vac. Sci. Technol.*, A12, 1079, (1994), BNL 60381.

Shi, X., Su, C., Heskett, D., Berman, L., Kao, C.-C., and Bedzyk, M.J., "Adsorption-Site Investigation of Rb/Cu(111) Using the X-rayStanding-Wave Method", *Phys. Rev. B*, 49(2), 638-642, (1994), BNL 60864.

Shleifer, M., Sharma, S., Woodle, M., Rotela, E., and Brite, C., "Design of a High-Precision Double Crystal Tunable Monochromator", *SPIE*, 1997, 361, (1993), BNL 49661.

Shleifer, M., Dilmanian, F.A., Staicu, F.A., and Woodle, M., "Mechanical Design of a High-Resolution Tunable Crystal Monochromator for the Multiple Energy Computed Tomography Project", *Synch. Rad. Instrum.*, 356, (1993), BNL 49519.

Shulze, C., Suortti, P., and Chapman, D., "Test of a Bent Laue Double Crystal Fixed Exit Monochromator", *Synch. Rad. News*, 7, 3, May 1994. BNL 60418.

Siddons, D.P., Johnson, E.D., and Guckel, H., "Precision Machine Using Hard X-Rays", *Synch. Rad. News*, 7/2, 16-18, (1994), BNL 60178.

Smith, N.V., Hulbert, S.L., Johnson, P.D., and Erskine, J.L., "Spherical-Grating Monochromator System with Circular-Polarization Capability for the U5U Undulator at Brookhaven", *Nucl. Instrum. Methods in Phys. Res.*, A347, 119, (1994), BNL 60858.

Thomlinson, W., "Medical Applications of Synchrotron Radiation at the National Synchrotron Light Source", Synchrotron Radiation in the Biosciences, edited by B. Chance, J. Deisenhofer, S. Ebashi, D.T. Goodhead, J.R. Helliwell, H.E. Huxley, T. Iizuka, J. Kirz, T. Mitsui, E. Rubenstein, N. Sakabe, T. Sasaki, G. Schmahl, H.B. Stuhrmann, K. Wuthrich, and G. Zaccai, Oxford University Press, New York, pp. 674-680, (1994), BNL 60609.

Thompson, A.C., Lavender, W.M., Rosso, V., Shulze, C., Chapman, D., Thomlinson, W., Rubenstein, E., and Giacomini, J.C., "A 1200 Element Detector System for Synchrotron-Based Coronary Angiography", *Nucl. Instr. And Meth. In Phys. Rev.*, A347, 545-552, (1994), BNL 60383.

Yu, L.H., Johnson, E., Li, D., and Umstadter, D., "Femtosecond Free-Electron Laser by Chirped Pulse Amplification" *Phys. Rev. A,* 49, 4480, (1994), BNL 60031.

BNL Formal and Informal Reports

Ben-Zvi, I., and Winick, H., "Towards Short Wavelength FELs Workshop", BNL 49651, October 1993.

Blum, E.B., "Storage Ring Based Inverse Compton Scattering Angiography Source", BNL 49587, October 1993.

Blum, E.B., "X-324: An Upgrade to the NSLS X-ray Ring Using B Factory Technology", BNL 49795, December 1993.

Blumberg, L.N., "Analysis of Magnetic Measurement Data by Least Squares Fit to Series Expansion Solution of 3-D Laplace Equation", BNL 60741, August 1994.

Blumberg, L.N., "H- Injection Simulation for a 5 MW Spallation Neutron Source", BNL 60071, February 1994.

Blumberg, L.N., "Ring Energy and Current Considerations for Spallation Neutron Source", BNL 60440, May 1994.

Fewell, N., "Maintenance Management Program National Synchrotron Facility Manual", BNL 49735, December 1993.

Gmur, N., "Studies of Magnetism at the National Synchrotron Light Source", BNL 60374, May 1994.

Johnson, E.D., "Concepts for UV-FEL Optics", BNL 49776, December 1993.

Foyt W. (edited by), "Conceptual Design Report for a Phase III Upgrade of the National Synchrotron Light Source", BNL 60158, March 1994.

Krinsky S. (edited by), "The Brookhaven National Laboratory DUV Free Electron Laser - A Fourth Generation Source in the Vacuum Ultra-Violet: Conceptual Design Report", BNL 49713, November 1993.

Hulbert, S.L., Lazarz, N.M., and Rothman E.Z., "National Synchrotron Light Source Activity Report 1993", BNL 52415, April 1994.

Reffner, J.A., and Williams, G.P., "First Workshop on Applications of Synchrotron Radiation to Infrared Microspectroscopy", BNL 60293, February 1994.

Stoner, R.E., "Radiation From Relativistic Electron Beams in Periodic Structures", BNL 60740, August 1994.

vanSteenbergen, A., "5 MW Pulsed Spallation Neutron Source Preconceptual Design Study, BNL Interdepartmental Study", BNL 60678, June 1994.